NUREG/CP-0131
ORNL/TM-12413
RF

Proceedings of the Joint IAEA/CSNI Specialists' Meeting on Fracture Mechanics Verification by Large-Scale Testing

Held at
Pollard Auditorium
Oak Ridge, Tennessee

Manuscript Completed: September 1993
Date Published: October 1993

Compiled by:
C. E. Pugh, B. R. Bass, J. A. Keeney

Oak Ridge National Laboratory
Managed by Martin Marietta Energy Systems, Inc.

Oak Ridge National Laboratory
Oak Ridge, TN 37831-8063

Prepared for
Division of Engineering
Office of Nuclear Regulatory Research
U.S. Nuclear Regulatory Commission
Washington, DC 20555-0001
NRC FIN B5703
Under Contract No. DE-AC05-84OR21400

ABSTRACT

This report contains 40 papers that were presented at the Joint IAEA/CSNI Specialists' Meeting-Fracture Mechanics Verification by Large-Scale Testing held at the Pollard Auditorium, Oak Ridge, Tennessee, during the week of October 26-29, 1992. The papers are printed in the order of their presentation in each session and describe recent large-scale fracture (brittle and/or ductile) experiments, analyses of these experiments, and comparisons between predictions and experimental results. The goal of the meeting was to allow international experts to examine the fracture behavior of various materials and structures under conditions relevant to nuclear reactor components and operating environments. The emphasis was on the ability of various fracture models and analysis methods to predict the wide range of experimental data now available. The international nature of the meeting is illustrated by the fact that papers were presented by researchers from CSFR, Finland, France, Germany, Japan, Russia, U.S.A., and the U.K. There were experts present from several other countries who participated in discussing the results presented. The titles for some of the final papers and the names of the authors have been updated in this report and may differ slightly from those that appeared in the final program of the meeting.

FOREWORD

This report provides the proceedings of a Specialists' Meeting on Fracture Mechanics Verification by Large-Scale Testing that was held in Oak Ridge, Tennessee, on October 23-25, 1992. The meeting was jointly sponsored by the International Atomic Energy Agency (IAEA) and the Nuclear Energy Agency (NEA) of the Organization for Economic Cooperation and Development. In particular, the International Working Group (IWG) on Life Management of Nuclear Power Plants (LMNPP) was the IAEA sponsor, and the Principal Working Group 3 (PWG-3) (Primary System Component Integrity) of the Committee for the Safety of Nuclear Installations (CSNI) was the NEA's sponsor. The IWG/LMNPP is chaired by L. M. Davies of the U.K., and L. Ianko is its Scientific Secretary. K. Torronen is chairman of the CSNI PWG-3 and J. Strosnider served (at the time of the meeting) as its Scientific Secretary.

This meeting was preceded by two prior international activities that were designed to examine the state-of-the-art in fracture analysis capabilities and emphasized applications to the safety evaluation of nuclear power facilities. The first of those two activities was an IAEA Specialists' Meeting on Fracture Mechanics Verification by Large-Scale Testing that was held at the Staatliche Materialprufungsanstalt (MPA) in Stuttgart, Germany, on May 25-27, 1988; the proceedings of that meeting were published 1991.[1] The second activity was the CSNI/PWG-3's Fracture Assessment Group's Project FALSIRE (Fracture Analyses of Large-Scale International Reference Experiments). The proceedings of the FALSIRE workshop that was held in Boston, Massachusetts, U.S.A., on May 8-10, 1990, was recently published by the Oak Ridge National Laboratory (ORNL).[2]

Those previous activities identified capabilities and shortcomings of various fracture analysis methods based on analyses of six available large-scale experiments. Different modes of fracture behavior, which ranged from brittle to ductile, were considered. In addition, geometry, size, constraint and multiaxial effects were considered. While generally good predictive capabilities were demonstrated for brittle fracture, issues were identified relative to predicting fracture behavior at higher temperatures.

The meeting in Oak Ridge was designed to allow leading specialists to share and review recent large-scale fracture experiments and to discuss them relative to verification of fracture mechanics methods. The objective was to assess the ability of analytical methods that may currently be used to model the fracture behavior of nuclear reactor components and structures. The meeting was organized into six technical sessions.

Session I.	CSNI Project FALSIRE - Current Results
Session II.	Large-Scale Experiments and Applications
Session III.	Assessments of Fracture Mechanics Analysis Methods
Session IV.	Large-Scale Plate Experiments and Analyses
Session V.	Fracture Modeling and Transferability
Session VI.	Large-Scale Piping Experiments and Analyses

[1] K. Kussmaul (Editor), *Fracture Mechanics Verification by Large-Scale Testing, Proceedings of IAEA Specialists' Meeting Held at the Staatliche Materialprufungsanstalt, University of Stuttgart, FRG*, May 1988, Mechanical Engineering Publications Limited, London, 1991.

[2] B. R. Bass, C. E. Pugh, J. Keeney-Walker, H. Schulz, and J. Sievers, CSNI Project for Fracture Analyses of Large-Scale International Reference Experiments (Project FALSIRE), NUREG/CR-5997 (ORNL/TM-12307) Martin Marietta Energy Systems, Inc., Oak Ridge National Laboratory and Gesellschaft fur Anlagen-und Reaktorsicherheit, June 1993.

This report records all the papers presented at this meeting along with two others whose authors could not be present. While the report does not include session dividers, the table of contents shows the grouping of papers by session. The final chapter of this report provides summaries that rapporteurs prepared on the day the papers were presented.

The organizing committee for the meeting included C. E. Pugh (Chairman), ORNL (U.S.A.), C. Z. Serpan, U.S. Nuclear Regulatory Commission (U.S.A.), L. M. Davies, Consultant (U.K.), K. Torronen, Technical Research Center of Finland (VTT) (Finland), B. R. Bass, ORNL (U.S.A.), L. Ianko, IAEA Headquarters, Vienna, and J. Strosnider, NEA Headquarters, Paris.

The organizing committee expresses appreciation to each of the contributing authors and their employers for making the meeting a great technical success. Thanks are also given to the U.S. Nuclear Regulatory Commission and the Oak Ridge National Laboratory for providing funding support and the staff to arrange and conduct the meeting. A special acknowledgment is given to S. J . Ranney and M. J. Woods of ORNL; their extraordinary efforts to arrange the details of the meeting and to process the technical papers into a comprehensive volume had a very positive impact on the success of the meeting.

LIST OF ATTENDEES FOR THE IAEA/CSNI SPECIALISTS' MEETING ON FRACTURE MECHANICS VERIFICATION BY LARGE-SCALE TESTING

AUSTRIA
L. Ianko
International Atomic Energy Agency
Wagramerstrassee 5
P.O. Box 100
A-1400 Vienna

BELGUIM
A. Fabry
SVK-CEN
200 Boeretang
2400 MOL

E. van Walle
SVK- CEN
200 Boeretang
2400 MOL

CANADA
B. Jarman
Atomic Energy Control Board
P.O. Box 1046, Station B
Ottawa, Ontario K1P 5S9

M. Kozluk
Ontario Hydro
Mail Stop H14
700 University Avenue
Toronto, Ontario M5G 1X6

B. Mukherjee
Ontario Hydro Research
800 Kipling Avenue-KR185
Toronto, Ontario M8Z 5S4

J. Pereira
Atomic Energy Control Board
P.O. Box 1046, Station B
Ottawa, Ontario K1P 5S9

CSFR
M. Brumovsky
Head, Reactor Integrity Division
Nuclear Machinery Plant
ŠKODA
31600 Plzeň

J. Joch
Head, Dept. of Integrity
Nuclear Research Institute
250 68 Rez

FINLAND
H. Keinänen
VTT of Finland
Metals Laboratory
Metallimiehenkuja 10
02150 ESP00

K. Wallin
VTT of Finland
Metals Laboratory
Kemistintie 3
02150 ESP00

FRANCE
M. Bethmont
Electricite de France
DER/Dpt. EMA
Route de Sens
77250 Ecuelles

S. Bhandari
Framatome
BAL 758A
Tour Fiat, Cedex 16
92084 Paris-La Defense

J. Brochard
C.E.A.
DMT/SEMT/LAMS
Centre D'Etudes De Seclay
91191 GIF-SUR-YVETTE

C. Faidy
EDF-Septent
12/14 Avenue Dutrievoz
69628 Villeurbanne Cedex

P. Gilles
Framatome
Tour Fiat, Cedex 16
92084 Paris La Defense

D. Miannay
C.E.A.-IPSN
DES/SAMS
Centre D'Etudes De Fontenay aux Roses
BP6 F92265 Fontenay aux Roses Cedex

D. Moulin
C.E.A.
DMT/SEMT/RDMS
Centre D'Etudes De Seclay
91191 GIF-SUR-YVETTE

G. Rousselier
Electricite de France
Direction des Etudes et Recherches
Les Renardieres-Dept. MTC
B.P. No 1-Route de Sens
F-77250 Moret-sur-Loing

GERMANY
H. Kordisch
Fraunhofer Institut für Wekstoffmechanik
Wohlerstrasse 11
D-7800 Freiburg

K. Kussmaul
MPA Stuttgart
Pfaffenwaldring 32
W-7000 Stuttgart 80

H. Schulz
Gesellchaft für Anlagen und Reaktorsicherheit
Schwertnergasse 1
D-5000 Köln 1

J. Sievers
Gesellchaft für Anlagen und Reaktorsicherheit
Schwertnergasse 1
D-5000 Köln 1

L. Stumpfrock
MPA Stuttgart
Pfaffenwaldring 32
W-7000 Stuttgart 80

HUNGARY
A. Fehévári
Research Institute for Ferrous Metals
1509 Budapest 119
P.O. Box 14

ITALY
A. Pini
ENEA-DISP
Rome, Italy
(On assignment at:
GE Nuclear Energy
175 Curtner Avenue M/C 781
San Jose, CA 95125)

JAPAN
Y. Igarashi
Hitachi, Ltd.
1-1, Saiwai-Cho3-Chome
Hitachi-Shi
Ibaraki-Ken, 317

K. Kashima
CRIEPI
11-1 Iwato Kita
2-Chome, Komae-Shi
Tokyo 201

N. Nakajima
Japan Atomic Energy Research Institute
Reactor Component Reliability Research Lab.
Dept. of Reactor Safety Research
Jaeri, Tokai-Mura, Naka-Gun
Ibaragi-Ken 319-11

Y. Urabe
Mitsubishi Heavy Industries
Takasago R&D Center
2-1-1, Shinhama, Arai-Cho
Takasago City, Hyogo Pref., 676

G. Yagawa
Dept. of Nuclear Engineering
University of Tokyo
7-3-1, Hongo, Bunkyo-ku
Tokyo 113

REPUBLIC OF KOREA
Y. Kim
Korea Inst. of Nuclear Safety
P.O. Box 16
Daeduk-Danji, Taejeon

J. Lee
Mgr, Reactor Systems Dept.
Korea Inst. of Nuclear Safety
P.O. Box 16
Daeduk-Danji, Taejeon

SWEDEN
B. Brickstad
The Swedish Plant Inspectorate
Box 49306
S-100 28 Stockholm

SWITZERLAND
S. Brosi
Paul Scherrer Institut
Abteilung 49
CH-5232 Villigen PSI

UNITED KINGDOM
J. Darlaston
Nuclear Electric plc
Berkeley Technology
Berkeley, GLOS GL13 9PB

L. Davies
Consultant
176 Cumnor Hill
Oxford, OX 29PJ

D. Lidbury
AEA Technology
Reactor Services
Risley, Warrington
Chesire WA3 GAT

A. Miller
UK Nuclear Installations Inspectorate
St. Peter's House
Balliol Road, Bootle
Merseyside, AB-L20 3LZ

E. Morland
AEA Technology
Reactor Services
Risley, Warrington
Chesire WA3 GAT

D. Wright
AEA Technology
Reactor Services
Risley, Warrington
Chesire WA3 GAT

UNITED STATES OF AMERICA
D. Ayres
ABB Combustion Eng. Nuclear Services
Dept 9393-404
1000 Prospect Hill Road
Windsor, CT 06095

B. Bass
Oak Ridge National Laboratory
P.O. Box 2009, MS-8056
Oak Ridge, TN 37831

J. Bloom
Babcock & Wilcox
1562 Beeson St.
Alliance, OH 44601

R. Cheverton
Oak Ridge National Laboratory
P.O. Box 2009, MS-8056
Oak Ridge, TN 37831

J. Clinard
Oak Ridge National Laboratory
P.O. Box 2009, MS-8051
Oak Ridge, TN 37831

J. Corum
Oak Ridge National Laboratory
P.O. Box 2009, MS-8051
Oak Ridge, TN 37831

W. Corwin
Oak Ridge National Laboratory
P.O. Box 2008, MS-6151
Oak Ridge, TN 37831

H. Couque
Southwest Research Institute
6220 Culebra Rd.
San Antonio, TX 78238

R. Dexter
Lehigh University
117 ATLSS Drive Room B159
Bethlehem, PA 18015-4729

R. Dodds
University of Illinois
3140 Newmark Lab
205 N. Mathews
Urbana, IL 61801

E. Hackett
US Nuclear Regulatory Commission
Office of Nuclear Regulatory Research
Mail Stop NLS217C
Washington, DC 20555

A. Hiser
US Nuclear Regulatory Commission
Office of Nuclear Regulatory Research
Mail Stop NLS217C
Washington, DC 20555

S. Iskander
Oak Ridge National Laboratory
P.O. Box 2008, MS-6151
Oak Ridge, TN 37831

J. Keeney
Oak Ridge National Laboratory
P.O. Box 2009, MS-8056
Oak Ridge, TN 37831

J. Landes
Dept. of Engineering
Science and Mechanics
Perkins Hall
University of Tennessee
Knoxville, TN 37966-2030

S. Malik
US Nuclear Regulatory
Commission
Office of Nuclear Regulatory
Research
Mail Stop NLS217C
Washington, DC 20555

M. Mayfield
US Nuclear Regulatory
Commission
Office of Nuclear Regulatory
Research
Mail Stop NLS217C
Washington, DC 20555

D. McCabe
Oak Ridge National Laboratory
P.O. Box 2008, MS-6151
Oak Ridge, TN 37831

J. Merkle
Oak Ridge National Laboratory
P.O. Box 2009, MS-8049
Oak Ridge, TN 37831

R. Nanstad
Oak Ridge National Laboratory
P.O. Box 2008, MS-6151
Oak Ridge, TN 37831

R. Olson
Battelle Memorial Institute
505 King Avenue
Columbus, OH 43201-2693

W. Pennell
Oak Ridge National
Laboratory
P.O. Box 2009, MS-8056
Oak Ridge, TN 37831

A. Poole
Oak Ridge National
Laboratory
P.O. Box 2009, MS-8051
Oak Ridge, TN 37831

C. Pugh
Oak Ridge National Laboratory
P.O. Box 2009, MS-8063
Oak Ridge, TN 37831

C. Schwartz
University of Maryland
Department of Civil Eng.
College Park, MD 20742

C. Shih
Brown University
Division of Eng., Box D
Providence, RI 02912

D. Shum
Oak Ridge National Laboratory
P.O. Box 2009, MS-8056
Oak Ridge, TN 37831

J. Strosnider
US Nuclear Regulatory
Commission
Office of Nuclear Reactor
Regulation
OWFN 7D26
Washington, DC 20555

S. Swamy
Westinghouse Electric Corp.
P.O. Box 355
Pittsburgh, PA 15230-0355

T. Theiss
Oak Ridge National Laboratory
P.O. Box 2009, MS-8056
Oak Ridge, TN 37831

K. Wichman
US Nuclear Regulatory
Commission
Office of Nuclear Reactor
Regulation
Mail Stop OWFN 7D4
Washington, DC 20555

G. Wilkowski
Battelle Memorial Institute
505 King Avenue
Columbus, OH 43201-2693

K. Yoon
B & W Nuclear Service Co.
3315 Old Forest Road
P.O. Box 10935
Lynchburg, VA 24506-0935

A. Zahoor
Zenith Corp.
7700 Goodfellow Way
Rockville, MD 20855-2259

PROCEEDINGS OF THE JOINT IAEA/CSNI SPECIALISTS' MEETING – FRACTURE MECHANICS VERIFICATION BY LARGE-SCALE TESTING

October 26–29, 1992

TABLE OF CONTENTS

Large-Scale Experiments and Applications
Chairmen: M. Davies and C. Pugh

Assessments of Fracture Mechanics Analysis Methods
Chairmen: G. Yagawa and J. Landes

Large-Scale Plate Experiments and Analyses
Chairmen: D. Miannay and A. Hiser

Fracture Modeling and Transferability
Chairmen: K. Kussmaul and W. Pennell

Opening Address

IAEA/CSNI Specialists' Meeting on

"Fracture Mechanics Verification by Large-Scale Testing"

Oak Ridge, Tennessee, USA, 26 - 29 October 1992

L. Ianko
Scientific Secretary, IWG-LMNPP
Division of Nuclear Power
International Atomic Energy Agency
Vienna

On behalf of the International Atomic Energy Agency, I would like to welcome you to this Specialists' Meeting jointly sponsored by the OECD/NEA and the IAEA.

We are meeting at a time of profound political and social changes in the world. Recent developments internationally portend the beginning of a new era of greater openness and growing public engagement in environmental matters and energy policy. This opening up of the energy decision making process offers unprecedented opportunities to rebuild public confidence in nuclear power as safe, well regulated and beneficial to human health and the environmental well-being of present and succeeding generations. This is a challenge which the nuclear community must - and can - meet.

Let me first express the Agency's gratitude to the Government of the USA for hosting this meeting, and for providing the opportunity to participants from all over the world to exchange information and experience. I would also like to state my appreciation to the OECD/CSNI for its traditional co-operation with the IAEA which has been demonstrated in the organization of this meeting.

The task you have before you this week - to enhance understanding of nuclear power plants ageing and lifemanagement - is both important and timely.

In order to continue and further develop the nuclear power utilization, it is essential to ensure safe and reliable operation of existing plants and at the same time lay foundations for excellent safety, reliability and economy of plants of the future. In view of the long lead times siting problems and the high costs in bringing new plants into service, securing the continued operation of existing plants after taking care of their age related degradation and obsolescence may be very important for meeting electrical power demands.

All components of nuclear power plants are subject to some form of ageing degradation; however, the rates of degradation and therefore component lifetimes vary considerably. Component deterioration due to ageing may significantly prejudice plant reliability and capacity factors unless failures are anticipated and prevented by timely maintenance, repair or replacement of components. If a life management programme is not

implemented to preserve ongoing reliability, then component failures may develop, which may impair one or more of the multiple levels of protection, provided by the defence in depth concept, as well as resulting in unavailability. This could result in a reduction in component safety margins, below the limits provided, and thus to the impairment of safety systems. On the other hand many components operate at a significant margin below design limit criteria, which are themselves significantly below safety limits. The ageing phenomena must be closely monitored if high performance in terms of reliability and availability, accompanied with low operating and maintenance costs, are to be achieved. It has to be ensured that the continued operation of, particularly, older plants does not pose an undue risk to public health and safety owing to obsolescence of equipment or in the safety standards and requirements to which they were built.

There is a common requirement for information in many areas, such as methods of economic assessment, and the data necessary to predict time-dependent degradation. Some problems, such as the ageing of pressure boundary components, have been studied for several decades. The difficulties in studying the subject are aggravated by the inability to realistically simulate the ageing environment in the laboratory. In addition, the process of ageing is slow in comparison to the time span in which, one would desire to observe and obtain data. Above mentioned realities have been taken into account for preparation of future IAEA programme in this area.

The Agency's Nuclear Power Programme in the field of Plant Life Management promotes technical information exchange between Member States with major development programmes, offers assistance to Member States with an interest in exploratory or research programmes, and publishes reports available to all Member States interested in the current status of devlopment. For countries with nuclear programmes, Agency activities are co-ordinated by the standing committee called the International Working Group.

In conclusion, it should be stressed that NPP life management is clearly a very important area of concern recognized by the IAEA and its Member States.

The main objective of this meeting is to provide a forum for exchange of information among the participating experts from Member States through their interactions both at this meeting and later through the publication of the proceedings which will reach a much wider audience. I believe that the information exchange in the coming days will make an important contribution to reaching our common goal of achieving a high level of nuclear performance and safety. The results of this meeting should help to clarify the main issues for future work, both for you and for us in the IAEA. I also hope that you will find some time to enjoy this beautiful country and learn from its rich culture.

Overview of the CSNI Project FALSIRE

by

H. Schulz

Gesellschaft für Anlagen- und Reaktorsicherheit (GRS)mbH,
Schwertnergasse 1, D-5000 Köln 1, FRG

Table of content

1 Objective of the CSNI fracture assessment group

For the safety assessment of primary circuit components the predictive capability of fracture mechanics methods play an important role. Within the scientific community active collaboration is going on in various fields of fracture mechanics. On behalf of the Principal Working Group No. 3 of CSNI the Fracture Assessment Group (FAG) has been given the task to review the capabilities of present fracture assessment methods in view of their application to nuclear pressure vessels. The different subtasks chosen to perform the work are shown in Table 1.

2 Project FALSIRE [1)]

To meet the outlined objectives the CSNI/FAG planned an international project to assess various fracture methodologies through interpretative analysis of selected large-scale fracture experiments. The selected large-scale experiments are all experiments which are directed to the structural response to combine mechanical and thermal loadings. These combined loading conditions - many times being refered to in the expression " thermal shock" or " pressurized thermal shock" - may arise in nuclear reactor pressure vessels as a consequence of the safety systems designed to cope with loss of coolant accidents. Furthermore these combined loading conditions may also occur in different components as a consequence of the application of accident management procedures. The relevance to nuclear safety was the main reason to select these experiments to evaluate present fracture prediction capabilities in these cases. Choosing this as a main topic of a round robin analysis the FAG took advantage that there was strong interest at the time into this topic and the number of experiments where not too large. It was also the intention to avoid any duplication of effort in the fracture mechanics area going on in different other international groups.

The CSNI/FAG established a common format for comprehensive statements of related experiments, including supporting information and available analysis results. The format of the common statements has been proven to be very helpfull in organizing such work, it is summarized in Appendix 1. Based on the information available the CSNI/FAG selected reference experiments for detailed analysis and interpretation, these are summarized in Table 2. Organizations which participated in the project FALSIRE are given in Table 3. The experiments utilized in Project FALSIRE were designed to examine various aspects of crack growth in RPV steels under pressurized-thermal-shock (PTS) loading conditions. These conditions were achieved in three of the experiments by internally pressurizing a heated vessel containing a sharp crack and thermally shocking it with a coolant on the inner (NKS-3 and 4) or outer (PTSE-2) surface. In the series of spinning cylinder experiments, a thick cylinder with a deep crack on the inner surface was thermally shocked with a water spray while simultaneously spinning the cylinder about its axis in a specially-constructed rig. The Japanese Step B test utilized a large surface-cracked plate subjected to combine mechanical loads of tension and bending coordinated with a thermal shock of the cracked surface to model PTS loading conditions. Data from the experiments provided in the CSNI/FAG problem statements included pretest material characterization, geometric parameters, loading histories, instrumentation, and measured results from temperatures, strains, crack-mouth opening displacements

[1)] FALSIRE Fracture Analyses of Large-Scale International Reference Experiments

(CMODs), and crack-growth histories. A summary of the material toughness, loading conditions, crack geometry and crack growth for each experiment is given in Table 2.

Based on the CSNI/FAG problem statements, 37 participants representing 26 organizations performed a total of 39 analyses of the experiments. The analysis techniques employed by the participants included engineering methods (R6,GE/EPRI estimation scheme, DPFAD) and finite-element methods; these techniques were combined with applications of J_R methodology and the French Local Approach. The finite element applications include both two-and three-dimensional models, as well as deformation plasticity and incremental thermo-elastic-plastic constitutive formulations. Crack growth models based on nodal release techniques were utilized to generate the application-mode and generation-mode solutions for several of the experiments. A summary of the analysis methods applied to each experiment is given in Table 4. For each of the experiments, analysis results provided estimates of variables including crack growth, CMOD, temperatures, strains, stresses and applied J and K values. Conditions of crack stability and instability were identified in the experiments. Where possible, computed values were compared with measured data.

All the information to the test itself, the performed analysis and comparison of the analysis data as well as conclusions are given in a final report which is accepted by CSNI and will be published soon. Detailed presentations of the results are subject of the following sessions and therefore are not commented in this presentation. Beside the results of the exercise itself (see Table 5) there are a number of valuable accompanying effects which could be summarized as follows:

- A common format to collect comprehensive information on large-scale experiments has been established which could also be used for other purposes.
- The information collected are a good startingpoint for a documentation of large-scale experiments related to combined thermal mechanical loading.
- The work has been very beneficial for the individual organisations in judging on their own computer codes, their individual capabilities to handle these codes and the quality assurance to be applied for such kind of analysis.

The work to be performed in the future and in a phase II of the FALSIRE Project is subject of another presentation of this meeting.

3 Documentation of large-scale experiments related to combined thermal mechanical loading

Large-scale experiments adressing the structural response to thermal shock-type loadings have been performed in many countries. Most of these programs have already been finished or will be finished soon. The compilation of information related to these large-scale tests as well as relevant information on analyses performed to the tests is within the objective of the CSNI/FAG. As already pointed out the FALSIRE Project fills up a solid ground floor on which a database could be established to compile the,information available on thermal shock tests. The work is going on and requires further cooperation by all the international partners. The NKS-3 experiment of the MPA Stuttgart is presented as an example how this kind of documentation could

be performed in a comprehensive way so that each user can easily assess the applicability of certain boundary conditions and results to the problem he is presently looking for. The example is summarized in Figures 1 and 2. This type of presentation shows the test cylinder geometry, the crack geometry, the loading and a material characterization. Concerning the fracture assessment Figure 3 shows the calculated stress intensity at the crack tip as a function of crack tip temperature and the measured fracture toughness (K_{IC}) as a function of temperature as well as ASME-curves based on the NDT-temperature of the material. Furthermore a line is drawn to characterize measured J_{IC} values and the crack resistance (J_R) at certain steps of crack growth (e.g. 1 mm) as a function of temperature. This kind of fracture assessment in a comprehensive way is presented in Figures 4 to 9 for the thermal shock experiments NKS-1, 4, 5, 6 and PTSE-1,2, all with axisymetric thermal loading. Furthermore a partly circumferential crack inserted into the HDR (Heißdampfreaktor, Kahl) -RPV was loaded by a thermal shock experiment with a guided injection into an artifical cooling canal (see. Fig. 10, comparison of measured and calculated CMOD see Fig. 11). The fracture assessment confirmes the experimental results of no crack growth and that the test stopped close to crack initiation (see. Fig. 12).

4 Reactor pressure vessel response to the thermal shock loading conditions

The safety concept of light-water reactors (LWR) is based on the so called "design basis accidents". As part of the design basis accidents loss of coolant of the primary as well as the secondary circuit is postulated, assuming different leak sizes and locations and boundary conditions. The goal of the safety analysis for design basis accidents with primary or secondary blowdown is

- to demonstrate sufficient cooling of the reactor core assuming the minimum injection capability according to safety criteria and
- to demonstrate the integrity of the reactor pressure vessel (RPV) assuming the injection capability which causes the maximum load, using end-of-life (EOL) material conditions and postulated cracks of a limited size.

The basic requirements for the integrity assessment of reactor pressure vessels are

- the evaluation of loads as a function of time and temperature
- the evaluation of material conditions as a function of temperature, time and environment with special emphasis on irradiation
- evaluation of state of defects with respect to the applied NDT- methods and the influence of time, loads and environment.

The main load cases to be analysed in the integrity assessment of reactor pressure vessels are:

- hydro test
- pressure-temperature limits
  (cold overpressurization system aspect)

- ECCS injection in case of primary or secondary blow-down
- rapid cooldown in case of secondary blowdown without ECCS injection.

Important parameters in the definition of conservative loads are the primary loop design (2-,3-,4-,6-loops), the blowdown transients, injection geometry, -temperature and rate, water level and temperature in the RPV as function of time and the width of the cold water path (tongue) along the vessel wall.

For the evaluation of material conditions distinctions have to be made between properties of base, weld and cladding material. Furthermore the directionality of the material properties have to be investigated. Major emphasis is given to the properties of the irradiated material. For a detailed analysis of the reactor pressure vessel under thermal shock loading conditions the dependency of the material properties from the temperature in the whole range has to be known quite well.

For the crack to be investigated (based either on design assumption or on indications of the performed NDT) the important parameters are size, shape, orientation and certainly the question of near surface or surface crack.

As an example of detailed RPV-analyses an axisymmetric and a 3d-FE-model as well as sector models with (partly) circumferential cracks, which are loaded by boundary conditions calculated in the global model, are shown in Figs. 13 and 14. The deformation of a vessel loaded by PTS with axisymmetric cooling assumption is presented in Fig. 15. In case of asymmetric/strip like cooling the deformation is shown in Figs. 16 and 17. The stress intensity of circumferential cracks with different assumptions concerning the loading is compared with the fracture toughness of the investigated weld material at begin-of-life (BOL) and for the case of an assumed highly irradiated condition at the end-of-life (EOL) in the same comprehensive way as discussed in chapter 3 (see Figs. 18 to 20).

Looking to all the variables important as indicated above it is very clear that there are a number of parameters and boundary conditions to be addressed as potentially important areas in large scale tests. In the practical safety case we have normally to judge a short near surface or surface crack surrounded by material showing considerable variations in properties in the thickness, axial and radial direction. Loading conditions may vary between highly nonuniform up to axisymmetric starting with steep radial temperature gradients at the surface at the beginning of the transient, with developing overtime temperature differences over small or large portions of the wall thickness in the axial and circumferential direction. Therefore the investigations of practical RPV transients are three dimensional problems from thermohydraulic, structural and fracture mechanics point of view.

5 Summary and future needs

From experimental and analytical modelling of the fracture process we have learnt worldwide a lot of details and have reached a certain state of the art to assess structural behaviour of specimens and components as well as fracture behaviour of cracks under thermal and mechanical loading. The database and the comparative

evaluations developed in FALSIRE-Phase I have shown the capabilities of the applied analysis methods and the necessity to improve fracture assessment methods concerning

- the transferability of small specimen fracture properties to large specimens and components (constraint problem)
- the crack behaviour in the transition region of fracture toughness
- non homogenous material (cladded and welded vessels) and
- different stages of crack extension (ductile/brittle).

Therefore a Phase II of FALSIRE Project is planned starting in first half of 1993.

The state of the art concerning assessment of RPV-integrity due to transient thermal and pressure loading show the necessity of three dimensional thermohydraulic, structural and fracture analyses and the comparison with simplified models and methods to quantify the safety margins.

Activities of CSNI/Fracture Assessment Group (FAG)

- compilation of large scale tests
- round robin analyses of selected tests
- review of state-of-the-art
- recommendations to methods applied in the safety review

Table 1

Table 2

CSNI: Fracture Analyses of Large-Scale International Reference Experiments (FALSIRE)

experiment (place)	material toughness	loading	crack geometry	crack growth
NKS-3 (MPA, FRG)	A_v=95 J, T_{NDT}=60 °C	thermal shock, axial tension, internal pressure (constant)	circumferential (a/t = 0.3)	ductile 3.8 mm (average)
NKS-4 (MPA, FRG)	A_v^{US}=65 J, T_{NDT}=120 °C	thermal shock, axial tension, internal pressure (constant)	partly circumferential (a/t = 0.15)	ductile 1.5 mm (center)
PTSE 2A/B (ORNL,USA)	A_v^{US}=60 J, T_{NDT}=75 °C	thermal shock, internal pressure (transient)	axial (a/t = 0.1/0.29)	ductile 11.1/3.7 mm brittle 16.8/32.7 mm unstable -/68.8 mm
Spin Cyl. I (AEA,UK)	A_v^{US}=90 J	rotation of the specimen	axial (a/t = 0.5)	ductile 2.8 mm (average)
Spin Cyl. II (AEA,UK)	A_v^{US}=110 J	thermal shock	axial (a/t = 0.52)	ductile 0 - 0.75 mm,
PTS (B) (JAPEIC,Japan)	A_v^{US}=100 J, T_{NDT}=139 °C	thermal shock tension bending	partly circumferential (a/t = 0.14)	ductile 0.3 - 1.0 mm

Table 3

CSNI/FAG: Workshop on Fracture Analyses of Large-Scale International Reference Experiments (FALSIRE), Boston, May 1990

Tests	Number of Analyses	Institutions
NKS-3	11	MPA, CENS (2x), Uni. Maryl., EDF, GRS, ABB-CE, Batelle, CEGB, Novetech, IWM
NKS-4	6	MPA, CENS, Uni. Maryl., ABB-CE, Novetech, IWM
PTSE-2	8	ORNL, GRS, ABB-CE, SWRI, PSI, CRIEPI, Novetech, ENEA
SC-I	6	AEA, ORNL, SWRI, VTT, Novetech; CRIEPI
SC-II	7	AEA, ORNL, B&W, VTT, Novetech, CRIEPI, IWM
PTS (B)	1	MHI

Participants: USA 17, FRG 5, France 4, UK 3, Japan 3, Finnland 2, Switzerland 1, Korea 1, Italy 1

Table 4

Summary of Project FALSIRE analysis techniques[a]

NKS-3 (10 analyses)	NKS-4 (6 analyses)	PTSE-2 (8 analyses)	SC-I (6 analyses)	SC-II (8 analyses)	STEP B PTS (1 analysis)
FE; JR	FE; JR	FE; JR	FE; JR	FE; JR	FE; JR
FE; JR, LA	FE; JR	FE; JR	FE; JR	FE; JR	
FE; JR	FE; JR	FE; JR	FE; JR	FE; ES	
FE; JR, LA	FE; JR	FE; JR	ES	FE; ES	
FE; JR	ES; J/T	FE; JR	ES	ES	
FE; JR	ES; R6/1	FE; JR	ES; WF	ES; R6/1	
FE; JR		ES; J/T		ES	
FE; JR		ES		ES	
ES; J/T					
ES; R6/1					

[a]FE = Finite Element Method
ES = Estimation Scheme
A1 = Analytic Solution with Numerical Integration
A2 = Handbook Analysis of Statically Indeterminate Model
JR = R-Curve Approach
J/T = J/Tearing Modulus Approach
LA = Local Approach
R6/1 = R6 Method/Option 1
WF = Weight Function Method

Fracture Analyses of Large-Scale International Reference Experiments (CSNI / FALSIRE)

Preliminary conclusions

- improved instrumentation for structure mechanical parameters of future experiments
- temperature dependence of material data necessary for thermal shock analyses
- differences in approximation of stress strain data,thermal expansion coefficient,reference temperature and other boundary conditions effect scatterbands in the FE-analysis results
- strong difference between 3D-FE-results and axisymmetric approximation,no important effect of model size (degrees of freedom) on the same level
- crack resistance of some investigated materials show significant dependence on temperature (PTSE-2) and specimen geometry (SC-I/II)
- refering to the transferability of specimen results to a component consideration of stress triaxility parameters (q,T) in the frame of the J-integral-concept or local approach is necessary

Table 5

Test cylinder geometry

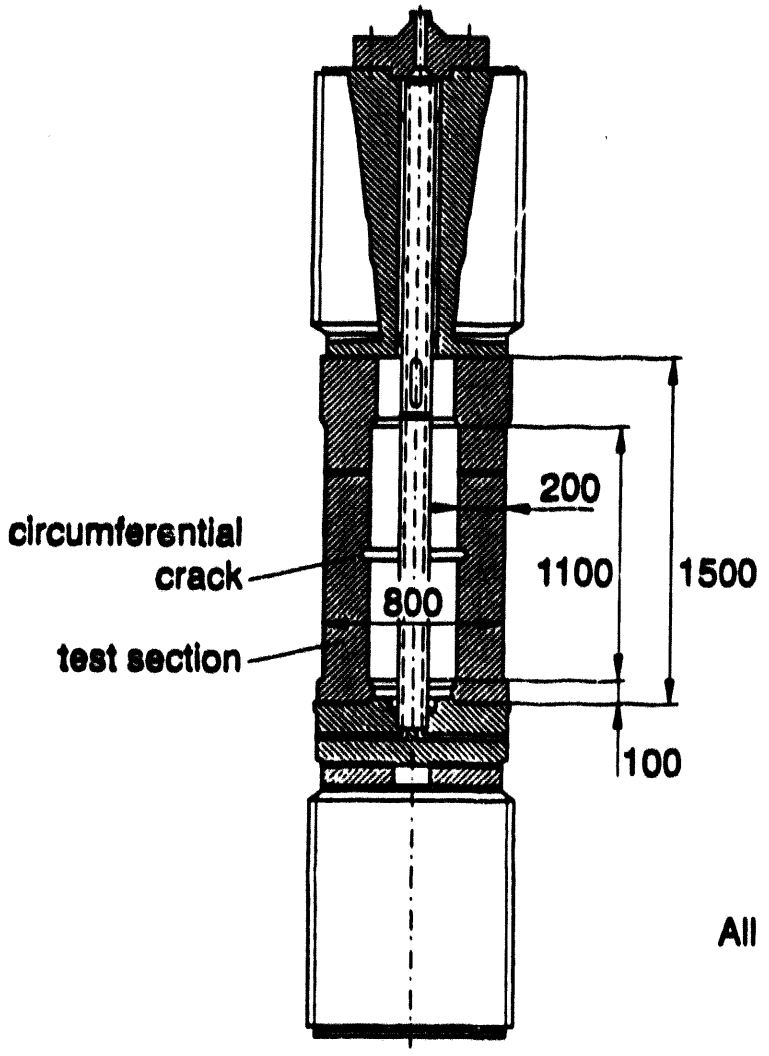

Crack geometry

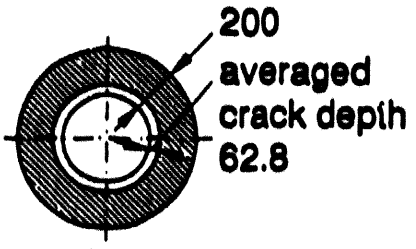

All measures in mm

3989K

CSNI - reference experiment
NKS-3, MPA-Stuttgart

Figure 1

Thermal and mechanical loading

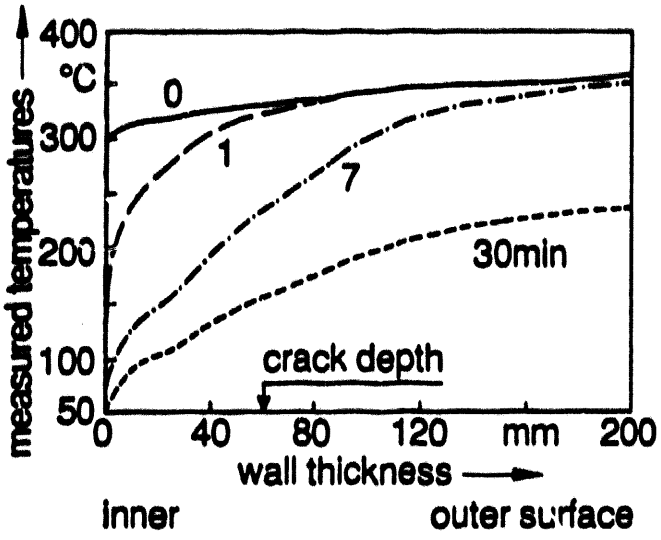

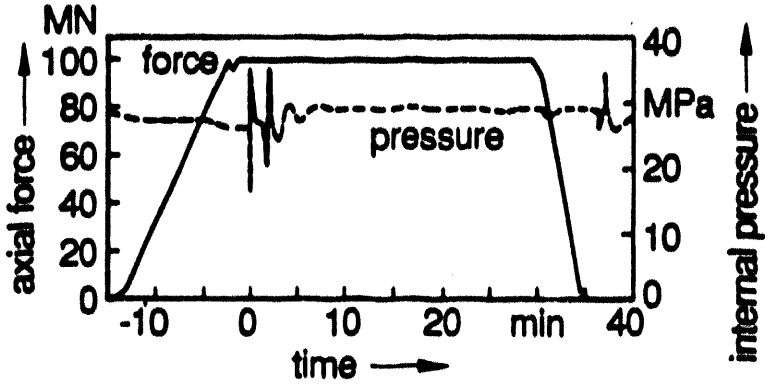

CSNI - reference experiment
NKS-3, MPA-Stuttgart

Material characterization of the test section 22 Ni Mo Cr 37

yield/ultimate stress at RT	563/723 MPa
charpy energy for upper shelf	95 J
NDT	60 °C

Figure 2

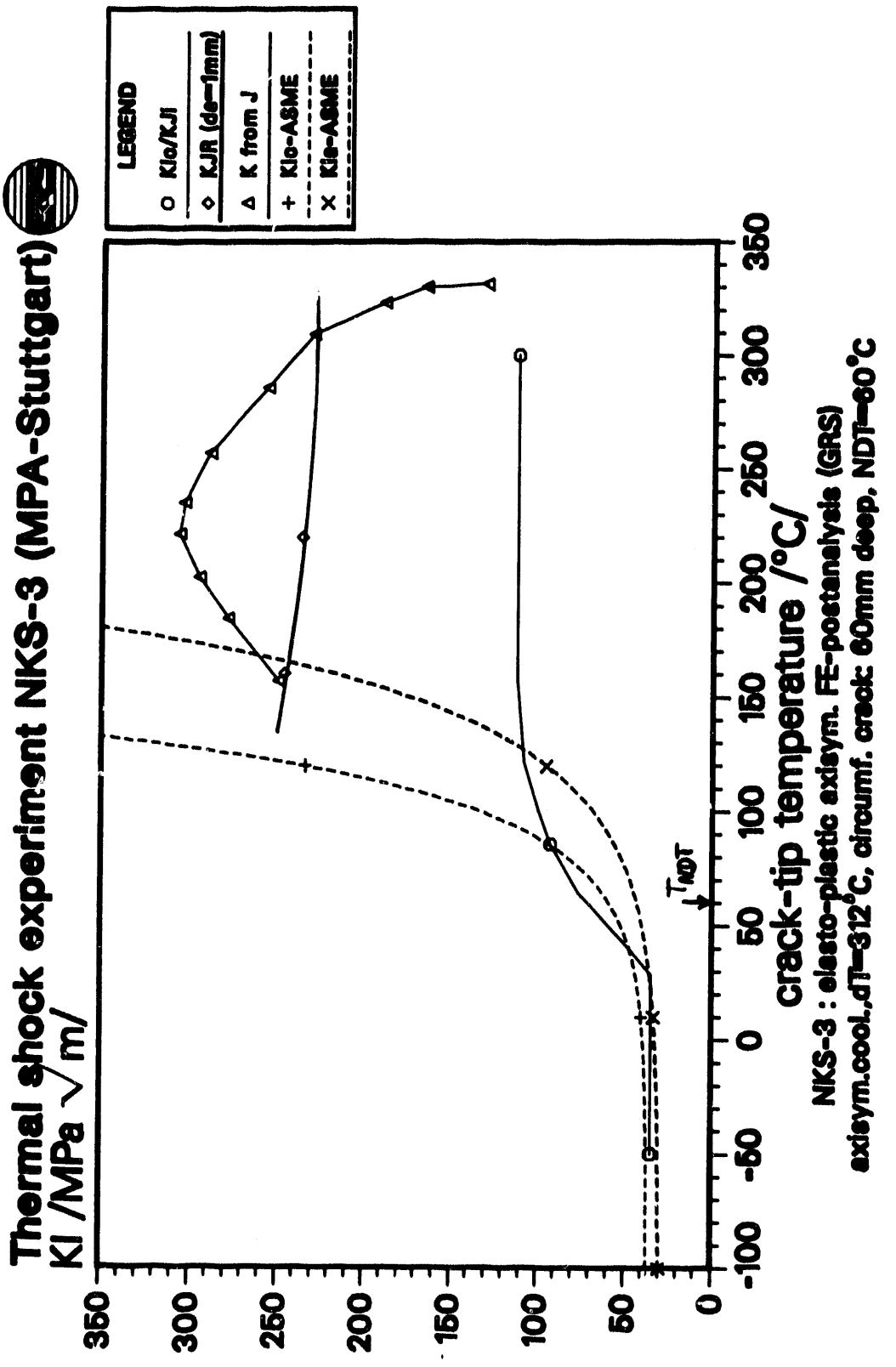
Thermal shock experiment NKS-3 (MPA-Stuttgart)
KI /MPa √m/
LEGEND
KIo/KJI
KJR (dc=1mm)
K from J
KIo-ASME
KIa-ASME
crack-tip temperature /°C/
NKS-3 : elasto-plastic axisym. FE-postanalysis (GRS)
axisym.cool.,dT=312°C, circumf. crack: 60mm deep, NDT=60°C
T NDT

Figure 3

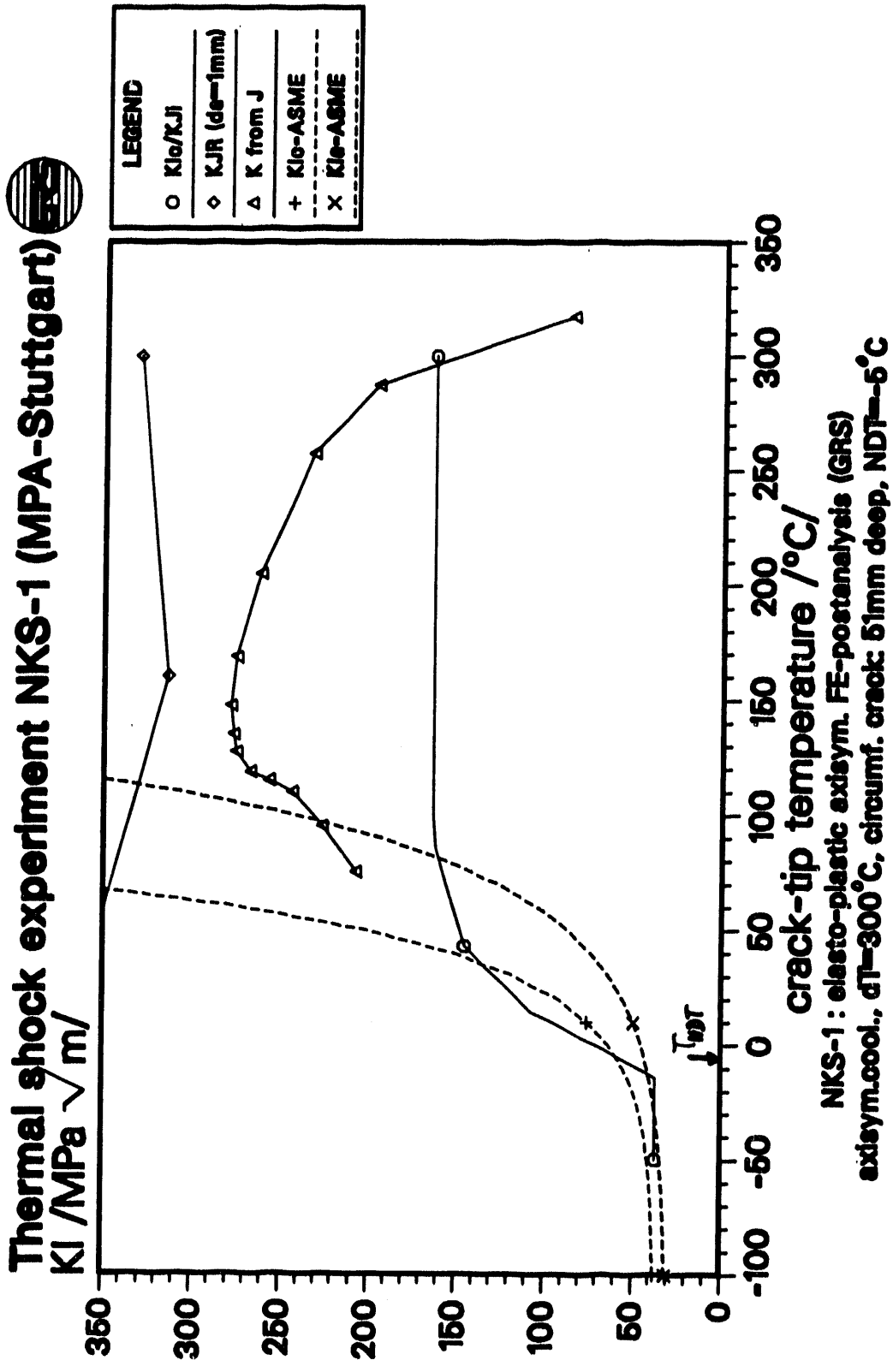
Thermal shock experiment NKS-1 (MPA-Stuttgart)
KI /MPa √m/
LEGEND
KIo/KJi
KJR (dc=1mm)
K from J
KIo-ASME
KIc-ASME
350
300
250
200
150
100
50
0
-100
-50
0
50
100
150
200
250
300
350
crack-tip temperature /°C/
T0
NKS-1 : elasto-plastic axisym. FE-postanalysis (GRS)
axisym.cool., dT=300°C, circumf. crack: 51mm deep, NDT=-5°C

Figure 4

Figure 5

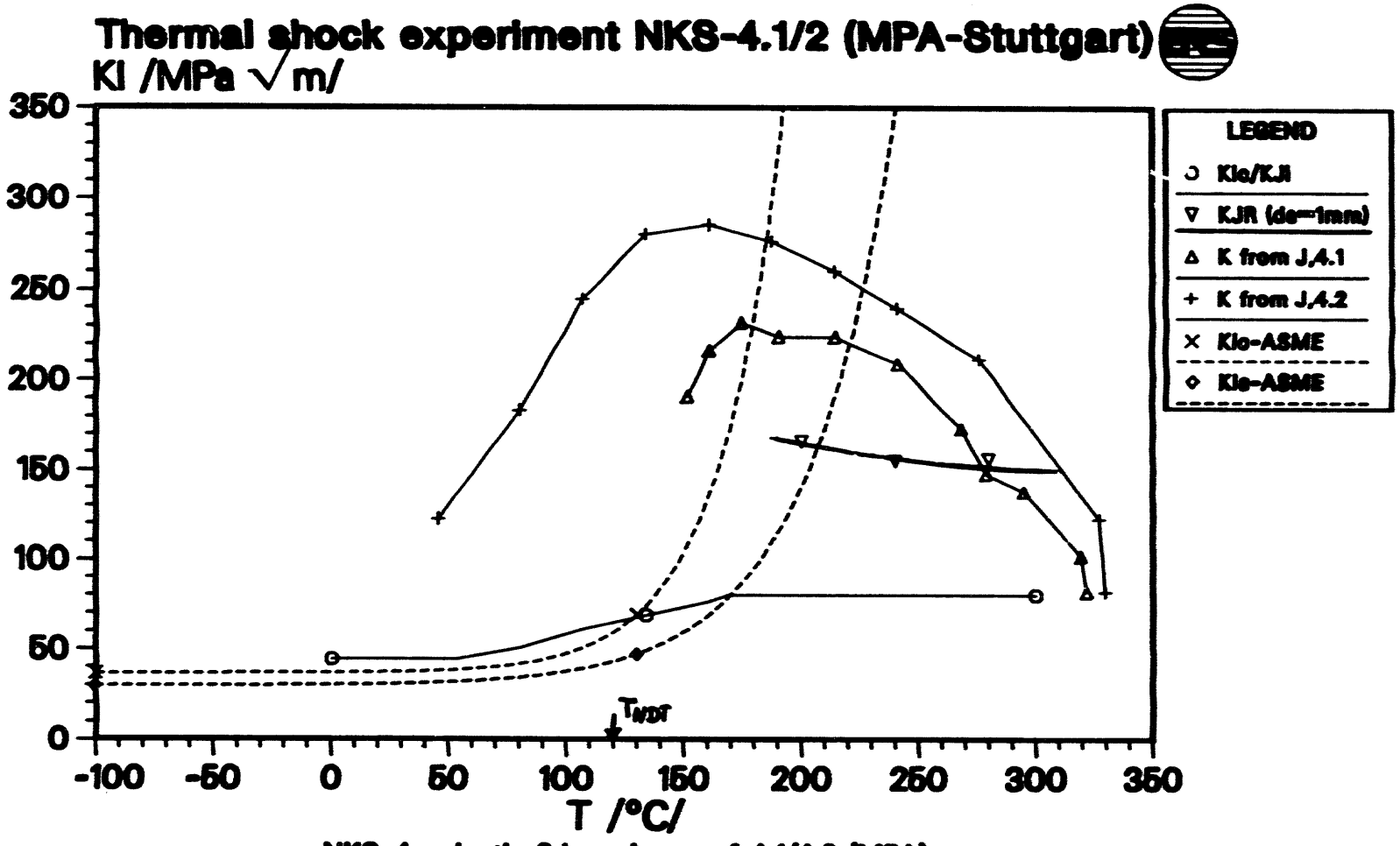
Thermal shock experiment NKS-4.1/2 (MPA-Stuttgart)
KI /MPa √m/
350
300
250
200
150
100
50
0
-100
-50
0
50
100
150
200
250
300
350
T /°C/
T_NDT
LEGEND
Klc/KJI
KJR (de=1mm)
K from J,4.1
K from J,4.2
Klc-ASME
Klc-ASME
NKS-4 : elastic 2d-analyses of 4.1/4.2 (MPA)
axisym c.,dT=310/325°C,part.circumf:30/31.5,180mm,NDT=120°C

Figure 6

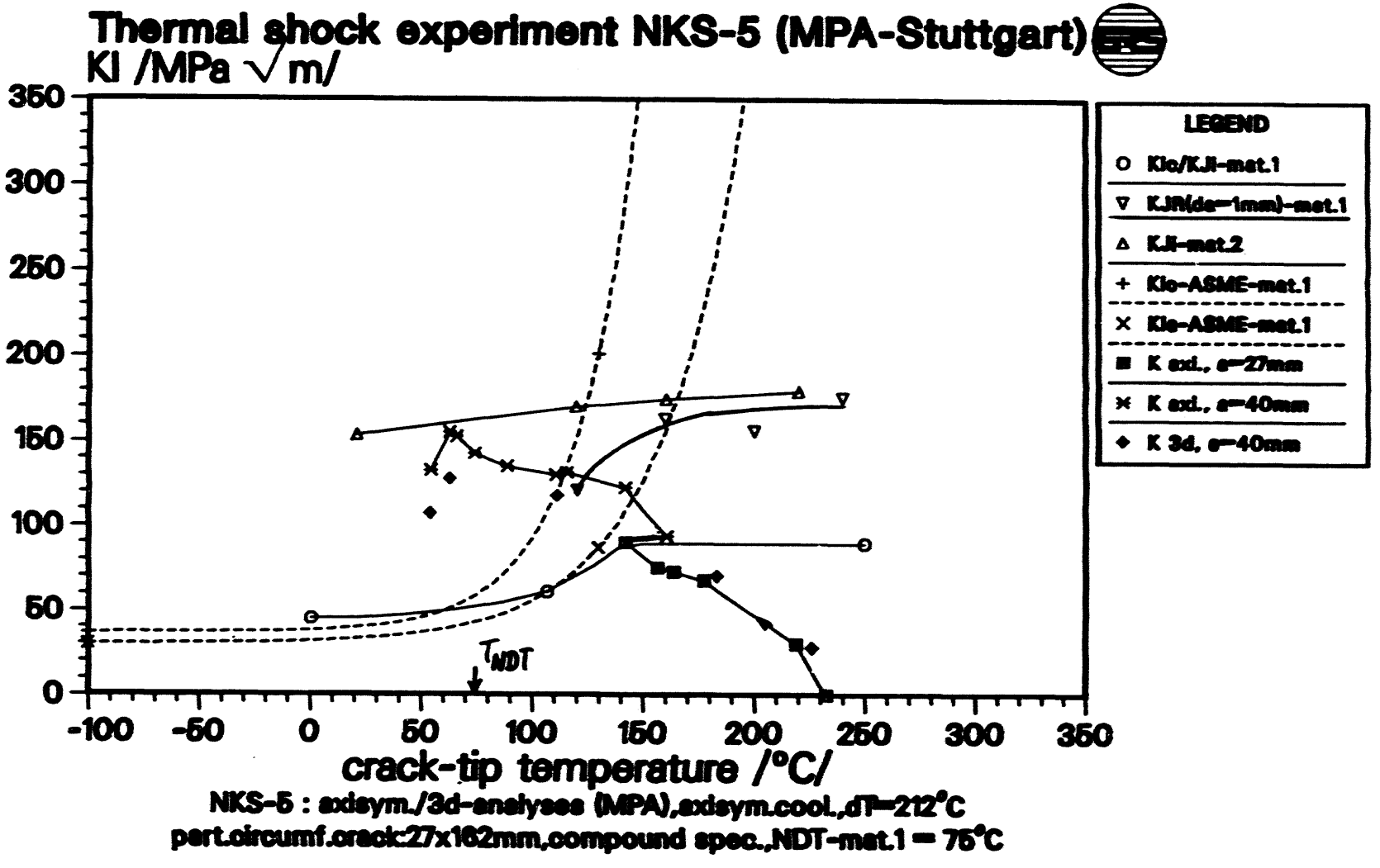
Thermal shock experiment NKS-5 (MPA-Stuttgart)
KI /MPa √m/
350
300
250
200
150
100
50
0
-100
-50
0
50
100
150
200
250
300
350
crack-tip temperature /°C/
T_{NDT}
LEGEND
Klc/KJI-mat.1
KJR(da=1mm)-mat.1
KJI-mat.2
Klc-ASME-mat.1
Kia-ASME-mat.1
K exi., a=27mm
K exi., a=40mm
K 3d, a=40mm
NKS-5 : axisym./3d-analyses (MPA),axisym.cool.,dT=212°C
part.circumf.crack:27x162mm,compound spec.,NDT-mat.1 = 75°C

Figure 7

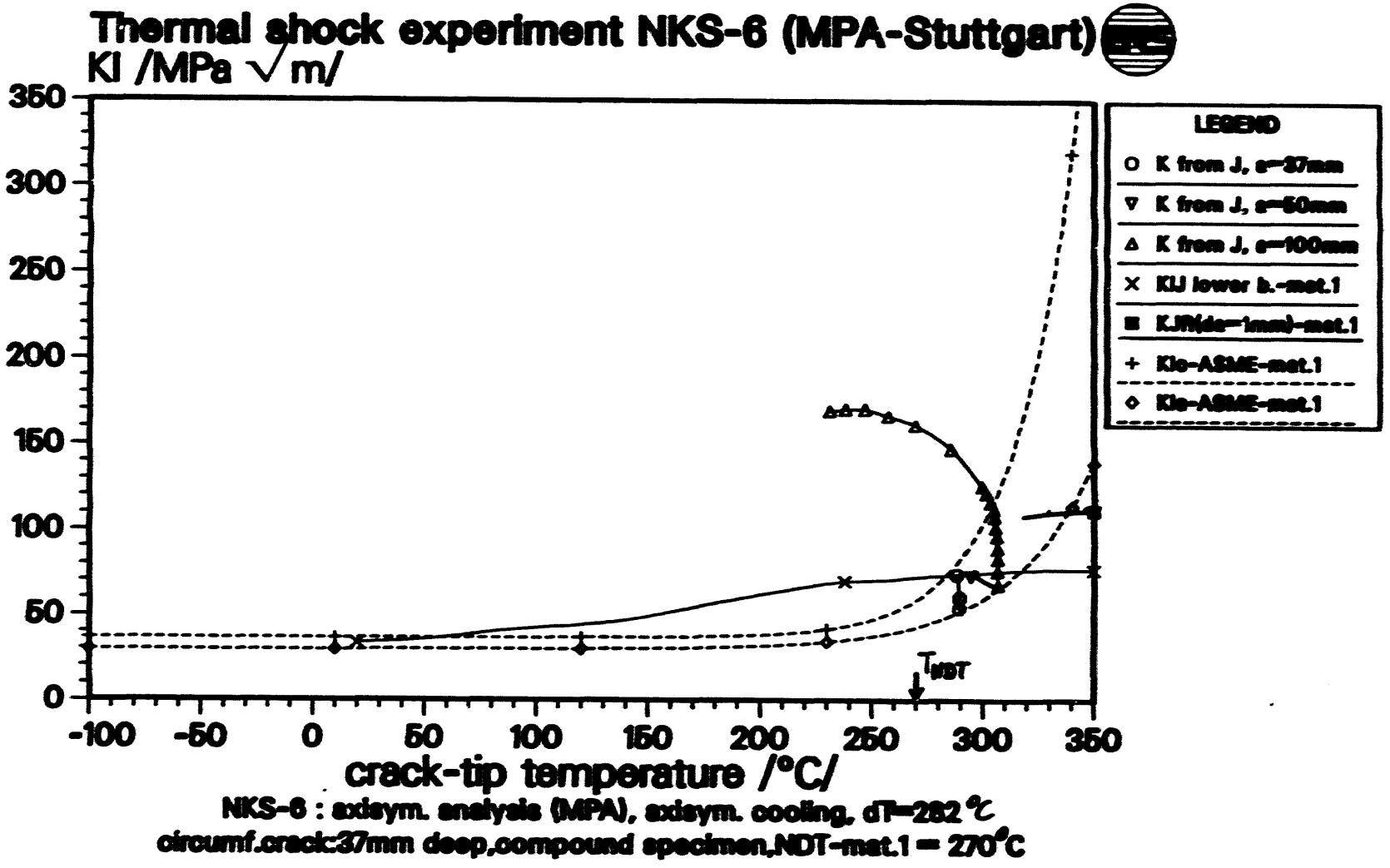
Thermal shock experiment NKS-6 (MPA-Stuttgart)
KI /MPa √m/
350
300
250
200
150
100
50
0
-100
-50
0
50
100
150
200
250
300
350
crack-tip temperature /°C/
LEGEND
K from J, a=37mm
K from J, a=50mm
K from J, a=100mm
KIJ lower b.-mat.1
KJR(da=1mm)-mat.1
KIa-ASME-mat.1
KIa-ASME-mat.1
T_NDT
NKS-6 : axisym. analysis (MPA), axisym. cooling, dT=282 °C
circumf.crack:37mm deep,compound specimen,NDT-mat.1 = 270°C

Figure 8

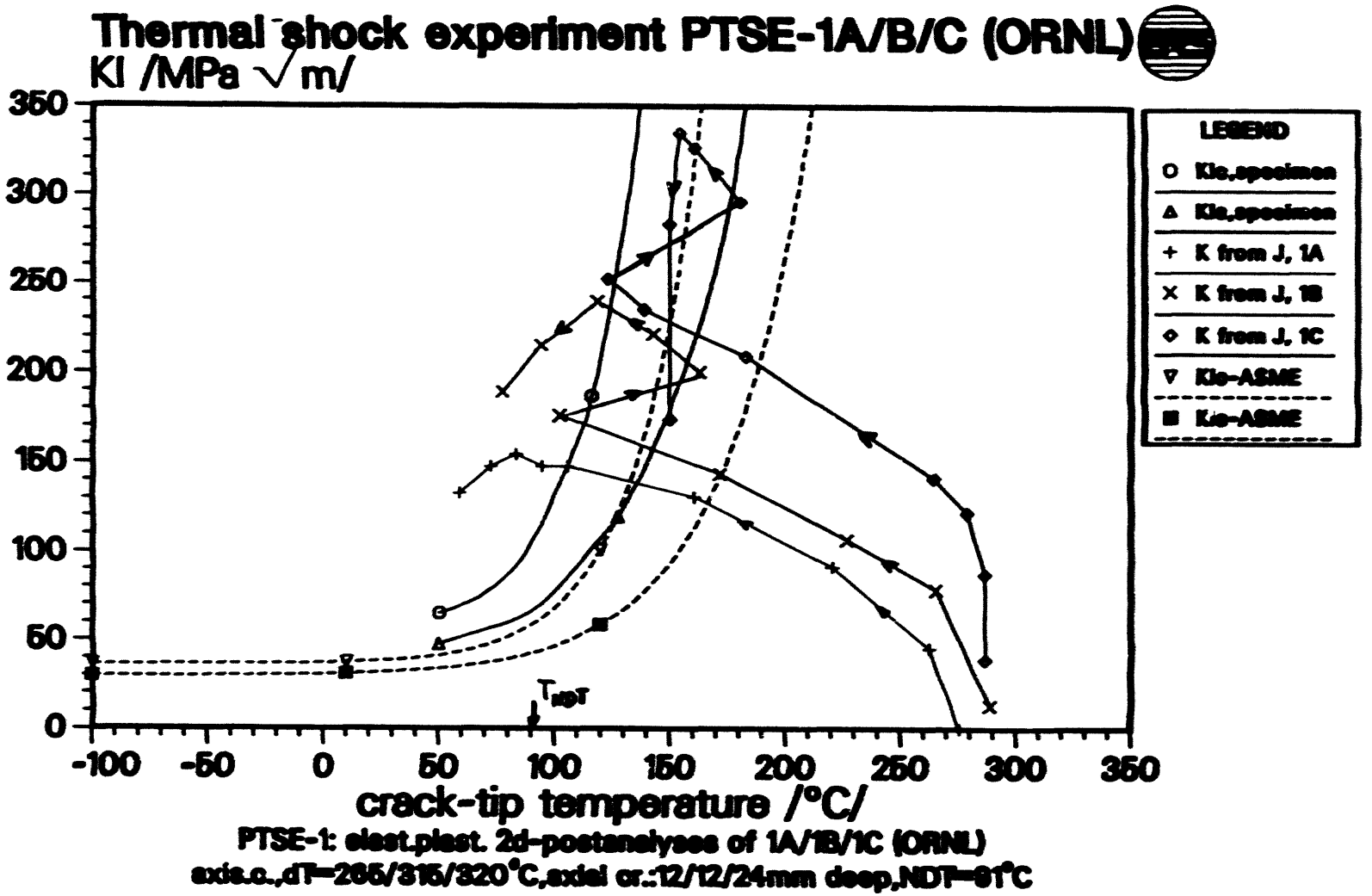
Thermal shock experiment PTSE-1A/B/C (ORNL)
KI /MPa √m/
350
300
250
200
150
100
50
0
-100
-50
0
50
100
150
200
250
300
350
crack-tip temperature /°C/
LEGEND
Kic,specimen
Kia,specimen
K from J, 1A
K from J, 1B
K from J, 1C
Kic-ASME
Kia-ASME
PTSE-1: elast.plast. 2d-postanalyses of 1A/1B/1C (ORNL)
axis.c.,dT=265/315/320°C,axial cr.:12/12/24mm deep,NDT=91°C

Figure 9

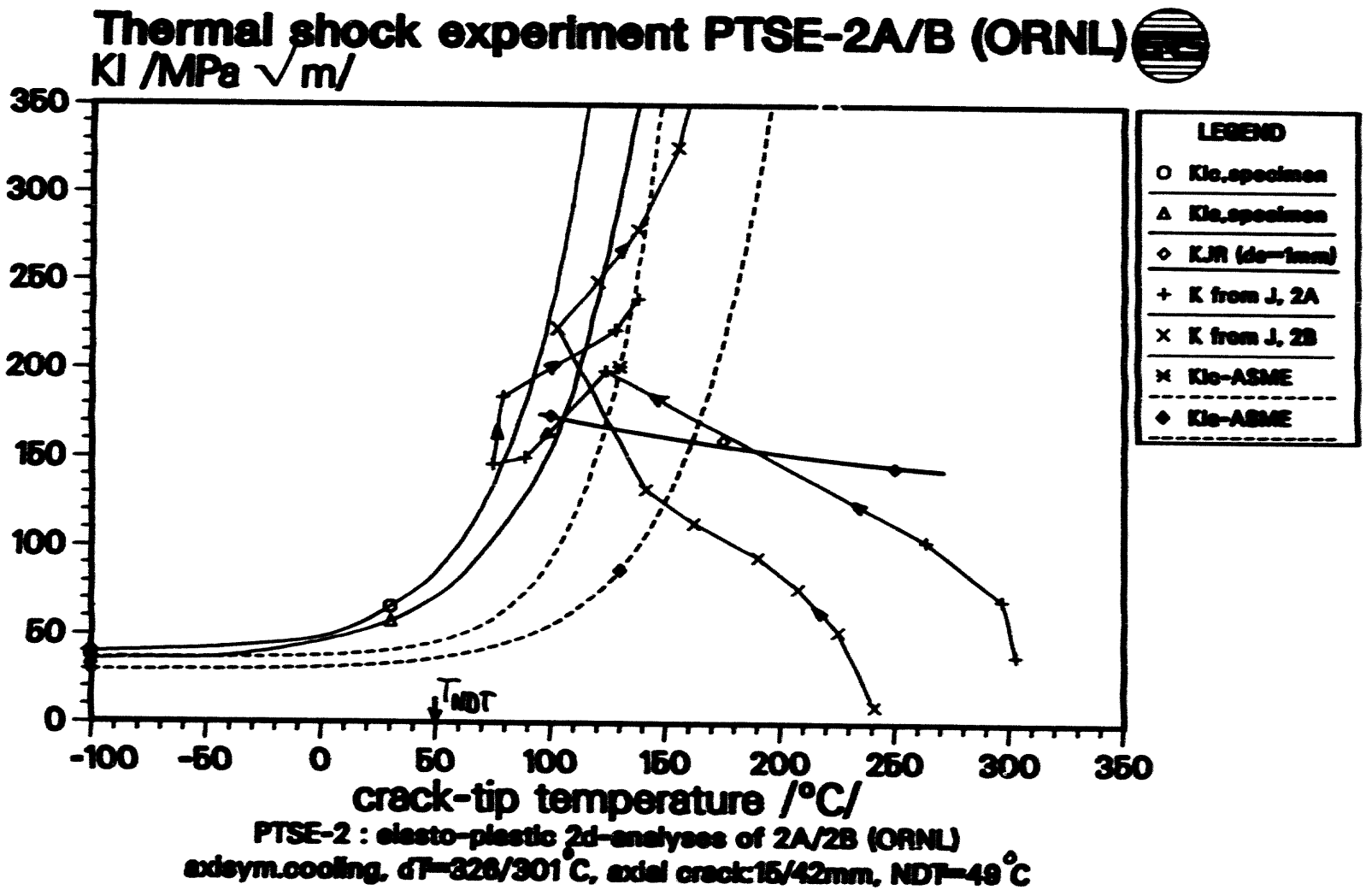
Thermal shock experiment PTSE-2A/B (ORNL)
KI /MPa √m/
350
300
250
200
150
100
50
0
-100
-50
0
50
100
150
200
250
300
350
T_NDT
crack-tip temperature /°C/
LEGEND
Klc,specimen
Klc,specimen
KJR (da=1mm)
K from J, 2A
K from J, 2B
Klc-ASME
Klc-ASME
PTSE-2 : elasto-plastic 2d-analyses of 2A/2B (ORNL)
axisym.cooling, dT=328/301°C, axial crack:15/42mm, NDT=49°C

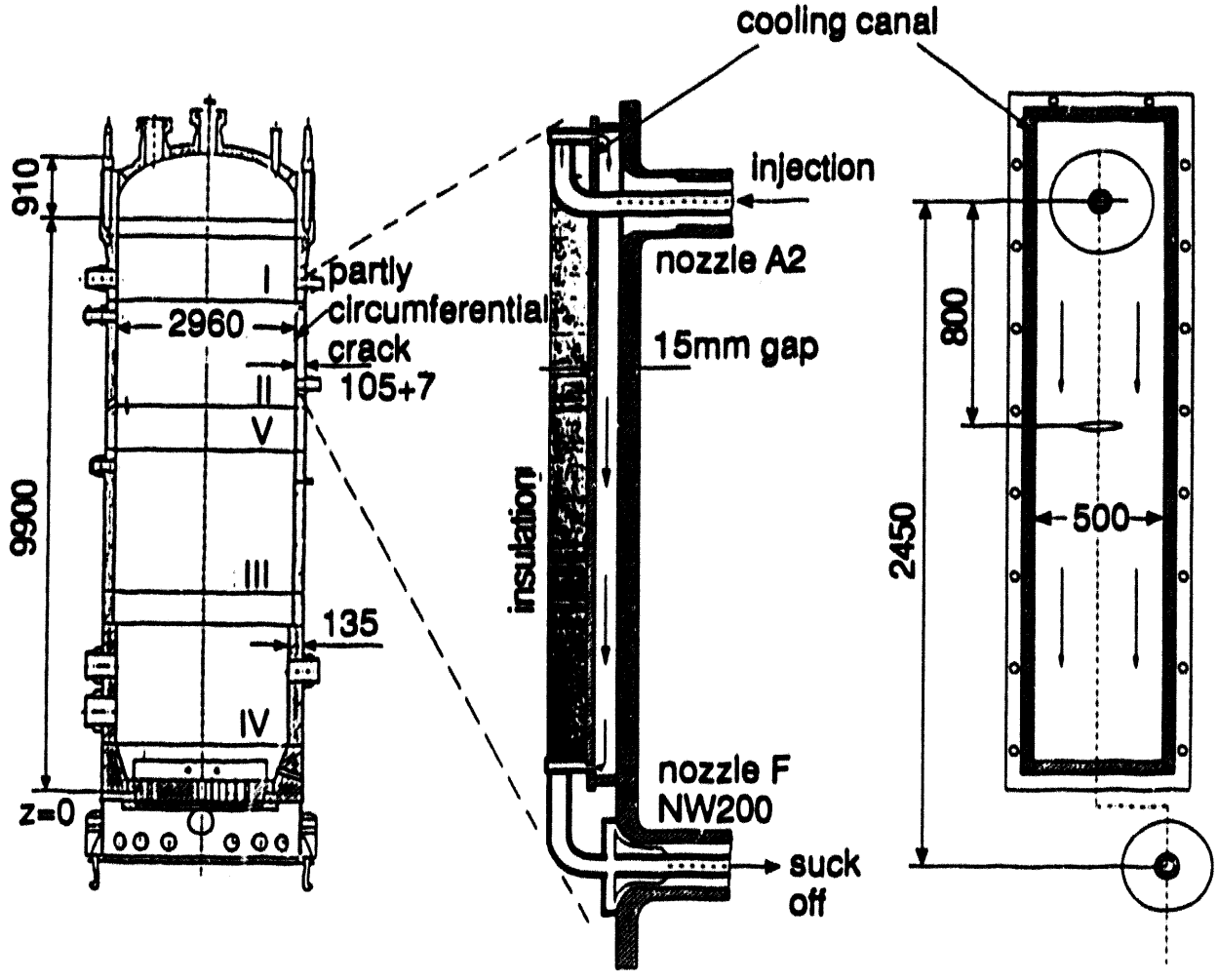

HDR-Thermal shock experiment THEL II
at the RPV, guided injection

Figure 10

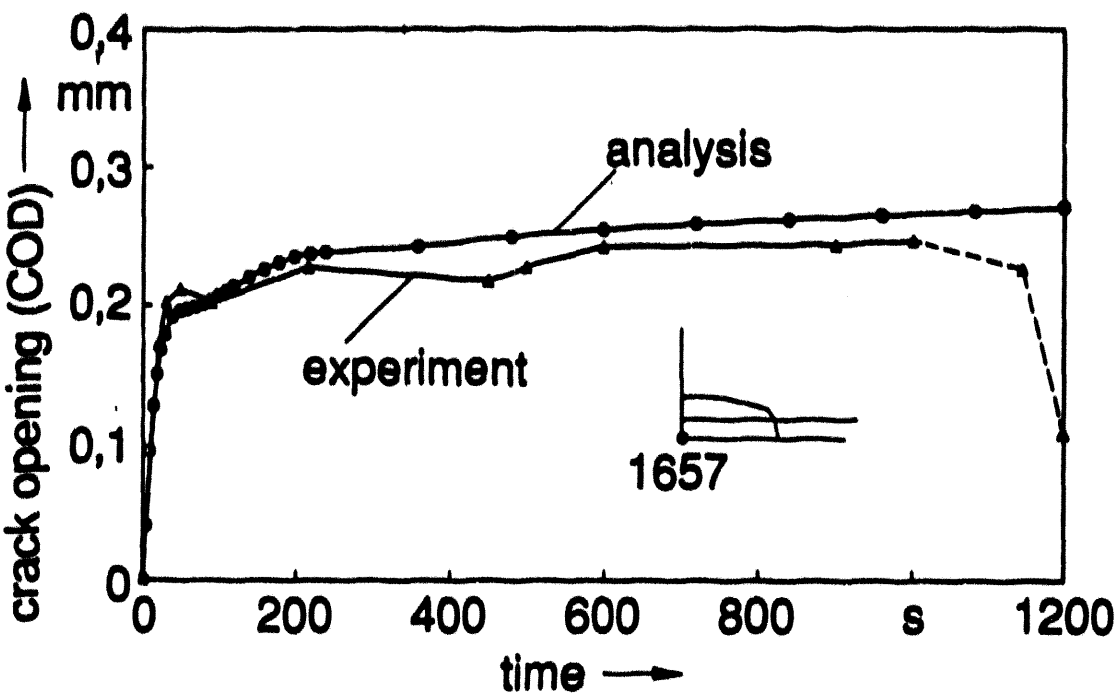

HDR-Thermal shock experiment THEL II at the RPV, crack mouth opening of partly circumferential crack (post-analysis)

Figure 11

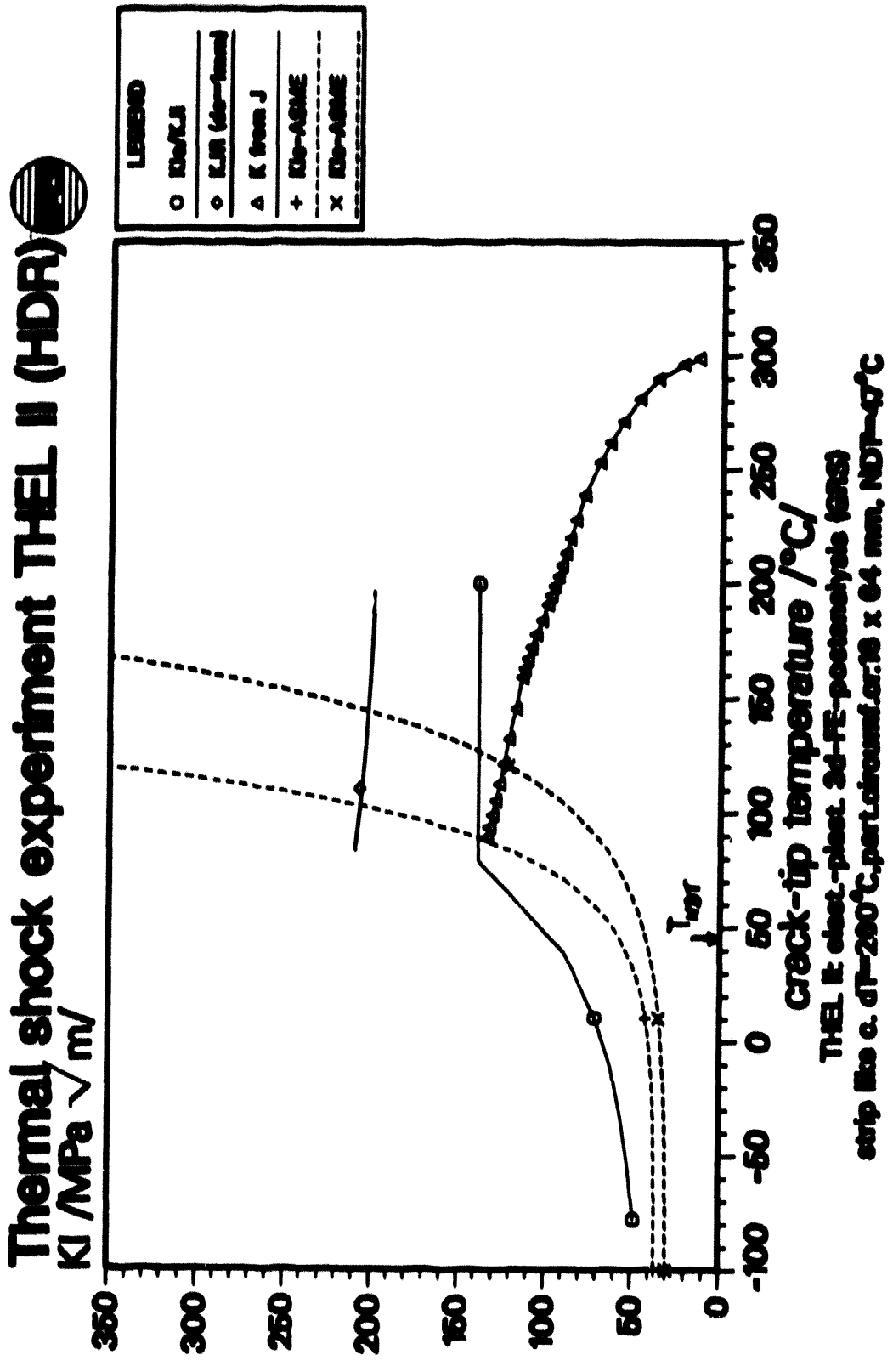
Thermal shock experiment THEL II (HDR)
KI /MPa √m/
crack-tip temperature /°C/
LEGEND
0
50
100
150
200
250
300
350
-100
-50
0
50
100
150
200
250
300
350

Figure 12

GRS
weld
crack depth 17mm
cladding
base metal
p_F
a
p
p
p
p
Loading
p: internal pressure
p_F: surface load due to internals
a: cooling region
RPV-1: Axisymm. model and sector model with assumed 360° circumf. crack

Figure 13

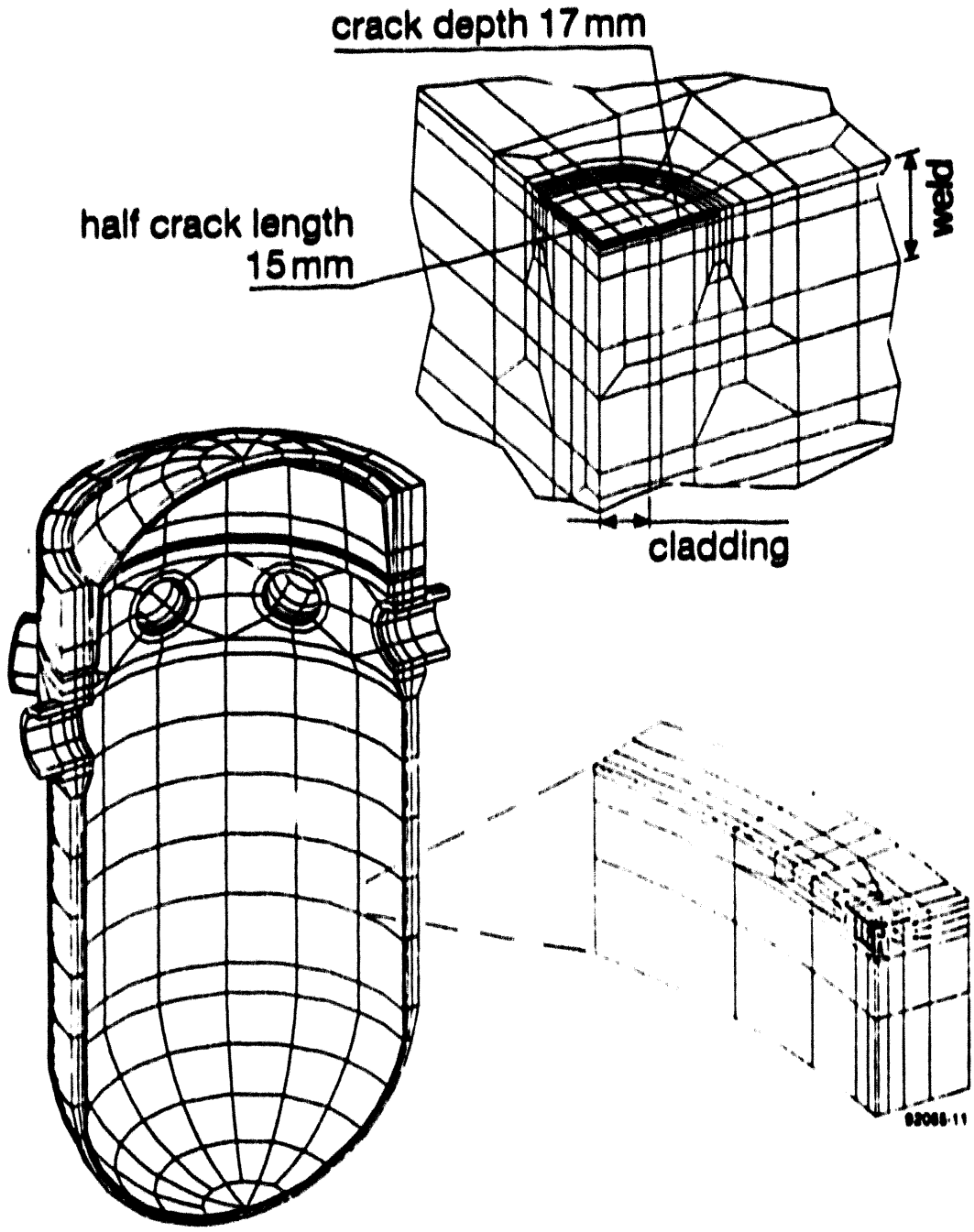

RPV-1: 3-D model and sector model with assumed partly circumferential crack

Figure 14

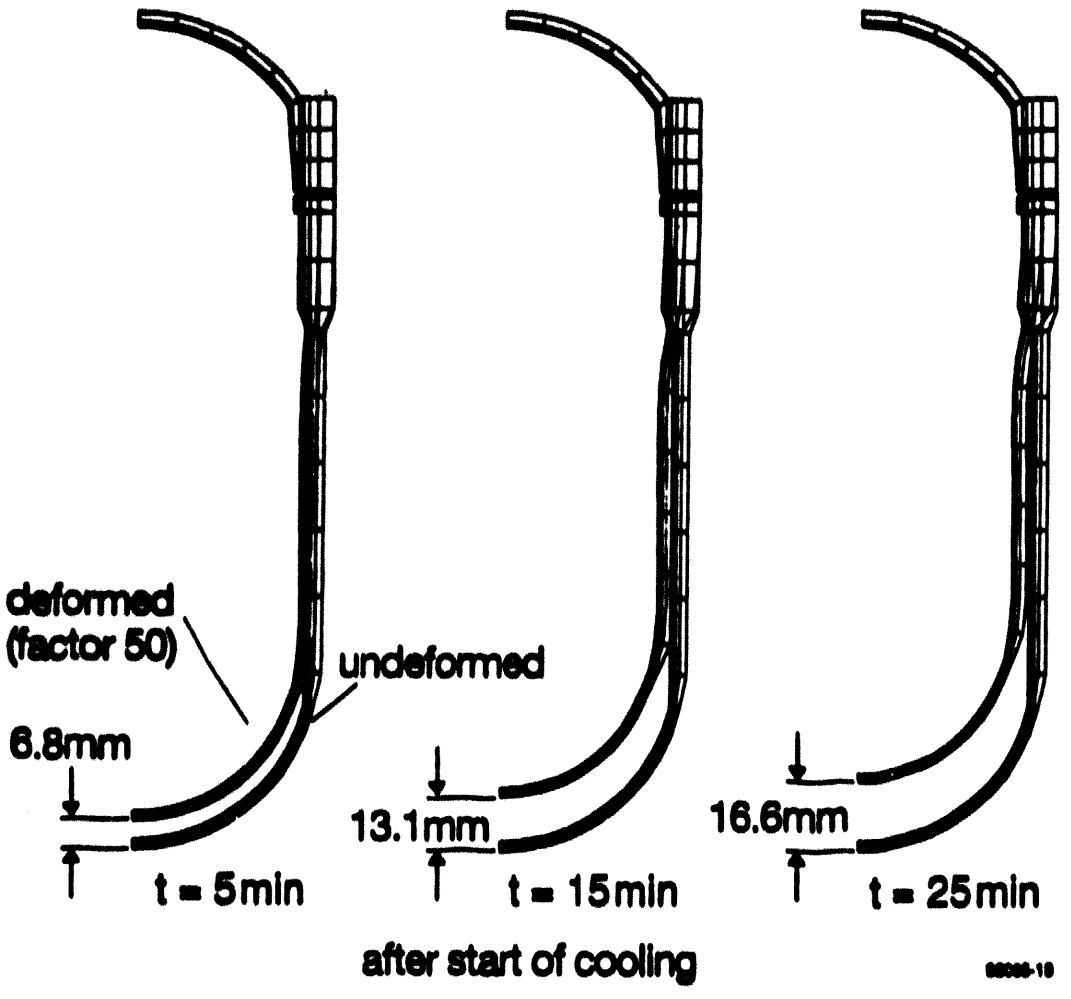

RPV-1: Cold water injection at low pressure with axisymmetric cooling

Figure 15

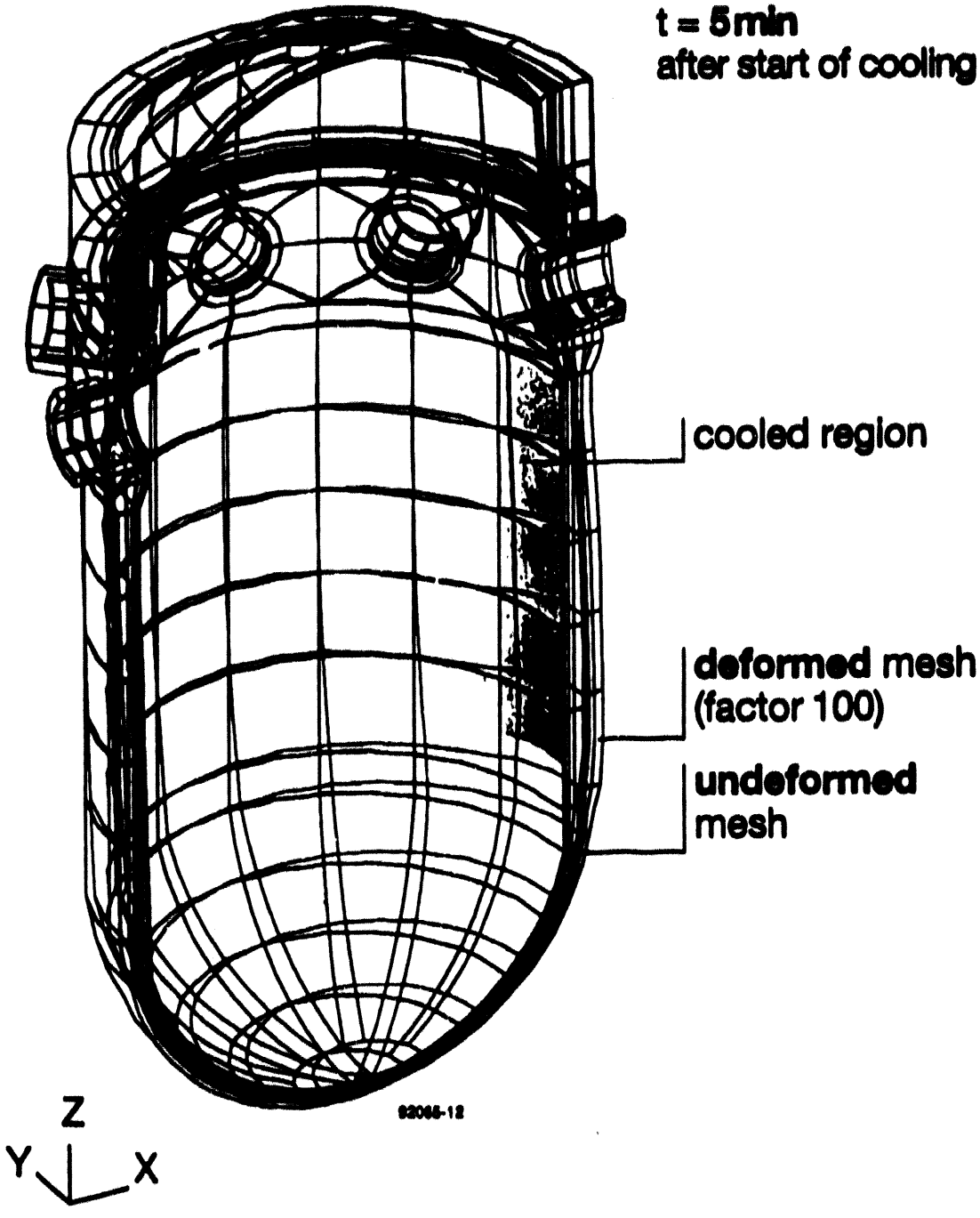

RPV-1: Cold water injection at low pressure with strip like cooling

Figure 16

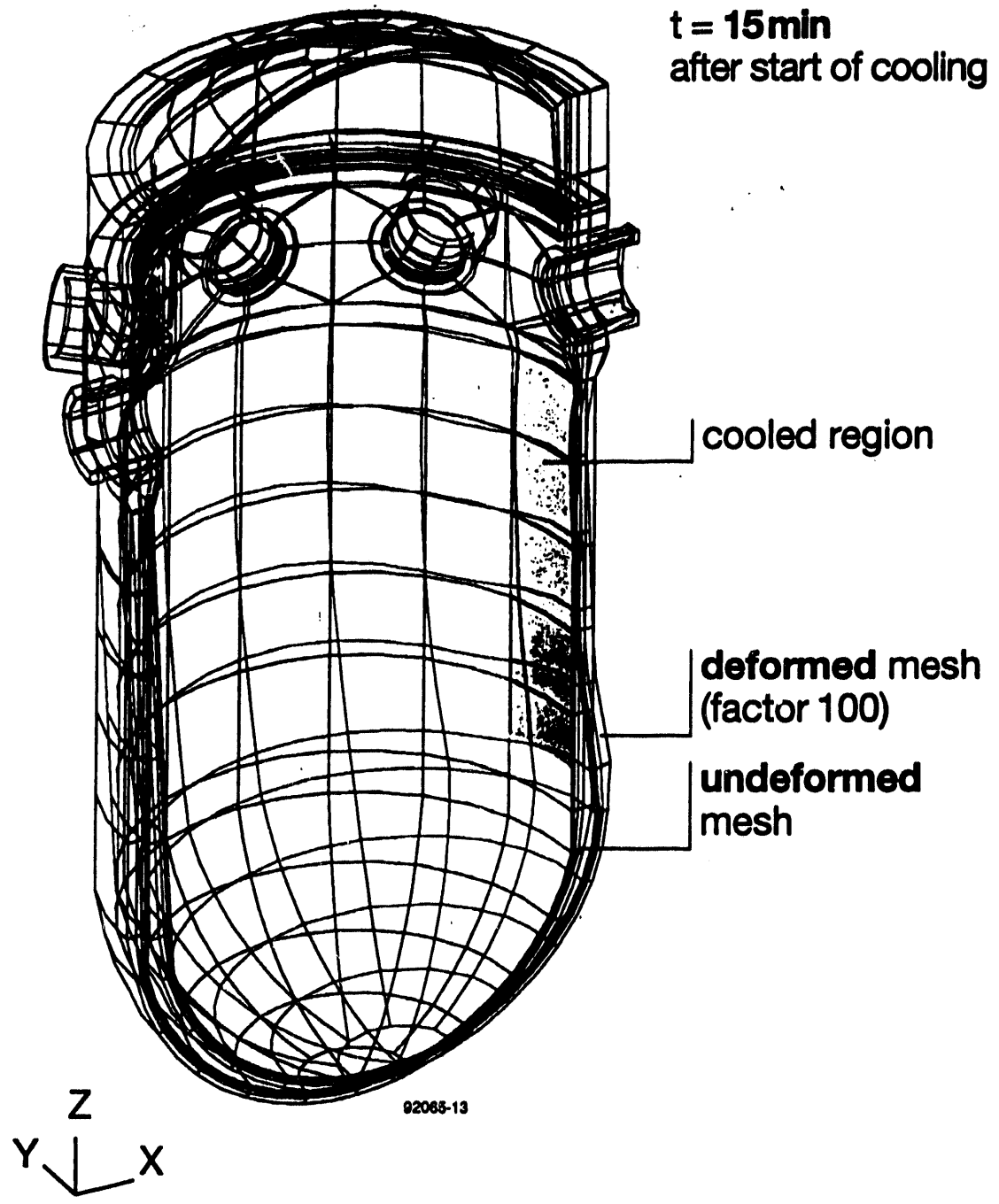

RPV-1: Cold water injection at low pressure with strip like cooling

Figure 17

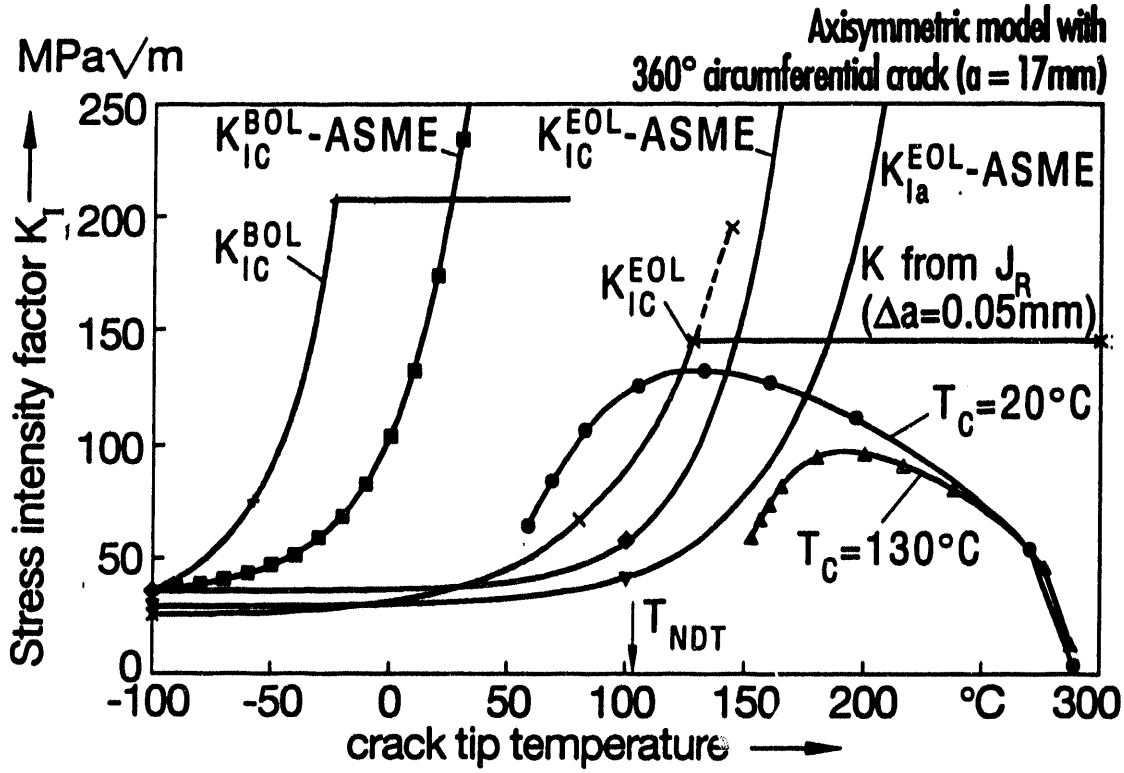

Parameters of the analyses:
T_C = 20°C - cooling temperature **without** mixing
T_C = 130°C - cooling temperature **with** mixing
values of curve are about 4% lower
in the region of the maximum

92065-03

RPV-1: Low pressure injection with variation of cooling temperature

Figure 18

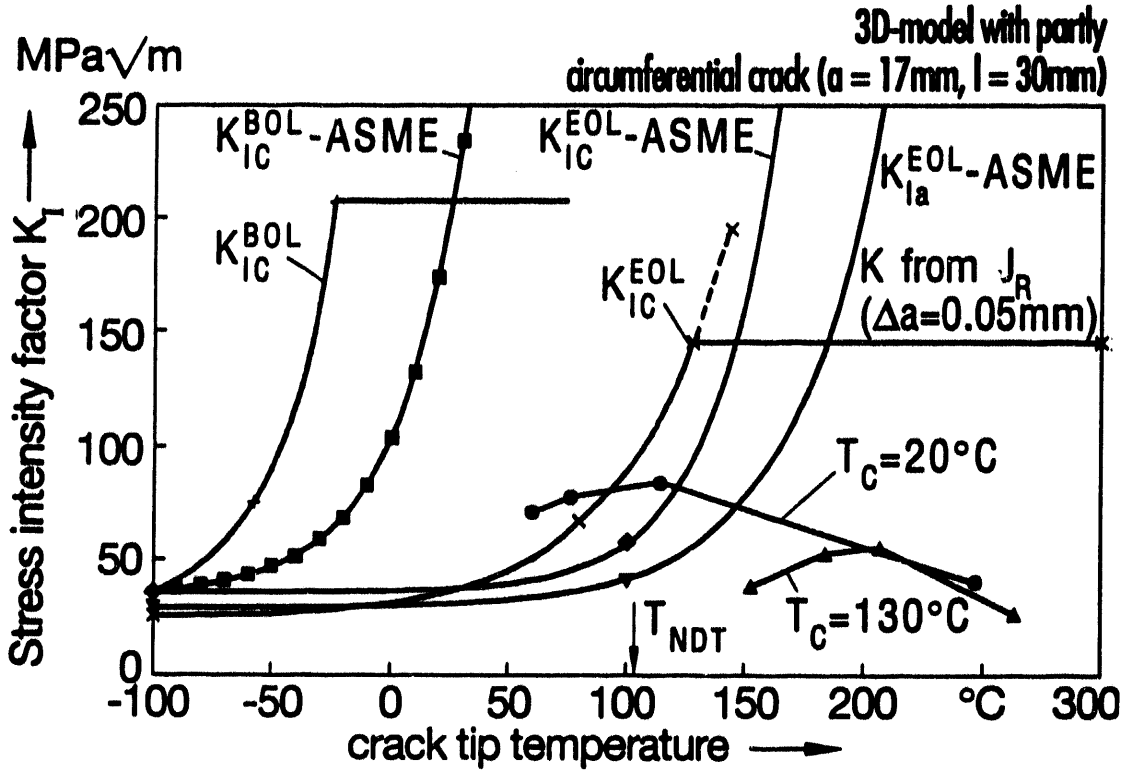

Parameters of the analyses:
T_C = 20°C - cooling temperature **without** mixing
T_C = 130°C - cooling temperature **with** mixing

92065-04

RPV-1: Low pressure injection (strip like) with variation of cooling temperature

Figure 19

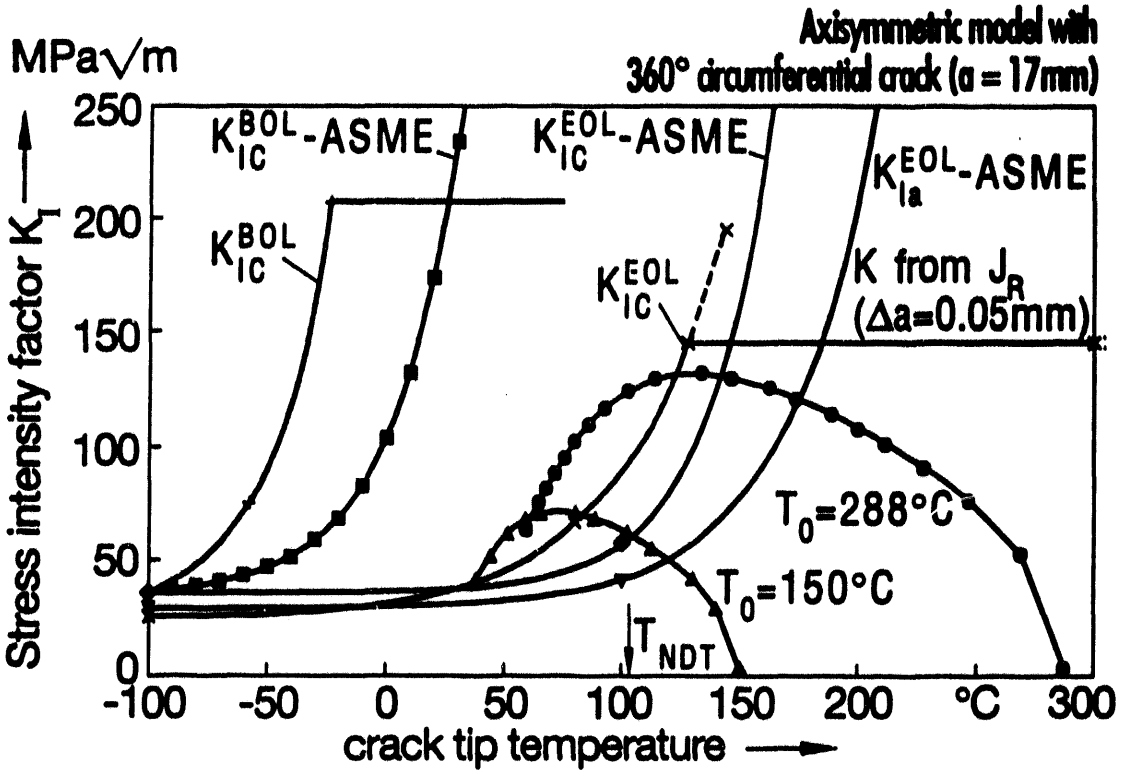

Parameters of the analyses:
T_0 = 288°C - initial temperature at operation
T_0 = 150°C - initial temperature at shutdown

RPV-1: Low pressure injection with cooling temperature 20°C

Figure 20

Appendix 1: Standard format for test and analysis documentation

	GENERAL INFORMATION	1

- general project title
- special project title
- aim of the special project
  (e.g. crack initiation, stable growth, arrest)
- institution / company
  (name, address, contactperson)
- dates of the special project
  (initiated, completed)

additional information:

references:

	GENERAL TEST INFORMATION	2

- test title
- date and location of the test
- description of the test
  (e.g. specimen, loading, environment, material)
- institution / company
  (name, address, contactperson)

additional information:

references:

	GENERAL INFORMATION ON DOCUMENTATION , DATE:	3

- description of documentation
  (experiment, pre/postcalculation)
- institution / company
  (name, address, contactperson)
- dates of the project
  (initiated, completed)

additional information:

references:

	LOADING CONDITIONS	4

- initial conditions
  (e.g. pressure, temperature, environment)
- loading during the test
  (e.g. pressure, temperature, axial force)

additional information:

INSTRUMENTATION 5

- temperature distribution
- forces / pressures
- stresses / strains
- deformation
- crack mouth opening
- crack tip opening angle
- crack growth

additional information:

GEOMETRICAL CHARACTERISTICS 6

- component geometry (figures)
  (e.g. radius, thickness)
- flaw characteristics (figure)
  (e.g. crack profile, direction)
- fatigue pre-cracking Y/N
- cladding Y/N
  (thickness)

additional information:

MATERIAL : IDENTIFICATION 7

- test material-identification (ASTM, etc)
- cladding material-identification (ASTM, etc)
- chemical analysis
- thermal treatment

additional information:

MATERIAL : MECHANICAL PROPERTIES 8

- test temperatures
- engineering and true stress - strain
  tensile data and curves, numerical approximation for analysis (temperature dependence, multi/bilinear...)

  E-Modul [MPa]

  $R_{p0.2}$ [MPa]

  R_m [MPa]

  A_g and Z

  Poisson'ratio

  Ramberg-Osgood-coefficients

additional information:

MATERIAL : PHYSICAL PROPERTIES — 9

- heat convection coefficient *)
  h [W/m**2 K]
- thermal conductivity *)
  λ [W/m K]
- specific heat capacity *)
  c_p [kJ/kg K]
- density *)
  ρ [kg/m**3]
- coefficient of thermal expansion *)
  α [1/K]

additional information
*) numerical approximation for analysis (time/temperature dependence, multi/bilinear)

MATERIAL : FRACTURE MECHANICS PROPERTIES — 10

- Charpy energy versus temperature (curve)
- Charpy impact energy for upper shelf
- RT-NDT
- K_{Ia} versus temperature (curve)
- K_{Ia} versus temperature (curve)

additional information

MATERIAL : FRACTURE MECHANICS PROPERTIES — 11

- J_R curve *) : specimen / geometry (a/w)
  - fatigue pre-cracking Y/N
- J_R curve determination method
  - J_i fracture initiation value
  - J_i determination method

additional information
*) with respect to the dependence of J_R - curves on specimen geometry a series of curves is desirable.

ANALYSIS : PARAMETERS AND RESULTS — 12

- kind of analysis (pre/postcalculation)
- analysis tools
  - FE-code (pre/postprocessor)
  - estimation scheme (e.g.catalogue, R6 ....)
- analysis method
  - temperature distribution analysis (e.g. nonlinear transient)
  - structural analysis (e.g. elastic-plastic)
  - fracture mechanics concept (e.g. J-integral, crack growth model)

additional information

ANALYSIS : PARAMETERS AND RESULTS 13

- FE-model: Temperature analysis / Structural analysis
  - dimensions (e.g. 1d, 2d plane stress..)
  - elements (number,type)
  - nodes
  - degrees of freedoms
  - integration scheme (type, order)
  - equilibrium iteration method
  - material / plasticity model
  - formulation of deformation and strain analysis
- boundary conditions
  - temperature (e.g. T = const, Q = 0)
  - mechanics (e.g.fixation, forces, ...)
  - fracture mechanics (e.g. crack pressure)

additional information

ANALYSIS : PARAMETERS AND RESULTS 14

- results (values,plots,diagrams,comparision with experiment)
  - temperature distribution (time history,radial,axial...)
  - deformed geometry
  - crack opening (time history)
  - stresses / strains (time history, plastic zone)
  - J-integral (time history, along crackfront,...)
  - J-path dependence
  - crack growth
  - maximum loads
  - failure assessment

additional information

EXPERIMENT : DETAILS AND RESULTS 15

- measured data (values, plots, diagrams, comparison with analysis)
  - temperature distribution (time history,radial,axial..)
  - deformation (time history)
  - crack opening (time history)
  - stresses / strain (time history)
  - forces (time history)
  - J-integral (method, time history)
  - crack opening angle
  - crack growth (time history)

additional information

COMPARISON OF EXPERIMENT AND ANALYSIS 16

- discrepancies
  - geometry
  - loading
- comments

additional information

Spinning Cylinder Experiments SC-I and SC-II : A review of results and analyses provided to the FALSIRE Project.

by

E. Morland* and A. H. Sherry*

A series of six large-scale experiments have been carried out at AEA Technology using the Spinning Cylinder test facility. Results from two of those experiments (SC-I and SC-II) have been provided to Project FALSIRE and are reviewed in this paper.

The Spinning Cylinder tests were carried out using hollow cylinders of 1.4m outer diameter, 0.2m wall thickness and 1.3m length, containing full-length axial defects and fabricated from a modified A508 Class 3 steel. The first Spinning Cylinder test (SC-I) was an investigation of stable ductile growth induced via mechanical (primary) loading and under conditions of contained yielding. Mechanical loading was provided in the hoop direction by rotating the cylinder about its major axis within an enclosed oven. The second test (SC-II) investigated stable ductile growth under severe thermal shock (secondary) loading again under conditions of contained yielding. In this case thermal shock was produced by spraying cold water on the inside surface of the heated cylinder whilst it was rotating.

For each experiment, results are presented in terms of a number of variables, eg. crack growth, temperature, stress, strain and applied K and J. In addition, an overview of the analyses of the FALSIRE Phase-1 report is also presented with respect to tests SC-I and SC-II.

* AEA Technology, Reactor Services, Risley, Warrington Cheshire, WA3 6AT, UNITED KINGDOM

1. INTRODUCTION

The Spinning Cylinder project is concerned with the investigation of fracture behaviour in thick-walled test specimens under severe thermal shock and simulated pressure loading conditions. The facility, located within AEA Technology's Structural Features Test Facility at Risley in the United Kingdom, has been designed to produce the appropriate loading conditions. Pressure loading is simulated by the rotation of a test cylinder about its own axis and the resulting hoop stress distribution resembles that in a larger diameter pressurized vessel of the same wall thickness. With regard to secondary (thermal) stresses, cold water can be directed, at controllable flow rates at the inside surface of a test cylinder. Test cylinders can be heated to temperatures of up to 350°C. These high flow rates, together with the centrifugal forces due to rotation, lead to very good heat transfer conditions whilst at the same time providing uniformity of cooling.

A schematic of the test rig given in Fig. 1 shows the main features of the facility. The central feature is the 8-ton cylindrical test specimen (1.3m long, 1.4m OD, 200mm wall thickness) which is suspended from a flexible shaft from a single pivoted bearing so that it is free to rotate about the vertical axis. The test cylinders are rotated by a 375kW DC motor through a 2:1 step up right angle gear box and are located in a heavily reinforced pit which acts as an oven enclosure. The motor is capable rotating the cylinder to a maximum design speed of 3500 rpm. A damping device (not shown) is attached to the bearing pivot to stabilize the rotor against aerodynamically-induced precessional motion. Eight 3kW heaters mounted vertically within the cylinder enclosure allow the cylinder temperature to be raised to a maximum of 350°C. A stationary water spray system, capable of delivering controllable flow rates of up to 300 gallons per minute, provides the mechanism for thermally shocking the rotating inner surface of test cylinders. Instrumentation for monitoring temperatures, strains and displacements within the test cylinder are mounted directly on the rotating specimen and signals are extracted via a 100-channel slip-ring unit mounted directly above the drive gearbox.

Within the Spinning Cylinder facility therefore, independent control of both primary and secondary loading permits a variety of PWR fault conditions to be examined, including large and small loss-of-coolant accidents. Extensive on-line data monitoring systems are available within the facility to provide immediate and permanent records of temperatures, strains and defect extensions realised during Spinning Cylinder experiments. To date a total of six Spinning Cylinder experiments have been performed. These have investigated a number of different combinations of transient type (eg PTS, large LOCA etc), defect configuration and fracture mechanism. Of these experiments, results from the first two (SC-I and SC-II) have been provided to Project FALSIRE and are reviewed in this paper.

2. TEST OBJECTIVES AND CONDITIONS

The basic objective of both Spinning Cylinder tests SC-I and SC-II was to compare the progress of stable ductile tearing under simulated PWR plant conditions, against that predicted from conventional fracture mechanics theory, based on data derived from small-scale fracture toughness specimens. In both cases the tests were performed on large scale test cylinders containing full-length axial defects penetrating over 50% through the 200mm wall thickness. Specimen details in respect of both tests are presented in Fig 2. The distinguishing feature between the two tests was the loading condition. SC-I was an isothermal test performed at 290°C where the driving force for crack extension was provided solely from specimen rotation (simulated pressurization). SC-II was a thermal shock test simulating a large loss-of-coolant accident, where the

driving force for crack extension was overwhelmingly provided by thermal loading. Additional details in respect of both tests are presented below.

2.1 SC-I

The first spinning cylinder experiment was an investigation of stable ductile tearing under contained yield conditions for a thick-section low alloy steel structure. The test was isothermal, being carried out at 290°C and crack growth was generated by progressively increasing the rotational speed of the test cylinder. With respect to the full length axial defect contained within the cylinder, this consisted of a machined notch with a sharpened tip produced via fatigue pre-cracking. The fatigue crack was generated by subjecting the cylinder to cyclic diametral loading in the plane of the notch using a 500-ton actuator. In order to avoid the possibility of brittle fracture, the test cylinder was maintained at around 90°C throughout fatigue cracking. Some 80,000 cycles were applied using a maximum load of 420 tons. This resulted in a reasonably uniform fatigue crack of mean depth 10mm over the central 1.0m of the defect length.

The instrumentation arrangements for monitoring stable crack extension in SC-I are shown in Fig 3. These consisted of three sets of alternating current potential drop (ACPD) probes situated 25mm above the bottom of the machined slot at different axial locations. The connections for the constant AC driving current (0.4A at 1kHz), were on opposite sides of the slot so that the current between them passed around the crack tip. Additional instrumentation on SC-I comprised five back-face strain gauges, three pairs of clip gauges to monitor slot opening adjacent to the ACPD stations (thereby providing a back-up indication of crack extension), digital and analogue tachometers to measure speed and an array of thermocouples to measure any cylinder temperature variations.

2.2 SC-II

The second spinning cylinder experiment was an investigation of stable ductile tearing under contained yield conditions for a thick-section low alloy steel structure subjected to a severe thermal shock. The test was designed in such a way as to ensure fully ductile upper shelf conditions at the crack tip, throughout the course of the experiment. With respect to the full length axial defect contained within the cylinder, as for SC-I this consisted of a machined notch with a sharpened tip produced via fatigue pre-cracking. Once again the fatigue crack was generated by subjecting the cylinder to cyclic diametral loading, the test cylinder being maintained at around 80°C throughout fatigue cracking. Some 15,000 cycles were applied using a maximum load of 420 tons. This resulted in a reasonably uniform fatigue crack of mean depth 5mm over the central 1.0m of the defect length. In order to prevent egress of water into the crack tip (and thus prejudice upper shelf conditions), the entire machine slot was packed with insulating wool and covered with a pleated steel shim.

As with SC-I, instrumentation for SC-II comprised ACPD, back-face strain gauges, clip gauges and thermocouples, although, in line with the different nature of the thermal shock loading of SC-II, the number and location of these various instruments was different to that employed in SC-I. The instrumentation layout for SC-II is shown in Fig 4.

3. MATERIAL PROPERTIES

Comprehensive characterisation of the physical and mechanical properties of cylinder materials was carried out in respect of the test cylinders for both SC-I and SC-II, these having been manufactured from separate large-scale forgings.

3.1 SC-I

After casting into a partially pre-formed geometry, the ingot used to produce test cylinder I was centrally pierced and then forged. Following detachment of a stepped end-piece (used for heat treatment studies), the residual forging comprised a centrally located test cylinder (SC-I) encompassed top and bottom by both AEA test prolongations and manufacturer's "buffer" rings, Fig. 5. AEA prolongations were parted from the test cylinder and buffer rings after forging, heat treatment and identification of a 0° datum line corresponding to the ultimate position of the full-length axial defect. Both top and bottom prolongations were subsequently bandsawn into four equi-sized segments. Details of the chemical composition of the forging and its heat treatment are given in Table 1.

All specimens used in the pre-test characterisation programme were extracted from the 0° segment of either the top or bottom AEA prolongations and from positions which were at least 50mm from cut surfaces. Tensile specimens were located on, or near to, the 0° datum line and extracted in either the circumferential (C), radial (R) or axial (Longitudinal (L)) orientations. A total of six tensile tests were performed, one specimen of each orientation being tested from each of the two AEA prolongations.

Resulting values of 0.2% proof stress ($\sigma_{0.2}$), ultimate tensile strength (σ_u), percentage elongation and reduction of area are presented in Table 2. Additional true stress-strain data are given in Fig 6.

Fracture toughness specimens were extracted so that all specimen crack tips lay exactly on the the 0° datum line, at a radial position and direction of crack advance in direct correspondence to the defect in the cylinder (ie. all C-R orientation). A total of six 20% sidegrooved 35mm thick compact specimens were tested, four from the top prolongation and two from the bottom prolongation. The tests were performed using combined multi-specimen/unloading compliance test techniques. Values of crack length, crack growth and corresponding values of J are given in Table 3. Individual unloading compliance J_R curves were characterized using power fits of the form

$$J=A\,(\Delta a)^B \qquad (1$$

values of the regression coefficients A and B are given in Table 4. A "composite" J_R curve for the material as a whole was also provided to the FALSIRE project and is included in Table 4.

3.2 SC-II

After casting into a partially pre-formed geometry, the ingot used to produce test cylinder II and test cylinder III (not reported here) was centrally pierced and then forged. The forging consisted of the two test cylinders separated centrally by a test ring and encompassed top and bottom by test rings and buffer rings. A diagram of the complete forging is shown in Fig 7. Test rings were parted from the cylinders after forging and heat treatment. Prior to any machining operations a 0° datum line was established corresponding to the defect position in the cylinder(s). Just as for SC-I, test rings were subsequently bandsawn into four equi-sized segments. Details of the chemical composition of the forging and its heat treatment are given in Table 5.

All small-scale specimens examined in the characterization programme were extracted from the 0° segment of either the top, middle or bottom test rings and from positions which were at least 50mm from cut surfaces. Tensile specimens were located on, or near to, the 0° datum line and were extracted from up to three different positions across the wall thickness. Specimens were extracted in either the circumferential (C) or axial (A) orientations depending upon the test ring. A total of twenty-six tests were performed. Specimens extracted from near the inner cylinder wall surface (t/8 position) (where temperature drops during thermal shock would be largest) were tested at three temperatures spanning the complete range of the thermal transient, ie. 20°C, 150°C and

350°C. Specimens from other positions within the wall thickness were only tested at 350°C. Individual exponential expressions of the form

$$\sigma = \alpha \, EXP(\beta T) \qquad (2$$

where is σ either 0.2% proof stress or ultimate tensile strength and T is the temperature, were fitted to the data via linear regression analysis. No effect of specimen orientation on properties was observed and both circumferential and axial test results were included in the analyses, resulting in the expressions given in Table 6. Values of engineering stress/strain and true stress/strain from these tensile tests are given in Table 7. Physical properties characterizing the behaviour of the test material under thermal shock conditions are given in Table 8.

Fracture toughness specimens were extracted so that all specimen crack tips lay exactly on the the 0° datum line, at a radial position and direction of crack advance in direct correspondence to the defect in the cylinder (ie. all C-R orientation). A total of eight 20% sidegrooved 35mm thick compact specimens were tested, two from the top, two from the bottom and four from the middle test rings. Values of crack length (ao) and ductile crack extension (Δa) were estimated both from unloading compliance measurements made during tests and from post-test fracture surface measurements. Results are presented in Table 9. For each test the data were characterized using a power curve fit of the form of equation 1. Resulting values of the coefficients A and B are given in Table 10. Composite J_R curves for the different test rings are included.

4. TEST RESULTS

4.1 SC-I

The plan for test SC-I was to proceed directly to a target speed at which a useful minimum amount of crack growth would be anticipated without incurring the risk of tearing instability, and then to proceed beyond that point as circumstances allowed. In the actual experiment, three speed increments beyond the target speed of 2285rpm, were required to reach the intended amount of stable tearing (3 to 5mm), resulting in an eventual maximum (terminal) speed of 2600 rpm.

Initiation of stable tearing in the experiment was related to a pronounced change in the rate of increase of ACPD at about 2250rpm (see Fig 8). Final crack extension at each ACPD station was defined from physical measurements of stable tearing made on the actual fracture surface of the cylinder, extracted after the test. The growth at the ACPD stations varied from 2.4mm to 3.1mm, with a mean of 2.75mm. The crack profile, based on post-test destructive examination of the entire full-length defect, is shown in Fig 9. On the basis of the predicted initiation points and measured final crack extensions at each ACPD location, angular velocity versus crack growth curves were developed as shown in Fig 10.

4.2 SC-II

Prior to commencement of SC-II, the cylinder was stabilized at a mean temperature of 312°C. The cylinder was then rotated to 530 rpm to provide for uniform cooling of the inner surface upon application of the water spray. The inner surface of the cylinder was then spray cooled with water of temperature 15°C and at a flow rate of 269 gallons per minute, thus producing an effective heat transfer coefficient in excess of 20kW/m^2°C and a large thermal gradient across the cylinder wall thickness.

Temperature data from the test are depicted graphically in Fig 11. The figure compares measured temperatures with those predicted from a one-dimensional finite difference analysis using a heat transfer coefficient of 22.75 kW/m^2°C. The extent of ductile crack extension attained during the test was variable along the length of the defect but

achieved a maximum growth level of approximately 2.0mm at a distance of around 400mm from one end of the cylinder. The crack profile, based on post-test destructive examination of the entire full-length defect, is shown in Fig 12.

5. FALSIRE ANALYSES OF SC-I AND SC-II

Within this section the analysis techniques used within Phase 1 of the FALSIRE programme for assessment of SC-I and SC-II are described, as are their results. In the interests of consistency, the terminology used to describe analysis methods and the numerical designation of individual analysts has been kept consistent with those used in Reference [1].

5.1 Description of Analytical Methods

With respect to tests SC-I and SC-II a total of seven separate analyses were performed within the FALSIRE programme. As Table 11 indicates, the primary structural analysis tool used was the finite element (FE) method. Additional details of the finite element methods used are given in Table 12, which identifies the finite element programme, the model dimension (2 or 3-D), the size of the mesh as defined by the number of equations (degrees of freedom), the constitutive relation, material model and stress-strain approximation, and the solution scheme (integration rule and iteration method) employed in the analysis of the model. Unfortunately, much of the information regarding the FE methods used in the analysis of Spinning Cylinder Tests SC-I and SC-II, is unavailable (N/A).

From inspection of Table 12 it is apparent that the sizes of the various finite element models varied to a large extent. For example, in the analysis of SC-II analysis number 8, using the ADINA FE code, a mesh with ≈3,800 degrees of freedom was used. By comparison, analysis number 16, using the ABAQUS FE code, used a mesh with only 890 degrees of freedom. One other variable of note is the stress-strain relation used as input data to the various analyses. In some cases, particularly analyses that utilised the ADINA FE code, a bilinear stress-strain relation was employed. In others a multilinear stress-strain relation was used.

All of the FE analyses employed a J-resistance curve methodology for modelling stable ductile crack growth. J was typically calculated within the FE code from a path-area integral or domain integral expression containing terms appropriate for the applied loading conditions (ie, mechanical loads, thermal gradients, centrifugal loads, etc.). Most analysts computed the J-parameter as a function of applied load for one or more fixed crack depths. Analysts number 8 employed a node-release technique to perform analysis of the ductile tearing process.

Several participating analysts performed structural analyses of the Reference Experiments using engineering estimation schemes (ES). These approaches, of specific interest to the analyses of the Spinning Cylinder Tests are summarised in Table 13. The fracture analysis methodologies employed in the estimation scheme applications were primarily based on the J-resistance curve approach, with the J parameter determined from a variety of published sources.

Analyst 11 determined K_I values from influence coefficients for a vessel having a wall thickness to inner radius ratio of 0.1; the corresponding ratio for Spinning Cylinder Test 2 was 0.4. Analyst 12 used K_I solutions from Reference [2], which were modified using the Irwin plastic zone correction. The modified K_I values were subsequently converted to equivalent J values using the expression $J=K^2/E'$, where $E'=E/(1-\nu^2)$ and ν is Poisson's ratio. Solutions provided by analyst 13 were based on option 1 of the R6 method described in Reference [3,4]. Analyst 14 employed results

from a statically indeterminate solution for a cylindrical shell to evaluate the J-parameter by defining it as the sum of elastic and fully plastic components. Analyst 16 used an analytical solution for the hoop stress distribution in a rotating cylinder to determine J from a weight function method. Further details of the analytical methods are contained in Reference [1].

5.2 Results and Discussion

Figure 13 illustrates the variation of the J-integral with the angular velocity, Ω, for Spinning Cylinder Test 1. The open circles denote the experimental variation of J with Ω determined at AEA Technology and as described in Reference [1]. With the exception of analysis 9, the scatter band of results is small. The stress-strain approximation of the plane strain FE analyses 8 and 9 are multilinear. The curve of analysis 9 has a weaker slope than the other analyses, a result which is still under discussion. Comparison of the ES solutions reveals that analyses 12 and 16 show differences of up to 50%, with analysis 12 overestimating the level of J for a given angular velocity. This difference is considered to be due to the ES's used, since the variation hoop stress with Ω was almost identical in each analysis.

Figure 14 illustrates the variation of the J-integral with time through the thermal shock. The weight function method used for analysis 16 gives a quite conservative result, and analysis 11, using the K_I solutions specific to a vessel with wall thickness to internal radius of 0.1 (SC-I = 0.4) shows the lowest values. The remaining analyses are located in a fairly tight scatter band. As in the analysis of SC-I, the fracture assessment is strongly dependent on the estimation scheme used.

The reasons for the magnitude of the scatter associated with these analyses are discussed in some detail in Reference [1]. Modelling requirements for the experiments incorporate history-dependent mechanical, thermal and body-force loadings, temperature-dependent material and fracture toughness properties, specially designed materials, residual stress states and three-dimensional effects. For these reasons, it could be anticipated that comparisons of analysis predictions with available structural data from the experiments would yield results that vary significantly.

However, a number of common explanations for some of the scatter are evident. One of the major influences on the finite element solutions was the precise materials property input data used in the analyses. Restrictions of some FE codes to use only bilinear approximations of the stress-strain behaviour, compared with the use of multilinear stress-strain curves, was one major source of scatter. Another major source of scatter was the use of temperature insensitive material properties data in the analysis of the thermal shock experiments. Both of these sources of scatter highlight the importance of obtaining, and using, high-quality material properties data in order to accurately model structural behaviour.

6. ACKOWLEDGEMENTS

Funding in support of the Spinning Cylinder programme and analyses carried out by AEA Technology as part of the FALSIRE programme was provided by the United Kingdom Department of Trade and Industry (formerly by the Department of Energy), Nuclear Electric (formerly CEGB) and the United Kingdom Health and Safety Executive.

7. REFERENCES

[1] B R Bass, C E Pugh, J Keeney Walker, H Schulz and J Sievers, "Final report on phase I of the CSNI multi-national project for fracture analyses of large-scale international Reference Experiments (FALSIRE)", 1992.

[2] A Zahoor, *Ductile fracture handbook*, Vol. 2 and 3, EPRI NP-6301-D, 1990 and 1991, Electric Power Research Institute, Palo Alto, CA.

[3] I Milne et al., "Assessment of the integrity of structures containing defects", *The International Journal of Pressure Vessels and Piping*, Vol. 32, pp3-104.

[4] I Milne et al., "Background to the validation of CEGB Report R/H/R6-Revision 3", *The International Journal of Pressure Vessels and Piping*, Vol. 32, pp105-196.

Table 1 SC-I Heat Treatment & Chemical Composition

Heat Treatment

Austenitise	6 hrs @1065°C
Quench	Water quench from 1065°C
Temper	7hrs @ 590°C +/- 10°C

Chemical Composition : Steelmakers Ladle Analysis

C	Si	Mn	S	P	Cr	Mo	Ni
0.22	0.20	1.32	0.012	0.012	0.08	0.57	0.78

Table 2

SC-1 Tensile Data at 290°C for First Spinning Cylinder Test Material

Spec. Ident.	Prolgn.	Orient.[a]	0.2% Proof Stress $\sigma_{0.2}$ (MPa)	Ultimate Stress σ_u (MPa)	Elongn. (%)[b]	Reduction of Area (%)
HU1	TOP	C	540	728	18	51
HU3	TOP	R	548	709	17	49
HU5	TOP	L	540	703	18	66
HW1	BOTTOM	C	529	702	16	52
HW3	BOTTOM	R	533	703	13	35
HW5	BOTTOM	L	543	711	17	59

[a] C = circumferential

R = radial

L = longitudinal

[b] None of the specimens failed within the middle third of the gage length.

Table 3

SC-I, J vs Δa Values From Unloading Compliance Tests with Physical Measurements of Final Crack Extensions (T = 290°C)

Crack Growth (mm)	J (MJ/m^2)	Crack Growth (mm)	J (MJ/m
Specimen HV1 (Top Ring)		Specimen HV2 (Top Ring)	
0	0.012	0	0.012
0.02	0.047	0.03	0.047
0.08	0.071	0.09	0.071
0.11	0.099	0.16	0.099
0.27	0.13	0.23	0.131
0.43	0.161	0.4	0.164
0.66	0.192	0.72	0.196
0.99	0.227	1.24	0.227
1.9	0.256	2	0.266
2.64	0.292	2.82 (2.44)	0.306
3.62 (3.34)	0.327		
Specimen HV3 (Top Ring)		Specimen HV4 (Top Ring)	
0	0.012	0.55[a]	0.183
0.07	0.047		
0.1	0.068		
0.15	0.087		
0.23	0.108		
0.3	0.134		
0.46	0.161		
0.7	0.19		
1.22	0.216		
1.73	0.243		
2.78 (2.79)	0.277		
Specimen HX1 (Bottom Ring)		Specimen HX2 (Bottom Ring)	
0	0.012	0	0.012
0.05	0.047	-0.01	0.046
0.08	0.072	0.04	0.069
0.15	0.099	0.09	0.098
0.24	0.131	0.23	0.129
0.47	0.162	0.44	0.161
0.77	0.196	0.68	0.195
1.12	0.227	1.43	0.225
2.22	0.258	2.21	0.264
2.88	0.288	2.89	0.302
4.52 (4.32)	0.323	3.92 (3.74)	0.316

[a]Measured final crack growth.

Note: () = measured value.

Table 4

SC-1 Regression Coefficients for Power-Law Curve Fit to J vs Δa Data for First Spinning Cylinder Test Materials[a] (T = 290°C)

Specimen	Coefficients		
	A	B	r^{2b}
HV1	0.213	0,339	0,985
HV2	0.215	0.326	0.996
HV3	0.201	0.356	0.970
HX1	0.207	0.306	0.991
HX2	0.209	0.314	0.990
Composite curve	0.208	0.320	0.976

[a] $J = A(\Delta a)^B$, where units of J and Δa are MJ/m^2 and mm

[b] Square of regression correlation coefficient (r)

Table 5 SC-II Heat Treatment & Chemical Composition

Heat Treatment

Austenitise	6 hrs @1065°C
Quench	Water quench from 1065°C
Temper	7hrs @ 540°C +/- 10°C
Temper	7hrs @ 590°C +/- 10°C

Chemical Composition : Steelmakers Ladle Analysis

C	Si	Mn	S	P	Cr	Mo	Ni
0.21	0.28	1.39	0.009	0.008	0.03	0.53	0.79

Table 6

SC-II Tensile Data for Second Spinning Cylinder Test Material[a]

Young's modulus, E (GPa)	212.35 - 0.0063T
0.2% proof stress, $\sigma_{0.2}$ (MPa)	560.3 exp (-3.356×10^{-4} T)
Ultimate stress, σ_u (MPa)	708.5 exp (-1.889×10^{-4} T)
Poisson's ratio, ν	0.275

[a]Temperature T has units of [°C]

Table 7 SC-II Engineering and True Stress/Strain Values

JU21/JU3 20C

Strain	Stress MPa	True Strain	True Stress MPa
JU21			
.0003	67	.0003	67
.0006	129.4	.0006	129.5
.0009	191.1	.0009	191.3
.0012	252	.0012	252.3
.0015	311.7	.0015	312.2
.0018	371.8	.0018	372.5
JU3			
.0024	503.1	.0024	504.3
.0033	546	.0033	547.8
.0041	551.4	.0041	553.6
.0049	557.1	.0049	559.8
.0070	586.8	.0070	590.9
.0138	615.7	.0137	624.1
.0202	637.4	.0200	650.3
.0261	657.8	.0258	675
.0325	675.3	.0320	697.3
.0389	687.2	.0382	714
.0453	698	.0443	729.6
.0521	707.7	.0508	744.6
.0584	715.6	.0568	757.5
.0652	720.1	.0632	767
.0728	724.4	.0703	777.1
.0800	724.6	.0769	782.5
.0871	728.3	.0835	791.7
.0947	728.7	.0905	797.7

JU22/JU4 20C

Strain	Stress MPa	True Strain	True Stress MPa
JU22			
.0002	50.9	.0002	50.9
.0005	115.3	.0005	115.3
.0008	177.3	.0008	177.4
.0011	237.8	.0011	238.1
.0014	297.9	.0014	298.3
.0017	358.8	.0017	359.4
JU4			
.0021	455.3	.0021	456.3
.0030	548.3	.0030	550.0
.0038	552.9	.0038	555.0
.0046	558.7	.0046	561.3
.0082	598.8	.0082	603.7
.0150	620.5	.0149	629.8
.0217	642.2	.0215	656.2
.0281	662.8	.0277	681.4
.0349	674.9	.0343	698.5
.0417	686.9	.0408	715.5
.0480	699.2	.0469	732.8
.0552	706.9	.0537	746.0
.0624	713.3	.0605	757.8
.0696	715.6	.0672	765.4
.0771	719.7	.0743	775.3
.0847	719.1	.0813	780.0
.0926	719.7	.0886	786.4

JU5 150C *

Strain	Stress MPa	True Strain	True Stress MPa
.0024	456.4	.0024	457.5
.0033	503.1	.0033	504.8
.0041	514.6	.0041	516.7
.0049	523.1	.0049	525.6
.0082	552.9	.0081	557.4
.0142	581.7	.0141	590.0
.0205	602.3	.0203	614.7
.0265	618.8	.0262	635.2
.0325	639.3	.0320	660.1
.0389	650.5	.0382	675.8
.0453	662.7	.0443	692.7
.0516	670.7	.0504	705.3
.0584	675.0	.0568	714.5
.0652	680.4	.0632	724.8
.0720	684.6	.0695	733.9
.0791	688.7	.0762	743.3
.0859	689.7	.0824	748.9
.0935	694.0	.0894	758.9
.1007	688.7	.0959	758.1

JU24/JU6 150C

Strain	Stress MPa	True Strain	True Stress MPa
JU24			
.0003	59.4	.0003	59.4
.0006	115.6	.0006	115.7
.0009	173.5	.0009	173.6
.0012	231.7	.0012	232.0
.0015	286.0	.0015	286.5
.0018	338.9	.0018	339.5
JU6			
.0024	466.5	.0024	467.6
.0033	504.2	.0033	505.9
.0041	517.7	.0041	519.8
.0049	526.6	.0049	529.2
.0101	558.0	.0101	563.6
.0167	576.7	.0166	586.3
.0229	603.1	.0227	617.0
.0291	619.9	.0287	637.9
.0357	632.4	.0351	655.0
.0423	646.2	.0415	673.6
.0485	656.1	.0474	687.9
.0551	665.8	.0537	702.5
.0621	674.2	.0603	716.1
.0692	678.4	.0669	725.3
.0766	681.1	.0738	733.3
.0836	685.3	.0803	742.6
.0910	687.5	.0871	750.1
.0989	686.7	.0943	754.6
.1051	690.3	.0999	762.8

Table 7 SC-II Engineering and True Stress/Strain Values

JU25/JU7 350C

Strain	Stress MPa	True Strain	True Stress MPa
JU25			
.0000	8.1	.0000	8.1
.0003	59.2	.0003	59.3
.0006	113.1	.0006	113.1
.0009	169.2	.0009	169.4
.0012	226.5	.0012	226.8
.0015	283.1	.0015	283.5
.0018	338.1	.0018	338.7
JU7			
.0024	431.5	.0024	432.6
.0033	480.8	.0033	482.4
.0041	507.3	.0041	509.4
.0049	524.2	.0049	526.8
.0130	559.9	.0129	567.1
.0193	588.4	.0191	599.8
.0265	608.8	.0262	624.9
.0357	627.2	.0350	649.5
.0444	642.1	.0435	670.6
.0532	653.9	.0518	688.7
.0731	660.3	.0705	708.5
.0930	665.8	.0889	727.8

JU14 350C *

Strain	Stress MPa	True Strain	True Stress MPa
.0029	470.2	.0029	471.6
.0037	498.9	.0037	500.8
.0045	517.7	.0045	520.0
.0102	548.7	.0101	554.3
.0157	574.7	.0156	583.8
.0221	597.9	.0219	611.2
.0289	614.3	.0285	632.1
.0353	634.2	.0347	656.6
.0416	643.0	.0408	669.8
.0484	651.2	.0473	682.7
.0556	655.3	.0541	691.7
.0627	660.7	.0609	702.2
.0703	663.5	.0679	710.1
.0779	667.5	.0750	719.5
.0858	669.5	.0823	726.9
.0942	668.9	.0900	731.9

Note: (1) Data up to strains of 0.2% taken from small specimens, data from 0.2% to 10.0% taken from large specimens.

(2) Elastic data for JU24/JU6 exhibits a discontinuity. This will lead to some errors in E values determined from this data.

* Small specimen data omitted - alignment errors.

Table 8

SC-II Physical Properties for Second Spinning Cylinder Test Material

Heat convection coefficient, $h(W/m^2K)$	22750 (during time relevant to crack growth)
Thermal conductivity, $\lambda(W/m^2K)$	$38.6 - 2.2 \times 10^{-2} T + 1.67 \times 10^{-5} T^2$
Specific heat capacity, $c_p(kJ/kg\ K)$	$4.1 \times 10^{-4} T + 0.432$
Density, $\rho(kg/m^3)$	7757 at 290°C
Coefficient of thermal expansion, $\alpha(1/K)$	Instantaneous: $(11.46 + 0.0105T) \times 10^{-6}$ Mean (20-T): $(11.59 + 5.161 \times 10^{-3} T) \times 10^{-6}$ where T is temperature in °C

Table 9 SC-II J - Δa Values from unloading compliance and physical measurements of final crack extension.

JT1 Btm. 290C

Δa mm	J MJm-2
0.03	0.100
0.09	0.135
0.19	0.173
0.34	0.216
0.55(P_{max})	0.264
0.86	0.314
1.49	0.364
2.10	0.409
2.98*	0.437
3.67	0.473
5.44*	0.493
6.34*(6.23)	0.518

JT3 Btm. 290C

Δa mm	J MJm-2
0.00	0.040
0.08	0.069
0.11	0.102
0.24	0.138
0.33	0.176
0.57(P_{max})	0.216
0.74	0.257
1.21	0.291
1.35*	0.33
2.54*	0.373
3.73	0.406
4.27	0.436
4.66	0.467
5.92(5.72)	0.487

JT4 Mid. 150C

Δa mm	J MJm-2
0.01	0.019
0.01	0.032
0.03	0.049
0.09	0.068
0.16	0.085
0.16	0.113
0.23	0.136
0.28	0.162
0.37	0.193
0.54	0.228
0.73	0.258
0.95	0.294
1.19	0.329
1.58	0.363
1.98	0.395
2.57	0.425
3.16	0.450
3.61	0.473
4.09(4.04)	0.501

JT5 Mid. 150C

Δa mm	J MJm-2
0.03	0.019
0.03	0.032
0.03	0.049
0.09	0.068
0.13	0.099
0.21	0.134
0.32	0.173
0.46	0.212
0.69	0.249
0.96	0.287
1.24	0.321
1.52	0.362
1.95	0.394
2.23	0.428
2.66	0.459
3.21	0.491
3.81(3.27)	0.511

( ) 9pt average measured values

Table 9 SC-II J - Δa Values from unloading compliance and physical measurements of final crack extension.

JT7 Mid. 290C

Δa mm	J MJm-2
0.08	0.090
0.12	0.126
0.26	0.168
0.40	0.213
0.65	0.265
0.90(P_{max})	0.317
1.73*	0.371
2.71*	0.414
3.22	0.459
3.85	0.493
4.52	0.524
** (5.79)	0.568

** Last unloading line not recorded

JT8 Mid. 290C

Δa mm	J MJm-2
0.01	0.050
0.02	0.071
0.03	0.092
0.11	0.114
0.24	0.151
0.35	0.191
0.49	0.233
0.79(P_{max})	0.275
1.11	0.313
1.60	0.351
2.22	0.391
2.76	0.429
3.48	0.463
4.33	0.496
5.64*(5.58)	0.521

JT10 Top 290C

Δa mm	J MJm-2
0.04	0.023
0.04	0.040
0.02	0.058
0.05	0.080
0.06	0.105
0.10	0.130
0.22	0.157
0.33	0.188
0.58(P_{max})	0.225
0.86*	0.264
1.75*	0.302
2.36*	0.335
3.36*	0.360
4.65*	0.384
5.51*	0.404
6.31*	0.553
6.88*(6.71)	0.534

JT11 TOP 290C

Δa mm	J MJm-2
0.02	0.041
0.03	0.060
0.06	0.082
0.11	0.105
0.20	0.131
0.37	0.161
0.56	0.195
0.84	0.231
1.07	0.270
1.31(P_{max})	0.313
2.58*	0.350
3.60*	0.374
5.25*	0.403
5.93	0.434
6.70*(6.23)	0.461

( ) 9pt average measured values

* Plastic Instability

Table 10 SC-II Regression Coefficients in the expression $J = A(\Delta a)^B$

Specimen	Temp	Ring	Individual Coefficients A	B	r^2	Composite Coefficients A	B	r^2
JT1	290	Bim	0.317	0.320	0.991	0.285	0.363	0.914
JT3	290	Bim	0.265	0.376	0.968			
JT4	150	Mid	0.286	0.429	0.985	0.289	0.442	0.989
JT5	150	Mid	0.291	0.458	0.996			
JT7	290	Mid	0.300	0.375	0.981	0.294	0.384	0.983
JT8	290	Mid	0.289	0.392	0.988			
JT10	290	Top	0.259	0.323	0.984	0.253	0.343	0.954
JT11	290	Top	0.248	0.385	0.969			

Notes (1) J has units (MJm^{-2}) and Δa has units (mm).
(2) Power curves performed using data within the limits $0.2mm \leq \Delta a \leq 4.5mm$ only.

TABLE 11
Summary of Project FALSIRE analysis techniques used to assess SC-I & SC-II [1]

SC-I/II (7 analyses)
FE; JR
FE; JR
A1; FE
WF;FE
ES;J/T
A2
ES;R6/1

FE = Finite element method
ES = Estimation Scheme
A1 = Analytical Solution with Numerical Intergration
A2 = Handbook Analysis of Statically Indeterminate Model
JR = R-Curve Approach
J/T = J/Tearing Modulus Approach
R6/1 = R6 Method/Option 1
WF = Weight Function Method

TABLE 12
Summary of finite element applications to analysis of Spinning Cylinder Tests 1 and 2 within Project FALSIRE [1]

Experiment	Analysis Number	Finite Element Program	Model Dimension	Number of Equations	Material Plasticity model	Stress-Strain Relation	Intergration Rule	Equilibrium Iteration Method	Fracture Method
Spinning Cylinder I	17	ABACUS	2-D (Plane Strain)	N/A	Von Mises, elastic-plastic, isotropic hardening	Multilinear	N/A	N/A	J_R-curve
	9	VISCRACK	2-D (Plane Strain)	N/A	Von Mises, elastic-plastic, isotropic hardening	Multilinear	N/A	N/A	J_R-curve
	8	ADINA	2-D (Plane Strain)	N/A	Von Mises, elastic-plastic, isotropic hardening	Multilinear	2x2/ 3x3	BFGS with line search	J_R-curve
Spinning Cylinder II	17	ABACUS	3-D	~3800	Von Mises, isotropic hardening, thermo elastic-plastic	N/A	N/A	N/A	J_R-curve
	8	ADINA	2-D (Plane Strain)	N/A	Von Mises, isotropic hardening, thermo elastic-plastic	Bilinear	2x2/ 3x3	BFGS with line search	J_R-curve
	11	ABACUS	2-D (Plane Strain)	890	Linear thermo-elastic	N/A	N/A	N/A	J_R-curve*
	16	ADINA	2-D (Axisym)	329	Linear thermo-elastic	N/A	N/A	N/A	J_R-curve

* Crack not modeled; K_I from VTTSIF program,
N/A = not available or not applicable
BFGS = Broyden-Fletcher-Goldfarb-Shanno

Table 13. Summary of estimation scheme applications to analysis of Spinning Cylinder Tests 1 and 2

Experiment	Analysis No.	Stress analysis methodology	Fracture methodology
SC-I	12	Analytic solution for hoop stress distribution in rotating cylinder	J_R curve; J from handbook
	14	Statically indeterminate solution for circumferential force and bending moment on end surface of cracked cylindrical shell	J_R curve; J from elastic and fully plastic solutions
	16	Analytic solution for hoop stress distribution in rotating cylinder	J_R curve; J from weight function method
SC-II	12	Superposition of closed form solutions for stress caused by pressure and thermal loading	J_R curve; J from handbook
	13	Thermal stresses calculated analytically for LOTUS 1,2,3	R6, Option 1
	14	Statically indeterminate solutions for circumferential force and bending moment on end surface of cracked cylindrical shell	J_R curve; J from elastic and fully plastic solutions
	11	Analytic solution for stress in a cylinder subjected to thermal gradient loading	J_R curve; J from influence functions
	16	Analytic and finite-element solutions for stress in a cylinder subjected to thermal gradient loading	J_R curve; J from weight function method

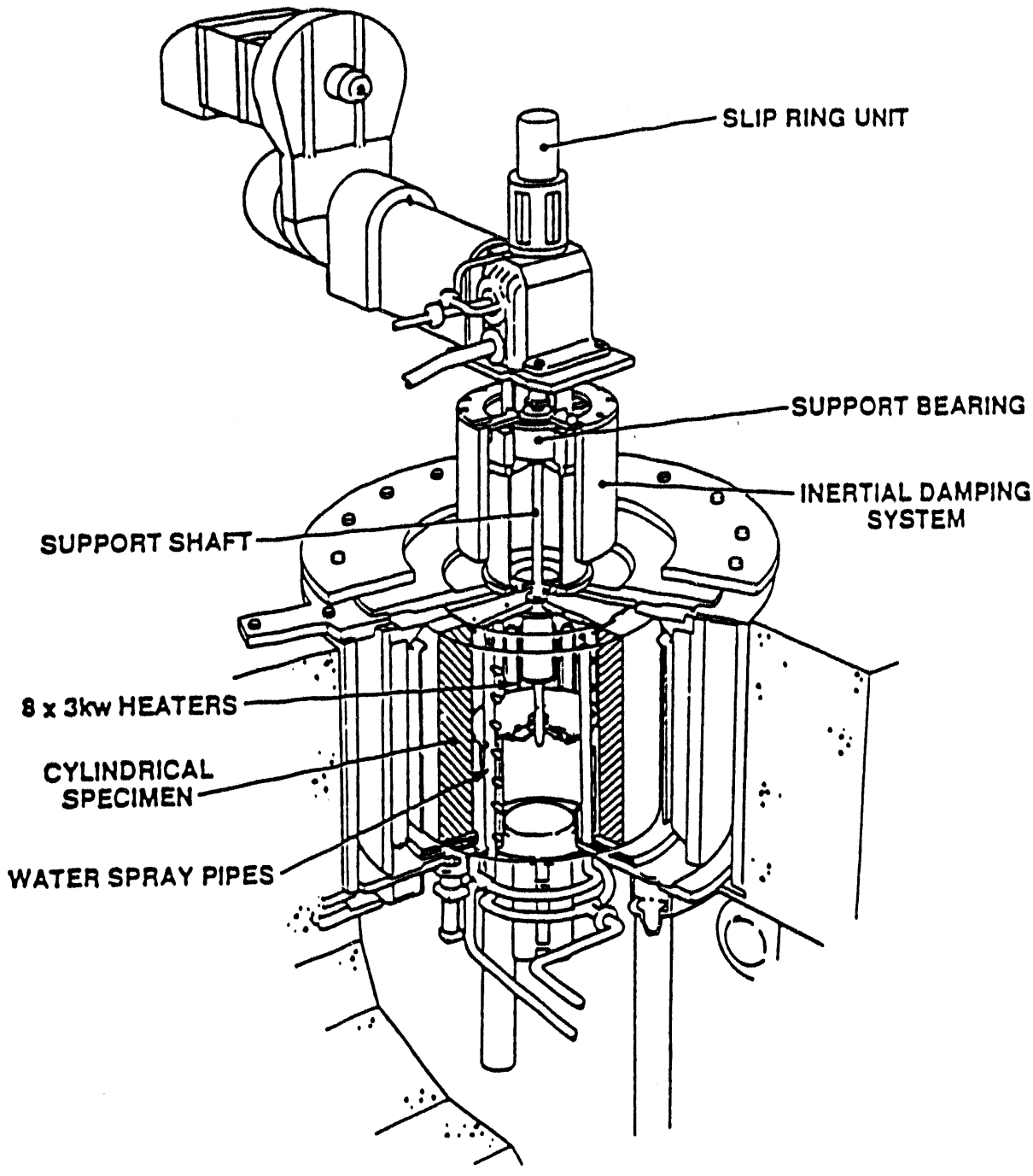

Fig. 1 The Spinning Cylinder Test Facility

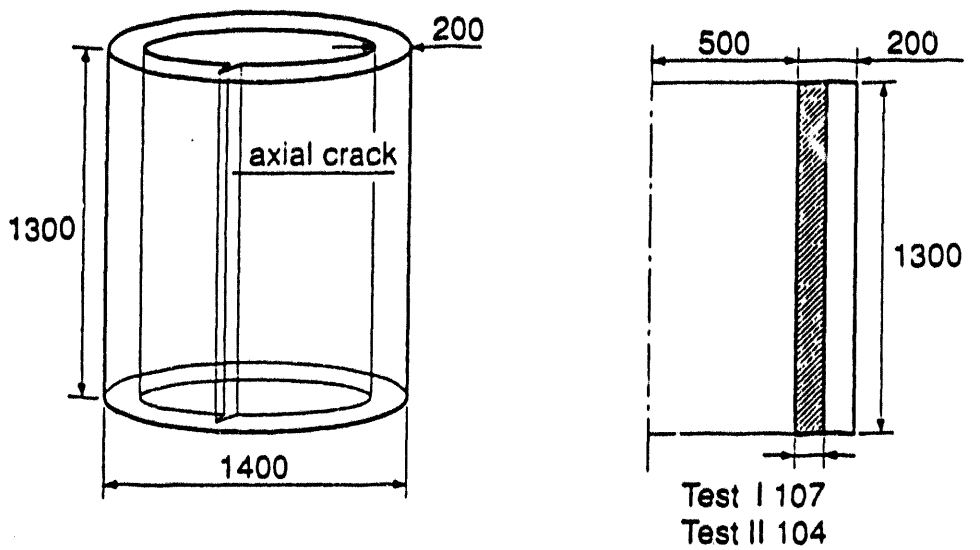

All measures in mm

Fig. 2 SC-I , SC-II Test Cylinder and crack geometries

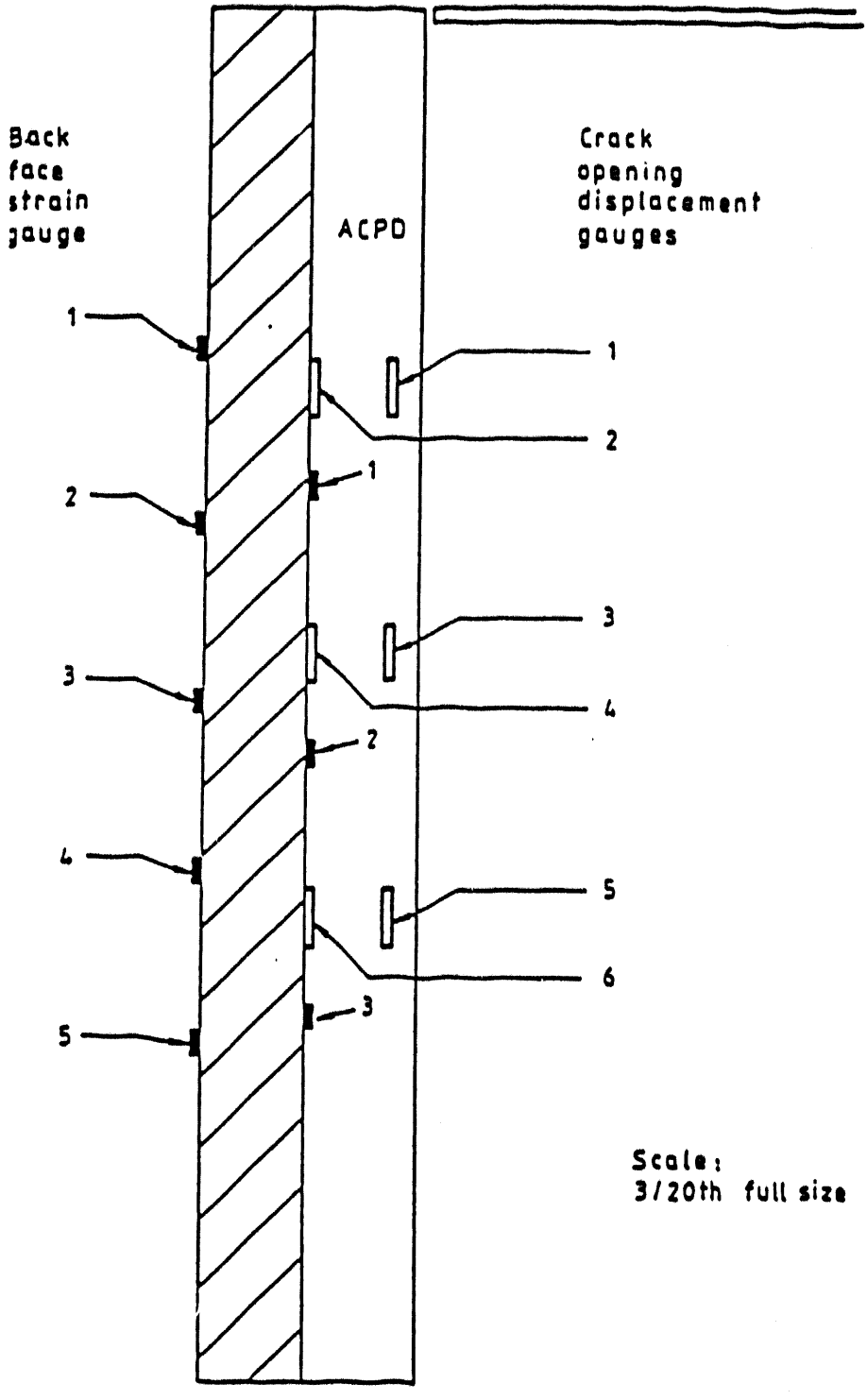

Fig. 3 SC-I, Instrumentation layout for the first spinning cylinder experiment

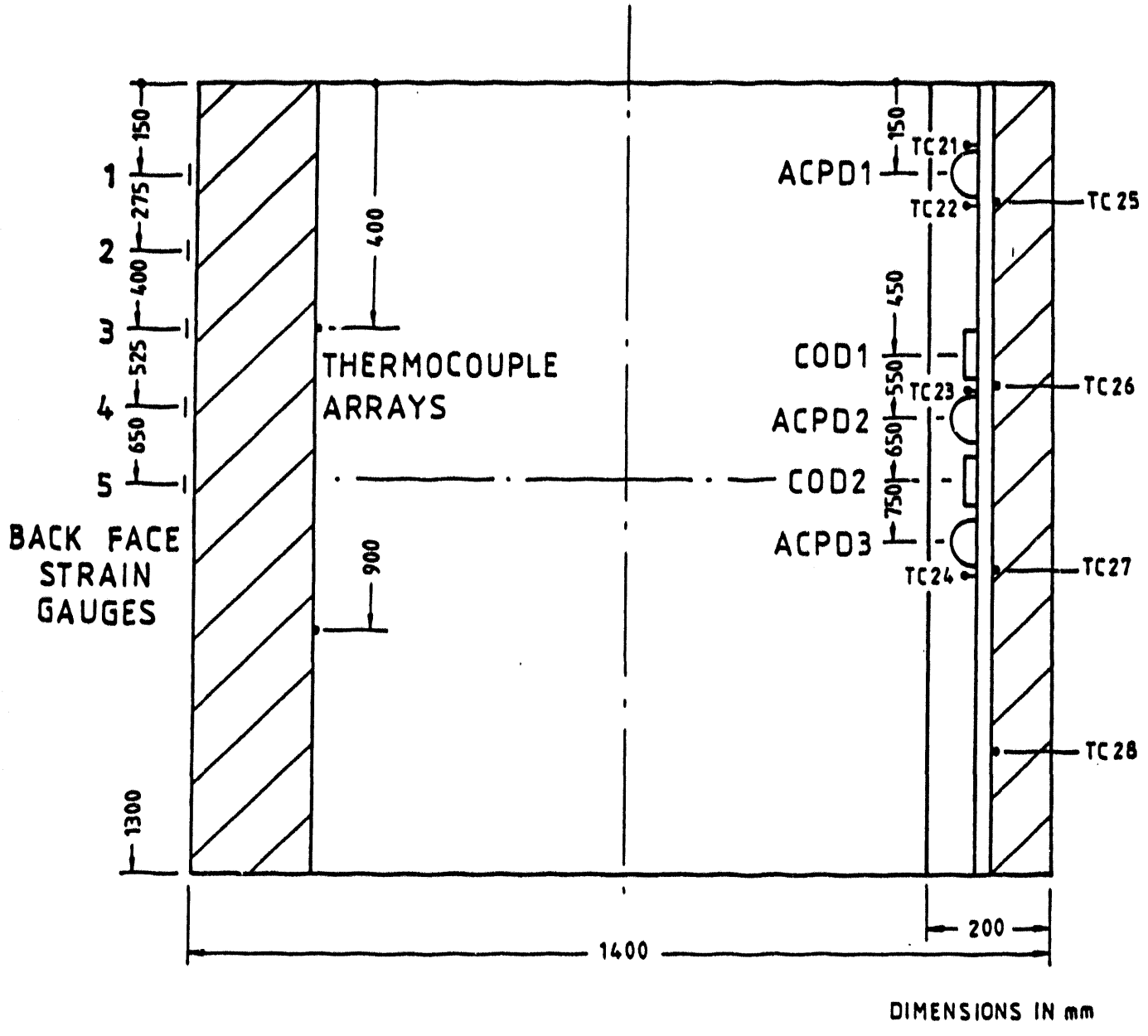

Fig. 4 SC-II, Instrumentation layout for the second spinning cylinder experiment

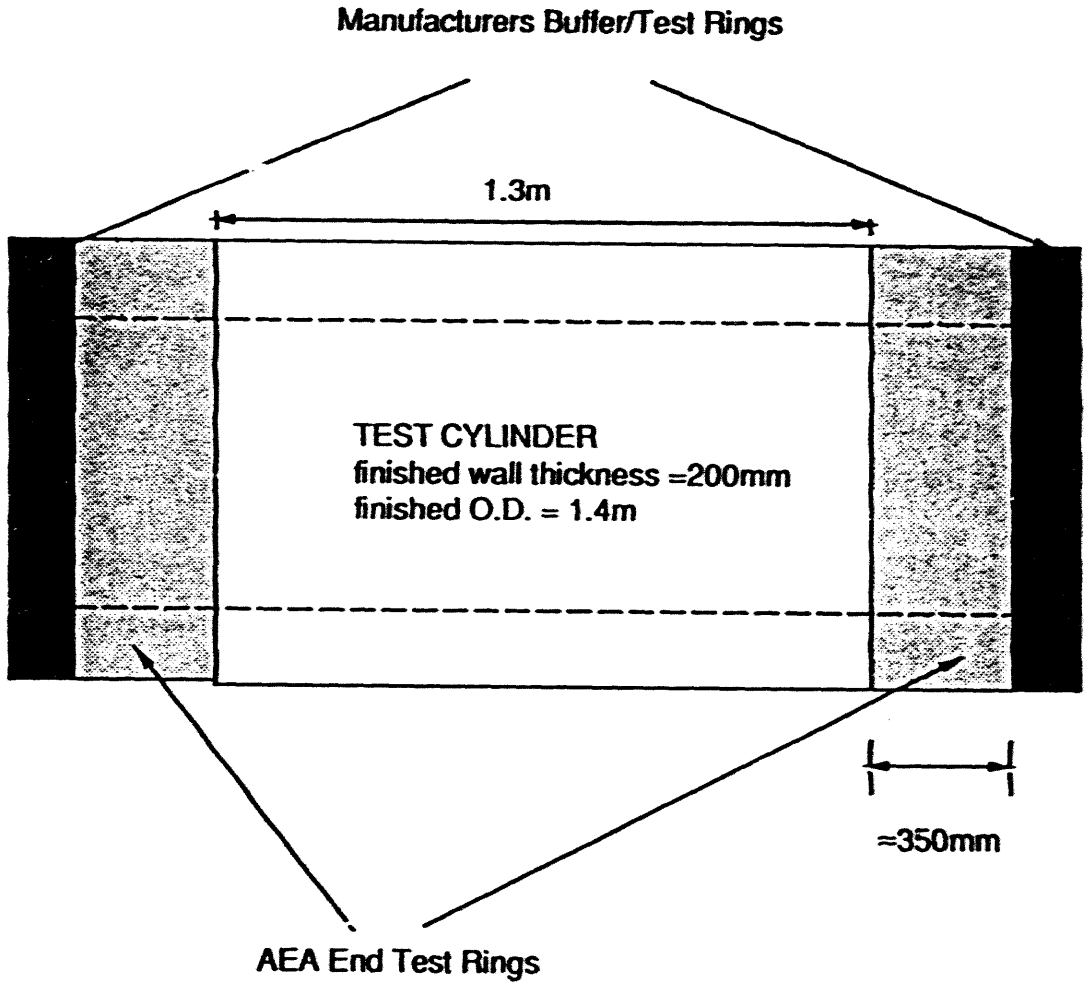

Fig. 5 Location of SC-I Test Cylinder within the large-scale forging

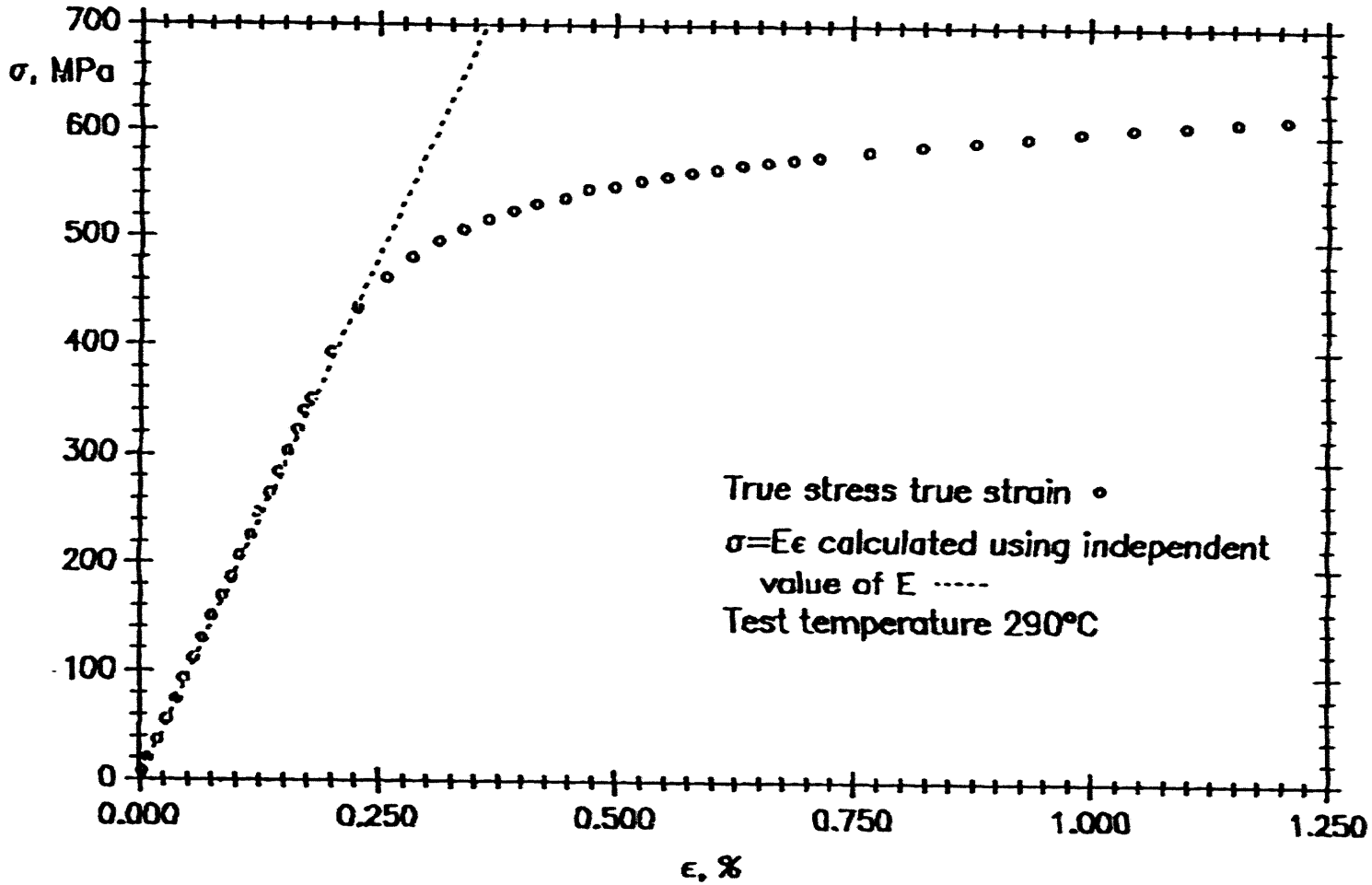

Fig. 6 SC-I, representative stress-strain data for the first spinning cylinder test specimen.

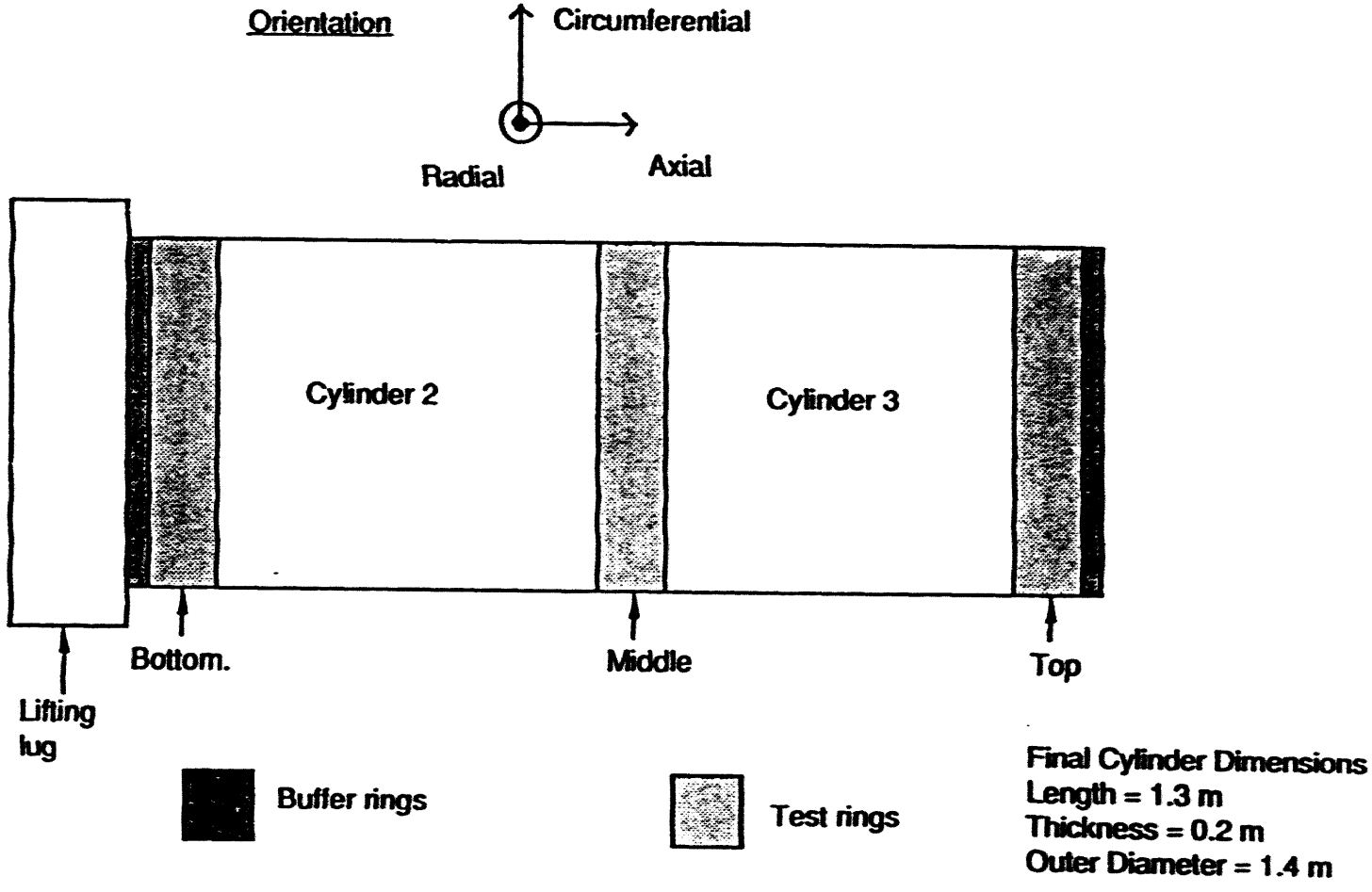

Fig. 7 Location of SC-II Test Cylinder within the large-scale forging

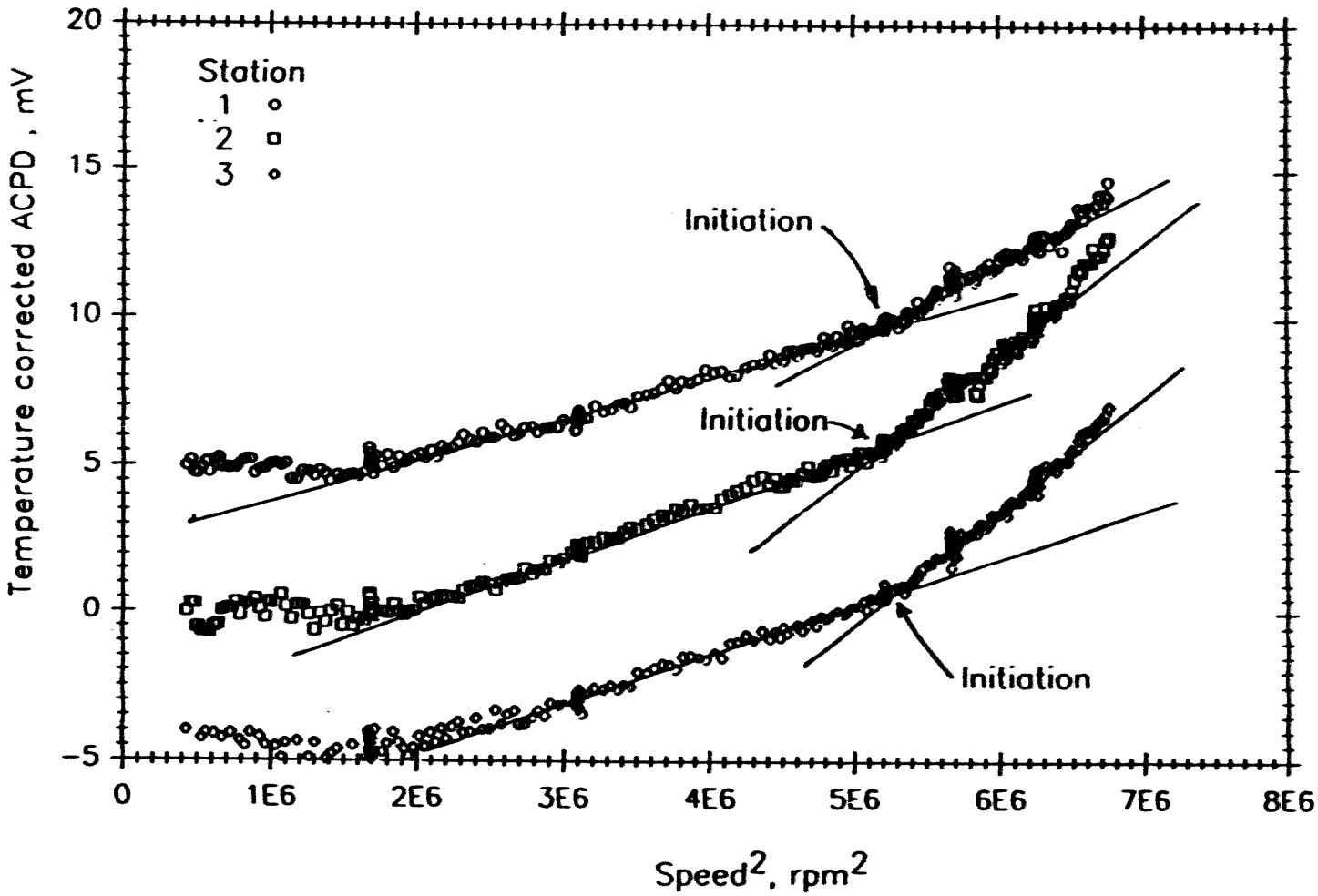

Fig. 8 SC-I, identification of initiation from alternating current potential drop (ACPD)

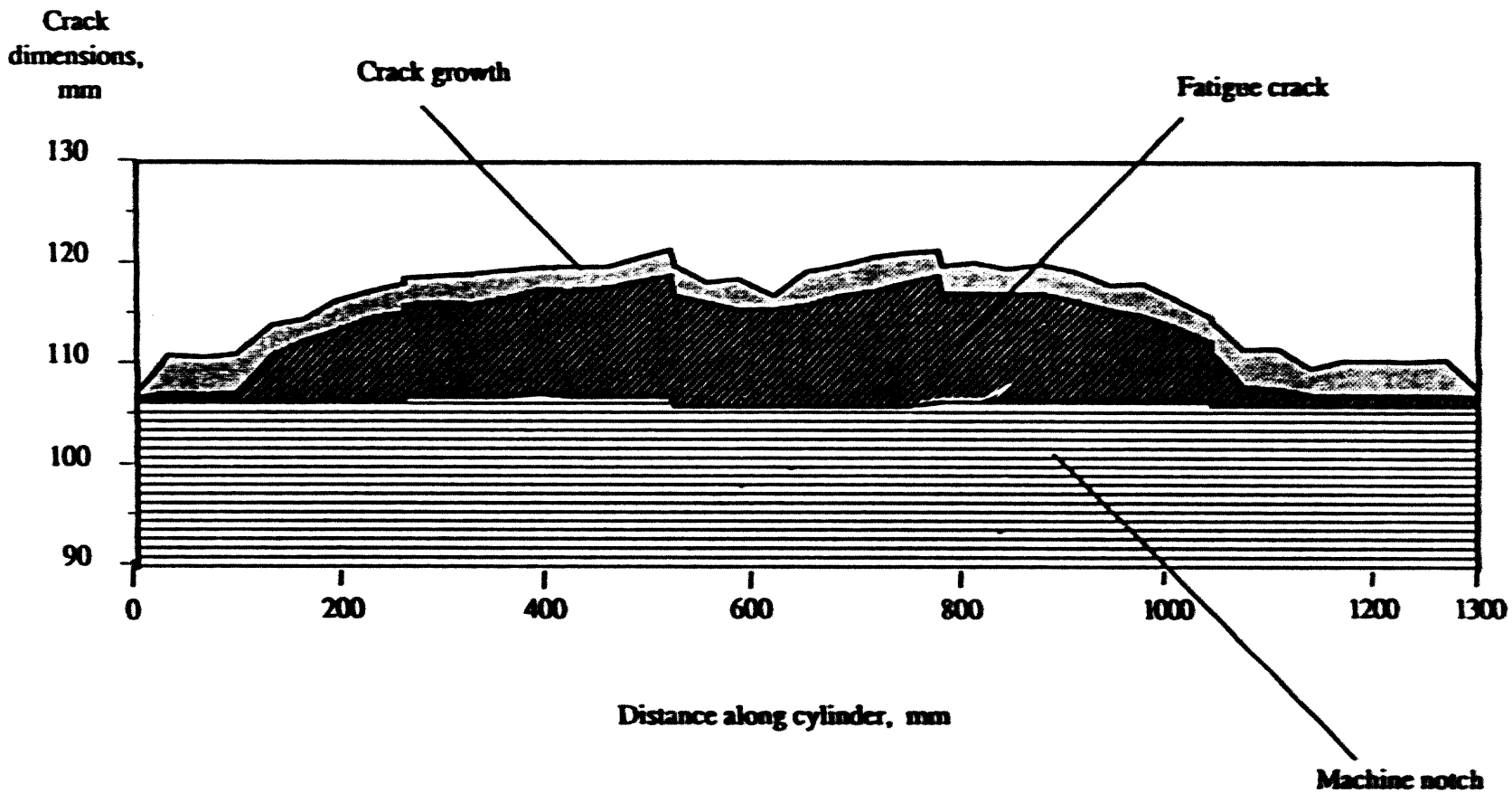

Fig. 9 SC-I, Crack Profile

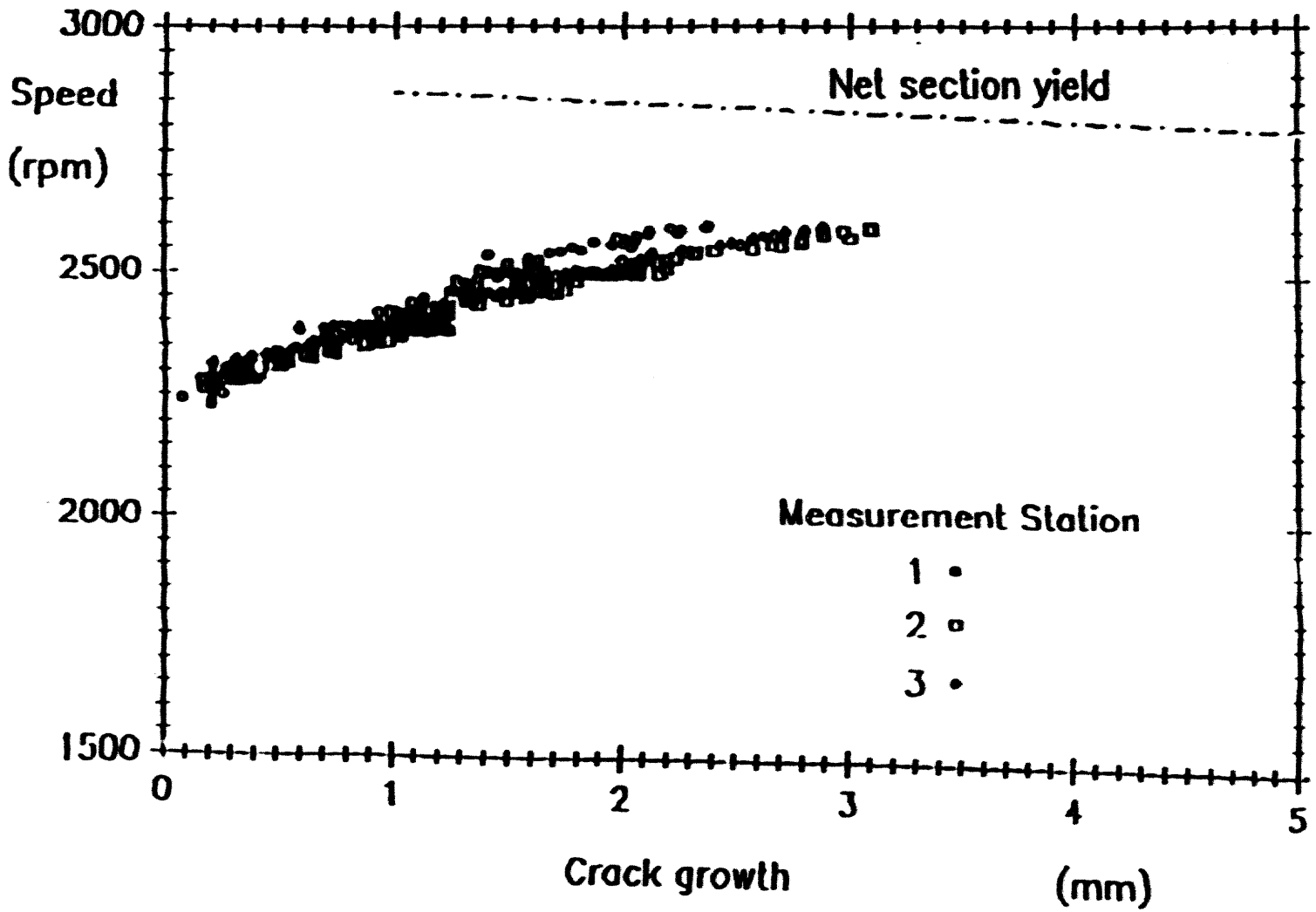

Fig. 10 SC-I, angular velocity vs. crack growth data from three ACPD measurement stations

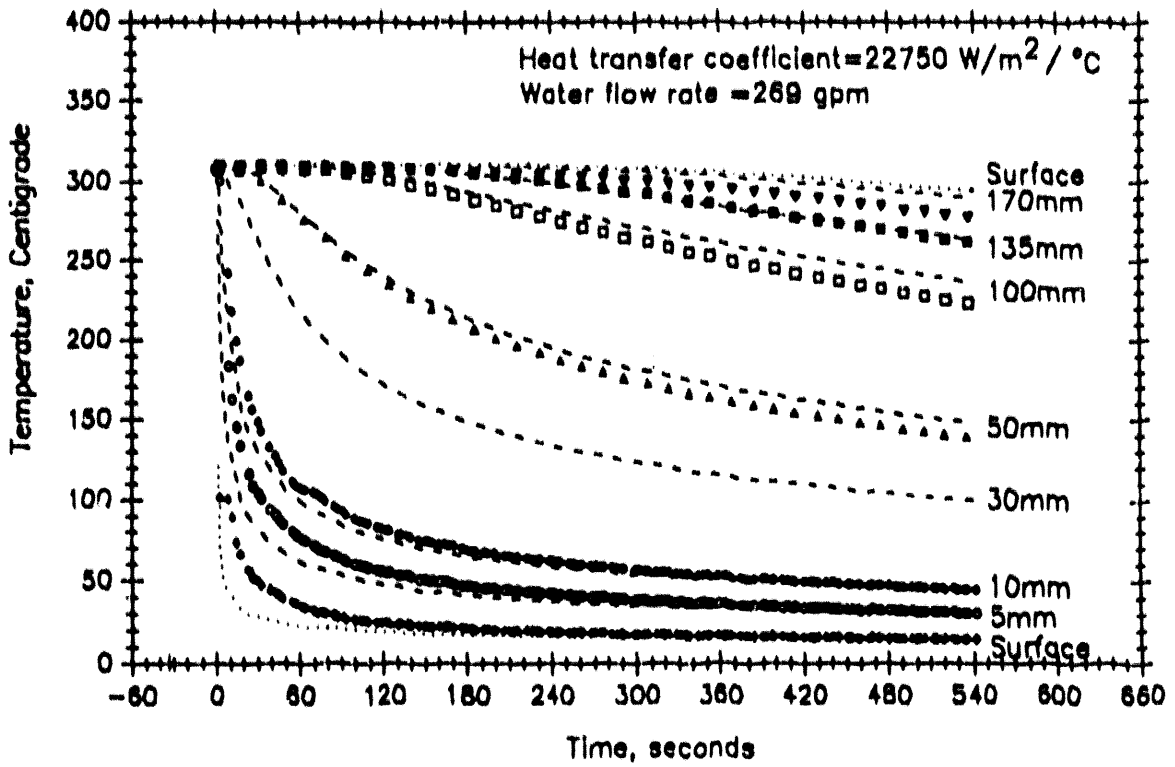

Fig. 11 SC-II,comparison of measured and computed temperature histories for the second spinning cylinder test (upper thermocouple array).

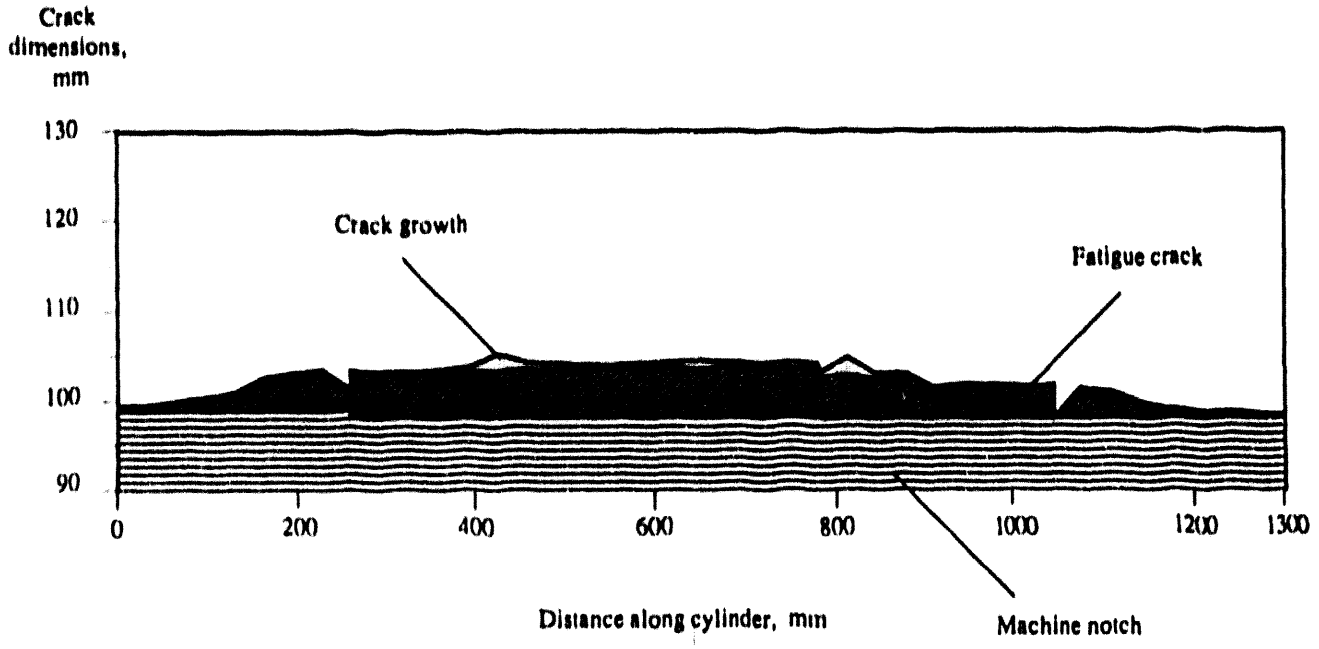

Fig. 12 SC-II, Crack Profile

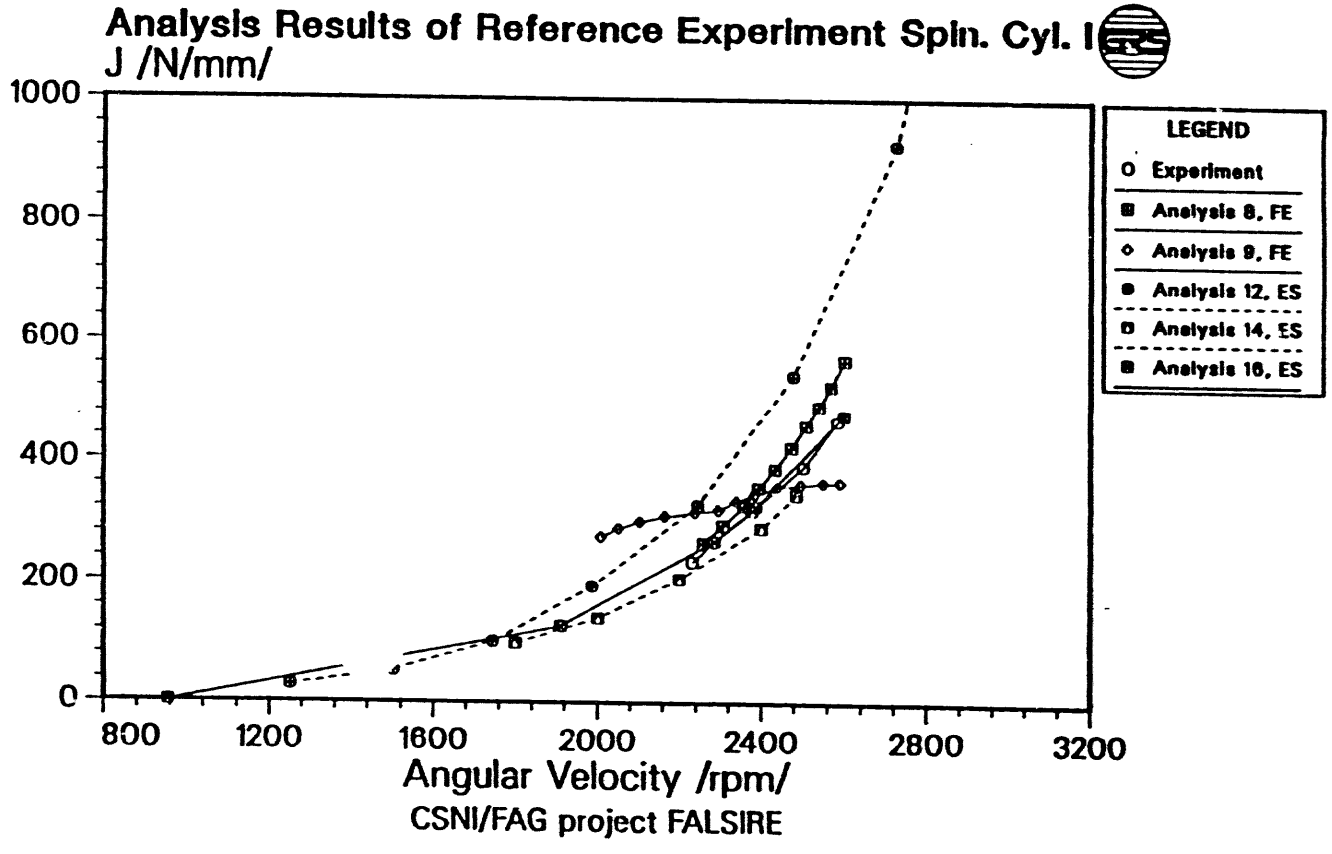

Fig. 13 SC-I, FALSIRE predictions of J-integral vs. angular velocity.

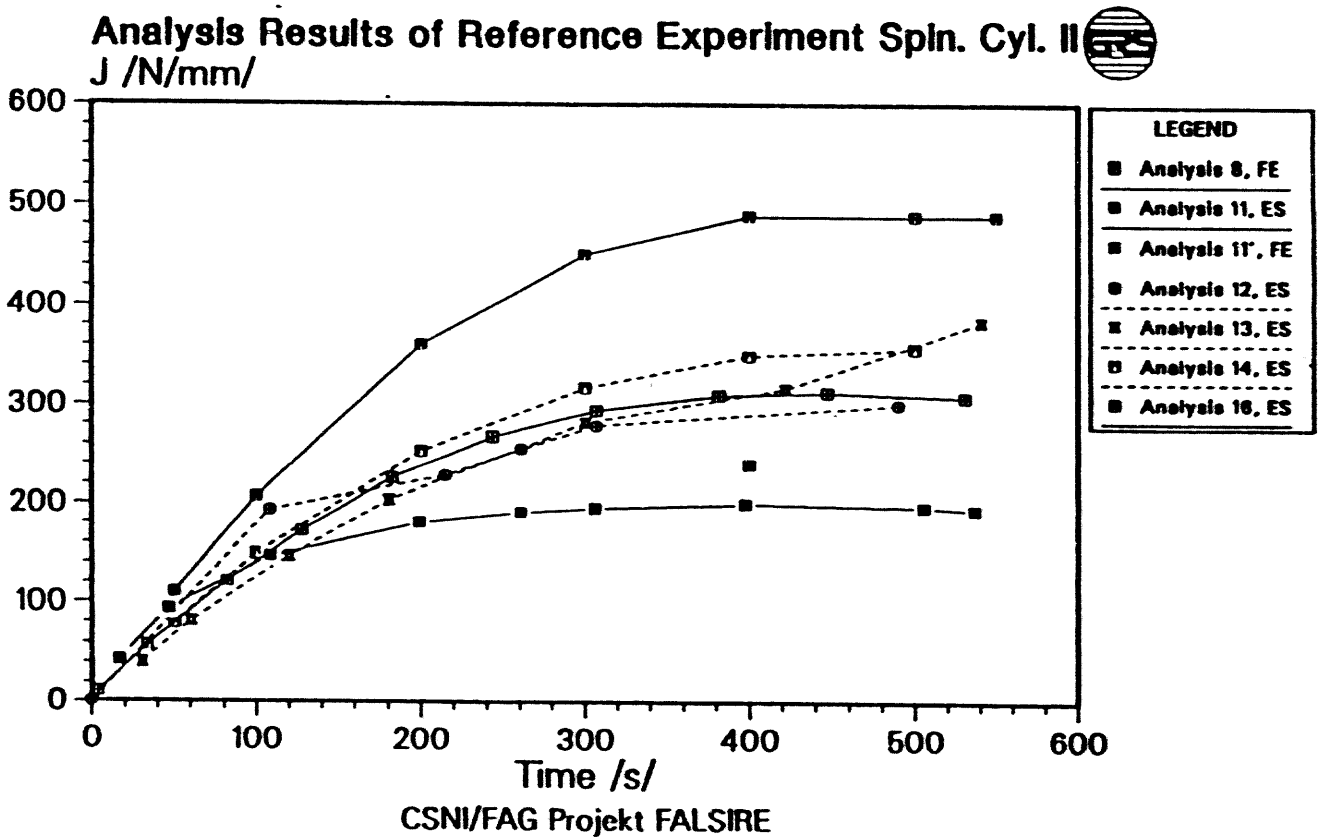

Fig. 14 SC-II, FALSIRE predictions of J-integral vs.time.

FIRST SPINNING CYLINDER TEST ANALYSIS BY USING LOCAL APPROACH TO FRACTURE

C. ERIPRET, G. ROUSSELIER

**Electricité de France (EDF), Service Réacteurs Nucléaires et Echangeurs (RNE),
Les Renardières,BP 1, 77250 Moret s/Loing , FRANCE.**

ABSTRACT

In recent years, several experimental programs on large scale specimens were organized to evaluate capabilities of the fracture mechanics concepts employed in structural integrity assessment of PWR pressure vessels. During the first spinning cylinder test, a geometry effect was experimentally pointed out and exhibited the problem of transferability of toughness data from small scale to large scale specimens. An original analysis of this test, by means of local approach to fracture is presented in this paper. Both compact tension specimen and spinning cylinder fracture behaviour were computed by using a continuum damage mechanics model developped at EDF. We confirmed by numerical analysis that the cylinder's resistance to ductile tearing was considerably larger than in small scale fracture mechanics specimens tests, about 50 percent. The final crack growth predicted by the model was close to the experimental value. Discrepancies in J-R curves seemed to be due to an effect of stress triaxiality and plastic zone evolution. The geometry effect inducing differences in resistance to ductile tearing of the material involved in the specimens can be investigated and explained by using local approach to fracture methodology.

INTRODUCTION

In recent years, several experimental programs on large scale specimens were organized to evaluate capabilities of the fracture mechanics concepts employed in structural integrity assessment of PWR pressure vessels [1,2,3,4]. Most of them aimed at investigate the upper shelf toughness fracture behaviour of low alloyed steels, and to assess the validity of the J-integral and J-resistance curve concepts regarding to ductile crack propagation.

Thus, it is now universally accepted that toughness may depend on thickness, loading patterns, degree of triaxiality, and geometry of the structure. The J-R curve concept was shown not to be an intrinsic characteritic of the material properties, but may vary in some circumstances.

It is, therefore, very important to identify the different factors that can make this toughness changing, and to quantify their influence. The following underlying questions should be posed :

- Is the J-R curve a representative measure of tearing toughness when crack propagation occured ?

- Is it possible to transfer the J-R curve provided from laboratory specimens tests to an other geometry or configuration ?

This paper doesn't fully answer to the questions mentionned above, but still highlights the importance of the problem and proposes an explanation to the geometry effect pointed out in the first spinning cylinder experiment. An interesting analysis performed by using a local approach to fracture methodology showed the influence of the near crack tip stress and strain fields on the fracture behaviour of steels, and explained the geometry effect observed.

THE FIRST SPINNING CYLINDER EXPERIMENT

The first spinning cylinder test, performed by Northern Research Laboratories, involved the rotation of a 200 mm thick cylinder containing a full length axial flaw to an angular speed of 2600 rpm at the temperature of 290°C [1]. This test aimed at generating ductile crack growth by increasing progressively the rotational speed, that created a membrane hoop stress loading across the thickness.

The first objective of this test was to provide experimental data that would permit the construction of a J-resistance curve. This has been achieved by using the measurement of an alternating current drop potential to determine the crack growth, and by performing a finite element analysis in order to associate to each rotational speed a corresponding value of J-integral.

In addition, a J-R curve was also derived from experimental results corresponding to small scale compact tension specimens tests and proved considerably lower J-values than the cylinder's J-resistance curve (figure 1). A geometry effect (scale, load, or size effect ?), was experimentally pointed out and exhibited the problem of transferability of toughness data from small scale to large scale specimens.

ANALYSIS BY LOCAL APPROACH METHODOLOGY

An original analysis of this test, by means of local approach to fracture is presented in this paper.

The model used in this paper refers to the generalised standard material constitutive relations [5], and enables to model material tearing and crack propagation whithout using any numerical technique such as node release. The main advantage of this approach is to assess the crack initiation and growth by using criteria derived from the near crack tip stress and strain fields (local values), which control the material damage. The evolution of the damage is governed by the competition of material hardening and softening. These effects are included in the constitutive relations by modifying the expression of the plastic potential as follows :

$$F = F_{hardening} + F_{damage} = \frac{\sigma_{eq}}{\rho} - R(p) + DB(\beta) \exp\left(\frac{\sigma_m}{\rho\, \sigma_1}\right)$$

$$\text{where} \quad \sigma_{eq} = \left(\frac{3}{2}\, \sigma_{ij}\, \sigma_{ij}\right)^{1/2} \quad \text{and} \quad \sigma_m = \frac{1}{3}\,(\sigma_{ii})$$

The constitutive relations are derived from F, and from the yield criterion F=0, through the help of the normality rule. In this expression, D and σ_1 are constants, p is the hardening variable, and β the damage variable. Material hardening is assumed to be isotropic, as well as damage. The second term R(p) represents the true stress - true strain curve of the material, and function $B(\beta)$ is equal to

$$B(\beta) = \frac{\sigma_1\, f_0 \exp \beta}{1 - f_0 + f_0 \exp \beta}$$

where f_0 is also a scalar that defines the initial volume fraction of cavities. Material softening caused by cavities growth is taken into account through the third term F_{damage}, which competes with the hardening part $F_{hardening}$.

As loading is increasing, the plastification effects make the cavities growing, and damaging the material. When the damage becomes important, softening of the material takes place and the stress strain relation is going down (figure 2). The material resistance becomes lower and lower, until the failure occurs.

From the calculation results, we can determine the instants at which the crack growth initiates, as well as the position of the crack tip during the propagation when the opening stress reach a maximum just before collapsing (figure 3). The first maximum observed defines the crack initiation, the second one occurs when the first element fails, the third maximum defines the failure of the second element, an so on... [6].

Then, combining numerical results and J-contour integral calculation provides a numerical J-R curve characteristic of the structure behaviour regarding to ductile tearing.

Using Rousselier's model, one needs to identify the three parameters that control the fracture behaviour :

- the cavities initial volume fraction f_0,
- the metallic matrix stiffness σ_1,
- and the characteristic length lc of the finite elements.

Usually, f_0 is estimated from the chemical composition of the material [7]. In fact, manganese sulfides inclusions play an essential role in the cavities growth and we can directly relate the initial volume fraction of cavities f_v with the percentage of Mn and S elements through the Franklin's formula :

$$f_0 = f_v = 0.054 \, (S \, \% - 0.001 / Mn \, \%)$$

The second parameter σ_1 may be estimated from the flow stress value but this gives a poor evaluation of it. In practice, mechanical testing is necessary to calibrate σ_1 [7]. The basic specimens used for it are axisymmetric notched tension specimens, for which the calibration procedure is depicted in figure 4. However, we couldn't follow the same procedure in this study, because we got neither coupons of material in which machining the notched specimens, nor experimental results (provided from axisymmetrcal notched specimen tension tests) to be compared to numerical computations.

Thus, calibration was made with help of results provided from Compact Tension specimens, and the model's parameters were determined so that calculated J-R curve (determined from CT specimen test simulation) fit the experimental one. The two curves, which are in a good agreement, are plotted on figure 5.

The mechanical properties were issued from [1] as well as the chemical composition of the material (table 1).

The parameters were found to be equal to :

$f_0 = 6.10^{-4}$, $\sigma_1 = 350$ MPa , and $l_c = 0.55$ mm

Then, a two-dimensionnal finite element computation was performed to analyse the fracture behaviour of the spinning cylinder. Obviously, the same parameters of the Rousselier's model were used to make this computation. The same size of element was kept to mesh the crack tip area, according to [6]. This condition ensures the crack propagation speed in the CT specimen and in the cylinder will be close.

As our finite element code did not enable to account for body forces, we replaced the rotation load by internal pressure that provided an equivalent hoop stress profile for an uncracked structure [8](at most 3.6 percent error at inner surface).

However, these loadings are not equivalent regarding to the radial stresses : the contraction due to pressure is very different from the contraction caused by spinning. This difference may influence

the stress and strain fields in the vicinity of the crack, and also the damage's evolution. The influence of the radial stress on ductile tearing will have to be clarified in further studies.

The equivalence between loadings provided from pressure or rotational speed is given by this expression [10]:

$$\sigma_{Pm} = \sigma_{\omega m} \Longrightarrow P = f(\omega) = \rho \frac{\omega^2}{3} \frac{(R_0^2 + R_i^2 + R_0 R_i)(R_0 - R_i)}{R_i}$$

where σPm and σωm are the average values of the hoop stress through the thickness generated respectively by internal pressure and by rotational speed :

$$\sigma_{Pm} = \int_{R_i}^{R_0} \frac{\sigma_{\theta\theta}(P)}{R_0 - R_i} dR \qquad \sigma_{\omega m} = \int_{R_i}^{R_0} \frac{\sigma_{\theta\theta}(\omega)}{R_0 - R_i} dR$$

We performed the numerical simulation of the behaviour of the cracked cylinder under internal pressure and translated results of both crack propagation and J-integral into values depending on rotational speed.

Then, the J-R curve numerically obtained is presented in figure 6, and compared with the J-R curve derived from CT specimens testing. We confirmed by numerical analysis that the cylinder's resistance to ductile tearing was considerably larger than in small scale fracture mechanics specimens tests, about 50 percent. The final crack growth (about 2.5 mm) obtained at 260(rpm (corresponding to an internal pressure of 85 MPa) was close to the experimental value (2.75 mm). Scatter in J-R curves seemed to be due to an effect of stress triaxiality and plastic zone evolution, which are very different in the two situations. It should be noted that we call stress triaxiality the ratio σ_m/σ_{eq}.

The CT specimen tests involved a quasi-pure bending loading of the structure, which is totally different to withstand than a membrane loading as generated by internal pressure or spinning.

This loading effect can be responsible for changing the J-resistance curve level, at initiation point as well as during crack propagation. The stress triaxiality around the crack tip is larger in the CT specimen than in the hollow structure (figure 7). Then, the material damage will increase earlier in the crack tip area of a CT specimen : the cavities growth, which is directly depending on the stress triaxiality level [9], will be quicker. The steel resistance to ductile tearing will be lower in that case.

DISCUSSION ABOUT THE DEPENDANCE OF FINITE ELEMENT ANALYSES RESULTS ON MESH SIZE

Through this numerical analysis carried out with local approach to fracture, it has been shown that an essential parameter of this kind of models is the mesh size. This finite element size plays an important role in local fracture mechanics concepts applications, and the dependance of finite element analyses results on it has to be highlighted and explained. In fact, this parameter is the most controversial one because people intuitively think that increasing the mesh refinement will provide more accurate results. Then, imposing to use a fixed mesh size, which is in some cases large when compared to the microstructure scale or to the stresses and strains gradients might shock.any physical reasoning.

However, it must be noticed that introducing a distance criterion for failure at crack tip is absolutely necessary when developping a model based on microstructured controlled fracture process. As far as local approach modelling is based on microscopical observations of damage mechanisms, and tries to relate the macroscopic fracture behaviour of an homogeneous material on the microscopic metallurgical heterogeneities, this way of modelling obeys to the rule and has to introduce a scale factor that averages the microscopic mechanisms and microstructural effects.

Previous works have already exhibited this conclusion. Rice and Johnson [11] and later Ritchie, Knott and Rice [12] mentionned that for cleavage fracture, where failure occurs on microstructural initiation sites, the critical fracture stress has to be achieved at a distance which is characteristic of the material microstructure. More recently, Neville [13] introduced a new definition of that critical distance, but demonstrating the same conclusion : introducing microstructural effects on failure in a continuum mechanics analysis requires a characteristic distance that relates the mechanical behaviour at microscopic scale to the macroscopic scale. The physical reason for it is that, for a sharp crack as well as for a blunted crack, the stresses or strains in the highly strectched zone will always overpass a critical value. Then, any failure criterion expressed in terms of critical stress for cleavage or critical strain for ductile tearing will be achieved in a process volume near the crack tip. Therefore, if no critical distance had to be introduced, the minimum toughness for any microstructured material would be zero.

As far as a scale factor must be introduced, the solution that has been retained for local approach to fracture models is to introduce it directly through the mesh size. This the simplest solution, but may be not the most satisfactory one from a physical point of view. Recent works on strain or damage localisation have shown that it is possible to make local models results independent on the mesh size by using a redistribution function in the finite element analysis [14]. Then, the critical distance appears in the "delocalisation" procedure by determining the width of the Gaussian shaped redistribution function. This way of modelling may be more satisfactory, but is still time consuming in numerical analyses, makes the finite element code more difficult to operate, and lastly exhibits the same difficulties in relating this characteristic distance to any microstructural scale. Then, although it is not physically justified, introducing this scale trough the mesh size seems to be the simplest solution and the most convenient for today's industrial applications. Thus, this parameter must be fitted numerically in order to account for coalescence of growing cavities (interactions between elementary cells containing an insolated cavity). The mesh size has therefore a limited influence on crack initiation, and a large one on propagation.

Another point deserves to be highlighted : it concerns the role played by the microsructure on material or industrial structures resistance to fracture. In order to predict structural integrity in connection with microstructural fracture processes, four different scales of observations must be considered. The first one is related to microstructure and material microscopic heterogeneities, the second one concerns the scale of continuum mechanics, the third one represents the scale of the process zone (damaged zone or yielded area), and the last one is the size of the structure. The microstructural distance can be related to mean spacing between inclusions or carbides, or any other particles that play a role in the microsructure fracture process. When comparing this distance with the process zone size, two cases must be considered. If the plastic zone, or crack tip opening displacement is much larger than the mean spacing between inclusions, the effect of microstructure on material failure is very limited. It can be considered that the material, observed at the scale of CTOD or mesh size, is rather homogeneous. In that case, the macroscopic tensile properties of the material, even if including damage, are determined at a scale which already averages microstrucural effects. On the other hand, if the continuum mechanics scale and the mean spacing are within the same order of magnitude, the characteristic distance will obviously play a greater role on crack initiation as well as crack growth. Moreover, if the distance between initiation sites is greater than CTOD or continuum mechanics scale, microstructure effects on fracture will be enhanced and any modelling attempt of the fracture process will have to include statistics on geometrical ditribution of inclusions in order to be able to account for structural resistance as well as for scatter associated to crack initiation and toughness measurements.

Once again, the simplest solution is to seize the opportunity that the mesh size is an averaging tool for stresses and strains gradients, but also for the effects of microstructure on failure.

CONCLUSION

This modelling, instead of applying criteria based on global loading parameters, describes the damage evolution from local values of stress and strain fields. For this reason, this method is able to account for local effects of the crack area loading factors, such as stress triaxiality.

The geometry effect inducing differences in resistance to ductile tearing of the material involved in the specimens can be investigated and explained by using local approach to fracture methodology. The Rousselier's model proved to be an efficient tool for understanding ductile tearing behaviour of steels, and brings answers where classical fracture mechanics concepts fail.

REFERENCES

[1] D.J. LACEY and R. E. LECKENBY - "Determination of Upper Shelf Fracture Resistance in the Spinning Cylinder Test Facility" -Transaction of the 10th Int. Conf. on Structural Mechanics in Reactor Technology, Division F, pp. 1-6, Anaheim, August 1989.

[2] K. KUSSMAUL and A. SAUTER. , "Application of Ductile Fracture Mechanics to Large-Scale Experiment Simulation and Analyses for Pressurized Thermal Shock Behaviour of RPV's.", Int. Conf. on Fatigue, Corrosion Cracking, Fracture Mechanics and Failure Analysis, American Society for Metals, Salt Lake City, USA, 2-6 Dec. 1985.

[3] R. H. BRYAN and al., "Pressurized Thermal Shock Experiment of 6 in.-thick Pressure Vessels - PTSE-2 : Investigation of Low Tearing Resistance and Warm-Prestressing.", NUREG CR-4888, ORNL-6377.

[4] H. OKAMURA and al., "Japanese Pressurized Thermal Shock Experiment Program", Specialists Meeting, CSNI/FAG Project for Fracture Analyses of Large-Scale International Reference Experiments (Project Falsire), Boston, May 8-10th 1990.

[5] G. ROUSSELIER - "Finite deformation constitutive relations including ductile fracture damage" in Three Dimensional Constitutive Relations and Ductile Fracture. North Holland Publishing Company, Amsterdam, 1981.

[6] G. ROUSSELIER et al. - "A Methodology for Ductile Fracture Analysis Based on Damage Mechanics: An Illustration of a Local Approach of Fracture". Nonlinear Fracture Mechanics. Volume II - Elastic-Plastic Fracture, ASTM STP 995, pp.332-354, 1989.

[7] F. MUDRY - "Etude de la rupture ductile et de la rupture par clivage d'aciers faiblement alliés". Thèse d'Etat, Université de Technologie de Compiègne, 23/03/82.

[8] R.J. DEXTER - "Analysis of the first spinning cylinder experiment" - CSNI/FAG Specialists meeting - FALSIRE Project - BOSTON - May 8-10th 1990.

[9] M. BETHMONT, G. DEVESA, G.ROUSSELIER - "A Methodology for Ductile Fracture Analysis Based on Damage Mechanics: An Application of Local Approach to Fracture to the NKS-3 thermal shock experiment". 5th MPA Seminar - STUTTGART - October 5,6th 1988

[10] G. PISSARENKO, A. YAKOVLEV, V. MATVEEV - Material Strength Memorendum - Editions MIR.

[11] J.R. RICE and M.A. JOHNSON - In "Inelastic Behaviour of solids", edited by Kanninen and al. - p. 641 - Mc Graw Hill - New York.

[12] R.O. RITCHIE, J.F. KNOTT, J.R. RICE - Journal of Mechanics and Physics of Solids - Vol 21,p. 395.

[13] D.J. NEVILLE, "On distance criterion for failure at the tips of cracks, minimum fracture toughness, and non-dimensionnal toughness parameters" - Journal of Mechanics and Physics of Solids - Vol 36, N°4, pp 443-457.

[14] G. PIJAUDIER-CABOT and Z.P. BAZANT - "Nonlocal Damage Theory " - ASCE Journal of Engineering Mechanics - Vol 113,pp. 1512-1533.

TABLE 1 – MECHANICAL PROPERTIES FOR SPINNING CYLINDER TEST MATERIAL.

- TEST MATERIAL IDENTIFICATION

Nominally A508 Class 3 composition in a nonstandard quenched and tempered condition

- CHEMICAL ANALYSIS

C	Si	Mn	S	P	Cr	Mo	Ni
0.22	0.20	1.32	0.012	0.012	0.08	0.57	0.78

- THERMAL TREATMENT

Austenitise	6 hours at 1065°C
Quench	Water quench from 1065°C
Temper	7 hours at 590 ± 10°C

- PROPERTIES-TEST TEMPERATURES

290°C

- ENGINEERING AND TRUE STRESS-STRAIN TENSILE DATA

E-Modulus [MPa]	193,000 (measured using an electrostatic resonance technique)
$R_{p0.2}$ [MPa]	540
R_M [MPa]	710
ν, Poisson's ratio	0.275 (determined from biaxial strain gage measurements of material strips loaded in tension)

TABLE 2 – TYPICAL STRESS-STRAIN DATA AT 290°C FOR FIRST SPINNING CYLINDER TEST MATERIAL.

True Strain %	True Stress N/mm^2
0.003906	7.9
0.05662	111.1
0.1054	207
0.1542	303.6
0.2007	393
0.228	433.8
0.2572	461.8
0.3118	496.2
0.3916	525.3
0.4985	548.4
0.6054	564.5
0.714	576.4
0.8225	587.5
0.9329	595.6
1.043	604.4
1.153	611.8
1.207	614.4
1.261	617.9

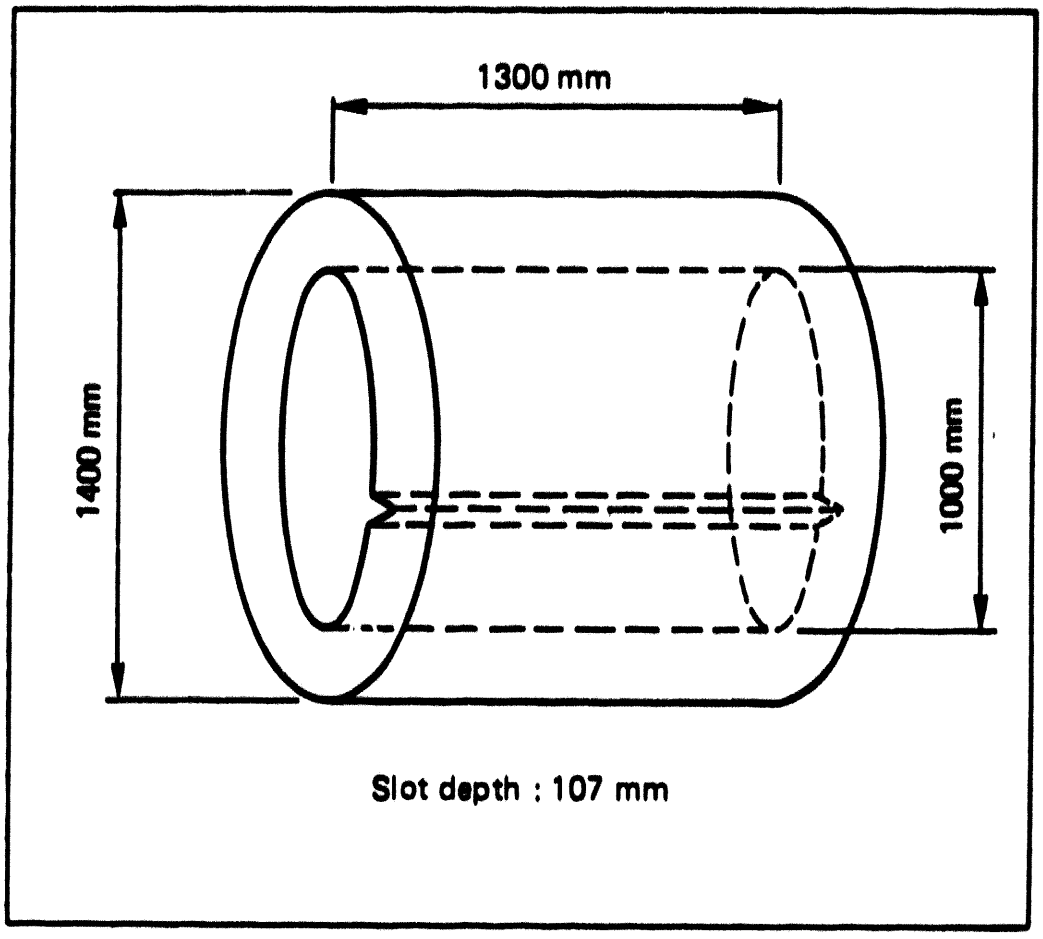

Figure 1 – Cylinder geometry for first spinning cylinder experiment.

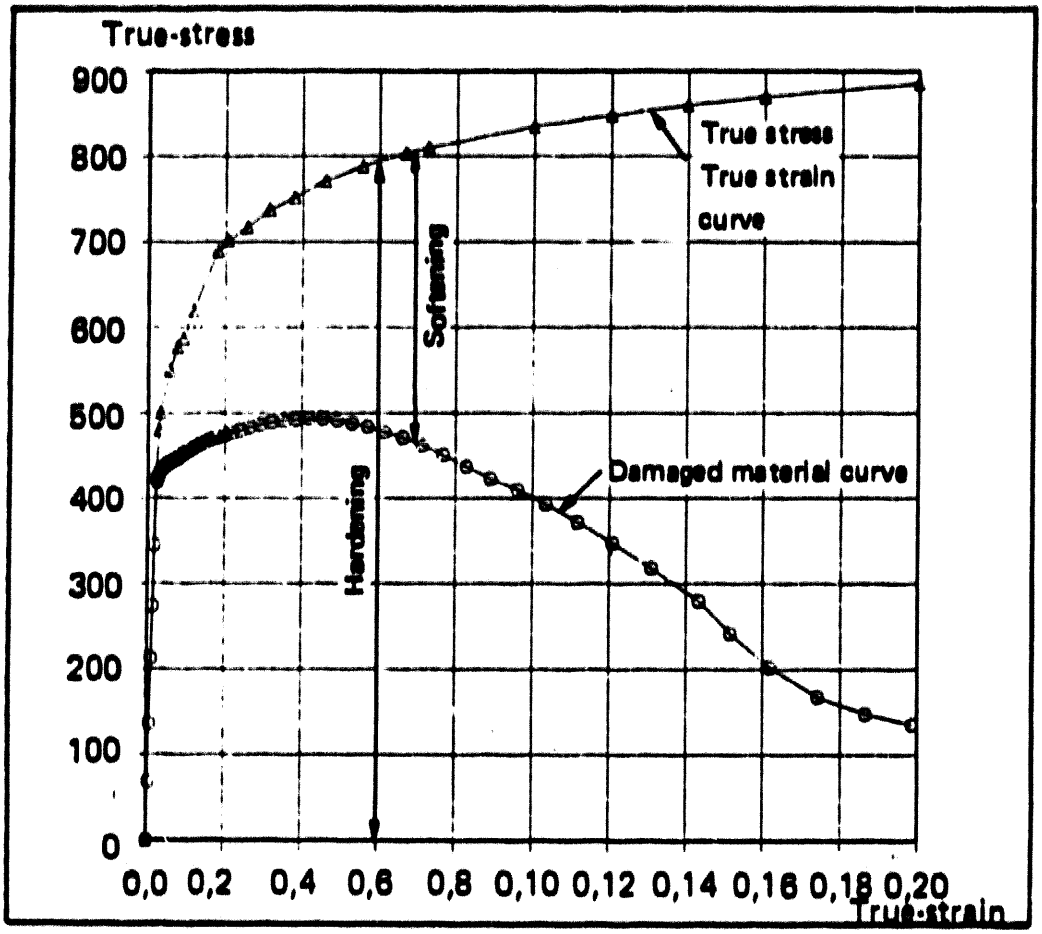

Figure 2 – Stress-strain curve accounting for damage.

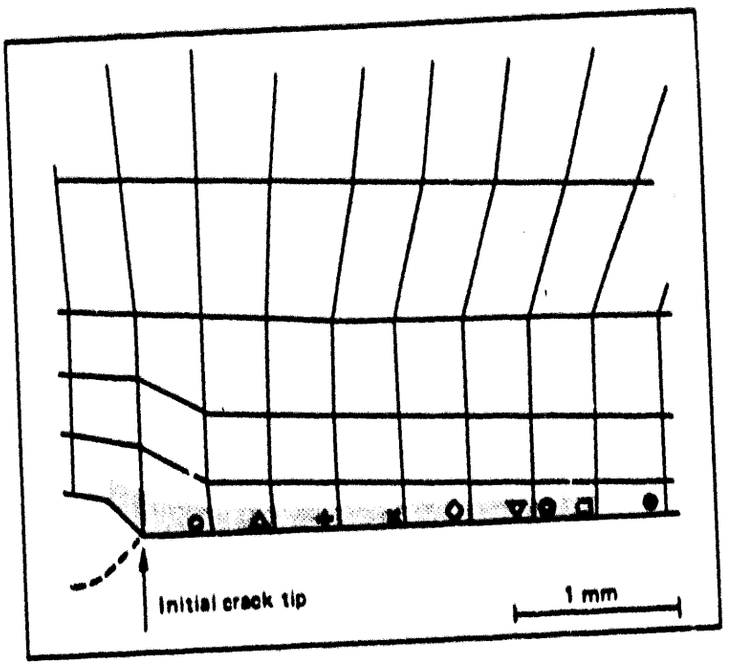

Figure 3a – Stable crack growth (damaged zone in grey).

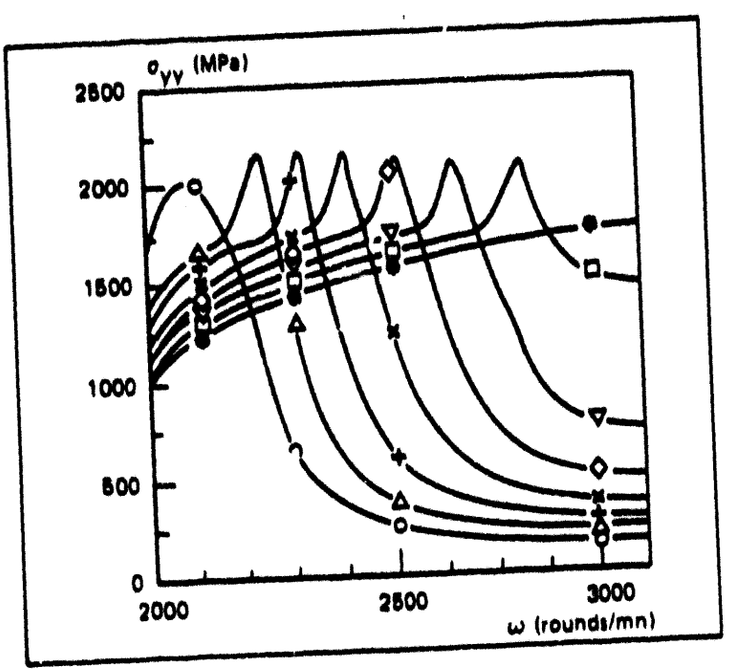

Figure 3b – Hoop stress at the crack tip (the symbols correspond to the locations of figure 3a).

Figure 3

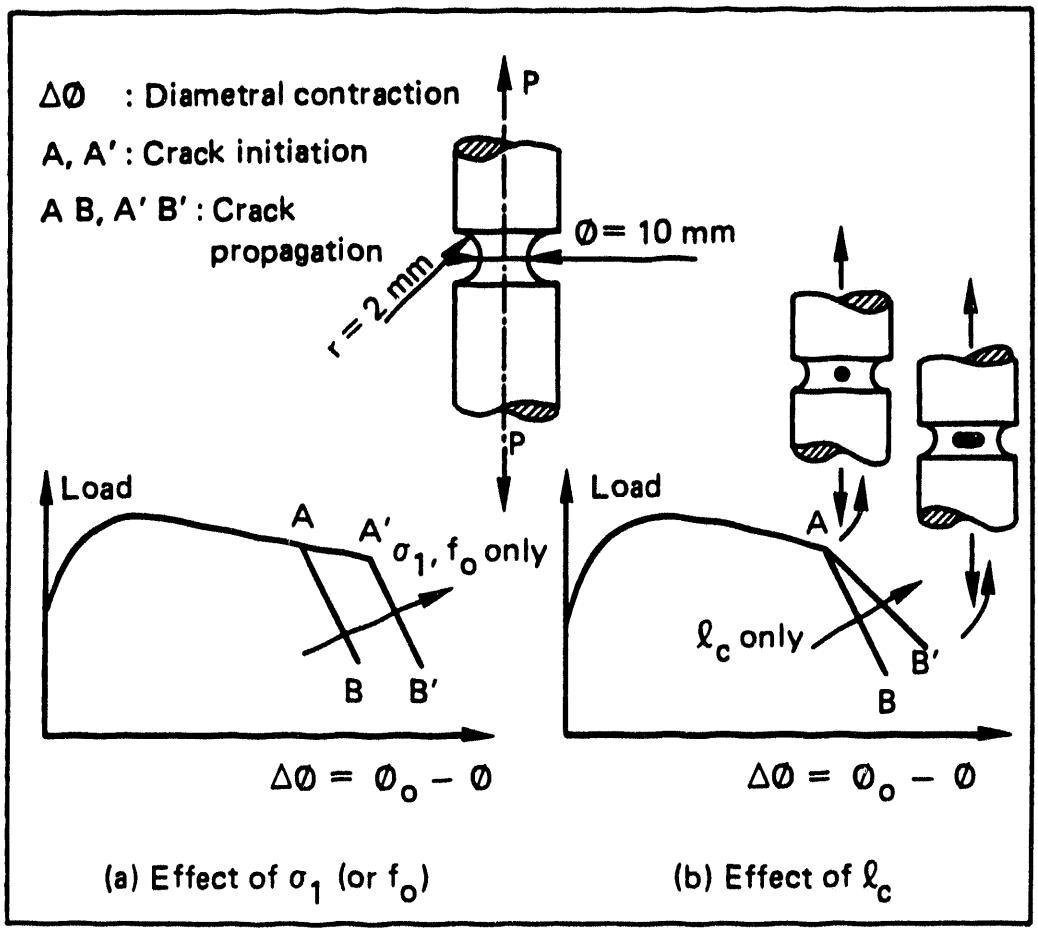

Figure 4 — Numerical load-displacement curves of a notched tension specimen (schematic).

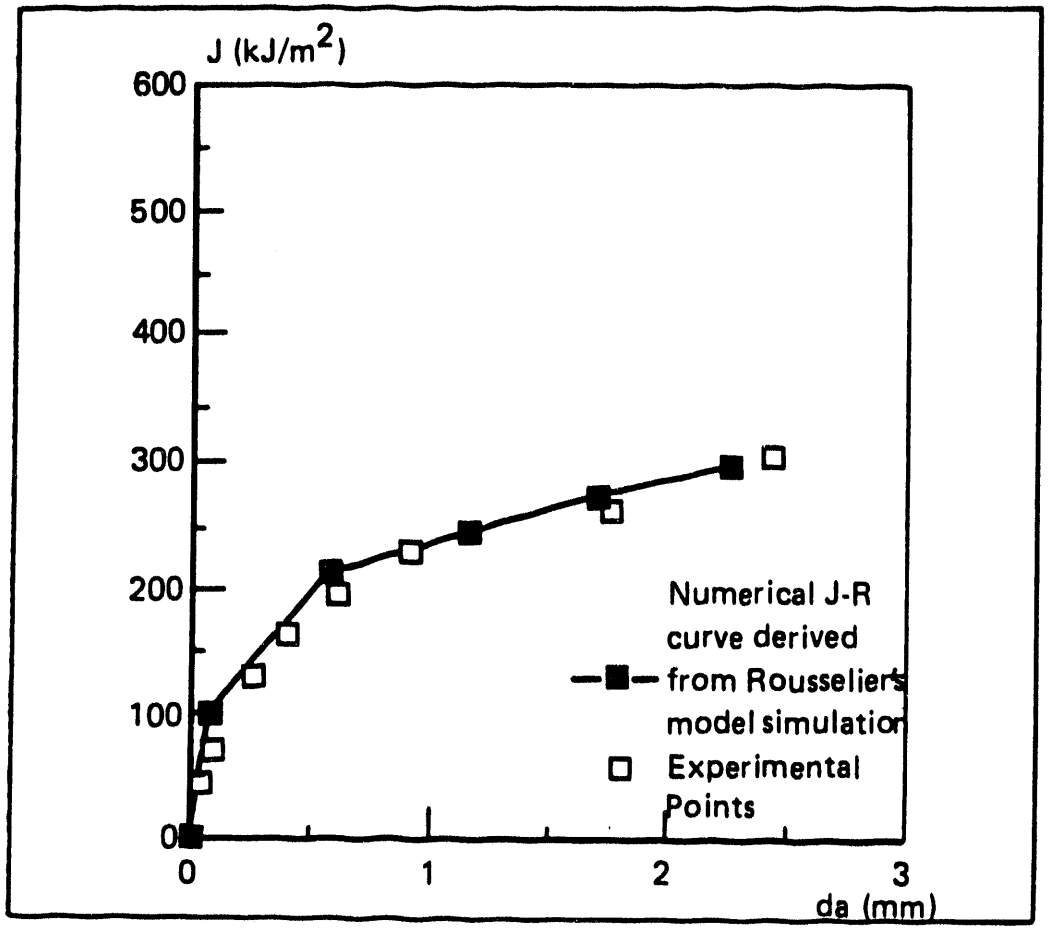

Figure 5 – Comparison of experimental and numerical J-R curves for CT specimens.

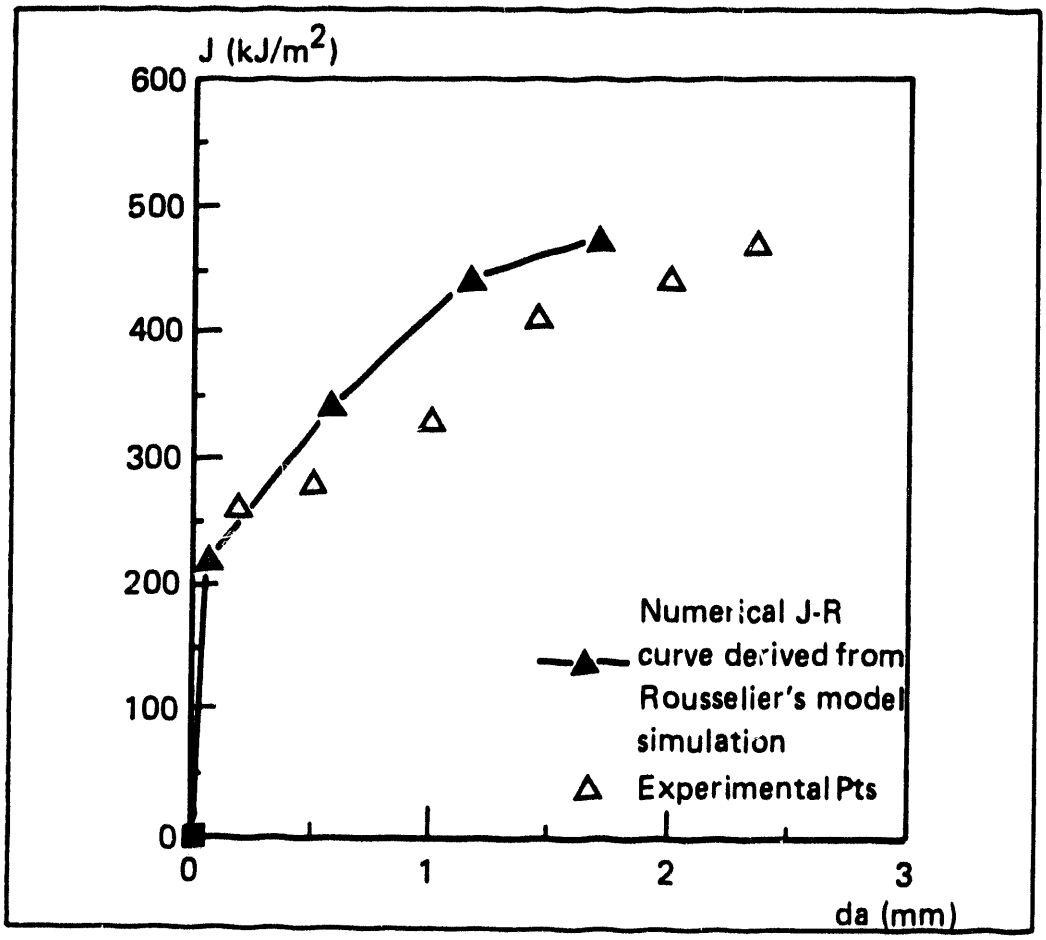

Figure 6 – Comparison of numerical and experimental J-R curves for spinning cylinder experiment.

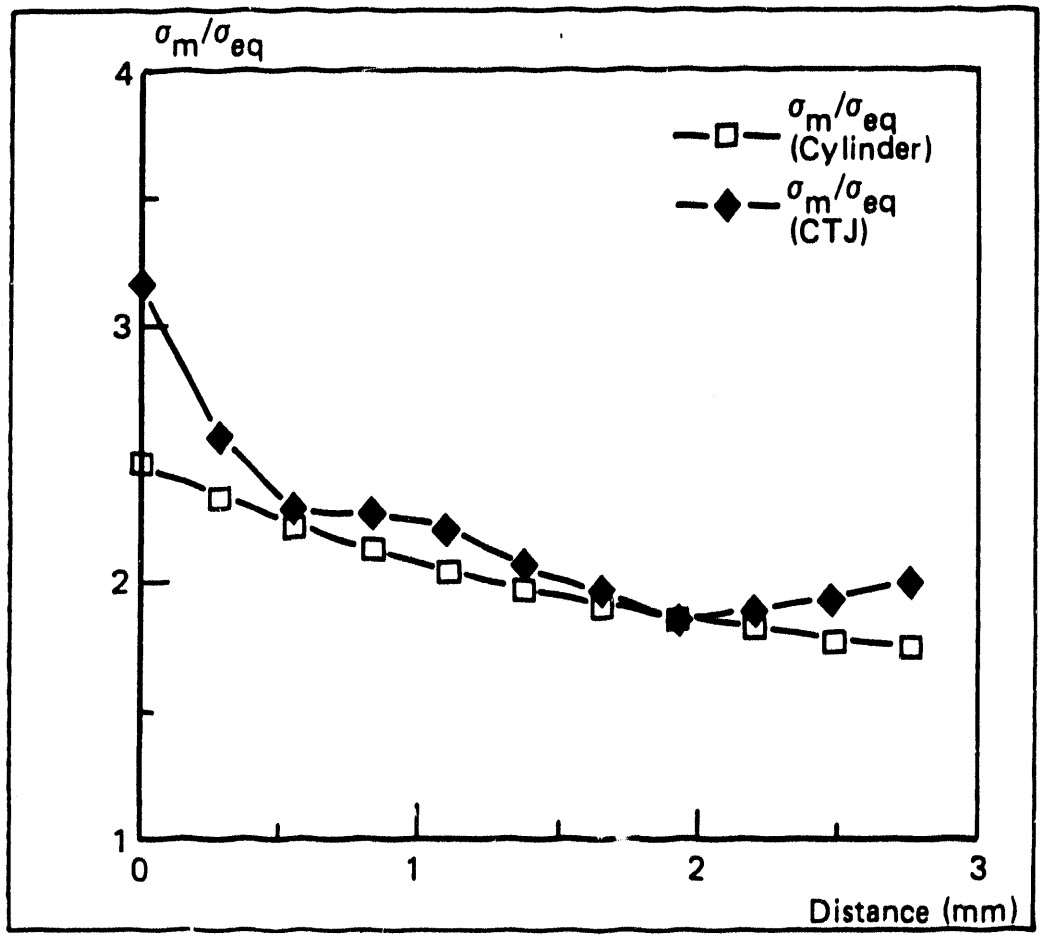

Figure 7 — Stress Triaxiality Evolution along the ligament for CT specimens and spinning cylinder experiment.

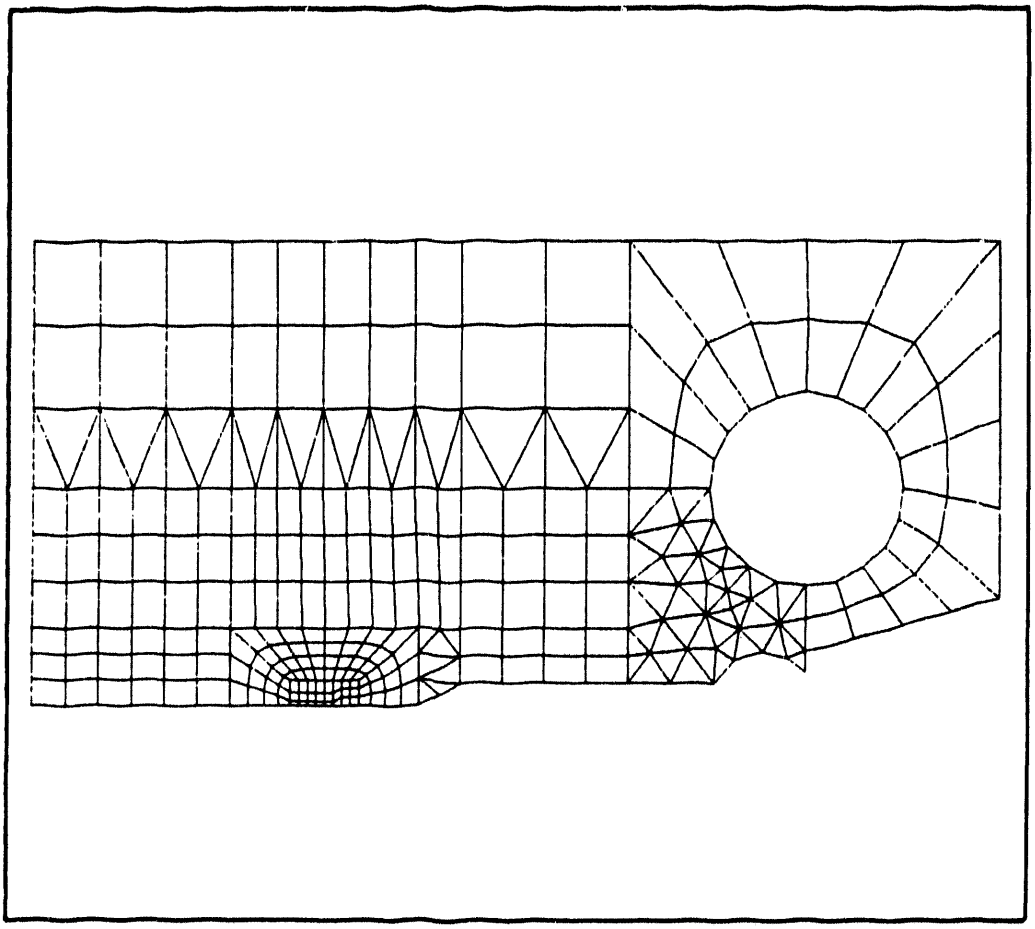

Figure 8 – Mesh of CT specimen.

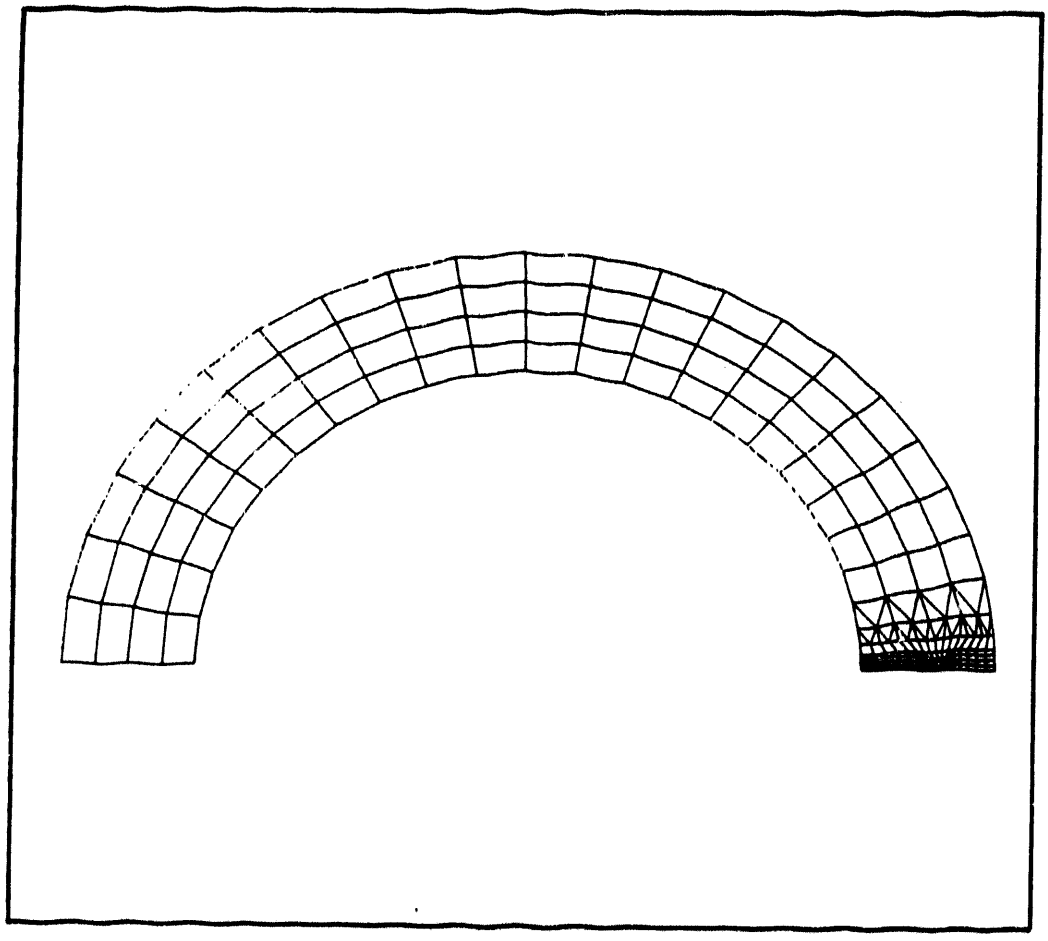

Figure 9 – Mesh of the cylinder.

A SUMMARY OF CSNI PROJECT FALSIRE ANALYSES OF THE SECOND HSST PRESSURIZED-THERMAL-SHOCK EXPERIMENT (PTSE-2)

B. R. Bass
Heavy-Section Steel Technology (HSST) Program
Oak Ridge National Laboratory
Oak Ridge Tennessee

J. Sievers
Gesellschaft für Anlagen-und Reaktorsicherheit
Köln, Germany

ABSTRACT

A comparative summary of Project FALSIRE Workshop analyses of the second pressurized-thermal-shock experiment (PTSE-2) is presented. All analytical predictions are found to underestimate the measured crack-mouth-opening displacement (CMOD) and crack propagation data for the first loading transient. Additional analyses performed subsequent to the FALSIRE Workshop are described that examine some possible explanations for these differences in predicted and measured structural response. Updated analysis results based on temperature-independent material and physical properties are shown to substantially underestimate measured data describing time histories of circumferential surface strains. No improvement in the comparisons is obtained by incorporating temperature-dependent properties into plane stress or plane strain models. However, two-dimensional models may not be adequate to represent the structural response of the vessel. A pronounced axial dependence of the measured CMOD and crack extension data from the first transient implies that significant three-dimensional loading effects may have played an important role in the experiment.

1. INTRODUCTION

The pressurized-thermal-shock experiments [1,2] (PTSEs) in the Heavy-Section Steel Technology (HSST) Program are part of a carefully planned series of fracture mechanics experiments that are of a scale large enough to produce restraint at the crack tip similar to that of full-scale water-cooled nuclear reactor pressure vessels (RPVs). Hypothetical PTS transients, when imposed on the thick-wall vessel, produce high tensile stresses on the cooled inner surface. In addition, irradiation embrittlement is greatest near the inner surface, so that in the case of some pressurized water reactor vessels, preexisting shallow flaws on the inner cooled surface may propagate in a fast fracture mode. If pressure is also present during the thermal transient, additional stresses are produced that become more dominant as the crack advances through the wall, and vessel integrity may be threatened in the absence of crack arrest or an action to reduce the load. The positive gradient in temperature and the lessening of neutron damage through the thickness provide increased material toughness to enhance crack arrest and terminate an incident without breaching the vessel wall. The primary objective of the HSST PTSEs is to provide an experimental basis for the confirmation of current fracture analysis methods or for the development of new methods.

The following fracture phenomena can be investigated through these tests.

1. The ability of RPV steels to exhibit sufficiently high crack-arrest toughness to halt crack propagation before instability.

2. The fracture mode transition as the crack propagates into ductile regions.

3. The propensity for ductile tearing, prior to initial cleavage crack propagation.

4. The inhibiting effects of warm pre-stressing on initiation of cleavage fracture.

5. The evolution of crack shape changes in clad vessels.

The second experiment [2] (PTSE-2) in this series was performed with a surface-cracked vessel having the geometry shown in Fig. 1. The PTSE-2 experiment was concerned, primarily, with characterizing crack propagation in material with low Charpy upper-shelf energy levels, and, secondarily, with warm pre-stressing. The test material in PTSE-2 was a specially heat treated 2-1/4 Cr-1 Mo plate, meeting SA-387 grade 22 specifications with a low Charpy impact energy ($\approx$ 50-70 J) on the ductile upper shelf, which ensured low ductile-tearing resistance. Vulnerability of existing reactor pressure vessels to damage in over-cooling accidents is a potential problem mainly in instances of vessel steels that have high copper contents and, consequently, high susceptibility to fast-neutron embrittlement. Coincidentally, these high-copper steels have low ductile tearing resistance at temperatures on the Charpy upper shelf.

The PTSE-2 experiment was designed to examine crack propagation and arrest in a material that exhibits low tearing resistance. One phase of the experiment was defined to produce cleavage arrest at temperatures above the onset of Charpy upper-shelf behavior followed by unstable tearing. Another objective was to achieve cleavage initiation of a warm pre-stressed crack. A third consideration was to evaluate tearing resistance models through interpretation of stable tearing that occurs prior to cleavage initiation and after arrest.

This paper presents a brief description of the pressurized-thermal-shock test facility at ORNL, a review of the test objectives, and a summary of the test results for PTSE-2. Results from analyses of PTSE-2 carried out in support of the CSNI/FAG Project FALSIRE are compared with the experimental observations. Consideration is given to the cleavage run-arrest events that occurred, and to the various ductile tearing phases of each test. Finally, some conclusions are presented based on the outcome of the studies.

2. PTSE-2 PRESSURIZED-THERMAL-SHOCK EXPERIMENT

2.1 PTSE-2A

The details of the PTSE-2 test vessel and the initial flaw geometry [2] are given in Fig. 1 and in Table 1. An HSST intermediate test vessel was prepared with a plug of specially heat-treated test steel welded into the vessel. The 1-m-long sharp flaw was implanted in the outside surface of the plug by cracking a shallow electron-beam weld under the influence of hydrogen charging. For the test, the vessel was extensively instrumented (e.g., see Figs. 2 and 3) to give direct measurements of CMOD, temperature profiles through the vessel wall, and internal pressure during the transient.

In the experiment, the flawed vessel was enclosed in an outer test vessel (OTV) as shown schematically in Fig. 4. The OTV is electrically heated to bring the flawed test vessel to the desired uniform initial temperature of about 290°C. A thermal transient is initiated by suddenly injecting a chilled methanol-water mixture through an annulus between the test vessel and the other vessel. The annulus between the vessel surfaces was designed to permit coolant velocities that would produce the appropriate convection heat transfer from the test vessel for a period of about 10 min. Pressurization of the test vessel is controlled independently by a system capable of pressures up to about 100 MPa. A detailed description of the ORNL PTS test facility, including the main coolant and pressurization systems, as well as the computer-controlled data acquisition systems, is given in Refs. 1 and 2.

In PTSE-2, the insert (test) material was taken from a 2 1/4 Cr-1 Mo plate, meeting SA-387 grade 22 specifications. The two pieces used for the insert and for properties characterization were subjected to the same heat treatment following welding of the insert into the vessel. The heat treatment was intended to provide the tensile and toughness characteristics desired for the experiment. The tensile strengths were undesirably low, but other properties, although somewhat uncertain, were satisfactory. True stress-strain tensile data are shown in Fig. 5 for the low upper-shelf (LUS) test material (A) and the tough carrier vessel material (B). (Concerning Fig. 5, note that the LUS material (A) set 5 data were from the properties characterization piece and used in pretest analyses, while set 7 data were obtained from actual vessel insert material after completion of PTSE-2.) Tensile and physical properties for the test vessel are given in Tables 2-3. Additional data characterizing the fracture properties of the PTSE-2 material are given in Tables 4-5 and in Figs. 6-7. Side-grooved specimens from the vessel insert and from the pretest characterization piece (PTC1) were tested at 175 and 250°C to obtain full J_R-curves (see Fig. 7). These unloading-compliance characterization tests were analyzed using procedures described in ASTM E1152, and the power-law curve fit parameters are given in Table 5.

Pretest crack arrest (K_{Ia}) and crack initiation fracture toughness (K_{Ic} and K_J) data are shown in Fig. 6. The K_{Ia} data were obtained from tests of 33- and 51-mm-thick specimens. K_{Ic} and K_J data are from tests of 25-mm-thick specimens. The upper- and lower-K_{Ia} curves shown in Fig. 6(a) were determined by least-squares fits to the raw data and to β-adjusted [3] data, respectively. The curves representing K_{Ic} at high transitional temperatures were presumed, in the absence of reliable data, to be positioned ~30°K lower in temperature than the respective K_{Ia} curves. It transpired that a K_{Ic} curve determined by the low-temperature K_{Ic} points and by the remaining β and rate-adjusted K_J data [2] in the transition region was suitably related to the upper K_{Ia} curve. This fitted K_{Ic} curve and a lower K_{Ic} curve, displaced upward by 30°K from the former (Fig. 6(b)), were adopted for planning the PTSE-2 experiment.

The experiment was planned to consist of two transients, of which the first would induce warm prestressing ($\dot{K}_I < 0$) followed by reloading ($\dot{K}_I > 0$) until the crack propagated by cleavage and arrested. The second transient was planned to produce a deep cleavage crack jump with an arrest occurring only after conditions conducive to subsequent unstable tearing were attained. The second transient was also necessary to provide a measurement of K_{Ic} that was not strongly affected by warm prestressing so that the effects of warm prestressing in the first transient could be evaluated. The experimentally-determined temperature profile and pressure data for transient A, as well as some material characterization of the test section, are given in Fig. 8 and in Table 6.

The time dependence of the heat transfer coefficient for transient A is given in Fig. 9. The thermal shock in the PTSE-2A transient started about 112 s after the initiation of the data scan. Subsequently and sequentially, the flaw experienced ductile tearing while K_I was increasing; tearing

ceased, presumably when K_I first decreased; tearing resumed at about the time K_I increased again; cleavage crack propagation and arrest occurred; and, finally, ductile tearing resumed after crack arrest until pressure was reduced. The succession of events identifiable from recorded transient data is summarized in Table 7. The most probable times of events were determined by detailed evaluation of all relevant data.

CMOD behavior for the entire PTSE-2A transient is typified by the plot shown in Fig. 10. More detail for the period of initial tearing that preceded the initial maximum K_I is represented by two typical CMOD measurements vs time shown in Fig. 11. The first maximum K_I was reached at point A, when CMOD reached a maximum. Examination of the fracture surface showed that ductile tearing enlarged the flaw depthwise with no significant axial tearing.

The second episode of ductile tearing transpired when CMOD again increased (from point B to C in Figs. 10 and 12). The crack propagated by cleavage, causing the rapid change in CMOD from C to C′. The final ductile tearing in PTSE-2A occurred while pressure and CMOD were increasing (from point C′ to D in Figs. 10 and 12).

2.2 PTSE-2B

The arrested crack from transient A was the initial crack geometry for transient B. Data describing the thermal and mechanical loading conditions in transient B are provided in Fig. 8 and Table 6. The thermal shock in PTSE-2B started at about 155 s after initiation of the data scan. Here, K_I increased monotonically until about the time of the rapid cleavage crack propagation. The extended crack that had developed during the PTSE-2A first tore depthwise and then converted to cleavage. The propagating cleavage crack arrested and then propagated by ductile tearing until the vessel ruptured. The events in this transient are summarized in Table 7. The CMOD behavior

typical of the time before cleavage is shown by the CMOD at the center of the flaw in Fig.13. The time of the start of the cleavage event is reasonably well defined by all of the active CMOD and strain gages.

The PTSE-2 experiment produced two fast crack jumps. The final crack propagation led to rapid ductile tearing that penetrated the vessel wall. Prominent features of the flaw are identified in Fig. 14 and Tables 8-9. The average depth of the flaw at several stages is given in Table 9. The experimental records of CMOD vs time in conjunction with finite-element calculations of displacements displacements for a range of crack depths and times were the basis for identifying fracture events. The time of vessel rupture is marked by a sharp drop in pressure and by abrupt changes in CMOD and strain gage outputs. Times of all events are given relative to the time of initiation of the computer-controlled data scans.

3. SUMMARY OF ANALYSIS RESULTS FROM CSNI/FAG WORKSHOP

In this chapter, the results of the finite-element (FE) and the estimation scheme (ES) analyses of PTSE-2 presented at the CSNI/FAG workshop in Boston in May 1990 and in Ref. 4 are discussed. The following discussion concentrates on reasons for the discrepancies among the various analyses of the PTSE-2 experiment.

3.1 PTSE-2A

The time histories of CMOD and the J-integral are presented in Figs. 15-16, and selected characteristics are summarized in Table 10. The comparisons in Fig. 15 show that all analyses underestimate the experimental results of CMOD. Note that the lack of temperature-dependent data concerning the stress-strain curve and the thermal expansion coefficient (α), as well as the use of an α-value based on a reference temperature of 20°C, could be important factors in this underestimation of CMOD. Also, recent evaluations of the PTSE-2 data indicate that the measured CMOD values show a strong dependence on axial position in the vessel.

The FE results are strongly dependent on the approximation of the stress-strain data, the effect of whether crack extension has been considered, and the coefficient of thermal expansion. Analysis 10 has ~30% lower CMOD at t = 185 s than analysis 5 and ~40% higher J-value. The reason is the different bilinear approximations of the stress-strain data. The measured onset of yield is very low (70 MPa) compared with the engineering yield stress (255 MPa) quoted for the vessel insert. The value used in the calculations ranges from 200 to 495 MPa, dependent on whether the small strain or the larger strain region of the stress-strain curve is approximated well. Furthermore, an increase of 50% in $\sigma_{0.2}$ was measured for the vessel insert after transients A and B. The artificially high yield stress used in analysis 10 results in higher stresses on the ligament (Figs. 17-20, especially Fig. 20), with smaller plastic zone and, therefore, smaller CMOD but higher J-integral. In analysis 5′, the final crack length after the first period of stable crack extension (5.1 mm after 185 s) was used, which produces an increase of CMOD at t = 185 s of ~30% compared with analysis 5. Based on the experiences with other calculations, a 20% higher coefficient of thermal expansion was used to demonstrate the effect of a change in reference temperature from room temperature to 300°C. This change produces a CMOD increase of 13%. The change in the approximation of the stress-strain data (pretest set 5) by a multilinear curve causes a CMOD decrease of ~13%. Perhaps because of uncertainties concerning the loading assumptions as indicated by the axial dependence of CMOD, a 17% underestimation of the measured CMOD remains at 185 s. The scatterband of the results is also enlarged because different assumptions concerning the crack depth have been chosen (initial depth or depth after first phase of stable crack extension).

Analysis 8 simulated the measured crack extension, but the higher yield stress makes the model more stiff, which results in lower CMOD values. ES analyses 15 and 15′ used influence coefficients based on infinitely long cracks and on finite-length 3-D cracks, respectively. Therefore, when the fracture assessment is done excluding analysis 15 (because the latter assumes infinite crack length) and analyses 5′ and 8 (because the latter already took crack extension into account), a crack extension estimate of 1 to 2.5 mm (measured 5.1 mm) is obtained from isothermal CT-25 specimen J_R curves (Fig. 7). The underestimation of crack loading and crack extension has to be considered in connection with the underestimation of CMOD; that is, without good structural mechanics simulations, a good fracture mechanics approximation cannot be achieved. The temperature dependence of J_R is strong, and it is not known what the effect of temperature gradient in the test cylinder is on the crack resistance.

Oscillations of q (Figs. 21-24) in front of the crack tip (e.g., analysis 5) can be reduced by a finer mesh on the ligament (e.g., analyses 7, 9, and 10). The necessary material properties, especially the temperature dependence, were not available totally. Therefore, reasons for the large difference between results of the analyses and the experiments could be provided only partly. However, some parameters that show significant influence on the analysis results have been identified.

3.2 PTSE-2B

Figures 25 and 26 show the time dependence of CMOD and the J-integral, and Table 11 shows selected characteristics of the FE analyses. The FE analyses underestimate CMOD (as in PTSE-2A), which may be because of the same reasons just discussed [e.g., lack of temperature-dependent material data for σ and α]. Differences in the stress behavior on the ligament, especially at the beginning of the transient (Figs. 27-29), are caused by the inclusion of residual stresses from transient A in analyses 5 and 8 but not in analysis 7. Furthermore, different material property sets were used, set 7 in analysis 5 and set 5 in analysis 7 (Fig. 5). These assumptions lead to differences in CMOD and J-integral values.

Negative J values are calculated at the beginning of the transient in analyses 5 and 8 because of the compressive residual stresses in front of the crack tip caused by transient A. The hoop stresses of analyses 12 and 15 (see Fig. 30) compare well, but the J values have large differences because of the ES methods applied.

A range of stable crack extension is calculated using isothermal J_R curves and the J-integral scatterband obtained by excluding analyses 12 and 15 from the set given in Fig. 26. Possibly, analysis 12 fails because of the deep crack and analysis 15 because of the assumption of infinite crack length (as compared with analysis 15', which assumed a finite crack length). The calculated crack extension ranges from 1.4 to 2.9 mm (measured 3.7 mm, i.e., 9% of the initial crack depth in PTSE-2B). The underestimation of the crack extension is not as large as in PTSE-2A, but another factor that could reduce the crack extension has not been considered. The stress state in front of a crack that has already seen transient (A) could be altered due to blunting and could lead to an increase in crack resistance compared to that of a standard specimen. To summarize, differences between the analysis results and the experimental data could not be clarified totally, but additional factors that could influence the quality of fracture assessment based on J_R methodology have been identified.

4. FURTHER ANALYSIS AND DISCUSSION

Results presented in the previous section from the Project FALSIRE Workshop and from Ref. 4 indicate that all analytical predictions underestimated the measured CMOD at the crack midplane and the crack propagation data for PTSE-2. Subsequent to the FALSIRE workshop, additional studies were performed at GRS to examine in more detail some of the possible explanations for the differences in predicted and measured structural response. These studies focused on the following factors related to the PTSE-2 experiment:

- Comparisons between measured and calculated circumferential strains in the vessel;
- Consideration of temperature-dependent tensile and physical properties (i.e., stress-strain curves, thermal expansion coefficient, etc.);
- Plane strain/plane stress approximation; and
- Axial/circumferential dependence of measured displacements and strains (i.e., 3-D load effects).

In Figs. 31 and 32, measured circumferential strains are compared with calculated values on the inner and outer surface of the vessel wall, respectively. The strain gages providing the measured

data are located in the axial plane of the crack, as shown in Figs. 31 and 32. The calculations were carried out assuming temperature-independent material properties and a multilinear stress-strain curve. Results are shown for two fixed crack depths of a = 14.5 and 19.6 mm. For both crack configurations, the computed values underpredict the magnitude of measured circumferential strain at both the inner and outer gage locations.

The potential influence of temperature-dependent material and physical properties on modeling the structural response of the vessel was discussed in the previous section. Additional analyses were performed using the temperature-dependent tensile properties depicted in Figs. 33-35 and presented in Table 12 for the insert material and for carrier vessel respectively. The temperature-dependent thermal expansion coefficient for the insert material is given by the relation

$$\alpha(T) = (10.2 + 12.496 \cdot 10^{-3}\, T) \cdot 10^{-6}$$

within the range 0 to 350° C, where α is per Kelvin and T is degrees Celsius.

The updated analyses were performed for both plane stress and plane strain assumptions using a fixed crack depth of a = 14 mm. In Figs. 36 and 37, results for calculated circumferential strains are compared with measured data from PTSE-2A at two locations remote from the crack. Apparently these results indicate that the discrepancy between measured and computed structural response cannot be explained satisfactorily in terms of temperature-dependent properties or 2-D plane strain/plane stress modeling assumptions.

Examination of measured data [2] from the PTSE-2A transient reveals an anomalous mismatch of the flows into and out of the shroud (Fig. 38) and a pronounced axial dependence in the measured CMOD and in the measured crack extension just prior to the first cleavage event. This axial dependence of CMOD and of crack extension is depicted in Figs. 39 and 40, respectively. These data imply that significant 3-D loading effects may have been active in the transient which preclude the use of 2-D models to represent the structural response of the vessel.

5. CLOSURE

All of the PTSE-2 finite element analysis results from the FALSIRE Workshop provided estimates of CMOD vs time that substantially underpredicted the measured data for the first phase of stable tearing. Additional analyses were described herein that examined in detail some of the possible explanations for the differences in predicted and measured structural response. In these updated analyses, calculated circumferential strains vs time for two different crack depths and for temperature independent material properties significantly underpredicted the measured data at two locations remote from the crack tip. When the analyses were repeated using temperature-dependent material properties and considering both the plane stress and plane strain assumptions, no improvement was observed in matching the measured data.

Published data indicate a pronounced axial variation in the measured CMOD and crack-extension for the PTSE-2A transient, implying the existence of significant 3-D loading effects. Additional studies should be performed to determine whether further advances in the understanding of events in the PTSE-2A transient can be extracted from models incorporating this axial dependence in the measured data.

REFERENCES

1. R. H. Bryan et al., Martin Marietta Energy Systems, Inc., Oak Ridge Natl. Lab., "Pressurized-Thermal-Shock Test of 6-in.-Thick Pressure Vessels, PTSE-1: Investigations of Warm Prestressing and Upper-Shelf Arrest," USNRC Report NUREG/CR-4106 (ORNL-6135), April 1985.

2. R. H. Bryan et al., Martin Marietta Energy Systems, Inc., Oak Ridge Natl. Lab., "Pressurized-Thermal Shock Test of 6-in.-Thick Pressure Vessels, PTSE-2: Investigation of Low Tearing Resistance and Warm Prestressing," USNRC Report NUREG/CR-4888 (ORNL-6377), December 1987.

3. J. G. Merkle, Union Carbide Corp., Nuclear Div., Oak Ridge Natl. Lab., "An Examination of the Size Effects and Data Scatter Observed in Small-Specimen Cleavage Fracture Toughness Testing," USNRC Report NUREG/CR-3672 (ORNL/TM-9088), April 1984.

4. B. R. Bass, C. E. Pugh, J. Keeney-Walker, H. Schulz and J. Sievers, "Final Report on CSNI Project for Fracture Analysis of Large-Scale International Reference Experiments (Project FALSIRE)," NUREG/CR-5997 (ORNL/TM-12307), Oak Ridge Natl Lab., Oak Ridge, TN (in publication).

Table 1. PTSE-2, geometric parameters of PTSE-2 vessel

Parameter	Value
Inside radius (mm)	343.0
Wall thickness (w) (mm)	147.6
Flaw length (mm)	1000.0
Flaw length (a) (mm)	14.5
a/w	0.098

Table 2. PTSE-2, tensile properties for PTSE-2 vessel

	Material A[a] (set 5)	Material A[a] (set 7)	Material B[b]
Elastic modulus, E (MPa)	2.111×10^5	1.98×10^5	2.023×10^5
Poisson's ratio, ν	0.3	0.3	0.3
RT[c] yield stress, σ_y (MPa)	255	375	430
RT[c] ultimate stress, σ_u (MPa)	518	?	?

[a] = Low upper shelf test material
[b] = Carrier vessel material
[c] = Room temperature

Table 3. PTSE-2, physical properties for PTSE-2 vessel

Heat convection coefficient	(See Fig. 9)
Thermal conductivity	$k = 41.54\ W \cdot m^{-1} \cdot K^{-1}$
Specific heat	$c = 502.4\ J \cdot kg^{-1} \cdot K^{-1}$
Density	$\rho = 7833\ kg \cdot m^{-3}$
Coefficient of thermal expansion	$\alpha = 14.4 \times 10^{-6}\ K^{-1}$

Table 4. PTSE-2, fracture properties for PTSE-2 material

Property	Value
NDT temperature (°C)	49
Onset of Charpy upper shelf (100% shear fracture appearance) (°C)	150
Charpy upper shelf Energy (J)	~50-75[a]
Charpy transition temperature (°C)	
At 50% shear fracture appearance	90
At 0.89-mm lateral expansion	98

[a]Range for all depths in plate. The average at 1/4 depth is ~68 J.

Table 5. PTSE-2, updated ductile-shelf fracture-toughness results for PTSE-2 2 1/4 Cr-1 Mo Steel (TS orientation)

Specimen[a]	Test temperature (°C)	J_{Ic}[b] (KJ/m^2)	$K_{J_{Ic}}$ ($MPa\sqrt{m}$)	Final extension (mm)	Tearing modulus[c]	A	B	C	D
PTSE-2 Vessel Insert									
PE75	175	34.7	82.7	8.54	33.5	136.0	0.0	0.235	-62.18
PE77	175	47.4	96.7	8.92	26.9	164.4	0.129	0.181	-90.39
PD79	175	32.3	79.8	9.17	37.1	87.4	0.016	0.445	-14.72
PD81	250	41.6	89.6	9.49	18.4	68.9	0.032	0.257	-7.88
PE83	250	25.2	69.7	8.76	27.8	100.0	0.0	0.252	-43.64
Characterization Piece, PTC1									
PI230	100	40.6	90.4	11.57	126.6	164.9	0.176	0.543	-64.61
PI250	100	39.4	89.2	8.06	134.4	491.2	0.163	0.186	-377.80
PI228	175	36.6	85.0	8.23	110.6	148.4	0.032	0.443	-48.29
PI256	175	37.8	86.4	9.69	117.7	295.9	0.168	0.259	-198.76
PI238	250	34.0	81.0	9.47	73.9	174.3	0.065	0.224	-100.48
PI235	250	43.0	91.7	9.86	77.3	236.0	0.288	0.216	-164.03

[a]25.4-mm-thick compact specimens.

[b]J_{Ic} determined by power-law curve intersection with 0.2 mm offset line; J is deformation theory J per ASTM E1152.

[c]Calculated using linear fit to data between exclusion lines.

[d]$J = A(\Delta a + B)C + D$, where Δa = crack extension in millimeters; power law curve fit to data from beginning of test up to 1.5 mm exclusion line, with obvious anomolous data in that region excluded from fit.

Table 6. PTSE-2, experimental pressure vs time values for PTSE-2A and -2B at selected time steps[a]

PTSE-2A		PTSE-2B	
Time (s)	Pressure (MPa)	Time (s)	Pressure (MPa)
110	60.0	157.2	2.7
120	60.5	159.6	2.9
130	61.2	161.9	3.0
140	61.8	164.3	3.0
150	62.2	167.9	3.1
160	62.6	171.5	3.1
170	63.0	178.7	3.2
180	63.2	185.8	3.4
185	62.8	193.0	3.2
200	46.5	200.2	2.9
220	31.5	214.5	2.5
240	21.5	228.8	2.5
260	14.8	243.2	2.6
280	10.4	271.8	2.4
310	10.8	300.5	3.1
340	11.1	329.2	5.5
345	16.7	350.7	9 3
350	26.5	365.0	11.2
355	36.5	386.5	16.3
360	45.8	400.8	20.1
365	52.5	451.0	34.9
370	49.4	501.2	50.0
		551.3	62.9
		572.8	66.9
		575.7	67.3
		576.0	65.1
		576.7	62.3

[a]Time t = 112 s and 155 s at start of thermal transient for PTSE-2A and -2B, respectively.

Table 7. PTSE-2, events identified by transient data in PTSE-2A and -2B

Event	Time[a] (s)	Evidence of event
	PTSE-2A	
Initiation of thermal shock	~112	Outside surface temperature
Initial tearing	112–184.6	Analysis and CMOD
First maximum K_I	184.6	Calculated K_I; CMOD, pressure
Minimum K_I	341.8	Calculated K_I; CMOD, pressure
Precleavage tearing	341.8–361.4	Analysis and CMOD
Initial cleavage propagation	361.4	CMOD
Crack arrest	361.4[b]	CMOD
Axial crack propagation	361.4	Strain and CMOD gages beyond ends of initial flaw
Postcleavage tearing	361.4–365.6	Analysis and CMOD
Final maximum K_I	365.6	Calculated K_I, CMOD, pressure
	PTSE-2B	
Initiation of thermal shock	~155	Outside surface temperature
Precleavage tearing	155–575.8	Analysis and CMOD
Cleavage propagation	575.82	CMOD
Crack arrest	575.82[b]	CMOD
Postcleavage tearing	576.2–576.7	Analysis and CMOD
Rupture of vessel wall	576.7	Pressure, CMOD, strain

[a]Time after start of scanning by the data acquisition system.
[b]Time intervals <10 ms cannot be resolved by the data acquisition system.

Table 8. Fracture features shown in Fig. 14.

Area	Deeper Boundary	Description
A	y_1	Cracked electron-beam weld, smooth dark gray
B	y_2	Precleavage ductile tear in PTSE-2A, dark gray, rough
C	y_3	Cleavage fracture in PTSE-2A, light gray
D	y_4	Postcleavage ductile tear in PTSE-2A, brown or gray band
E	y_5	Precleavage ductile tear in PTSE-2B, medium gray
F	y_6	Cleavage fracture in PTSE-2B, light gray
G	y_6	Narrow band of ductile tearing, medium gray
H	y_7	Same as F
I	y_8	Postcleavage ductile tear in PTSE-2B
J	y_9	Light-gray shear lip in ruptured portion; unbroken ligament, very light gray, near both ends of flaw

Table 9. PTSE-2, dimensions of fracture features of the PTSE-2 flaw

Feature	Depth[a] (mm)
EB weld crack (y_1)	14.5
Initial ductile tear (y_2)	22.5
First cleavage crack (y_3)	39.3
Intermediate tear	
First phase (y_4)	42.4
Second phase (y_5)	46.1
Second cleavage crack (y_7)	78.8
Momentary arrest site[b] (y_6)	69.2

[a]Average total depth of feature over the central part (~400 mm long) of the flaw.

[b]This linear feature is distinct for 500 mm in both directions from the beltline. It is generally an area of ductile tearing from 0.5 to 1.5 mm wide.

Table 10: PTSE-2A, selected characteristics of FE analyses

Analysis Number	Degrees of Freedom in FE-Model	Crack Depth in FE-Model (mm)	Approximation of Stress-Strain Data of Vessel-Insert T(°C)	Bilinear $\sigma y/E_T$(MPa)	Multilinear σy(MPa)	Expansion ($10^{-6}K^{-1}$)	Reference Temperature (°C)
5	515 (2D-plane strain)	14.5	Averaged	200/12087 (set 5)		14.4	300
5′	515 (2D-plane strain)	19.6	Averaged		70 (set 5)	17.3	300
7	3200 (2D-plane strain)	19.6	Averaged		70 (set 5)	14.4	
8	3800 (2D-plane strain)	14.5-19.6	Averaged	400/2637 (set 5)		14.4	300
9	1922 (2D-plane strain)	14.5-19.6	Averaged		375 (set 7)	14.4	290
10	2419 (2D-plane strain)	14.5	Averaged	495/2300 (set 7)		14.4	300

Table 11: PTSE-2B, selected characteristics of FE analyses

Analysis Number	Degrees of Freedom in FE-Model	Crack Depth in FE-Model (mm)	Residual Stress Considered	Approximation of Stress-Strain Data of Vessel-Insert T(°C)	Bilinear $\sigma y/E_T$(MPa)	Multilinear σy(MPa)	Expansion ($10^{-6}K^{-1}$)	Reference Temperature (°C)
5	551 (2D-plane strain)	42.4	Yes	Averaged	373/7313 (set 7)		14.4	275
7	3200 (2D-plane strain)	42.4	No	Averaged		70 (set 5)	14.4	
8	3800 (2D-plane strain)	42.4-46.1	Yes	Averaged	400/2637 (set 5)		14.4	275

Table 12. Stress-plastic-strain modules H′ for HSST wide-plate material (HSST plate 13A of A 533 grade B class 1 steel)

Plastic strain interval (%)	Temperature interval (°C)	$H' = \Delta\sigma/\Delta\epsilon^p$ (MPa/%)
<1	-125.00 < T < -72.78	0.345
	-72.78 ≤ T < 37.78	16.044 + 0.214 T
	37.78 ≤ T < 148.89	21.787 + 0.062 T
	148.89 ≤ T < 260.00	-24.407 + 0.372 T
1-2	-125.00 < T < 260.00	37.23
2-4	-125.00 < T < 260.00	26.579 - 0.00776 T
4-8	-125.000 < T < 37.78	11.228 - 0.0599 T
	37.78 ≤ T < 260.00	8.96
8-12	-125.00 < T < -17.78	-0.0276 - 0.0403 T
	-17.78 ≤ T < 260.00	0.689

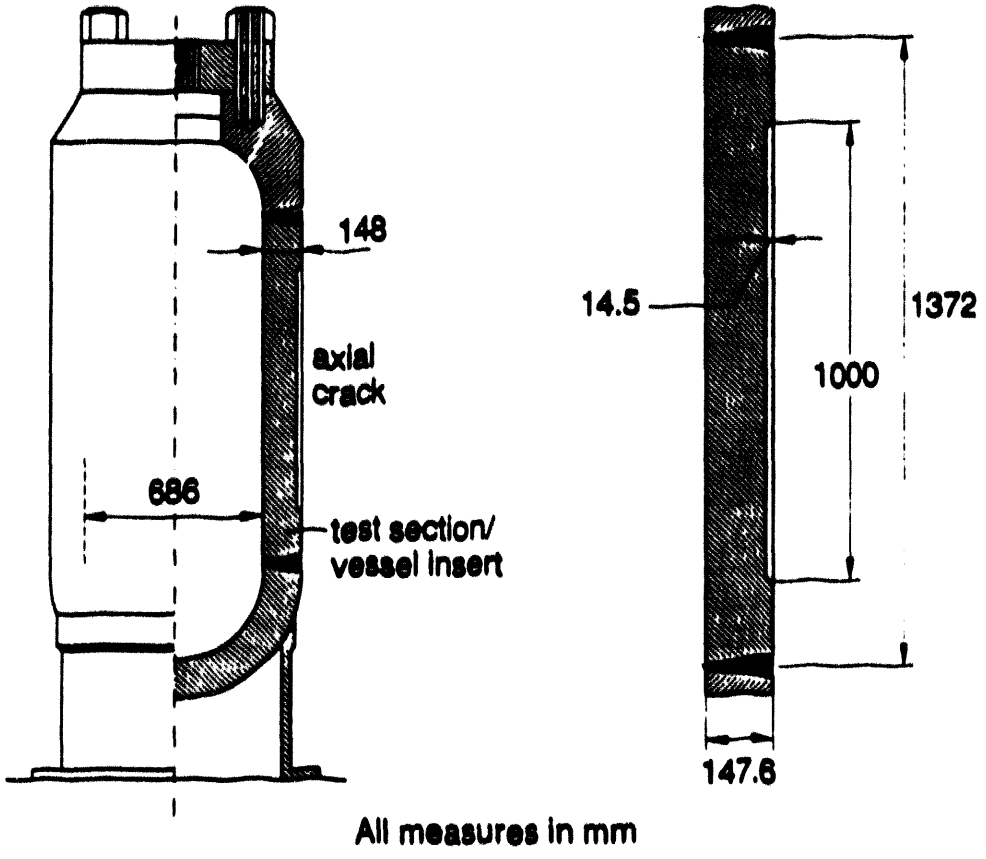

Fig. 1 PTSE-2A, test vessel and crack geometry for transient A (ORNL, USA).

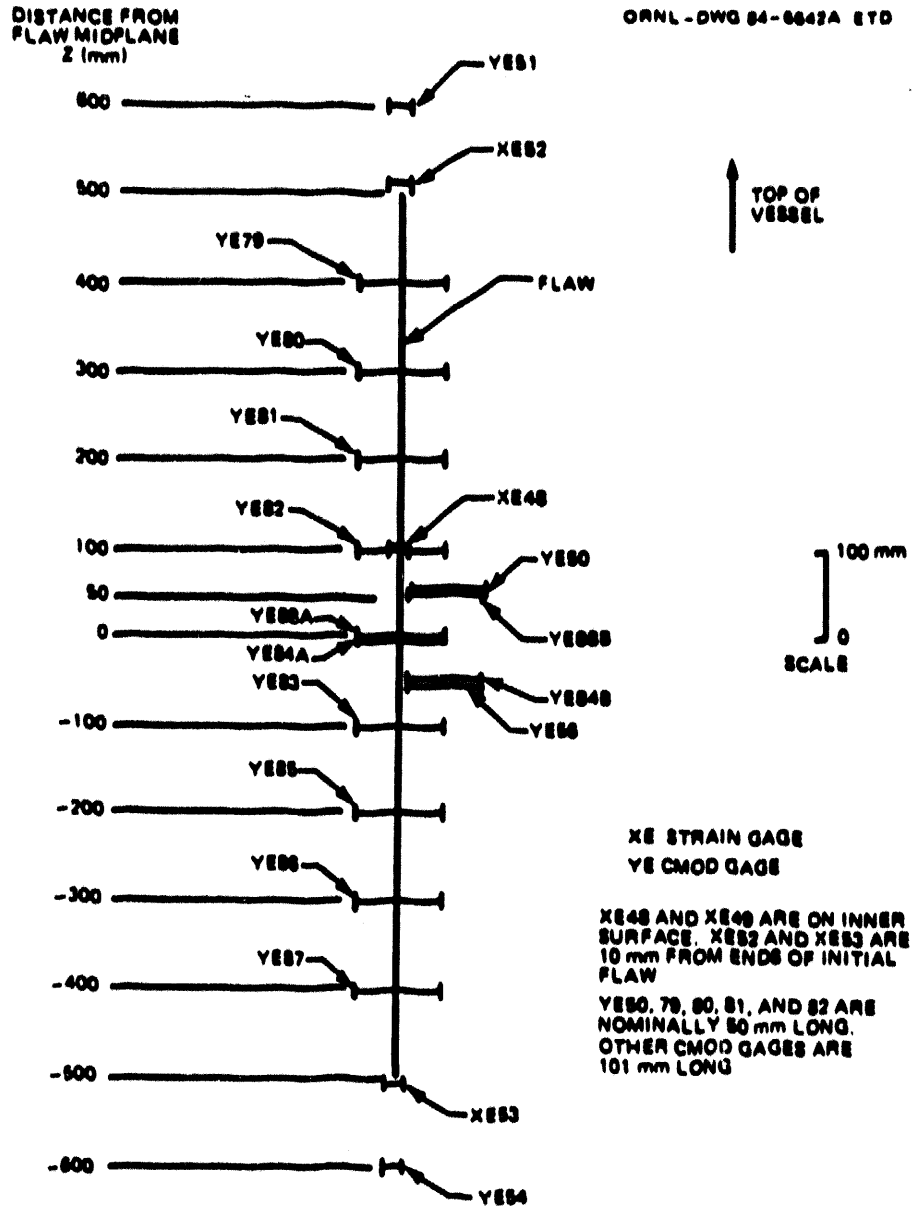

Fig. 2 PTSE-2, locations of CMOD gages and strain gages near flaw on PTSE-2 vessel.

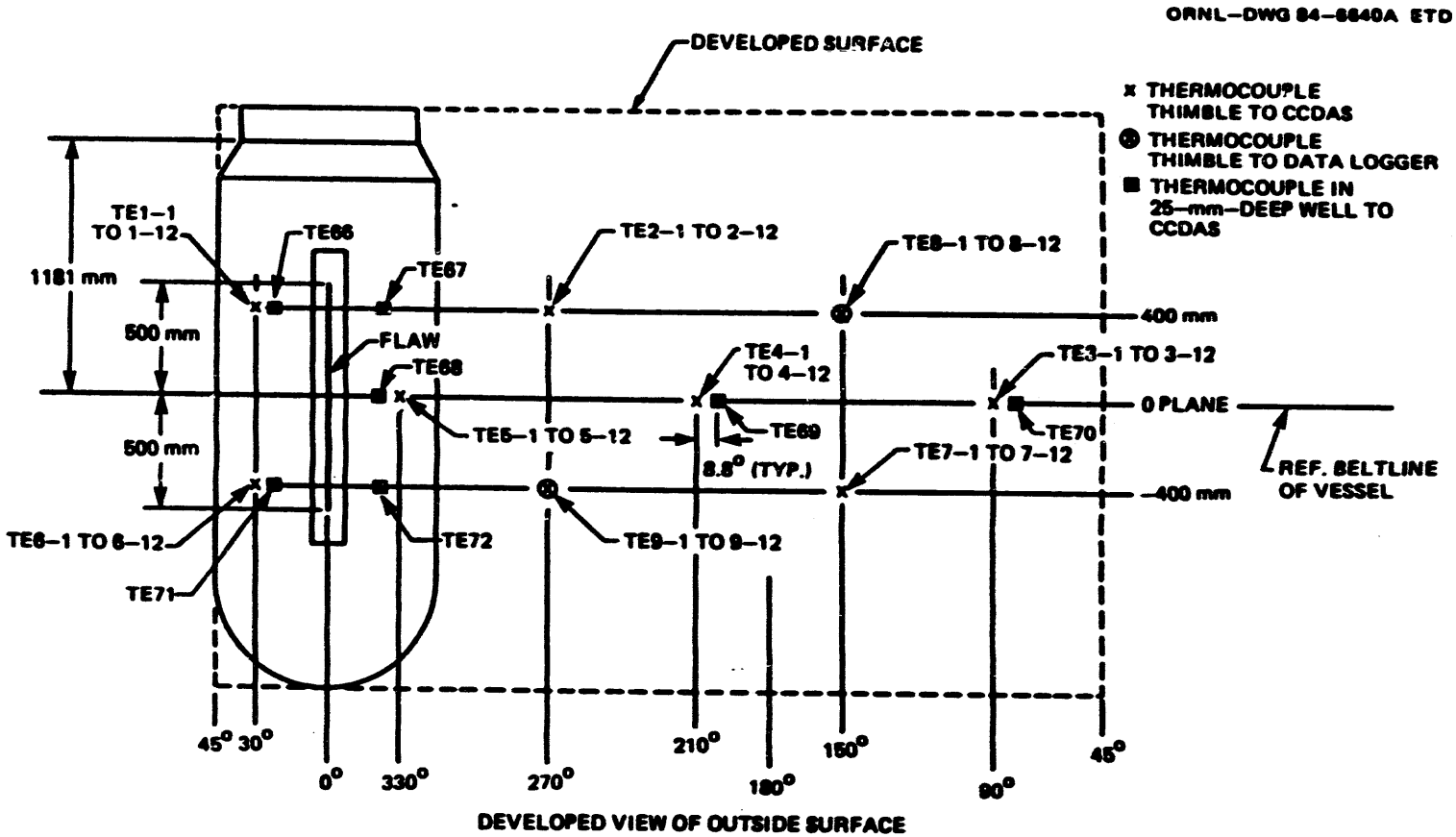

Fig. 3 PTSE-2, thermocouple thimble and near-surface thermocouple locations in PTSE-2.

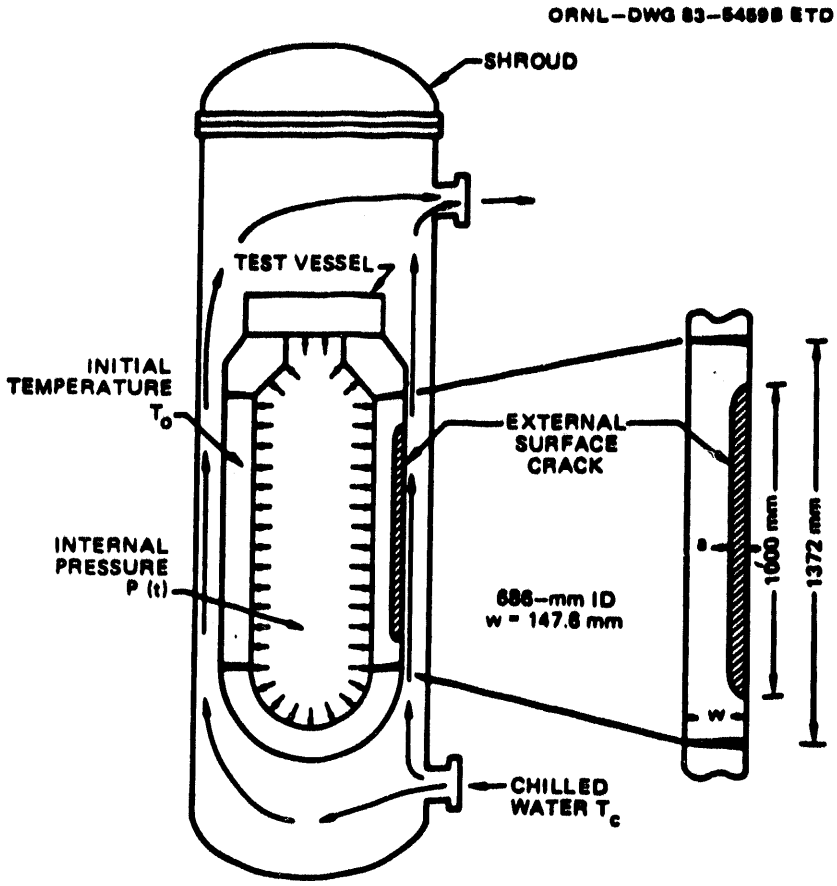

Fig. 4 PTSE-2, schematic view of pressurized-thermal-shock vessel inside shroud.

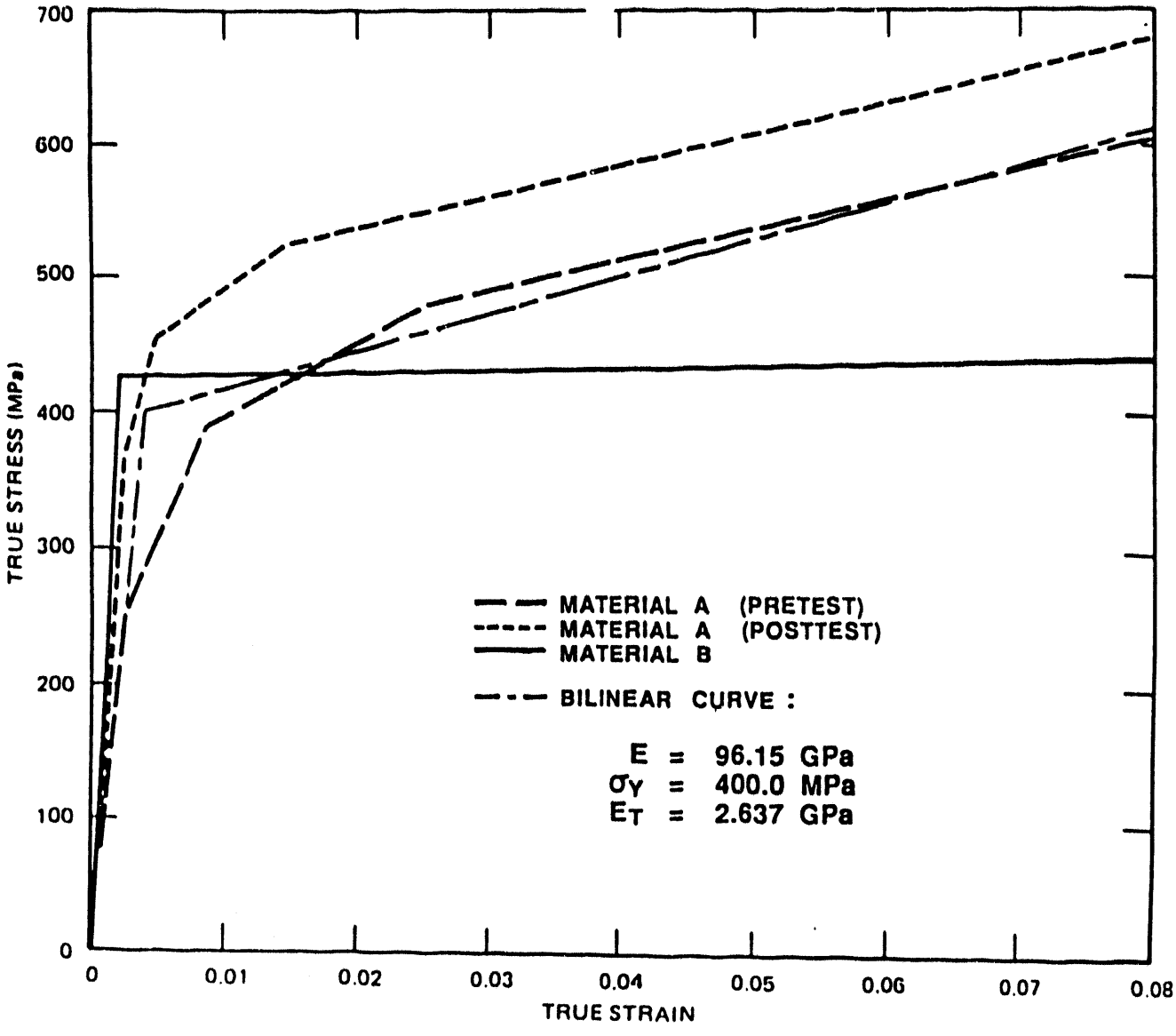

Fig. 5 PTSE-2, stress-strain curves used in analyses of the PTSE-2 experiment.

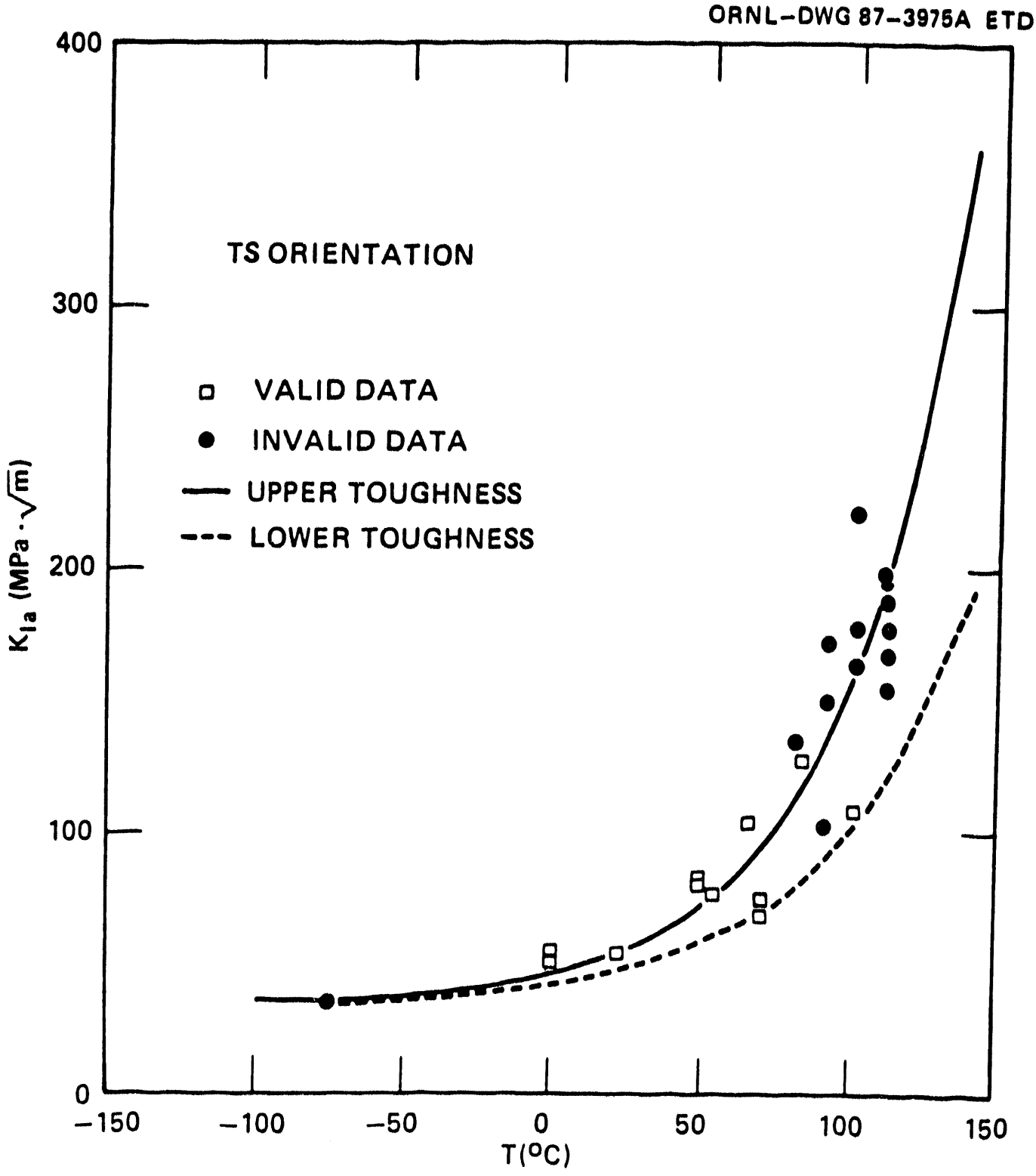

Fig. 6(a) PTSE-2, crack-arrest toughness data for characterization piece PTC1. Upper-toughness curve is least-squares fit to data shown. Lower-toughness curve is similar fit to β-adjusted data (points not shown).

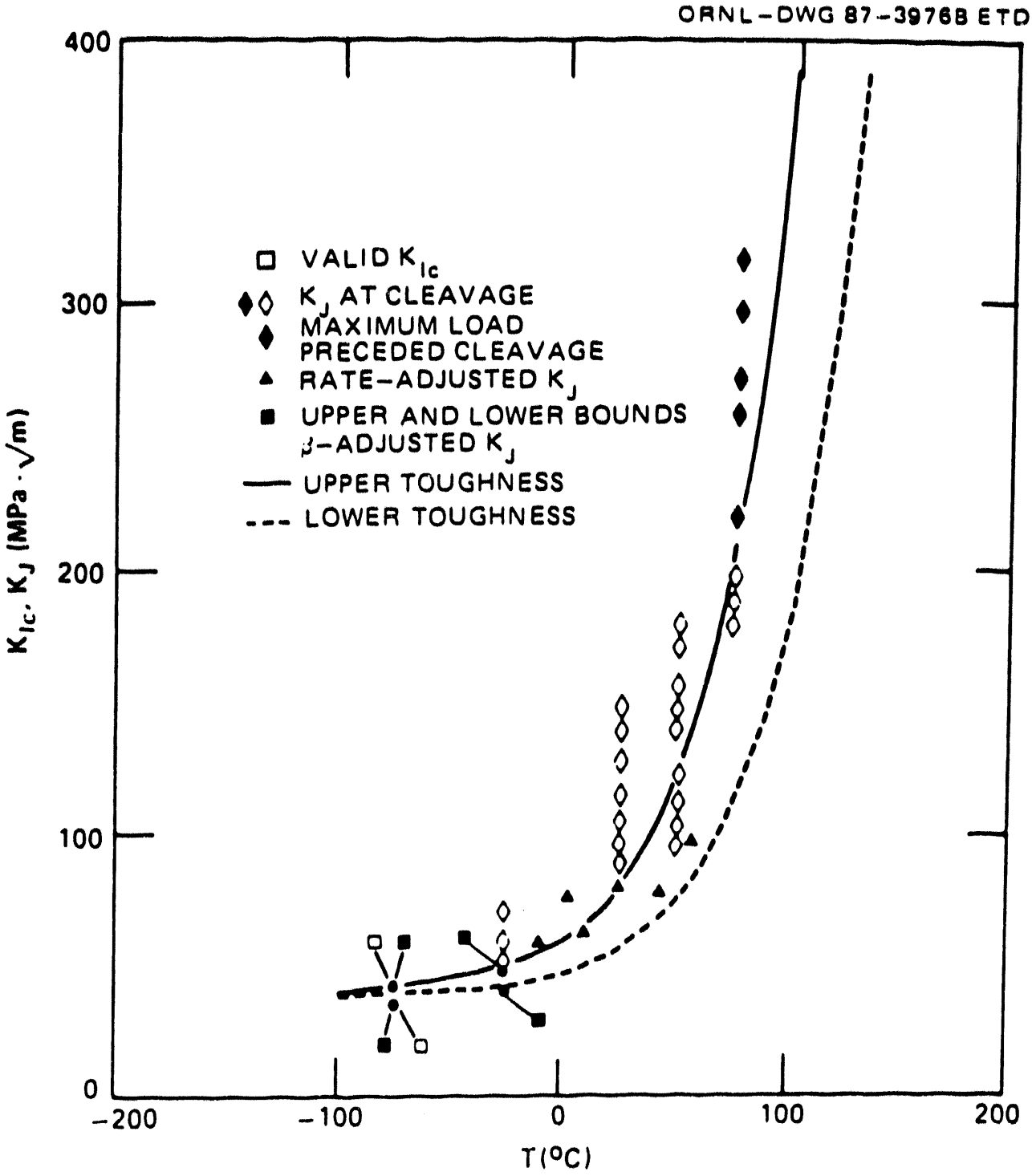

Fig. 6(b) PTSE-2, fracture toughness data for characterization piece PTC1. Two lowest points are only valid K_{Ic} data. Upper-toughness curve is least-squares adjusted and rate adjusted points.

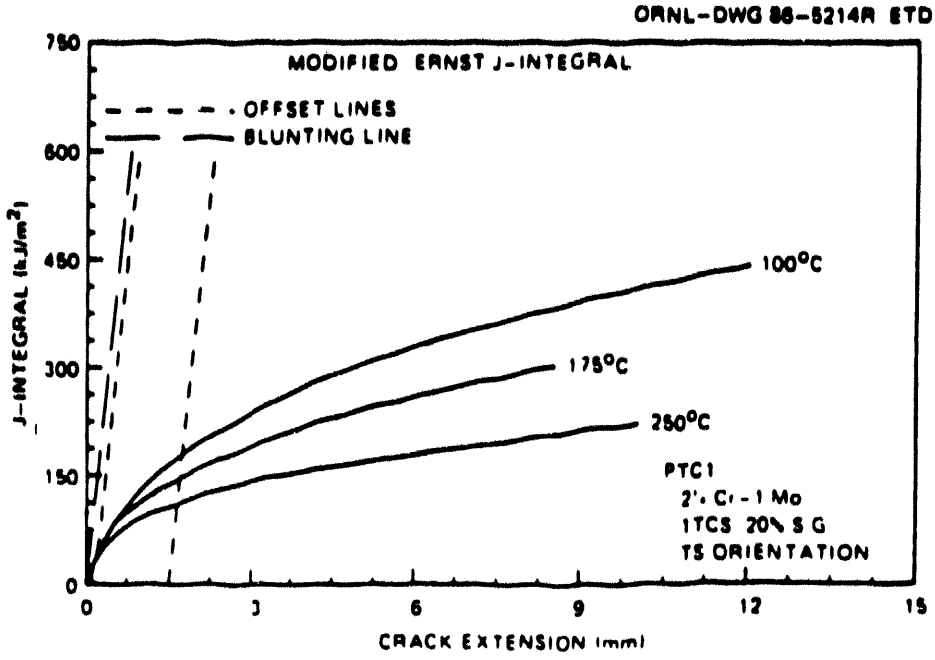

Fig. 7 PTSE-2, comparison of J-integral (J_m) resistance curves at three test temperatures for TS orientation near plate surface of characterization block PTC5.

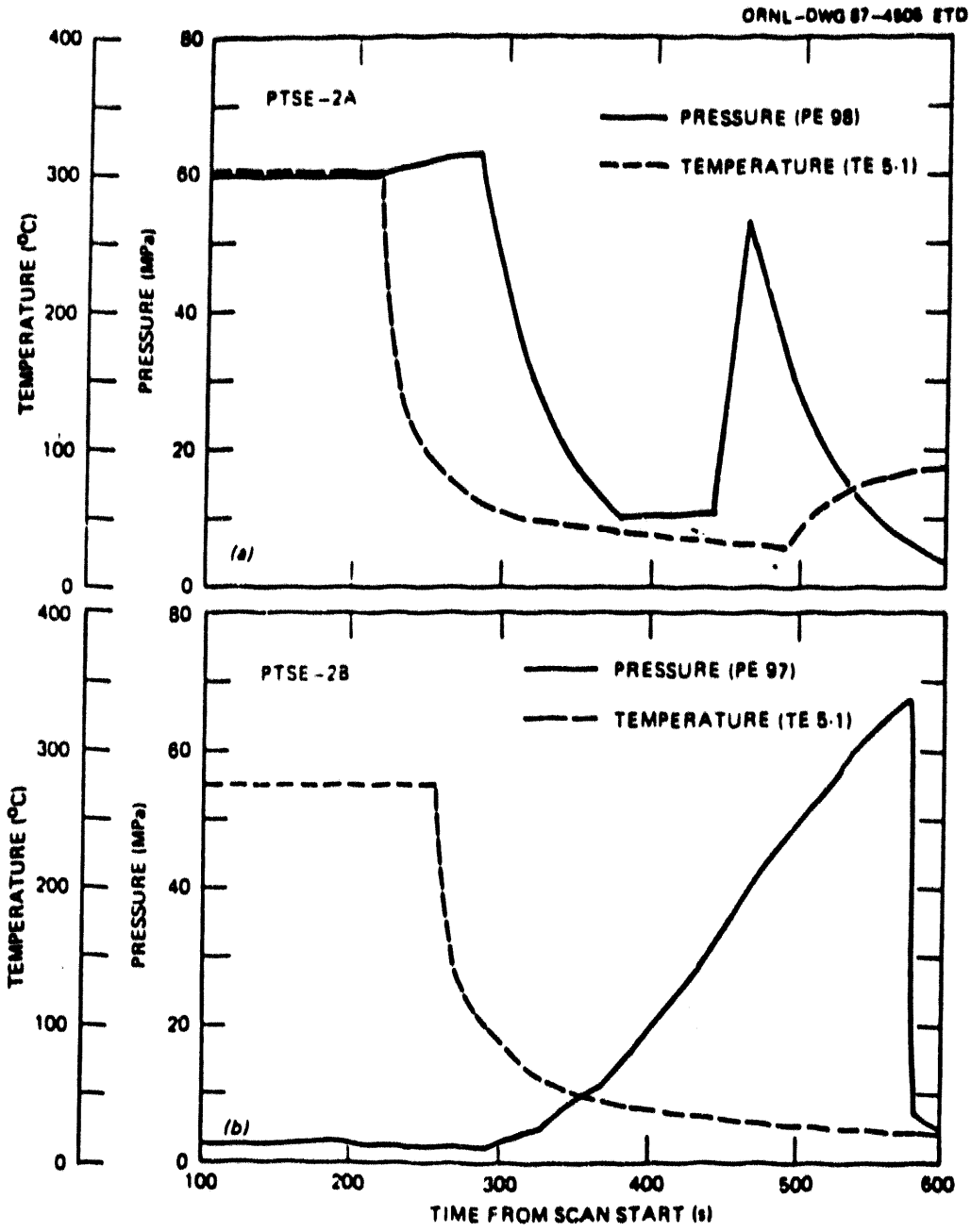

Fig. 8 PTSE-2, temperature and pressure vs time data recorded by PTSE-2 transients: (a) PTSE-2A and (b) PTSE-2B.

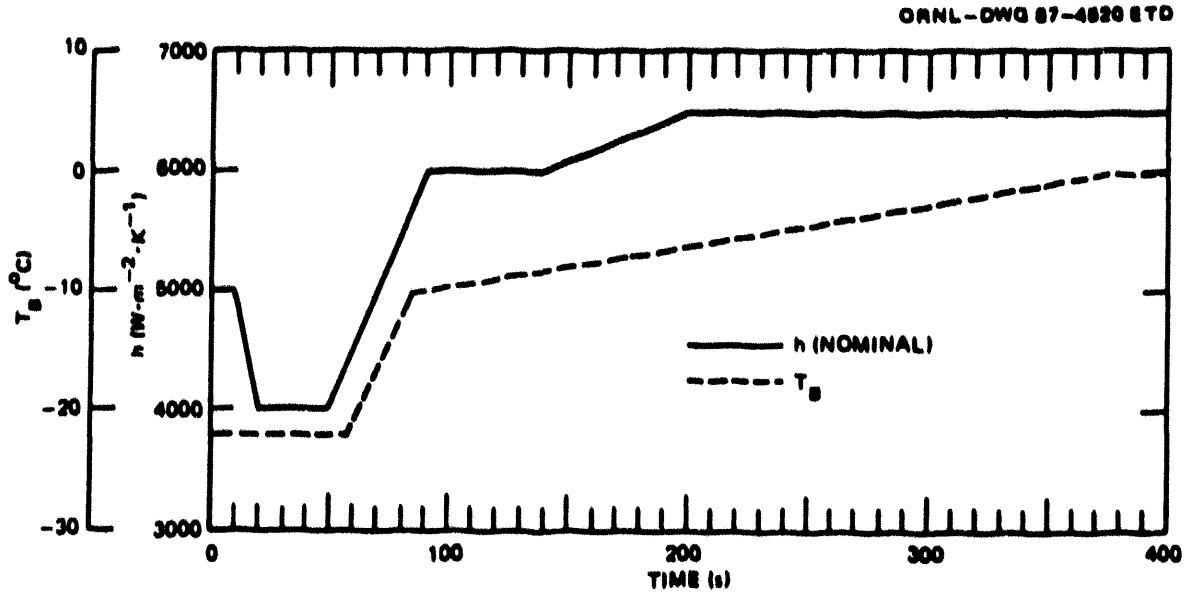

Fig. 9 PTSE-2A, time-dependent values of h (heat convection coefficient) and T_B (bulk coolant temperature) established from pretest thermo-hydraulic measurement and heat transfer analyses. Final ORNL pretest analyses included variants of h 10% above and below normal.

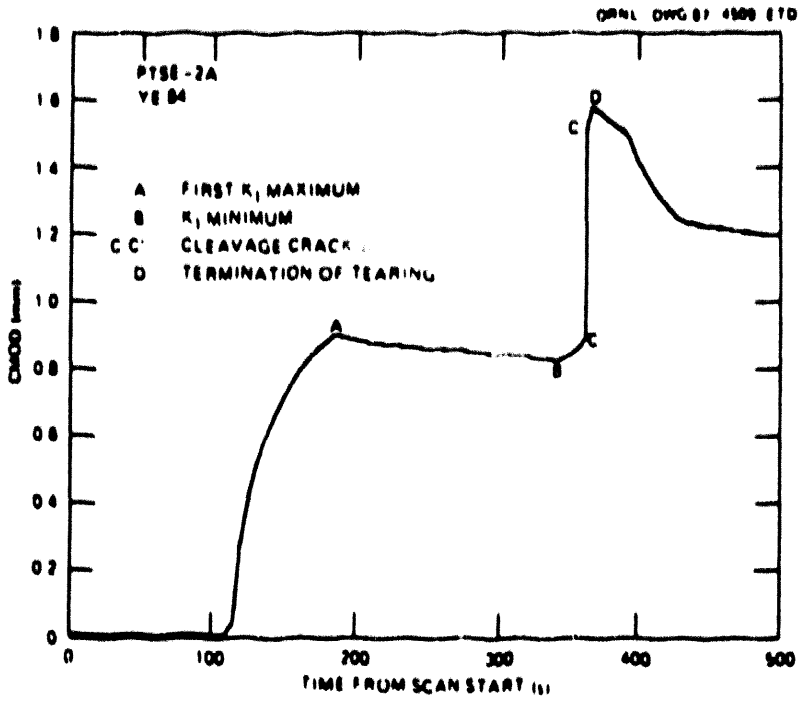

Fig. 10 PTSE-2A, CMOD vs time at center of flaw for PTSE-2A transient.

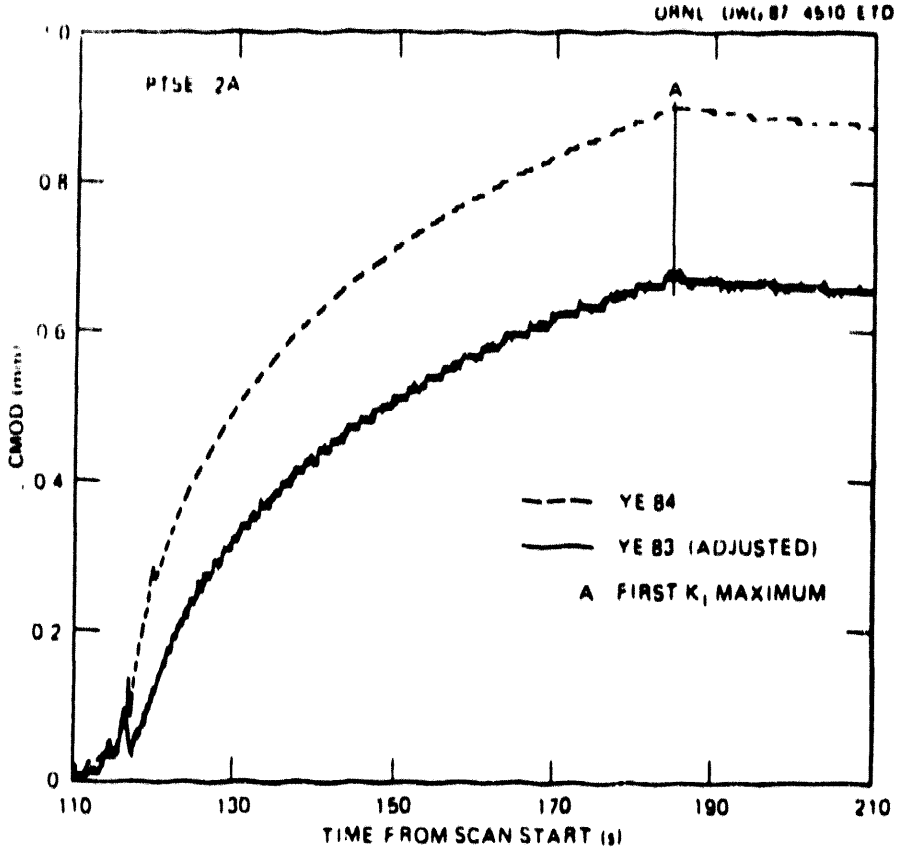

Fig. 11 PTSE-2A, CMOD vs time during early phase of PTSE-2A measured at center of flaw (z = 0) and 100 mm below center (z = -100 mm) by gages YE84 and YE83, respectively (see Fig. 2). The YE84 output was naturally biased by incorporation of a dummy gage in the bridge circuit. The YE83 output has been adjusted by subtracting the output of a dummy gage (YE56).

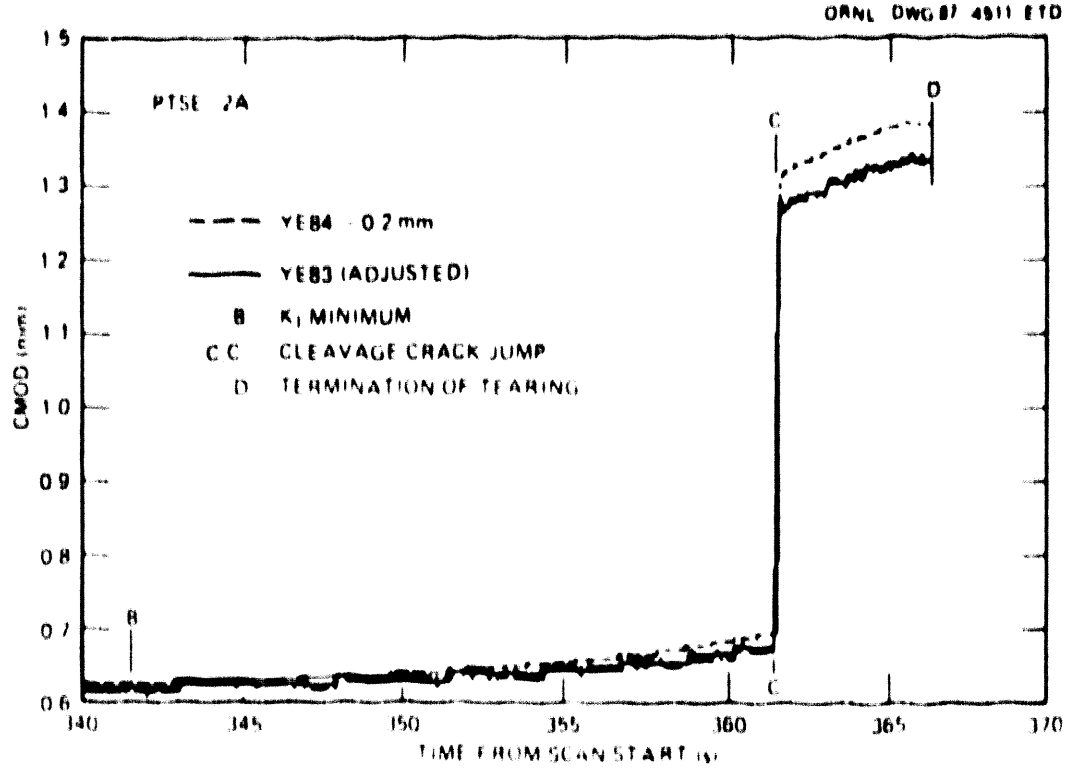

Fig. 12 PTSE-2A, CMOD vs time for final phase of PTSE-2A. The effects of precleavage tearing, cleavage crack propagation, and posteleavage tearing are shown. The output of gage YE84 has been shifted by 0.2 mm to facilitate comparison of the changes in CMOD at two proximal points while the crack was growing.

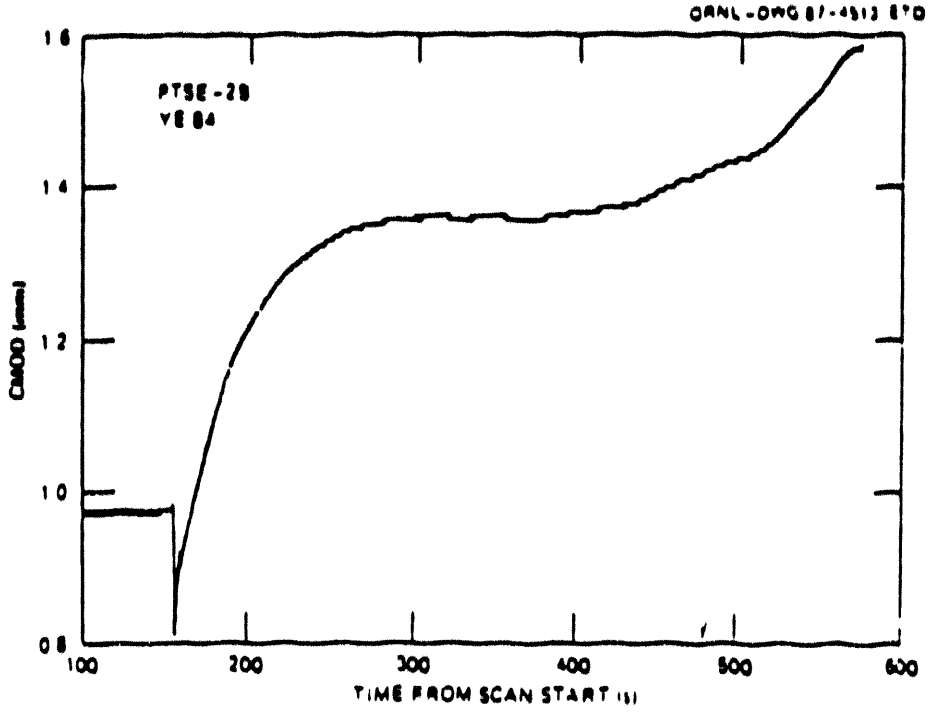

Fig. 13 PTSE-2B, typical CMOD behavior during the PTSE-2B transient. CMOD gage YE84 is at the center of the flaw.

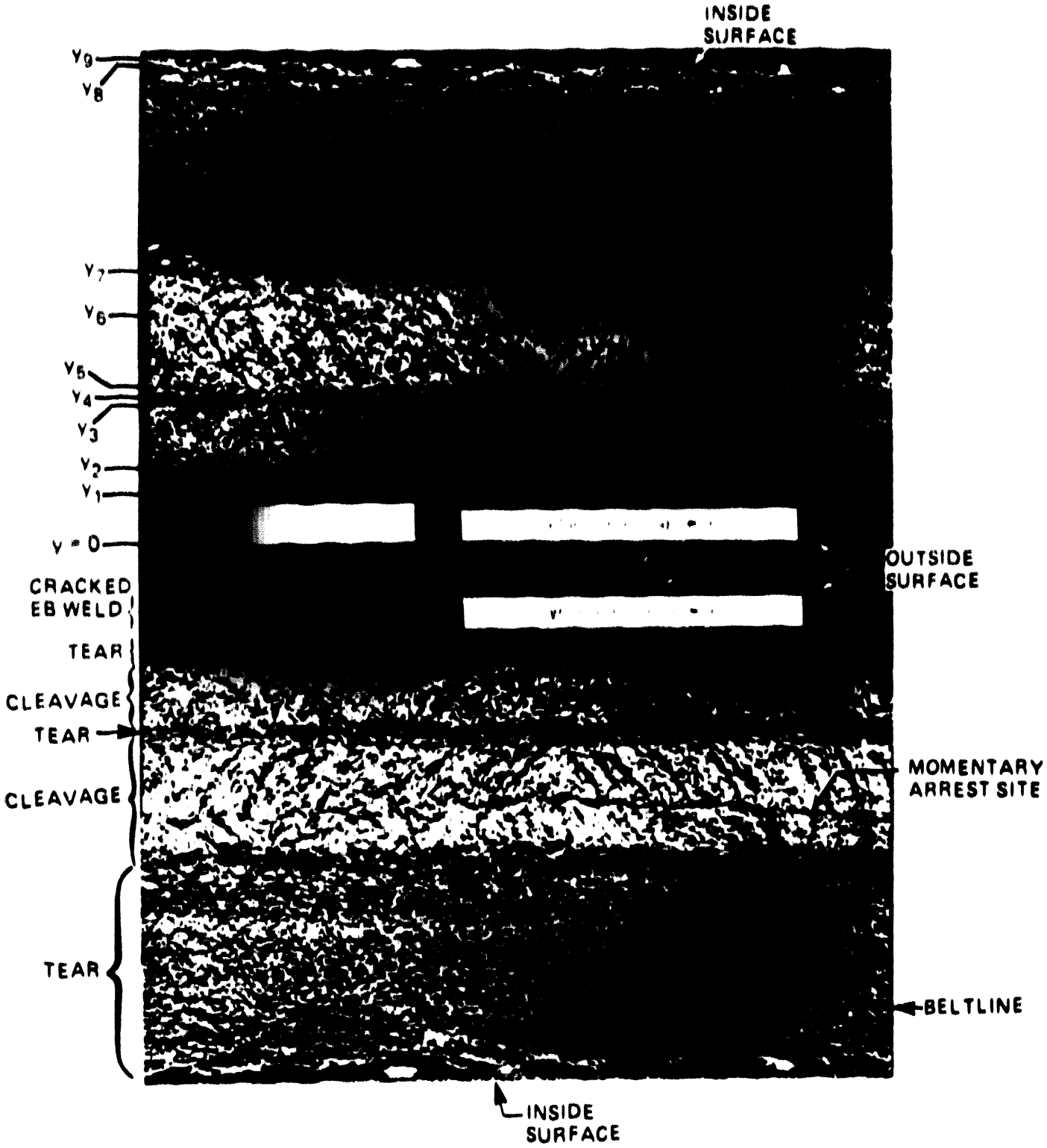

Fig. 14 PTSE-2, photograph of a central segment of PTSE-2 fracture surfaces. The depths (y) are described in Table 8.

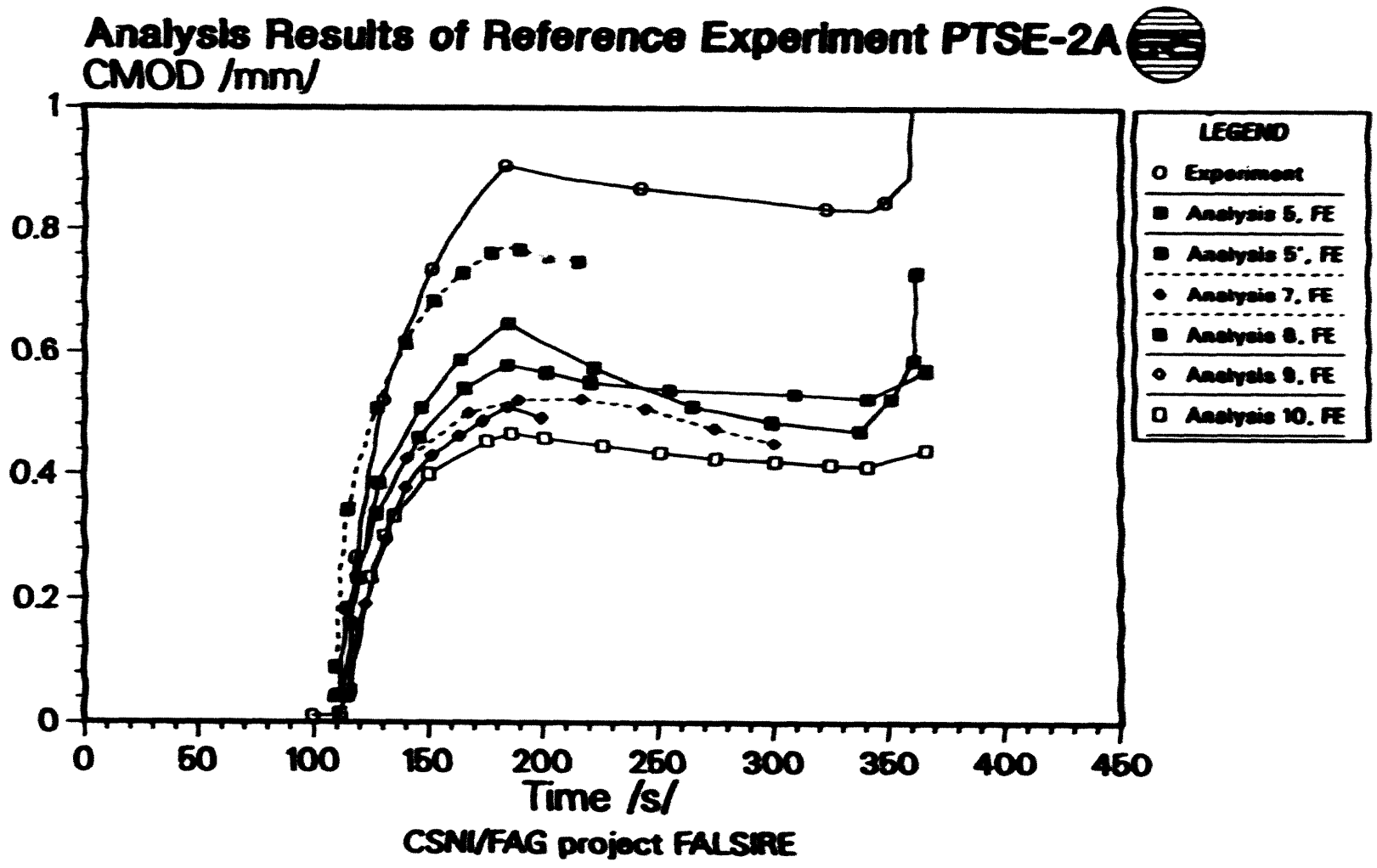

Fig. 15 PTSE-2A. CMOD vs time.

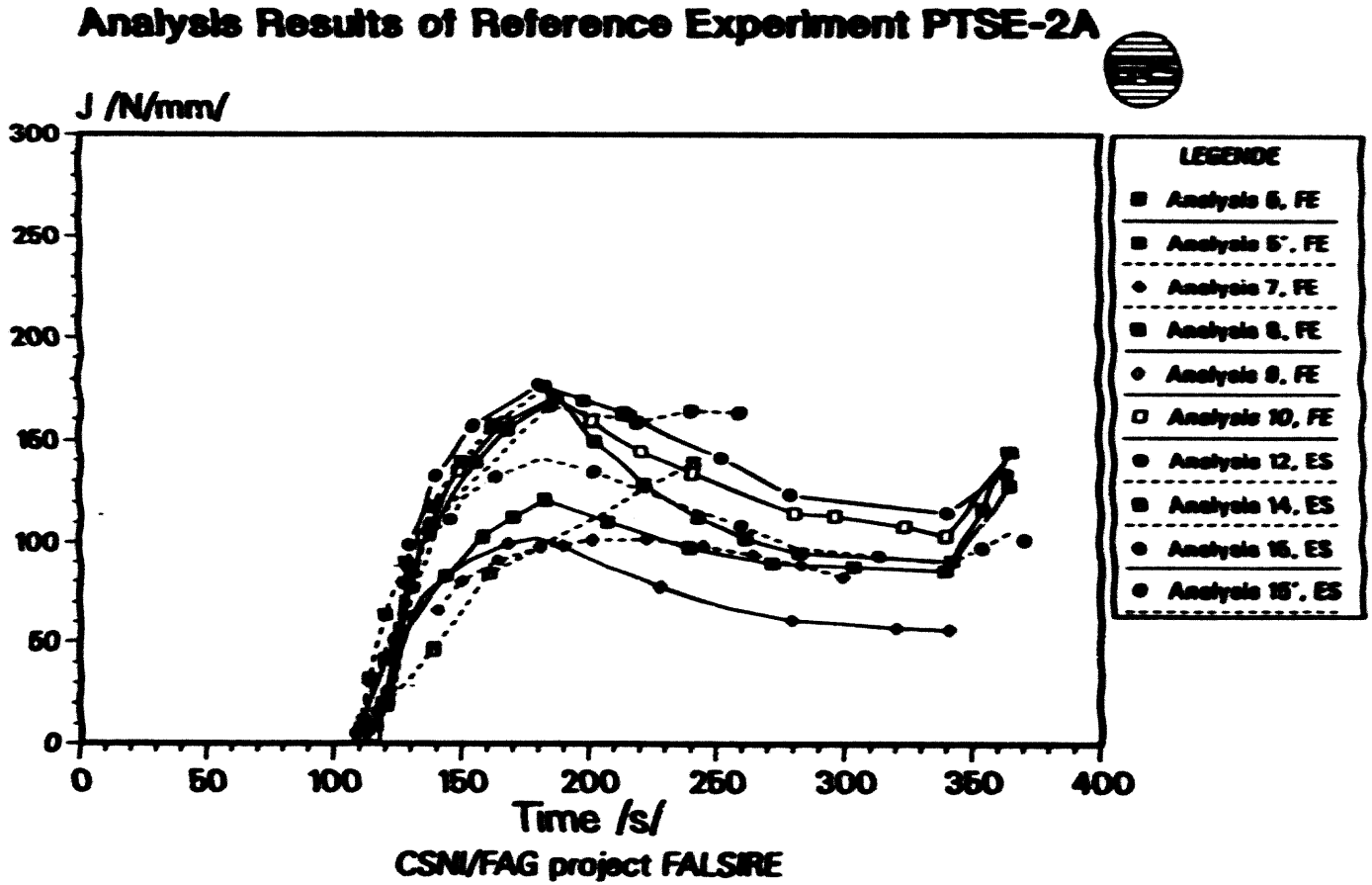

Fig. 16 PTSE-2A, J-integral vs time.

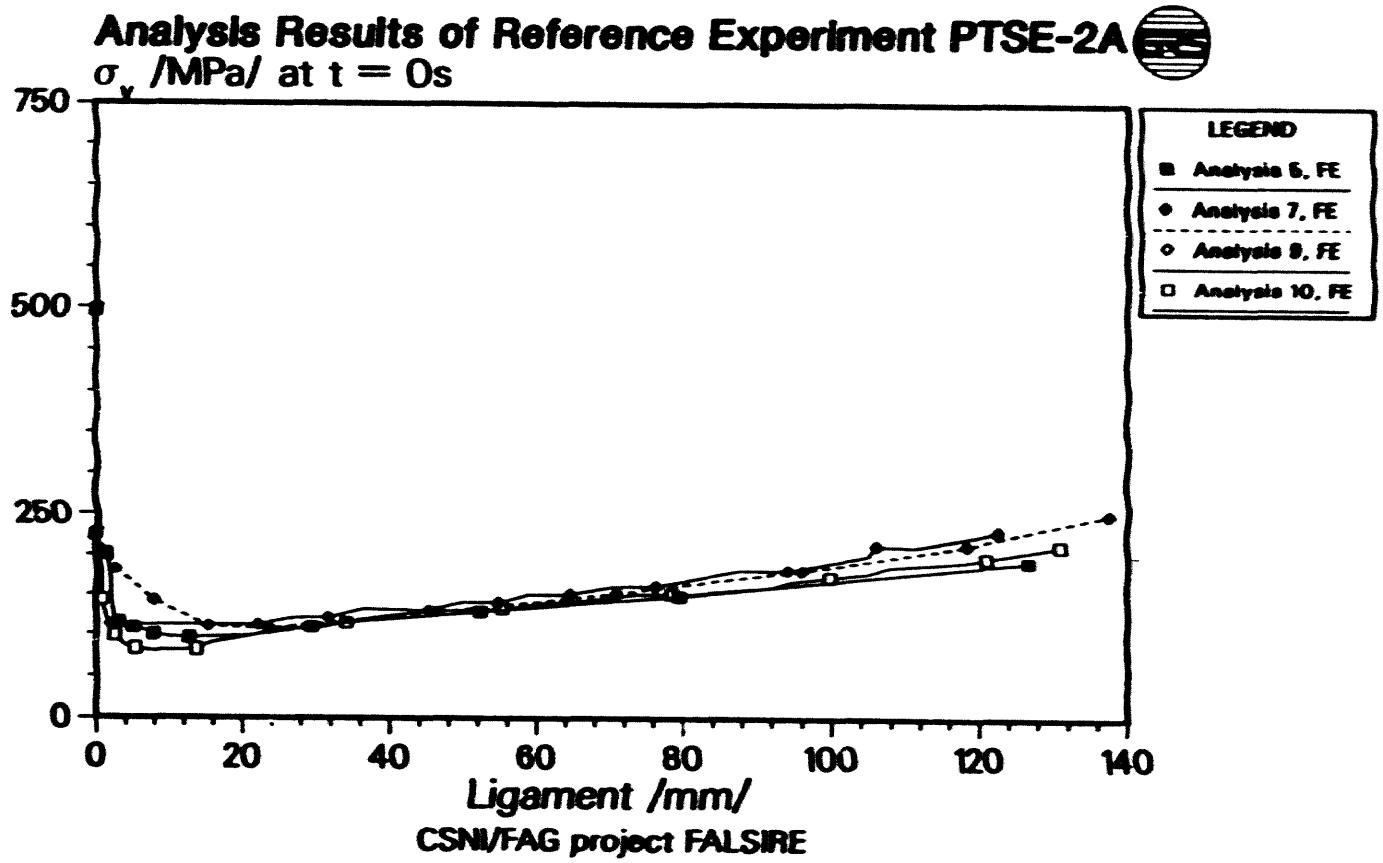

Fig. 17 PTSE-2A, effective stresses on the ligament t = 0 s.

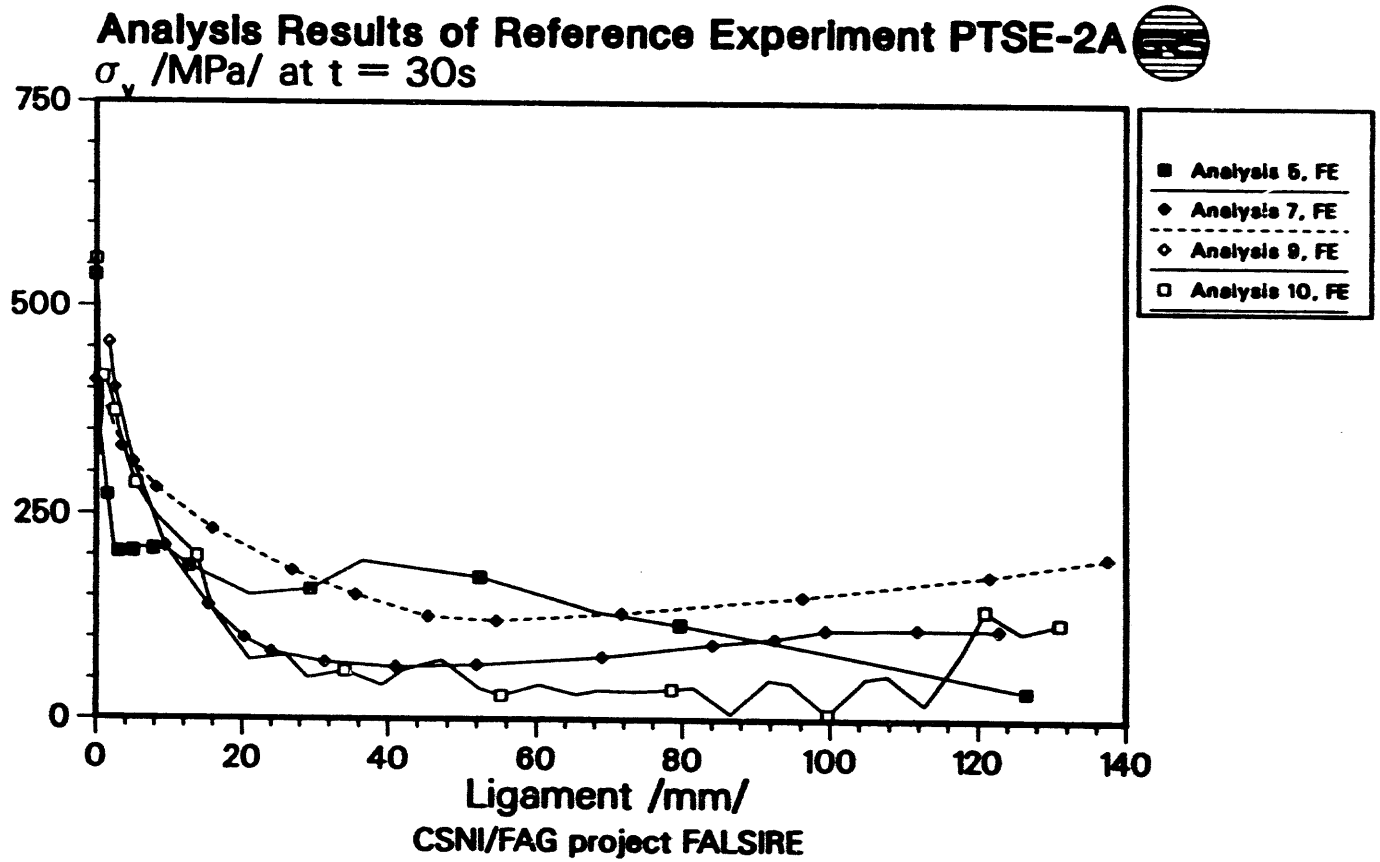

Fig. 18 PTSE-2A, effective stresses on the ligament t = 30 s.

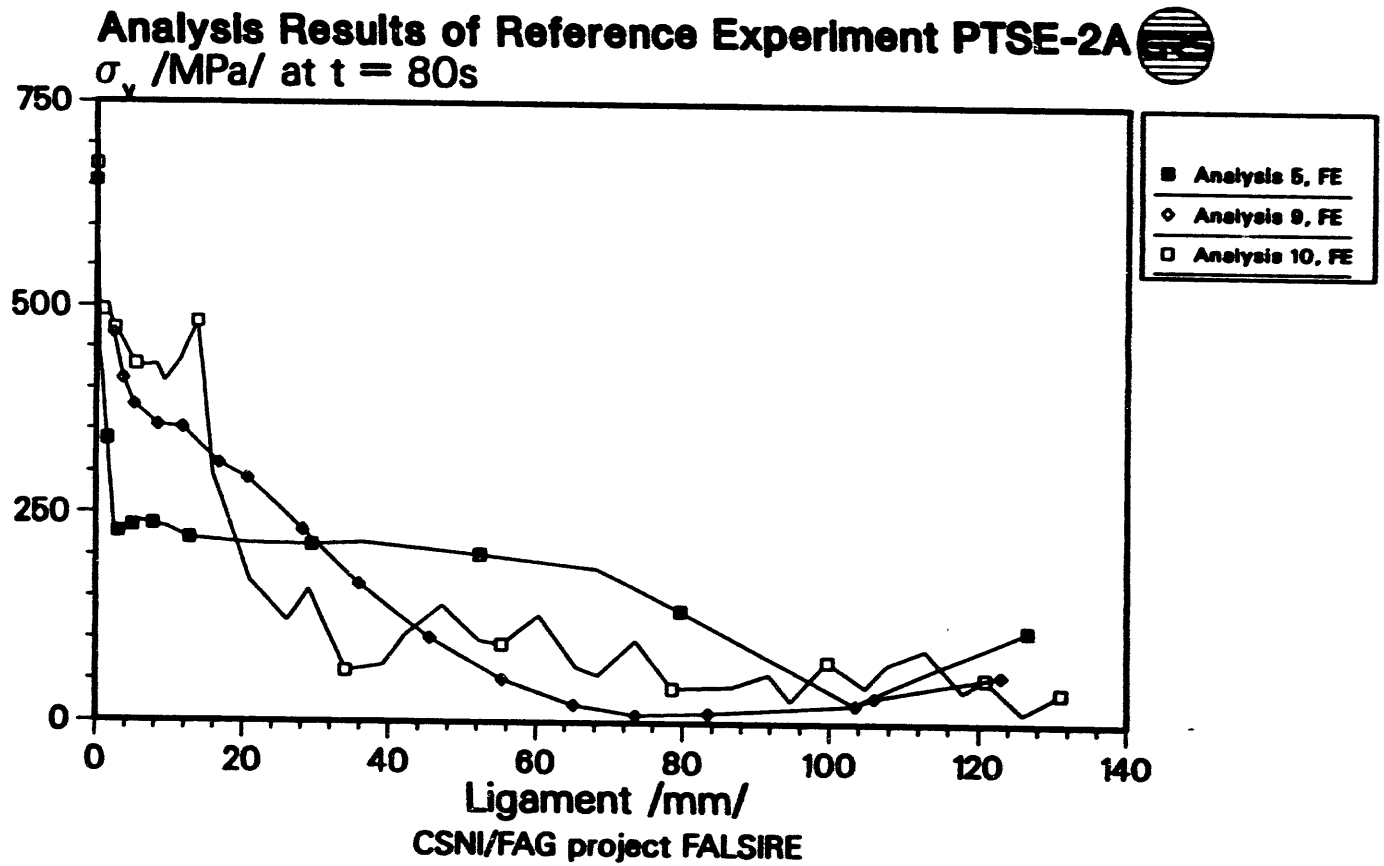

Fig. 19 PTSE-2A, effective stresses on the ligament t = 80 s.

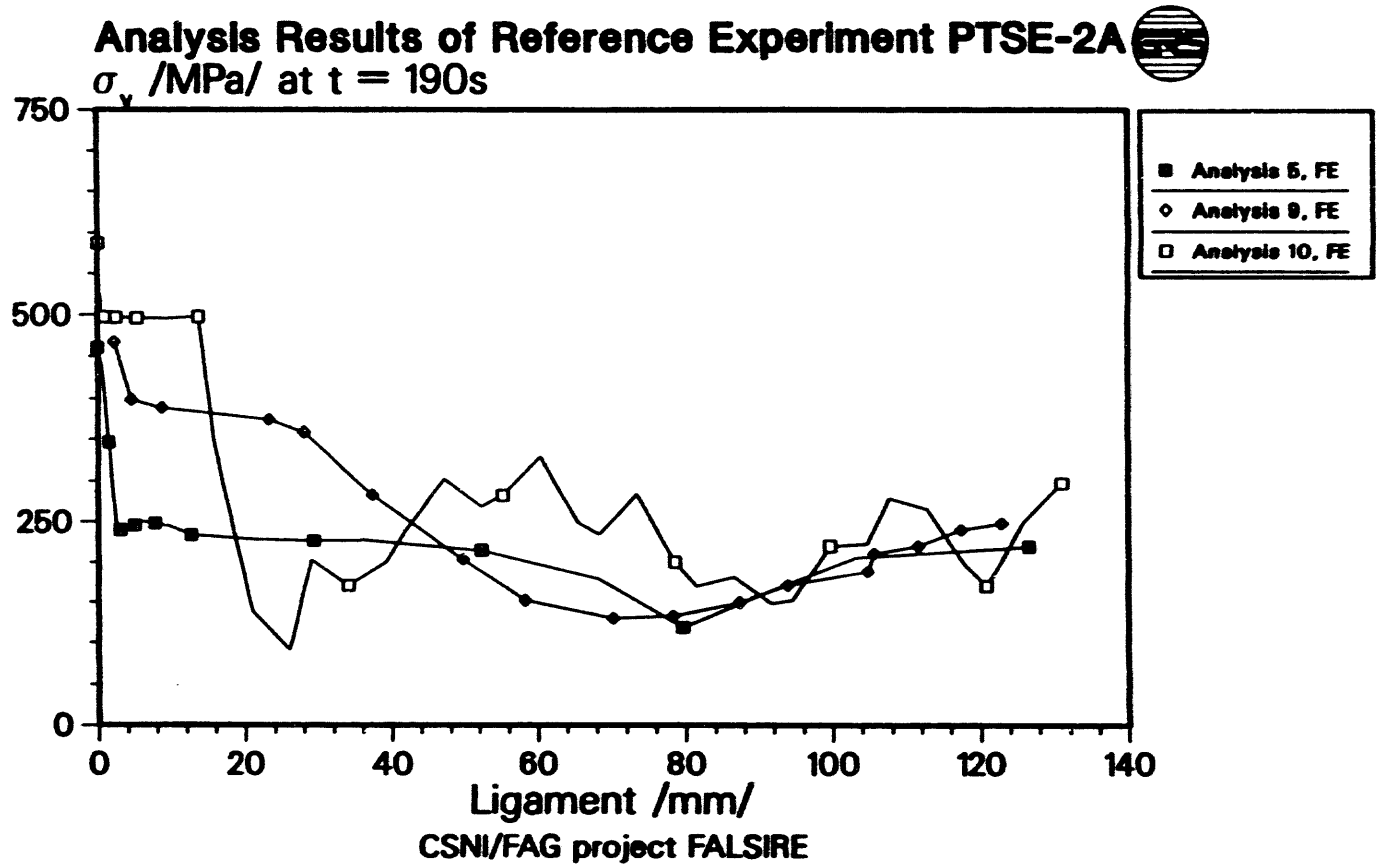

Fig. 20 PTSE-2A, effective stresses on the ligament t = 190 s.

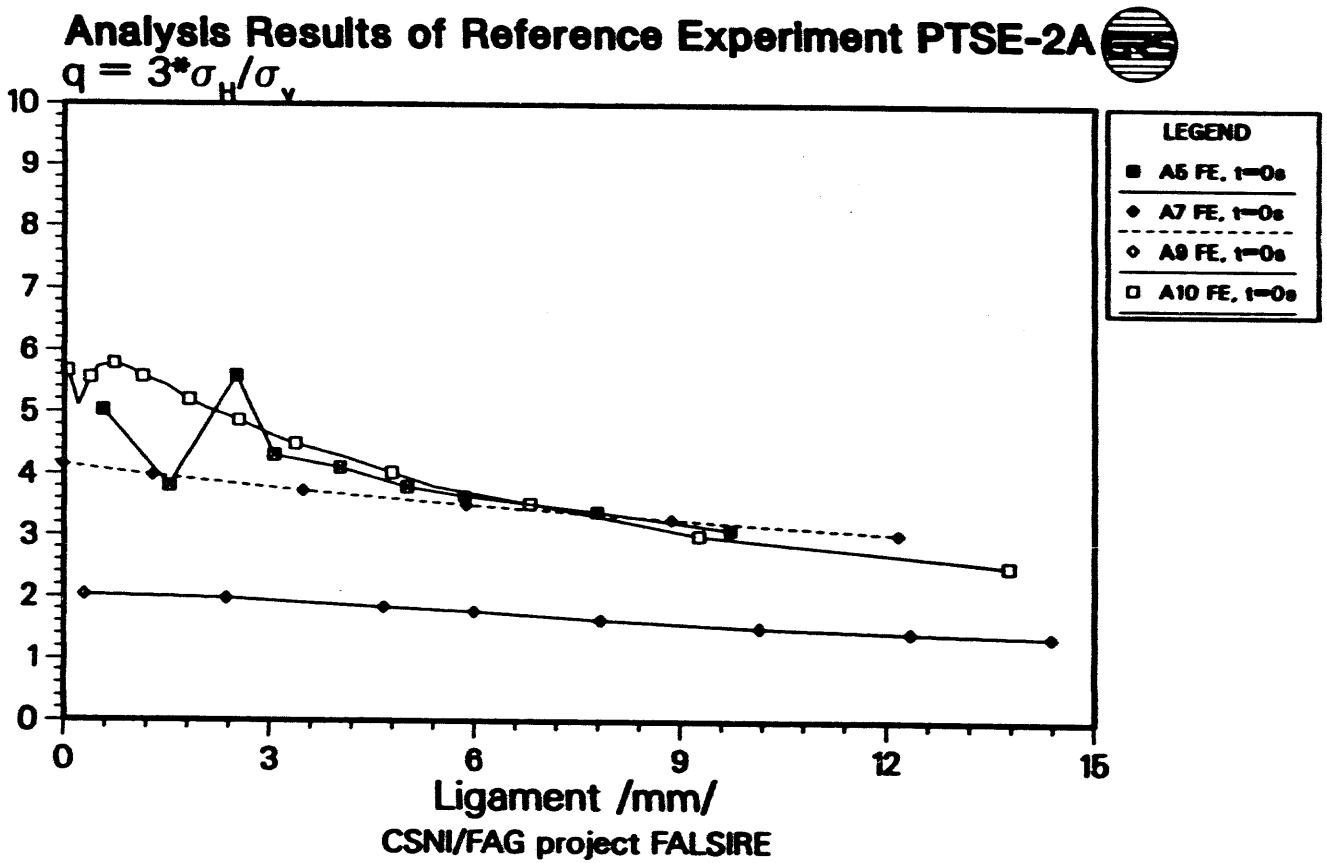

Fig. 21 PTSE-2A, stress triaxiality on the ligament t = 0 s.

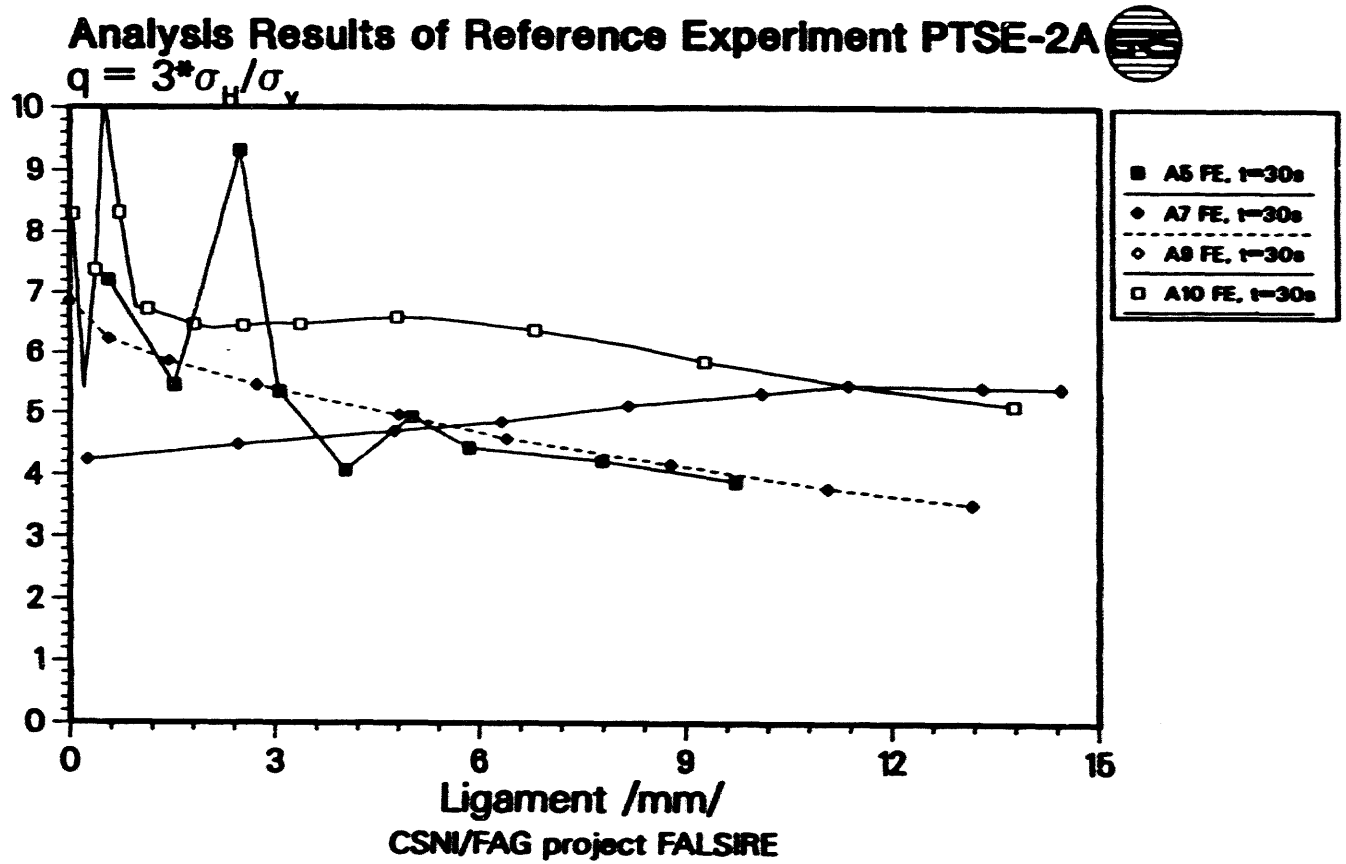

Fig. 22 PTSE-2A, stress triaxiality on the ligament t = 30 s.

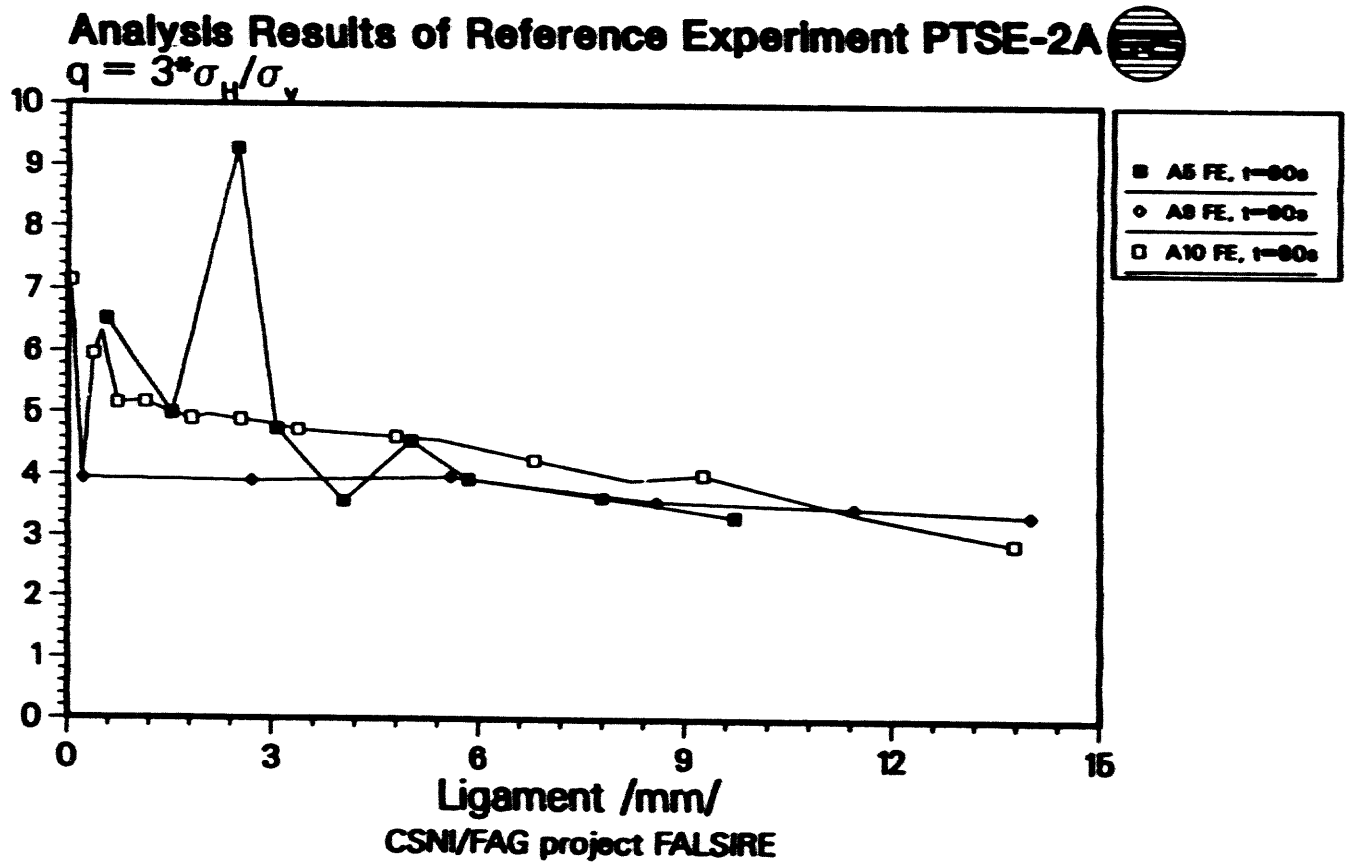

Fig. 23 PTSE-2A, stress triaxiality on the ligament t = 80 s.

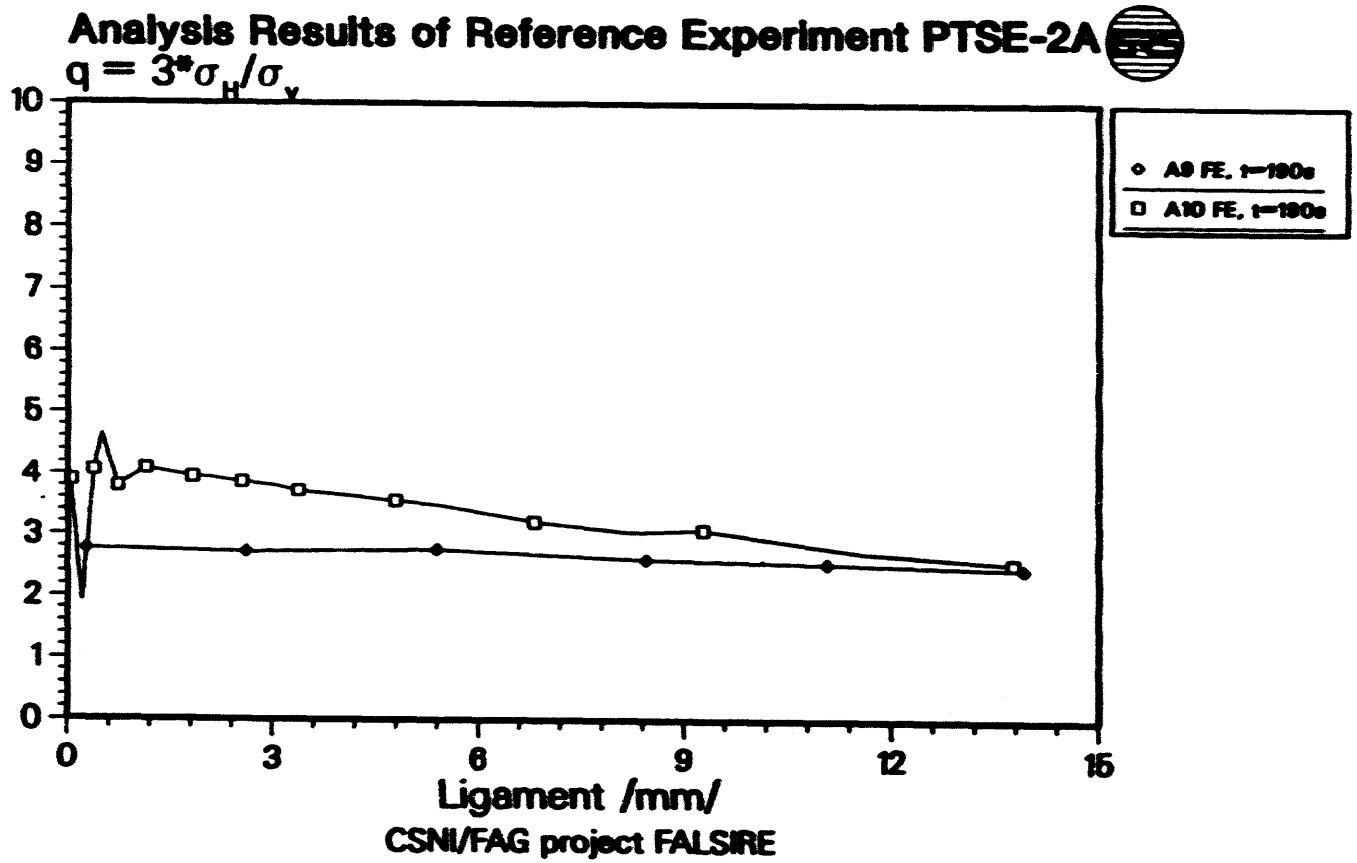

Fig. 24 PTSE-2A, stress triaxiality on the ligament t = 190 s.

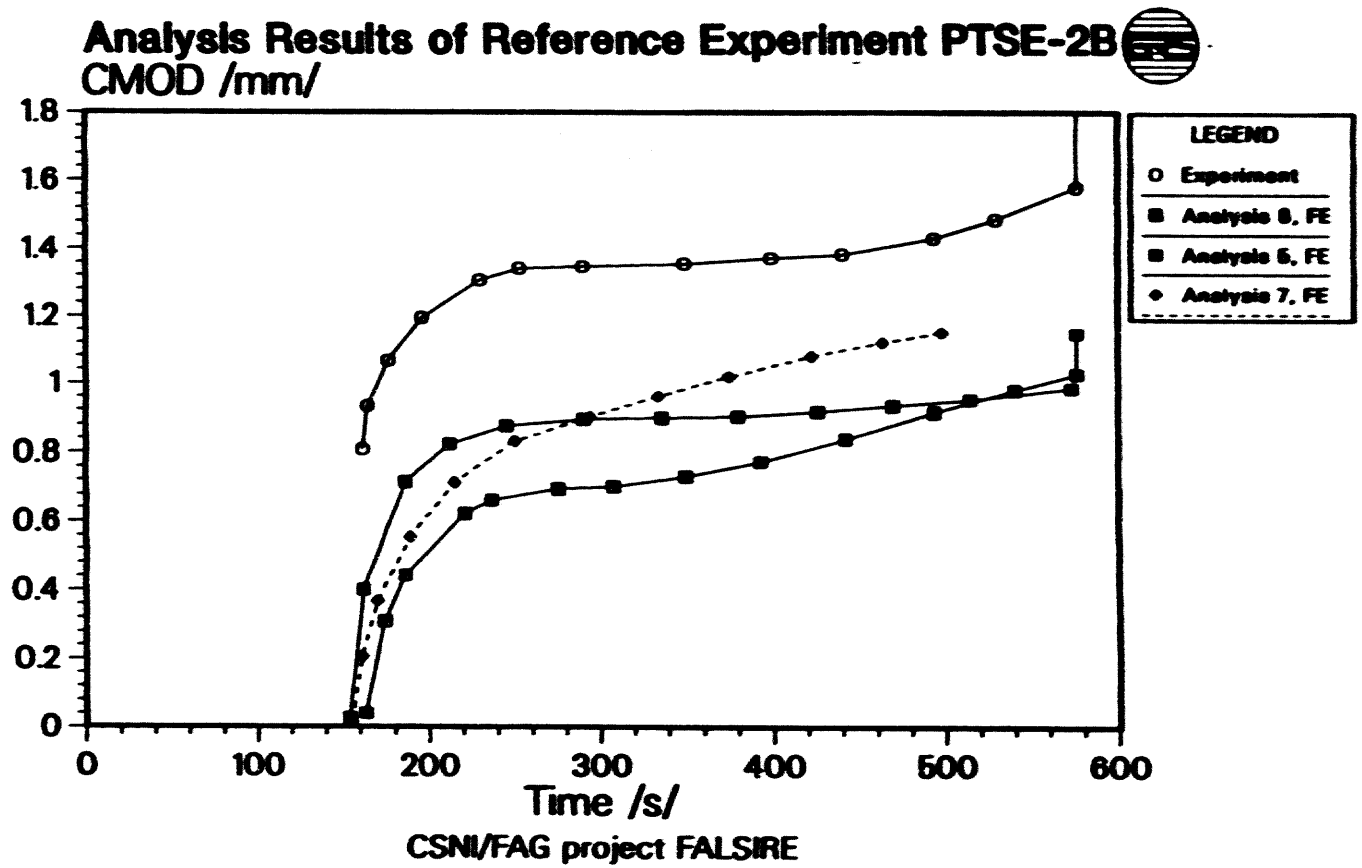

Fig. 25 PTSE-2B, CMOD vs time.

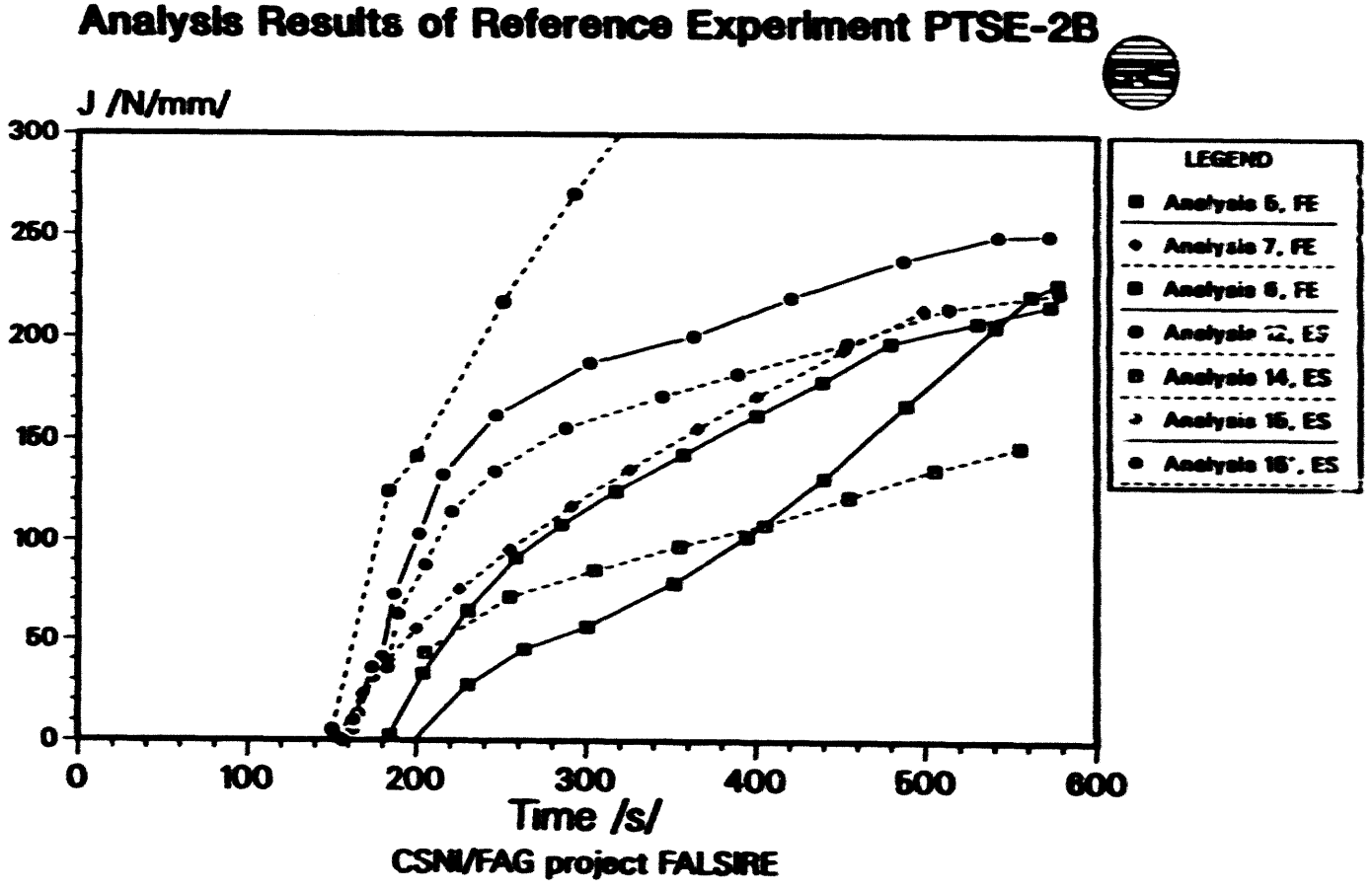

Fig. 26 PTSE-2B, J-integral vs time.

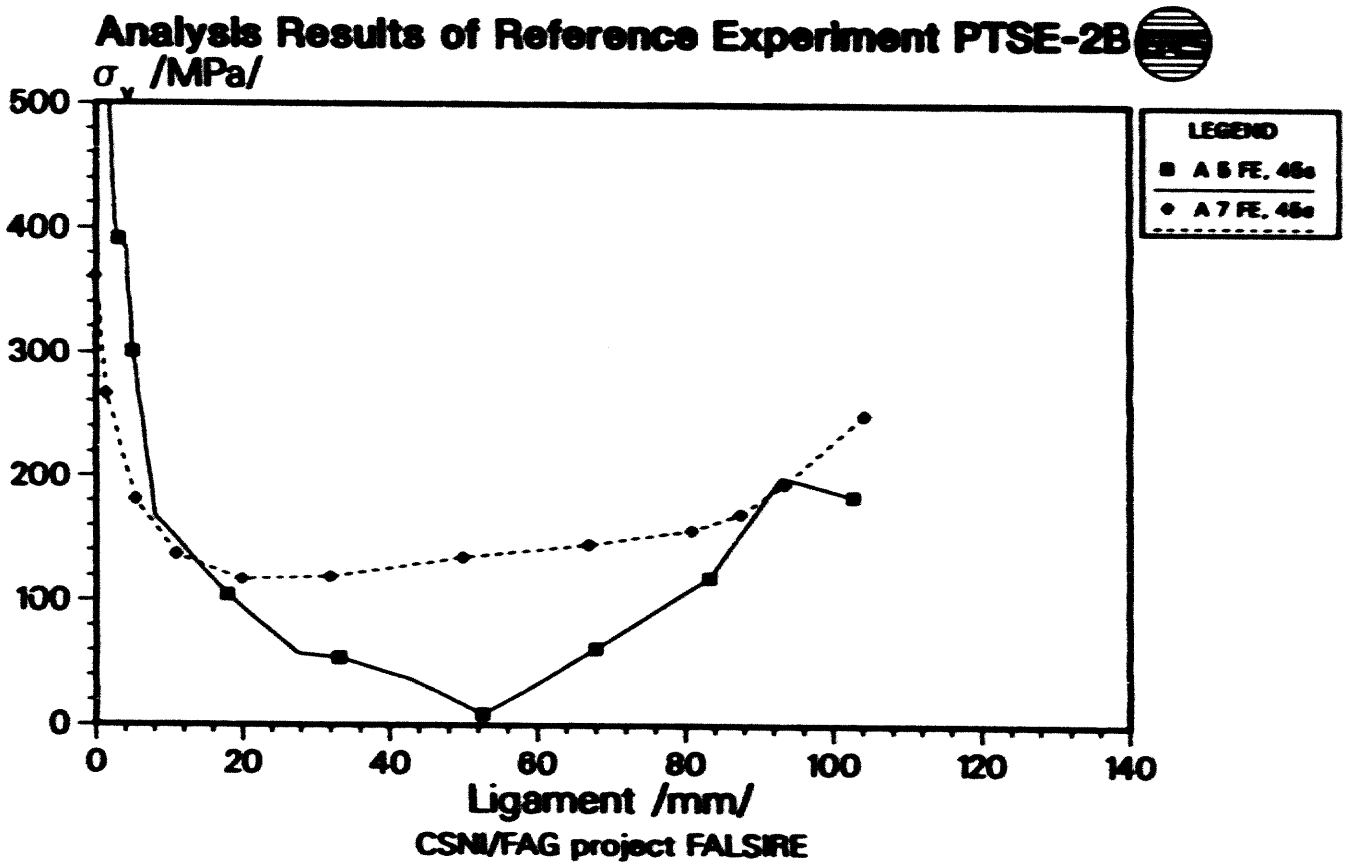

Fig. 27 PTSE-2B. effective stresses on the ligament t = 45 s.

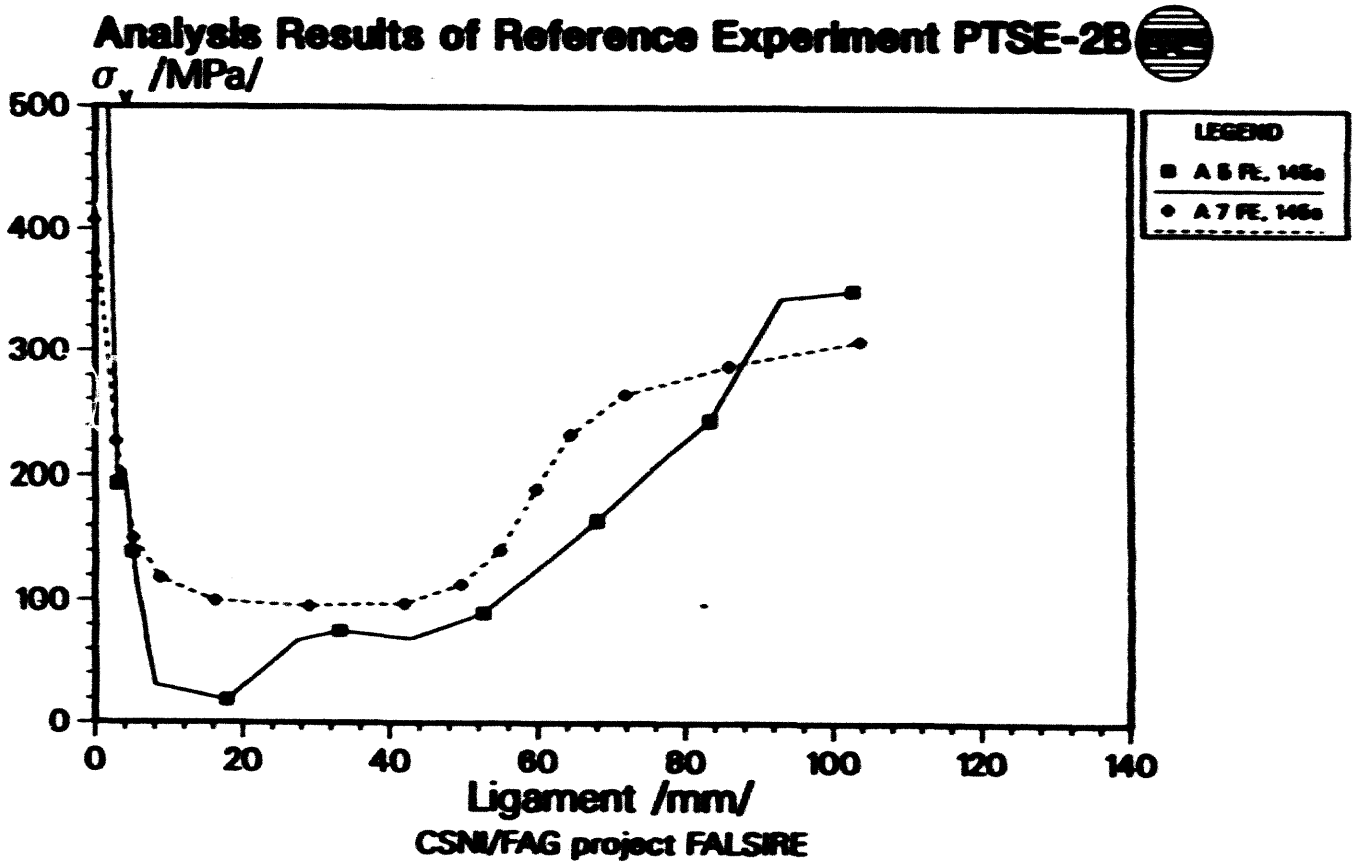

Fig. 28 PTSE-2B, effective stresses on the ligament t = 145 s.

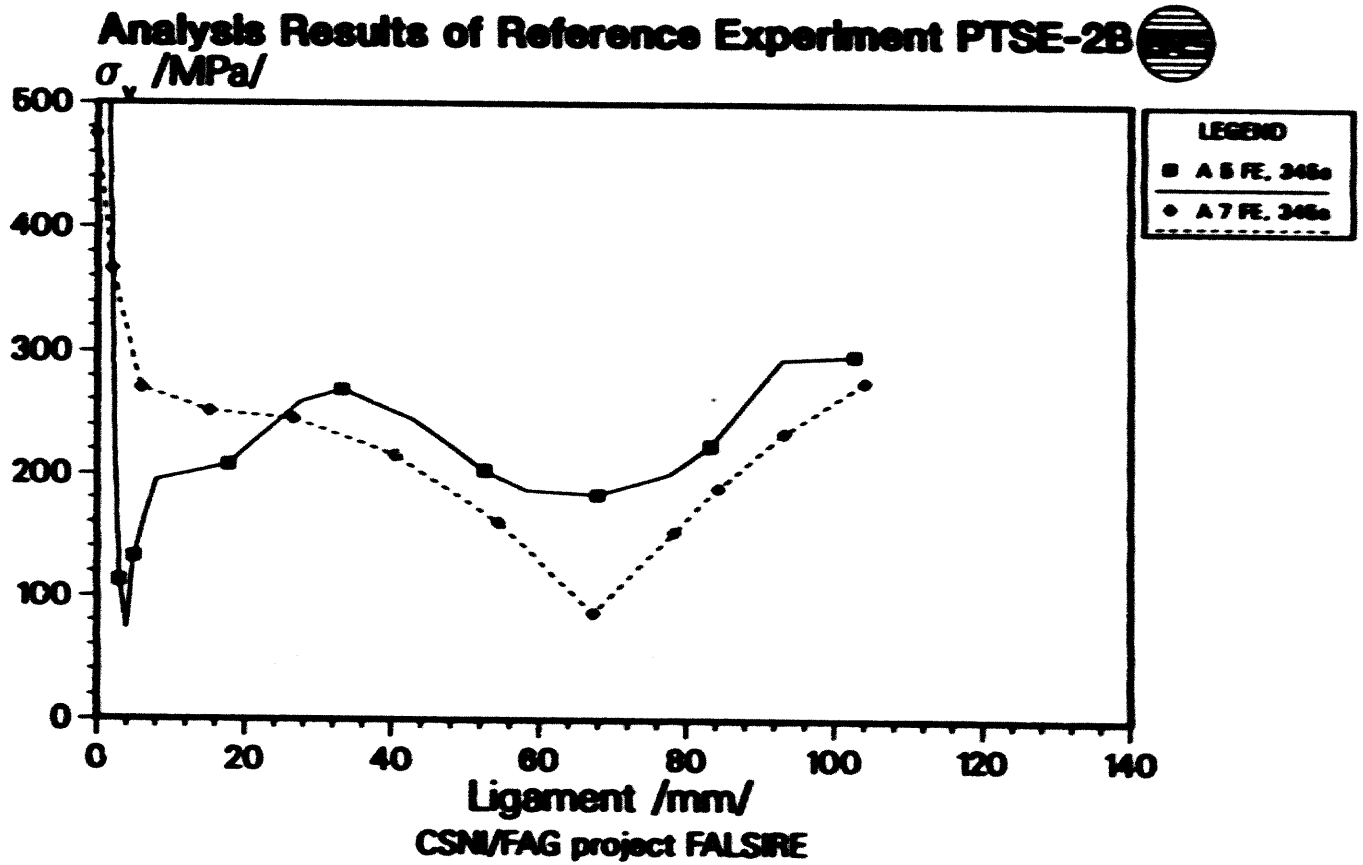

Fig. 29 PTSE-2B, effective stresses on the ligament t = 345 s.

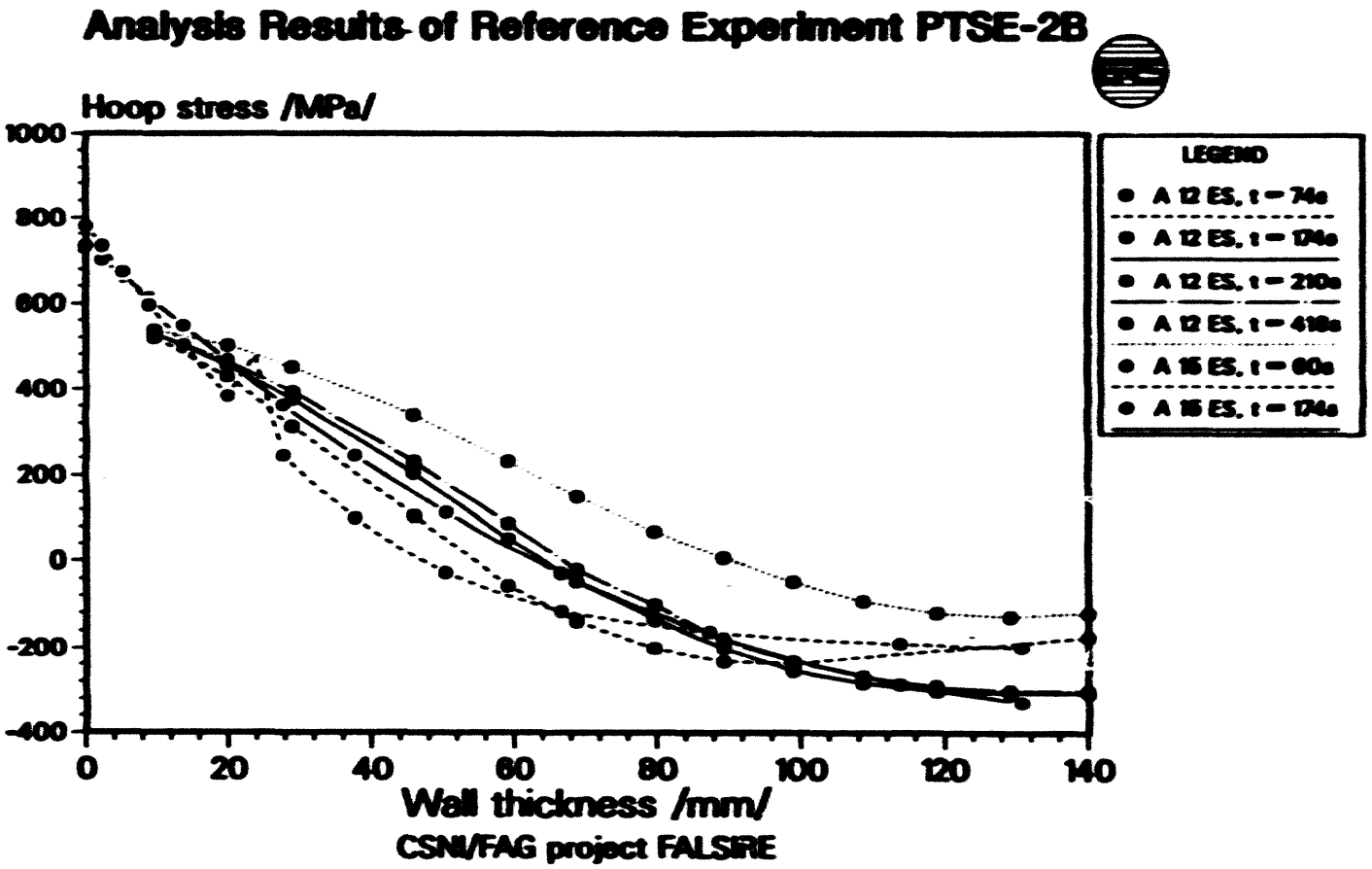

Fig. 30 PTSE-2B, hoop stresses vs wall thickness.

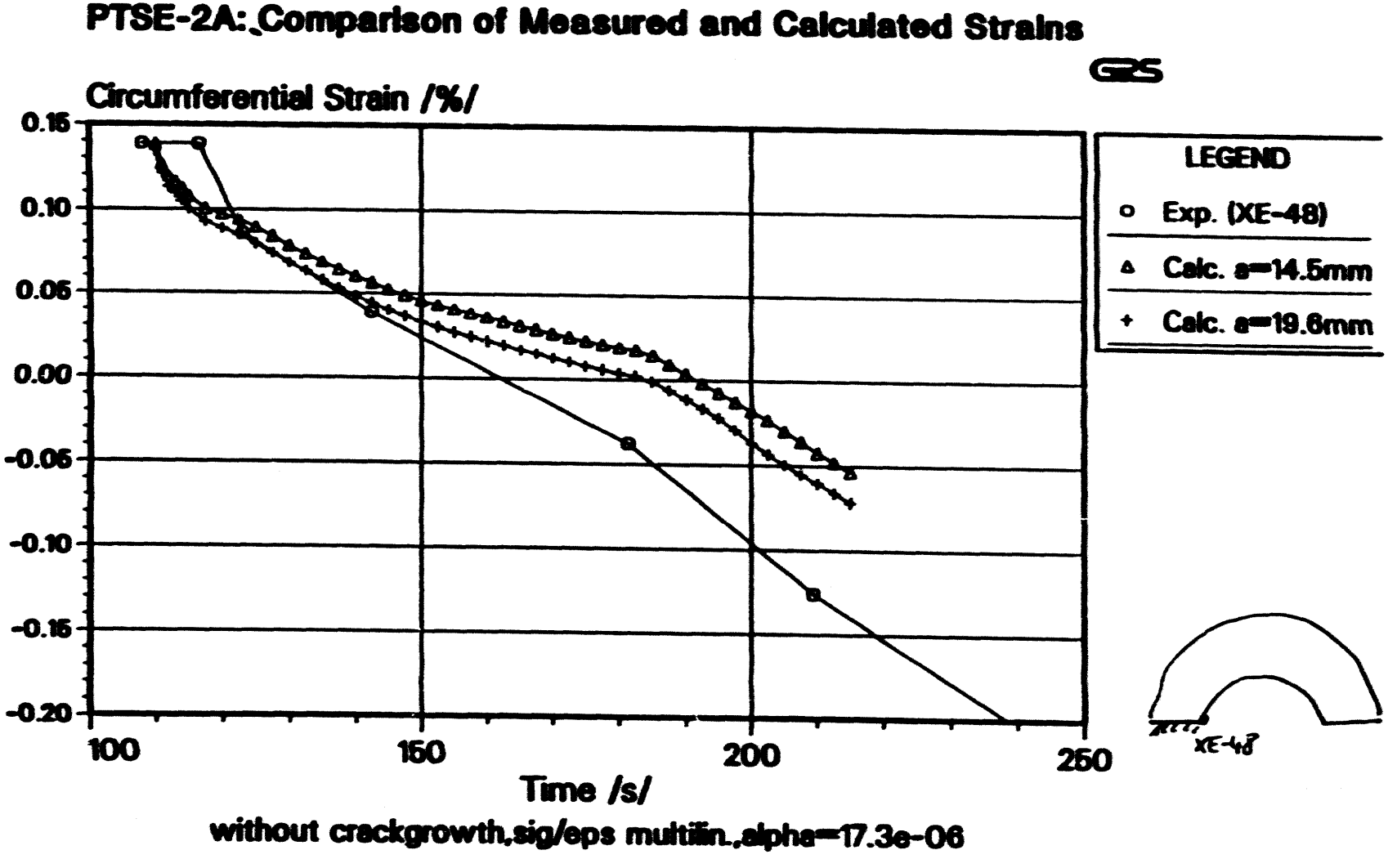

Fig. 31 PTSE-2A, comparison of calculated circumferential strain vs time with measured data from strain gage XE-48 for two crack depths and temperature-independent material properties.

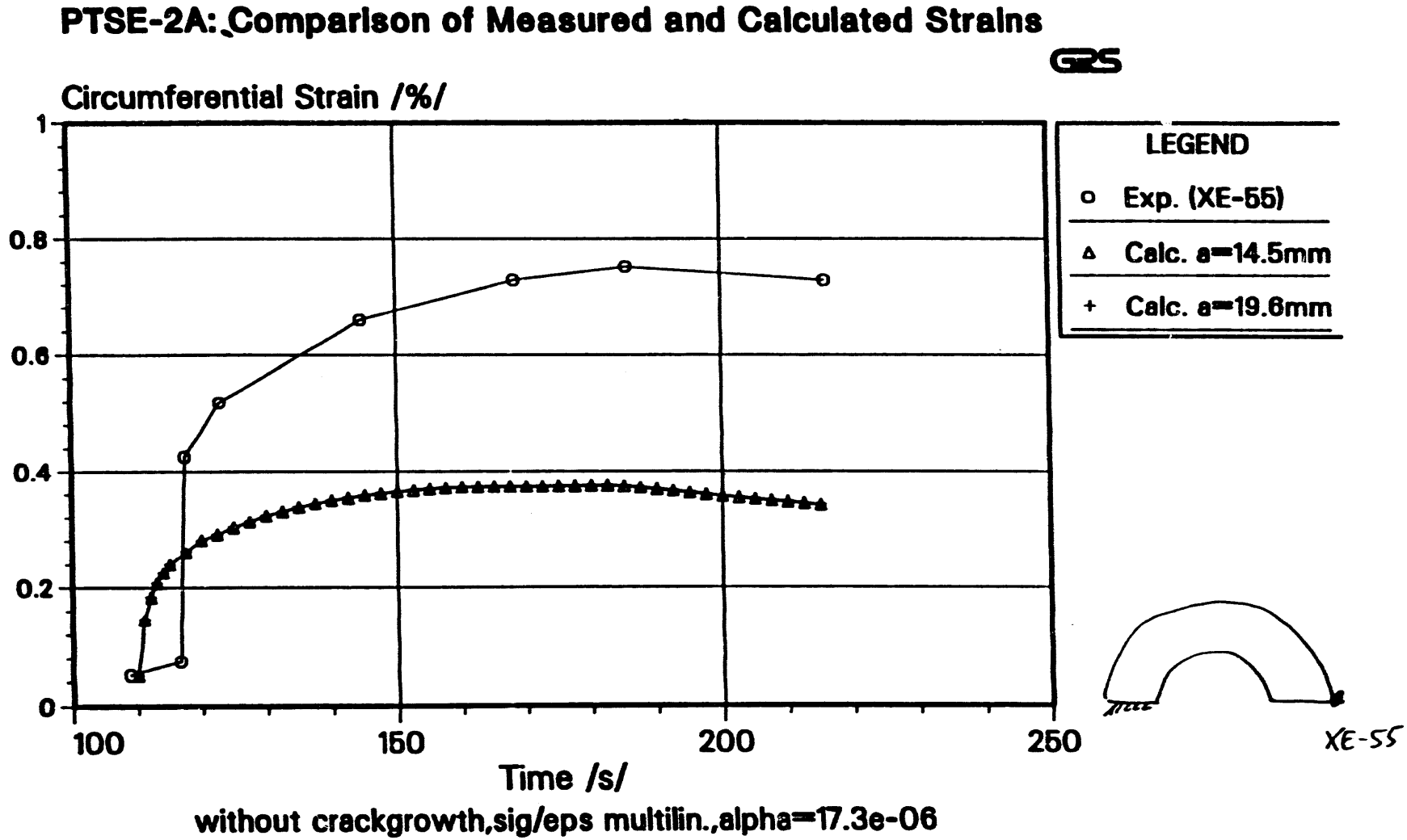

Fig. 32 PTSE-2A, comparison of calculated circumferential strain vs time with measured data from strain gage XE-55 for two crack depths and temperature-independent material properties.

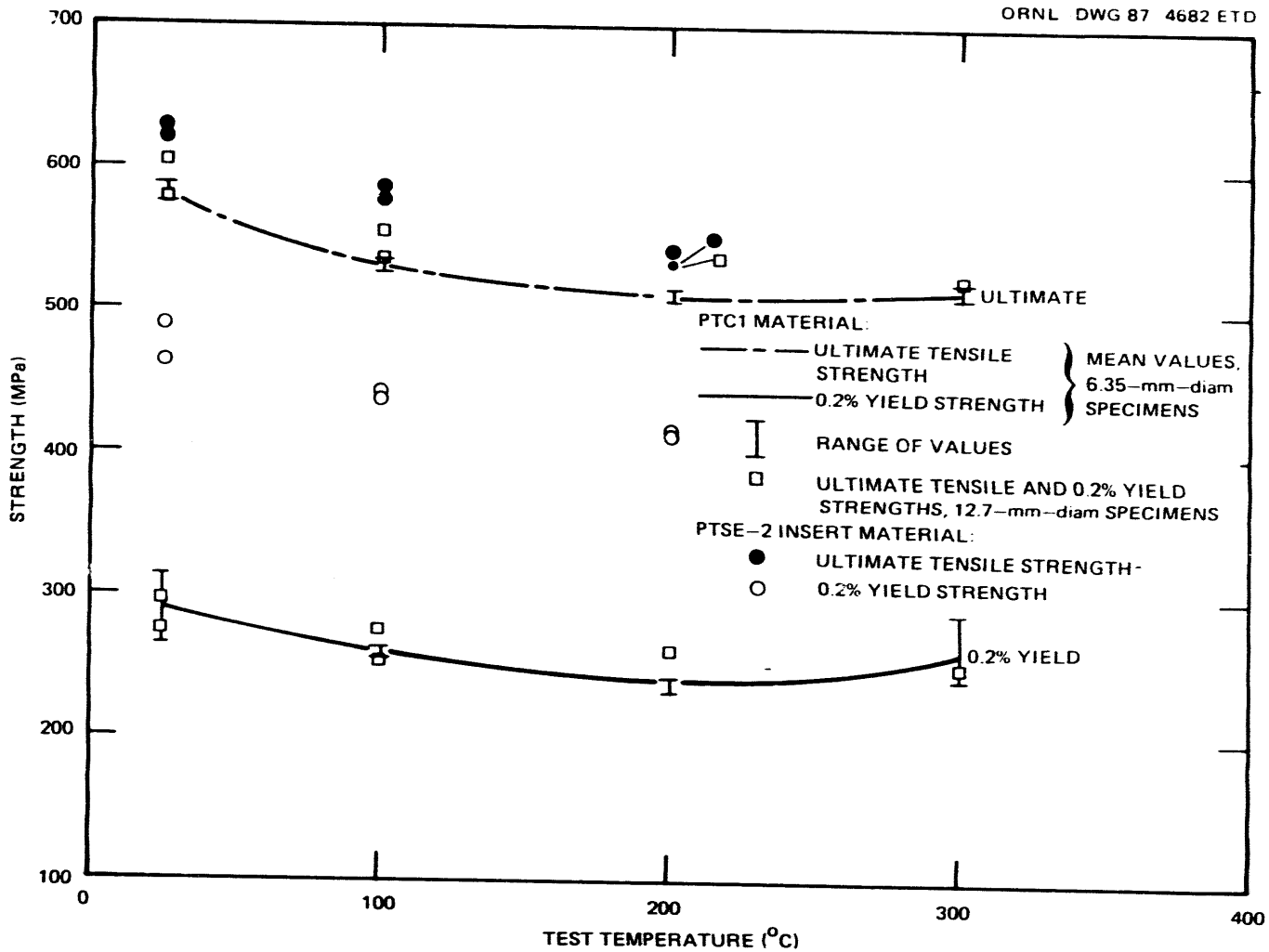

Fig. 33 Comparison of tensile strengths of PTC1 characterization block to flaw insert material, all from 1/4t depth and T orientation. The values for the yield strength are from extensometer data.

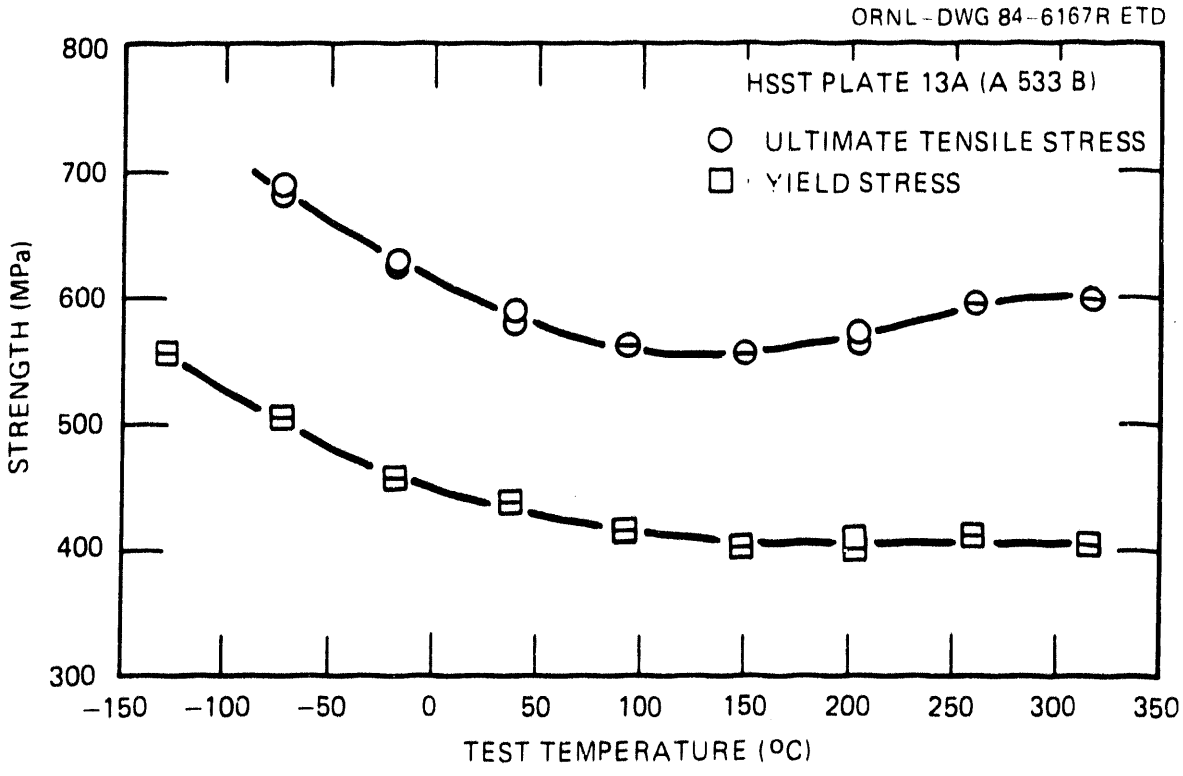

Fig. 34 Effect of temperature on longitudinal tensile properties for HSST plate 13A, A 533 grade B class 1 steel (specimens from center half of 18.7-cm-thick plate).

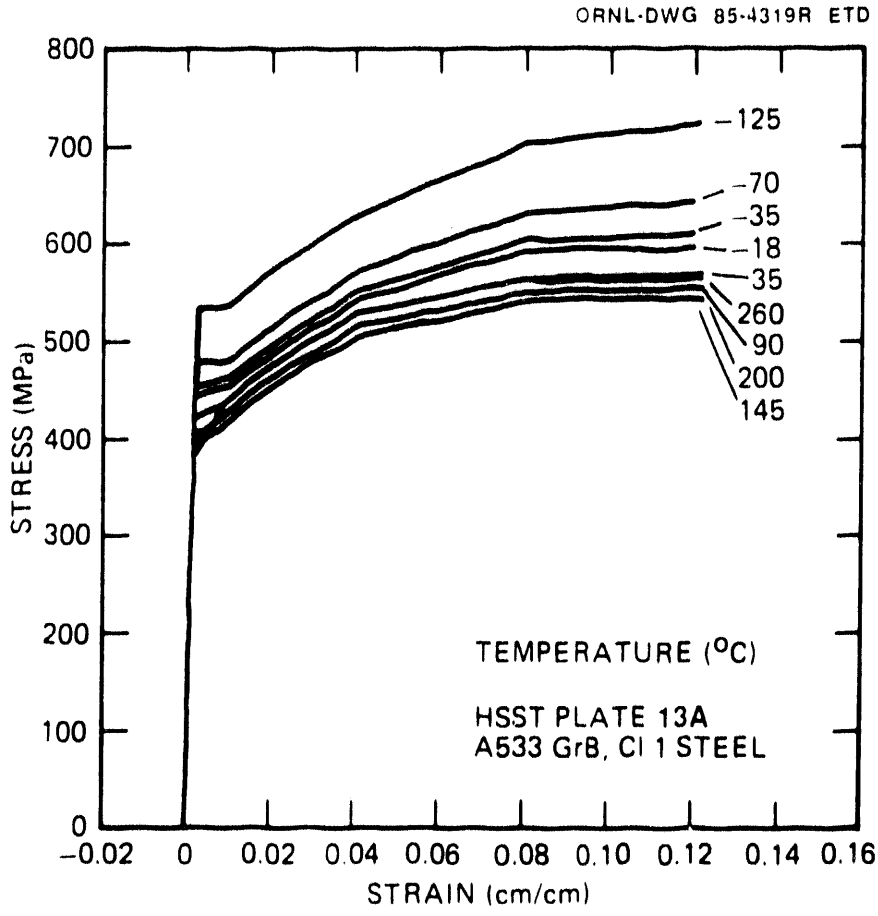

Fig. 35 Multilinear representations of uniaxial stress-strain behavior of HSST plate 13A of A533 grade B class 1 steel.

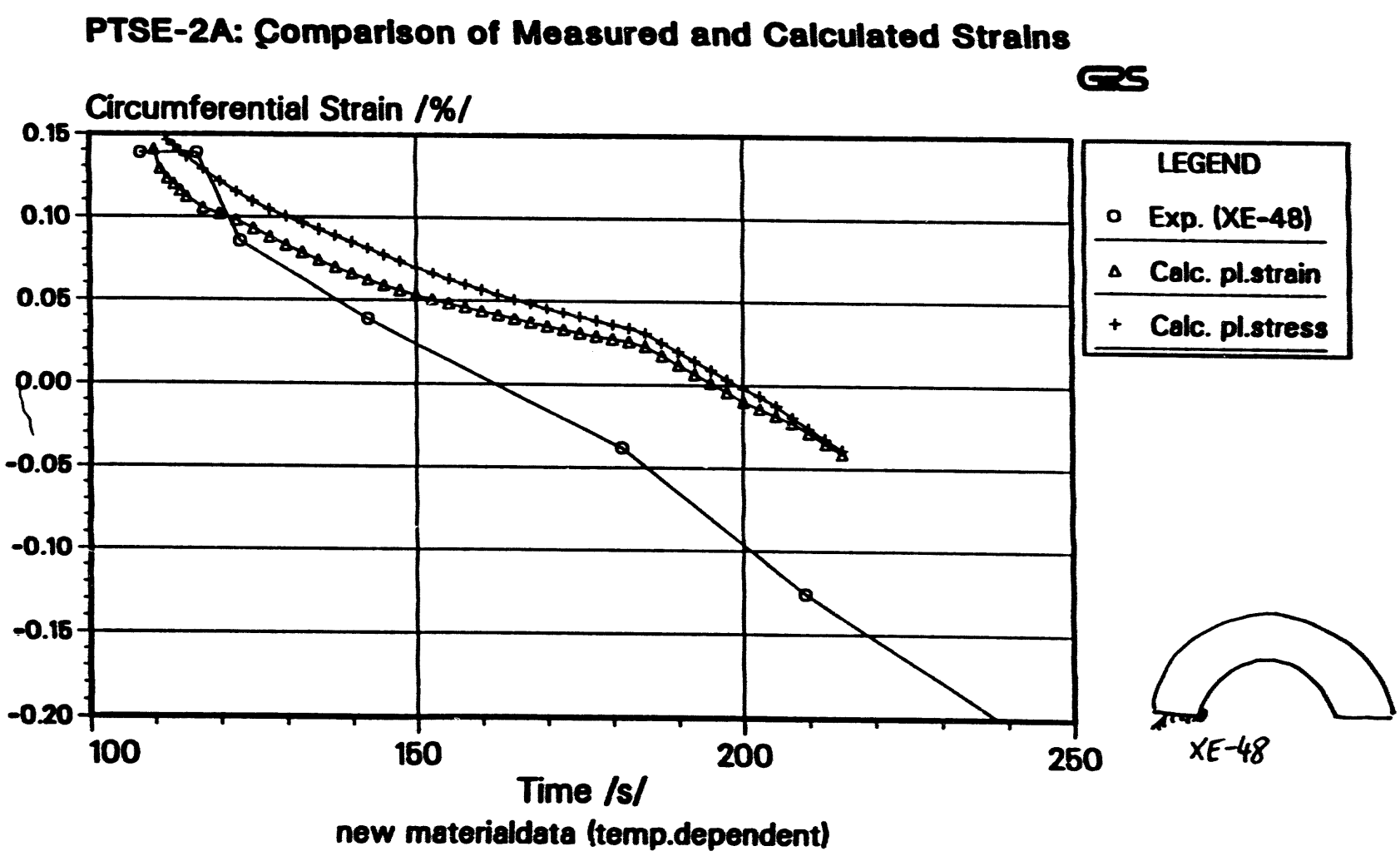

Fig. 36 PTSE-2A, comparison of measured circumferential strains vs time from gage XE-48 with calculated strains based on plane stress and plane strain models and temperature-dependent material properties.

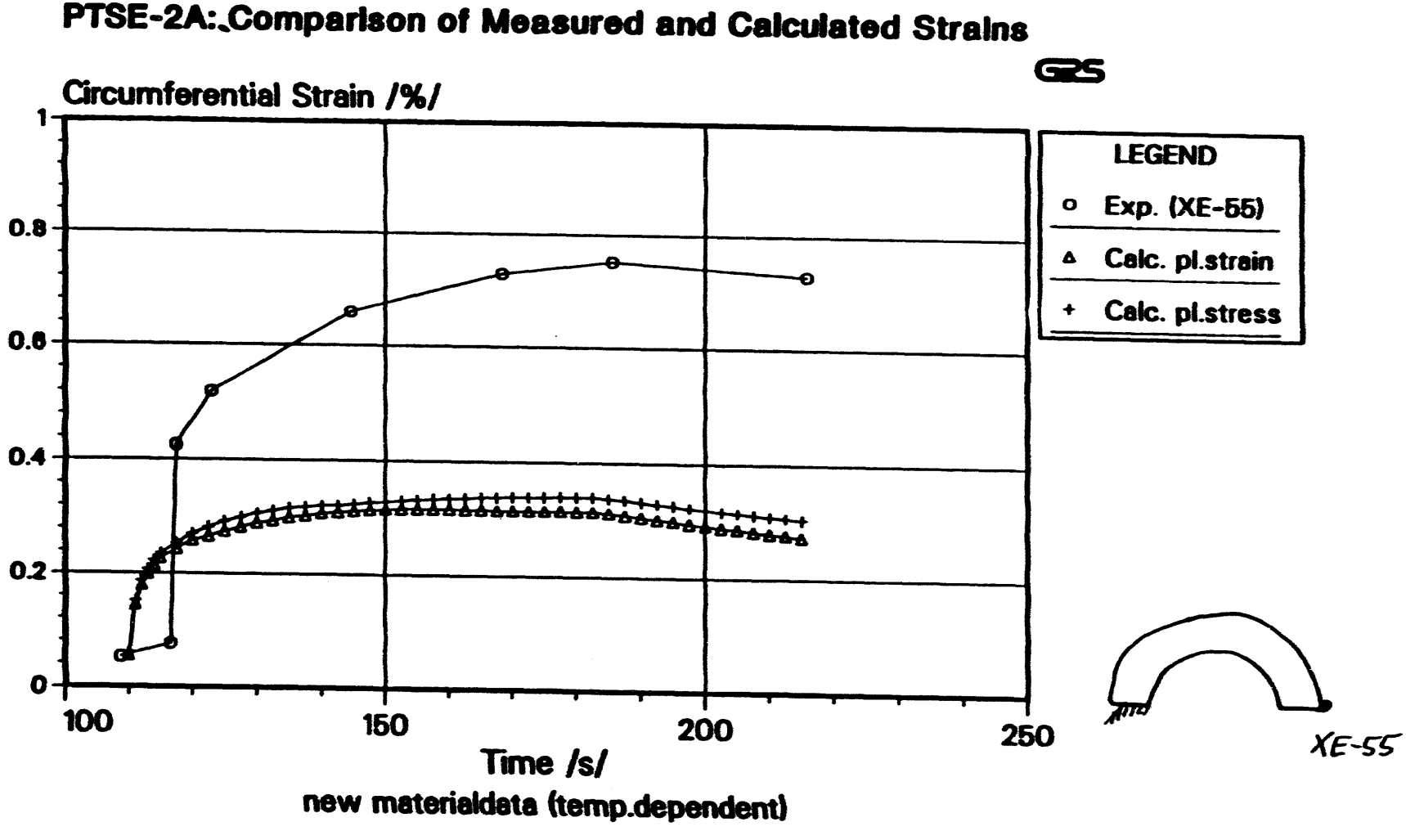

Fig. 37 PTSE-2A, comparison of measured circumferential strains vs time from gage XE-55 with calculated strains based on plane stress and plane strain models and temperature-dependent material properties.

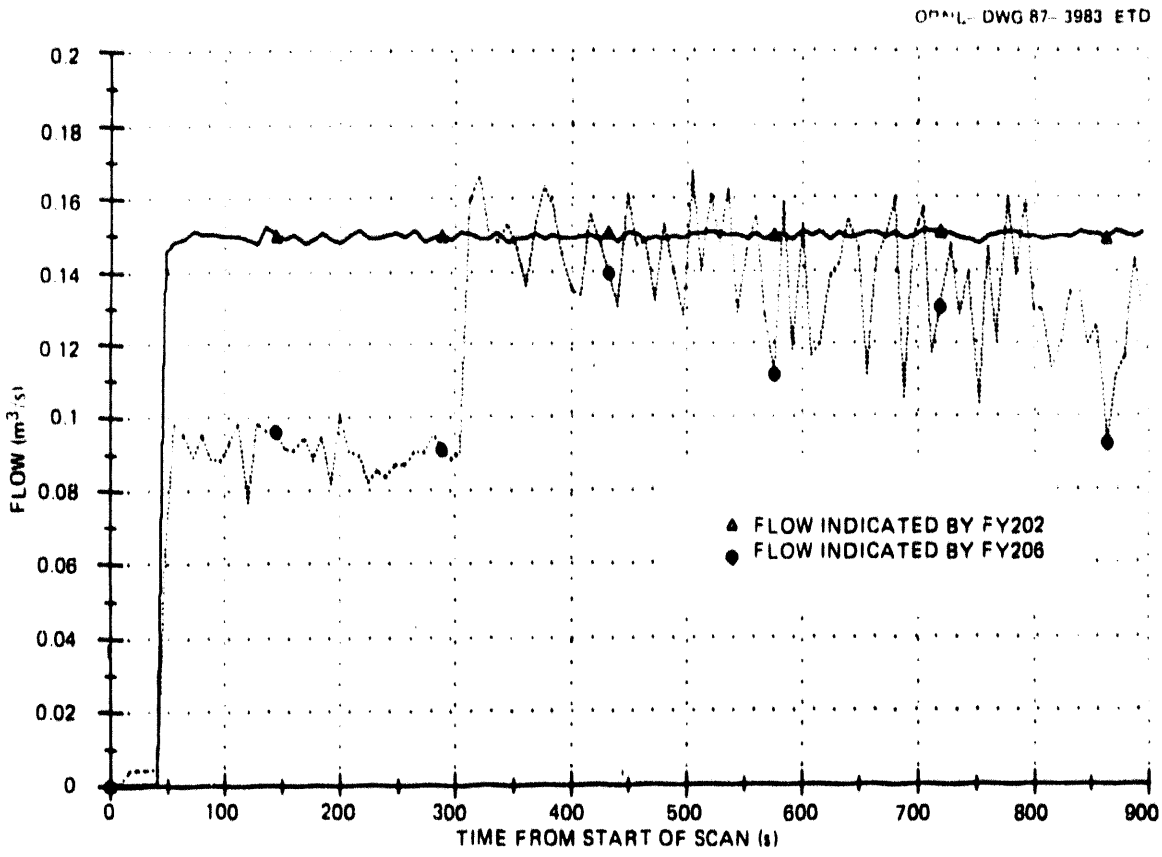

Fig. 38 Unsatisfactory recirculation pump flow-time response. This shows an anomalous mismatch of flows into and from the shroud.

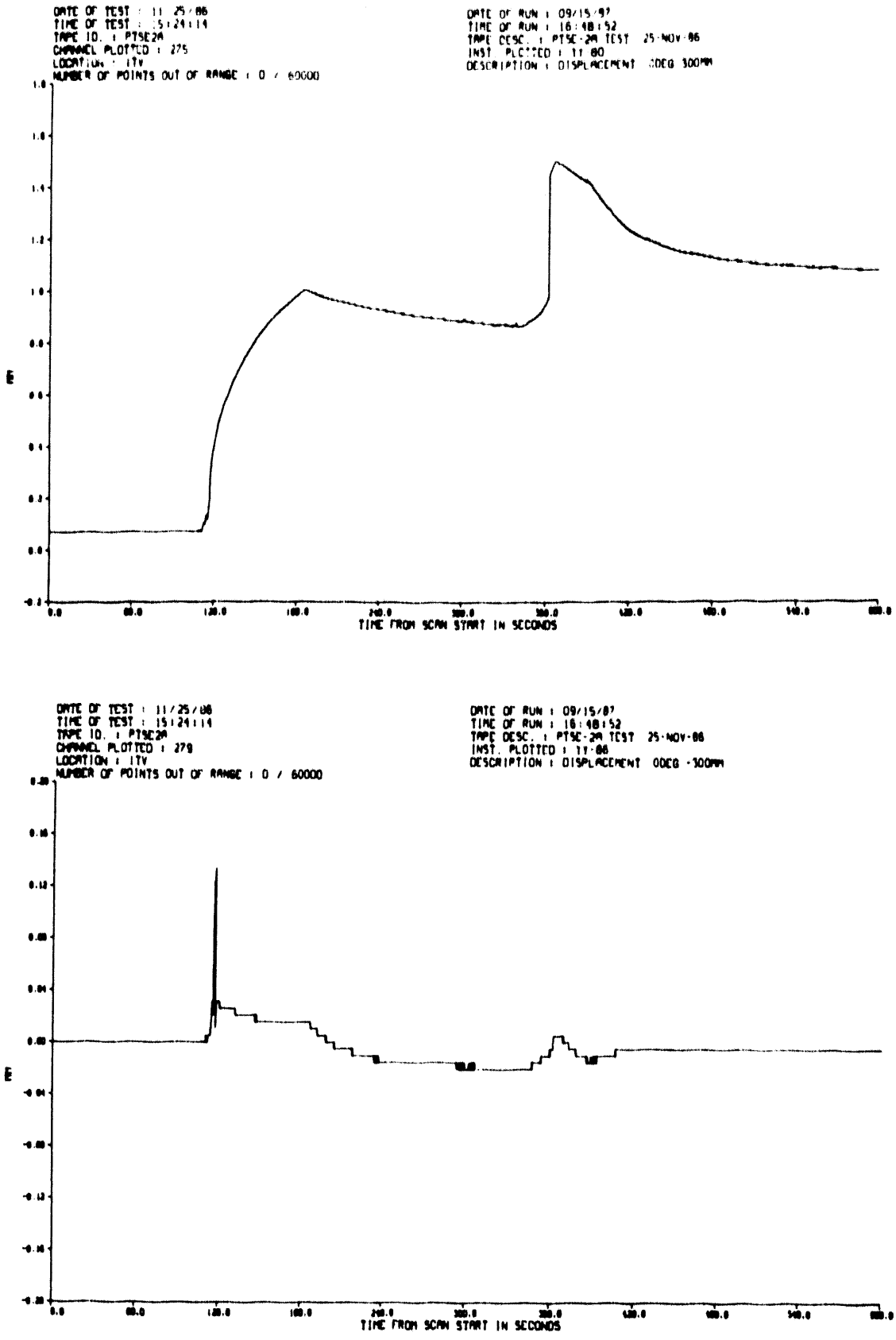

Fig. 39 PTSE-2A, measured CMOD vs time at two gage locations in Fig. 2 showing axial dependence of data: (a) gage YY-80; and (b) gage YY-86.

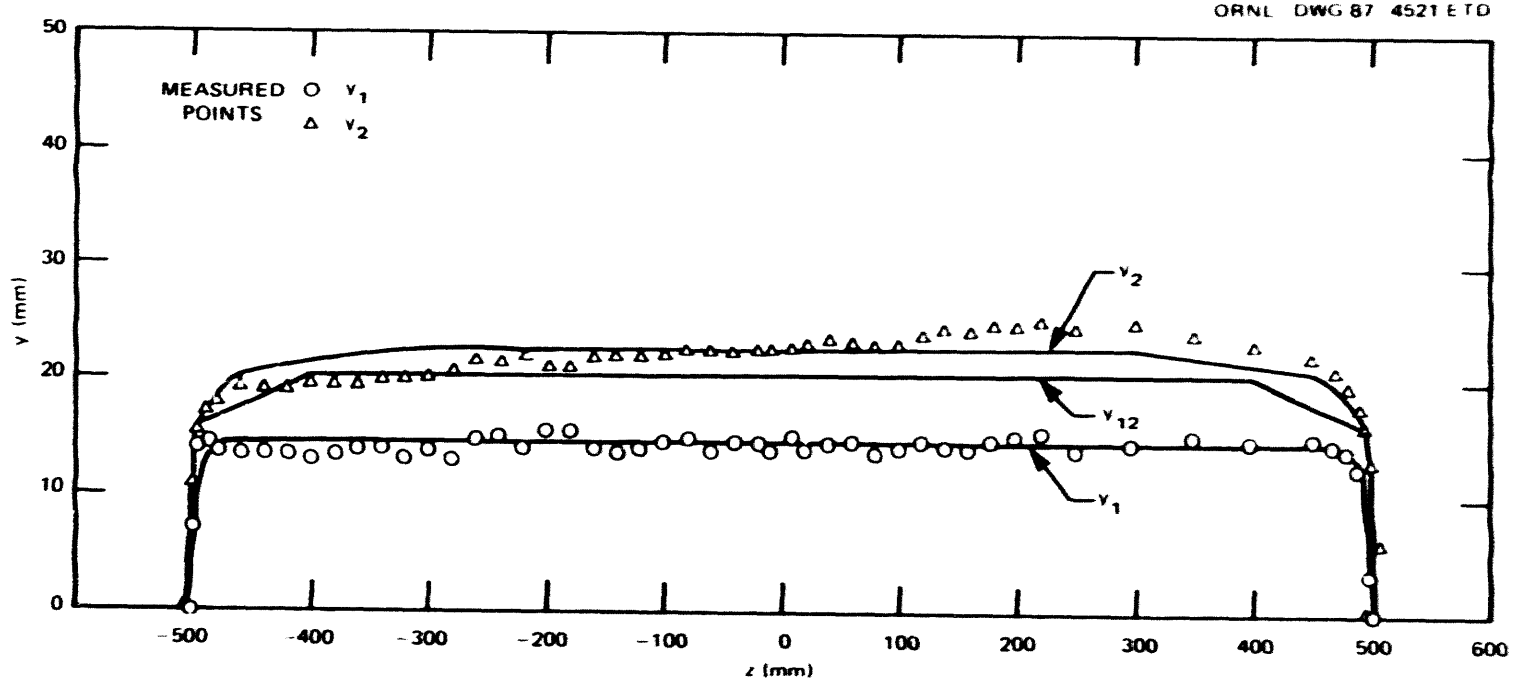

Fig. 40 Crack geometries of precleavage cracks in PTSE-2A

FALSIRE Results for NKS-3 and NKS-4

Ludwig Stumpfrock

MPA Stuttgart

University of Stuttgart, Federal Republic of Germany

Abstract

In the framework of the project NKS funded by the Federal Minister of Research and Technology, MPA Stuttgart conducted up to now 7 pressurized thermal shock experiments. The purpose of the experimental and numerical investigations in the research project was to study the crack propagation behaviour of circumferential flaws on the inner surface of the test specimens. Experiments NKS-3 and NKS-4 were selected as reference experiments in the project FALSIRE.

In this paper we give a review of the experiments and the experimental results and an overview of the analysis results presented at the FALSIRE workshop in 1990.

It is shown that the post calculations of the NKS 3 specimen during the CSNI project FALSIRE provided fracture mechanics results in a relatively small scatterband. The NKS 4 results showed a greater scatterband, but the main reasons could be explained.

1 Introduction

The pressurized thermal shock (PTS) research in the Federal Republic of Germany was initiated in the mid seventies. In the framework of the HDR-safety research program /1/ cyclic thermal shock experiments on plates, intermediate-sized test vessels and later on a

nozzle of the HDR pressure vessel, have been performed. In 1982, a research program was launched at MPA /2/, to study the variation of material parameters like upper shelf energy or nil ductility temperature, figure 1. Also the crack configuration was varied while cooling with the same temperature and the same pressure (except one specimen), table 1.

Beside the experimental investigations extensive numerical studies have been done to verify fracture mechanics methods like the J-integral method or the two criteria method.

2 Description of the experiments

In all the experiments the test specimen was a thick walled hollow cylinder with original (RPV) wall thickness of 200 mm, outer diameter of 800 mm and length of 1100 mm, figure 2, see e.g. /3, 4/. In the NKS3 experiment a 360° circumferential prefatigued notch with a/t = 0,3 was investigated. The NKS 4 crack form was semielliptical with a/2c ~ 1/6 and a/t = 0,15, figure 3.

The actual specimen was lengthened with pass-throughs for the measurement cabels and the cooling pipes, resp., and welded on grips for the 100 MN tensile machine. The specimen was heated on the outer surface with an electrical resistance heating up to about 300°C at the inner surface. The cooling water flowed vertically from the lower side to the upper side of the specimen. The relaxed cooling water flowed in a 100 m^3 water reservoir. A low pressure pump fed the high pressure injection pumps which pressed the water into a spraying device, figure 4. The cooling of the inner surface of the specimen via this spraying device was even in longitudinal and circumferential direction, resp.

The behaviour of the specimens under the PTS loading was recorded with various measurement techniques. Measured data such as temperature profiles through the wall thickness, strains on inner and outer surface and crack mouth opening displacement were used for the detailed post-test analyses during the research program or afterwards in the FALSIRE project.

3 Experimental results

3.1 NKS 3

Figures 5a and 6a show the internal pressures and the outer axial load, resp., vs. time. The measured temperature profiles near the crack section is delineated in figure 7. A similar distribution of temperature was provided in nearly all experiments. The axial strain on the inner surface in a section 184 mm above the crack section is shown in figure 8. The thermal strain is subtracted. The strain increases slowly proportional to

the mechanical load. Following PTS a sudden increase in the strain measured on the inner surface is provided (as expexted). The maximum values are reached after about 3 minutes and then the strains decrease slowly. The same performance shows the measured CMOD, except the maximum was reached after about 7 minutes, figure 9.

The crack depth measurement on the crack face following the laboratory induced brittle fracture provides an averaged crack extension of 3.6 mm. The crack depth before PTS experiment was between 55 mm and 70 mm, and after the test between 61 mm and 78 mm, figure 10.

3.2 NKS 4

Figure 5b and 6b show the internal pressure and the outer axial load, resp., vs. time. The measured temperature profiles near the crack section is delinated in figure 11. The axial strain on the inner surface in a section 184 mm above the crack section is shown in figure 12. The thermal strain is subtracted. Following PTS a sudden increase in the strain measured on the inner surface is provided (as expected). The maximum values are reached after about 3 minutes and then the strains decrease slowly. The same performance shows the measured CMOD except the maximum was reached after about 7 minutes, figure 13.

The crack growth measurements on the crack surface provide maximum stable crack extension of about 1,5 mm and 0,8 mm for the two surface cracks, figure 14.

4 Numerical results

The following results were presented at the FALSIRE workshop in Boston, 1990, and partly compiled in the Final Report /5/.

4.1 NKS 3

Table 2a shows the summary of the finite element applications including the essential data about the number of unknowns, the basic material law, the integration rule on element level and the iteration method. All models are 2D axisymmetric (7 applications). Different commercial and inhouse finite element packages were used. The fracture mechanics analysis is based on the J-integral or local approach. Table 3a shows the summary of the estimation scheme applications (2 applications). There the fracture mechanics analysis is based on J_R-curve and on the R6-method.

Table 4a gives the material characteristics used in the different FE analyses.

Figures 15 - 17 show the time history of CMOD, axial strain at the inner surface 184

mm above the crack section and the J-Integral. The difference between the FE results are quite little. The J-Integral values calculated with estimation scheme methods lay in the scatterband of the FE results. In figure 18 the effective stress due to von Mises, σ_v, on the ligament of the crack section is given for one characteristic time step (5 minutes after starting the thermal shock transient). As expected, the stress distribution strongly depends on the approximation of the stress-strain data. In one analysis a very low yield stress is used which results in lower stresses on the ligament during the transient. The difference in the effective stress calculated are little in the ligament, except in front of the crack tip.

Figure 19 shows the stress triaxiality parameter q in front of the crack tip for the same time step. The stress triaxiality q is defined as $q = 3\,\sigma_H/\sigma_v$, where $3\sigma_H$ is the first invariant of the stress tensor (σ_H is called the hydrostatic stress portion). The course of q in the ligament is similar for all time steps in all analyses.

For a typical CT 25-specimen and the NKS 3 specimen, resp., the stress triaxiality is depicted in figure 20, expressed by $\sqrt{3}/q$. The crack growth value is determined by comparing the J_R-curve and the $J_{applied}$ course vs. time, figure 21. The q-values are close to plane strain values, therefore, crack growth can be evaluated with crack resistance curves of CT 25 specimens. The analyses give crack growth values of about 3 to 4.8 mm similar to the scatterband of the other results.

The uncertainty of the calculated crack growth is about 3 % of the initial crack depth. In this case, therefore, the analysis results show a scatterband which is acceptable in comparison with the experimental data.

4.2 NKS 4

Table 2b shows the summary of the finite element applications including the essential data about the number of unknowns, the basic material law, the integration rule on element level and the iteration method. All models are 3D, except 1 (4 applications). Different commercial and inhouse finite element packages were used. The fracture mechanics analysis is based on the J-Integral. Table 3b shows the summary of the estimation scheme applications (2 applications). There fracture mechanics analysis is based on $J_R$and on the R6-method.

Table 4b gives the material characteristics used in the different FE analyses.

Figures 22 - 24 show the time history of CMOD, axial strain at the inner surface 184 mm above the crack section and the J-Integral. The difference between the FE results are considerable and result from missing rotational restraints, from an artificially high yield stress or from different reference temperatures. The J-Integral values provided by estimation scheme methods lay in the scatterband of the FE results. In figure 25 the effective stress due to von Mises, sv, on the ligament of the crack section at the

deepest point of the crack is given for the time step 10 minutes after starting the thermal shock transient. The stress distributions calculated are quite similar.

Figure 26 shows the stress triaxiality parameter q at the crack center in front of the crack tip for the time step 10 minutes after starting the thermal shock transient. The differences in q are greater than in the NKS 3 calculations. Only for the time step 10 minutes the coincidence in q is satisfactory.

The stress triaxiality values at the deepest point of the crack in front of the crack tip is very close to plane strain values as in a standard CT 25-specimen. In figure 27 the stress triaxiality is expressed by $\sqrt{3}/q$. Near the surface there are nearly plane stress conditions, and therefore the crack resistance can be described by a CT 25-specimen with reduced thickness of 10 mm, see figure 27. The crack growth value is determined by comparing the J_R and the $J_{applied}$ course vs. time, figure 28. The analyses give crack growth values of about 2 to 3.2 mm. The uncertainty of the calculated crack growth is about 4 % of the initial maximum crack depth.

5 Conclusions

The analysis of the PTS experiment NKS 3 via finite element methods or estimation scheme methods represents an acceptable scatterband in the fracture mechanical parameters.

This is due to the relatively simple geometry of the test specimen (axisymmetric), and due to sufficient input data like material parameters, fracture mechanics parameters and due to the good description of the transient temperature data. Stable crack growth could be well predicted with the J_R-curve based on the standard CT-Specimen due to the comparable state of stress triaxiality.

In case of NKS 3 Loacal Approach as alternative to J_R-curve performs well in fracture mechanics evaluation too.

The analysis of the PTS experiment NKS 4 via finite element methods or estimation scheme methods represents an large scatterband in the fracture mechanical parameters.

This is due to the complex 3D geometry of the test specimen. The input data like material parameters, fracture mechanics parameters and the good description of the transient temperature data have been sufficient. Stable crack growth could be well predicted with the J_R-curve based on standard or modified CT-Specimen due to the comparable state of stress triaxiality.

References

/1/ Katzenmeier, G. and W. Müller-Dietsche: HDR-Sicherheitsprogramm: Gesamtprogramm Phase II. PHDR-Arbeitsbericht 05.19/84. Kernforschungszentrum Karlsruhe, 1984.

/2/ BMFT-Project 1500 618: Experimental and Numerical Fracture Analyses for Reactor Pressure Vessels Subjected to Pressurized Thermal Shock Loading.MPA Stuttgart, Final Report, 1990.

/3/ Sauter, A., T. Nguyen-Huy, U. Weber and H. Huber: Behaviour of Surface Flaws under Thermal-Mechanical Loading.14th MPA-Seminar, Stuttgart FRG, 1988.

/4/ Sauter, A.:Recent Progress in PTS Research at MPA Stuttgart. French-German Seminar, EDF-Moret sur Loing, France, 1987.

/5/ Bass, B.R., C.E. Pugh, J. Keeney-Walker, H. Schulz and J. Sievers: Final Report on Phase I of the CSNI Multi-National Project for Fracture Analyses of Large-Scale International Reference Experiments (Falsire).Oak Ridge National Laboratory ORNL, USA, Juni 1992.

specimen	material	upper shelf energy (J)	NDT (°C)	crack geometrie	initial crack depth (mm)	stable crack growth (mm)
NKS1	20 MnMoNi 5 5	175	- 5	360° circum. crack	50.9	0,8
NKS2	20 MnMoNi 5 5	140	0	360° circum. crack	30.0	0,46
NKS3	22 NiMoCr 3 7	95	65	360° circum. crack	62.8	3,6
NKS4	22 NiMoCr 3 7	65	120	semi-elliptical surface crack	crack A: 31.2 crack center crack B: 29.5 crack center	crack A: 3,1 crack B: 1,8
NKS5 bm wm	22 NiMoCr 3 7 S 3 NiMo 1	90 220	75 -30	semi-elliptical surface crack	crack A: 27.0 crack center crack B: 27.0 crack center	crack A, B: 40,0 220° circum. direction

bm: base material

wm: weld material

Table 1: Specimens in NKS programme

Experiment	Analysis Number	Finite Element Program	Model Dimension	Number of Equations	Material/Plasticity Model	Stress-Strain Relation	Integration Rule	Equilibrium Iteration Method	Fracture Method
NKS-3	1	ADINA (Ref. 1)	2-D Axisym.	1968	Von Mises, isotropic hardening, thermo-elastic-plastic	Bilinear	2 X 2	BFGS with line search	J_R-curve
	2	CASTEM 2000 (Ref. 2)	2-D Axisym.	1938/4044	Von Mises, isotropic hardening, thermo-elastic-plastic	Multilinear	3 X 3	Initial stress	(1) J_R-curve (2) Local approach
	3	ADINA	2-D Axisym.	7054	Von Mises, isotropic hardening, thermo-elastic-plastic	Bilinear	2 X 2	BFGS with line search	J_R-curve
	4	ALIBABA (Ref. 3)	2-D Axisym.	~ 4300	Von Mises, isotropic hardening, thermo-elastic-plastic	Multilinear	2 X 2	N/A	(1) J_R-curve (2) Local approach
	5	ADINA	2-D Axisym.	886	Von Mises, isotropic hardening, thermo-elastic-plastic	Bilinear	2 X 2	Full Newton with line search	J_R-curve
	6	BERSAFE (Ref. 4)	2-D Axisym.	1718	Von Mises, isotropic hardening, thermo-elastic-plastic	Multilinear	2 X 2	Full Newton-Raphson method	J_R-curve
	7	MARC (Ref. 5)	2-D Axisym.	8800	Von Mises, isotropic hardening, thermo-elastic-plastic	Multilinear	3 X 3	Secant stiffness, residual load correction	J_R-curve
	19	ABAQUS (Ref. 6)	2-D Axisym.	~ 2500	Von Mises, isotropic hardening, thermo-elastic-plastic	N/A	3 X 3	Modified Newton-Raphson method	J_R-curve

Table 2a: Summary of finite element applications (NKS 3)/5/

Experiment	Analysis Number	Finite Element Program	Model Dimension	Number of Equations	Material/Plasticity Model	Stress-Strain Relation	Integration Rule	Equilibrium Iteration Method	Fracture Method
NKS-4	1	ADINA	3-D (90°)	21175	Von Mises, isotropic hardening, thermo-elastic-plastic	Bilinear	2 X 2 X 2	BFGS with line search	J_R-curve
	2	CASTEM-2000	3-D (90°)	5094	Von Mises, isotropic hardening, thermo-elastic-plastic	Multilinear	3 X 3 X 3	Initial stress method	J_R-curve
	3	ADINA	3-D (90°)	35370	Von Mises, isotropic hardening, thermo-elastic-plastic	Bilinear	2 X 2 X 2	BFGS with line search	J_R-curve
	7	MARC	2-D Axisym.	8800	Von Mises, isotropic hardening, thermo elastic-plastic	Multilinear	3 X 3	Secant stiffness, residual load correction	J_R-curve

Table 2b: Summary of finite element applications (NKS 4)/5/

Experiment	Analysis Number	Stress Analysis Methodology	Fracture Methodology
NKS-3	12	Superposition of closed form solutions for stresses due to pressure and thermal loading (from Refs. 11-13)	J_R-curve; J from handbook (Ref. 32)
	13	Thermal stresses calculated analytically from LOTUS 123	R6, Option 1 (Refs. 38-39)

Table 3a: Summary of estimation scheme applications (NKS 3)/5/

NKS-4	12	Superposition of closed form solutions for stresses due to pressure and thermal loading (from Refs. 11-13)	J_R-curve; J form handbook (Ref. 32)
	13	Thermal stresses calculated analytically from LOTUS 123	R6, Option 1 (Refs. 38-39)

Table 3b: Summary of estimation scheme applications (NKS 4)/5/

Analysis Number	Degrees of Freedom of FE-Model	Approximation of stress strain data				Coefficient of Thermal Expansion	Reference Temperature (°C)
			Bilinear	Multilinear			
		T(°C)	σy/E_T (MPa)	σy (MPa)	T(°C)	α($10^{-6}K^{-1}$)	
1	1968 (axisym.)	20 160 260 400	563/3555 519/4388 536/5489 506/6383			14.4	330
2	1938 (axisym.)	20		350*		14.4	330
3	7054 (axisym.)	20 350	607/1167 643/469			14.4	355
4	2232 (axisym.)	20 160 220 260 290 320		444 400 411 419 413 406	20 160 220 260 290 320	11.2 13.0 14.0 14.6 15.2 15.7	330
5	886 (axiysm.)	20 160 260 320	563/3436 519/3804 536/4540 523/5291			14.4	332
6	1718 (axisym.)	20 160 220 260 320		563 519 504 536 523		14.4	330
7	8800 (axisym.)						

Table 4a: Material characteristics in FE applications (NKS 3)/5/

Analysis Number	Degrees of Freedom of FE-Model	Approximation of stress strain data			Coefficient of Thermal Expansion		Reference Temperature (°C)
		T(°C)	Bilinear σy/E_T (MPa)	Multilinear σy (MPa)	T(°C)	α(10⁻⁶K⁻¹)	
1	21175 (3D-90°)	20	618/3013		20	12.00	
		120	619/3013		120	12.53	
		160	578/3013		160	12.73	330
		280	629/3013		280	13.37	
		320	608/3013		320	13.58	
2	5094 (3D-90°)	20	temperature independent	350*		14.4	330
3	35370 (3D-90°)		692/2140 temperature independent			14.4	20
7	8800 (axisym.)						

* engineering stress-strain curve

Table 4b: Material characteristics in FE applications (NKS 4)/5/

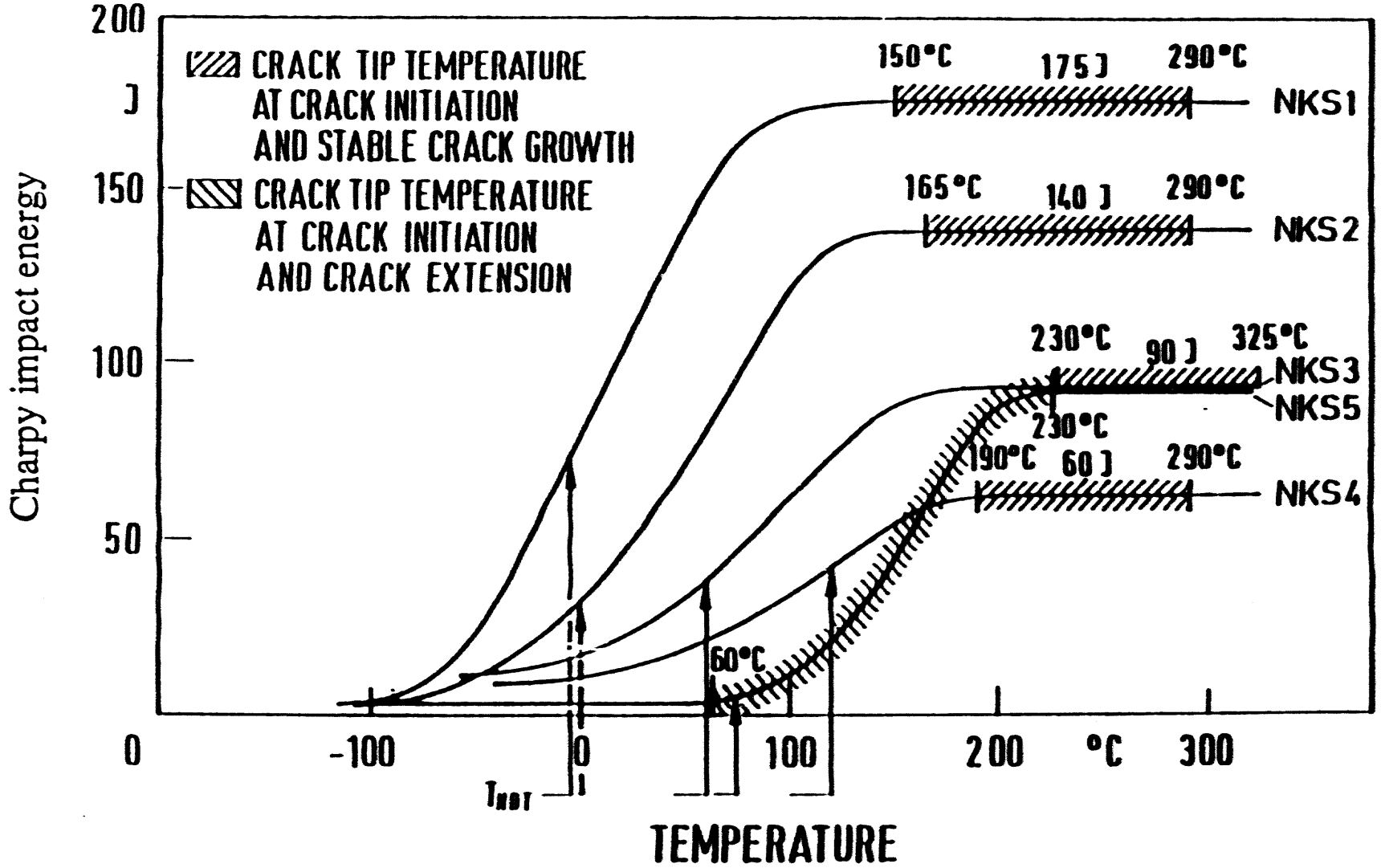

Figure 1: Charpy-V notch impact energy

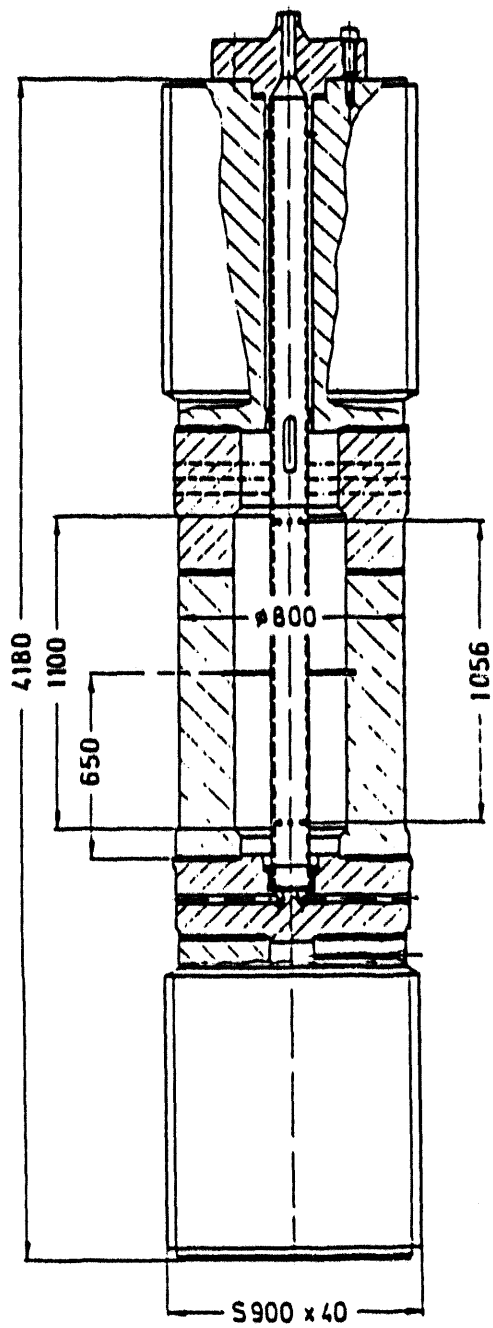

Figure 2: NKS test specimen

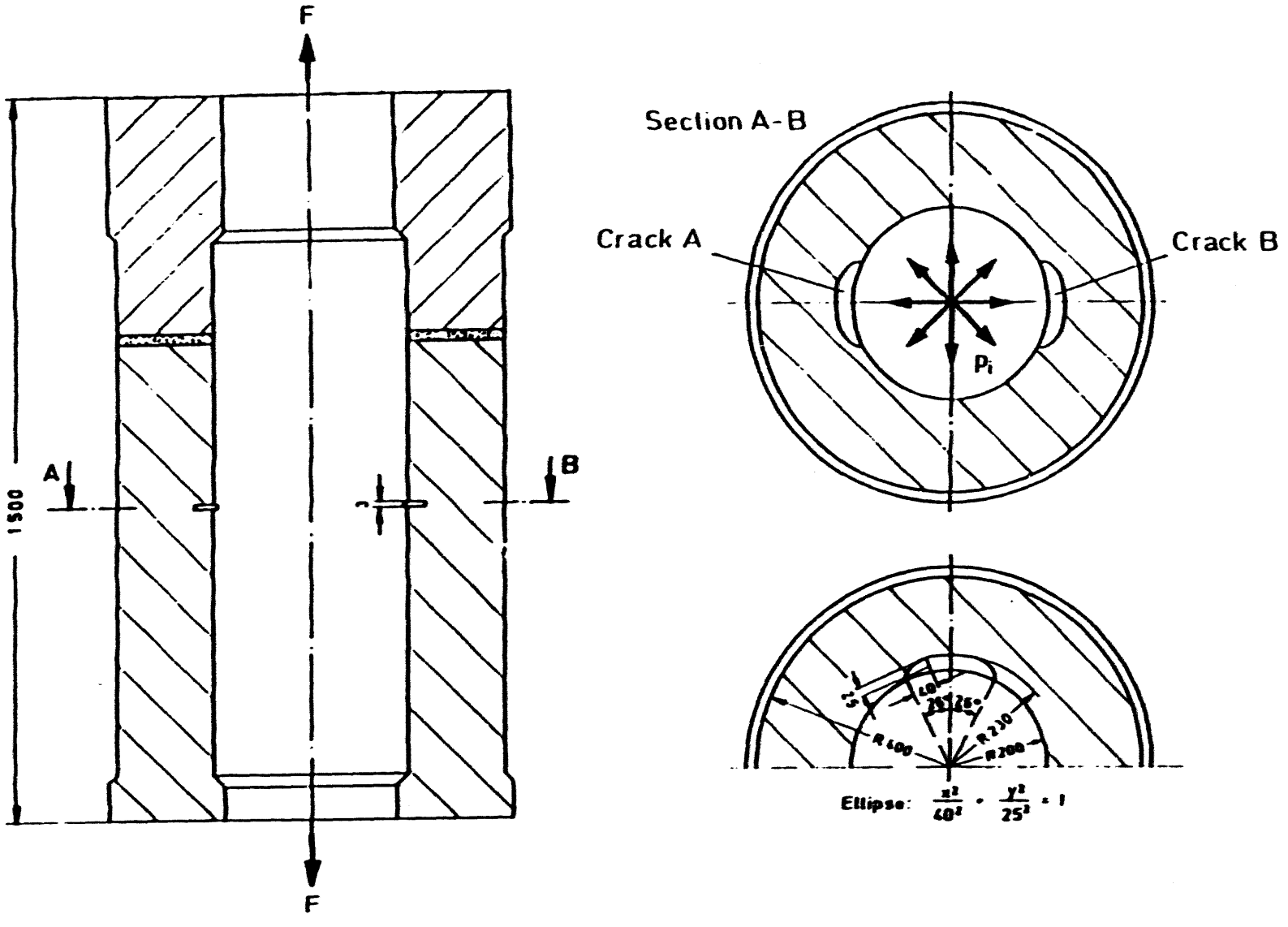

Figure 3: NKS 4 crack section

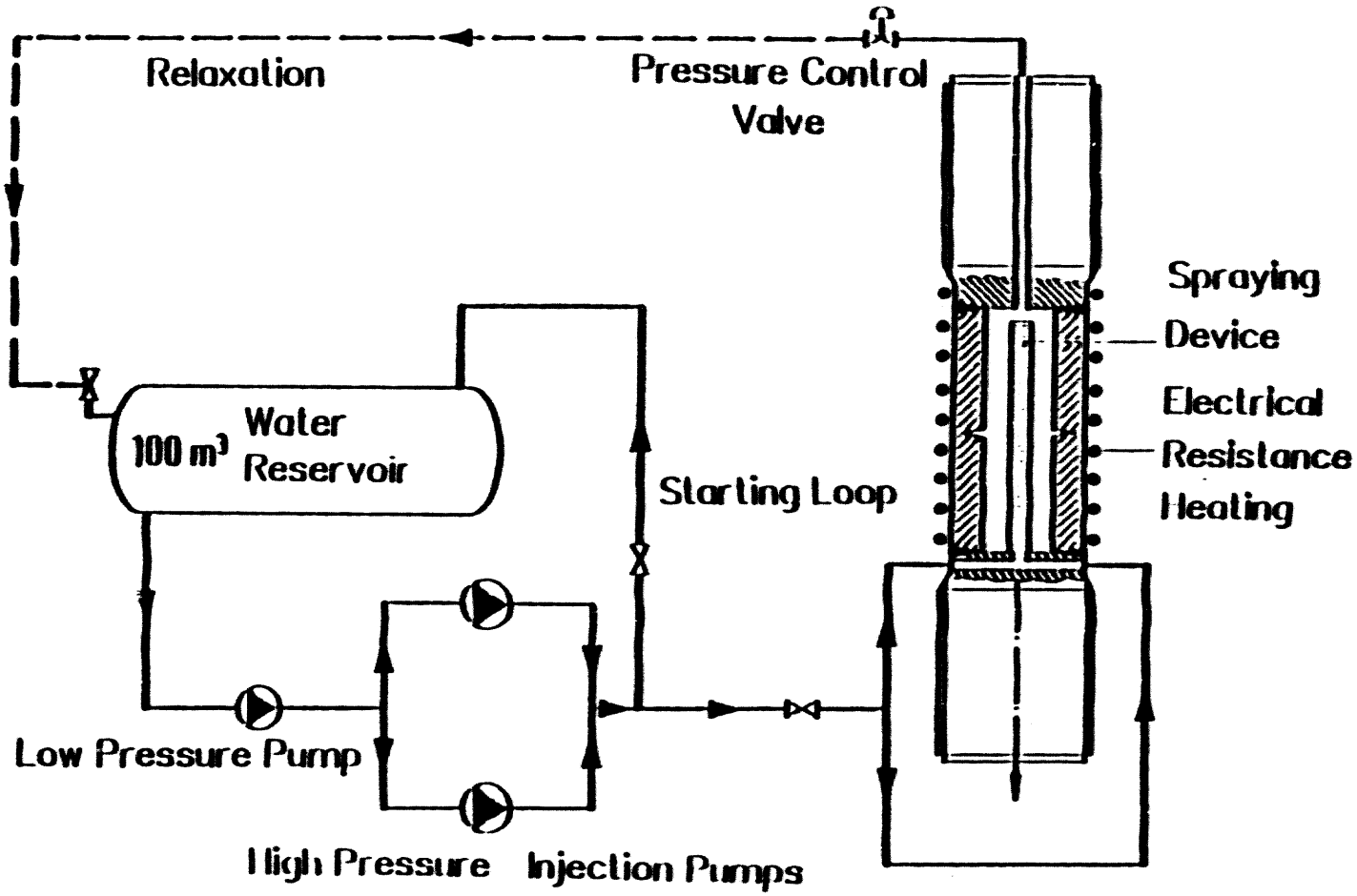

Figure 4: NKS test loop

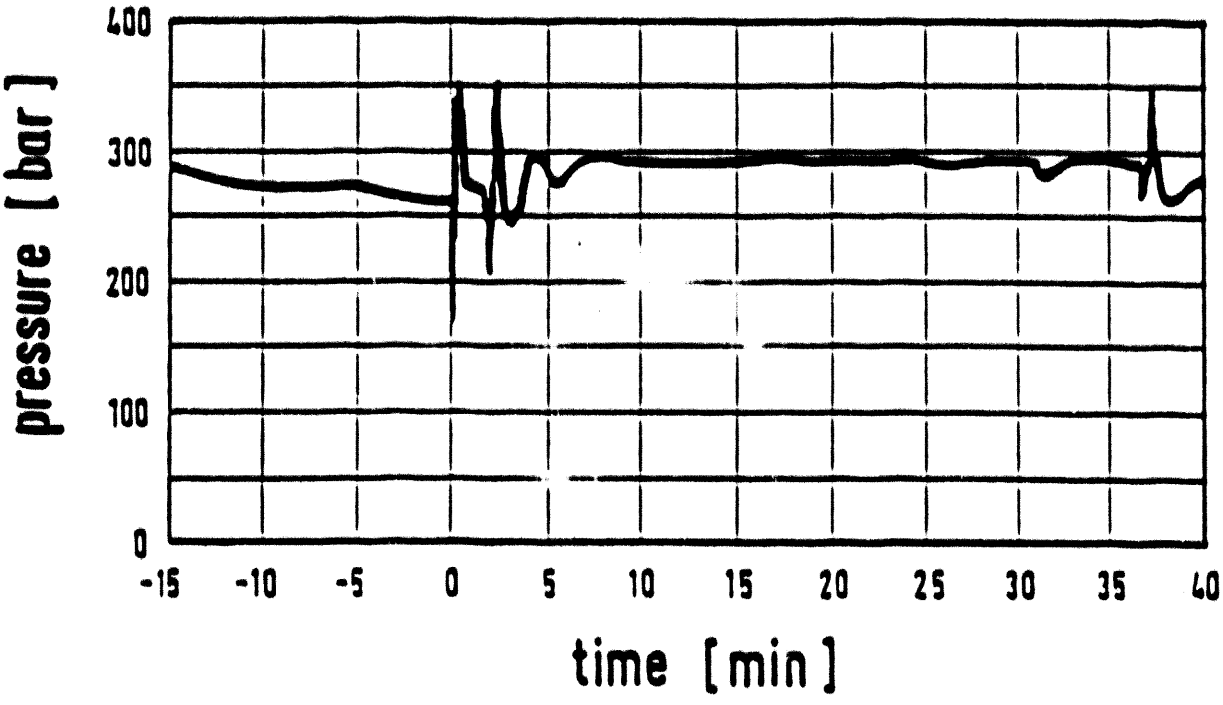

Figure 5a: Internal pressure vs time (NKS 3)

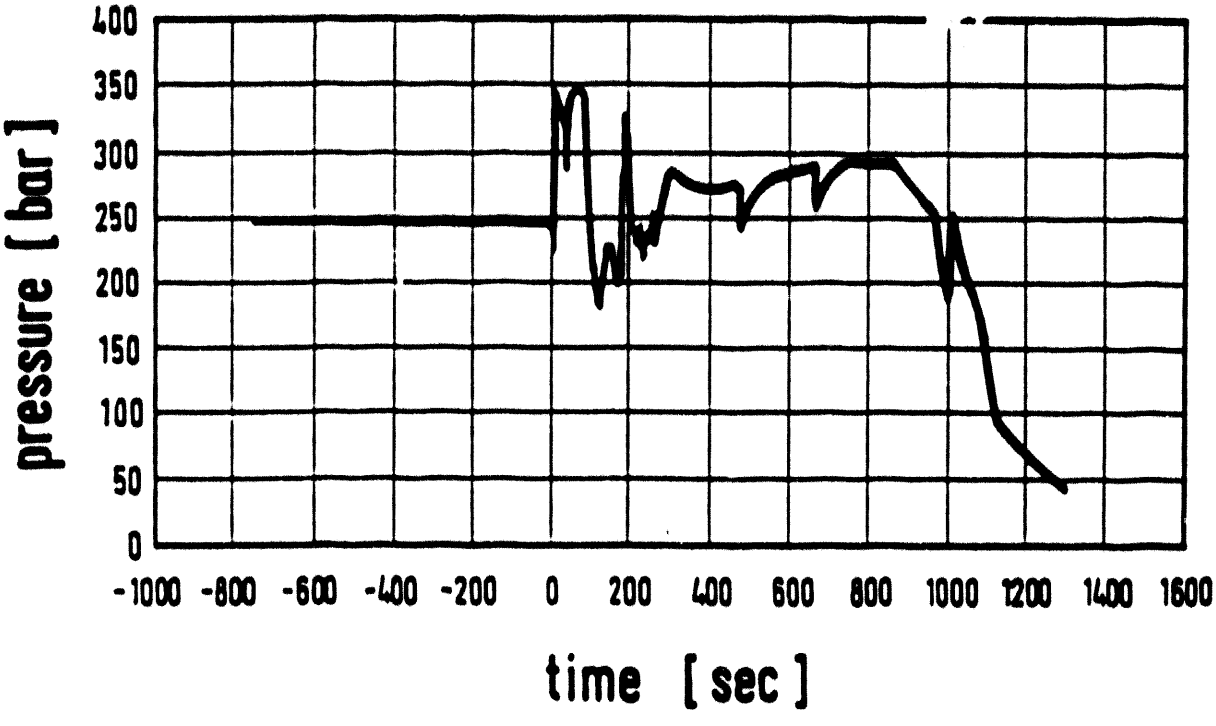

Figure 5b: Internal pressure vs time (NKS 4)

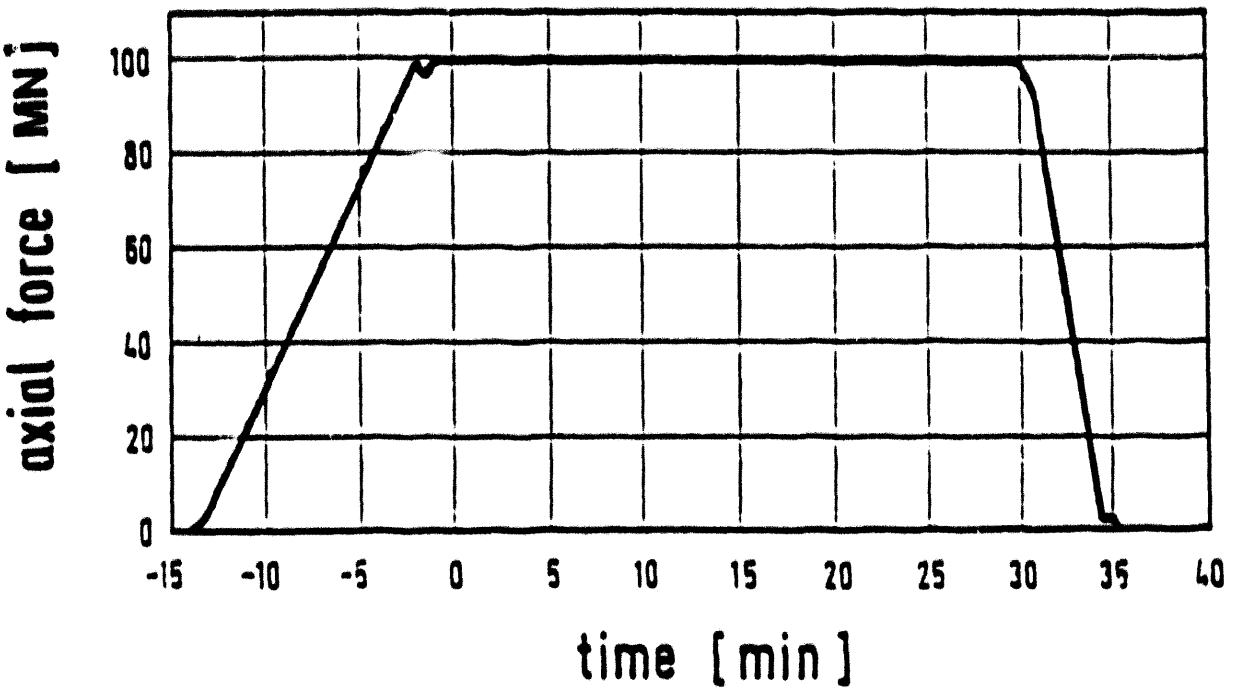

Figure 6a: Axial load vs time (NKS 3)

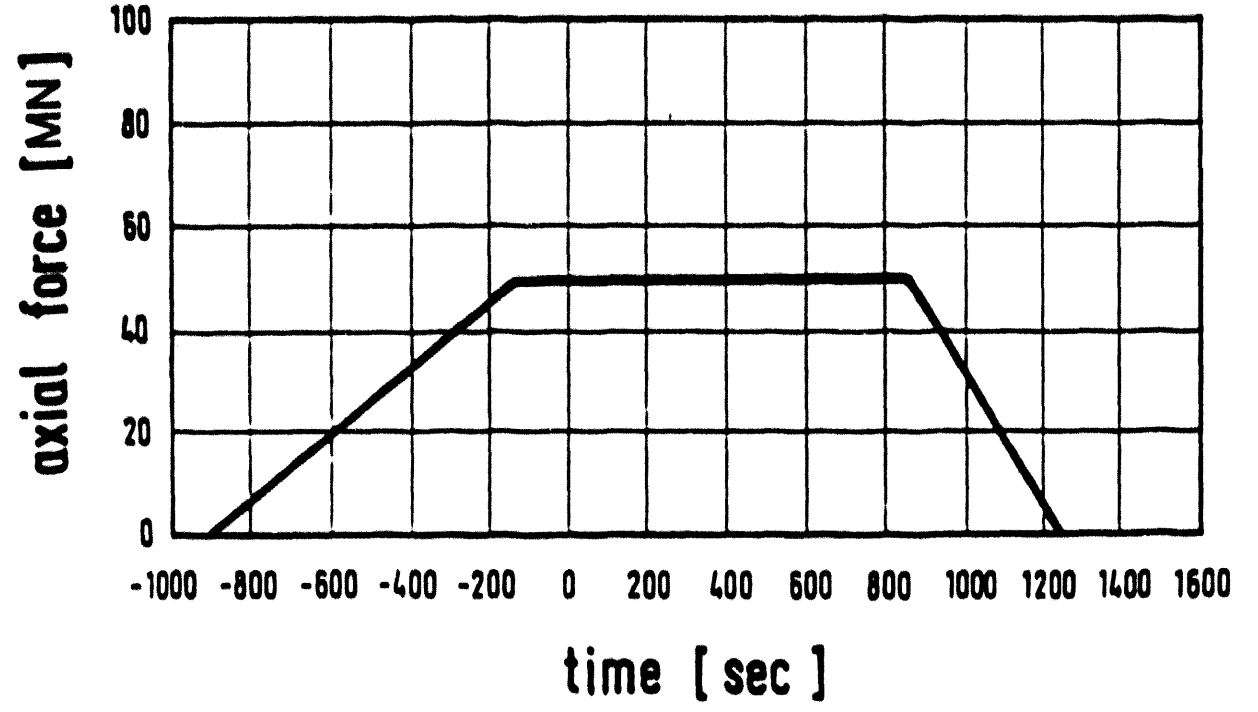

Figure 6b: Axial load vs time (NKS 4)

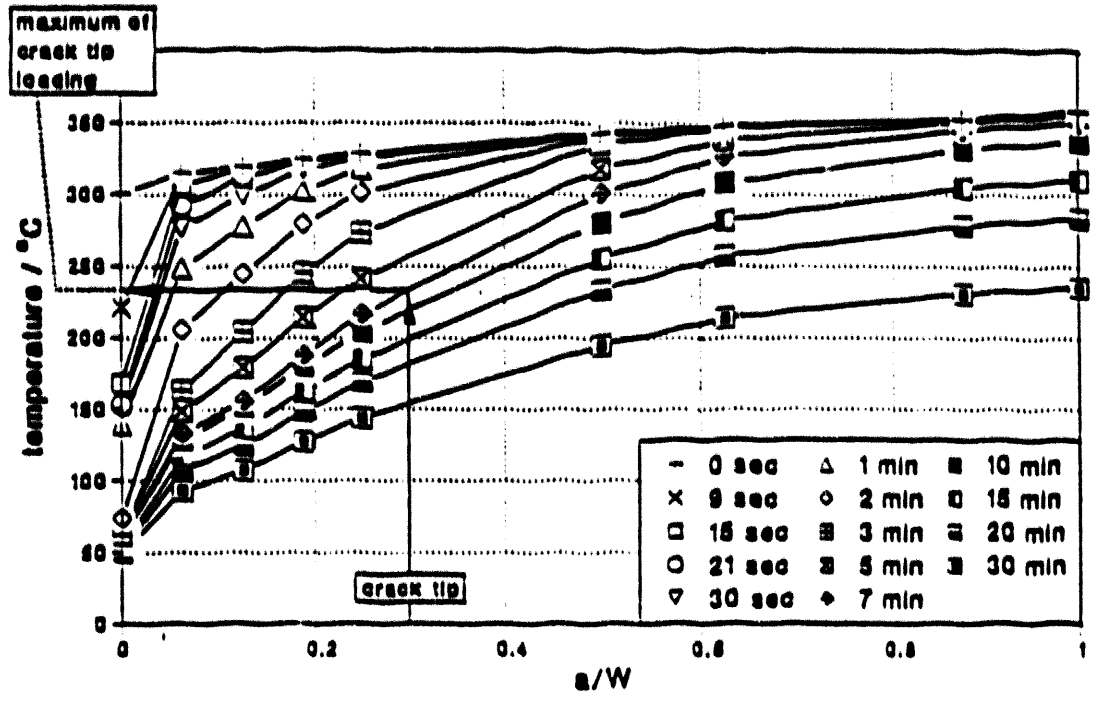

Figure 7: Measured temperature profile near crack section (NKS 3)

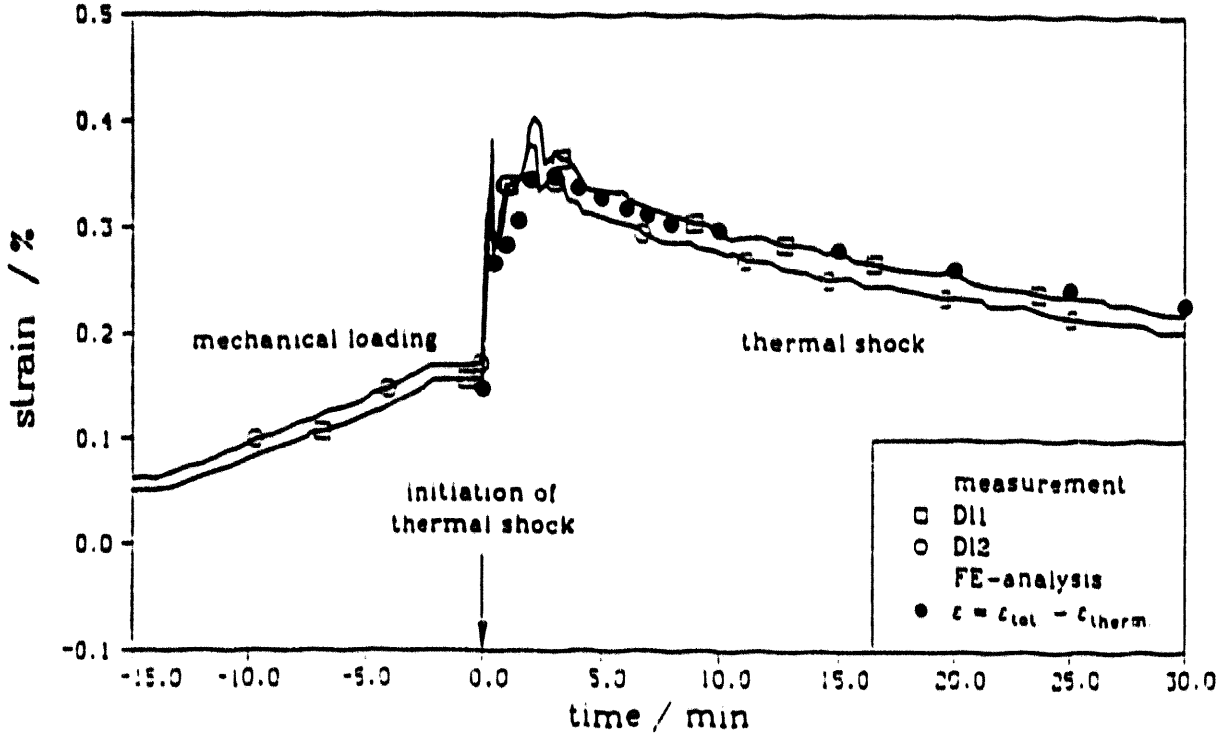

Figure 8: Measured axial strain vs time (NKS 3)

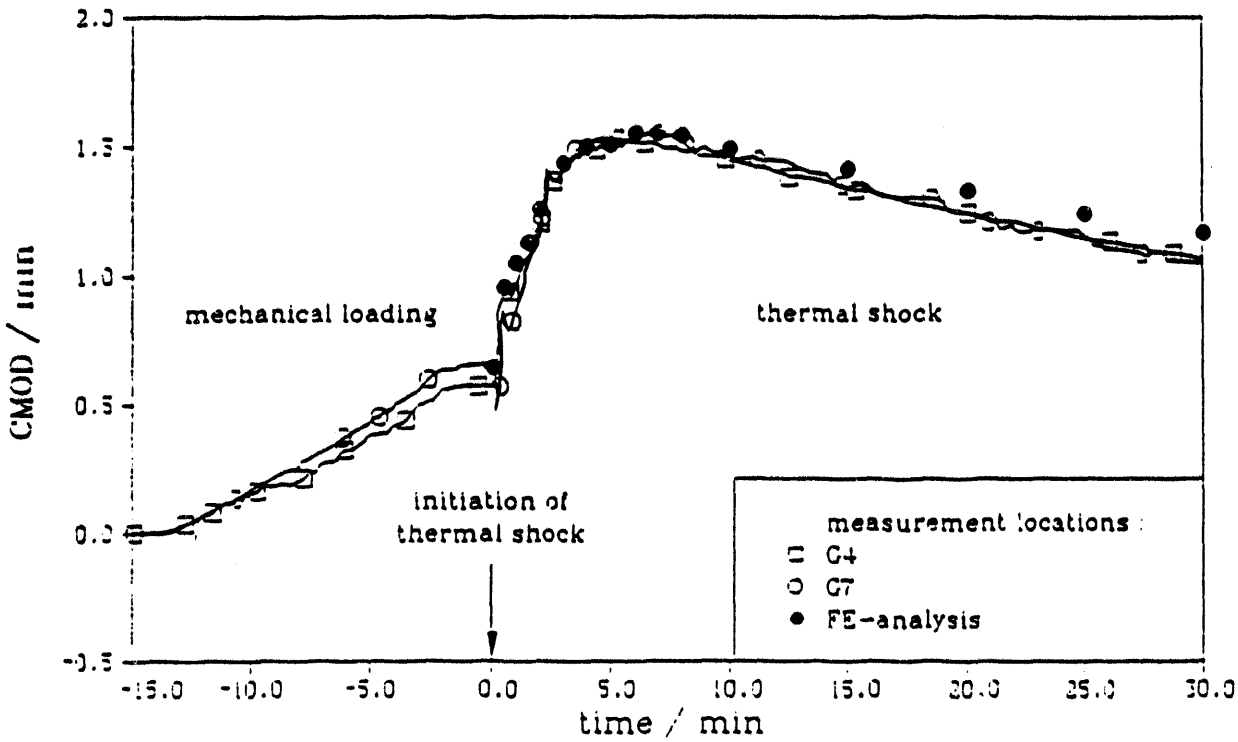

Figure 9: Measured crack opening displacement vs time (NKS 3)

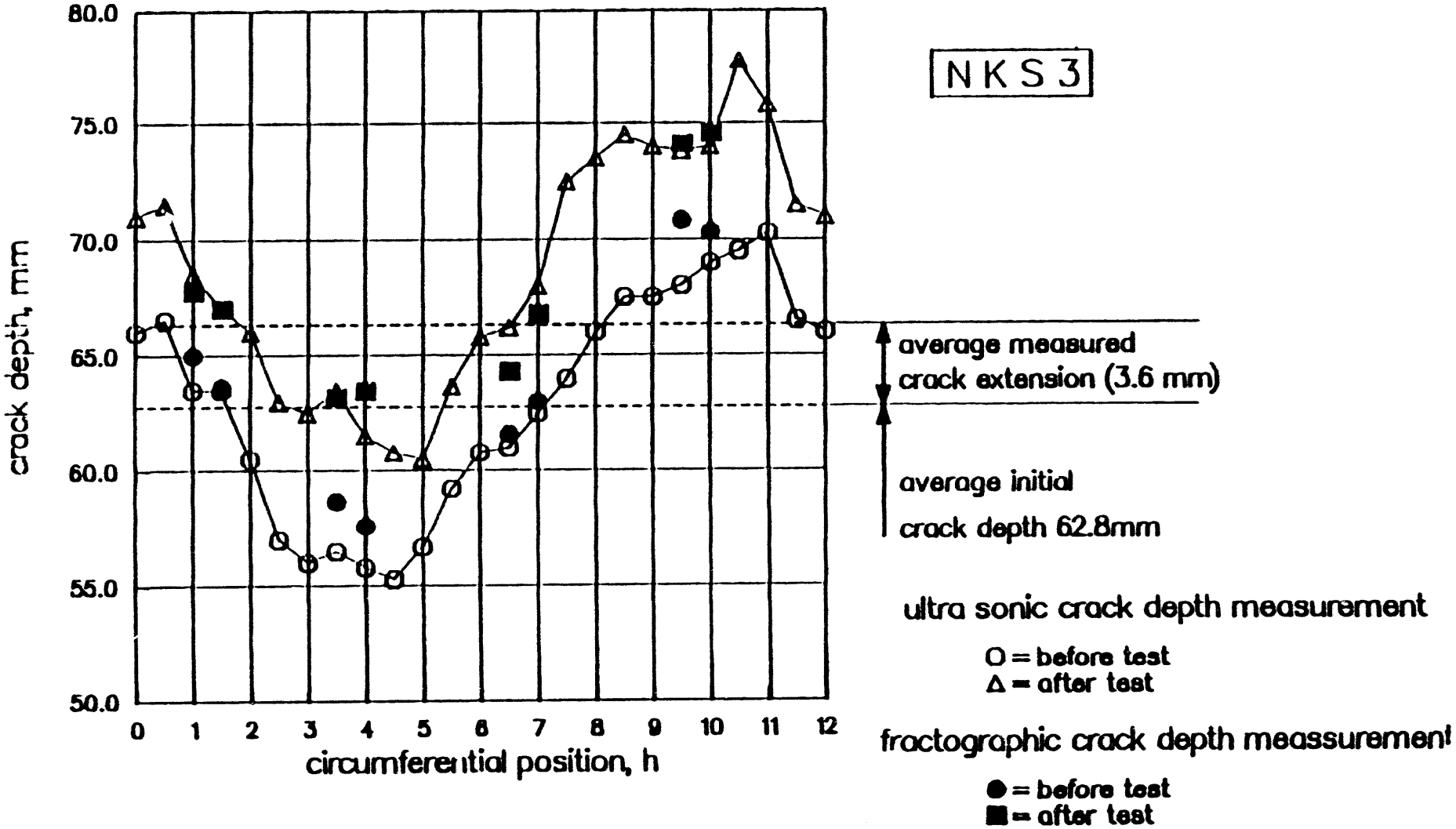

Figure 10: Crack depth measurement (NKS 3)

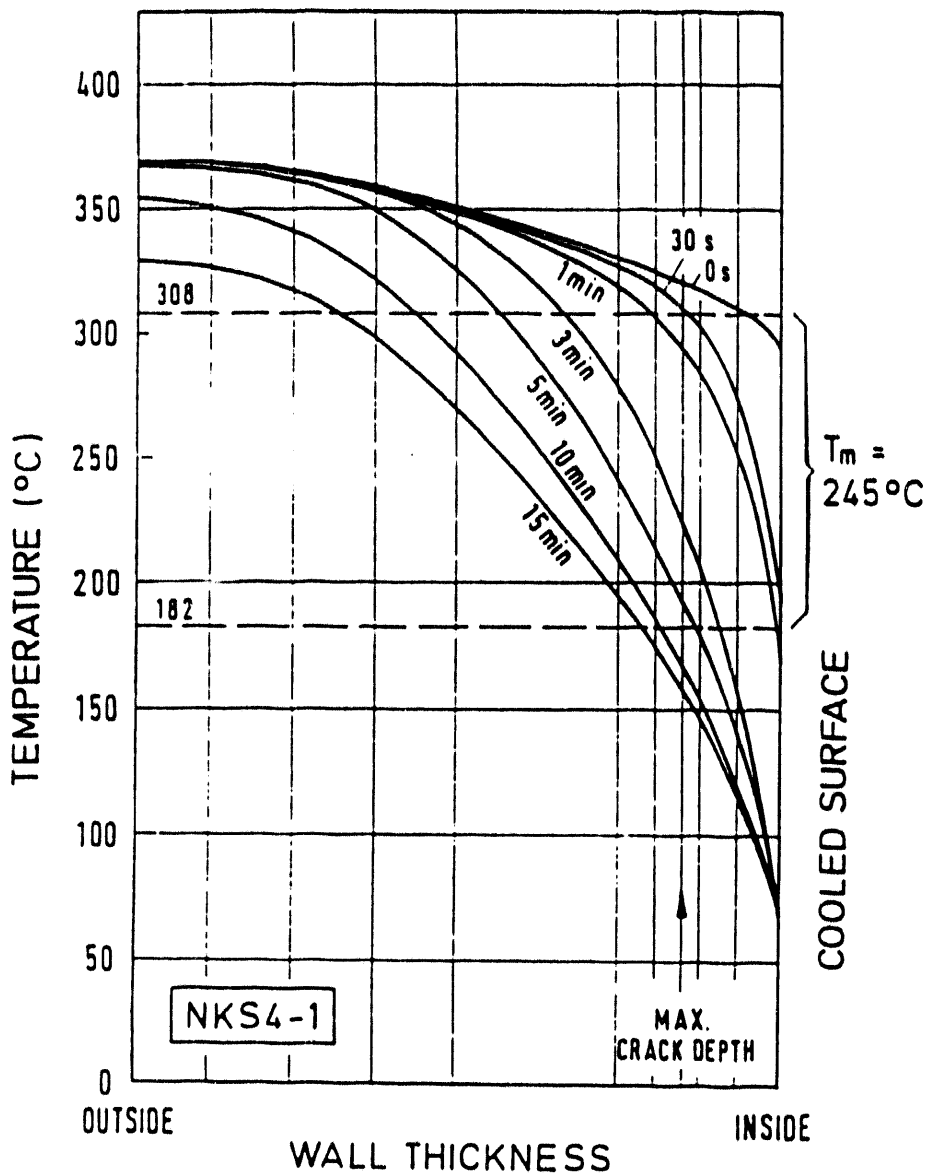

Figure 11: Measured temperature profile near crack section (NKS 4)

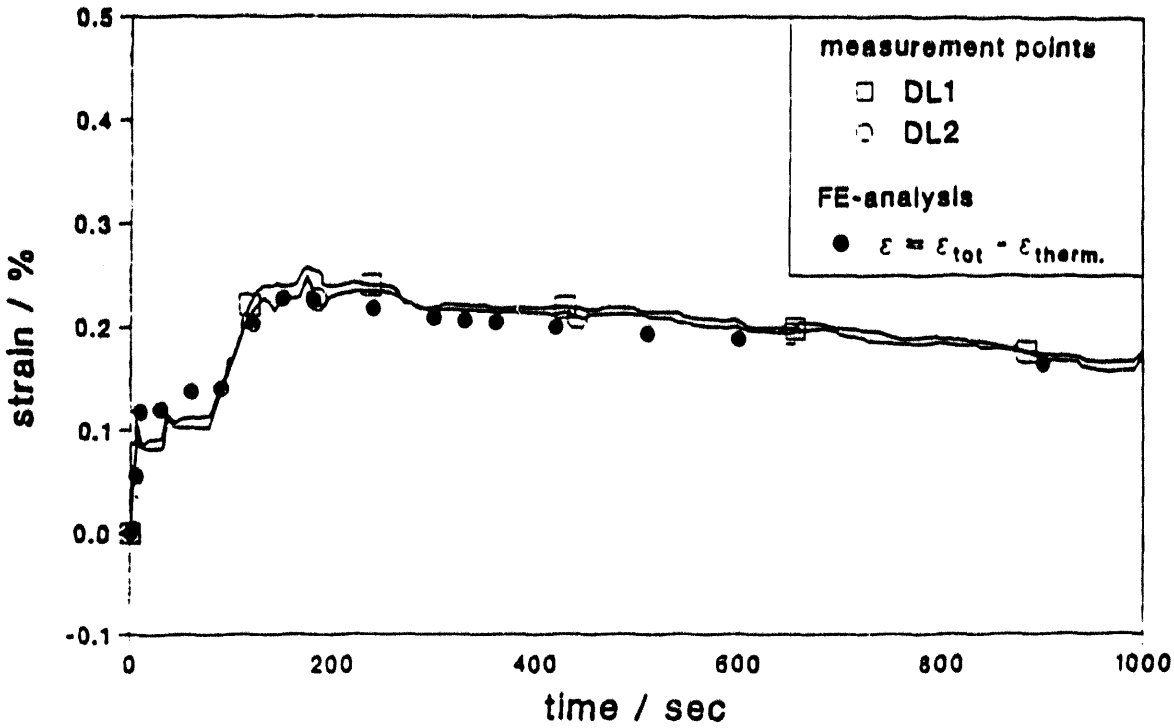

Figure 12: Measured axial strain vs time (NKS 4)

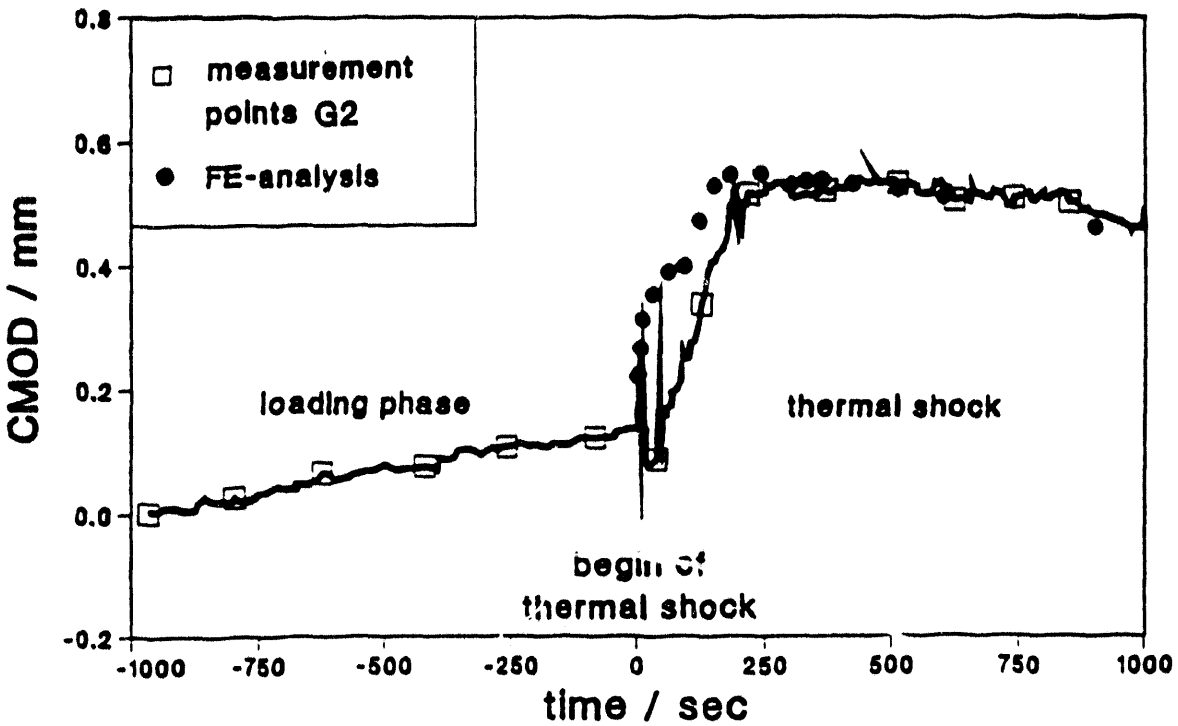

Figure 13: Measured crack opening displacement vs time (NKS 4)

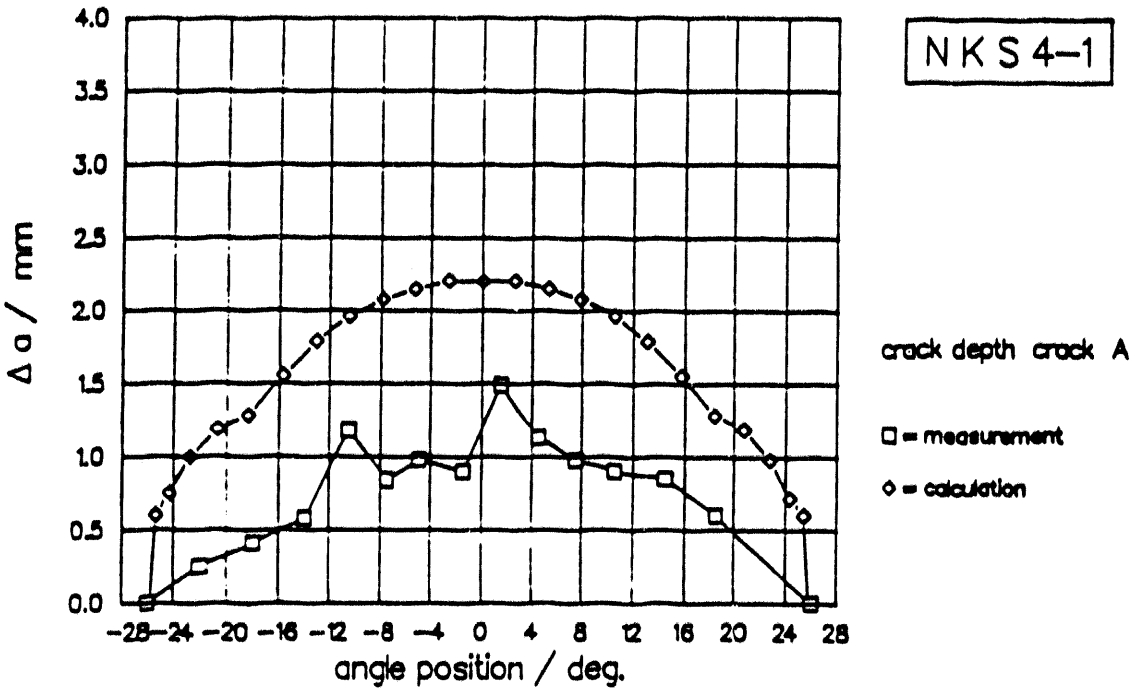

Figure 14: Crack depth measurement (NKS 4)

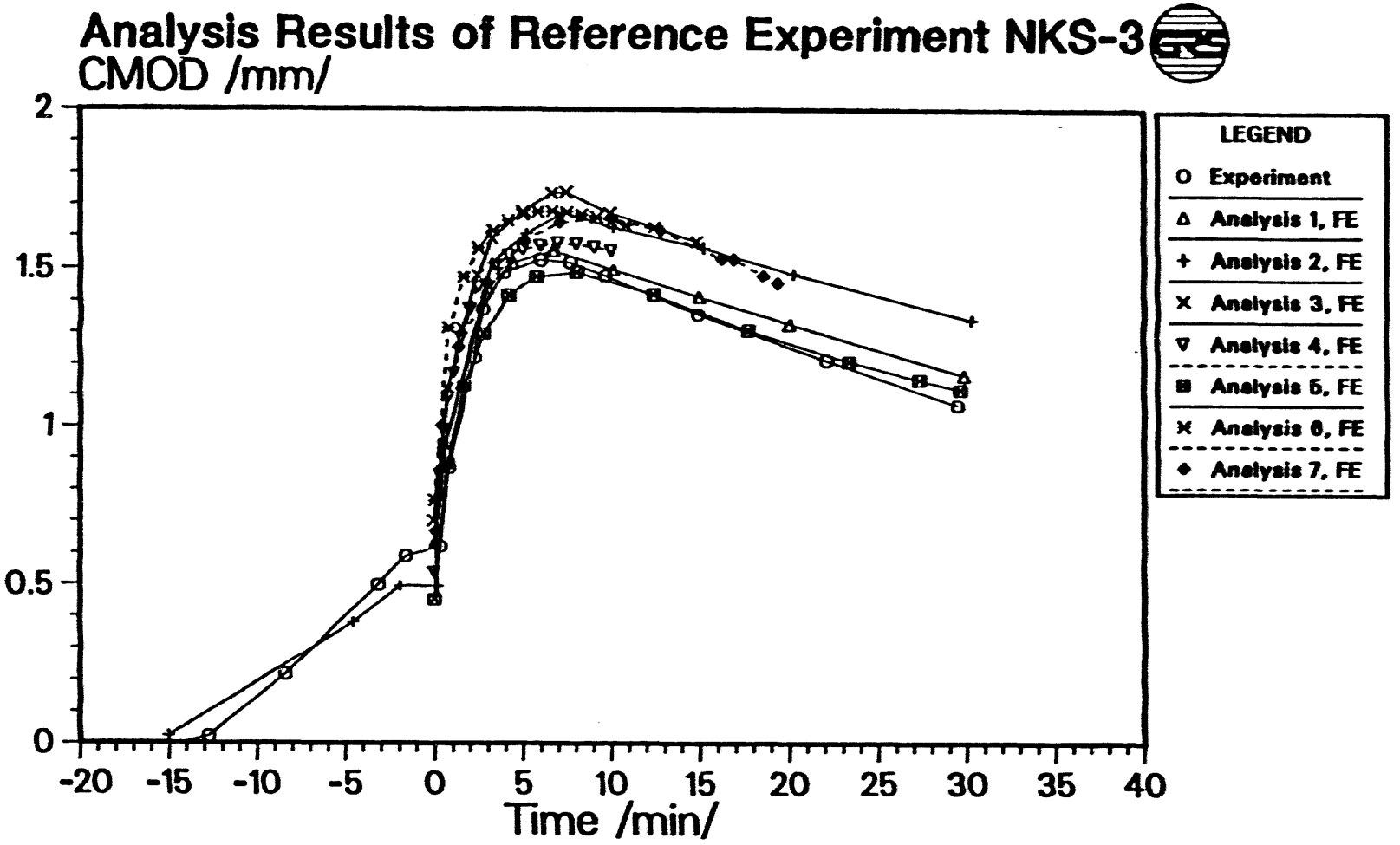

Figure 15: Calculated crack opening displacement vs time /5/

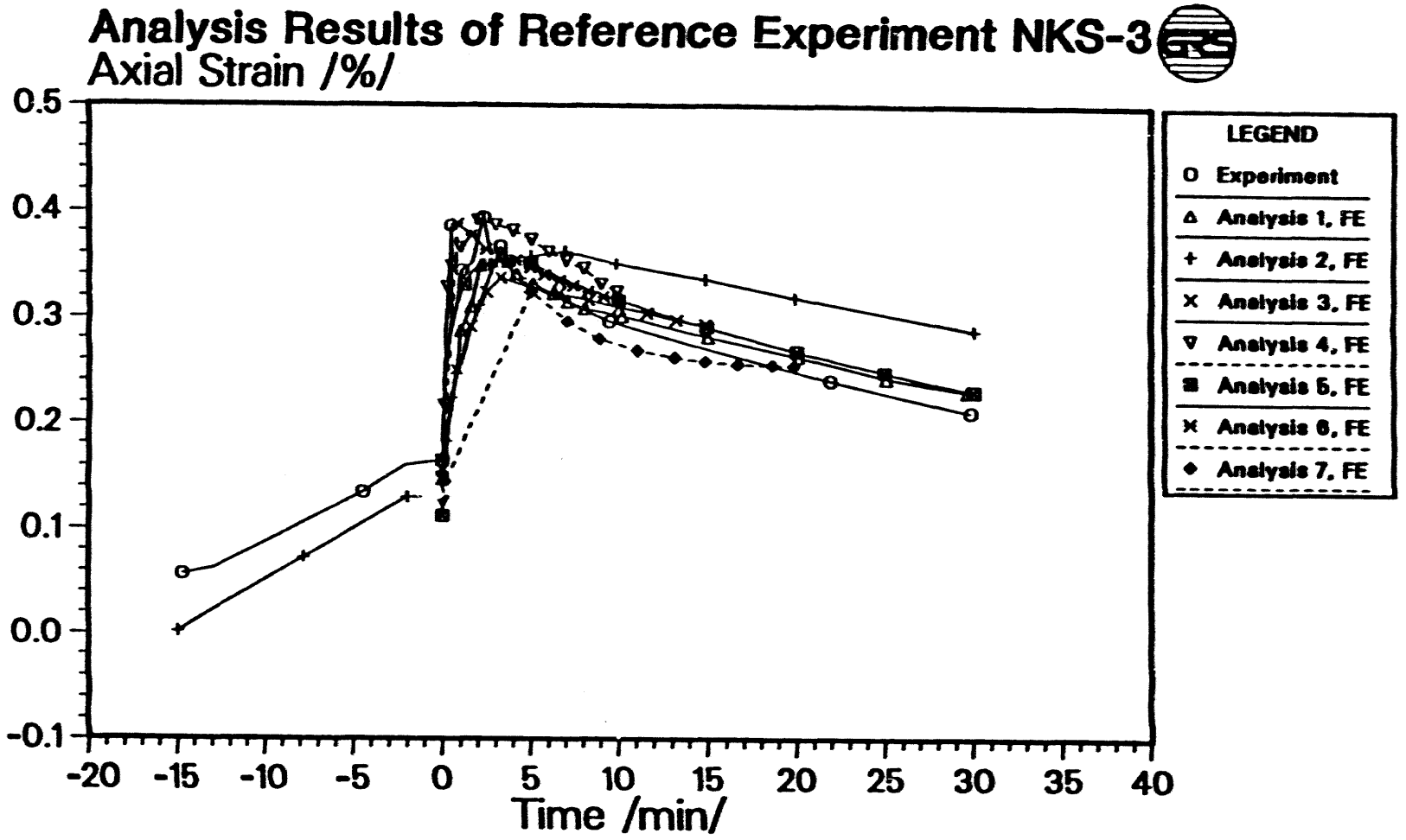

Figure 16: Calculated axial strain vs time /5/

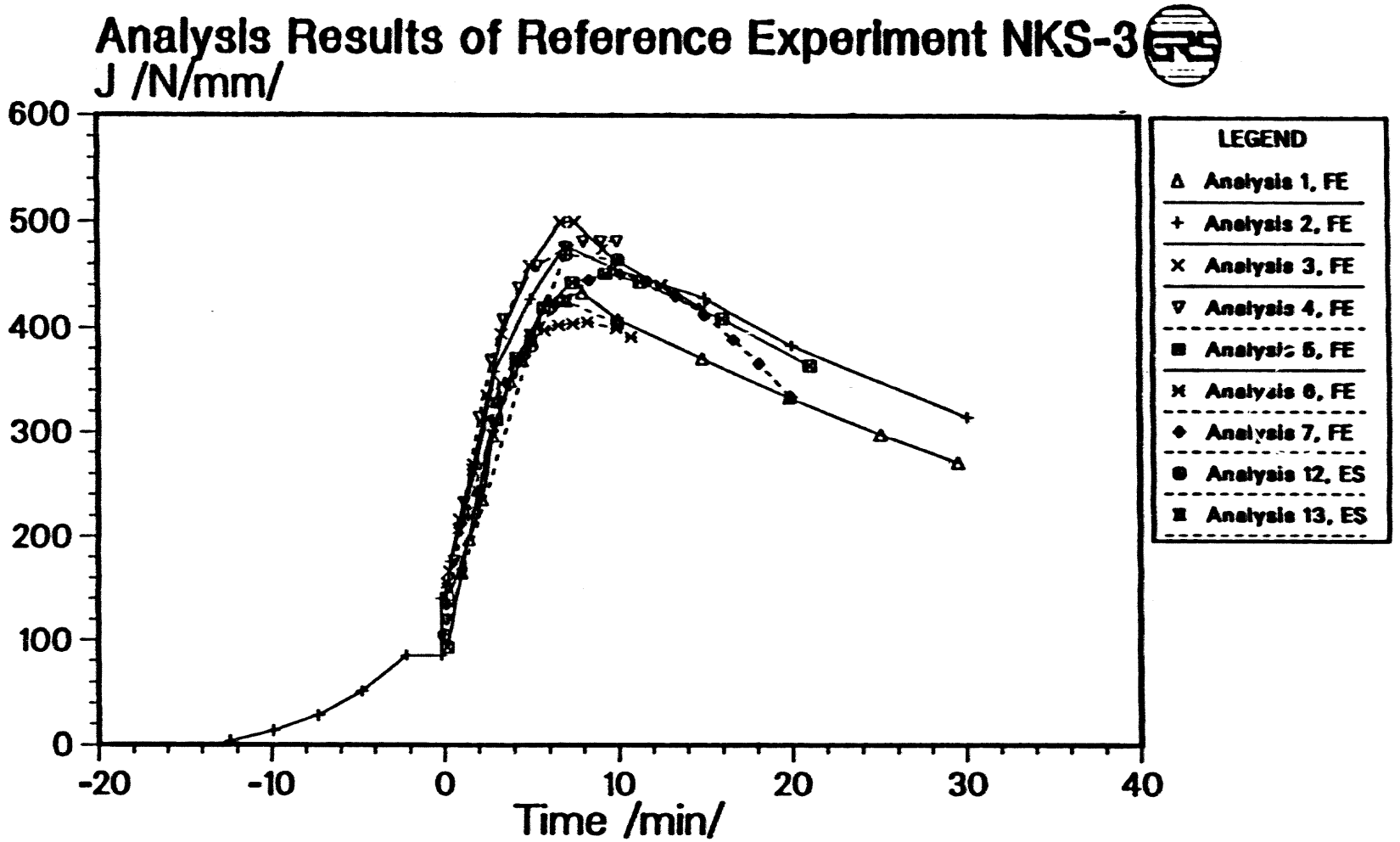

Figure 17: J-Integral vs time /5/

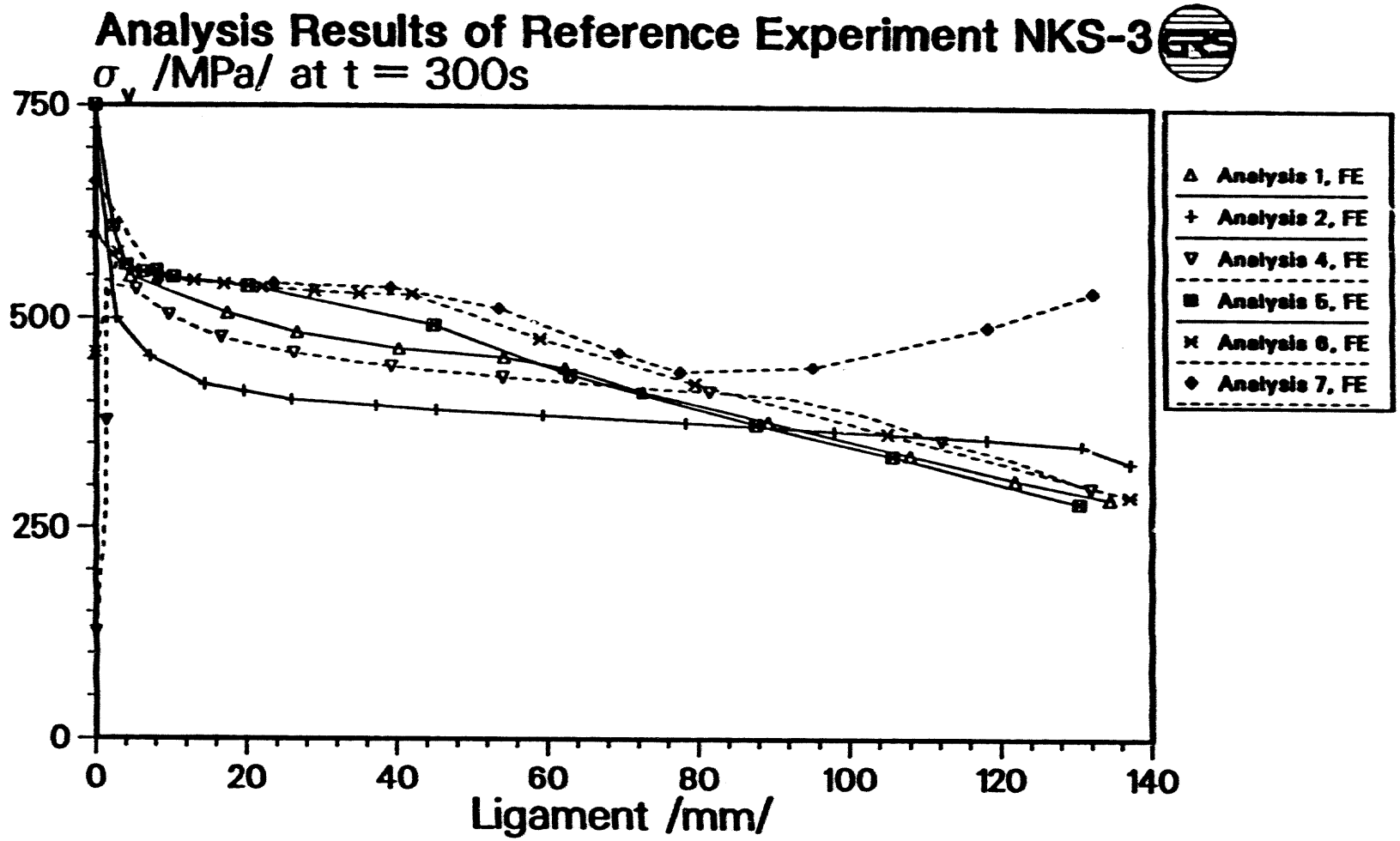

Figure 18: Effective stress at t = 5 min /5/

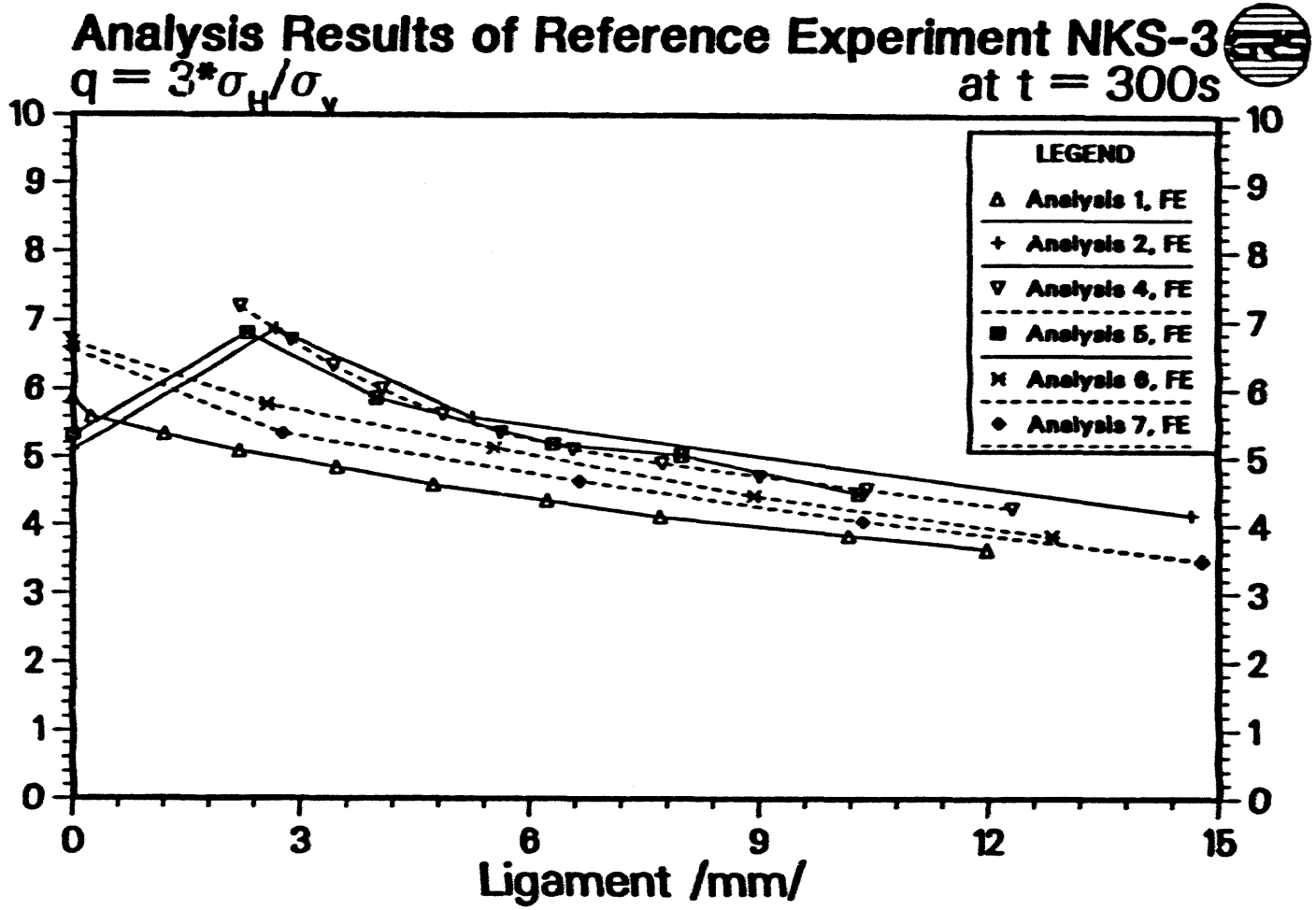

Figure 19: Stress triaxiality vs ligament at t = 5 min /5/

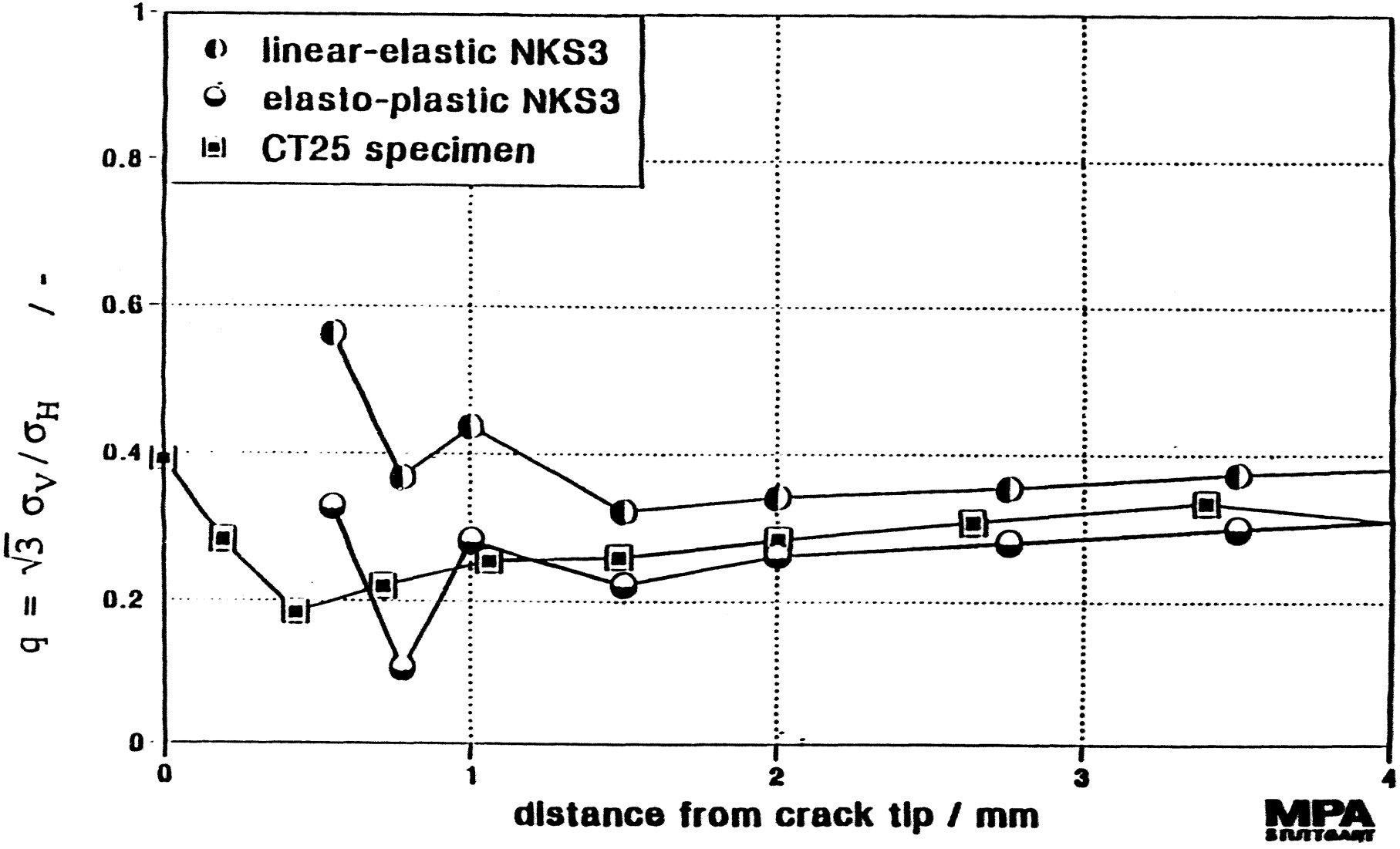

Figure 20: Stress triaxiality vs ligament at t = 7 min and in CT specimen

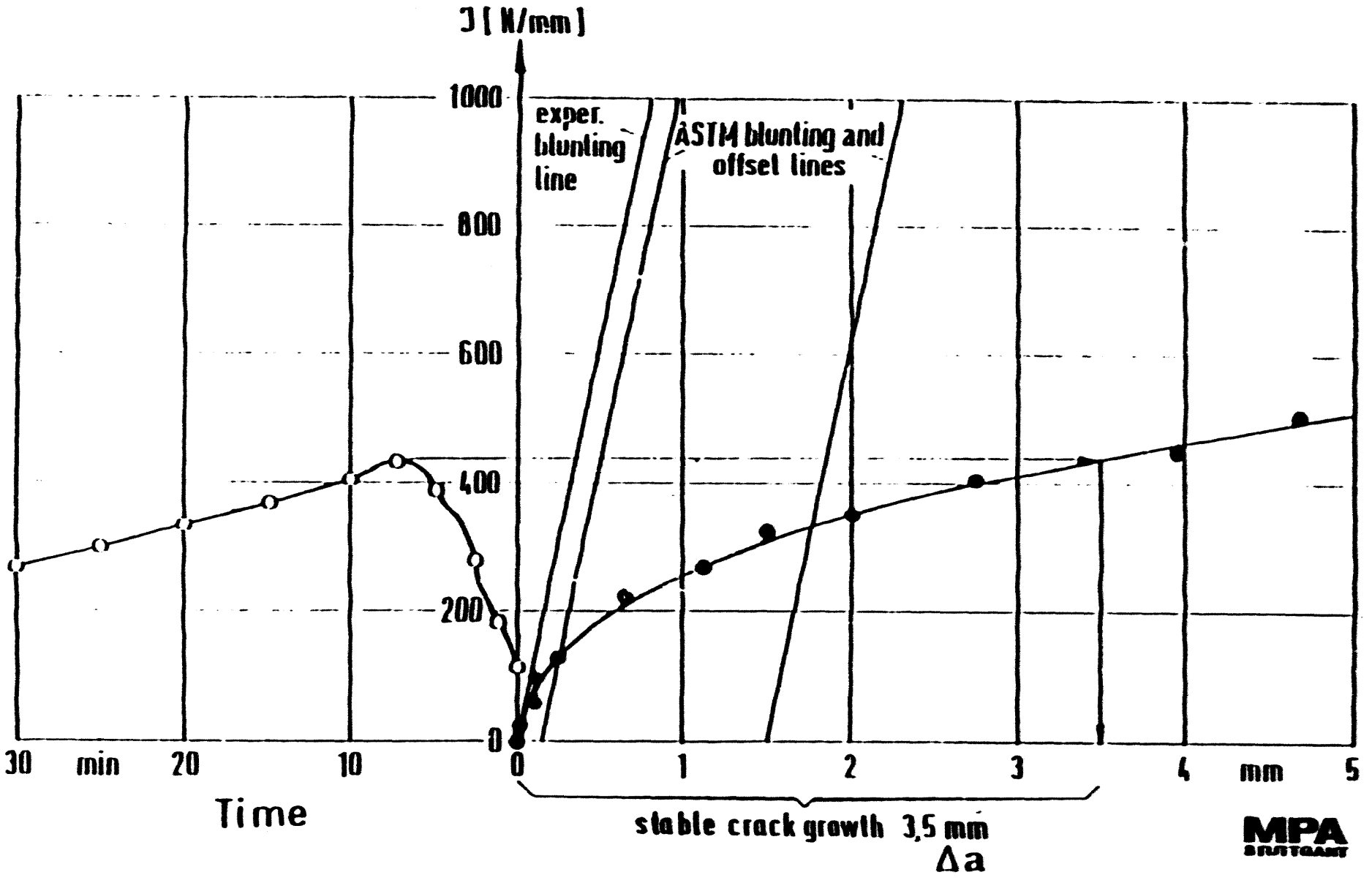

Figure 21: Comparison of crack driving force and crack resistance

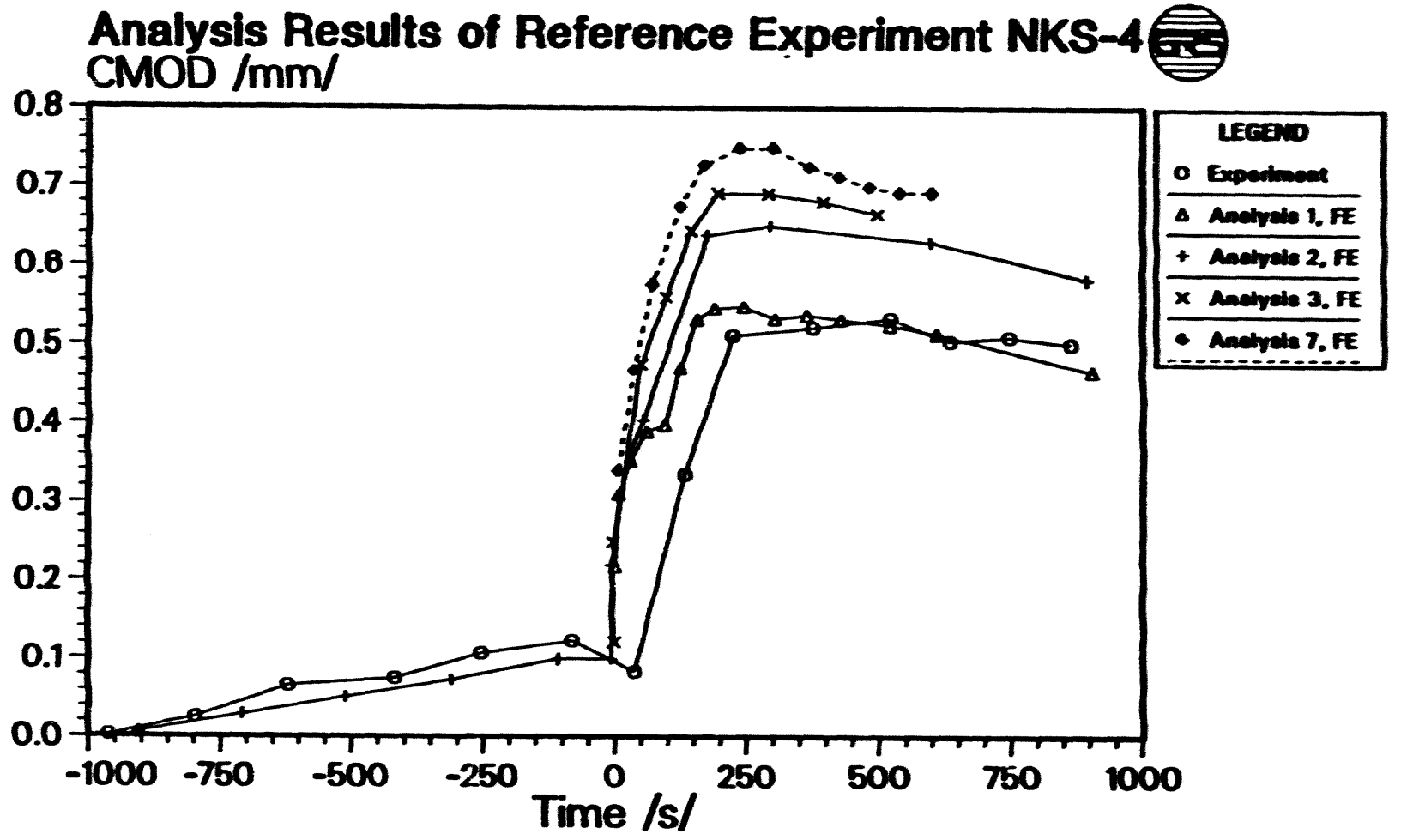

Figure 22: Calculated crack opening displacement vs time /5/

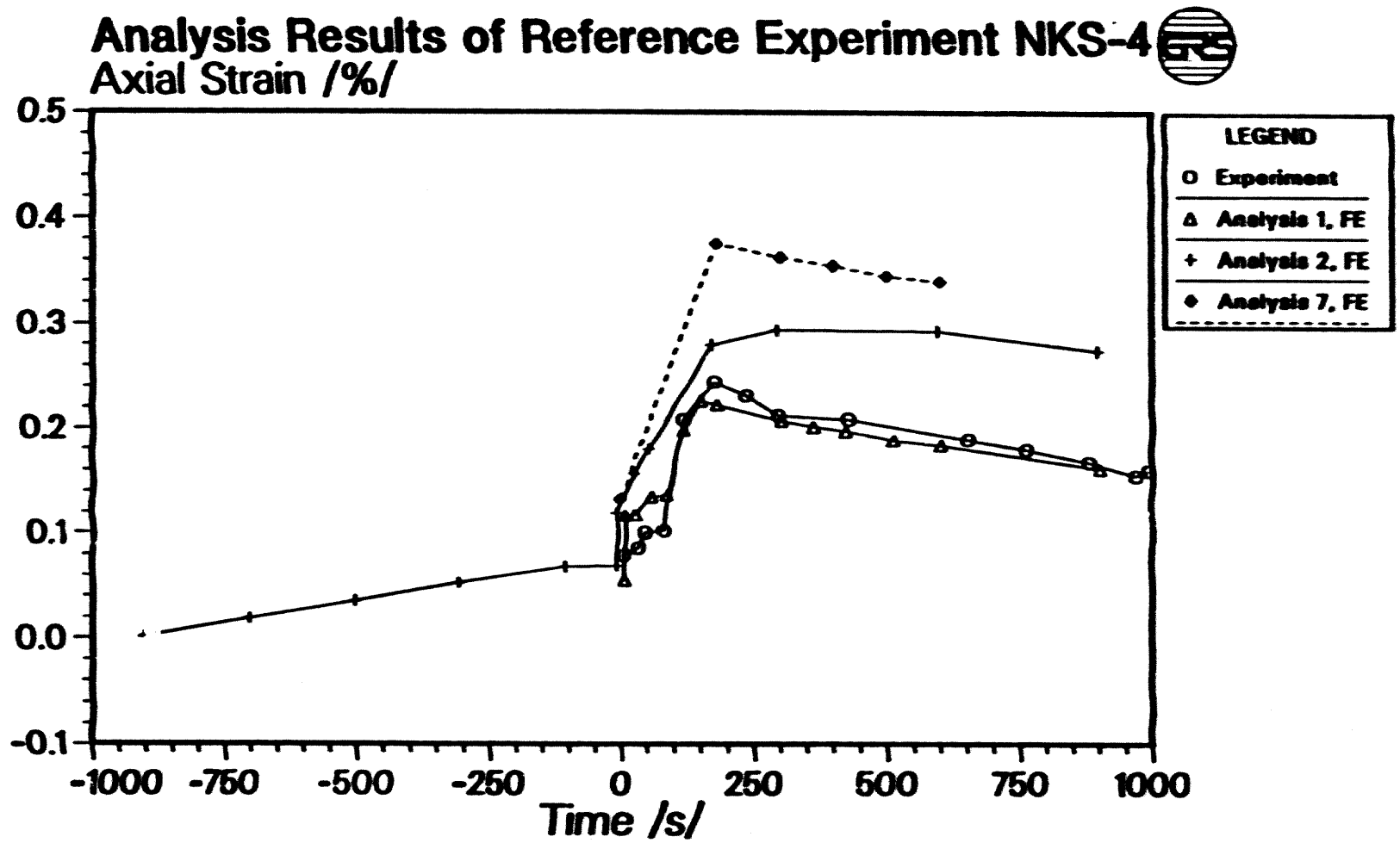

Figure 23: Calculated axial strain vs time /5/

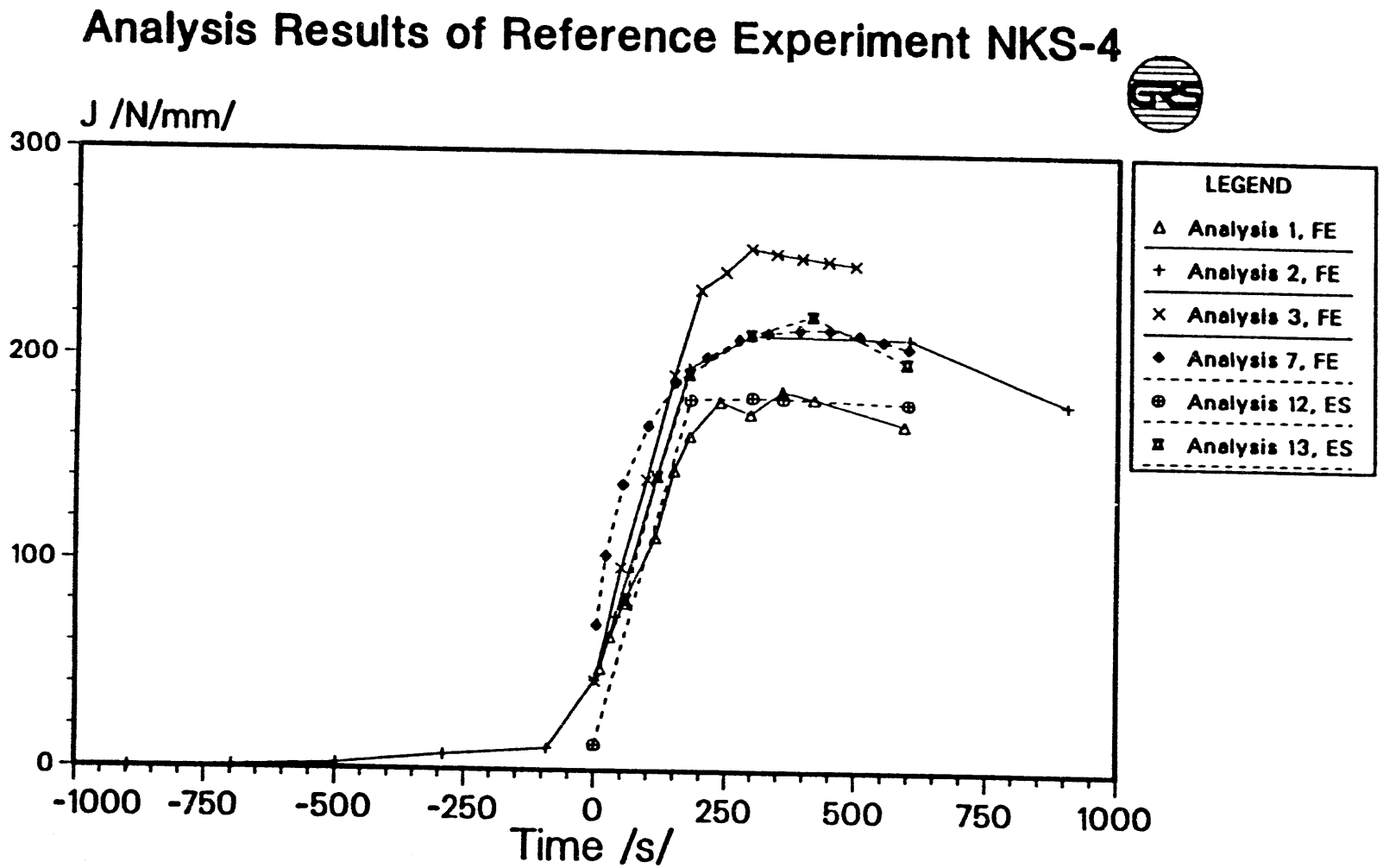

Figure 24: J-Integral vs time /5/

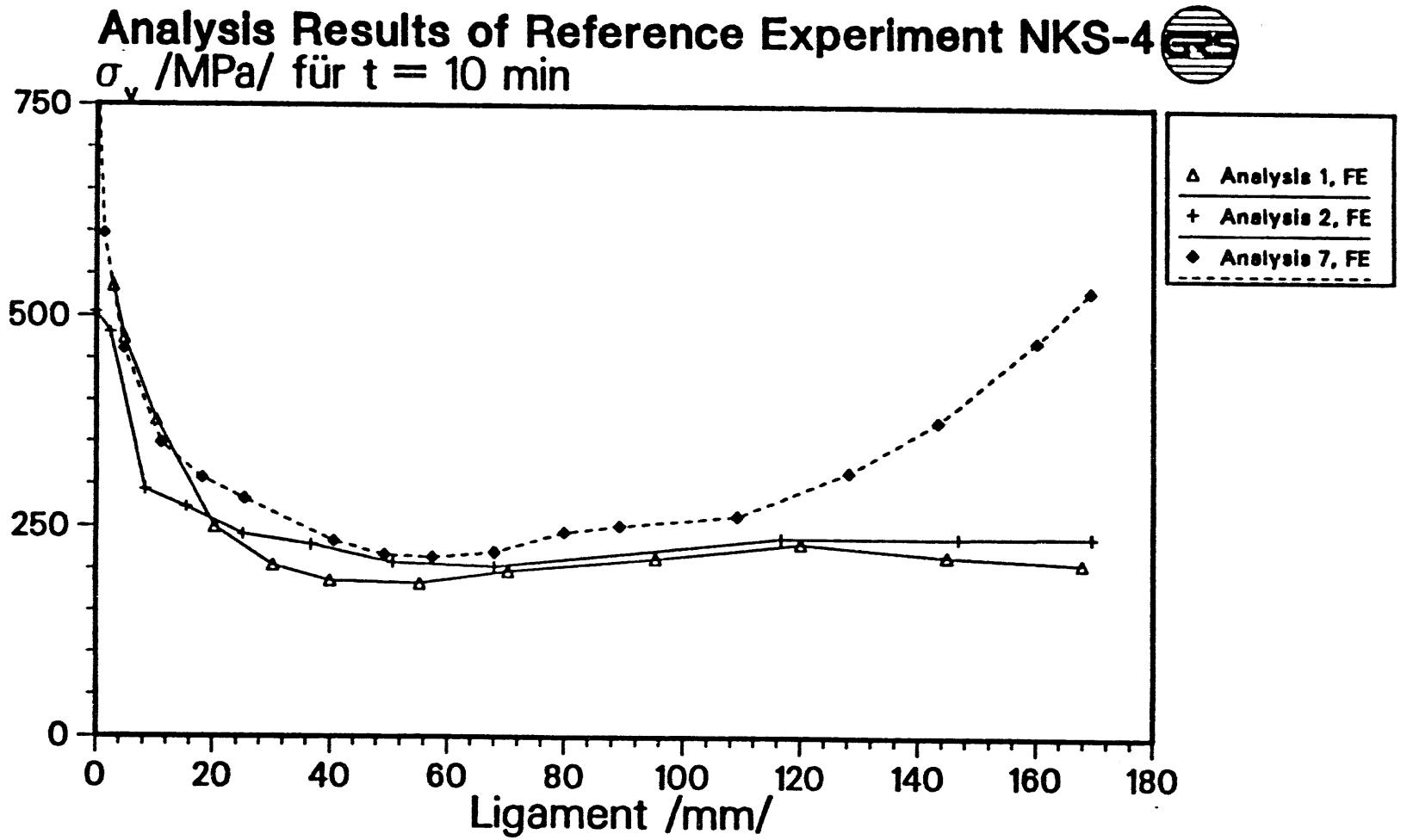

Figure 25: Effective stress at t = 10 min /5/

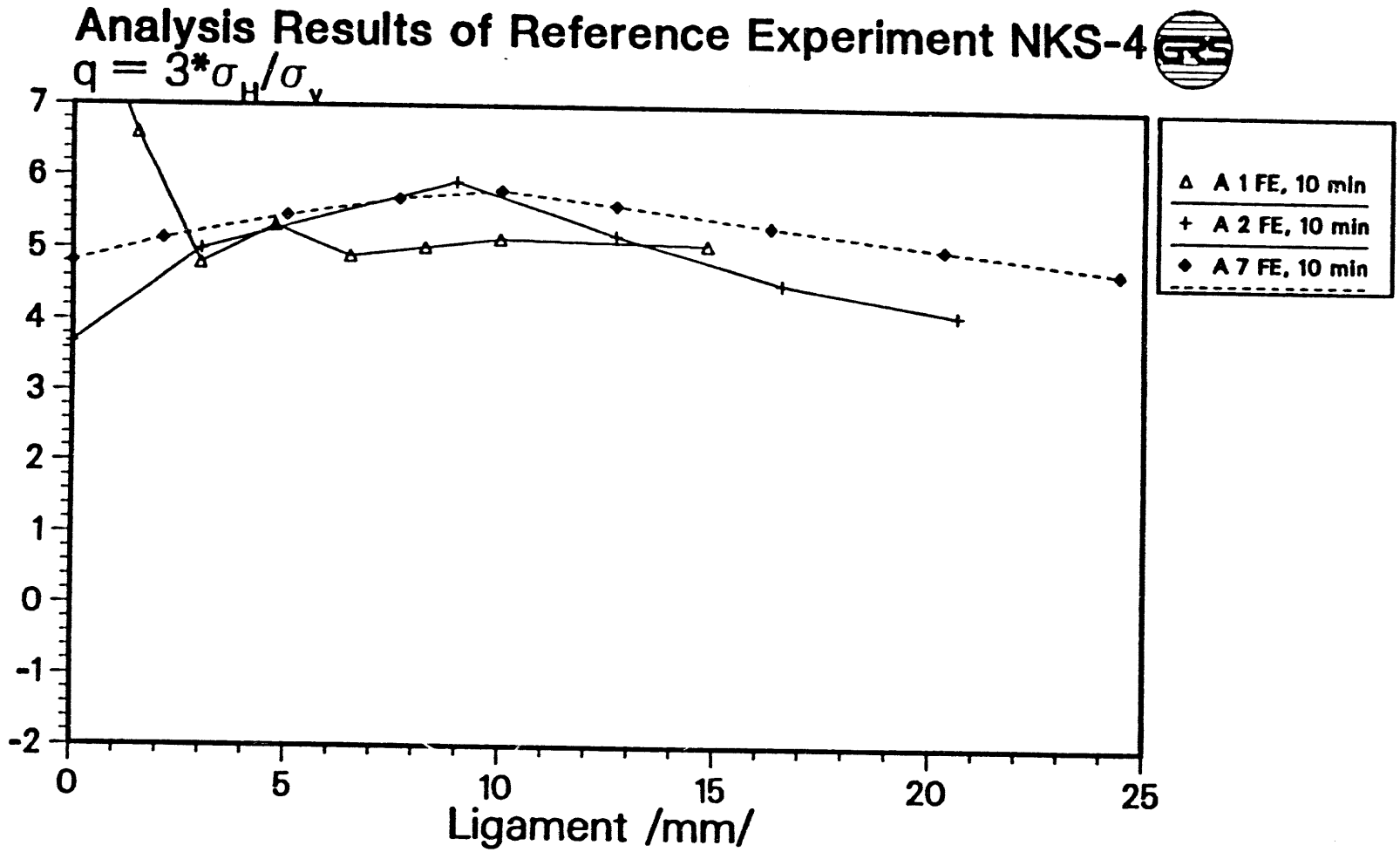

Figure 26: Stress triaxiality vs ligament at t = 10 min /5/

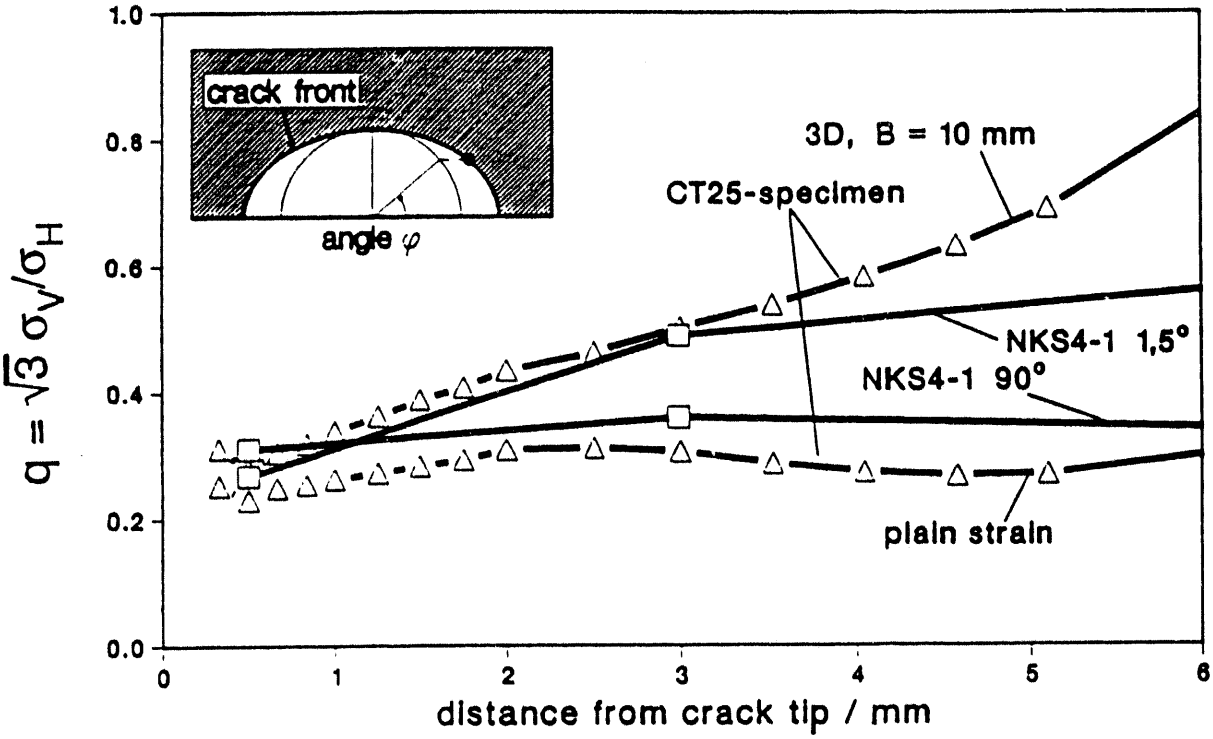

Figure 27: Stress triaxiality vs ligament (NKS 4) and in CT-specimen

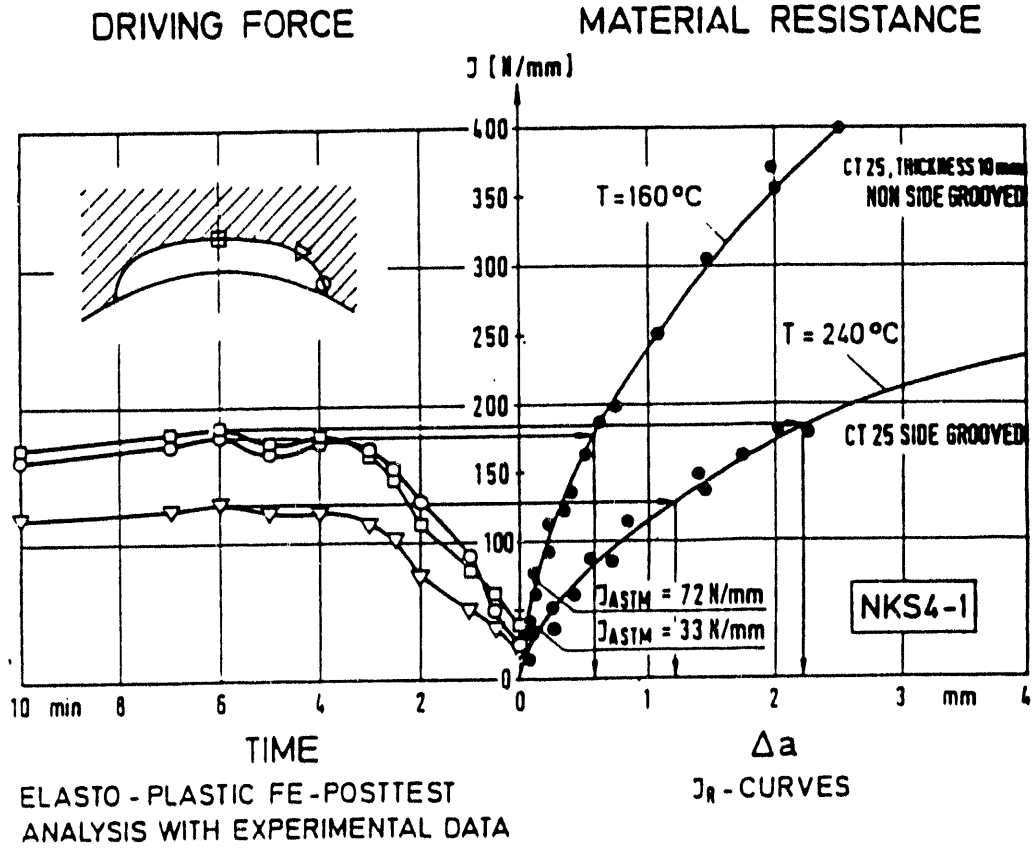

Figure 28: Comparison of crack driving force and crack resistance

COMPLEMENTARY RESULTS FOR NKS PRESSURIZED THERMAL SHOCK ANALYSES

J. BROCHARD

CEA, CE Saclay, Gif-sur-Yvette, France

X.Z. SUO

EUROSIM SARL, Les Ulis, France

H. HOROWITZ

CEA, CE Fontenay, Fontenay-aux-Roses, France

INTRODUCTION

In the framework of the CSNI project FALSIRE, we performed bidimensional and tridimensional finite element computations to analyse NKS3 and NKS4 experiments respectively. Results were presented at the FALSIRE workshop in 1990. After the workshop, we performed a new calculation, for the NKS4 analysis, with a more refined mesh to try to explain some discrepancies between the fracture mechanics parameters we obtained and values presented by other participants. In this paper, we review briefly the NKS3 results and then we turn to the NKS4 problem.

COMPUTATIONAL TECHNIQUES

Calculations of NKS tests were performed in two steps :

- incremental non linear computation to determine stress and strain fields at each time of the thermal transient,

- from these stress ans strain fields, computation of the G energy release rate.

The finite element computer code developped by CEA and called CASTEM 2000 was used.

We didn't performe thermal computations to determine the temperature distributions, but we interpolated the measured temperatures at each nodes of the meshes.

The meshes modelised a part of 550 mm high of the cylindrical vessels, and appropriate boundary conditions were used : symetry in the crack plane and rigid movement in the axial direction in the upper plane.

The elastic-plastic computations were performed with the hypothesis of small displacements ans small strains, and consequently the engineering stress-strain curve was considered. For plastic flow, the Von Mises criterion was used and isotropic hardening was assumed. Material properties dependance with temperature was not taken into account, and we took the stress-strain curve at room temperature, which is almost the average curve.

The multilinear stress-strain approximation used in our analyses is plotted in figure 1. The limit of linearity was defined by 2/3 the conventionnal yield stress.

ANALYSIS OF NKS3 TEST

The bidimensionnal model used to analyse the circumferential defect is shown in figure 2. The size of the quadratic elements near the crack tip is 5 mm.

The computed G values are plotted in figure 3. The G value exceeds the J_{1c} value (J_{1c} = 43 N/mm) during the application of the tractive effort and becomes maximum 7 minutes after the beginning of the thermal shock.

The evolution of the equivalent stress along the ligament at different times of the transient is one of the additional informations used, in the Final Report [1], to compare the different numerical results. A typical curve five minutes after the beginning of the thermal shock is plotted in figure 4. Just after the peak, values are very low in comparison with results of other participants : the small yield stress we put in the stress-strain relation gives an explanation of this discrepancy.

Another additional information is the stress triaxiality in the ligament (figure 5). In front of the crack tip, values are high, almost equal to 6, as for a plane strain configuration.

An estimation of the stable crack growth was done, transferring the applied J values on a CT-25 specimen resistance curve. The predicted value, 4.2 mm, is in good agreement with the measured one : 3.6 mm (figure 6).

ANALYSIS OF NKS4 TEST

Due to the symetry of the defects, just a quarter of the vessel was modelled, using quadratic elements. The first model presented at the workshop, in 1990, was very coarse, the ratio between the size of the smallest element at the crack front and the crack depth being equal to 1/4. The new 3D model is shown in figure 7 ; the size of each element is two times smaller than in the first mesh : almost 4 mm at the crack front (about 20000 degrees of freedom).

Results of the new elastic-plastic computation are compared with the experimental values by means of comparison of displacements ans strains. Figure 8 shows the axial strain at 184 mm from the crack plane versus time, and figure 9 the crack mouth opening displacement versus time. Like with the initial mesh, the numerical analysis overestimates, by almost 15 %, the crack mouth opening displacement.

The computed G values at the deepest point of the crack front are plotted in figure 10. This figure explains the discrepancy, pointed out at the workshop, with values of the other participants. In fact, in the first study, the G-value was calculated with a virtual crack advance restricted to the node at the crack front ; the evolution of G versus time was equivalent to the lowest curve of figure 10. In the new study, four virtual crack advances were tested. The first one is localized on the deepest point as previously, and the others are more and more extended in the row of elements leaning on the deepest point and perpendicular to the crack front. The maps, figure 10, are iso-value representations of the θ-fields used to simulate the crack advance. The corresponding evolutions of G versus time show up a stabilization tendency, but the G value obtained with the fourth θ-field is almost 30 % higher than the initial value with the first θ-field. So the discrepancy in our first study was due to an underprediction of the G values because not stabilized.

The equivalent stress and the stress triaxiality in the ligament are plotted in figures 11 and 12. In front of the deepest point of the crack, the stress triaxiality is almost equal to 6, characterizing a plane strain configuration.

According to comparison of the stress triaxiality values computed from CT specimens and from NKS4 experiment, Huber and Guth [3] recognized two resistance curves for the NKS4 experiment fracture assessment. Following these indications, we put our stabilized G values, for the deepest point, on the recommended (J, Δa) curve. The predicted crack growth is equal to 2.8 mm, though higher, by a factor 2, than the measured value 1.5 mm.

CONCLUSION

The global elastic plastic response measured during NKS3 and NKS4 experiments is well predicted by finite element computations.

For NKS3, the J_R methodology based on CT specimen data gives crack growth assessment in good agreement with the measured values.

For NKS4, the CMOD is somewhat overpredicted by the FE analysis and, in correlation, the crack advance prediction using the J_R concept is also too high.

REFERENCES

[1] Bass, B.R. et al.
Final report on phase I of the CSNI Multi-National Project for Fracture Analyses of Large-Scale International Reference Experiments (FALSIRE), June 1992.

[2] Huber, H.
CSNI reference experiment n° 1 : NKS3 pressurized thermal shock experiment (1989).

[3] Huber, H. and Guth, W.
CSNI reference experiment n° 4 : NKS4 pressurized thermal shock experiment (1989).

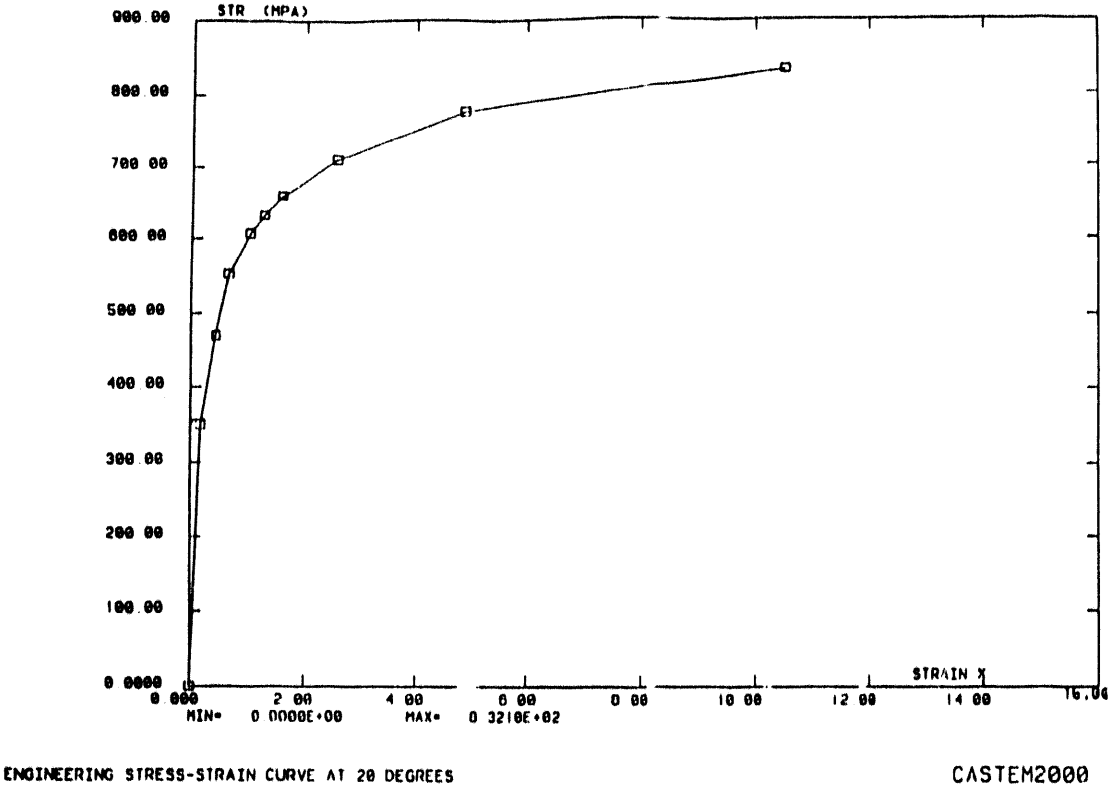

Figure 1 : Multinear stress-strain approximation for NKS analyses

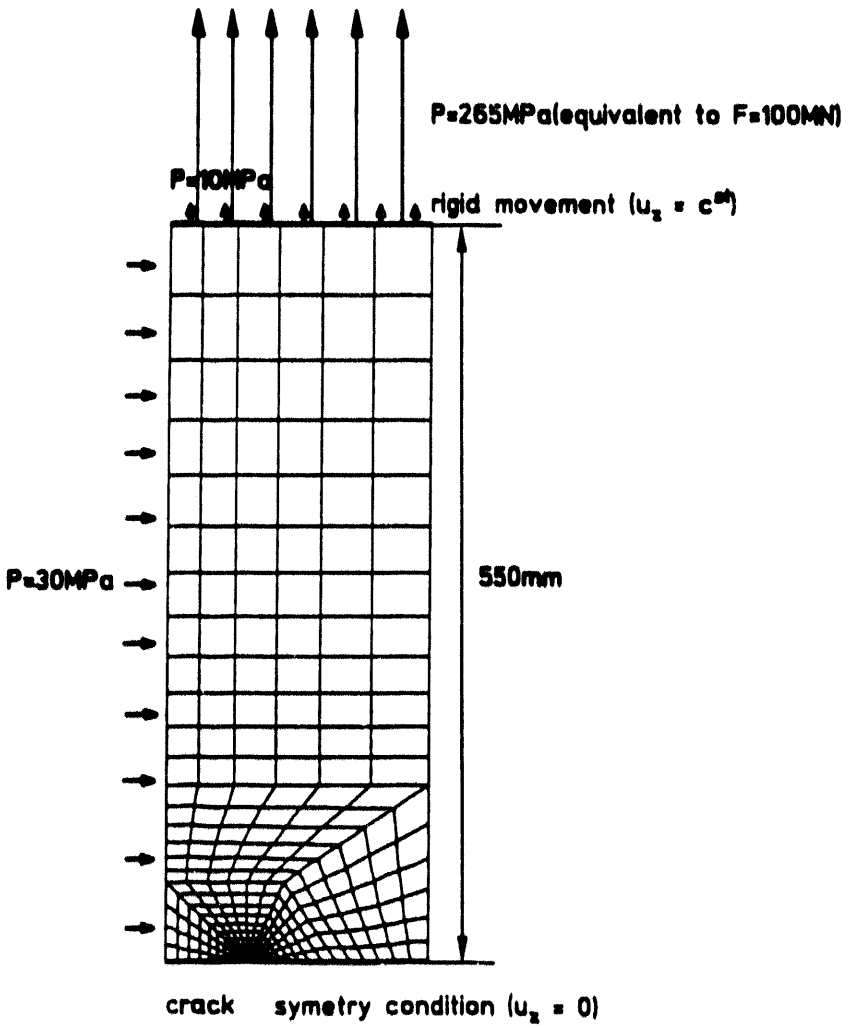

Figure 2 : Finite element model for NKS3 analysis

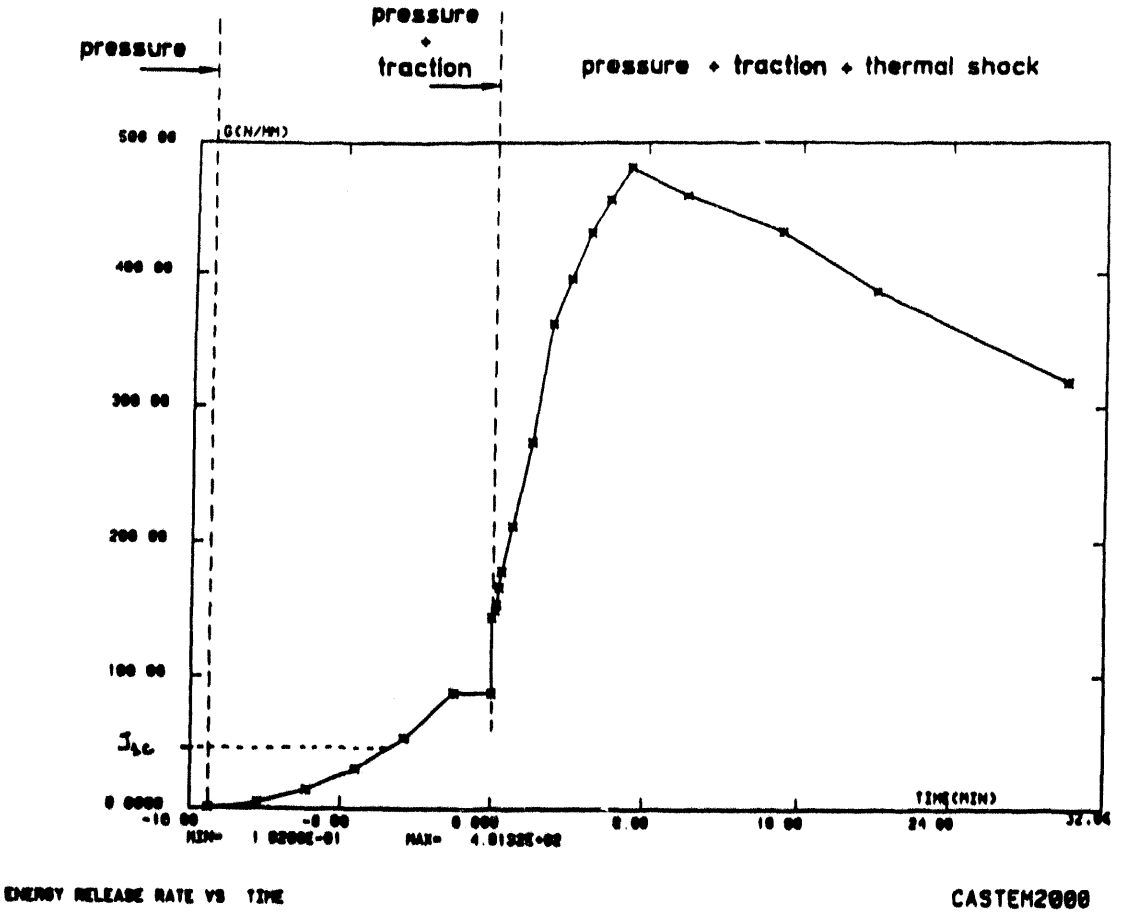

Figure 3 : Energy release rate versus time for NKS3 analysis

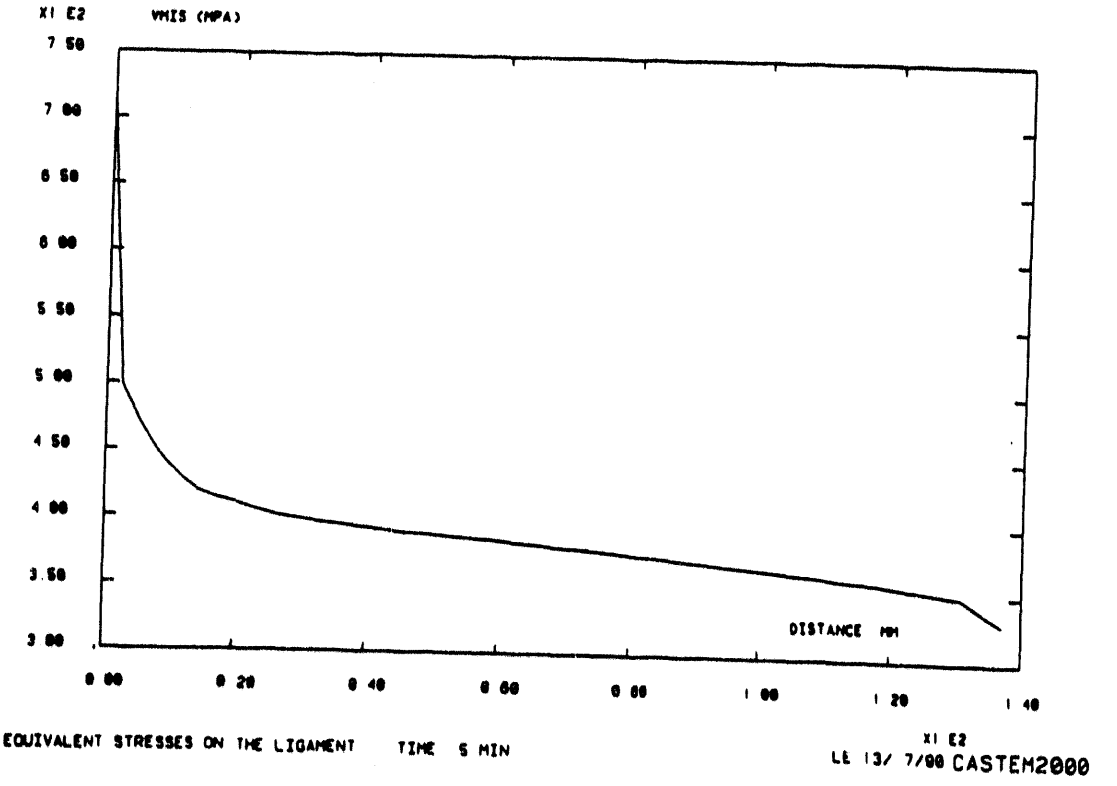

Figure 4 : Equivalent stress in the ligament for NKS3 analysis (time 5 minutes)

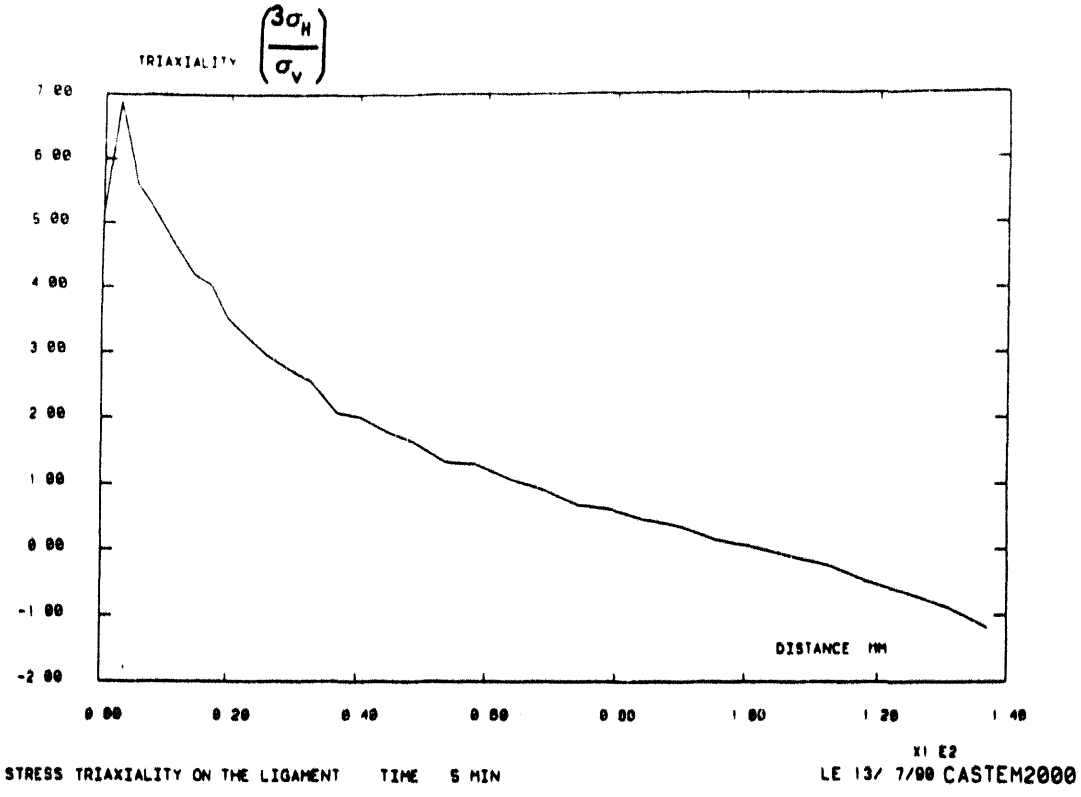

Figure 5 : Stress triaxiality in the ligament for NKS3 analysis (time 5 minutes)

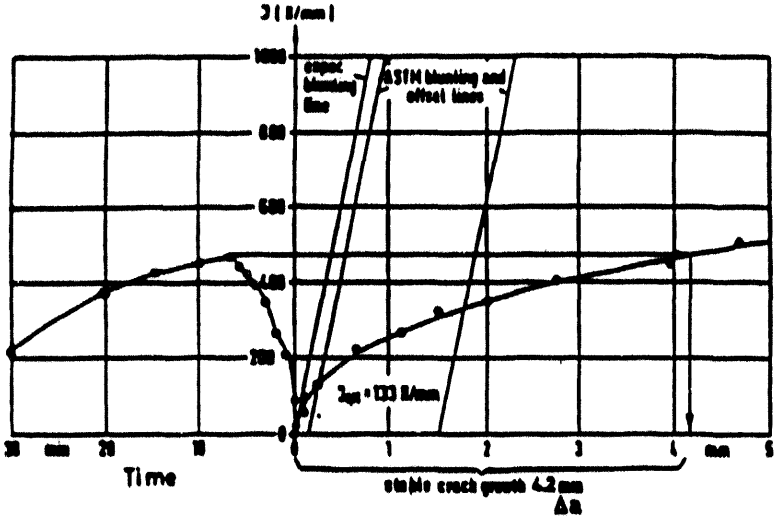

Computed G. values and J_R curve for NKS - 3 experiment

predicted stable crack growth : 4.2 mm

average measured crack extension : 3.6 mm

Figure 6 : Crack growth assessment for NKS3 analysis

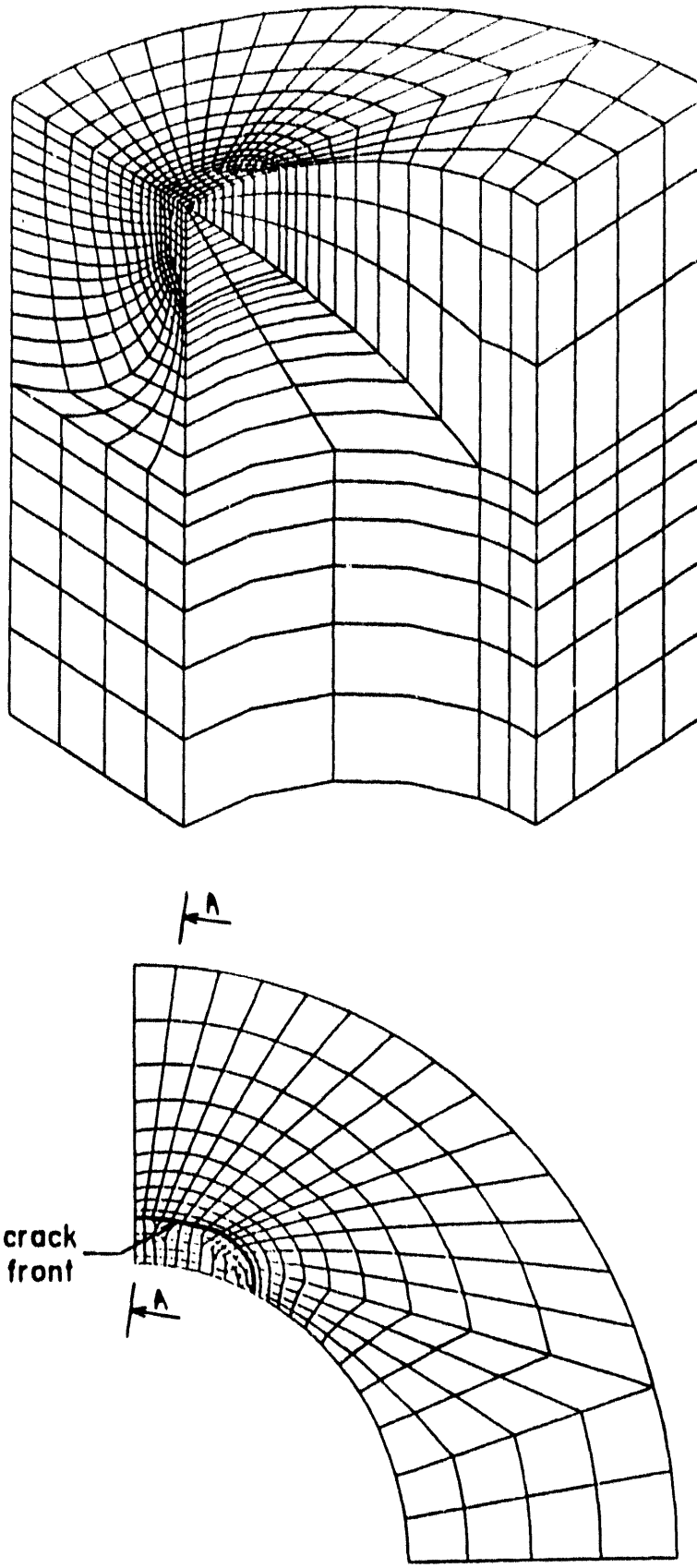

Figure 7 : New finite element model for NKS4 analysis

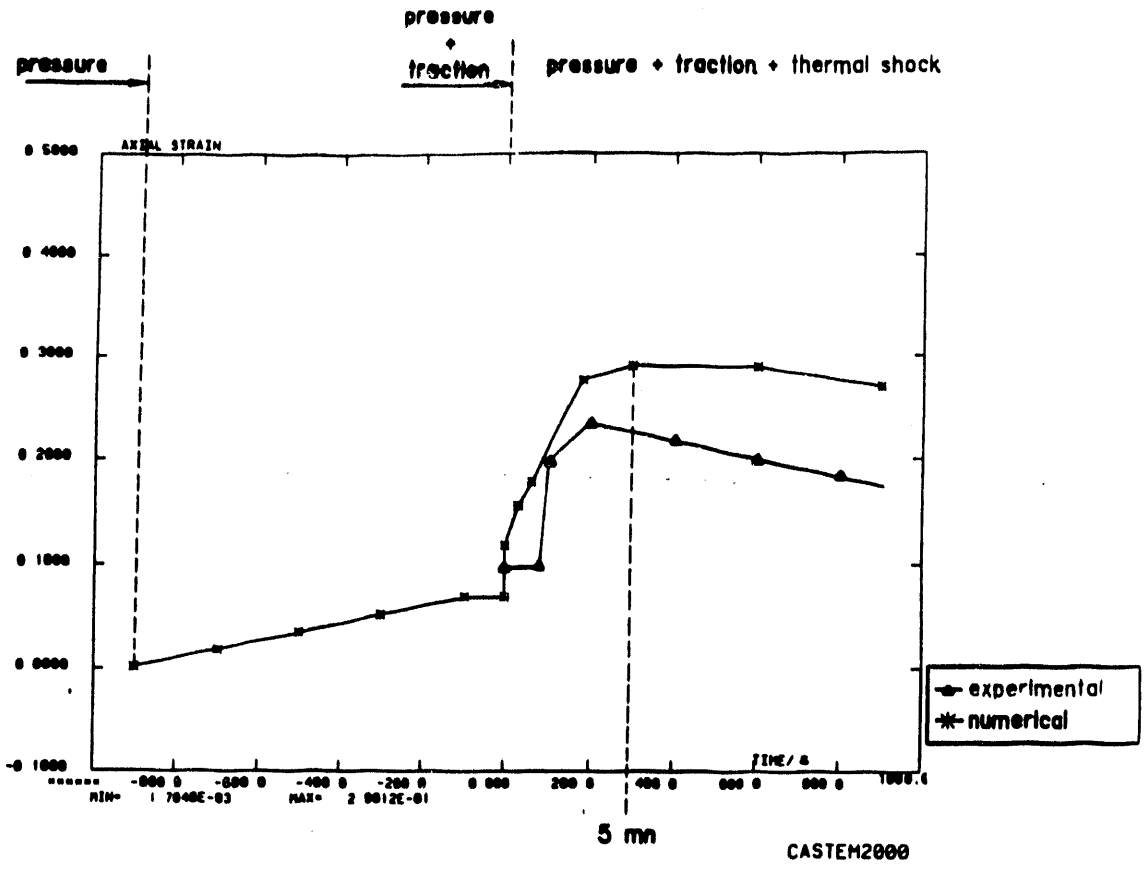

Figure 8 : Axial strains at 184 mm from the crack plane for the new NKS4 analysis

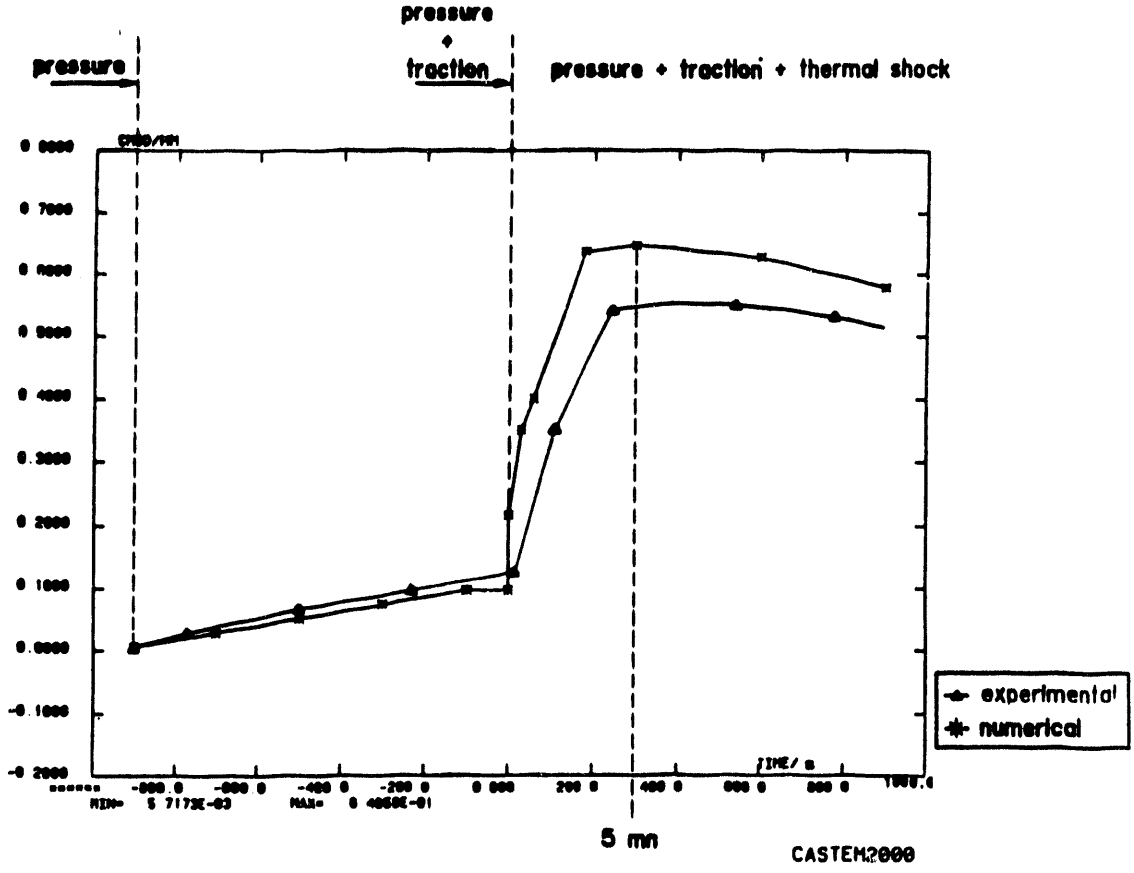

Figure 9 : Crack mouth opening displacement vs.time for the new NKS4 analysis

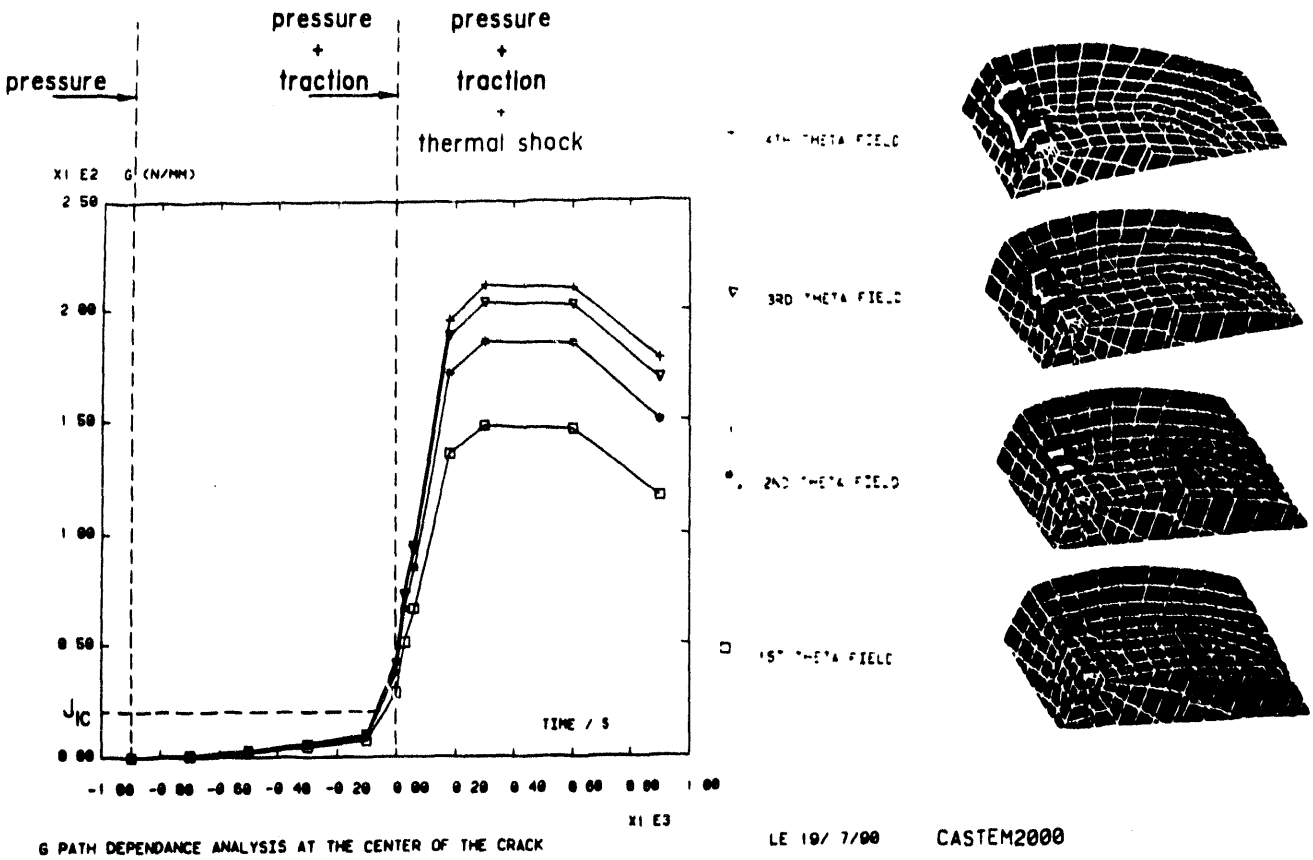

Figure 10 : Energy release rate at the deepest point for the new NKS4 analysis

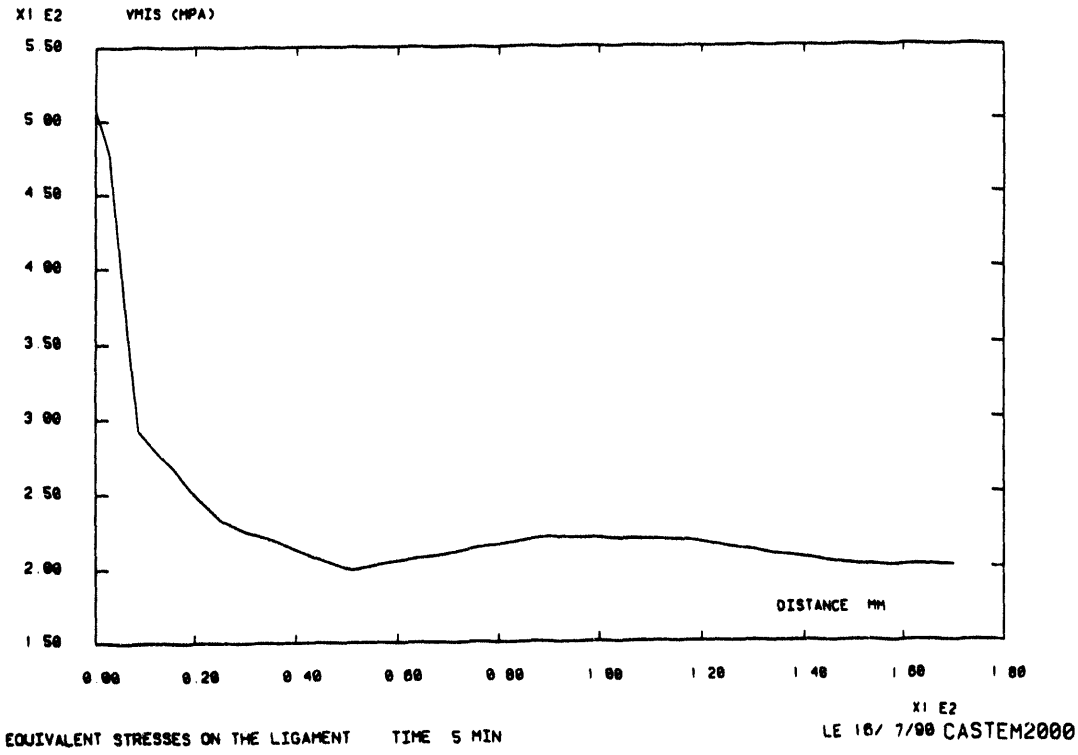

Figure 11 : Equivalent stress in the ligament for the new NKS4 analysis

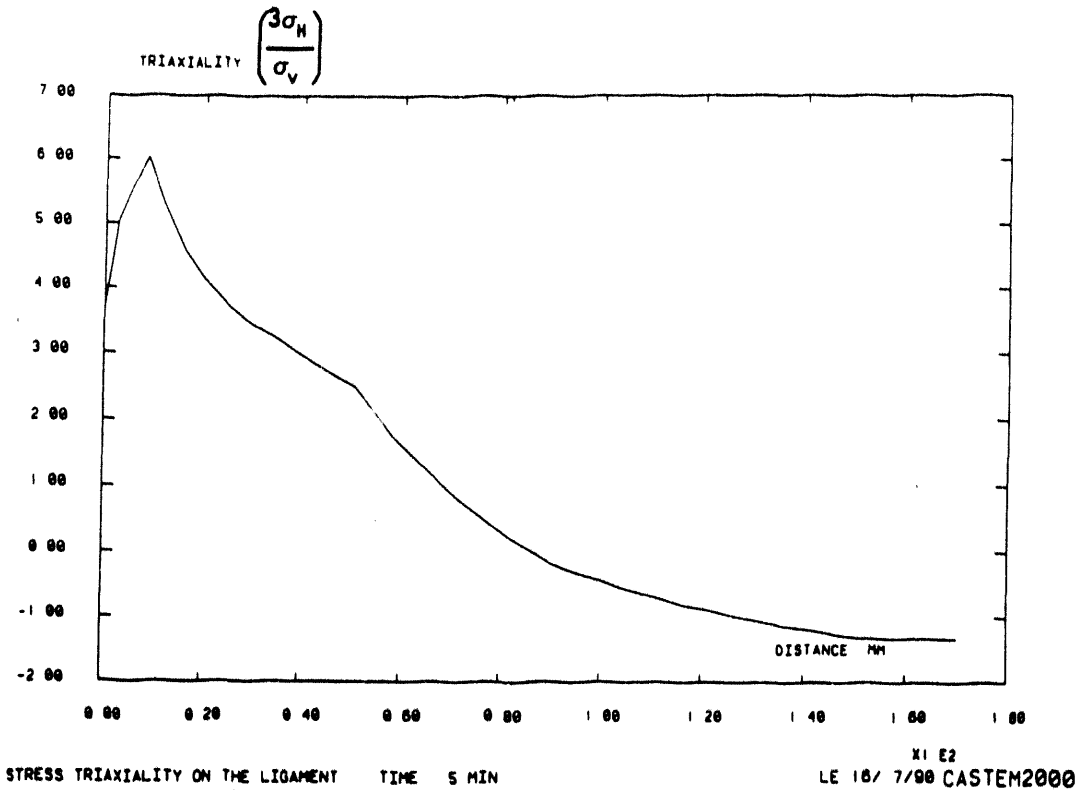

Figure 12 : Stress triaxiality in the ligament for the new NKS4 analysis

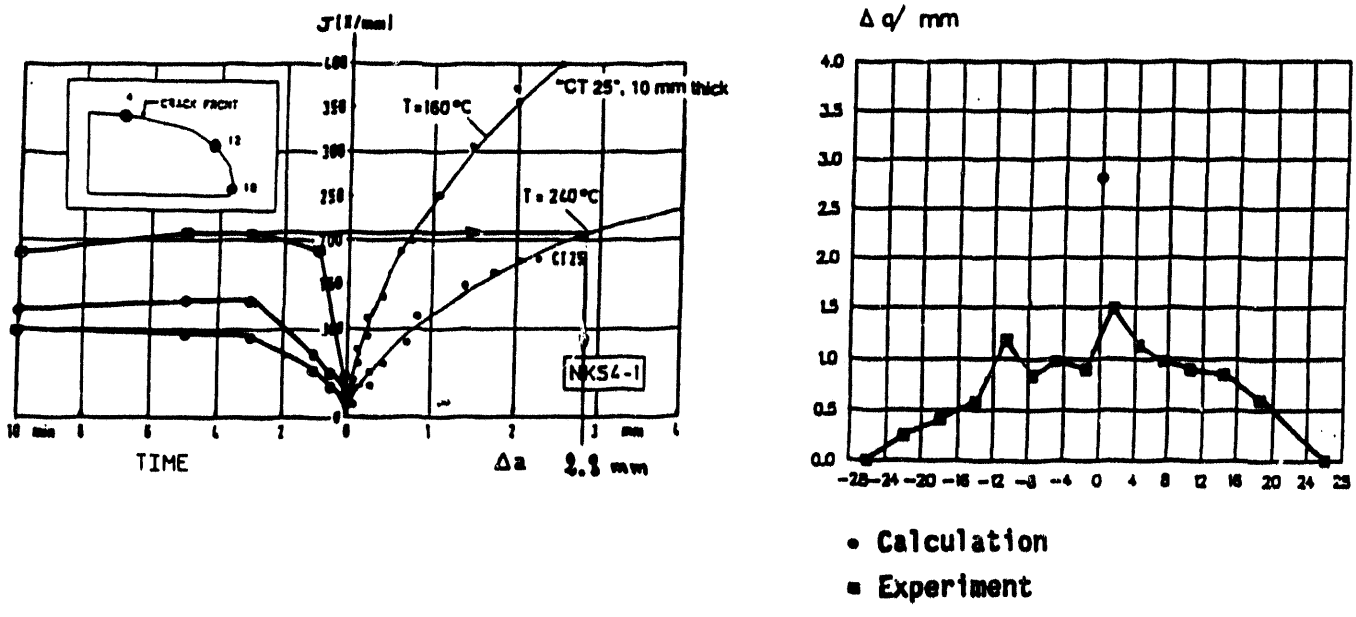

Figure 13 : Crack growth assessment at the deepest point for the new NKS4 analysis

EPFM Verification by a Large Scale Test

by

Prof. H. Okamura[*1], Prof. G. Yagawa[*1], Mr. T. Hidaka[*2], Dr. Y. Urabe[*3], Mr. M. Sato[*2] and Mr. M. Iida[*4]

*1 Faculty of Engineering, University of Tokyo, 7-3-1, Hongo, Bunkyo-ku, Tokyo, 113, Japan

*2 Japan Power Engineering and Inspection Corporation, 1-5-11, Akasaka, Minato-ku, Tokyo, 107, Japan

*3 Takasago R & D Center, Mitsubishi Heavy Industries, Ltd., 2-1-1, Shinhama, Arai-cho, Takasago City, Hyogo Pref., 676, Japan

*4 Kobe Shipyard and Machinery Works, Mitsubishi Heavy Industries, Ltd., 1-1, Wadasaki-cho, Hyogo-ku, Kobe City 652, Japan

Abstract

Step B test was carried out as one of the EPFM study in Japanese PTS integrity research project. In step B test bending load was applied to the large flat specimen with thermal shock. Tensile load was kept constant during the test. Estimated stable crack growth at the deepest point of the crack was 3 times larger than the experimental value in the previous analysis. In order to diminish the difference between them from the point of FEM modeling, more precise FEM mesh was introduced. According to the new analysis, the difference considerably decreased.

That is, stable crack growth evaluation was improved by adopting precise FEM model near the crack tip and the difference was almost same order as that in the NKS4-1 test analysis by MPA.

1. Introduction

Reactor pressure vessels (RPVs) used for Japanese PWR plants have lower copper contents and preliminary research showed that no PTS concern existed on Japanese RPVs during their design service lives. However, it is required to get public acceptance about the integrity by analyses and experiments and it is very useful to establish an analytical method and a database for life extension of Japanese RPVs. Japanese PTS integrity study was carried out from FY 1983 to FY 1991 as a national project by Japan Power Engineering and Inspection Corporation (JAPEIC) under the contract with Ministry of International Trade and Industry (MITI) in corporation with LWR utilities and vendors.

This project is composed of model tests and fracture mechanics tests which include PTS transient study. Model tests are planned to investigate crack behaviors under PTS conditions, using flat plate specimens with an actual vessel thickness.

According to preliminary integrity analyses for PTS conditions, the following test items were selected.

(1) PTS preliminary test
   * Verification of fracture mechanics analytical method and our test methodology by brittle crack initiation test

(2) Step A test
   (a) A-1 test
      * Verification of no crack initiation under PTS events at the end of design service life (It corresponds to the neutron fluence of 6×10^{19}n/cm^2 at the inner surface of the typical PWR pressure vessel.)
   (b) A-2 test
      * Verification of no crack initiation under PTS events at the extended service life (It corresponds to the neutron fluence of 1×10^{20}n/cm^2 at the inner surface of the typical PWR pressure vessel.)
   (c) A-3 test
      * Investigation of crack depth margin for crack initiation (2 times of crack depth margin for A-1 test was demonstrated.)

(3) Step B test
   * Investigation of crack behavior in the upper shelf region and elastic plastic fracture mechanics (EPFM) method

(4) Step C test
   * Investigation of crack arrest behavior by using of fracture toughness gradient material

(5) WPS test
   * Investigation of warm prestressing (WPS) effect

Some of the above test results have been published elsewhere [1], [2], [3], [4].

Our main concern is to verify no brittle crack initiation under PTS events at the end and some extended design lives and it has been verified by the Step A test series. However, still we have an interest on crack behavior in the upper shelf region from the viewpoints of reactor vessel integrity under level A and B conditions and general fracture mechanics assessment for heavy section steel components.

There are some investigations on applicability of EPFM for RPV integrity in the upper shelf region [5], [6], [7]. However, still more experimental data and analyses are needed to verify and demonstrate the usefulness of EPFM. So, Step B test was carried out in order to investigate fundamental crack behavior in the upper shelf region. We have already published test data and analytical result using a new developed schematic EPFM method in Reference [3]. Its conclusion is that the stable crack growth of the Step B test is conservatively estimated using the J resistance curves obtained by 1TCT specimens.

However, the estimated crack growth is almost three times larger than the experimental value. This big difference may be caused by finite element mesh, triaxiality and scatter of fracture toughness. It is very difficult to discuss these three factors at the same time. So, in this paper Step B test is reanalyzed using finer finite element than in the previous analysis and influence of the FEM breakdown on the estimation of stable crack growth is discussed.

2. Material Characterization

An A533B cl.1 type steel with low toughness and high strength was specially produced by controlling the chemical compositions and heat treatments. Chemical compositions and heat treatments are shown in Table 1.

Tensile tests, Charpy tests, drop weight tests and fracture toughness tests were carried out at room temperature to 300°C. Fracture toughness data in the upper shelf region were obtained by 1TCT specimens according to ASTM E813-81. Table 2 shows typical material properties for the test material. Obtained J resistance curves at 200°C, 250°C and 300°C are shown in Fig.1. Lower bound of K_{IC} vs. temperature curve in the transition region is expressed in Eq.(1).

$$K_{IC} = 20.2 + 129.9\exp\{0.0161(T-138)\} \quad (1)$$

where

K_{IC} : fracture toughness $\left[MPa\sqrt{m}\right]$
T : evaluation temperature [°C].

Table 1 Chemical compositions and heat treatments

(wt. %)

C	Si	Mn	P	S	Ni	Mo
0.24	0.39	1.53	0.030	0.002	0.56	0.60

Quenching	970-985°C × 6 hr 50 min	Water Cooling
Tempering	545-555°C × 6 hr 35 min	Air Cooling

Table 2 Mechanical properties of the test material

Tensile Properties			Charpy Value						Drop Weight Test	
σ_y (MPa)	σ_u (MPa)	El (%)	*1 vTr30 (°C)	*2 vTr50 (°C)	*3 vTr35 mils (°C)	*4 vTrs (°C)	*5 USE (J)	TCV-33 (°C)	TNDT (°C)	RTNDT (°C)
777	943	19.4	95	130	151	109	101	139	70	139

*1 30ft-lb (41 J) transition temperature
*2 50ft-lb (68 J) transition temperature
*3 35mils (0.9mm) transition temperature
*4 50% shear transition temperature
*5 Upper shelf energy

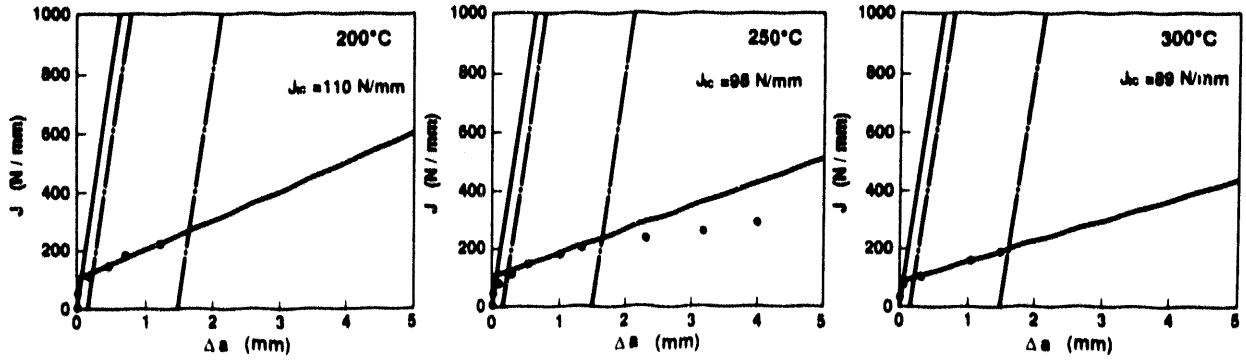

Fig.1 J_R curves of the low toughness A533B cl.1 steel

3. Experiment and Its Results

3.1 Experimental Facility

Fig.2 shows the experimental facility which consists of a tensile and bending load test rig, a coolant storage tank, a refrigerator, a coolant pump, a steam line, piping and equipments for welding and instrumentation of specimens.

Maximum capacities of tensile and bending loads are 19.62MN and 4.90MN, respectively. Coolant is water or ethyleneglycol and temperature can be controlled from about 90°C to 0°C by using the steam line or the refrigerator.

A test specimen is settled between two pin joints of the test rig. The joints have ball bearings and the specimen is simply supported even under the tensile loading in engineering sense.

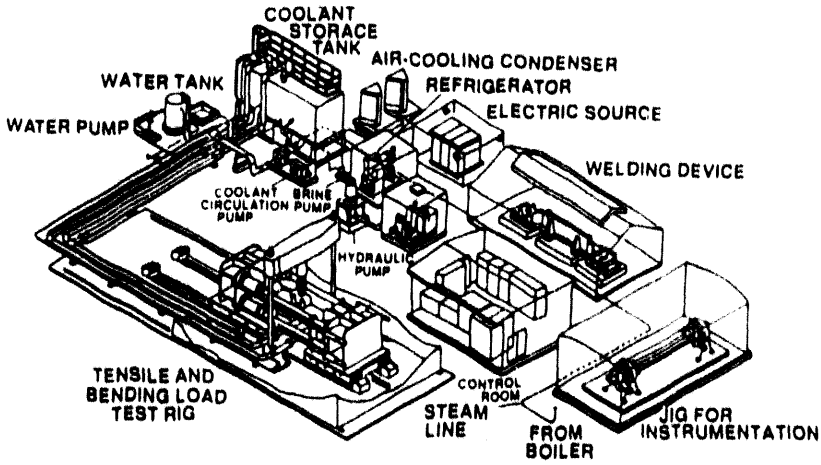

Fig.2 Experimental facility for the model test

3.2 Test Specimen

A schematic drawing of the test specimen is shown in Fig.3. The specimen is 170mm in thickness, 750mm in width and 6900mm in whole length. An initial crack was prepared at the center of the specimen surface by electric discharge machining and cyclic four-point bending load.

Initial crack depth by non-destructive inspection was 20.1mm. Thermocouples and strain gages were installed and the cooled surface was sprayed with a kind of coating material. A coolant channel was settled in order to cool the lower surface with the initial crack and the whole specimen was wrapped in insulation.

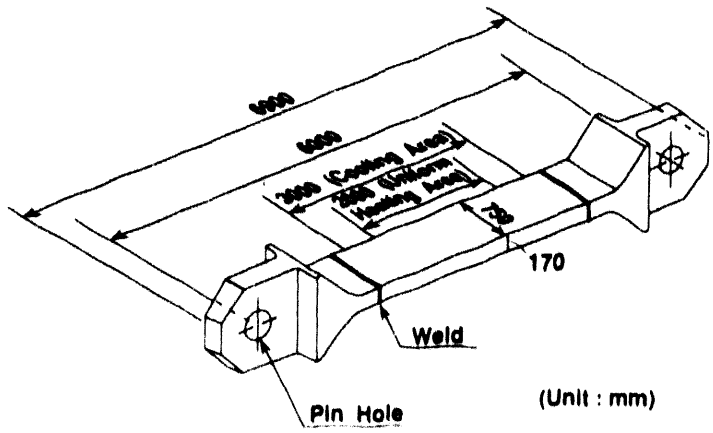

Fig.3 Detail of a large scale flat plate specimen

3.3 Test Procedures and Results

The test specimen was settled between two pin hole joints of the test rig and maintained at a temperature about 322°C prior to the test. A tensile load of 17.87MN was applied and kept constant during the test. Bending load was applied with thermal shock loading simultaneously. Coolant was water and initial temperature was 91°C. Bending load was automatically controlled according to the intended loading program by the previous analysis in order to generate stable crack growth.

Electronic potential output to check the crack initiation suddenly changed at 93 sec. and it suggests that ductile crack initiation took place at that time.

Solid lines in Fig.4 are temperature distributions through the thickness at the cross section of 200mm away from the center of the specimen. At 140 sec. after the start of thermal shock, bending load reached a load of 3.13MN and 10 sec. later the bending load was gradually decreased by manual control. Bending load was completely unloaded at 200 sec. and tensile load also completely unloaded at 315 sec.. The above-mentioned loading history during the test is shown in Fig.5.

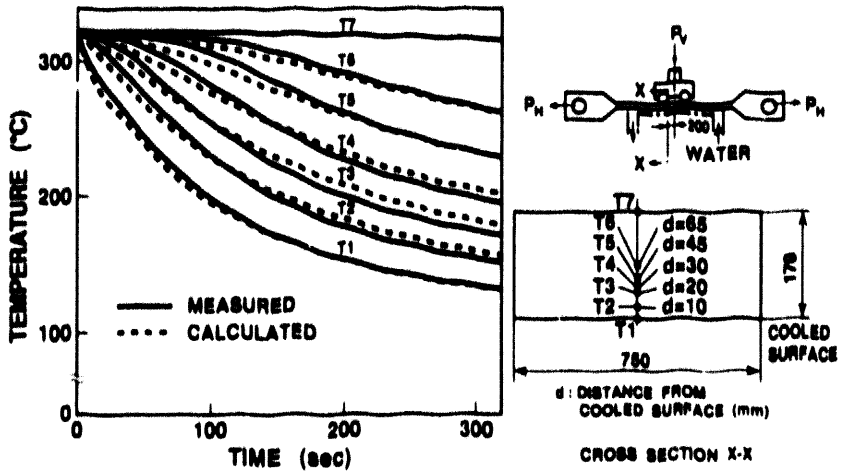

Fig.4 Time history of temperature distribution

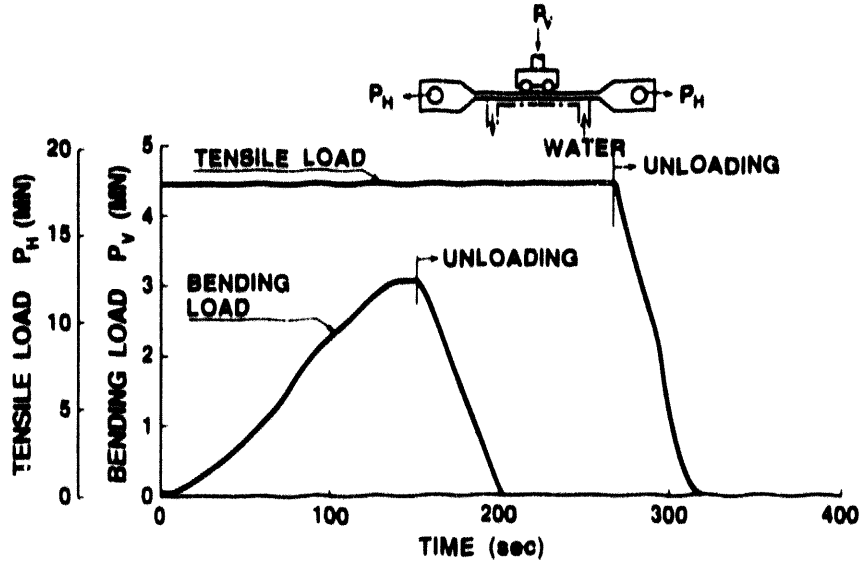

Fig.5 Time history of tensile load and bending load

A solid line in Fig.6 is a measured value of the deflection at the center of the specimen. A strain gage output at the cooled surface is shown in Fig.7 by a solid line. The location of the strain gage is also shown in the same figure.

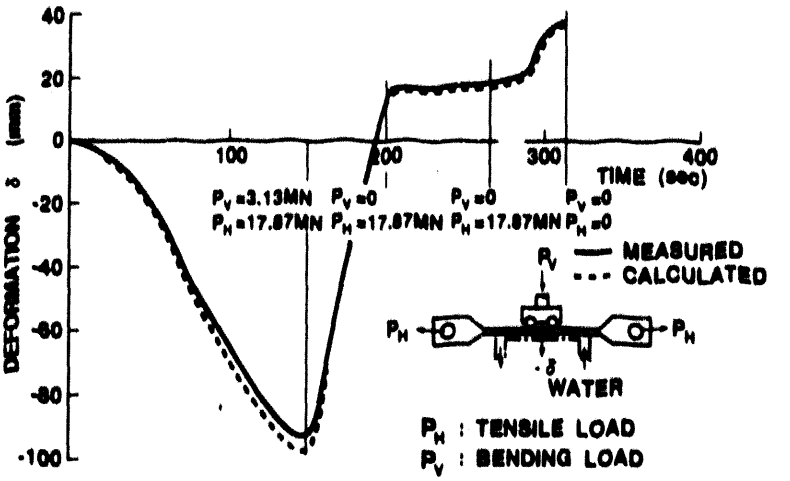

Fig.6 Time history of deformation at the center of the specimen

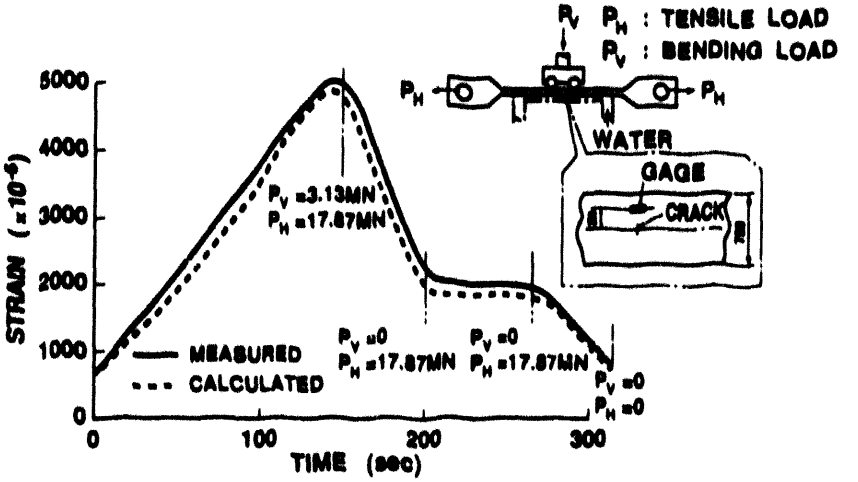

Fig.7 Time history of a strain gage

3.4 Fracture Surface

After the test, in order to distinguish the stable crack growth during the test from the enforced fracture surface, cyclic bending load was applied. After generating fatigue

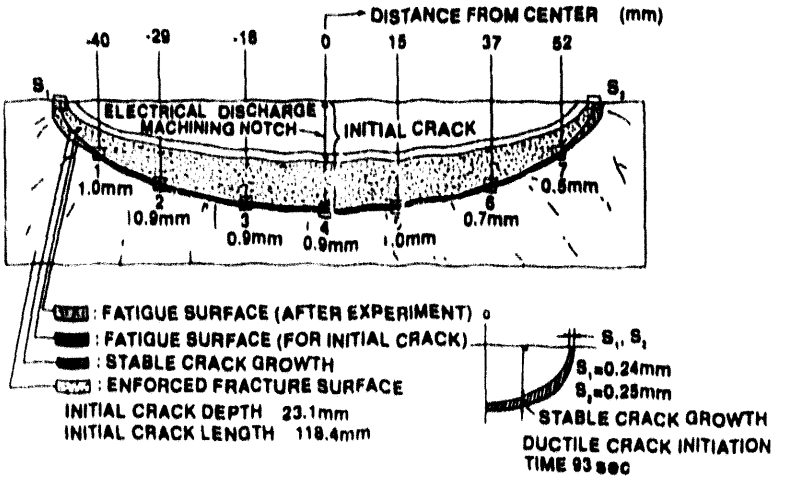

Fig.8 Initial crack and stable crack growth (schematic drawing of the fracture surface)

crack growth the specimen was broken at −34°C. A schematic drawing of the fracture surface is shown in Fig.8. Measured initial crack was 118.4mm in length and 23.1mm in depth and these values agreed well with the above-mentioned non-destructive inspection results. The maximum stable crack growth was 0.9mm to 1.0mm and it took place at the deepest point of the crack or near by. The stable crack growths at the crack edges were 0.24mm and 0.25mm, respectively.

4. Analysis

Fig.9 shows the typical three-dimensional finite element model used for the new analyses. According to the symmetry, one fourth of the specimen is modelled. A three-dimensional 20-node brick element of MARC program was used. In the new finite element model, element number and node number are 1114 and 5103, respectively. Crack front is divided by twelve. The minimum node length near the crack is 0.5mm and is almost 22% of that of the previous finite element mesh size.

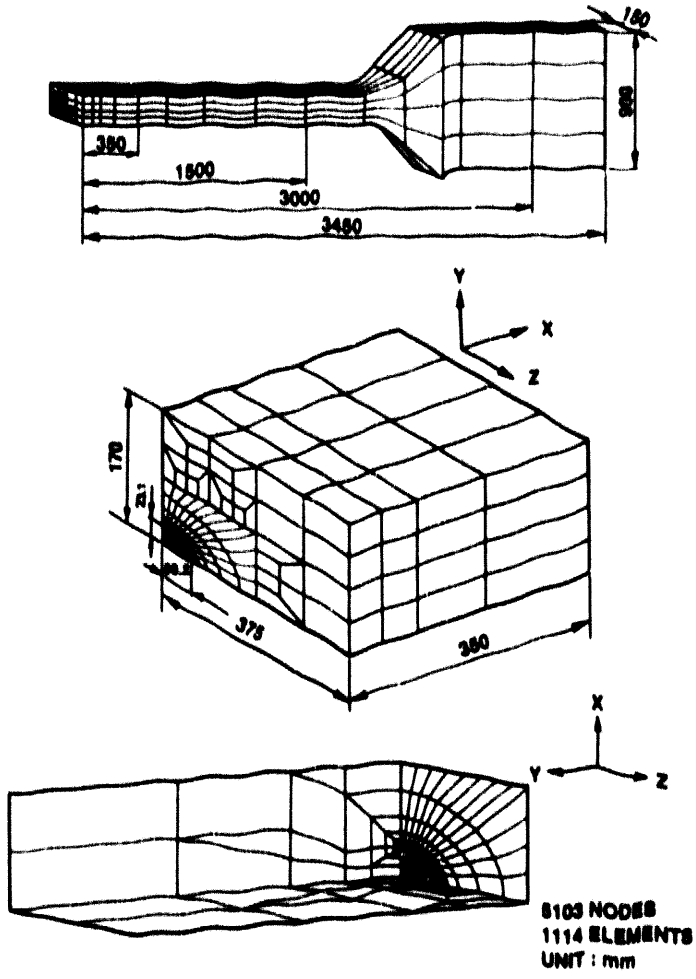

Fig.9 Finite element breakdown of the test specimen with an initial crack

Fig.10 shows the history of the measured heat transfer coefficient on the cooled surface. As the first step, temperature distribution during the test was calculated using the heat transfer coefficient.

Initial temperature of the specimen is 322°C and a coolant temperature of 91°C is kept constant during the test. Boundary conditions for the analysis are shown in Fig.11. Material properties used for the analysis are shown in Table 3.

Calculated temperature distribution is shown in Fig.4 by dotted lines. Again calculated values agree well with the measured values.

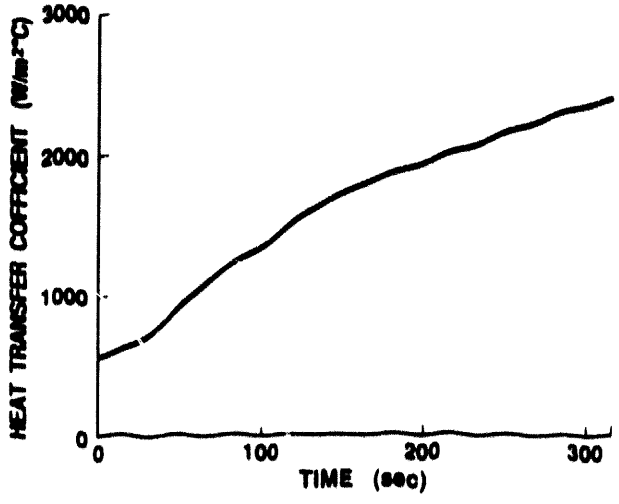

Fig.10 Time history of heat transfer coefficient

As the second step, thermo-elasto-plastic stress analysis was carried out. Same finite element model as for the temperature analysis was used. Boundary conditions for the analysis are shown in Fig.12.

Calculated temperature distribution in Fig.4 and loading condition in Fig.5 were used for the analysis. Material properties for the analysis are shown in Table 4 and Table 5.

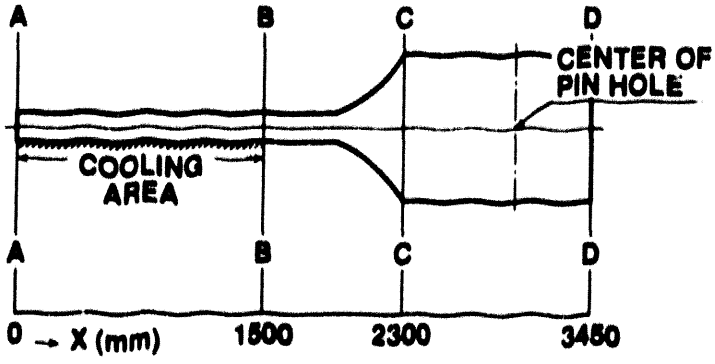

- INITIAL TEMPERATURE OF TEST SPECIMEN
  SECTION A-B 322°C
  SECTION B-C LINEARLY DECREASED FROM 320°C TO 50°C
  SECTION C-D 50°C
- COOLANT TEMPERATURE 91°C
  HATCHED AREA IS COOLED.
- OTHER PARTS OF THE SPECIMEN ARE INSULATED.

Fig.11 Boundary conditions of the thermal load

ONE FOURTH OF THE SPECIMEN IS MODELED

P_H = 17.87 MN

TIME HISTORY OF P_V IS GIVEN IN FIG. 5

Fig.12 Boundary conditions of mechanical loads

Table 3 Material properties for temperature analysis

thermal conductivity λ [W/m°C]	specific heat capacity C_p [KJ/kg°C]	density ρ [kg/m^3]
39.54	0.502	7850

Table 4 Young's modulus and coefficient of thermal expansion

TEMPERATURE (°C)	YOUNG'S MODULUS (MPa)	COEFFICIENT OF THERMAL EXPANSION $(1/°C)\times10^{-5}$
30	205900	1.106
75	204000	1.178
100	203000	1.210
150	200000	1.280
200	197100	1.351
250	194200	1.420
300	190300	1.484

Table 5 True stress-true strain relation

30°C PLASTIC STRAIN	STRESS (MPa)	75°C PLASTIC STRAIN	STRESS (MPa)	100°C PLASTIC STRAIN	STRESS (MPa)
0.0	677	0.0	647	0.0	628
0.0025	780	0.0025	760	0.0025	755
0.005	809	0.005	789	0.005	780
0.01	843	0.01	814	0.01	809
0.02	885	0.02	863	0.02	858
0.04	929	0.04	932	0.04	922
0.06	981	0.06	971	0.06	961
0.10	1035	0.10	1013	0.10	1000

150°C PLASTIC STRAIN	STRESS (MPa)	200°C PLASTIC STRAIN	STRESS (MPa)	250°C PLASTIC STRAIN	STRESS (MPa)
0.0	598	0.0	598	0.0	598
0.0025	740	0.0025	736	0.0025	736
0.005	770	0.005	760	0.005	780
0.01	794	0.01	792	0.01	814
0.02	843	0.02	836	0.02	858
0.04	902	0.04	897	0.04	912
0.06	941	0.06	939	0.06	951
0.10	983	0.10	990	0.10	990

300°C PLASTIC STRAIN	STRESS (MPa)
0.0	579
0.0025	726
0.005	765
0.01	814
0.02	873
0.04	929
0.06	964
0.10	990

A dotted line in Fig.6 is the calculated deformation at the center of the specimen and it agrees well with the measured value. Also shown by a dotted line in Fig.7 is a calculated axial direction strain. The calculated strain agrees well with the measured value but the value is slightly smaller than that in the previous analysis.

As the third step, using the thermo-elasto-plastic stress analysis results, fracture mechanics analysis was carried out. $\hat{J}$-integral developed by Aoki and others [8] was used as a fracture mechanics parameter. Paths to calculate $\hat{J}$-integrals around the initial crack tip were taken as shown in Fig.13. Fig.14 shows $\hat{J}$-integrals at the deepest point of the crack in three paths. Even in case of unloading, $\hat{J}$-integral still has good path independency as expected and path independency is improved than that in the previous analysis.

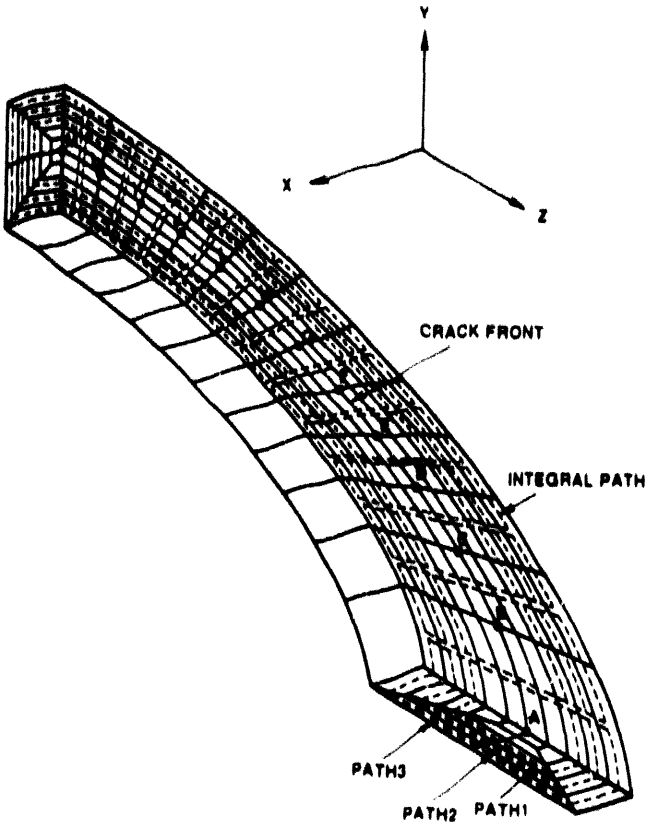

Fig.13 Paths for $\hat{J}$-integral analyses

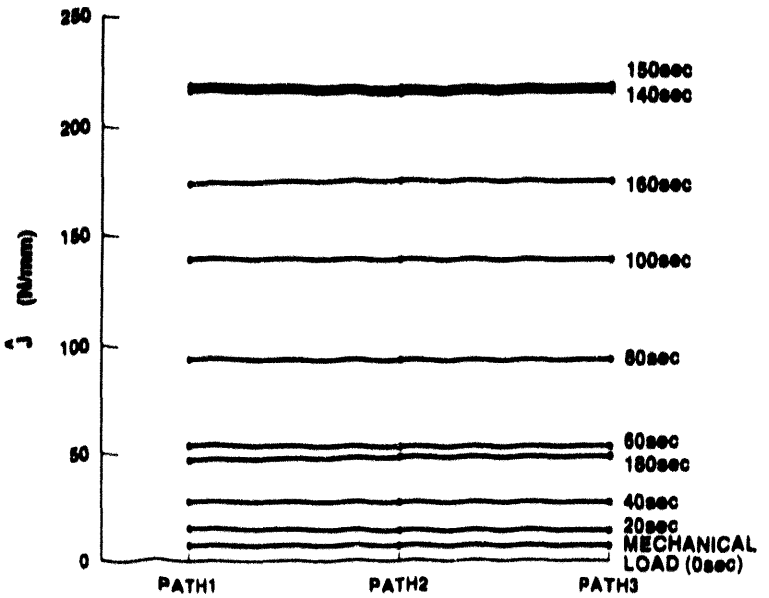

Fig.14 Path independency of $\hat{J}$-integral at the deepest point of the initial crack

Fig.15 shows the mean value of $\hat{J}$-integrals at three paths on the crack front. As shown in Fig.15, $\hat{J}$-integral is slightly oscillating but the configuration of $\hat{J}$-integral distribution on the crack front is reasonable.

From these analyses, it is judged that FEM mesh size near the crack tip is sufficiently small for stable crack growth analysis.

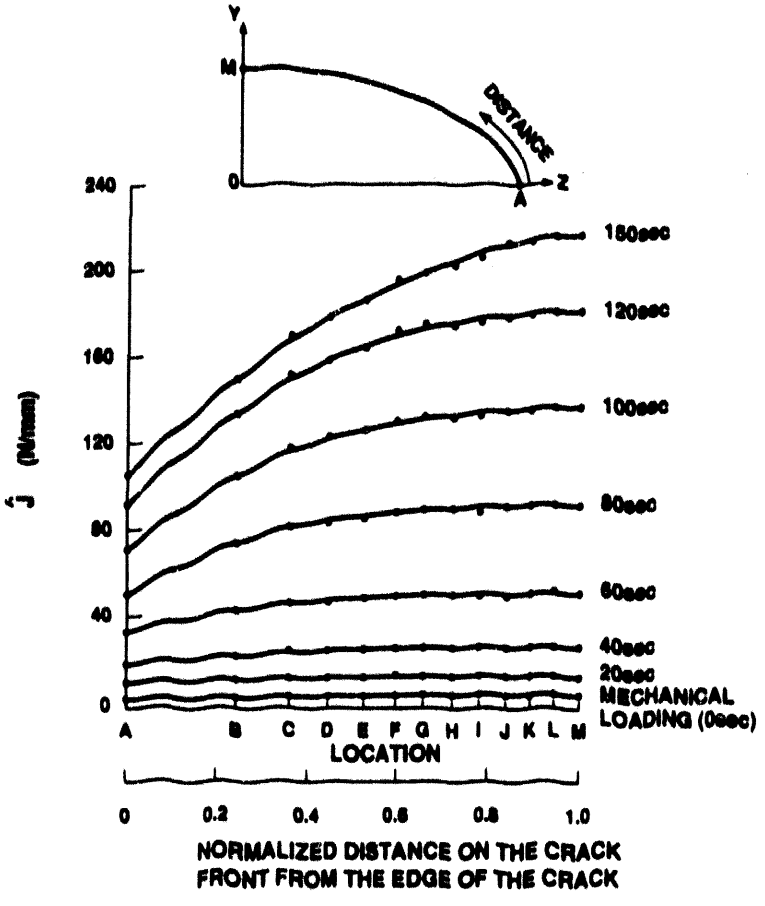

Fig.15 $\hat{J}$-integral distribution on the crack front

Unfortunately we have no fracture toughness data corresponding to the crack edge temperature available. So only ductile crack growth at the deepest point of the crack was analyzed. According to the previously developed schematic evaluation method of ductile crack behavior under mechanical and thermal loading, stable crack growth of the Step B test specimen was again evaluated. The concept of the method is mentioned in Reference [3].

Crack shapes for the stationary crack model is shown in Fig.16. It is assumed that the crack grows at the same ratio in the normal direction of the crack front as the measured stable crack growth from the initial crack.

Same finite element models as that of the initial crack were used for the analyses to reduce numerical errors. Loading condition in Fig.5 was used. Fracture toughness curves at upper shelf temperatures were prepared using Fig.1.

Average J-integrals of three paths at the deepest points for initial crack and postulated crack configurations in Fig.16 are plotted as $\hat{J}$-integral vs. crack tip temperature curves. Obtained results are shown in Fig.17. From this figure stable crack growth is estimated to be 2.0mm at the deepest point of the crack, while measured crack growth is approximately 0.9mm. On the while, in the previous analysis, the estimated stable crack growth is 2.5mm [3]. It means that stable crack growth analysis is considerably sensitive to the crack tip mesh size and overestimation of the ductile crack growth reduces by adopting finer mesh near the crack tip. In NKS4-1 analysis of one of the PTS experiments in MPA, the experimental crack growth at the deepest point of the crack is almost 50%

of the estimated value and that in average near the deepest point of the crack is about 40% of the experimental one. [5] These data have good coincidence with difference between the experimental crack and estimated value in Step B test.

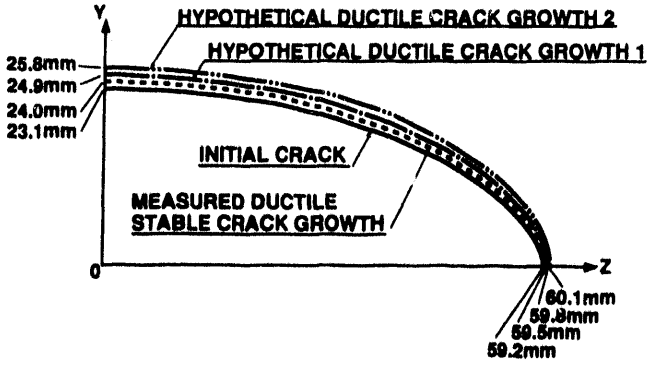

Fig.16 Models of crack shapes for stable crack growth analysis

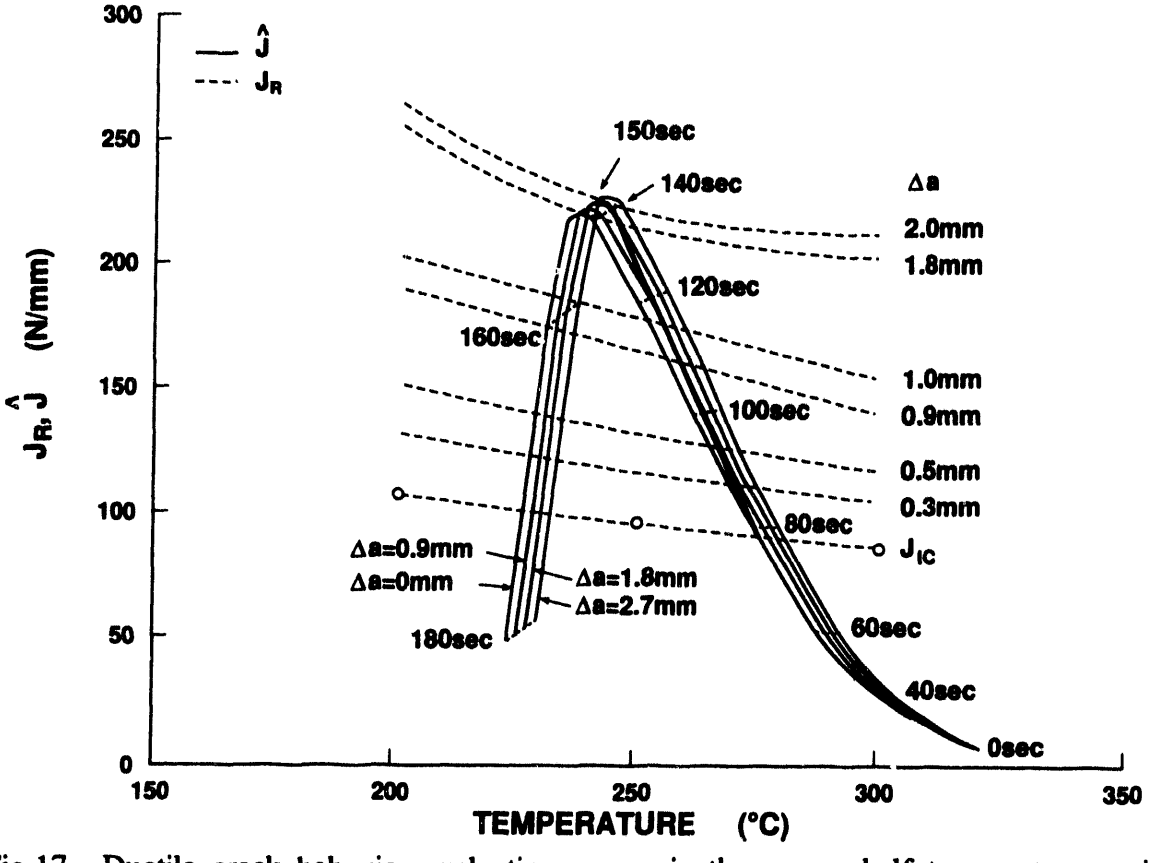

Fig.17 Ductile crack behavior evaluation curves in the upper shelf temperature region and predicted crack growth at the deepest point of the crack

5. Conclusion

As one of the test items of Japanese PTS project, a fundamental study of EPFM using a flat plate specimen was carried out. A semielliptical surface crack was prepared by fatigue and tensile and bending loads were applied with simultaneous thermal shock in the upper shelf region. According to the post test fracture surface observation, the stable crack growth at the deepest point was 0.9mm.

In the previous analysis estimated stable crack growth at the deepest point of the crack was 2.5mm and it was considerably larger than the experimental value. This big

difference may be caused by finite element mesh, triaxiality and scatter of fracture toughness. In this paper, from the point of mesh refinement, reanalysis was carried out. In the new analysis, the minimum node length is 0.5mm near the crack tip and is almost 22% of that of the previous mesh size. Material properties for the analysis are exactly same as those of the previous analysis.

According to the new analysis, path independency is improved and estimated ductile crack growth becomes 2.0mm. That is, overestimation of the ductile crack growth reduces by adopting finer mesh near the crack tip. The difference between the experimental crack growth and the estimated value is in the same order as that in the NKS4-1 test analysis by MPA. To reduce overestimation still more, it is necessary to investigate the effects of the other two factors.

Acknowledgement

The authors would like to express their hearty thanks to members of the PTS research committee [Chairman: Prof. Mishima, Y.] for their useful advice and discussion.

References

[1] H. Okamura, G. Yagawa, T. Kawakami, T. Funada, "PTS Integrity Study in Japan," Transaction of the 9th International Conference on Structural Mechanics in Reactor Technology, G, 1987, pp.395-400.

[2] H. Okamura, G. Yagawa, T. Hidaka, Y. Urabe, "PTS Integrity Study in Japan (Part 2)," Transaction of the 10th International Conference on Structural Mechanics in Reactor Technology, F, 1989, pp.7-12.

[3] H. Okamura, G. Yagawa, T. Kawakami, Y. Urabe, "Ductile Crack Growth under a PTS Event," 16. MPA-Seminar, 1989, pp.45.1-45.19.

[4] H. Okamura, G. Yagawa, T. Kawakami, J. Sano, Y. Urabe, M. Sato, "A Crack Arrest Test Using a Toughness Gradient Steel," ASME Pressure Vessel and Piping Conference, June 23-27, 1991, San Diego, CA., PVP-Vol.213, pp.47-52.

[5] A. Sauter, T. Nguyen-Huy, U. Weber, H. Huber, "Behavior of Surface Flaws under Thermal-Mechanical Loading," Nucl. Engrg. Des. 119, 1990, pp.287-305.

[6] R. H. Bryan, B. R. Bass, S. E. Bolt, J. W. Bryson, W. R. Corwin, J. G. Merkle, R. H. Nanstad, G. C. Robinson, "Pressurized-Thermal-Shock Test of 6-in.-Thick Pressure Vessels. PTSE-2: Investigation of Low Tearing Resistance and Warm Prestressing," NUREG-CR-4888, 1987.

[7] D. J. Lacey and R. E. Leckenby, Determination of Upper Shelf Fracture Resistance in the Spinning Cylinder Test Facility, "Transactions of the 10th International Conference on Structural Mechanics in Reactor Technology," F, 1989, pp.1-6.

[8] S. Aoki, K. Kishimoto, M. Sakata, "Energy Release Rate in Elastic-Plastic Fracture Problem," Transaction of the ASME Journal of Applied Mechanics, 48, 1981, pp.825-829.

ANALYSIS OF JAPANESE PRESSURIZED THERMAL SHOCK EXPERIMENT (STEP B TEST)

Charles W. Schwartz

Department of Civil Engineering
University of Maryland
College Park, MD 20742

INTRODUCTION

Two different 3D fracture analyses of the Japanese Step B pressurized thermal shock experiment have already been performed by Okamura *et al* [1,2]. As it is unlikely that a third 3D analysis will produce results significantly different from these prior studies, the focus of the present investigation is on the reasonableness of 2D analytical approximations to the Step B experiment. The evolution of crack tip constraint during the PTS transient is also evaluated using the 2D analytical approximation.

Details of the experimental configuration, mechanical and thermal loadings, material properties, and measured results are described by Okamura *et al.* [1,2] and will not be repeated in detail here.

ANALYSIS MODEL

The initial flaw in the Step B experiment was a semi-elliptical surface crack having a half-width of approximately 59.2 mm and a maximum depth of approximately 23.1 mm. In the present investigation, this surface crack is modeled as an equivalent 2D through-thickness crack. However, the crack depth is adjusted in the 2D case because the crack driving forces (K or J) for a through-thickness crack will be greater than those for an equivalently deep surface crack under the same applied mechanical loading (tension and/or bending). The adjusted 2D crack depth is determined by equating the analytical LEFM K values for a through-thickness crack and the deepest point for the actual surface crack (analytical solutions tabulated in [3,4]). For the Step B test, this procedure yields an adjusted 2D crack length of 15.5 mm, a 33% reduction from the actual 23.1 mm maximum depth of the 3D surface crack. The computed adjustment is essentially the same for both tension and bending analytical solutions.

Note that for PTS loadings, such as those in the Step B test, the 2D crack depth adjustment outlined above can only be justified as a very crude approximation. The adjusted crack tip location will now be shifted relative to the PTS temperature fields, and thus the thermal stresses at the adjusted 2D crack tip will be greater from those at the deepest point in the 3D surface crack. This should translate into higher crack driving forces in the 2D analysis, even though the crack depth adjustment procedure is based upon equating the crack driving forces caused by the mechanical loads.

The finite element mesh used to analyze the cracked specimen is shown in Figure 1. Due to the symmetry of the problem geometry and loading about the crack plane, only one-half of the specimen was modeled in the 2D analyses. The mesh contains 3141 nodes and 978 8-node reduced integration (2x2) plane strain isoparametric elements. The full specimen geometry including the loading pins and tabs is modeled in the analysis (Figure 1a). Eight fans of elements converge on the crack tip (Figure 1b) and the 17 initially coincident crack tip nodes are free to deform independently during the analysis. The discretization is sufficiently fine to permit adequate resolution of the stresses and strains within distances on the order of 5 crack tip opening displacements (CTODs) from the crack tip; the radial dimension of the elements at the crack tip is on the order of 0.05 mm (r/a on the order of 0.003). All finite element calculations were performed using the ABAQUS analysis code [5], and all pre- and post-processing was performed using PATRAN [6].

The material stress-strain behavior was modeled using a Ramberg-Osgood deformation plasticity constitutive model:

$$\varepsilon/\varepsilon_o = \sigma/\sigma_o + \alpha(\sigma/\sigma_o)^n \qquad (1)$$

Very little significant temperature dependence was found in the reported stress-strain properties for the Step B plate material over a temperature range of 30 to 300°C. The material constants were therefore assumed independent of temperature, with the actual values weighted toward the measured values at the higher temperature levels (appropriate for the Step B test conditions). The values used in the analysis for the material constants are as follows:

$$E = 192{,}250 \text{ MPa} \qquad (2a)$$
$$\nu = 0.3 \qquad (2b)$$
$$\sigma_o = \sigma_y = 588.5 \text{ MPa} \qquad (2c)$$
$$\alpha = 0.065 \qquad (2d)$$
$$n = 11.9 \qquad (2e)$$

The thermal expansion coefficient was set at 1.452×10^{-5}/°C. As shown in Figure 2, the agreement between the Ramberg-Osgood uniaxial stress-strain curve and the measured stress-strain curves at the various temperatures is quite good.

The measured PTS transient was used as the loading conditions for the analysis. A transient thermal analysis was not performed; instead, the measured temperature profile history was used as input to the analysis. The measured temperature profiles were assumed to apply uniformly over the central heated/cooled section of the specimen and to vary linearly between the edge of this section and the remote loading tabs. The present study analyzed the PTS transient up to the peak response of the specimen only.

A large displacement, small strain formulation was employed in all of the finite element calculations. As will be shown later, the large displacement part of the formulation is required to model adequately the P-δ bending moments in the specimen in the deflected condition (P = applied axial tension force; δ = centerline deflection). The small strain part of the formulation was adopted in part to eliminate convergence problems often encountered in large

strain analyses of highly refined meshes loaded over large ranges. More importantly, the small strain formulation was adopted because it provides an adequate model for the phenomena being studied in this analysis. Although the small strain formulation cannot correctly model the stress and strain fields and crack tip blunting in the very high strain region immediately surrounding the crack tip, the stress and strain fields predicted by small and large strain formulations are similar at distances greater than approximately 3 CTODs from the crack tip under plane strain conditions [7,8]. This is sufficient for the purposes of the present study.

Because the ABAQUS code does not include a large displacement small strain analysis option, an iterative approximate method for including the P-δ effect was employed for the calculations. During the initial analysis, no P-δ effects are included. The computed δ values from this analysis are then used to compute the first estimate of the P-δ moments, the applied bending loads are reduced accordingly, and the problem is reanalyzed. The process is repeated, with the computed δ at each cycle used to update the P-δ moments and applied bending load corrections at the next cycle, until convergence.

J-integral values were computed using the virtual crack extension algorithm as implemented in ABAQUS [5,9]. Ten contours were evaluated to establish path independence of the J-integral value. Variation of the computed J values among the contours was negligible.

RESULTS

The measured response parameters in the Step B experiment (in addition to temperatures) consisted of the centerline deflection, the extreme fiber axial tension strain (at a location midway between the surface crack and the edge of the plate), and the crack advance (from post-experiment examination of the fracture surface). Comparisons between the predicted and measured centerline deflections are summarized in Figure 3. The measured values (solid line), predicted values by Okamura *et al.* [2] from a 3D elastoplastic finite element analysis (dotted line), and predicted values from the present 2D analysis (solid circles) are all in very close agreement. Moreover, these values are also in very close agreement with results from a 2D analysis of an *uncracked* test specimen (hollow circles in Figure 3). As might be intuitively expected, the presence of a small crack on the surface of a wide (750 mm) and deep (170 mm) plate has little effect on a gross response measure such as centerline deflection.

Also shown in Figure 3 is the effect of the P-δ moments on the predicted response. The centerline deflections obtained from 2D analyses based on small displacement theory--i.e., no P-δ effects included--are shown by triangles in Figure 3. At the peak response, the centerline deflections computed in the small displacement theory analyses are approximately three times larger than those computed in the corresponding large displacement theory analyses (circles in Figure 3) that incorporate the full P-δ effects.

Comparisons between the predicted and measured extreme fiber tension strains are summarized in Figure 4. The 2D results are all from analyses of an *uncracked* test specimen geometry because the through-thickness crack runs across the strain gauge location in the 2D approximation. However, as shown previously in Figure 3 for the centerline deflections, a

gross response measure such as the extreme fiber tension strain at a location remote from the crack is little affected by the presence or absence of the crack. As was the case for centerline deflection, the measured, 3D predicted (Okamura *et al.* [2]), and 2D predicted tension strains are all in very close agreement. The differences between large displacement (circles) and small displacement theory (triangles) analysis assumptions are also again clear in the figure.

J-integral values computed in the analyses are summarized in Figure 5. The peak response of the specimen occurred at approximate 140-150 seconds into the transient. The peak J value computed by Okamura *et al.* [2] from their 3D analysis at the deepest part of the crack was approximately 220 N/mm. The corresponding value computed from the large displacement theory 2D analysis is approximately 310 N/mm, or approximately 40% larger than the 3D value. It is believed that much of this discrepancy is due to the shallower crack depth in the 2D analysis, which places the crack tip in a higher thermal stress region than that at the deepest point of the 3D surface crack.

The computed J values can be combined with the measured J-R curves to estimate the crack advance during the test. The measured J-R data are shown in Figure 6. Only a slight temperature dependence is observed over the three sets of data in the 200-300°C range. The predicted Δa at the deepest part of the surface crack using Okamura *et al.*'s 3D analysis results and the data in Figure 6 is approximately 1.5-2.0 mm (Okamura *et al.*'s own estimate is 2.0 mm). This is 70-120% greater than the actual 0.9 mm of crack advance measured at this location from post-experiment examination of the fracture surface. The predicted Δa from the large displacement theory 2D analysis is approximately 3-5 mm, substantially greater than both the experimentally measured value and Okamura *et al.*'s prediction.

One possible explanation for the discrepancies between the measured and predicted values of crack advance may lie in the different constraint conditions at the crack tip in the Step B configuration vs. the CT specimens used to derive the J-R curves. These differences in constraint can be quantified using the Q-stress approach of O-Dowd and Shih [10,11]:

$$\sigma_{ij}/\sigma_o = (\sigma_{ij}/\sigma_o)_{SSY} + Q(r/(J/\sigma_o))^q \hat{\sigma}_{ij}(\theta) \qquad (3)$$

Equation (3) represents a two-parameter expansion of the *near*-tip elastic-plastic stress fields in a power law hardening material. The first term represents the small scale yielding (SSY) singular fields--e.g., the fields obtained from a boundary layer analysis [12] (alternatively, this can be taken as the HRR analytical fields [10,11]). The second order term represents the difference between the actual stress fields and the SSY (or HRR) reference fields. The second order term, which has the dimensionless parameter Q as its amplitude, captures *all* constraint influences on the in-plane near-tip stress fields. The $\hat{\sigma}_{ij}(\theta)$ functions represent the angular variation of the second order stress fields and are expected to depend also upon the material hardening; the $\hat{\sigma}_{ij}(\theta)$ functions are normalized such that $\hat{\sigma}_{00}$ equals 1 at $\theta = 0$.

The second order fields are extracted by subtracting the SSY solution [12] from the numerical solution for the Step B crack tip stresses. Figure 7 illustrates the crack opening stress fields from the 2D large displacement theory Step B analysis at several times during the PTS transient. Figure 7a shows the total stresses computed from the finite element analysis and the first-order SSY

stresses. Figure 7b depicts the second-order stress fields computed by subtracting the SSY stresses from the total stresses. The crack opening stresses computed from the finite element analyses are similar in functional form to the SSY distributions but are lower in magnitude at all radial distances ahead of the tip. These differences in stress magnitude increase with time during the PTS transient--i.e., with increasing J. This is reflected in the increasingly negative second order stresses in Figure 7b at later times during the transient.

The second-order stress field parameters Q and q in Eq. (3) can be obtained from regression analyses of the form:

$$\ln[(\sigma_{yy}/\sigma_o)-(\sigma_{yy}/\sigma_o)_{SSY}] = \ln(Q) + q \ln[r/(J/\sigma_o)] \qquad (4)$$

The regression for Eq. (4) was estimated over the range $1.5 < r/(J/\sigma_o) < 10$. Additionally, the first three nodal points ahead of the crack tip were excluded from the regressions because of lack of fidelity of the numerical solution in this region. The fit of the computed regressions was very good in all cases.

The evolution of J and Q during the PTS transient up to the peak response as computed using the above approach and the results from the 2D large displacement theory analyses is depicted in Figure 8. Q has a small negative value at the start of the transient, but by the peak has decreased to a value of approximately -1.0, indicating substantial loss of constraint at the crack tip at peak response. Part of this constraint loss is undoubtedly due to the shallow depth of the flaw. Detailed examination of the computed stress fields suggests that additional constraint loss may be associated with the gross yielding of the cooled (cracked) face of the Step B plate at the peak of the response.

Virtually no experimental data exist on the influence of constraint loss on J-R curves for ductile fracture, so it is impossible to evaluate quantitatively the influence of this constraint loss on the analytical predictions for crack advance. Some qualitative indications may be obtained from the influence of constraint on cleavage fracture, however. Data from Theiss and Bryson [13] from cleavage-dominated SENB fracture tests on A533B steel suggest that a reduction of Q from 0 (plane strain conditions) to -1.0 may elevate the effective fracture toughness K_c by approximately 80% (or, alternatively, reduces the effective driving force by a similar amount); in terms of J_c, this increase in effective cleavage fracture toughness is approximately 200%. Re-examination of the J-R data in Figure 6 suggests that if ductile fracture follows these same trends and the ductile fracture resistance is increased by even only a small fraction of the cleavage toughness increase, the crack advance predicted by the 3D and 2D finite element analyses may be well within range of the 0.9 mm measured value.

CONCLUSIONS

The principal conclusions drawn from this study are as follows:

(1) Large displacement P-δ effects are important for this experimental geometry and must be considered in the analyses.

(2) There was excellent agreement between the measured, 3D predicted, and 2D predicted values for the measured specimen response, i.e., the centerline deflection and the extreme fiber tension strain. These excellent predictions of the gross speciment response can be a achieved without even including the presence of the crack.

(3) The predicted values of J from the 2D (large displacement theory) analyses are substantially larger than those computed from the 3D analyses at the deepest part of the crack; much of this discrepancy is believed due to the shallower adjusted crack depth in the 2D analysis, which places the crack tip in a higher thermal stress region.

(4) The predicted values of J from both the 3D and 2D analyses substantially overpredict crack advance when using the J-R data obtained from small scale CT tests.

(5) There is a significant loss of constraint in the Step B specimen at the peak of the PTS transient. This loss of constraint is likely due primarily to the shallowness of the flaw and the gross yielding of the cracked surface of the specimen at the peak of the transient. Although there is virtually no data with which to evaluate quantitatively the effect of this constraint loss on the ductile fracture resistance of the material, intuitively the qualitative effect should be to increase the effective fracture resistance. This in turn may produce a smaller predicted crack advance that is more in agreement with the experimentally measured values.

The results from this study also suggest several recommendations for future large-scale reference experiments:

(1) Adequate instrumentation must be included in the experiment. Particular emphasis should be placed on instrumentation to measure near-crack response, as opposed to gross specimen response. Examples include CMOD gauges, near-crack strain gauges, etc.

(2) From an analyst's perspective, phenomena such as the significant P-δ effect in the Step B experiment needlessly complicate the analysis (and do not necessarily have any counterpart in prototypical RPV scenarios) and should be avoided in the experiment design.

(3) Additional small specimen fracture toughness data are required. Interpretation of the large-scale test predictions and results becomes very uncertain when only limited fracture property characterization data are available. The intermingled influences of inherent variability, temperature dependence, constraint effects, etc. cannot be isolated and interpreted unless sufficient small scale test data exist.

REFERENCES

1. Okamura, H., G. Yagawa, T. Kawakami, and Y. Urabe (1990) "Japanese Pressurized Thermal Shock Experiment (Step B Test)," *CSNI PAG Workshop on Fracture Analyses of Large-Scale International Reference Experiments*, Boston, MA, May.

2. Okamura, H., G. Yagawa, T. Hidaka, Y. Urabe, M. Sato, and M. Iida (1992) "EPFM Verification by a Large Scale Test," *CSNI IAEA Specialists Meeting*, Oak Ridge, TN, October.

3. Barsom, J.M. and Rolfe, S.T. (1987) *Fracture and Fatigue Control in Structures* (2nd ed.), Prentice-Hall, Inc., Englewood Cliffs, NJ.

4. Broek, D. (1982) *Elementary Engineering Fracture Mechanics*, Martinus Nijhoff Publishers, London.

5. *ABAQUS User Manual--Version 4.8.5* (1989), Hibbit, Karlsson, and Sorenson, Inc., Providence, RI.

6. *PATRAN Plus User Manual--Release 2.4* (1989) PDA Engineering, Inc., Costa Mesa, CA.

7. Rice, J.R., and Johnson, M.A. (1970) "The Role of Large Crack Tip Geometry Changes in Plane Strain Fracture," *Inelastic Behavior of Solids* (Kanninen *et al.*, eds.), McGraw-Hill, New York, NY, pp. 641-670.

8. McMeeking, R.M. (1977) "Finite Deformation Analysis of Crack Tip Opening in Elastic-Plastic Materials and Implications for Fracture," *Journal of the Mechanics and Physics of Solids*, Vol. 25, pp. 357-381.

9. Parks, D.M. (1977) "The Virtual Crack Extension Method for Nonlinear Material Behavior," *Computer Methods in Applied Mechanics and Engineering*, Vol. 12, pp. 353-364.

10. O'Dowd, N.P., and Shih, C.F. (1991) "Family of Crack-Tip Fields Characterized by a Triaxiality Parameter: Part I--Structure of Fields," *Journal of the Mechanics and Physics of Solids*.

11. Shih, C.F. and O'Dowd, N.P. (1992) "A Fracture Mechanics Approach Based on a Toughness Locus," *TWI/EWI/IS International Conference on Shallow Crack Fracture Mechanics*, Cambridge, UK, September.

12. Dodds, R.H., Anderson, T.A., and Kirk, M.T. (1991) *International Journal of Fracture*, Vol. 48, pp. 1-22.

13. Theiss, T.J., and Bryson, J.W. (1991) "Influence of Crack Depth on the Fracture Toughness of Reactor Pressure Vessel Steel," *ASTM Symposium on Constraint Effects in Fracture*, Indianapolis, IN, May (in press).

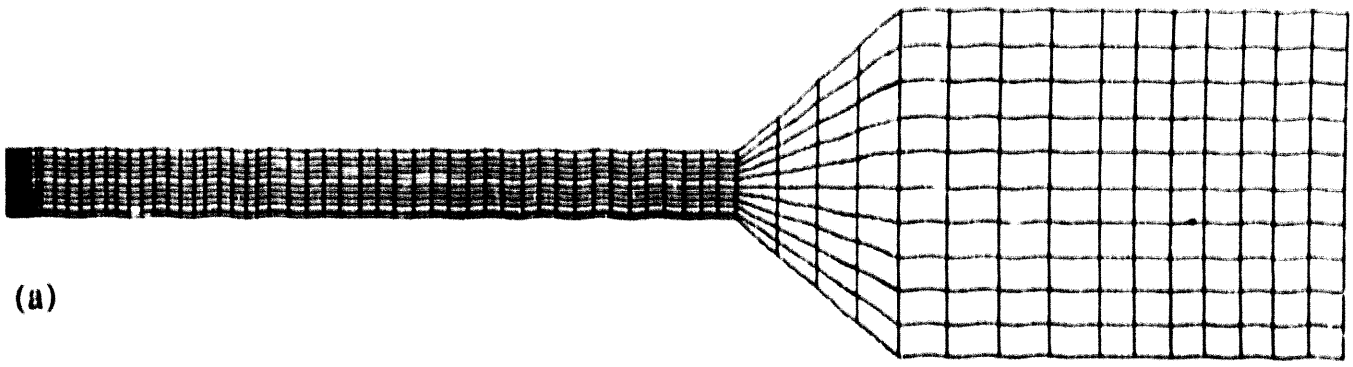

(a)

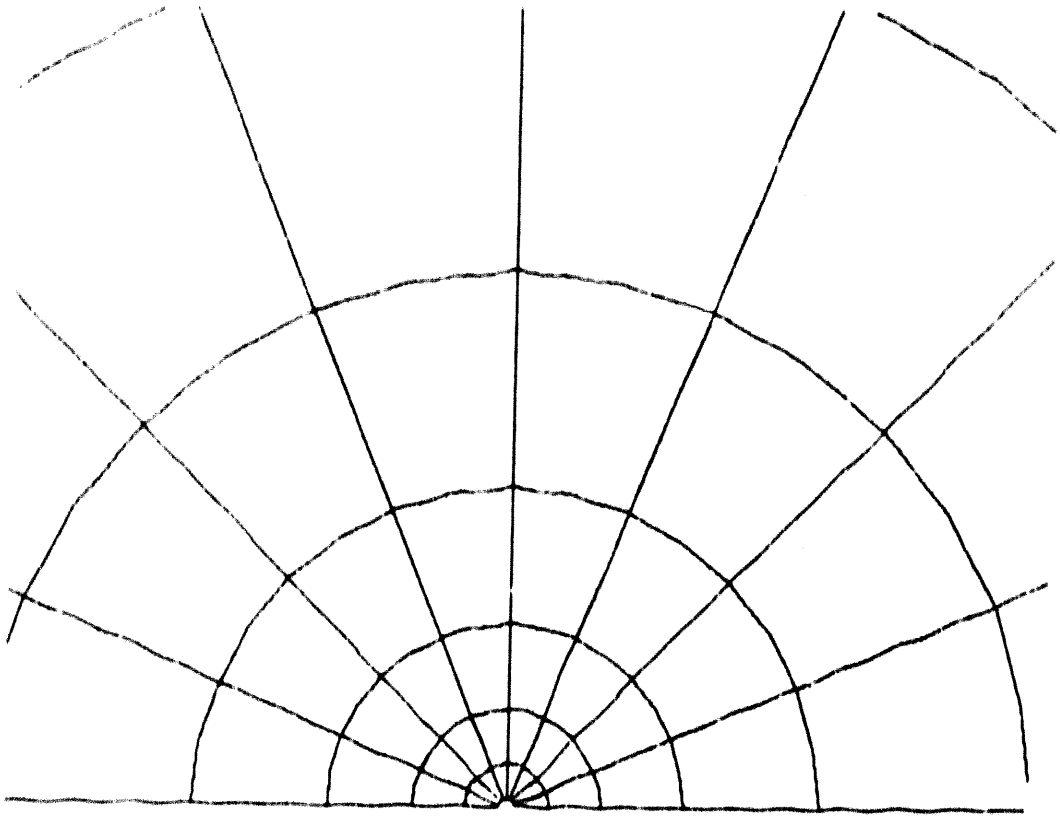

(b)

Figure 1. Finite element mesh for all analyses: (a) overall mesh; (b) detail of the crack-tip region.

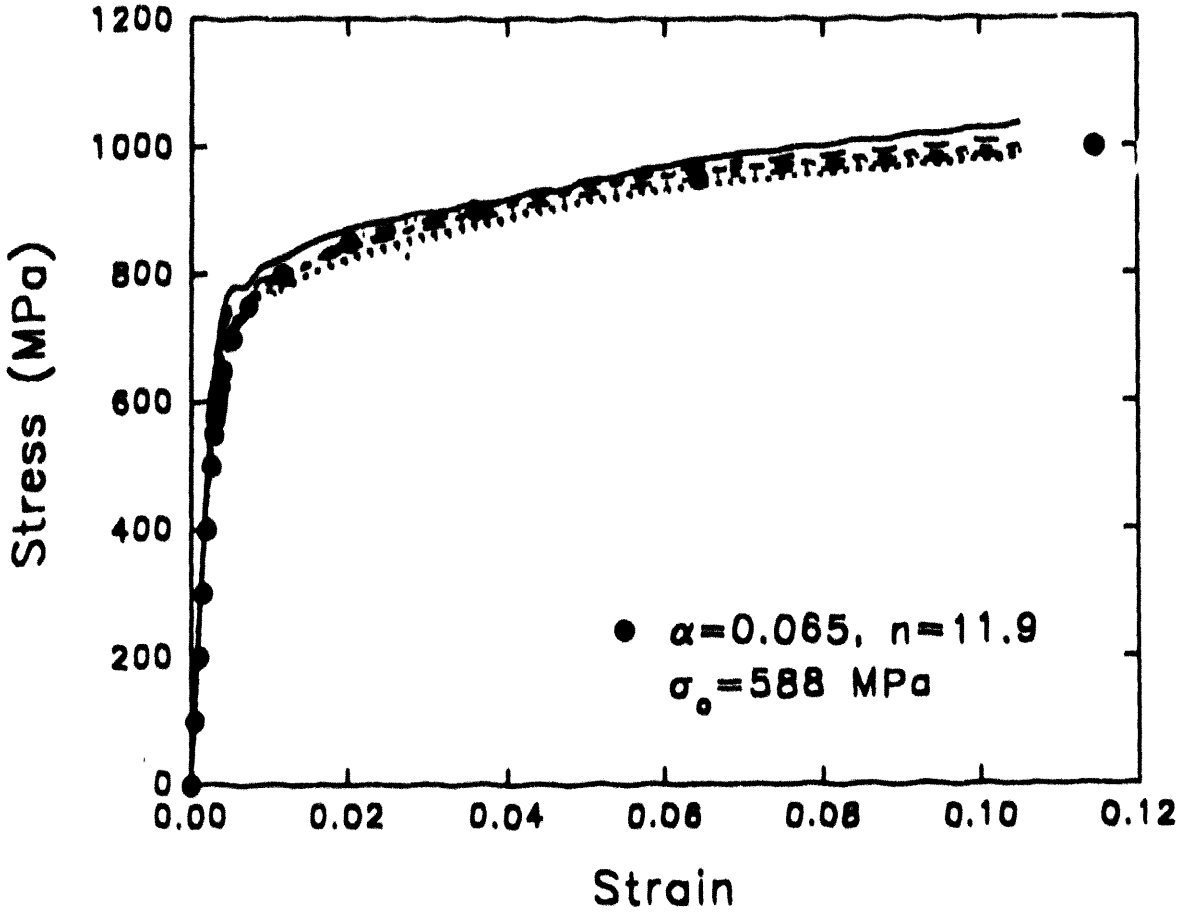

Figure 2. Stress-strain relations for Ramberg-Osgood material and for Step B test material (at various temperatures between 30°C and 300°C).

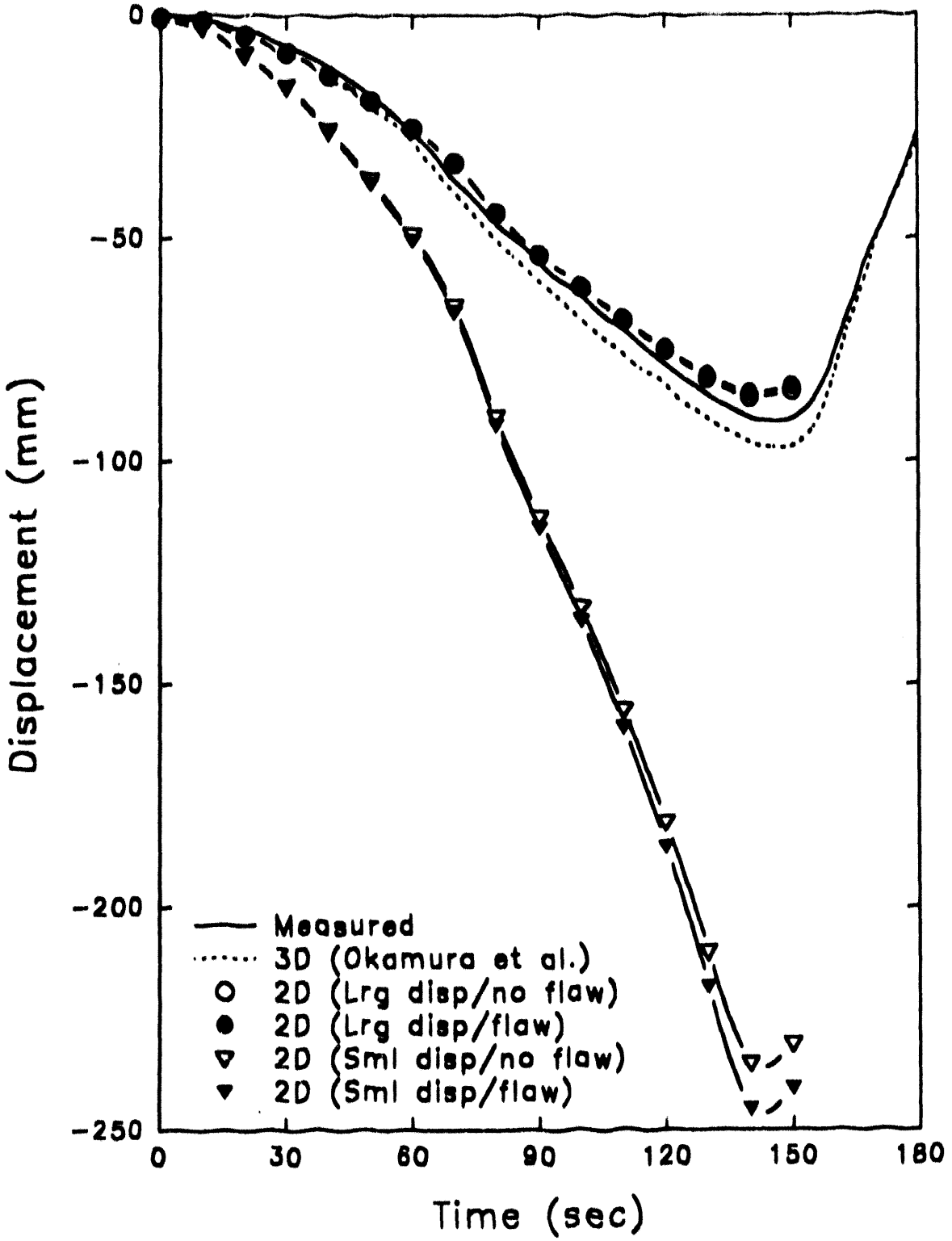

Figure 3. Measured and predicted centerline deflections vs. time for Step B PTS experiment.

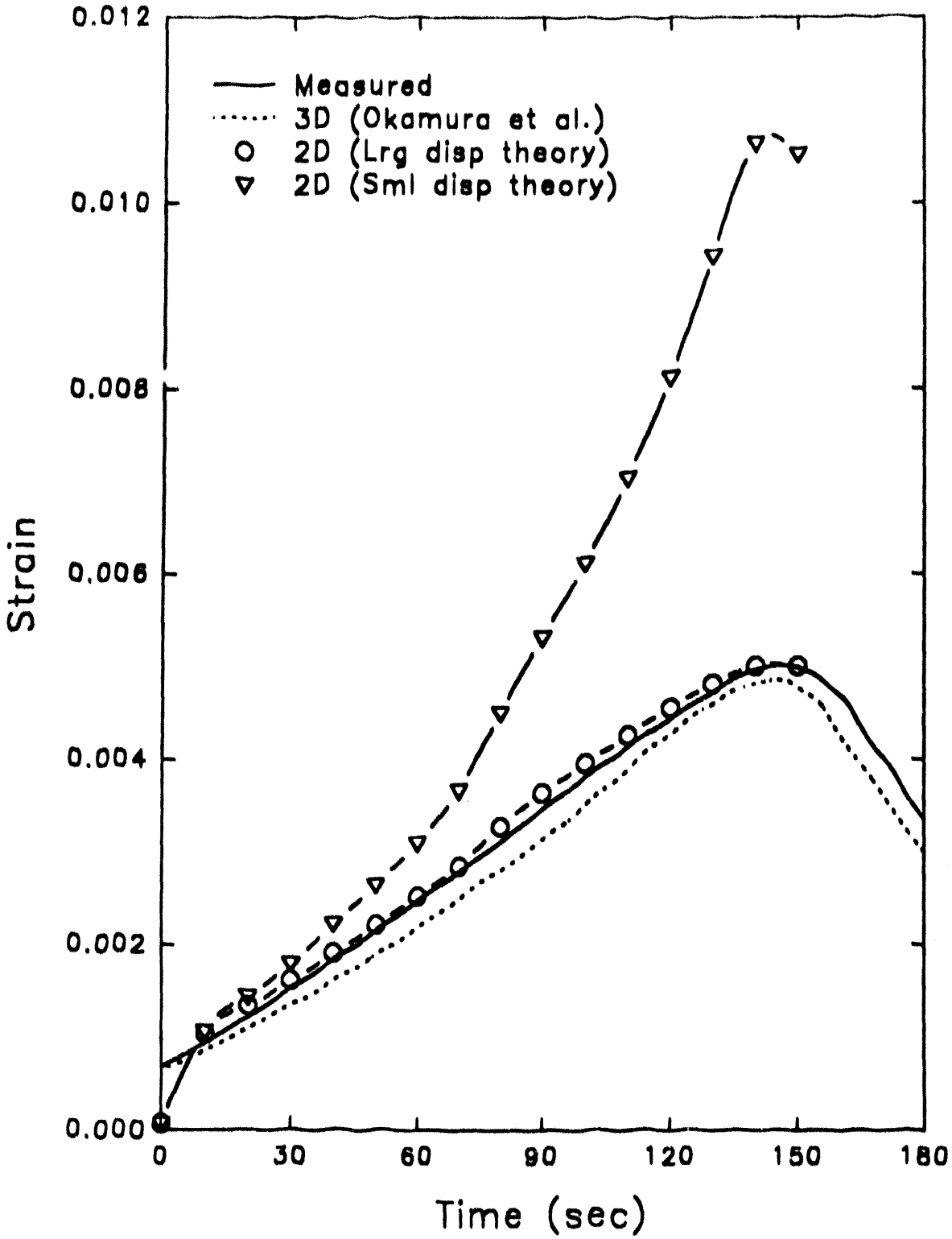

Figure 4. Measured and predicted extreme fiber tension strains vs. time at strain gauge location for Step B PTS experiment.

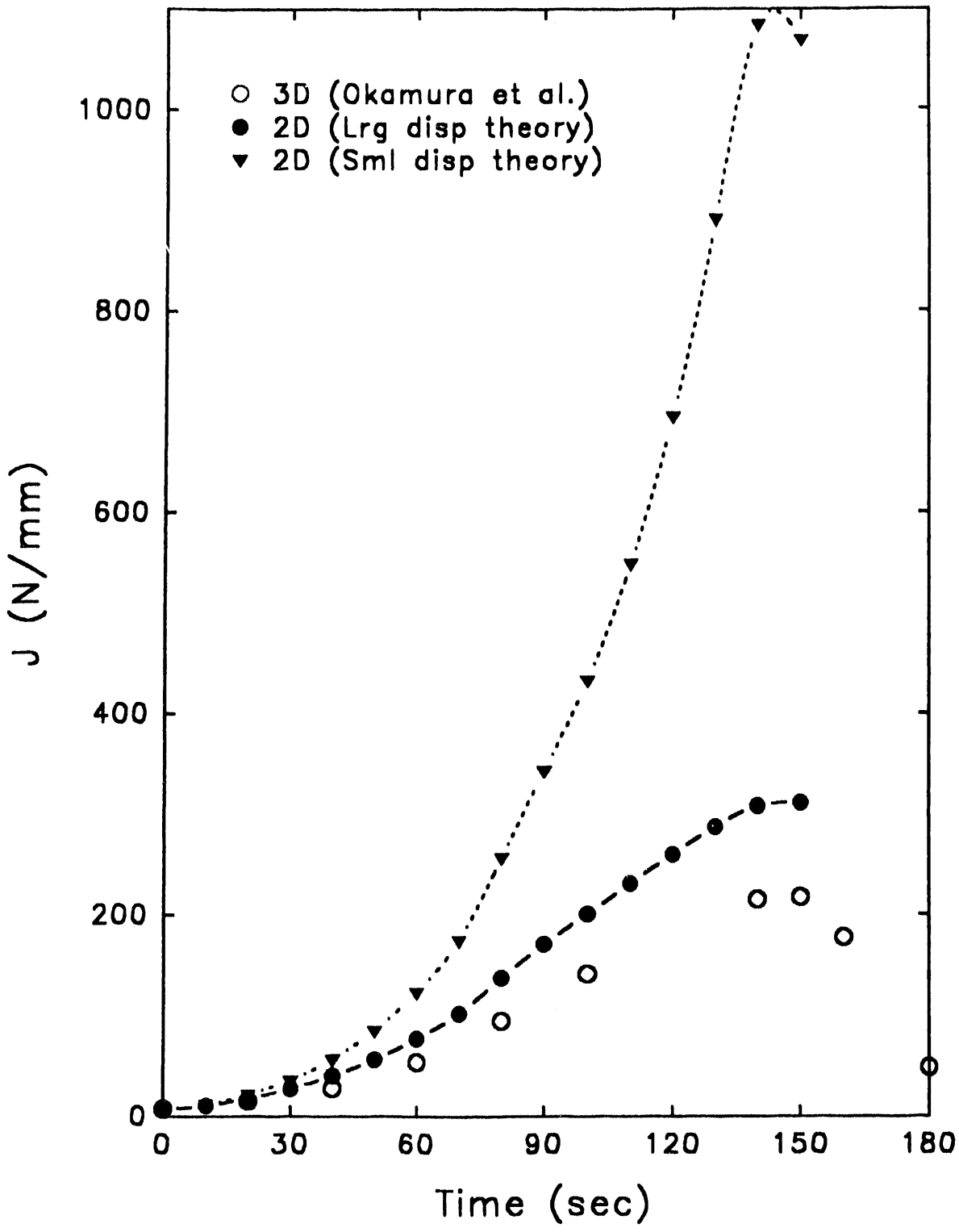

Figure 5. Computed J-integral values vs. time for Step B PTS experiment (up to peak response).

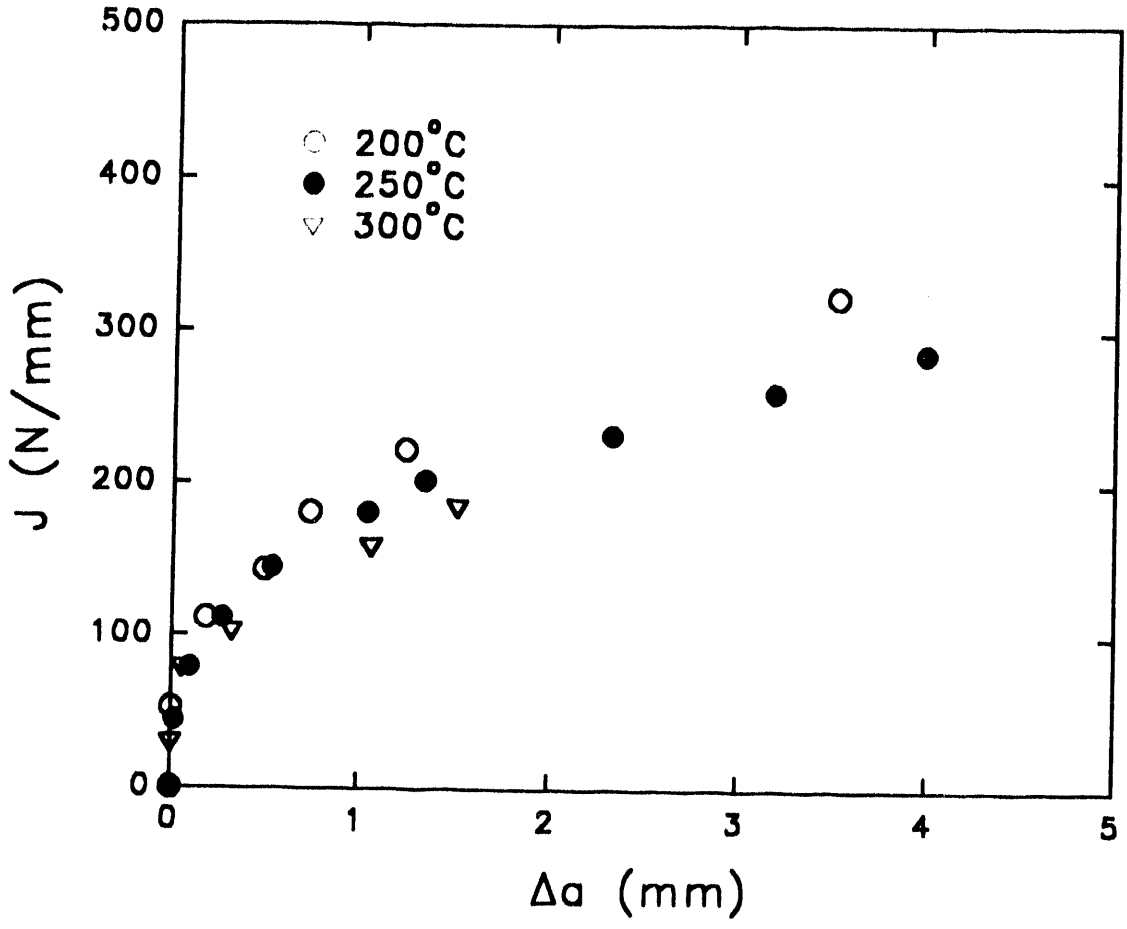

Figure 6. Measured J-R data for Step B test material.

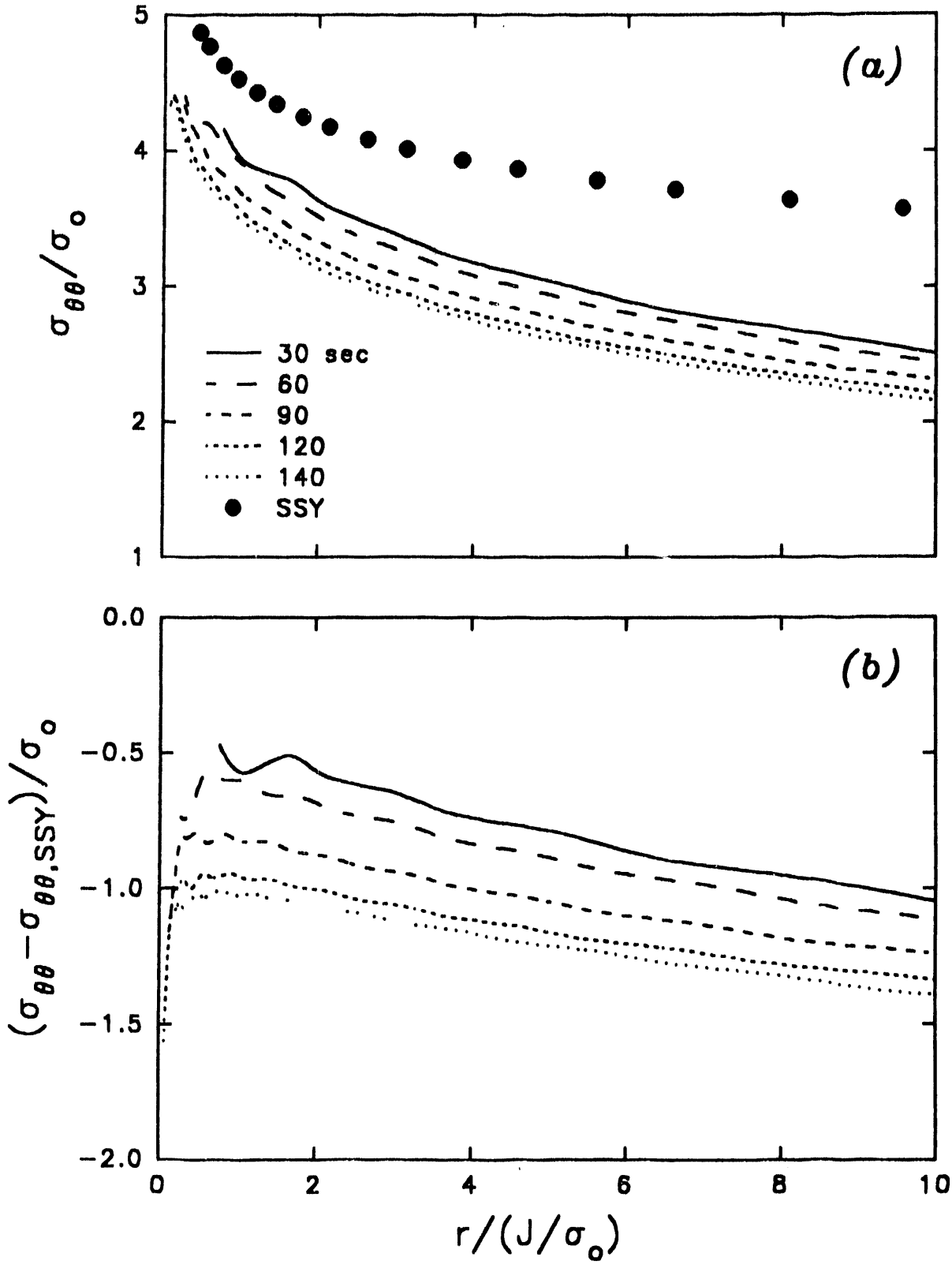

Figure 7. Total and second-order tangential normal stresses (i.e., crack opening stresses) along the crack plane $\theta = 0$ at various times during the Step B PTS transient.

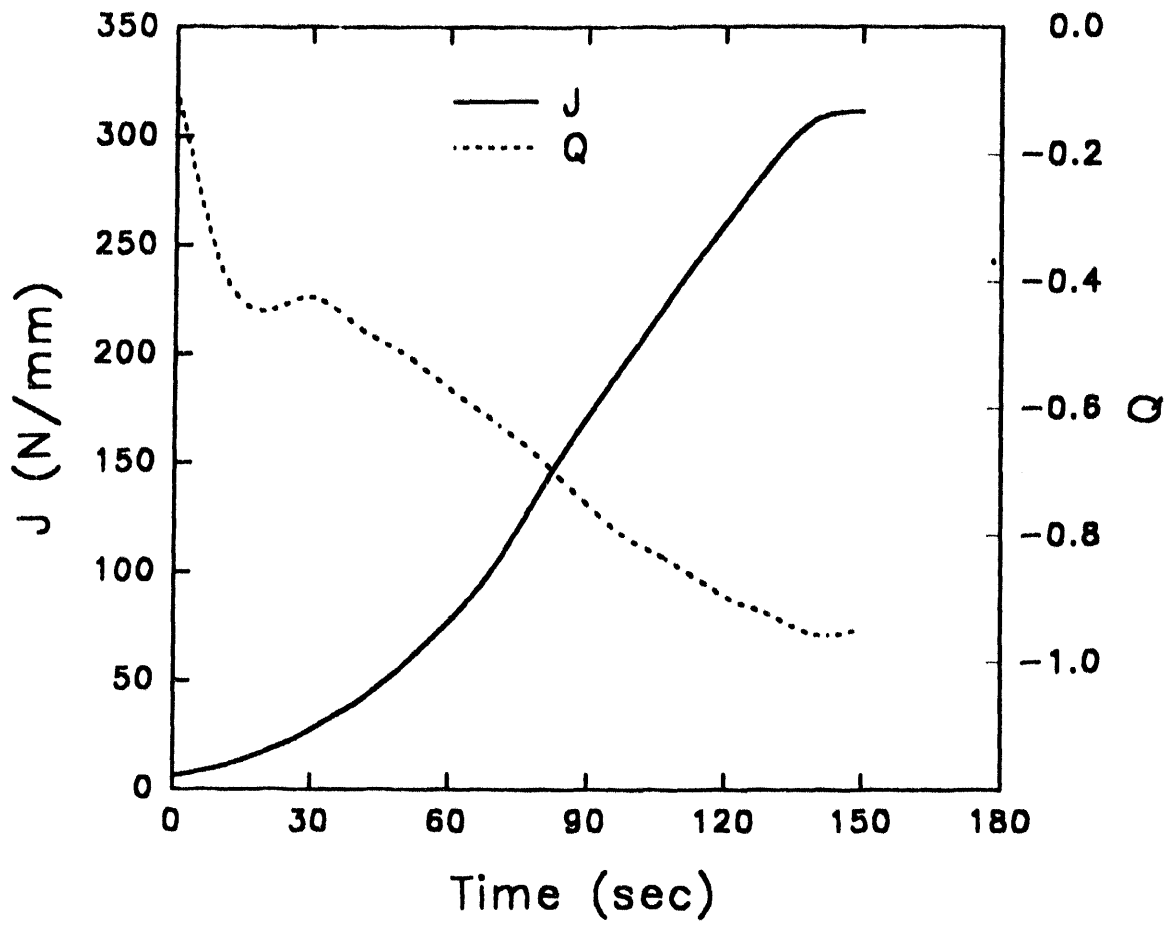

Figure 8. Computed J and Q vs. time for Step B PTS experiment (up to peak response).

Comparative Assessment of Project FALSIRE - Results

by

Dr. J. Sievers*, Dr. B.R. Bass**

*Gesellschaft für Anlagen- und Reaktorsicherheit (GRS)mbH,
Schwertnergasse 1, D-5000 Köln 1, FRG
**Oak Ridge National Laboratory (ORNL), P.O. Box 2003,
Oak Ridge, Tennessee 37831, USA

Abstract

The analysis results of the recently completed Phase I for the Project Fracture Analysis of Large Scale International Reference Experiments (FALSIRE) are summarized in a comparative manner. Thirty-nine analyses of the pressurized thermal shock experiments NKS-3 and NKS-4 from MPA-Stuttgart (FRG), PTSE-2 from ORNL (USA) and spinning cylinder SC-I and SC-II from AEA-Technology (UK) have been evaluated. The discussion of the results has been focused on the discrepancies of the finite element results and on comparisons with the estimation scheme analyses. A set of quantities like crack mouth opening (CMOD), strains, stresses, J-integral and constraint have been selected and compared for the different analyses to approximate the structural behaviour of the test specimens and the fracture behaviour of the cracks. A database of the results has been established. The influence of boundary conditions, approximation of material properties and calculational methods is shown in detail.

The structure mechanics behaviour of the test specimens could be approximated well in case of NKS experiments but not in PTSE-2. Most differences between the various analyses could be explained. In SC tests structural mechanics results could not be compared with experimental measures. The applications of J_R methodology to predict crack extension was partially successful in some cases (NKS experiments) but not in others (PTSE-2). The quality of fracture assessment is closely connected with the structural mechanics simulation. In all analyses with a good structural mechanics approximation, the fracture prediction was reasonable.

Fracture assessments based on CT-specimens overestimate stable crack growth in the case of NKS-4 and SC-I/II, because the crack resistance in the large scale test specimens is bigger than predicted by small specimens (e.g. CT-25). SC-I/II fracture results show that crack growth can be described quite well with the J-integral and the J_R-curves of the large scale test specimen. Therefore, future work has to be concentrated on extension of the J_R methodology by a parameter which controls the geometry and load dependence of the crack resistance. This can only be achieved by close connection between numerical simulation and fracture mechanics testing.

Introduction

Project FALSIRE was created by the Fracture Assessment Group (FAG) of Principal Working Group No. 3 (PWG/3) of the Organization for Economic Cooperation and Development (OECD)/Nuclear Energy Agency's (NEA's) Committee on the Safety of Nuclear Installations (CSNI). The CSNI/FAG was formed to evaluate fracture prediction capabilities currently used in safety assessments of nuclear vessel components. Members are from laboratories and research organizations in Western Europe, Japan, and the U.S.A. To meet its obligations, the CSNI/FAG planned Project FALSIRE to assess various fracture methodologies through interpretive analyses of selected large-scale fracture experiments. The six experiments utilized in Project FALSIRE (performed in Federal Republic of Germany, United States, United Kingdom, and Japan) were designed to examine various aspects of crack growth in reactor pressure vessel (RPV) steels under pressurized-thermal-shock (PTS) loading conditions.

These conditions were achieved in three of the experiments by internally pressurizing a heated cylindrical vessel containing a sharp crack and thermally shocking it with a coolant on the inner (NKS-3 and-4, from MPA, Germany) or outer (PTSE-2 from ORNL, USA) surface. In a series of spinning cylinder experiments (SC from AEA Technology, UK), a thick cylinder with a deep crack on the inner surface was rotated about its axis in a specially-constructed rig (SC-I) and thermally shocked with a water spray (SC-II). A Japanese test (Step B from JAPEIC, Japan) utilized a large surface-cracked plate subjected to combined mechanical loading of tension and bending, coordinated with a thermal shock of the cracked surface to model PTS loading conditions. A summary of the material toughness, loading conditions, crack geometry and crack growth for each experiment is given in Table 1.

The CSNI/FAG established a common format for comprehensive statements of these experiments, including supporting information and available analysis results. These statements formed the basis for evaluations that were performed by an international group of analysts using a variety of structural and fracture mechanics techniques. A three-day workshop was held in Boston, MA (USA) during May 1990, at which thirty-seven participants representing twenty-six organizations (Table 2) presented a total of thirty-nine analyses of the experiments. The analysis techniques employed by the participants (Table 3) included engineering and finite-element methods, which were combined with J_R fracture methodology and the French local approach. For each experiment, analysis results provided estimates of variables such as CMOD, temperature, stress, strain, crack growth and applied J and K values and have been stored in a results database. The comparative assessment of the analysis results is summarized and the discussion concentrates on reasons for the discrepancies among the various analyses. Further details on the description of the reference experiments, the applied analysis methods and the comparative assessments of the analysis results are given in the recently finished final report on Project FALSIRE Phase I (Ref. 1).

NKS-3 Pressurized-Thermal-Shock Experiment

The NKS-3 PTS experiment (Ref. 2) was performed with a thick-walled hollow cylinder (thickness 200 mm; inner diameter 400 mm) containing a 360° circumferential flaw on the inner surface having an average depth of approximately 62.8 mm (see Fig. 1). The test piece was first loaded with an axial tensile load of 100 MN and by internal pressure using water (30 MPa, 330° C) in the cylinder volume. Thermal shock cooling of the inner cylinder surface was performed by means of two high pressure pumps, spraying cold water (20° C) towards the inner cylinder surface over the whole test length of the cylinder through evenly distributed nozzels. Loading and test material data are summarized in Fig. 2.

Figures 3-5 show the time history of CMOD, axial strain at the inner surface 184 mm above the crack ligament and the calculated J-integral. Analyses 1-7 used FE[1] methods and analyses 12 and 13 used ES[2] methods. The difference between the results from FE methods are quite small. Table 4 summarizes some selected characteristics of the FE analyses. Due to restrictions of the FE-code versions, the approximations of the stress-strain data are different. Multilinear temperature-dependent approximations in analyses 1 and 5 are very similar, as are the calculated results. The FE models differ in the number of degrees of freedom by a factor of 10. This number ranges between 886 (analysis 5) and 8800 (analysis 7). Therefore, the results in this case do not depend very much on the model size. The J-integral results of the ES analyses are in the scatter band of the FE results. The stress distribution is strongly dependent on the approximation of the stress-strain data. In analysis 2, a very low yield stress is used which results in lower stresses on the ligament during the transient. Crack growth has been evaluated with crack resistance curves of CT-25 specimens, giving values of about 3 to 4.8 mm (average measured: 3.6 mm, i.e. about 6 % of the initial crack depth) due to the scatterband of the analyses results. The uncertainty of the calculated crack growth is about 3 % of the initial crack depth. Therefore, these analysis results show a scatterband which is acceptable in comparison with the experimental data. The neccessary material properties to calculate the structure mechanics behaviour were available. The J_R-methodology based on small specimens gives suitable results for the analyses.

NKS-4 Pressurized-Thermal-Shock Experiment

The PTS experiment NKS-4 (Ref. 3) examined crack-growth behaviour of two symmetrically opposed semi-elliptical surface cracks in a low-toughness material. Figure 6 shows the geometry of the test cylinder and the two circumferential cracks located on the inner surface. Each crack has a ratio of length to depth of 6:1 and a maximum depth of approximately 30 mm. The cracks were produced by means of spark erosion and fatiguing procedures.

The test rig and loading procedures used to test the NKS-4 specimen were essentially the same as for NKS-3. The NKS-4 experiment was performed using two thermal-shock transients, the first of which produced a reduced thermal loading due to mechanical problems with the cooling water flow. In Fig. 7 the loading of the analyzed transient and the material characterization is summarized.

Comparisons of calculated CMOD, axial strain and J-integral at the center of the partially circumferential crack versus time are shown in Figs. 8-10. Selected characteristics of the FE analyses are summarized in Table 5. Analysis 1 fits the experimental data best. Analysis 2 used a temperature independent stress-strain curve with a very low yield stress and a higher thermal expansion coefficient which produces higher CMOD. The J values of small evaluation regions show about 30 % lower values than presented in Fig. 10 (very recent results). Analysis 3 is characterized by an artificially high yield stress and a reference temperature of 20° C, contrary to the other analyses; but most important are the differences in the deformation boundary conditions. Missing rotational restraints are responsible for the significantly higher J-integral values. Analysis 7 is an axisymmetric solution of the 3-D problem with an approximation of the partially circumferential crack by a 360° fully circumferential crack. Therefore the results overestimate the measured data. The J-integral results of ES analyses 12 and 13 are in the scatterband of the 3-D FE results. The crack growth at the center of the crack calculated from an isothermal J_R-curve (T = 240° C) of a CT-25 specimen ranges from 2 to 3.2 mm (measured: 1.5 mm, i.e. 5 % of the initial crack depth).

[1] FE finite element

[2] ES estimation sheme

In conclusion, the results show that with the available material properties, the structure and fracture mechanics behaviour of this 3-D problem were analyzed quite well. The scatter of the results is quite large but the main reasons could be identified. Crack growth assessment based on J_R-methodology at the center of the crack overestimates the measured value.

PTSE-2A Pressurized-Thermal-Shock Experiment

The details of the PTSE-2 test vessel (Ref. 4) and the initial flaw geometry of the axial crack in the outside surface are given in Fig. 11. A test vessel was prepared with a plug of specially heat-treated test steel welded into the vessel. In the experiment the flawed vessel was loaded by outside cooling and an internal pressure transient (Fig 12). Furthermore a summary of the material data of the test section are given. The tensile strengths were undesirably low, but other properties, although somewhat uncertain, were satisfactory. The flaw experienced two stages of ductile tearing interrupted by a period of warm prestressing ($\dot{K}_I < 0$) followed by cleavage and arrest. The comperative assessment of the analyses has been concentrated on the first three minutes of the thermal transient with one period of stable crack growth. The time histories of CMOD and J-integral are presented in Figs. 13-14 and selected characteristics are summarized in Table 6. In comparison with the experiment, all analyses underestimate the experimental results of CMOD. In this connection it has to be mentioned that the temperature dependence of the stress-strain curve and the thermal expansion coefficient (α) were not available for the analysts. Recent investigations show that the measured CMOD values are strongly axial dependent, i.e. the thermal loading conditions have to be checked in further detail.

The FE results are strongly dependent on the approximation of the stress-strain data, the effect of whether crack growth has been considered, and the coefficient of thermal expansion. Analysis 10 has about 30 % lower CMOD at t = 185 s than analysis 5 and about 40 % higher J-value. The reason is the different bilinear approximation of the stress strain data. The measured onset of yield is very low (70 MPa) compared with the engineering yield stress (255 MPa) quoted for the vessel insert. The value used in the calculations ranges from 200 MPa to 495 MPa, dependent on whether the small strain or the larger strain region of the stress curve is approximated well. Furthermore, an increase in $\sigma_{0.2}$ of 50 % from the vessel insert after transients A and B has been found. The artificially high yield stress used in analysis 10 results in higher stresses on the ligament (see Figs. 15-16) with a smaller plastic zone and therefore smaller CMOD but higher J-integral. In analyses 5', the final crack length after the first period of stable crack growth (5.1 mm after 185 s) was used which produces an increase of CMOD at t = 185 s of about 30 % compared with analysis 5. Due to the experience with other calculations, a 20 % higher coefficient of thermal expansion was used to demonstrate the effect of a change in reference temperature from room temperature to 300° C. This change produces a CMOD increase of 13 %. The change in the approximation of the stress-strain data (pretest set 5) by a multilinear curve causes a CMOD decrease of about 13 %. The scatter band of the results is also enlarged because different assumptions concerning the crack depth have been chosen (initial depth after first phase of stable crack growth).

Analysis 8 simulated the measured crack growth, but the higher yield stress makes the model more stiff, which results in lower CMOD values. ES analysis 15 and 15' used influence coefficients based on infinitely long cracks and on finite-length 3-D crack, respectively. Therefore, when the fracture assessment is done excluding analysis 15 (because the latter assumes infinite crack length) and excluding analyses 5' and 8 (because the latter took crack growth already into account), then a crack growth estimation of 1-2.5 mm (measured 5.1 mm) is obtained from isothermal CT-25 specimen J_R-curves. The underestimation of crack loading and crack growth has to be considered in connection with the underestimation of CMOD, i.e.

without good structure mechanics simulations a good fracture mechanics approximation cannot be achieved. The temperature dependence of J_R is strong and it is not known what the effect of temperature gradient in the test cylinder has on the crack resistance. The necessary material properties, especially the temperature dependence, were not available totally. Therefore, reasons for the large difference between results of the analyses and the experiment could be only partly provided. However, some parameters which show significant influence on the analysis results have been identified.

PTSE-2B Pressurized-Thermal-Shock Experiment

The arrested crack from transient A was the initial crack geometry for transient B. Data describing the thermal and mechanical loading conditions in transient B are provided in Fig. 17. The extended crack that had developed during the PTSE-2A first tore depthwise and then converted to cleavage. The propagating cleavage crack arrested and then propagated by ductile tearing until the vessel ruptured. Figures 18-19 show the time dependence of CMOD and J-integral and Table 7 shows selected characteristics of the FE-analyses. The FE-analyses underestimate CMOD (as in PTSE-2A) which may be due to the same reasons discussed above, e.g. lack of temperature-dependent material data for $\sigma(\varepsilon)$ and α. Differences in the stress behaviour on the ligament, especially at the beginning of the transient, are due to the inclusion of residual stresses from transient A in analyses 5 and 8, but not in analysis 7. Furthermore, different material property sets have been used, the post-test set in analyses 5, and the pre-test set in analysis 7 (see Fig. 12). That also leads to differences in CMOD and J-integral.

Negative J-values are calculated at the beginning of the transient in analyses 5 and 8 because of the compressive residual stresses in front of the crack tip due to transient A. The hoop stresses of analyses 12 and 15 compare well, but the J-values have large differences due to the ES methods applied.

A range of stable crack growth is calculated using isothermal J_R-curves and the J-integral scatterband obtained by excluding analyses 12 and 15 from the set given in Fig. 19. Possibly, analysis 12 fails due to the deep crack and analysis 15 due to the assumption of infinite crack length (as compared with analysis 15', which assumed a finite crack length). The calculated crack growth ranges from 1,4 to 2,9 mm (measured 3,7 mm, i.e. 9 % of the initial crack depth in PTSE-2B). The underestimation of the crack growth is not as large as in PTSE-2A, but is again closely connected with the underestimation of CMOD and another factor which could reduce the crack growth has not been considered. The stress state in front of a crack which has already seen a transient (A) could be altered due to blunting and lead to an increase in crack resistance compared to that of a standards specimen with fatigued crack. Therefore, as in PTSE-2A, differences between the analysis results and the experimental data could not be clarified totally, but additional influence factors concerning the quality of fracture assessment based on J_R-methodology have been pointed out.

SC-I Spinning Cylinder Experiment

The first spinning cylinder experiment (Ref. 5) was an investigation of stable ductile crack growth in contained yield for a thick section low alloy steel structure. Crack growth was generated by progressively increasing the rotational speed of a cylindrical specimen with an axial flaw at the inner surface maintained at a uniform temperature of 290°C (see Fig. 20). The loading and material characterization data for SC-1 are summarized in Fig. 21.

In Fig. 22 J-integral values are plotted versus the angular velocity which represents the loading of the test. The stress-strain approximation of the plane strain FE analyses 8 and 9 are multilinear. Measured CMOD or strain values were not available to the analysts. Some CTOD data were made available only after evaluation of the analysis results of the Project FALSIRE Workshop. The J-integral results of the FE and ES analyses show a small scatterband around the experimental curve extracted from the J_R-curve measured with the SC-I test cylinder. The curve of analysis 9 has a weaker slope, which could not be explained. Analyses 12 and 16 show differences up to 50 % due to different ES-fracture methods used in the analyses; it should be noted that the hoop stresses are the same.

In conclusion, only fracture results could be compared with the experiment. They show that crack growth based on J_R-methodology can be described with the crack resistance curve of the large scale test specimen quite well. However, the fracture toughness measured with small-scale CT specimens is substantially lower than that obtained for the large-scale spinning cylinder which should be explained by a constraint parameter controlling the geometry dependence of crack resistance.

SC-II Thermal-Shock Spinning Cylinder Experiment

The second spinning cylinder experiment was an investigation of stable crack growth in contained yield for a thick section low alloy steel structure subjected to a severe thermal shock. The configuration of the cylindrical specimen used is shown in Fig. 20. In the SC-II test, the cylinder was stabilized at a mean temperature of 312°C. The cylinder was then rotated to 530 revolutions per minute to provide for uniform cooling of the inner surface. The thermal gradient in the wall is given in Fig. 23.

The time dependence of the J-integral is presented in Fig. 24. For the deep crack, the weight function method used for fracture assessment in analysis 16 gives quite conservative results, primarily due to stress calculations resulting from the assumption of free-end boundary conditions. Analysis 11, which used the Bamford and Buchalet K_I solution given for a wall thickness to internal radius (t/R) ratio of 0.1 (but SC-II, t/R = 0.4), shows the lowest values. Due to the scatterband, the crack growth calculated from the SC-II specimen J_R-curve ranges from 0.0 mm to 1.4 mm (measured value in the middle of the crack, 0.75 mm i.e., 0.7 % of the initial crack depth), but the four analyses 8, 12, 13 and 14 range from 0.2 to 0.8 mm.

As in SC-I, the fracture assessment based on the large scale test specimen J_R-curve gives suitable results, but the crack loading is strongly dependent on the estimation scheme method used and the boundary conditions assumed for the model. In particular, free-end boundary conditions, which best fit the test conditions, produce an axial decrease of crack loading. Measured crack opening and hoop strains were made available only after evaluation of the analysis results of the Project FALSIRE Workshop.

Conclusion

Based on results from the Project FALSIRE Workshop, several observations can be made concerning predictive capabilities of current fracture assessment methodologies as reflected in the large-scale experiments described in the previous sections.

The discussion of the analysis results has been focused on the discrepancies of the finite element results and on comparisons with the estimation scheme analyses. Examples of these comparisons were shown in CMOD vs time plots for experiments NKS-3, 4 , and PTSE-2 A/B. The structural mechanics behaviour of the test specimens could be approximated well in case of NKS experiments but not in PTSE-2 (see Table 8). In SC tests structural mechanics results could not be compared with experimental measures. The largest differences are seen to occur in the PTSE-2 A transient. The restrictions in some finite element codes to input stress-strain curves only by bilinear approximations produced scatter bands in the results (CMOD and J-integral) dependent on the level of plasticity reached.

All the analyses of PTSE-2 assumed material and physical properties to be independent of temperature, because corresponding measured data have not been made available. These analysis results highlight the importance of obtaining high-quality material properties and structural response data (CMOD, strains, etc.) from the experiments to model structural behaviour of the specimen prior to performing fracture mechanics evaluations. In particular, variables must be carefully selected and reliably measured to provide a minimum set of data for validating these structural models. This requirement was not uniformly achieved in all of the large-scale experiments examined in the Project FALSIRE Workshop.

In applications of J_R methodology based on small specimen data, all analyses correctly distinguished between stable crack growth and ductile instability conditions for each experiment. These include both estimation schemes and detailed finite element analyses. However, as a technique to predict crack extension, J_R methodology was partially successful in some cases (NKS experiments) but not in others (PTSE-2, spinning cylinder experiments). The quality of fracture assessment is closely connected with the structural mechanics simulation. In all analyses with a good structure mechanics approximation the fracture prediction was reasonable. Fracture assessments based on CT-specimens overestimated stable crack growth in the case of NKS-4, SC-I/II, and Step B-PTS because the crack restistance in the large scale test specimens is bigger than predicted by small specimens (e.g. CT-25). SC-I/II fracture results show that crack growth can be described quite well with the J-integral and the J_R-curves of the large scale test specimen. A summary of the fracture results are given in Table 9.

In PTSE-2A, the first phase of stable crack growth is underestimated because the crack loading also represented in CMOD is underestimated. Recent investigations show a strong axial dependence of the measured CMOD value. Therefore especially the thermal loading conditions have to be checked for further studies. Furthermore, differences between pretest characterization data and posttest in situ data for material and fracture toughness properties gave rise to questions concerning whether J_R curves from CT specimens were representative of the flawed region of the vessel. None of these temperature-dependent J_R-curves were consistent with all phases of ductile tearing observed in PTSE-2. It should be pointed out that the PTSE-2A transient included load-history (i.e., warm-prestressing) effects that were not incorporated into the J_R methodology. The substantial differences between fracture toughness curves generated from the spinning cylinders and from CT specimens focussed attention on other factors. These included the possibility that crack-tip behaviour in the spinning cylinder is not characterized by a single correlation parameter. Alternative criteria under consideration include two-parameter models in which K or J is augmented by the next higher-order in the

series expansion of the stresses around the crack tip (Ref. 6). Other measures considered in dealing with the transfer of small specimen data to large structures include the stress triaxiality parameter, which is proportional to the rate of hydrostatic to effective stress (Ref. 7).

Therefore, future work has to be concentrated on extension of the J_R methodology by a parameter which controls the geometry and load dependence of the crack resistance. In fracture analyses it has to be investigated how the crack resistance in large scale test specimens can be approximated by small scale fracture test specimens. This can only be achieved by close connection between numerical simulation and fracture mechanics testing.

References

1. B.R. Bass, C.E. Pugh, J. Keeney-Walker, H. Schulz, J. Sievers
"Final Report on Phase I of the CSNI Multi-National Project for Fracture Analysis of Large-Scale International Reference Experiments (FALSIRE)", will be published by NUREG

2. A. Sauter, "Recent Progress in PTS Research at MPA Stuttgart", French-German Seminar, Technical Presentation 1.4, EDF - Moret sur Loing, France, 1987.

3. A. Sauter, T. Nguyen-Huy, U. Weber and H. Huber, "Behavior of Surface Flaws under Thermal-Mechanical Loading", 14th MPA Seminar, Stuttgart, FRG, 1988.

4. R.H. Bryan et al., "Pressurized-Thermal Shock Test of 6-in.-Thick Pressure Vessels, PTSE-2: Investigation of Low Tearing Resistance and Warm Prestressing", NUREG/CR-4888 (ORNL-6377), Martin Marietta Energy Systems, Inc., Oak Ridge Nat'l. Lab., December 1987.

5. D.J. Lacey and R.E. Leckenby, " Determination of Upper Shelf Fracture Resistance in the Spinning Cylinder Test Facility", Tenth International Conference on Structural Mechanics in Reactor Technology, Vol. F, pp. 1-6, 1989.

6. N.P. O'Dowd and C.F. Shih, "Family of Crack-Tip Fields Characterized by a Triaxiality Parameter: Part I-Structure of Fields", Journal of the Mechanics and Physics of Solids Vol. 39, No. 8, pp 989-1015, 1991.

7. H.Clausmeyer, K. Kussmaul and E. Roos, "Influence of Stress State on the Failure Behavior of Cracked Components Made of Steel", ASME Book No. AMR 090, Appl. Mech. Rev. Vol. 44, no. 2, February 1991.

Tables and Figures

Table 1: Summary of Project FALSIRE Reference Experiments

Experiment (Place)	Material[a] Toughness	Loading	Crack Geometry	Crack Growth
NKS-3 (MPA, FRG)	A_V^{US} = 95 J, T_{NDT} = 60°C	Thermal shock axial tension, internal pressure (constant)	Circumferential (a/t = 0.3)	Ductile 3.6 mm (Average) $\Delta a/a$ = 0.06
NKS-4 (MPA, FRG)	A_V^{US} = 60 J, T_{NDT} = 120°C	Thermal shock axial tension, internal pressure (constant)	Partly circumferential (a/t = 0.15)	Ductile 1.5 mm (Center) $\Delta a/a$ = 0.05
PTSE 2A\B (ORNL, USA)	A_V^{US} = 60 J T_{NDT} = 49°C[b] = 75°C[c]	Thermal shock, internal pressure (transient)	Axial (a/t = 0.1\0.29)	Ductile 11.1\3.7 mm Brittle 16.8\32.7 mm Unstable -\68.8 mm $\Delta a/a$ = 0.35\0.09 (first phase of A\B)
Spin. Cyl. I (AEA, UK)	A_V^{US} = 90 J	Rotation of specimen	Axial (a/t = 0.54)	Ductile 2.8 mm (Average) $\Delta a/a$ = 0.03
Spin. Cyl. II (AEA, UK)	A_V^{US} = 110 J	Thermal shock	Axial (a/t = 0.52)	Ductile 0.0 - 0.75 mm $\Delta a/a$ = 0.01 (max)
Step B PTS (JAPEIC, JAPAN)	A_V^{US} = 100 J, T_{NDT} = 139°C	Thermal shock Tension, and	Surface crack (a/t = 0.14) bending	Ductile 0.3 - 1.0 mm $\Delta a/a$ = 0.04 (max)

[a] A_V^{US} = Charpy V-notch upper shelf energy

[b] pretest

[c] posttest

Table 2: Organizations participated in the Project FALSIRE Workshop, Boston, May 1990

Organization	Country
Atomic Energy Authority (AEA)	UK
AZ/EPRI	USA
B&W Nuclear Services	USA
Battelle Columbus Division	USA
Central Research Institute of Electric Power Industry (CRIEPI)	Japan
Centre D'Etudes Nucleaires de Saclay	France
Combustion Engineering (CE)	USA
Electricite de France (EDF)	France
Fraunhofer Institut fur Werkstoffmechanik (IWM)	FRG
Gesellschaft für Anlagen-und Reaktorsicherheit (GRS)	FRG
Japan Power and Engineering Inspection Corporation (JAPEIC)	Japan
Korea Institute of Nuclear Safety	Korea
Materialprüfungsanstalt (MPA) Universität Stuttgart	FRG
Mitsubishi Heavy Industries (MHI)	Japan
National Committee for Nuclear and Alternative Energies (ENEA-DISP)	Italy
Nuclear Electric	UK
Nuclear Energy Agency-OECD	France
Nuclear Installations Inspectorate	UK
Nuclear Regulatory Commission (NRC)	USA
Oak Ridge National Laboratory (ORNL)	USA
Paul Scherrer Institut	Switzerland
Southwest Research Institute (SWRI)	USA
Technical Research Centre of Finland (VTT)	Finland
University of Maryland	USA
University of Tennessee	USA
University of Tokyo	Japan

Participants: USA 17, FRG 5, France 4; UK 3, Japan 3, Finland 2, Switzerland 1, Korea 1, Italy 1; Total 37

Table 3: Summary of Project FALSIRE analysis techniques

NKS-3 (10 analyses)	NKS-4 (6 analyses)	PTSE-2 (8 analyses)	SC-I (6 analyses)	SC-II (8 analyses)	STEP B PTS (1 analysis)
FE; JR	FE; JR	FE; JR	FE; JR	FE; JR	FE; JR
FE; JR, LA	FE; JR	FE; JR	FE; JR	FE; JR	
FE; JR	FE; JR	FE; JR	FE; JR	FE; ES	
FE; JR, LA	FE; JR	FE; JR	ES	FE; ES	
FE; JR	ES; J/T	FE; JR	ES	ES	
FE; JR	ES; R6/1	FE; JR	ES; WF	ES; R6/1	
FE; JR		ES; J/T		ES	
FE; JR		ES		ES	
ES; J/T					
ES; R6/1					

FE = Finite Element Method
ES = Estimation Scheme
A1 = Analytic Solution with Numerical Integration
A2 = Handbook Analysis of Statically Indeterminate Model
JR = R-Curve Approach
J/T = J/Tearing Modulus Approach
LA = Local Approach
R6/1 = R6 Method/Option 1
WF = Weight Function Method

Table 4: NKS-3, selected characteristics of FE analyses

Analysis Number	Degrees of Freedom of FE-Model	Approximation of stress strain data			Coefficient of Thermal Expansion		Reference Temperature (°C)
			Bilinear	Multilinear			
		T(°C)	σ_y/E_T (MPa)	σ_y (MPa)	T(°C)	$\alpha(10^{-6}K^{-1})$	
1	1968 (axisym.)	20	563/3555			14.4	330
		160	519/4388				
		260	536/5489				
		400	506/6383				
2	1938 (axisym.)	20		350*		14.4	330
3	7054 (axisym.)	20	607/1167			14.4	355
		350	643/469				
4	2232 (axisym.)	20		444	20	11.2	330
		160		400	160	13.0	
		220		411	220	14.0	
		260		419	260	14.6	
		290		413	290	15.2	
		320		406	320	15.7	
5	886 (axiysm.)	20	563/3436			14.4	332
		160	519/3804				
		260	536/4540				
		320	523/5291				
6	1718 (axisym.)	20		563		14.4	330
		160		519			
		220		504			
		260		536			
		320		523			
7	8800 (axisym.)						

* Engineering stress-strain curve of NKS-4 material (stress values used are about 10% higher than e.g. in analysis 4).

Table 5: NKS-4, selected characteristics of FE analyses

Analysis Number	Degrees of Freedom of FE-Model	Approximation of stress strain data			Coefficient of Thermal Expansion		Reference Temperature (°C)
		T(°C)	Bilinear $\sigma y/E_T$ (MPa)	Multilinear σy (MPa)	T(°C)	$\alpha(10^{-6}K^{-1})$	
1	21175 (3D-90°)	20	618/3013		20	12.00	
		120	619/3013		120	12.53	
		160	578/3013		160	12.73	330
		280	629/3013		280	13.37	
		320	608/3013		320	13.58	
2	5094 (3D-90°)	20	temperature independent	350*		14.4	330
3	35370 (3D-90°)		692/2140 temperature independent			14.4	20
7	8800 (axisym.)						

* engineering stress-strain curve

Table 6: PTSE-2A, selected characteristics of FE analyses

Analysis Number	Degrees of Freedom in FE-Model	Crack Depth in FE-Model (mm)	Approximation of Stress-Strain Data of Vessel-Insert T(°C)	Bilinear $\sigma y/E_T$(MPa)	Multilinear σy(MPa)	Expansion ($10^{-6}K^{-1}$)	Reference Temperature (°C)
5	515 (2d-plane strain)	14.5	Averaged	200/12087 (set 5)		14.4	300
5′	515 (2d-plane strain)	19.6	Averaged		70 (set 5)	17.3	300
7	3200 (2d-plane strain)	19.6	Averaged		70 (set 5)	14.4	
8	3800 (2d-plane strain)	14.5-19.6	Averaged	400/2637 (set 5)		14.4	300
9	1922 (2d-plane strain)	14.5-19.6	Averaged		375 (set 7)	14.4	290
10	2419 (2d-plane strain)	14.5	Averaged	495/2300 (set 7)		14.4	300

Table 7: PTSE-2B, selected characterisitcs of FE analyses

Analysis Number	Degrees of Freedom in FE-Model	Crack Depth in FE-Model (mm)	Residual Stress Considered	Approximation of Stress-Strain Data of Vessel-Insert T(°C)	Bilinear $\sigma y/E_T$(MPa)	Multilinear σy(MPa)	Expansion ($10^{-6}K^{-1}$)	Reference Temperature (°C)
5	551 (2d-plane strain)	42.4	Yes	Averaged	373/7313 (set 7)		14.4	275
7	3200 (2d-plane strain)	42.4	No	Averaged		70 (set 5)	14.4	
8	3800 (2d-plane strain)	42.4-46.1	Yes	Averaged	400/2637 (set 5)		14.4	275

Table 8: Comparative assessment of structure behaviour in Project FALSIRE Reference Experiments

	[illegible]		[illegible]		[illegible]	
	x		1.5	x	17	13
	x		0.54	x	8	7
		x	0.9	x	35[5]	-
		x	1.6	x	21[5]	-
	x		-[2]	-	-	-
	x		-[2]	x[2]	-	-

[1] T - Temperature

[2] some data of crack tip opening have been provided after evaluation of the analyses

[3] relative to measured value

[4] analysis results with wrong boundary conditions or crack assumptions ignored

[5] - underestimation of measured data

Table 9: Comparative assessment of fracture behaviour in Project FALSIRE Reference Experiments

	[illegible]	[illegible]	[illegible]	[illegible]
[illegible]	CT-25, T=160/220°C CT-50, T=220°C	3.6 (averaged)	410 - 500	3 - 4.8
[illegible]	CT-25, T=160/240/280°C CT-25(10mm thick), T=160°C	1.5[2]	180 - 220[2]	2 - 3.2[2]
[illegible]	CT-25, T=100/175/250°C	5.1 3.7	100 - 175 145 - 225	1 - 2.5 1.4 - 2.9
[illegible]	CT-35, T=290°C SC-I test specimen	2.8 (averaged)	470 - 560	3.2 - 4.2[4]
[illegible]	CT-35, T=150/290°C SC-II test specimen	0.75	200 - 490	0.2 - 0.8[4]

[1] - analysis results with wrong boundary conditions or crack assumptions ignored

[2] - deepest point of partly circumferential crack

[3] - middle of axial crack

[4] - determined with J_r-curves of SC-test specimen

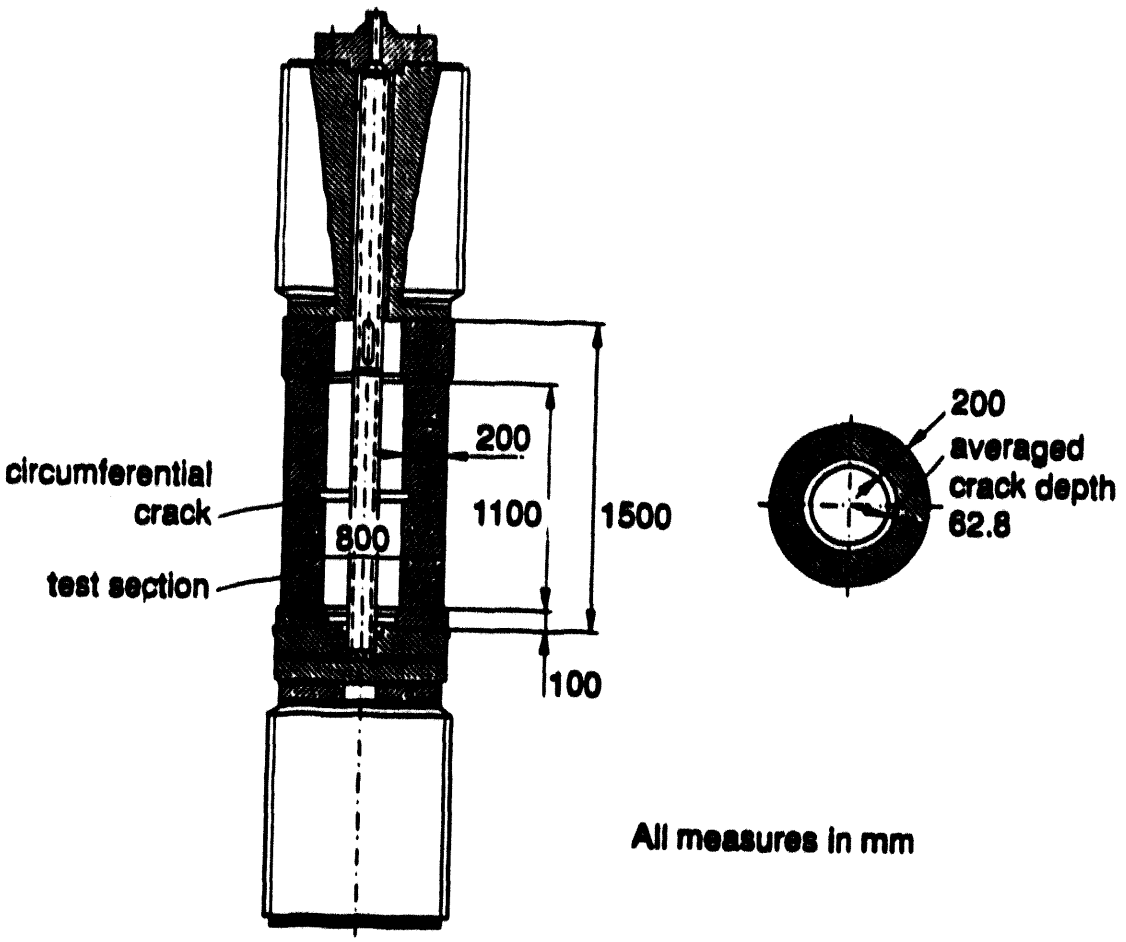

Figure 1: NKS-3, Test cylinder and crack geometry (MPA Stuttgart, FRG)

Thermal and mechanical loading

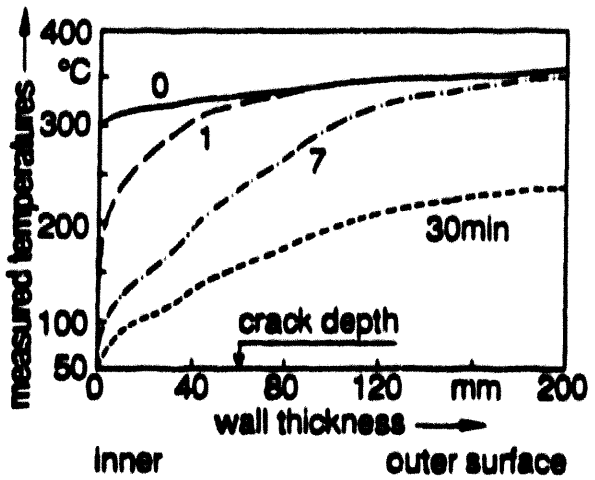

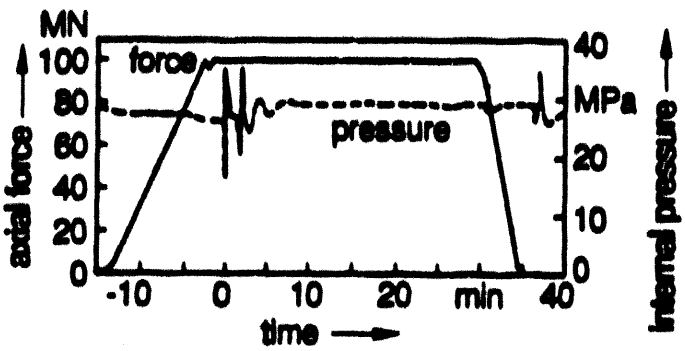

Material characterization of the test section 22 Ni Mo Cr 37

yield/ultimate stress at RT	563/723 MPa
charpy energy for upper shelf	95 J
NDT	60 °C

Figure 2: NKS-3, loading and test material data

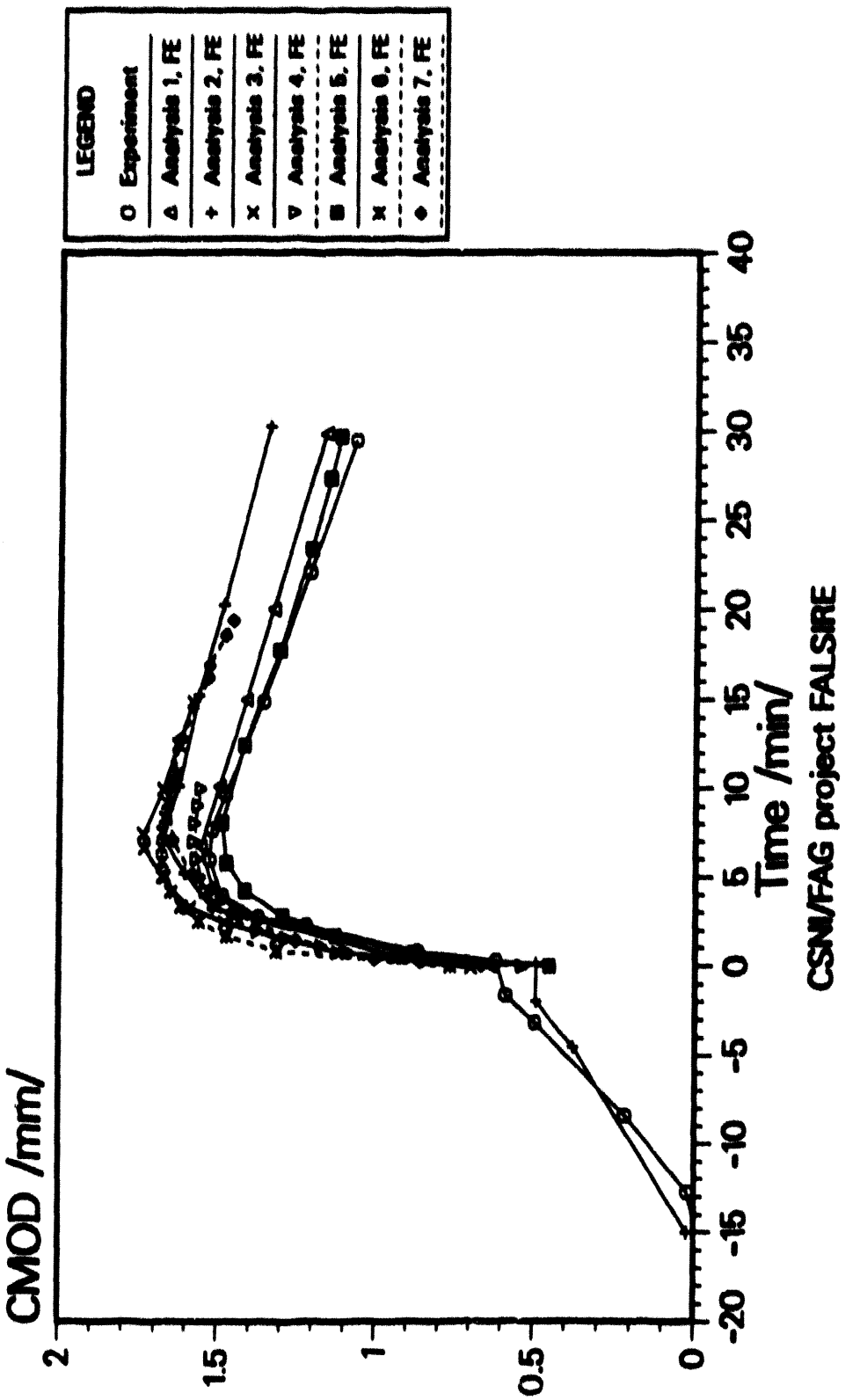

Figure 3: NKS-3, CMOD vs time

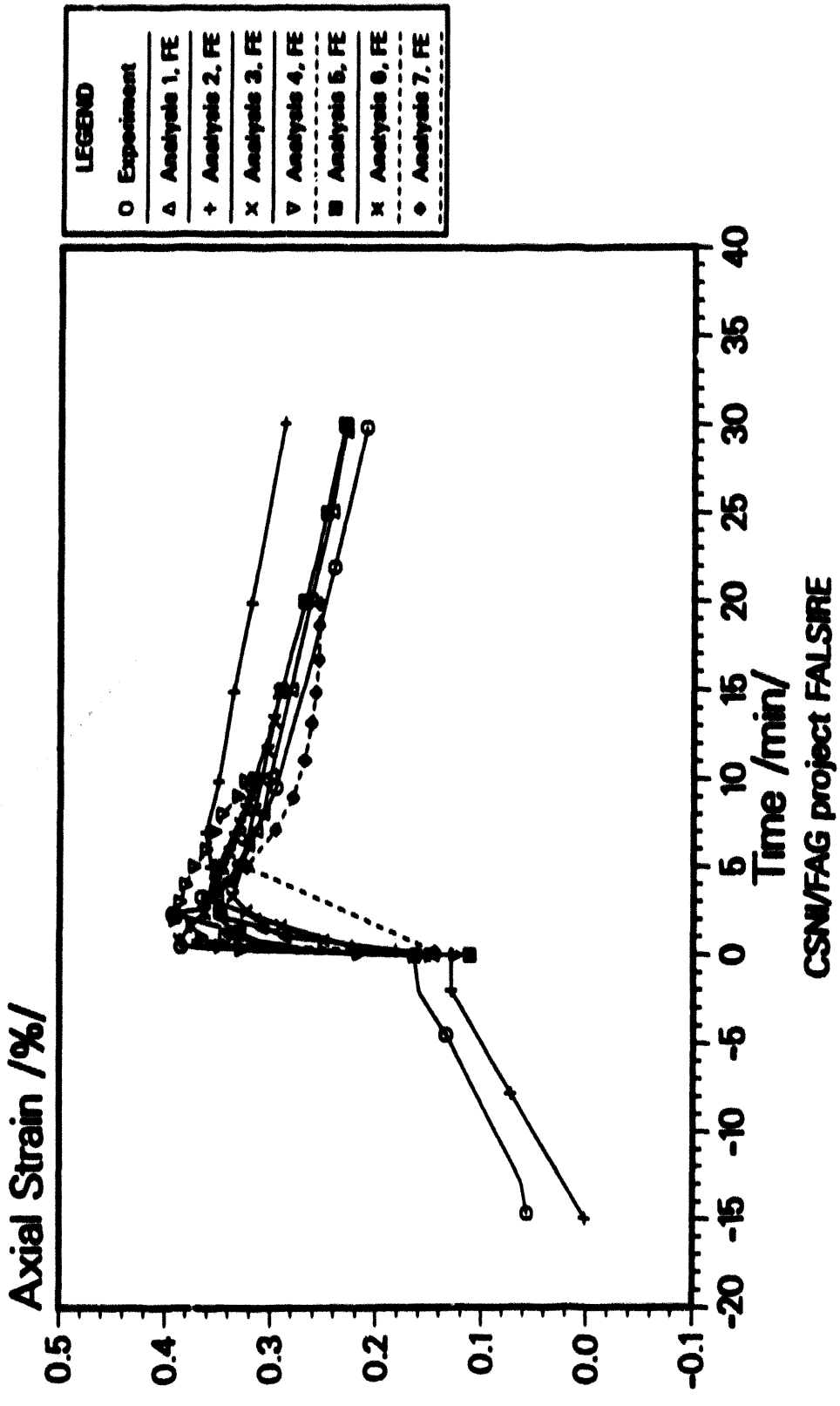

Figure 4: NKS-3, axial strains at the inner surface 184 mm above the crack ligament vs time

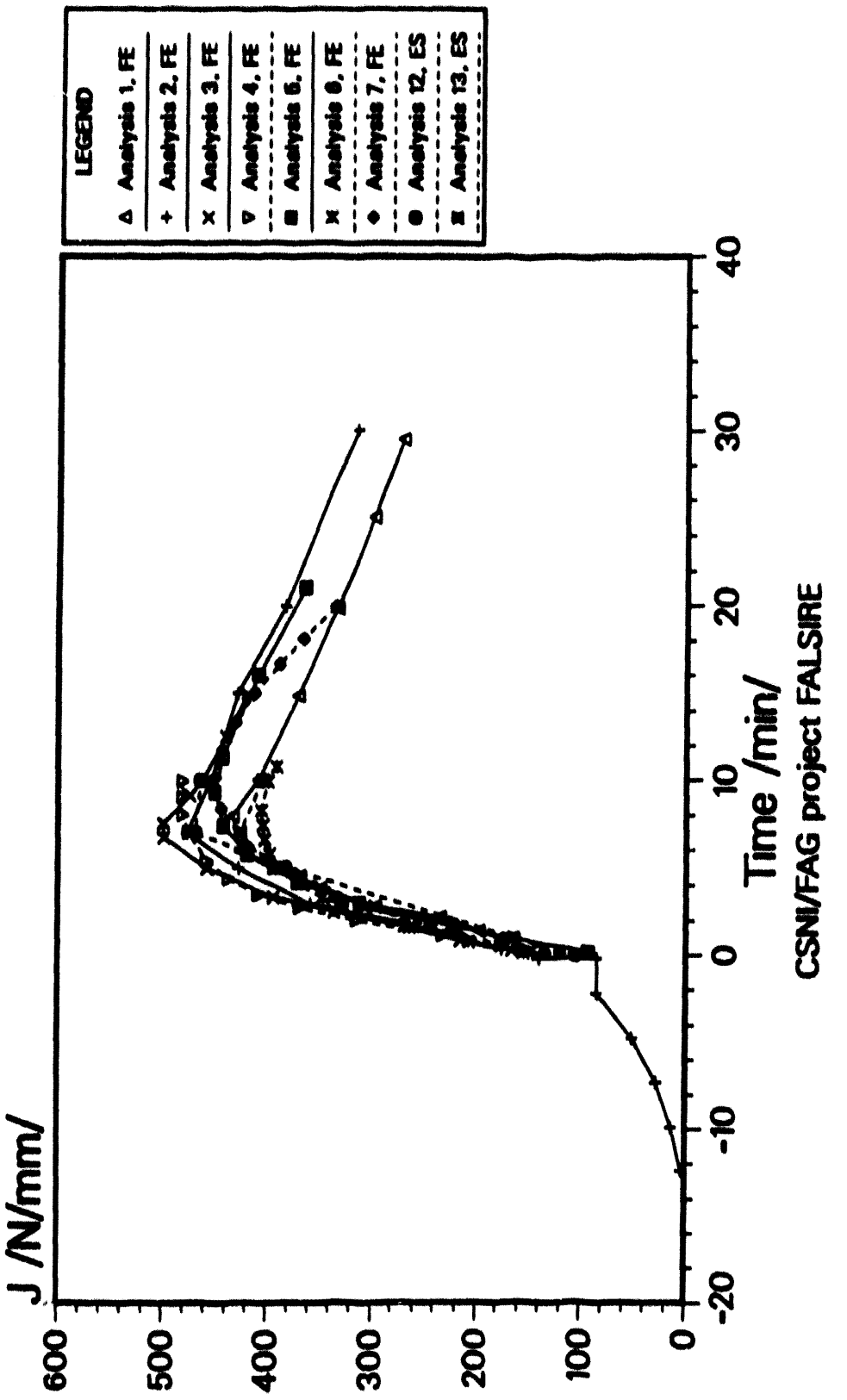

Figure 5: NKS-3, J-integral vs time

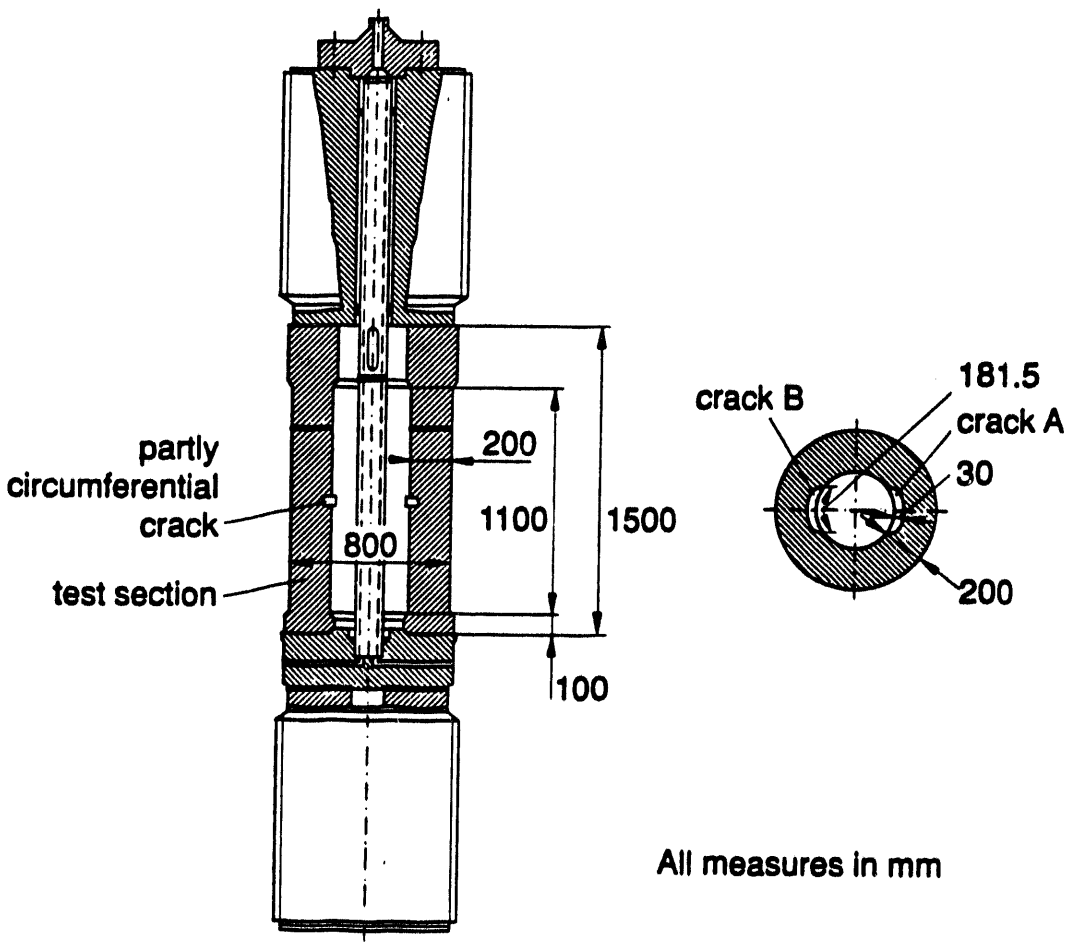

Figure 6: NKS-4, test cylinder and crack geometry (MPA Stuttgart, FRG)

Thermal and mechanical loading

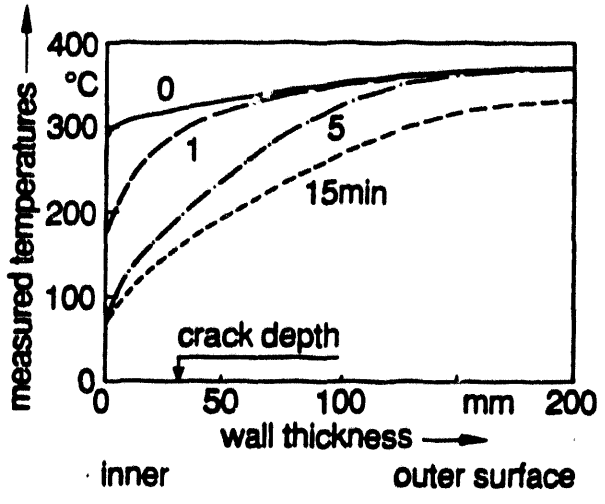

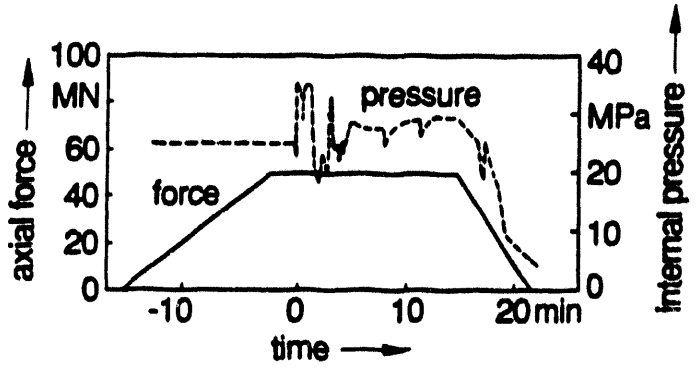

Material characterization of the test section 22 Ni Mo Cr 37, KS07

yield/ultimate stress at RT	506/798 MPa
charpy energy for upper shelf	60 J
NDT	120 °C

Figure 7: NKS-4, loading and material data

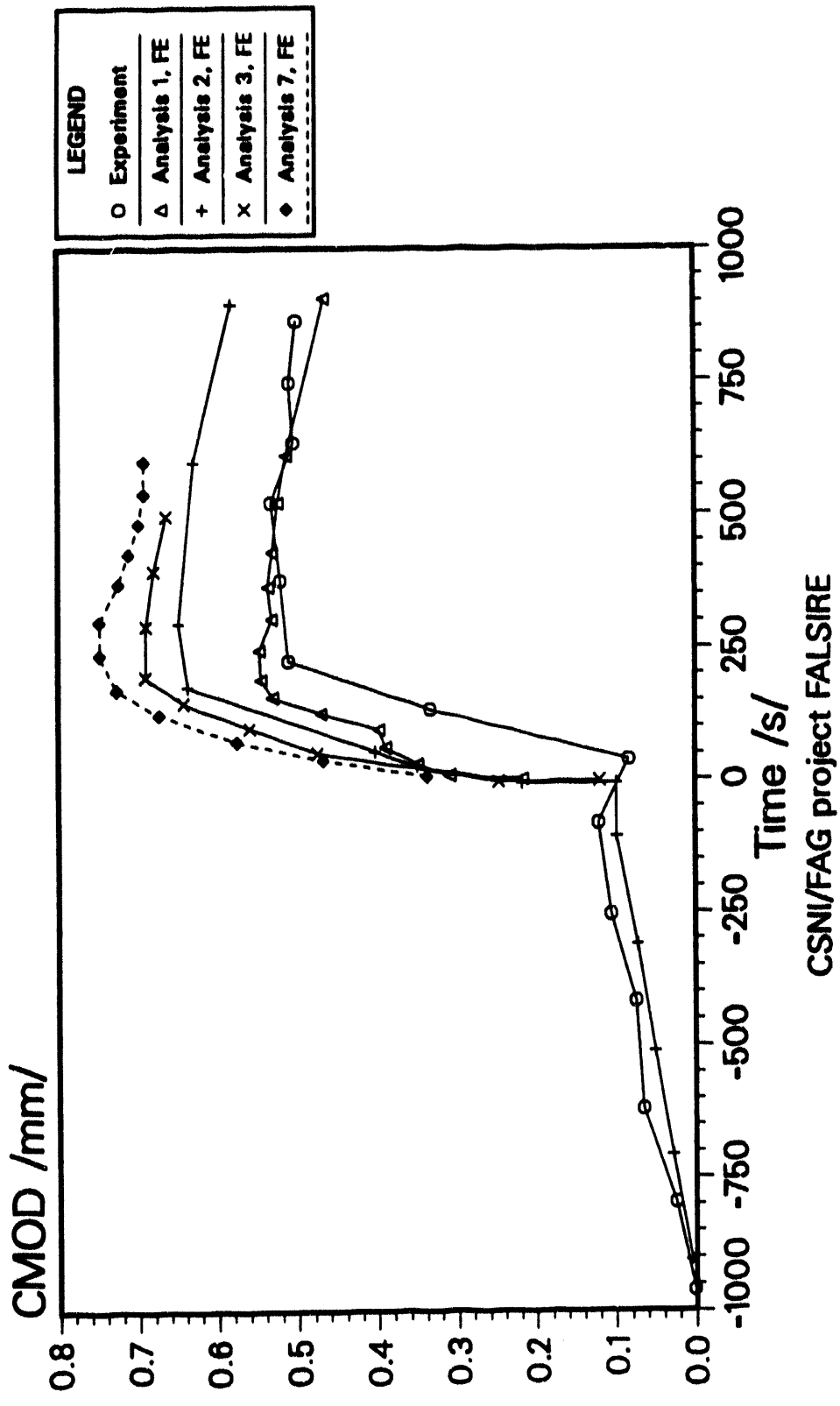

Figure 8: NKS-4, CMOD vs time

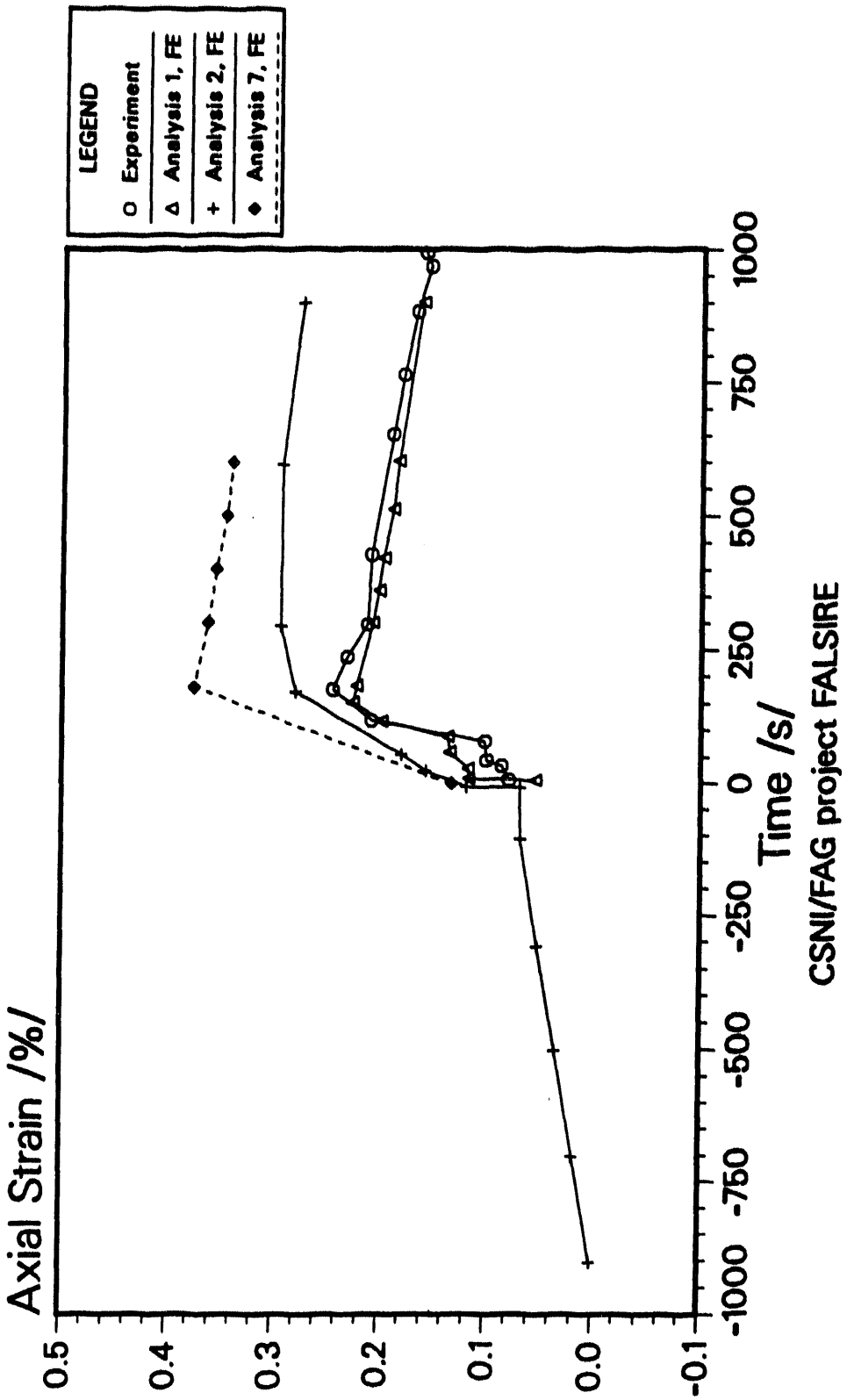

Figure 9: NKS-4, axial strains at the inner surface 184 mm above the crack ligament vs time

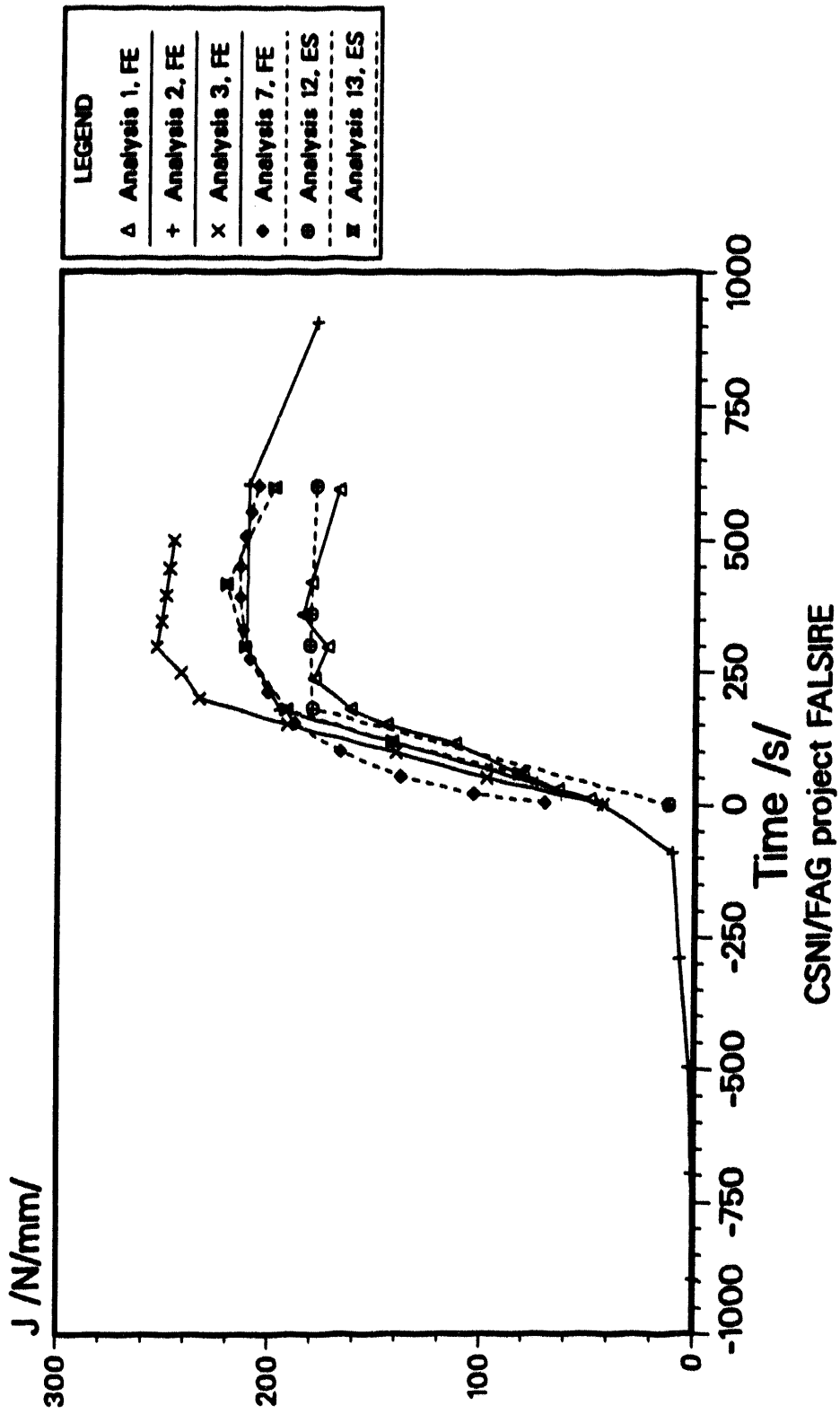

Figure 10: NKS-4, J-integral vs time

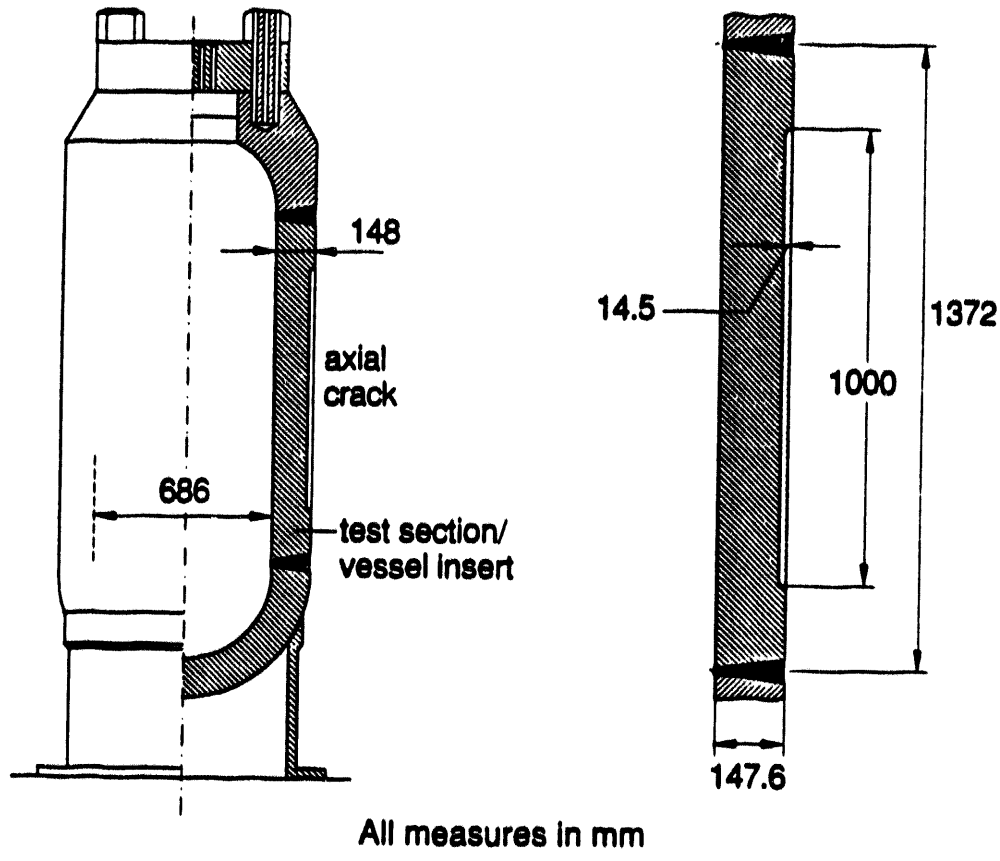

Figure 11: PTSE-2A, test vessel and crack geometry for transient A (ORNL, USA)

Thermal and mechanical loading

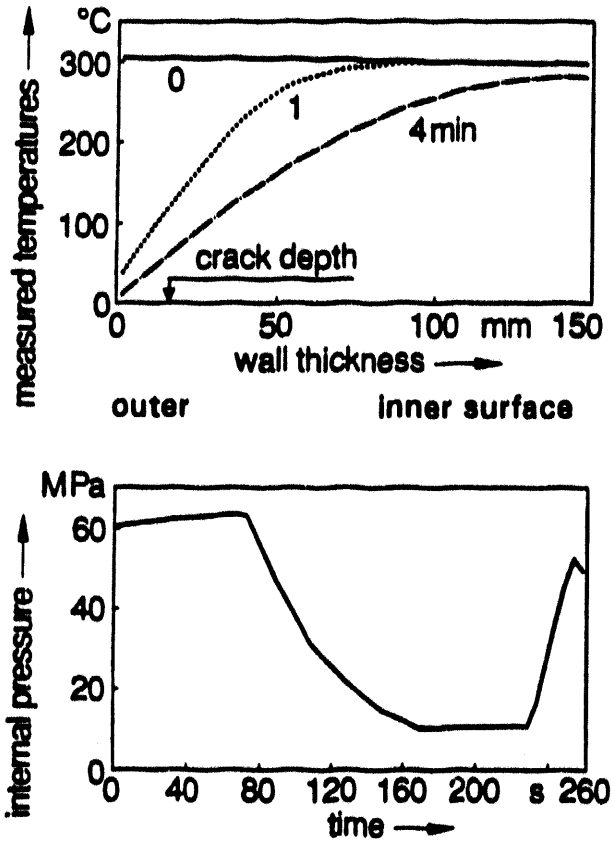

Material characterization of 2 1/4 Cr-1 Mo (SA-387 grade 22) (test section/vessel insert)

yield/ultimate stress at RT	255/518 MPa (pretest) 375/ ? MPa (posttest)
charpy energy for upper shelf	50-75 J
NDT	49 °C (pretest) 75 °C (posttest)

Figure 12: PTSE-2A, loading of transient A and material data of the test section before and after the PTSE-2 transients

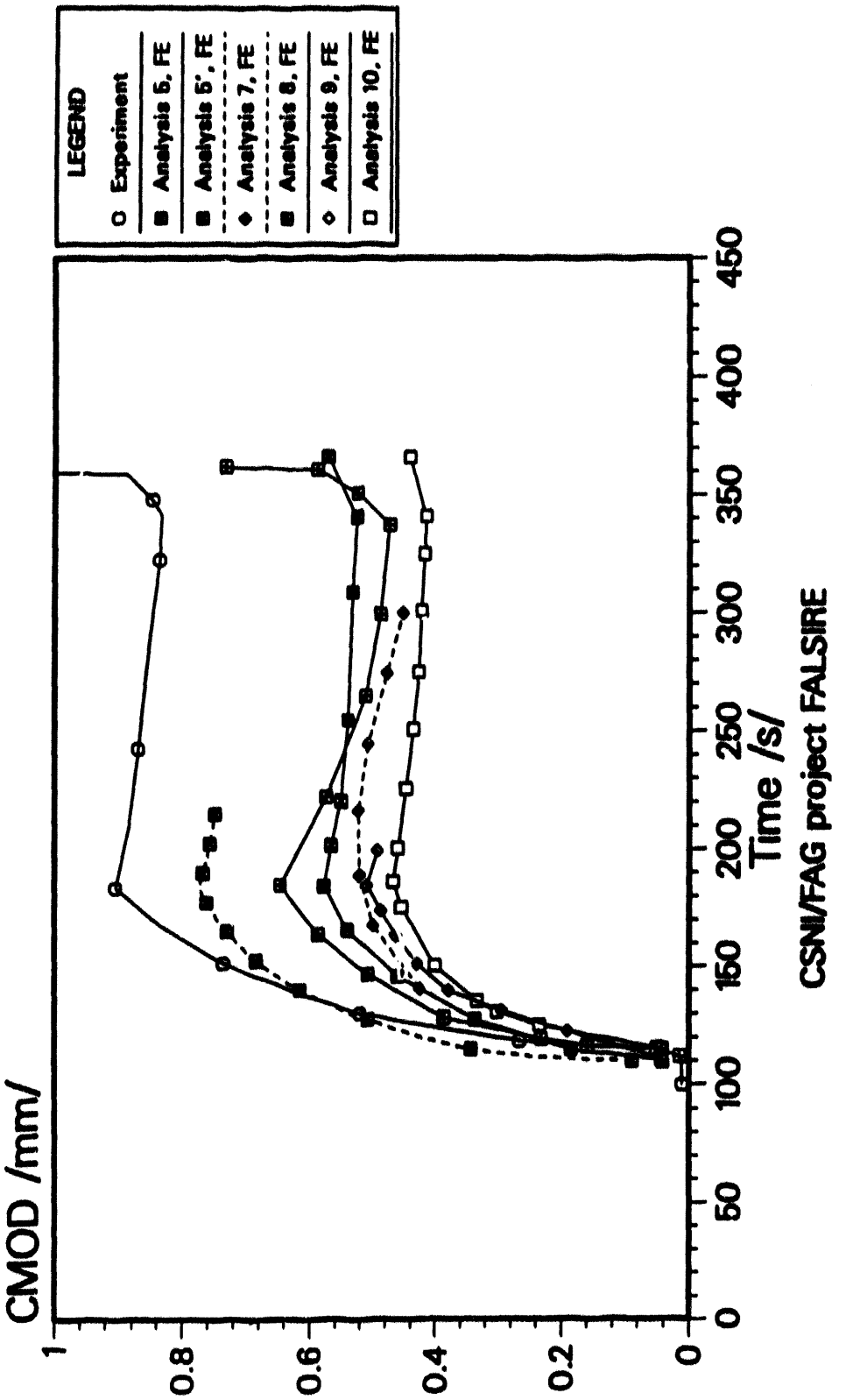

Figure 13: PTSE-2A, CMOD vs time

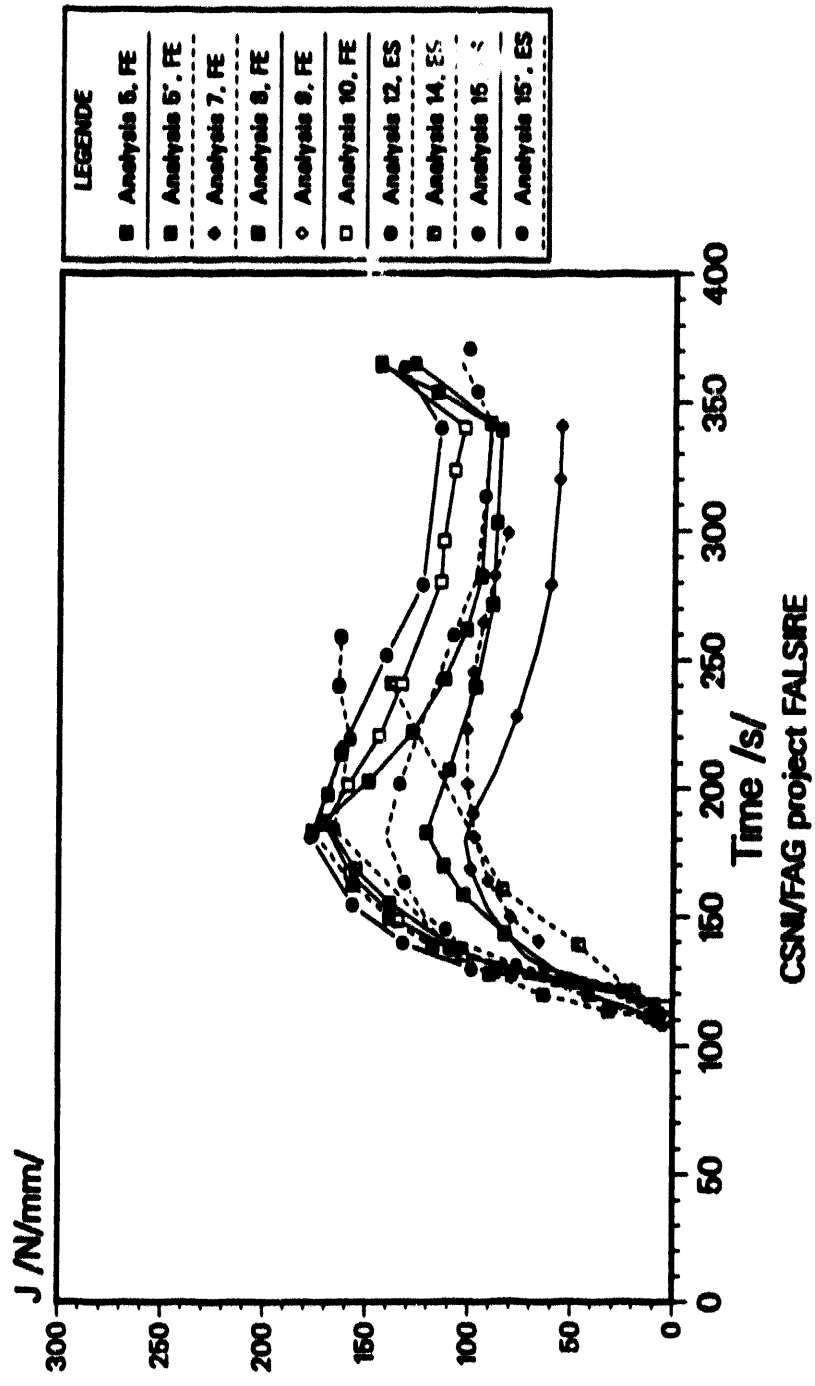

Figure 14: PTSE-2A, J-integral vs time

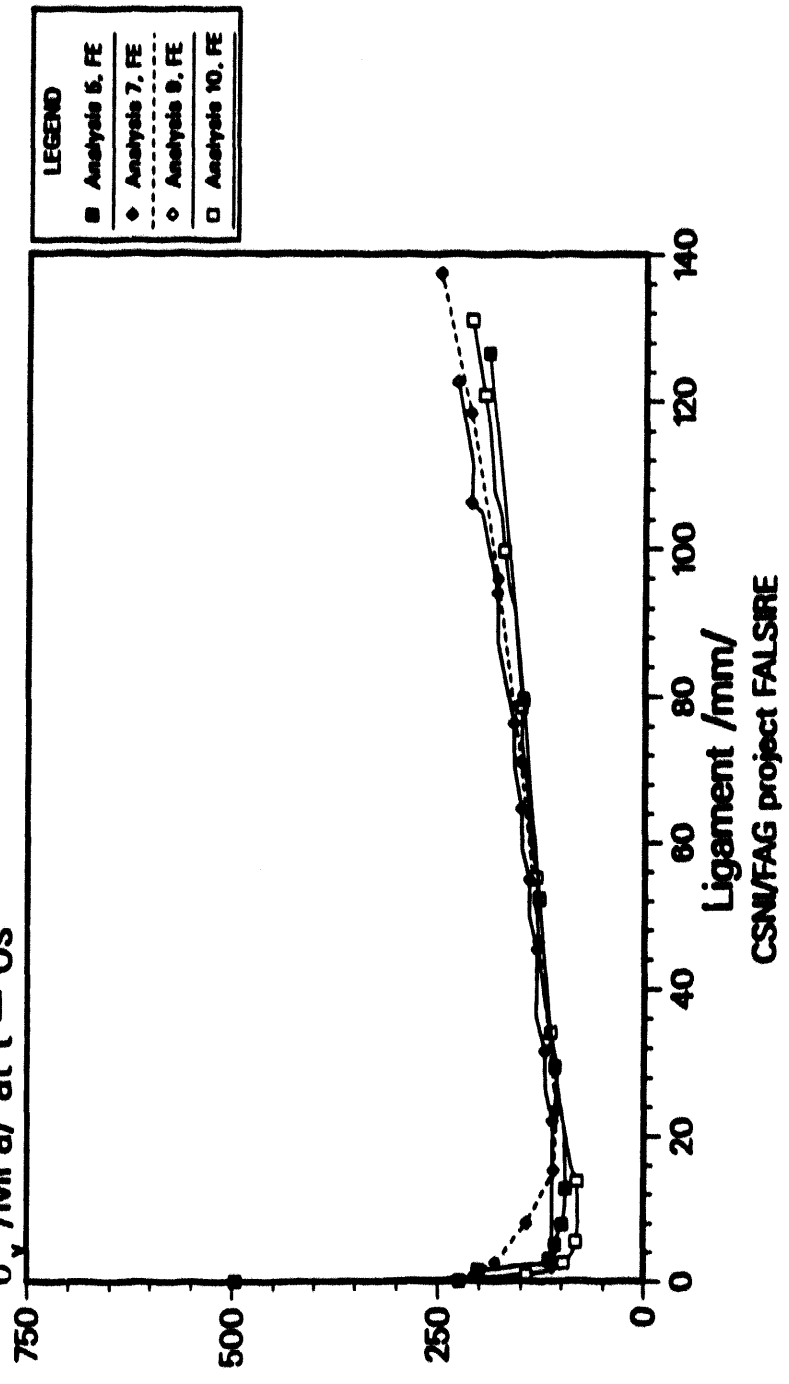

Figure 15: PTSE-2A, effective stresses on the ligament t = 0 s

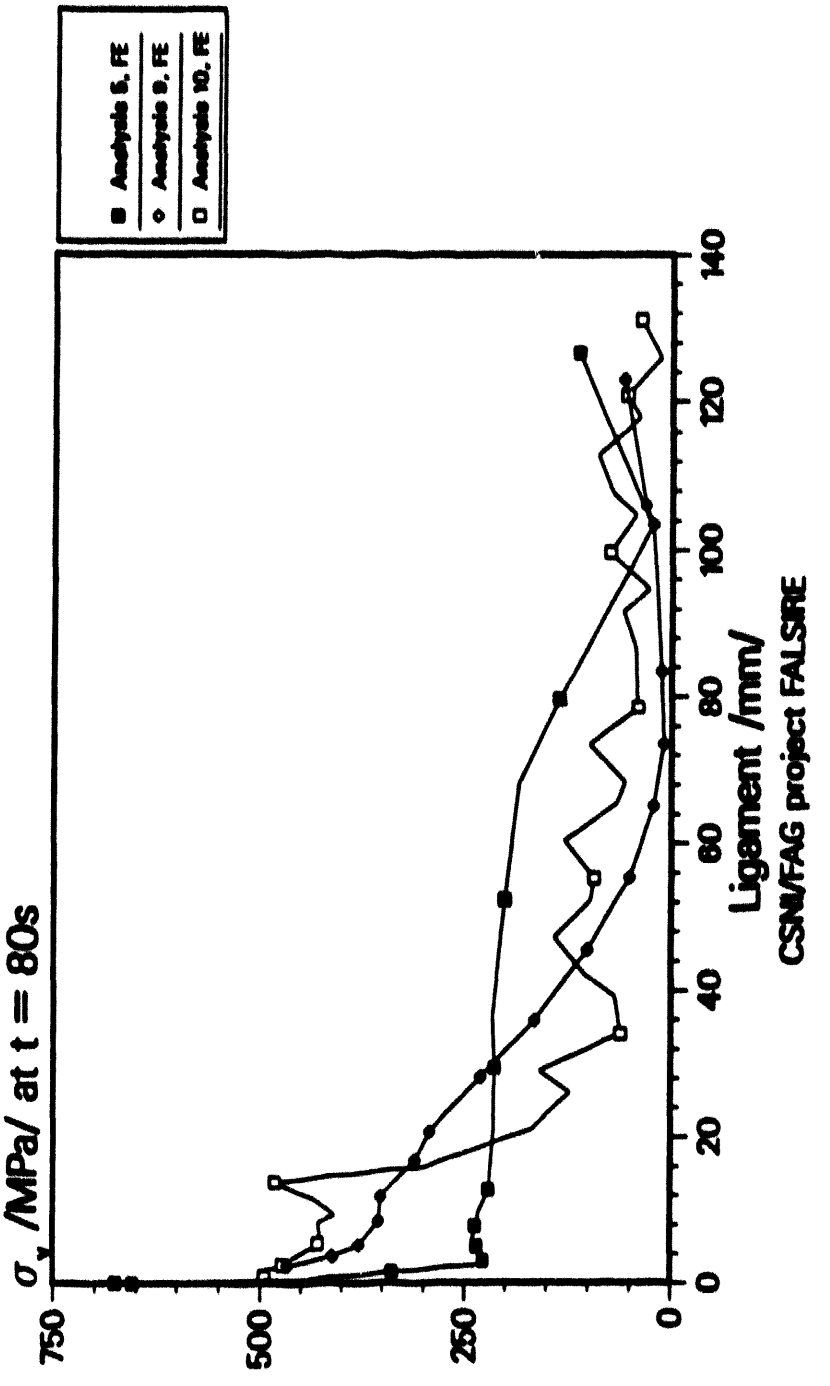

Figure 16: PTSE-2A, effective stresses on the ligament t = 80 s

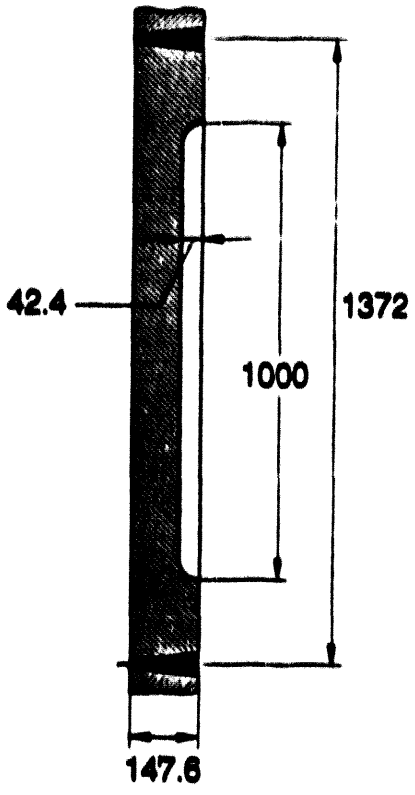

All measures in mm

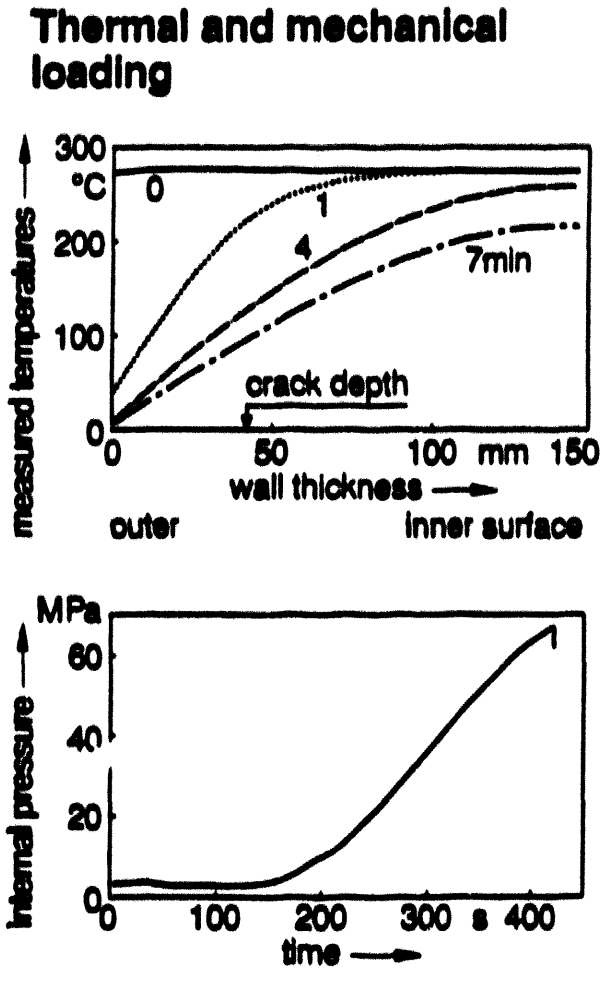

Figure 17: PTSE-2B, crack geometry and loading data for transient B

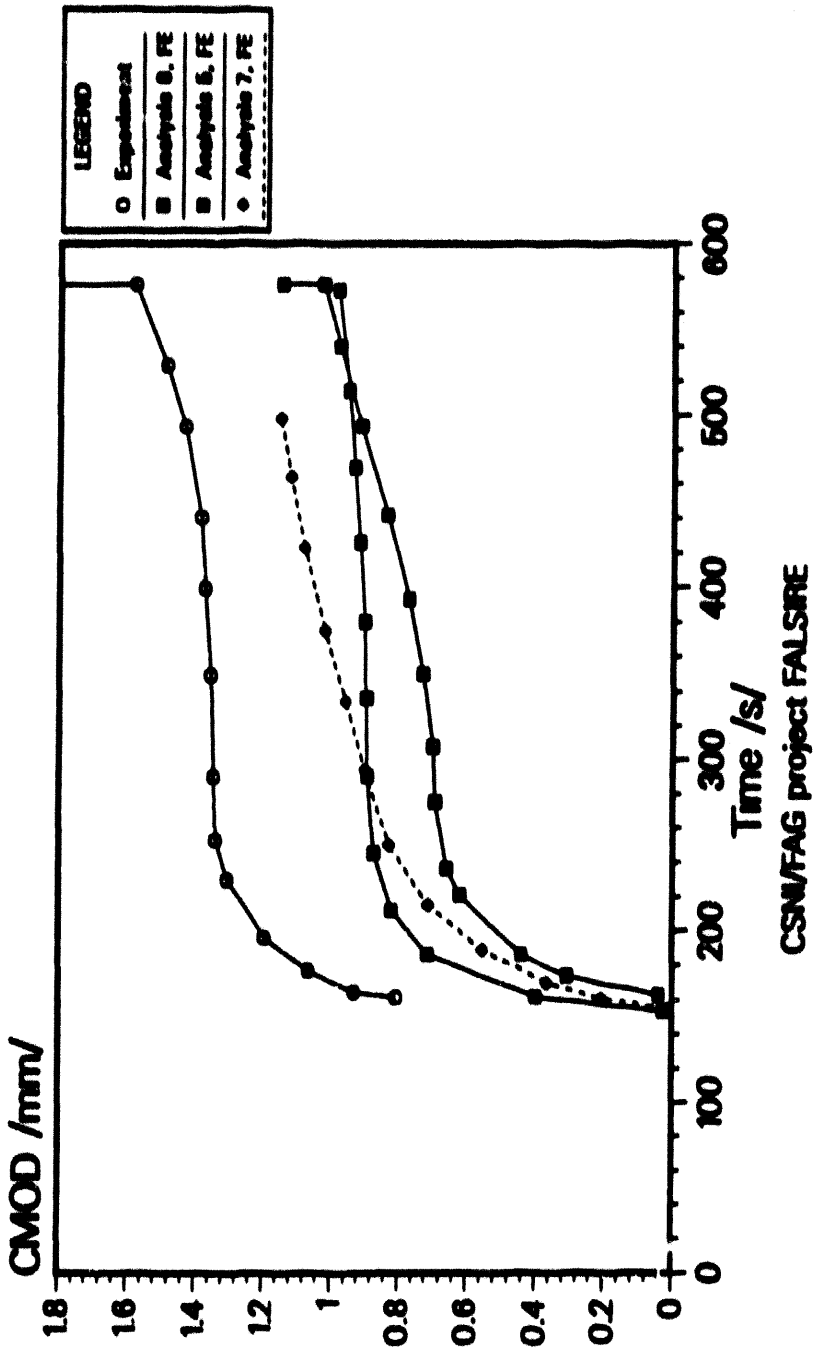

Figure 18: PTSE-2B, CMOD vs time

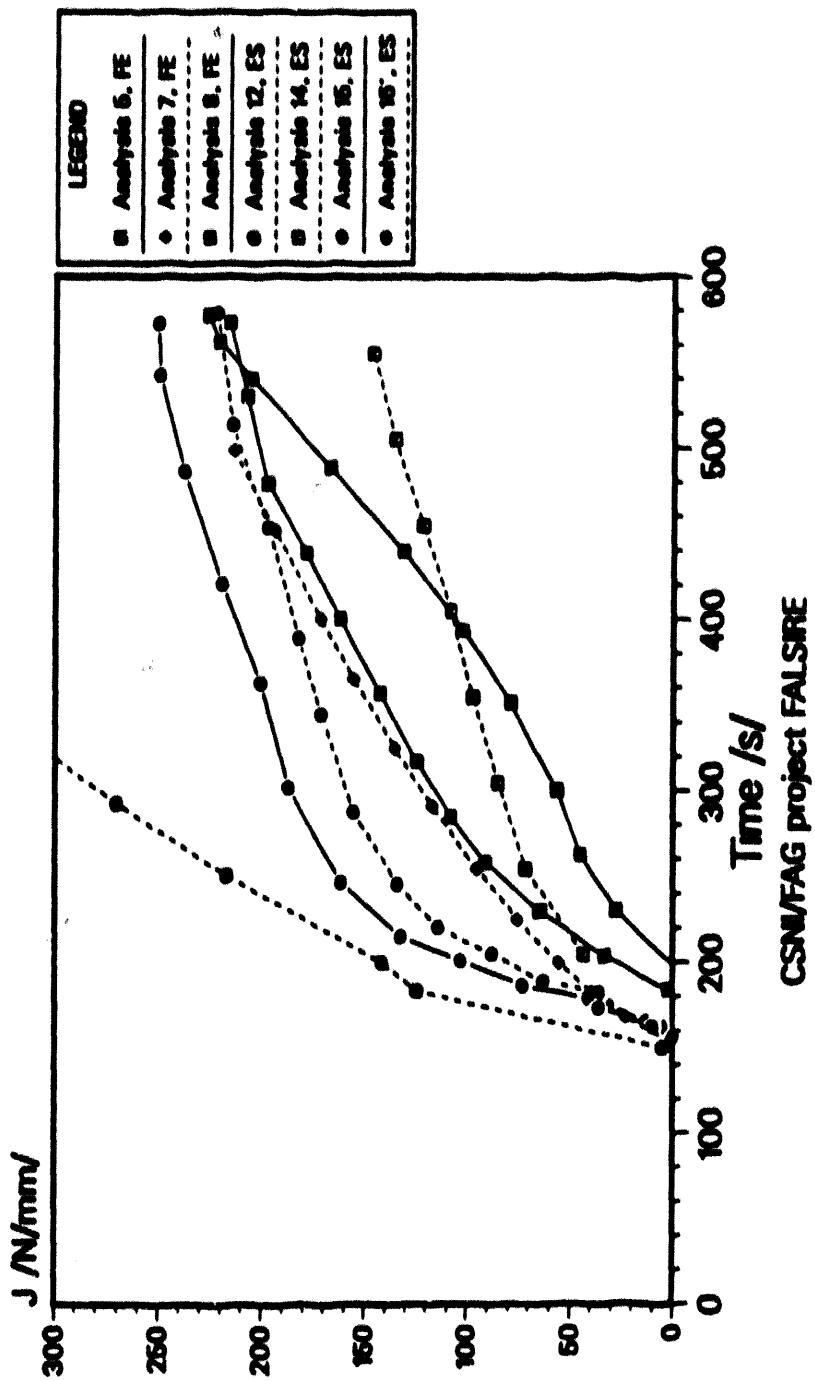

Figure 19: PTSE-2B, J-integral vs time

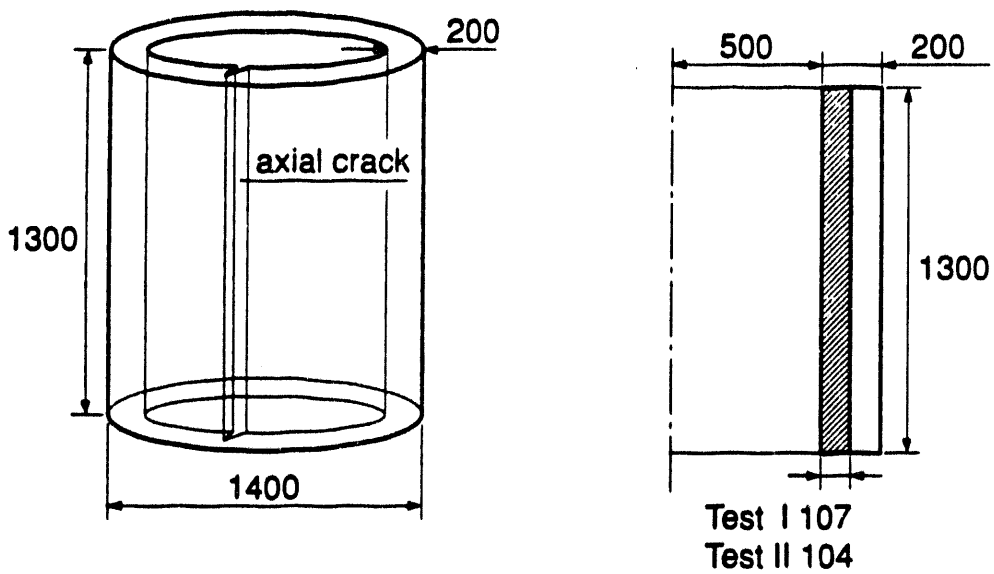

Figure 20: SC, test cylinder and crack geometry (AEA-Risley, UK)

Thermal and mechanical loading

Test I:
rotational speed:
ω = 0-2600 rpm at T=290°C

Material characterization of A 508 class 3 type steel (nonstandard quenched and tempered)

yield/ultimate stress at 290°C	540/710 MPa
charpy energy for upper shelf	90 J
NDT	?

Figure 21: SC-I, loading and material data for test I

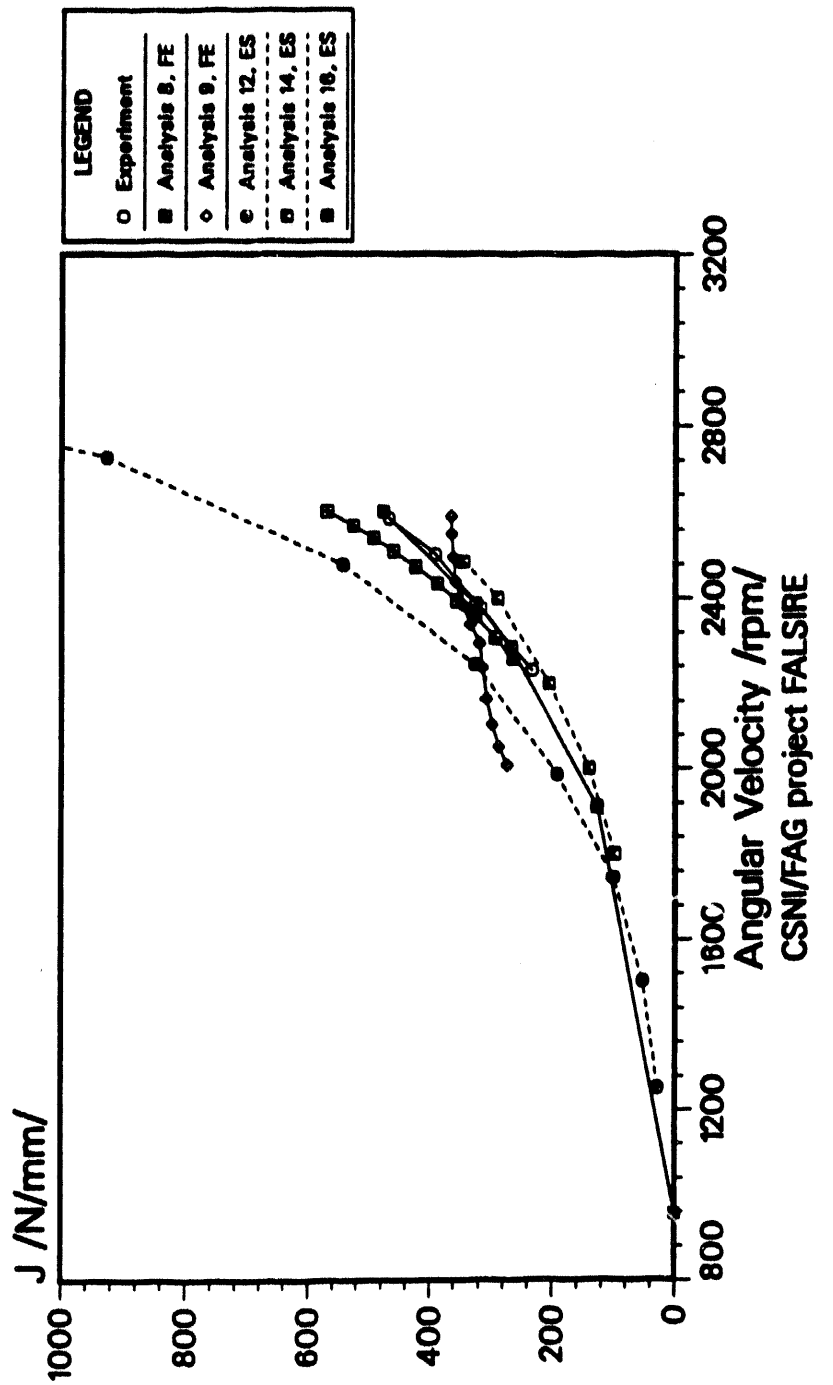

Figure 22: SC-I, J-integral vs angular velocity

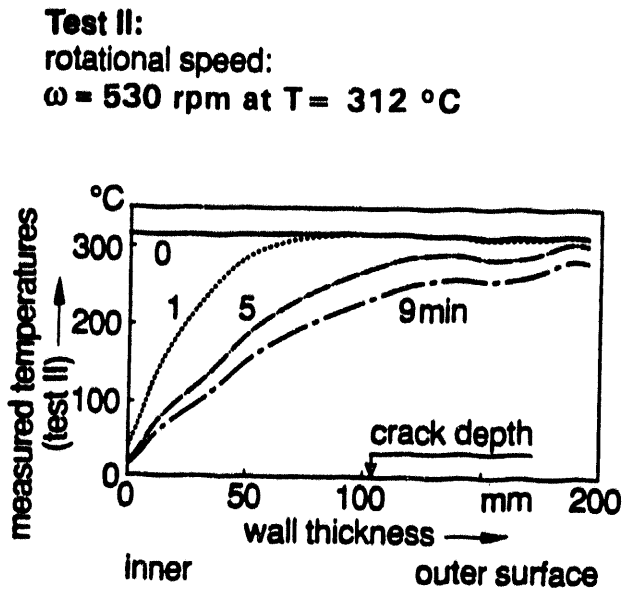

Figure 23: SC-II, loading data

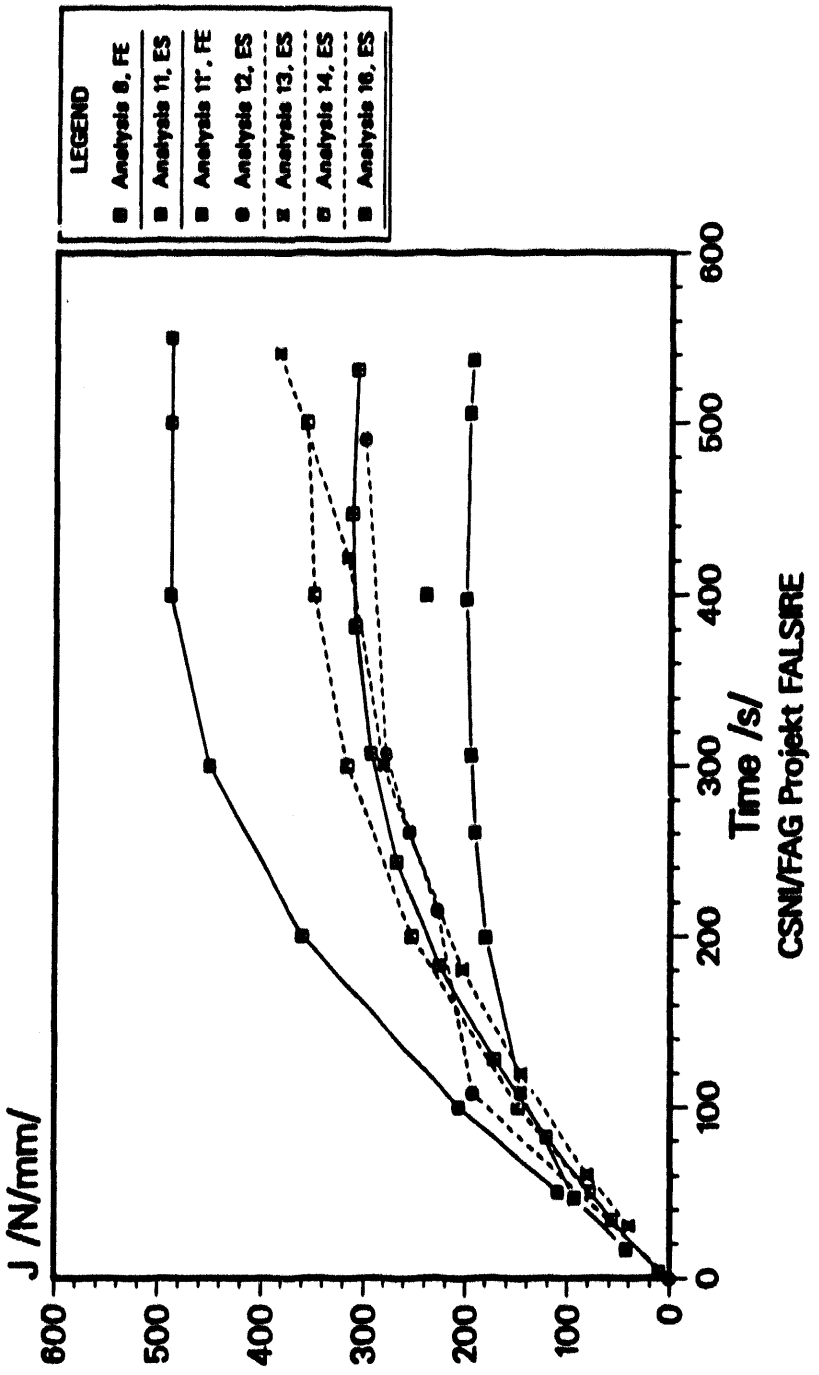

Figure 24: SC-II, J-integral vs time

PRESSURIZED THERMAL SHOCK TESTS WITH MODEL PRESSURE VESSELS MADE OF VVER-440 REACTOR PRESSURE VESSEL STEEL

by
H. Keinänen*, H. Talja*, R. Rintamaa*,
R. Ahlstrand**, P. Nurkkala**,
G. P. Karzov***, A. A. Bljumin*** and B. T. Timofeev***.

ABSTRACT

A reactor pressure vessel may be exposed to the most severe loading during its operational life, when in emergency cooling cold water is injected into it. The very high thermal stresses combined with the stresses due to internal pressure may cause initiation of an existing crack and its propagation into the pressure vessel wall which in the worst case leads to catastrophic failure of the reactor vessel.

A joint pressure vessel integrity research programme between three partners has been going on since 1990. The partners are the Prometey Institute from Russia, the Imatran Voima Oy (IVO) from Finland and the Technical Research Centre of Finland (VTT). The main objective of the research programme is to increase the reliability of the VVER-440 reactor pressure vessel safety analysis. This is achieved by providing the material property data for the VVER-440 pressure vessel steel and by producing experimental knowledge of the crack behaviour in pressurized thermal shock loading for the validation of different fracture assessment methods.

The programme is divided into four parts: pressure vessel tests, material characterization, computational fracture analyses and evaluation of the analysis methods. The testing programme comprises tests on two model pressure vessels with axial surface flaws. The second model vessel has an austenitic steel cladding. A special heat treatment is applied to the vessels prior to the tests in order to simulate the end of life toughness state of a real reactor pressure vessel.

The Prometey Institute conducts the pressure vessel tests, IVO is responsible for the test instrumentation and VTT performs the material characterization and the computational analyses. The evaluation part is carried out together. The Finnish work is funded by the Finnish Centre for Radiation and Nuclear Safety, Imatran Voima Oy and the Ministry of Trade and Industry. The pressure vessels have been manufactured in the Izorsky factory in St. Petersburg. The same factory manufactures VVER-440 reactor pressure vessels.

In this paper, the results of the tests and the computational analyses considering the first (uncladded) model vessel are discussed. Extensive three-dimensional finite-element analyses as well as simple engineering assessments are performed. The fracture behaviour of the model vessel based on fractographic examinations and test measurements is described. Both the results of pre-test analyses using initial material properties and post-test analyses using actual material properties are compared with the experimental observations. Finally, evaluation of the fracture assessment methods is performed.

*Technical Research Centre of Finland, Metals Laboratory, Metallimiehenkuja 10, 02150 Espoo, Finland
**Imatran Voima Oy, PL 112, 01601 Vantaa, Finland
***Central Research Institute of Structural Materials "Prometey", 193167, St. Petersburg, nab. reki Monastyrki 1, Russia

INTRODUCTION

Seven pressurized thermoshock tests were made with the first model pressure vessel (Fig. 1) using five different flaw geometries, Table 1. The initial flaws have all been shallow, outer-surface, axially oriented flaws at the midlength of the vessel, partially in the base metal and in a circumferential weld. In the first three tests the flaw was actually a blunt notch made by grinding. In the following tests a sharp pre-crack was used.

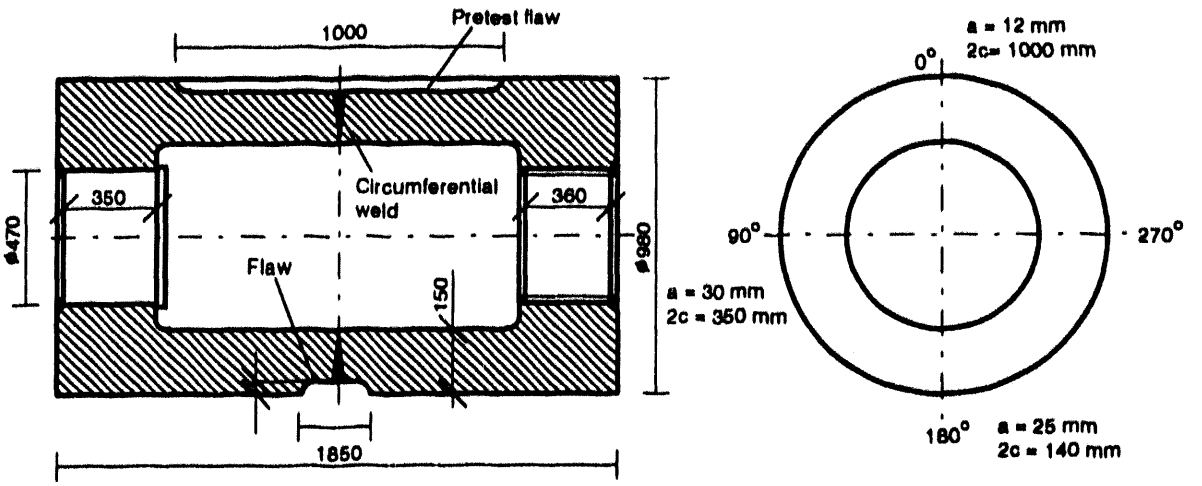

Fig. 1. The first model vessel.

Table 1. Different tests and flaw geometries. a is crack depth, 2c is crack length, p is pressure, T_c is coolant (water) temperature and T_{ini} is initial temperature.

Test nr.	1	2	3	4	5	6	7
a (mm)	12	12	25	26	30[e]	30[e]	*[d]
2c (mm)	1000	1000	250	140	350[e]	350[e]	*[d]
Flaw nr.	1	1	-	2	3	3	4
Type	notch[a]			crack[b]			
p (bar)	60	300..90[c]	335	300..40[c]	560..0[c]	600	600
T_{ini} (°C)	240	262	266	266	280	300	300
T_c (°C)	13	13	20	9	7	15	15

*[a] Mechanical notch. [b] Sharp crack produced by a special crack initiating welding technique (Rintamaa et al. 1988). [c] Due to leaks constant pressure was not maintained. *[d] The old (extended) flaw was used. [e]The values of crack depth and length were determined by ultrasonic measurement.*

MATERIAL PROPERTIES

The pressure vessel material is VVER 440 type reactor pressure vessel steel 15X2MFA. The circumferential weld has been made by submerged arc welding using wire Sv-10XMFT and flux AH-42. The vessel has been subjected to thermal heat treatment to simulate the radiation

embrittlement of the steel: annealing 1000 °C, holding 4 hours, cooling in oil, tempering 620 °C 10 hours, cooling in air.

The thermal material property values for the analyses were obtained from the Prometey Institute, Table 2. The measured stress-strain curves for both base and weld material are presented in Fig 2. Fig. 3 presents the Charpy-V impact energy at different temperatures. Unfortunately, at the time of preparation of this manuscript, the results of J-R testing are not yet available.

Table 2. Thermal material property values. T is temperature, α is thermal expansion coefficient, λ is thermal conductivity and d is thermal diffusivity.

T (C°)	20	150	300
α (10^{-6}1/°C) (base and weld)	11.7	12.15	12.7
λ (W/(m°C)) (base and weld)	37	37	37
d (mm^2/s) (base and weld)	9.970	9.775	9.550

FLAW PREPARATION

In tests 1, 2, 3 and 4 the flaw was a blunt notch manufactured by grinding. In tests 4, 5, 6 and 7 a sharp crack was used. The crack was manufactured by filling the grinded notch by weld deposites. Welding data and parameters are given in Table 3.

Table 3. Welding data and parameters for crack preparation (manual metal arc welding).

Electrode	Fox Dur 500 ϕ 3,25 mm
Chemical composition	0,4 % C, 1,2 % Si, 1,2 % Mn, 2,8 % Cr
Current and velocity	215 A DC, 12 cm/min

TEST CONFIGURATION

The pressure vessel is first heated to approximately 300 °C using resistors. At the same time the vessel is pressurized by water. Just before the test the heating resistors are lifted up. The vessel is subjected to sudden flow of cold (0...20 °C) water around the outer surface. Due to the capacity of cooling water tanks the coolant flow is effective during the first two minutes. The test configuration is presented in Fig. 4.

MEASUREMENTS DURING THE TESTS

The measurements were performed by Imatran Voima Oy (Nurkkala 1991a, 1991b). Temperatures were measured on the outside surface of the vessel and inside the vessel wall using thermocouples. Strains were measured on the outside surface using weldable strain gages. In addition, crack opening displacement and pressure was measured in tests 6 and 7. All transducers were set to zero after pressurization before the beginning of the thermal transient.

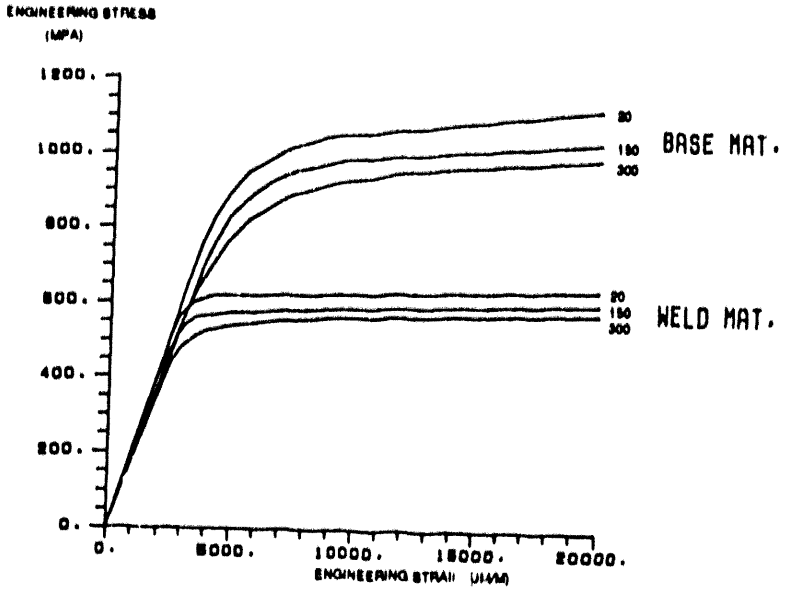

Fig. 2. *The measured stress-strain curves for the base and weld materials.*

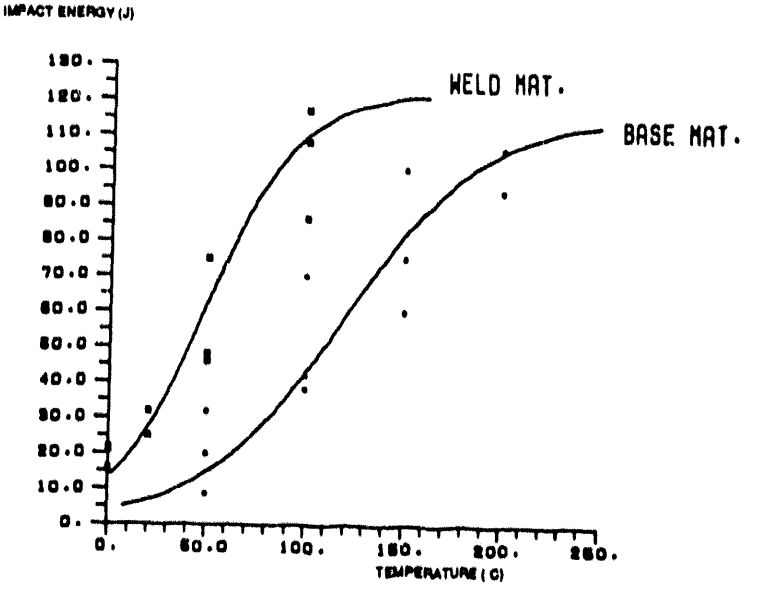

Fig. 3. *The measured Charpy-V impact energy at different temperatures.*

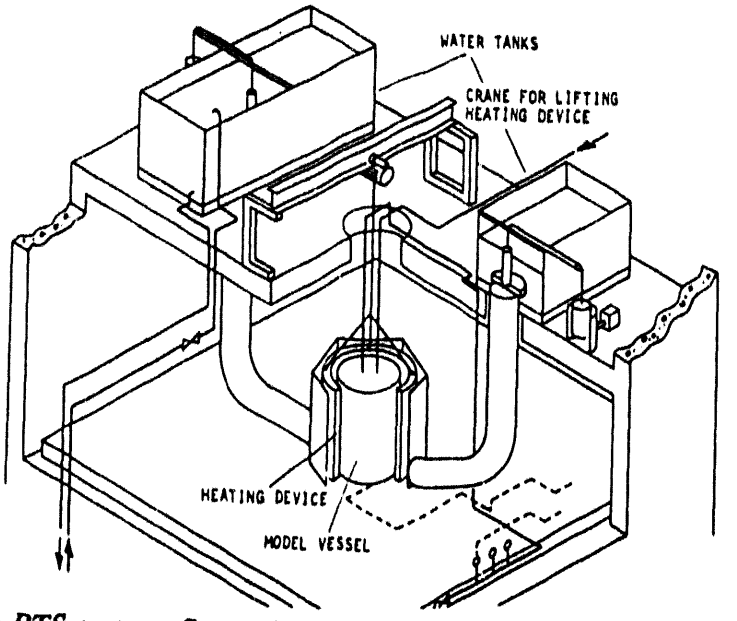

Fig. 4. *The PTS test configuration.*

PRE-TESTS CALCULATIONS

The temperature field calculations were made using a computer code based on the Fourier series (Raiko & Mikkola 1991). As the next step, the hoop stresses due to internal pressure and thermal transient were calculated analytically using the normal "thick shell"- formula. The hoop stress due to temperature transient was obtained from (Timoshenko & Goodier 1982)

$$\sigma_h = \frac{\alpha E}{1-\nu}\left[\frac{r^2+a^2}{(b^2-a^2)r^2}\int_a^b T(r)rdr + \frac{1}{r^2}\int_a^r T(r)rdr - T(r)\right] , \qquad (1)$$

where α is the thermal expansion coefficient ($12{,}0 \cdot 10^{-6}$), E is Young's modulus (195 GPa), ν is Poisson's ratio (0,3), T(r) is the function describing the temperature variation in the wall, b is the outside radius, a is the inside radius and r is the radius of the location of interest.

Linear elastic fracture mechanics was applied to assess the severity of the flaws. The VTTSIF program (Kantola 1986) based on the influence function method (Besuner 1977) was used to calculate stress intensity factor values. For the calculation the stress distribution in an unflawed structure and geometry-dependent influence functions were needed. Flaws 2 and 3 (Table 1) were considered as semi-elliptical flaws, and the stress intensity factor formulae presented by Newman and Raju (1983) were used.

The initial shape of flaw 2 (Table 1) was idealised as a semi-ellipse with semi-axes of 25 mm and 70 mm. The calculated stress intensity factor values at the deepest point are shown in Fig. 5. Flaw 3 was idealised as a semi-ellipse with semi-axes of 30 mm and 175 mm. The results for the stress intensity factor value at the deepest point of the crack are shown in Fig. 6.

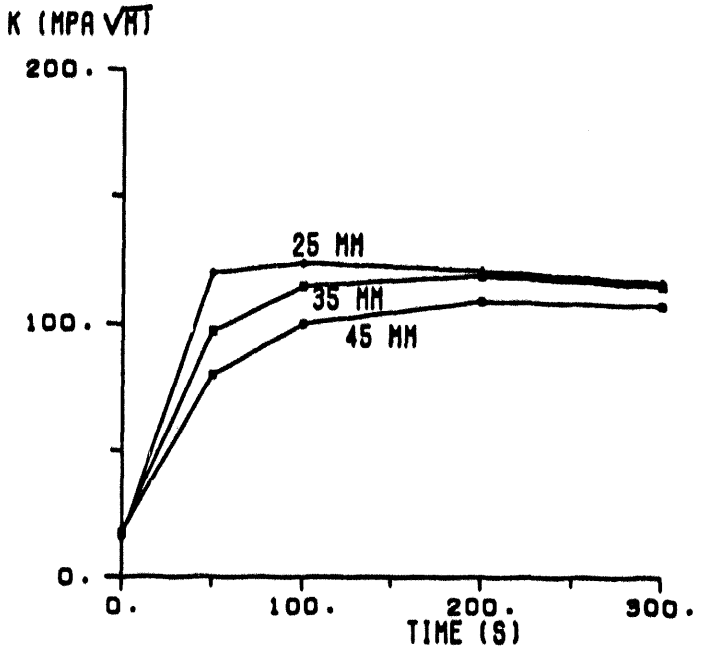

Fig. 5. The values of stress intensity factor due to internal pressure 300 bar and thermal shock, flaw 2.

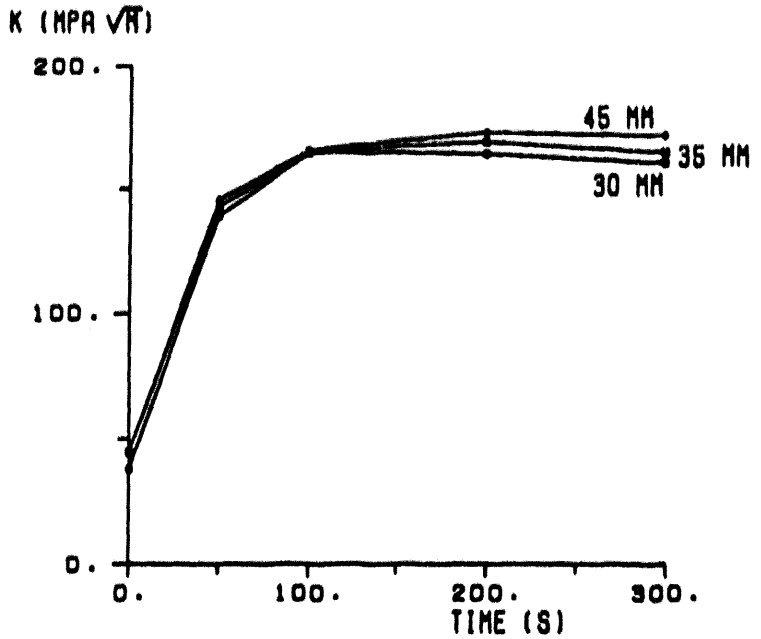

Fig. 6. *The values of stress intensity factor due to internal pressure 600 bar and thermal shock, flaw 3.*

The calculated stress intensity factor for flaw 3 is presented as a function of crack tip temperature for pressure loads of 300 bar and 600 bar (including thermal transient) in Fig. 7 together with the estimated fracture initiation toughness values of the weld material provided by the Prometey Institute.

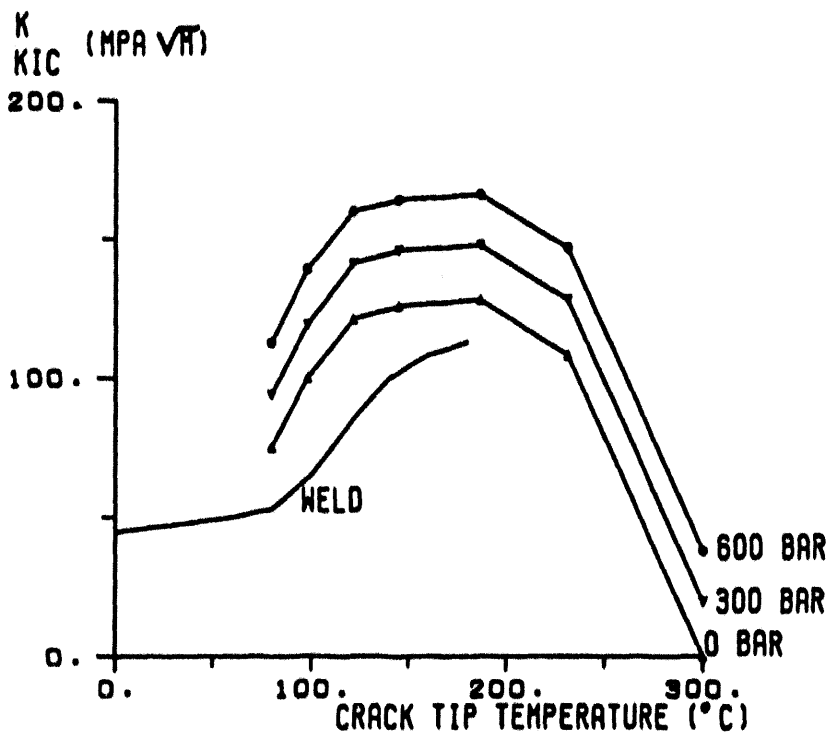

Fig. 7. *The calculated stress intensity factor for flaw 3 as a function of crack tip temperature for different pressure loads (including thermal transient) together with the preliminary fracture initiation toughness values of the weld material provided by the Prometey Institute.*

FLAW BEHAVIOUR

According to the measurements and other observations, no crack initiation occurred in tests 1 - 5. In tests 1, 2 and 3 the crack was actually a blunt notch. In tests 4 and 5 a sharp crack was inroduced but constant pressure was not maintained during the tests due to leaks. According to the measured strain and crack mouth opening displacement values the crack already tested in test 5 initiated and propagated in test 6. The crack initiation occurred at the time of round 155 s from the start of cooling. In test 7 no o[illegible]itions of crack initiation could be observed on the basis of the measurements.

On the basis of the macroscopic examination of the fracture surface (see Appendix) following conclusions were made:

- Before test 6 the initial depth of the crack has been approximately 30-40 mm in the middle area of the crack. The initial crack length has been 350 mm.
- The crack has initiated and arrested during test 6. The fracture surface reveals brittle or brittle/ductile morphology.
- Considerable amounth of crack propagation has been developed in both ends of the crack ('tunneling').

POST-TESTS CALCULATIONS

Numerical post-test calculation was made for studying the case of test 6, in which crack initiated to grow and arrested. In the finite-element calculation the ADINA-T and ADINA codes were used. The VTTVIRT code (Talja 1987) was used to calculate J-integral values.

The temperature field was calculated using a fine meshed line model. The inside surface of the vessel was assumed to be insulated. The heat transfer between the vessel wall and the coolant was modelled for the outside surface. The heat transfer coefficient h between the cooling water and the vessel outside surface is presented in Table 4. These values were determined on the basis of pre-test experiments (Prometey) and the measured surface temperatures. These values are consistent with those presented in literature (e.g. Kordisch et al. 1990). The calculated temperatures are compared to measured ones in Fig. 8.

Table 4. The heat transfer coefficient between the cooling water and the vessel wall.

T (°C)	40	80	90	95	100	105	110	300
h (kW/(m^2°C))	2.5	3.3	6.0	8.0	15.0	20.0	30.0	40.0

The three dimensional model is presented in Fig. 9. Only the straight part of the vessel was modelled (length of the model was 385 mm), because the end effects were small (Talja & Keinänen 1991). The flaw was modelled having a constant depth and quarter-circular ends. The appropriate symmetry boundary conditions and the axial traction due to internal pressure were modelled and the measured pressure-time-dependency was used. Fig. 10 compares the calculated crack opening displacement to the measured one in the middle of the crack. Fig. 11 compares the calculated hoop strain far from the crack to the measured one.

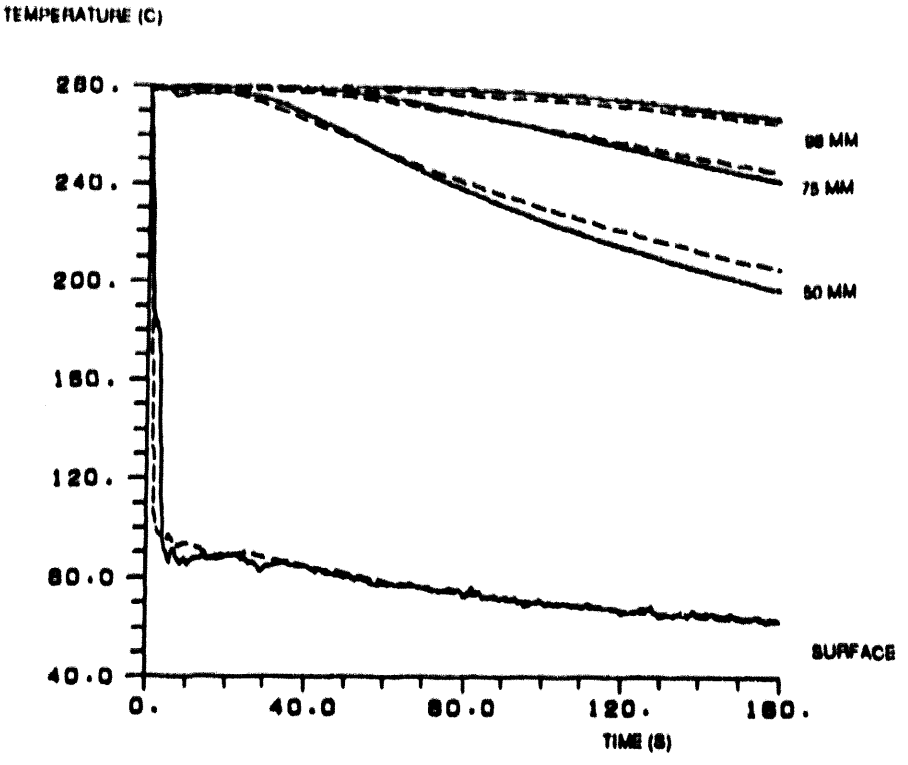

Fig. 8. *Comparison of calculated temperatures to measured ones, test 6. Dashed lines present calculated values and solid lines measured values.*

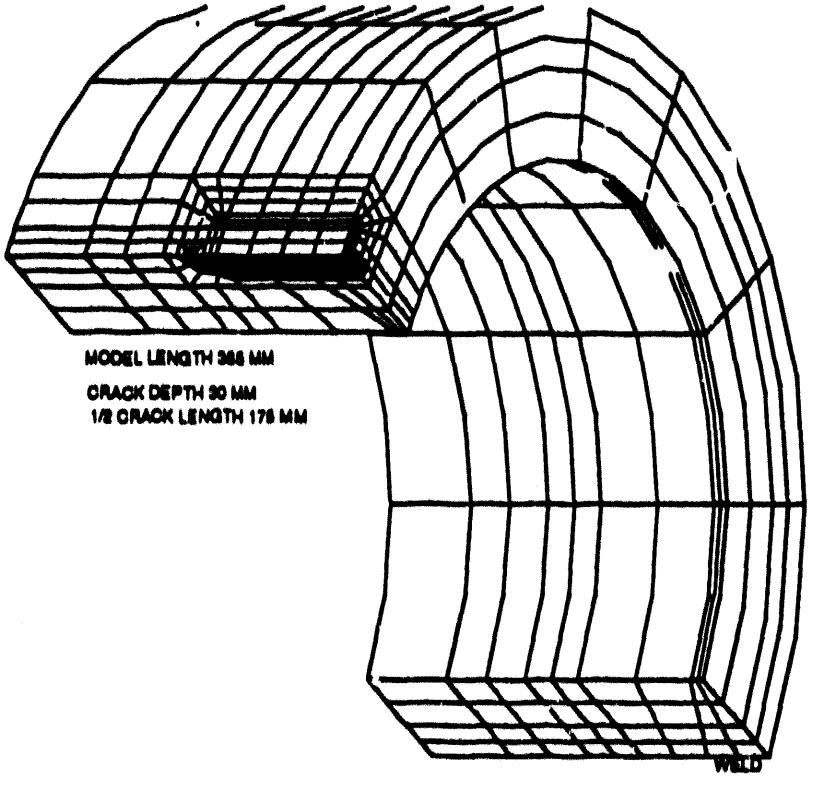

Fig. 9. *The three dimensional model.*

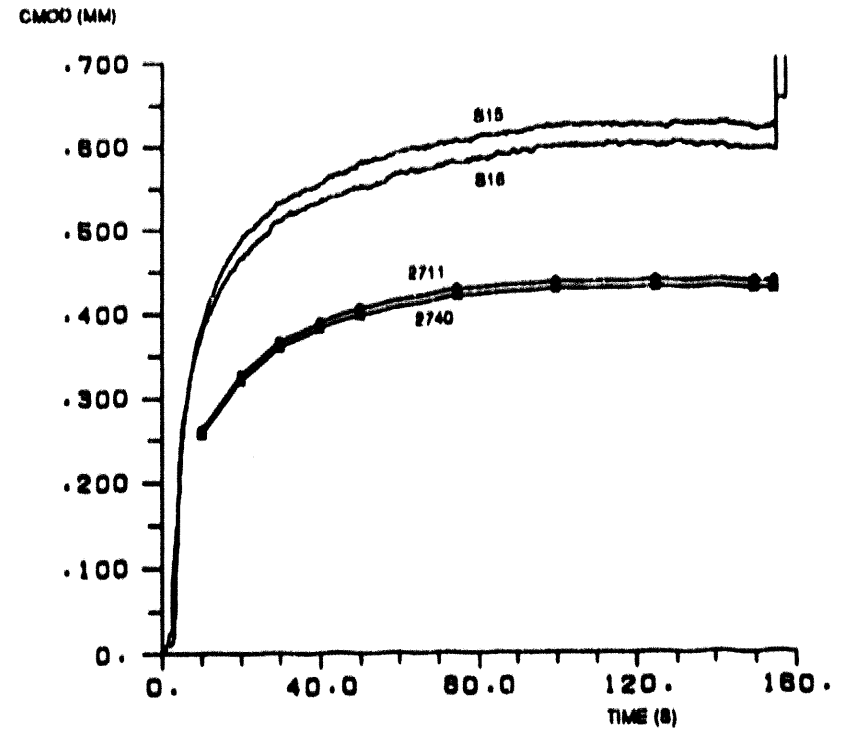

Fig. 10. *Comparison of calculated and measured crack mouth opening displacement in the middle of the crack.*

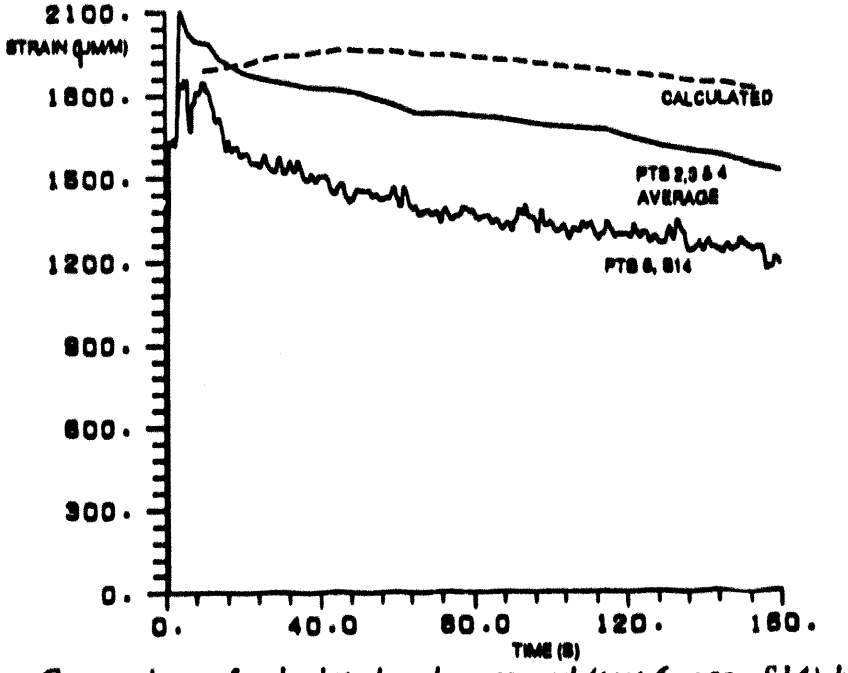

Fig. 11. *Comparison of calculated and measured (test 6, gage S14) hoop strain far from the crack. The average of the hoop strain measurements in tests 2, 3 and 4 is also presented.*

J-integral values were calculated using the VTTVIRT-code (Talja 1987) in which the calculation of the J-integral is done by the virtual crack extension method. The stress intensity factor was calculated assuming a plane strain condition and small scale yielding, thus

$$K = \sqrt{\frac{E}{1-\nu^2} J} \qquad (2)$$

The calculated stress intensity factors in two locations are compared to the preliminary material fracture toughness data in Fig. 12. The reasons for that the stress intensity factor value according to the finite-element calculation exceeds the analytical value are the larger crack area in the finite-element model and the linear elasticity in the analytical calculation.

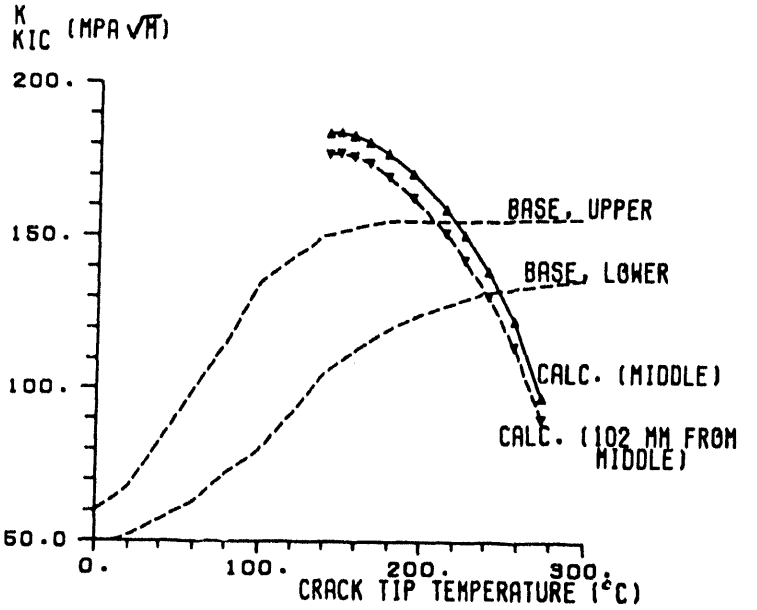

Fig. 12. Calculated stress intensity factors (tests 6) and the preliminary material fracture toughness data.

DISCUSSION AND FUTURE PLANS

The behaviour of a model pressure vessel made of a steel 15X2MFA has been studied in a pressurized thermal shock loading. Seven PTS tests were performed with the same model pressure vessel using five different flaw geometries. According to the measurements and a post-test ultrasonic examination of the crack front, the successful sixth test led to remarkable crack extension followed by crack arrest. Due to the lack of the relevant material property data at the time of preparation of this manuscript only some preliminary conclusions can be made:

- Generally good agreement was observed between the calculated and measured values.
- The crack initiation time corresponded the time at which the calculated stress intensity factor reached its maximum.
- Main crack extension was observed near the crack ends. To clarify this effect the actual crack shape should be modelled more precisely.
- The circumferential weld located at the midlength of the vessel was much tougher than the base material.

The analytical stress intensity calculations showed that in the case of a PTS loading the crack geometry (aspect ratio (a/c)) has a strong effect on the arrest behaviour: a short crack has a clear tendency to arrest because the K_I value decreases with increasing crack depth. In the case of a long crack, the situation is the reverse: an initiated crack would more probably penetrate the wall or at least extend significantly.

The differences between calculated and measured crack mouth opening displacement values stem from two reasons. One is the uncertainty in the measurement due to large strains. The other is the real initial depth of the crack which varies from 30 to 40 mm. In the analysis crack depth was 30 mm.

The three-dimensional finite-element analysis will be repeated using a deeper crack. Also, the measured material toughness properties, which are available in the beginning of October 1992, will be used in the results interpretation. The conditions for crack arrest will also be studied in the near future.

The next PTS-test will be performed using a cladded model vessel. The results of the test and analyses will be available next year.

ACKNOWLEDGEMENT

The participants of this co-operation are the Central Research Institute for Structural Materials "Prometey" from Russia, Imatran Voima Oy (IVO) from Finland and the Technical Research Centre of Finland (VTT). The Finnish part is funded by the Finnish Centre for Radiation and Nuclear Safety, the Imatran Voima Oy and the Ministry of Trade and Industry. The pressure vessels have been manufactured in the Izorsky factory in St. Petersburg.

REFERENCES

Besuner, P. M. 1977. The influence function method for fracture mechanics and residual fatigue life analysis of cracked components under complex stress fields. Nuclear Engineering & Design 43, pp. 115 - 154.

Kantola, K. 1986. Calculation of stress intensity factors using the influence function method. Helsinki. Technical Research Centre of Finland, Nuclear Engineering Laboratory, Research Notes YRT-2/86, 35 p (in Finnish).

Keinänen, Heikki, Talja, Heli, Lehtonen, Mikko, Rintamaa, Rauno, Ahlstrand, Ralf, Nurkkala, Pekka, Rajamäki, Pentti, Bljumin, Alexander & Timofeev, Boris. Finite-element pre-analyses for pressurized thermoshock tests. Vessel I: Tests 4, 5 and 6. Espoo 1992, VTT, VTT Publications 103. 35 p.

Kordisch, H., Talja, H. & Neubrech, G. E. 1990. Analysis of initiation and growth of a circumferential crack in the HDR-RPV-cylinder under pressurized thermal shock. Nuclear Engineering and Design 124, pp. 171-192.

Newman, J. C. & Raju, I. S. 1983. Stress-intensity factor equations for cracks in three-dimensional bodies. In: ASTM STP 791, Fracture Mechanics, Volume I: Theory and analysis. J. C. Lewis and George Sines (eds.). Philadelphia, PA, American Society for Testing and Materials, pp. 238 - 265.

Nurkkala, P. 1991a. Prometey PTS #1...#5 yhteenveto. Imatran Voima Oy, Work Report DLM1-G320-0299 (in Finnish).

Nurkkala, P. 1991b. Termoshokkikoe PTS #6, Prometey. Imatran Voima Oy, Work Report DLM1-G320-0361 (in Finnish).

Raiko, H. & Mikkola, T. P. J. 1991. Fracture assessment program system for practical engineering applications. IV Suomen Mekaniikkapäivät, Lappeenranta 6.6.1991. Lappeenranta. Lappeenranta University of Technology. pp. 335 - 349.

Rintamaa, R., Törrönen, K., Keinänen, H., Sarkimo, M., Sundell, H., Talja, H. & Ikonen, K. 1988. Prevention of catastrophic failure of pressure vessels and piping. Results of pressure test with a large vessel (HC1 test), Espoo, Technical Research Centre of Finland, Research Reports 515, 52 p.

Talja, H. 1987. Elastis-plastiset murtumisparametrit ja niiden laskeminen elementtimenetelmällä. Espoo, Helsinki University of Technology, Licenciate Thesis. 113 s (in Finnish).

Talja, H. & Keinänen, H. 1991. Pre-test analyses for pressurized thermoshock tests. Vessel I. Espoo, Technical Research Centre of Finland, Research Reports 746. 38 p.

Timoshenko, S. P. & Goodier, J. N. 1982. Theory of Elasticity. 3rd edition. Tokyo, Japan, McGraw-Hill. 567 p.

One half of the fracture surface of vessel I.

The real wall thickness is reduced (initially 150 mm). The initial crack is shown by a solid line.

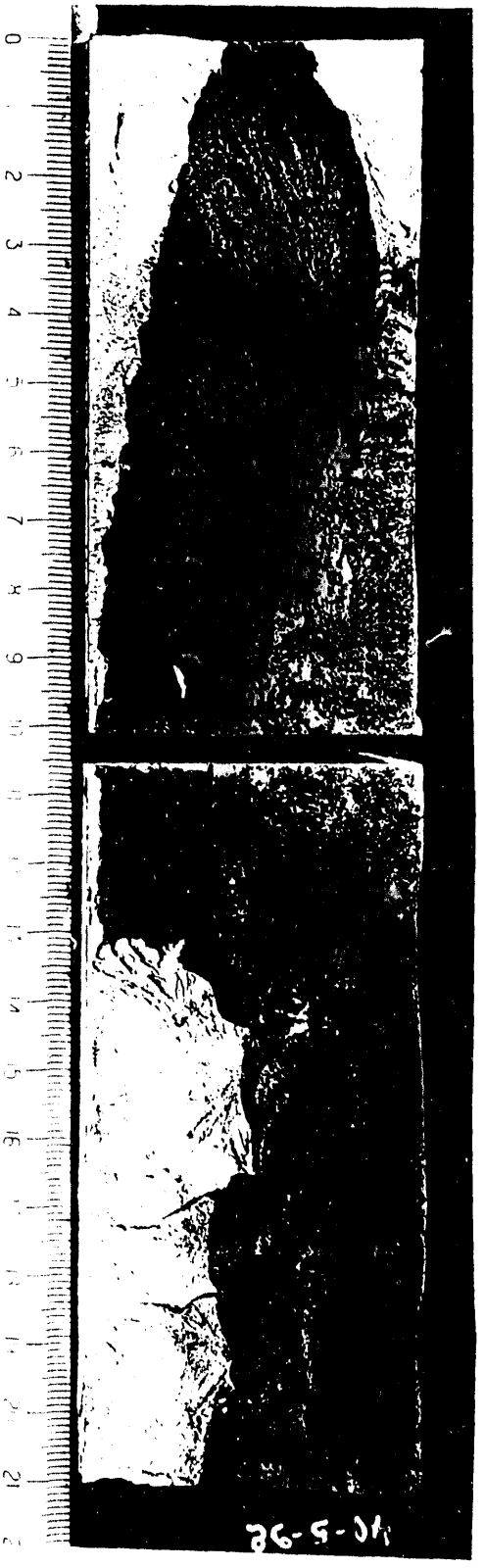

← OUTSIDE SURFACE

HAK/d:\pts\reports\oakridge.tex

LARGE-SCALE THERMAL-SHOCK EXPERIMENTS WITH CLAD AND UNCLAD STEEL CYLINDERS*

R. D. Cheverton
Oak Ridge National Laboratory
Oak Ridge, Tennessee

Abstract

Flaw behavior trends associated with pressurized-thermal-shock (PTS) loading of pressurized-water-reactor pressure vessels have been under investigation at the Oak Ridge National Laboratory for nearly 20 years. During that time, twelve thermal-shock experiments with thick-walled (152 mm) steel cylinders were conducted as a part of the investigations. The first eight experiments were conducted with unclad cylinders initially containing shallow (8–19 mm) two-dimensional and semicircular inner-surface flaws. These experiments demonstrated, in good agreement with linear elastic fracture mechanics, crack initiation and arrest, a series of initiation/arrest events with deep penetration of the wall, long crack jumps, arrest with the stress intensity factor (K_I) increasing with crack depth, extensive surface extension of an initially short and shallow (semicircular) flaw, and warm prestressing with $\dot{K}_I \leq 0$.

The remaining four experiments were conducted with clad cylinders containing initially shallow (19–24 mm) semielliptical subclad and surface flaws at the inner surface. In the first of these experiments one of six equally spaced (60°) "identical" subclad flaws extended nearly the length of the cylinder (1220 mm) beneath the cladding (no crack extension into the cladding) and nearly 50% of the wall, radially. For the final experiment, four of the semielliptical subclad flaws that had not propagated previously were converted to surface flaws, and they experienced extensive extension beneath the cladding with no cracking of the cladding.

Information from this series of thermal-shock experiments is being used in the evaluation of the PTS issue.

*Research sponsored by the Office of Nuclear Regulatory Research, U.S. Nuclear Regulatory Commission under Interagency Agreement 1886-8011-9B with the U.S. Department of Energy under Contract DE-AC05-84OR21400 with Martin Marietta Energy Systems, Inc.

THERMAL-SHOCK EXPERIMENTS WITH LARGE, CLAD AND UNCLAD TEST CYLINDERS

1. INTRODUCTION

The pressurized thermal shock (PTS) issue pertaining to pressurized water reactors (PWRs) has been under intensive investigation by the Nuclear Regulatory Commission (NRC), reactor vendors, and utilities since the early 1970s, and these efforts resulted in issuance, by the NRC, of the PTS Rule[1] and Regulatory Guide 1.154 (Ref. 2). As an aid in formulating the rule and Regulatory Guide, the NRC sponsored the Integrated Pressurized Thermal Shock (IPTS) Program, which involved development of probabilistic models and the subsequent calculation of the frequency of vessel failure for three specific plants.[3–5] The validity of the deterministic aspects of the probabilistic fracture mechanics model included in the IPTS methodology was established to a large extent on the basis of a series of thermal-shock experiments conducted with thick-walled steel cylinders.[6] These experiments were conducted without cladding, which normally exists on the inner surface of PWR pressure vessels and presumably influences the behavior of flaws in the proximity of the cladding. An "acceptable" method for including cladding in the IPTS studies was to account for its relatively low thermal conductivity in the thermal analysis and its relatively high coefficient of thermal expansion in the stress analysis, and to assume that initial flaws penetrated the cladding (surface flaws) and that the cladding had the same fracture toughness properties, including irradiation effects, as the base material. More recently, there has been a desire to obtain a better understanding of the role of cladding. To address this need, "typical" cladding material has been irradiated,[7] clad-plate[8,9] and clad-beam[10] tests with mechanical loading have been conducted, and thermal-shock experiments, similar to the earlier ones, but with cladding on the inner surface, have been conducted.[11]

There has also been a growing interest in the effect of constraint on fracture toughness for PTS-related conditions. The IPTS studies indicated that most flaws resulting in calculated failures were very shallow (crack depth <15 mm), and beam experiments[12] indicate that such flaws may have elevated toughness (relative to plane-strain values) associated with them (attributed to reduced constraint). Yet, there is some concern that out-of-plane tensile stress, a relatively high yield stress, and/or a steep gradient in stress[13,14] could, at least to some extent, negate the elevation. The thermal-shock experiments tend to address these phenomena because shallow flaws, steep stress gradients, a relatively high yield stress, and a biaxial stress state are involved.

Another area of recent interest pertains to the possible existence and effects of low-toughness sites, which, in principle, could result in a structure effective crack-initiation fracture toughness as low as the crack arrest toughness of the material surrounding the low-toughness site.[15] The thermal-shock experiments tend to address this subject because of the extensive length of crack front involved, which increases the chances of a low-toughness site existing. However, no welds, other than the cladding (weld deposition), were included in the test cylinders, and it may be that low-toughness sites are more likely to exist in welds than base material.

The purpose of this paper is to review and compare the thermal-shock experiments with and without cladding, particularly in light of present interests in flaw-depth, stress-gradient, yield-stress, and stress-state effects on effective fracture toughness and the concern over low-toughness sites. Detailed analyses of the experiments are still being conducted, and thus this paper does not represent a final evaluation. Presumably there is more to be learned from these experiments as our insights and analytical tools are improved.

2. OBJECTIVES OF THERMAL-SHOCK EXPERIMENTS

As indicated in Figs. 1 and 2 and discussed in Ref. 11, a linear elastic fracture mechanics (LEFM) analysis of a PWR vessel subjected to PTS loading indicates (1) essentially a biaxial stress state; (2) steep gradients in temperature, stress, stress intensity factor (K_I) and critical values of K_I corresponding to initiation (incipient propagation) (K_{Ic}) and arrest (K_{Ia}); (3) a series of initiation and arrest events; (4) initiation of very shallow flaws; (5) arrest with K_I increasing with increasing crack depth (in a standard crack-arrest test K_I decreases with increasing crack depth); (6) warm prestressing (WPS) with $\dot{K}_I < 0$; (7) the possibility of long crack jumps that might introduce dynamic effects; and (8) at least in the absence of cladding a short surface crack could extend on the surface to become a long flaw with an increased potential for propagating radially. These indicated events and features raised questions about the applicability of lab-specimen K_{Ic} and K_{Ia} data for PTS analyses (constraint effects associated with shallow flaws and steep stress gradients; arrested crack fronts; arrest with $dK_I/da > 0$) and about whether warm prestressing, dynamic events, and extensive surface extension would take place under PTS conditions. Obtaining answers to these questions was a major part of the objective of the thermal-shock program.

The objective also included, of course, a determination of the behavior of flaws in the presence of cladding. By comparison with an unclad vessel, the presence of cladding (1) reduces the severity of the PTS thermal shock (relatively low thermal conductivity) and thus tends to reduce the potential for propagation of flaws; and (2) introduces high thermal stresses near the surface (relatively high coefficient of thermal expansion) and thus tends to increase the potential for propagation of surface flaws. As suggested in Refs. 16–18, the cladding provides a crack-mouth closing force for subclad flaws (Fig. 3) that reduces K_I relative to that for a surface flaw. The crack-mouth closing force is essentially equal to the stress in the cladding times the thickness of the cladding, and for severe thermal-shock loading conditions this stress is the "yield" stress. The possible benefit of cladding for a subclad flaw, relative to a surface flaw and in terms of reducing K_I for the portion of the crack front in the base material, is dependent on the extent of stretching of the cladding over the crack. As the stretching increases, the benefit decreases. Because of complexities associated with modeling of the crack tip at the clad/base interface, the accuracy of the calculated extent of stretching is quite uncertain. Thus, an experimental determination is necessary and was included in the scope of the thermal-shock experiments with a clad cylinder.[11]

Another cladding-related phenomenon that is difficult to model at the present time is the tendency for either a surface or subclad flaw to propagate beneath the cladding. If subclad propagation (tunneling) is restricted, limiting the length of the flaw, the potential for radial propagation will be less.

3. DESCRIPTION OF EXPERIMENTS

3.1 Test Cylinders

Nine thermal-shock experiments (TSE-4, 5, 5A, 6–11) are discussed in this paper. Each was conducted with a test cylinder fabricated from A508 steel with class-2 chemistry. Three different heat treatments were used, the difference being in the tempering temperature following quenching in water from the austenitizing temperature (860°C). At the time of quenching, the cylinders were oversize so that final machining would preclude significant residual stresses. The length of the cylinders was sufficient to eliminate significant end effects in the central portion of the cylinder. New, unclad, test cylinders were used for each of the first five experiments (TSE-4, 5, 5A, 6, and 7), and one additional cylinder, clad on the inner surface, was used for TSE-8, 9, 10, and 11. Two cladding materials were used for the clad cylinder (Fig. 4), and both were applied by the strip-cladding, submerged-arc process. Stainless steel 304L was applied to a 90° segment, while the remaining 270° was clad with Inconel 600. All test cylinders but the one for TSE-4 were

the same in length and outside diameter. The test cylinder for TSE-4 was smaller and had a small enough ratio of diameter to wall thickness to preclude deep penetration of the flaw. A summary of descriptive material is provided in Table 1, and more detail is given in Refs. 6, 11, 19, 20, and 21. Photographs of a clad and unclad test cylinder are shown in Figs. 5 and 6.

Table 1. Summary of test conditions for ORNL thermal shock experiments

Parameter	Experiment					
	TSE-4	TSE-5	TSE-5A	TSE-6	TSE-7	TSE-8,9,10,11
Cylinder dimensions, mm						
Outside diameter	533	991	991	991	991	991
Wall thickness	152	152	152	76	152	152
Length	914	1220	1220	1220	1220	1220
Cladding thickness						5.6
Cylinder material						
Designation			A508, Class 2 chemistry			
Tempering temperature, °C	AQ[a]	613	679	613	704	620
RT_{NDT}, °C	75	66	10	66	−1	66
Yield stress at 22°C, MPa	900	682	581	682	449	520
Flaw (initial)						
Type	LS[b]	LS, SS[c]	LS	LS	SCS[d]	SES,[e] SESC[f]
Orientation	axial	axial, circum.	axial	axial	axial	axial
Length, mm	914	1220, 10	1220	1220	37	114, 38 } Fig. 7
Depth, mm	11	16	11	7.6	14	19 }
Thermal shock						
Initial temperature of cylinder, °C	288	96	96	96	96	96
Initial temperature of coolant, °C	−25	−196	−196	−196	−196	−196
Quench medium	W/A[g]	LN_2[h]	LN_2	LN_2	LN_2	LN_2

[a]AQ = as quenched.
[b]LS = long, surface.
[c]SS = short, surface
[d]SCS = semicircular, surface.
[e]SES = semielliptical, surface.
[f]SESC = semielliptical, subclad.
[g]W/A = water/alcohol.
[h]LN_2 = liquid nitrogen.

3.2 Flaws

Initial flaws for the experiments were "shallow" (≤19 mm) and were generated with the electron-beam, hydrogen-charge technique,[22] which results in a sharp, arrested crack for the initial flaw. All intended flaws were oriented in an axial direction. For experiments TSE-4, 5, 5A, and 6, the intended initial flaws were surface cracks that extended the length of the test cylinder with uniform depth. The flaw for TSE-7 was a semicircular surface crack. The test cylinder used for TSE-8, 9, 10, and 11 had multiple flaws with arrestor holes in close proximity in an attempt to control interaction effects after flaw extension. As indicated in Figs. 4 and 7, there were six,

equally spaced (60°), 6/1 semielliptical, subclad flaws for TSE-8. Following TSE-8, two semicircular surface flaws were added, and following TSE-10 four of the subclad flaws in the Inconel-clad area were converted to surface flaws by slitting the cladding; these latter flaws had not propagated previously.

3.3 Experiment Technique

To simulate radiation embrittlement and otherwise provide appropriate conditions for propagation of flaws, it was necessary to use a low-temperature thermal-shock medium and, for some experiments, a low-tempering temperature (both of which contributed to low-fracture toughness) and a severe thermal shock (high stress intensity factors). This is not surprising when we recall that flaw propagation in PWR vessels is predicted only when considering high fluences, high copper and nickel concentrations, lower-bound fracture toughness, and severe transients.

The desired thermal-shock conditions were achieved for TSE-4 by heating the test cylinder to 288°C and quenching the inner surface with an alcohol/water mixture at –25°C. For all successive experiments the test cylinder was heated to 96°C and quenched with liquid nitrogen (–196°C). For the latter experiments, the ends and outer surface of the test cylinder were thermally insulated. After heating, and with all instrumentation attached, the test cylinder assembly was lowered into a tank of liquid nitrogen. (A special surface coating was used to promote nucleate boiling, which provided the necessary high heat transfer coefficient.) The thermal shock was delayed, until full submergence of the test cylinder, by a gas bubble, trapped in the cavity, that was released after complete submergence was achieved. This procedure resulted in a very uniform thermal shock to the inner surface.

Instrumentation included 15 thermocouple thimbles with 12 thermocouples each for measuring the temperature distribution in the wall during a transient; weldable strain gages, as crack-opening-displacement gages, for detecting the times of initiation/arrest events, and, indirectly, for determining crack depth; and ultrasonic instrumentation for detecting time of events and crack depth.

After the final experiment with a specific test cylinder, the flawed region was removed and the fracture completed, by mechanical means, at liquid-nitrogen temperature to reveal the fracture surfaces. In some cases, examination of the fracture surfaces was aided by scanning electron microscopy.

3.4 Specific Purpose of Each Experiment

Generic: to demonstrate that linear elastic fracture mechanics (LEFM) is valid for application to PTS loading. One way of doing this is to compare the thermal-shock-experiment critical values of K_I corresponding to the initiation and arrest events with K_{Ic} and K_{Ia} data measured with standard specimens. This could be an oversimplification, however, if, for instance, out-of-plane stress, a relatively high yield stress, and/or very steep stress gradients, all of which were characteristic of the specific thermal-shock experiments,[6] nullified lack-of-constraint enhancement of fracture toughness associated with the shallow flaws tested under uniaxial, shallow-gradient-stress conditions.[12]

TSE-4: to demonstrate initiation and arrest. It was not anticipated that more than one initiation/arrest event would take place because of the stiffness of the wall (low ratio of radius to wall thickness).

TSE-5: to demonstrate a series of initiation/arrest events with deep penetration of the wall and with warm prestressing limiting the number of events.

TSE-5A: the same as that for TSE-5, with the addition of arrest with $dK_I/da > 0$. The fracture toughness was purposely greater than for TSE-5 (RT_{NDT} = 10°C for TSE-5A compared to 66°C for TSE-5).

TSE-6: to demonstrate that as a result of a very long crack jump, dynamic effects would not be large enough to drive the flaw completely through the wall. A thinner wall (higher radius-to-wall-thickness ratio) was required to achieve the long crack jump.

TSE-7: to demonstrate that in the absence of cladding an initially short surface flaw would extend on the surface in a single event to become a long flaw.

TSE-8: to evaluate the behavior of subclad flaws.

TSE-9: to evaluate the behavior of shallow, semicircular, surface flaws in the presence of cladding. The intent was to terminate the experiment after the first event so that the fracture contour associated with the first event could be determined. (The occurrence of a subsequent event might prevent that determination.)

TSE-10: to evaluate the behavior of shallow, semicircular, surface flaws in the presence of cladding. As opposed to TSE-9, the duration of the transient was to be sufficient for all possible events to take place.

TSE-11: to evaluate the behavior of shallow, 6/1 semielliptical, surface flaws in the presence of cladding.

4. RESULTS AND DISCUSSION

4.1 Temperature Transients

The temperature transients achieved (Figs. 8 and 9) were such that within 2 min the inner-surface temperatures dropped 270°C for TSE-4 and 170–240°C for the subsequent experiments. The rather large variation for the latter experiments was not intentional but was due in part to unintended variations in the surface coating that must be used to enhance the fluid-film heat transfer coefficient. The initial rate of decrease in surface temperature was greater for the clad test cylinder because of the insulating effect of the cladding, and was greater yet for TSE-4 because of forced-convection cooling. In all cases, the initial difference in temperature between test cylinder and quench medium was about the same (~300°C).

4.2 Fracture Behavior

The evaluation of the actual flaw behavior involves a calculation of K_I, K_{Ic}, and K_{Ia}. To minimize uncertainties, these parameters were calculated using the measured temperature distributions. Also, some fracture-toughness data were obtained specifically for the test-cylinder materials, and these data were used in conjunction with an existing data base[23] to obtain best-estimate values. LEFM two- and three-dimensional (2-D and 3-D) finite-element models were used for calculating K_I values for TSE-4, 5, 5A, 6, and 7, but for TSE-8, 9, 10, and 11 elastic-plastic fracture mechanics (EPFM) models were used to account for the large amount of plasticity in the cladding. Values of K_I/K_{Ic} mentioned below are consistent with this approach.

4.2.1 TSE-4

During TSE-4 there was one initiation/arrest event (Figs. 10 and 11). It took place at 152 s into the transient, and the best-estimate value of K_I/K_{Ic} at the time of initiation was 1.06. A second initiation event was prevented by WPS. The flaw extended 10 mm and arrested with $dK_I/da \cong 0$. As indicated by the set of critical crack depth curves (Fig. 11),* there is reasonably good agreement between predicted (using actual temperatures) and actual flaw behavior.

* A set of critical-crack-depth curves consists of a plot of crack depths corresponding to initiation and arrest events and incipient WPS ($\dot{K}_I = 0$), all as a function of time in the transient.

4.2.2 TSE-5

During TSE-5 there were three initiation/arrest events associated with the intended long, axial flaw, and WPS prevented a fourth event (Figs. 12 and 13). As indicated in Fig. 13, the second event was delayed, indicating an elevated toughness and thus resulting in a rather long crack jump. The long jump introduced the possibility of dynamic effects, but the good agreement between calculated (static analysis) and actual arrested crack depth indicates dynamic effects were not significant.

An unintended and initially undetected surface flaw with a surface length of only 10 mm, a depth of 16 mm, and a circumferential orientation (a cross crack in the EB-weld fusion zone used to generate the long axial flaw) extended on the surface, bifurcating many times, to become a very long flaw (Fig. 14). This confirmed a predicted behavior that was to be investigated in a later experiment (TSE-7). Propagation of this flaw occurred after propagation of the long axial flaw and thus did not influence propagation of the latter flaw.

4.2.3 TSE-5A

During TSE-5A there were four initiation/arrest events with WPS preventing a fifth event (Fig. 15). Following incipient WPS ($\dot{K}_I = 0$), K_I/K_{Ic} reached a maximum value of 2.3, and yet initiation did not take place. Thus, WPS (no initiation with $\dot{K}_I < 0$) was demonstrated in a reasonably convincing manner, and once again there was good agreement between prediction and experiment.

4.2.4 TSE-6

During TSE-6 there were two initiation/arrest events with a final arrest 95% of the way through the wall (Figs. 16 and 17). The static LEFM analysis predicted the deep arrest, but there was concern that dynamic effects might drive the flaw completely through the wall. Apparently, dynamic effects were negligible.

4.2.5 Comparison of fracture-toughness data from TSE-4, 5, 5A, and 6

A comparison of standard-specimen K_{Ic} and K_{Ia} data* with the critical K_I values corresponding to the initiation and arrest events detected during the ORNL thermal-shock experiments and a similar French experiment[24] (Figs. 18 and 19) shows good agreement and thus indicates that LEFM is valid for PTS loading, assuming that the shallow initial flaws would not exhibit a substantially elevated toughness. Shallow-flaw data obtained with beams subjected to bending[12] indicate that the first initiation events for TSE-5 and TSE-6 were at too low a temperature to exhibit elevated toughness; however, for TSE-4, TSE-5A and the French experiment, they were not. Even so, there is no evidence in Fig. 18 of elevated toughness. A possible explanation is that out-of-plane stresses (nearly equal biaxial stresses under thermal-shock loading), and/or the relatively high yield stress,** and/or the steep gradient in stress over the depth of the flaw resulted in a reduction in fracture toughness based on the single fracture parameter K_I (Refs. 13 and 14). This possibility is under investigation at ORNL.

---

*The data used for the comparison discussed herein are those used to define the ASME lower-bound K_{Ic} and K_{Ia} curves.[23]

**The room-temperature yield stress for the shallow-flaw beams was ~420 MPa, which is low compared to the values for the test cylinders (Table 1).

The two relatively high data points in Fig. 18 correspond to the initiation events that preceded the two long crack jumps (TSE-5 and TSE-6), and in Fig. 19 it is not evident that the long crack jumps had a significant effect on crack arrest (data points are within the scatter band).

Two other data points of particular interest in Fig. 19 are those corresponding to arrest with $dK_I/da > 0$. There is not a discernible difference between these data points and data obtained from a standard crack-arrest test ($dK_I/da < 0$). Thus, the latter data appear to be valid for PTS loading.

During TSE-5, 5A, 6, and 7, there were more than 12 initiation events involving crack fronts totaling more than 1000 mm in length, and yet the existence of low-toughness sites is not apparent; that is, K_{Ic} values deduced from the experiments do not fall below the ASME lower-bound K_{Ic} curve. On the other hand, there is considerable overlap of the K_{Ic} and K_{Ia} scatterbands, which implies that the lower part of the K_{Ic} scatterband includes the effect of low-toughness sites.[15] This is consistent with the notion that if a compact specimen containing a low-toughness site fails, as opposed to exhibiting a pop-in, the existence of the low-toughness site results in a relatively low value of K_{Ic} but otherwise is not recognized. A pop-in eliminates the low-toughness site without failure and presumably is not recorded as a K_{Ic} value. Thus, perhaps the ASME lower-bound K_{Ic} curve includes essentially all low-toughness sites that can result in failures.

4.2.6 TSE-7

During TSE-7, the shallow, semicircular flaw experienced three major initiation/arrest events and, during the first event, extended on the surface, bifurcating many times, to become a very long flaw (Fig. 20). The pretest analysis, which could not include the potential for bifurcation, indicated that the flaw would extend on the surface nearly the full length of the test cylinder in a single event and subsequently experience two more initiation/arrest events with a fourth event being prevented by WPS (Fig. 21). (The 2-D analysis presented in Fig. 21 is reasonably accurate because the maximum value of K_I/K_{Ic} for the semicircular and 2-D flaws of the same depth are about the same, and the first event extends the surface length of the initial flaw.) Thus, there was good agreement between prediction and experiment.

4.2.7 TSE-8

During TSE-8, one of the six flaws (flaw 3) experienced two initiation/arrest events, extending both the length and depth of the flaw (Fig. 22). Although there were obvious stretch marks in the cladding over the extended flaw, there was no penetration of the cladding. The maximum value of K_I/K_{Ic} along the original crack front at the time of the initial initiation was at the deepest point and was 0.8. The maximum values achieved for the other five flaws occurred somewhat later and were nominally 1.0 (as a result of the extensive extension of flaw 3, there was a loss of symmetry that increased K_I slightly for some flaws and decreased K_I slightly for others). This experiment demonstrated that even in the presence of tough cladding, a short flaw could extend in length beneath the cladding to effectively become a 2-D subclad flaw. Comparing TSE-8 with TSE-7 indicates that the presence of the cladding reduces the tendency for bifurcation and thus the extent of "surface" extension.

The calculation of K_I for the portion of the crack front in the base material required modeling of the crack front at the clad/base interface, and this was done using a crack-tip blunting model.[11] The low calculated value of K_I/K_{Ic} for the first event (0.8) indicates that stretching of the cladding over the flaw was greater than calculated.

4.2.8 TSE-9 and TSE-10

TSE-9 and TSE-10 included two semicircular surface flaws, one of which extended slightly during TSE-9. Immediately following this event, which was nothing more than completion of crack generation in the EB-weld fusion zone, the transient was terminated by withdrawing

the test cylinder from the liquid nitrogen. Although of greater duration, the thermal transient for TSE-10 was less severe (Fig. 9), and there was no further propagation. The maximum value of K_I/K_{Ic} during TSE-9 for the portion of the crack front in the base material occurred at the clad/base interface and was 1.3. This value, however, is based on the toughness of the base material in essentially a quench-only condition, and it may be that the heat affected zone at the clad/base interface was tempered to a higher toughness. In any case, because the TSE-7 test cylinder was fully temperated ($RT_{NDT} = -1°C$), and because the TSE-9 transient was somewhat more severe (Figs. 8 and 9), it appears that the presence of cladding reduced the potential for propagation of the semicircular surface flaw. This is further supported by the lack of propagation during TSE-11, which had a more severe transient.

4.2.9 TSE-11

The thermal transient for TSE-11 was substantially more severe than those for the other experiments (Fig. 9). During the transient, the four 6/1, semielliptical, surface flaws propagated, extending in length and depth without penetrating the cladding (Fig. 23 and Table 2). There was some bifurcation that permitted flaw 6 to bypass the arrestor holes and extend nearly to the ends of the cylinder. There is evidence in Table 2 that at 124 and 230 s initiation of one flaw triggered others, presumably as a result of stress waves. Values of K_I/K_{Ic} at the times of the first initiations were 1.1 (clad/base interface) and 0.8 (deepest point) at 86 s and 1.3 (clad/base interface) and 1.1 (deepest point) at 124 s, all based on $RT_{NDT} = 66°C$. The extension of flaw 2 at 86 s was restricted, as intended, by arrestor holes and thus had a negligible effect on the events associated with the other flaws at 124 s.

Table 2. Events during TSE-11

Flaw	Time (s)				
	86	124	192	230	390
2	E[a]	E			
3		E	E	E	E
4		E			
5		E			
6		E		E	

[a]E indicates initiation/arrest events.

Flaw 3, which had propagated during TSE-8, experienced four additional initiation/arrest events, while the subclad flaw in the stainless-steel-clad region (flaw 1) and the two semicircular surface flaws (flaws 7 and 8) did not propagate. The maximum value of K_I/K_{Ic} for flaw 1 prior to WPS (~230 s) and prior to extensive propagation of other flaws (124 s) was 1.0, and it was at the deepest point. For the semicircular flaws, the corresponding value was 1.5 at the clad base interface (based on $RT_{NDT} = 66°C$) and 0.8 at the deepest point.

5. SUMMARY

The thermal-shock experiments confirmed the validity of LEFM for severe thermal-shock loading conditions by demonstrating the following flaw behavior trends in good agreement with analysis:

a. initiation of very shallow flaws;
b. arrest of both short- and long-crack jumps;
c. a series of initiation/arrest events with deep penetration of the wall;
d. the inability of a flaw to initiate with $\dot{K}_I < 0$, even though $K_I/K_{Ic} >> 1.0$ (Type-1 WPS);
e. arrest with $dK_I/da > 0$;
f. extensive surface extension in a single event and in the absence of cladding of an initially short and shallow surface flaw; and
g. extensive subclad extension at the clad/base interface of an initially short and shallow surface or subclad flaw, although the analytical model for subclad propagation is suspect because of geometric complexities.

The validity of LEFM is illustrated in a quantitative sense by the good agreement between critical values of K_I, corresponding to initiation and arrest events, and K_{Ic} and K_{Ia} values measured with standard procedures. The good agreement in K_{Ia} values for a long crack jump should not, however, be interpreted to mean that dynamic effects are necessarily negligible for PWR pressure vessels, which have higher ratios of vessel radius to wall thickness.[25,26] Also, the good agreement of K_{Ic} values should not be interpreted to mean that constraint effects associated with shallow flaws will not be significant under more nearly typical PWR PTS conditions. This issue is presently under investigation at ORNL.

There was no evidence of low-toughness sites other than the observation that some of the K_{Ic} values deduced from the thermal shock experiments approached the ASME lower-bound K_{Ic} curve.

6. REFERENCES

1. "Fracture Toughness Requirements for Protection Against Pressurized Thermal Shock Events," *Federal Register*, Vol. 50, No. 141, Section 50.61, pp. 29937–29945 (July 23, 1985).

2. *Regulatory Guide 1.154*, "Format and Content of Plant-Specific Pressurized Thermal Shock Safety Analysis Reports for Pressurized Water Reactors," U.S. Nuclear Regulatory Commission, Office of Nuclear Regulatory Research, January 1987

3. T. J. Burns et al., *Pressurized Thermal Shock Evaluation of the Oconee-1 Nuclear Power Plant*, NUREG/CR-3770 (ORNL/TM-9176), Martin Marietta Energy Systems, Inc., Oak Ridge National Laboratory, May 1986.

4. D. L. Selby et al., *Pressurized Thermal Shock Evaluation of the Calvert Cliffs Unit 1 Nuclear Power Plant*, NUREG/CR-4022 (ORNL/TM-9408), Martin Marietta Energy Systems, Inc., Oak Ridge National Laboratory, September 1985.

5. D. L. Selby et al., *Pressurized Thermal Shock Evaluation of the H. B. Robinson Unit 2 Nuclear Power Plant*, NUREG/CR-4183 (ORNL/TM-9567), Vols. 1 and 2, Martin Marietta Energy Systems, Inc., Oak Ridge National Laboratory, September 1985.

6. R. D. Cheverton, S. K. Iskander, and D. G. Ball, "Review of Pressurized-Water-Reactor-Related Thermal-Shock Studies," pp. 752–766 in *Fracture Mechanics: Nineteenth Symposium*, ASTM STP 969, T. A. Cruse, Ed., American Society for Testing and Materials, Philadelphia, 1988.

7. W. R. Corwin et al., "Fracture Behavior of a Neutron-Irradiated Stainless Steel Submerged Arc Weld Cladding Overlay," *Nucl. Engrg. Des.*, 89, pp. 199–221 (1985).

8. W. R. Corwin, "Reactor Vessel Cladding Separate Effects Studies," *Nucl. Engrg. Des.*, 98, pp. 171–193 (1987).

9. S. K. Iskander et al., *Experimental Results of Tests to Investigate Flaw Behavior of Mechanically Loaded Stainless Steel Clad Plates*, NUREG/CR-5785 (ORNL/TM-11950), Martin Marietta Energy Systems, Inc., Oak Ridge National Laboratory, April 1992.

10. D. E. McCabe, *Fracture Evaluation of Surface Cracks Embedded in Reactor Vessel Cladding*, NUREG/CR-4841 (MEA-2200), Materials Engineering Associates, Inc., May 1987.

11. R. D. Cheverton et al., "Thermal Shock Experiments with Flawed Clad Cylinders," *Nucl. Engrg Des.*, 124, pp. 109–119 (1990).

12. T. J. Theiss, D. K. M. Shum, and S. T. Rolfe, *Experimental and Analytical Investigation of the Shallow-Flaw Effect in Reactor Pressure Vessels*, NUREG/CR-5886 (ORNL/TM-12115), Martin Marietta Energy Systems, Inc., Oak Ridge National Laboratory, July 1992.

13. W. E. Pennell, "Aging Impact on the Safety and Operability of Nuclear Reactor Pressure Vessels," in *Proceedings of the Aging Research Information Conference*, Holiday Inn Crowne Plaza, Rockville, Maryland, March 24–27, 1992, NUREG/CP-0122, Vol. 1.

14. D. K. M. Shum and B. R. Bass, *Absence of Toughness Elevation in Thermal-Shock Experiment TSE-5A: Preliminary Explanation Based on Crack-Tip Constraint*, ORNL/NRC/LTR-92/24, October 1992.

15. R. D. Cheverton and S. K. Iskander, "Thermal Shock Investigations" pp. 87–93 in *Heavy-Section Steel Technology Program Quarterly Progress Report for January–March 1981*, NUREG/CR-2141/V1 (ORNL/TM-8722), Martin Marietta Energy Systems, Inc., Oak Ridge National Laboratory, June 1981.

16. R. D. Cheverton et al., *Heavy Section Steel Technology Program Quarterly Progress Report for July–September 1981*, NUREG/CR-2141, Vol. 3 (ORNL/TM-8145), pp. 91-93, February 1982.

17. E. Smith, "The Effect of Austenitic Cladding on the Extension of an Under-Clad Crack into the Wall of a Water-Cooled Nuclear Reactor Pressure Vessel During a Hypothetical Loss of Coolant Accident," *Trans. 7th Int. Conf. on Structural Mechanics in Reactor Technology*, Vol. G, pp. 143–148, August 1983.

18. E. Smith, "The Restraining Effect of Austenitic Cladding on the Extension of a Three-Dimensional Crack into the Wall of a Water-Cooled Nuclear Reactor Pressure Vessel During a Hypothetical Overcooling Accident," *Nucl. Engrg. Des.*, 78, pp. 79–84 (1984).

19. R. D. Cheverton and S. E. Bolt, *Pressure Vessel Fracture Studies Pertaining to a PWR LOCA-ECC Thermal Shock: Experiments TSE-3 and TSE-4 and Update of TSE-1 and TSE-2 Analysis*, ORNL/NUREG-22, Marietta Energy Systems, Inc., Oak Ridge National Laboratory, December 1977.

20. R. D. Cheverton et al., *Pressure Vessel Fracture Studies Pertaining to the PWR Thermal-Shock Issue: Experiments TSE-5, TSE-5A, and TSE-6*, NUREG/CR-4249 (ORNL-6163), Marietta Energy Systems, Inc., Oak Ridge National Laboratory, June 1985.

21. R. D. Cheverton et al., *Pressure Vessel Fracture Studies Pertaining to the PWR Thermal-Shock Issue: Experiment TSE-7*, NUREG/CR-4304 (ORNL-6177), Marietta Energy Systems, Inc., Oak Ridge National Laboratory, August 1985.

22. P. P. Holz, "Preparation of Long Axial Flaw for TSE-5A," pp. 35–37 in *Heavy-Section Steel Technology Program Quarterly Progress Report July–September 1980*, NUREG/CR-1806 (ORNL/NUREG/TM-419), Marietta Energy Systems, Inc., Oak Ridge National Laboratory, December 1980.

23. *Flaw Evaluation Procedures – Background and Application of ASME Section XI, Appendix A, NP-719-SR*, Prepared by American Society of Mechanical Engineers, Section XI Task Group on Flaw Evaluation, T. U. Marson, Ed., Special Report, August 1978.

24. A. Pellissier-Tanon, P. Sollogoub, and B. Houssin, "Crack Initiation and Arrest in an SA 508 Class-3 Cylinder Under Liquid Nitrogen Thermal-Shock Experiment," *Transactions of the 7th International Conference on Structural Mechanics in Reactor Technology*, Vols. G and H., North Holland Publishing Co., Amsterdam, The Netherlands, August 1983.

25. J. Keeney-Walker and B. R. Bass, *A Comparison of Analysis Methodologies for Predicting Cleavage Arrest of a Deep Crack in a Reactor Pressure Vessel Subjected to Pressurized-Thermal-Shock Loading Conditions*, NUREG/CR-5793 (ORNL/TM-11969), Marietta Energy Systems, Inc., Oak Ridge National Laboratory, September 1992.

26. D. J. Ayres et al., *Tests and Analyses of Crack Arrest in Reactor Vessel Materials*, Final Report, NP-5121M on EPRI Research Project 2180-3, April 1987.

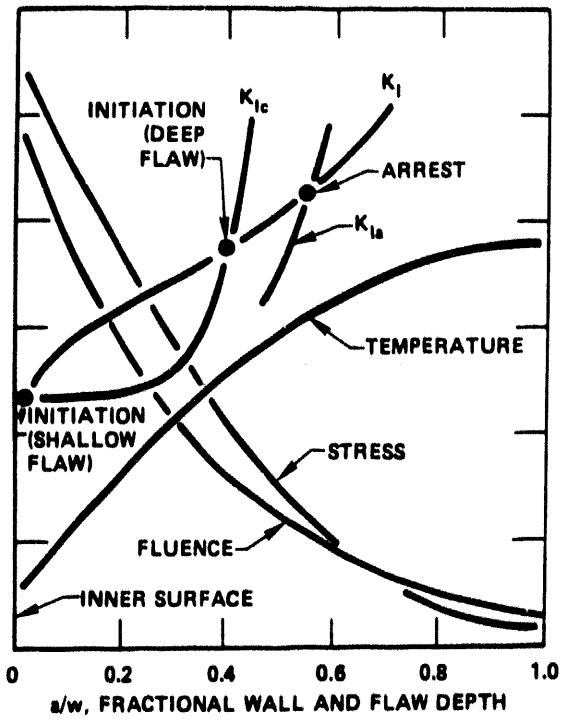

Fig. 1. Fracture parameters vs flaw depth and radial position in wall at specific time in severe PTS transient (high copper, nickel, and fluence).

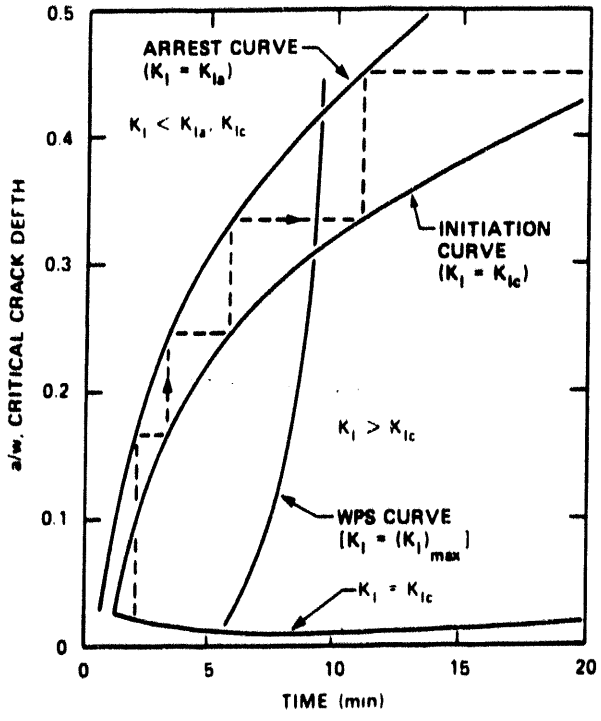

Fig. 2. Critical-crack-depth curves for severe PTS transient (high copper, nickel, and fluence).

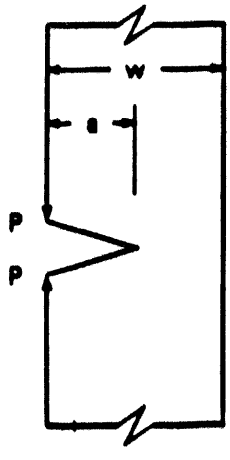

Fig. 3. Crack-mouth closing force associated with tensile stress in cladding over subclad flaw.

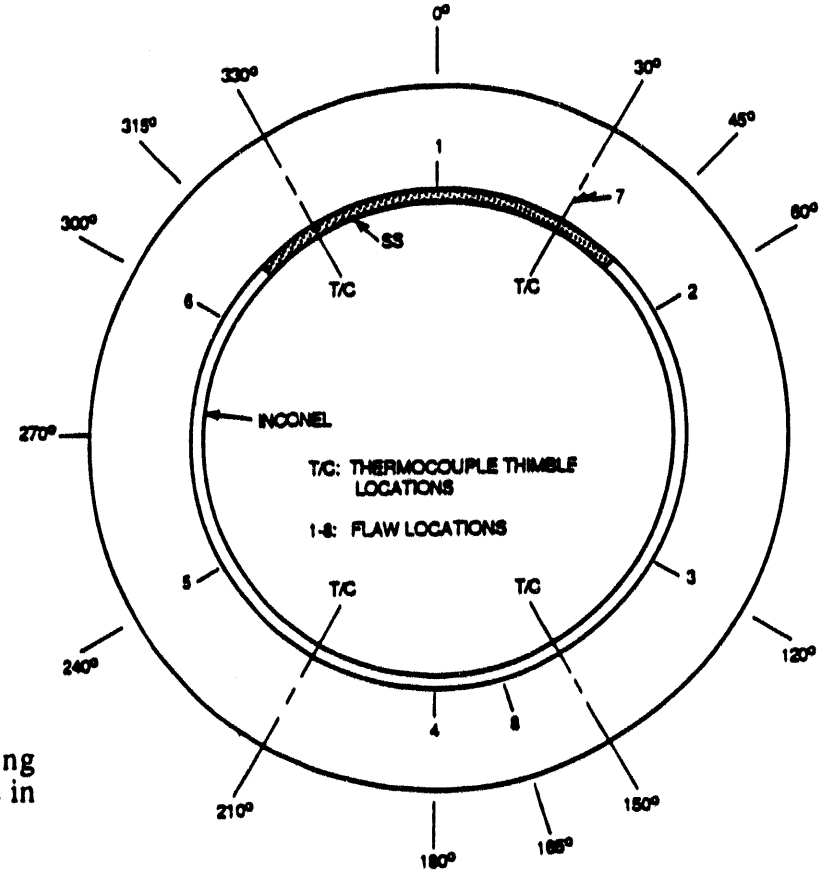

Fig. 4. Cladding configuration and flaw locations in test cylinder for TSE-8, 9, 10, and 11.

Fig. 5. Typical test cylinder used for TSE-5, 5A, 6, 7 (no cladding).

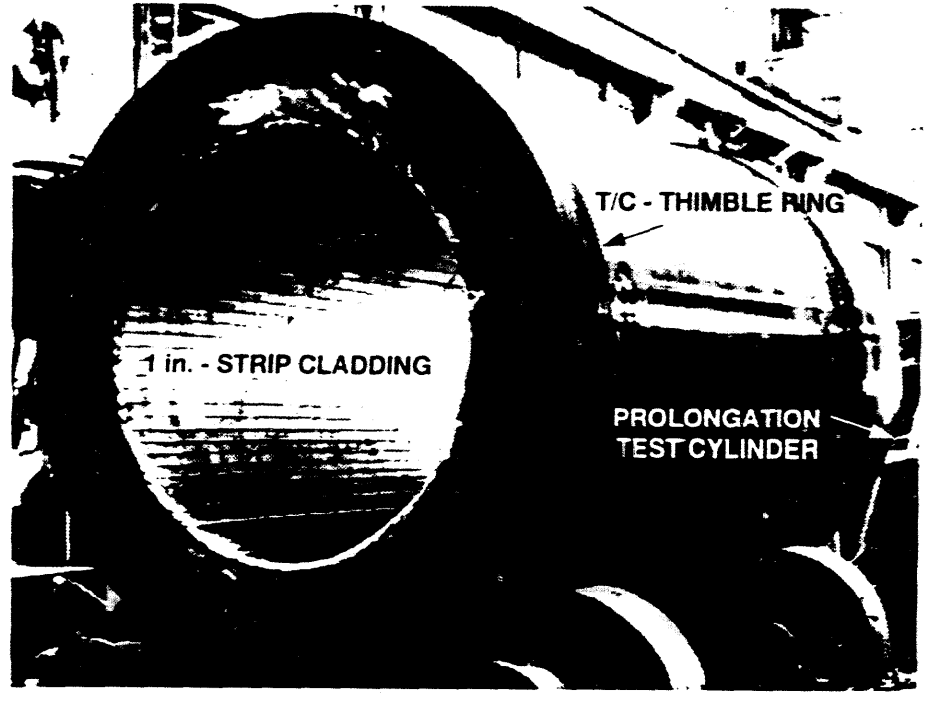

Fig. 6. Test-cylinder/prolongation assembly showing strip cladding before machining.

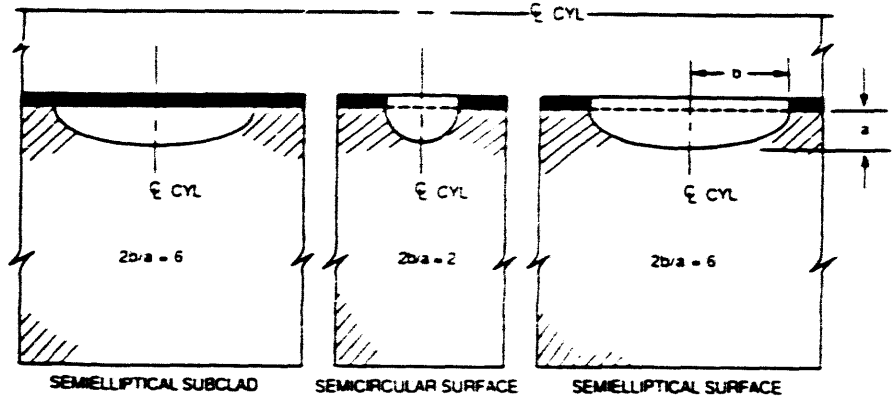

Fig. 7. Types of flaws for the clad-cylinder series of experiments.

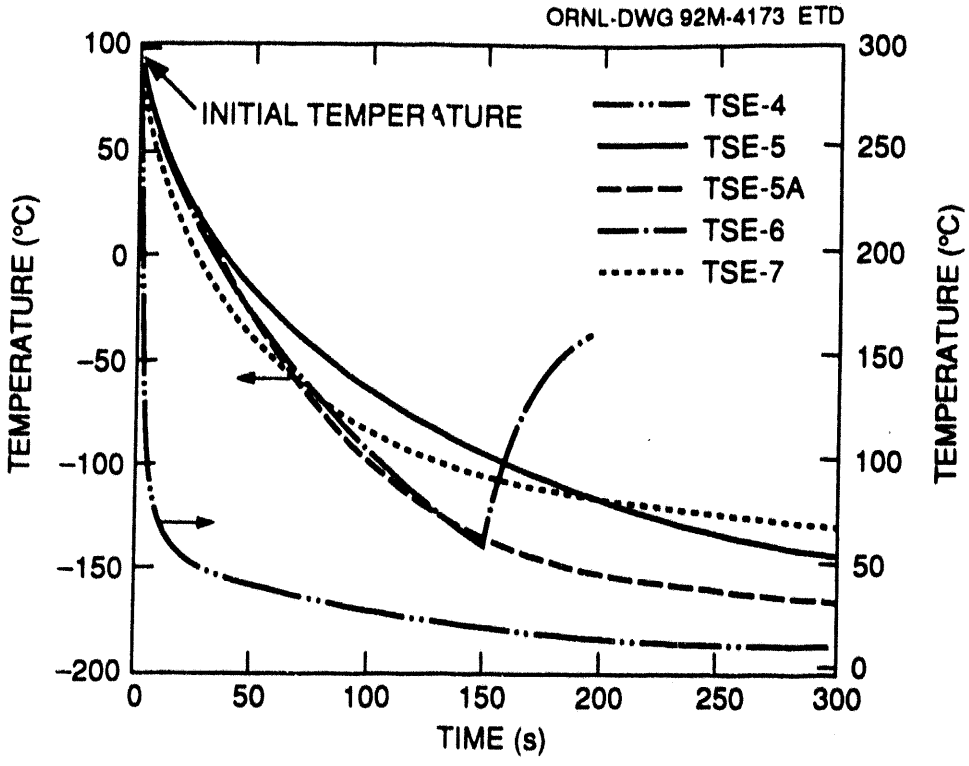

Fig. 8. Inner-surface temperature vs time for TSE-4, 5, 5A, 6, and 7.

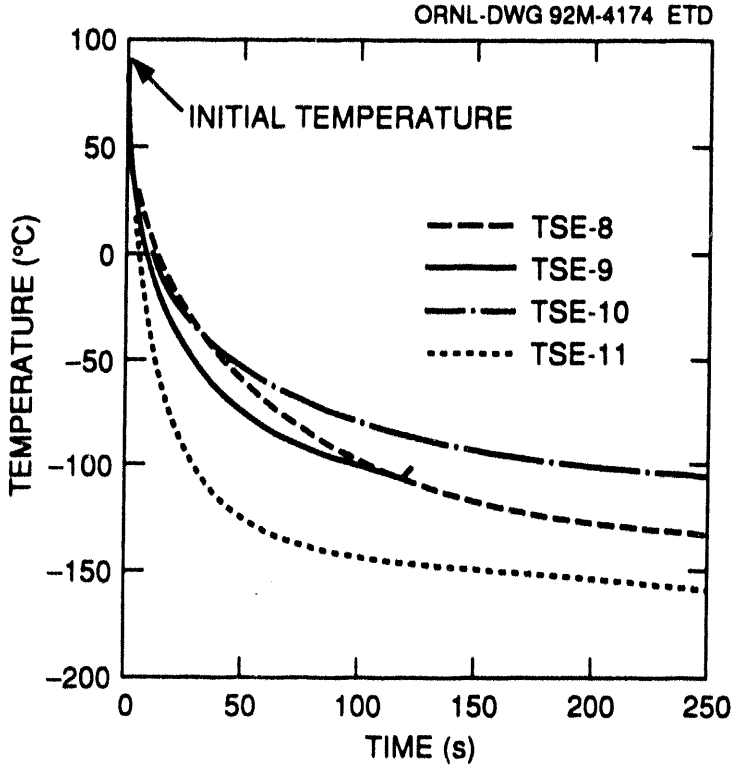

Fig. 9. Inner-surface temperature vs time for TSE-8, 9, 10, and 11.

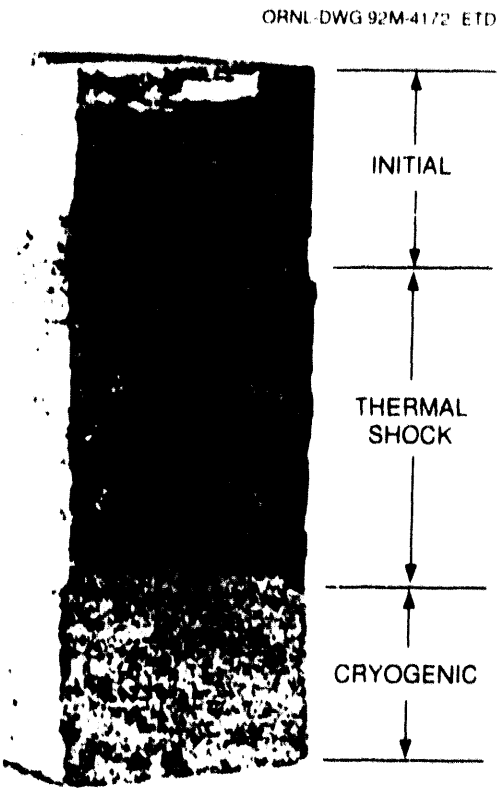

Fig. 10. Fracture surface for TSE-4.

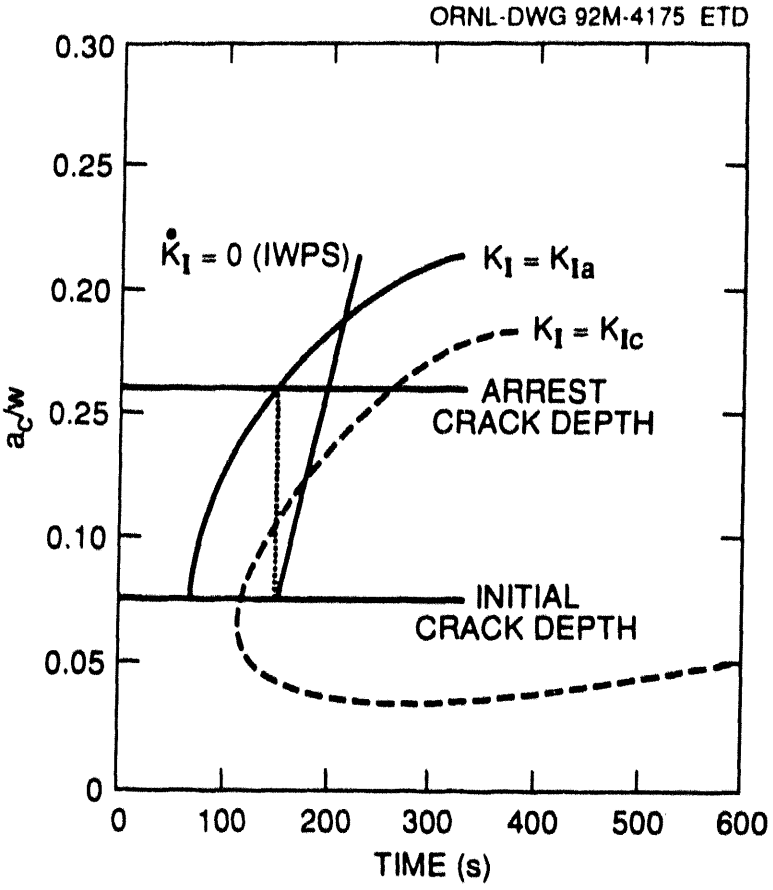

Fig. 11. Critical-crack-depth curves from posttest analysis of TSE-4.

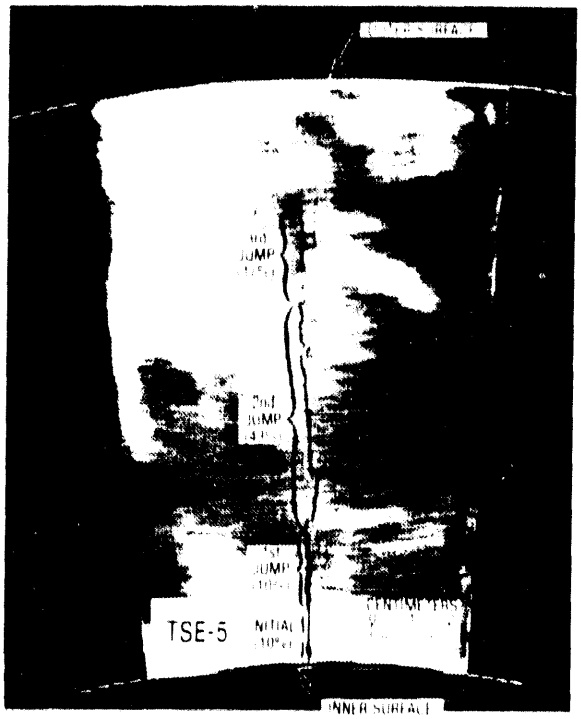

Fig. 12. Fracture profile for TSE-5.

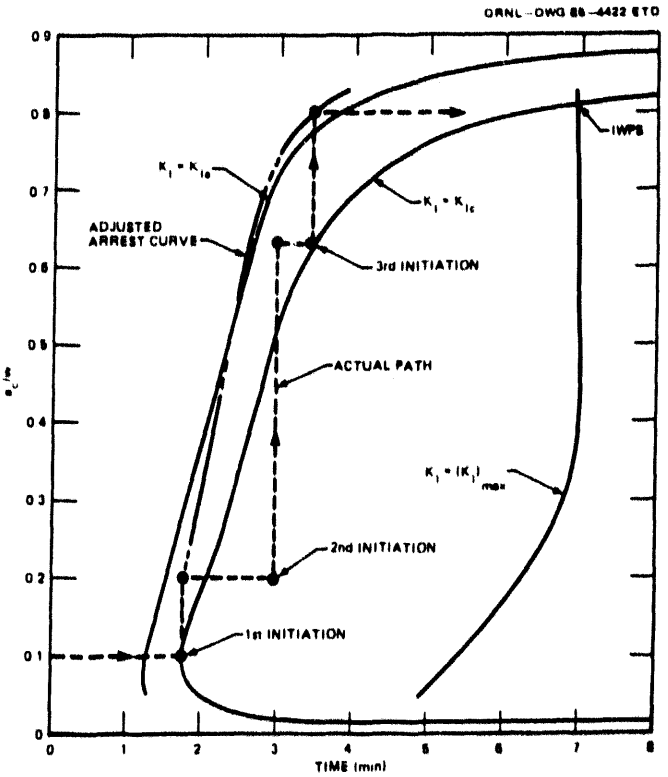

Fig. 13. Critical-crack-depth curves from posttest analysis of TSE-5.

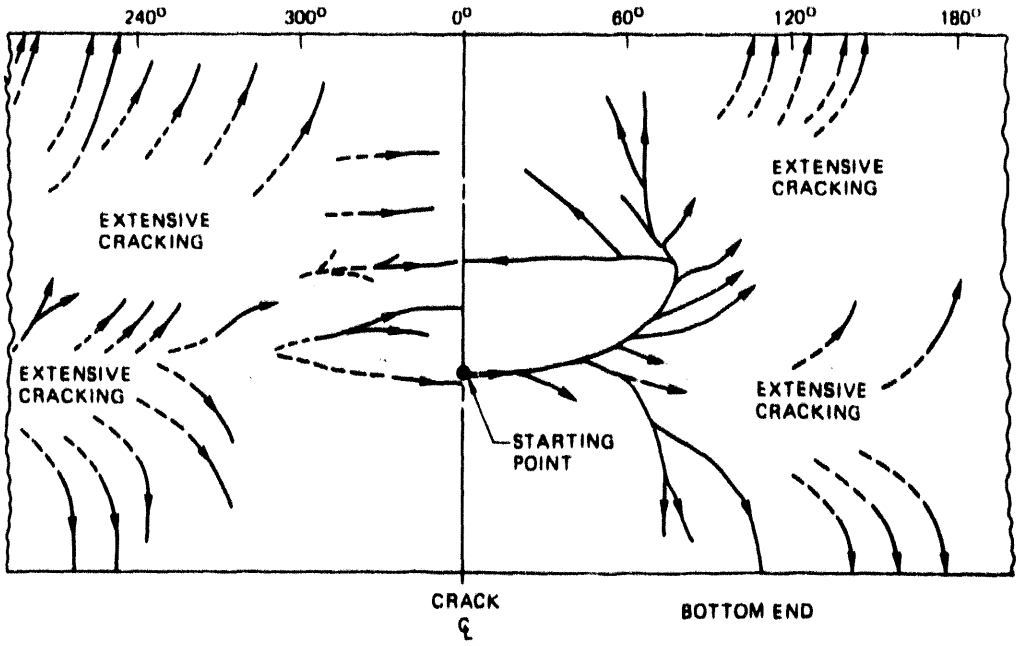

Fig. 14. Developed view of inner surface of TSE-5 test cylinder showing surface extension of initially small (10 mm long × 16 mm deep), circumferential, surface flaw.

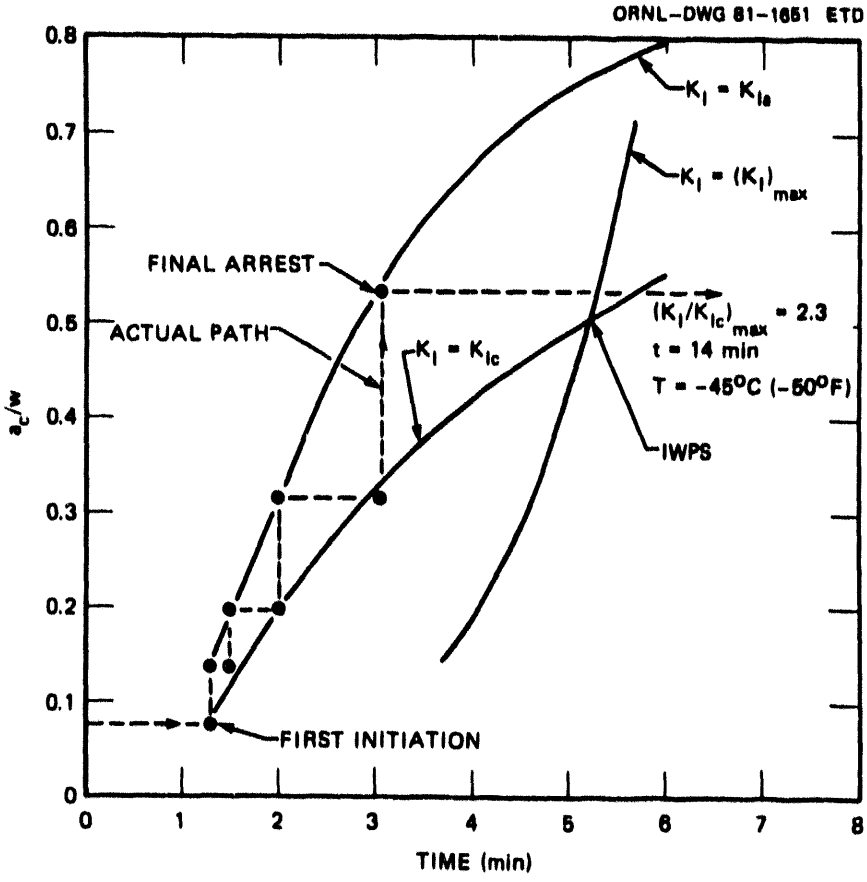

Fig. 15. Critical-crack-depth curves from posttest analysis of TSE-5A.

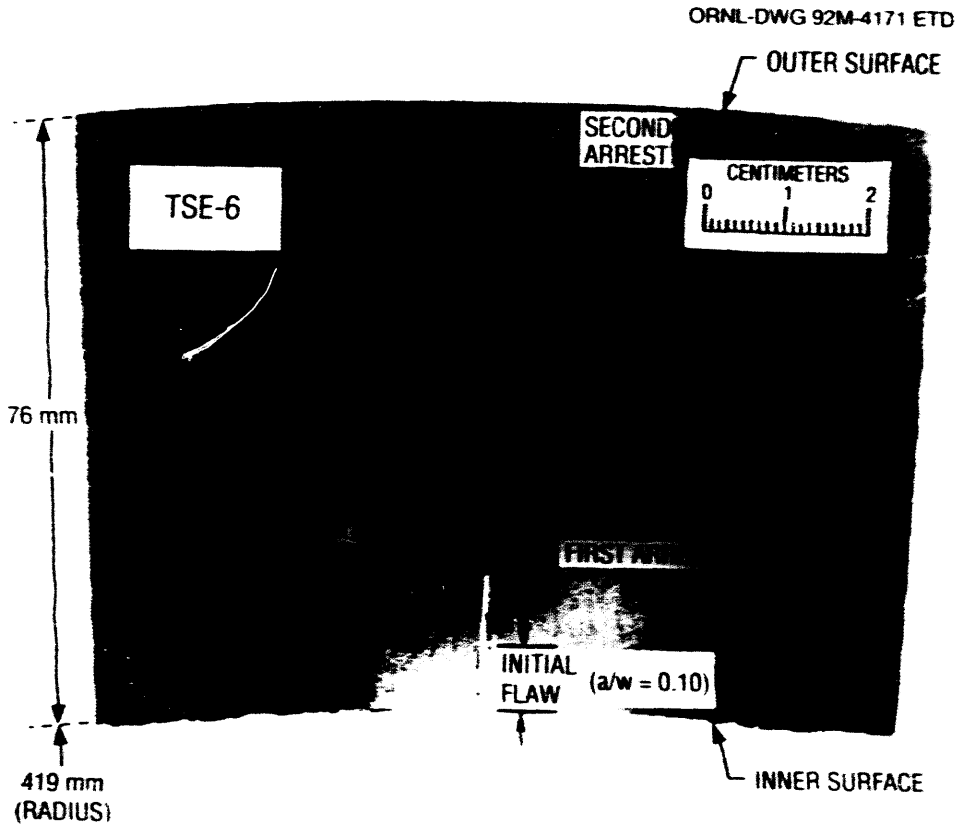

Fig. 16. Fracture profile for TSE-6.

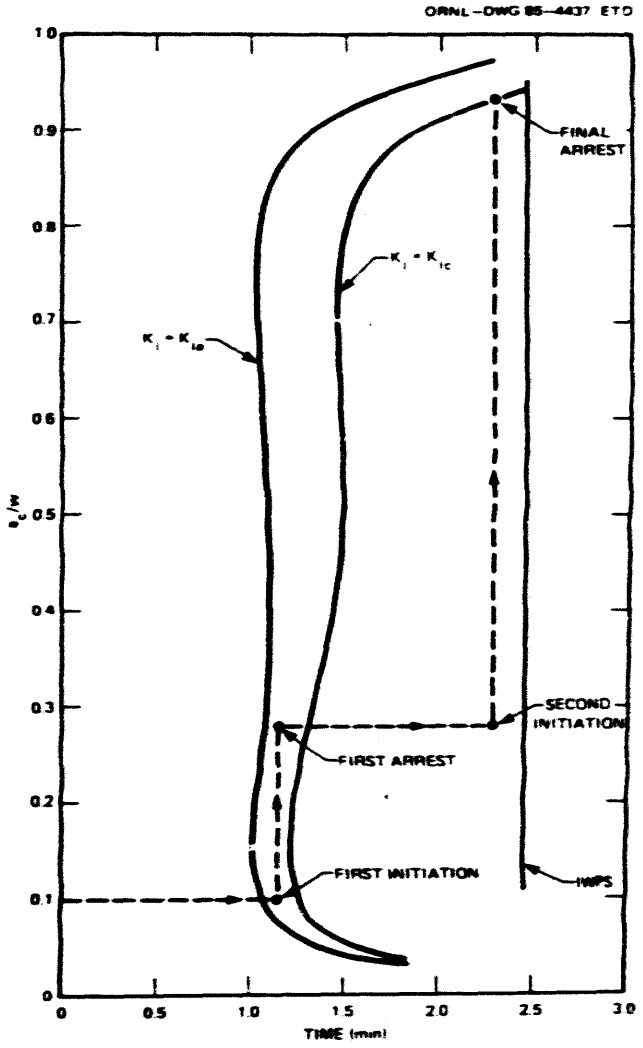

Fig. 17. Critical-crack-depth curves from posttest analysis of TSE-6.

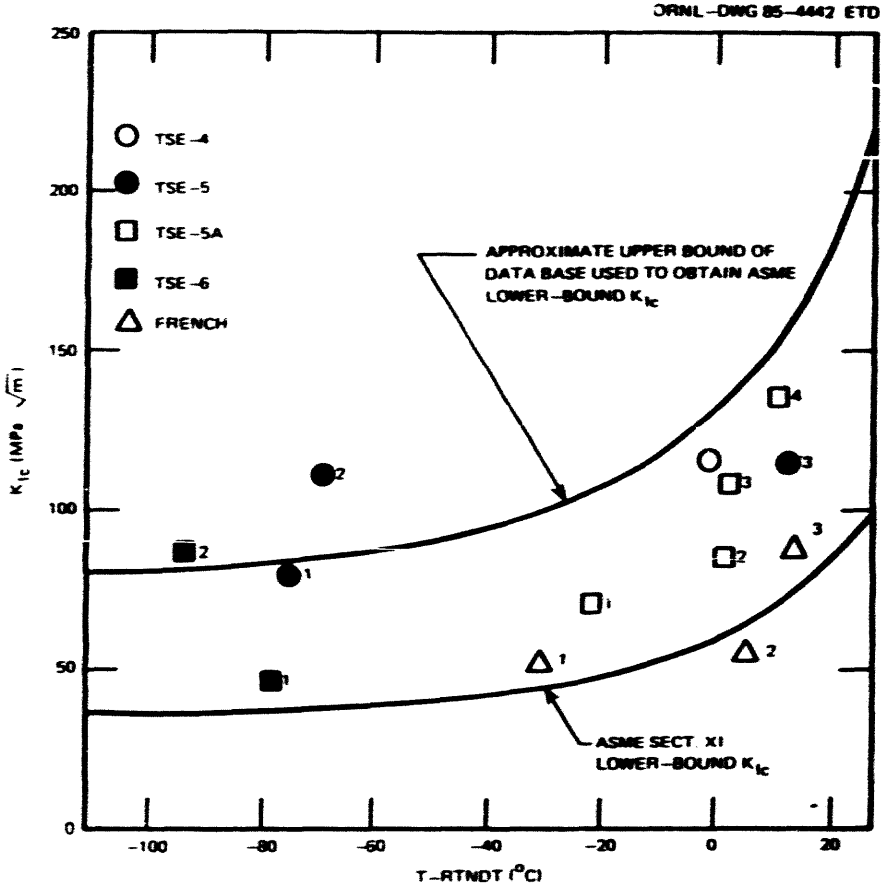

Fig. 18. Comparison of small-specimen and large-specimen K_{Ic} data.

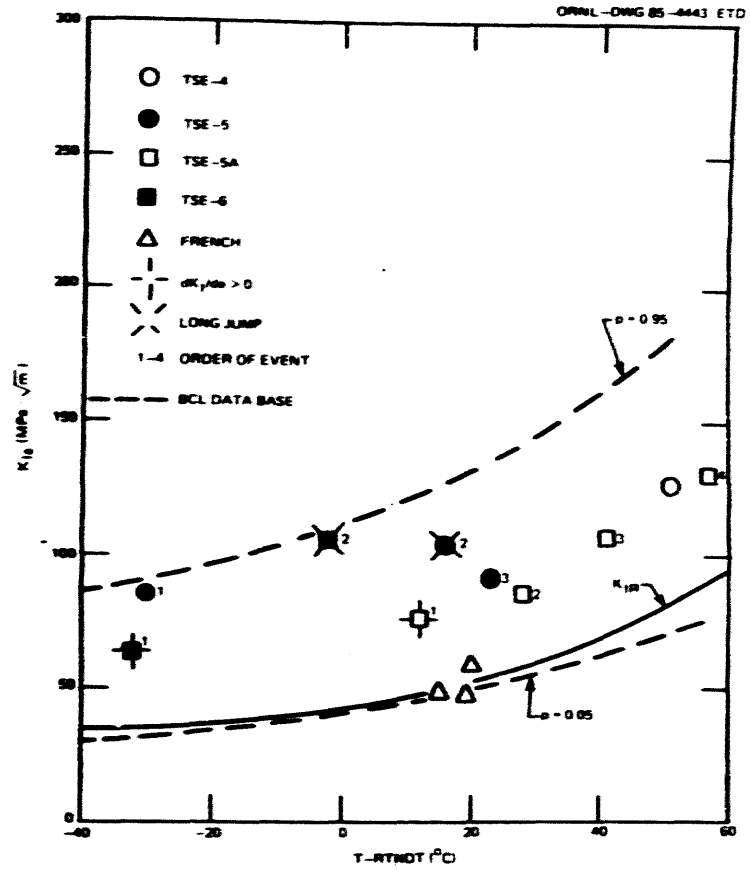

Fig. 19. Comparison of small-specimen and large-specimen K_{Ia} data.

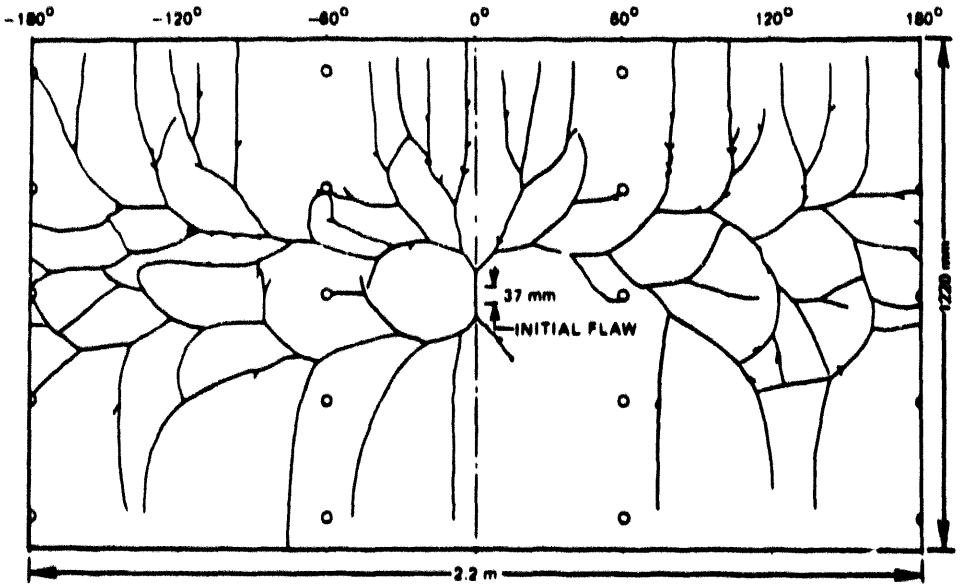

Fig. 20. Developed view of inner surface of TSE-7 test cylinder showing surface extension of initially small flaw (37 mm long × 14 mm deep).

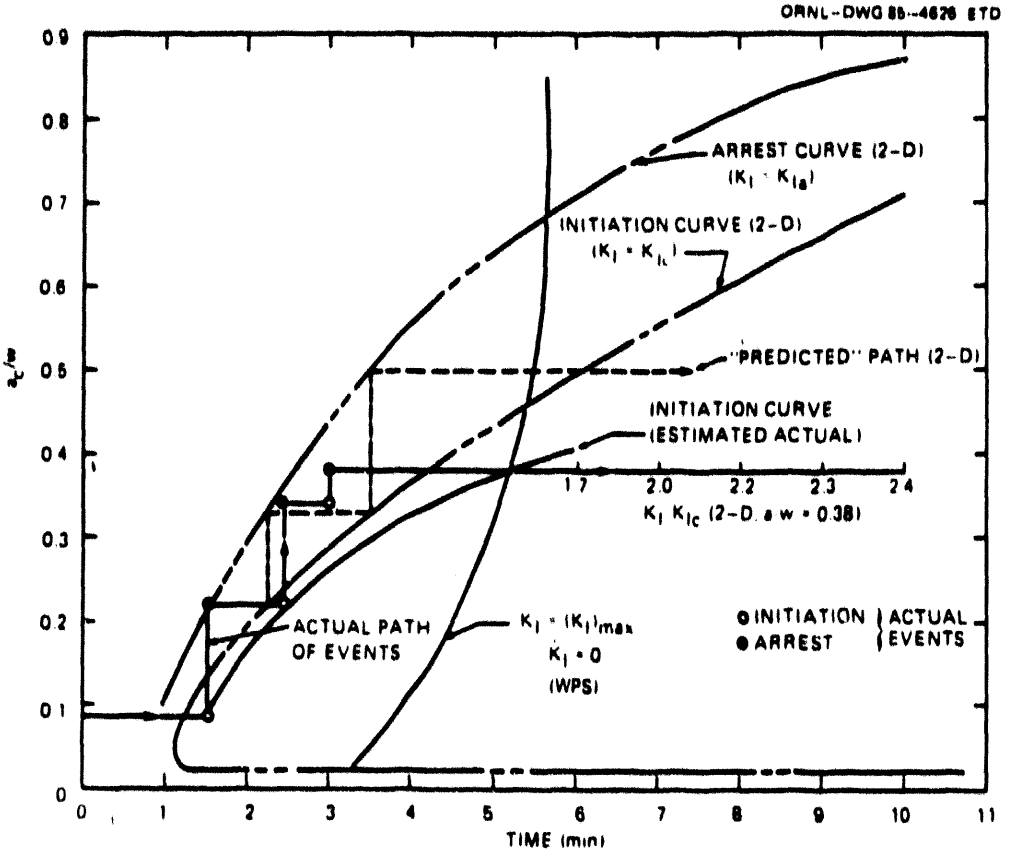

Fig. 21. Critical-crack-depth curves from posttest analysis of TSE-7 (2-D analysis).

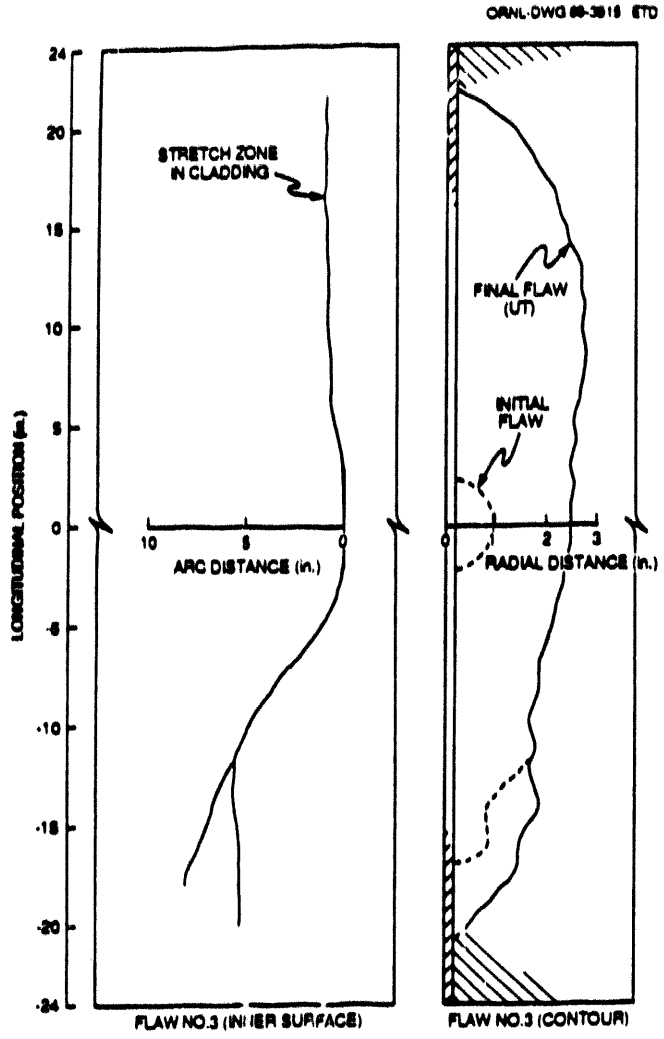

Fig. 22. Stretch-zone and ultrasonic-inspection indications of flaw 3 extension during TSE-8.

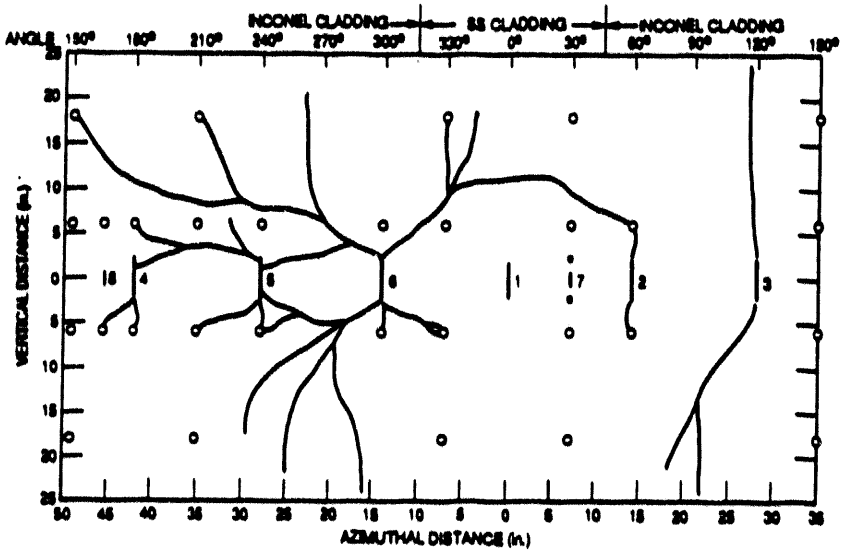

Fig. 23. Developed view of inner surface of test cylinder showing under-clad cracking pattern following TSE-11.

THE INFLUENCE OF FINITE-LENGTH FLAW EFFECTS ON PTS ANALYSES*

J. Keeney-Walker
T. L. Dickson

Oak Ridge National Laboratory
Oak Ridge, Tennessee 37831

ABSTRACT

Current licensing issues within the nuclear industry dictate a need to investigate the effects of cladding on the extension of small finite-length cracks near the inside surface of a vessel. Because flaws having depths of the order of the combined clad and heat affected zone thickness dominate the frequency distribution of flaws, their initiation probabilities can govern calculated vessel failure probabilities. Current pressurized-thermal-shock (PTS) analysis computer programs recognize the influence of the inner-surface cladding layer in the heat transfer and stress analysis models, but assume the cladding fracture toughness is the same as that for the base material. The programs do not, therefore, recognize the influence cladding may have in inhibiting crack initiation and propagation of shallow finite-length surface flaws. Limited experimental data and analyses indicate that cladding can inhibit the propagation of certain shallow flaws. This paper describes an analytical study which was carried out to determine (1) the minimum flaw depth for crack initiation under PTS loading for semicircular surface flaws in a clad reactor pressure vessel and (2) the impact, in terms of the conditional probability of vessel failure, of using a semicircular surface flaw as the initial flaw and assuming that the flaw cannot propagate in the cladding.

The analytical results indicate that for initiation a much deeper critical crack depth is required for the finite-length flaw than for the infinite-length flaw, except for the least severe transient. The minimum flaw depths required for crack initiation from the finite-length flaw analyses were incorporated into a modified version of the OCA-P code. The modified code was applied to the analysis of selected PTS transients, and the results produced a substantial decrease in the conditional probability of failure. This initial study indicates a significant effect on probabilistic fracture analyses by incorporating finite-length flaw results.

1. INTRODUCTION

The Nuclear Regulatory Commission (NRC) established the PTS rule[1] (10 CFR 50.61) to insure the integrity of reactor pressure vessels (RPVs) under PTS loading conditions based on results from the Integrated Pressurized-Thermal-Shock (IPTS) Program[2–4] and other studies. According to this document, plant-specific analyses must be performed for any plant that is intended to operate beyond the screening criteria [limiting values of the reference nil ductility temperature (RT_{NDT})]. Furthermore, *Regulatory Guide 1.154*[5] provides guidance on the

*Research sponsored by the Office of Nuclear Regulatory Research, U.S. Nuclear Regulatory Commission under Interagency Agreement 1886-8011-9B with the U.S. Department of Energy under Contract DE-AC05-84OR21400 with Martin Marietta Energy Systems, Inc.

methodology for performing plant-specific safety analyses and references the IPTS methodology as acceptable for the probabilistic fracture-mechanics (PFM) portion of the analyses.

A typical methodology for performing deterministic and probabilistic fracture mechanics analyses is embodied in the OCA-P computer program,[6] which is referenced in the IPTS study. The OCA-P program was developed at Oak Ridge National Laboratory (ORNL) specifically for simulating the cleavage fracture response of an RPV subjected to a PTS event. The program is based on linear-elastic fracture-mechanics (LEFM) theory and uses superposition techniques and influence coefficients for calculating stress-intensity factors (K_I) for both two- and three-dimensional (2-D and 3-D) flaws. In the IPTS studies[2–4] the cladding was assumed to have the same fracture-toughness characteristics as that for the base material. In an experiment performed on an unclad cylinder with RT_{NDT} = −1°C (30°F) [TSE-7 (Ref. 7)], a 19-mm-deep (0.75-in.) semicircular flaw propagated extensively along the surface and in three initiation-arrest events propagated radially ~40% through the 152-mm (6-in.) wall. Based on early 3-D calculations and the results of TSE-7, it was concluded that, if the fracture toughness of the cladding were less than or equal to that for the base material, shallow semicircular surface flaws would extend on the surface to effectively become long flaws and that this would occur prior to the time that a long flaw of the same depth would propagate radially. Thus, it was only necessary to calculate the potential for the long flaw to propagate (for subsequent initiation/arrest events the actual length of the flaw was considered).

More recent analytical studies[8] have shown that for more realistic PTS transients than previously considered, K_I for an infinitely long surface flaw may be greater than that for semi-elliptical surface flaws of identical depth. Furthermore, a comparison of TSE-7 with a more recent thermal-shock experiment[9] and with a study[10] that makes use of recent cladding irradiation data indicate that the toughness of the cladding may be sufficient to prevent propagation in the cladding under PTS loading conditions. In the TSE-9 experiment[9] [similar test cylinder to TSE-7 with cladding on the inner surface, base-material RT_{NDT} = 66°C (150°F), and essentially the same thermal shock] there was a single event with only 6 mm (0.25 in.) of crack extension, and this event was attributed to completion of the initial flaw in the electron-beam-weld fusion zone created for generating initial flaws. Consequently, the IPTS methodology in Refs. 2–4 tends to predict a greater potential for propagation of initial shallow flaws than would actually exist. For the present study, the possible benefit of using a finite-length surface flaw as the initial flaw, as opposed to a 2-D surface flaw, and of assuming no propagation of the flaw in the cladding was investigated. A semicircular flaw was selected for the finite-length flaw because earlier studies indicated that, at least in the absence of cladding, the maximum K ratio $(K_I/K_{Ic})^*$ for a semicircular flaw was greater than that for longer flaws of the same depth during a PTS transient. By contrast with the longer flaws, the maximum K ratio occurs at or near the surface rather than the deepest point, and thus there is a tendency for the shorter flaw to extend in surface length.

The specific objectives of this initial study are to determine for PTS loading conditions (1) which surface flaw (semicircular or 2-D of the same depth) has the greatest potential for initiation, (2) the minimum flaw depth resulting in initiation of semicircular surface flaws in a clad RPV under PTS loading, and (3) the impact, in terms of the conditional probability of vessel failure, of using a semicircular surface flaw as the initial flaw. Part (2) provides a means for incorporating 3-D flaw effects in the ORNL PFM code, which at the present time does not include stress-intensity-factor influence coefficients for the specific 3-D flaws of interest in this study. With the 3-D capability at hand, it is then possible to perform Part (3).

*K_{Ic} = static crack initiation toughness.

2. INPUT DATA

The transients included in the studies were defined by an exponential decay of the primary-system coolant temperature, a constant heat-transfer coefficient for the fluid film at the coolant-vessel interface, and a constant primary-system pressure. The coolant-temperature transient is described mathematically as

$$T_C = T_f + \left(T_i - T_f\right) e^{-nt}, \tag{1}$$

where

T_C = temperature of primary-system coolant in downcomer (°C),
T_f = final temperature of primary-system coolant in downcomer (°C),
T_i = initial temperature of primary-system coolant in downcomer (°C),
t = time in transient (min), and
n = exponential decay constant (min^{-1}).

For this study the exponential decay constant (n) was 0.15 min^{-1}, which, based on the IPTS studies,[2–4] represents a typical rapid PTS transient; there were three final temperatures [65.6, 100, and 119.4°C (150, 212 and 247°F)] and a single initial temperature [288°C (550°F)] for the coolant and vessel. The coefficient of convective heat transfer was 2839 $W \cdot m^{-2} \cdot K^{-1}$ (500 $Btu/h \cdot ft^{2} \cdot °F$), which is typical for some reactors. The duration of the transient was 100 min in all cases with a pressure of 6.895 MPa (1.0 ksi). The pressure was obtained from a NRC/Electric Power Research Institute (EPRI) PTS computer-code benchmarking activity* currently in progress. Graphical representations of the thermal transients are shown in Fig. 1.

The geometry and material properties of the vessel were obtained from the NRC/EPRI PTS activity. The geometry of the vessel is given in Table 1 and the material properties in Table 2. The adjustment in reference temperatures caused by radiation through the vessel wall was determined by the procedure in Regulatory Guide 1.99 Revision 2 (Ref. 11) with the following equations:

$$RT_{NDT} = -6.67 + \Delta RT_{NDT}, \tag{2}$$

$$\Delta RT_{NDT} = 0.56\,(CF)\left[\Phi^{(0.28-0.1\log\Phi)}\right], \tag{3}$$

and

$$\Phi = \Phi_o \left[e^{(-0.0094\,a)}\right], \tag{4}$$

where

a = crack depth measured from inner surface (mm),
Φ = fast-neutron fluence (E > 1 MeV) at depth a/10^{19} (neutrons/cm^2),
Φ_0 = Φ at a = 0,
ΔRT_{NDT} = increase in RT_{NDT} at depth a (°C), and
CF = chemistry factor.

*Letter, T. J. Griesbach, Electric Power Research Institute, to T. L. Dickson, ORNL, "Definition of PTS Benchmark Problem," dated March 3, 1992.

The chemistry factor is a function of copper and nickel content and, assuming for these analyses a typical high value of copper (0.3 wt%) and a typical value of nickel (0.75 wt%), was determined to be 217.3 from Ref. 11. For $\Phi_0 = 1.73$ (typical for some reactors near end of license period), at the inner surface $\Delta RT_{NDT} = 139°C$ (250°F) and $RT_{NDT} = 132°C$ (270°F), which corresponds to the screening criteria for axial flaws, as specified by the PTS rule.[1] (The specific values for Φ_0, copper, and nickel are those used in the NRC/EPRI PTS activity.)

Predictions of crack initiation were based on a range of American Society of Mechanical Engineers (ASME)-based fracture initiation toughness curves. The mean K_{Ic} curve was the one used in the IPTS studies[2–4] and is defined by assuming that the ASME lower-bound curve[12] represents the mean minus two standard deviations. One standard deviation is defined as 0.15 (K_{Ic} mean). The range of K_{Ic} curves used in these analyses were:

$$-3\sigma = 0.787 \text{ (ASME lower-bound } K_{Ic} \text{ curve)}, \tag{5}$$

$$-2\sigma = \text{ASME lower-bound } K_{Ic} \text{ curve}, \tag{6}$$

$$-1\sigma = 1.22 \text{ (ASME lower-bound } K_{Ic} \text{ curve)}, \tag{7}$$

$$0\sigma = 1.43 \text{ (ASME lower-bound } K_{Ic} \text{ curve)}, \tag{8}$$

and

$$K_{Ic}\text{ (ASME)} = 36.5 + 3.083 \exp\left[0.036\,(T - RT_{NDT} + 55.56)\right], \tag{9}$$

where K_{Ic} is in $MPa\sqrt{m}$.

Vessel dimensions and material properties (in addition to K_{Ic}) used in this study are given in Tables 1 and 2.

Table 1. Geometry of the vessel used in the PTS analyses

Inner vessel radius, mm (in.)	2286.0 (90.0)
Wall thickness (with cladding), mm (in.)	228.6 (9.0)
Cladding thickness, mm (in.)	4.1 (0.16)

3. DETERMINISTIC-ANALYSIS METHODOLOGY FOR LONG FLAWS

OCA-P was used to perform the fracture analysis for the 2-D flaws. OCA-P performs one-dimensional (1-D) finite-element thermal and stress analyses to determine the time and wall-depth-dependent temperatures and stresses that are required for a fracture analysis. OCA-P then utilizes stress-intensity-factor influence coefficients and superposition techniques to calculate K_I values as functions of crack depth and transient time. OCA-P also calculates the time- and wall-depth-dependent values of K_{Ic} based on the attenuated fluence, chemistry, and initial (unirradiated) value of RT_{NDT}, and determines critical flaw depths and corresponding transient times.

Table 2. Material properties

	Cladding	Base metal
Modulus of elasticity (E), MPa (ksi)	186,160 (27,000)	193,050 (28,000)
Poisson's ratio (ν)	0.3	0.3
Thermal expansion coefficient (α), per °C (per °F)	17.82×10^{-6} (9.9×10^{-6})	14.49×10^{-6} (8.05×10^{-6})
Thermal conductivity (k), W/m·°C (Btu/hr·ft·°F)	17.3 (10)	41.52 (24)
Specific heat (c_p), J/kg·°C (Btu/lb·°F)	502 (0.12)	502 (0.12)
Density (ρ), kg/m^3 (lb/ft^3)	7833 (489)	7833 (489)

4. 3-D FINITE-ELEMENT ANALYSES

Semielliptical axial surface cracks having length-to-depth ratios of 2:1 and depths ranging from 4.572 mm (0.18 in.) to 44.45 mm (1.75 in.) were evaluated in this study. The 3-D finite-element model of the cylinder was generated with the ORMGEN[13] mesh generating program. From symmetry conditions, only one-fourth of the cylinder (180° model) is included in the finite-element model (Fig. 2). A detailed plot of the crack-tip region of a 12.7-mm-deep (0.5-in.) flaw is shown in Fig. 3. This model has a modified semicircular crack front in which the crack-front profile through the thickness of the cladding is represented by a straight line normal to the surface. This straight-line profile affects the modeling of shallow semicircular flaws. Comparisons were made between the 3-D analyses and closed-form K_I solutions[14] developed for semicircular part-through surface cracks. There was good agreement between the two results for deeper flaws [12.7 mm to 25.4 mm (0.5 to 1.0 in.)], but the solutions diverged as the flaw depth becomes more shallow [6.35 mm (0.25 in.)]. This is because of the modeling assumptions discussed earlier (the deviation of the 3-D crack front from a semicircular configuration becomes more pronounced as the flaw becomes more shallow). Hence the 3-D results will deviate from closed-form solutions for a semicircular flaw. The comparisons are summarized in Table 3 for T_f = 119.4°C (247°F) at a time of 17.5 min [3-D K_I values were not available for the 4.572 mm (0.18 in.) flaw with this transient]. The vessel dimensions are given in Table 1. The cylinder was analyzed with the ADINA[15] finite-element program, using special constraints on the nodal displacements to approximate generalized-plane-strain boundary conditions opposite the symmetry plane. This boundary condition is used to simulate the closed end of an RPV. The model depicted in Fig. 2 consists of 8161 nodes and 1688 twenty-noded isoparametric elements.

The 3-D model of the cylinder was analyzed using the material properties in Table 2, which were assumed to be constant throughout the transient. Thermoelastic analyses were performed using a 3 × 3 × 3 Gauss point rule to compute the global stiffness matrix. The temperatures through the wall for each transient were obtained from the OCA-P thermal analyses and applied to the cylinder by interpolation. The "stress free" temperature was taken as the initial operating temperature of the RPV, which is a reasonable approximation to the lifetime load history effects.

The pressure of 6.897 MPa (1.0 ksi) was applied to the model using 3-D element pressure surfaces. For each time step of the calculations, energy release rates were determined around the crack front using a virtual crack-extension technique developed by deLorenzi[16] and implemented

in the ORVIRT[17] program. (The ORVIRT program functions as a postprocessor of a conventional finite-element solution obtained from the ADINA program.)

The through-wall circumferential and axial stress distributions from the ADINA and OCA-P solutions were compared for T_f = 119.4°C (247°F), and a time of 17.5 min into the transient. This comparison is depicted in Fig. 4 and shows good agreement.

Table 3. Comparisons of 3-D finite-element analyses with closed-form K_I solutions of semicircular part-through surface cracks

Location	a = 25.4 mm (1.0 in.)			a = 15.875 mm (0.625 in.)			a = 12.70 mm (0.5 in.)			a = 6.35 mm (0.25 in.)			a = 4.572 mm (0.18 in.)		
	K_I (MPa$\sqrt{m}$)			K_I (MPa$\sqrt{m}$)			K_I (MPa$\sqrt{m}$)			K_I (MPa$\sqrt{m}$)			K_I (MPa$\sqrt{m}$)		
	3-D	CF*	% Diff	3-D	CF	% Diff	3-D	CF	% Diff	3-D	CF	% Diff	3-D	CF	% Diff
Surface	98	99	1	82	80	3	74	72	3	46	52	12	—	44	—
Clad/Base Interface	86	90	4	67	71	6	58	64	9	28	44	36	—	37	—
Deepest Point	62	65	5	55	59	7	51	54	6	36	41	12	—	36	—

*CF = closed-form solution.

As mentioned in the introduction, to be able to perform the PFM analysis with OCA-P, considering 3-D as well as 2-D flaws, it was necessary to provide a means for including 3-D-flaw effects in OCA-P for the specific flaws of interest. This was done by first calculating the minimum flaw depth that would result in initiation during the specific PTS transients of interest for the study. In so doing, the effects of warm prestress were neglected, consistent with the requirement in NRC *Regulatory Guide 1.154* and thus consistent with the way in which the OCA-P PTS analyses are performed with 2-D and other 3-D flaws.

5. DETERMINISTIC COMPARISON OF POTENTIAL FOR INITIATION OF 2-D AND 3-D FLAWS

Values of K_I/K_{Ic} were calculated for flaw depths of 12.7 and 25.4 mm (0.5 and 1.0 in.), and for the two PTS transients corresponding to T_f = 65.6 and 100.0°C (150 and 212°F). For the 3-D (semicircular) flaw, the maximum value of K_I/K_{Ic} occurs at the clad/base interface, and thus the 3-D flaw initially tends to grow in length. Thermal-shock experiments[9] with clad cylinders indicate that in a single event the flaw could grow in length beneath the cladding to become a long (2-D) flaw. Thus, the interface point on the initial crack front was used in the present study for the comparison.

Results of the analyses, shown in Fig. 5 (a)–(d), indicate that for a flaw depth of 25.4 mm (1.0 in.) and T_f = 100.0°C (212°F) the maximum values of K_I/K_{Ic} (maximum with respect to time) are somewhat greater for the 3-D flaws, and for the more severe transient the 25.4-mm (1.0

in.) 3-D values are only slightly less than for the 2-D values, with the 2-D values occurring a few minutes later in both transients. For shallower flaws, the maximum values for the 3-D flaws are substantially less than for the 2-D flaws. Previous IPTS-type studies [2-4] using only 2-D flaws for initial flaws, indicate that most initial flaws resulting in vessel failure have depths less than 15 mm. Thus, use of the presumably more likely 3-D flaw could result in a smaller calculated value of the probability of vessel failure. A preliminary estimate of the effect is included in Section 8.

6. CALCULATION OF MINIMUM CRITICAL FLAW DEPTH FOR 2-D FLAWS

The minimum flaw depth that resulted in cleavage fracture as predicted by OCA-P is illustrated in Fig. 6 for infinite-length axial-oriented surface flaws and for the various transients and K_{Ic} curves, assuming RT_{NDT} at the vessel inner surface of 132°C (270°F). From Fig. 6 it can be seen that as the toughness increases (-3σ to 0σ) and T_f increases, the minimum flaw depth that will initiate increases, as would be expected for the specific transients.

7. CALCULATION OF MINIMUM CRITICAL FLAW SIZE FOR 3-D FLAWS

In performing a series of 3-D analyses for each transient to determine the minimum crack depth that would result in initiation, K_I was calculated along all of the crack front. Values are plotted as a function of time and selected points along the crack front in Fig. 7 (a)–(c) for crack depths of 25.4 mm (1.0 in.), 10.16 mm (0.4 in.), and 6.35 mm (0.25 in.), respectively, and for T_f = 100°C (212°F). As indicated, K_I values are highest at the surface. For the deepest flaw, the maximum value in the base material is at the clad/base interface, and for the shallowest flaw, it is at the deepest point.

In Fig. 8, values of K_I and K_{Ic} at the clad/base interface for a = 15.875 mm (0.625 in.) and T_f = 100°C (212°F) are shown as functions of time. The K_I curve is tangent to a K_{Ic} curve slightly above the -1σ curve. The corresponding time and K_I value are approximately 30 min and 66 MPa$\sqrt{m}$ (60 ksi$\sqrt{in.}$). By interpolation, crack depths corresponding to tangent points with each of the indicated K_{Ic} curves were obtained and are reported in Table 4. These crack depths are the minimum values that will result in initiation for the specified conditions, and the maximum K_I value from along the crack front. All the initiations took place at the clad/base interface except for the -2σ and -3σ cases and T_f = 65.6°C (150°F), since K_I was higher at the deepest point. As discussed earlier, there is a divergence from the closed-form solution for the shallow-flaw 3-D model at the clad/base interface. The results in Table 3 for shallow flaws indicate that the value of K_I at the clad/base interface is close to the value at the deepest point for the closed-form solution. Consequently, for these analyses, the minimum flaw depth that will result in initiation would not change for the -3σ case, but would decrease from 7.37 mm (0.29 in.) to 6.35 mm (0.25 in.) for the -2σ case. For any subsequent analyses, it is recommended that a 3-D model of a true semicircle be used.

The results from the 3-D and IPTS/OCA-P analyses are plotted together in Fig. 9. The 3-D results, using the -3σ fracture toughness curve, predict that a much deeper minimum critical flaw size (by 80%) is needed for initiation than is indicated by the 2-D results for the three transients. But, as toughness increases (-3σ to 0σ), and the final temperature increases, the 3-D results predict flaws to initiate which are shallower than those predicted by the 2-D analyses.

Table 4. 3-D finite-element results

Temperature		0σ		−1σ		−2σ		−3σ	
°C	(°F)	a	K	a	K	a	K	a	K
65.6	(150)	10.92 (.43)	63 (57)	9.14 (.36)	53 (48)	7.37 (.29)	47 (43)	5.08 (.20)	36 (33)
100.0	(212)	21.84 (.86)	77 (70)	15.75 (.62)	66 (60)	11.68 (.46)	54 (49)	8.89 (.35)	45 (41)
119.4	(247)	42.93 (1.69)	98 (89)	29.97 (1.18)	83 (76)	20.07 (.79)	69 (63)	13.46 (.53)	54 (49)

Note: Values of a in mm (in.)
Values of K in MPa$\sqrt{m}$ (ksi$\sqrt{in.}$)

8. OCA-P PROBABILISTIC ANALYSES

The possible net benefit of using 3-D as opposed to 2-D initial flaws in a PTS analysis is most accurately evaluated in terms of the probability of vessel failure. PFM calculations, using OCA-P, were performed using both 2-D and semicircular flaws as initial flaws. The results, shown in Fig. 10, indicate that P(F|E) is substantially less for the semicircular flaw: a factor of 3 for the most severe transient considered and a factor of 20 for the least severe.

For these studies, the semicircular flaws was included in the OCA-P analysis in an approximate manner that underestimated the benefit of using the specific 3-D as opposed to the 2-D flaw. [The minimum crack depths for initiation determined in the 3-D deterministic analysis (Section 7) were used as a filter to eliminate initiation of 2-D flaws of a shallower depth. Flaws that were not filtered out were treated as infinitely long surface flaws.[19]]

9. DISCUSSION AND SUMMARY

Analyses were performed to determine the effect of using semicircular surface flaws as initial flaws in a PTS analysis as opposed to 2-D flaws. A deterministic analysis indicated that deeper 3-D (semicircular) than 2-D flaws were required for initiation, except for the least severe transient. P(F|E) was reduced by a factor of 3 for the most severe transient and a factor of 20 for the least severe transient. When the closed-form semicircular flaw K_I solutions were evaluated, the minimum flaw depth required for initiation did not change significantly. Consequently, P(F|E) was not affected. This initial study indicates that incorporating finite-length flaw results into probabilistic fracture analyses significantly affects the analyses.

10. REFERENCES

1. *Code of Federal Regulations*, Title 10, Part 50, Section 50.61 and Appendix G.

2. D. L. Selby et al., *Pressurized-Thermal-Shock Evaluation of the H. B. Robinson Nuclear Power Plant*, NUREG/CR-4183, Vol. 1 (ORNL/TM-9567/V1), Martin Marietta Energy Systems, Inc., Oak Ridge Natl. Lab., September 1985.

3. D. L. Selby et al., *Pressurized-Thermal-Shock Evaluation of the Calvert Cliffs Unit 1 Nuclear Power Plant*, NUREG/CR-4022 (ORNL/TM-9408), Martin Marietta Energy Systems, Inc., Oak Ridge Natl. Lab., September 1985.

4. T. J. Burns et al., *Preliminary Development of an Integrated Approach to the Evaluation of Pressurized-Thermal-Shock as Applied to the Oconee Unit 1 Nuclear Power Plant*, NUREG/CR-3770 (ORNL/TM-9176), Martin Marietta Energy Systems, Inc., Oak Ridge Natl. Lab., May 1986.

5. U. S. Nuclear Regulatory Commission, *Regulatory Guide 1.154*, "Format and Content of Plant-Specific Pressurized Thermal Shock Safety Analysis Reports for Pressurized Water Reactors."

6. R. D. Cheverton and D. G. Ball, *OCA-P, A Deterministic and Probabilistic Fracture-Mechanics Code for Application to Pressure Vessels*, NUREG/CR-3618 (ORNL-5991), Martin Marietta Energy Systems, Inc., Oak Ridge Natl. Lab., May 1984.

7. R. D. Cheverton et al., "Thermal Shock Experiment TSE-7," pp. 57–74 in *Heavy Section Steel Technology Program Quarterly Progress Report for April–June 1983*, NUREG/CR-3334 Volume 2 (ORNL/TM-8787/V2), December 1983.

8. R. D. Cheverton and D. G. Ball, *A Parametric Study of PWR Pressure Vessel Integrity During Overcooling Accidents, Considering Both 2-D and 3-D Flaws*," NUREG/CR-4325 (ORNL/TM-9682), Martin Marietta Energy Systems, Inc., Oak Ridge Natl. Lab., August 1985.

9. R. D. Cheverton et al., "Thermal-Shock Experiments with Flawed Clad Cylinders," *Nuclear Engineering and Design* 124, pp. 109–119, North-Holland, 1990.

10. J. Keeney-Walker, B. R. Bass, and W. E. Pennell, "Evaluation of the Effects of Irradiated Cladding on the Behavior of Shallow Flaws Subject to Pressurized-Thermal-Shock Loading," *Proceedings of the 11th Conference on Structural Mechanics in Reactor Technology*, Tokyo, Japan, August 18–22, 1991.

11. U. S. Nuclear Regulatory Commission, *Regulatory Guide 1.99 Revision 2*, "Radiation Embrittlement of Reactor Vessel Materials."

12. The American Society of Mechanical Engineers Boiler and Pressure Vessel Code, Section XI, "Rules for Inservice Inspection of Nuclear Power Plant Components," 1986.

13. B. R. Bass and J. W. Bryson, Applications of Energy Release Rate Techniques to Part-Through Cracks in Plates and Cylinders, Volume 1, ORMGEN-3D: A Finite-Element Mesh Generator for 3-Dimensional Crack Geometries, NUREG/CR-2997/V1 (ORNL/TM-8527), Union Carbide Corp. Nuclear Div., Oak Ridge Natl. Lab., December 1982.

14. J. G. Merkle, *A Review of Some of the Existing Stress Intensity Factor Solutions for Part-Through Surface Cracks*, ORNL/TM-3983, Union Carbide Corp., Nuclear Div., Oak Ridge Nat'l. Lab., January 1973.

15. K. J. Bathe, *ADINA – A Finite-Element Program for Automatic Dynamic Incremental Nonlinear Analysis*, Report 82448-1, Massachusetts Institute of Technology, 1975, revised 1978.

16. H. G. deLorenzi, *On the Energy Release Rate and the J-Integral for 3-D Crack Configurations*, TIS Report 80CRD 113, General Electric Company, 1980.

17. B. R. Bass and J. W. Bryson, *Applications of Energy Release Rate Techniques to Part-Through Cracks in Plates and Cylinders, Volume 2, ORVIRT: A Finite-Element Program for Energy Release Rate Calculations for 2-D and 3-D Crack Models*, NUREG/CR-2997/V2 (ORNL/TM-8527), Union Carbide Corp. Nuclear Div., Oak Ridge Natl. Lab., February 1983.

18. J. G. Merkle, *Experimental Observations of Cladding Effects on Crack Extension*, ORNL/NRC/LTR-92/16, Martin Marietta Energy Systems, Inc., Oak Ridge Natl. Lab., June 30, 1992.

19. J. Keeney-Walker, J. G. Merkle, S. K. Iskander, and T. L. Dickson, *Finite-Length Surface Crack Propagation in Clad Cylinders*, NUREG/CR-5915 (ORNL/TM-12166), Martin Marietta Energy Systems, Inc., Oak Ridge Nat'l. Lab.(to be published).

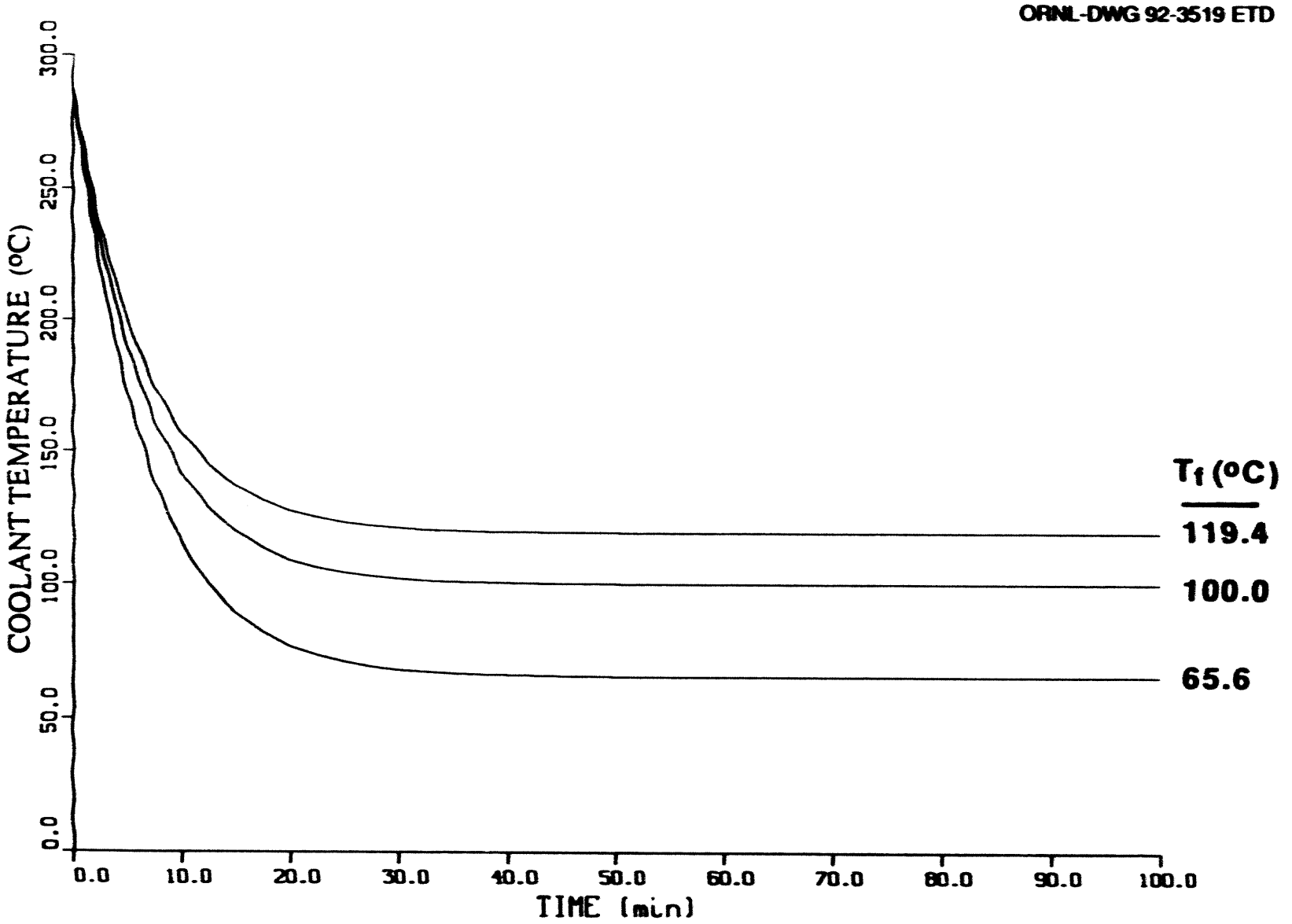

Fig. 1. Postulated thermal transients with an exponential decay constant of 0.15 min^{-1}.

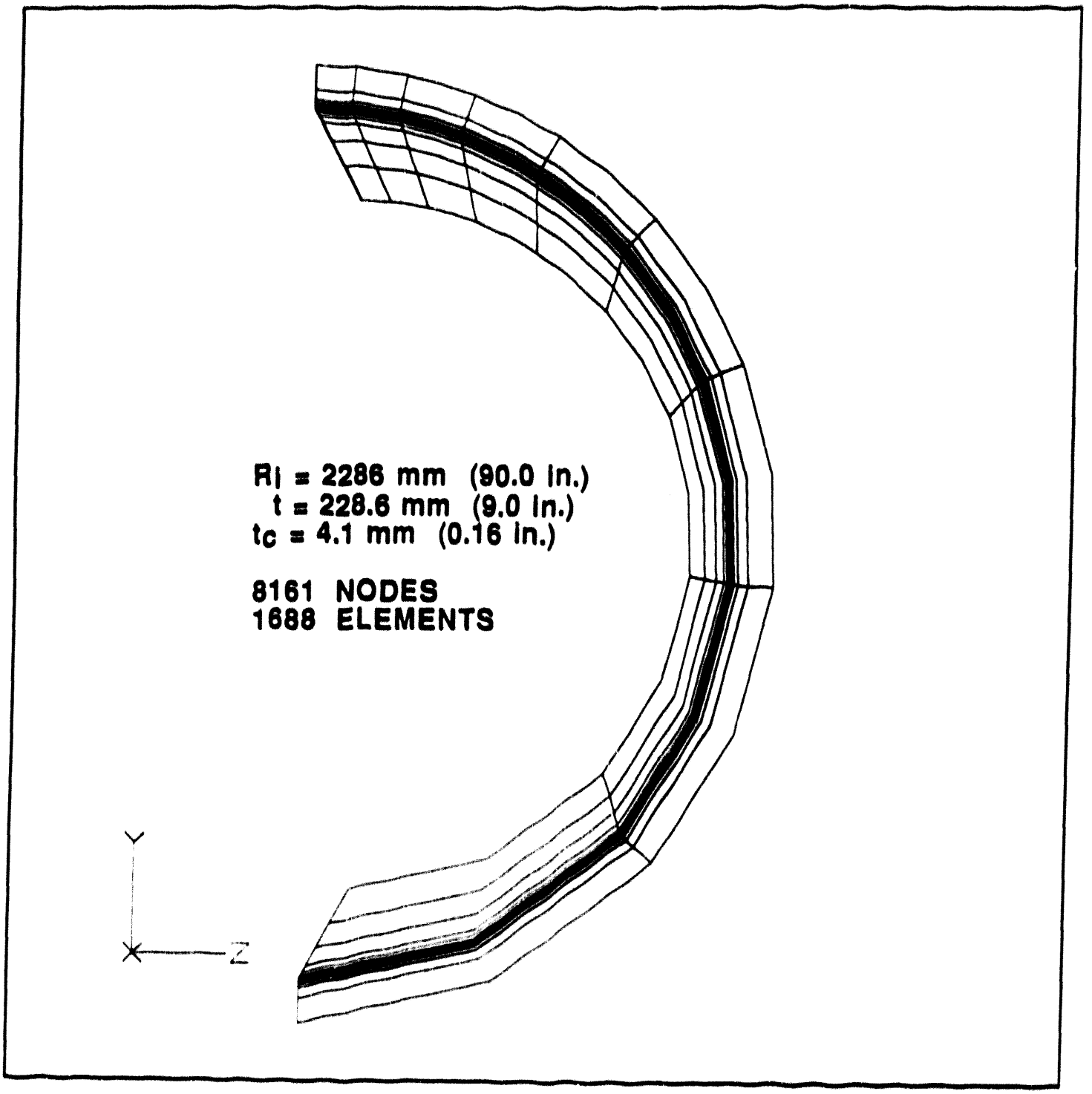

Fig. 2. 3-D finite-element model of a clad cylinder subjected to PTS loading.

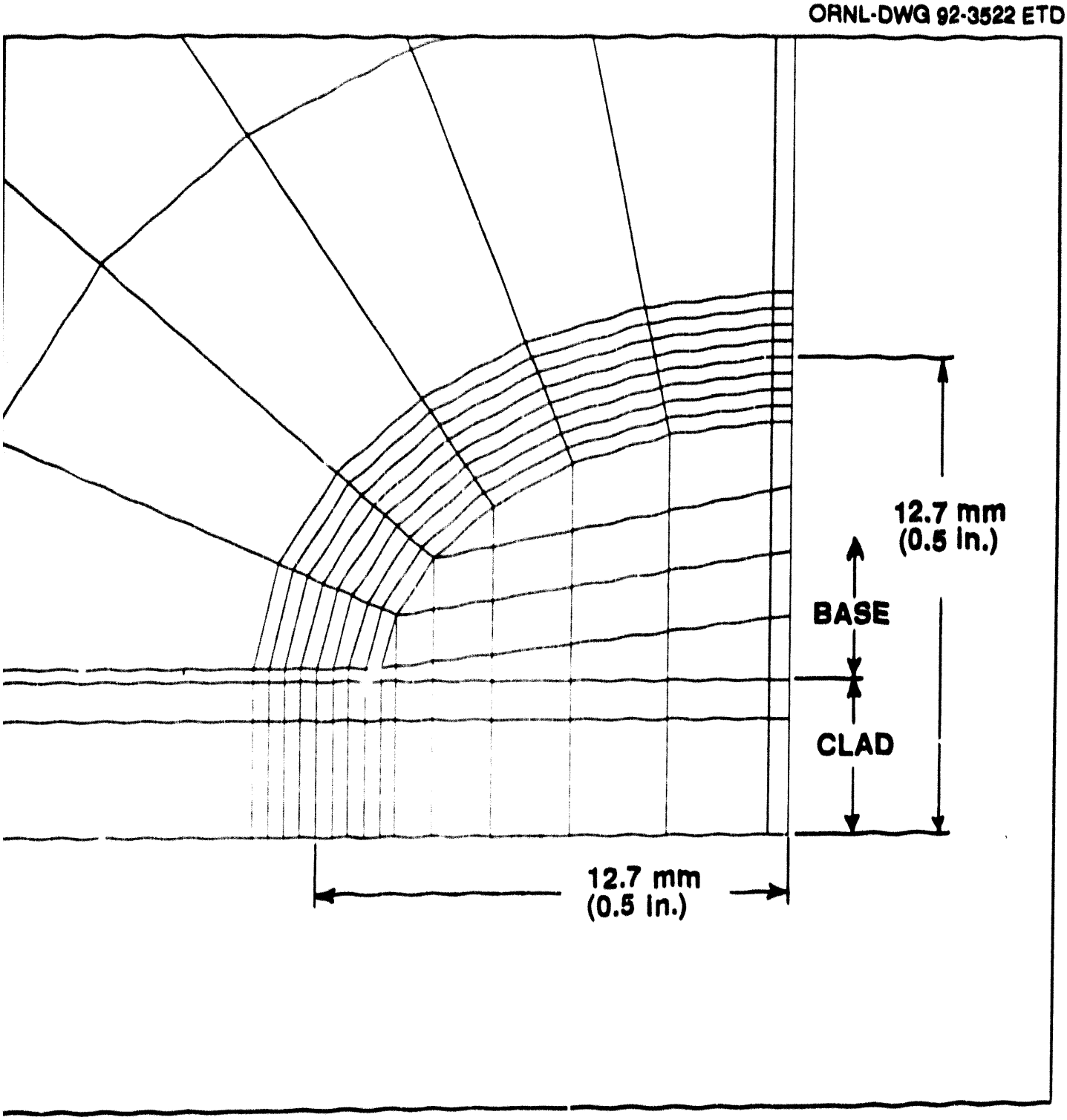

Fig. 3. Detail of crack-tip region for the finite-element model of a clad cylinder with a 12.7-mm-deep (0.5-in.) flaw.

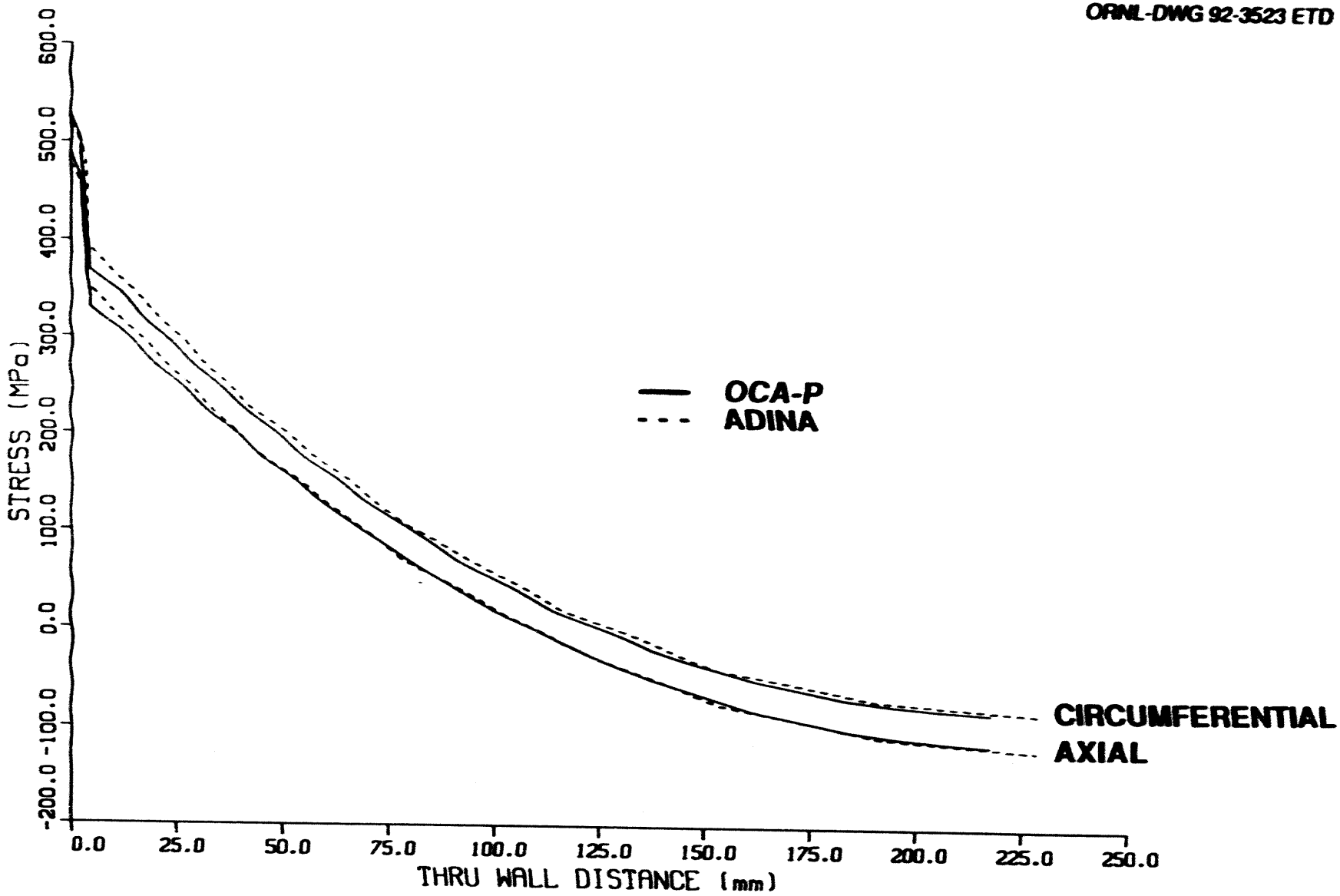

Fig. 4. Comparison of the through wall stresses for an OCA-P and 3-D finite-element analysis.

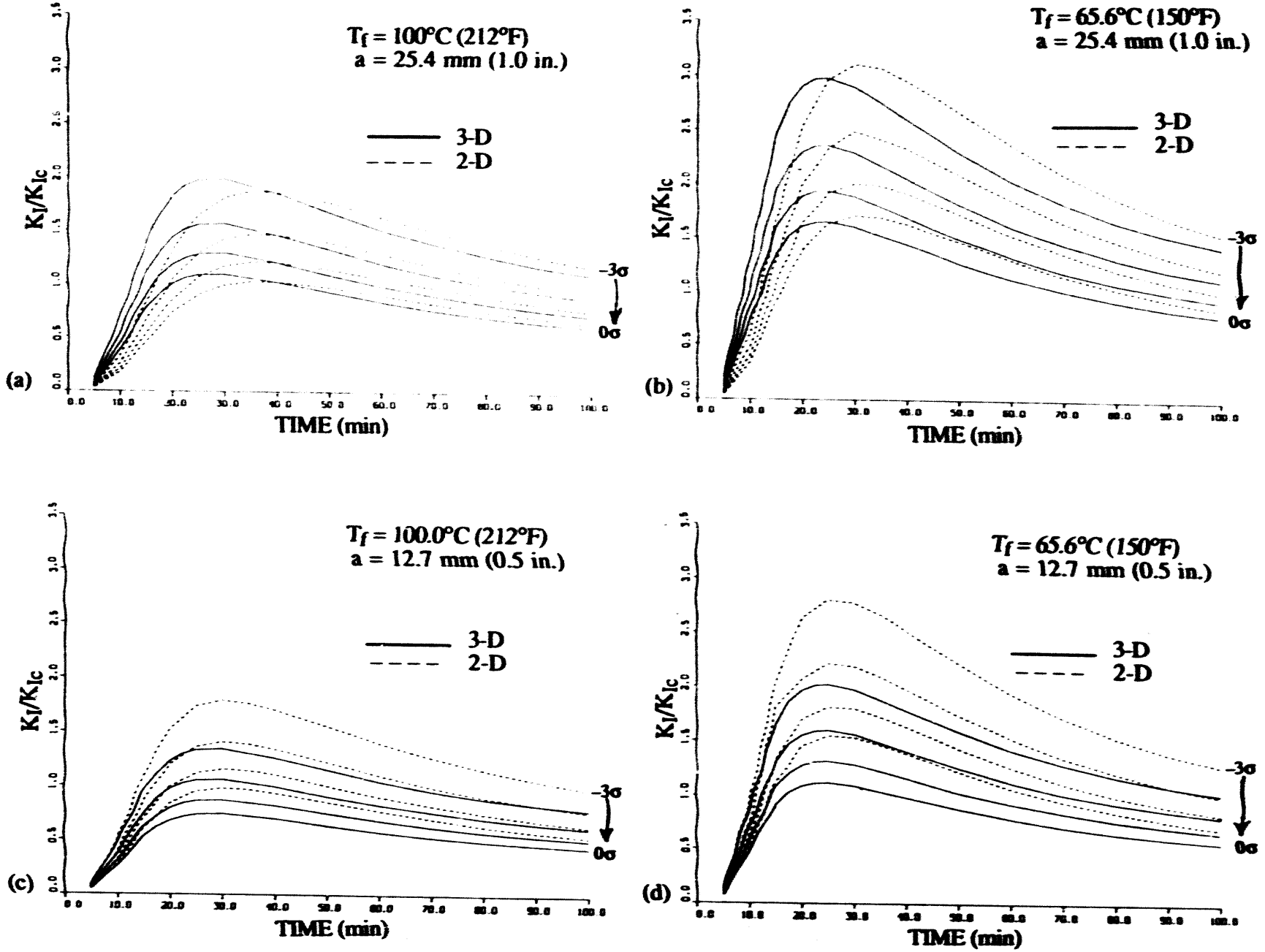

Fig. 5. Values of K_I/K_{Ic} ratios as a function of time: (a) 25.4 mm (1.0 in.), T_f = 100°C (212°F); (b) 25.4 mm (1.0 in.), T_f = 65.6°C (150°F); (c) 12.7 mm (0.5 in.), T_f = 100°C (212°F); and (d) 12.7 mm (0.5 in.), T_f = 65.6°C (150°F).

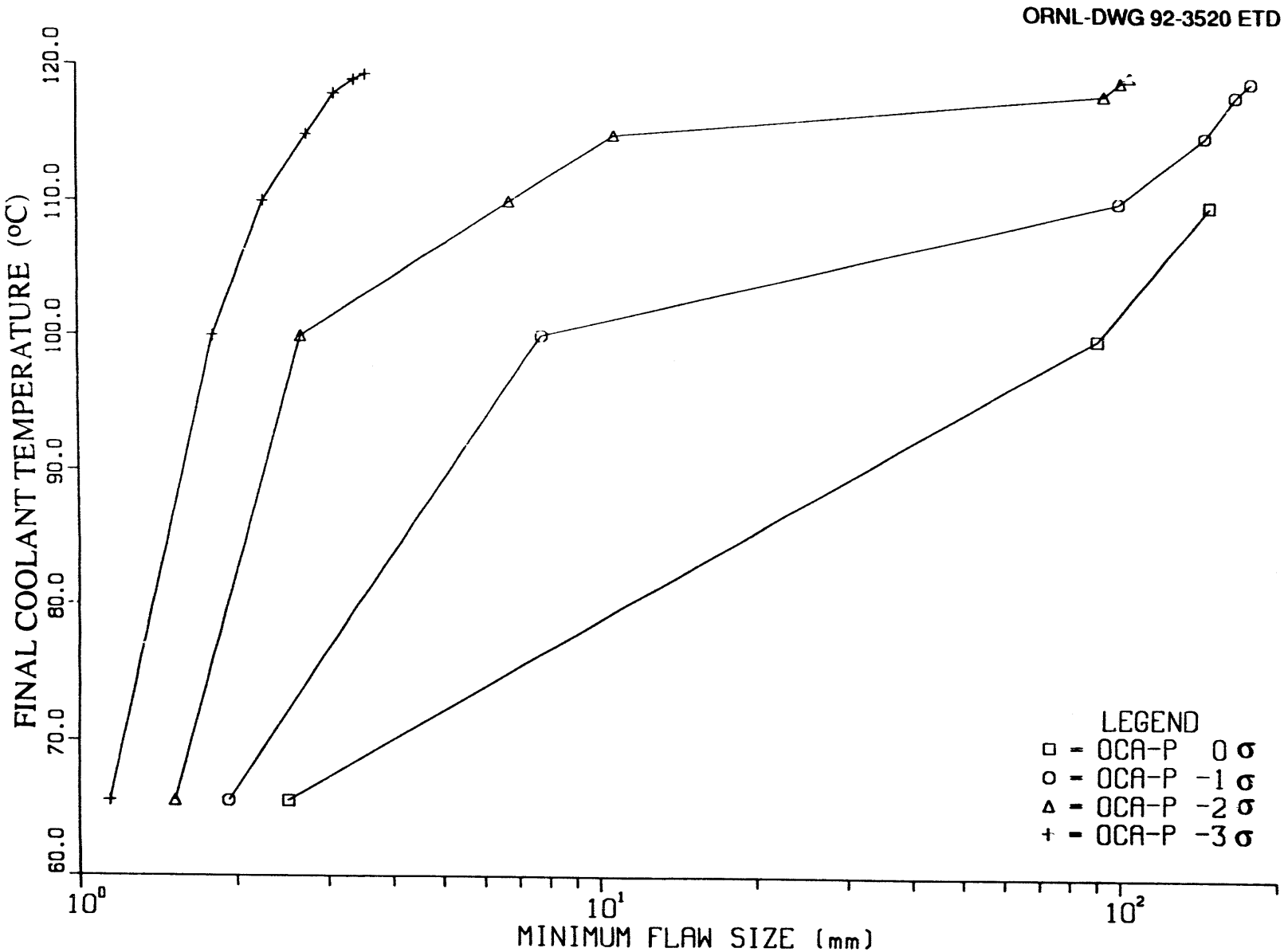

Fig. 6. Minimum flaw depth that will initiate in cleavage as predicted by OCA-P for infinite-length axial surface flaws.

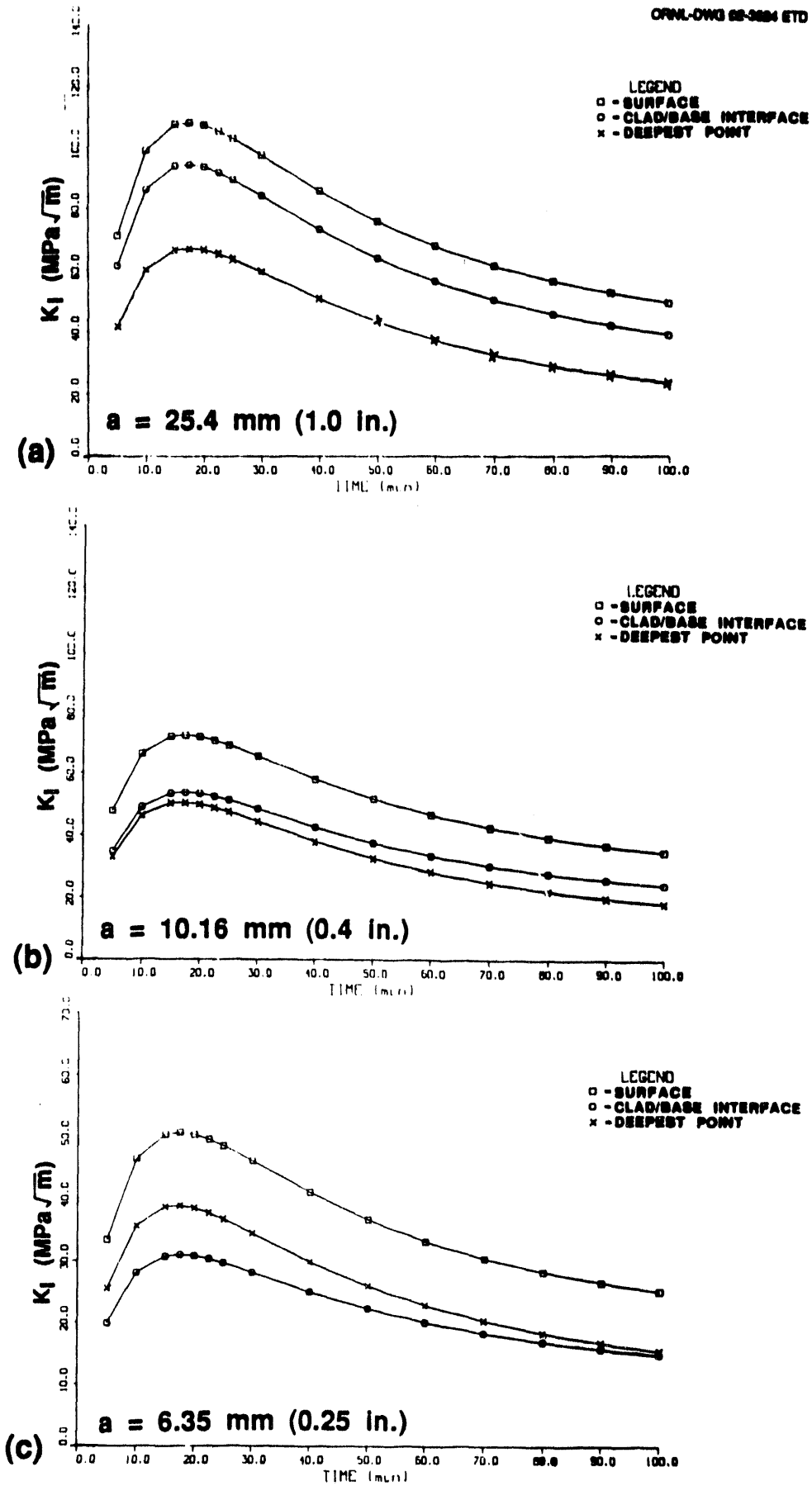

Fig. 7. Values of applied K_I as a function of time for three flaw depths: (a) 25.4 mm (1.0 in.); (b) 10.16 mm (0.4 in.); and (c) 6.35 mm (0.25 in.); T_f = 100°C (212°F).

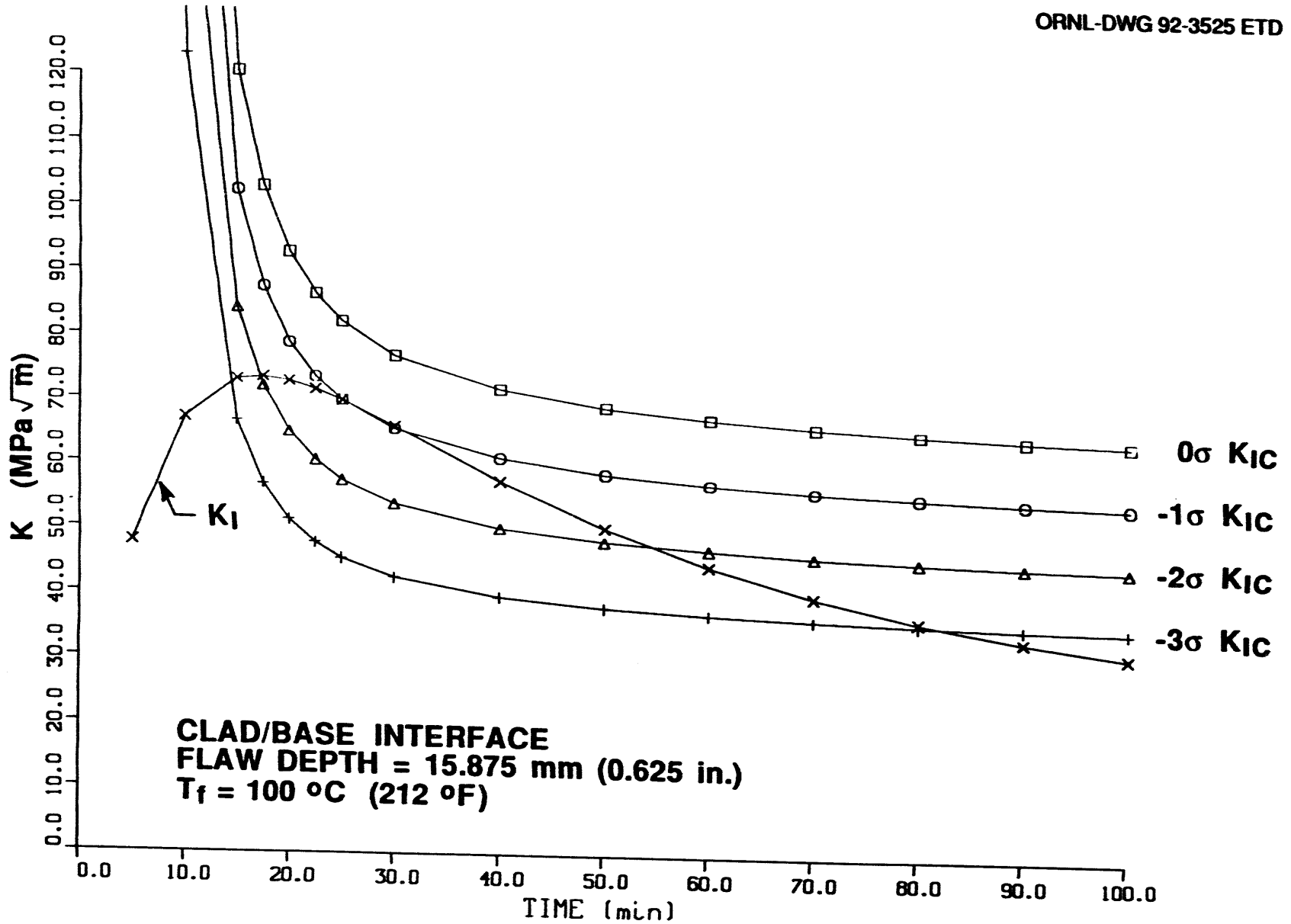

Fig. 8. Comparison of K_I and K_{Ic} at the clad/base interface for a 15.875-mm-deep (0.625-in.) flaw.

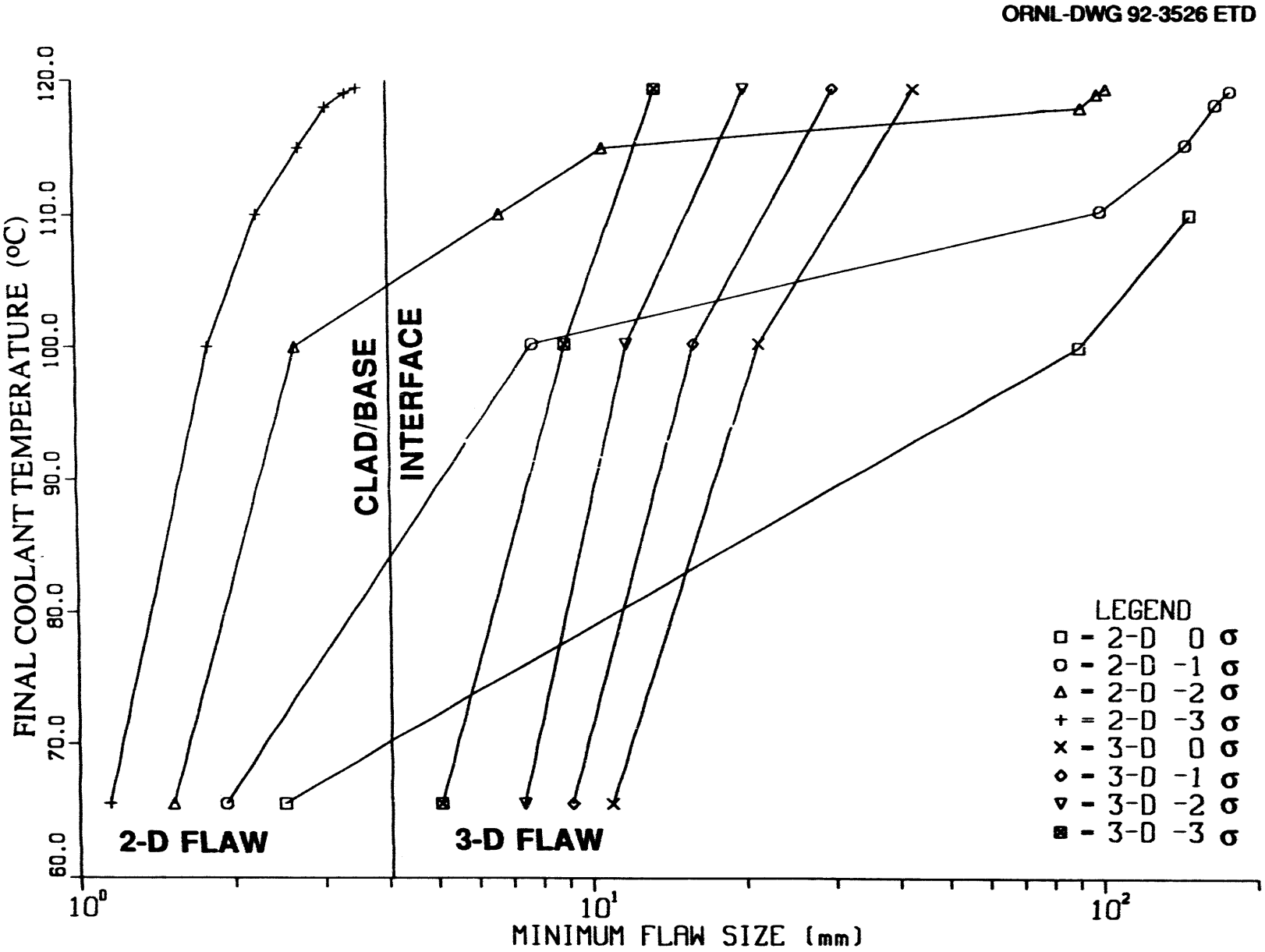

Fig. 9. Comparison of predictions for the minimum flaw depth that will initiate in cleavage by OCA-P and 3-D finite-element analyses.

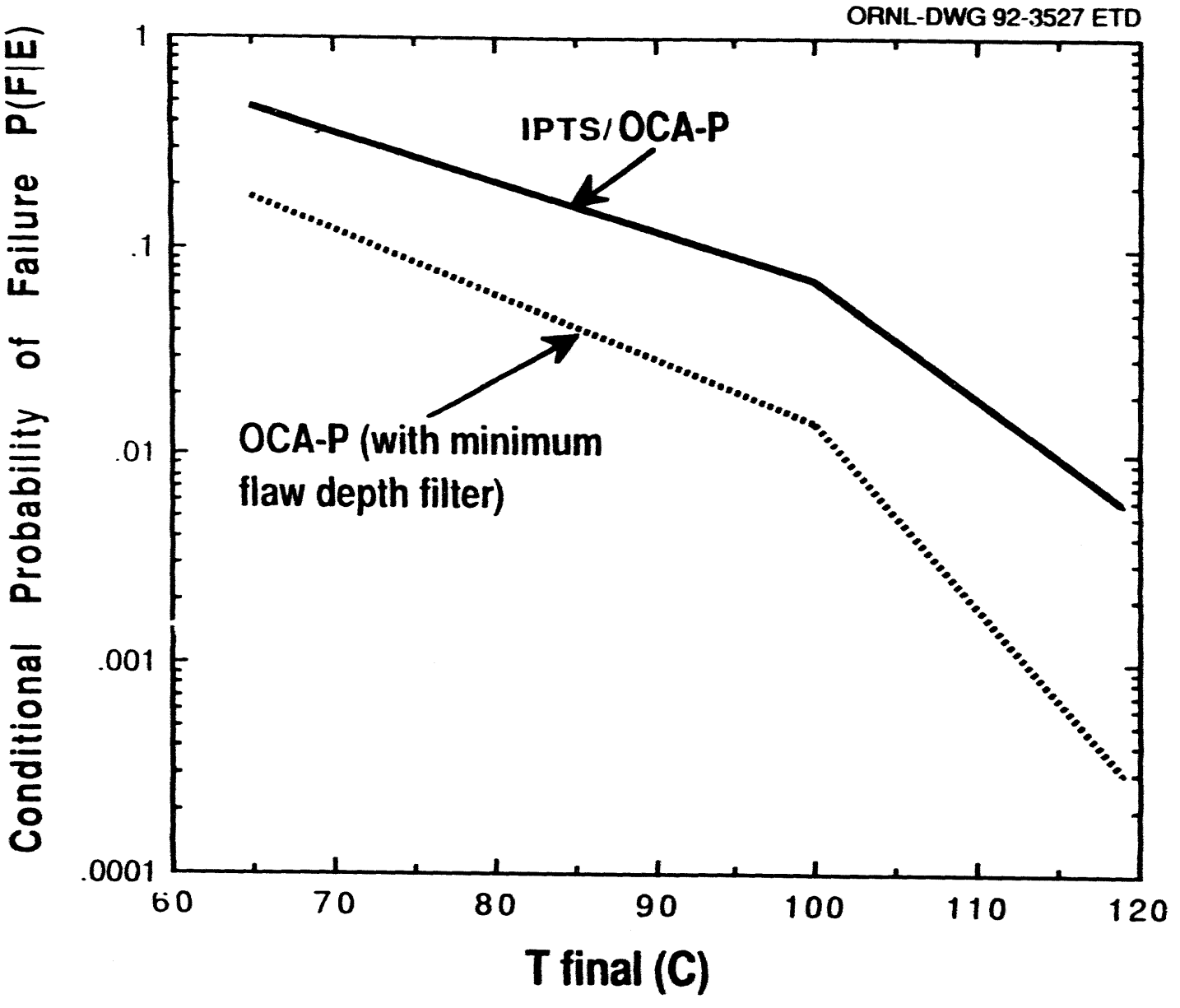

Fig. 10. P(FIE) as a function of transient as predicted by OCA-P and OCA-P with filter.

LARGE-SCALE TESTING OF VVER REACTOR PRESSURE VESSEL MATERIALS - VERIFICATION OF FRACTURE MECHANICS CALCULATIONS

Milan BRUMOVSKÝ
ŠKODA Concern, Nuclear Machinery Plant
Czech and Slovak Federal Republic

ABSTRACT

Large-scale fracture mechanics experiments have been carried out in cooperation between ŠKODA Concern, OKB Gidropress and CNIITMASH (both former USSR) to establish reliable and precise fracture mechanics calculations for VVER reactor pressure vessel behaviour.

The programme included testing of base materials, electroslag and submerged arc weldments from both 15Kh2MFA (VVER-440) as well as from 15Kh2NMFA (VVER-1000) types of steels. The most important part of the experiments were performed on 150 mm thick specimens (with section of 150 × 600 mm in ŠKODA tested in tension, and with sections 150 × 400 up to 150 × 650 mm in CNIITMASH tested by spinning) with different surface defects. Testing temperatures were within the interval of -30 and +80°C, with defect depths between 15 and 100 mm, all of semielliptical form.

Fracture behaviour of these tests varied between fully brittle (cleavage) to ductile, with/or without any subcritical crack growth.

These large-scale tests were completed by standard fracture mechanics tests, and in the case of VVER-440 materials also by small-scale specimens testing.

Evaluation of results has been carried out on the basis of linear-elastic fracture mechanics, elastic-plastic fracture mechanics as well as two-criteria (R6) methods with respect to uniaxial as well as biaxial loading.

INTRODUCTION

One of the most important tasks with respect to ensuring reactor pressure vessel (RPV) safe operation is to eliminate any possibility of fast (brittle or semi-brittle) fracture. Nuclear codes used nowadays are based on Linear Elastic Fracture Mechanics (LEFM) only. This approach seems to be very conservative, especially in the area of elastic-plastic loading. Such type of loading is characteristic not only for normal operation conditions, but also for cases of emergency cooling - pressurized thermal shock. Moreover, operating conditions (relatively high temperatures with respect to material transition temperatures) as well as steels of medium strength create a situation such that conditions of plane strain are not fulfilled even for high thicknesses of RPV walls. Thus, the LEFM approach is no longer fully suitable and should be replaced by some more appropriate approach like CEGB R6, for example.

Tests of large-scale specimens of real thickness (equal to the thickness of RPV wall) are very useful to determine real conditions of fast fracture initiation. In cases when these specimens have surface semielliptical defects, their results can be compared with calculated parameters received directly from Codes.

A coordinated research programme has been carried out mainly in ŠKODA Concern, Nuclear Machinery Plant, Plzeň, ČSFR with the aim of checking conditions for fracture initiation in materials of RPVs for VVER-440 and VVER-1000 MW units. This programme was carried out in a close cooperation with the OKB "Gidropress", Podolsk, Russia (General Designer of VVER reactors) and CNIITMASH, Moscow, Russia (Material Research Organization).

TESTED MATERIALS

Large scale specimens were manufactured from 150 mm thick plates taken from materials used for RPV of VVER-440 (15Kh2MFA type) as well as for VVER-1000 MW (15Kh2NMFA type) units. Base metals (BM) as well as welding joints were tested; included were electroslag (ES) and submerged arc (A/S) welds.

Main characteristics if these materials are given in Tables 1 and 2.

Table 1. Chemical composition of tested materials (mass %)

material									
15Kh2MFA steel	0.15	0.48	0.35	0.013	0.016	2.77	0.14	0.60	0.34
15Kh2NMFA steel	0.13	0.41	0.23	0.010	0.018	2.06	1.32	0.63	0.07

Table 2. Mechanical properties of tested materials at 20°C

material	$R_p0.2$ (MPa)	R_m (MPa)	A_5 (%)	Z (%)	KCV (Jcm^{-2})	T_{ko} (°C)	K_{IC} ($MPa\sqrt{m}$)
15Kh2MFA steel	575	680	21.2	72.8	210	-30	150-200
S/A weld metal	425	565	25.4	66.4	30	+30	80
ES weld metal	550	665	20.4	73.0	30	+40	80
15Kh2NMFA steel	570	660	21.4	70.0	200	-30	220-250
S/A weld metal	500	610	21.0	64.0	85		180
ES weld metal	650	750	18.5	71.0			135

Transition temperature T_{k0} - *critical temperature of brittleness* - is, in principle, defined as follows:

- mean value of KCV from three tests at temperature equal to T_{k0} should be equal to 60 Jcm^{-2} (for steels with yield strength at room temperature between 550 and 700 MPa),

- mean value of KCV from three tests at temperature equal to T_{k0} + 30°C must not be lower than 90 Jcm^{-2} and mean value of shear fracture appearance must be larger than 50%.

This transition temperature lies within an interval of RT_{NDT} +/-10°C, as was demonstrated for both types of steels.

TESTING EQUIPMENTS AND PROCEDURES

Large-scale specimens of two different types were tested:

- flat specimens in special testing equipment ZZ 8000 in ŠKODA Concern,

- disc specimens in special spinning equipment in CNIITMASH.

Testing equipment ZZ 8000 in ŠKODA Concern was designed and made by ŠKODA and is in operation since October 1962, i.e., 30 years. Maximum tensile force is 80 MN, maximum dimensions of testing specimens -350 × 1,200 mm in section, and up to 4,000 mm in length. Specimen are usually welded to the specimen heads by electroslag type of welding. For this programme, flat tensile specimens with testing section equal to 150 × 600 mm were chosen - see Fig. 1. This thickness was chosen as a representative one for the whole programme, as it is very close to both RPV wall thicknesses (thickness of RPV VVER-440 is 140 mm, while VVER-1000 is equal to 200 mm in their cylindrical parts).

These specimens contained surface semielliptical crack-type defects with two different a/2c ratios:

- 1:3 for RPV VVER-440 materials, as the main purpose was to obtain supporting results for a newly prepared "USSR Standard for strength calculations..",
- 1:5 for RPV VVER-1000 materials, as comparison with ASME Code should have to be established.

Specimens were tested in temperature range of T_{k0} +/-50°C in case of VVER-440 materials or at room temperature for VVER-1000 materials. Defects in these specimens were manufactured using electric erosive spark method - it was shown, that behaviour of such defects is similar to fatigue cracks with respect to their fracture toughness values for tested materials.

Conditions of fast fracture initiation as well as of subcritical crack growth were determined by measuring the following parameters: force, temperature, crack opening displacement, extension, strain field, acoustic emission and electrical potential drop. Also in some cases TV observation of crack deformation was used.

To obtain more complex information about tested materials and to be able to compare old (transition temperature) and new (LEFM) approaches in USSR Standards, tests for determination of Crack Arrest Temperature in flat type specimens of testing section equal to 150 × 1,200 mm were also carried out and a Fracture Analysis Diagram was determined. For these tests the ESSO type method was chosen with temperature gradient across specimen width.

Disc type specimens were tested in two testing machines in CNIITMASH, Moscow. Disc models of diameter equal to 650 mm were tested in spinning machine VRD-1500, and models of diameter 400 mm in the machine VRD-500. In both cases specimens had similar thickness - 150 mm. Defects were prepared using electron-beam melting of titan wire in defect tip.

All these tests were carried out at room temperature. Loading of models was performed by rotation (spinning disc) using step-by-step increase of frequency of rotation by about 500 to 1,000 revolutions/minute. After every step in the region of expected fracture, all specimens were stopped and their geometrical dimensions and defect depth were measured. Increase of rotation frequency then continued up to specimen fracture.

In both types of testing, fracture type, subcritical crack growth value and its shape was determined after failure and documented by photos.

While testing of flat tensile specimens was fully uniaxial, testing of rotating (spinning) disc was characterized by biaxial type of loading - in disc centre, where fracture was mostly initiated, ratio of both stresses is equal to 1:1.

RESULTS AND DISCUSSION

The relatively wide set of large-scale tests shows some interesting and important facts, the most pronounced are as follows.

Testing of flat tensile specimens

Fracture surfaces are in all cases (with the exception of one test of base metal at a temperature equal to +75°C, where large subcritical crack growth through the whole thickness followed by fast shear failure was observed - in this case testing temperature was equal to the FAT) were of brittle or semi-brittle character with pronounced "half-moon" type of subcritical crack-growth. Fracture surfaces are practically fully flat, in cases of weld metals of submerged arc welding joint these surfaces are slightly undulated and corresponded to individual welding "beads". Fracture surfaces of base metal and electroslag welding metal are very similar (electroslag welding joint was quenched and tempered after welding, i.e., has practical similar structure of metal). Initiation of final failure started, in most cases, from the deepest point, i.e., from place with maximum value of stress intensity factor. In cases of submerged arc welds, only, this initiation point is often shifted to some further bead, probably to the weakest point of the weld. There was practically no difference between fracture surface characteristics of 15Kh2MFA and 15Kh2NMFA types of steels.

Main results from testing of 15Kh2MFA type of materials are shown in Fig. 2. In this figure solid curves represent mean values of fracture toughness determined from tested materials by standard fracture toughness specimens (mostly of thickness 25 nd 75 mm), dashed line represents the design (allowed) fracture toughness curve according to the USSR Code /1/. Experimental points show, that, in most cases, an initiation of subcritical crack growth starts close to the mean value curves. In the case of submerged arc weld, their initiation was observed at values lower than the mean curve, in general, as this weld metal is very nonhomogeneous and the initiation starts at the weakest bead but practically in all cases at values beyond the design curve. These results fully support the necessity of large-scale specimen testing, as standard specimens cannot catch such weakest points, or, mean curves are of course higher as they include test results of tougher materials.

Figures 3 and 4 summarize results from the same steel but in the form of critical netto(net)-stresses vs. initial crack depth for testing at room temperature. This type of diagram represents so-called "Defect Analysis Diagram - DAD"; it is an isotermic type of diagram. Figure 3 for base metal as well as Figure 4 for weld metals show that initiation netto(net)-stresses are practically equal to yield strength of materials while fracture netto(net)-stresses are practically equal to ultimate tensile strength of tested materials, if testing temperature was higher than critical temperature T_{ko}. The effect of a crack on these stresses is observed only for temperature below T_{ko}, i.e., the LEFM approach can be observed only in this temperature region.

Similar results are shown in Fig. 5 for specimens from 15Kh2NMFA type of steel and its welding joints. All tests were performed, in this case, only at room temperature, i.e., with relatively high fracture toughness values (see Table 2). Some effect of crack size on critical stresses is seen only for electroslag weldment, i.e., for materials with the lowest toughness values (only about 135 MPa$\sqrt{m}$). In all cases, for both types of steels, some effect of crack size on critical netto(net)-stresses can be observed for conditions with lower fracture toughness values of materials, as well as for crack sizes larger than 40 mm in depth.

Quite different situations can be encountered when brutto(gross)-stresses are used in design of such diagrams. Figure 6 shows the Defect Analysis Diagram for 15Kh2MFA type of steel tested at room temperature. Comparison of experimental values with calculated stresses (for fracture toughness according to Table 2) using LEFM approach is also shown. It is clearly seen that practically all experimental data lie beyond the calculated curve. Moreover, as it was also seen in Figure 4, specimens with defects smaller than about 40 mm are not, at this temperature, practically affected by these defects. Figure 7 shows further results for specimens with defect depths equal to 40 and 100 mm, tested at different temperatures. This diagram represents part of the Fracture Analysis Diagram but in netto(net)-stresses.

Detailed Defect Analysis Diagrams for 15Kh2NMFA type of steels are given also in Figs. 8-10; in all cases for room temperature testing, brutto(gross)-stresses have been used. Figure 8 summarizes results from base metal testing; Fig. 9 gives results from electroslag weld; and Fig. 10 from submerged arc weld. Experimental results are compared with calculated trends, using fracture toughness values from Table 2. In all cases open symbols are used for subcritical crack initiation, full symbols for fracture. Comparing experimental results with calculated trends, one can conclude that experimental values lie beyond calculated ones, i.e., it is demonstrated that the LEFM approach even for thick walled RPVs is conservative, especially in cases when the design fracture toughness curves according to Nuclear Codes are used. It was shown, for example, that for 15Kh2MFA type of steel with crack depth equal to 100 mm, its critical stress is higher than 400 MPa, i.e., more than twice

design stress value of this material. For crack depth close to the "postulated defect" size (in case of VVER-440 RPVs it is equal to 35 mm), i.e., 40 mm, this fracture stress is even higher than 500 MPa for temperature close to critical temperature T_{k0}. Thus, a sufficiently high safety factor was demonstrated.

Comparing results from Figs. 8-10 (15Kh2NMFA type steel) with Fig. 6 (15Kh2MFA type steel) it can be concluded that similar effects of crack depth on initiation/fracture stresses are found. In principle, base metals defects of depth smaller than about 40 mm have no pronounced effect on brutto(gross)-stress, while for welding joints this crack depth value is somewhat smaller - between 15 and 30 mm.

Another evaluation of results was carried out using two-criteria approach - CEGB R6 method, Rev. 3 /2/. A design curve, according to this approach, is given as:

$$K_R = (1-0.14\ L_R^2) \cdot (0.3 + 0.7\ \exp(-0.65\ L_R^6)$$

where

$$K_R = K_I/K_{IC}\ ,\ \text{and}\ L_R = \sigma/R_e\ .$$

In Fig. 11 all results received for both types of steels and their welding joints are summarized. For calculations only mean real fracture toughness values of tested materials (see Table 2) have been applied, as well as mean yield strength values. Relatively good correlation of experimental points and the design curve has been established - practically in all cases initiation points are close to the design curve. This conclusion has been reached independent of crack depth and testing temperatures. Safety factors, determined with respect to stress intensity factors K_I or with respect to stresses, lie in interval between one and two. Of course, if design fracture toughness values would be used, then all results would lie substantially higher than the R6 design curve and safety factors would be at least twice as large, i.e., safety would be fully reliable.

Comparison of tensile and spinning specimens

Comparison of these two different type of testing (uniaxial and biaxial) can be performed only for 15Kh2NMFA type of steels, tested at room temperature. This fact was based on experimental capabilities of spinning testing equipment.

Results from both types of testing are summarized also in Figs. 8-10 Practically in all cases, results from biaxial type of testing (i.e., from spinning disc specimens) lie lower in comparison with tensile ones. Moreover, in some tests, like in Fig. 9, it can also be seen that size effect plays some role, i.e., specimens of larger diameter of 600 mm (i.e., with conditions closer to plane strain) were fractured at lower stresses than specimens with smaller diameter of only 260 mm.

Thus, this small comparison shows that biaxial type of loading is less favourable than uniaxial loading. Results from biaxial loading lie closer to calculated line than those from uniaxial testing. Situations in RPVs are characterized by loading conditions that are mostly between these two boundary cases - i.e., between uniaxial (tensile flat specimens) and biaxial (spinning discs) with loading ratio 1:1. Thus, use of LEFM approach with only the first type of loading (K_I) is very conservative, closer

results are received from biaxial type of testing. So, the LEFM approach is strongly conservative, and an elastic-plastic approach is necessary to apply.

Subcritical crack growth

Testing of both types of specimens showed that final failure was preceded by some subcritical crack growth in most cases. This growth was mostly of "half-moon" type, i.e., it followed the course of stress intensity factor values: largest values of K_I for tensile tests lie in the deepest point, while the lowest value is on the specimen surface. Dependence of maximum crack growth values on initial defects depth can be found practically in all diagrams. Special attention should be given to Figs. 6 and 7, their lower parts summarize crack growth values for 15Kh2MFA type of material, in Fig. 6 as a function of initial defect size at room temperature testing, in Fig. 7 as a function of testing temperature for two initial defect sizes: 40 and 100 mm. For this type of steel, this crack growth value is increasing with initial defect size, independently on testing temperature (with exception of very low testing temperatures, where fully brittle failure occurred). At the same time, with increasing temperature this crack growth value is, naturally, also increasing.

A different situation was found for 15Kh2NMFA type of steel as shown in Fig. 12. Crack growth values are, on contrary, decreasing with increasing initial defect size. This trend is valid for base metal as well as for submerged arc weld. For electroslag weld metal, results can be somewhat different, but lack of further data caused these results not so fully representative.

Comparing these two different trends in crack growth data, it is necessary to compare also R-curves (J-da) for both materials. Both steels are, in principle, characterized by similar fracture toughness values, not only at room temperature, but in the whole temperature region. While 15Kh2MFA type of steel is characterized by somewhat lower strength properties, its R-curve is less steeper in comparison with 15Kh2NMFA type. These trends fully correspond with dependencies of crack growth values - steeper R-curve results in smaller crack growth values and vice versa.

CONCLUSIONS

Testing of large-scale specimens made of steels used for RPVs of VVER-440 and VVER-100% MW units shows the following results:

- fracture behaviour in temperature transition region (around critical temperature T_{k0}) is mostly semi-brittle with some extent of subcritical crack growth,
- netto(net)-stresses for crack growth initiation are close to yield strength of materials while netto(net)-stresses for final failure are close to ultimate tensile strength of tested materials,
- critical brutto(gross)-stresses for crack growth initiation for "postulated defect" are much larger than allowable stress values in given materials,
- specimens with defects smaller than 40 mm in depth (for base materials) and smaller than 15 to 20 mm for weld metals behaved like without these defects - their initiation stresses do not depend on crack size,

- comparison of experimental results with calculated values based on LEFM approach shows a large conservatism of the approach, as practically all tests failed in elastic-plastic region of loading, at higher stresses than calculated ones,

- use of two-criteria CEGB R6, Rev. 3 approach was found to be well consistent with experimental data if mean values of experimentally determined fracture toughness of materials was used into calculation,

- comparison of uniaxial tensile tests (flat specimens with section of 150 × 600 mm) with biaxial tests (spinning discs with section up to 150 × 600 mm) shows that biaxial loading is less favourable: failure stresses are lower than for uniaxial loading and they are closer to calculated results from LEFM approach for uniaxial loading,

- subcritical crack growth values depend strongly on type of material and its R-curve: while for 15Kh2MFA type of steels these values are increasing with increasing crack size, on the contrary, for 15Kh2NMFA type of steel these crack growth values have a decreasing trend, in both cases these values are growing with temperature increase,

- main task of this coordinated programme has been achieved: these tests demonstrated that USSR Code for strength calculations is conservative with a sufficient degree of additional safety with respect not only to real but also to design values of fracture toughness.

LITERATURE

/1/ USSR Standard for Strength Calculation of Components and Piping of Nuclear Power Plants, (1989), Moscow.

/2/ Milne, I., Ainsworth, E. A., Dowling, A. R., Stewart, A. T. - Assessment of the Integrity of Structures Containing Defects, CEGB Report R/H/R6-Revision 3 (1986).

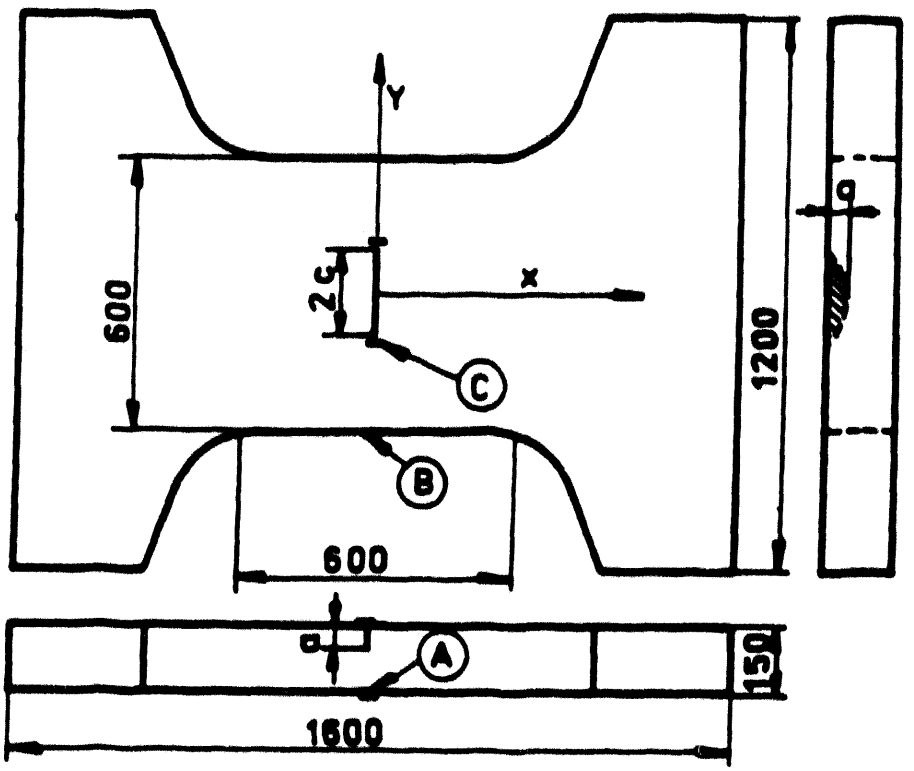

Fig. 1. Flat tensile specimen with surface defect.

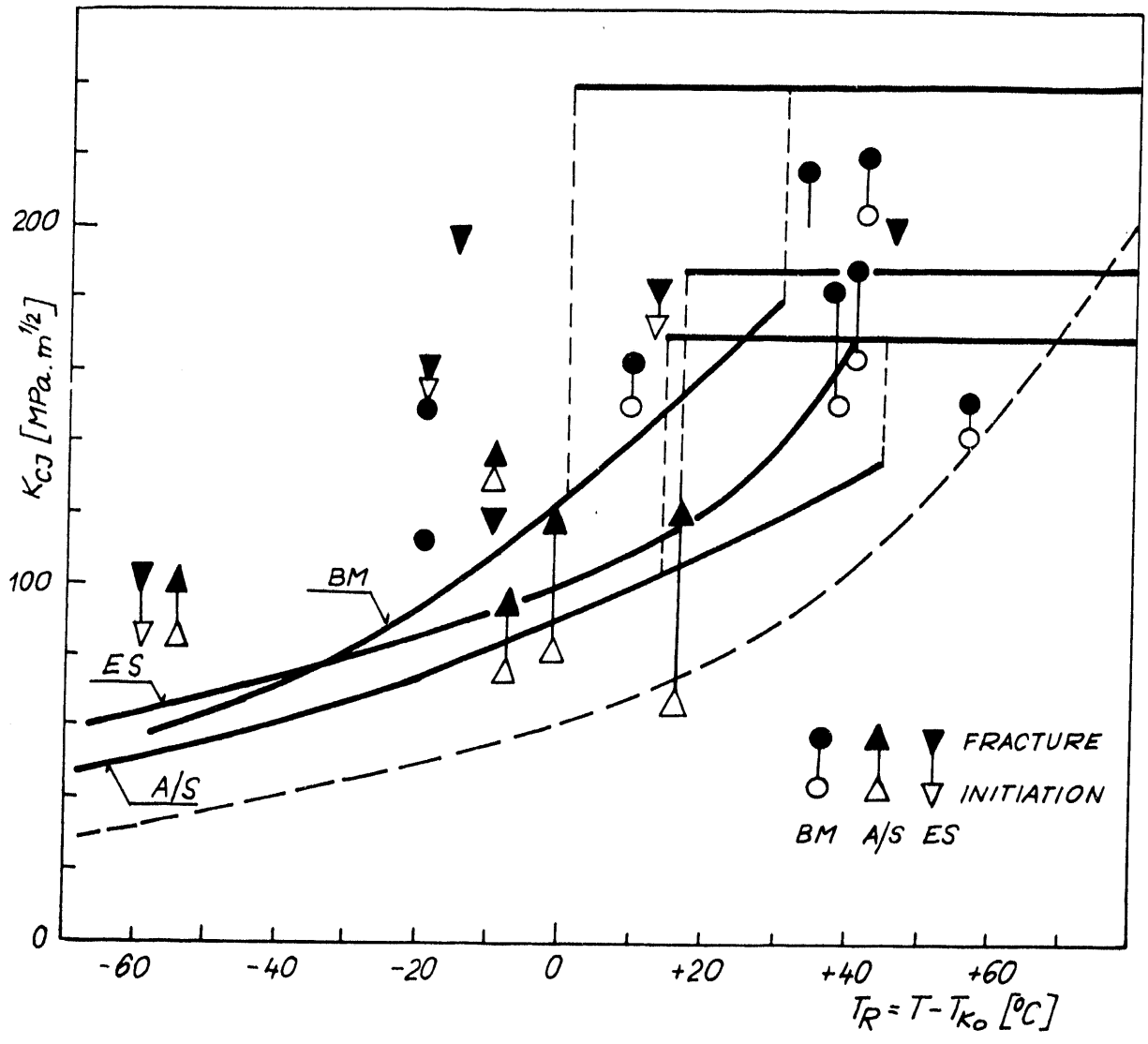

Fig. 2. Results of testing of 15Kh2MFA type of steel.

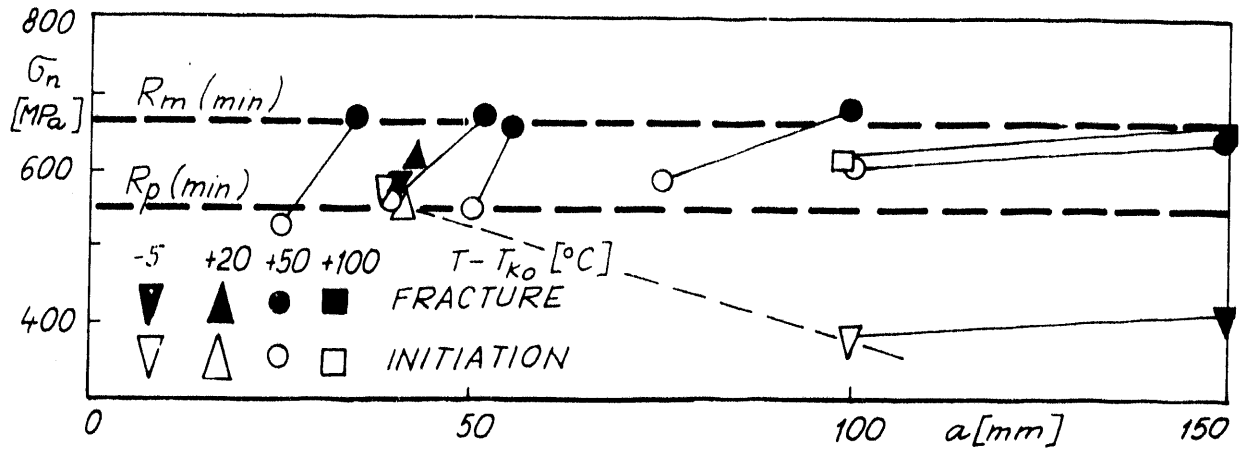

Fig. 3. Results of testing of 15Kh2MFA type of steel a/2c = 1/3.

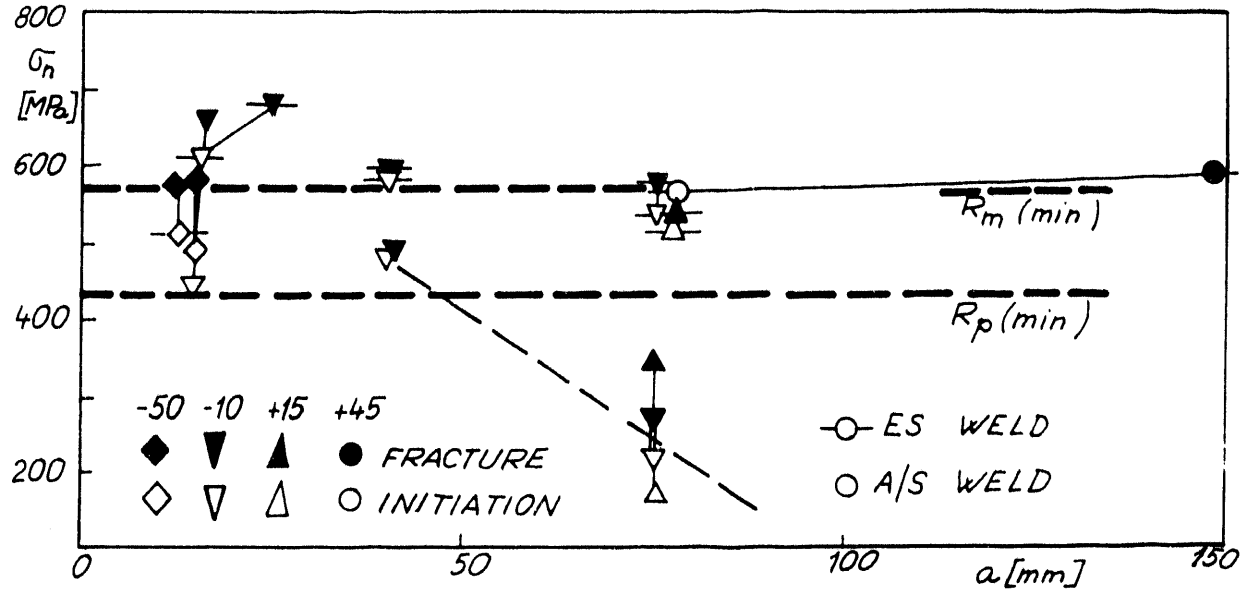

Fig. 4. Results of testing of welding joints of 15Kh2MFA type of steel a/2c = 1/3.

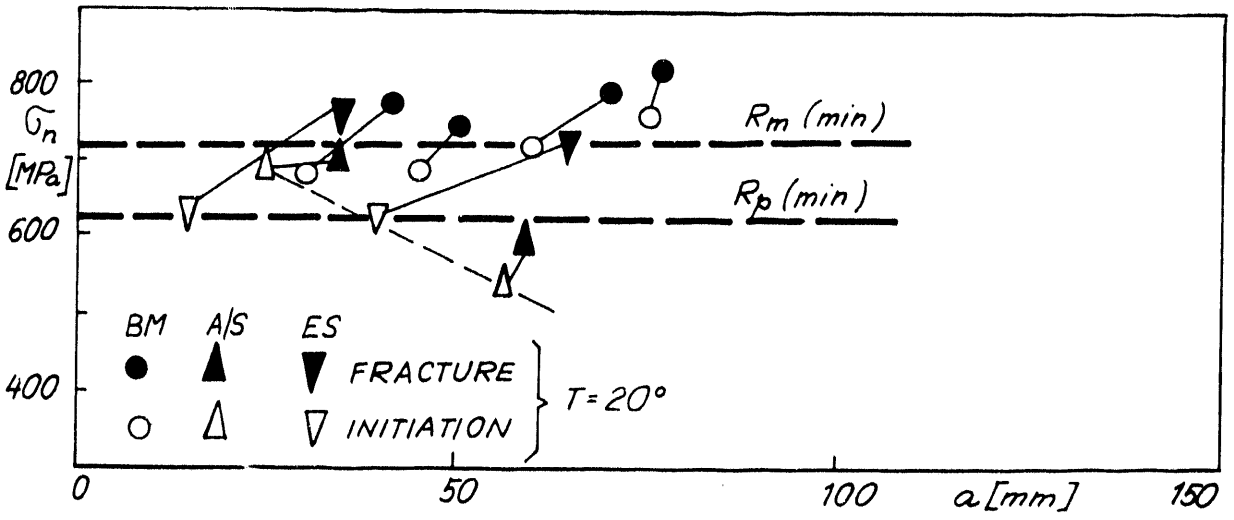

Fig. 5. Results of tests of 15Kh2NMFA type of steel and its welding joints at room temperature a/2c = 1/5.

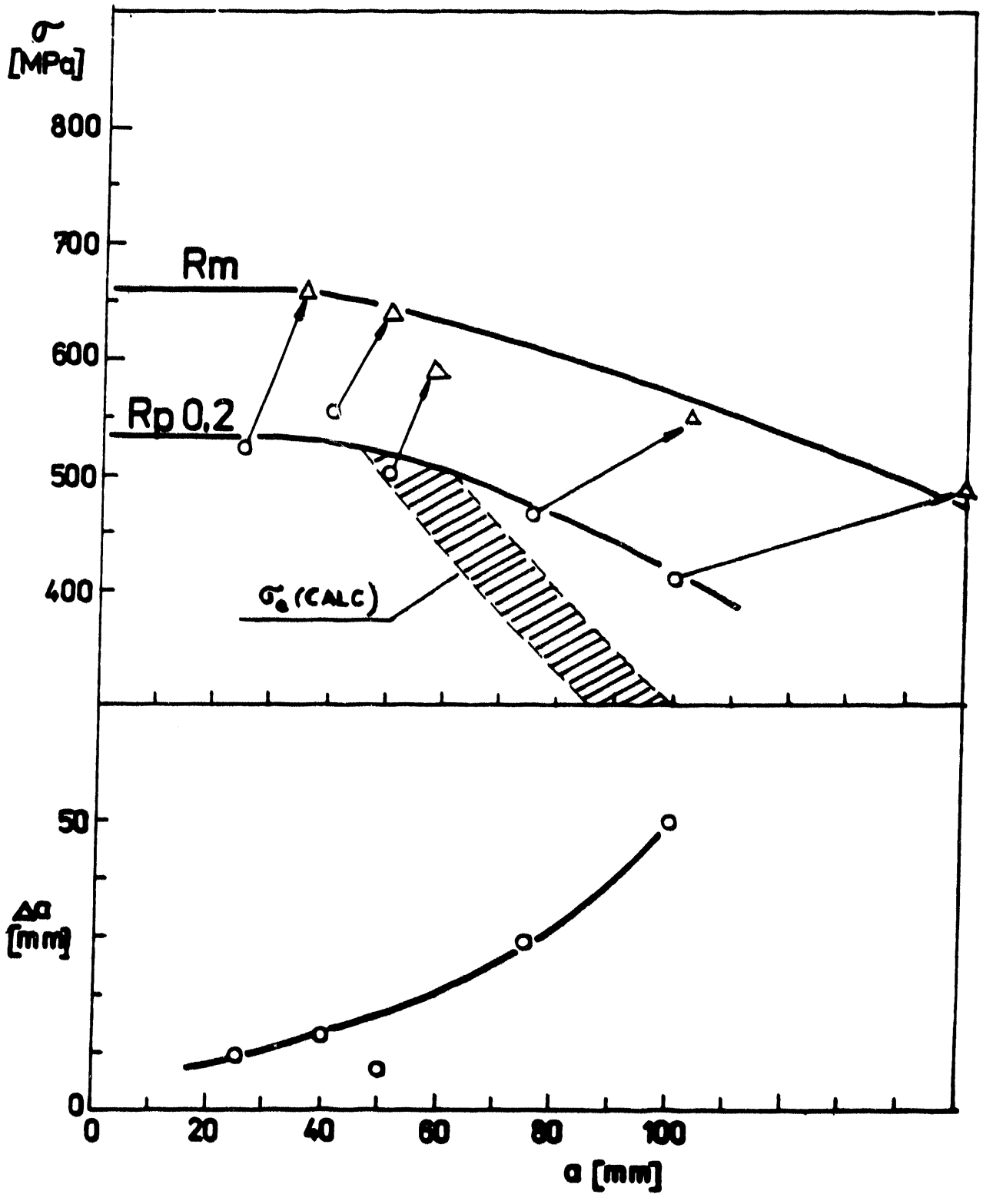

Fig. 6. Defect Analysis Diagram for 15Kh2MFA type of steel at room temperature for 150 mm thickness.

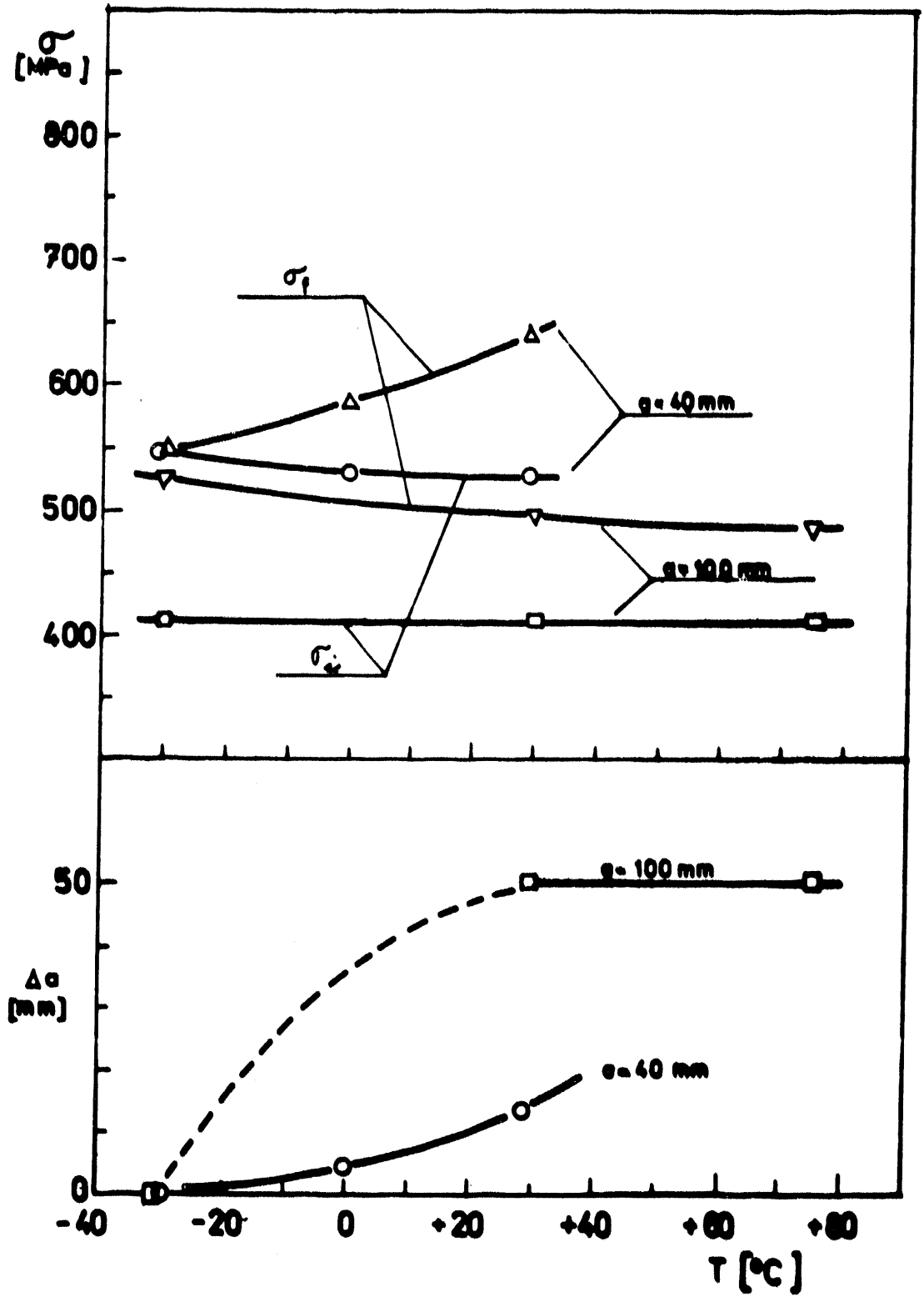

Fig. 7. Part of Fracture Analysis Diagram for 15Kh2MFA type of steel with 150 mm thickness.

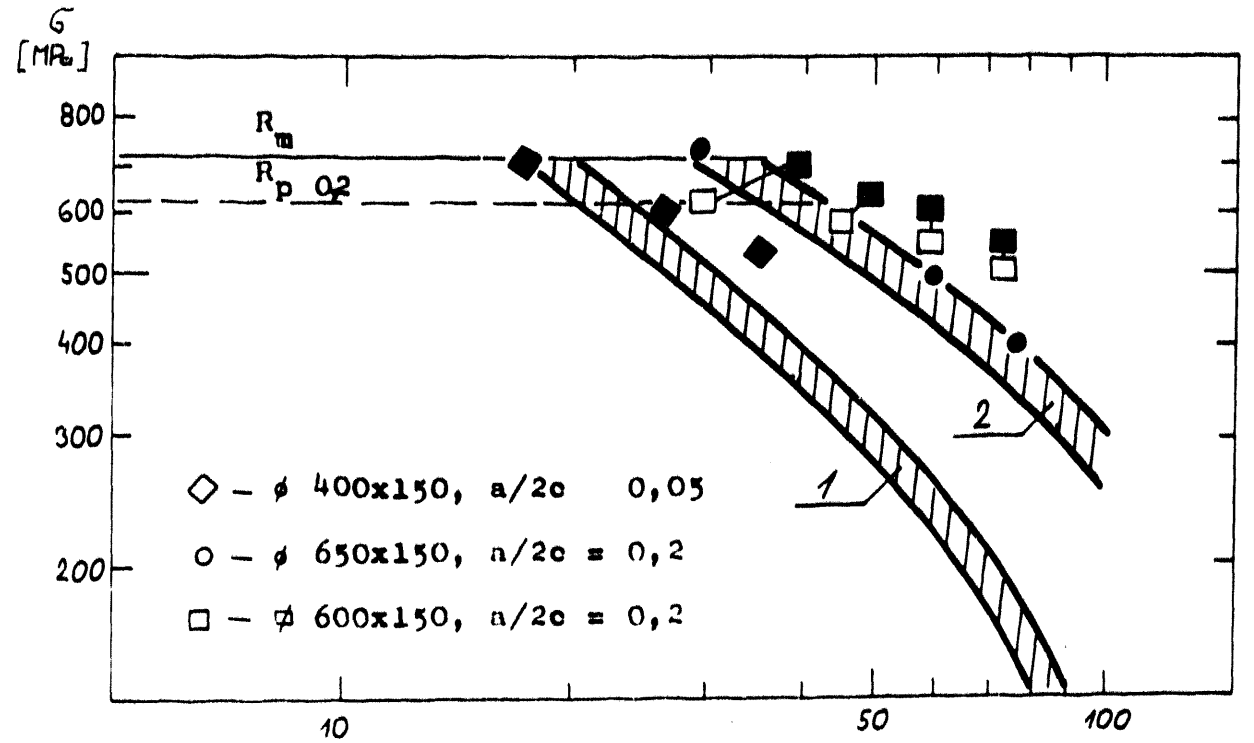

Oceł: 15Kh2NMFA, T = + 20°C

1 - a/2c = 0.05
2 - a/2c = 0.20

K_{CJ} = (220 + 250) MPa*m$^{1/2}$

Fig. 8. Defect Analysis Diagram of 15Kh2NMFA type of steel (base metal) at room temperature - 150 mm thickness.

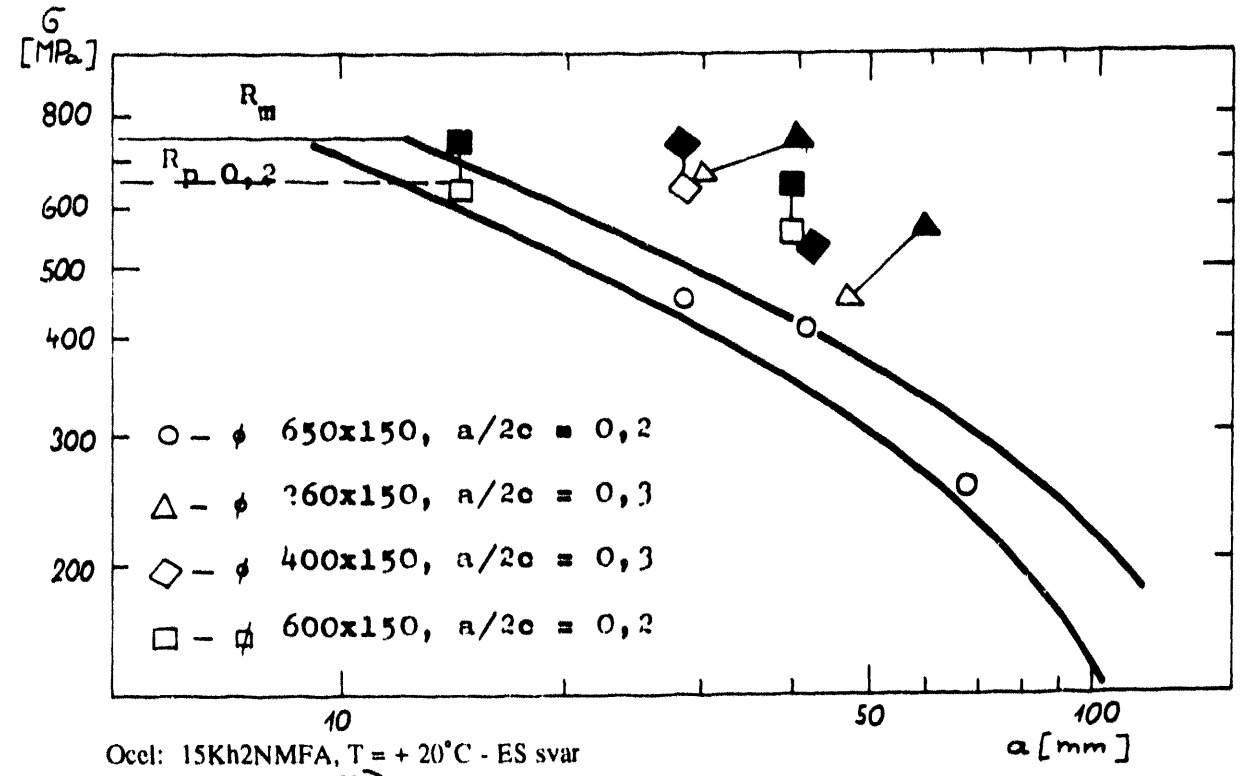

Oceł: 15Kh2NMFA, T = + 20°C - ES svar

1 - a/2c = 0.20
2 - a/2c = 0.30

K_{CJ} = + 135 MPa*m$^{1/2}$

Fig. 9. Defect Analysis Diagram of 15Kh2NMFA type of steel (electroslag weld metal) at room temperature - 150 mm thickness.

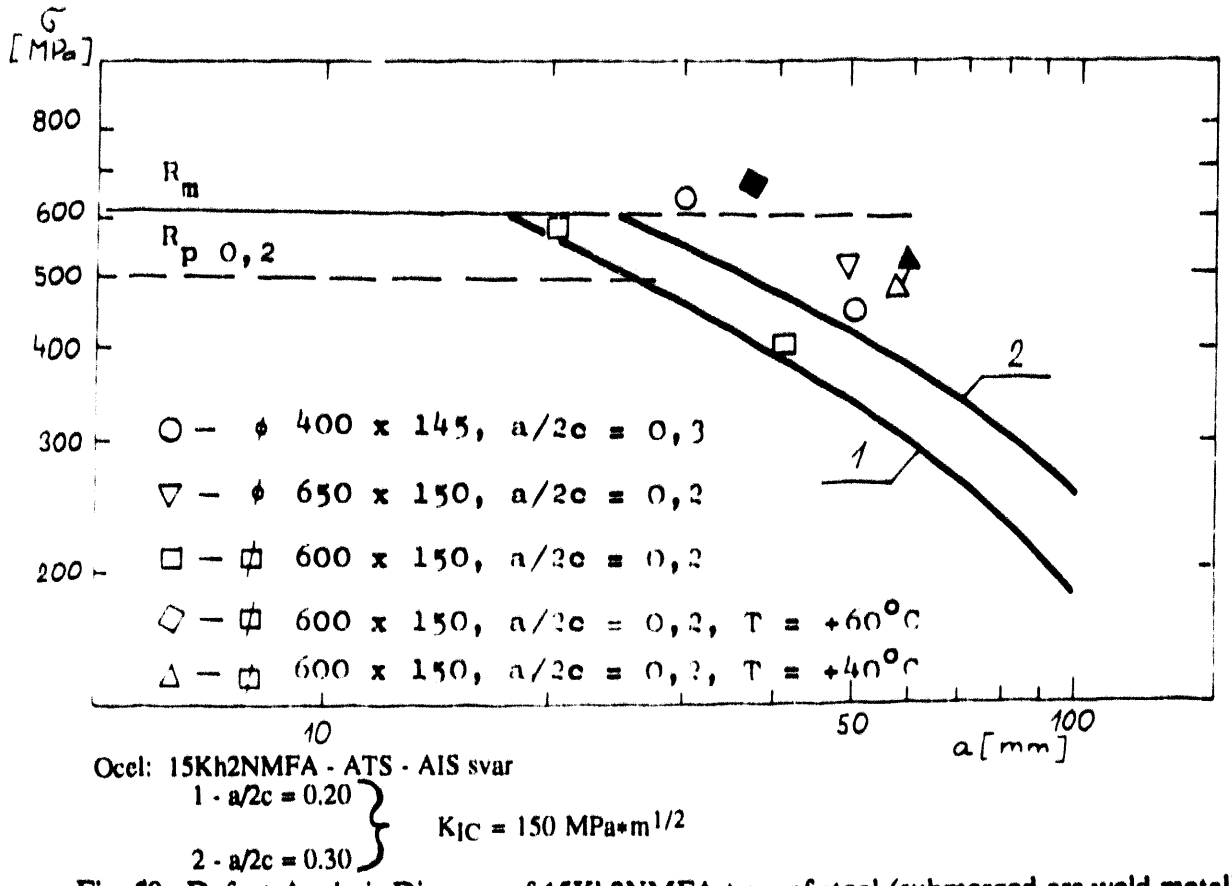

Fig. 10. Defect Analysis Diagram of 15Kh2NMFA type of steel (submerged arc weld metal) at room temperature - 150 mm thickness.

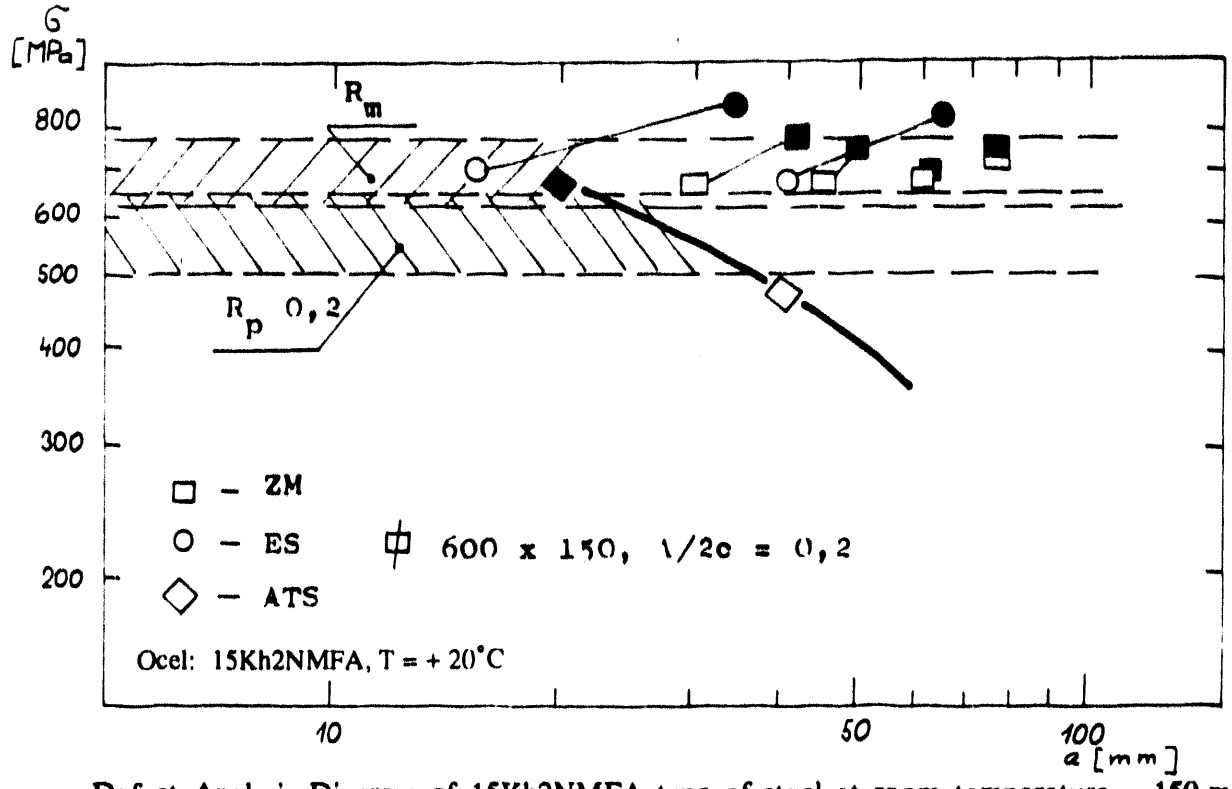

Defect Analysis Diagram of 15Kh2NMFA type of steel at room temperature - 150 mm thickness.

BM - base metal

ES - electroslag weld metal

A/S - submerged arc weld metal

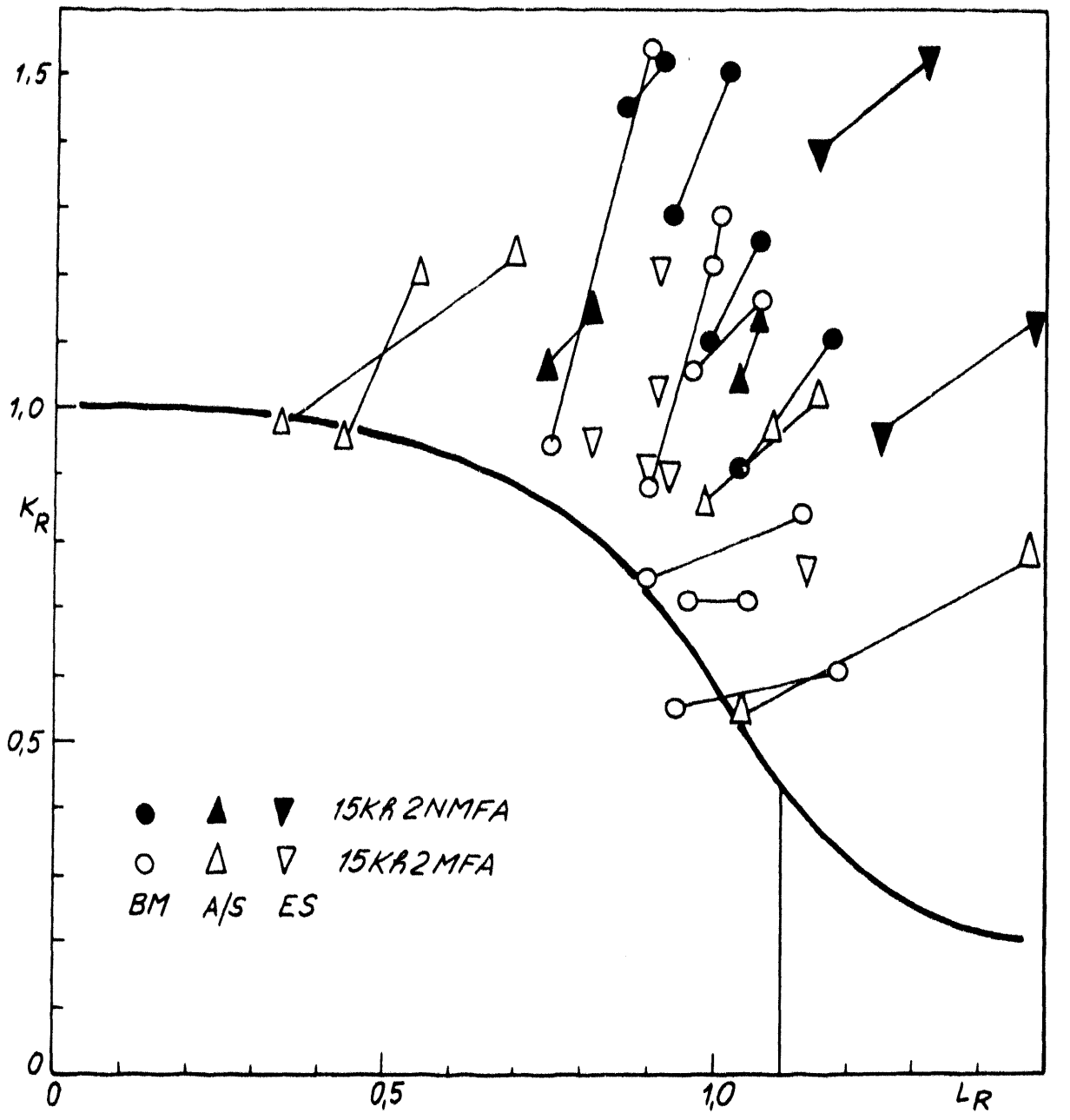

Fig. 11. Summarization of all experimental results with the design curve according to the R6, Rev. 3 model.

BM - base metal

A/S - submerged arc weld metal

ES - electroslag weld metal

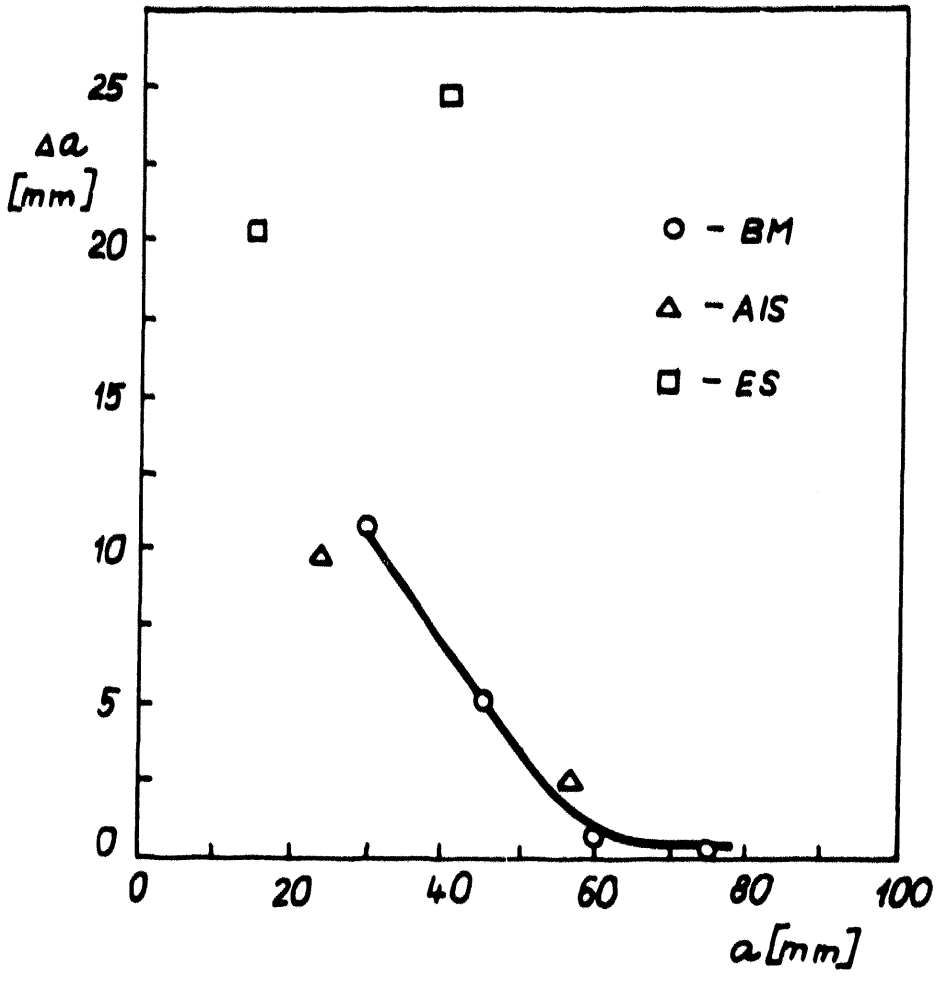

Fig. 12. Subcritical crack growth values for 15Kh2NMFA type of steel for testing at room temperature

BM - base metal

A/S - submerged arc weld metal

ES - electroslag weld metal

FULLY PLASTIC J-INTEGRAL SOLUTIONS FOR PRESSURIZED CYLINDRICAL VESSELS HAVING SEMI-ELLIPTICAL SURFACE FLAWS

by

J. M. Bloom, D. R. Lee
Babcock & Wilcox
Research and Development Division
Alliance, OH, U.S.A.

ABSTRACT

The application of elastic-plastic fracture mechanics to safety analysis of pressurized vessels has been developed based on limited, published finite element solutions. These limited solutions have not necessarily been verified to be accurate. This paper presents new, accurate, finite element solutions. These solutions are based on ABAQUS fully-plastic finite element J-integral solutions presented in terms of calibration constants, h_1. These calibration constants are a function of crack depth to thickness, aspect ratio of the flaw, Ramberg-Osgood hardening exponent, and thickness to inside radius ratio.

An evaluation of the published J-integral solutions lead to the conclusion that these earlier solutions were not taken far enough out in applied pressure to produce valid fully plastic J-integral solutions. This is shown to produce higher, more conservative h_1 values than are presented in this paper.

In addition to comparisons with these published results, the effect of strain hardening was examined. The earlier work was limited to a strain hardening value of n=8.6. The work presented here includes the range of values of n=5, 7, 8.6, and 10 representative of both austenitic and ferritic pressure vessel and piping steels.

INTRODUCTION

A critical part of the assessment of defects in power plant components is the knowledge of the crack driving force. The crack driving force is measured by the stress intensity factor, K_I, for structures operating in the linear elastic range of applied stresses, or the J-integral for flawed structures operating in the elastic-plastic stress regime. While the determination of K_I or J is possible using finite element analyses, finite element methods can be prohibitive for many practical engineering applications. This is especially true for part-through-the-wall flaws (semi-elliptical) where three-dimensional finite element modeling is required.

An alternate approach referred to as the engineering approach or estimation scheme(1) allows the engineer to superpose solutions obtained from linear elastic solutions such as from handbooks(2) and fully plastic solutions determined from the J-integral solutions. For a power law hardening material, Il'yushin(3) has demonstrated that the J-integral can be represented by a geometry factor times the remote applied load taken to the "n+1" power or as stated in (1) by an "h_1" calibration function times the ratio of the applied remote load

strain hardening exponent for elastic-plastic problems. The value of "h_1" is a function of the geometry and hardening exponent. General Electric, under Electric Power Research Institute (EPRI) support, developed and published many of these fully plastic solutions (1) for 2-D geometries in the h_1 format. However, there are few solutions in the literature for part through axial flaws in pressurized cylinders or flat plates (4), (5), (6), (7), and (8). Of these solutions only (4), (7), and (8) present solutions in a systematic format of the h_1 functions as presented in (1).

The finite element program ABAQUS (9) was used to evaluate the J-integral at the deep point of the axial interior part-through wall semi-elliptical flaw in a pressurized cylinder with pressure acting on the crack face. Several different flaw depths were modelled as a fraction of the pressure vessel wall thickness, t (a/t=1/8, 1/4, 1/2) for a fixed aspect ratio of a/ℓ=1/6, where ℓ is the surface length of the semi-elliptical flaw. The cylinder geometry chosen had an inside radius to thickness ratio of 10. In addition, the range of strain hardening values chosen for n was 5 to 10 which is representative of commonly used austenitic and ferritic steels. This range is consistent with the values given in the EPRI Elastic-Plastic Fracture Handbook (1) for both test specimen geometries (2D) and flawed cylinders (axisymmetric geometries). From the J-integral values generated, h_1 functions were determined and compared to those found in (4) and (5).

BACKGROUND THEORY

The J-integral procedure in ABAQUS is based on the virtual crack extension method of Parks (10). The J-integral procedure is simple to use, adds little to the cost of the analysis, and provides excellent accuracy. ABAQUS provides a Ramberg-Osgood deformation theory plasticity model, which, when used with the J-integral evaluation capability, allows the determination of fully plastic J solutions, J_p. Convergence to J_p is generally rapid with this model, so that analyses in support of the simplified "engineering approach" are readily obtainable.

The finite element model was generated using a Fortran program (ORMGEN-3D) developed at Oak Ridge National Lab (ORNL). ORMGEN-3D (11)is capable of generating six different flaw geometries. These geometries include flat plates with straight or curved surface cracks and cylinders with part-through flaws on the outer or inner surfaces.

Most fracture problems lend themselves to previously solved geometries and loadings contained in various references (1,2). However, elastic-plastic structural response in terms of h_1 for some geometries and loadings are not available in the published literature. For these cases, h_1 can be determined from the ABAQUS generated J-integral analyses.

As described in Reference 1, the total J-integral (J_t) can be estimated by separating the J-integral into an elastic part and a fully plastic part.

$$J_t = J_e + J_p \qquad (1)$$

The fully plastic portion can be written as:

$$J_p = h_1(a/t, a/\ell, R_i/t, n) * (P/P_o)^{(n+1)} \quad (2)$$

where:
- a = flaw depth
- t = cylinder wall thickness
- ℓ = surface length of flaw
- R_i = inside radius
- n = strain hardening exponent
- P = internal pressure
- P_o = reference limit pressure

If h_1 is known as a function of a/t, a/ℓ, R_i/t and n, J_p can be calculated for any load level. The J_p expression contains other terms such as yield offset (α), yield stress (σ_o), yield strain (ε_o), and a/t. For the calculation of h_1, the values used in ABAQUS for σ_o and α will not effect the values of h_1, so any reasonable values can be used to determine J_p.

The Ramberg-Osgood deformation theory plasticity material model was used in conjunction with the J-integral evaluation capability to determine the fully plastic J-integral. The stress-strain relation for the Ramberg-Osgood model is

$$\varepsilon/\varepsilon_o = \sigma/\sigma_o + \alpha(\sigma/\sigma_o)^n \quad (3)$$

The term σ/σ_o is the elastic term and $\alpha(\sigma/\sigma_o)^n$ is the fully plastic term. In order to determine the fully plastic J-integral, the structure must be stressed sufficiently such that the plastic portion dominates and the elastic portion is insignificant.

DETERMINATION OF h_1 AND COMPARISONS WITH PUBLISHED DATA

The fully plastic J-integral expression for a pressurized cylinder with an axial interior surface semi-elliptical part-through flaw was obtained from (7) as given by

$$J_p = \alpha*\sigma_o*\varepsilon_o*a*(1-(a/t))*h_1(a/t, a/\ell, R_i/t, n)*(P/P_o)^{n+1} \quad (4)$$

$$P_o' = (2/\sqrt{3})*\sigma_o*(t-a')/(R_i+a') \quad (5)$$

$$a' = a*[\,1-(1+(\ell^2/2t^2))^{-n}]\,/\,[\,1-(a/t)(1+(\ell^2/2t^2))^{-n}] \quad (6)$$

where:
- a = flaw depth
- t = cylinder wall thickness
- ℓ = surface length of flaw
- R_i = inside radius
- n = strain hardening exponent
- P = internal pressure
- P_o = reference limit pressure
- α = yield offset
- σ_o = yield stress
- ε_o = yield strain

To obtain a fully plastic value (J_p) for the structure for a Ramberg-Osgood material, a large load is applied such that the elastic

portion (J_e) of J_t becomes insignificant compared to J_p. Using the calculated J-integral value from ABAQUS and equations (1) and (4), the value for h_1 can be calculated from equation (4) directly when J_e in equation (1) is insignificant.

An alternate approach is to determine J_e directly (the stress intensity factor squared for a plastically adjusted crack size) and subtract J_e from J_t to obtain J_p. The value of h_1 can then be determined directly from equation (4). This approach is used in (4) as well as in (7) and (8).

ABAQUS calculates J_t along the crack front and for each defined path. The calculated J_t values provide the user with the variation in J_t along the crack front from the surface point to the deep point. The maximum J_t occurs at the deep point. Only results from the deep point are presented here. The J paths used are illustrated in Figure 1 for Case 1. For Case 1 ($a/t=1/4$, $a/\ell=1/6$, $R_i/t=10$) the mesh used allowed only 3 valid paths to be defined. The element transitioning from 2 elements to 1 element precluded the use of a fourth path. For the 3 paths defined only the results from paths 2 and 3 were used in the determination of h_1. The exclusion of path 1, containing the crack tip elements, was based on recommendations found in guidelines given at an HKS Fracture Mechanics course. The h_1 values given in Table 1 are based on an average of the J-integral values for paths 2 and 3.

The following subsections describe the finite element models used as well as the J-integral (and h_1) results for each a/t ratio examined. In all cases the crack aspect ratio was $a/\ell=1/6$. This value of 1/6 is based on a postulated flaw shape used in the ASME Nuclear Pressure Vessel Code (Section III). In all cases, strain hardening values of n= 5, 7, 8.6, and 10 were run. Each case is presented in the order of analysis.

Case 1: a/t=1/4

The finite element model, 36 inches in length, contained 4808 nodes and 8 elements along the crack front.

Since the J_t results from the literature (4), (5) were for n=8.6 the results for n=8.6 are presented and discussed first. Table 1 shows the calculation of h_1 at each load level.

The finite element model was of the same length as used in (4) and (5). This length was required to sufficiently isolate the displacements at the uncracked end of the model from localized disturbances in the vicinity of the crack. The modeled length was based on the comparison of the displacements at the uncracked end of the flaw model with those from an uncracked cylinder model. Based on (5), for the end effects to be small, the cylinder length must be at least 16 times the maximum crack depth or 2.667 times the maximum surface length for an $a/\ell=1/6$.

Table 1

Axial Semi-Elliptical Flaw in a Cylinder With Ri/t=10, a/t=1/4, and n=8.6

R_i= 90 in.
t= 9 in.
ℓ=2c= 13.5 in.
a= 2.25 in.
α = 1.4
n= 8.6
E= 30.0E06 psi
v= 0.3
σ_o = 60000 psi
a*= 0.8527 in.
P_o= 6212.88 psi

Length of Cylinder - 36 in.

P (psi)	J1 (in-lb/in²)	J2 (in-lb/in²)	J3 (in-lb/in²)	J_{avg} (in-lb/in²)	P/P_o	$(P/P_o)^{n-1}$	h_1
2260	149.26	152.3	152.6	152.45	0.363	0.0000607	8845.
4520	735.14	763.1	772.31	767.705	0.727	0.0471754	57.40
6780	5525.9	5949.7	6135.3	6042.5	1.091	2.3130879	9.21
9040	57154	63464	66896	65180	1.455	36.610360	6.27
11300	4.319E5	484850	518780	501815	1.818	311.84596	5.67
13560	2.376E6	2.684E6	2.9212E6	28028E7	2.182	1795.0646	5.50
15820	1.019E7	1.167E7	1.2974E7	12323E7	2.546	7884.4114	5.51
18080	3.585E7	4.197E7	4.7588E7	447805E7	2.910	28411.356	5.56
20000	9.240E7	1.1066E8	1.2709E8	118875E8	3.219	74864.346	5.60

The first column in Table 1 shows the applied internal pressure for that load increment. The next four columns show the J_t values from paths 1 through 3 and the average J_t from paths 2 and 3, respectively. Columns 6 and 7 show the ratio of the applied pressure to the limit pressure, and the pressure ratio to the n+1 power, respectively. Using the values in column 7, the geometry dimensions, and material properties in conjunction with the equation for J_p, h_1 is calculated and shown in column 8.

Theoretically, h_1 should not be a function of pressure and indeed, as the applied pressure increases, h_1 converges to a constant value. There was a small amount of variation at the higher pressures where h_1 begins to increase slightly, but the variation was small, on the order of 2% (5.5 vs 5.6).

It can be observed from Table 1 that the J values are nearly path independent. Based on discussions with Professor Dodds, differences between J values from each path should be within 5%. The significance of this will be discussed in Case 3.

The method for determining h_1 in (4) was based on the estimation scheme formula (1) for J_t. J_p was determined by subtracting the J_e value adjusted for the plastic zone correction. The problem with this method is that the plastic zone correction (a_{eff}) is a function of the internal pressure through the following expressions.

$$\phi = 1/(1+(P/P_o)^2) \tag{11}$$

$$a_{eff} = a + \phi\, r_y \tag{12}$$

where r_y is the Irwin plastic zone correction. This dependence of J_e on pressure, results in h_1 being a function of pressure.

The h_1 value reported in (4) of 7.45 was determined at a pressure of 5000 psi. From Figure 2 and Table 1 the converged h_1 value was 5.5. It can be observed from Figure 2 that when h_1 is plotted against P/P_o, h_1 levels out at about $P/P_o \approx 2$. This is equivalent to an applied pressure of 12,500 psi. Reference (4) only went up to a pressure of 5000 psi, not nearly high enough to eliminate the contributions due to J_e. If the model from (4) would have gone to a higher pressure, their calculated value of h_1 would have decreased. In other words, (4) did not go out far enough in pressure to obtain a fully plastic solution. When the Ramberg-Osgood material strain hardening law is used (as in the this work and (4)), the pressure must be large enough to minimize the amount of elastic contribution so that J_t is almost entirely made up of J_p (fully plastic solution). An alternate approach would be to use a pure power law material model (currently not available in ABAQUS).

Note that only one strain hardening value of n=8.6 was reported in (4). The present work includes values of 5, 7, and 10, as presented in Table 2.

Table 2

h_1^* Versus a/t and n

a/t	n			
	5	7	8.6	10
1/8	7.0 (6.5)	7.5 (7.1)	7.9 (7.6)	9.0 (8.1)
1/4	6.3 (6.1)	6.1 (5.8)	6.3 (5.5)	6.4 (5.2)
1/2	1.6** (1.4)	0.8 (0.8)	0.4** (0.3)	0.8** (0.2)

* values of h_1 determined using the 5% J-integral path independency criteria
values in parentheses were determined by the constant value of h_1 vs P/P_o plots

** 10% J-integral path independency criteria

The only other comparison for case 1 is found in (5). As in (4), the results in (5) are for n=8.6. In (5), the value of h_1 is not calculated directly. Therefore, comparison values using the J_t-integral results from (5) for h_1 were determined using the computer code PCFAD (12), a failure assessment diagram approach (7). Reference (8) discusses this approach. In (7), h_1 was determined as 6.9 for a/t=1/4 and n=8.6, using the finite element J_t-integral values in (5). In (5), the pressure used was not large enough to obtain a converged fully plastic J-integral value. However, the h_1 values shown in Table 1 for pressures between 6780 and 9040 psi (note the maximum pressure in (5) was only 7500 psi) were between 9.2 and 6.3.

Other possible reasons why h_1 values from both (4) and (7) (using the J_t results from (5)) were different from the value found and reported in this paper may be due to grid refinement. Unless the mesh is very refined, the crack tip elements do not provide sufficient accuracy to give good path-independent J_t values. This is especially true for nonlinear problems. The finite element grid for case 1 contains 4,808 nodes and 8 elements along the crack front. The model used in (5) contained 2,983 nodes and 6 elements along the crack front. The model used in (4) contained 3,043 nodes and 6 elements along the crack front.

Case 2: a/t=1/8

Case 2 is the same geometry as Case 1 except a/t=1/8. The same number of nodes and elements was maintained for case 2 as was used in case 1. This means that the refinement around the crack was increased and the model length (36 inches) was twice the required length of 16 times the crack depth.

As with Case 1 (a/t=1/4), comparisons for to n=8.6, as reported in (4) and (5). The reported h_1 value from (4) of 11.9 was based on a pressure of 5000 psi. From Table 3, a converged value of 7.6 was obtained at a pressure of 16,000 psi. If (4) had used a higher pressure, the resulting h_1 value would be lower. A pressure of at least 16,000 psi would be required. Table 3 shows the value of h_1 at each pressure level. Note that there was a small amount of variation at the higher pressures where h_1 begins to increase slightly, but the variation was small, on the order of 1.5% (7.57 vs 7.68).

The models from (5) were limited to a/t=1/4 and 3/4. The value of h_1 determined from (7) for a/t=1/8 (a/ℓ=1/6) and n=8.5 is 9.06. This was based on engineering judgement and extrapolation of h_1 from other a/t values. This h_1 value (9.06) is consistent with the more accurately calculated h_1, (7.6), from the present finite element analysis. Table 2 shows the results for n=5, 7, and 10.

Case 3: a/t=1/2

The geometry for this case was identical to Cases 1 and 2 except a/t=1/2. Three different finite element models were developed for this case. The need for a more refined finite element grid for the deeper crack (a/t=1/2) is discussed below. The initial finite element model used the same number of nodes and elements as in Cases 1 and 2. Table 4 presents the J-integral values for n=8.6 as well as the calculated h_1 values for the initial model (Model 1). However, it can be observed from Table 4 that the resultant h_1 values varied erratically with increasing pressure. This is thought to be due to the larger flaw depth configuration which produces an effectively decreasing grid refinement along the crack front. Because of the observed erratic behavior of h_1, a second model (Model 2) was generated with 12 elements (as opposed to 8) along the crack front. This resulted in an increased number of nodes from 4808 to 7166. This second model was executed using smaller pressure steps (for improved accuracy). The results for Model 2 for n=8.6 are shown in Table 4. Note that the second model (Model 2) eliminated the erratic behavior observed in Model 1.

For the pressure levels run (up to 13,5600 psi for model 2), the h_1 values appear to vary smoothly and converge to a value of 0.33. However, on closer investigation of Table 4 (Model 2), the J_t values from paths 2 and 3 exhibit large differences for pressure levels greater than 7500 psi. These differences in J_t were much larger than observed in the previous cases (a/t=1/4 and a/t=1/8). At a pressure of 13,560 psi, J_t from path 2 is approximately twice as large as the value from path 3. The variation between paths for Case 1 and 2 did not appear to be a problem in the determination of converged h_1 values for these cases. The maximum difference in Case 1 between paths for J_t was 15% occurring at a maximum pressure of 20,000 psi.

Due to these observed differences in the J_t-integral values for the different paths in Model 2, a third more refined grid model (Model 3) was generated. A newly developed program ORMTIP (obtained from ORNL) was used as the originally used grid generator ORMGEN-3D does not easily allow the evaluation of the effects of refinement of the mesh around the crack tip. ORMTIP was used to create additional

Table 3

Axial Semi-Elliptical Flaw in a Cylinder With Ri/t=10, a/t=1/8, and n=8.6

R_i= 90 in.
t= 9 in.
ℓ=2c= 6.75 in.
a= 1.125 in.
α = 1.4
n= 8.6
E= 30.0E06 psi
v= 0.3
σ_o = 60000 psi
a*= 0.1474 in.
P_o= 6803.59 psi

Length of cylinder - 36 in.

P (psi)	J1 (in-lb/in²)	J2 (in-lb/in²)	J3 (in-lb/in²)	J_{avg} (in-lb/in²)	P/P_o	$(P/P_o)^{n-1}$	h_1
2000	51.907	52.923	53.03	52.9765	0.294	0.000	4.07E4
4000	234.2	241.26	243.11	242.185	0.588	0.006	239.98
7000	2838.2	3032.3	3108.7	3070.5	1.029	1.314	14.12
10000	52309	57744	60464	59104	1.469	40.337	8.86
13000	5.690E5	6.357E5	6.736E5	6.546E5	1.911	500.68	7.91
16000	3.873E6	4.421E6	4.790E6	4.606E6	2.352	3675.0	7.58
19000	1.916E7	2.297E7	2.534E7	2.415E7	2.793	19131.	7.63
20000	3.086E7	3.780E7	4.180E7	3.980E7	2.940	31303.	7.69

Table 4

Axial Semi-Elliptical Flaw in a Cylinder With Ri/t=10, a/t=1/2, and n=8.6

R_i= 90 in.
t= 9 in.
ℓ=2c= 27. in.
a= 4.5 in.
α = 1.4
n= 8.6
E= 30.0E06 psi
v= 0.3
σ_o = 60000 psi
a*= 3.2806 in.
P_o= 4247.93 psi

Length of cylinder - 81 in. (Model 1)
8 elements along crack front

P (psi)	J1 (in-lb/in²)	J2 (in-lb/in²)	J3 (in-lb/in²)	J_{avg} (in-lb/in²)	P/P_o	$(P/P_o)^{n-1}$	h_1
6000	7400.1	7417	7162.2	7289.6	1.412	27.526	0.701
12000	3.76iE6	3.551E6	1.977E6	2.764E6	2.825	21361.5	0.342
18000	3.655E8	1.806E7	5.017E7	3.411E7	4.237	1.047E6	0.086
24000	6.54E+09	6.51E+09	8.819E8	3.69E+09	5.650	1.658E7	0.589
30000	2.40E+10	9.92E+10	1.51E+10	5.72E+10	7.062	1.412E8	1.071
36000	5.36E+10	5.97E+11	9.12E+10	3.44E+11	8.475	8.128E8	1.119
42000	3.30E+11	2.07E+12	2.80E+11	1.18E+12	9.887	3.57E+09	0.871
43500	5.14E+11	2.67E+12	3.43E+11	1.51E+12	10.24	5.00E+09	0.797
45000	7.60E+11	3.40E+12	4.02E+11	1.90E+12	10.59	6.92E+09	0.727

Length of cylinder - 81 in. (Model 2)
12 elements along crack front

P (psi)	J1 (in-lb/in²)	J2 (in-lb/in²)	J3 (in-lb/in²)	J_{avg} (in-lb/in²)	P/P_o	$(P/P_o)^{n-1}$	h_1
600	24.373	24.655	24.584	24.6195	0.141	0.000	9.41E6
1200	98.224	98.596	98.369	98.4825	0.282	0.000	48554.
2100	306.18	306.64	304.93	305.785	0.494	0.001	700.04
3450	904.04	905.56	894.75	900.155	0.812	0.136	17.54
5475	4420.9	4434.1	4319.2	4376.65	1.289	11.428	1.01
7500	40944	40955	37686	39320.5	1.766	234.46	0.44
9540	3.834E5	3.797E5	2.868E5	3.332E5	2.246	2361.34	0.37
11580	2.689E6	2.552E6	1.479E6	2.015E6	2.726	15173.8	0.35
13560	1.458E7	1.153E7	5.779E6	8.654E6	3.192	69053.6	0.33

concentric rings of elements around the crack tip. By adding only concentric rings of elements, the total number of additional nodes is minimized.

Figure 3 illustrates the crack tip elements after ORMTIP divided the original two rings of elements into six rings. The additional paths provide a better average J_t value than was obtained using only two paths from the use of ORMGEN-3D. The refinement around the crack tip increased the number of nodes from 7166 to 8950.

Model 3, however, was run for n=7; results are presented in Table 5. Note the J-integral values are now within 5 percent for each path up to the maximum pressure of 15,000 psi. Note that the corresponding h_1 values are converged at the three pressures of 9000, 12,000 and 15,000 psi.

For comparison with Model 3 results, Model 2 was also run for n=7; results are presented in Table 5. The Model 2 results (n=7) show the path independence was not obtained (J2 versus J3). Thus, Model 2 lacks path independence for both n=7 and n=8.6. Model 2 was also run for n=5 and n=10; the same lack of path independence was observed. The obvious conclusion is that Model 2 lacks adequate refinement for the determination of accurate h_1 values for deep cracks ($a/t \geq 1/2$).

Even though Model 3 was not run for n=8.6, values from Model 2 (Table 4) were somewhat consistent with values of h_1 reported in (4) of 0.664. A value of 0.75 was reported in (7). This value was obtained from the finite element database from (5) which interpolated J-integral results from a master curve approach. Both these values of h_1 are comparable to Model 2 results reported in Table 2.

DISCUSSION OF RESULTS

Before discussing the accuracy of the h_1 values reported in Table 2, a brief explanation of the importance of J-integral path independence at high pressures is in order. According to Professor Dodds, ABAQUS calculation of the J-integral includes the results of the crack tip elements in the calculation of each J path. This produces path dependence at high loads. Due to the large strain gradients in the vicinity of the crack tip, the error in the crack tip elements increases with load. Since this error is included in the J-integral calculation for each path, the J_t values lose path independence at the higher pressures. However, for 2D models, this is not a problem only the elements contained in each path are used in the calculation of J_t. The crack tip elements are only included in the first path. This path is usually excluded in the calcultion of J_t. According to Professor Dodds, for path independence, if the J_t-integral values for the various paths differ by more than 5%, the average J_t-value from the previous pressure should be used to calculate h_1. The selection of this value is referred to as Dodds' 5% J-integral path criterion.

In addition to the three test cases discussed above, the impact of the strain hardening coefficients (n) on h_1 was studied. In addition to n=8.6, Case 1 (a/t=1/4) and 2 (a/t=1/8), models were run for n values of 5, 7 and 10. These values cover the range of strain

Table 5

Axial Semi-Elliptical Flaw in a Cylinder With Ri/t=10, a/t=1/2, and n=7

R_i= 90 in.
t= 9 in.
ℓ=2c= 27. in.
a= 4.5 in.
α = 1.4
n= 7.
E= 30.0E06 psi
v= 0.3
σ_o = 60000 psi
a*= 3.2806 in.
P_o= 4247.93 psi

Length of cylinder - 81 in. (Model 2 using ORMGEN-3D grid generator)
8 elements along crack front
2 concentric rings of elements

P (psi)	J1 (in-lb/in²)	J2 (in-lb/in²)	J3 (in-lb/in²)	J_{avg} (in-lb/in²)	P/P_o	$(P/P_o)^{n-1}$	h_1
6000	7404.1	7415.8	7179	7297.4	1.412	15.841	1.2
12000	1.219E6	1.189E6	7.990E5	9.943E5	2.825	4055.34	0.65
18000	3.979E7	2.797E7	1.444E7	2.120E7	4.237	103934.	0.54
24000	6.341E8	5.043E7	9.489E7	7.266E7	5.649	1038169.	0.19
30000	4.76E9	2.28E9	4.812E8	1.38E+09	7.062	6187970.	0.59

Length of cylinder - 81 in. (Model 3 using ORMTIP grid generator)
12 elements along crack front
6 concentric rings of elements

P (psi)	J1	J2	J3	J4	J5	J6	J7	J_{avg} (in-lb/in²)	P/P_o	$(P/P_o)^{n-1}$	h_1
3000	673.69	673.93	674.77	675.06	675.18	675.24	667.93	674.83	0.706	0.062	28.85
6000	7595.9	7562.6	7590	7598.4	7603.2	7606.3	7353.5	7592.1	1.412	15.84	1.27
9000	1.220E5	1.181E5	1.197E5	1.197E5	1.197E5	1.203E5	1.049E5	1.195E5	2.119	405.99	0.78
12000	1.261E6	1.195E6	1.211E6	1.217E6	1.225E6	1.242E6	8.486E5	1.218E6	2.825	4055.34	0.79
15000	7.785E6	7.655E6	7.473E6	7.617E6	7.772E6	7.841E6	4.346E6	7.671E6	3.531	24171.7	0.84

hardening of interest for common pressure vessels and piping steels. For Case 3 (a/t=1/2), n=8.6 was run for Models 1 and 2 and n=7 was run for Models 2 and 3. In addition, n=5 and n=10 were run for Model 2. Table 2 presents the results in terms of h_1 values per a/t and n.

The h_1 values in Table 2 were based on three criteria:

- Dodds 5% J-path independent criterion at the highest pressure run.
- Minimum or constant value of h_1 based on an h_1 versus P/P_o plot given by numbers in the parentheses in Table 2.
- 10% J-path independence criteria at the highest pressure run shown by ** in Table 2.

For Cases 1 (a/t=1/4) and 2 (a/t=1/8), the J_1-integral values are well behaved and converged values of h_1 for n=5, 7, 8.6 and 10 were obtained and are given in Table 2. For Case 3 (a/t=1/2), Model 3, n=7, the J_1-integral values were well behaved and the converged value of h_1 is given in Table 2.

The 10% criterion was needed to estimate an accurate h_1 value for Case 3 (a/t=1/2, Model 2) for values of n=5, 8.6, and 10. This was because no values of h_1 were available at high enough pressures to meet the 5% J-path independence criterion. Only for n=7 where Model 3 was used did an h_1 value meet the 5% J-path criterion.

Note that for a/t=1/8, 1/4 the h_1 values do not differ significantly using either the 5% criteria or the minimum/constant value criteria. Only in Case 3 (a/t=1/2, Model 2) do the h_1 values significantly deviate from each other using the different criterion, except, of course, for n=7 where the results from the more refined grid model were used.

CONCLUSIONS

Based on the discussion of the results, it can be concluded that those values selected on the basis of the Dodds' 5% J-path independence criterion are the most accurate. The values of h_1 based on the minimum or constant h_1 criterion found from plotting h_1 versus P/P_o give slightly lower values of h_1 with the exception of Case 3 (a/t=1/2) where only one value of n (n=7) met Dodds' criterion. A larger h_1 value produces a slightly more conservative J-applied for the flawed structure.

In any case, the values in Table 2 give lower values than those previously reported. The use of these newly generated values for part-through-the-wall flaws in pressurized vessels and/or piping would give more accurate flaw assessment with the attendant acceptance of larger defects found during inspection.

References

1. V. Kumar, M. D. German, C. F. Shih, "An Engineering Approach for Elastic-Plastic Fracture Analysis", EPRI Topical Report NP-1931, Research Project 1237-1, Electric Power Research Institute, Palo Alto, CA, July 1981.

2. H. Tada and P. Paris, The Stress Analysis of Crack Handbook, Del Research Corporation, Hellertown, Pennsylvania, 1973.

3. A. A. Il'yushin, "The Theory of Small Elastic-Plastic Deformations," Prikadnaia Matematika i Mekhanida, P. M. M., Vol. 10, 1947.

4. K. K. Yoon, D. Killian, "Development of 3-D Elastic-Plastic Finite Element Methodology for the Analysis of Reactor Vessel Longitudinal Flaws", BAW-2103, 77-1178004-00, February 1990.

5. W. W. Wilkening, H. G. deLorenzi, M. Barishpolsky, "Elastic-Plastic Analyses of Surface Flaws in a Reactor Vessel", ASME 83-WA/PVP-2, August 1983.

6. G. Yagawa, Y. Kitajima and H. Ueda, "J-Integral Database for Surface Cracks", Fracture Mechanics, London and New York, Elsevier Applied Science, 1991, p. 195-215.

7. J. M. Bloom, "Extensions of the Failure Assessment Diagram Approach Semi-Elliptical Flaw in Pressurized Cylinders - Part II, Journal of Pressure Vessel Technology, Vol. 108, November 1986, p485.

8. J. M. Bloom, " Extensions of the Failure Assessment Diagram Approach - Semi-Elliptical Flaw in Pressurized Cylinder", ASME Journal of Pressure Vessel Technology, Vol. 107, Feb. 1985, pp. 25-29.

9. ABAQUS Version 4.8, 1989, Hibbit, Karlsson and Sorensen, Inc., Providence, R.I.

10. D. M. Parks, "The Virtual Crack Extension Method for Nonlinear Material Behavior," Computer Methods in Applied Mechanics and Engineering, Vol. 12, pp. 353-364, 1977.

11. B. R. Bass, J. W. Bryson, "Applications of Energy Release Rate Techniques to Part-Through Cracks in Plates and Cylinders - Volume 1. ORMGEN-3D: A Finite Element Mesh Generator for 3-Dimensional Crack Geometries", NUREG/CR-2997, ORNL/TM-8527/V1

12. J. M. Bloom and D. R. Lee, "User's Guide for the Failure Assessment Diagram - Computer Code FAD", Babcock & Wilcox Research and Development Division, Revision 4, April 1990.

FIGURE 1. VALID J PATHS

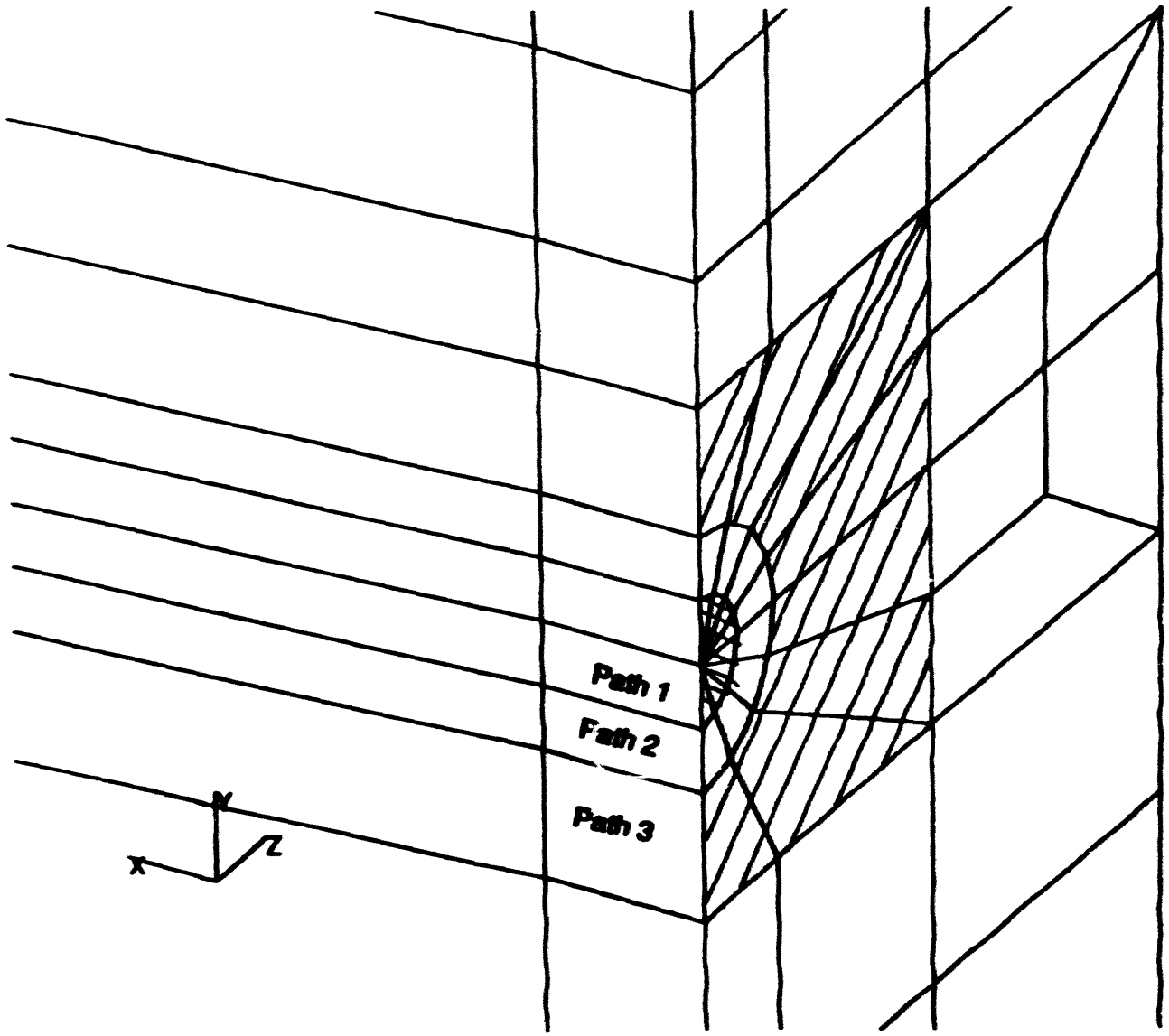

FIGURE 2. VARIATION OF h_1 WITH P/P_o RATIO

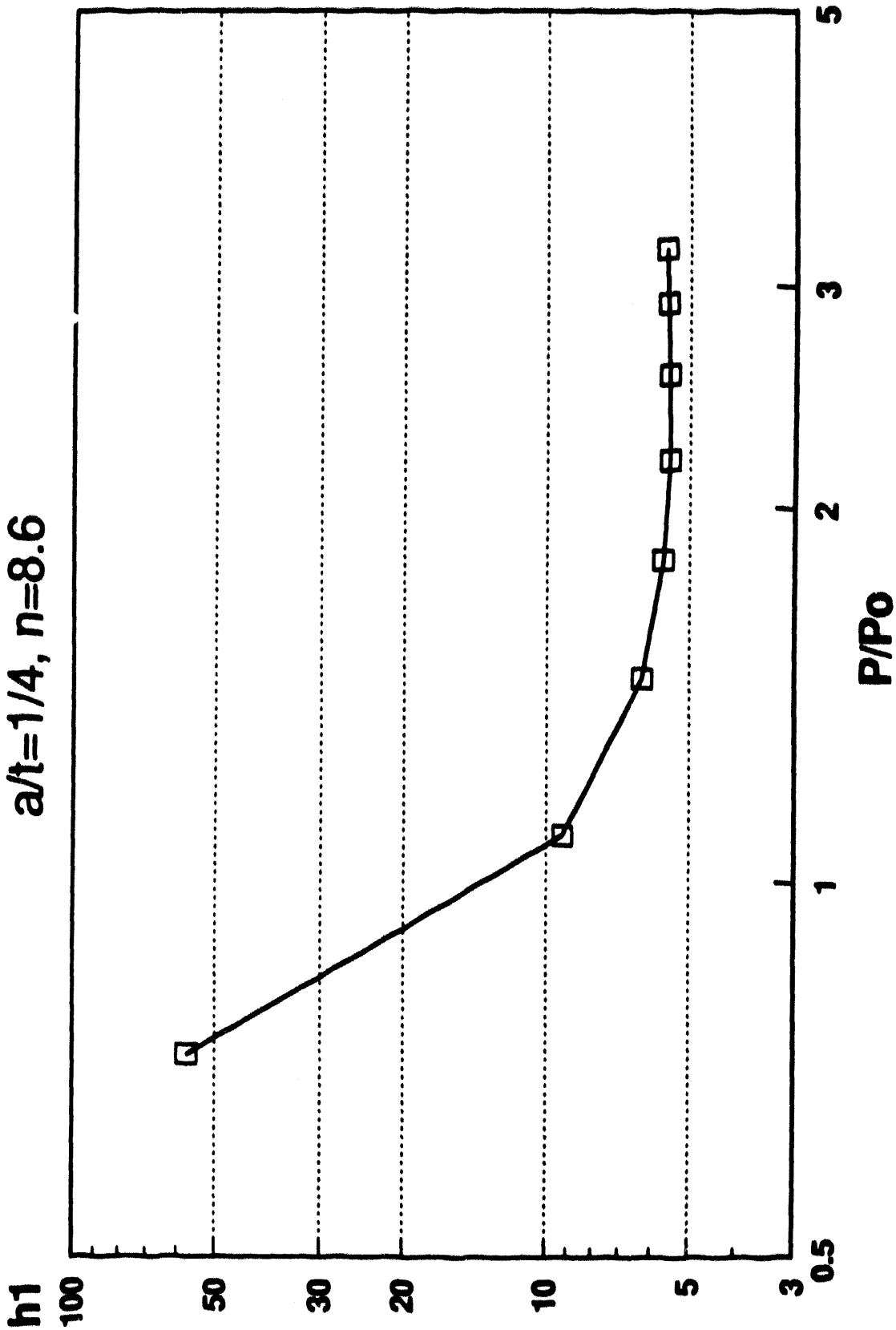

FIGURE 3. REFINEMENT AROUND CRACK TIP USING ORMTIP

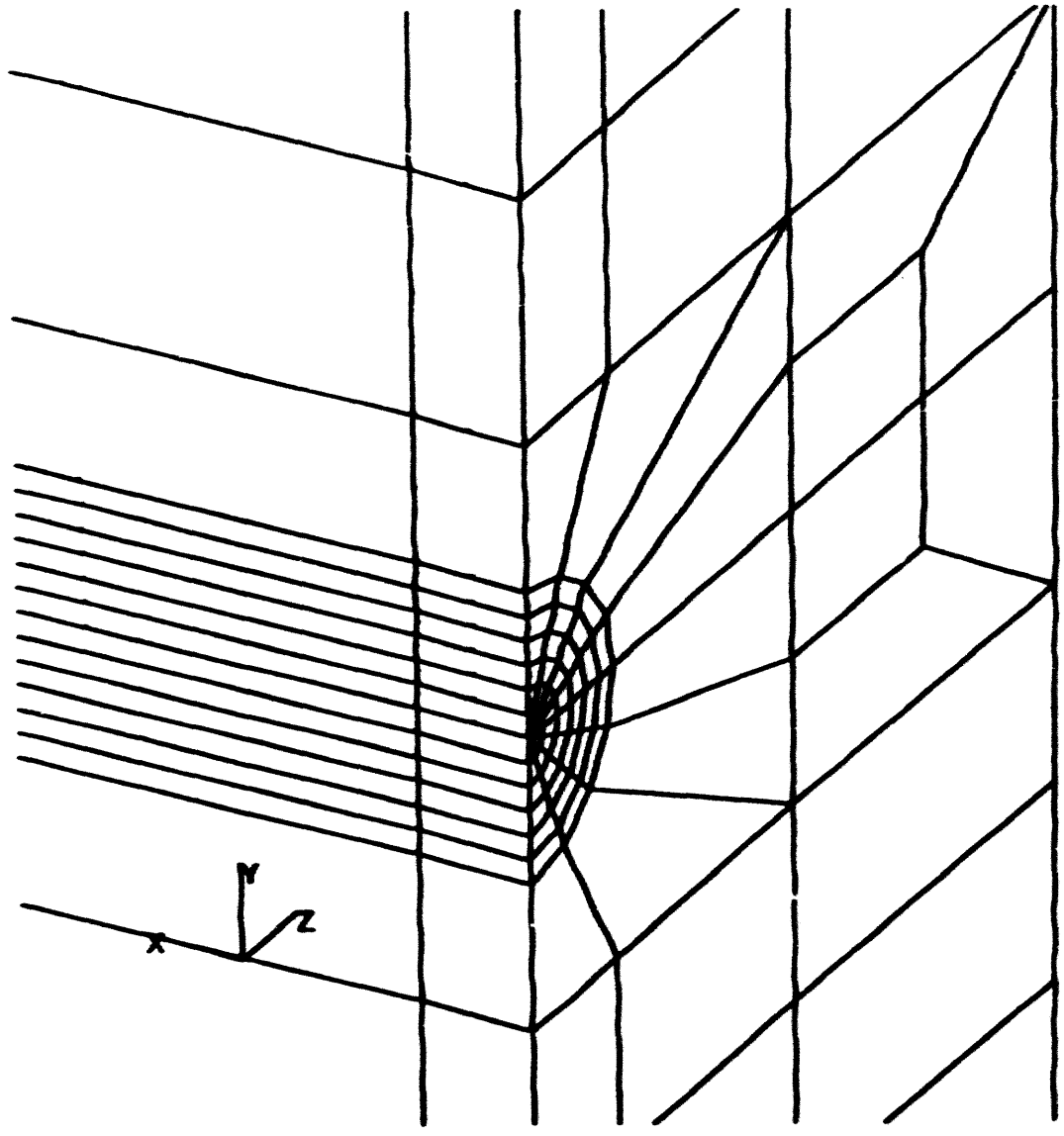

VALIDATION OF THE R6 DEFECT ASSESSMENT PROCEDURES BY WIDE PLATE AND PRESSURE VESSEL TESTS

By: A J Carter and T C Chivers
Nuclear Electric
Berkeley Technology Centre
Berkeley
Gloucestershire
United Kingdom

J B Wintle
AEA Technology
Risley
Warrington
Cheshire
United Kingdom

SUMMARY

The R6 Procedure for the assessment of the integrity of structures containing defects is widely accepted and used.

Continuing development includes validation work to both assess the methodology and to reduce inbuilt conservatisms. In this paper pressure vessel and wide plate tests are reported. The former tests address a defect in a repair weld, and a through wall defect in a strain ageing steel. For each case the R6 Procedure is shown to give reasonable assessments of performance. The wide plate tests assess the interaction between multiple defects and show that the currently employed recharacterisation rules can lead to over-conservative assessments.

1. INTRODUCTION

The R6 Procedure for the Assessment of Structures Containing Defects (1) was produced by the former Central Electricity Generating Board (CEGB) and is now maintained by Nuclear Electric plc, one of the successor companies to the CEGB. Development of R6 is now performed by Nuclear Electric plc, in collaboration with AEA Technology, British Nuclear Fuels plc and Scottish Nuclear plc in the UK. Historically, assessment of a defective structure was based either on Linear Elastic Fracture Mechanics or on plastic collapse. The R6 Procedure combines these two aspects since in any real structure they will interact. The overall objective in developing this procedure has been to produce an engineering tool which is relatively simple to use, thus avoiding the difficulties associated with precise and detailed analysis.

R6 employs a two parameter Failure Assessment Diagram (FAD). The user is required to calculate K_r, a measure of proximity to elastic failure, and L_r a measure of proximity to plastic collapse. Using these co-ordinates a datum point is plotted; if it falls within the diagram then "failure avoidance" can be claimed.

The procedure permits the user to choose from three FADs.

Option 1 - is a general curve, and its cut-off is determined by knowledge of the yield stress and the ultimate tensile stress only. This curve was chosen as an empirical but generally lower bound to a number of Option 2 curves. Thus in use it can be over-pessimistic. It can, however, be used for a first assessment of a problem. The major restriction on its use relates to materials with a large yield plateau; for these materials the Option 2 curve should be used, as in some area of the diagram Option 1 may be non conservative.

Option 2 - is a material-specific curve and full stress-strain characteristics for the material are required to calculate the boundary. In deriving this curve conservative approximations were made. Thus Option 2 is expected to give a closer assessment of performance than Option 1, whilst remaining generally conservative for all materials.

The Option 3 FAD is based on the equivalence of the failure assessment curve to a J-integral analysis. It is thus not only material specific, but also geometry specific. Its generation requires computer modelling and its validity depends on the validity of the code used in the computation.

An additional FAD is included in R6 for materials, such as C-Mn(Mild) Steels, which exhibit a high rate of hardening in the initial stages of the stress-strain curve. For these a user would be expected to use an Option 2 approach

initially. However, in many instances the specific stress-strain data may not be available. Hence an alternative FAD is included in R6 specifically for application to C-Mn steel structures. This diagram is based on typical Option 2 diagrams for these materials.

When using R6 the simplest route is to undertake an assessment using Option 1 (providing it is valid for the material). Should the evaluated L_r, K_r datum point not provide an adequate margin, then it is legitimate to move to Options 2 and/or 3 in order to calculate higher margins.

The Procedure offers advice on the determination of fracture toughness; the calculation of stress intensity factors, plastic collapse solutions, the treatment of secondary stresses, fatigue, and mixed mode loading. Appended to R6 are sub Procedures dealing with leak-before-break and probabilistic fracture mechanics.

An important aspect of assessment is how to characterise a defect, or collection of defects so that a calculation can be performed. Here R6 also offers advice to the user.

A number of assumptions are built into the Procedure which make it inherently conservative, and this results in the calculation of lower margins than actual. This conservatism is demonstrated in the Validation Section of R6 which describes a number of structural experiments including pressure vessel tests. As leak-before-break safety arguments become more important to plant operations it is necessary to move closer to predicting behaviour rather than failure avoidance. Thus further validation is important to the development of R6. In this paper three aspects of validation are addressed;

- the performance of a defect in C-Mn steel
- the performance of a defect in a repair weld
- the re-characterisation of defects

2. PRESSURE VESSEL TESTS

The work reported in this section was carried out in Nuclear Electric's pressure vessel testing facilities. Two tests were conducted using vessels with section thicknesses and materials typical of those in the primary pressure circuit of the Magnox power stations. They have shown R6 to be inherently safe in predicting failure loads.

2.1 C-Mn Steel Vessel

This vessel, figure 1, included a plate from the construction of a Magnox nuclear power station pressure vessel.

This strain ageing material was welded to modern boiler plate, and the whole formed into the barrel section of a pressure vessel; separate end caps were then added. An axially orientated fully penetrating defect (Figure 3) was cut into the strain ageing material, and lightly sealed on the inner wall with a foil cap. The machined notch was fatigue sharpened by pressure cycling at 50°C. The vessel pressure test to failure was then conducted at 200°C, a temperature at which strain ageing effects were apparent. In this test, oil was used as the pressurizing medium to minimize stored energy by avoiding boiling of the liquid once leakage occurred.

Destructive testing of the vessel stopped when the pumping system failed to keep pace with leakage, as the foil seal became dislodged. The degree of stable tearing induced by the overpressure test was measured from the fracture surfaces, after these had been machined from the surrounding plate and broken open by fatigue (Figure 3).

2.1.1 R6 Analyses of the C-Mn Vessel

Mean material properties (Table 1) were used in the R6 analyses, to provide the best burst pressure estimates. Failure assessments were based on the general purpose (option 1) failure assessment curve, the material specific (option 2) curve, and the carbon-manganese failure curve. Stable tearing limits in the R6 analyses were the values measured from the fracture surfaces; these were 3.6 mm of stable tearing which occurred at each end of the penetrating defect. J integral versus crack growth (J-Δa) data were measured from fracture toughness specimens.

Failure estimates based on initiation (category 1) and with stable tearing (category 3) appear in Table 2 and Figure 6. The point shown inside the diagram corresponds to the upper pressure in the fatigue cycle (1769psi).

The R6 analyses were conducted with the FRACTURE.TWO computer code (Ref. 3), with limit loads based on the Battelle formulae (Ref. 4) and stress intensity factors computed by the weight function method.

2.1.2 Discussion

Failure pressure estimates in the strain ageing vessel, based on initiation (category 1), are all significantly lower than the measured burst pressure, but in good agreement with each other. The category 3 assessments, corresponding to 3.6 mm of stable tearing, are nearer the true burst pressure; best agreement is obtained with the C-Mn failure assessment curve, which marginally underestimated the failure pressure. Both the option 1 and 2 category 3 analyses give slightly conservative answers and are in close agreement with one another.

2.2 Weld Repair Vessel

The vessel was made from modern boiler plate (Figure 2) and incorporated an axial repair weld, 50 mm deep and running along the length of the barrel. Post weld heat treatment was deliberately avoided, leaving significant residual hoop stresses in the repair weld (Figure 5). A surface defect was machined into the weld (Figure 4) and sharpened by fatigue; the vessel was failed at 50°C with water as the pressurising medium.

Destructive testing ceased when the pumping system failed to keep pace with leakage when the defect snapped through the vessel wall. The extent of stable tearing induced by the overpressure was measured from the fracture surfaces.

2.2.1 R6 analyses of the weld repair vessel

Mean material properties as included in (Table 1) were used in the R6 analyses, to provide the best burst pressure estimates. In this instance failure assessments were based on the general purpose (option 1) failure assessment curve only. The stable tearing limit in the analyses was assessed from the fracture surfaces as 25.4 mm (the remaining ligament) at the bottom of the surface defect. The J integral versus crack growth ($J-\Delta a$) relationship for the plate was only available from a handbook (Ref.2).

Failure estimates based on initiation (category 1) and with stable tearing (category 3) appear in Table 2 and Figure 7. Initiation is envisaged in the weld region, with the defect tearing through plate material, at the deepest point.

As before, the R6 analyses were conducted with the FRACTURE.TWO computer code (Ref. 3). Limit loads were based on the Battelle formulae (Ref. 4) and stress intensity factors computed by the weight function method. The effect of secondary (residual) stresses in the cold weld repair vessel were most pronounced at the surfaces, and they had little effect at the deepest point on the crack front. Points inside the diagram correspond to the upper pressure of 3950 psi in the fatigue cycle.

2.2.2 Discussion

Failure pressure estimates in the cold weld repair vessel are considerably lower than the measured burst pressure. Here the amount of stable tearing covered in the analysis was only 9mm, (compared with over 20mm in the test) and this was restricted by the cut off in the R6 diagram (Fig.7). This result suggests that either the limit load solution or the flow stress (the mean of the yield and ultimate tensile stresses) is conservative.

3. RE-CHARACTERISATION OF DEFECTS

The work reported in this section was carried out in the AEA Technology Structural Features Test Facility at Risley.

3.1 Embedded Flaws in Brittle Fracture

A series of four tests have been carried out on flat mild steel rectangular specimens containing embedded flaws. In each case the R6 Procedure would require the flaws to be recharacterised as surface breaking. The tests were undertaken at low temperatures where failure occurred by brittle fracture. The flaw geometries are illustrated in Fig. 8 and were as follows:

(a) A single circular embedded flaw.

(b) A single circular flaw as in (a) above but located nearer to the free surface and therefore having a smaller ligament.

(c) An elliptical flaw at the same depth as (a).

(d) Two adjacent coplanar flaws of the same radii and depth below the surface as (a).

The material used for the tests was a carbon steel containing 0.36% carbon with a relatively low fracture toughness of 38MPa$\sqrt{m}$, as assessed by Charpy impact tests, in relation to its yield stress of 310MPa.

Each specimen was manufactured from a pair of blocks each containing appropriately sized surface breaking semi-circular or semi-elliptical slot(s) cut by electro discharge machining. The blocks were aligned to match the slots in each and the assembly diffusion bonded to form a large block containing the required flaw(s). After bonding, end pieces were attached by electron beam welding to form the test specimen.

The test specimens were mounted in a 2.5MN servo hydraulic testing machine with constraints to minimise out of plane bending. The slots were sharpened into defects by cyclic loading at a stress intensity factor range of approximately 20 MPa$\sqrt{m}$.

The specimens were then cooled to a temperature between -30 and -35°C and loaded slowly in tension until failure occurred. Afterwards the fracture surfaces were cut from the specimens and the final (post fatigue) dimensions of the flaws were measured.

Although a small amount of yielding occurred prior to failure (as evidenced from the load/displacement and load/strain traces) examination of the fracture surface confirmed that all specimens had failed by brittle fracture.

3.1.1 R6 Analyses

An assessment of the load to failure was undertaken using the generalised R6 Rev 3 Option 1 Failure Assessment Diagram. The flaws were first analysed in their true geometry (i.e. uncharacterised) and then analysed as recharacterised surface flaws according to Section 9.4.1(i) of R6. The two circular flaws in specimen (d) were also analysed as a combined embedded flaw according to Section 9.4.1(ii) of R6.

The stress intensity factor solution for these flaw geometries were derived from standard published sources and the limit load was based on the reduction of cross section area.

Table 3 gives the actual failure loads from each of these tests and the predicted failure load from the R6 analysis.

3.1.2 Discussion

From Table 3 the following observations can be made.

- The actual loads required to fail the specimens exceeded the failure loads assessed by R6 in all cases demonstrating the R6 procedures to be conservative. This was true also for the un-recharacterised defects and suggest that the use of modern formulations for stress intensity factors, in conjunction with nett section stresses for collapse, adequately describe behaviour.

  The actual failure loads and the assessed failure loads for the non re-characterised flaws were consistent with the different features of the flaw geometries: the failure load reduced with decreasing ligament (specimens (a) and (b)); the failure load reduced with increasing aspect ratio (specimens (a) and (c)); the failure load reduced with the presence of a second flaw in close proximity (specimens (a) and (d)).

- The assessed failure loads for the recharacterised flaws were less than those assessed for the original flaws thereby demonstrating conservatism in the recharacterisation procedures. However, the assessed failure load for specimen (b) was higher than for specimen (a) contrary to the actual behaviour. This could indicate an inconsistency in the treatment of deep flaws relative to shallow flaws which may result in an overly conservative assessment. However, the differences are small bearing in mind that the data for specimen (a) have been adjusted for comparative purposes, and definitive conclusions cannot be drawn from this data alone.

3.2 Multiple Surface Flaws in Plastic Collapse

A series of tests have been carried out on plates, 12.5mm thick by 125mm wide, containing pairs of identical co-planar, surface breaking semi-circular flaws. Four types of flaw configuration with varying separations were tested, Fig. 9. The separations were such as to require recharacterisation under the procedures of R6.

Two materials were used in the tests, 0.36% C mild steel and stainless steel, representing materials with a distinct yield and with high work hardening, respectively. The mild steel was tested at 80°C while the stainless steel was tested at ambient temperature. At these temperatures, the respective yield stresses were 308MPa and 339MPa. The crack growth resistance of these materials indicated that high fracture toughness was attained after a small amount of tearing - a necessary condition to obtain failure by plastic collapse.

The flaws were spark machined into the plates and sharpened by fatigue. The flawed plates were mounted in a 100 tonne servo-hydraulic machine in such a way so as to minimise out of plane bending. The plates were strain gauged with flaw growth determined using an ACPD technique. The plates were loaded in tension until through wall cracking had occurred and the load was reducing. Two loads were determined from the tests: the load at which tearing of the flaws initiated and the peak load. It is noted that high values of toughness are required to achieve plastic collapse and this is consistent with the tearing resistance of the material.

3.2.1 Analyses

An analytical prediction of the failure load was made solely on a simple reduction of area criteria. The failure load of each flaw configuration was estimated in five different ways:

(a) Single flaws - global section. Based on the actual area of both flaws as a ratio of the full cross section of the plate. This is the least conservative treatment as it does not take account of the proximity of the flaws to each other or to the back surface of the plate.

(b) Single flaws - local section. Based on the area of both flaws as a ratio of the total of the ligament area associated with each flaw (as defined in Fig. 10)). When the flaws are in close proximity such that the ligament areas overlap, the area of the overlap is only counted once.

(c) Recharacterised as through flaws - global section. This case is based on a strict interpretation of the procedure outline in British Standard PD 6493. The pair of separate flaws are recharacterised as through thickness flaws having an area equal to the local section. Collapse is calculated on the basis of the

area of the recharacterised flaws as a ratio of the full (global) cross sectional area of the plate. This is the most conservative treatment.

(d) Recharacterised as a semi-elliptical flaw - local section. This case follows the guidance given in R6. The pair of surface breaking flaws is recharacterised as a single semi-elliptical flaw when S < 2a. Collapse is calculated on the basis of the area of the semi-elliptical flaw as a ratio of the local section area.

(e) Recharacterised as a semi-elliptical flaw - global section. This calculation is based on the flaws recharacterised as a semi-elliptical flaw (as in (d) above). Collapse is determined from the ratio of the area of the semi-elliptical flaw to the full (global) cross section.

Table 4 details the experimentally obtained initiation and peak loads for comparison with the collapse predictions.

3.2.2. Discussion

The following observations can be made from Table 4.

- The loads for initiation of tearing and maximum loads determined in the tests increase with increasing flaw separation.

- The separation effect is not modelled correctly by the collapse loads assessed from recharacterising the flaws.

- All the approaches for estimating the collapse load are conservative (i.e. give under estimates) with respect to the observed peak load. The approach based on recharacterising the flaws as through thickness flaws (BS PD 6493, Ref. 5) is the most conservative. The R6 approach is less conservative and is consistent with the other alternatives.

- This work does not resolve the issue as to when global or local limit loads are appropriate for these geometries and further study of this aspect is desirable.

4. CLOSURE

A number of experiments have been described which underwrite the R6 Procedure for the assessment of structures containing defects. All results show the basic procedure to be conservative. The data also indicate areas that permit more accurate assessments to be made and these include:

- the use of stable tearing provided valid J-Δa data is available

- detailed attention to re-characterisation of defects and the calculation of stress intensity factors
- accurate definition of appropriate limit loads, although here there may be a paucity of data.

5. ACKNOWLEDGEMENTS

The authors gratefully acknowledge the contributions made by colleagues in the preparation of this paper.

This paper is published by permission of Nuclear Electric plc and AEA Technology.

6. REFERENCES

1. I Milne, R A Ainsworth, A R Dowling and A T Stewart, Assessment of the Integrity of Structures Containing Defects, CEGB Report R/H/R6 - Revision 3 (1986). Int. J Pres. Ves. and Piping 32, 3-104 (1988)

2. Magnox Pressure Circuit Materials Data Handbook R51, Issue 4, Nuclear Electric Document.

3. G G Chell, R6 Code: A Computer Program for Performing an R6 (REV 3) Analysis: User Guide for FRACTURE TWO, National Power Report TEC/L/0162/M91, September 1991.

4. A G Miller, Review of Limit Loads of Structures Containing Defects, CEGB Report TPRD/B/0093/N82 - Revision 2 (1987). Int. J. Pres. Ves. and Piping 32, 197-327, (1988)

5. British Standards Institution, Guidance on methods for assessing the acceptability of flaws in welded structures, Published Document PD6493 (1991)

TABLE 1

MATERIAL PROPERTIES

	STRAIN AGEING VESSEL (MEAN DATA, 200°C)	COLD WELD REPAIR VESSEL (MEAN DATA, 50°C)	
		WELD METAL	PARENT PLATE
YIELD STRESS (MPa)	249	442	277
ULTIMATE TENSILE STRESS (MPa)	433	518	440
YOUNG'S MODULUS (GPa)	162	208	208
POISSON'S RATIO	0.3	0.29	0.29
INITIATION FRACTURE TOUGHNESS (MPa$\sqrt{m}$)	156	223	178
STABLE TEARING RELATIONSHIP J(MNm^{-1}) VS. Δa(mm)	$J = 0.122 + 0.068\ \Delta a$	NOT USED	$J = 0.113 + 0.129\ \Delta a$

TABLE 2

FAILURE PRESSURE ESTIMATES

	STRAIN AGEING VESSEL FAILURE PRESSURE (psi)	COLD WELD REPAIR VESSEL FAILURE PRESSURE (psi)
OPTION 1 - CATEGORY 1	2085	5250
OPTION 2 - CATEGORY 1	2124	NOT INVESTIGATED
C-Mn - CATEGORY 1	1995	NOT INVESTIGATED
OPTION 1 - CATEGORY 3	2627	6003
OPTION 2 - CATEGORY 3	2671	NOT INVESTIGATED
C-Mn - CATEGORY 3	2538	NOT INVESTIGATED
MEASURED DURING TEST	2542	7300

TABLE 3

EXPERIMENTAL AND ASSESSED FAILURE LOADS

ALL LOADS IN MN

Specimen	R6 Option 1 FAD			Experimental Failure Load
		Section 9.4.1(i)	Section 9.4.1(ii)	
	No recharac-terisation	Defects recharacterised as:		
		Surface	Embedded	
(a)	1.965	1.977		2.30 (2.53)
(b)	1.991	1.990		2.447
(c)	1.524	1.308		2.099
(d)	2.076	1.490	1.655	2.171

The load value in brackets has been derived from the actual failure making an allowance for a difference in the size of the flaw relative to the flaws in the other specimens.

TABLE 4

COMPARISON OF INITIATION AND PEAK LOADS WITH COLLAPSE PREDICTIONS

Material	Flaw Separation	Experimental		Assessed Failure Load				
		Init. Load	Peak Load	Single		Recharacterised		
						Semi-elliptical		Through
				Local	Global	Local (R6)	Global	Global (BS)
	mm	kN	kN	kN	kN	kN	kN	kN
Stainless Steel	0	480	773	558	698	558	698	454
Stainless Steel	6.25	490	814	587	698	545	683	379
Stainless Steel	12.50	680	850	608	698	535	683	303
Mild Steel	0	470	610	473	591	473	591	385
Mild Steel	6.25	520	635	497	591	462	579	321
Mild Steel	12.50	653	676	516	591	453	566	256
Mild Steel	25.00	685	707	516	591	-	-	385

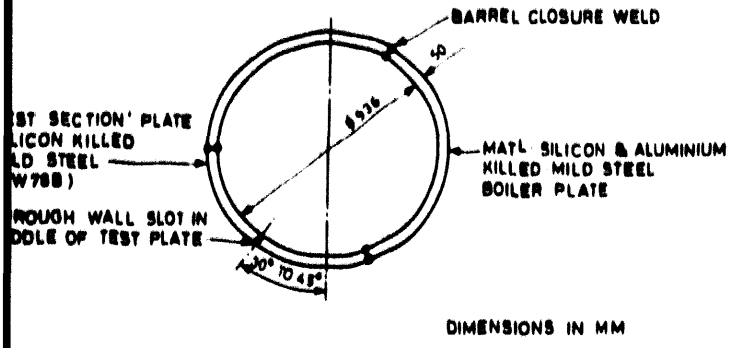

FIG.1. THE STRAIN AGEING VESSEL

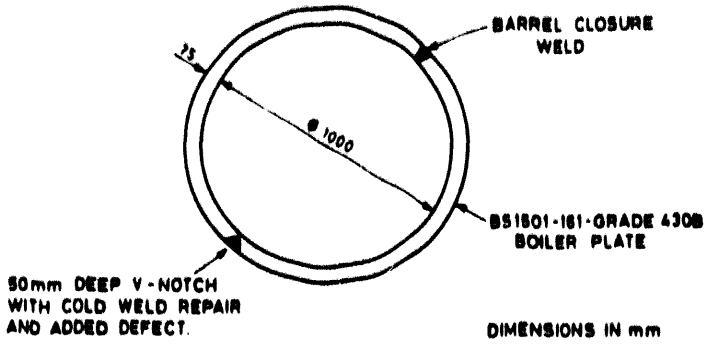

FIG.2. THE COLD WELD REPAIR VESSEL

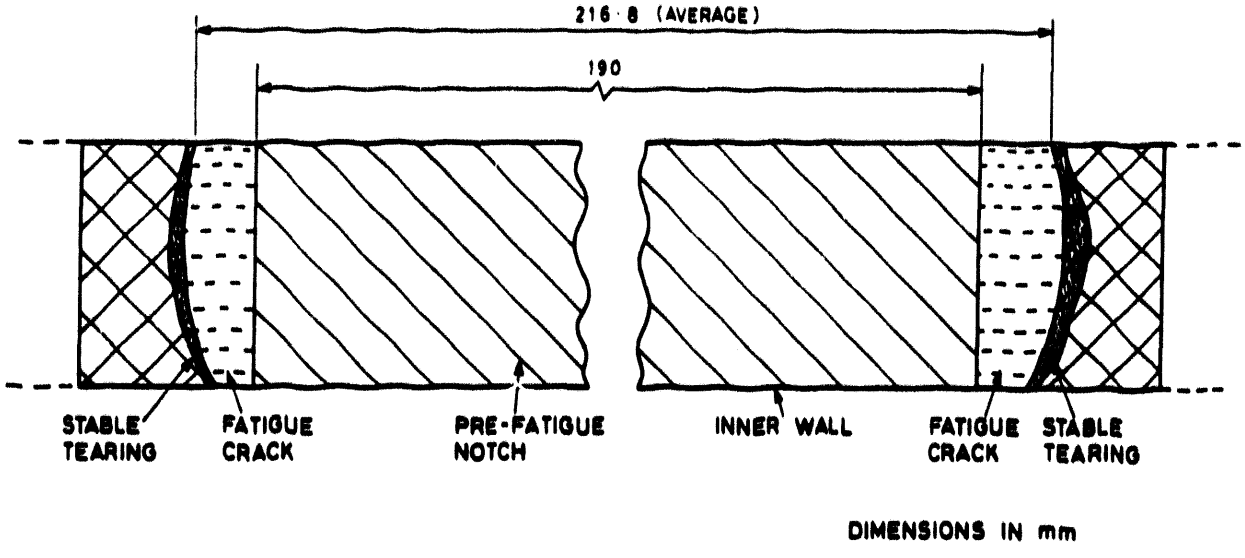

FIG. 3. THE STRAIN AGEING VESSEL FRACTURE SURFACE

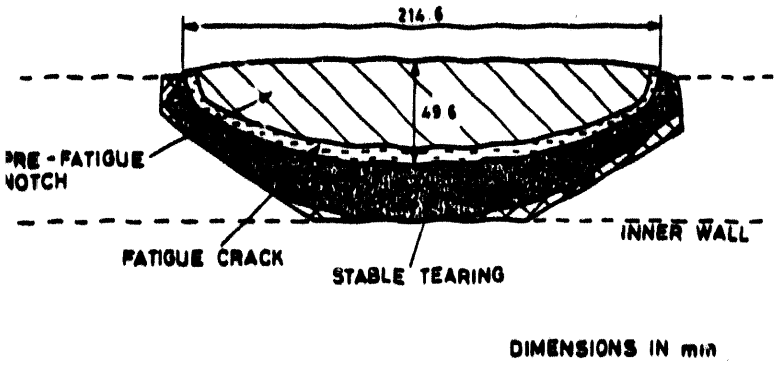

.4. THE COLD WELD REPAIR VESSEL FRACTURE SURFACE

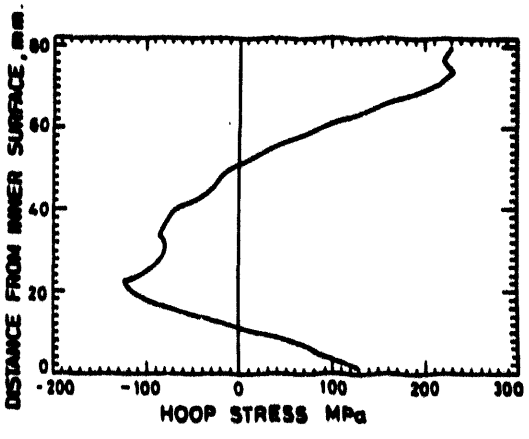

FIG.5. THROUGH-WALL DISTRIBUTION OF RESIDUAL STRESS ON REPAIR WELD CENTRELINE

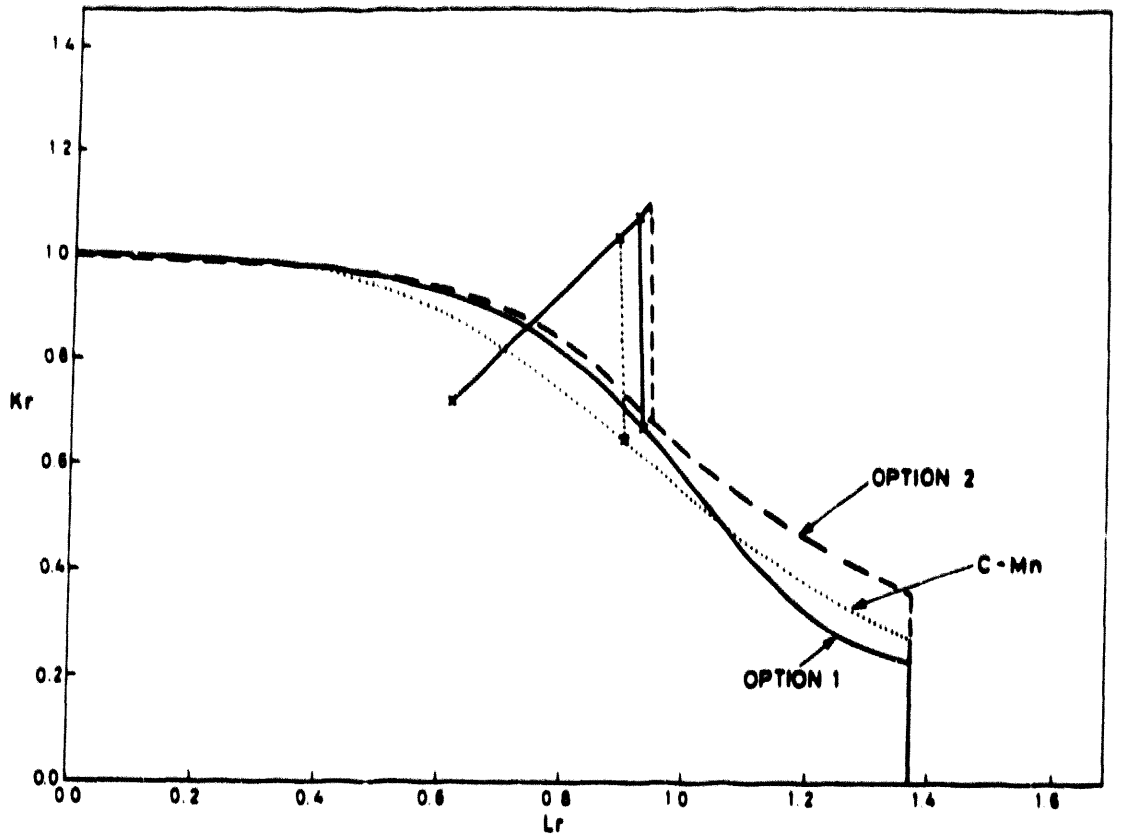

FIG.6. THE STRAIN AGEING VESSEL FAILURE DIAGRAM

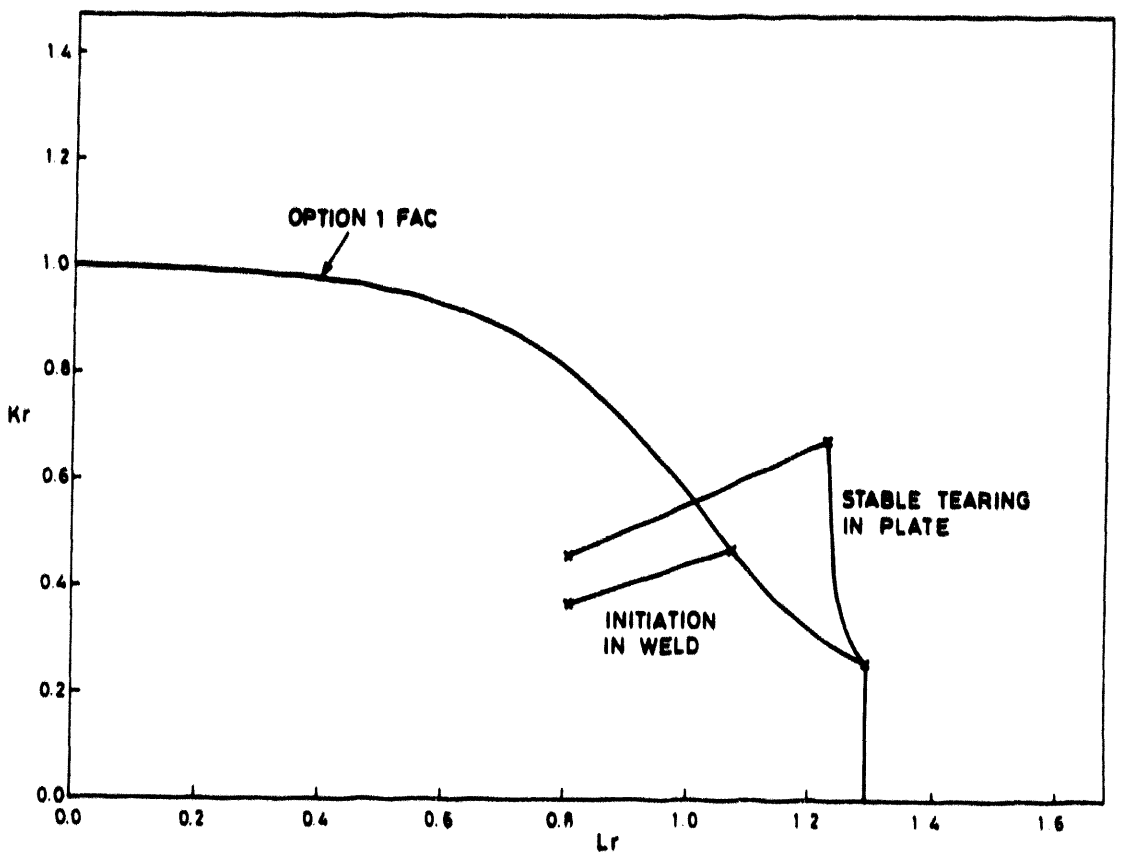

FIG. 7. THE COLD WELD REPAIR VESSEL FAILURE DIAGRAM

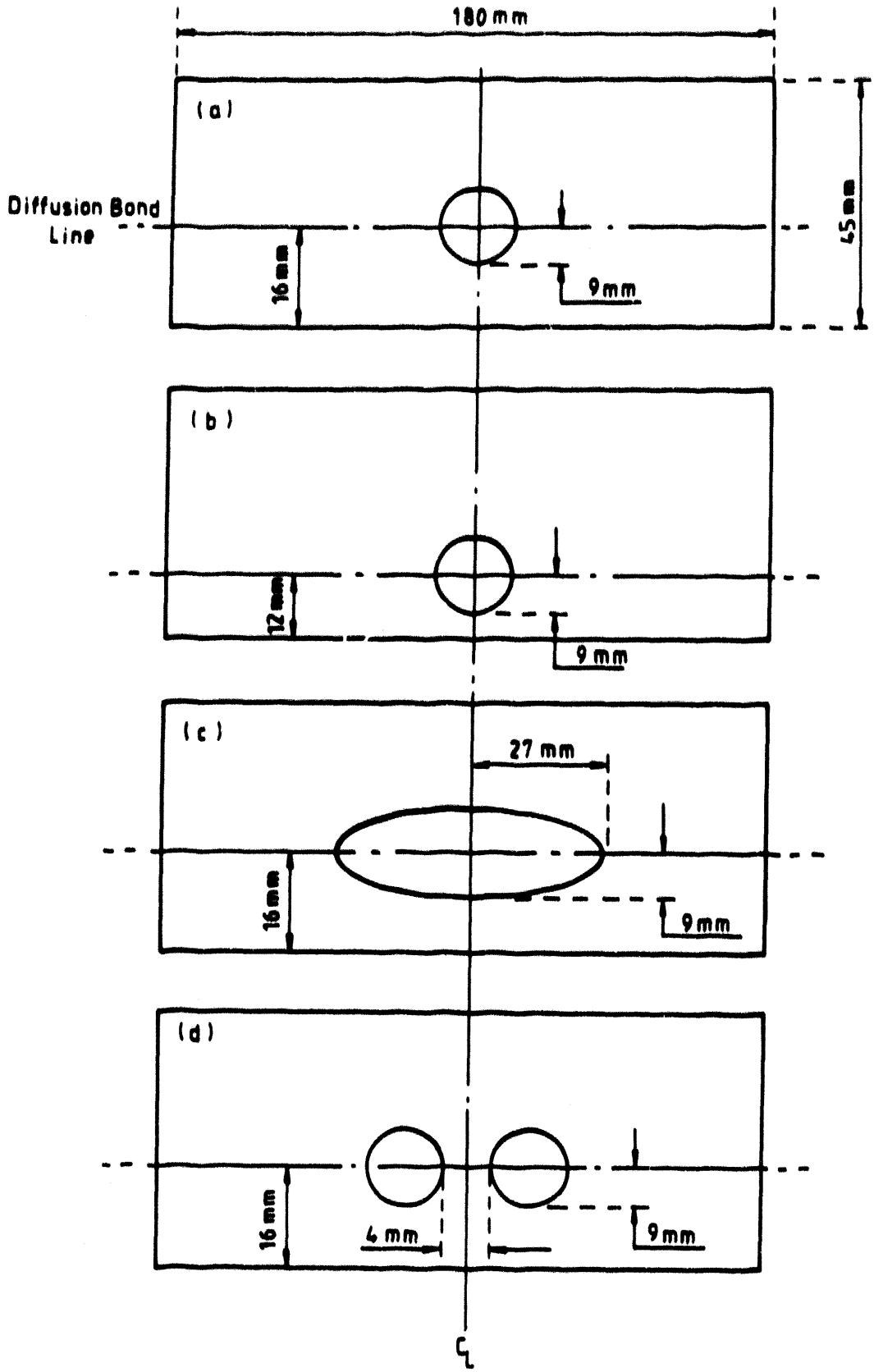

The above dimensions are for the as-machined defects

FIG.8. SPECIMEN CROSS SECTIONS

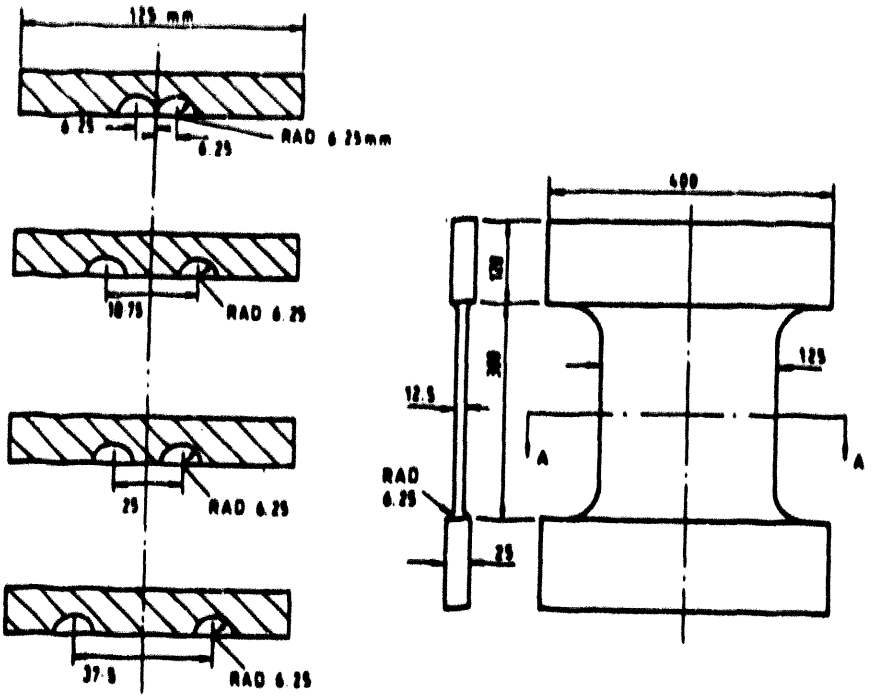

Part sections on A-A

Nb Dimensions in mm

FIG. 9. SPECIMEN AND DEFECT DIMENSIONS

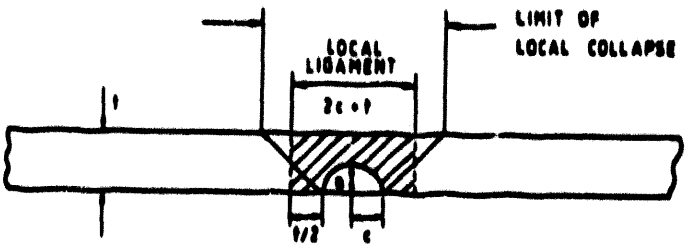

SINGLE DEFECT

LIGAMENT AREA = t (2c + t)

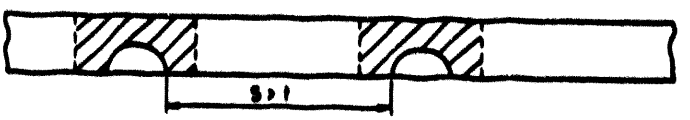

MULTI DEFECT WIDE SPACING

LIGAMENT AREA = 2t (2c + t)

MULTI DEFECT CLOSE SPACING

LIGAMENT AREA = 2t (2c + t) - OVERLAP

FIG.10.DEFINITION OF 'LOCAL' LIGAMENT

TEST OF LARGE-SCALE SPECIMENS AND MODELS AS APPLIED TO NPP EQUIPMENT MATERIALS

Boris T. Timofeev, Georgy P. Karzov

Central Research Institute of Structural Materials "Prometey"
St. Petersburg, Russia, 193167

Abstract

The paper presents the test results on low-cycle fatigue, crack growth rate and fracture toughness of large-scale specimens and structures, manufactured from steels, widely applied in power engineering industry and used for the production of NPP equipment with VVER-440 and VVER-1000 reactors. The obtained results are compared with available test results of standard specimens and calculation relations, accepted in "Calculation Norms on Strength." At the fatigue crack initiation stage the experiments were performed on large-scale specimens of various geometry and configuration, which permitted to define 15X2MFA steel fracture initiation resistance by elastic-plastic deformation of large material volume by homogeneous and inhomogeneous state. Besides the above mentioned specimen tests in the regime of low-cycle loading, the tests of models with nozzles were performed and a good correlation of the results on fatigue crack initiation criterium was obtained both with calculated data and standard low-cycle fatigue tests.

The scale factor effect on the fatigue crack kinetics stage for reactor steels and their welded joints was estimated on compact specimens of 20-100 mm thickness. It was noted that on the Paris part of the fatigue fracture diagram a specimen thickness increase does not influence fatigue crack growth resistance by tests in air both at 20 and 350°C. The estimation of the comparability of the results, obtained on specimens and models was also carried out for this stage of fracture.

At the stage of unstable crack growth by static loading the experiments were conducted on specimens of various thickness from 15X2MFA and 15X2NMFA steels and their welded joints, produced by submerged arc welding, in as-produced state (the beginning of service) and after embrittling heat treatment, simulating neutron fluence attack (the end of service). The compact specimens of 25-150 mm thickness - up to 120 mm) were used for these tests. The obtained results give evidence of the possibility of the reliable prediction of structure elements brittle fracture using fracture toughness test results on relatively small standard specimens.

Scale Factor Effect On Low Cycle Fatigue Resistance

Fatigue fracture initiation and development in real structures occurs, as a rule, in stress concentration zones, and fatigue life to a crack nucleation is determined by the amplitude of local strains for loading cycle. In spite of the sufficient accuracy and good experimental study of fatigue failure criteria, some problems, arising by service life estimation of real structures, should be discussed. It concerns, first of all, the effect of absolute sizes of plastically deformed metal zone on service life to failure initiation.

A series of experiments was performed on large-scale specimens of various geometry and configuration (Fig. 1). The specimens made from the type 15X2MFA steel (which is widely used for pressure vessel production) were tested in MYG-3000 and ZDM-1200 machines by elastic-plastic deformation of material large volume both by homogeneous and inhomogeneous stressed states, which are characteristic to real structures. A sufficiently inhomogeneous stressed state, generated by the interaction between several stress concentrators and defects, was simulated by the test of specimens (Fig. 1c) which contained the second stress concentrator in the form of a hole in the field of an outer concentrator action. To provide different concentrators effect on each other, the distance between was varied.

Under the conditions of homogeneous stressed state and rigid loading low cycle fatigue tests of large-scale specimens (net section - 4800 mm^2) made from 15X2MFA steel showed that the material fatigue life to crack initiation is in good agreement with the results obtained from small specimens (net section - 48 and 300 mm^2). Figure 2 shows experimental results obtained on large-scale specimens from 15X2MFA steel as compared with analogous test results for ten melts of this steel on standard cylindrical specimens (curves 1-3). The given results demonstrate the absence of special peculiarities of the material fracture by low cycle loading with the increase of the deformed material volume. More correct understanding of the dependence of fatigue life to crack initiation on specimen scale factor gives the comparison with the results of serial tests of similar in configuration specimens (net section - 300 and 48 mm^2) represented in Fig. 2 in the form of real distribution fatigue life curves. In this case the average values to crack initiation are practically similar for these types of specimens which differ in scale.

Thus, the increase of metal deformed volume by elastic-plastic loading approximately by 100 times did not change the value of fatigue life to crack initiation in the investigated material. By specimen scale factor variation, a very small tendency to life decrease is observed which does not permit us to consider the effect of scale factor on fatigue fracture characteristics, associated with the average statistic distribution of material structure imperfections to be reasonable (as it was done in earlier investigations).

The effect of an inhomogeneous stressed state on fracture resistance by large volumes of deformed material, under the conditions of cyclic loading was experimentally and theoretically investigated on specimens, containing lateral notches (net section - 60 $\times$ 600 mm). As related to the applied loading regimes, the size of material elastic-plastic deformation zone in the field of stress concentrators was equal to 20-70 mm. The typical distribution of longitudinal and transversa strains and stresses in the minimum section of specimens with concentrators, received with the use of transducer measurements and the finite element method analysis, is presented in Fig. 3. The comparison of calculated and experimental results demonstrate the finite element method application permits to conduct the analysis of the stressed state in stress concentration zones with a sufficiently high degree of accuracy. In this case, both in elastic and elastic-plastic deformation zones the complete coincidence of results

is observed. The stress-strain calculations by elastic-plastic deformation in stress concentration zones permitted to analyze the variation of the stressed/strained state in specimens by the steady regime of cyclic loading. Figure 3 gives the stress and strain distribution at the moment when the load on the specimen is equal to zero by a pulsating loading cycle. The specimens stressed-strained state for three regimes of loading is characterized by the generation of compression by stresses break down exceeding the material yield strength. Thus, in the steady regime by a mild pulsating cycle of the loading variation in concentration zones, a symmetrical deformation cycle is realized with a given deformation amplitude (rigid loading). Such type of material deformation occurs in the concentrator in the case when the maximum local strain exceeds $2\epsilon_T$, where ϵ_T is the strain corresponding to the material yield strength. It is confirmed with calculated results.

Elastic-plastic strain and stress values obtained as the result of experiments and calculations give the possibility to determine the strain concentration factors (K_ϵ - the relation of the maximum local strains to the nominal ones) and the stress concentration factors (K_σ) - the relation of the maximum local stresses to the nominal ones) and to observe their variation versus the material loading degree. By elastic deformation, when the stresses in the concentration zones do not exceed the material yield strength, the stress and strain concentration factors are equal to the theoretical concentration factor α_σ. The variation of K_ϵ and K_σ versus the degree of operating nominal stresses is shown in Fig. 4. By the increase of nominal stresses, K_σ decreases and approximates to the unit, and K_ϵ attains the value of 8 - 10. It is necessary to note some difference in the variation of K_ϵ and K_σ by testing with the monotonic and stepped (with intermediate break downs) loading increase. In the second case a rapid development of plastic deformations and correspondingly the K_ϵ increase are observed (the K_ϵ increase becomes slower by the high values of σ_{nom}/YS). Theoretical curves of the correlation K_ϵ versus nominal stresses, calculated in accordance with the loading history of each specimen by testing process, agree with experimental results. The strain concentration factors in the steady regime of cyclic loading appear to be lower than the maximum value and differ sufficiently from α_σ. The calculated and experimental values of K_ϵ^{cycle} for the steady deformation process are presented in Fig. 4.

As at the stage of repeated static loading the material resistance of elastic-plastic deformation is defined by the generalized diagram of cyclic deformation (for which the cyclic yield strength $S_T \approx 2$ YS), then the corresponding values of K_ϵ^{cycle} to compare with the static values should be considered in the coordinates of σ_{nom} (S_T), i.e. σ_{nom} (2 YS).

Based on this fact, Fig. 4 shows the location of steady K_ϵ^{cycle} values. For the given loading conditions one observes an agreement of K_ϵ values, obtained by static monotonous loading, with the corresponding steady values of K_ϵ^{cycle}, calculated, based on the generalized diagram of cyclic deformation. The variation of stress and strain concentration factors in the elastic-plastic zone is well described by the equation, proposed by N. A. Makhutov.[1]

For scale factor estimation and verification of deformation criteria, both local strain amplitudes and number of cycles to crack initiation were registered for all specimens. The experimental results were compared with the 15X2MFA steel low cycle fatigue data, obtained on small specimens, from the crack initiation moment under the conditions of the homogeneous stressed state (Fig. 2). It is evident, that the life to fatigue failure of large-scale specimens in the inhomogeneous stressed state regime is defined by the amplitude of local deformations and there is a good agreement with the test results of small specimens by rigid loading. The performed investigations confirm that low cycle fatigue crack initiation is independent of scale factor both under the conditions of homogeneous stress field and in stress concentration zones.

In real structures an interaction of two concentrators may occur, namely, for example, when a production flaw is located in the zone of a design stress concentrator effect. The character of elastic-plastic deformation and fracture resistance by cyclic loading, under the conditions of two stress concentrators interaction was investigated on specimens with 300 × 15 mm net section (Fig. 1). The distribution of longitudinal, transversa and shearing strains and stresses in the concentrators interaction zone, obtained by the use of the finite element method calculation results, indicates that a stressed and strained state for an inner concentrator depends greatly on the distance from an outer concentrator, which provides a constant field of stress and strain disturbance (Fig. 5). At the distance between concentrators less than two diameters of an inner hole an evident concentrators interaction may be observed. In this case, a sharp stress and strain increase occurs for the hole edge, nearest to the concentrator, especially by elastic-plastic deformation. At the largest distance from the outer concentrator hole by elastic loading, the concentrators do not interact with each other; at the same time a joining of ductility zones occurs in the elastic-plastic zone and the stresses in the crosspiece between concentrators exceed the material yield strength. However, it does not result in the sufficient strain increase on the surface of the hole (Fig. 5). Thus, the analysis shows that the mutual effect of two concentrators in the elastic-plastic zone takes place by the interaction of their strain fields. The stressed state in the crosspiece between concentrators is practically not changed, because longitudinal stresses and stress intensity exceed the material yield strength by a sufficient degree.

The information about the stressed-strained state in the region of interacting concentrators permits to analyze the variation of stress and strain concentration factors by the increase of nominal stresses. Fig. 6 demonstrates the dependence of K_σ and K_ϵ for the typical points of two concentrators on the level of nominal stresses by the various distances of an inner hole from an outer concentrator. Here, the variation of K_σ and K_ϵ, illustrating only the outer concentrator effect, is also presented. Within the material elastic deformation range a sufficient increase of stress concentration factor (α_σ) on the surface of a hole is observed in the case when the interaction of two concentrators occurs. By other investigation conditions the stress concentration factors near the hole are comparable with theoretical values,[2,3] obtained by biaxial loading. By the development of elastic-plastic deformations within the zones of interacting concentrators K_ϵ increase and K_σ decrease take place. The character of K_ϵ versus σ_{nom}/YS variation by the interaction of concentrators differs from the similar data, obtained for non-interacting concentrators. Beginning with a definite moment the tempo of strain concentration factor increase for a highly loaded point of hole surface becomes slower (Fig. 6). The analysis of local strain variation versus outer concentrator range in the points corresponding to the edge of an outer hole (Fig. 7), and also strain concentration factors $K_{\epsilon i}^M$ (calculated as related to local strains, obtained with regard to the outer concentrator effect) showed that the strain concentration in the vicinity of a hole after the general plastic deformation development in this region is decreased significantly. And it results in the retarding of strain concentration factors increase by static loading for interacting stress concentrators.

By steady cyclic loading (Fig. 6), strain concentration factors K_ϵ^{cycle} appear to be lower than the maximum values, observed by static deformation. In this case (as it was mentioned before) the values of K_ϵ^{cycle}, calculated with the diagram of cyclic deformation, are in a good agreement with the values of K_ϵ, corresponding to the σ_{nom}/S_T coordinates, is indicated by arrows, parallel to axis of abscissas. The material deformation analysis near the edges of interacting concentrators (Fig. 8) show that by cyclic loading both for an outer (dot A) and for an inner (dot B) concentrators a rigid symmetrical cycle of material elastic-plastic deformation is realized. In this case the range of cyclic elastic-plastic strains near the hole edge appear to be higher than for an outer concentrator, which is in an agreement with the values of K_ϵ^{cycle}. In the case when the concentrators interaction does not take place, in spite of high plastic strains in "0"-semicycle, the metal is elastically deformed near the inner

concentrator - by cyclic loading. The character of material elastic-plastic deformation near the side of an outer concentrator is practically not changed. The variation of stress and strain concentration factors in the elastic-plastic deformation region for the interacting concentrators is being compared with the calculation results with the use of the following equations:[1-5]

$$K_\sigma = 1 + (\alpha_\sigma - 1)\frac{E_2}{E_1}, \qquad (1)$$

where α_σ - theoretical stress concentration factor;
E_1 - secant modulus of nominal strain;
E_2 - secant modulus for the maximum strain in concentration zone.

$$\frac{K_\sigma \cdot K_\epsilon}{\alpha_\sigma^2} = \frac{1}{(\alpha_\sigma \cdot \sigma_{nom})^{n(1-m)[1-(\sigma_{nom}-1/\alpha_\sigma)]}} \qquad (2)$$

where σ_{nom} - nominal stress;
m - exponent by power approximation of strain diagrams;
n - constant, equal to $\approx$ 0.5.

The dependence of K_ϵ/α_σ on $\alpha_\sigma \cdot \sigma_{nom}/YS$ parameter (Fig. 9) for an inner concentrator is not satisfactorily described with these equations by α_σ variation in the investigated range. The strain concentration change for single outer concentrator agrees with the results, obtained with Eq. (2), which corresponds to the above described results for large-scale specimens. Thus, for the complex conditions of some stress concentrators interaction in the elastic-plastic region, the available correlations, describing the variation of strain concentration factor with stress increase, appear to be unapplicable, as they give a mistake in the dangerous direction. The limited volume of performed investigations does not permit to obtain the generalized correlations, reflecting the stress and strain concentration factors variation by the mutual effect of concentrators on each other. However, the given results demonstrate that by the analysis of interacting concentrators effect on each other the simplest approaches basing on an arithmetical summation or multiplication of stress and strain factors can not be applied.

The experimental investigation of fatigue failure initiation under the conditions of inhomogeneous stressed-strained state by interaction of stress concentrators, performed on the specimens being considered, confirmed the theoretical results, described earlier. The results for fractured specimens containing two stress concentrators are given in Table 1, where the calculation data of strain range in various points of a concentrator by steady cyclic loading are also presented. The character of failure initiation reflects the conditions of interaction and uninteraction of stress concentrators. The available fatigue life results to crack initiation depending on local strain amplitude are compared in Fig. 2 with the low cycle fatigue test results, obtained on specimens from 15X2MFA steel by homogeneous stressed state. The results, discussed above, illustrate the possibility to use strain criteria for the determination of life to fatigue crack initiation under the conditions of inhomogeneous stressed state by the presence of very high strain gradients. However, in this case the values of local strains can be defined only on the basis of special calculation or strain measurement because the

available analytical correlations do not permit to estimate reliably the strain concentration by such complex conditions.

Table 1. Test results of specimens with two interacting stress concentrators

Number of specimen	Distance between concentrators (mm)	Local strain range			Number of cycles to crack initiation	Kind of fracture
		Outer concentrator	Inner cross piece side	concentrator opposite edge		
1	-	1.47	-	-	1600	Crack from outer concentrator
2	2	2.21	4.22	2.0	100	Crack from inner concentrator
3	4	1.45	1.67	0.9	430	Crack from inner concentrator
4	9	1.50	0.63	0.58	1450	Crack from outer concentrator
5	14	1.35	0.52	0.52	2540	Crack from outer concentrator

The obtained results permit to estimate the effect of loaded components design forms and their absolute sizes on the material fatigue failure resistance. A good agreement between the results, obtained on specimens of various sizes and geometry, show the reliability of fatigue failure strain criteria, being obtained on small specimens to describe the performance of full-sized structure components. In this case the construction of lines for permissible stresses could be carried out on the basis of the obtained mean square correlations, and the introduced safety factors should consider the dispersion of real materials fatigue failure resistance with regard to the effect of production and operation factors and also the possible inaccuracy in the estimation of the maximum amplitude range of cycle deformation. This inaccuracy may be as a result of calculation errors and also as a result of the presence of initial production defects in real metal.

Along with large-sized specimens, the tests of pressure vessel models with nozzles were performed in the regime of low cycle loading. The model sizes are given in Fig. 10.[6] The metal volumes in concentration zones exceeded the cross section area of specimens, tested on low cycle fatigue. However, the moment of fatigue crack initiation in the concentration zone is well predicted based on test results of small specimens (Fig. 11). Consequently, the test results of large-scale specimens under the conditions of homogeneous and inhomogeneous stressed state, and also the test results of pressure vessel models showed that scale factor does not effect practically on low cycle fatigue resistance with the use of crack initiation criterium.[7]

Scale Factor Effect On Fatigue Crack Growth Rate

The published investigations[8-17] show that a specimen thickness, along with other factors, could effect fatigue crack growth. However, the authors express different views. Some investigators note the fatigue crack growth increase with a specimen thickness increase,[8-12] the others note its decrease,[13-15]

and some scientists consider the crack growth rate to be independent of specimen thickness.[16] As a whole, the data indicate that specimen size effect on the fatigue crack growth regularities may be revealed for all three zones of the fatigue failure diagram and has a complex character. In this investigation the study of scale factor effect on 15X2MFA steel cyclic crack resistance was conducted. The specimens of the thicknesses t=10, 15, 25, and 50 mm were tested with three-point bending at room temperature. By the selection of other specimen sizes the following requirements were fulfilled:[18] $2t < b < 4t$; $b > 15$ mm; $L = 4b$, where b - specimen width, L - distance between supports.

In this investigation the applied specimen width was always equal to two thicknesses. The correlations between dl/dN and K for 15X2MFA steel, obtained on specimens of various thickness are given in Figs. 12 and 13 and the characteristics of cyclic crack resistance are presented in Table 2.

Table 2. The parameters of 15X2MFA steel cyclic crack resistance at room temperature

R	t (mm)	ΔK_{th} (MPa$\sqrt{m}$)	$\Delta K_{(eff)th}$ (MPa$\sqrt{m}$)	m	C
0.05	10	10.5	3.8	3.2	2.3×10
	15	7.5	3.5	2.9	7.7×10
	25	6.8	3.3	2.7	1.2×10
	50	8.5	3.4	2.6	2.0×10
0.7	10	4.2	-	2.6	3.4×10
	25	3.4	-	2.0	1.5×10
	50	3.5	-	1.8	2.5×10

The presented data demonstrate that for both coefficients of loading cycle asymmetry R experimental data are considered in the narrow scatter band independent on a specimen thickness. And we may speak about a cyclic crack resistance sensitivity to a scale factor in a second region of the fatigue failure diagram. At the same time in the range, being near to the threshold rates by R = 0.05 a sufficient specimen thickness effect on ΔK_{th} (Fig. 14) is evident. This correlation has no monotonous character. The minimum ΔK_{th} value was obtained on 25 mm thickness specimens, the maximum - for 10 mm thickness. By R = 0.7 in the range of low crack growth rates in a specimen of 10 mm thickness, the maximum fracture development resistance was also found, the further specimen thickness increase does not influence the threshold stress intensity factor value. The obtained results agree well with the data,[10,17] where the scale factor effect on crack growth rate was investigated in 15X2MFA, 15X2NMFA steels and their welded joints (Figs. 15 and 16). Compact specimens of 25 and 100 mm thickness were tension tested at room temperature. For metal after standard heat treatment (YS ≈ 600 MPa) the maximum effect was evident for the threshold ΔK_{th} values with specimen thickness increase the threshold ΔK_{th} values with specimen thickness increase the threshold ΔK_{th} increase was obvious. The high strength 15X2MFA steel (YS ≈ 1000 MPa) did not show the remarkable difference in ΔK_{th} by testing of specimens of 25 and 15 mm thickness.

As at present the precularities of fatigue crack growth (by low K values) in structural materials, as a rule, are analysed with the use of crack closing concept,[17,19-21] by testing on cyclic crack resistance,

crack closing was estimated with the use of an electrotensometric displacement transducer of high sensitivity, located on the both sides from the crack tip in previously drilled holes of 0.2 mm depth. The distance between was 4 mm, the distance from the crack tip was not more than 2 mm.

The value of stress intensity factor, by which a crack is opening, K_{op}, the effective range $\Delta K_{(eff)}$ were determined in accordance with the procedure, described in Ref. 22. The obtained values $\Delta K_{(eff)}$ at R = 0.05 are given in Table 2. By R = 0.7 the K_{op} values were lower than the minimum stress intensity factor, independent of specimen thickness. Thus, the given results show the absence of scale factor effect when considering crack closing and it indicates that the scale factor effect is responsible for K variation with specimen thickness variation.

Scale Factor Effect On Fracture Toughness

At present there is no direct answer on the problem of scale factor effect on metal crack resistance. In most published investigations, concerning the scale factor effect on metal crack resistance, they were performed mainly on specimens with thickness up to 60 mm. Based on these results it is impossible to make a conclusion about the crack resistance of structure components of greater thickness. In this case "scale factor effect" means material properties variation by similar loading conditions versus investigated specimen sizes by the retaining of geometrical similarity.

In accordance with the models[23-26] (based on the main concepts of LMF) with the increase of a specimen thickness (i.e. by the transition from fracture in plane stressed state to fracture by plane deformation) the stress intensity factor values decrease, approaching to the material constant - K_{IC}. These models were experimentally confirmed for many aluminum and titanium alloys and steels. However, in some investigations[27-30] K_Q increase was observed with a specimen thickness increase. As applied to reactor materials such experiment is described in Ref. 31. In our country for the type 15X2MFA steel the Scientific and Methodical Commission on Fracture Mechanics of GOSTSTANDARD carried out the basic experiments on specimens of 16-150 mm thickness to verify the comparability of test results obtained in six laboratories. Three-point bending and tension tests were performed by the development of a standard for K_{IC} determination by plane deformation with the use of the following testing machines: ZDM-300/600PY, ZDM-200/400PY, ZDM-100PY, Instron-1255, IMC-30, and YME-10TM.

The application of 15X2MFA steel specimens of various types and sizes permitted to establish the correct boundaries of test results, obtained with different criteria. As a most stringent condition for correctness a sharp loading break down on the diagram "loading - displacement" was taken. Figure 17 indicates with arrows the temperature boundaries for the fulfillment of this condition using the basic experiment results. In this case no difference was found between test results on bend and compact specimens. Figure 17 also shows the curves of $K_Q = f(T)$ parameter, determined with 5% secant from 16 to 150 mm as compared with the temperature K relation. The disagreement of $K_Q = f(T)$ and $K_{IC} = f(T)$ curves is associated with the plane deformation loss at the crack tip in specimens with various thickness - t. In the right part of the figure the values of K_Q correspond to the relation $K_Q = K_{max} = C \cdot YS\sqrt{t}$, characterizing the plastic stability loss of specimens, having various sections. In Fig. 18 the basic experiment data, corresponding to the correctness condition, are plotted on the scatter band of experimental results for more than ten 15X2MFA steel melts after base and additional heat treatment. The results for the melt, which was used for the basic experiment performance are located in the coordinates "K_{IC} - $(T - T_K)$" in the upper part of the figure, describing the scatter between melts. The low envelope can be described by the equation $K_{IC} = 32\exp \cdot 0.024$ *

$(T - T_K) + 26$. In Ref. 33, the estimation of static materials crack resistance was carried for nuclear power plants. The following structural materials were considered: - the type 08X18N10T steel of a high ductility (YS = 272 MPa, UTS = 556 MPa, A= 54%, Z = 68% at 20°C), - the type 15X2MFA steel after standard heat treatment (YS = 548 MPa, UTS = 700 MPa, A = 27%, Z = 75% at 20°C) and the same steel after the embrittling heat treatment, simulating the neutron fluence attack for VVER-440 reactors to the end of service life (YS = 981 MPa, UTS = 1069 MPa, A = 15.5%, Z = 65.4% at 20°C). The tension tests of these steels were performed on specimens with 25 to 150 mm thickness. The testing procedure is presented in detail in Ref. 34. In Fig. 18 the diagrams in reduced coordinates "load P - crack opening" are given, they are obtained by static loading of specimens manufactured from the above mentioned materials. The possibility to fulfill the plane deformation conditions was verified with the criterium:[35]

$$K_I \leq \sqrt{B \cdot YS^2/2.5} \quad , \tag{3}$$

where B - specimen thickness, YS - the material yield strength; and with the criterium:[28]

$$\frac{\Delta B}{B} \cdot 100\% \leq 1.5\% \quad , \tag{4}$$

where ΔB - specimen thickness variation in front of the crack tip.

The static test results analysis shows that the scale effect for the high strength 15X2MFA (KP100) steel, for which the plane deformation conditions are fulfilled with both criteria, is not revealed. For the middle strength 15X2MFA steel and the low strength 08X18N10T steel, for which the plane deformation conditions are not fulfilled with two criteria at the same time, specimens thickness increase results in K_Q increase.

P - V diagrams for 15X2MFA steel (KP100) were linear for both specimen thicknesses, for 08X18H10T steel - are sufficiently non-linear for both thicknesses. For 15X2MFA (KP60) steel the diagram P-V was non-linear by fracture of 25 mm thickness specimens. It should be noted that in spite of the fact, that the values of K, obtained from 150 mm thickness specimens from 15X2MFA (KP60) steel, are higher than the stress intensity factor values, by which the plane deformation conditions are satisfied with the criterium (3), the diagram was linear up to fracture. The verification of plane deformation conditions with the criterium (4) confirmed that by the fracture of 15X2MFA (KP60) steel specimens of 150 mm thickness, the plane deformation condition was fulfilled.

The values for 08X18H10T steel, defined with the approach of 5% secant on 150 mm thickness specimens satisfy the criterium (3). However, the sufficient non-linearity of P-V diagram, the tough character of fracture and unsatisfactory of the criterium (4) indicate that for 08X18H10T the plane deformation conditions were not fulfilled by 25 mm and 150 mm specimens, and the criterium (3) for 08X18H10T steel is not applicable.

Despite the fact that 15X2MFA steel (KP 100) at temperatures lower than room temperature is brittle (T = + 100°C) and the scale effect is not realized in this temperature range, by higher

temperatures, close to service temperatures, this effect may be visible. This is confirmed by the test results of compact specimens (thickness - 50 and 150 mm), made from the above mentioned steel (Fig. 20). To obtain more reliable fracture toughness results for embrittled 15X2MFA steel, it is necessary to perform the investigation of thicker specimens. The results of such experiments on compact 150 mm thickness specimens containing a through thickness crack and 150 mm thickness bend specimens with a semi-elliptical crack are given in Fig. 21. These are the results to consider by pressure vessel brittle strength estimation.

The brittle strength test results of a pressure vessel are also of an interest. The tested pressure vessel sizes are given in Fig. 22 and Fig. 23, which compare the test results of these pressure vessel failures with specimen test results. There is a good agreement between these results for an embrittled model from 15X2MFA steel and a model with a circumferential weld. However, for the model from 15X2MFA (KP60) steel a significant safety margin is evident by the pressure vessel test as compared with the analogous specimens tests.

References

1. N. A. Makhutov, "Strain Criteria of Low Cycle and Brittle Fracture," Moscow, IMash, p. 71 (1974).

2. G. Neiber, "Stress Concentration," Moscow, Gostechizdat, p. 204 (1947).

3. R. Peterson, "Stress Concentration Factors", Moscow, Mir, p. 302 (1977).

4. "Strength Calculation Standard for Equipment and Pipelines of Energetic Units," Moscow, Energoatomizdat, p. 525 (1989).

5. G. P. Karzov, V. P. Leonov, and B. T. Timofeev, "Welded Pressure Vessels: Strength and Endurance." Leningrad, Mashinostroenije, p. 287 (1982).

6. M. S. Druskin, G. P. Karzov, M. P. Rozanov, and B. T. Timofeev, "Experimental Investigation of Welded Vessels Strength by Cyclic Loading with Inner Pressure," Welding, No. 13, p. 114-126 (1970).

7. C. Ruiz, "Design of Pressure Vessel Against Fatigue," Engineer, Vol. 28, No. 5818, p. 362-371 (1967).

8. S. P. Malashenkov, A. G. Vovnjanko, and G. Yu. Bengus, "Effect of Specimen Width and Thickness on Fracture Toughness and Fatigue Fracture Diagrams of Al Alloy Semifinished Products," Kiev, Naukova Dumka, p. 269-273 (1980).

9. V. I. Trufjakov, P. P. Mikheev, and A. Z. Kuzmenko, "Scale Factor and Residual Stresses Effect on Fatigue Crack Growth," Problemy prochnosti, Nr. 6, p. 20-22 (1980).

10. V. T. Troshchenko, V. V. Pokrovskij, V. G. Kaplunenko, and B. T. Timofeev, "Specimens Size Effect on Pressure Vessel Heat Resistant Steel Crack Resistance," Problemy Prochnosti, Nr. 10, p. 3-11 (1982).

11. F. A. Heiser and W. Mortimer, "Effect of Thickness and Orientation on Fatigue Crack Growth Rate in 4340 Steel," Met. Trans., No. 8, p. 2119-2123 (1972).

12. P. N. Thielen and E. F. Morris, "Fatigue Crack Propagation in 4140 Steel," Met. Trans. A, No. 11, p. 2133-2141 (1975).

13. M. N. Georgiev, V. Yu. Dogadushkin, and N. Ya. Mezhova, "Fatigue Crack Rate Dependence on Specimen Size and Orientation in the Type 3sp Steel," FKHMM. Nr. 3, p. 18-24 (1981).

14. W. G. Clark and H. E. Trout, "Influence of Temperature and Section Size on Fatigue Crack Growth Behaviour in Ni-Mo-V Alloy Steel," Eng. Fract. Mech., No. 2, p. 107-123 (1970).

15. A. R. Jack and A. T. Price, "Effects of Thickness on Fatigue Crack Initiation and Growth in Notched Mild Steel Specimens," Acta Met., No. 7, p. 857-866 (1972).

16. A. M. Sillivan and T. W. Crooker, "The Effect of Specimen Thickness Upon Fatigue Crack Growth Rate of A516-60 Pressure Vessel Steel," Trans. ASME Journal, No. 2, p. 248-252 (1977).

17. V. T. Troshchenko, V. V. Pokrovskij, and V. G. Kaplunenko, "Specimen Size Effect on Cyclic Crack Resistance of Heat Resistant Seels," Problemy Prochnosti, Nr. 4, p. 3-9 (1986).

18. RG 50-345-82, "Methodic Instructions, Strength Calculation and Tests, Methods of Metal Mechanical Tests, Definition of Crack Resistance Characteristics (Fracture Toughness by Cyclic Loading)," Izdatelstvo standartov, p. 93 (1983).

19. J. J. McGowan and H. W. Liu, "The Role of Three-Dimensional Effects in Constant Amplitude Fatigue Crack Growth Testing," Trans. ASME H, No. 4, p. 341-346 (1980).

20. P. K. Liaw, T. R. Leax, R. S. Williams, and M. G. Peck, "Near-Threshold Fatigue Crack Growth Behaviour in Copper," Met. Trans., No. 9, p. 1607-1618 (1983).

21. O. N. Romaniv, A. N. Tkach, and Yu. N. Lenetz, "Fatigue Crack Closing Effect on Near-Threshold Structural Steel Crack Resistance," Problemy Prochnosti, Nr. 5, p. 3-9 (1987).

22. O. N. Romaniv, G. N. Nikiforchin, and B. N. Andrusiv, "Crack Closing Effect and Estimation of Structural Alloys Cyclic Crack Reistance," Phisiko-Khimicheskaja Mechanika Materialov, Nr. 3, p. 47-61 (1983).

23. D. Broek, "Fracture Mechanics Concepts," Moscow, Vysshaja Shkola. p. 368 (1980).

24. D. E. Srouli, "Fracture Toughness by Plane Deformation," In Book: Failure, Moscow, Vol. 4, p. 47-67 (1977).

25. G. P. Cherepanov, A. B. Kaplun, and Yu. I. Puchkov, "Scale Factor Effect on Brittle Fracture, Problemy Prochnosti, No. 7, p. 36-41 (1970).

26. J. I. Bluhm, "A Model for the Effect of Thickness on Fracture Toughness," in Proc. ASTM, Philadelphija, Vol. 61, p. 1324-1331 (1961).

27. N. N. Bokman, Yu. M. Dahl, and L. S. Moroz, "Fracture Toughness Estimation of Low and Middle Strength Steels," In Book: Some Problems of Metals Strength, Leningrad, p. 62-75 (1975).

28. B. A. Drozdovsky and E. M. Morozov, "Methods of Fracture Toughness Estimation," Zavodskaja Laboratorija, 42, No. 8, p. 995-1004 (1976).

29. A. Ya. Krasovsky, "Metals Brittleness at Low Temperatures," Kiev, Naukova Dumka, p. 340 (1980).

30. G. S. Pisarenko, V. P. Naumenko, and G. S. Volkov, "Strain Constraint Effect on Fracture Toughness of Ductile Steels," Problemy Prochnosti, No. 11, p. 45-51 (1977).

31. V. A. Volkov, A. M. Orestov, and G. P. Karzov, et al. "Experimental Verification of Methodic Instructions Applicability for the Definition of Low Strength Steels Crack Resistance, Unification of Metal Test Methods on Crack Resistance," Moscow, Izdatelstvo Standartov, vyp. 2, p. 10-31 (1982).

32. GOST 25.506-85, "Calculation and Strength Tests, Metals Mechanical Test Methods, Definition of Crack Resistance Characteristics (Fracture Toughness) by Static Loading," Moscow, p. 61 (1985).

33. V. V. Pokrovsky, V. G. Kaplunenko, B. T. Timofeev, and V. A. Ignatov, "Effect of Scale and Cycle Loading Regimes on Crack Resistance Characteristics of High-Temperature Steels," Proc. of the 7-th Colloquium on Mechanical Fatigue of Metals, Miskolc, Vol. 2, p. 103-119, September 6-10, 1983.

34. V. P. Troshchenko, V. V. Pokrovsky, and V. T. Kaplunenko, et al., "Specimen Size Effect on Pressure Vessel Heat Resistant Steels Crack Resistance," Problemy Prochnosti, No. 10, p. 3-11 (1982).

35. "Standard Test Method for Plane-Strain Fracture Toughness of Materials," In: 1976 Annual Book of ASTM Standards, E399-74, p. 471-490.

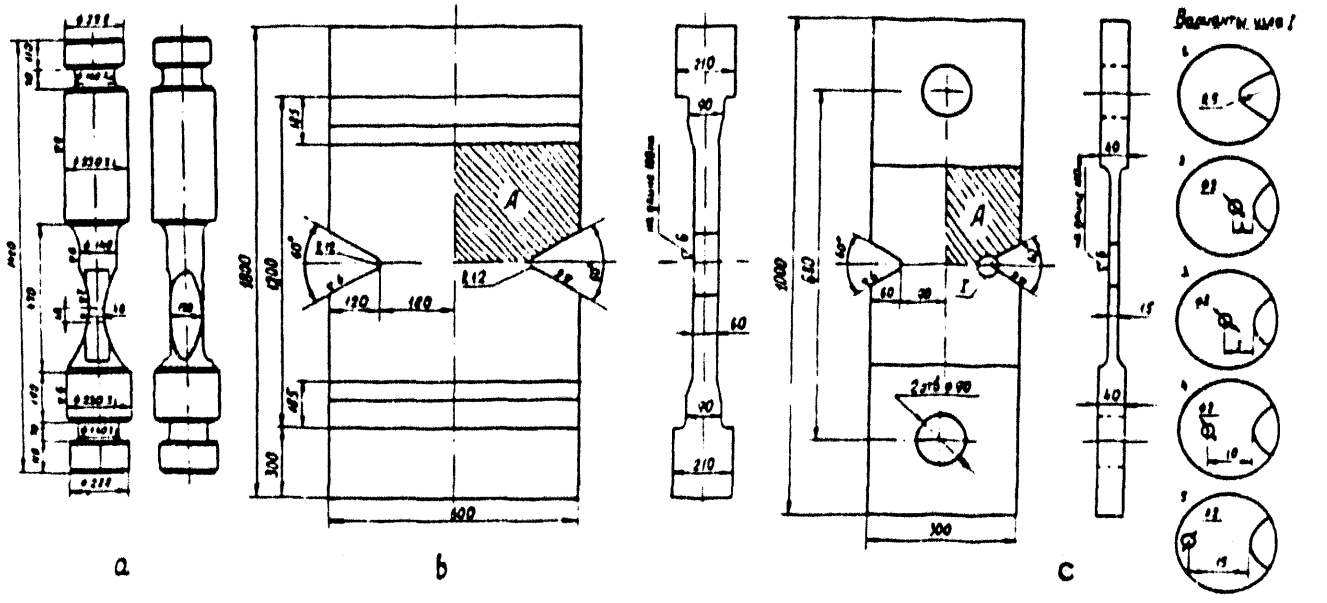

Fig. 1. Types of large-scale specimens from 15X2MFA steel.

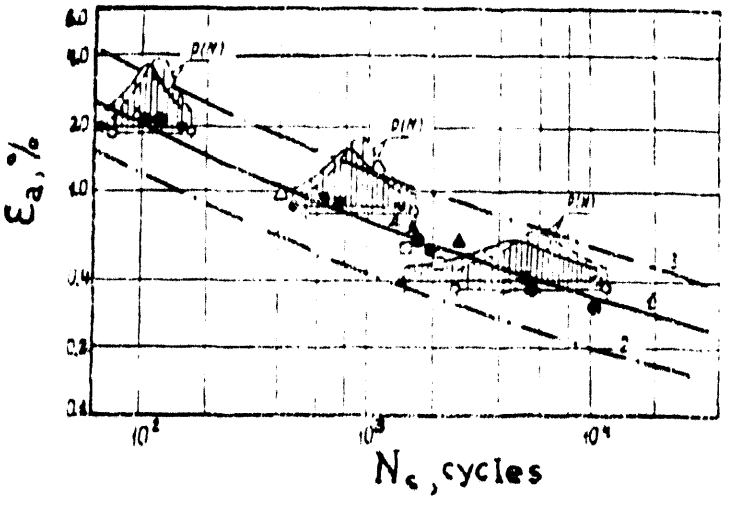

Fig. 2. Low-cycle fatigue resistance of 15X2MFA steel specimens by homogeneous and inhomogeneous stressed state:

1, 2, 3 - mean square life to failure values and boundaries of 95% scatter band, obtained on the base of 10 melts tests;

●, ●—●, ϕ—ϕ - smooth specimens with net sections 4800, 300 and 48 mm^2, respectively;

□ - specimens with concentrators 60 × 600 mm;

Δ, ▲ - specimens with interacting concentrators

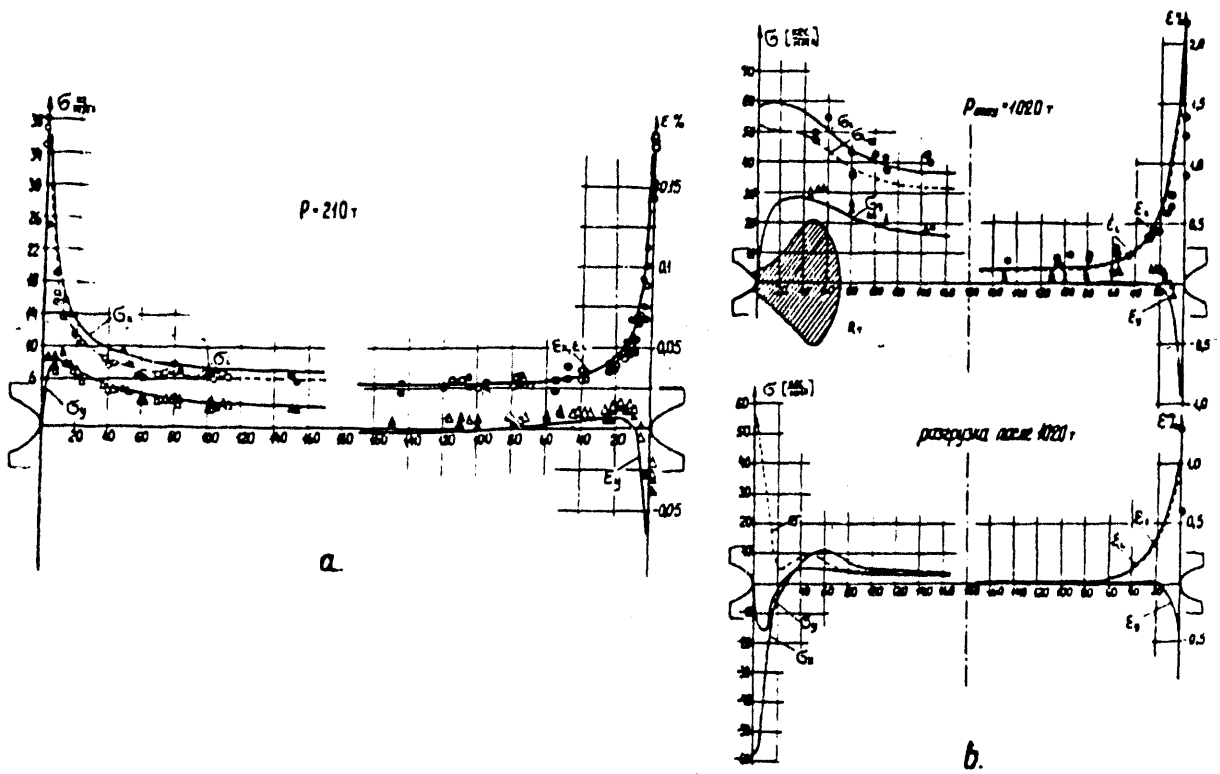

Fig. 3. Theoretical and experimental strain and stress distribution in concentration zone in the minimum specimen section:

A - elastic deformation,

B - elastic-plastic deformation.

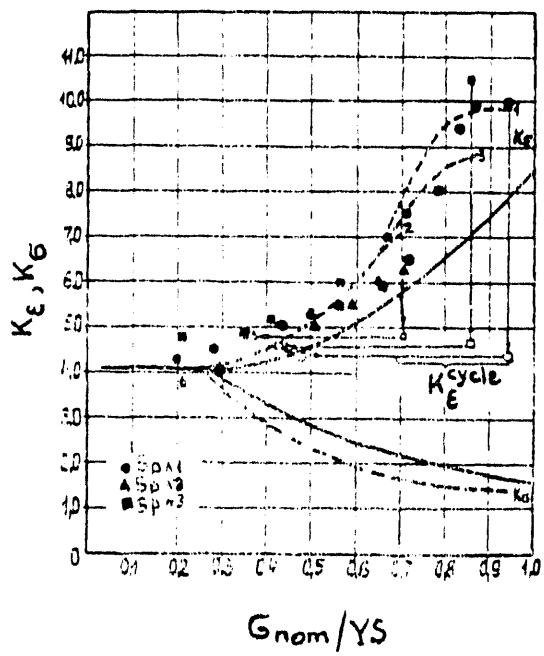

Fig. 4. The dependence of strain K_ϵ and K_σ concentration factors on the level of nominal stresses: dots - experimental results, — and --- -calculation results by monotonous and stepped loading.

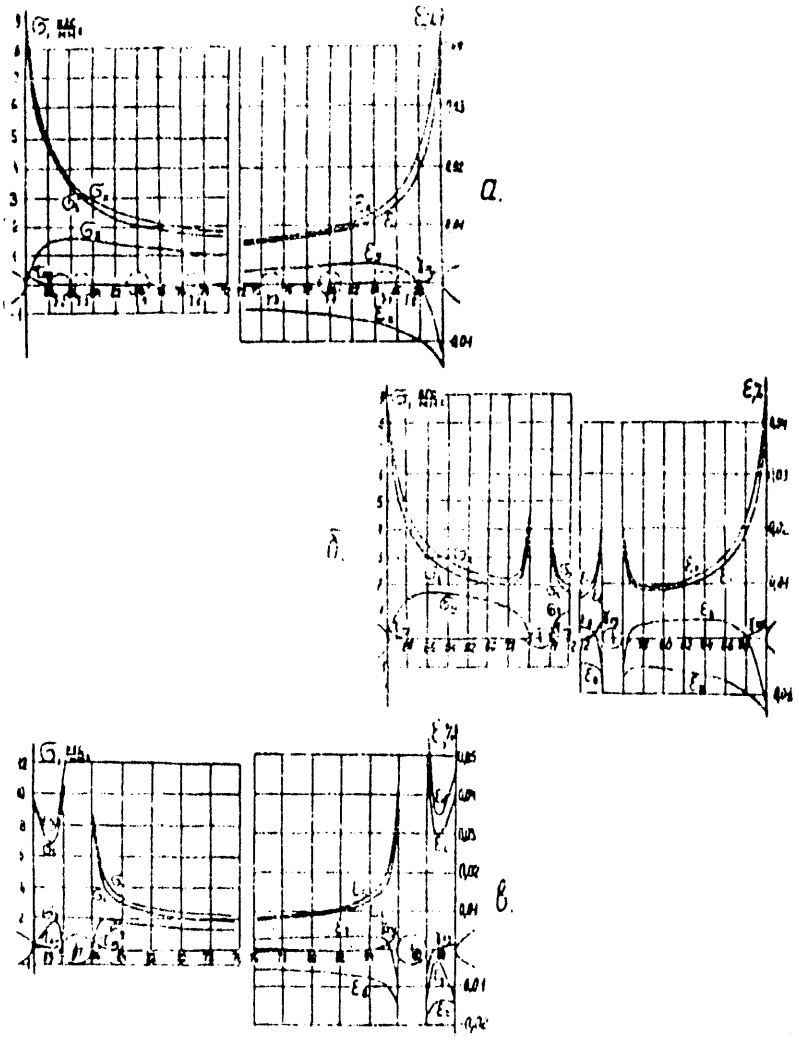

Fig. 5. Elastic stress and strain distribution in specimens with interacting concentrators: a,b,c - for units 1-1, 1-5, 1-2, respectively.

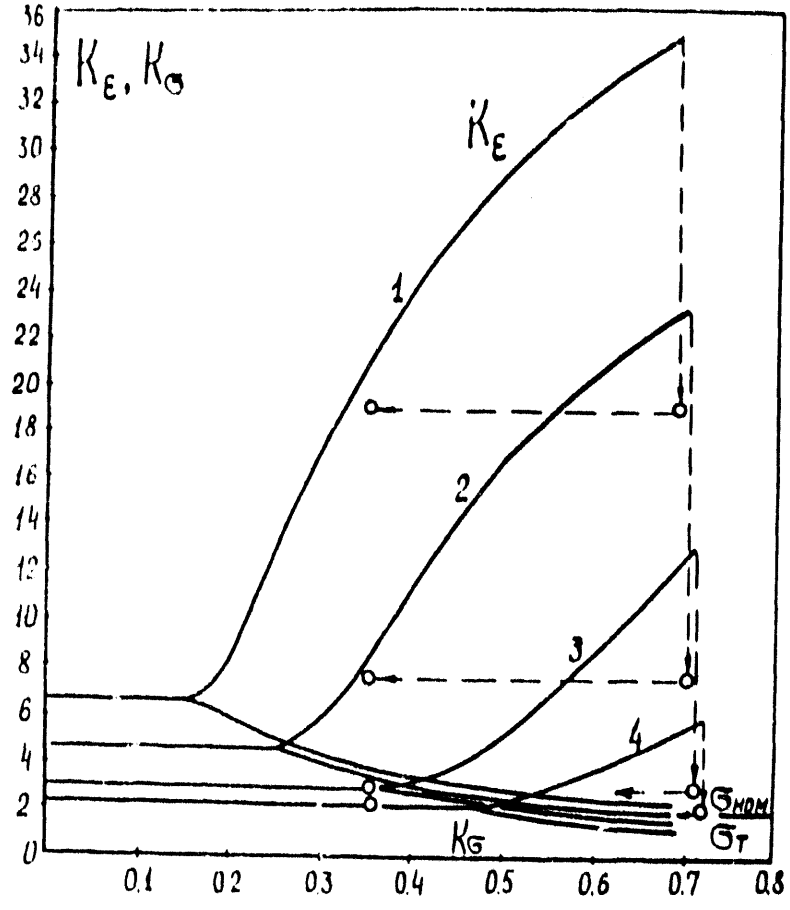

Fig. 6. The dependence of strain K and K stress K concentration factors on the level of nominal stresses.

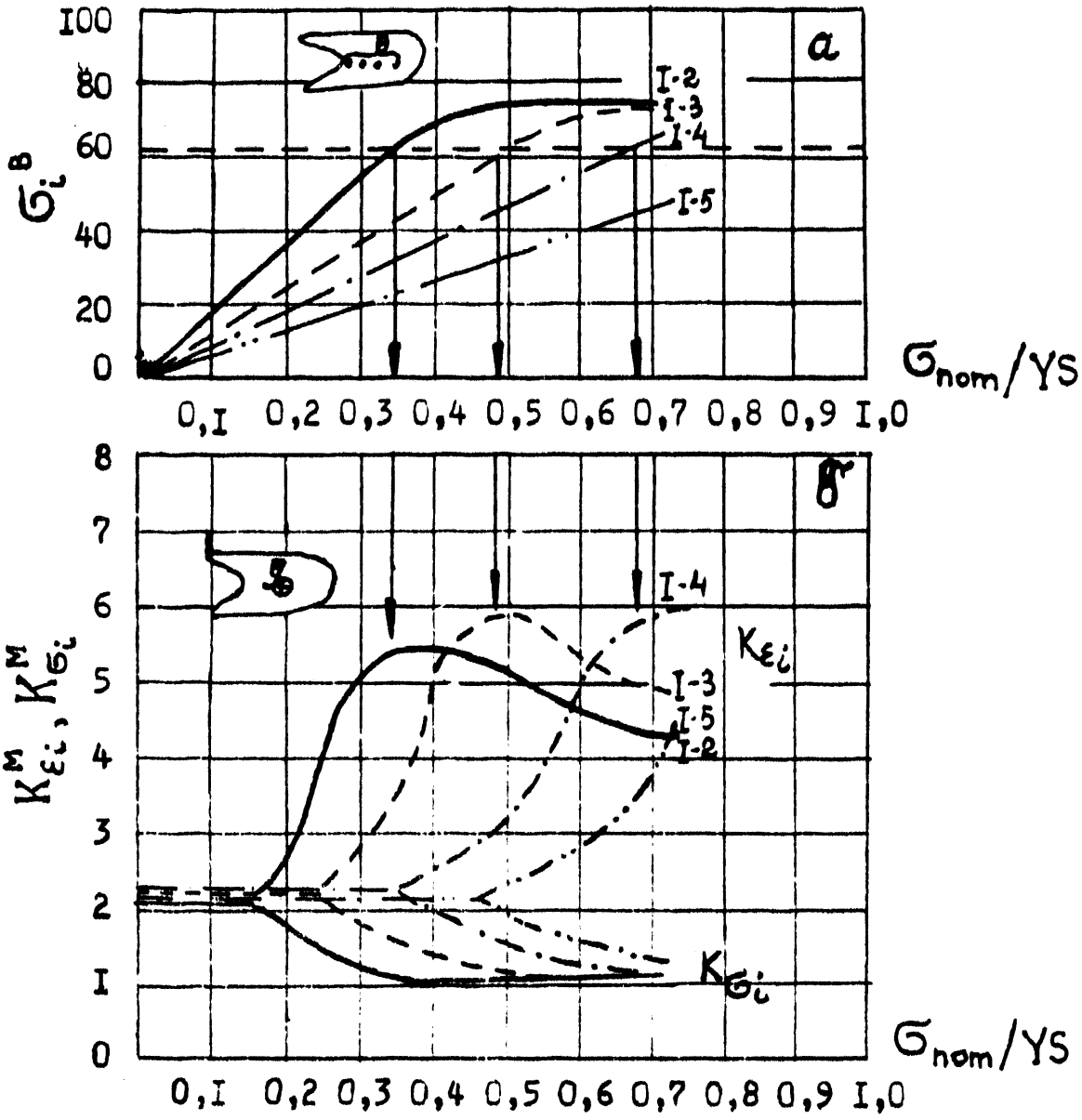

Fig. 7. Stress variation versus outer concentrator (a) and strain concentration factors (b) versus nominal stress values.

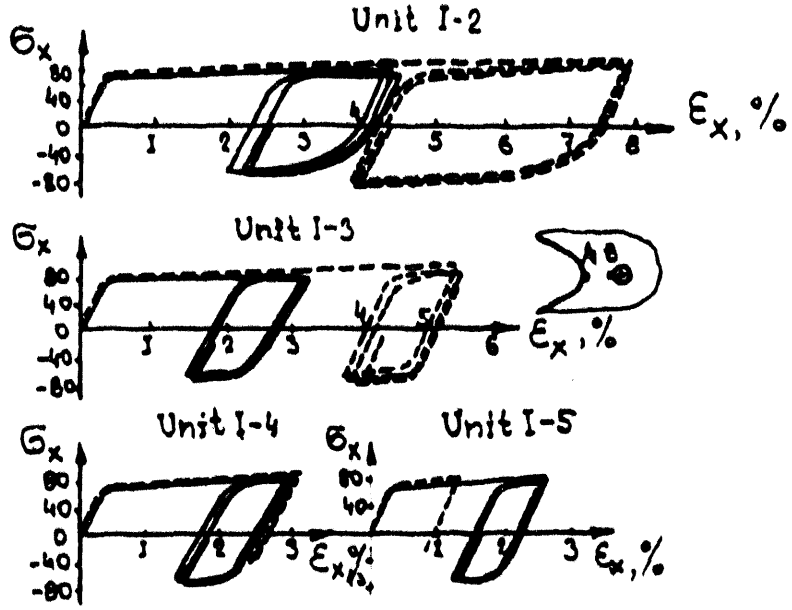

Fig. 8. The character of material deformation near the inner concentrator edge for the investigated structure components:

— - deformation in dot A,

--- - deformation in dot B.

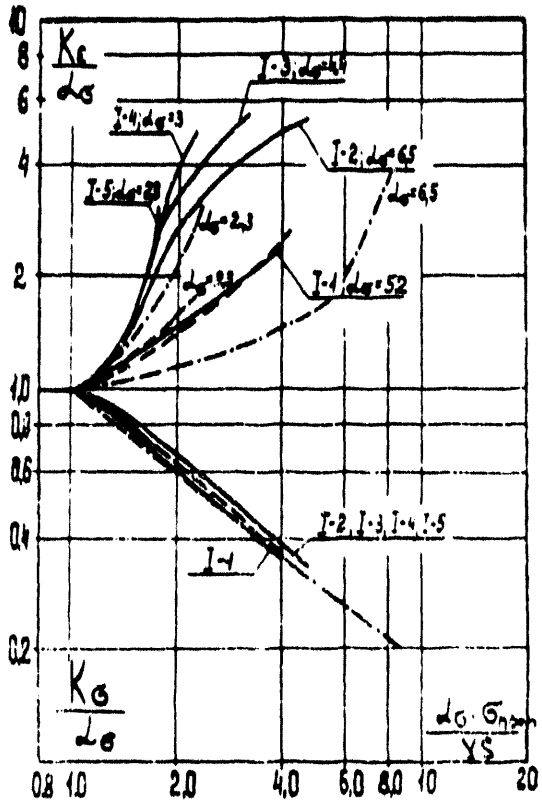

Fig. 9. The generalized $\frac{K_{\varepsilon i}}{\alpha_{\sigma i}}$ and $\frac{K_{\sigma i}}{\alpha_{\sigma i}}$ correlation versus $\frac{\alpha_\sigma \cdot \varepsilon_{anom}}{\varepsilon_T}$ parameter:

Dots - calculation results ●, ■, ▲ and ○, Δ, □ for defects ρ = 5 mm, ρ = 1.8 mm, ρ = 0.2 mm by $\frac{\varepsilon_{anom}}{\varepsilon_T} < 1$ and $\frac{\varepsilon_{anom}}{\varepsilon_T} \geq 1$ respectively.

—, -·-, --- according to theoretical correlation.

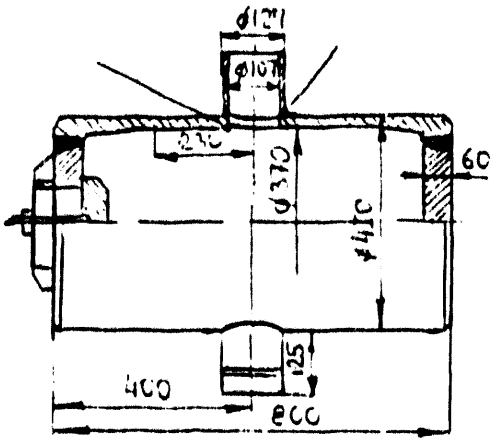

Fig. 10. Sketch of 12X1MF steel model for hydrocyclic pressure tests.

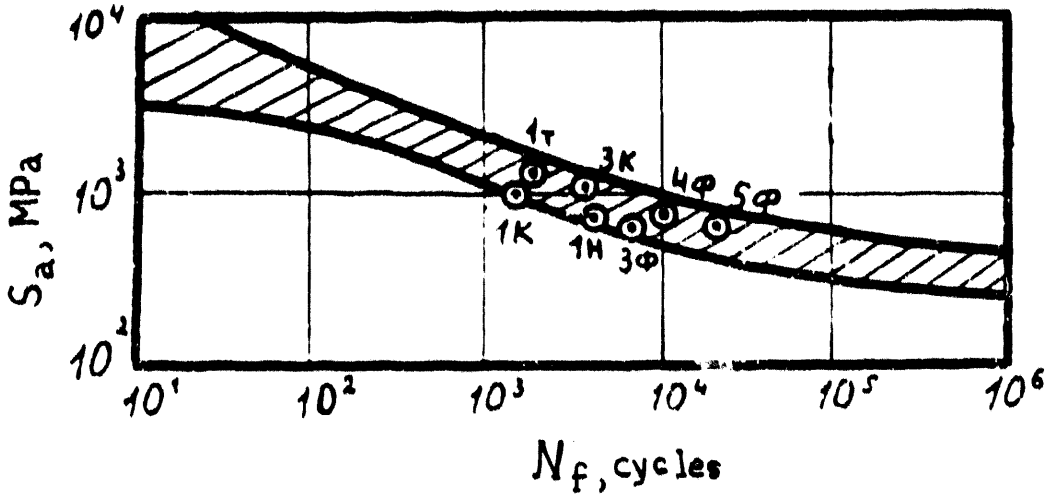

Fig. 11. The comparison of test results of vessels and pipings, obtained in our country with test results of full-scaled structures, obtained abroad in the coordinates "stress range - number of cycles to failure":

//// - scatter band of experimental data according to Ruiz [7],

3, 4, 5 - vessels from 12X1MF steel,

1K, 3K - vessels from 22K steel,

1T - vessel from 15X2MFA steel,

1H - vessel from 15X3NMFA steel.

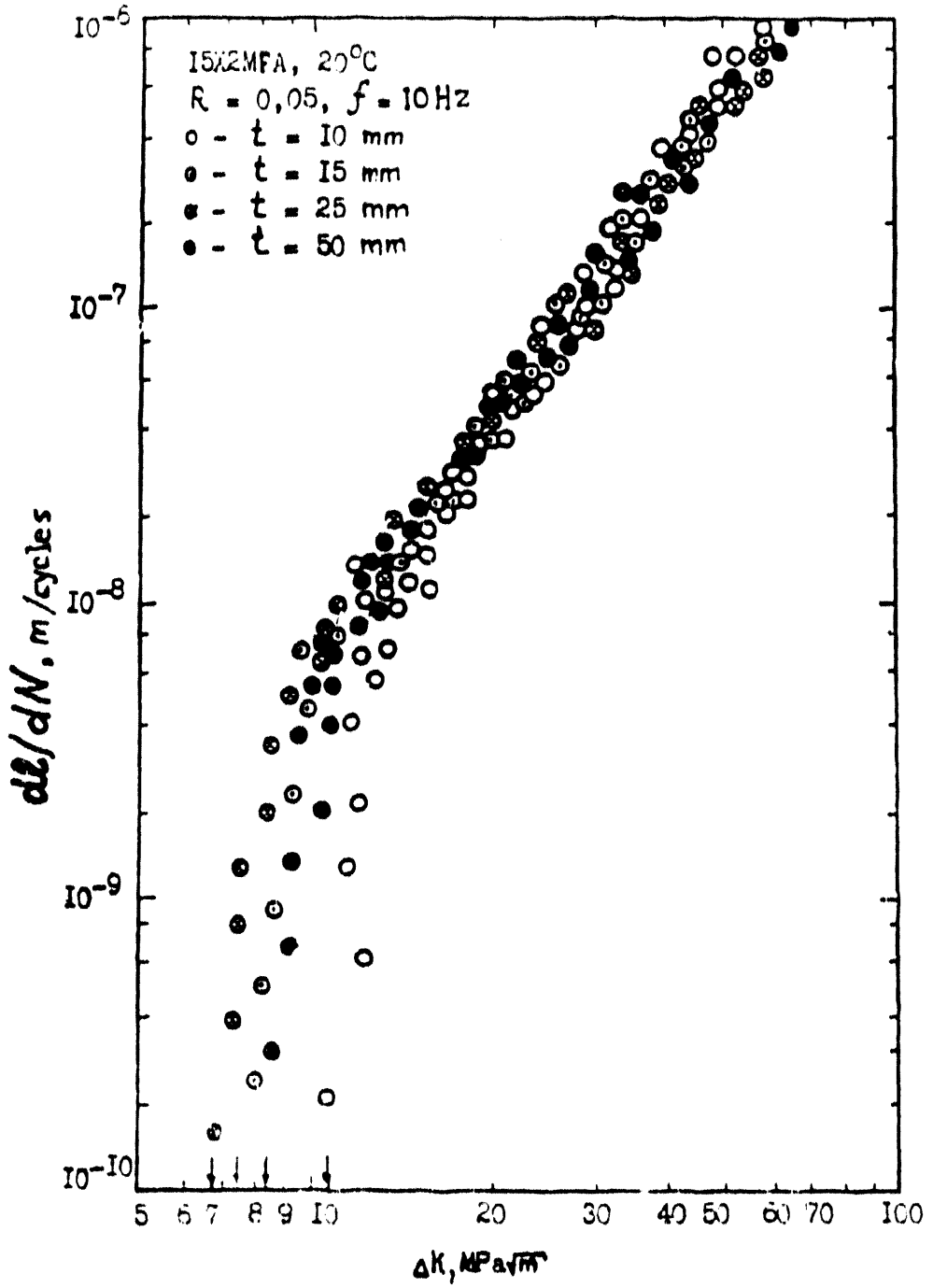

Fig. 12. Specimen thickness effect on fatigue crack growth in 15X2MFA steel in air (R = 0.05).

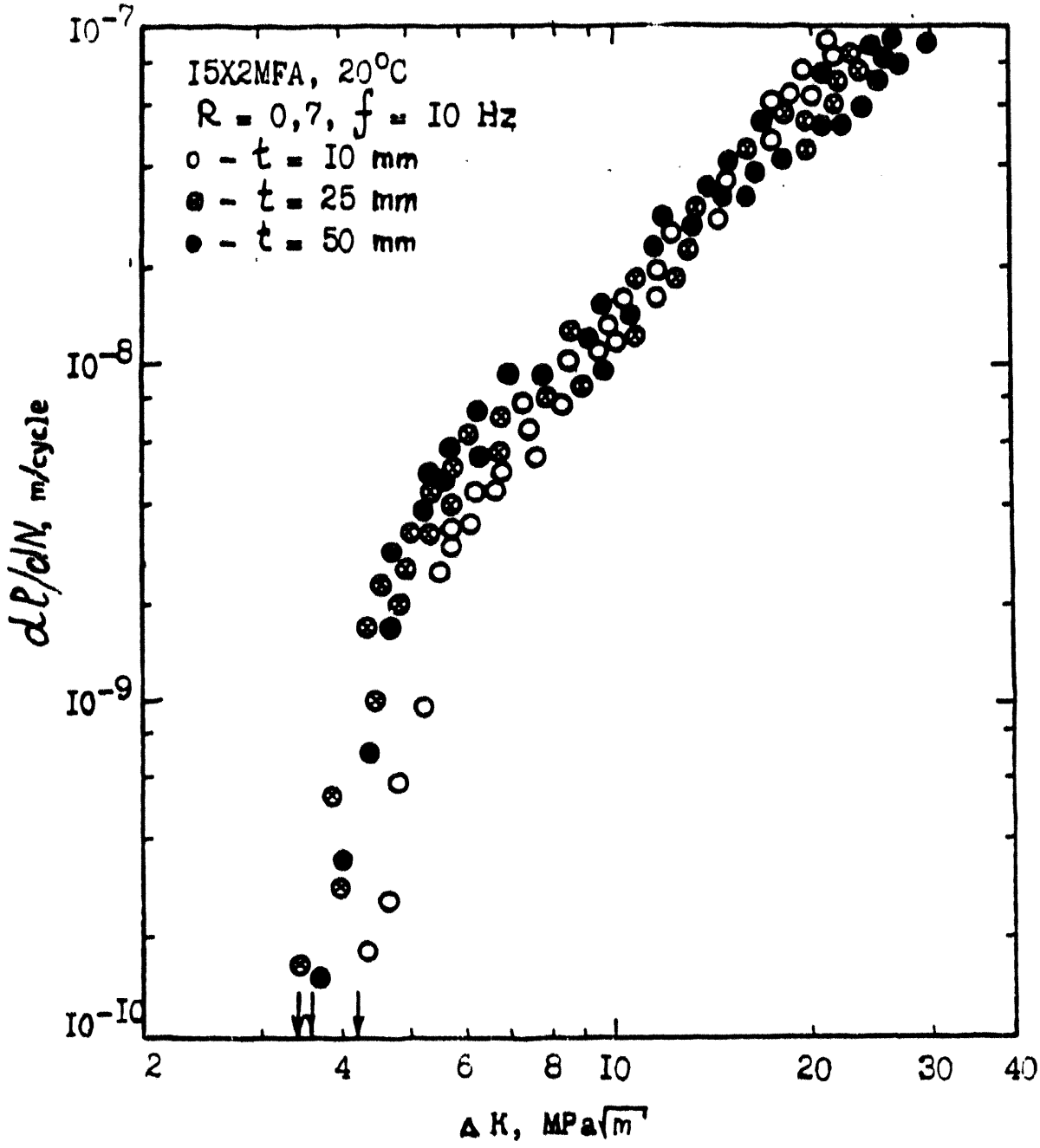

Fig. 13. Specimen thickness effect on fatigue crack growth in 15X2MFA steel in air (R = 0.7).

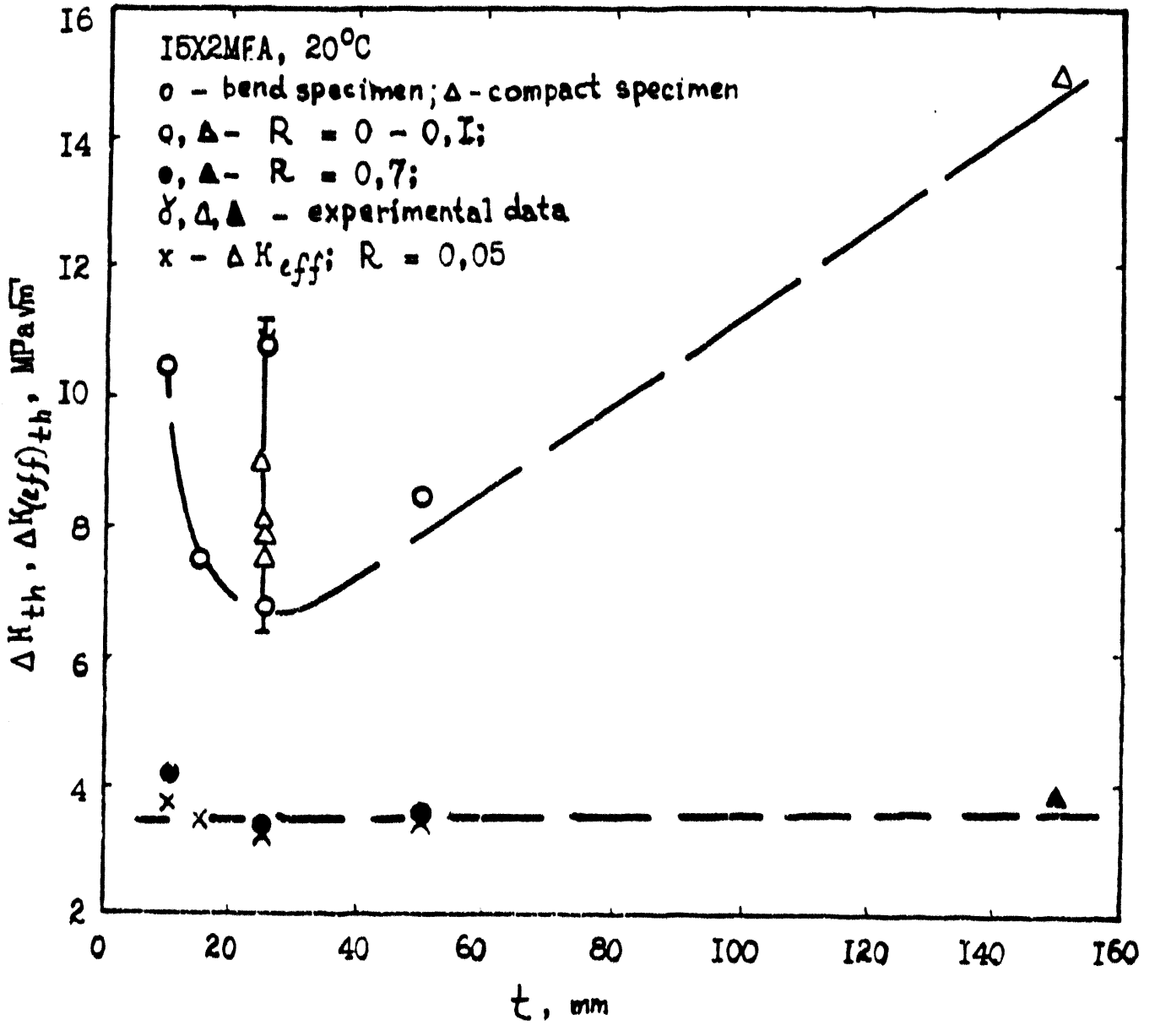

Fig. 14. Specimen thickness effect on threshold stress intensity factor ΔK_{th}.

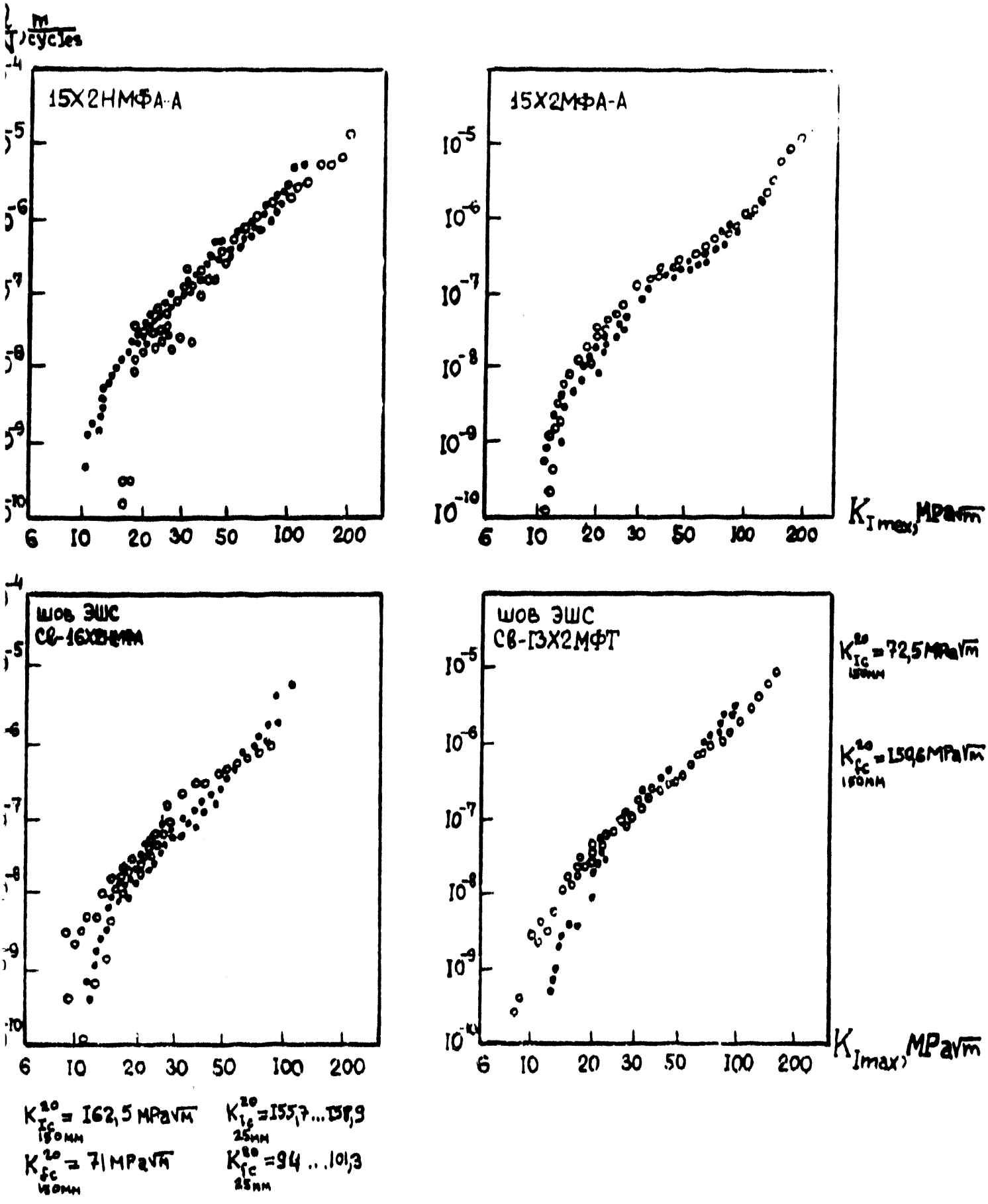

Fig. 15. Scale factor effect on fatigue crack growth rate for reactor steels and their welded joints:

R = 0.1, T = 20°C, ● - t = 25 mm, ○ - t = 150 mm.

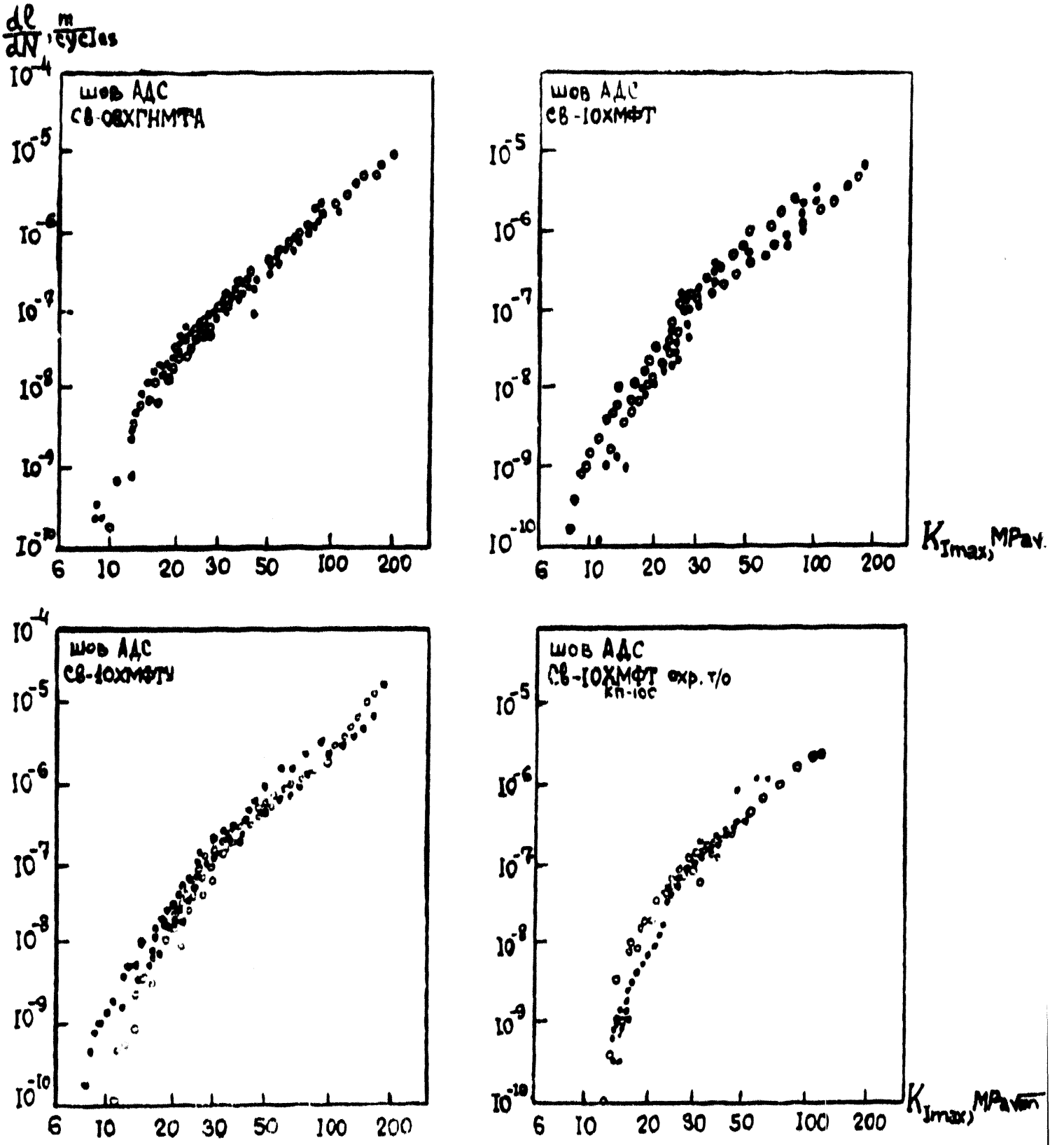

Fig. 16. Scale factor effect on fatigue crack growth rate for welds manufactured by submerged arc welding:

R = 0.1, T = 20°C, ● - t = 25 mm, ○ - t = 150 mm.

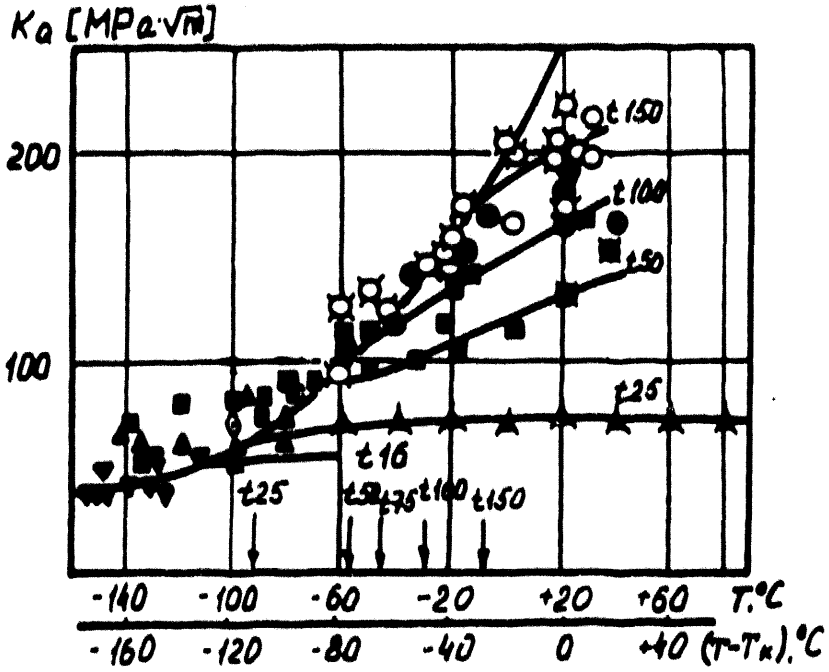

Fig. 17. Fracture toughness temperature dependence for 16-150 mm thickness specimens on the base of the basic experiment results [31].

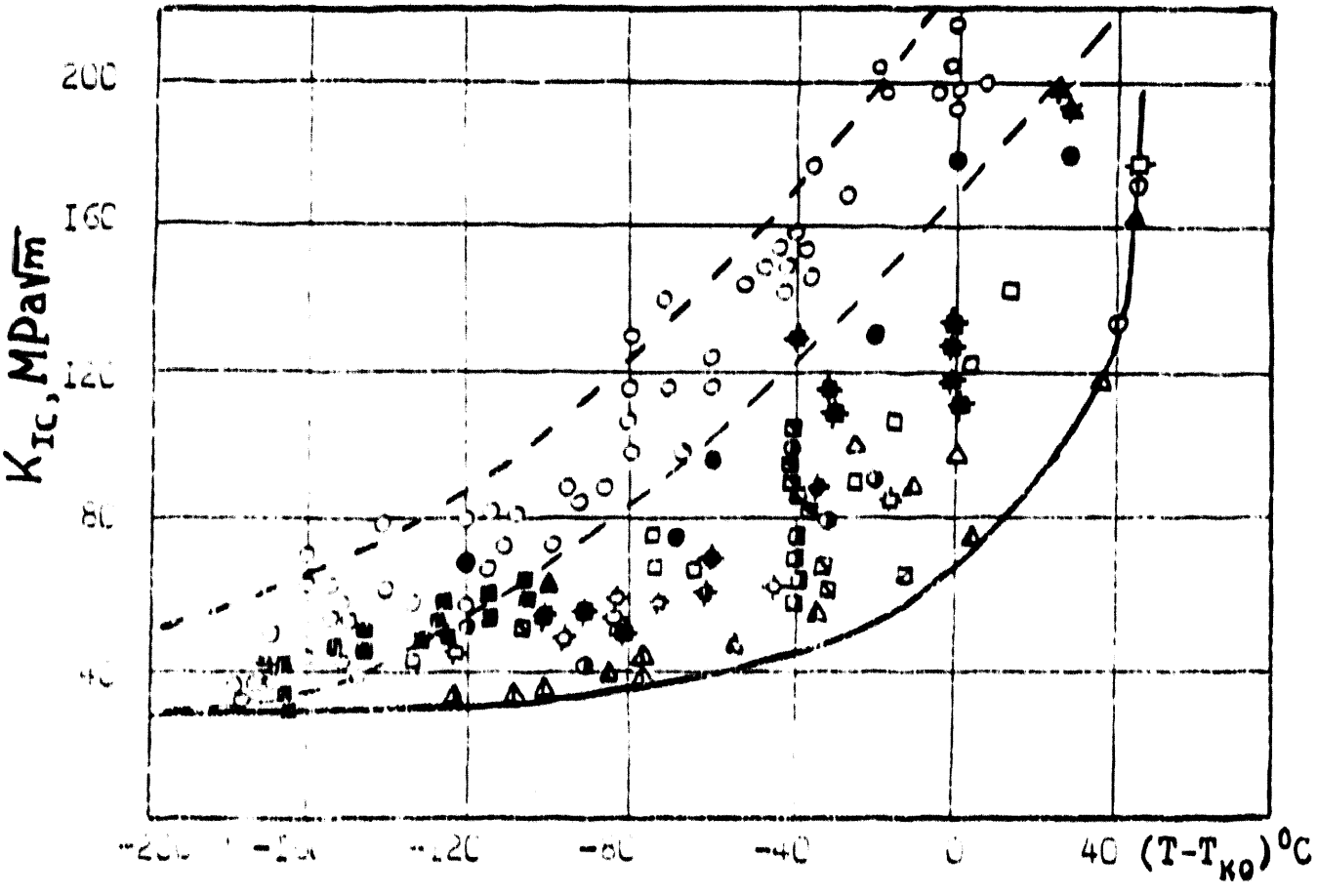

Fig. 18. Comparison of the basic experiment results with the generalized fracture toughness result for 15X2MFA steel.

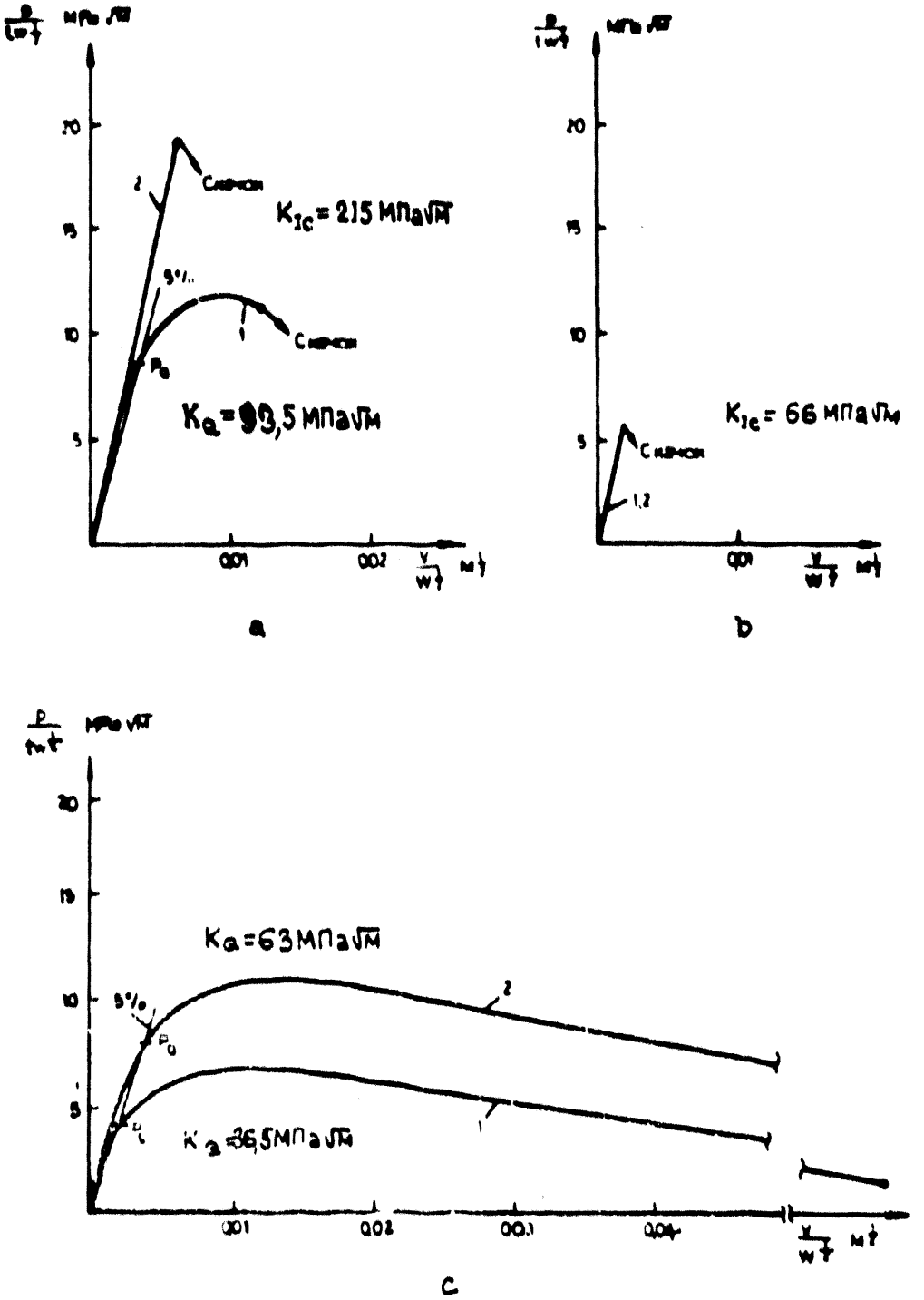

Fig. 19. Diagram "load P - crack opening along V action line" at test temperature 20°C: a - 15X2MFA (KP 60) steel, b - 15X2MFA (KP 100) steel, c - 08X18N10T steel.

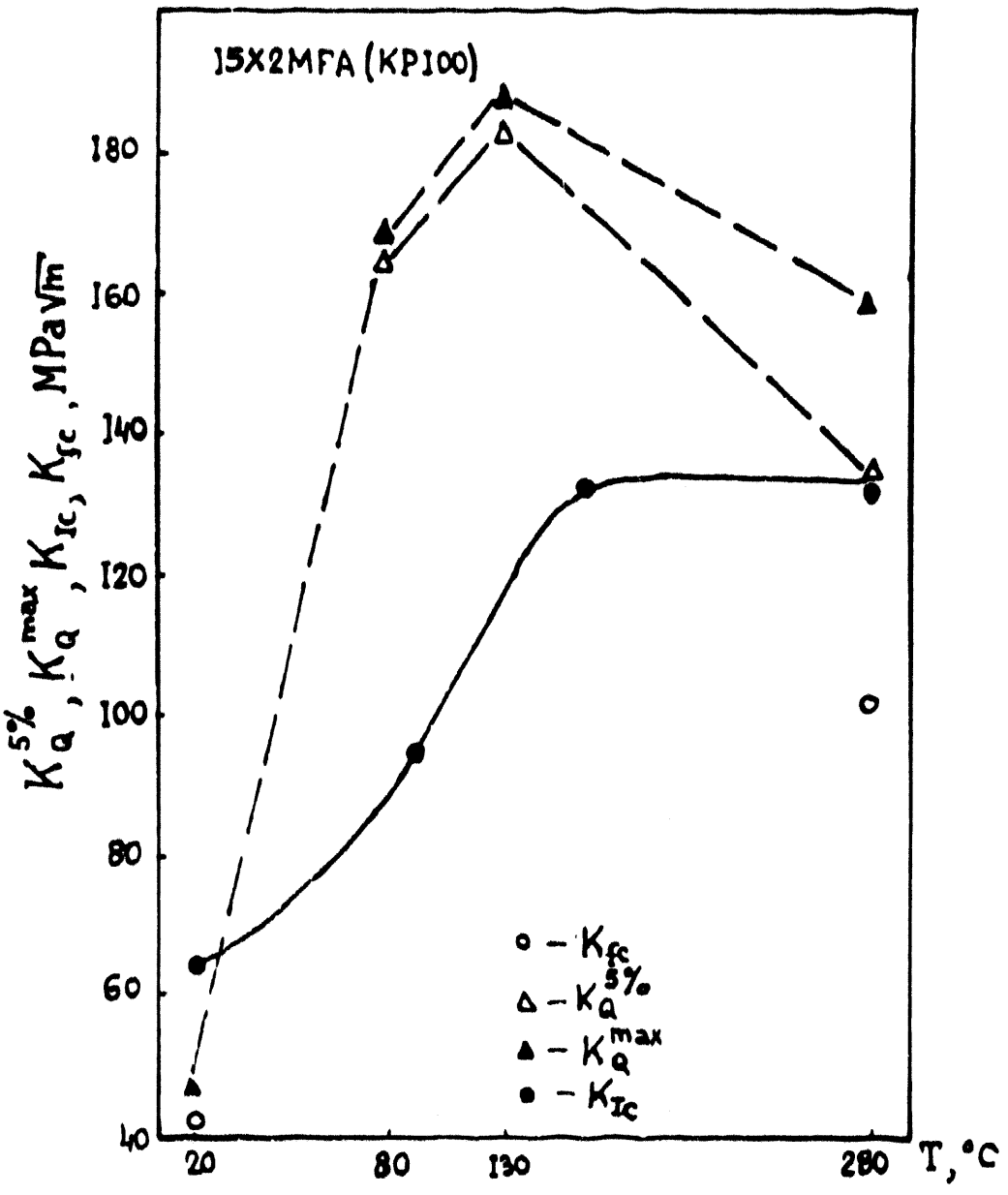

Fig. 20. Temperature critical stress intensity factor dependence for 50 mm (Δ, ▲) and 150 mm (●, ○) thickness specimens from 15X2MFA steel.

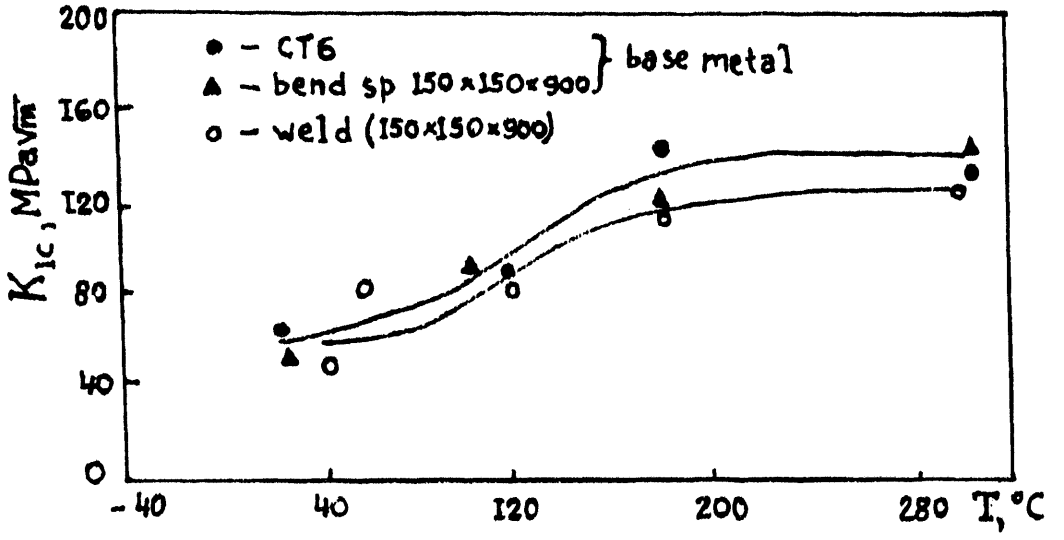

Fig. 21. Fracture toughness temperature dependence of welded joints from 15X2MFA steel after embrittling heat treatment of 150 mm thickness specimens.

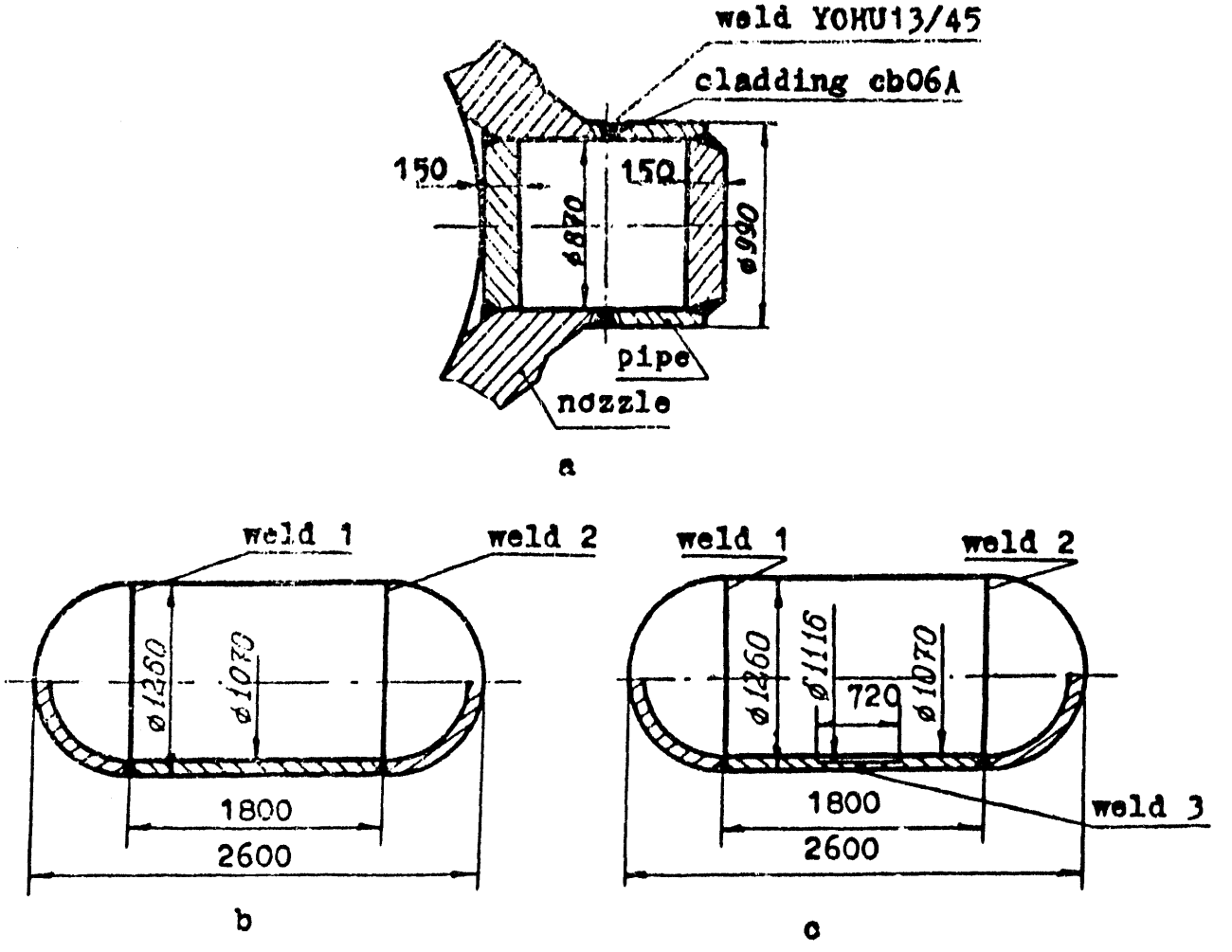

Fig. 22. Model types tested to failure:
a = nozzle zone
b = shell
c = shell complete with a circumferential weld seam

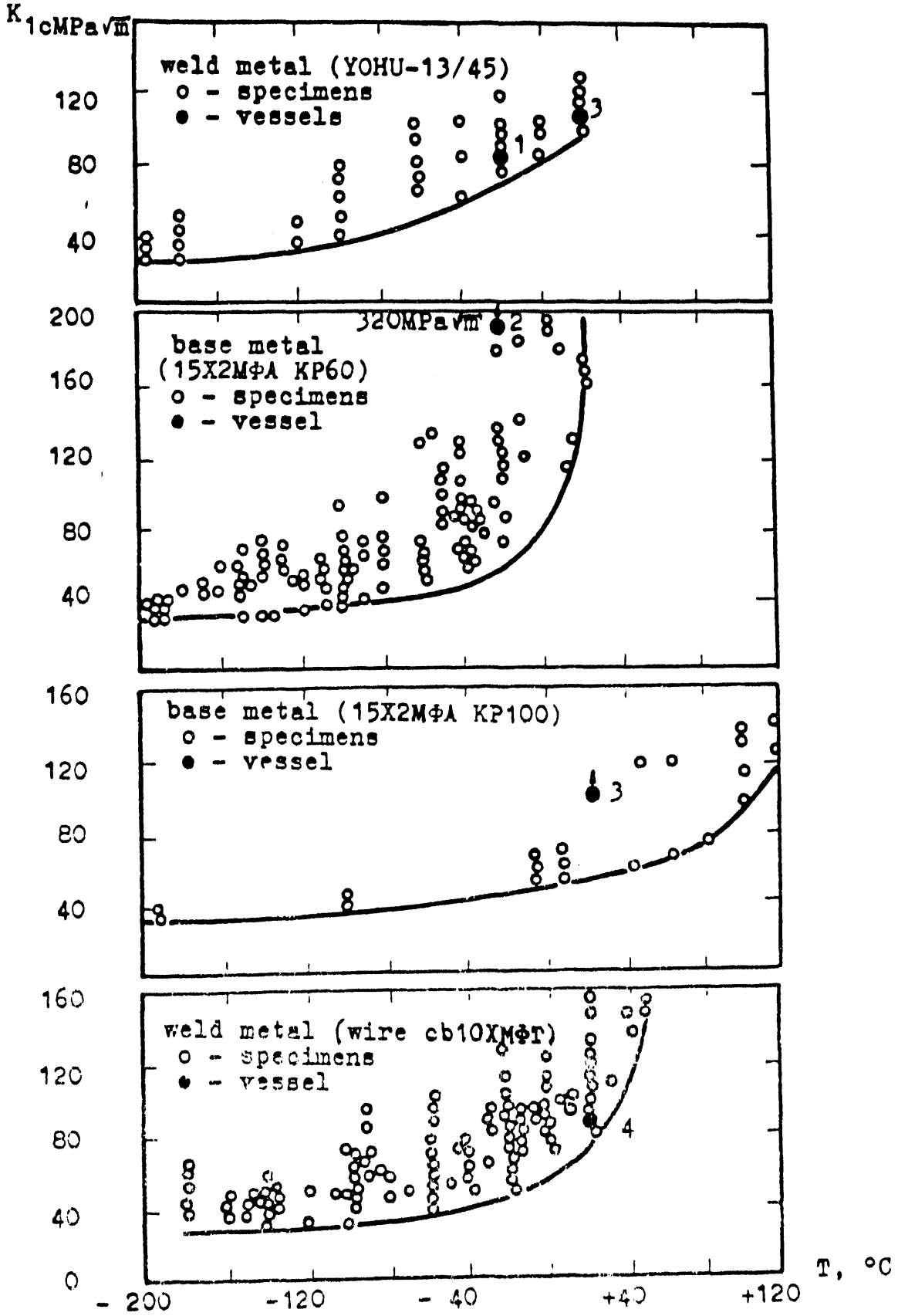

Fig. 23. Fracture toughness of materials based on the test results obtained on small-sized specimens and large-sized pressure vessel models.

PERSPECTIVES ON FRACTURE:

CORRELATION vs. FIRST PRINCIPLES

and LENGTH SCALES

C. FONG SHIH

DIVISION OF ENGINEERING
BROWN UNIVERISTY

Presentation at

IAEA/CSNI Specialists' Meeting on
Fracture Mechanics Verification by Large Scale Testing
Oak Ridge, Tennessee, October, 1992

PERSPECTIVES ON FRACTURE

MECHANISM-BASED FIRST PRINCIPLES	MIXED APPROACH	CORRELATION APPROACH IRWIN
Quantum Mechanics Molecular Dynamics	Mechanism/Correlation	Stress Intensity Factor, K J-integral
$10^{-9} \sim 10^{-5}$ m Cleavage fracture Ductile tearing Damage Mechanics Local Approach	Constraint Correction Dodds/Anderson	Two-parameter Approaches J-T theory J-Q theory

FIRST PRINCIPLES and LENGTH SCALES

- Physicists relate macroscopic behavior in terms of atomic and electronic structure and properties via Schrödinger's equation.
- Fracture involves competing physical processes too complex for this approach.
- Fracture is not determined by the average behavior of the atoms, but by the exceptional behavior of the relatively few atoms/defects situated at lattice/material irregularities.
- Develop concepts involving length scales $10^{-9} \sim 10^{-5}$ m.
- Cohesion of a solid in terms of force-displacement relations between a pair of atoms.

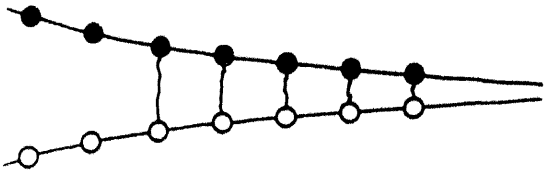

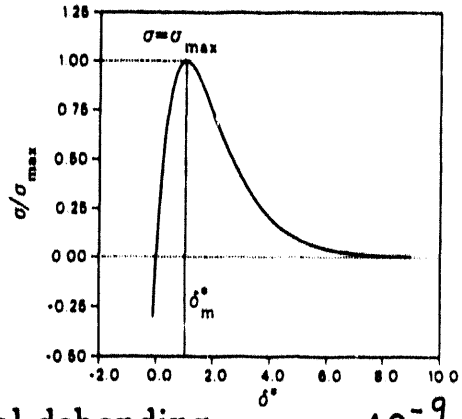

Applications: ideal brittle fracture, interfacial debonding. 10^{-9} m

- Cohesion of a solid in terms of force-displacement relations derived from the relevant micromechanical processes.

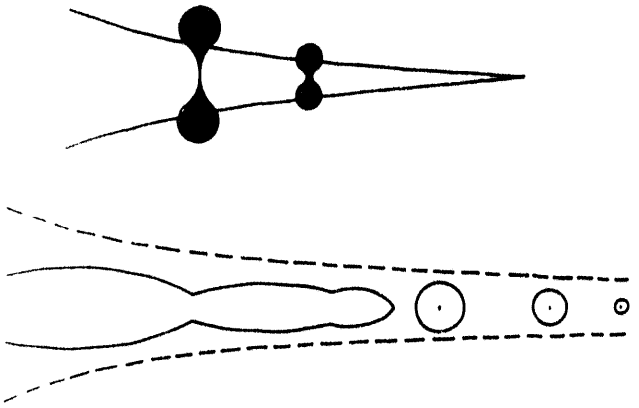

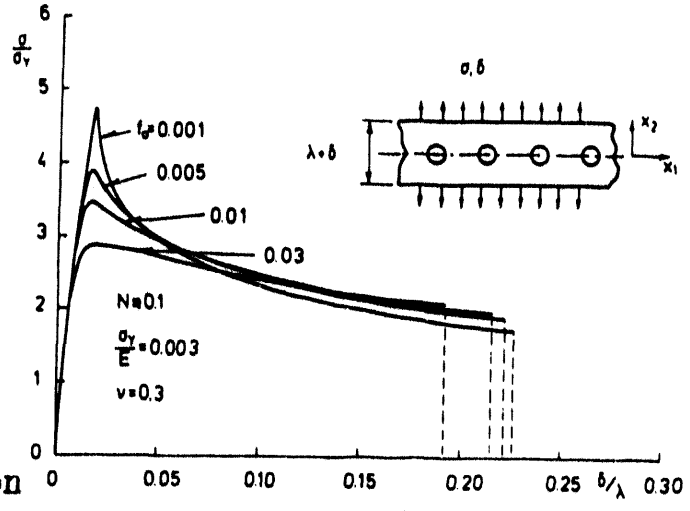

Applications: brittle/ductile transition
ductile fracture. $10^{-6} \sim 10^{-4}$ m

Irwin's Approach

- $K = K_{Ic}$, $J = J_{Ic}$ $\Rightarrow$ onset of fracture

This criterion is a physical postulate on material response, on the same level as the stress-strain curve, e.g.,

- $\sigma = \sigma_0$ $\Rightarrow$ onset of yield

However, fracture process occurs in a highly non-uniform stress, strain field.

Therefore, a size scale must enter into the fracture description. Indeed, an important idea in fracture mechanics concerns the size scale over which different phenomena dominate a fracture process. The idea is implicit in Irwin's stress intensity factor concept.

Scale of Observation: δ_t or J/σ_0

- Focus on the prospective fracture region on the length scale of the crack opening displacement or J/σ_0 since $\delta_t \propto J/\sigma_0$.

- Discuss fields which represent the environment in which the failure mechanisms are operative.

One-Parameter J Theory

- J scales the deformation and process zone size, and the stress triaxiality ahead of the crack
- J_{IC} is the fracture toughness
- J is the load parameter

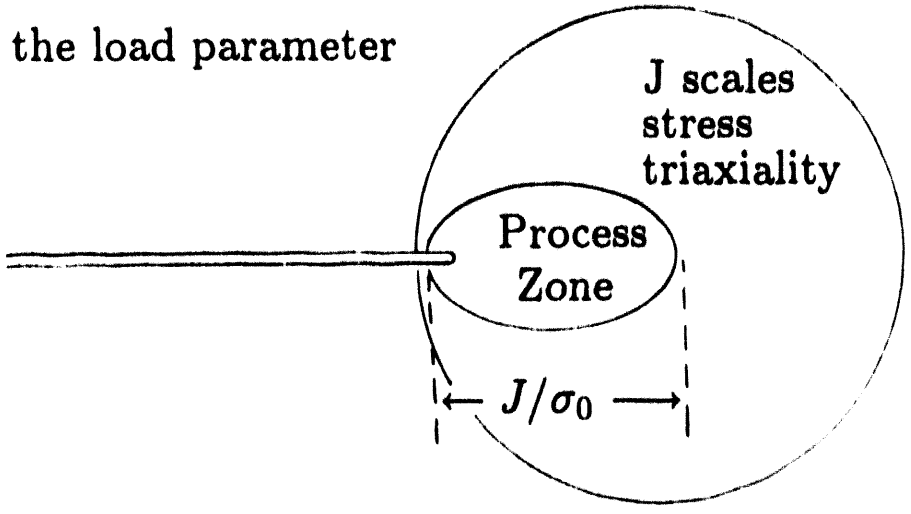

Two-Parameter J-Q Theory

- J scales the deformation and process zone size
- Q scales the stress triaxiality ahead of the crack
- $J - Q$ locus is the fracture toughness
- J and Q are the load parameters

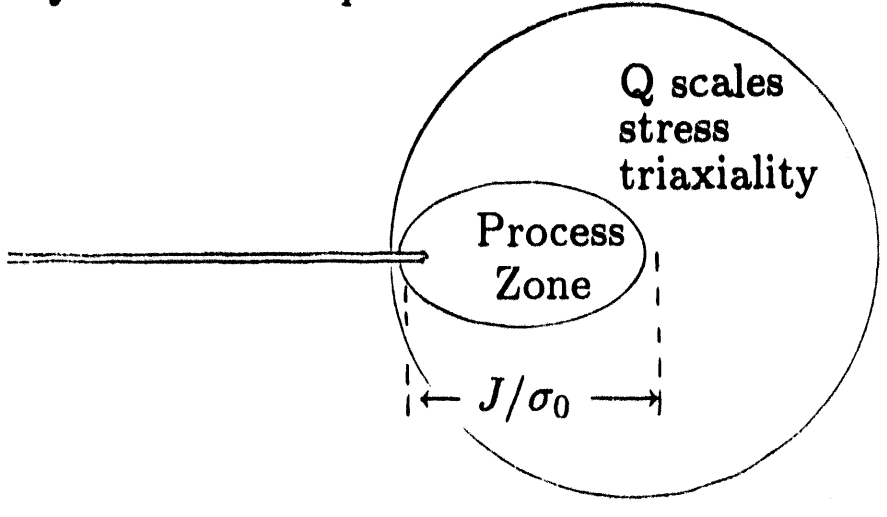

Two-Parameter Fracture Theory

Deformation and Stress Triaxiality } are weakly coupled under plastic yielding

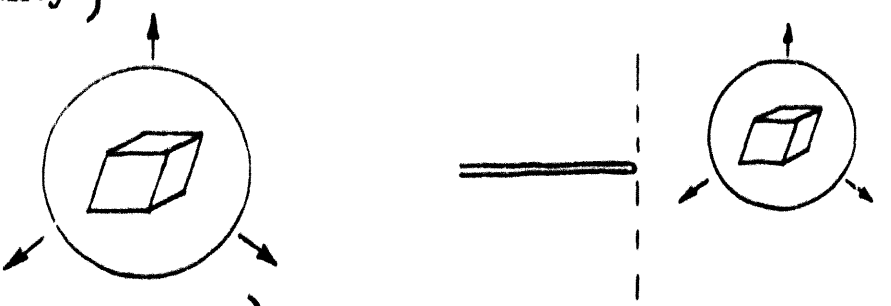

$\Longrightarrow$ Near-Tip Deformation and Stress Triaxiality } cannot be scaled by K_I or J alone

Two Parameter Theory:

K or J scales near-tip deformation

A second parameter scales near-tip stress triaxiality

Elasticity parameters: K_I and T

Plasticity parameters: J and Q

Equivalence Under Small Scale Yielding:

$$J = \frac{1-\nu^2}{E} K_I^2$$

$$Q = F(T/\sigma_0; n)$$

That is, a strict one-to-one correspondence exists between Q and T.

J-Q Fields

O'Dowd and Shih, JMPS 1991, 1992
Xia, Wang and Shih, 1992

$$\sigma_{ij} = \sigma_0 \left(\frac{J}{\alpha \epsilon_0 \sigma_0 I_n r} \right)^{1/(n+1)} \tilde{\sigma}_{ij}(\theta; n) + \underbrace{\text{higher order terms}}_{\text{Difference Field: } Q\sigma_0 \hat{\sigma}_{ij}(\theta)}$$

FORWARD SECTOR, $|\theta| < \pi/2$:

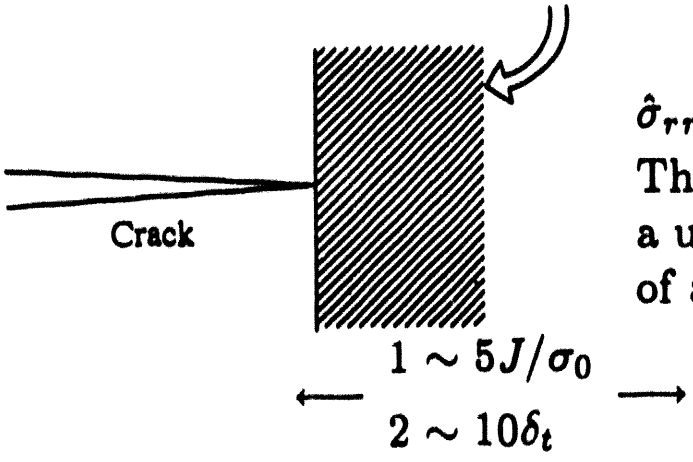

$\hat{\sigma}_{rr} \approx \hat{\sigma}_{\theta\theta} \approx$ constant, $\hat{\sigma}_{r\theta} \ll \hat{\sigma}_{\theta\theta}$
The difference field is essentially a uniform hydrostatic stress state of adjustable level.

Xia, Wang and Shih matched a four term asymptotic series to the form:

$$\sigma_{ij} = \sigma_0 \left(\frac{J}{\alpha \epsilon_0 \sigma_0 I_n r} \right)^{1/(n+1)} \tilde{\sigma}_{ij}(\theta; n) + Q\sigma_0 \delta_{ij}$$

$$\sigma_{ij} = (\sigma_{ij})_{\text{HRR}} + Q\sigma_0 \delta_{ij}$$

$$\sigma_{ij} = (\sigma_{ij})_{\text{SSY}} + Q\sigma_0 \delta_{ij}$$

That is, Q scales the near-tip triaxiality relative to a high triaxiality reference stress state

Definition of Q

Q is evaluated just outside the finite strain zone

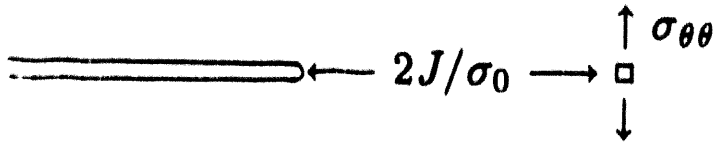

Two Reference Stress States:

$$Q \equiv \frac{\sigma_{\theta\theta} - (\sigma_{\theta\theta})_{\text{HRR}}}{\sigma_0} \qquad \text{at} \quad \theta = 0,\ r = 2J/\sigma_0$$

$$Q \equiv \frac{\sigma_{\theta\theta} - (\sigma_{\theta\theta})_{\text{SSY}}}{\sigma_0} \qquad \text{at} \quad \theta = 0,\ r = 2J/\sigma_0$$

Using standard SSY distribution as the reference state:

$$\sigma_{ij} = \underbrace{(\sigma_{ij})_{\text{SSY}}}_{\text{Reference State}} + \underbrace{Q\sigma_0\delta_{ij}}_{\text{Difference Field}}$$

$\therefore$ Negative (positive) $Q \Longrightarrow$ hydrostatic stress level is lowered (elevated) by $Q\sigma_0$ from the reference stress state.

Q Based on the Mean Stress:

$$Q_{\text{m}} \equiv \frac{\sigma_{\text{m}} - (\sigma_{\text{m}})_{\text{SSY}}}{\sigma_0} \qquad \text{at} \quad \theta = 0,\ r = 2J/\sigma_0$$

Q_{m} differs insignificantly from Q.

Construction of Q-Family of Fields

Modified Boundary Layer (MBL) Formulation

$$\sigma_{ij} = \frac{K_I}{\sqrt{2\pi r}} f_{ij}(\theta) + T\delta_{1i}\delta_{1j}$$

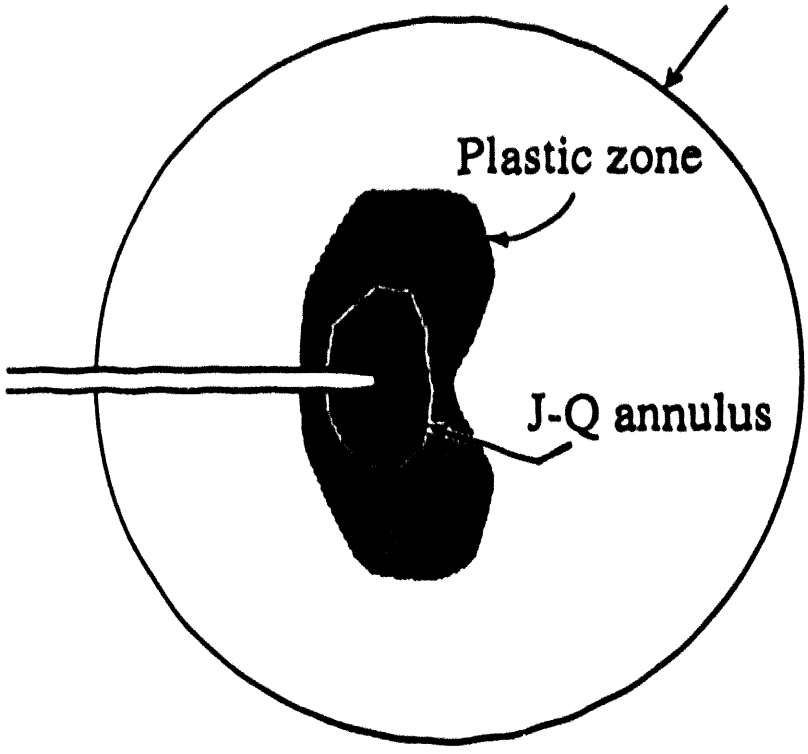

Q–family of fields obtained by applying different values of K_I and T/σ_0

$$J = \frac{1-\nu^2}{E} K_I^2$$

$$Q = F(T/\sigma_0; n)$$

Small Scale Yielding: Equivalence of J-T and J-Q

$$J = \frac{1-\nu^2}{E} K_I^2$$

$$Q = F(T/\sigma_0; n)$$

That is —

the connection between Q and T

is similar to that between J and K_I

$Q - T$ Relation

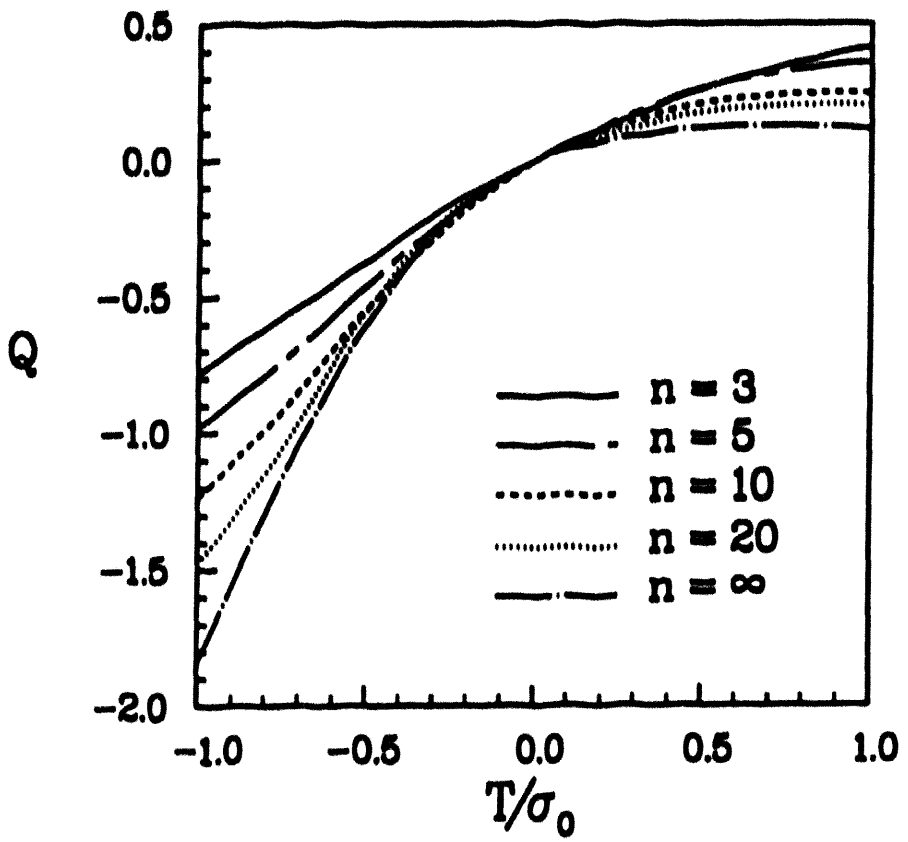

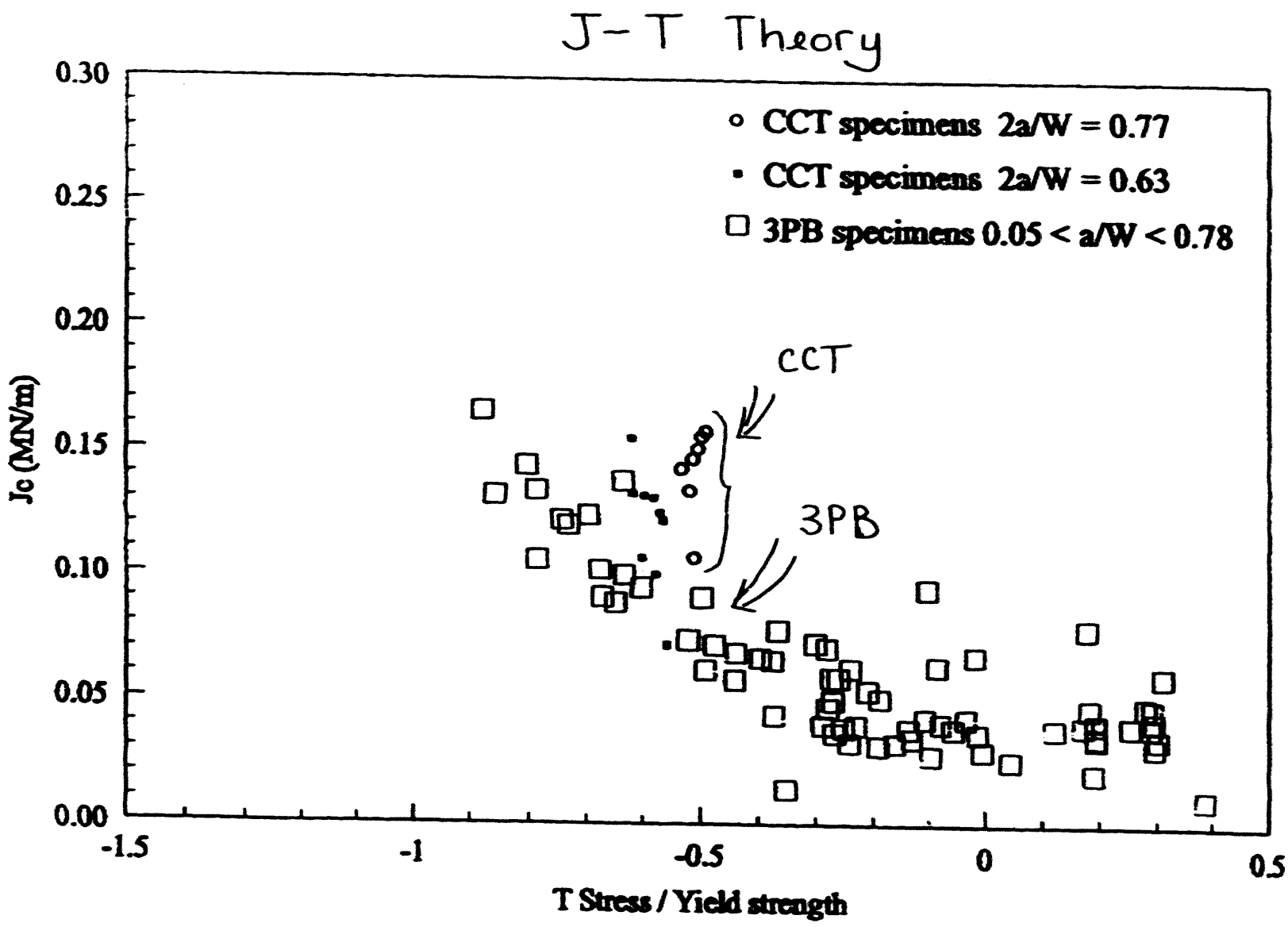

Cleavage Toughness Data — Sumpter and Forbes (1992)

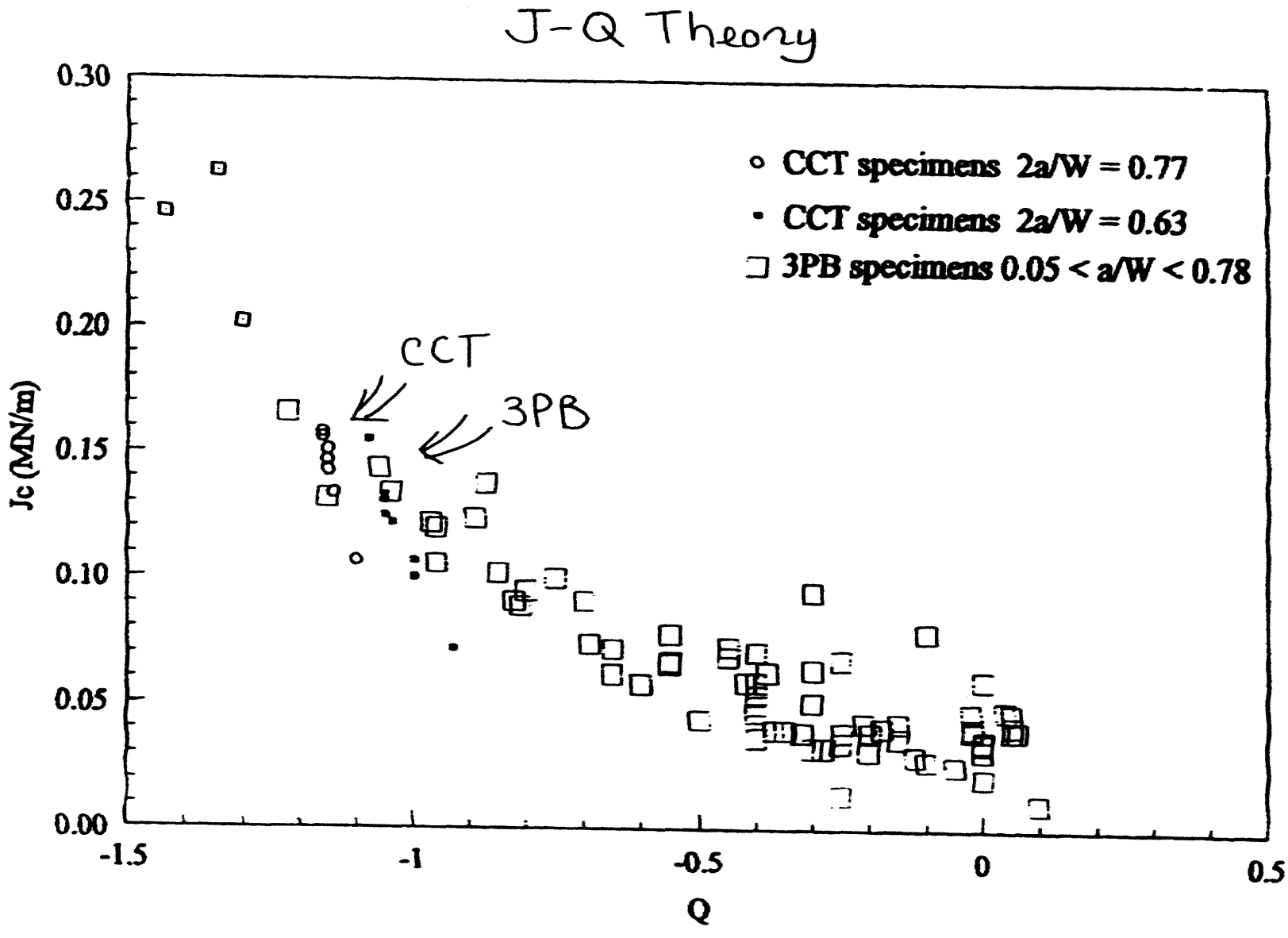

Cleavage Toughness Data — Sumpter and Forbes (1992)

Cleavage Toughness Locus

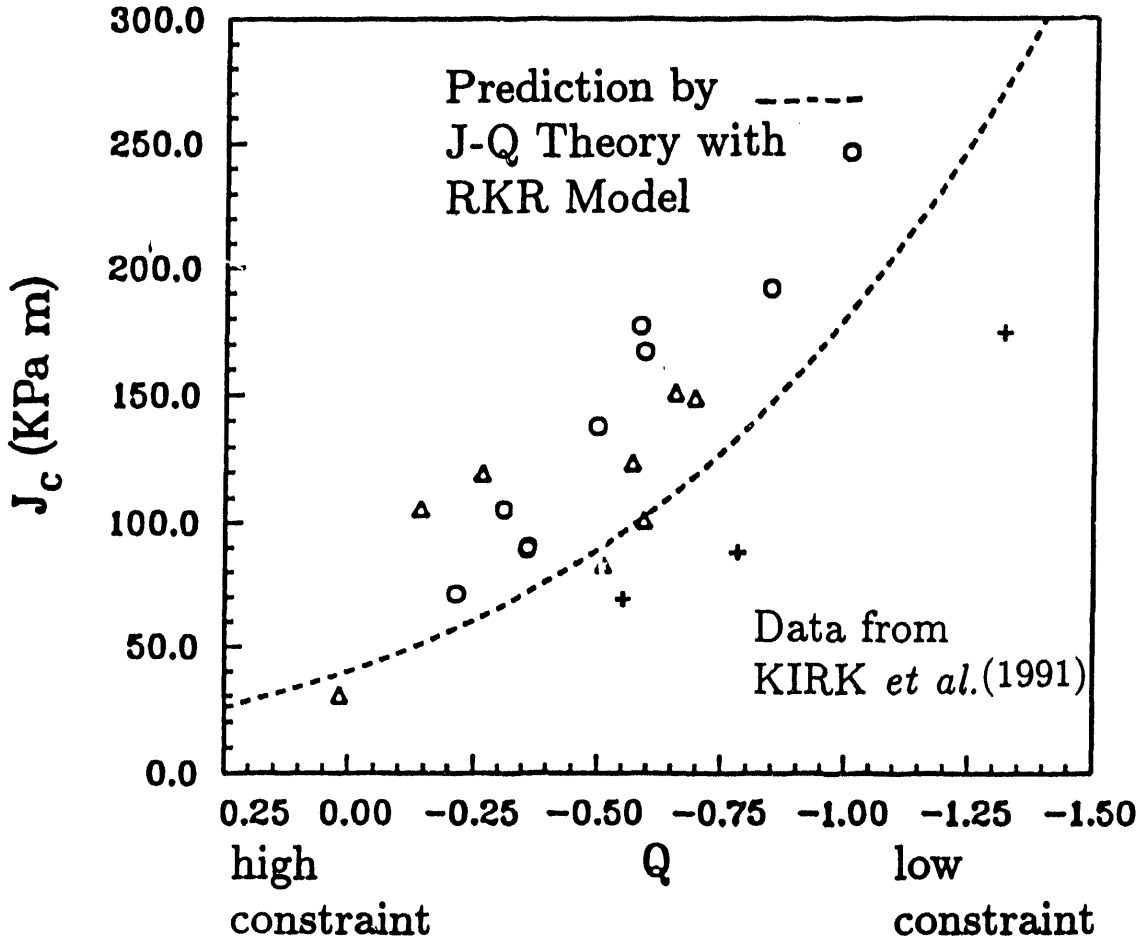

Cleavage toughness data for ASTM A515 Grade 70 steels tested at 20°C using edge-cracked bend bar for three thicknesses (KIRK *et al.*, 1991). + for B=10 mm, O for B=25.4 mm, Δ for B=50.8 mm.

Two Representations of J–Q Field for Engineering Analysis

HRR distribution as the $Q = 0$ solution:

$$\sigma_{ij} = (\sigma_{ij})_{\text{HRR}} + Q\sigma_0\delta_{ij} \qquad \text{for} \quad |\theta| < \pi/2$$

SSY ($T = 0$) distribution as the $Q = 0$ solution:

$$\sigma_{ij} = (\sigma_{ij})_{\text{SSY}} + Q\sigma_0\delta_{ij} \qquad \text{for} \quad |\theta| < \pi/2$$

Preferred form

$\therefore$ **Negative (positive) Q $\Rightarrow$ hydrostatic stress is reduced (increased) by $Q\sigma_0$ from the reference state**

NOTES :

i) The $Q = 0$ reference state is also referred to in the existing literature as the J-dominant state.

ii) The second representation provides a more accurate description of the Q-family of fields.

iii) The reference field $(\sigma_{ij})_{\text{SSY}}$ can be evaluated for an actual stress-strain relation and finite deformation.

Q-Solutions Generated By Finite Element Analyses Are Available For Several Crack Geometries

Q-T-J Handbook, Editors: Bob Dodds and Fong Shih, will contain solutions to 2-D and 3-D crack problems

Q-Solutions Available For These Geometries:

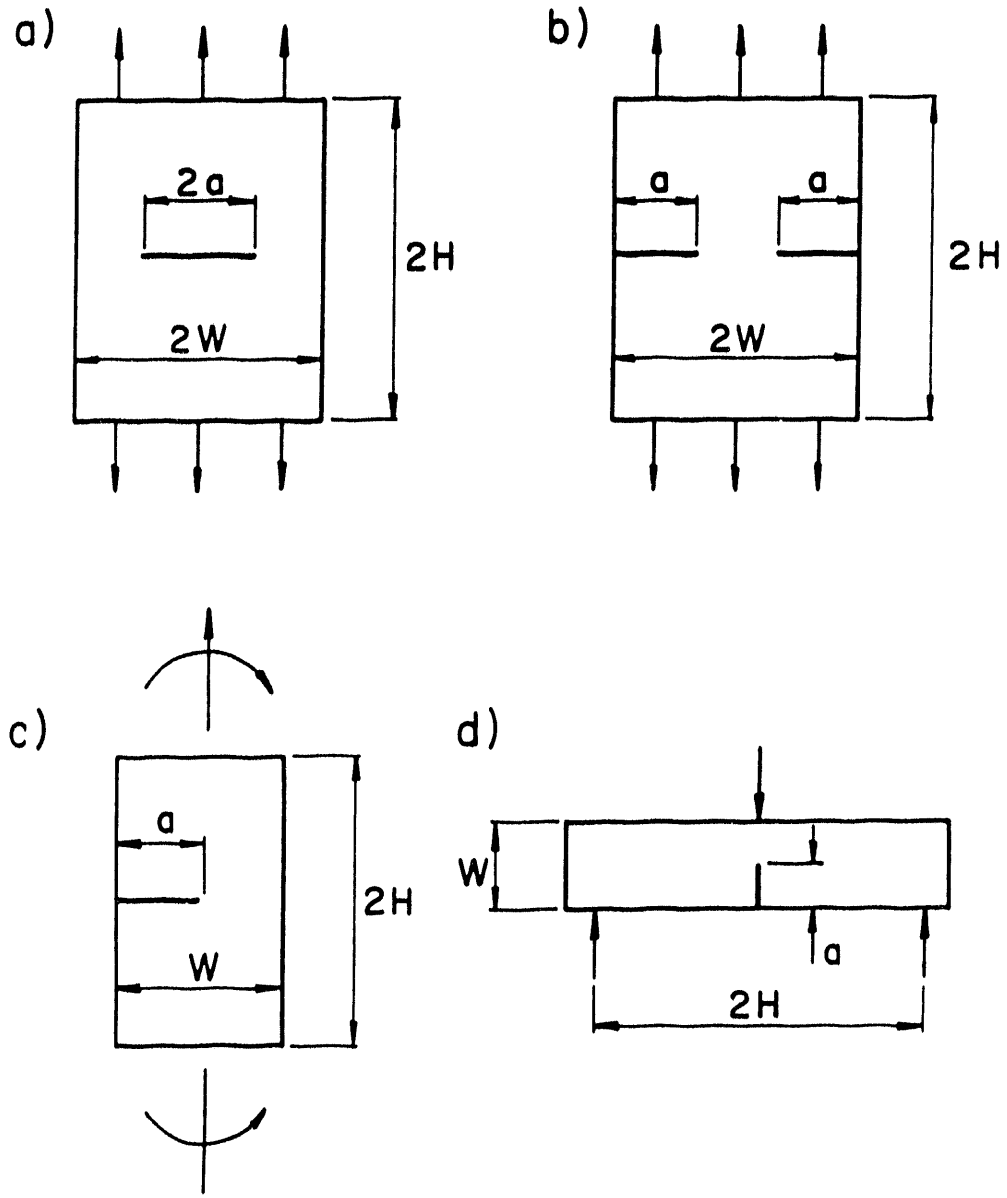

J-Q Methodology

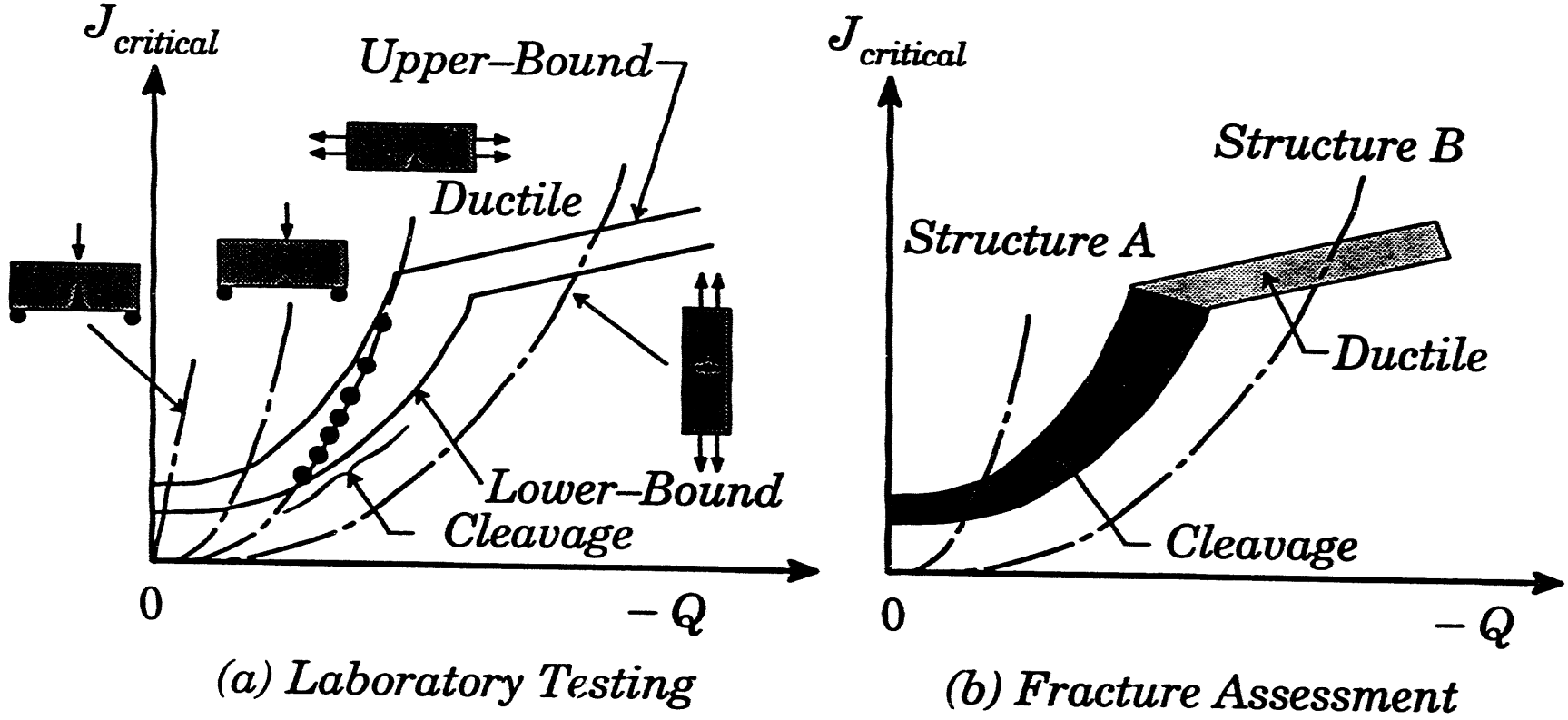

(a) Laboratory Testing

(b) Fracture Assessment

FRACTURE in the BRITTLE/DUCTILE TRANSITION REGION

- Strain rate effects on flow strength
- Strain rate effects on competing fracture mechanisms
- Material inertia effects on stress and strain fields
- Temperature effects on flow strength
- Crack growth effects on constraint

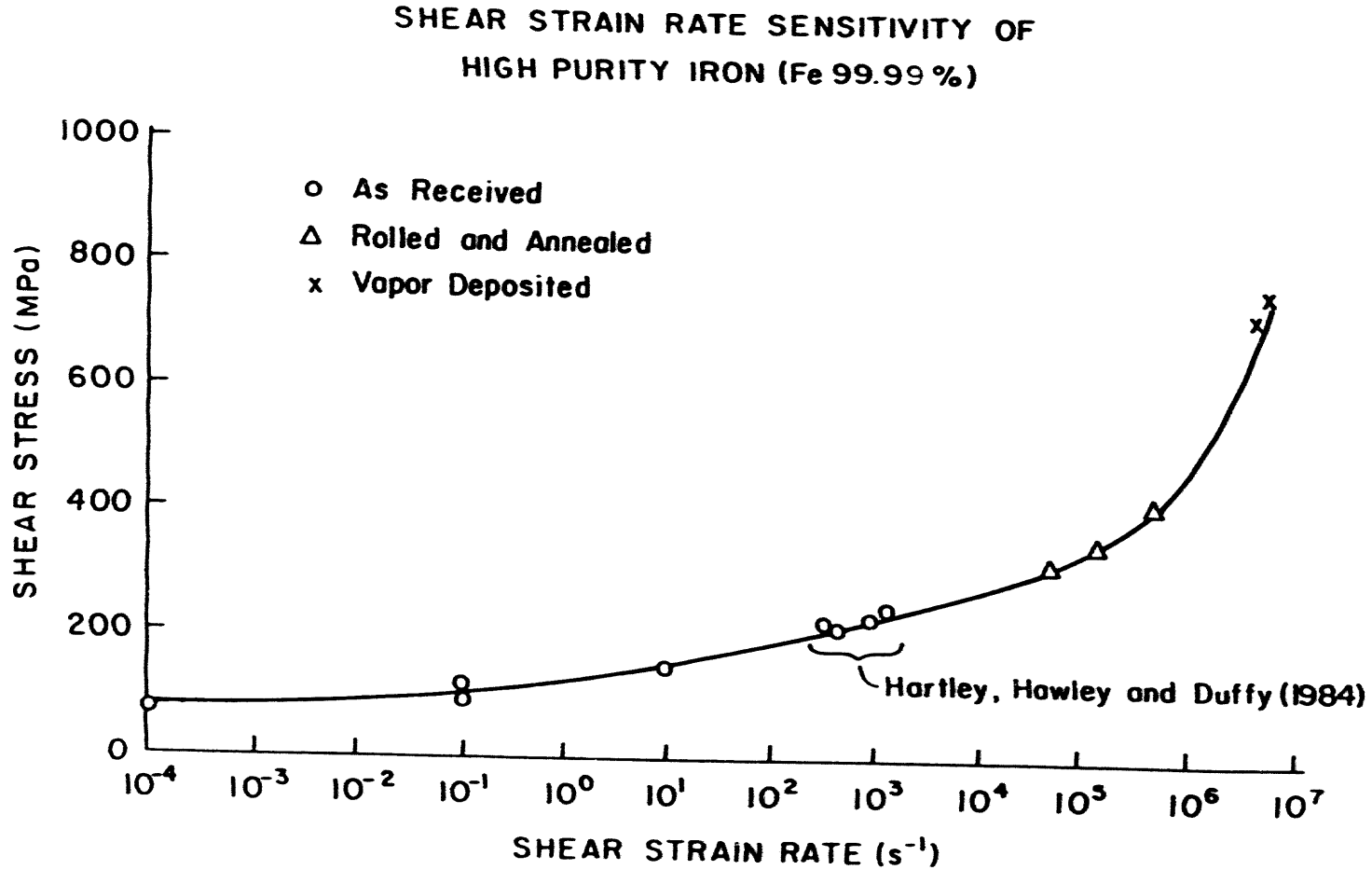

From Klopp, Clifton and Shawki (1985), Mechanics of Materials, Vol. 4, pp. 375-385.

$$\dot{\bar{\epsilon}} = \dot{\bar{\epsilon}}_2 + (\dot{\bar{\epsilon}}_1 - \dot{\bar{\epsilon}}_2) \exp\left(-\frac{\bar{\sigma}}{H}\right)$$

$$H(\bar{\epsilon}) = \sigma_0 \left(\frac{\bar{\epsilon}}{\epsilon_0} + 1\right)^{1/n}$$

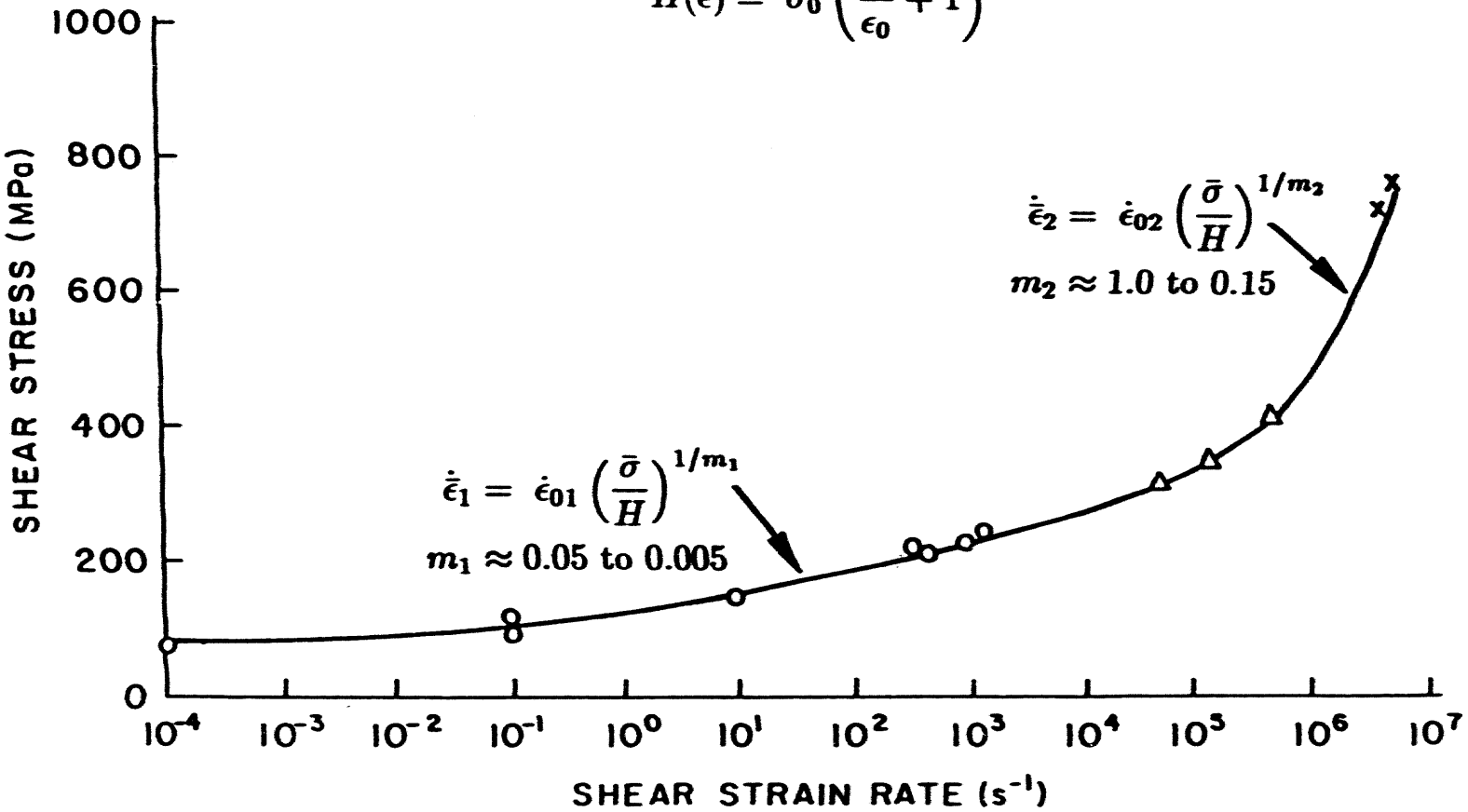

Constitutive relation which provides a smooth transition from the low strain rate range to the high strain rate range.

Material constants: $\dot{\epsilon}_{01}$, $\dot{\epsilon}_{02}$, m_1, m_2, n and σ_0

FRACTURE in the BRITTLE/DUCTILE TRANSITION REGION

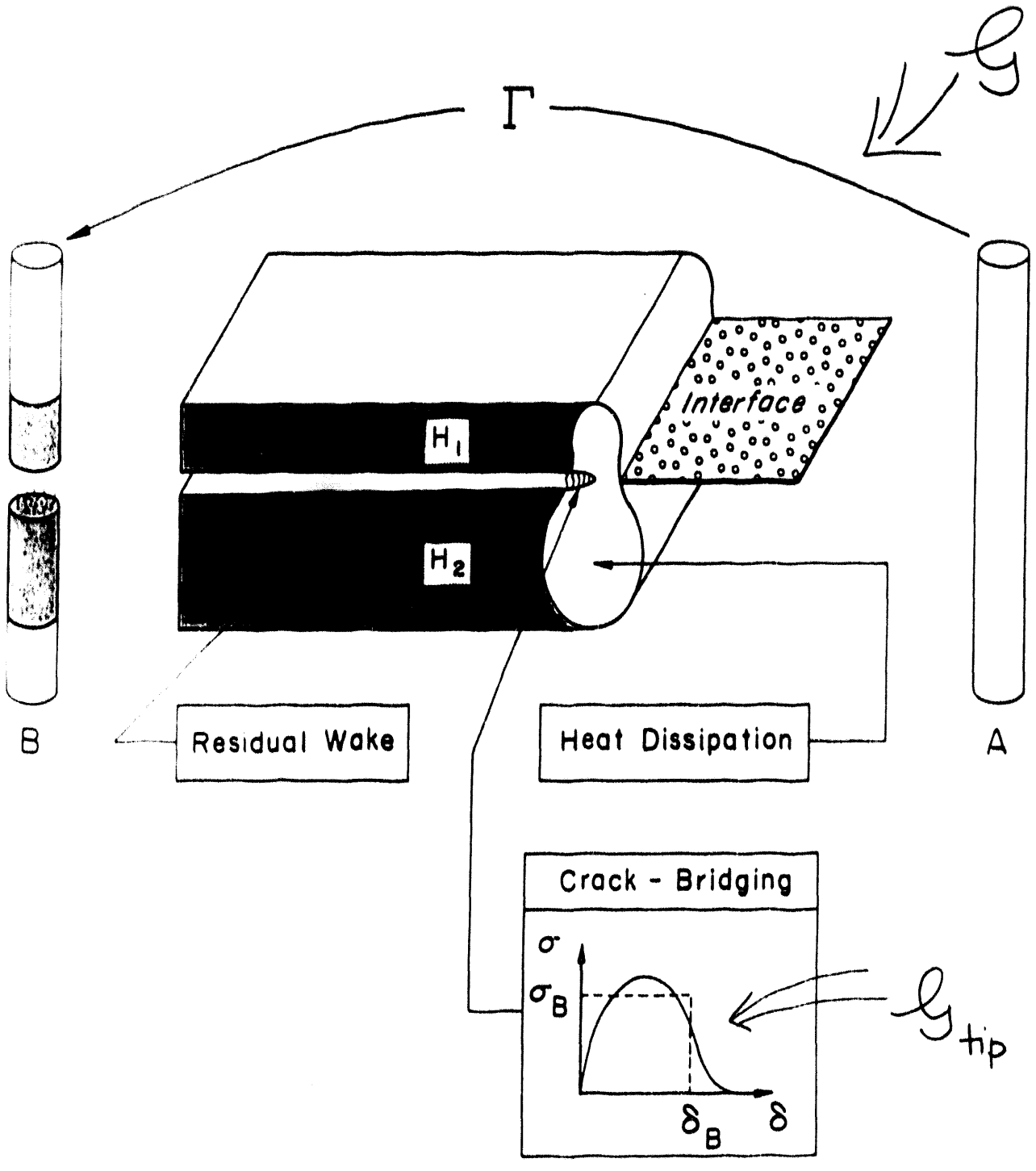

Inelastic processes acompanying crack propagation.

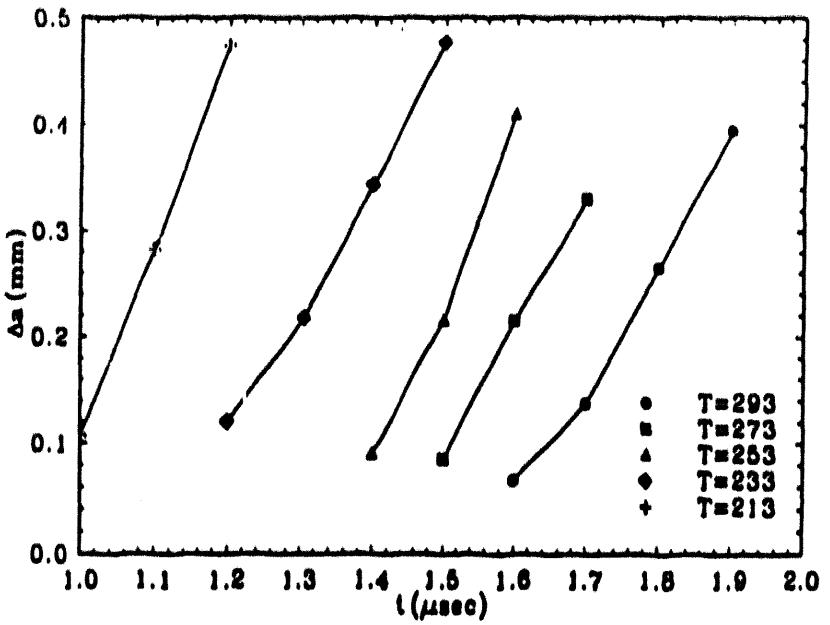

(a)

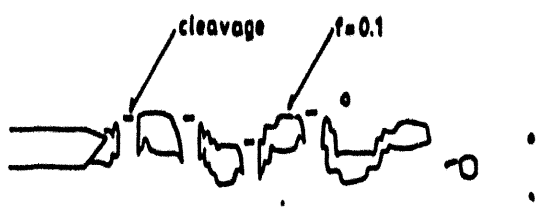

(b)

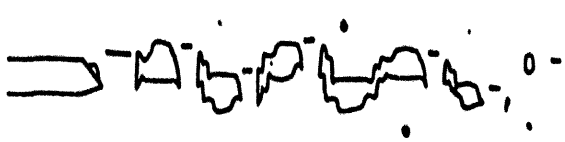

(c)

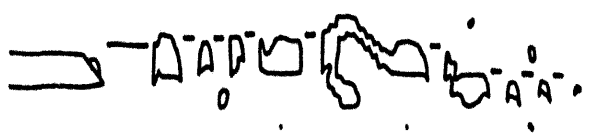

(d)

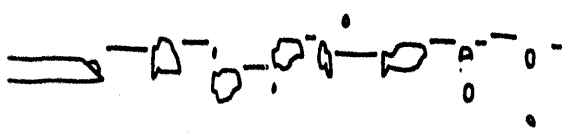

From Tvergaard and Needleman (1992)

CRACK TIP SHIELDING BY PLASTICITY

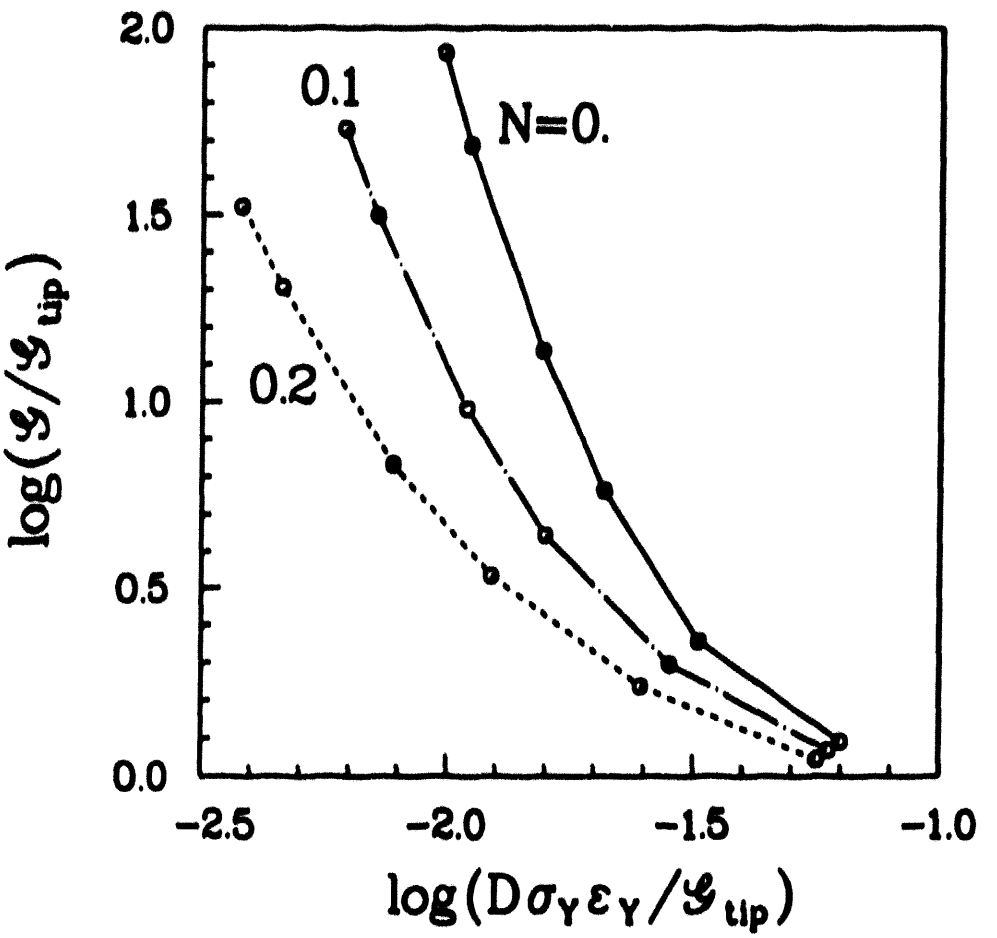

Suo, Shih and Varias (1992). Acta Metall. Mater. To appear.

Continuum and Micro–Mechanics Treatment of Constraint in Fracture

Robert H. Dodds, Jr.

Department of Civil Engineering
University of Illinois at Urbana-Champaign
Urbana, Illinois 61801 USA

C. Fong Shih

Division of Engineering
Brown University
Providence, Rhode Island 02912 USA

1. INTRODUCTION

Two fundamental concepts underlie both linear–elastic fracture mechanics and elastic–plastic fracture mechanics: [1] the relevant crack–tip singularity dominates over microstructurally significant size scales and [2] the parameter K_I, or J, uniquely scales the amplitude of the near–tip fields. In an actual structure, the crack–tip field must be perturbed by the external boundary and the loading distribution (*from afar*), and by the zone of inelasticity and small–scale heterogeneities, e.g., grains, microcracks, crack face roughness (*from within*). However, when the zone of inelasticity and small–scale heterogeneities remains small compared to the external geometry, the asymptotic field is approximately unperturbed in an annulus which is larger than the zone of inelasticity and small–scale heterogeneities, but much smaller than the external geometry. Strain–stress fields in such an annulus are determined completely by the singularity solution (see review article by Hutchinson [1]). Under this condition, the effects of remote loading and external boundaries are communicated to the crack tip through K_I, or J, alone. Moreover, when linear elasticity prevails at the macro–scale, then boundary loading as well as traction free boundaries exert their influence on the near–tip field through K_I alone, with no effect on the actual distribution. Similarly, the plastic fields for well–contained yielding sense external boundaries and loading only through J [2,3,4]. However, for large–scale yielding in finite bodies, the relationship between the scaling parameter, J, and the near–tip fields loses the one–to–one correspondence [5,6,7] This loss of uniqueness, often termed *loss of constraint*, produces the increases in fracture toughness observed for tension geometries and for shallow notch bend specimens. The mismatch of constraint conditions at the crack tip apparently plays a dominant role in the often disappointing correlation between fracture specimen behavior [C(T), SE(B)] and the behavior observed in large–scale, tension loaded tests.

Constraint effects are most pronounced for low–to–medium strength structural steels (and their weldments) operating in the ductile–to–brittle transition region where unstable fracture occurs by the micromechanism of transgranular cleavage. Many nuclear, civil and marine structures operate in the transition region over significant portions of their lifetimes. Unlike the more ductile mechanism of slow stable tearing, cleavage fractures most often trigger catastrophic failure of even highly redundant structural systems. Extensive experimental studies (see, for example [8–12]) have readily demonstrated the much greater sensitivity of cleavage fracture toughness, J_c, to constraint than is observed for ductile initiation toughness, J_{Ic}, and for ductile crack growth resistance J–Δa.

In the past three years, new approaches have appeared to quantify constraint and to predict the effects of constraint changes on macroscopic (engineering) fracture toughness characterized by J and the crack tip opening displacement, CTOD or δ. Very detailed, elas-

tic–plastic finite element analyses provide correlations of crack–tip stress fields over distances $r \leq 2–8\delta$ with loading level (J), loading mode (tension *vs.* bending), specimen geometry and strain hardening. Such computations stimulated development of the J–Q continuum mechanics framework [13–19] to describe the near–tip fields under very general conditions of loading in finite bodies. Within this framework, the J–integral sets the scale of deformation at the crack tip (i.e., the CTOD) while the hydrostatic stress parameter, Q, quantifies the level of stress triaxiality over distances $r \leq -2–8\delta$ ahead of the tip in which the microseparation processes occur. Under increased loading, each fracture specimen for a specific material/temperature follows a characteristic J–Q driving force curve which defines the evolution of crack–tip deformation and constraint. Specimens fracture at a critical J–value denoted J_c which depends on Q (J_c determined by laboratory testing, Q determined from analysis). By testing fracture specimens that exhibit a wide–range of constraint conditions (e.g. shallow–to–deep notch SE(B) specimens), the toughness locus for the material is constructed, i.e., the curve connecting all J_c *vs.* Q points.

Another two–parameter approach also receiving considerable attention utilizes J and the elastic T–stress [7,20–25]. These studies propose to correlate crack–tip stress triaxiality in contained and fully–yielded cracked bodies using the the elastic T–stress. The J–T and J–Q approaches are equivalent under well–contained yielding conditions [14–16]. However, under fully–yielded conditions the T–stress becomes undefined; moreover, T is proportional to K_I and near limit load K_I (and thus T) approaches a saturation value independent of additional plastic deformation. In contrast, the Q–parameter continues to evolve over the entire range of plastic yielding. Numerical studies have shown that the J–T approach overestimates the actual stress triaxiality for some geometries and underestimates it in other cases so that there is not a consistent trend [16,26]. An extensive study of the limits of applicability of the T–stress as a correlator of near–tip stress triaxiality can be found in [26]. Readers are referred to the publications [7,20–25] and references therein for details of the J–T approach. This paper focuses on continuum and micro–mechanics approaches believed to have broader applicability.

The J–Q approach may become prohibitively expensive as the number of specimens and temperatures of interest increases. To reduce the cost, a micromechanics model for cleavage fracture is introduced to predict the toughness locus using the finite element stress fields and the J_C values from a few fracture toughness tests. Recent developments [27,28] in the formulation of a robust micromechanics model focus on the observation of a strong, spatial self–similarity of crack–tip principal stresses under increased loading and across different fracture specimens. While the spatial variation remains self–similar, the magnitudes of principal stresses vary dramatically as crack–tip constraint evolves under loading. The micromechanics model employs the volume of material bounded within principal stress contours at fracture to correlate J_c values for different specimens and loading modes. The similarity of principal stress contours as constraint evolves under loading is entirely consistent with the J–Q description of the crack–tip stress fields. For an applied J–value, the size, but not the shape, of principal stress contours is altered by the near–tip, uniform hydrostatic stress states of adjustable magnitude characterized by Q. These observations imply that values specified for metallurgical parameters in the micromechanics model, such as the critical fracture stress and the distance to the critical particle, have only a weak influence on the relative variation of fracture toughness, J_c, with constraint for a given material and temperature.

This paper explores the fundamental concepts of the J–Q description of crack–tip fields, the fracture toughness locus and micromechanics approaches to predict the variability of

macroscopic fracture toughness with constraint under elastic–plastic conditions. While these concepts derived from plane–strain considerations, initial applications in fully 3–D geometries are very promising. Computational results are presented for a surface cracked plate containing a 6:1 semi–elliptical, $a=t/4$ flaw subjected to remote uniaxial and biaxial tension. Crack–tip stress fields consistent with the J–Q theory are demonstrated to exist at each location along the crack front. The micromechanics model employs the J–Q description of crack–front stresses to interpret fracture toughness values measured on laboratory specimens for fracture assessment of the surface cracked plate. The computational results suggest only a minor effect of the biaxial loading on the crack tip stress fields and, consequently, on the propensity for fracture relative to the uniaxial loading.

2. J–Q THEORY

Consider a cracked body of characteristic dimension L loaded remotely by a stress denoted $\sigma\infty$. The scale of crack–tip deformation is measured by J/σ_0 where σ_0 is the material's tensile yield stress ($\delta \propto J/\sigma_0$). At a sufficiently low load, $L \gg J/\sigma_0$ and it can be shown from dimensional grounds that all near–tip fields are members of a single family of crack–tip fields. Each member field is characterized by its level of deformation as measured by J/σ_0 and by its level of crack tip stress triaxiality as measured by Q, which also identifies that field as a particular member of the family. For example, the self–similar solution of Rice and Johnson [29] and McMeeking [30] (as well as the HRR field [3,4]) is the $Q=0$ member field. The Q–family of fields provides the proper characterizing parameter for the full range of near–tip stress states.

In the following discussion, attention is directed to the prospective fracture region ahead of the crack tip on the scale of several crack opening displacements, δ, representing the environment in which the failure mechanisms are active.

2.1 Q–Family of Fields–MBL Formulation

The Q–family of fields is constructed using a modified boundary layer (MBL) formulation in which the remote tractions are given by the first two terms of the small–displacement–gradient linear elastic solution (Williams [31]),

$$\sigma_{ij} = \frac{K_I}{\sqrt{2\pi r}} \tilde{f}_{ij}(\theta) + T\delta_{1i}\delta_{1j} \tag{2.1}$$

Here r and θ are polar coordinates centered at the crack tip with $\theta=0$ corresponding to a line ahead of the crack is shown in the insert in Fig. 2.1. Cartesian coordinates, X and Y with the X–axis running directly ahead of the crack, are used when it is convenient. Within the MBL formulation,

$$J = \frac{1-\nu^2}{E} K_I^2 \tag{2.2}$$

under plane strain conditions, where J is Rice's J–integral [1], E is Young's modulus and ν is Poisson's ratio.

Fields of different crack tip stress triaxialities can be induced by applying different combinations of K and T. From dimensional considerations, these fields can be organized into a family of crack tip fields parameterized by T/σ_0:

$$\sigma_{ij} = \sigma_0 \tilde{f}_{ij}\left(\frac{r}{J/\sigma_0}, \theta; T/\sigma_0\right) . \tag{2.3}$$

That is, the load parameter T/σ_0 provides a convenient means to investigate and parameterize specimen geometry effects on near-tip stress triaxiality under conditions of well-contained yielding. Such studies have been carried out by Betegon and Hancock [20], Bilby *et al.* [32] and Harlin and Willis [33]. Nevertheless, the result in (2.3) cannot have general applicability since the elastic solution (2.1), upon which the T-stress is defined, is an asymptotic condition which is increasingly violated as plastic flow progresses beyond well-contained yielding.

Recognizing the above limitation, O'Dowd and Shih [13,14], referred to as OS, identified members of the family of fields by the parameter Q which arises naturally in the plasticity analysis. OS write:

$$\sigma_{ij} = \sigma_0 f_{ij}\left(\frac{r}{J/\sigma_0}, \theta; Q\right), \quad \varepsilon_{ij} = \varepsilon_0 f_{ij}\left(\frac{r}{J/\sigma_0}, \theta; Q\right), \quad u_i = \frac{J}{\sigma_0} h_i\left(\frac{r}{J/\sigma_0}, \theta; Q\right) . \tag{2.4}$$

The additional dependence of f_{ij}, g_{ij} and h_i on dimensionless combinations of material parameters is understood. The form in (2.4) constitutes a one-parameter family of self-similar solutions, or in short a Q-family of solutions. The annular zone over which (2.4) accurately quantifies the actual field is called the J-Q annulus.

2.2 Difference Field and Near-Tip Stress Triaxiality

Using the modified boundary layer formulation, and considering a piecewise, power-law hardening material, OS generated the full range of small scale yielding, plane strain solutions, designated by $(\sigma_{ij})_{SSY}$. OS considered the difference field defined by

$$\Delta\sigma_{ij} = (\sigma_{ij})_{SSY} - (\sigma_{ij})_{HRR} \tag{2.5}$$

where $(\sigma_{ij})_{HRR}$ is the HRR field. They systematically investigated the difference field within the forward sector $|\theta| < \pi/2$ of the annulus $J/\sigma_0 < r < 5J/\sigma_0$, since this zone encompasses the microstructurally significant length scales for both brittle and ductile fracture[34]. Remarkably, the difference field in the forward sector displayed minimal dependence on r. Noting this behavior, OS expressed the difference field within the forward sector in the form

$$\Delta\sigma_{ij} = Q\sigma_0\hat{\sigma}_{ij}(\theta) , \tag{2.6}$$

where the angular functions $\hat{\sigma}_{ij}$ are normalized by requiring $\sigma'_{ij}(\theta=0)$ to equal unity. Moreover, the angular functions within the forward sector exhibit these features: $\sigma_{rr} \approx \sigma_{\theta\theta} \approx$ constant and $|\sigma_{r\theta}| \ll |\sigma_{\theta\theta}|$ (see Figs. 3, 4, and 5 in [13]).

Thus the difference field within the sector $|\theta| < \pi/2$ and $J/\sigma_0 < r < 5J/\sigma_0$, correspond effectively to a spatially uniform hydrostatic stress state of adjustable magnitude, i.e. $\Delta\sigma_{ij} = Q\sigma_0\delta_{ij}$. Therefore Q defined by

$$Q \equiv \frac{\sigma_{\theta\theta} - (\sigma_{\theta\theta})_{HRR}}{\sigma_0} \quad \text{at } \theta = 0, \quad r = 2J/\sigma_0 \tag{2.7}$$

is a natural measure of near-tip stress triaxiality, or crack tip constraint, relative to a high triaxiality reference stress state. In words, Q is the difference between the actual hoop stress and the corresponding HRR stress component at $r=2J/\sigma_0$, the difference being normalized by σ_0. The distance chosen for the definition of Q lies just outside the finite strain blunting zone. It is preferable that Q be defined at a distance which is some multiple of the crack tip opening displacement; the present definition suffices for our purposes.

OS also considered the difference field whereby the reference solution is the standard small scale yielding solution, $(\sigma_{ij})_{SSY;T=0}$ which is driven by K_I alone, i.e.,

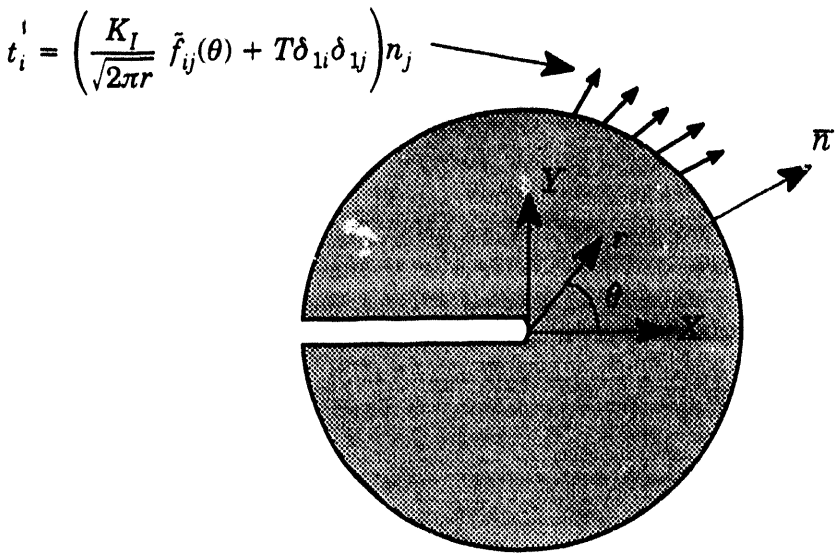

Figure 2.1 Definition of the Modified Boundary Layer (MBL) problem.

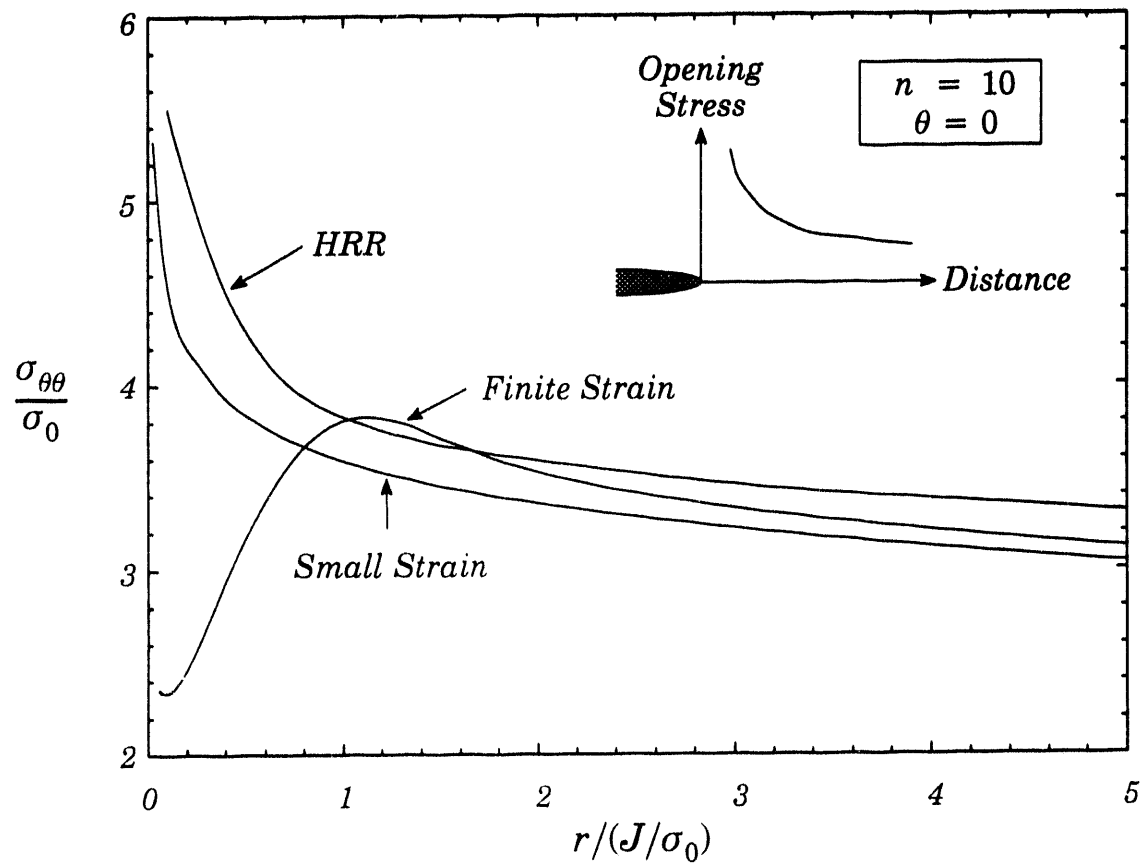

Figure 2.2 Plane strain reference fields for n=10, E/σ_0=500, ν=0.3. Table 2.1 provides differences in the three fields for various n at each $r/(J/\sigma_0)$. The material stress–strain curve has the form given in (2.10).

$$\Delta\sigma_{ij} = (\sigma_{ij})_{SSY} - (\sigma_{ij})_{SSY;T=0} \tag{2.8}$$

In this case the difference field in the forward sector matches a spatially uniform hydrostatic stress state even more closely. Thus an alternative definition of Q is

$$Q \equiv \frac{\sigma_{\theta\theta} - (\sigma_{\theta\theta})_{SSY;T=0}}{\sigma_0} \quad \text{at } \theta = 0, \; r = 2J/\sigma_0 \; . \tag{2.9}$$

Representative stress distributions of the Q–family of fields can be found in [13,14].

2.3 Choice of Reference Field

The value of Q is slightly affected by the choice of reference field. Thus a small increment (or decrement) must be applied to the Q–values if the reference field is changed from $(\sigma_{\theta\theta})_{HRR}$ to $(\sigma_{\theta\theta})_{SSY;T=0}$, or vice versa. The reference field distributions according to the HRR singularity and the small scale yielding solutions for small strain and finite strain are given in Table 2.1. The material's uniaxial stress–strain response is represented by an elastic power–law model having the form

$$\varepsilon = \begin{cases} \sigma/E & \text{if } \sigma \le \sigma_0 \\ \varepsilon_0(\sigma/\sigma_0)^n & \text{if } \sigma > \sigma_0 \end{cases} \; ; \; \varepsilon_0 = \sigma_0/E \tag{2.10}$$

with values of E/σ_0=500, ν=0.3 adopted in the computations. Figure 2.2 shows typical reference fields determined from the MBL formulation with T=0.

In practice it really does not matter whether we use $(\sigma_{\theta\theta})_{HRR}$ (2.7), or $(\sigma_{\theta\theta})_{SSY;T=0}$ (2.9), for the definition of Q so long as it is applied consistently. In other words, the evaluation and tabulation of Q solutions for test specimens, the determination of the toughness locus from test data, and subsequent applications of such data to predict fracture in structural components should be based on the same reference field. Nevertheless, use of (2.9) can extend the range of applicability of the J–Q approach and is preferable when it is desired to assess the spatial extent of the J–Q annulus. A parameter which can ascertain the robustness of the J–Q field is discussed in the next Section.

A reference distribution determined from a small–displacement–gradient analysis is adequate for most applications. However, accurate descriptions of fields near the zone of finite strains may be desirable in some applications, e.g. computational studies on the micromechanisms of ductile initiation. In such cases it is preferable to calculate $(\sigma_{\theta\theta})_{SSY;T=0}$ by a finite deformation analysis and to use (2.9) for the definition of Q. More importantly for practical applications, the evolution of stress triaxiality in a finite–width, cracked body can be evaluated for an actual stress–strain relation, not just the power–law relation, if the $(\sigma_{\theta\theta})_{SSY;T=0}$ reference field for the MBL model is determined with the same stress–strain relation. This extends the applicability of the approach to a much broader range of material responses. In contrast, the reference field $(\sigma_{\theta\theta})_{HRR}$ is defined for an elastic power–law hardening material and the calculations in the finite body also must employ an elastic power–law hardening relation.

2.4 Variation of Q with Distance

Because Q scales the difference field relative to a reference stress state, it provides a sensitive measure of the evolution of near–tip stress triaxiality in finite width cracked bodies. It also can be used to detect changes in the stress triaxiality that deviates from the pattern that develops under MBL loadings. For this purpose, we consider $Q(r)$ defined by

$$Q(\tilde{r}) \equiv \frac{\sigma_{\theta\theta}(\tilde{r}) - [\sigma_{\theta\theta}(\tilde{r})]_{SSY;T=0}}{\sigma_0}, \quad \text{at } \theta = 0 \tag{2.11}$$

where $\tilde{r} \equiv r/(J/\sigma_0)$. Note that $(\sigma_{\theta\theta})_{SSY;T=0}$ is chosen as the reference field.

The mean gradient of Q over $1 < \tilde{r} < 5$,

$$Q' = \frac{Q(\tilde{r} = 5) - Q(\tilde{r} = 1)}{4}, \tag{2.12}$$

can be used to monitor changes in the pattern of the stress triaxiality ahead of the crack that do not conform to a spatially uniform hydrostatic stress field of adjustable magnitude. Q' provides a measure of the robustness of the J–Q fields in the application of interest. For example, Q'=0.04 means $\Delta\sigma_{\theta\theta}$ varies by less than $0.16\sigma_0$ over the interval $1 < \tilde{r} < 5$; that is, $\Delta\sigma_{\theta\theta}$ is effectively constant over those distances. On the other hand, an $|Q'|$ much larger than 0.1 implies that the variation of $\Delta\sigma_{\theta\theta}$ over the interval $1 < \tilde{r} < 5$ can be comparable to σ_0. This is unacceptably large if the theory is employed to predict cleavage fracture which is very sensitive to changes in the hoop stress.

Table 2.1: Reference stresses, $\sigma_{\theta\theta}/\sigma_0$, for MBL problem, T/σ_0=0.

n	$r/(J/\sigma_0)$	HRR	Small Strain	Finite Strain
3	1	5.99	5.46	5.95
	2	5.04	4.53	4.72
	3	4.55	4.06	4.19
	4	4.24	3.76	3.85
	5	4.01	3.53	3.61
5	1	4.77	4.42	4.83
	2	4.25	3.90	4.06
	3	3.97	3.63	3.73
	4	3.79	3.44	3.52
	5	3.65	3.29	3.36
10	1	3.83	3.57	3.79
	2	3.59	3.35	3.52
	3	3.46	3.22	3.33
	4	3.38	3.12	3.20
	5	3.31	3.03	3.11
∞	1	–	2.83	2.50
	2	–	2.80	2.97
	3	–	2.77	2.91
	4	–	2.74	2.86
	5	–	2.71	2.82

2.5 Simplified Forms for Engineering Applications

Two simplified representations for the Q–family of fields within the forward sector have been proposed by OS. The first is

$$\sigma_{ij} = (\sigma_{ij})_{HRR} + Q\sigma_0\delta_{ij} \tag{2.13}$$

where δ_{ij} is the Kronecker delta. This form is consistent with (2.7). The second form is

$$\sigma_{ij} = (\sigma_{ij})_{SSY;T=0} + Q\sigma_0\delta_{ij} \tag{2.14}$$

which is consistent with (2.9). The physical interpretation of (2.13) and (2.14) is this: *negative (positive) Q value mean that the hydrostatic stress ahead of the crack is reduced (in-*

creased) by $Q\sigma_0$ from the J-dominant stress state, or the standard small scale yielding stress state. This interpretation is precise when $|Q'| \ll 1$.

Our numerical studies show that (2.14) provides a more accurate representation of the full range of near-tip fields so that a fracture methodology based on (2.14) with (2.9) has a greater range of validity. Q values presented in this paper are based on the definition in (2.9). To simplify subsequent discussions, the term small-scale yielding (SSY) will refer to the reference field $(\sigma_{ij})_{SSY;T=0}$ or equivalently $(\sigma_{ij})_{SSY;Q=0}$. Fields corresponding to $T \neq 0$ or $Q \neq 0$ will be explicitly stated as such.

2.6 Difference Field and Higher-Order Terms of the Asymptotic Series

The connection between the difference field and higher-order terms of the asymptotic series can be understood in the context of the MBL formulation. Here the stress fields obey the functional form

$$\sigma_{ij} = \sigma_0 \, f_{ij}\left(\frac{r}{J/\sigma_0}, \theta; Q\right) \tag{2.15}$$

which also should apply to finite-width crack geometries as long as the characteristic crack dimension L is sufficiently large compared to J/σ_0. Now, if one assumes a product dependence on the first argument in (2.15) and works with deformation plasticity theory with power law hardening behavior, then one obtains a series in $r/(J/\sigma_0)$:

$$\sigma_{ij} = \sigma_0 \left(\frac{J}{a\varepsilon_0\sigma_0 I_n r}\right)^{1/(n+1)} \tilde{\sigma}_{ij}(\theta, n) \; + \text{second-order terms} \; + \text{higher-order terms} \tag{2.16}$$

where ε_0 is a reference strain, α a material constant (equal to unity for the stress-strain response defined by (2.10)) and I_n is an integration constant. By definition, the asymptotic series beyond the first term is equivalent to the difference field since (see Section 2.2)

$$\sigma_{ij} = (\sigma_{ij})_{HRR} + \text{difference field} \; . \tag{2.17}$$

Thus the HRR field and (only) the second-order term provide a two-term approximation to the solution for the MBL problem and this point appears not always to be understood.

The higher order asymptotic analysis of Li and Wang [17] and Sharma and Aravas [18] has been extended by Xia, Wang and Shih [19]. They have obtained a five term expansion for the series in (2.16) for $n = 3$ and a four term series for $n=10$. The four term series accurately matches the radial and angular variations of the difference field given in Fig 3 and Fig. 5 by O'Dowd and Shih [13] for an $n = 10$ material. Indeed, in the forward sector $|\theta| < \pi/2$, the collective behavior of the second, third and fourth order terms is effectively equivalent to a spatially uniform hydrostatic stress state so that (2.16) can be approximated by the simpler form in (2.13).

Finally, it may be noted that an admissible range of stress states for an elastic-perfectly plastic material can be written in the form

$$\sigma_{ij} = (\sigma_{ij})_{Prandtl} + Q\sigma_0\delta_{ij} \; , \quad |\theta| \leq \pi/4 \; , \tag{2.18}$$

where $(\sigma_{ij})_{Prandtl}$ designates the Prandtl slip-line solution and the difference field corresponds simply to a uniform hydrostatic stress state scaled by Q [14,21]

2.7 J-Q Material Toughness Locus

The J-Q theory provides the quantitative framework to characterize a material's fracture resistance over a range of crack-tip stress triaxiality. The experimental determination of the toughness locus and its utilization in engineering applications are discussed below.

The competition between fracture by cleavage and ductile tearing controls the fracture resistance of ferritic steels in the ductile–to–brittle transition region. Now consider test conditions where both mechanisms are operative. Fracture by (stress–controlled) cleavage generally requires higher crack–tip constraint while ductile tearing develops at low constraint; this is illustrated by the two distinct segments to the toughness locii shown in Fig. 2.3a. Since measured toughness values generally exhibit scatter, both the lower and higher toughness locii are indicated which define bands for brittle and ductile failure. Toughness values over the full range of crack–tip constraints can be measured by using the test geometries depicted in Fig. 2.3a. As an example, deeply–cracked SE(B) specimens generate high crack–tip stress triaxiality, i.e., $Q \approx 0$. They produce driving force curves which rise steeply and therefore intersect the toughness locii within a well–defined, narrow zone of the J–Q diagram. In contrast, center–cracked panels and single–edge cracked panels loaded in tension are low constraint crack geometries. They produce driving force curves which rise with more shallow slopes and thus intersect the toughness locii over a broad zone in the J–Q diagram. The shallow driving force curves of low constraint geometries imply considerably greater scatter in cleavage toughness values (J_c), a phenomenon commonly observed in testing SE(B) specimens with small a/W ratios, for example.

Utilization of the toughness locus in fracture assessments is illustrated in Fig. 2.3b. Suppose that the material's fracture resistance under service conditions is characterized by the indicated cleavage–ductile failure band. The driving force curve for a structure of high crack–tip constraint, structure A, rises rapidly in the J–Q space so that cleavage fracture occurs when the driving force curve intersects the failure locus. In contrast a low constraint geometry such as structure B, induces a gradually rising driving force curve so that ductile tearing is the likely event at overload.

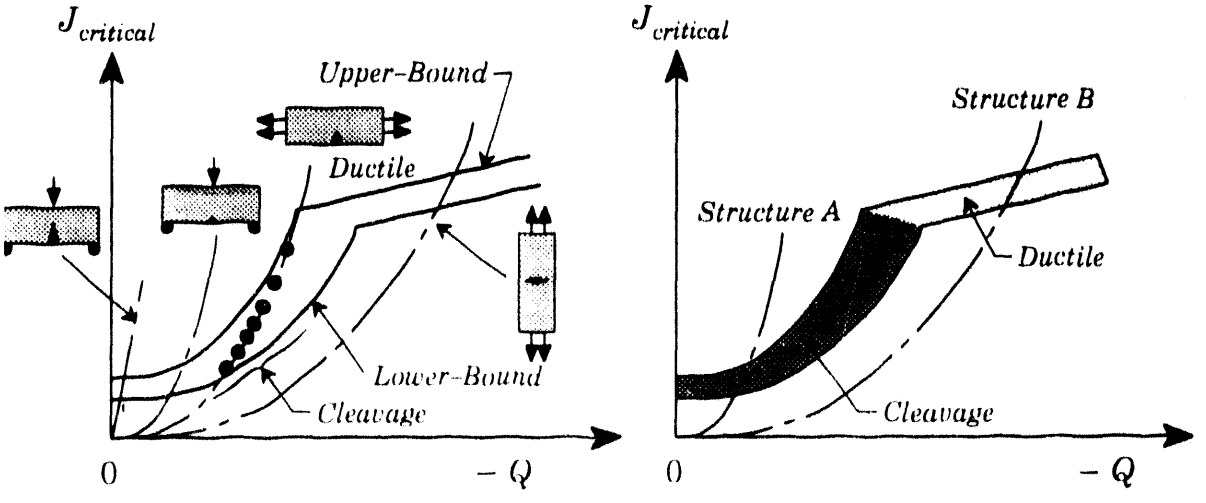

Figure 2.3 Application of the J–Q methodology in fracture assessments. (a) Laboratory testing of specimens with varying constraint to measure the material's fracture resistance. Circles indicate anticipated scatter which define upper–lower bounds. (b) Evaluation of structural flaws using measured toughness locus and predicted J–Q response for two structural configurations. Cleavage fracture is predicted for Structure A; ductile tearing is predicted for Structure B.

3. MICROMECHANICAL CONSTRAINT CORRECTIONS

Dodds and Anderson [27,28] show that by quantifying the effects of finite size on the relationship between micro–scale crack driving force (e.g. near–tip stresses and strains) and macro–scale crack driving force (e.g. J, CTOD), the apparent size effect on fracture toughness can be predicted rigorously without resort to empirical arguments. These size effects become steadily more pronounced as load increases due to the deviation of crack–tip region deformations from the small scale yielding conditions essential for single parameter fracture mechanics (SPFM) to apply. When SPFM becomes invalid, a micromechanics failure criteria is required to establish the near–tip conditions at fracture. Finite element analysis, or alternatively the near–tip stresses described by the J–Q theory, provides a means to quantify the geometry dependent relations between these micromechanical failure conditions and macro–scale crack driving force. This permits (in principle) prediction of fracture in any body from toughness values measured using standard specimens.

For steels operating at temperatures where cleavage occurs after significant plastic deformation but before the initiation of ductile growth (lower to mid–transition), attainment of a critical stress over a microstructurally relevant volume is an appropriate micromechanical failure criteria [35–37]. A number of important engineering structures can fail by this mechanism, including high strength rails, offshore oil platforms, ships, storage tanks, and nuclear pressure vessels after years of neutron irradiation embrittlement. Techniques for predicting the apparent size effects on cleavage fracture toughness developed by Dodds and Anderson are described in the following sections.

3.1 Transgranular Cleavage Mechanism

A number of micro–mechanical models for transgranular cleavage fracture have been proposed, most derive from weakest–link statistics. The weakest–link models assume the largest or most favorably oriented fracture–triggering particle controls the cleavage failure. The actual trigger event involves a local Griffith instability of a microcrack which forms at a microstructural feature such as a carbide or inclusion; satisfaction of of the Griffith energy balance occurs when the critical stress is reached in the vicinity of the microcrack. The size and location of the triggering microstructural feature(s) dictate the fracture toughness and produces the scatter routinely observed in results of cleavage fracture tests.

The Griffith instability criterion implies fracture at a critical normal stress near the crack tip; the statistical sampling aspect of the mechanism (i.e., the probability of finding a triggering micro–feature near the crack tip) suggests a dominant role for the volume of material within a process–zone over which the opening mode stress exceeds a threshold value sufficient to initiate cleavage. The probability of cleavage fracture in a cracked specimen may then be expressed in the following general form:

$$F = F[V(\sigma_1)] \tag{3.1}$$

where F is the failure probability, σ_1 is the maximum principal stress at a point and $V(\sigma_1)$ is the cumulative volume sampled over which the principal stress is equal to or greater than σ_1. This form of F applies to any fracture process controlled by maximum principal stress, not just weakest–link failure which is now being questioned [38,39]. In particular, the F criterion of (3.1) does not require material–specific assumptions for the distribution and strength of cleavage triggering particles.

Unlike other micromechanics models, the present methodology does not attempt to predict absolute values of J_c from metallurgical parameters that describe the distribution and

strength of cleavage triggering particles. Rather, the micromechanical model predicts the variation of fracture toughness with constraint changes for a given material/temperature by scaling to a reference condition. The crack–tip stress fields in a test specimen are compared to the limiting solution of SSY. A J–like parameter, denoted J_0, is obtained from this comparison to the reference solution. J_0 is the J to which the SSY model (infinite body) must be loaded to achieve the same stressed volume, and thereby the same likelihood of cleavage fracture, as in a finite body.

A critical value of J_0 represents the fracture toughness of an infinitely large specimen; the ratio of applied $J/J_0 > 1$ implies that the specimen has experienced a constraint loss that causes the commonly observed increase in measured fractured toughness.

3.2 Constraint Corrections

By employing the family of near–tip states in the form of (2.4), the maximum principal stress also has the form

$$\frac{\sigma_1}{\sigma_0} = f_1\left(\frac{r}{J_0/\sigma_0}, \theta; Q\right) . \tag{3.2}$$

For any given value of Q and θ, σ_1/σ_0 decreases monotonically once r extends beyond the finitely deformed region of $r \leq J/\sigma_0$. Rearrangement of the above expression furnishes a relation for the distance r as a function of θ and σ_1/σ_0 as

$$r = \frac{J}{\sigma_0} g_1(\theta; \sigma_1/\sigma_0, Q) . \tag{3.3}$$

Consider a particular level of the principal stress σ_1/σ_0. The area A over which the principal stress is greater than σ_1/σ_0 is given by

$$A = \frac{J^2}{\sigma_0^2} h(\sigma_1/\sigma_0; Q), \quad h = \frac{1}{2}\int_{-\pi}^{\pi} g_1^2(\theta; \sigma_1/\sigma_0, Q) d\theta . \tag{3.4}$$

The area enclosed by the contour of level σ_1/σ_0 depends on J as well as the triaxiality of the near–tip fields identified with Q. To fix ideas, let A_0 and J_0 designate the area and J associated with the Q=0 field, and let A_{FB} and J_{FB} designate the area and J associated with a crack in a finite body with $Q \neq 0$. Then we have

$$A_0 = \frac{J_0^2}{\sigma_0^2} h_0(\sigma_1/\sigma_0); \quad h_0 = \frac{1}{2}\int_{-\pi}^{\pi} g_1^2(\theta; \sigma_1/\sigma_0, Q = 0) d\theta \tag{3.5}$$

and

$$A_{FB} = \frac{J_{FB}^2}{\sigma_0^2} h_{FB}(\sigma_1/\sigma_0); \quad h_{FB} = \frac{1}{2}\int_{-\pi}^{\pi} g_1^2(\theta; \sigma_1/\sigma_0, Q) d\theta . \tag{3.6}$$

Upon initial loading of the finite body, Q=0 so that h_{FB}=h_0; compare expressions (3.5b) and (3.6b). As the load increases, plasticity spreads over the body, Q becomes non–zero, and h_{FB} begins to deviate from h_0.

For a given material and temperature, the present micromechanics model requires the attainment of equivalent stressed volumes (A_{FB} × thickness B) for cleavage fracture in different specimens. The ratio of applied J–values in a finite body and the reference Q=0 stress state that generate equivalent stressed volumes is found by equating areas in (3.5) and (3.6) to yield

$$\frac{J_{FB}}{J_0} = \sqrt{\frac{h_0(\sigma_1/\sigma_0)}{h_{FB}(\sigma_1/\sigma_0)}} \quad . \tag{3.7}$$

The results thus far are generally applicable and do not rely upon any particular form of the J–Q fields.

The J ratios are evaluated using (3.7) at each loading level and for a range of principal stress values. The ratio quantifies the size and geometry dependence of cleavage fracture toughness. Consider, for example, a test specimen that fails at J_c=200 kPa · m. Suppose the computed ratio J_{FB}/J_0=2 at fracture (J_{FB}=J_c) in the test specimen; then a very large specimen made from the same material and tested at the same temperature is predicted to fail at J_c=100 kPa · m. Similarly, the fracture toughness ratios for test specimens with the same absolute size but varying crack–depths to specimen–widths, a/W, may be quantified. The model predicts a sharp increase in fracture toughness with decreasing a/W ratio.

Self–Similar Principal Stress Contours

The character of the near–tip fields has been investigated by O'Dowd and Shih [13,14] and Xia, Wang and Shih [19]. From their results, e.g., (2.14), we write

$$\frac{\sigma_1}{\sigma_0} = f_1\left(\frac{r}{J_0/\sigma_0}, \theta; Q\right) \tag{3.8a}$$

$$= f_0\left(\frac{r}{J_0/\sigma_0}, \theta\right) + Q \tag{3.8b}$$

where the form in (3.8b) describes the fields in the forward sector, $|\theta| < \pi/2$ and $r < 5J/\sigma_0$. Detailed computational studies have shown that principal stresses of sufficiently high level, say $\sigma_1/\sigma_0 > 2.0$, are found only in the forward sector. The form in (3.8b) is applicable in the preceding micromechanics analysis if we confine attention to $\sigma_1/\sigma_0 > 2.0$. Rearranging (3.8b) yields

$$\frac{\sigma_1}{\sigma_0} - Q = f_0\left(\frac{r}{J_0/\sigma_0}, \theta\right) \quad . \tag{3.9}$$

The form in (3.9) constitutes a self–similar field for $\sigma_1/\sigma_0 - Q$. Moreover, the behavior of $\sigma_1/\sigma_0 - Q$ obeys the form governing the Q=0 reference solution, which has been determined by small–scale yielding analysis.

To understand the implications of (3.9), we focus on a particular value of σ_1/σ_0, say σ_1/σ_0=3. Consider the behavior of $\sigma_1/\sigma_0 - Q$ as the deformation level, measured by J, increases. Suppose for the moment that Q remains constant; then the contour for a fixed level of $\sigma_1/\sigma_0 - Q$, presented in the normalized distances $X/(J/\sigma_0)$ and $Y/(J/\sigma_0)$, remains unaltered in size *and* shape with increasing deformation level. As an example, the outermost contour in Fig. 3.1 corresponding to the reference solution, fixed $Q \equiv 0$, maintains its size and shape as the deformation level is increased.

Now let Q evolve with increasing deformation as happens in a finite size body. Q decreases gradually corresponding to a loss of stress triaxiality as the deformation level increases; $\sigma_1/\sigma_0 - Q$ must increase since σ_1/σ_0 is fixed. Therefore the evolution (size reduction) of a contour, associated with a fixed value of σ_1/σ_0, under increasing plastic yielding can be described by contours, associated with increasingly higher levels of $\sigma_1/\sigma_0 - Q$, governed by (3.9). The sequence of diminishing contours associated with increasing levels of $\sigma_1/\sigma_0 - Q$, corresponding to a fixed level of σ_1/σ_0=3, is depicted in Fig. 3.1 for a shallow notch SE(B) specimen.

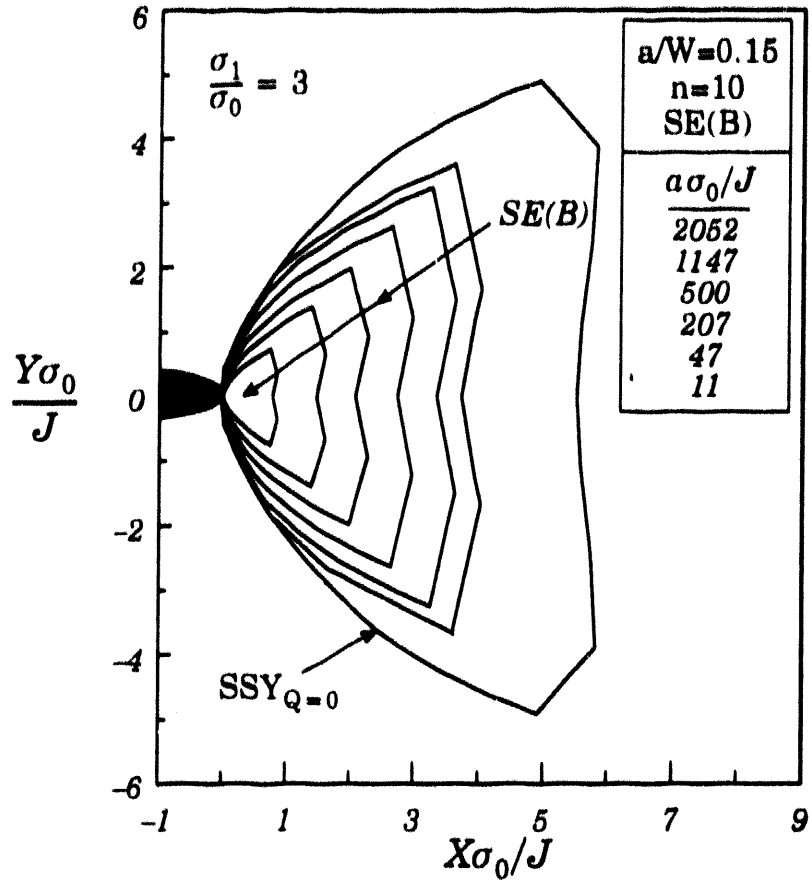

Figure 3.1 Comparison of a maximum principal stress contour for SSY$_{Q=0}$ with those for an a/W=0.15, n=10 SE(B). SE(B) contours decrease in size with increasing deformation (i.e. with decreasing $a\sigma_0/J$).

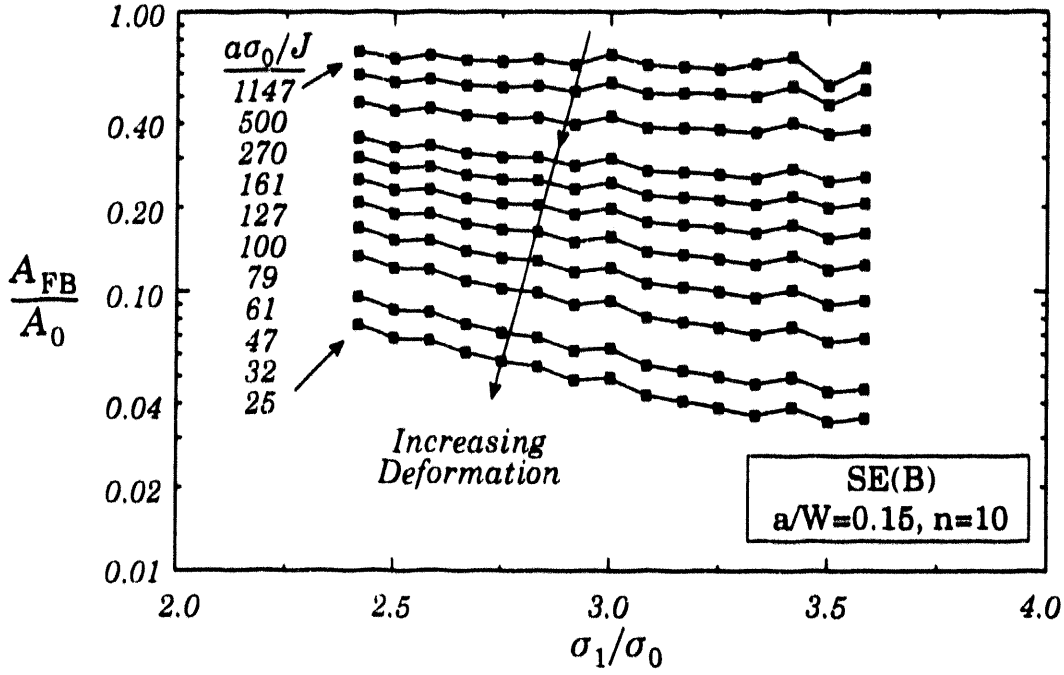

Figure 3.2 Areas within principal stress contours for an a/W=0.15, n=10 SE(B). Values are normalized by area within contour for SSY$_{Q=0}$ at same J-value.

Finally, the asymptotic studies show f_0 is nearly separable in r and θ when $r/(J/\sigma_0)$ is sufficiently small (HRR field). Consequently, the shape of a contour is maintained as its size diminishes. The self–similarity of $\sigma_1/\sigma_0 - Q$ prevails only to the extent that the J–Q form in (2.14) remains applicable.

Inverted Relationships

A specialized form of (3.3) is developed by noting the dependence of r on σ_1/σ_0 and Q involve them in the combination $\sigma_1/\sigma_0 - Q$, i.e.,

$$r = \frac{J}{\sigma_0} g_1(\theta; \sigma_1/\sigma_0 - Q) \ . \tag{3.10}$$

The results in (3.4) through (3.7) are simplified by using the form in (3.10).

The key question to resolve with this approach concerns the sensitivity of the A_{FB}/A_0 and J_{FB}/J_0 ratios to σ_1/σ_0. Let J^*_{FB} denote the value associated with $(\sigma_1/\sigma_0)^*$. Then to first–order,

$$\frac{J_{FB} - J^*_{FB}}{J_0} \propto Q\left[\left(\frac{\sigma_0}{\sigma_1}\right)^* - \left(\frac{\sigma_0}{\sigma_1}\right)\right] \ . \tag{3.11}$$

When $Q \approx 0$, the ratio J_{FB}/J_0 is insensitive to σ_1/σ_0 since the quantity in [ ] is scaled by Q. When Q is large (negative), the J_{FB}/J_0 exhibits a small sensitivity to σ_1/σ_0. The weak dependence of J_{FB}/J_0 on σ_1/σ_0 has been confirmed by analyzing the evolution of near–tip fields in common fracture specimens. Figures 3.1–3.3 provide typical results obtained through finite element modeling. The specimen is a single–edge notched bend bar containing a shallow notch, $a/W = 0.15$, with a strain hardening exponent of $n = 10$. Figure 3.2 shows the area enclosed by principal stress contours (A_{FB}). The SE(B) areas are normalized by the area, A_0, defined by the same contour of the reference solution ($Q = 0$) when loaded to the same J as the SE(B); $J_0 = J_{FB}$. The area ratios remain relatively insensitive to σ_1/σ_0 until the deformations become excessive. J_0 is calculated for each line of this figure using (3.7). J_{FB}/J_0 ratios are independent of the principal stress selected for computation over a wide range as shown in Fig. 3.3. In practice, the computation of J_{FB}/J_0 ratios is terminated when the values differ by more than 10% at the smallest and largest principal stress values as indicated on the figure. A larger deviation indicates breakdown in the similarity of the SE(B) and SSY stress fields and thus an unacceptably large dependence on the critical fracture stress.

To simplify applications of this methodology, the SSY areas within principal stress contours are expressed as a function of principal stress (σ_1) and strain hardening coefficient (n) as:

$$\frac{A_0 \sigma_0^2 \varepsilon_0^2 a^2}{J_0^2} = 10^{\beta}/250000 \tag{3.12}$$

where the curve fitting function is given by

$$\beta\left(\frac{\sigma_1}{\sigma_0}, n\right) = H_0 + H_1\left(\frac{\sigma_1}{\sigma_0}\right) + H_2\left(\frac{\sigma_1}{\sigma_0}\right)^2 + H_3\left(\frac{\sigma_1}{\sigma_0}\right)^3 + H_4\left(\frac{\sigma_1}{\sigma_0}\right)^4 \tag{3.13}$$

with fitting coefficients H_i given in Table 3.1 for a range of hardening exponents.

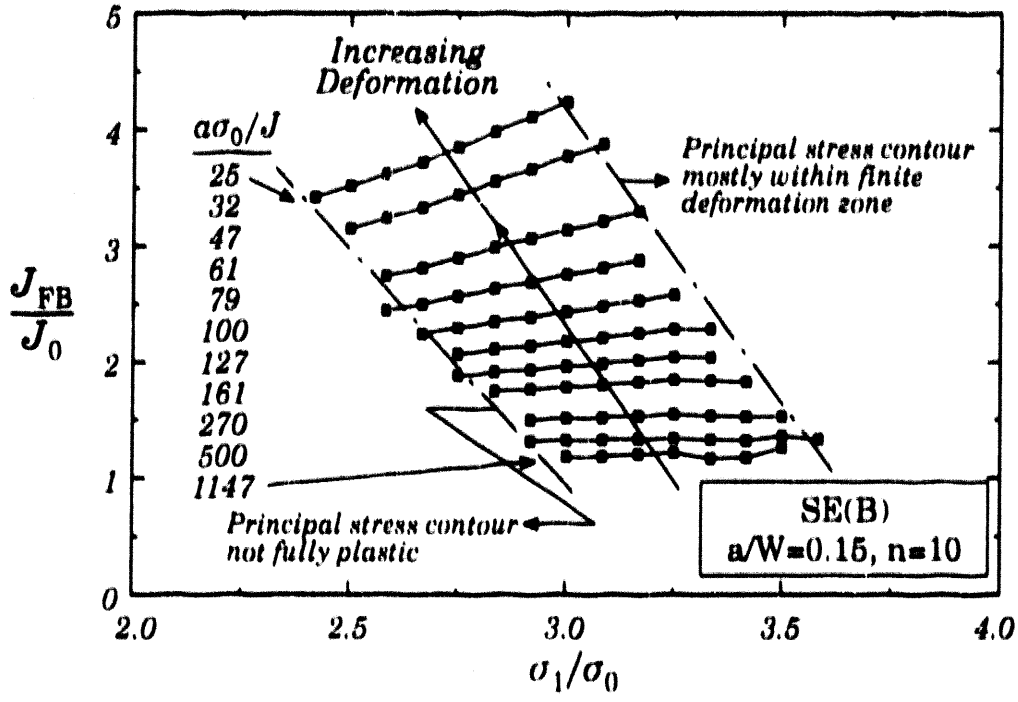

Figure 3.3 Influence of specified critical stress on the micromechanics prediction of fracture toughness variation with constraint for an a/W=0.15, n=10 SE(B).

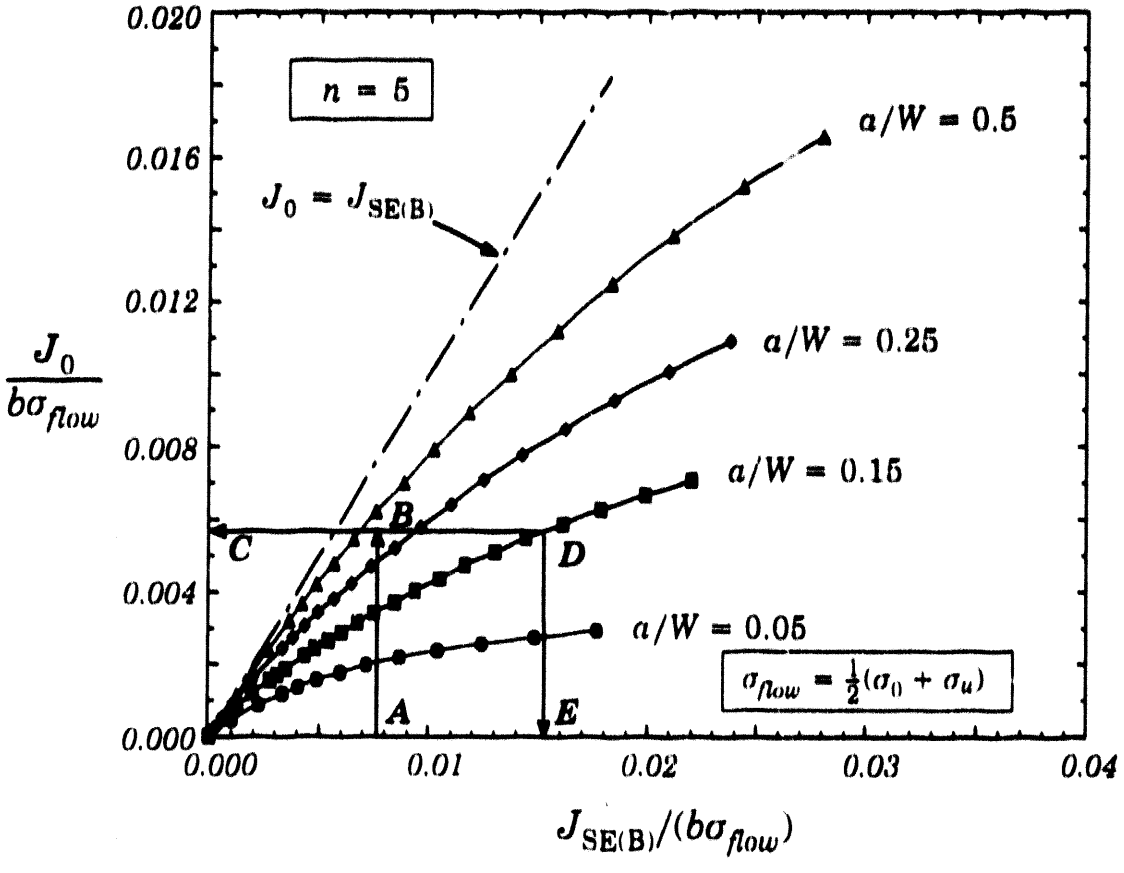

Figure 3.4 Micromechanics prediction of a/W effects on cleavage fracture toughness for an n=5, SE(B) fracture specimen.

Table 3.1: Fit coefficients for (3.13)							
n	H_0	H_1	H_2	H_3	H_4	Minimum σ_1/σ_0	Maximum σ_1/σ_0
4.0	6.4306	-2.4711	0.5037	-0.07975	0.00552	2.0	4.0
5.0	6.2579	-2.1653	0.3749	-0.06603	0.00505	2.0	4.0
10.0	7.6641	-4.3138	1.7368	-0.43685	0.03560	2.0	3.6
20.0	-3.2613	14.4338	-10.2659	3.01033	-0.34420	2.0	3.2

These expressions are obtained by curve fitting the results of small-displacement gradient, finite element analyses conducted on the MBL problem with T/σ_0=0. The material stress-strain curve employed in the analyses follows the conventional Ramberg-Osgood model given by

$$\frac{\varepsilon}{\varepsilon_0} = \frac{\sigma}{\sigma_0} + \alpha\left(\frac{\sigma}{\sigma_0}\right)^n \tag{3.14}$$

which exhibits a slightly different behavior than the elastic power-law model defined in (2.10).

3.3 Application of the Constraint Corrections in Fracture Testing

The computational procedures outlined above have been applied to generate J_{FB}/J_0 ratios for a variety of test specimens and material properties [26,27]. Figure 3.4 provides the results of such computations for SE(B) specimens having a range of a/W ratios modelled with an n=5 strain hardening material. Values of J_{FB} and J_0 are plotted on separate axes to facilitate removal of the size effect in experimental data. Points on the curves describe (J_{FB}, J_0) pairs that produce equal stressed volumes of material in the finite-size test specimen and in the SSY model. Upon initial loading, crack-tip plasticity is well contained within a surrounding elastic field and identical values for J_{FB} and J_0 correspond to the same stressed volume of material at the crack tip. This 1:1 line is shown on the figure for reference. At higher loads and as constraint relaxes under extensive plastic flow, the finite-size test specimen requires more applied-J ($J_{FB} > J_0$) to achieve the same conditions for cleavage (same stressed volume) as in SSY.

Information of this type is useful for both analysis of fracture test data and for assessing the defect integrity of structures. Path A-B-C on Fig. 3.4 illustrates the procedure to remove geometry dependence from experimental cleavage fracture toughness data (J_c value at A) by determining the geometry independent cleavage fracture toughness (J_0 value at C) corresponding to a measured J_c value. Alternatively, Fig. 3.4 permits determination of the apparent fracture toughness for an SE(B) with any a/W ratio from a known, J_0 value (path C-D-E for example).

Figure 3.5a shows the J_c values measured by Sumpter and Forbes [10] for a BS4360 43A steel (n = 5) using SE(B) specimens tested over a wide range of a/W ratios. The data readily demonstrate the dramatic increase in cleavage fracture toughness with decreasing a/W ratio. To remove the constraint effect on toughness, each experimental data point is processed using a path similar to A-B-C in Fig. 3.4 to obtain the corresponding J_0 value. Figure 3.5b shows these "constraint corrected" toughness values. The toughness variation with a/W ratio is effectively removed with this technique. The small remaining scatter in

the experimental data for different a/W ratios may be attributed to true metallurgical variations in the material and the unavoidable procedural variations in testing a large number of specimens. Application of this technique to other materials including A36, A515 and A533B [40] have been equally successful in removing the geometry dependence of J_c values.

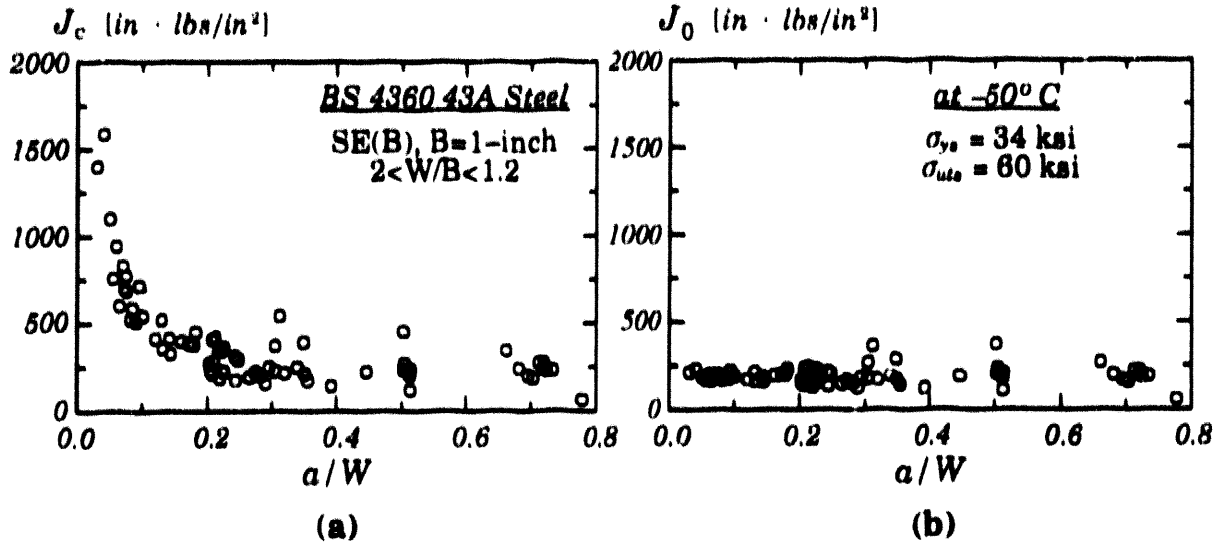

Figure 3.5 (a) Effect of initial crack depth on cleavage fracture toughness in a mild steel (Sumpter and Forbes [10]); (b) J_0 values (specimen size independent fracture toughness) calculated from experimental J_c data using the micromechanics constraint correction.

3.4 Engineering Use of *J–Q* Fields in the Micromechanics Model

When available, a J–Q description of the crack-tip stresses for a test specimen or structural component may be readily employed to generate the constraint corrections for fracture toughness of the type shown in Fig. 3.4. Here we outline a procedure that is computationally simpler than the stressed volume approach defined by (3.2)–(3.7) but which yields essentially the same result.

Figure 3.6 shows the variation of opening mode stress on the crack plane with distance from the crack tip for several deformation levels for an SE(B) specimen with a/W=0.15, n=10. The SE(B) stresses are normalized by the stress in the SSY model at the same relative distance ahead of the crack tip when the SSY model is loaded to the same J as the SE(B). Distances are normalized by the similarity length-scale $r/(J/(a\sigma_0\varepsilon_0))$. The independence of these normalized stresses with distance from the crack tip indicates again the similarity of the SSY and SE(B) stress distributions. J_0 is calculated at a number of points along each line on this graph as the J value required in the SSY model to achieve the same opening mode stress as in the finite body. The following equation is solved iteratively for J_0 using a simple nonlinear root solver:

$$\frac{(\sigma_{\theta\theta})_{FB}}{\sigma_0} = \frac{(\sigma_{\theta\theta})_{SSY}}{\sigma_0}, \quad \text{at } \theta = 0 \tag{3.15}$$

where a closed-form fit to the crack-plane stresses in SSY is given by

$$\frac{(\sigma_{\theta\theta})_{SSY}}{\sigma_0} = G_1(\hat{r})^{G_2}\exp(G_3\hat{r}) \tag{3.16}$$

where

$(\sigma_{\theta\theta})_{FB}$ stress at distance r from the tip at loading J_{FB} in finite body;

$\hat{r}$ normalized distance from tip: $\hat{r} = \dfrac{r}{J_0/a\sigma_0\varepsilon_0}$;

G_i SSY fit coefficients summarized in Table 3.2.

The finite-body stresses needed in (3.15) are given by

$$\frac{(\sigma_{\theta\theta})_{FB}}{\sigma_0} = \frac{(\sigma_{\theta\theta})_{SSY}}{\sigma_0} + Q(r) \tag{3.17}$$

where the SSY term in (3.17) is given by the expression on the right side of (3.16) with J_0 replaced by J_{FB}. The potential for a small radial dependence of Q under large-scale yielding is included in (3.17). The J_{FB}/J_0 ratio is computed over a range of distances ahead of the tip at each load level, typically $1\text{–}2 \le r/(J/\sigma_0) \le 4\text{–}5$ with the specific values dependent upon the degree of strain hardening. The objective is to sample the stress field at locations outside the finitely deformed zone, $r \ge 2\delta$, but within the process zone applicable for cleavage fracture. Herrens and Read [41]; Miglin, et al. [42] determined fractographically the limit of the cleavage process zone as $r \approx 8\delta$.

Figure 3.7 shows the J_{FB}/J_0 ratios computed using this approach for each loading level indicated in Fig. 3.6. The similarity between the SSY and finite-body stress distributions makes the specific r/δ value used in the calculations unimportant over a wide range of deformation. In practice, J_0 calculated by (3.15) is considered valid when the values calculated at $r=3\delta$ and at $r=8\delta$ differ by less than 10%. A larger deviation signals too great a dependence of J_0 on the critical distance selected and, consequently, a breakdown of the method. Figure 3.8 compares the constraint corrections for fracture toughness computed using the simpler approach with crack-plane stresses given by a J–Q analysis and the more complex approach requiring computation of stressed volumes within principal stress contours. Differences in the constraint corrections are insignificant for engineering applications..

Table 3.2: Fit coefficients for $SSY_{Q=0}$ in (3.16)

n	G_1	G_2	G_3	n	G_1	G_2	G_3
4.0	0.842	-0.2817	-0.926	10.0	1.801	-0.1169	-5.169
5.0	1.077	-0.2312	-2.181	18.0	2.219	-0.0668	-6.165
7.0	1.422	-0.1687	-3.952	50.0	2.646	-0.0255	-6.810

4. SURFACE CRACKS UNDER BIAXIAL LOADING

Bass, et. al [43] recently outlined current deficiencies in the understanding of constraint effects on the crack-initiation toughness of shallow surface cracks subjected to uniaxial and biaxial far-field tension loadings. In nuclear applications, the internal pressure alone generates a 1:0.5 biaxial tension loading while the pressurized thermal shock (PTS) event may generate the more severe case of 1:1 biaxial tension in addition to a locally severe bending field. The very few testing programs (see Bass, et. al [43] for a review) conducted on biaxially loaded surface cracks report a 25–40% reduction in toughness values (K_c) relative to the values obtained from SE(B) and C(T) specimens containing cracks of similar relative depth. These results imply a significantly increased crack-tip constraint under biaxial loading relative to uniaxial loading. Moreover, the biaxial test results appear to negate the now well established increases in fracture toughness for shallow notch, SE(B) specimens relative to deep notch toughness.

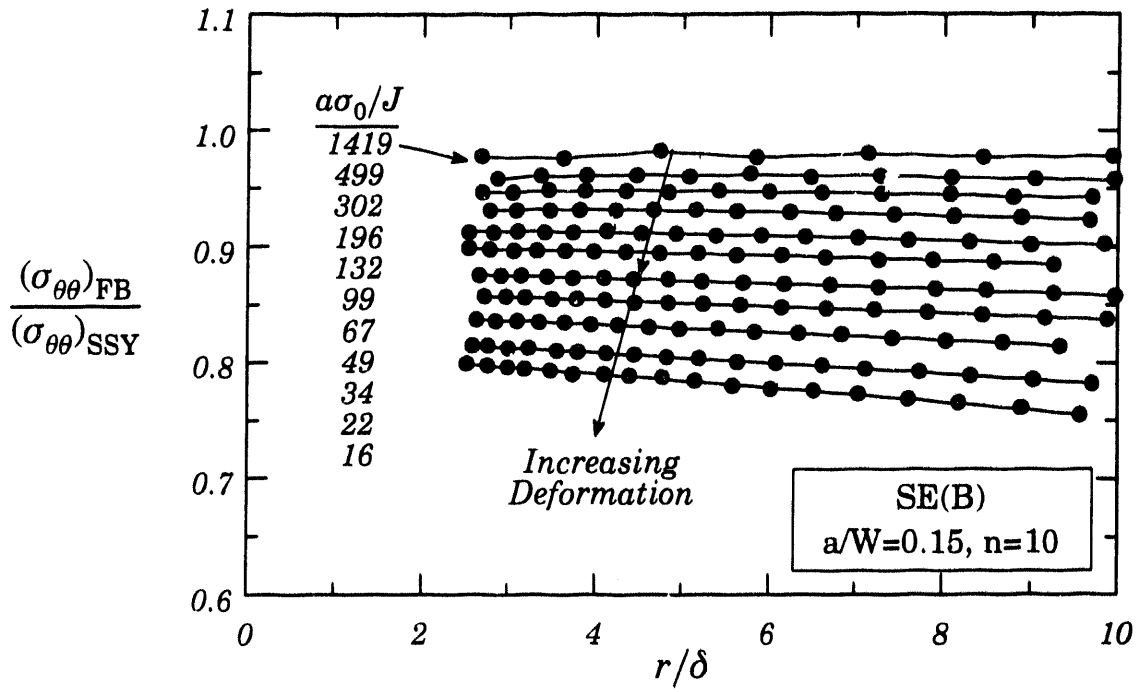

Figure 3.6 Opening stress on the crack plane normalized by $SSY_{Q=0}$ at same J-applied. a/W=0.15, n=10 SE(B).

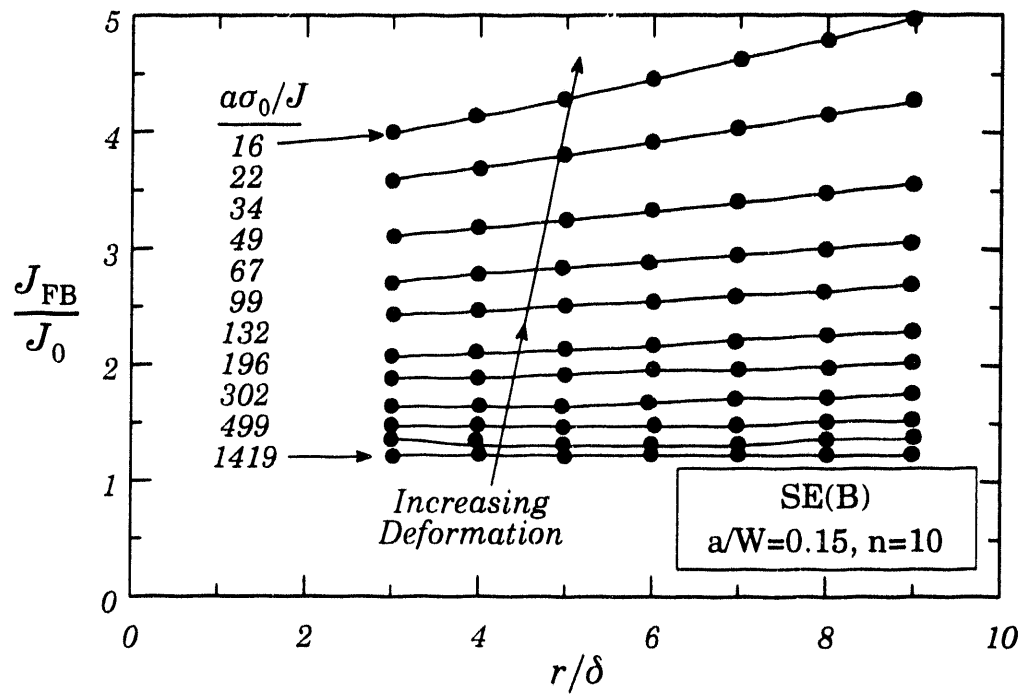

Figure 3.7 Variation of fracture toughness predicted by the micromechanics model using crack-plane stress shown in Fig. 3.6. a/W=0.15, n=10 SE(B).

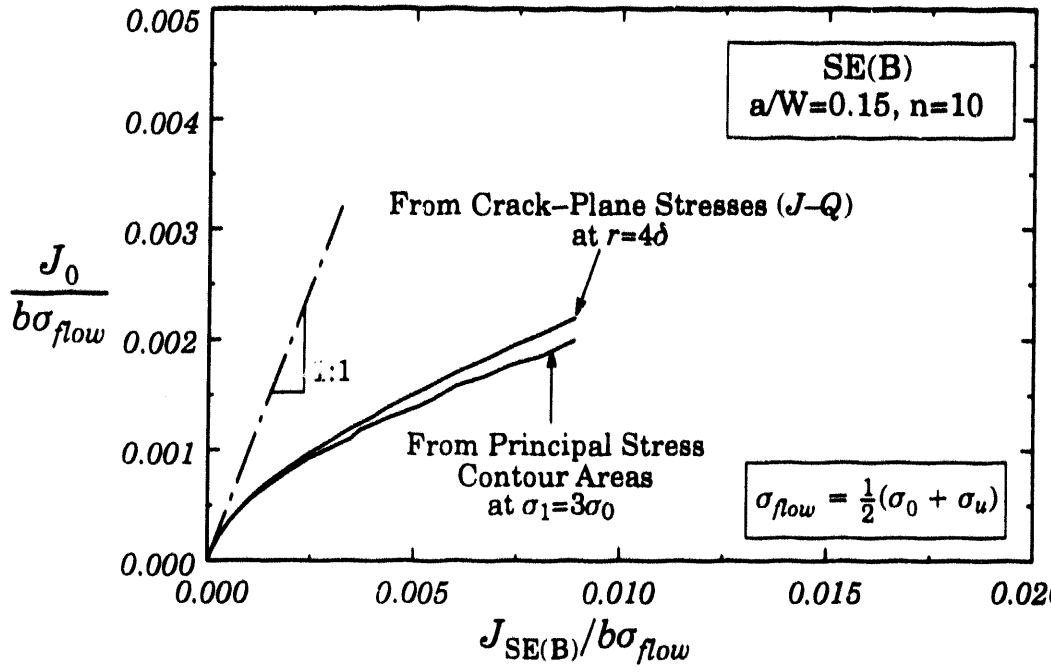

Figure 3.8 Comparison of J_0 values determined using the crack–plane stress from J–Q and stressed volume techniques for an a/W=0.15 n=10 SE(B).

Researchers currently frame discussions of the biaxial *vs.* uniaxial loading influence on constraint in terms of *in–plane* and *out–of–plane* effects. Shallow crack SE(B) specimens, for example, exhibit a strong in–plane effect on constraint; the small crack depth relaxes crack–tip stresses when plastic zones sense the nearby free surfaces behind the crack. Out–of–plane effects refer to tensile stresses acting parallel to the crack front. While these stresses exist and vary along the front of uniaxially loaded specimens, test programs demonstrate the much smaller influence of thickness (B), which governs the out–of–plane stress, relative to the crack–depth effect once B exceeds a significant fraction of the specimen width (W), usually $B \geq W/2$. The biaxial test results suggest that mechanically applied, remote out–of–plane stress restores crack–tip triaxiality lost to the shallow–crack in–plane effect. Strength–of–materials type models have been proposed to examine the interaction of in–plane and out–of–plane stresses. Such methods are severely limited since they rely on superposition of stresses which does not apply under elastic–plastic conditions at the crack tip.

The scarcity of testing programs that address biaxial loading effects on fracture toughness and their significant complexity (large plate specimens, scale–model pressure vessels, thermo–mechanical loading, etc.) leave open an experimental resolution of this issue. However, the J–Q and micromechanics concepts described in Sections 2 and 3 provide the analytical framework to clarify the in–plane and out–of–plane effects on crack–tip stress fields (using J–Q) and on cleavage fracture toughness (using micromechanics).

4.1 Part–Through Surface Crack Model

Figure 4.1 shows a flat plate containing a part–through surface crack considered in an initial analytical investigation. The semi–elliptical surface crack has geometric parameters a/t=0.25, $2c/a$=6.0. ϕ=0 and ϕ=90° correspond to lines along the free surface and directly ahead of the front at the point of maximum depth. Radial distances ahead of (and normal

to) the crack front are denoted r. The plate is loaded by a remote uniaxial tension, σ_{zz}^{∞} in one case, and by a remote biaxial tension, $\sigma_{zz}^{\infty} = \sigma_{xx}^{\infty}$ in the second case. The material response is modeled with small–strain, deformation plasticity; the uniaxial flow properties obey a Ramberg–Osgood relationship with hardening exponent n=10 and α=1.

Symmetry conditions enable consideration of only one–quarter of the full specimen in the finite–element model as shown if Fig. 4.1. The element mesh contains 1980 20–node, isoparametric elements and 9800 nodes. The level of mesh refinement in r at each point along the crack front matches the refinement employed in previous models [14,27] of two–dimensional specimens. The innermost ring of elements incident on the crack front contains degenerate 20–node elements with edge nodes retained in the mid–point location. Initially coincident nodes along the crack front are unconstrained to permit blunting deformations. Uniform reduced integration (2x2x2) in all elements performed satisfactorily in these models.

The intensity of local deformation at each point s along the front is given by [44]

$$J_{local}(s) = \lim_{\Gamma_\varepsilon \to 0} \int_{\Gamma_\varepsilon} \left[W n_1 - \sigma_{ij} \frac{\partial u_i}{\partial x_1} n_j \right] d\Gamma \tag{4.1}$$

where, W denotes the strain–energy density, Γ_ε is a vanishingly small contour in the principal normal plane at s, n is a unit normal vector to Γ_ε, σ_{ij} and u_j are Cartesian components of stress in the crack front coordinate system. Numerical evaluation of (4.1) is accomplished with a domain integral method [44,45].

Figure 4.2 shows the overall load–displacement response in terms of Crack Mouth Opening Displacement (CMOD). Under SSY, CMOD remains unaffected by the biaxial loading. With the onset of gross plasticity, however, the biaxial loading provides a significant stiffening effect; at σ^{∞}/σ_0=1.1 the biaxial CMOD is only 55% of the uniaxial value.

A similar effect of the biaxial loading on the J–values can be seen in Fig. 4.3. At the point of maximum crack depth (ϕ=90°), the uniaxial J–value is twice the biaxial value when both models are loaded to σ^{∞}/σ_0=1.1. The comparison of biaxial and uniaxial distributions for J_{local} along the crack front is shown in Fig. 4.4. The distributions are identical under SSY but reveal considerable differences under large scale yielding in the region of sharpest front curvature ($\phi < 30°$). The biaxial loading depresses the level of J relative to the uniaxial loading in this region of the crack front.

4.2 Crack–Front Stress Triaxiality

Figure 4.5 shows the behavior of near–tip stress triaxiality along radial lines normal to the crack front at ϕ=17° and 90° for the uniaxial and biaxial loadings. At ϕ= 90°, the variation of Q with r remains negligible up to the maximum applied load of σ^{∞}/σ_0=1.1. At loadings $\sigma^{\infty}/\sigma_0 \leq 0.4$, the model lacks sufficient refinement to resolve stresses over the region $2 \leq r/(J_{local}/\sigma_0) \leq 5$. The crack–tip constraint steadily decreases with increased global loading and plastic deformation (Q becomes more negative). The biaxial loading exerts only a minor influence toward reducing the constraint loss under large–scale yielding at ϕ= 90°.

The ϕ=17° location on the crack front has high curvature and lies a small distance from the traction–free face of the plate (see Fig. 4.1). Under increased uniaxial loading, Q steadily decreases indicating a gradual loss of stress triaxiality. Q develops a weak dependence on radial distance as the maximum applied loading is approached; Q varies by ± 6.7% from the mean value over $2 \leq r/(J_{local}/\sigma_0) \leq 5$ at σ^{∞}/σ_0=1.1. The biaxial loading maintains

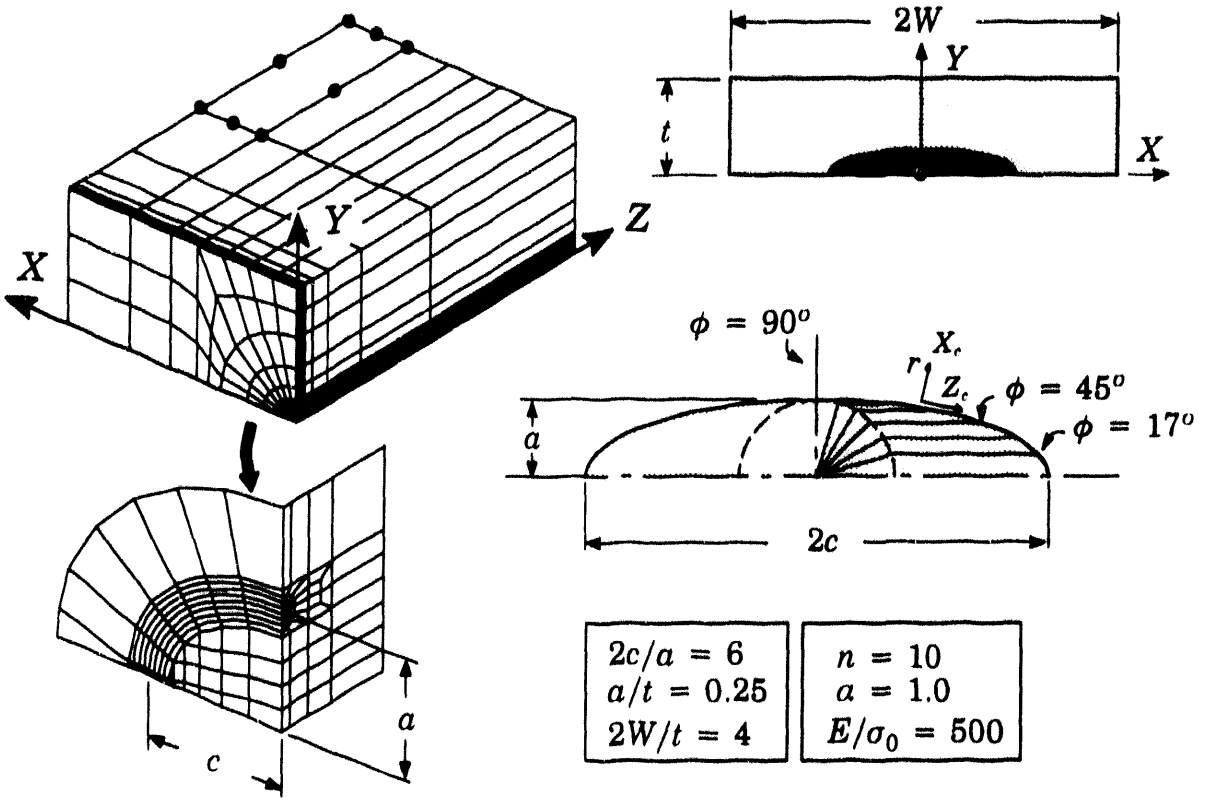

Figure 4.1 Finite–element model for investigation of constraint in surface cracked plate subjected to uniaxial and biaxial remote tension loadings.

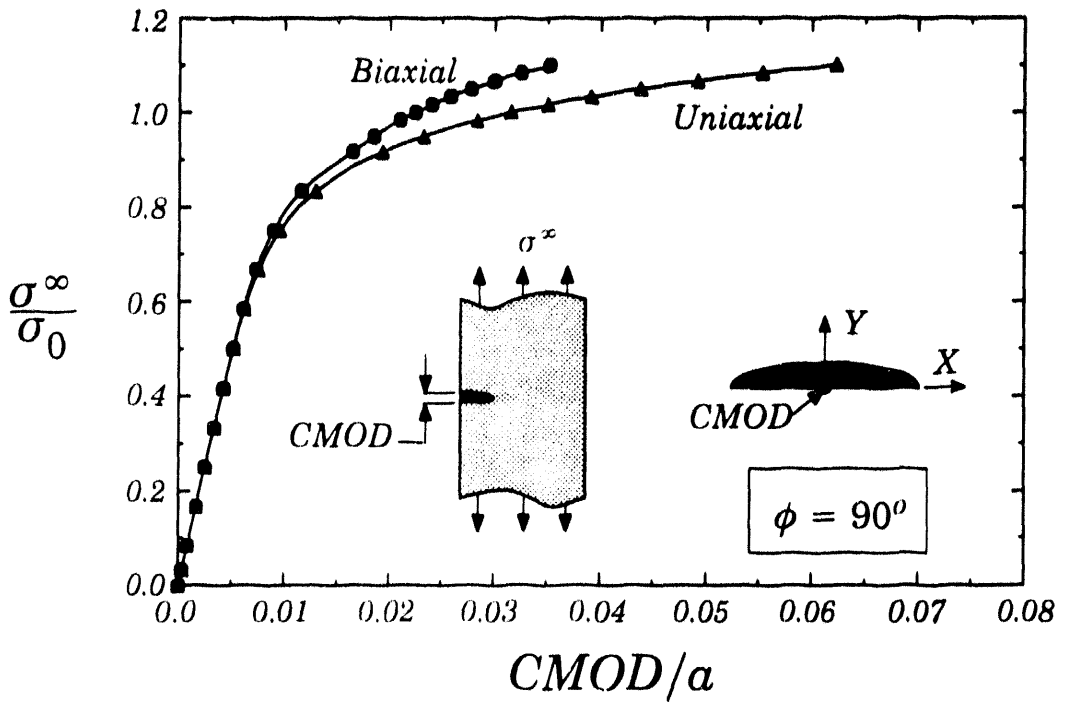

Figure 4.2 Global load–displacement (Crack Mouth Opening Displacement, CMOD) response for surface cracked plate.

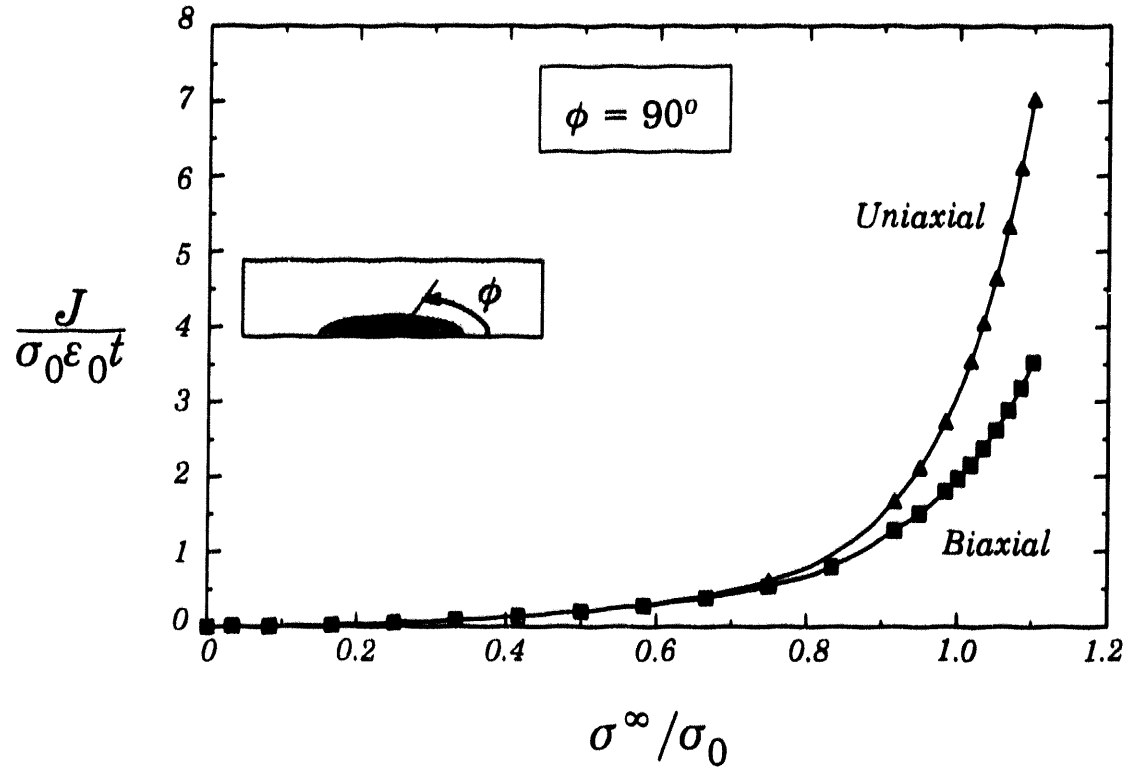

Figure 4.3 *J*–integral values at point of maximum crack depth for uniaxial and biaxial tension loading of surface cracked plate model.

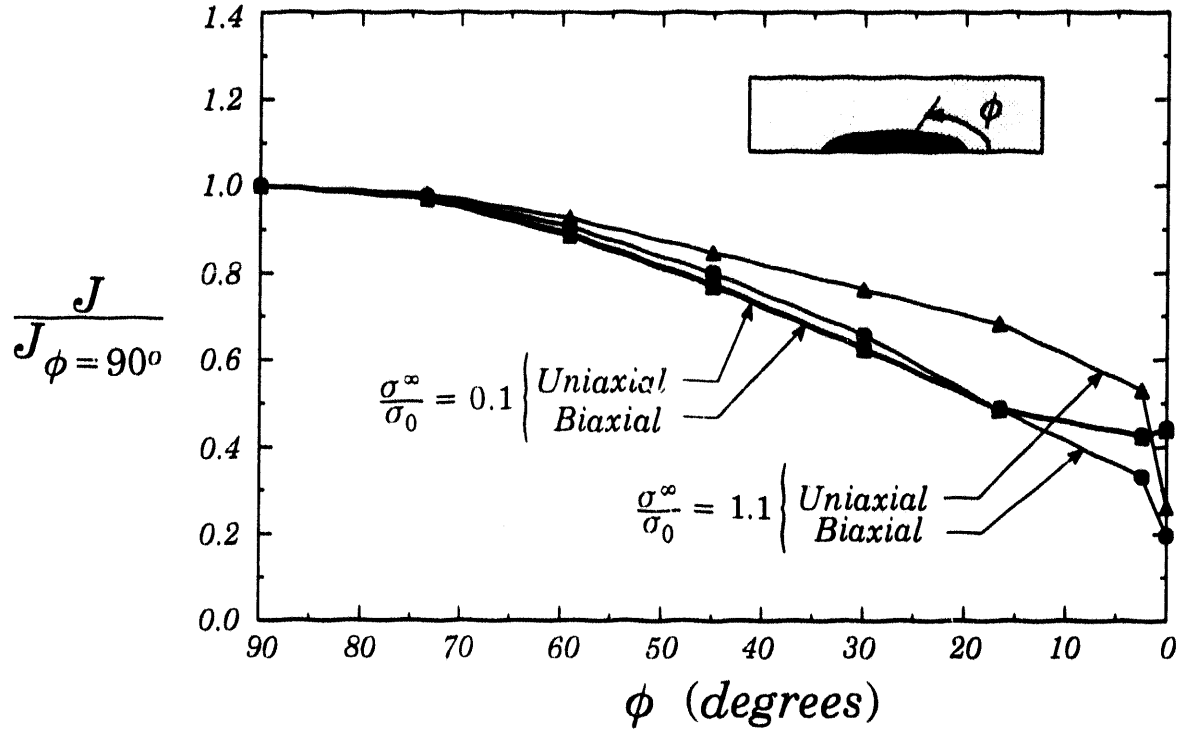

Figure 4.4 *J*–integral along crack front at SSY and LSY load levels normalized by corresponding *J* at maximum crack depth for each loading level.

stress triaxiality at significantly higher levels as plastic flow progresses from well–contained through large–scale yielding. The radial dependence increases to ± 17% over $2 \leq r/(J_{local}/\sigma_0) \leq 5$ at σ^∞/σ_0=1.1. The radial dependence of Q when large–scale yielding prevails is induced, in large part, by the nearby free surface.

Figure 4.6 summarizes the J–Q description of stress triaxiality at different points along the crack front. Both the uniaxial and biaxial cases are taken to the same load level, i.e., σ^∞/σ_0=1.1. Q is evaluated at $r/(J_{local}/\sigma_0) = 2$ ahead of the crack front. Under uniaxial loading, Q values for $\phi \geq 45^\circ$ saturate at –0.8 for large–scale yielding. Near the free surface, ϕ=0, stress triaxiality is reduced to a level approaching the yield stress even at relatively low loads ($Q \rightarrow$ –2.0). Biaxial loading promotes essentially uniform stress triaxiality, Q= –0.7, over much of the crack front. However, at the ϕ=2.4° and 17° locations, the influence of biaxial loading is very pronounced. Final Q–values for these two locations reveal an increase in stress triaxiality on the order of the yield stress relative to the uniaxial loading response.

For crack front locations $\phi \rightarrow 0$, the mechanically imposed biaxial stress, σ^∞_{xx}, corresponds to a positive T–stress (a stress parallel to X_c, see Fig. 4.1). Under SSY conditions in the surface–cracked plate, the T–stress elevates Q slightly above zero in accord with the discussion in Section 2. Under LSY conditions, the T–stress brings about a higher level of stress triaxiality near the free surface; however, the Q–values are still negative indicating a loss of stress triaxiality relative to the high constraint, reference condition of plane–strain $SSY_{T=0}$. Thus, at an identical value of applied–J in uniaxial and biaxial loading, the the crack front region with maximum opening mode stress occurs near $\phi \approx 17^\circ$ for the biaxial loading. However, the magnitude of remote loading required to generate the equivalent J–values is larger for the biaxial case (see Fig. 4.3 and 4.4; note the overall larger J–values for uniaxial loading).

4.3 Matching Structural and Test Specimen Constraint

Consider the fracture assessment of a structural configuration which is modeled adequately by the surface cracked plate subjected to uniaxial or biaxial loading. The J–Q and micromechanics concepts provide quantitative frameworks to select a corresponding laboratory test specimen, an SE(B) for example, which produces the same crack front constraint as the structural configuration. The cleavage fracture toughness, J_c, measured with such a specimen should then be employed in fracture assessments of the structure. These two approaches are illustrated in Figs. 4.7 and 4.8.

Figure 4.7 compares the computed J–Q driving force curves for SE(B) specimens having a range of a/W ratios with the driving force curves at ϕ=90° (uniaxial loading) and ϕ=17° (biaxial loading) for the surface cracked plate. An SE(B) with a/W=0.05 best matches the evolution of stress triaxiality for the uniaxially loaded plate while an $a/W \approx 0.20$ best matches triaxiality for the biaxial loading. By using the J–Q description of crack front stresses as input to the micromechanics model (as described in Section 3.4), the effects of constraint on cleavage fracture toughness for the surface cracked plate and SE(B) specimens of selected a/W ratios are predicted as shown in Fig. 4.8. An SE(B) with a/W=0.05 very closely matches the uniaxial loading curve for ϕ=90° while an $a/W \approx 0.20$ SE(B) specimen closely matches the biaxial loading curve for ϕ=17°.

The potential advantage offered by the micromechanics approach becomes clear from Fig. 4.8. It is not necessary to determine which laboratory specimen matches the structural constraint; rather, any a/W ratio SE(B) can be tested to measure the size independent fracture toughness, J_o, from which the structural toughness, J_c, for each loading case (uniaxial

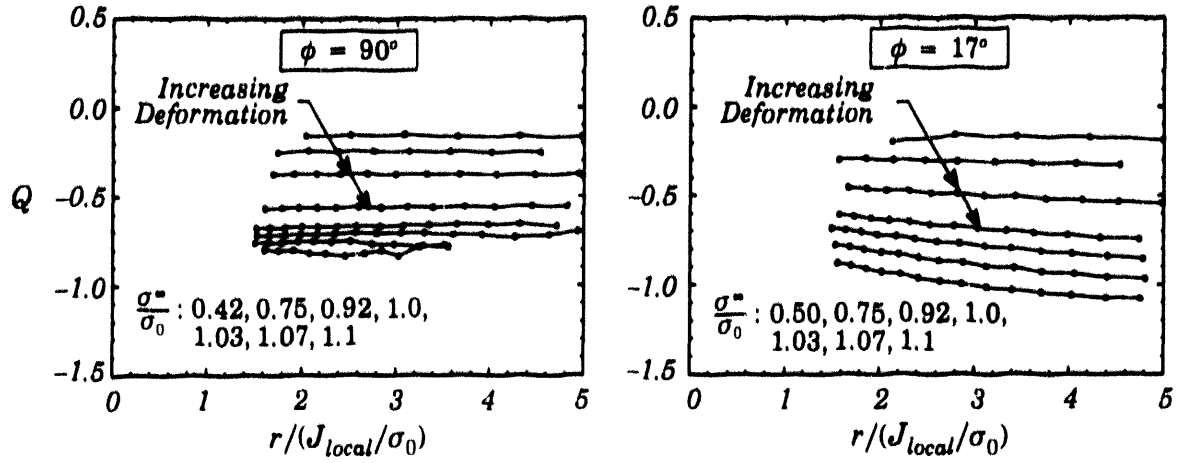

(a) Uniaxial Tension

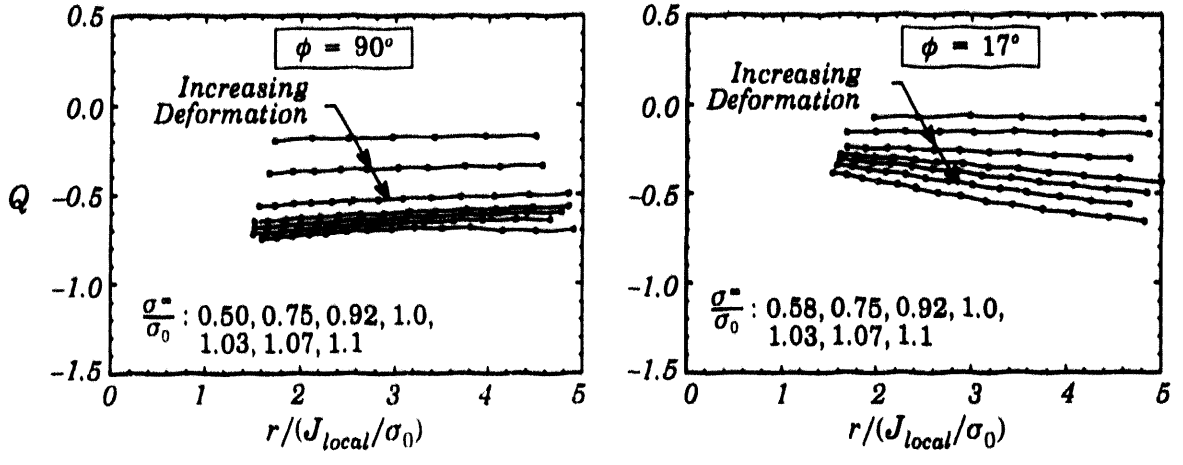

(b) Biaxial Tension

Figure 4.5 Evolution of stress triaxiality in surface cracked plate ahead of crack tip at ϕ=90° and 17°.

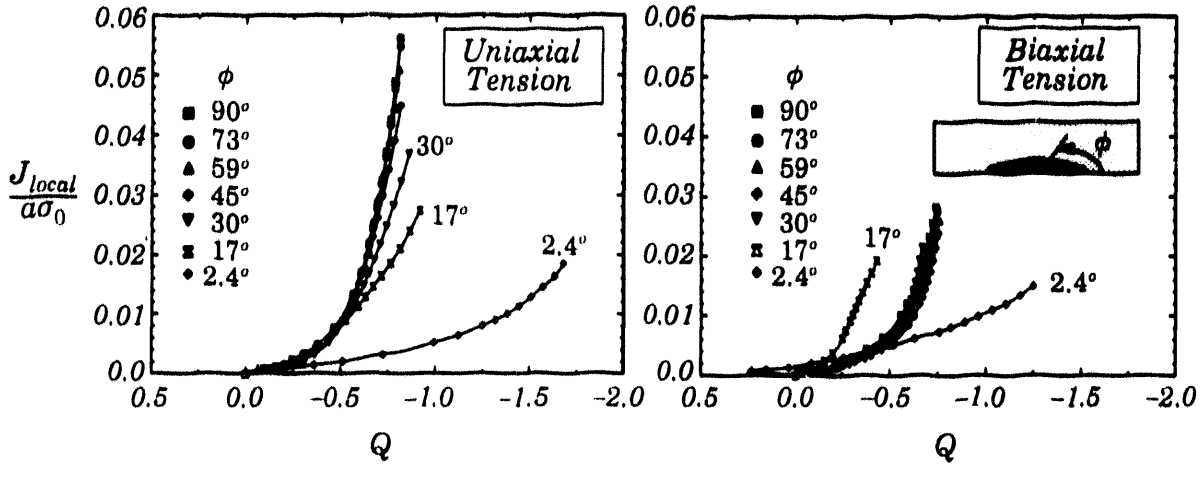

Figure 4.6 Evolution of stress triaxiality in surface–cracked plate with increasing local deformation, as measured by $J_{local}/a\sigma_0$, along radial lines emanating from different points on the crack front. Q is evaluated at $r/(J_{local}/\sigma_0)$=2. Both geometries are loaded to the same level $\sigma\infty/\sigma_0$=1.1.

and biaxial) is predicted from the corresponding structural response curves shown in Fig. 4.8. When deep notch SE(B) data is already available, from material qualification tests for example, no additional shallow–crack testing is needed to apply the micromechanics approach. *Such applications of the micromechanics model imply that the same fracture mode (cleavage) occurs in both the laboratory specimen and the structural configuration.* The current model cannot predict the effects of specimen geometry and loading mode on the fracture toughness (J_{Ic}) which characterizes the initiation of stable, ductile tearing. However, the model does predict when fracture by cleavage becomes highly unlikely. Consider the response for the a/W=0.5 SE(B) specimen shown in Fig. 4.8; if the J_0 measured with this specimen is sufficiently large, the driving force curve for a shallow notch SE(B) specimen or for the surface–cracked plate never attain such a large value of J_0. The model predicts that cleavage, without prior tearing, does not occur, i.e., the interaction of crack–tip plastic zones and nearby free surfaces prevents near–tip stresses from achieving the critical levels needed to trigger cleavage.

The SE(B) responses employed in this discussion are obtained from 2–D, plane–strain computations. In such cases, constraint matching with a structural configuration is accomplished by varying the absolute specimen size and/or the a/W ratio. For the same a/W ratio, large specimens increase constraint at a given J–value relative to small specimens. Similarly, for a fixed specimen size, large a/W ratios increase constraint at a given J–value relative to small a/W ratios. Different thicknesses provide yet another means to vary constraint in test specimens, although experimental and computational evidence suggest the thickness effect is much less significant than absolute size or a/W effects when specimens of usual proportions are employed ($B \geq W/2$).

5. CONCLUSIONS

Our investigations have shown that two–parameters, J and Q, suffice to characterize the full range of near–tip environments at the onset of fracture. J sets the size scale of the zone of high stresses and large deformations while Q scales the near–tip stress level relative to a high triaxiality reference stress state. The structure of the J–Q fields has been established by higher–order asypmtotic analysis and full–field numerical calculations within the context of the modified boundary layer formulation. Detailed analyses of finite–width, crack bodies show that the J–Q fields dominate over physically significant size scales, i.e. they represent the environment in which the ductile and brittle mechanisms are operative. Therefore, the J–Q fields furnish the theoretical basis to address onset of clevage fracture, the initiation of ductile tearing, as well as the competition between cleavage fracture and ductile tearing. Indeed, the J–Q theory can provide a framework which allows the cleavage and ductile toughness loci to be measured and utilized in engineering applications.

Constraint effects on cleavage fracture have been the subject of a number of recent studies. The J–Q theory together with a micromechanical model for cleavage predicts that cleavage fracture toughness depends sensitively on near–tip stress triaxiality. The cleavage toughness locus has been measured, for example by Sumpter and Forbes [10] for a mild steel and by Kirk, et al. [40] for A515 steel. The toughness data do show a strong dependence on Q. Toughness elevations of about 5 or so have been measured in low constraint crack geometries. Constraint is also expected to exert an influence on the initiation of ductile tearing; however, mechanistic studies of ductile tearing and the limited experimental data suggest that ductile initiation toughness depends less strongly on stress triaxiality. Systematic experimental studies are required to quantify constraint effects on the initiation of ductile tearing.

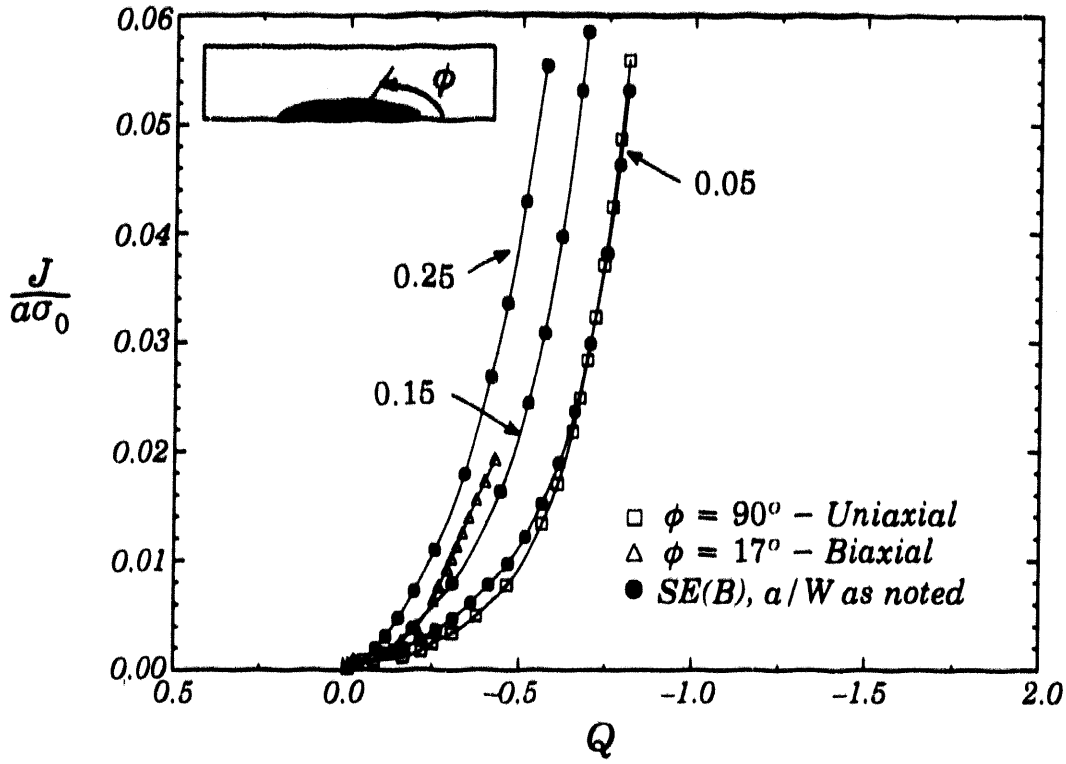

Figure 4.7 Application of J–Q methodology to select a/W ratio in SE(B) specimen for testing that matches stress triaxiality in structural configuration represented by a surface cracked plate loaded in uniaxial or biaxial tension.

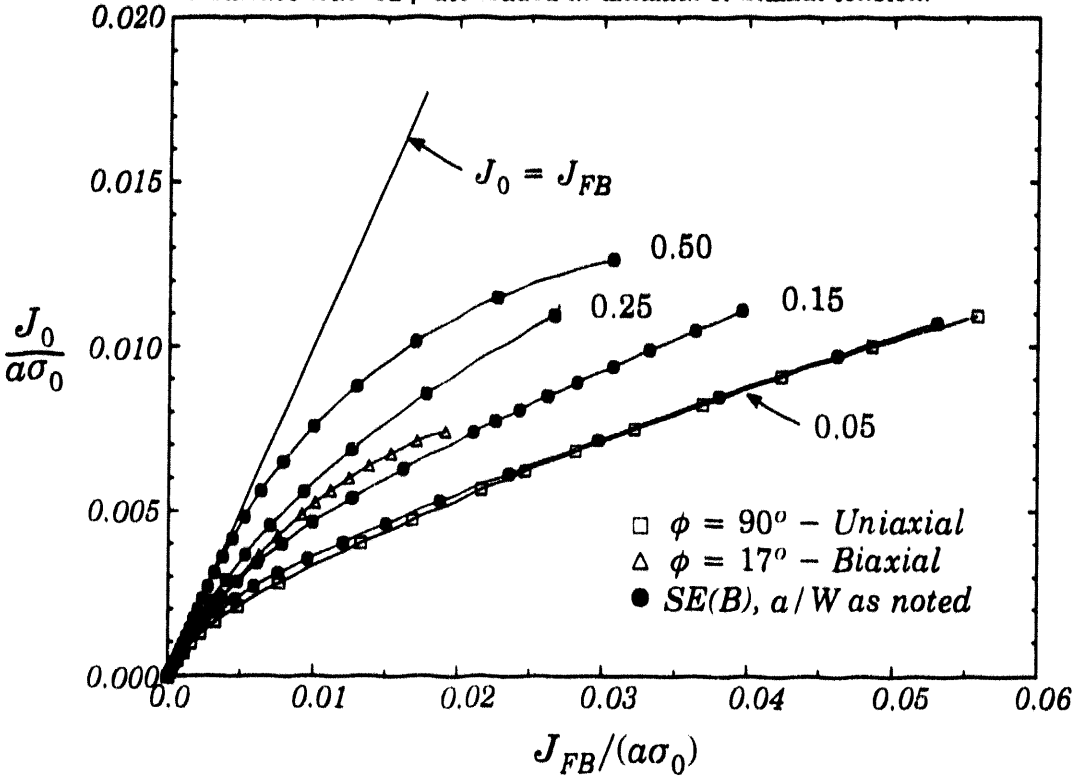

Figure 4.8 Application of micromechanics methodology to select a/W ratio in SE(B) specimen for testing that matches effective driving force for cleavage fracture in structural configuration represented by a surface cracked plate loading in uniaxial or biaxial tension.

The experimental determination of a toughness locus can become very costly, requiring considerable material and testing time, especially if toughness data are required for a number of temperatures. An alternative approach for cleavage fracture appears feasible. The constraint correction procedure advocated here uses a limited experimental database to predict cleavage toughness over a broad range of stress triaxiality. The procedure has been applied to several series experiments and the results are very encouraging. The procedure and its theoretical basis are discussed in Section 3. Though it has not been discussed, a similar procedure can be developed (in principle) for the initiation of ductile tearing. As is the case for cleavage fracture toughness, the procedure can be used in conjunction with the J–Q fields to determine geometry– and load–dependent ductile fracture toughness data.

Procedures such as the one in Section 3 hold promise for predicting toughness loci for cleavage and ductile fracture and can facilitate engineering applications of the J–Q approach. However, the incorporation of micromechanics failure criterion in a fracture mechanics methodology is not without its limitations. It is essential that the failure criterion be a sufficiently realistic model of the actual fracture process. In applications where cleavage and ductile failure modes are operative, competing failure processes also must be considered. Unfortunately, the initiation of ductile tearing is also a process involving several competing mechanisms, such as void formation *vs.* void growth and coalescence, void sheet formation and shear localization, and as yet there is no general agreement as to the essential features of a realistic model. Micromechanical models for ductile tearing are necessarily more complex, involving more metallurgical properties for a material, than the models for cleavage fracture. Considering the enormous economic payoffs, however, greater efforts are warranted to establish realistic, robust micromechanical models for ductile fracture.

ACKNOWLEDGEMENTS

This investigation was supported by grants from the Nuclear Regulatory Commission, the David Taylor Research Center and the Office of Naval Research. The authors acknowledge the many useful discussions and contributions of their colleagues Prof. Ted Anderson, Drs. Noel P. O'Dowd and Mark T. Kirk.

REFERENCES

1. Hutchinson, J.W., "Fundamentals of the Phenomenological Theory of Nonlinear Fracture Mechanics," *Journal of Applied Mechanics*, Vol. 50, pp. 1042–1051, 1983.
2. Rice, J.R., "A Path Independent Integral and the Approximate Analysis of Strain Concentration by Notches and Cracks," *Journal of Applied Mechanics*, Vol. 35, pp. 379–386, 1968.
3. Rice, J.R., and Rosengren, G.F., "Plane Strain Deformation Near a Crack Tip in a Power–Law Hardening Material," *Journal of Mechanics and Physics of Solids*, Vol. 16, pp. 1–12, 1968.
4. Hutchinson, J.W., "Singular Behavior at the End of a Tensile Crack in a Hardening Material," *Journal of Mechanics and Physics of Solids*, Vol. 16, pp. 13–31, 1968.
5. McMeeking, R.M., and Parks, D.M., "On Criteria for J–Dominance of Crack–Tip Fields in Large–Scale Yielding," *Elastic-Plastic Fracture, ASTM STP 668*, J.D. Landes, J.A. Begley, and G.A. Clark, Eds., American Society for Testing and Materials, Philadelphia, Pennsylvania, pp.175–194, 1979.
6. Shih, C.F. and German, M.D., "Requirements for a One Parameter Characterization of Crack Tip Fields by the HRR Singularity," *International Journal of Fracture*, Vol. 17, No. 1, pp. 27–43, 1981.

7. Al-Ani, A.M., and Hancock, J.W., "*J*-Dominance of Short Cracks in Tension and Bending," *Journal of Mechanics and Physics of Solids*, Vol. 39, pp. 23–43, 1991.

8. Sorem, W.A., Dodds, R.H., and Rolfe, S.T., "Effects of Crack Depth on Elastic Plastic Fracture Toughness," *International Journal of Fracture*, Vol. 47, pp. 105–126, 1991.

9. Sumpter, J.D.G., "J_c Determination for Shallow Notch Welded Bend Specimens," *Fatigue and Fracture of Engineering Materials and Structures*, Vol. 10, No. 6, pp. 479–493, 1987.

10. Sumpter, J.D.G., and Forbes, A.T., "Constraint Based Analysis of Shallow Cracks in Mild Steel," *Proceedings of the International Conference on Shallow Crack Fracture Mechanics Tests and Applications*, TWI, Cambridge, England, September 1992.

11. Theiss, T.J., and Bryson, J.R., "Influence of Crack Depth on Fracture Toughness of Reactor Pressure Vessel Steel," to appear in the ASTM STP resulting from the *Symposium on Constraint Effects in Fracture*, held May 8–9 1991, Indianapolis, Indiana.

12. DeCastro, P.M.S.T., Spurrire, J., and Hancock, P., "An Experimental Study of the Crack Length / Specimen Width (a/W) Ratio Dependence of the Crack Opening Displacement (COD) Test Using Small–Scale Specimens," *Fracture Mechanics, ASTM STP 677*, C.W. Smith, Ed., American Society for Testing and Materials, Philadelphia, Pennsylvania, pp. 486–497, 1979.

13. O'Dowd, N.P., and Shih, C.F., "Family of Crack–Tip Fields Characterized by a Triaxiality Parameter: Part I – Structure of Fields," *Journal of the Mechanics and Physics of Solids*, Vol. 39., No. 8, pp. 989–1015, 1991.

14. O'Dowd, N.P., and Shih, C.F., "Family of Crack–Tip Fields Characterized by a Triaxiality Parameter: Part II – Fracture Applications," *Journal of the Mechanics and Physics of Solids*, Vol. 40, pp. 939–963, 1992.

15. Shih, C. F., O'Dowd, N. P. and Kirk, M. T., "A Framework for Quantifying Crack Tip Constraint," to appear in the ASTM STP resulting from the *Symposium on Constraint Effects in Fracture*, held May 8–9 1991, Indianapolis, Indiana.

16. O'Dowd, N. P. and Shih, C. F., "Two–Parameter Fracture Mechanics: Theory and Applications." to appear in the ASTM STP resulting from the *National Fracture Symposium on Fracture Mechanics*, Gatlinburg, Tennessee, June 29–July 3, 1992.

17. Li, Y.C. and Wang, T.C., *Scientia Sinica (Series A)*, Vol. 29, pp. 941–955, 1986.

18. Sharma, S.M. and Aravas, N. *Journal of Mechanics and Physics of Solids*, Vol. 39, pp. 1043–1072, 1991.

19. Xia, L., Wang, T.C. and Shih, C.F., "Higher–Order Analysis of Crack–Tip Fields in Power Law Hardening Materials," to appear in *Journal of Mechanics and Physics of Solids*.

20. Betegon, C., and Hancock, J.W., "Two–Parameter Characterization of Elastic–Plastic Crack Tip Fields," *Journal of Applied Mechanics*, Vol. 58, pp. 104–113, March 1991.

21. Du, Z.–Z., and Hancock, J. W., *Journal of Mechanics and Physics of Solids*, Vol. 39, pp. 555–567, 1991.

22. Hancock, J.W., Reuter, W.G., and Parks, D.M., "Constraint and Toughness Parameterized by T–Stress," to appear in the ASTM STP resulting from the *Symposium on Constraint Effects in Fracture*, held May 8–9 1991(a), Indianapolis, Indiana.

23. Parks, D.M., "Advances in Characterization of Elastic–Plastic Crack–Tip Fields," to appear in *Topics in Fracture and Fatigue*, Springer Verlag, 1992.

24. Wang, Y.Y., "On the Two–Parameter Characterization of Elastic–Plastic Crack–Front Fields in Surface–Cracked Plates," to appear in the ASTM STP resulting from the *Symposium on Constraint Effects in Fracture*, held May 8–9 1991(a), Indianapolis, Indiana.

25. Wang, Y.Y., "A Two–Parameter Characterization of Elastic–Plastic Crack–Tip and Applications to Cleavage Fracture," Ph.D. Thesis, Department of Mechanical Engineering, MIT, 1991.

26. Kirk, M.T., and Dodds, R.H., "Approximate Techniques for Prediction of Size Effects on Cleavage Fracture Toughness," to appear in the ASTM STP resulting from the *National Fracture Symposium on Fracture Mechanics*, Gatlinburg, Tennessee, June 29–July 3, 1992.

27. Dodds, R.H., Anderson, T.L., and Kirk, M.T., "A Framework to Correlate a/W Ratio Effects on Elastic-Plastic Fracture Toughness (J_c)," *International Journal of Fracture*, Vol. 48, pp. 1–22, 1991.

28. Anderson, T.L., and Dodds, R.H., "Specimen Size Requirements for Fracture Toughness Testing in the Ductile–Brittle Transition Region," *Journal of Testing and Evaluation*, Vol. 19, pp. 123–134, 1991.

29. Rice, J.R., and Johnson, M.A. in *Inelastic Behavior of Solids*, (M.F. Kanninen, et al., Eds.), McGraw–Hill, New York, pp. 641–671, 1970.

30. McMeeking, R.M., "Finite Deformation Analysis of Crack–Tip Opening in Elastic–Plastic Materials and Implications for Fracture," *Journal of the Mechanics and Physics of Solids*, Vol. 25, pp. 357–381, 1977.

31. Williams, M.L., *Jounal of Applied Mechanics*, Vol. 24, pp. 109–114, 1957.

32. Bilby, B.A., Cardew, G.E., Goldthorpe, M.R. and Howard, I.C., "Size Effects in Fracture," *Institution of Mechanical Engineers*, London, England, pp. 36–46, 1986.

33. Harlin, G., and Willis, J.R., *Proceedings of the Royal Society*, Vol. A415, pp. 197–226, 1988.

34. Ritchie, R.O., and Thompson, A.W., *Metallurgical Transactions A*, Vol. 16A, pp. 233–248, 1985.

35. Ritchie, R.O., Knott, J.F., and Rice, J.R., "On the Relationship Between Critical Tensile Stress and Fracture Toughness in Mild Steel," *Journal of the Mechanics and Physics of Solids*, Vol. 21, pp. 395–410, 1973.

36. Beremin, F.M, "A Local Criterion for Cleavage Fracture of a Nuclear Pressure Vessel Steel," *Metallurgical Transactions*, Vol. 14A, pp. 2277–2287, 1983.

37. Wallin, K., Saario, T., and Torronen, K., "Statistical Model for Carbide Induced Brittle Fracture in Steel," *Metal Science*, Vol. 18, pp. 13–16, 1984.

38. Anderson, T.L., and Stienstra, D., "A Model to Predict the Sources and Magnitude of Scatter in Toughness Data in the Transition Region," *Journal of Testing and Evaluation*, Vol. 17, pp. 46–53, 1989.

39. Wallin, K., "Statistical Aspects of Constraint with Emphasis on Testing and Analysis of Laboratory Specimens in the Transition Region," to appear in the ASTM STP resulting from the *Symposium on Constraint Effects in Fracture*, held May 8–9 1991, Indianapolis, Indiana.

40. Kirk, M.T., Koppenhoeffer, K.C., and Shih, C.F., "Effect of Constraint on Specimen Dimensions Needed to Obtain Structurally Relevant Toughness Measures," to appear in the ASTM STP resulting from the *Symposium on Constraint Effects in Fracture*, held May 8–9 1991, Indianapolis, Indiana.

41. Herrens, J., and Read, D.T., "Fracture Behavior of a Pressure Vessel Steel in the Ductile–to–Brittle Transition Region," NISTIR 88–3099, National Institute for Standards and Technology, Boulder, Colorado, December, 1988.

42. Miglin, M.T., Wade, C.S., and Van Der Sluys, W.A., "Analysis of Fracture Toughness Data for Modified SA508 C12 in the Ductile–to–Brittle Transition Region,"*Fracture Mechanics: Twenty-First Symposium, ASTM STP 1074*, J.P. Gudas, J.A. Joyce, and E.M. Hackett, Eds., American Society for Testing and Materials, Philadelphia, Pennsylvania, pp. 238–263, 1990.

43. Bass, B.R., Shum, D.K.M., and Keeney-Walker, J., "Constraint Effects on Fracture Toughness for Circumferentially Oriented Cracks in Reactor Pressure Vessels," *NUREG/CR-6008, ORNL/TM-12131*, Oak Ridge National Laboratory, June 1992.

44. Moran, B., and Shih, C.F., "Crack Tip and Associated Domain Integrals from Momentum and Energy Balance," *Engineering Fracture Mechanics*, Vol. 27, pp. 615–642, 1987.

45. Shih, C.F., Moran, B., and Nakamura, T., "Energy Release Rate Along a Three–Dimensional Crack Front in a Thermally Stressed Body," *International Journal of Fracture*, Vol. 30, pp. 79–102, 1986.

RECOMMENDATIONS FOR THE APPLICATION OF FRACTURE TOUGHNESS DATA FOR STRUCTURAL INTEGRITY ASSESSMENTS

by

Dr. Kim Wallin*

ABSTRACT

Large scale testing for the purpose of fracture mechanics verification is essentially directed towards the validation of the transferability of material data obtained with small specimens. Unfortunately the results are sometimes controversial, insinuating that the transferability is imprecise at the very least. However, it seems that in many cases the controversy is due to an improper application of the small specimen data.

Present testing standards do not give any recommendations for the correct application of fracture toughness data and yet this is a crucial point for successful structural integrity assessment and fracture mechanics verification.

In this presentation the topic concerning recommendations is addressed, focussing on the application of brittle (cleavage type) fracture data. Simple guidelines for obtaining optimum "best-" and "safe-" estimates of the behavior of the actual structure based on small specimen data are presented.

* Technical Research Centre of Finland (VTT), Metals Laboratory, P.O.Box 26, Espoo, Finland, SF-02151.

INTRODUCTION

Present testing standards do not give any recommendations for the correct application of fracture toughness data for structural integrity assessments and yet this is a crucial point for a successful assessment and fracture mechanics verification. Standardization bodies have been reluctant to produce what they call application documents. Their single interest have been the test performance. Unfortunately, this state of affairs has reduced the credibility of fracture mechanical parameters due to a lacking verification.

Large scale testing for the purpose of fracture mechanics verification has as a goal the validation of the transferability of material data obtained with small specimens. Unfortunately, due to the lack of application documents, the results are often controversial, insinuating that the transferability is imprecise at the very least. However, in many cases the controversy is only due to an improper application of the small specimen data.

In this presentation the topic concerning recommendations is addressed, focussing on the application of brittle (cleavage type) fracture data. Simple guidelines for obtaining optimum "best-" and "safe-" estimates of the behavior of the actual structure based on small specimen data are presented.

General Considerations

Fracture mechanics parameters are widely used to determine materials' resistance to fracture. Presently a number of both standardized as well as nonstandardized parameters are used. Their main ambition is to be able to describe the material's fracture resistance with one single factor. Examples of such interrelated parameters are the plane-strain fracture toughness, K_{IC}, the critical J integral, J_{IC}, and the critical crack-tip opening displacement ($CTOD_c$ or δ_c).

The parameters can be divided into two different categories, namely those parameters based on linear elastis fracture mechanics (LEFM) and those based on elastic plastic fracture mechanics (EPFM). LEFM requires that the plastic zone in front of the crack is much smaller than the smallest structural dimension, i.e. the structure behaves in a linear elastic manner. EPFM allows the structure to yield to some extent. In principle the EPFM parameters are valid also in the case LEFM, but not vice versa.

Parameter validity

All the different parameters are assumed to describe the critical stress and strain fields ahead of a sharp crack at fracture, i.e. they are supposed to represent a material characteristic. By definition, they should all be geometry independent for a constant stress state. A large number of investigators, however, have found a distinct effect of specimen size and geometry on the test results [1-5]. These geometry effects have been

reported for both brittle cleavage fracture [6-8] and ductile fracture [9-11]. The specimen size and geometry have also been found to affect the ductile/brittle transition temperatures [1, 5, 12]. Many of the results are contradictory, with some indicating no geometry and/or size effect and others indicating either an increasing or decreasing toughness.

Depending on the method and the parameter chosen, one may observe quite different specimen size and geometry effects. Different parameters also show different characteristic scatter. Some frequently used toughness parameters and their characteristics are listed in Table 1 [13].

Table 1. Commonly used fracture toughness parameters exhibiting different size and geometry effects.

TYPE	PARAMETER	SCATTER	SIZE EFFECT	CRACK LENGTH EFFECT	USEFULLNESS
LEFM	K_{IC}	medium	small	small	good
	K_Q	small	unpredictable	medium	poor
	K_m	small	unpredictable	medium	poor
	K_i	small	unpredictable	medium	good ➡ poor
EPFM	J_{IC}	medium	small	small	good preferable
	J_i	medium	small	small	good
	$CTOD_i/\delta_i$	medium	small	small	good
	J_C	large predictable	large predictable	small	good preferable
	$CTOD_C/\delta_C$	large predictable	large predictable	small	good preferable
	J_m	small	large unpredictable	large	negligible
	$CTOD_m/\delta_m$	small	large unpredictable	large	negligible
	J_u	large	large	medium	medium
	$CTOD_u/\delta_u$	large	large	medium	medium

In Table 1, K_{IC} and K_Q are the valid and the invalid fracture toughness, respectively determined by ASTM Method E 399. Both parameters are determined by constructing a 95 % secant to the load - crack mouth opening curve. K_m and K_i are determined by using the K_{IC} linear-elastic fracture mechanics LEFM-formulas together with the load

maximum and load at ductile fracture initiation, respectively. Both K_i and especially K_m can be very inferior parameters and should not be used for integrity assessment. The parameter J_{IC} is the valid critical J-integral value determined by ASTM E 813. The parameters J_i and δ_i are the values of the J integral and the crack-tip opening displacement at ductile crack growth initiation. J_C and δ_C correspond to the onset of brittle fracture occurring without ductile tearing. Finally, J_u and δ_u correspond to the onset of cleavage fracture which has been preceded by some amount of ductile tearing. Not all of the parameters are "valid" according to existing test standards and recommendations, but often results referring to invalid parameters are quoted without mentioning their invalidity.

Furthermore, also parameters that are "valid" according to testing standards show size and geometry effects. It should be pointed out that the characteristic scatter of a parameter is not a direct measure of the usefulness of the parameter. The invalid LEFM parameters K_Q, K_m and usually also K_i show a small scatter but are yet undependable.

Most of the observed size effects are due to the poor nature of the parameters. The only test parameters that correctly describes the material from a fracture resistance point of view are K_{IC}, J_C, δ_C, J_{IC}, J_i, δ_i and to some extent J_u and δ_u. The other parameters do not correspond to the initiation of crack extension. Instead they rather describe the size effects on specimen plasticity together with ductile crack growth. As such they cannot be regarded to represent parameters describing the materials true fracture resistance.

One must remember that different parameters describe different fracture micromechanisms, and that one must know which micromechanism is the relevant one for the structural detail in question.

Fracture micromechanisms

The two main micromechanisms encountered in fracture resistance testing are ductile fracture and cleavage fracture. A third micromechanism i.e. grain boundary fracture is also possible, but it is of lesser relevance. This is fortunate, because the fracture mechanical modelling of grain boundary fracture is still incomplete.

There is a widely recognized view that ductile fracture proceeds by a continuous mechanism of microvoid nucleation and coalescence. Therefore it is impossible to detect the first physical initiation point. The initiation point is instead usually taken as a point at which there already has been some small amount of detectable ductile tearing. Probably the best known example of such a method is the J_{IC}-determination procedure in accordance to ASTM E 813.

Microvoid coalescence is a critical strain-controlled mechanism. As such, it is strongly governed by the maximum strain state along the crack front. For the crack to propagate macroscopically, microvoid coalescence must occur along the whole crack front. The macroscopic fracture resistance to ductile fracture is thus governed by the

mean toughness properties of the material. This means that for a macroscopically homogeneous material, the parameters related to ductile fracture (J_{IC}, J_i, δ_i) should show only a small amount of scatter. Also, as long as the J-integral and crack-tip opening displacement describe the strains in front of the crack, the parameters should also be specimen size and geometry independent.

Brittle cleavage fracture differs completely in mechanism from ductile fracture. It is assumed that cleavage fracture is initiated by a weakest link type critical stress-induced mechanism governed by locally situated cleavage initiators or "weak spots" [14 - 19]. As such, cleavage fracture will be affected, besides by changes in the stress distribution, also by the probability of finding a critical cleavage initiator. This weakest link type statistical nature of cleavage fracture unfortunately denotes that fracture toughness in the case of cleavage fracture is not a simple material property. Firstly, cleavage fracture initiation toughness exhibits a large amount of scatter [20], and secondly, it shows a characteristic statistical size effect associated to the length of the crack front [14]. Because of this statistical size effect one must always correct the experimental toughness values to correspond to the relevant crack front length. A few test results indicate that the statistical size effect may disappear at very low temperatures, but since the findings are somewhat controversal, it is safer to assume the existence of a size effect also in the case of lower shelf toughness.

FRACTURE RESISTANCE FOR LEFM APPLICATIONS

Fracture resistance for LEFM applications is ordinarily expressed in the form of a critical stress intensity factor K_I, denoted "fracture toughness". The validity of the stress intensity factor to describe the stress field in front of a crack is well documented and also the stress intensity factor equations used in the different testing standard are accurate. As such the stress intensity factor is well suited for determination of fracture resistance for LEFM applications.

The fracture toughness K_{IC} is classically supposed to be a material constant, but in reality this is not the case. Ordinary K_{IC}-tests according ASTM E 399 and related standards apply LEFM-formulas and allow the use of the 95 % secant procedure. The secant procedure is based on the assumption that the deviation from linearity in the load-displacement trace is in practice only due to stable ductile crack growth. A K_{IC} value corresponding to the 95 % secant is assumed to be related to a toughness value corresponding to a 2 % crack growth in the ligament. The size criterions in the standard are actually included to ensure that the load-displacement response of the specimen will be unaffected by plasticity effects. Parameters violating the K_{IC} size criterions (K_Q, K_{max} and possibly K_I) usually describe mainly specimen plasticity effects and as such they should not be used. The problem with K_{IC} is that it does not distinguish between ductile fracture and brittle cleavage fracture.

In the case of ductile fracture the K_{IC} will correspond to a 2 % crack growth in the ligament. This causes that a larger specimen will correspond to more actual ductile crack growth. Because ductile fracture always has an increasing R-curve ($dK/da > 0$),

a large specimen will yield a higher K_{IC} than a small specimen, even for valid tests. On the other hand, the validity criteria in the testing standards are such that a K_{IC} value for ductile fracture is obtainable only for materials whose R-curve is very flat. Thus the size effect in the case of K_{IC} corresponding to ductile fracture is relatively small and therefore it can be regarded nearly as a material characteristic. If it is possible to determine the true ductile initiation value K_i it is more preferable than K_{IC} provided that it otherwise fulfills the validity criteria for K_{IC}.

For ferritic steels K_{IC} corresponds usually to brittle cleavage fracture. In this case K_{IC} is a measure of a true critical event and as such it is a preferable parameter for LEFM fracture resistance determination. However, because the probability of cleavage fracture initiation is specimen and crack size dependent, one must always correct the fracture toughness to correspond to the relevant crack size. The need for statistical modelling of cleavage fracture initiation has been acknowledged during the last few years. A number of models for describing the behaviour of fracture toughness in the cleavage fracture temperature region have been presented [3, 7, 13-37]. Most of these are based on the assumption of cleavage fracture initiation to behave according to weakest link statistics i.e. one single critical event is sufficient to cause macroscopic failure. Even though the models may differ quite a lot in their basic assumptions of the microscopic fracture mechanism, macroscopically they still yield similar results.

In the case of brittle fracture, the fracture toughness can be thickness corrected with an equation like [14]

$$K_{B_2} = (K_{B_1} - K_{min}) \cdot (B_1/B_2)^{1/4} + K_{min} \qquad (1)$$

where K_{min} is a lower bound fracture toughness. The exact value of K_{min} is not known, but for steels a value of 20 MPa$\sqrt{m}$ has been successfully used for describing experimental test data.

The above equation has been validated for a large number of both low and high strength structural steels and for specimen thicknesses ranging from 10 mm to 200 mm [14]. Even though definitive proof of a statistical model based equation is very difficult, the successful application of the equation for more than 100 materials might be considered as a comparatively strong validation.

Based on the same assumptions the scatter of brittle fracture toughness results can be described with the equation [20]

$$P_f = 1 - \exp\{-\left(\frac{K_J - K_{min}}{K_0 - K_{min}}\right)^4\} \qquad (2)$$

where P_f is the cumulative failure probability at al load level K and K_0 is a specimen thickness and temperature dependent normalization parameter which is related to the

mean approximately by $K_0 \approx 1.1 \cdot \bar{K}_{IC}$.

With the help of equations 1 and 2 it is possible to handel cleavage fracture K_{IC} results in the assessment of component integrity by fracture mechanics.

The restricting property about the K_{IC} test is the demand for linear elasticity. Linear elastic K_{IC} values are usually possible to obtain only on the lower shelf of the fracture toughness transition curve. Often LEFM assessment of components may be performed also at higher toughness levels where it is impossible to measure a valid K_{IC} value. In such cases one must rely on an indirect determination of K_{IC} or EPFM parameters corresponding to cleavage fracture initiation.

FRACTURE RESISTANCE FOR EPFM APPLICATIONS

The fracture resistance for EPFM applications must be determined by use of EPFM parameters like the J-integral or the crack tip opening displacement. Analogous to the LEFM case, the valid parameters should correspond to fracture initiation, ductile or brittle. If something else than an initiation parameter is desired for description of ductile fracture resistance, the whole tearing resistance curve (J-Δa curve) should be determined.

The accuracy of the equations for the determination of J and δ from test records is not as well validated as in the case of the stress intensity factor K_I, but their accuracy seems to be of less concern than other experimental error sources. This is the case especially for the determination of ductile tearing resistance.

Brittle fracture

EPFM parameters describing brittle cleavage fracture initiation are J_c, J_u, δ_c and δ_u. Of the two definitions the one corresponding to cleavage fracture initiation after some ductile tearing is less reliable even though it relates to a catastrophic type of failure event, for which the occurrence is not directly dependent on the load bearing capacity of the structural detail. The one thing that deteriorates the relevance of J_u and δ_u is the ductile tearing preceding cleavage fracture, because this ductile tearing in itself affects the brittle fracture probability [38]. This effect has not been quantitatively clarified until recently. Presently the CTOD-standards (the only testing standards applicable in the transition region) do not even require the measurement of the amount of ductile tearing in the test.

Recently, a method to account for the effect of ductile tearing on cleavage fracture probability has been developed [38,39]. The methodology is originally developed for the J-integral and it results in a correction function for the ductile crack growth [38] as well as a minimum specimen ligament size requirement [39]. The ligament size requirement gives the maximum measuring capacity of the specimen regarding cleavage fracture. If the ligament is smaller than given by the size requirement a corrected value of the

fracture toughness should be used in the crack growth correction expression. The methodology has been shown to yield promising results, but it still needs some further validation and possible refining. Just recently, the size requirements have been further refined by detailed FEM-calculations by Anderson and Dodds [40]. Their size requirements are much more stringent than the ones deduced based on experimental data. Thus there seem to exist some open questions regarding the size criterion in the case of cleavage fracture.

Otherwise the EPFM parameters describing brittle cleavage fracture are well suited for the determination of fracture resistance. The relation between J and δ is usually written as $J = m \cdot \sigma_{flow} \cdot \delta$, where σ_{flow} is the flow stress of the material and m is a proportionality factor, which in theory is 1 for plane stress and 2 for plane strain. In reality the value of m is mainly controlled by the testing standards used for determination of J and δ. The value of m is dependent of load level, but it can still roughly be approximated by $m \approx 1.5$ [41].

Often one is forced to apply EPFM material parameters with LEFM integrity assessment procedures. In such cases it is relatively safe to estimate the critical stress intensity factor for cleavage fracture from J_C by the equation

$$K_{JC} = \sqrt{E' \cdot J_C} \tag{3}$$

provided that the fracture resistance is corrected to correspond to the relevant crack front length with equation 1.

The validity of equation 3 has been comparatively well verified, both directly by comparing small specimen EPFM data with large specimen LEFM data [42], as well as indirectly by showing that a Charpy-V - K_{IC} correlation is equally valid for K_{IC} and K_{JC} [43].

Equation 3 also basically makes it unnecessary to use full thickness specimens in the fracture toughness tests, in the case of brittle fracture. The standard arguments why full thickness specimens are required are based on constraint effects. It has however been shown, both experimentally [14] and numerically [44] that the main reason for thickness effects on cleavage fracture toughness is the statistical size effect.

Ductile fracture

The parameters used in connection with ductile fracture are either representing ductile fracture initiation or the specimen load maximum.

It is commonly recognized that the load maximum fracture toughness is a geometry dependent toughness value. It has, however, been argued that under specified conditions it is possible to use J_m or δ_m values to obtain a safe flaw size evaluation [45]. A special requirement is that the test must be performed with a full thickness specimen ie. specimen thickness must be equal to the structural thickness.

The maximum load occurs when the load increase caused by the increasing strain hardening is balanced by the reducing ligament area because of crack growth and/or necking of the bend specimen [41]. Thus the load maximum toughness is a measure of the specimens tearing instability. Of the two causes for ligament reduction necking is normally not important in the case of fracture toughness testing. Necking becomes possible only at load levels well beyond any validity criteria for fracture toughness. The load maximum toughness can actually be used to determine the materials tearing characteristics, but it demands that a full tearing instability analysis of the test specimen is performed [41,46]. If an analysis allowing for crack extension is needed, it is preferable to use the whole tearing resistance (J-Δa) curve.

As noted before, there exists a variety of definitions for the ductile initiation toughness. This is not however a very large problem as long as it can be shown that the structure will not fail by brittle fracture. All the different definitions of ductile initiation toughness will produce safe estimates with regard to ductile failure instability of the structure and therefore they can well be applied for failure assessment.

RECOMMENDATIONS FOR DETERMINING "BEST- " AND "SAFE-" BRITTLE FRACTURE TOUGHNESS ESTIMATES

The fracture toughness to be used in the fracture mechanics analysis can be based upon K_{IC}, J_C, δ_C, J_u or δ_u. Regardless of parameter it is preferable to express the fracture toughness in terms of it's equivalent K-value (equation 3). Equation 2 contains only two parameters. Unfortunately, a reliable estimation of the minimum fracture toughness K_{min} from test results is impossible. This is the main reason for fixing it's value to 20 MPa$\sqrt{m}$. If it can be shown that the minimum fracture toughness is higher than 20 MPa$\sqrt{m}$ that value can be applied. Otherwise the use of K_{min} = 20 MPa$\sqrt{m}$ is recommended. Thus, the only entity requiring estimation is K_0. A bias corrected maximum likelihood expression for K_0 is of the form

$$K_0 = \left[\frac{\sum (K_C^i - K_{min})^4 + (n-r)\cdot(K_C^r - K_{min})^4}{r - 1 + \log(2)} \right]^{1/4} + K_{min} \qquad (4)$$

where the summation is performed from i=1 to i=r. The equation denotes a so called censored sample, where not all results are included in the analysis. The total sample size is n and the uncensored sample size is r, which consists of all values that are lower than the lowest censored value. Equation 4 is especially well suited for use with data sets where part of the results have been affected by eg. large scale yielding.

Equation 4 yield a so called best estimate of K_0, i.e. it corresponds to a confidence level of 50 %. The standard deviation, corresponding to the lower tail of the K_0 distribution is approximately $\sigma_{K_0-K_{min}} \approx 28\ \%/\sqrt{n}$. The lower tail of the K_0 distribution is well described by a normal distribution. Thus, a safe estimate corresponding to a

desired confidence level can be determined (Figure 1).

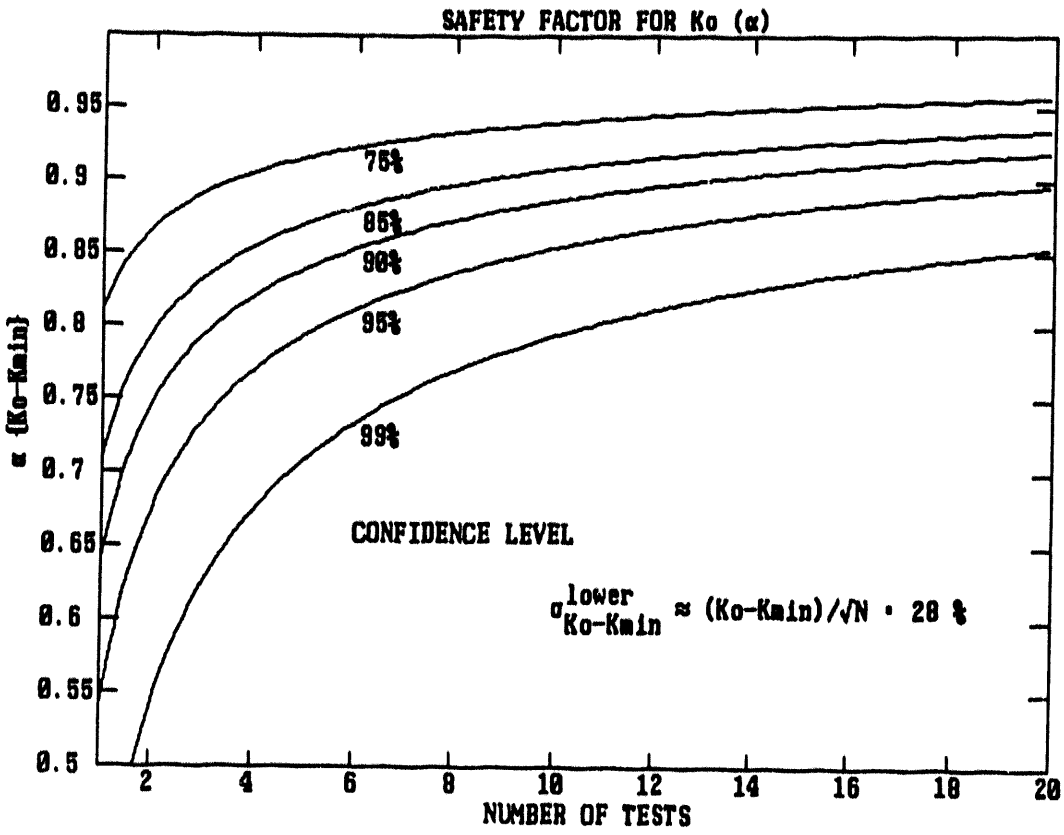

Fig. 1 Safety factor for K_0.

If the major part of the data set is censored, or if the material is suspected to be macroscopically unhomogeneous, K_0 can also be estimated directly from the lowest measured fracture toughness value K_{low} according to

$$K_0 = \{K_{low}-K_{min}\} \cdot [-n/\log(1-P_{conf})]^{1/4} + K_{min} \quad (5)$$

where P_{conf} is the desired confidence level eg. 0.9 (Figure 2).

Since the above K_0 estimate is based on only one toughness value, it will have the same scatter as a single test. Thus, the use of equation 2 is endorsed when ever possible.

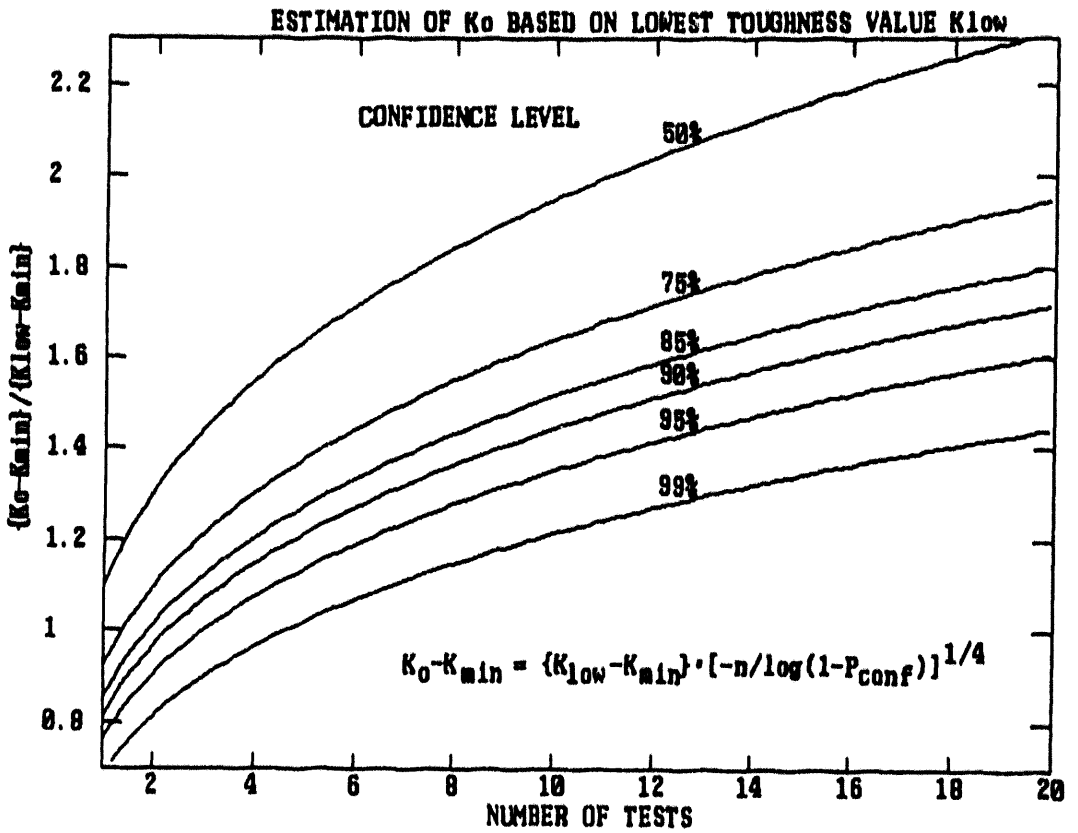

Fig. 2 Estimation of K_0 based on lowest toughness value.

Often knowledge of the fracture toughness at a single temperature is not enough, but instead the temperature dependence of K_0 is requested. The temperature dependence of K_0 in MPa$\sqrt{m}$ can be described with [47]

$$K_0 = \alpha + \beta \cdot \exp[\gamma \cdot (T - T_0)] \qquad (6)$$

where $\alpha + \beta = 108$ MPa$\sqrt{m}$ (for 25 mm thick specimens), T_0 is the temperature (in °C)

at which the mean fracture toughness is 100 MPa$\sqrt{m}$ and γ is a material constant.

Experimentally it has been found that the shape of the fracture toughness transition curve for steels is only slightly material and yield strength dependent. Therefore the values of α, β and γ are practically material independent. The resulting equation for the temperature dependence of K_0, corresponding to 25 mm thickness, can thus be written as [47]

$$K_0 = 31 + 77 \cdot \exp [0.019 \cdot (T - T_0)] \quad (7)$$

Verification of equation 7 is presented in figure 3.

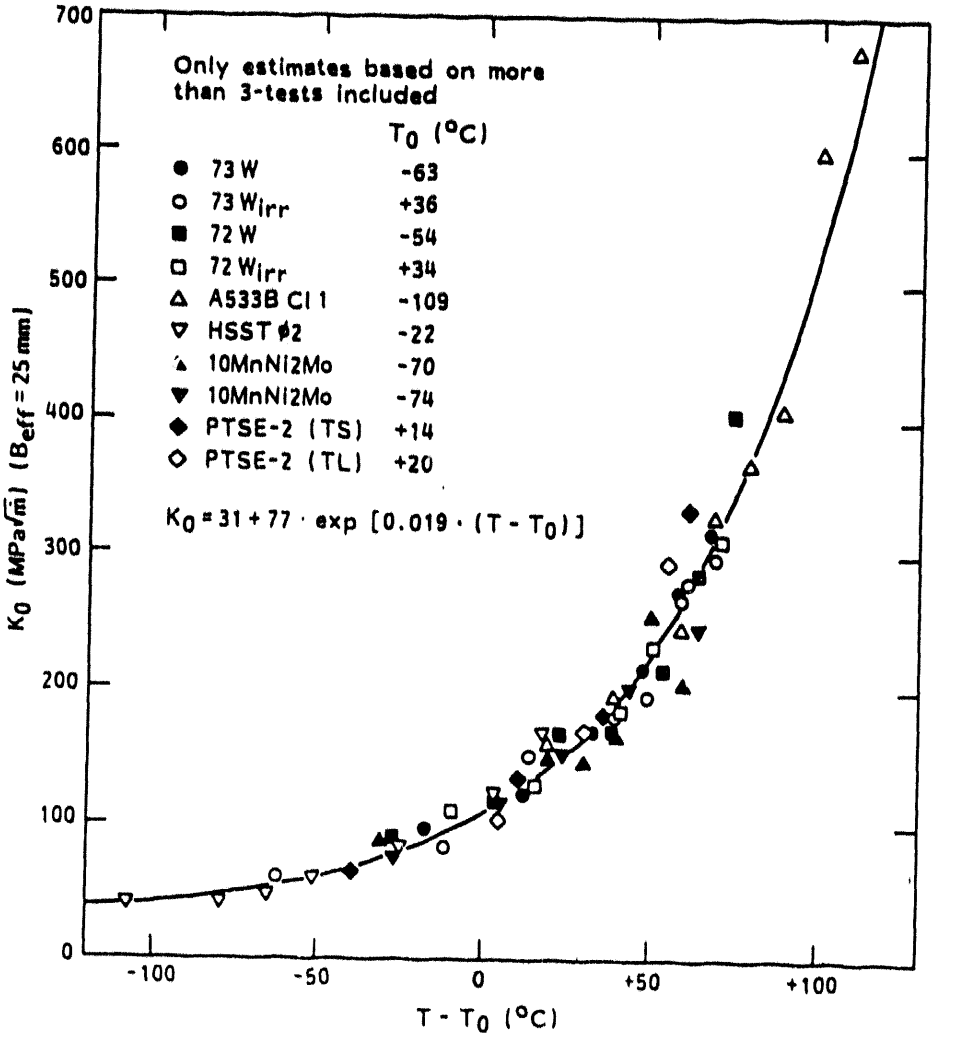

Fig. 3 Temperature dependence of K_0 for 25 mm thick specimens [47].

If T_0 is estimated based on equation 7, the estimate will have a standard deviation $\sigma_{T_0} \approx 18$ °C and it will be slightly biased towards higher temperatures (≈ 3 °C). If the upper tail of the T_0 temperature distribution is approximated by a normal distribution, its standard deviation is $\sigma_{T_0}^{upper} \approx 24$ °C/√n and the safety factor ΔT corresponding to any desired confidence level can be determined (Figure 4).

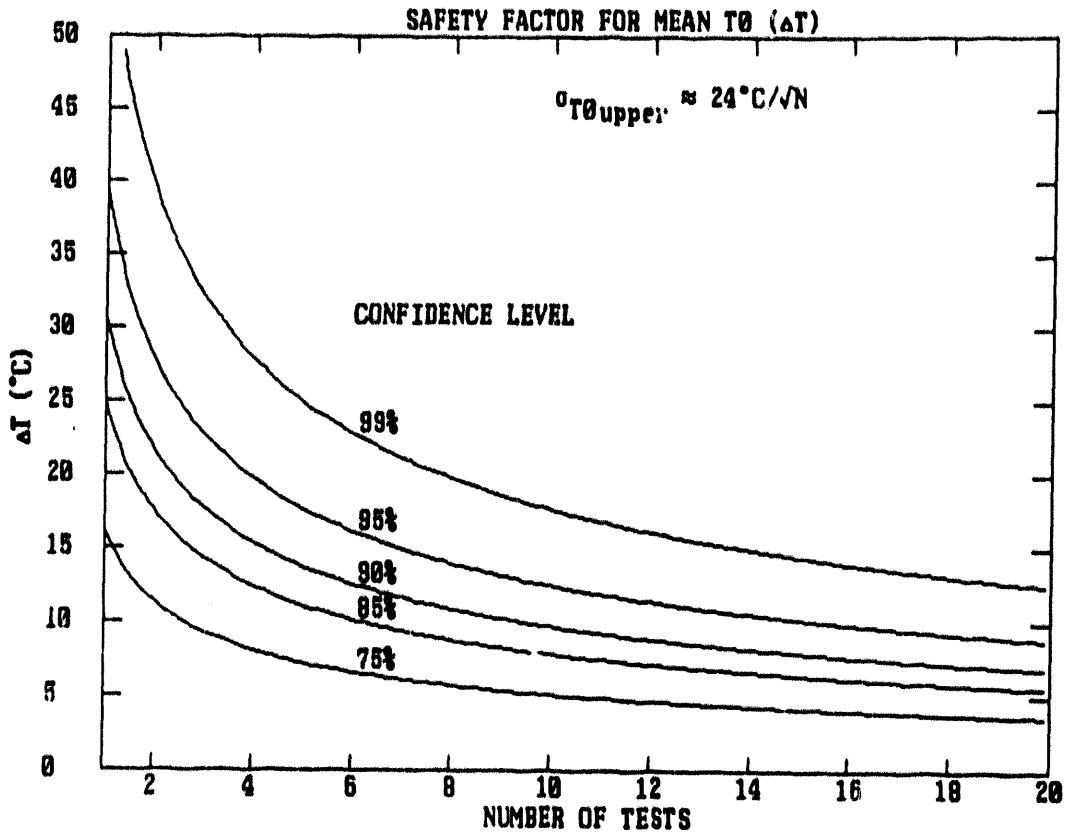

Fig. 4 Safety factor for estimate of T_0.

VALIDATION

Validation of the above recommendations require a validation of equations 1,2,3 and 7. Even though a rather comprehensive verification of the equations have already been presented elsewhere e.g. [14,18,20,29-31,38,39,42,43,47,49], additional validation is presented here. A number of large data sets including different size specimens were thickness corrected according to equation 1 and the temperature T_0 was estimated for each specimen size. If the equations are valid, they should correctly describe the materials scatter and temperature dependence. Furthermore, specimen size independent estimates for T_0, should be obtained. The validation is presented in figures 5-11.

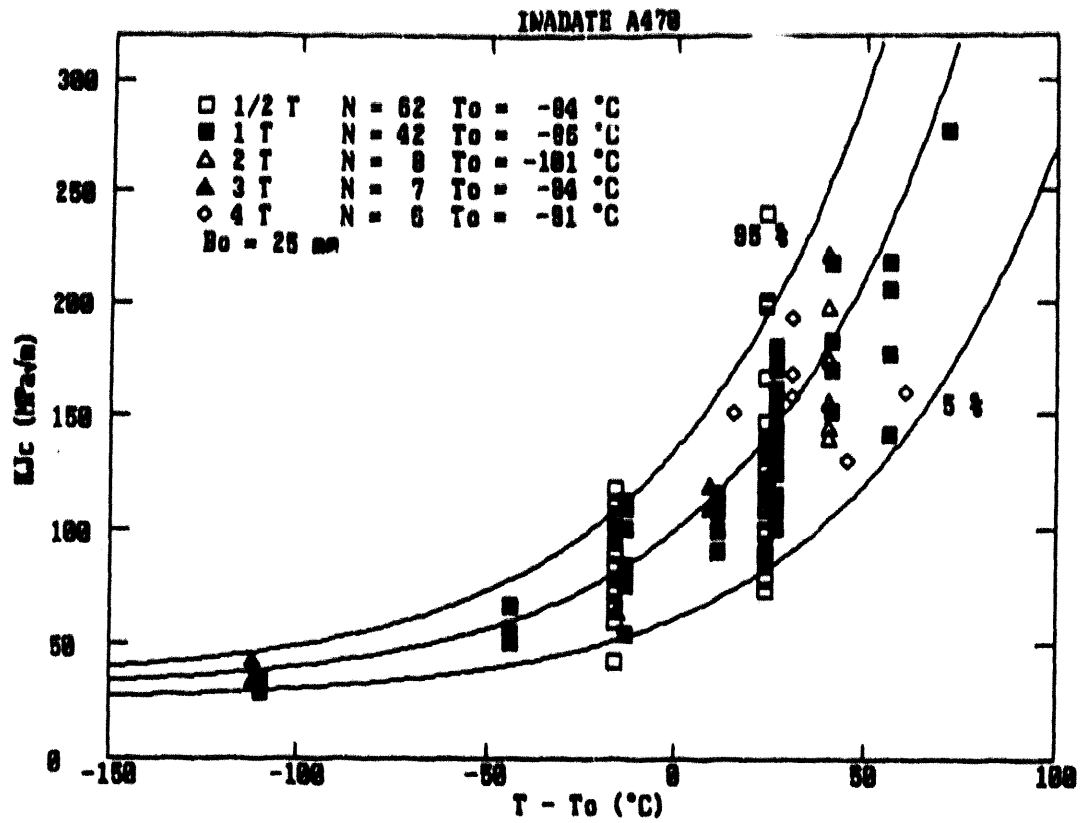

a)

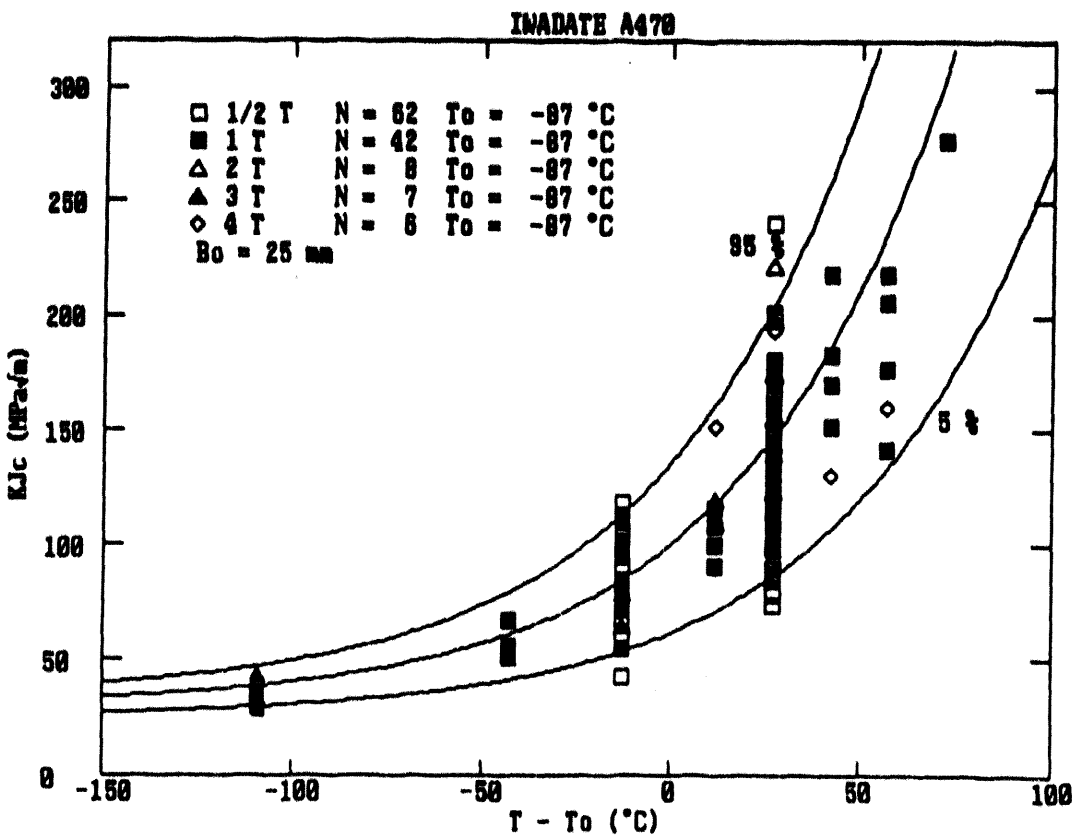

b)

Fig. 5 Iwadate data A470 [48]. Only statistical thickness correction performed. a) T_0 fitted, b) T_0 fixed

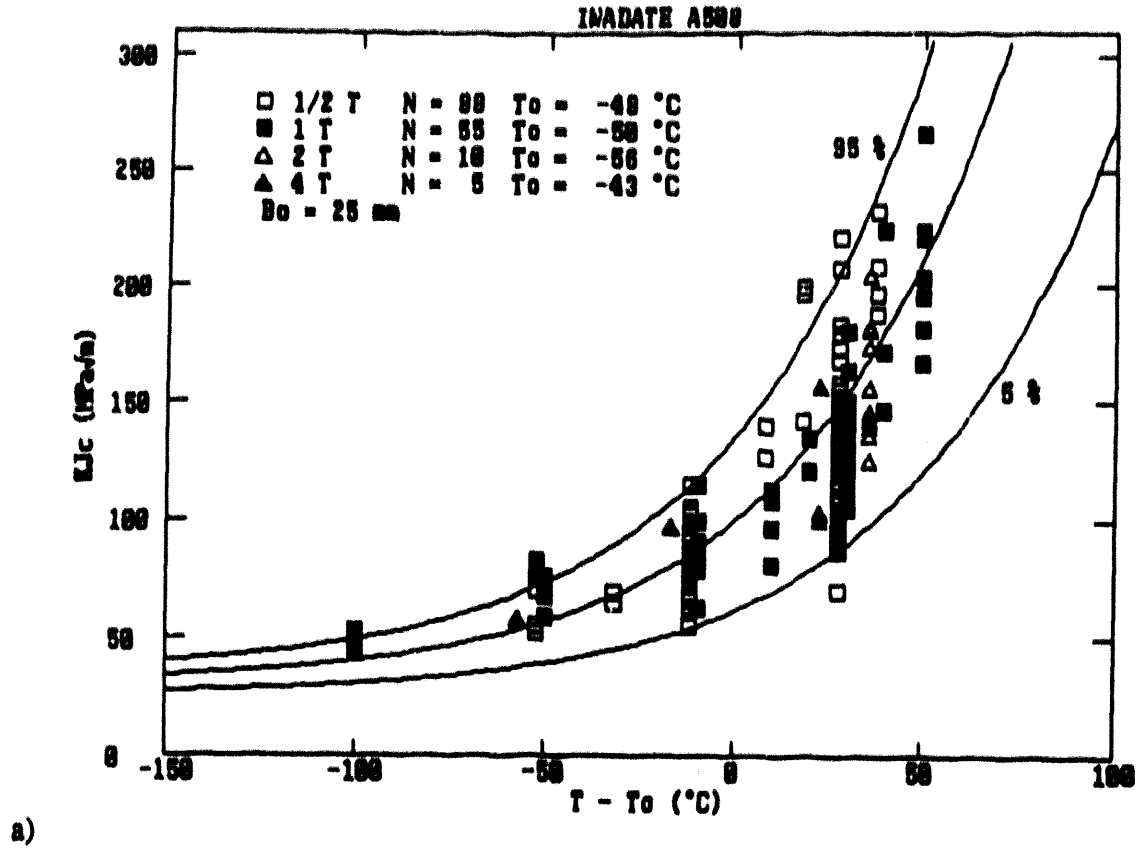

a)

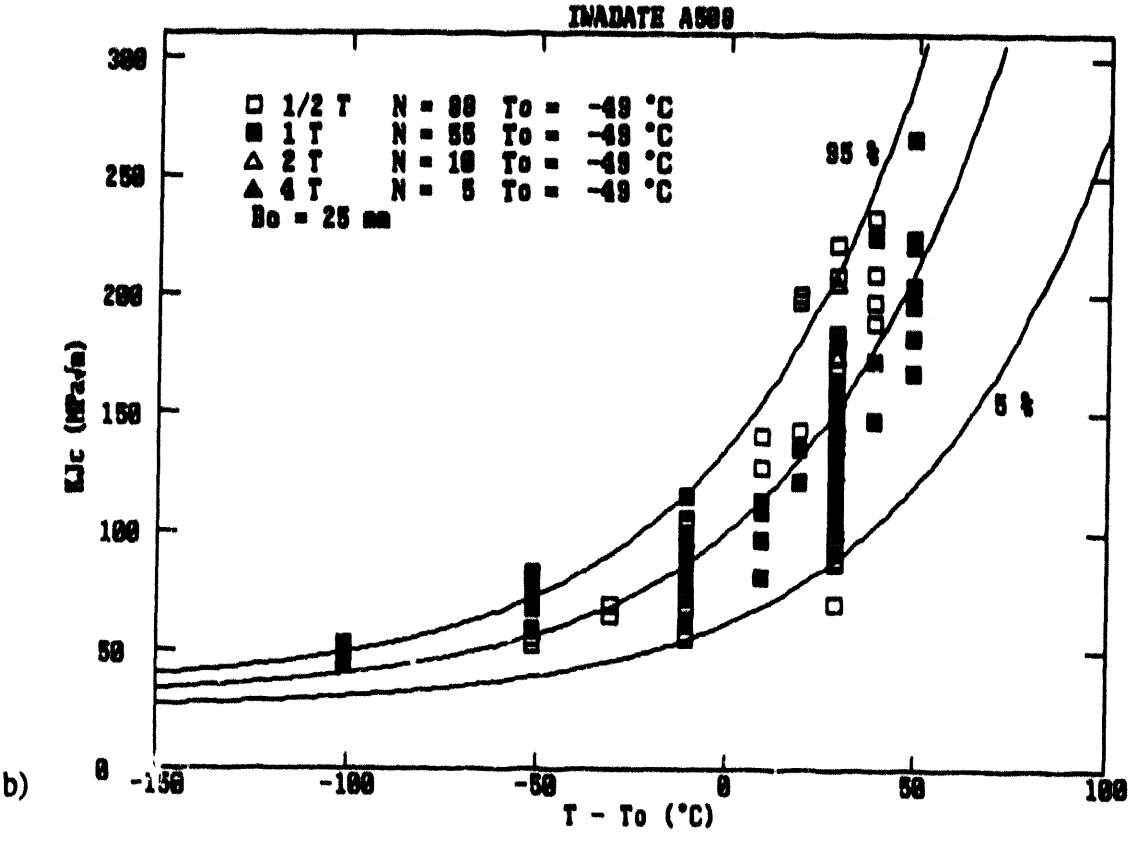

b)

Fig. 6 Iwadate data A508 [48]. Only statistical thickness correction performed. a) T_0 fitted, b) T_0 fixed

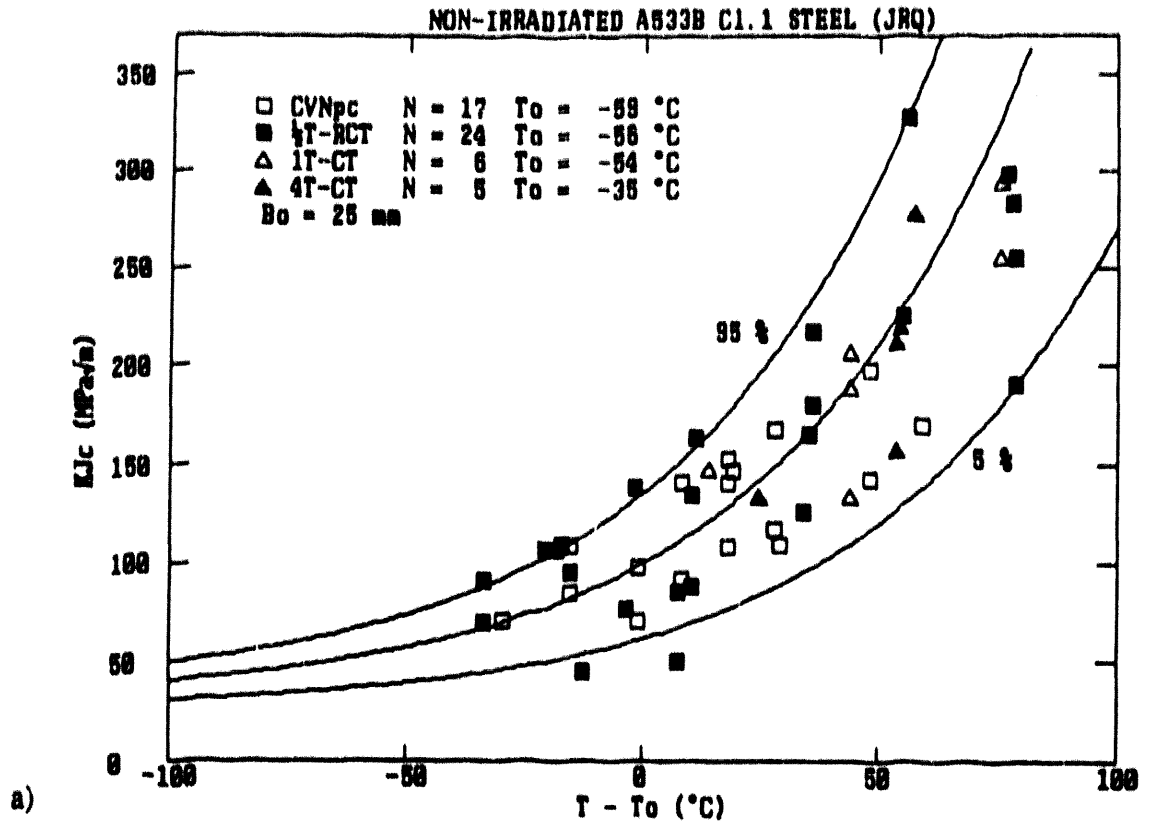

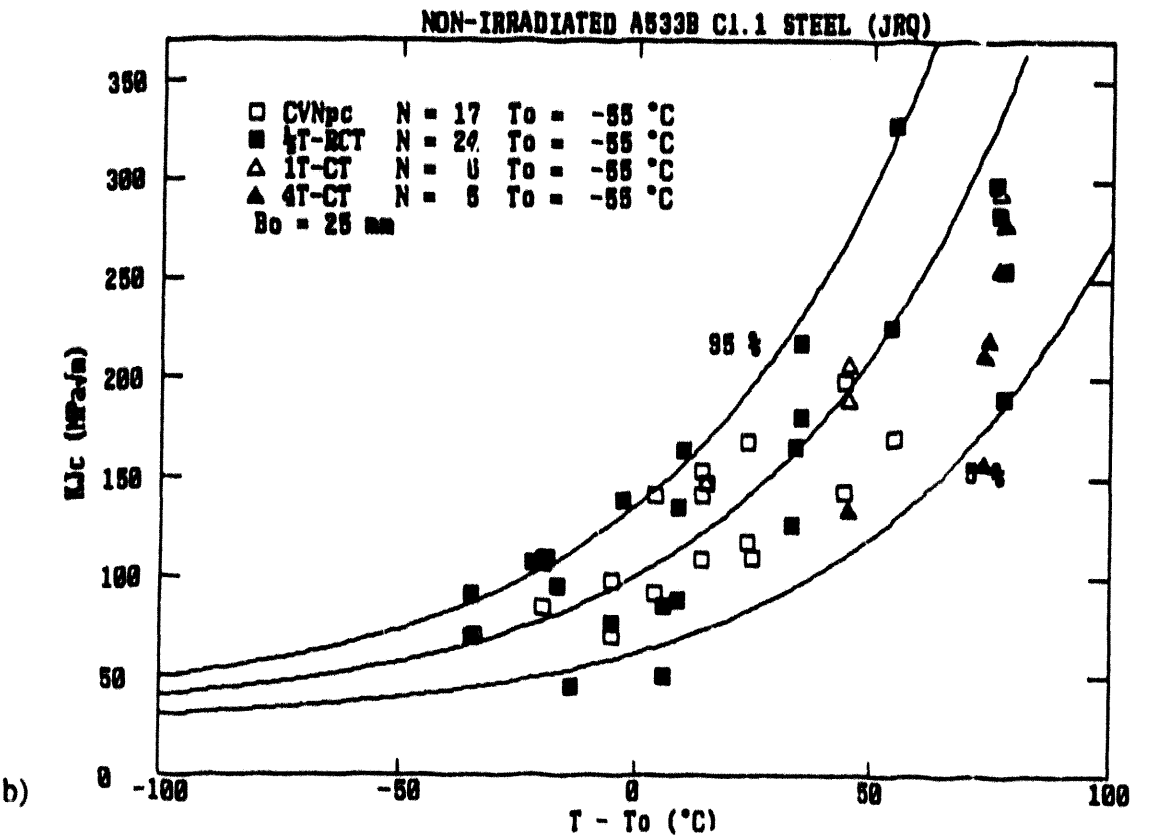

Fig. 7 VTT data A533B [49]. Only statistical thickness correction performed.
a) T_0 fitted b) T_0 fixed

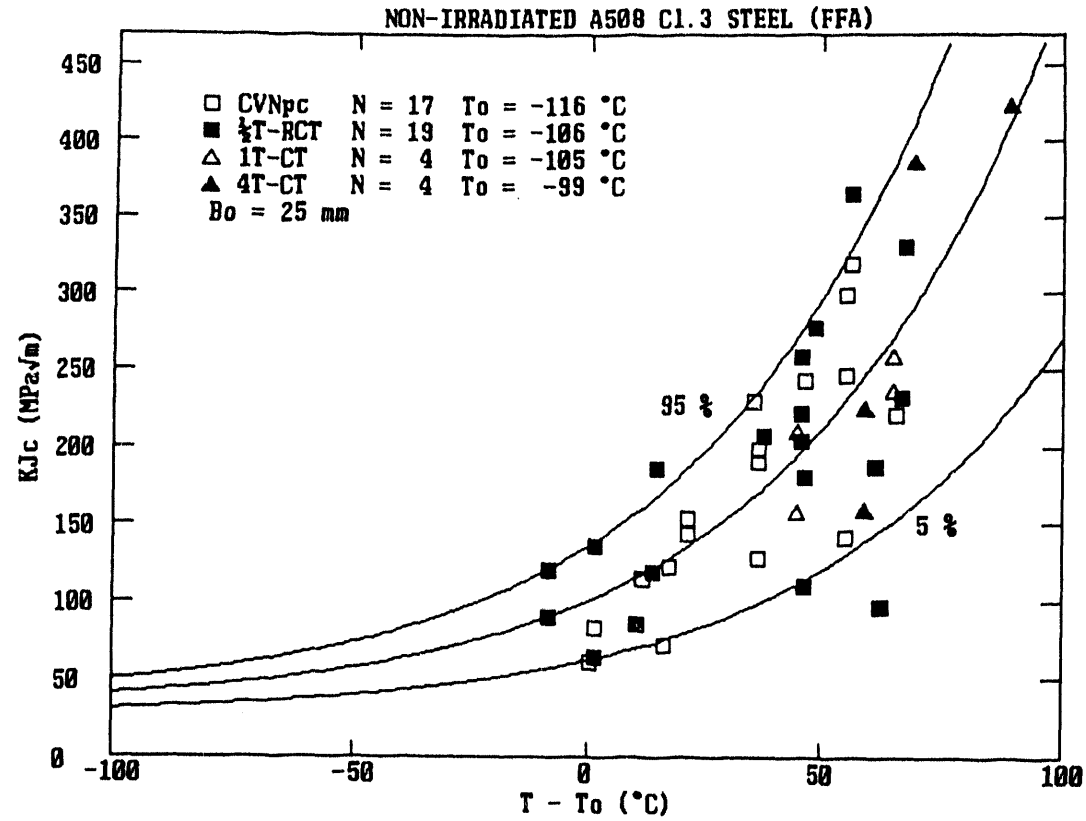

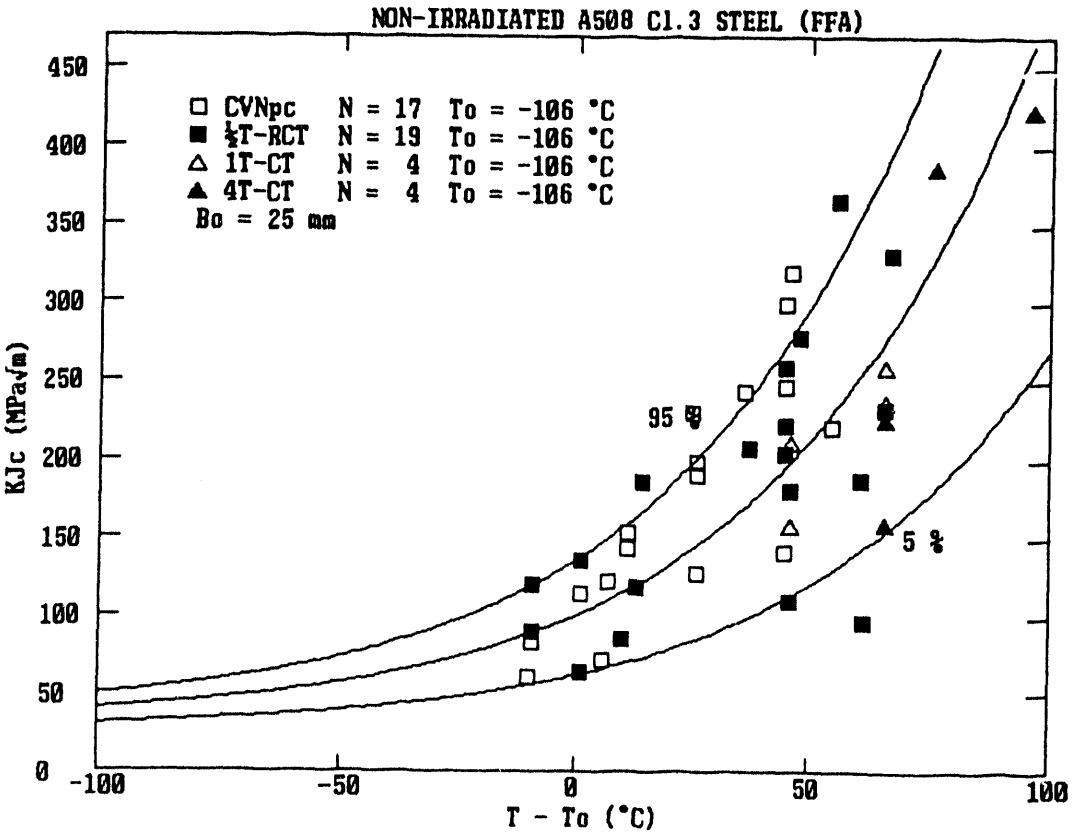

Fig. 8 VTT data A508 [49]. Only statistical thickness correction performed.
a) T_0 fitted, b) T_0 fixed

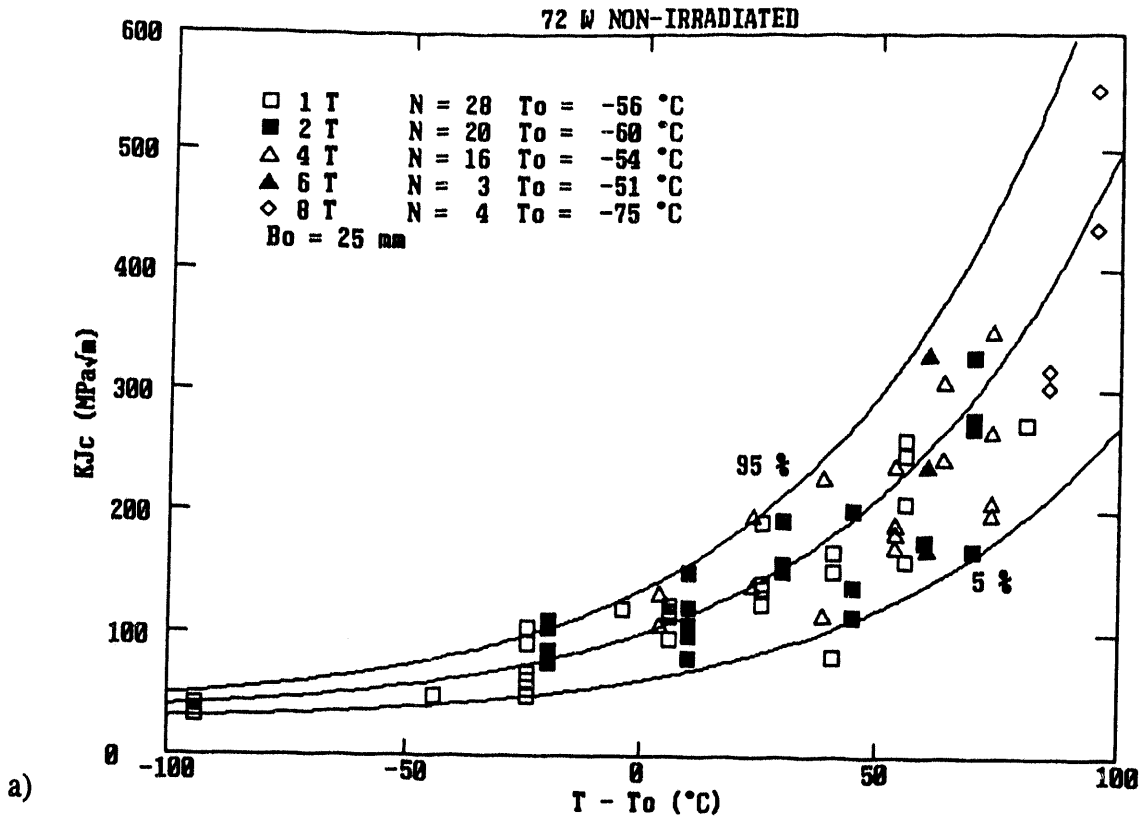

a)

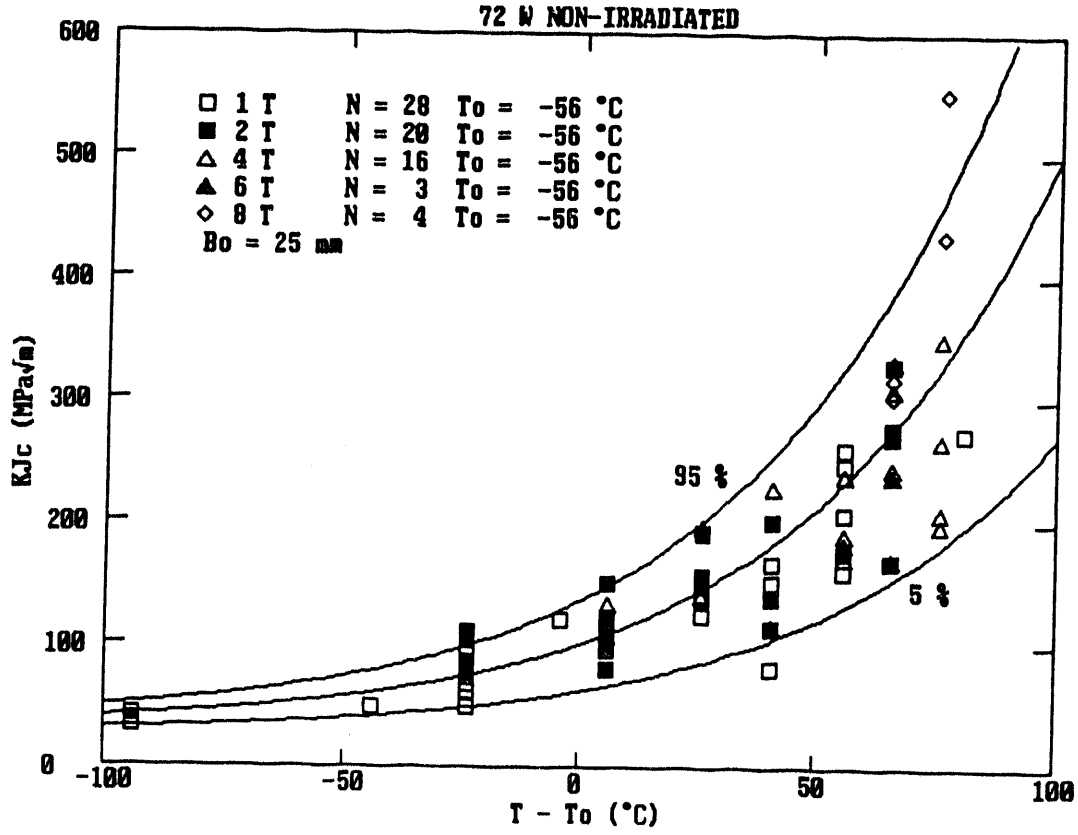

b)

Fig. 9 ORNL data 72W [50]. Only statistical thickness correction performed. a) T_0 fitted, b) T_0 fixed

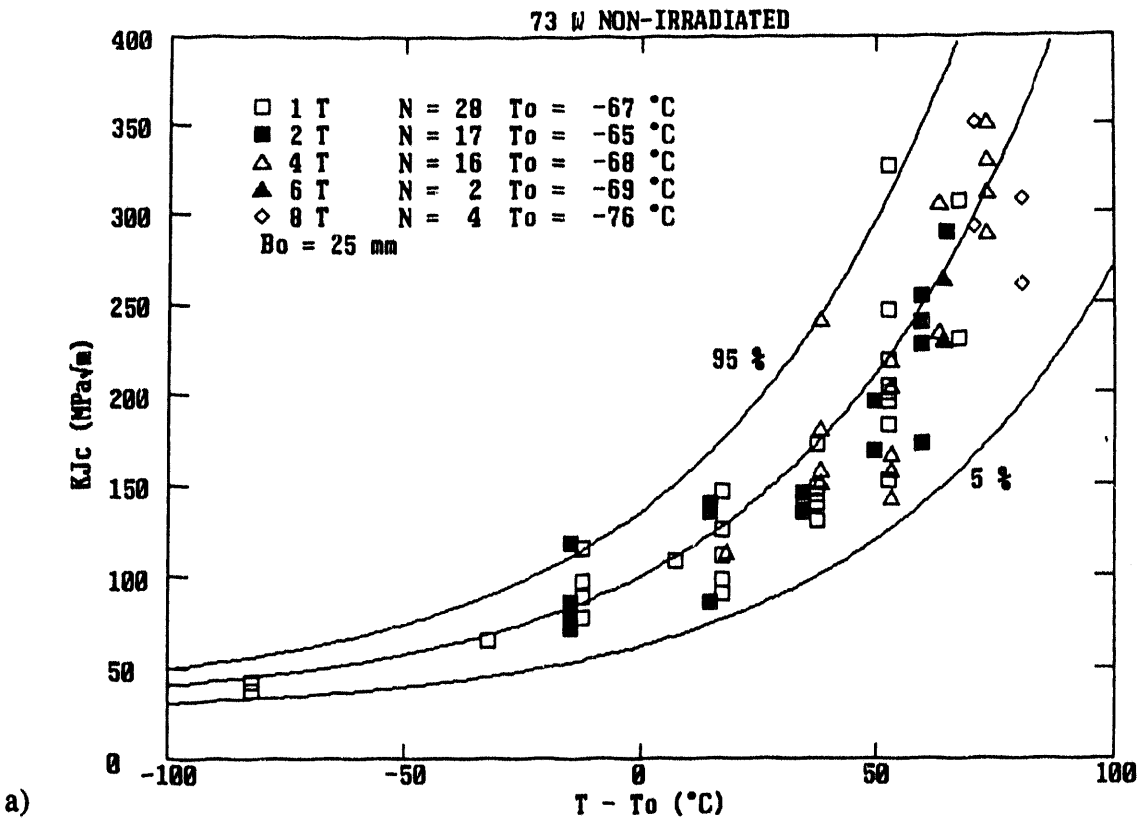

a)

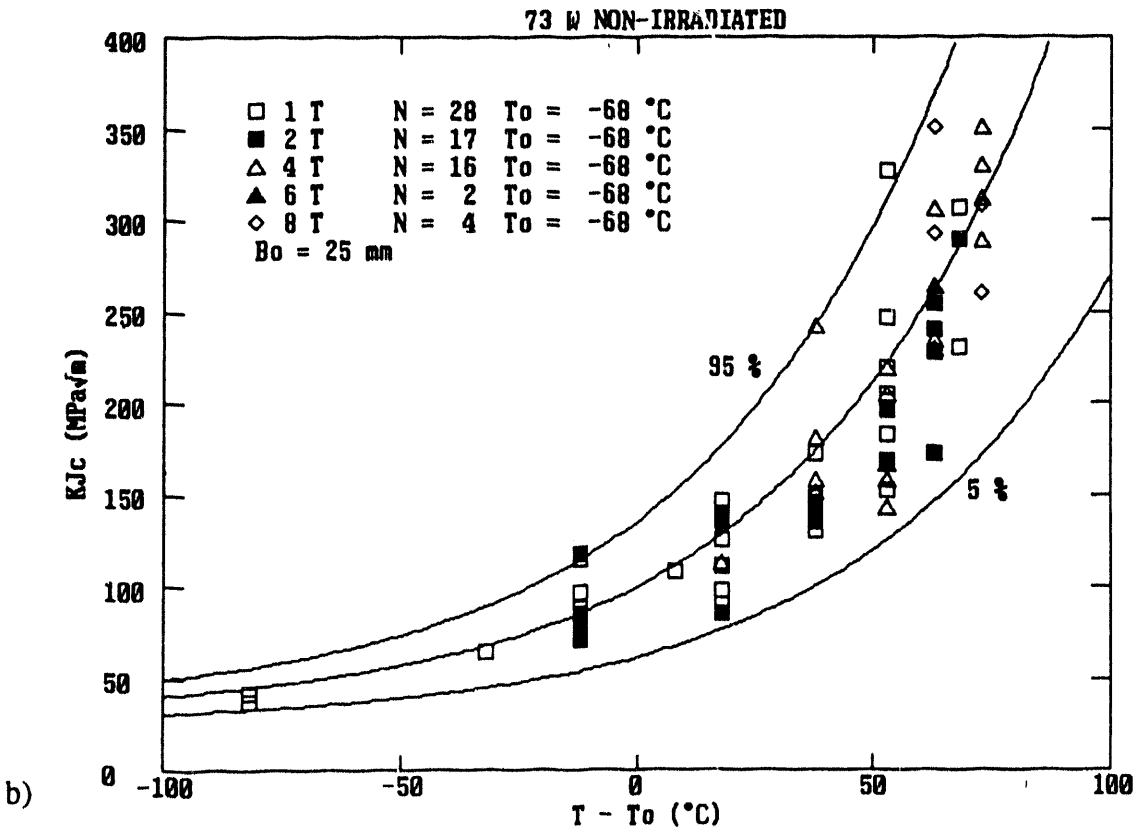

b)

Fig. 10 ORNL data 73W [50]. Only statistical thickness correction performed.
a) T_0 fitted, b) T_0 fixed

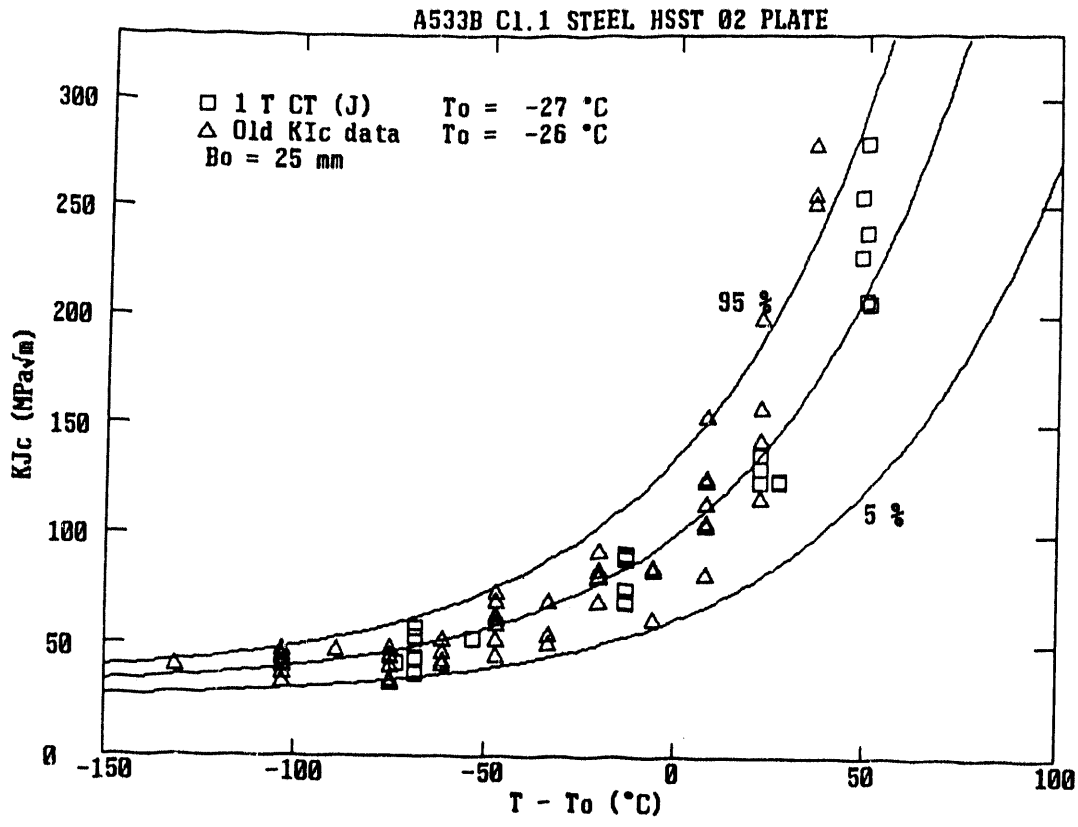

Fig. 11 HSST 02 plate data. Only statistical thickness correction performed.

Considering the fact that no corrections regarding loss of constraint and/or ductile crack growth have been perforemed, the estimated T_0 values are remarkably specimen size indpendent. The largest discrepancy are shown by the 100 mm thick specimens corresponding to Japanese A533B Cl.1 steel (JRQ) tested by VTT (figure 7). In this case the discrepancy is likely to be caused by a observed toughness gradient through the plate thickness. Figure 11 depicts both K_{IC} test results as well as K_{JC} test results. The specimen thickness for the K_{IC} data varied in the range 25 mm - 300 mm. Both parameters yield practically the same T_0 estimate. Thus, also equation 3 is validated. For all materials, the measured fracture toughness scatter follows comparatively well the theoretical scatter lines that have been included in the figures.

The reason why loss of constraint and ductile tearing effects do not seem to play a major role upon the fracture toughness is likely to be due to the fact that the effects contradict each other. Thus, it appears to be possible to relax the existing specimen size requirements quite considerably.

As an attempt to try to establish a new size requirement a large data set generated by Ingham & al. was analysed. The specimens where square section bend specimens with B/(W-a) ≈ 2. For this type of specimens the ligament is likely to be the critical dimension limiting the specimens measuring capacity. The size corrected data are presented in figure 12. No significant specimen size effects are visible despite the fact

that the fracture toughness levels are quite high. Figure 13 depicts the K_0 values based on equation 4. Even though a slight specimen size effect now is visible, no conclusions regarding size requirements can be drawn based on the results. Next, the lowest fracture toughness values at each temperature were applied together with equation 5 (figure 14). Even, when analyzed in this way the estimated T_0 values do not indicate any clear loss of constraint effects. If any, the data indicate a reverse size effect with the smallest specimen yielding the highest transition temperature. The scatter of K_0 is, however, large, because each estimate relates only to one specimen. Comparing the T_0 estimates in figures 13 and 14 it is seen that equations 4 and 5 yield not too significantly differing results. This offers further validation of the recommendations.

At the highest test temperatures in figure 14 the estimated K_0 values seem to rise more rapidly than predicted. When the K_0 estimates are normalized by a fixed temperature the rise is even more clear (figure 15). Also, smaller specimens begin the rise at lower toughness levels. For each specimen size it is possible to determine the highest toughness level where the rise have not begun and the lowest level were it has begun. The specimen size requirement should then lie between these values. This selection is presented in figure 16. Based on the results, the following size requirement seems realistic

$$b \geq 1/\pi^2 \cdot \{K_{JC}/\sigma_y\}^2 \qquad (8)$$

The materials yield stress is approximately 500 MPa. Thus, in terms of J, eqation 8 indicates an α-value of 46. This is surprisingly close to a value of 50 as proposed earlier for cleavage fracture [39,42].

The above analysis validates effectively the presented recommendations. Equation 8 can be applied as a size criterion for elastic plastic brittle fracture toughness. If the transition temperature T_0 is determined it appears possible to relax the size criterion further, without significantly affecting the reliability of the analysis.

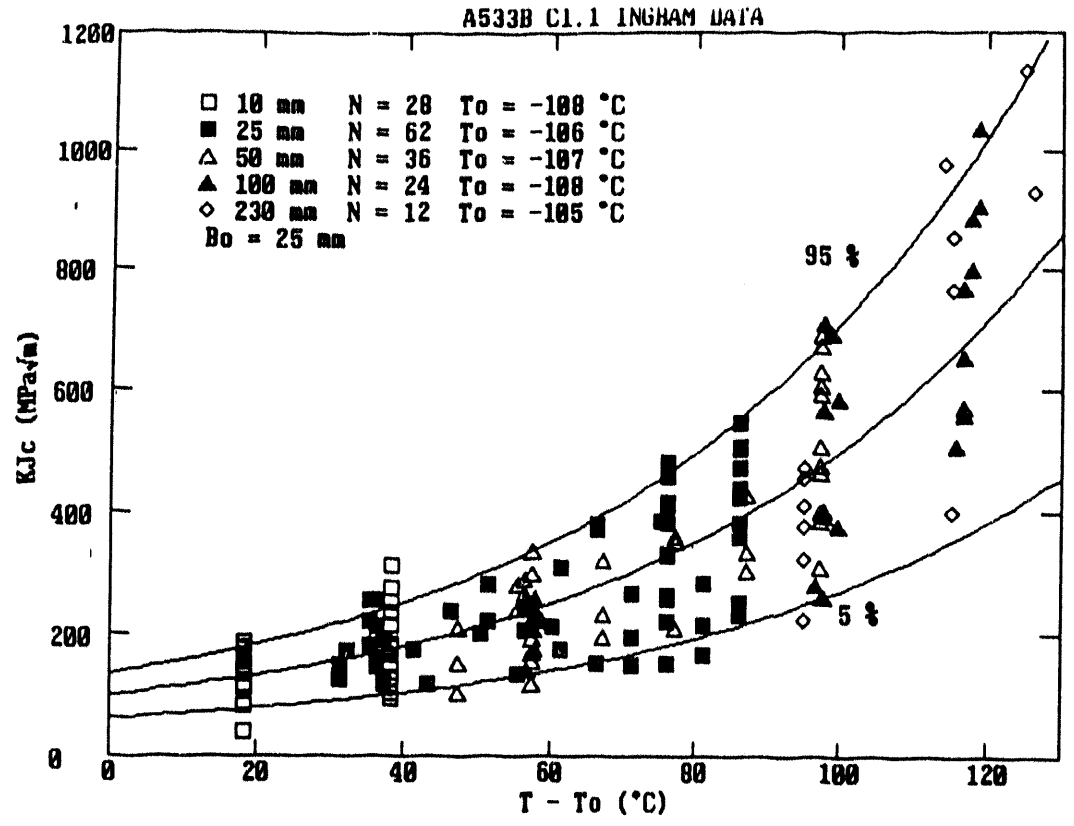

Fig. 12 Ingham data A533B [51]. Only statistical thickness correction performed.

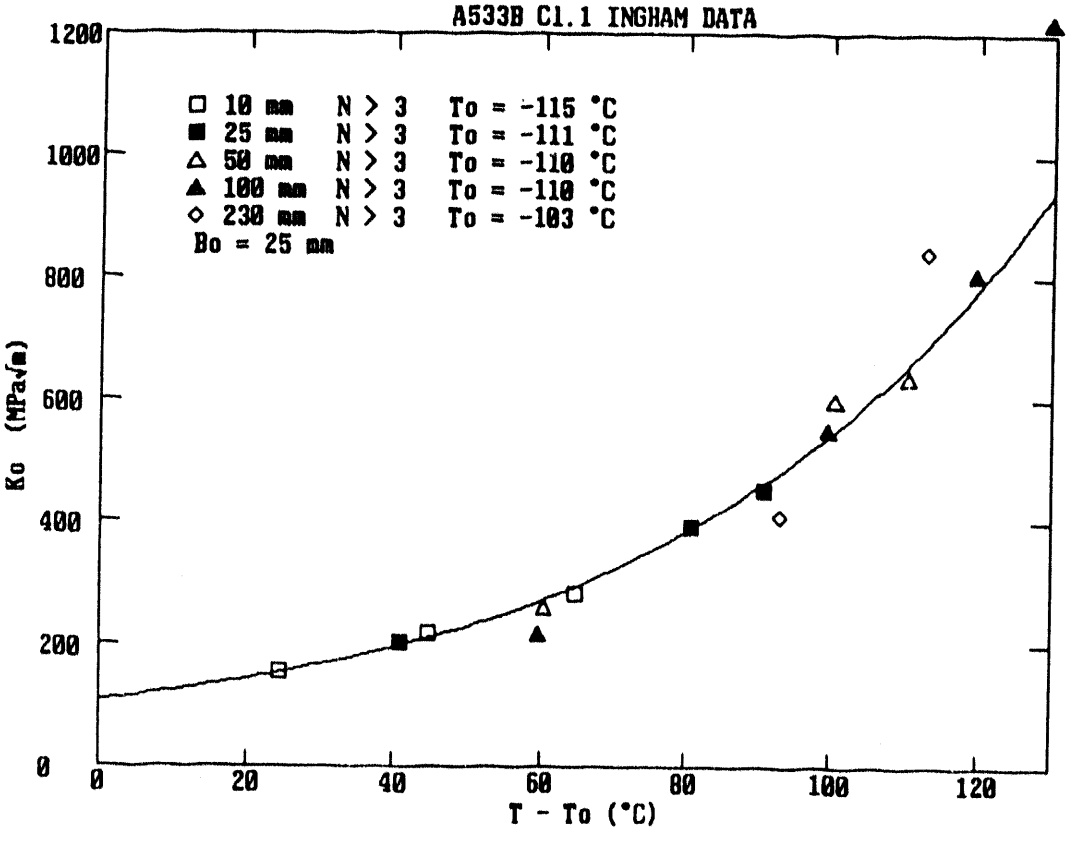

Fig. 13 Ingham data A533B [51]. K_0 estimated based on equation 4.

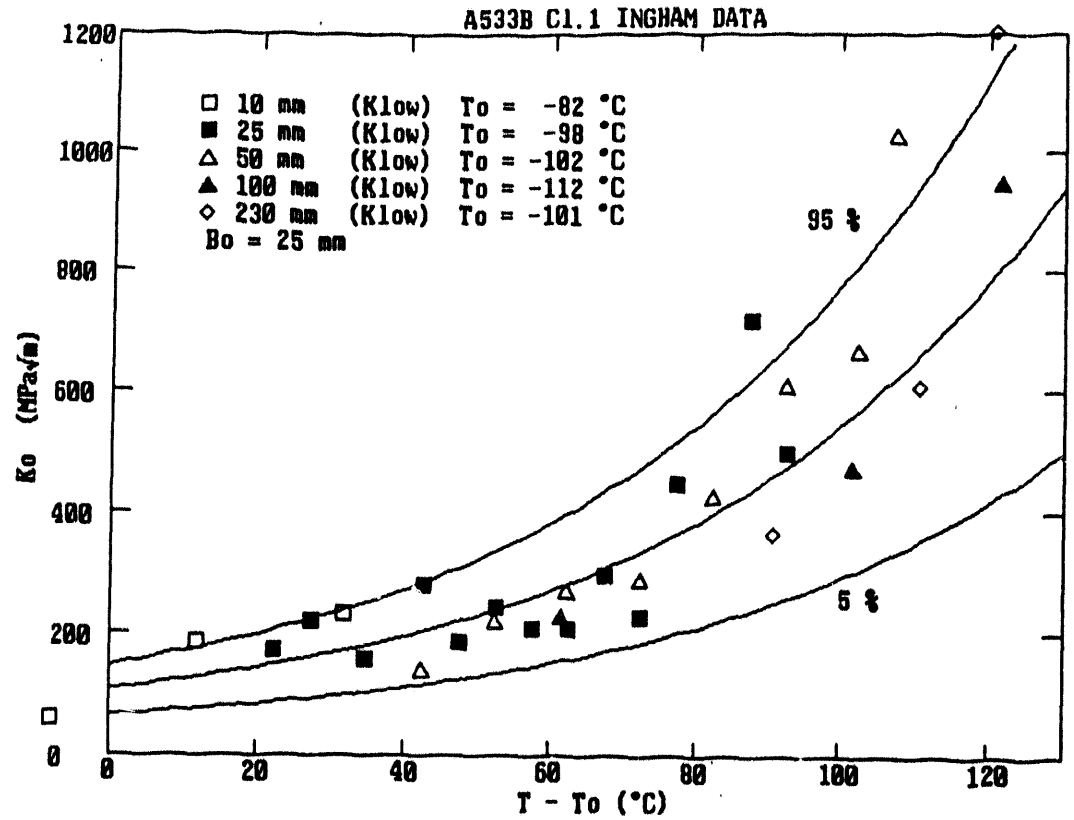

Fig. 14 Ingham data A533B [51]. K_0 estimated based on lowest fracture toughness.

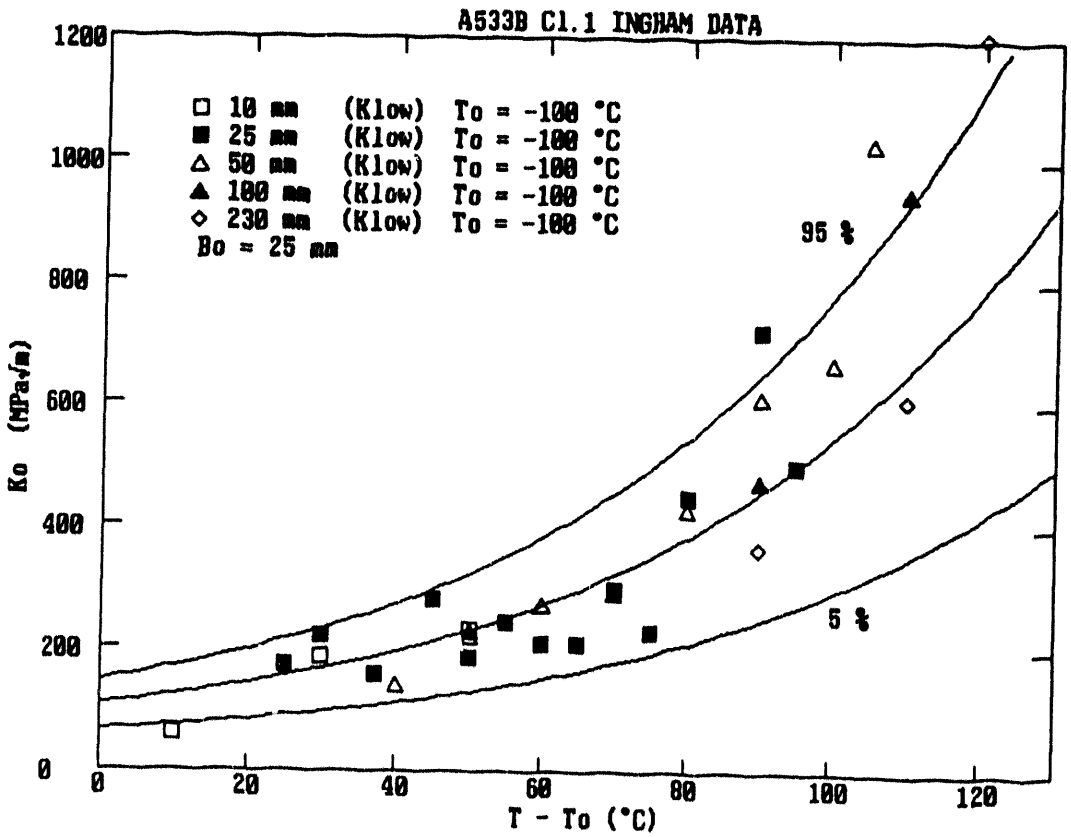

Fig. 15 Ingham data A533B [51]. K_0 estimated based on lowest fracture toughness. T_0 fixed.

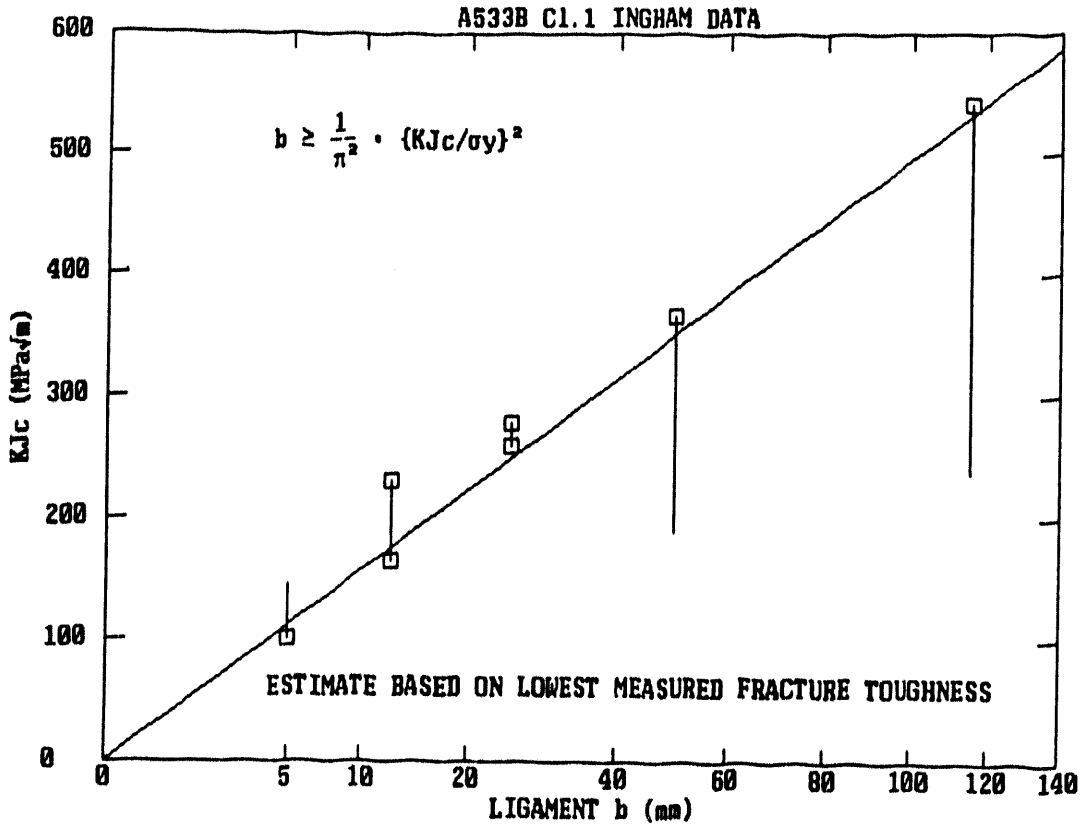

Fig. 16 Ingham data A533B [51]. Size criterion based on behavior of lowest fracture toughness.

SUMMARY AND CONCLUSIONS

The topic concerning recommendations for the application of fracture toughness data for structural integrity assessments have been addressed, focussing on the application of brittle (cleavage type) fracture data. Simple guidelines for obtaining optimum "best-" and "safe-" estimates of the behavior of the actual structure based on small specimen data have been presented and validated.

The following main conclusions can be made

- Weakest link statistics based models produce realistic descriptions of the fracture toughness scatter and specimen size effects.

- The elastic plastic K_{JC} yield equivalent results with valid K_{IC} results.

- The following size requirement, for elastic plastic brittle fracture, seems realistic

$$b \geq 1/\pi^2 \cdot \{K_{JC}/\sigma_y\}^2$$

- If the transition temperature T_0 is determined it appears possible to relax the size criterion further, without significantly affecting the reliability of the analysis.

ACKNOWLEDGEMENTS

This work is a part of the Nuclear Power Plant Structural Safety Program performed at the Technical Research Centre of Finland (VTT) and financed by the Ministry of Trade and Industry in Finland, the Finnish Centre for Radiation and Nuclear Safety (STUK) and the Technical Research Centre of Finland (VTT).

REFERENCES

1 Irwin G. R., Fracture Mode Transition for a Crack Traversing a Plate. *J. Basic Engng* ASME 82, 1960, pp. 417-425.

2 Nagai K., Shimizu S., Iwadate M. and Kawano S., The Size Effect on the Brittle Fracture Toughness Under the Large Scale Yielding. *Trans. Japan Welding Soc.* 12, 1981, pp. 14-18.

3 Landes J. D. and Shaffer D. H., Statistical Characterization of Fracture in the Transition Region. *Fracture Mechanics: Twelfth Conference, ASTM STP 700*, American Society for Testing and Materials, Philadelphia, 1980, pp. 368-382.

4 Nakasa K. and Takei H., The Sheet Thickness Dependency of Fracture in High Strength Steels. *Trans. ISIJ* 18, 1978, pp. 25-32.

5 Munz D. and Keller H. P., Effect of Specimen Size on Fracture Toughness in the Ductile Brittle Transition Region of Steel. Fracture and fatigue. *Proc. 3rd Colloquium on Fracture , ECF3.* J.C. Radon, Ed., 1980, pp. 105-117.

6 Hagiwara Y., Fracture Mechanics Approach to Evaluate the Effect of Thickness on Fracture in Heavy Sectioned Steel. *Tetsu-to-Hagané*. 69, (6), 1983, pp. 141-148.

7 Andrews W., Kumar V. and Little M. M., Small-Specimen Brittle-Fracture Toughness Testing. *Fracture Mechanics: Thirteenth Conference, ASTM STP 743*, R. Roberts, Ed., American Society for Testing and Materials,

Philadelphia, 1981, pp. 576-598.

8 Ohtsuka N., Development of J_{IC} Test in Transition Temperature Region. *Transactions of the 7th International Conference on Structural Mechanics in Reactor Technology*, 22-26 August 1983, Chicago, Vol. G, pp. 55-62.

9 Keller H. P. and Muntz D., Effect of Specimen Size on J-Integral and Stress Intensity Factor at the Onset of Crack Extension. *Flaw Growth and Fracture, ASTM STP 631*, American Society for Testing and Materials, 1977, pp. 217-231.

10 Lai M. O. and Ferguson W. G., The Inadequacy of the Plain-Strain Fracture Toughness Test Requirements. *Engng Fracture Mech.* 13, 1977, pp. 285-292.

11 Gilmore C. M., Provenzano V., Smidt F. A., Jr. and Hawthorne J. R., Influence of Thickness and Temperature on Stretched Zone Size in J_{IC} Test. *Metal Sci.* 17, 1983, pp. 177-185.

12 McCabe D. E., Landes J. D. and Ernst H. E., Prediction of Heavy Section Performance of Nuclear Vessel Steel from Surveillance Size Specimens. *Transactions of the 7th International Conference on Structural Mechanics in Reactor Technology*, 22-26 August 1983, Chicago, Vol. G, pp. 47-54.

13 Wallin K. and Törrönen K., Mechanism Based Statistical Requirements for Fracture Toughness Testing. *ECF6, Fracture control of engineering structures. Vol. 1.* H.C. van Elst and A. Bakker, Eds., Engineering Materials Advisory Services Ltd, U.K. 1986, pp. 563-576.

14 Wallin K., The Size Effect in K_{IC} Results. *Engng Fracture Mech.* 22, (1), 1985, pp 149-163.

15 Curry D. A. and Knott J. F., Effect of Microstructure on Cleavage Fracture Toughness of Quenched and Tempered Steels. *Metal Sci.*, 13, 1979, pp. 341-345.

16 Curry D. A., Comparison Between Two Models of Cleavage fracture. *Metal Sci.*, 14, 1980, pp. 78-80.

17 Rosenfield A. and Shetty D., Lower Bound Fracture Toughness of a Reactor-Pressure-Vessel Steel. *Engng Fracture Mech.* 14, 1981, pp. 833-842.

18 Wallin K., Saario T. and Törrönen K., Statistical Model for Carbide Induced Brittle Fracture in Steel. *Metal Sci.*, 18, (1), 1984, pp. 13-16.

19 Wallin K., A Quantitative Statistical Model for Cleavage Fracture Initiation in Carbide Strengthened Steels. *Dr thesis*. Espoo, 1987, 14 p.

20 Wallin K., The Scatter in K_{IC}-Results. *Engng Fracture Mech.*, 19, (6), 1984, pp. 1085-1093.

21 Ritchie R. O., Knott J. F. and Rice J. R., On the Relationship Between Critical Tensile Stress and Fracture Toughness in Mild Steel. *J. Mech. Phys. Solids*, 21, 1973, pp. 395-410.

22 Brückner A. and Munz D., Prediction of Failure Probabilities for Cleavage Fracture From the Scatter of Crack Geometry and of Fracture Toughness Using the Weakest Link Model. *Engng. Fracture Mech.*, 18, 1983, pp. 359-375.

23 Satoh K., Toyoda M. and Minami F., A Probabilistic Approach to Evaluation of Fracture Toughness of Welds with Heterogeneity. *Trans. Japan Welding Society*, 16, 1985, pp. 70-81.

24 Landes J. D. and McCabe D. E., Effect of Section Size on Transition Temperature Behavior of Structural Steels. *Fracture Mechanics: Fifteenth Symposium, ASTM STP 833*, R. J. Sanford, Ed., American Society for Testing and Materials, Philadelphia, 1984, pp. 378-392.

25 Beremin F. M., A Local Criterion for Cleavage Fracture of a Nuclear Pressure Vessel Steel. *Met. Trans.*, 14A, 1983, pp. 2277-2287.

26 Pineau A., Review of Fracture Micromechanisms and a Local Approach to Predicting Crack Resistance in Low Strength Steels. *Advances in Fracture Research, 5th International Conference on Fracture*, D. Francois, Ed., vol. 2, 1981, pp. 553-577.

27 Mudry F., A Local Approach to Cleavage Fracture. *Seminaire International sur L'Approche Locale de la Rupture*, Moret-sur-Loing 1986, pp. 165-186.

28 Evans A. G., Statistical Aspects of Cleavage Fracture in Steel. *Met. Trans.*, 14A, 1983, pp. 1349-1355.

29 Wallin K., Saario T., Törrönen K. and Forstén J., A Microstatistical Model for Carbide Induced Cleavage Fracture. *Technical Research Centre of Finland, Research Reports 220*, Espoo 1983. 15 p.

30 Törrönen K., Wallin K., Saario T., Hänninen H., Rintamaa R. and Forstén J., Optimization of Metallurgical Variables in Fracture Prevention. *Nucl. Eng. Design*, 87, 1985, pp. 225-237.

31 Saario T., Wallin K. and Törrönen K., On the Microstructural Basis of Cleavage Fracture Initiation in Ferritic and Bainitic Steels. *J. Eng. Mat. Tech.*, 106, 1984, pp. 173-177.

32 Slatcher S., A Probabilistic Model for Lower-Shelf Fracture Toughness - Theory and Application. *Fatigue & Frac. of Eng. Mat. & Struc.*, 9, 1986, pp. 275-289.

33 Lin T., Evans A. G. and Ritchie R. O., A Statistical Model of Brittle Fracture by Transgranular Cleavage. *J. Mech. Phys. Solids*, 34, 1986, pp. 477-497.

34 Tyson R. T. and Marandet B., Cleavage Toughness Variability and Inclusion Size Distribution of a Weld Metal. *Fracture Mechanics: Eighteenth Symposium, ASTM STP 945*, D. T. Read and R. P. Reed, Eds., American Society for Testing and Materials, Philadelphia, 1988, pp. 19-32.

35 Anderson T. L., A Combined Statistical and Constraint Model for the Ductile-Brittle Transition Region. *Nonlinear Fracture Mechanics: Vol. II - Elastic-Plastic Fracture, ASTM STP 995*, J. D. Landes, A. Saxena and J. G. Merkle, Eds., American Society for Testing and Materials, Philadelphia, 1989, pp. 563-583.

36 Anderson T. L. and Stienstra D., A Model to Predict the Sources and Magnitude of Scatter in Toughness Data in the Transition Region. *J. Testing and Eval., JTEVA*, 17, 1989, pp. 46-53.

37 Godse R. and Gurland J., A Statistical Model for Low Temperature Cleavage Fracture in Mild Steels. *Acta Metall.*, 37, 1989, pp. 541-548.

38 Wallin K., The Effect of Ductile Tearing on Cleavage Fracture Probability in Fracture Toughness Testing. *Engng. Fracture Mech.* 32, (4), 1989, pp. 523-531.

39 Wallin K., The Effect of Ligament Size on Cleavage Fracture Toughness. *Engng. Fracture Mech.* 32, (3), 1989, pp. 449-457.

40 Anderson T. and Dodds S., Specimen Size Requirements for Fracture Toughness Tseting in the Transition Region. *J. Testing and Eval., JTEVA*, 19, (2), 1991, pp. 123-134.

41 Thaulow C., Debel C., Søvik O., Wallin K., Holmgren M., Olofsson O. and Anderson H., Recommendations on Fracture Mechanics Testing. *NT TECHNICAL REPORT 109*. Nordtest 1989, 32 p. + 184 p. app.

42 Wallin K., Statistical Modelling of Fracture in the Ductile to Brittle Transition Region. *Defect Assessment in Components - Fundamentals and Applications, ESIS/EGF9*, J. G. Blauel & K.-H. Schwalbe, Eds., Mechanical Engineering Publications, London, 1991, pp. 415-445.

43 Wallin K., A Simple Theoretical Charpy-V - K_{Ic} Correlation for Irradia-

tion embrittlement. *Innovative Approaches to Irradiation Damage and Fracture Analysis. PVP-Vol.170*, D.L. Marriott, T.R. Mager & W.H. Bamford, Eds., The American Society of Mechanical Engineers, 1989, pp.93-100.

44 Braam H. and Prij J., A Statistical Evaluation of the Thickness Effect of SENB4 Using the J-Distribution Along the Crack Front. *Transactions of the 9th International Conference on Structural Mechanics in Reactor Technology*, 17-21 August 1987, Lausanne, Ed. F.H. Wittman, vol. G, pp. 33-38.

45 Towers O. L. and Garwood S. J., The Significance of Maximum Load Toughness. *The Welding Institute Research Bulletin*, 20 (10) 1979, pp. 292-299.

46 Anderson T. L., Gordon J. R. and Garwood S. J., On the Application of R-Curves and Maximum Load Toughness to Structures. *Fracture Mechanics: Nineteenth Symposium ASTM STP 969*. T.A. Cruse, Ed., American Society for Testing and Materials, Philadelphia, 1988, pp. 291-317.

47 Wallin K., Fracture Toughness Transition Curve Shape for Ferritic Structural Steels. *Fracture of Engineering Materials & Structures.*, S.T. Teoh & K.H. Lee, Eds., Elsevier Applied Science. 1991, pp. 83-88.

48 Iwadate T., Tanaka Y., Ono S. and Watanabe J., An Analysis of Elastic-Plastic Fracture Toughness Behavior of J_{IC} Measurement in the Transition Region. *Elastic-Plastic, Fracture: Second Symposium, Volume II-Fracture Resistance Curves and Engineering Applications, ASTM STP 803*. C.F. Shih and J.P. Gudas, Eds., American Society for Testing and Materials, Philadelphia, 1983, pp. II-531 - II-561.

49 Wallin K., Valo M., Rintamaa R., Törrönen K. and Ahlstrand R., IAEA Coordinated Research Programme on "Optimizing of Reactor Pressure Vessel Surveillance Programmes and Their Analyses" Phase 3 - Results of the Finnish Contribution, Technical Research Centre of Finland, to be published.

50 Nanstad R. K., McCabe D. E., Haggag F. M., Bowman K. O. and Downing D. J., Statistical Analysis of Fracture Toughness Results for Two Irradiated High-Copper Welds. *Effects of Radiation on Materials: 15th International Symposium, ASTM STP 1125*. R.E. Stoller, A.S. Kumar and D.S. Gelles, Eds., American Society for Testing and Materials, Philadelphia, 1992, pp. 270-291.

51 Ingham T., Knee N., Milne I. and Morland E., Fracture Toughness in the Transition regime for A533B Steel: Prediction of Large Specimen Results from Small Specimen Tests. *Fracture Mechanics: Perspectives and*

Directions: Twentieth Symposium, ASTM STP 1020. R.P. Wei and R.P. Gangloff, Eds., American Society for Testing and Materials, Philadelphia, 1989, pp. 369-389.

CONSTRAINT EFFECTS IN HEAVY-SECTION STEELS*

B. R. Bass, D. K. M. Shum, J. Keeney-Walker, and T. J. Theiss

Heavy-Section Steel Technology Program
Oak Ridge National Laboratory
Oak Ridge, Tennessee 37831

Abstract

A focal point of the Nuclear Regulatory Commission-funded Heavy-Section Steel Technology (HSST) Program is the development of technology required for accurate assessment of fracture-prevention margins in commercial nuclear reactor pressure vessels (RPVs). In a series of investigations, the HSST Program is seeking to obtain an improved understanding of the relationships governing transfer of fracture toughness data from small-scale specimens to large-scale structures. Current pressure vessel fracture-prevention technology relies on the use of fracture-correlation parameters such as the stress-intensity factor (K) and the Hutchinson, Rice, and Rosengren intensity parameter (J) to characterize both the applied load and the resistance of material to crack initiation. Shortcomings of these conventional one-parameter fracture-correlation methods, which impact issues associated with the transferability of small-specimen toughness data to large-scale structural applications, are being addressed through development of various two-parameter methods. This paper describes two analytical approaches to the transferability issues that are being evaluated in the HSST Program. One is a continuum correlative methodology based on two-parameter descriptions (K-T or J-Q) of the near crack-tip fields that incorporate effects of the higher-order T-stress for linear-elastic fracture mechanics conditions or the Q-stress for more general elastic-plastic fracture mechanics conditions. The second approach utilizes a micromechanical predictive methodology that relates cleavage crack initiation to the attainment of a critical volume enclosed within a selected maximum principal stress contour surrounding the crack tip. In preliminary evaluations, these methodologies were applied to experimental data taken from several intermediate- and large-scale testing programs. Results and conclusions from these applications are discussed in the paper. Applications of the methodologies to analytical studies concerning biaxial stress effects on fracture toughness and safety margin assessments of an RPV subjected to pressurized-thermal-shock transient loadings are also presented. While these fracture methodologies appear to show promise in being able to differentiate among crack-tip constraint levels, numerous issues were identified in the HSST studies that require further investigation. Recommendations are given concerning future work intended to resolve several of these issues.

1 Introduction

The Nuclear Regulatory Commission (NRC)-funded Heavy-Section Steel Technology (HSST) Program seeks to develop the technology required for accurate assessment of fracture-prevention margins in commercial nuclear reactor pressure vessels (RPVs). Pressurized-thermal shock (PTS) has emerged as a loading condition of primary concern in RPV fracture-margin

*Research sponsored by the Office of Nuclear Regulatory Research, U.S. Nuclear Regulatory Commission under Interagency Agreement 12886-8011-9B with the D.S. Department of Energy under Contract DE-AC05-84OR21400 with Martin Marietta Energy Systems, Inc.

safety assessments. A number of fracture-technology issues, which have the potential for significant impact on analyses of PTS events, are being addressed in the HSST Program. The issue of concern in this paper is the role of crack-tip constraint in fracture toughness data transfer. In a series of investigations,[1] the HSST Program is working to obtain an improved understanding of relationships governing the transfer of fracture toughness data from small-scale specimens to large-scale structures.

Current pressure vessel fracture-prevention technology relies on the use of correlation fracture parameters such as the stress-intensity factor (K) and the Hutchison[2] and Rice and Rosengren[3] (HRR) intensity parameter (J) to characterize both the applied load and the resistance of material to crack initiation. The parameter K applies to linear-elastic fracture mechanics (LEFM) conditions, whereas J is the relevant parameter for either LEFM or more general elastic-plastic fracture mechanics (EPFM) conditions. Provided that the near-tip stress and strain fields display an annular region characterizable by K or J, and that the annular region is of sufficient size so that a continuum description is physically meaningful (Fig. 1), the magnitude of this parameter at crack initiation is assumed to be a material property. The existence and/or dimensions of these annular regions depend on structural geometry, crack geometry, material properties, and loading conditions. The influence of these various factors on local crack-tip stress and strain fields is the primary consideration in the study of constraint effects on fracture.

These conventional one-parameter fracture correlation methods have been validated for moderately deep-crack, high-constraint geometries loaded under LEFM conditions. However, difficulties associated with applications of the methods to cracks in relatively low-constraint geometries are well known.[4] The impact of constraint conditions on apparent fracture toughness is illustrated in Fig. 2 for deep- and shallow-crack beams in bending, respectively, that were tested in the HSST Program and described in Ref. 4. Thirty-eight relatively large laboratory beam specimens were tested to compare the behavior of specimens with shallow cracks with that of specimens with deep cracks. All specimens were 100 mm deep (W). Shallow-crack beams had

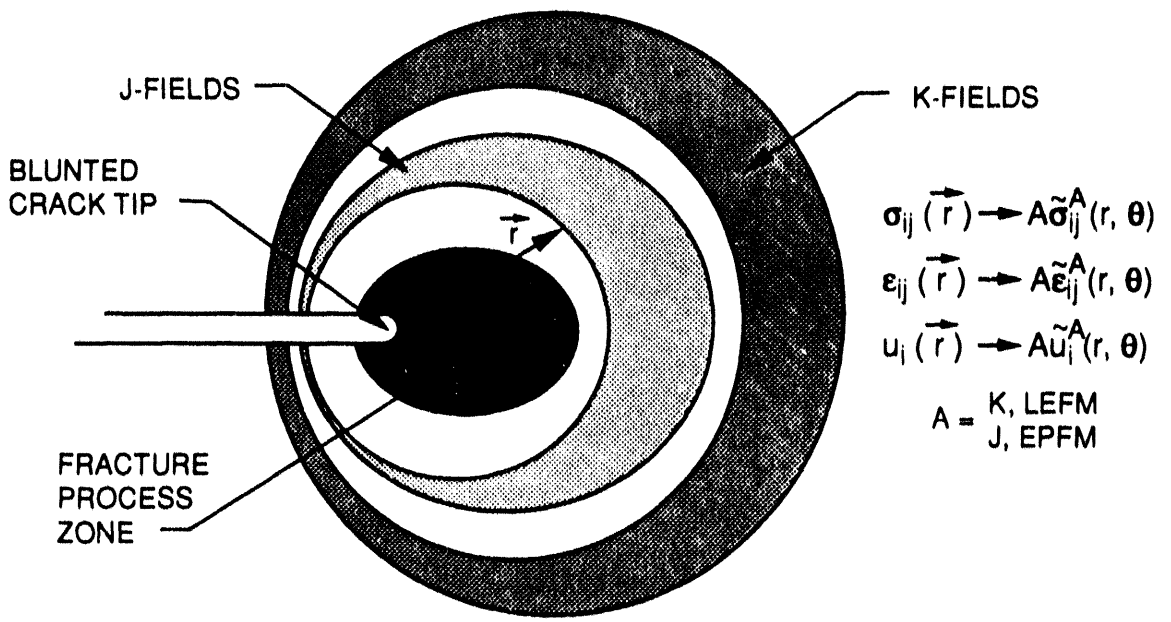

Fig. 1. Depiction of near-crack-tip fields displaying annular regions characterizable by K or J.

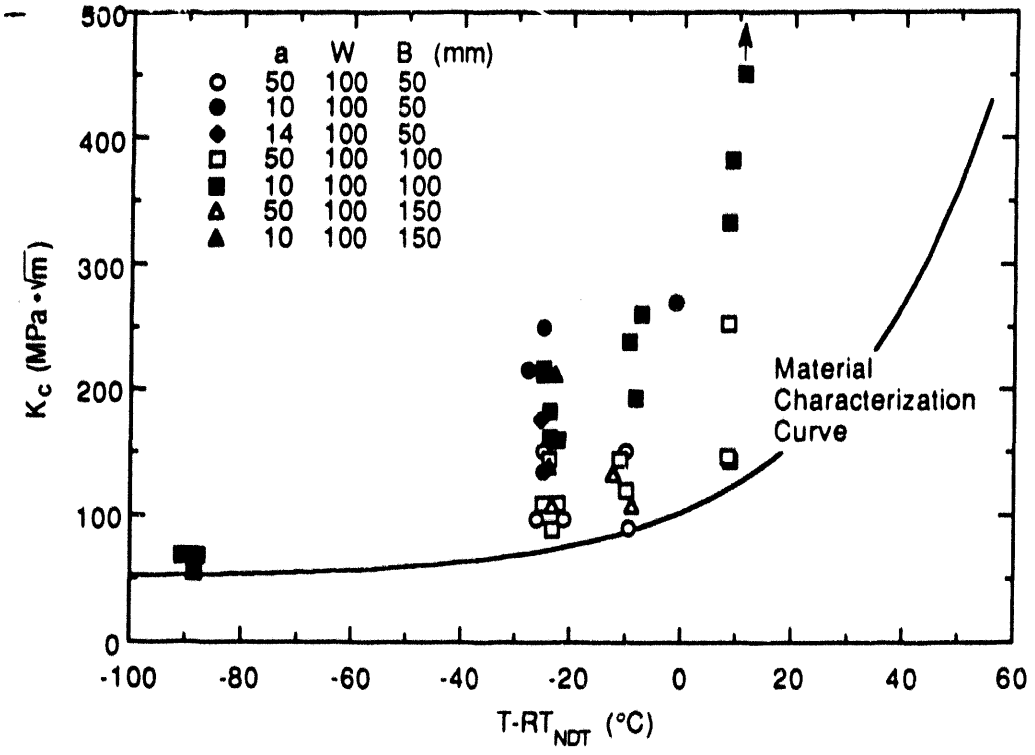

Fig. 2. Fracture-toughness (K_c) data vs normalized temperature for shallow- and deep-crack specimens.

crack depths ranging from 9 to 14 mm (a/W ~ 0.1 to 0.14), while deep-crack beams had 50-mm-deep cracks (a/W ~ 0.5). The toughness data presented in Fig. 2 are expressed in terms of K_c vs temperature (along with a material characterization curve for HSST Plate 13A[5]). All of the specimens failed in cleavage except the data point indicated with the arrow in Fig. 2. The shallow-crack specimens tested on the lower shelf showed little or no toughness increase relative to the material characterization curve. The results showed conclusively that shallow-crack beam specimens made of A 533 grade B (A 533 B) class 1 steel have a significant increase in crack-tip-opening displacement (CTOD) or J_c toughness (~150%) and K_c toughness (~60%) in the transition region. Analysis results presented in Ref. 4 indicate that crack initiation for the deep-crack beams occurred under essentially K-dominant conditions, whereas conditions in the shallow-crack beams are outside the domain of validity of the one-parameter characterization methods summarized in Fig. 1.

The influence of crack-tip constraint on fracture toughness as manifested in the shallow-crack effect may have important implications for PTS analyses. Probabilistic fracture-mechanic analysis of RPVs have shown that shallow cracks dominate the conditional probability of vessel failure in PTS evaluations,[6–8] with up to 95% of all initial crack initiations originating from cracks having depths of 25 mm or less (Fig. 3). Thus, a clear und standing of the constraint conditions associated with shallow cracks is required for an improved probabilistic PTS assessment.

Shortcomings of the conventional one-parameter methods, as demonstrated in the deep- and shallow-crack beam applications described above, are being addressed by the HSST Program through development and evaluation of two different analytical approaches. One is a continuum

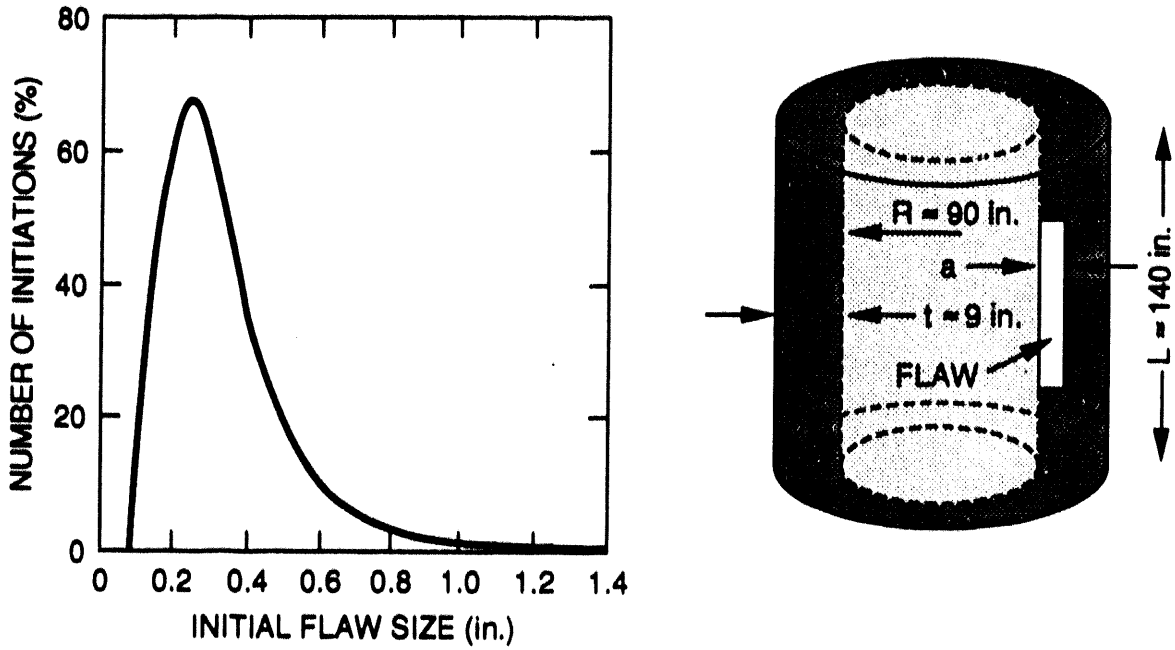

Fig. 3. Distribution (%) of flaw size, initiation, and failure in probabilistic fracture mechanics analysis of RPV.

correlative approach that addresses crack initiation by focusing on the near-crack-tip fields, along the crack plane, within a region extending a few CTODs directly ahead of the tip. The two-parameter descriptions of the near-crack-tip fields incorporate effects of the higher-order T-stress for LEFM conditions or the Q-stress for more general EPFM conditions. The T-stress parameter is the second term in the Irwin-Williams[9,10] series expansion of the opening-mode stress about the crack tip. The Q-stress plays the role of higher-order terms in the HRR series expansion and is readily interpreted as a hydrostatic stress superimposed on the HRR solution.[11] Detailed results for these near-crack-tip fields are obtained using the boundary-layer method. A boundary-layer method does not involve explicit consideration of loading and geometry but incorporates these factors through imposition of displacement and stress boundary conditions taken from asymptotic solutions.

The second approach[12] focuses on the development of parameters that relate fracture toughness within a volume of material loaded above threshold values of nominal stress states. Candidate parameters include, but are not limited to, those based on a critical maximum principal stress contour methodology. This methodology predicts the onset of cleavage crack initiation based on the attainment of a critical volume enclosed within a selected maximum principal stress contour surrounding the crack tip. A relationship between fracture toughness and this numerically determined volume parameter is obtained through applications of the methodology to cleavage-initiation data.

These two approaches are described in more detail in Sects. 2 and 3 and evaluated through applications to a variety of HSST test data in Sects. 4 and 5. Section 3 includes a description of the Ritchie-Knott-Rice (RKR) micromechanical fracture model that is used for predictions of cleavage fracture initiation in two of these applications.

As described in Sect. 4, the J-Q technique was employed extensively in posttest assessments of the HSST shallow-crack fracture toughness program.[4] The Q-stress parameter

was used to correlate crack-tip constraint in both deep- and shallow-crack specimens tested in the program. Both the J-Q and the stress-contour methodologies were applied to the cleavage-initiation data obtained from the WP-1 series of HSST wide-plate crack-arrest tests.[5,13] Loads required to initiate cleavage fracture in the Series I wide plates were substantially higher than had been predicted from small specimen data, with K_c/K_{Ic} ratios as high as ~4. The fracture methodologies were used to quantify the discrepancy between predicted and observed crack-initiation toughness. In the case of J-Q applications, the $J_c(Q)$ toughness locus (described in Sect. 2) from the wide-plate data is also compared with that determined from the shallow- and deep-crack beam data. For both the wide-plate and shallow-crack beam specimens, predictions of fracture toughness from the RKR model are compared with measured data.

In Sect. 5, another application[14,15] of the J-Q methodology is described that concerns the development and validation of analytical methods for estimating the potential impact of out-of-plane biaxial far-field stresses on crack-initiation toughness of shallow inner-surface cracks in nuclear RPVs. Motivation for this study comes from the observation that, while existing fracture toughness data are largely obtained under nearly plane strain conditions in compact tension (CT) test specimens, far-field tensile stresses are present in RPVs that act in a direction parallel to the crack front for both axial and circumferential flaws. The components of a typical far-field stress distribution existing in the wall of an RPV during a PTS transient are shown in Fig. 4 (from

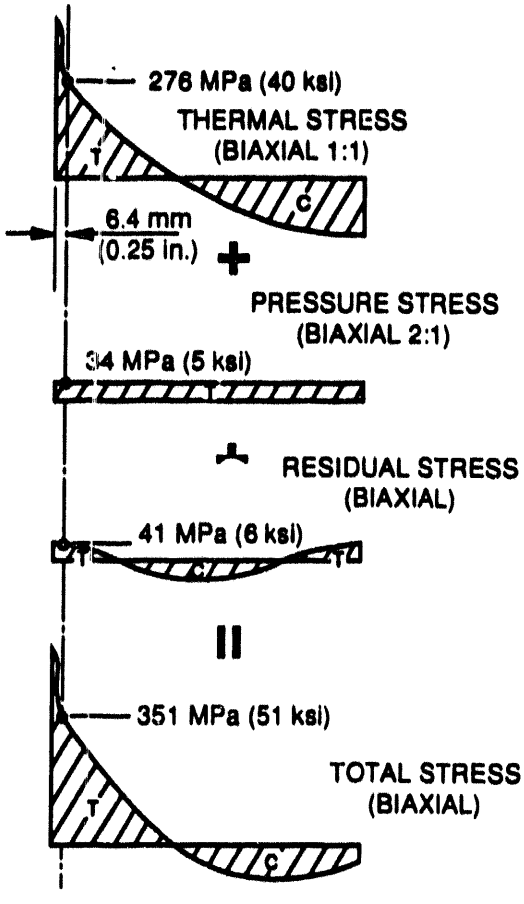

Fig. 4. Components of far-field stress distribution existing in reactor vessel wall during PTS transient.

Ref. 16). The thermal, pressure, and residual stresses are all biaxial, with both in-plane and out-of-plane components. This biaxial stress distribution occurs both during the normal operation of an RPV and under postulated PTS conditions. In Fig. 5 (from Ref. 16), tensile out-of-plane stresses acting parallel to a shallow longitudinal crack in an RPV are on the order of 350 MPa in a PTS transient. These far-field out-of-plane stresses have no equivalence in compact specimens used in conventional fracture toughness testing. Any potential increase in crack-tip constraint resulting from these out-of-plane biaxial stresses presumably would act in opposition to the in-plane constraint relaxation that has been previously demonstrated for shallow cracks.[4] Consequently, understanding of both in-plane and out-of-plane crack-tip constraint effects is necessary to a refined analysis of fracture initiation from shallow cracks under PTS transient loading. A summary overview of the HSST investigation of biaxial effects on constraint, including overall conclusions and recommended plans for further development and validation, are given in Sect. 5.

Section 6 describes analyses that were performed to evaluate the utility of the J-Q approach for characterizing the crack-tip fields in an RPV during a PTS transient. The PTS transient simulates the pressure-temperature history during a small-break loss-of-coolant accident (SBLOCA). In conjunction with these analyses, a methodology is described that incorporates small-specimen $J_c(Q,T)$ toughness locus data into the safety-margin assessment of an RPV.

Finally, conclusions and recommendations concerning future work to resolve some important RPV-related constraint issues are given in Sect. 7.

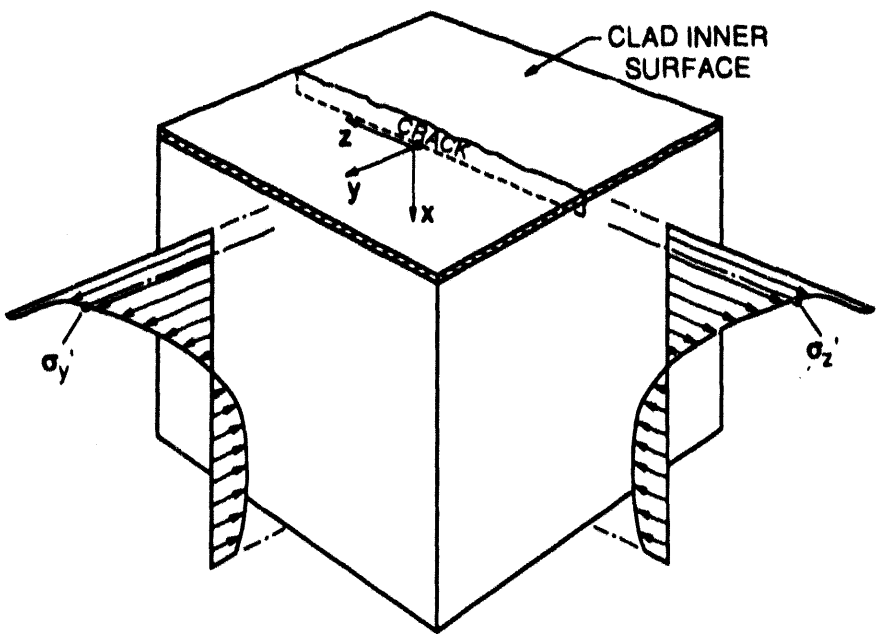

Fig. 5. Vessel wall biaxial far-field stresses during PTS transient with one component aligned parallel to front of longitudinal crack.

2 Definition of T-Stress and Q-Stress Parameters

2.1 Definition of T-Stress Parameter

Within the context of LEFM, the asymptotic two-dimensional (2-D) near-crack-tip fields, as a function of position relative to the crack tip, can be expressed in the form of infinite series. Let (r,θ) denote the position of a material point relative to the crack tip in polar coordinates. The infinite series denoting the Mode I stress components then take the form

$$\sigma_{ij}a = \frac{K_I}{\sqrt{2\pi r}}\tilde{\sigma}_{ij}(\theta) + T\delta_{ij}\delta_{i1} + \ \ldots\ , \tag{1}$$

where $\tilde{\sigma}_{ij}(\theta)$ are functions that are dependent on the angular coordinate θ only. These infinite series are commonly referred to as the Irwin-Williams series.[9,10] The first terms in these series become unbounded as the crack tip is approached. The stress-intensity factor K is the amplitude of the first terms in Eq. (1), and its value is undetermined from the asymptotic expansion.

The T-stress term is the next higher-order term in the series expansion for the opening-mode stress component. The T-stress term describes a stress field that is independent of position relative to the crack front and represents a uniform stress field parallel to the plane of the idealized 2-D crack. Within the context of three-dimensional (3-D) LEFM, the Irwin-Williams asymptotic expansion concept can be generalized, resulting in three T-stress-like terms.[17,18]

2.2 Definition of Q-Stress Parameter

Within the context of EPFM, the counterpart to the Irwin-Williams series in two dimensions is the HRR solution for a deformation-theory material, for which the uniaxial stress-strain relation is of the Ramberg-Osgood form.[2,3] The infinite series denoting the Mode I stress components have the form

$$\sigma_{ij} = \left(\frac{J}{\alpha\sigma_0\varepsilon_0 I_n r}\right)^{\frac{1}{n+1}}\hat{\sigma}_{ij}(\theta) + \ \ldots\ , \tag{2}$$

where $\hat{\sigma}_{ij}(\theta)$ are universal functions dependent on the angular coordinate θ only. In the HRR solution, the first terms are also singular with an amplitude undetermined from the asymptotic analysis, which corresponds to the value of the J-integral. Because the J-integral is path-independent for all deformation-theory material, its value can be evaluated from locations remote from the crack front. It is the path-independence of the J-integral, and its identification with the amplitude of the HRR field, that forms the basis of conventional one-parameter EPFM theory.

In a manner somewhat analogous to T-stress, the Q-stress term[11] plays the role of higher-order terms in the HRR expansion in the sense that the Mode I stress components in these series are assumed to take the form

$$\sigma_{ij} = \sigma_0\left(\frac{J}{\alpha\sigma_0\varepsilon_0 I_n r}\right)^{\frac{1}{n+1}}\hat{\sigma}_{ij}(\theta) + Q\sigma_0\delta_{ij} \quad \text{for } |\theta| < \pi/2,\ 2J/\sigma_0 \le r \le 5J/\sigma_0\ . \tag{3}$$

Unlike the T-stress term, the Q-stress term is not an analytic consequence of the asymptotic expansion. Instead, use of the Q-stress parameter in the context of Eq. (3) follows from the

following numerical observation. Detailed finite-element analyses performed for power-law hardening materials indicate that the near-crack-tip solutions appear to be consistent with the assumed expansion indicated in Eq. (3).[11] This assumed form generally applies only to the forward sectors symmetric about the crack plane ahead of the crack tip, extending ~90° to either side of the crack plane and over distances of the order $2 \le r/(J/\sigma_0) \le 5$. Consequently, the utility of a Q-stress description of the near-crack-tip fields requires that the physical micromechanisms of fracture be confined to this same region. The Q-stress term is readily understood as a state of hydrostatic tension superimposed on the HRR solution. As described in Ref. 11, the Q-stress is related to the T-stress under conditions for which the T-stress can be defined. The methodology for extending the Q-stress concept into 3-D fracture analysis is still an open issue.

Due to the numerical nature of its definition, determination of the Q-stress term is not without ambiguity. In its original development, the Q-stress term was defined as the difference between the full-field stress solution of a given problem and the reference HRR stress solution along the crack plane. (The full-field solutions are the stress and strain distributions within a structure obtained by explicitly considering the influence of the finite geometry of the structure and the crack.) It is observed that the Q-stress term thus determined is nearly constant over a distance up to 5 J/σ_0 ahead of the original crack tip. Definition of the Q-stress term is then made more precise by identifying Q-stress as the difference between the opening-mode stress component of the full-field and reference solutions at a distance of $2J/\sigma_0$ ahead of the crack front.

A more recent approach[19,20] is to define a second form for the Q-family of fields using the small-scale yielding (SSY) solutions as the reference (Q = 0) solution:

$$\sigma_{ij} = \left(\sigma_{ij}\right)_{SSY} + Q\sigma_0\delta_{ij} \quad \text{for } |\theta| < \pi/2,\ 2J/\sigma_0 \le r \le 5\ J/\sigma_0\ . \tag{4}$$

The Q-stress term is then defined as the difference between the opening-mode stress component of the full-field distribution and the corresponding quantity in the associated SSY problem at a distance of 2 J/σ_0 ahead of the crack front.

Conditions of SSY are present in a fracture mechanics application when an annular region surrounding the crack tip can be located for which the combined influence of geometry, material behavior, and loading conditions can be expressed in terms of an "applied" value K that characterizes the magnitude of the near-crack-tip fields. Plane-strain fracture toughness is identified with the magnitude of K at the onset of crack initiation under conditions of SSY. Adoption of the SSY crack-tip fields as the reference distributions from which the Q-stress parameter is evaluated thus represents a natural measure of deviation from plane-strain constraint.

Shih* has presented an interpretation of the two-parameter J-Q theory that spans the range of stress states extending from linear-elastic through elastic-plastic conditions. In this interpretation, J is a measure of the deformation that scales the size of the fracture process zone, while Q scales the triaxiality level ahead of the crack tip. For essentially LEFM conditions, the deformation fields and triaxiality are tightly coupled, so that the imposition of tensile or compressive out-of-plane stresses can affect triaxiality. Under conditions of substantial plastic deformation, however, the deformation fields and stress triaxiality are independent parameters, with triaxiality being affected only by the imposition of a state of pure hydrostatic stress (Fig. 6).

*C. F. Shih, "J-Q Fracture Methodology," presented at the Workshop on Constraint Effects in Fracture, sponsored by U.S. Nuclear Regulatory Commission, Rockville, Md., March 3, 1992.

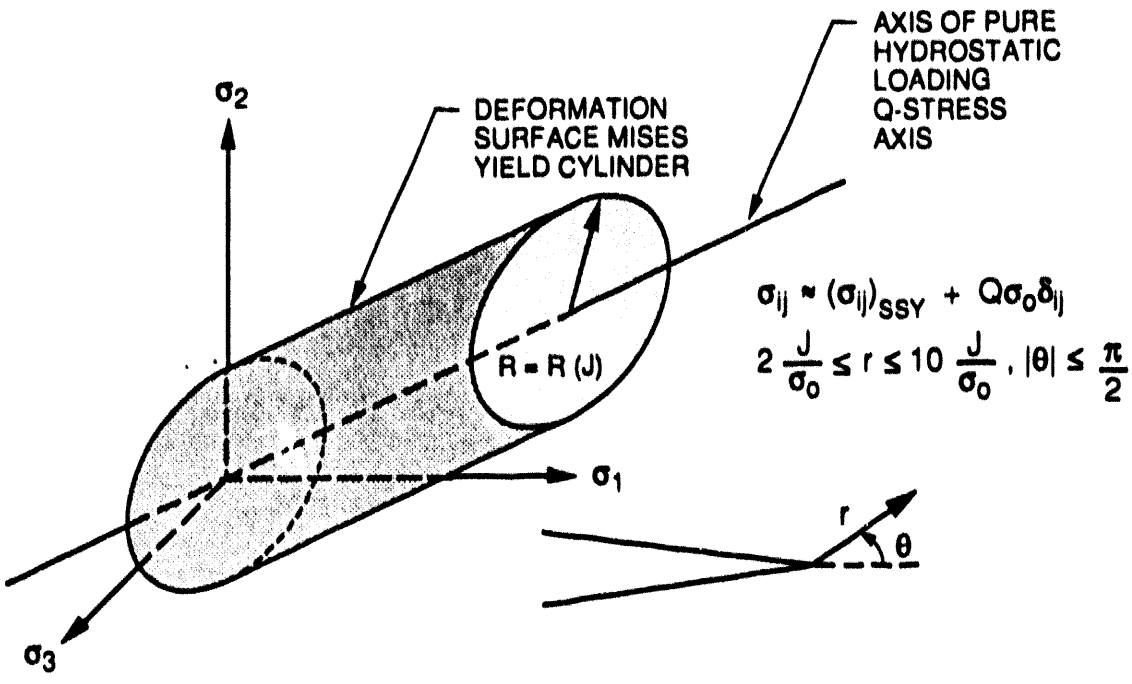

Fig. 6. Interpretation of near-crack-tip stress state in terms of J-Q theory.

2.3 J_c (Q) Fracture Toughness Locus and J-Q Trajectory

It has been proposed that the conventional concept of fracture toughness expressed in terms of a critical value of J, for example, be extended to a fracture locus involving combinations of J and Q. As illustrated in Fig. 7 (fro n O'Dowd and Shih*), the $J_c(Q)$ toughness locus characterizing the material resistance tc fracture as a function of constraint is constructed from application of J-Q methodology to measured toughness data from carefully selected specimen geometries. Detailed fracture assessments of a crack in a structure under applied load are performed by determining a J-Q trajectory that is compared with the $J_c(Q)$ toughness locus to determine the propensity for initiation.

Applications to deep- and shallow-crack small-scale fracture specimens demonstrate that the J-Q approach can provide a unified description of crack-tip fields and fracture toughness, at least for moderate levels of toughness. In Fig. 8, $J_c(Q)$ toughness loci are compared for single-edge-notched tension (SENT) and three-point bend (TPB) specimens from HY80 welds containing shallow through cracks. The $J_c(Q)$ toughness loci were determined from relations between T-stress and Q-stress for the material and from T-stress data given in Ref. 21. These data exhibit progressively more negative values of Q-stress with increasing values of critical crack-tip loading. However, beyond moderate load levels, the trends from the two specimens in Fig. 8 diverge, implying that the J-Q characterization is no longer valid.

*N. P. O'Dowd and C. F. Shih, "Two-Parameter Fracture Mechanics: Theory and Applications" (to be published).

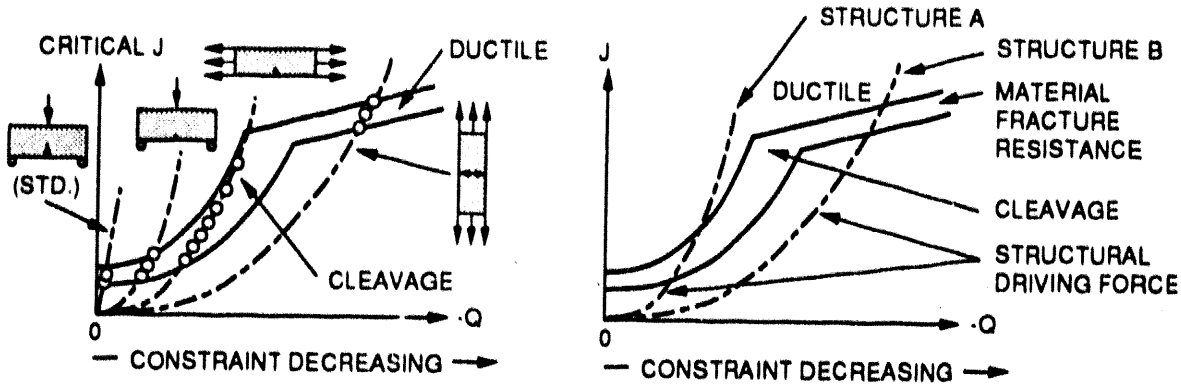

Fig. 7. Structural application of J-Q methodology based on careful selection of specimen geometries to map out J-Q toughness locus and detailed analysis of structure to determine structural J-Q trajectory.

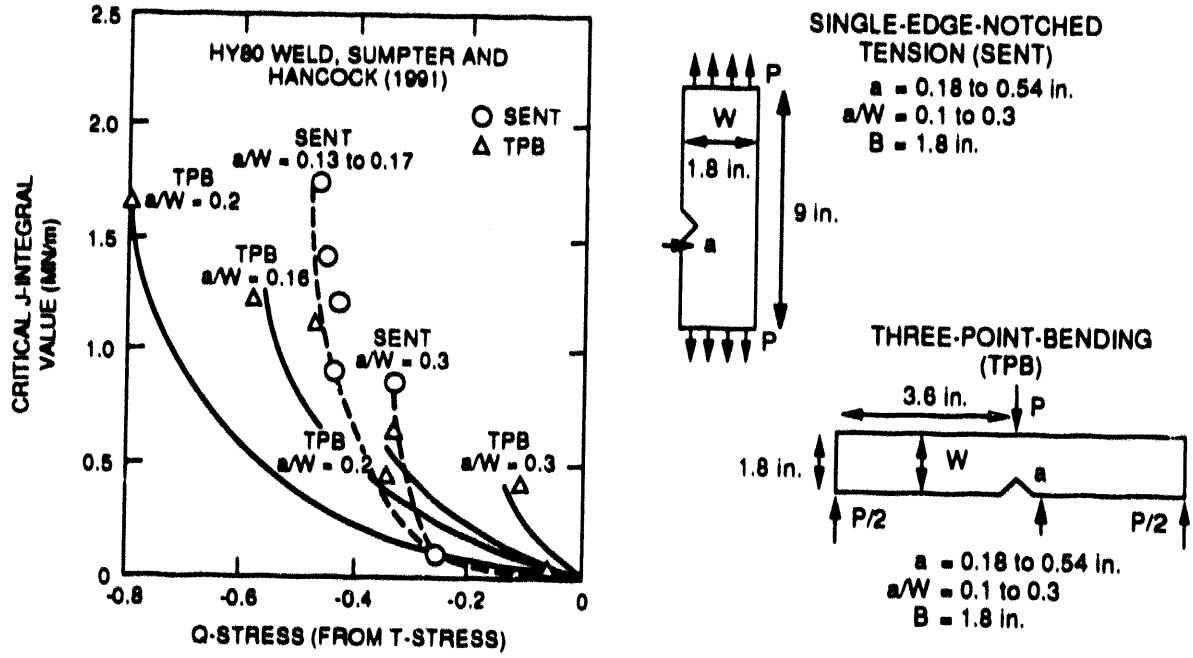

Fig. 8. Comparison of $J_c(Q)$ toughness loci for SENT and TPB specimens from HY80 welds.

3 Fracture Prediction Models

3.1 Micromechanical Model for Cleavage Fracture

The RKR model[22] is adopted herein as one means for the prediction of cleavage fracture initiation in applications to measured data. This model was chosen because it has been applied to

A 533 B material in the lower-transition and upper-shelf regions, respectively, with some success under nonirradiated and irradiated conditions.[23–25] Successful application of the RKR model to the analysis of fracture in the lower-shelf and in the ductile-to-brittle transition region for a German RPV-grade steel is also noted.[26] On the other hand, some recent investigations appear to cast doubt on the applicability of the RKR model to A 508 class 3, another RPV-grade steel, in the lower-shelf and transition regions.[27]

The RKR fracture model hypothesizes that crack initiation can be expressed in terms of the attainment of critical values of global stress measures determined from a continuum elastic-plastic fracture analysis. The RKR model postulates that cleavage fracture under Mode I conditions is governed by the attainment of a temperature-independent critical level of opening-mode stress over a minimum physical distance ahead of the crack front. The minimum distance necessary for cleavage fracture is often identified with the distance from the original crack front to cleavage-initiation sites. It has been suggested in Ref. 26 that both the steep gradient and the scatter in fracture toughness that are characteristic of the transition region can be attributed to the experimentally observed scatter in cleavage-initiation sites, thereby providing further justification for using the RKR model for examining cleavage fracture. However, available data suggest that both the nature and location of the cleavage-initiation sites vary considerably for nominally identical RPV-grade materials.[26,27] Consequently, a proper consideration of the micromechanics of fracture, along with continuum constraint effects such as the Q-stress, are integral elements in applications of this fracture model.

3.2 Stress Contour Correlation Model

A second approach is employed to predict cleavage fracture initiation in test specimens. The methodology applied herein is based on a procedure constructed by Anderson and Dodds[28] to remove the geometry dependence of cleavage fracture toughness values for single-edge-notched bend (SENB) specimens of A 36 steel for a range of crack depths. This procedure utilizes a local stress-based criterion for cleavage fracture and detailed finite-element analysis. From Ref. 28, dimensional analysis for SSY implies that the principal stress ahead of the crack tip can be written as

$$\frac{\sigma_{p1}}{\sigma_0} = f\left(\frac{J^2}{\sigma_0^2 A}\right), \tag{5}$$

where σ_0 is the 0.2% offset yield strength derived from a uniaxial stress-strain curve, σ_{p1} is the maximum principal stress at a point, and A is the area enclosed by the contour on which σ_{p1} is a constant. The strategy employed in Ref. 28 utilizes a fracture criterion dependent upon achieving a critical volume V_{CR} within which the principal stress is $>\sigma_{p1}$. For a specimen subjected to generalized-plane-strain conditions such that σ_{p1} does not vary in the thickness direction, the volume is equal to the specimen thickness B times the critical area A_{CR} within the σ_{p1} contour on the midplane ($V_{CR} = B \bullet A_{CR}$). This technique was successfully employed by Keeney-Walker et al.[12] to correlate cleavage-initiation toughness data from CT specimens with data from the large-scale WP-1 series of HSST wide-plate specimens.[5]

4 Validation Experiences with J-Q Methodology and Fracture Prediction Models

4.1 Comparison of Unirradiated A 533 B $J_c(Q)$ Toughness Loci from Shallow-Crack and WP-1 Testing Programs

Detailed posttest 2-D plane strain analysis results for two specimen geometries are presented in this section. The primary objectives of these analyses are to evaluate the utility of the two-parameter J-Q concept to characterize the crack-tip fields up to the onset of crack initiation in specimens with different crack depths and to provide a framework for interpreting and ordering the observed toughness differences between the deep- and shallow-crack geometries. Specifically, detailed 2-D finite-strain, finite-element analyses were performed for

1. seven specimens from the WP-1 series of HSST wide-plate experiments, and
2. six specimens from the production phase of the HSST shallow-crack fracture toughness testing program. (Three of the specimens contain deep cracks with nominal crack depth to specimen width ratio a/W = 0.5, while the remaining three are shallow-crack specimens with nominal a/W = 0.1.)

The ORNL WP-1 tests[5,13] provide a set of crack-initiation data against which comparison can be made with the deep- and shallow-crack data obtained in the shallow-crack[4] study. The WP-1 specimens were of single-edge-notched (SEN) geometry and fabricated from A 533 B steel plate (HSST-13A). The WP-1 specimens were 1 m wide, ~10.8 m long, and 0.1 to 0.15 m thick. Each side of the specimens was side-grooved to a depth equal to 12.5% of the specimen thickness, and in most cases the crack front was cut into a truncated chevron configuration.

The shallow-crack beam tests[4] were performed to produce fracture toughness data that would quantify the relaxation of crack-tip constraint associated with shallow-crack geometries. Beam specimens were fabricated from A 533 B steel plate (HSST 13B and WP-CE), with dimensions that varied from 40.6- to 86-cm length, 10.2-cm depth, and thicknesses of 5, 10, and 15 cm. Sharp cracks of depths 1 and 5 cm (a/W ≈ 0.1 and 0.5) were installed in the beams, which were then tested in TPB loading at temperatures corresponding to the lower-shelf and the lower-transition region of the plate material. Figure 2 summarizes the data from the testing program and illustrates the substantial elevation in effective toughness of the shallow-crack beams at temperatures in the lower-transition region when compared with those of the deep-crack beams.

Finite-element analyses of the wide-plate and shallow-crack beam experiments were performed using loading conditions measured in the tests. Full-field finite-strain solutions based on plane strain assumptions were generated from models having a highly refined crack-tip region and a crack-tip profile with an initial root radius to facilitate numerical convergence. Distributions of the opening-mode stress component for a deep-crack beam in bending, along the crack plane directly ahead of the crack tip, are indicated in Fig. 9 for three loading conditions up to crack initiation. The stress component is normalized by the initial yield stress, σ_0, and the distance ahead of the crack tip is expressed in terms of the normalized distance parameter, $r/(J/\sigma_0)$. In Fig. 9, J is the value of the J-integral associated with the given loading condition, and P_c is the experimentally determined critical value of the applied load P at cleavage initiation. The SSY distribution for the specimen material, obtained from a K-dominant boundary-layer formulation,[4] is also given in this figure. The analysis results in Fig. 9 indicate that crack initiation for the deep-crack beam occurred under essentially SSY conditions.

Figure 10 demonstrates an application of Eq. (4) to the near-crack-tip fields of a shallow-crack beam for the determination of Q-stress as a function of applied loading. For the opening-mode stress component, the Q-stress component is computed as the difference between the SSY and the full-geometry stress component at a given normalized distance ahead of the crack tip. For

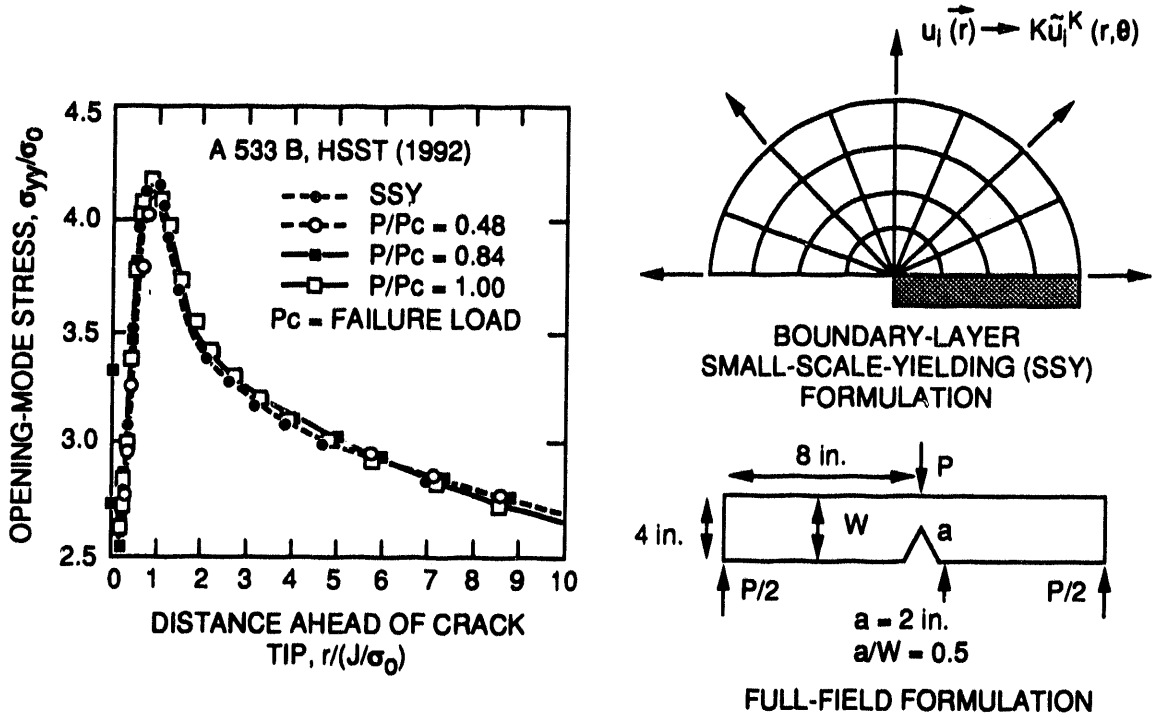

Fig. 9. Distribution of opening-mode stress component for deep-crack beam in bending for three loading conditions.

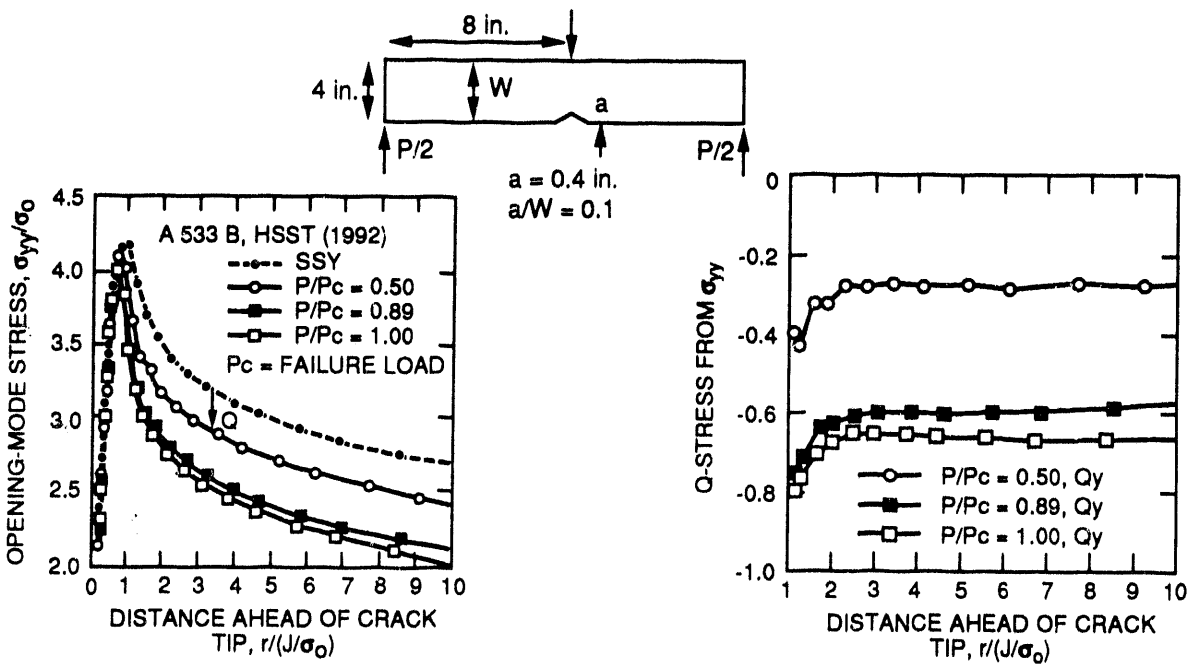

Fig. 10. Determination of Q-stress as function of applied loading from near-crack-tip stress fields of a shallow-crack beam.

a given value of applied load, the Q-stress component is relatively uniform over a distance of $2J/\sigma_0 < r < 10J/\sigma_0$ in front of the crack tip. The Q-stress component becomes more negative with increasing load, reflecting a progressive loss of constraint in the shallow-crack beam.

Crack initiation for the WP-1 specimens occurred over a narrow temperature range that envelops the test temperature of the deep- and shallow-crack specimens. Current understanding of the J-Q approach would suggest that the $J_c(Q)$ toughness loci from the WP-1 and the deep- and shallow-crack specimens should be very similar. Instead, reanalysis of the ORNL WP-1 tests using the J-Q approach indicates a very different $J_c(Q)$ toughness locus for the WP-1 tests as compared to the deep- and shallow-crack locus (see Fig. 11). The WP-1 results are based on 2-D plane-strain assumptions. Toughness values are expressed in terms of K, and they are further normalized by the plate 13-A small-specimen characterization toughness K_{Ic}.

When the wide-plate and shallow-crack beam results are evaluated separately, each set of crack-initiation toughness data appears to support a J-Q interpretation. That is, higher toughness values correspond to more negative Q-stresses, which imply a decrease in triaxiality and crack-tip constraint. Collectively, however, results in Fig. 11 indicate that the WP-1 $J_c(Q)$ toughness

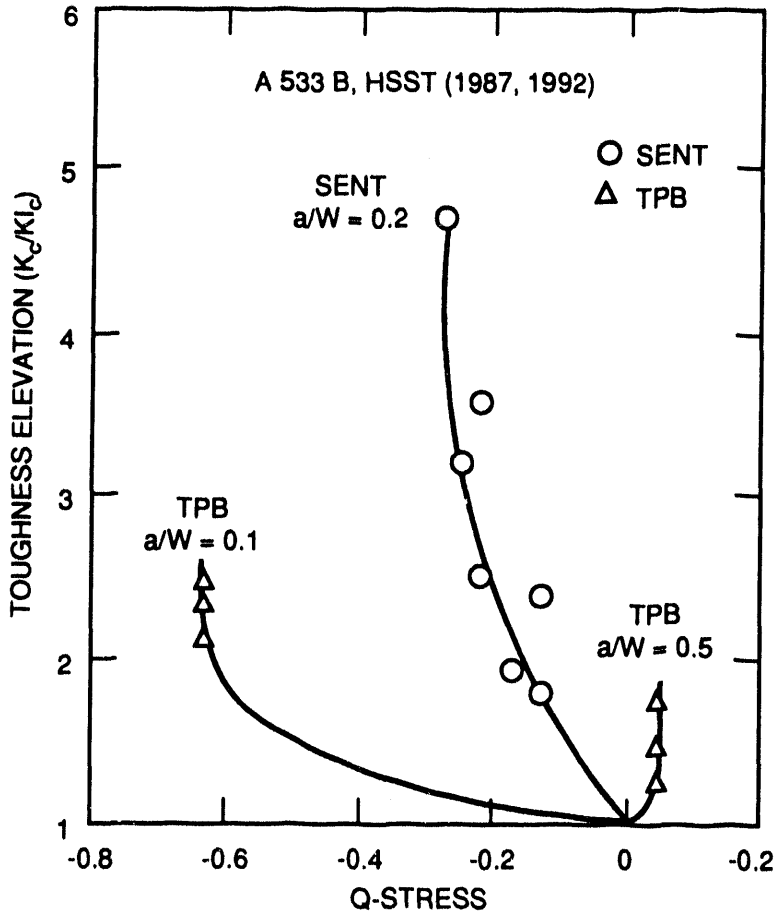

Fig. 11. Comparison of shallow-crack and wide-plate crack-initiation-toughness data.

locus is much steeper than that for the deep- and shallow-crack specimens. The presence of 3-D effects in the WP-1 specimens is hypothesized to provide at least a partial explanation for the observed differences between the two $J_c(Q)$ toughness loci. (Tests were performed on three different thicknesses of the shallow-crack beams, and no 3-D effects were detected in the toughness data.)

Preliminary results from analyses of CT specimens suggest that a 3-D methodology is needed to extend the J-Q concept to high toughness cases where crack-tip fields deviate significantly from 2-D plane strain assumptions.* In these analyses, the J-Q methodology was applied to fracture-toughness data for A 533 B steel previously generated by McCabe and Landes[29] for a study of thickness effects in the transition region. Analyses of 3-D models of CT specimens having a common planform of a 4T specimen and thickness of 5.08 and 10.16 cm were performed and the results compared with those from a 2-D plane strain model. The 2-D analysis results given in Fig. 12 indicate the absence of in-plane Q-stress constraint effects at measured fracture toughness values given in Ref. 29. However, results in Fig. 13 for a 3-D model of the 10.16-cm-thick 4T specimen indicate a significant Q-stress constraint effect through the thickness of the model at the higher fracture load.

*D. K. M. Shum, "3-D Q-Stress Effects in Compact-Tension Geometry," Joint Task Group Meeting of ASTM Committees E-24.08.03 and E24.08.04, Pittsburgh, Pa., May 1992.

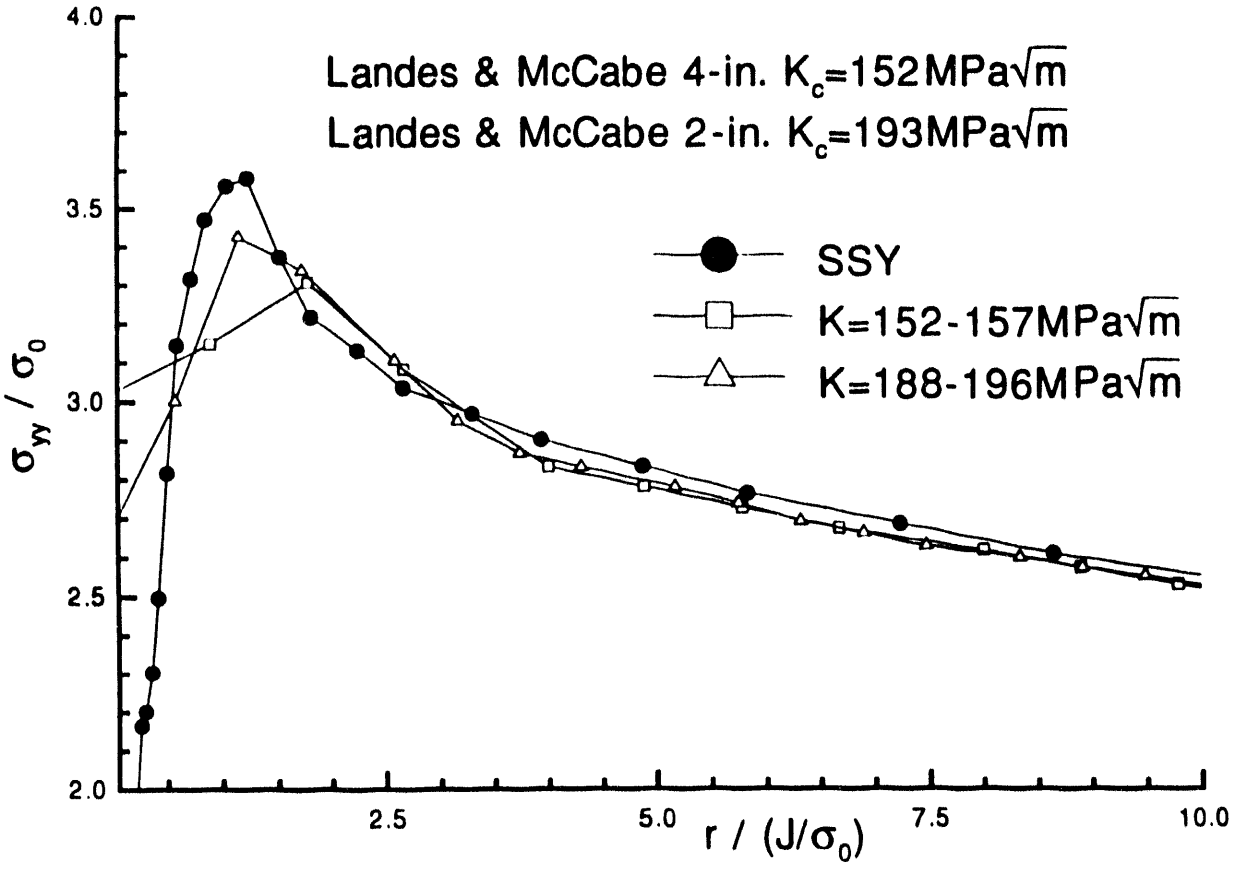

Fig. 12. Results from 2-D plane strain model of 4T-CT indicating absence of in-plane Q-stress constraint effects.

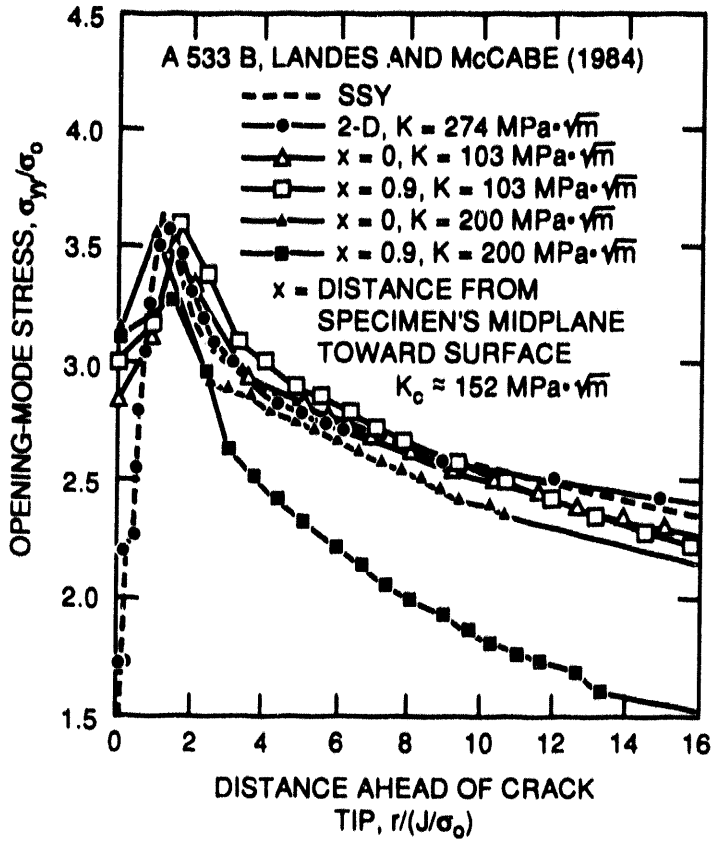

Fig. 13. Results from 3-D analysis of 4T-CT specimen indicating significant Q-stress constraint effect through thickness of model at higher loads.

4.2 Applications of Fracture Prediction Models to Measured Data

4.2.1 RKR Methodology

Results from application of the RKR prediction model to the WP-1 series of experiments are given in Fig. 14. Correlations of measured and predicted toughness for the experiments based on the Q-stress parameter are expressed in terms of K-factors normalized by SSY values. For the WP-1 series (Fig. 14), toughness predictions are given for three values of the critical stress ratio, σ_c/σ_0 = 2.2, 2.6, and 3.4, where σ_0 = 465 MPa. Results for the WP-2 series of HSST wide-plate experiments are given in Ref. 15. For both series of experiments, the RKR-model predictions fall substantially below the toughness values determined from the measured data. Fracture toughness predictions from the RKR model for the shallow-crack beam specimens are compared with measured toughness values in Fig. 15. Again the RKR model predictions fall below measured values, but not to the extent indicated for the wide-plate specimens. Note that these results were obtained based on 2-D plane strain assumptions, which were the basis for development of the J-Q methodology. It has not been established to what extent these differences are due to problems associated with representing 3-D stress states by a 2-D model or to problems with the RKR prediction model. As discussed previously, applications of the RKR prediction model to measure

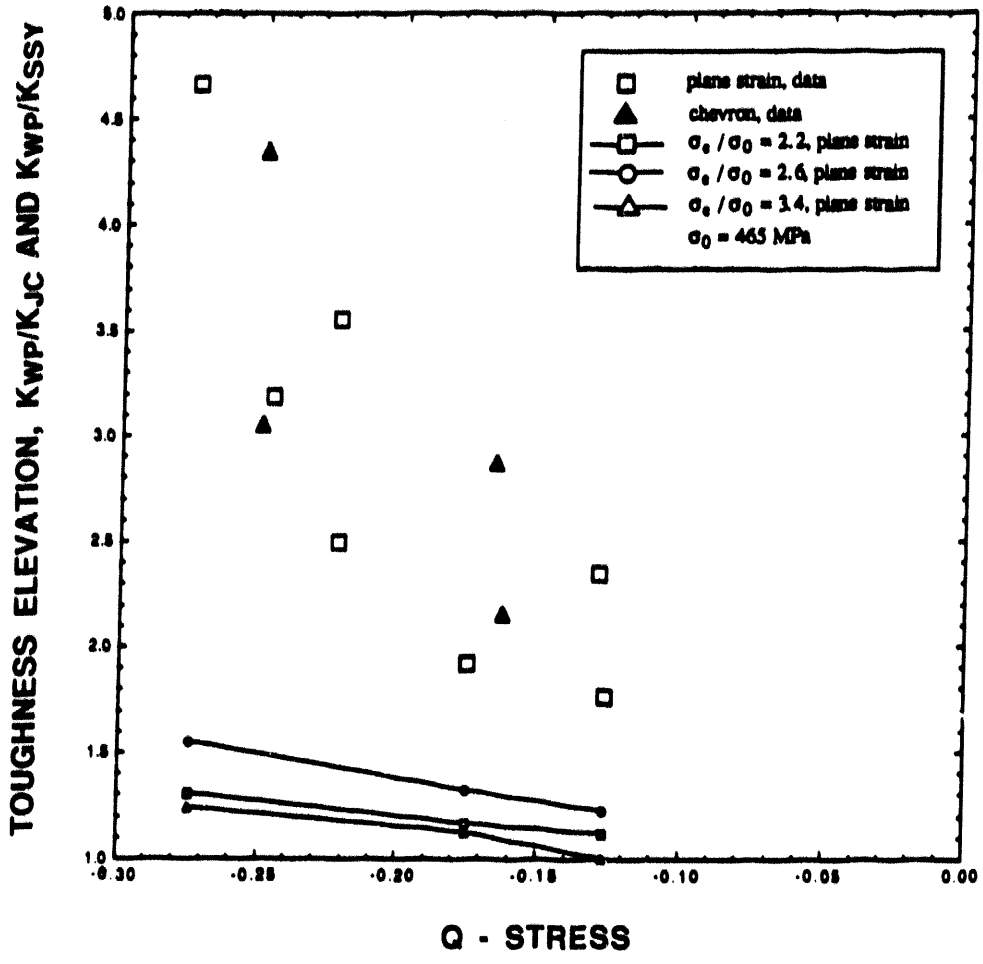

Fig. 14. Correlation of measured and predicted toughness for WP-1 wide-plate series based on Q-stress parameter.

data have been confined to small-scale laboratory specimens. There may be difficulties with applications of the model to large-scale structures subjected to nominal 3-D stress states that have not yet been identified.

4.2.2 Stress Contour Correlation Methodology

In this section, correlations are developed between local crack-tip fields in CT and wide-plate specimens utilizing parameters discussed in Sect. 3.2. Specifically, a volumetric or area maximum principal stress criterion, based on volume, $V(\sigma_1)$, or area $A(\sigma_1)$, and a critical stress, σ_1 is applied to analysis results from CT and wide-plate specimen geometries[12] that were tested in the HSST Program.

Two-dimensional plane-stress and plane-strain and fully 3-D finite-element models were employed to generate the local crack-tip fields for the CT and wide-plate specimens.[12] The numerical analysis techniques utilized both small- and large-strain formulations and the constitutive model representation for A 533 B steel described in Ref. 5. Detailed descriptions of

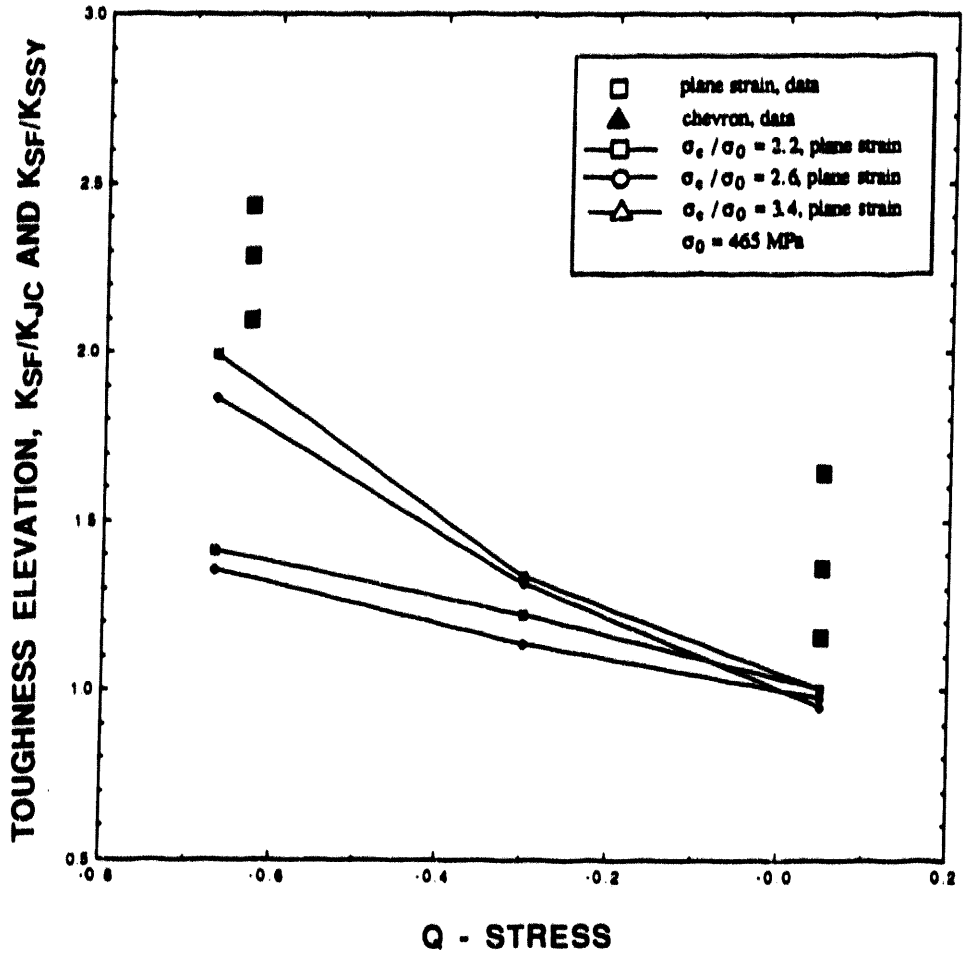

Fig. 15. Correlation of measured and predicted toughness for shallow-crack beam specimens based on Q-stress.

these models are given in Ref. 12, as well as the loading conditions for each analysis performed. Interpretations of the results are discussed in terms of the fracture parameters that were evaluated from the local crack-tip fields of the finite-element analyses.

The fracture model described in Sect. 3.2 is based upon achieving an A_{CR}, within which $\sigma_{p1} > \sigma_1$. This criterion was applied to the analyses of the CT and wide-plate specimens, and a portion of the results is summarized in Table 1. A maximum principal stress of σ_{p1} = 1400 MPa was used to generate the contour areas in Table 1. This critical stress is based on the average maximum principal stress calculated for the 2-D and 3-D analyses of the CT specimens. Also, Hahn et al.[30] estimated that the cleavage microcrack propagation stress for individual grains of ferrite is 1380 MPa. In Table 1, the area within the stress contour σ_{p1} = 1400 MPa is tabulated as a function of load for the 2-D and 3-D finite-element solutions. When these areas are normalized with respect to the factor $(\sigma_0/J)^2$, the normalized values vary slightly for the 2T-CT specimen over the range of loading. By contrast, the normalized results for the wide-plate specimens decrease significantly with increasing load after an initial increase, indicating loss of constraint with respect to SSY.

Table 1. Cumulative area within the maximum principal stress contour σ_{p1} = 1400 MPa for CT and WP specimens

Specimen	Load (MN)	J (MJ/m^2)	Area (mm^2)	Normalized area, $A^*(\sigma_o/J)^2$
2T-CT[a]	0.144	0.0480	0.1316	13.4
	0.158	0.0586	0.2166	14.8
	0.162	0.0615	0.2278	14.0
	0.180	0.0775	0.3572	14.0
2T-CT[b]				
	0.203	0.1075	0.2774	4.4
	0.207	0.1149	0.3002	4.4
WP-1.3[c]				
	7.63	0.0476	0.0328	3.2
	8.44	0.0583	0.0328	2.6
	8.84	0.0640	0.1186	6.2
	9.64	0.0764	0.1268	4.6
	11.25	0.1044	0.1428	2.8
WP-1.6[d]				
	7.46	0.0455	0.0090	0.8
	8.29	0.0563	0.0202	1.2
	8.70	0.0621	0.0338	1.8
	9.53	0.0748	0.0338	1.2
	14.50	0.1754	0.2538	1.6
WP-1.2[e]				
	8.81	0.0512	0.0202	1.6
	9.48	0.0595	0.0212	1.2
	10.16	0.0685	0.0338	1.4
	10.84	0.0780	0.0506	1.8
	18.90	0.2440	0.2452	0.8

[a]Two-dimensional elastic-plastic static analysis at T = –75°C.
[b]Two-dimensional elastic-plastic static analysis at T = –18°C.
[c]Two-dimensional elastic-plastic static analysis at T = –51°C.
[d]Two-dimensional elastic-plastic static analysis at T = –19°C.
[e]Two-dimensional elastic-plastic static analysis at T = –33°C.

In the 2-D analyses of the CT specimens, the area corresponding to the smallest initiation load (0.144 MN) is given by A_{CR} = 0.1316 mm^2. Comparing this with the area from the wide-plate analyses, the same critical area is achieved at an applied load of ~15.7 MN for WP-1.2, 10.06 MN for WP-1.3, and 10.83 MN for WP-1.6; the critical areas corresponding to the initiation loads are 0.2452, 0.1428, and 0.2538 mm^2, respectively. In Fig. 16, the applied J values calculated from the 2-D analyses for the 2T-CT and wide-plate specimens are plotted vs the area within the critical stress contour, σ_{p1} = 1400 MPa, at each load step. For given values of A_{CR} and temperature T, values of the J-integral for the wide-plate specimen lie above those for the CT specimen, reflecting the differences in crack-tip constraint in these two geometries.

Using the critical areas at initiation for the 2T-CT specimen at –75 and –18°C, a prediction can be made for J at initiation of the wide-plate specimens. From the CT specimen results, the

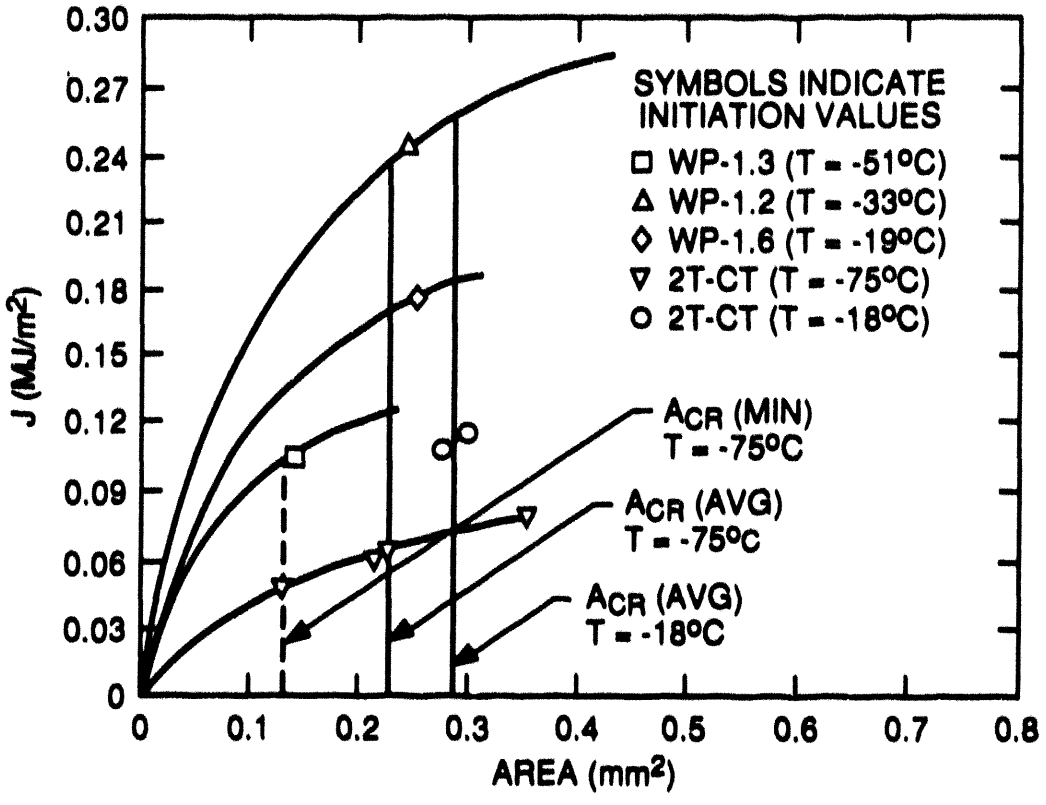

Fig. 16. J-integral values vs critical area within critical stress contour of 1400 MPa in 2T-CT and WP specimens.

predicted A_{CR} values at initiation, at –75 and –18°C, are 0.234 and 0.288 mm^2, respectively. This implies that the J value at initiation for the wide-plate specimen with a crack-tip temperature of –33°C should lie in the interval (0.233, 0.255) MJ/m^2. The calculated J value at initiation for WP-1.2 was 0.244 MJ/m^2. Thus, the 2-D analyses of the 2T-CT specimens at –75°C and at –18°C provide contour areas corresponding to initiation that are consistent with the values calculated from the 2-D of WP-1.2 and -1.6.

5 Biaxial Tensile Stress Effects on Fracture Toughness

5.1 Objectives, Scope, and Structure of the Study

In Ref. 15, the specific objectives of the HSST investigation concerning biaxial tensile stress effects on fracture toughness are summarized in the following elements:

1. identification and evaluation of existing biaxial fracture toughness data,
2. selection of fracture parameters suitable for characterizing the fracture process,
3. selection of fracture prediction models potentially capable of incorporating the effects of out-of-plane stresses on fracture initiation,
4. applications of the fracture prediction models to existing measured data in the plane stress-to-plane strain domain and comparisons between the predicted and measured results, and

5. applications of fracture prediction models from element (4) to the prediction of positive out-of-plane stress and strain effects on fracture initiation toughness.

Assessments of studies devoted to each of these elements are given in the following sections.

5.2 Interpretations of Existing Experimental Data

This section provides a summary of experimental data from several testing programs that were identified as potentially relevant to issues concerning the effects of out-of-plane biaxial stress on fracture toughness. Only limited evaluations of these data have been performed using the fracture methodologies described herein. Thus far, these data and evaluations have not provided a consistent and unambiguous basis for understanding the relationship between biaxiality and toughness.

Pennell[16] has suggested that results from thermal-shock cylinder experiments[31] and shallow-crack beam tests[4] conducted in the HSST Program provide insight into the impact of biaxial far-field stress distributions on fracture toughness. Results from the shallow-crack testing program, shown in Figs. 2 and 17, indicate that the lower-bound to the shallow-crack beam fracture data is ~60% greater than that of the deep-crack data in the lower-transition region. [Analyses[32] of PTS transients have shown that crack initiation is most likely to occur at a temperature relative to the reference nil-ductility transition temperature (RT_{NDT}) associated with the lower-transition region of the fracture toughness curve.] The thermal-shock experiments[31] also employed shallow cracks having depths comparable to those in the shallow-crack beam tests, but with a very long crack front. In Fig. 17, results from these tests show crack-initiation

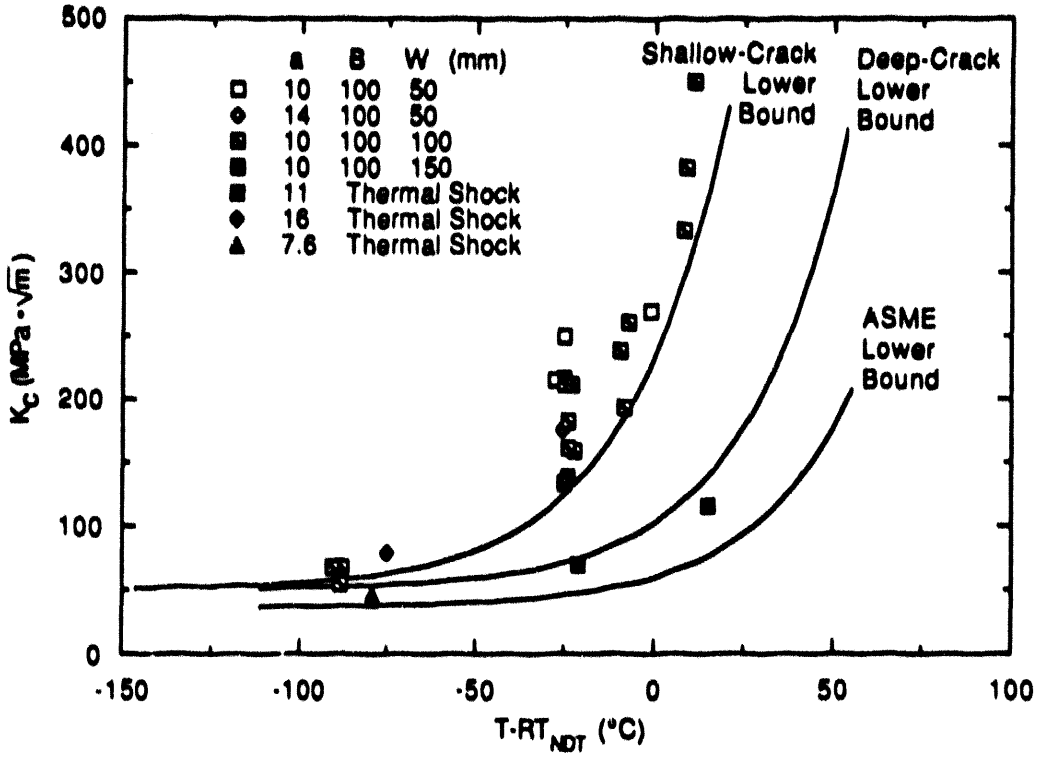

Fig. 17. HSST shallow-crack and thermal-shock data with ASME lower-bound curve.

toughness values from the thermal-shock experiments that are substantially lower in magnitude than toughness values that would have been inferred from the shallow-crack data.

Tensile out-of-plane biaxial stresses have been linked to a decrease in effective fracture toughness in other applications. Experimental and analytical studies[33–38] were performed at Bundesanstalt für Materialprüfung (BAM), Germany, to determine the influence tensile out-of-plane biaxial stresses on fracture toughness of engineering structures. The program at BAM utilized several different test specimens, beginning with a double-T-shaped geometry loaded in uniaxial tension. A biaxial nominal stress state was attained in the 50- by 80-mm cross section of the specimen via a transverse bending stress that develops in conjunction with the uniaxial tension component. The ratio of the tensile component to the transverse component of stress along the crack front had a maximum value of 1:0.3 and a mean value of 1:0.15. For comparison purposes, SEN specimens of the same cross section as the double-T specimens were fabricated from the same material (22 NiMoCr37 steel) and tested. Aurich et al.[34] reported that fracture toughness (K_c) values of the biaxially loaded specimen were ~25% lower than those of the SEN specimen.

A later study reported by Aurich et al.[38] focused on a plate-shaped specimen having dimensions 1000 × 1000 × 140 mm with a canoe-shaped (flat-bottom) surface crack of depth a = 83 mm and length 2c = 480 mm. The plates were loaded in eight-point bending to produce a biaxial stress state along portions of the crack front. For comparison, CT specimens from the same material as the plates were tested over the same temperature range as the plates. Toughness data vs temperature for the biaxial plates are compared with CT-100 specimen data[38,*] in Fig. 18. The toughness values of the biaxial plates are lower than those obtained from a very limited number of uniaxially loaded CT-specimens tested at low temperatures, but the large scatter in the CT specimen data precludes a similar interpretation at temperatures above –40°C. Because the nominal bending stresses along the flat-bottom portion of the crack front were compressive, cleavage-crack initiation always occurred at points on the end radius of the crack. In this region, the far-field stress components were oblique (or normal), rather than parallel, to the crack front. These characteristics of the stress fields cast doubt on any interpretation of out-of-plane stress effects on fracture toughness from the data in Fig. 18.

Unpublished data from CNITMASH, Russia, concerning fracture toughness under biaxial loading conditions were reported by M. Brumovsky.[†] Biaxial loading was produced in a spinning-disk facility that utilized circular disks with a diameter of 450 to 600 mm, a thickness of 150 mm, and surface cracks of 40-mm maximum depth and 200-mm length. In these experiments, an estimated 37% reduction in K_c was reported for the biaxially loaded spinning disks, as compared with data from uniaxially loaded specimens.

Figure 19 depicts the reduction in fracture toughness (in percent of K_c) expressed as a function of biaxiality ratio (out-of-plane stress/normal stress) inferred from a portion of the testing programs described above. Detailed finite-element analyses employing the methodologies described in this paper have not been performed to provide updated interpretations of the biaxial test results from BAM and CNITMASH. Some preliminary results from reanalysis of ORNL thermal-shock data using the J-Q methodology are described Ref. 39.

---

*Personal communication, D. Aurich, BAM, Berlin, Germany, to J. G. Merkle, Oak Ridge National Laboratory, August 3, 1991.

†Personal communication to W. E. Pennell, Oak Ridge National Laboratory, from M. Brumovsky, Skoda Works, Czechoslovakia, May 11, 1992.

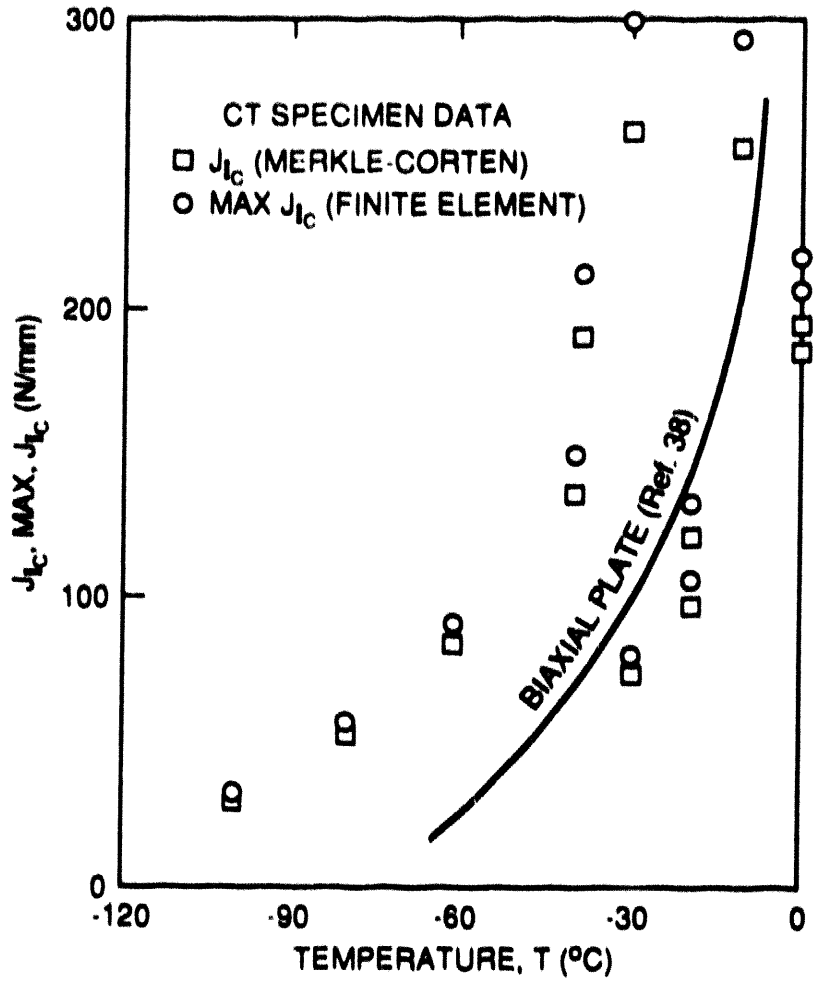

Fig. 18. Comparison of fracture-toughness data vs temperature from BAM biaxial plates with CT-100 specimen data.

5.3 Status Assessment of Investigation on Biaxial Stress Effects

Experimental data summarized in Sect. 5.2 from several different testing programs have been proposed by researchers as evidence of a significant decrease in fracture toughness due to positive out-of-plane biaxial stress effects. Estimates of reduced toughness for specimens subjected to equilibiaxial loading have ranged as high as 40%, when compared to uniaxial loading conditions (Fig. 19). Some preliminary analyses employing the methodologies described herein were performed to provide interpretations of biaxial test results from the thermal-shock and shallow-crack beam data.

Two different analytical approaches to the biaxial stress problem were selected for evaluation through applications to measured data from intermediate- and large-scale experiments. The K-T and J-Q fracture methodologies were employed to correlate fracture initiation in these experiments. Also, a stress contour methodology was used to relate cleavage crack initiation to the attainment of a critical area enclosed within a selected maximum principal stress contour ahead of the crack tip.

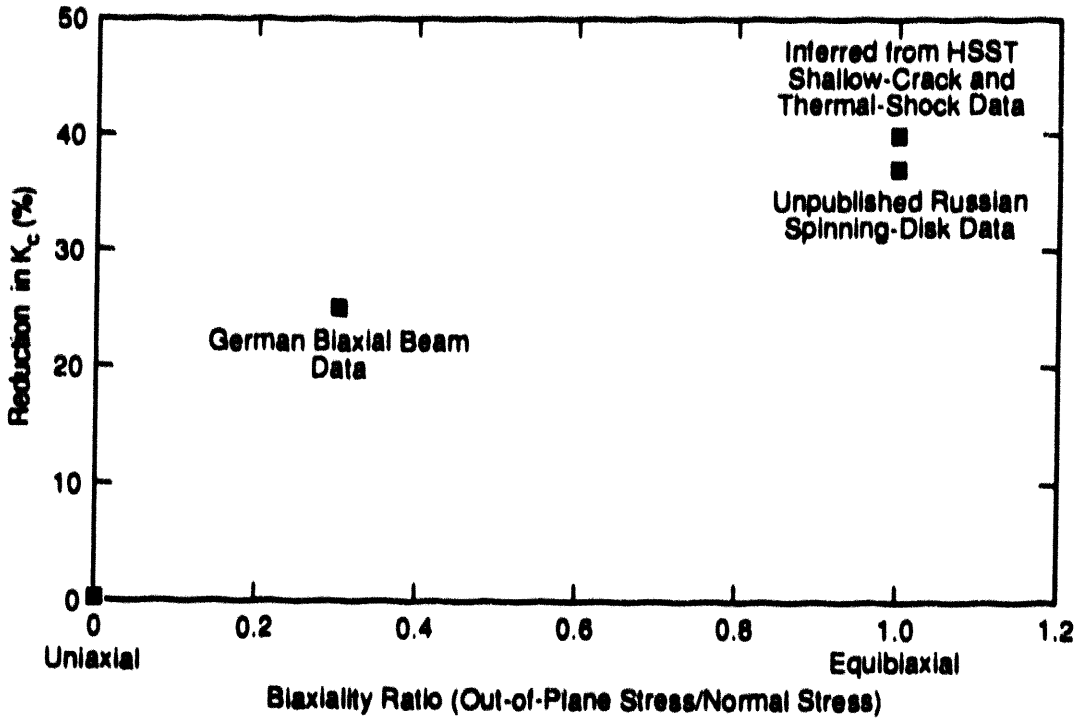

Fig. 19. Experimental data indicating decrease in fracture toughness due to effects of out-of-plane biaxial stresses.

In Sect. 4, the RKR model was applied to fracture-initiation-toughness data generated in the HSST Program from large-scale wide-plate experiments and shallow-crack beam tests. Comparisons of measured and predicted toughness for the WP-1 and -2 series of wide-plate experiments indicate that the RKR model predictions fall substantially below the toughness values determined from analysis of the measured data. Fracture toughness predictions from the RKR model for the shallow-crack beam specimens were compared with measured toughness values for three values of critical stress. Again, the RKR model predictions were below measured values, but not to the extent observed in the wide-plate specimens.

In Ref. 39, preliminary results from analyses of the TSE-5A experiment imply that transverse loading of the cylinder due to thermal shock did not significantly influence crack-tip constraint as measured by the in-plane Q-stress parameter. Also, fracture prediction models based on attainment of a critical *in-plane* stress would not predict a significant influence of transverse loading on fracture toughness of the cylinder. These results are consistent with the experimentally observed toughness data from TSE-5A.

The maximum principal stress criterion based on achieving a critical area within a selected principal stress contour successfully correlated the cleavage-initiation toughness values for wide-plate tests WP-1.2 and -1.6 with measured toughness values from 2T-CT specimen tests. However, attempts described in Ref. 15 to calibrate the stress contour model based on a very limited set of measured data from 4T-CT specimens of A 533 B steel were unsuccessful. In the latter case, the experimental data were not reported in sufficient detail to permit adequate modeling of the load vs load-line displacement curves of the test specimens.

The general finding is that applications of these fracture models to existing small- and large-scale fracture test results did not produce consistent results in predicting fracture behavior.

Thus, the effects of biaxial out-of-plane stresses on fracture toughness cannot be predicted here on the basis of validated models. Notwithstanding these general findings, toughness predictions implied by these models for out-of-plane strain effects were provided in Ref. 15 for reference purposes. Within the assumptions of the various models and analyses presented here, tensile transverse strains are predicted to produce a relatively small decrease in effective cleavage fracture toughness when compared with that of identical specimens loaded uniaxially. Applications of the RKR model (described in Appendix C of Ref. 15) and the stress contour methodology (described in Appendix D of Ref. 15) support a reduction in cleavage toughness of ~9 to 20% due to positive strains. However, because the fracture methodologies considered in this study have not been successfully validated using fracture data that involve out-of-plane straining, uncertainties remain with these estimates such that they cannot be applied with confidence in addressing questions that affect licensing and regulatory issues for RPVs.

5.4 Proposed Biaxial Testing Program

Based on the foregoing assessment, it is apparent that testing of RPV steels is required (1) to determine the magnitude of out-of-plane biaxial loading effects on fracture toughness and (2) to provide a basis for development of predictive models. The most desirable program would involve suitable test specimens and loading conditions for which the only variables are imposed biaxial loading components. This course of action is necessary to support a refined treatment of in-plane and out-of-plane constraint effects on crack initiation from shallow cracks under PTS loading conditions. As a consequence, a testing program is described herein that is designed to provide data to explain differences between theoretical predictions and measured material behavior.

The objective of the proposed biaxial fracture testing program is to obtain fracture toughness data under conditions of uniform far-field biaxial stresses for comparison with toughness data from uniaxial loading conditions. In addition, the experimental data from the proposed testing program will provide much needed data for the purpose of verifying and refining the fracture prediction methodologies that form the basis of the analytical predictions described in previous chapters.

The configuration and dimensions of a biaxial bend specimen proposed for the HSST biaxial testing program are depicted in Fig. 20. The biaxial bend specimens are fabricated from A 533 B steel plate previously employed in an HSST wide-plate testing program. The specimens have a cruciform-shaped geometry with a cross section of dimensions ~10.2 × 10.2 cm and a straight through-crack of depth 1.02 cm. A statically determinant five-point loading system produces equibiaxial stresses on the crack. These dimensions and loading conditions allow for a direct comparison of the biaxial bend specimen results with those from the previously tested HSST shallow-crack uniaxial bend specimens.[4] An assessment of the influence of out-of-plane biaxial tensile stresses on fracture toughness can be made from a comparison of results from biaxial and uniaxial loading conditions. A discussion of the test matrix, the structural and fracture analysis results, and the interim test data will be given in future HSST reports.

6 RPV Analysis

This section presents detailed 2-D plane strain analysis results for an RPV with an inner-surface axial flaw subject to a postulated PTS transient.[4] The PTS transient simulates the pressure-temperature history of an RPV during an SBLOCA. The primary objectives of these analyses are to (1) evaluate the utility of the two-parameter J-Q approach to characterize the crack-tip fields in an RPV throughout a PTS transient and (2) present a methodology that incorporates small-specimen $J_c(Q,T)$ toughness locus data in the safety-margin assessment of an RPV.

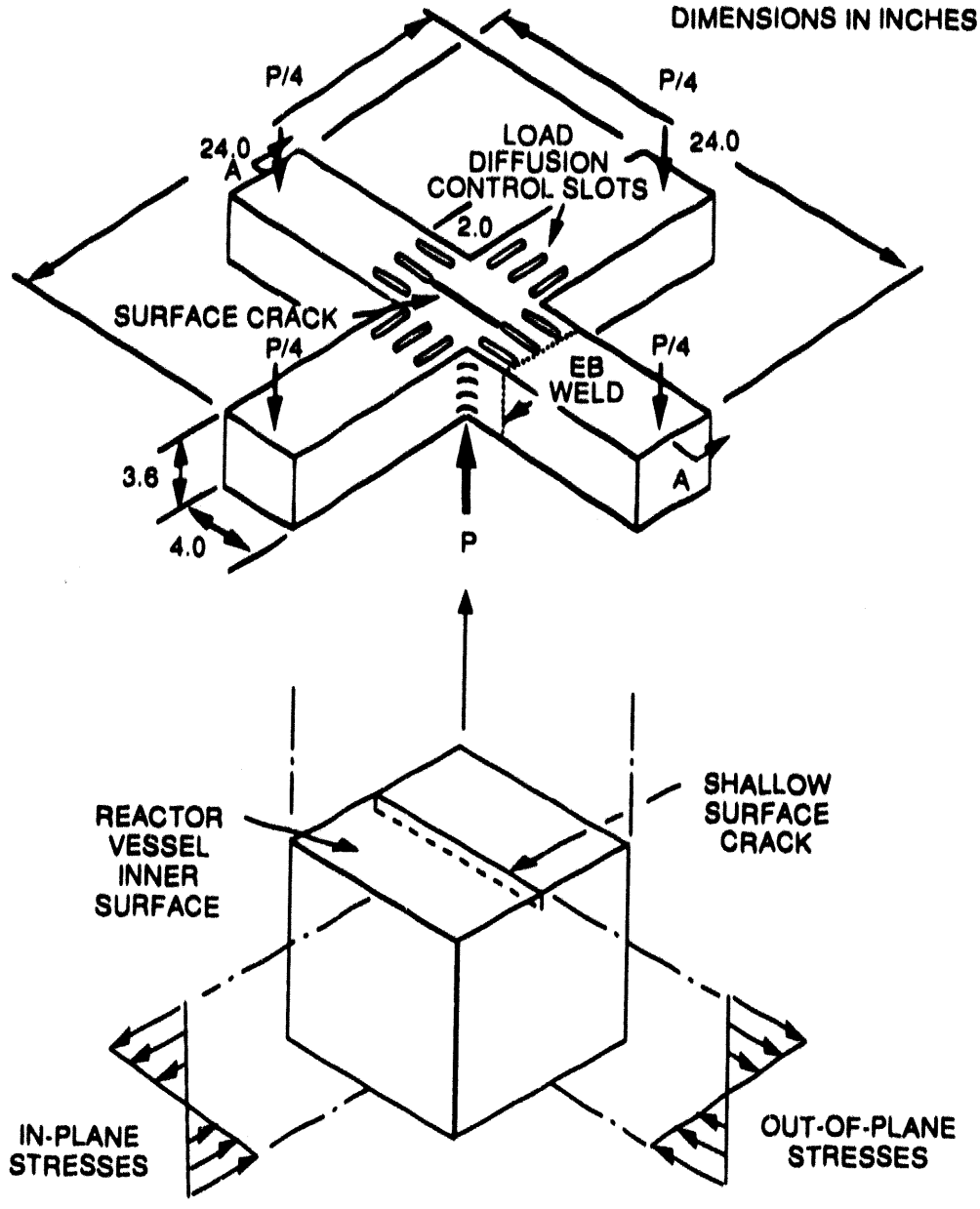

Fig. 20. Configuration and dimensions of biaxial bend specimen proposed for biaxial testing program.

6.1 Material Models and Analysis Assumptions

Three material models that simulate a wide range of tensile properties for RPV-grade materials have been considered. The first material model simulates the unirradiated tensile properties of A 533 B steel plate (HSST plate 13B) at –40°C and can be considered as a lower-shelf temperature material model.[4] In subsequent discussions this material model is referred to as Case 1. The second material model (Case 2) simulates the unirradiated tensile properties of

A 533 B steel plate (HSST plate 13A) at 180°C and can be considered an upper-shelf-temperature material model.[13] The third material model (Case 3) simulates the irradiation-embrittled tensile properties of A 533 B (HSST plate 13A).[40,41] The uniaxial true-stress, true-plastic-strain curves in tension are modeled for Cases 1, 2, and 3 as indicated in Fig. 21.

The RPV being considered in this study has an inner radius of 1384 mm and a wall thickness of 200 mm. A 2-D inner-surface axial flaw with a depth of 10.2 mm is assumed to exist in the vessel, representing a flaw-depth-to-wall-thickness ratio of a/W = 0.05. The PTS transient indicated in Fig. 22 simulates the pressure-coolant temperature history of an RPV during an SBLOCA. The operating pressure and temperature of the RPV before the onset of the transient are 14.1 MPa and 268°C, respectively. Analysis of the fracture response of the RPV was based on the three material models depicted in Fig. 21.

6.2 RPV Crack-Tip Stress Fields Under PTS Conditions

The effects of the PTS loading on the RPV as reflected in the J-integral vs time relation is relatively insensitive to the material model adopted in the analysis. The magnitude of the J-integral at operating conditions J_{op}, and its maximum value at ~1200 s into the transient J_{max}, are listed in Table 2 for the three material models. The magnitude of the J-integral increases monotonically with transient time up to ~1200 s; unloading of the crack tip as characterized by a decrease in the magnitude of the J-integral occurs after that time.

Distributions of the "opening-mode" stress component for the RPV based on Case 1–3 material models, along the crack plane directly ahead of the blunting notch tip, are indicated in Figs. 23–25 for various times during the transient up to ~1200 s. The stress distribution

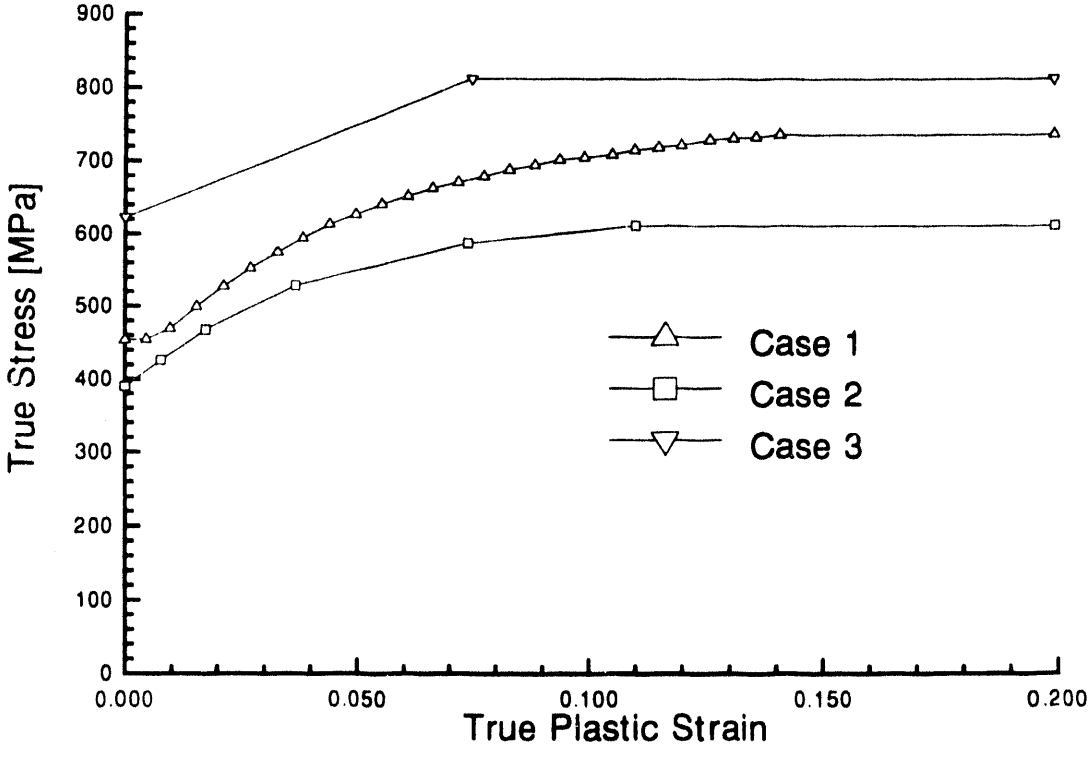

Fig. 21. Uniaxial true stress–true plastic strain curve in tension for Cases 1, 2, and 3.

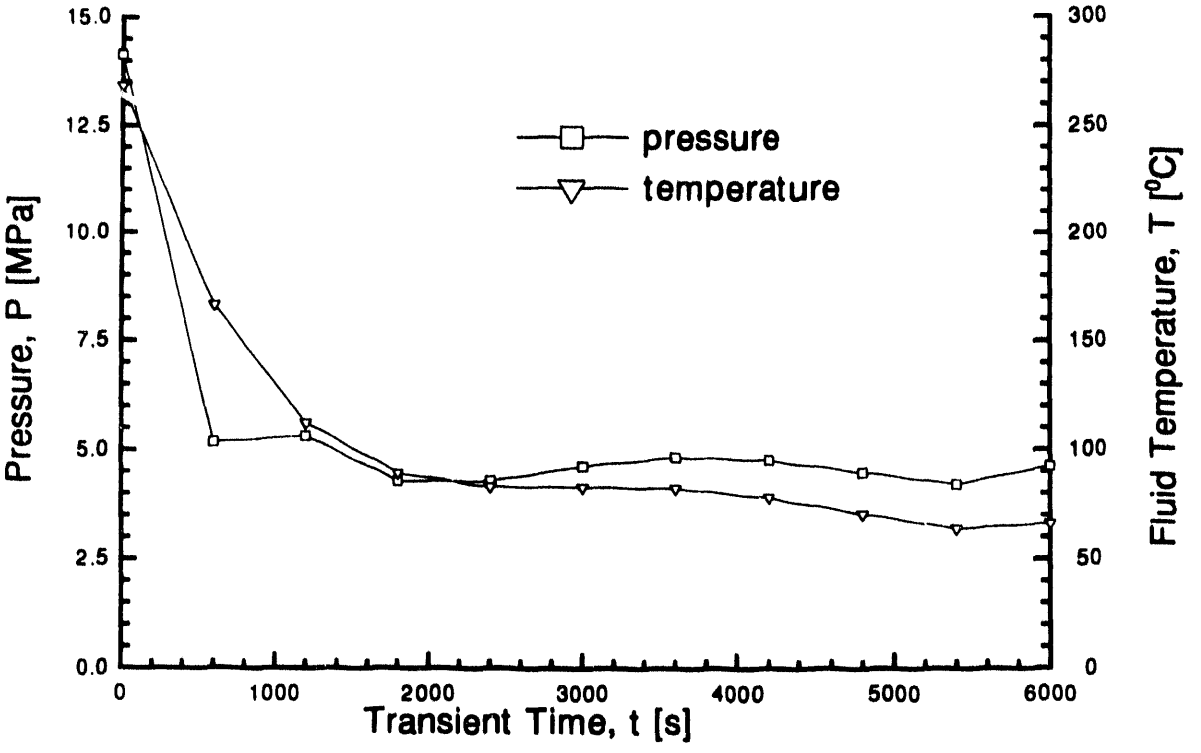

Fig. 22. SBLOCA pressure and bulk coolant temperature (P-T) history.

Table 2. Magnitude of the J-integral at operating conditions J_{op} and its maximum value J_{max} at ~1200 s into the transient for Cases 1, 2, and 3

	J_{op} (kJ/m^2)	J_{max} at ~ 1200 s (kJ/m^2)
Case 1	2.05	20.3
Case 2	2.14	19.5
Case 3	2.2	17.9

associated with the RPV operating pressure and temperature is labeled as t = 0 s. Also, the SSY distribution for each material model is indicated in Figs. 23–25.

Analysis results in Fig. 23–25 indicate that the crack-tip fields in the RPV have deviated from the SSY distribution even under operating conditions. The extent of the deviation from SSY conditions increases as the transient progresses through time. These results indicate that should crack initiation occur for Cases 1 and 2 in the neighborhood of 1200 s into the transient, it would do so under substantially non-SSY conditions. However, for up to 1200 s into the transient, the deviation of the crack-tip fields for Case 3 from the SSY distribution is not as significant as either Cases 1 or 2.

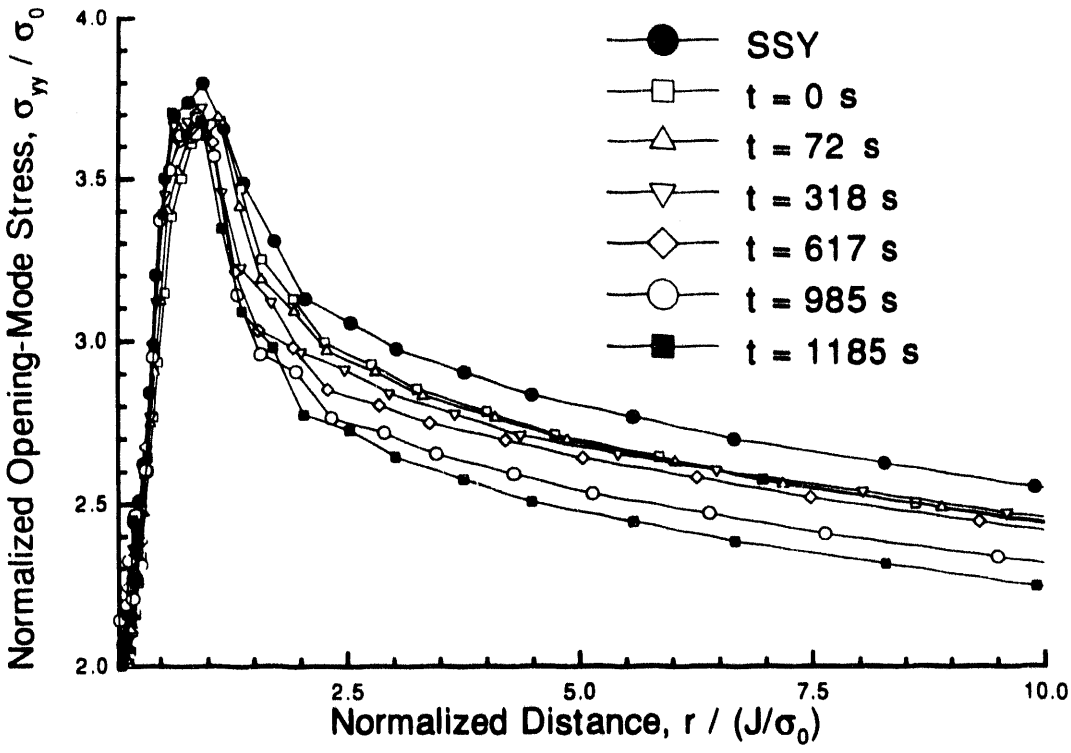

Fig. 23. Distributions of opening-mode stress component for Case 1 material model: SSY and PTS loading up to maximum loading at ~1200 s into transient.

The results from Figs. 23–25 indicate that a calculated value of the Q-stress, based on a single location in the range of $2 \le r/(J/\sigma_0) \le 10$, is somewhat sensitive to the exact location. This sensitivity decreases with increase in loading time and essentially disappears by 1200 s into the transient. A factor that may contribute to the observed sensitivity is that a PTS transient involves thermal-mechanical loads. Available analyses on the evaluation of the Q-stress thus far involve only mechanical loads. However, it is emphasized that the utility of the Q-stress approach is not per se dependent on the nature of the applied loading (e.g., mechanical vs thermal-mechanical) but depends only on the existence of crack-tip fields of the J-Q type as discussed in Sect. 2.

6.3 Effects of PTS Loading on the RPV in Terms of J-Q Values

Analysis results appear to support the applicability of the J-Q approach and interpretation method under PTS conditions. Results from Figs. 23-25 indicate that the Q-stress parameter [from Eq. (4)] can be defined up to maximum loading ($t \le 1200$ s) as characterized by the value of the J-integral during the transient. The effects of PTS loading on the RPV in terms J-Q values are indicated in Fig. 26 for all three material models up to ~1200 s into the transient. Although not explicitly indicated, both transient time and crack-tip temperature are parametric variables along the three J-Q trajectories indicated in Fig. 26. Also, values of the J-integral are only slightly different for the three material models throughout the transient up to maximum loading (see Table 2). On the other hand, the differences in the assumed tensile response associated with the three material models result in greater differences in terms of Q-stress values. Specifically,

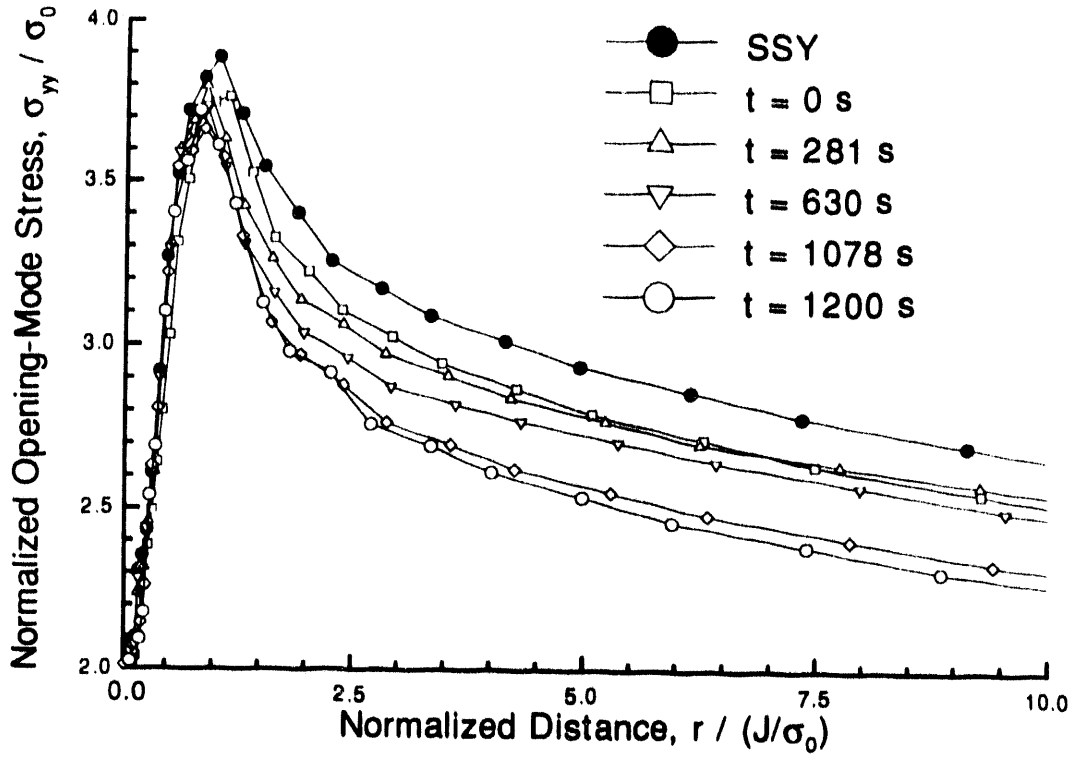

Fig. 24. Distributions of opening-mode stress component for Case 2 material model: SSY and PTS loading up to maximum loading at ~1200 s into transient.

the absolute value of the Q-stress in Fig. 26 for Case 3 conditions (simulated irradiation embrittlement) is much lower than for either Cases 1 or 2 (unirradiated).

6.4 Incorporation of Small-Specimen $J_c(Q,T)$ Toughness Locus Data in RPV Safety-Margin Assessment

A methodology to incorporate small-specimen $J_c(Q,T)$ toughness locus data in the safety-margin assessment of an RPV is presented in this section. For simplicity, it is assumed that type-I warm prestress (WPS) is operative during the unloading phase of this transient, so attention is focused on the PTS transient only up to ~1200 s.[42] It will be shown that the predicted margin of safety in RPVs under PTS conditions is then greater based on the two-parameter approach than that based on the conventional one-parameter approach. A schematic illustrating the differences between the one- and two-parameter safety-margin assessment methods is given in Fig. 26, in which the applied J-Q trajectories for Cases 1 to 3 illustrate possible RPV responses as a function of (simulated) irradiation embrittlement of the vessel.

During a PTS transient, the crack-tip temperature, and hence fracture toughness, decreases monotonically with transient time. A curve that schematically illustrates the locus of one-parameter irradiated fracture toughness, denoted as $J_c(T)$, is shown in Fig. 26. The one-parameter $J_c(T)$ toughness locus does not depend on the Q-stress parameter, but its indicated variation with Q-stress is strictly an indication of the dependence $J_c(T)$ on crack-tip temperature. The margin of safety can then be established based on comparing the value of the applied J-integral to $J_c(T)$ as

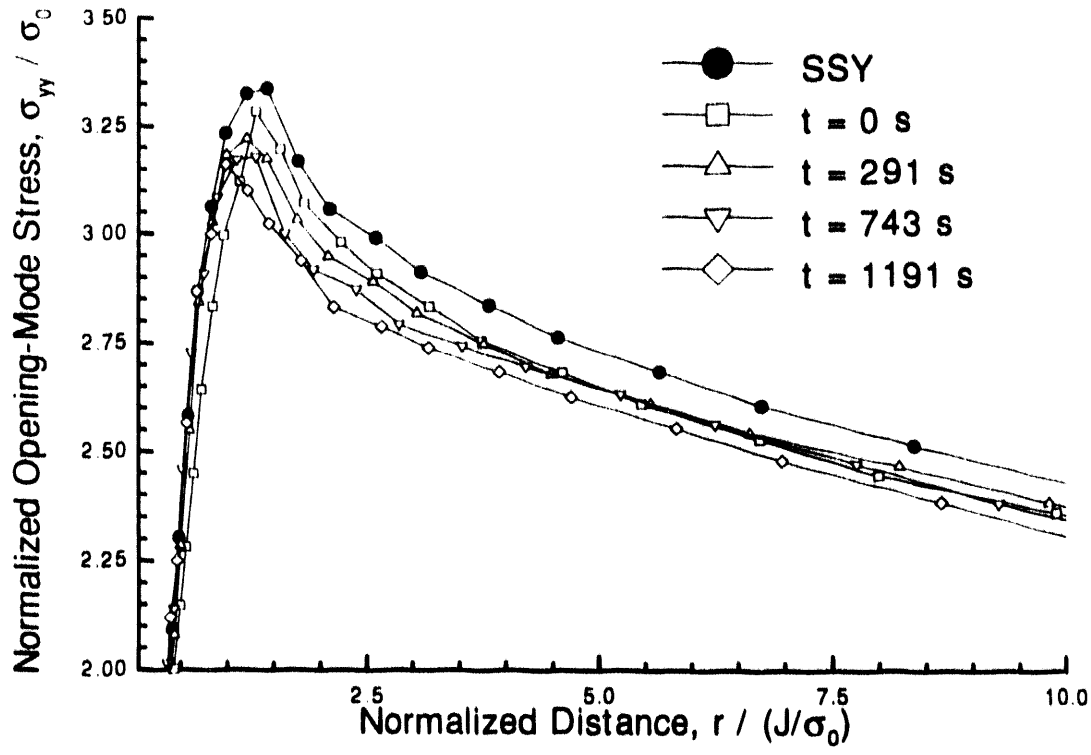

Fig. 25. Distributions of opening-mode stress component for Case 3 material model: SSY and PTS loading up to maximum loading at ~1200 s into transient.

indicated in Fig. 26. Thus, the transient may be most severe, and the margin of safety at a minimum, at the transient time associated with the maximum value of the applied J-integral.

Also schematically indicated in Fig. 26 is a curve denoted as $J_c(Q,T)$ that, based on available small-specimen *unirradiated* toughness data such as those from the HSST shallow-crack testing program, is believed to *qualitatively* illustrate the anticipated $J_c(Q,T)$ toughness locus trend for *irradiated* RPV-grade materials. Available (isothermal) unirradiated results suggest that the $J_c(Q,T)$ toughness locus depends weakly on the Q-stress for the approximate range of $Q > -0.2$ (see, for example, Ref. 21). This weak dependence is reflected in the near coincidence of the $J_c(Q,T)$ and J_c locus in that Q-stress regime. Further, it is assumed that "shallow-crack" toughness enhancement dominates over the toughness degradation associated with decreasing crack-tip temperature. For values of the Q-stress in the range $Q < -0.2$, the experimentally observed "shallow-crack" or Q-stress effects on toughness are reflected in the elevation of the $J_c(Q,T)$ locus above the $J_c(T)$ locus. The indicated $J_c(Q,T)$ toughness locus is qualitative in nature due to the absence of irradiated experimental data. However, the point is that the margin of safety, for example, at the transient time when the applied J-integral is maximum, is predicted to be larger based on the two-parameter $J_c(Q,T)$ approach as compared with the conventional one-parameter $J_c(T)$ approach. Furthermore, depending on the actual shape of $J_c(T)$, $J_c(Q,T)$, and the applied J-Q trajectory, the time at which the PTS transient is most severe in a J-Q approach, defined as the minimum margin of safety, might differ with that determined using the one-parameter J-only approach. Most importantly, a crack that is predicted to initiate in a PTS scenario based on the $J_c(T)$ approach might be predicted to be stable based on the more general $J_c(Q,T)$ approach. However, it is emphasized that the requisite $J_c(Q,T)$ toughness locus is

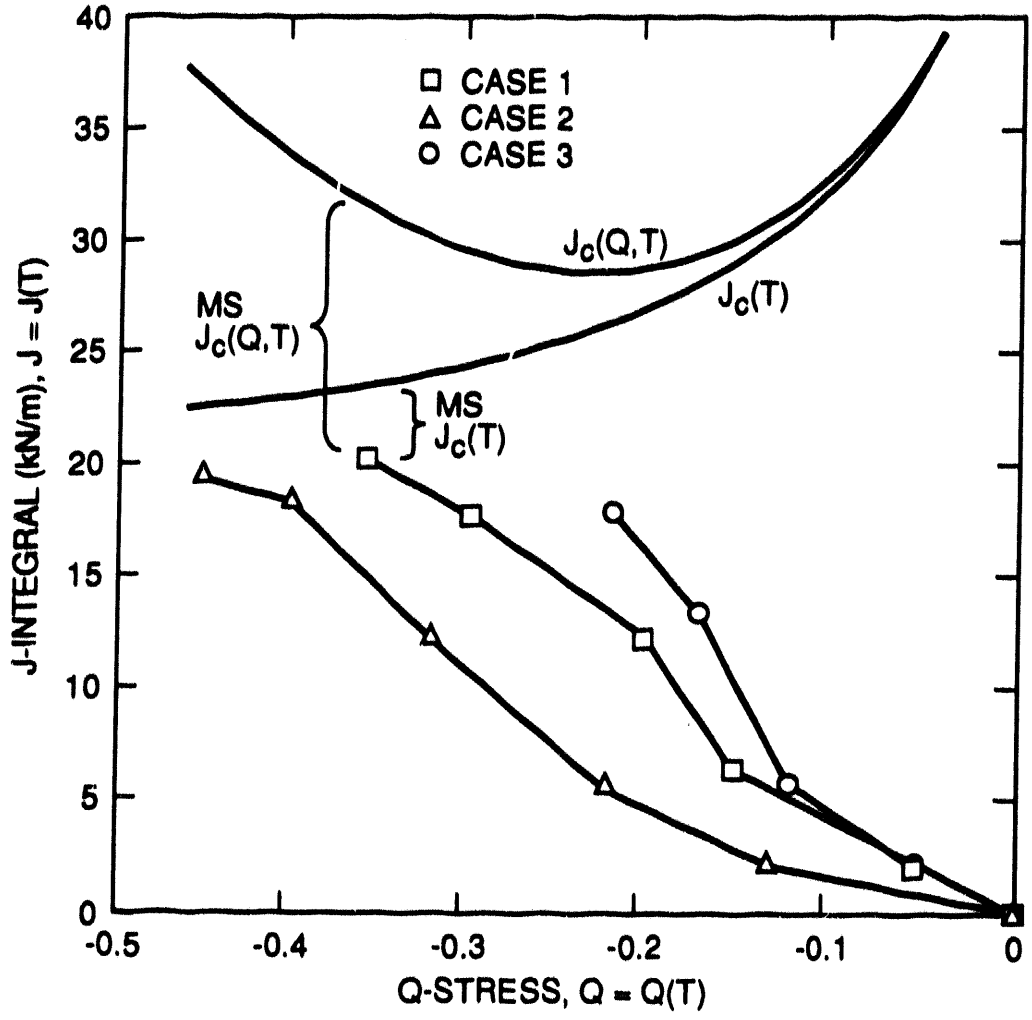

Fig. 26. Schematic illustrating margin of safety based on J-only or J-Q toughness data.

not yet available for either unirradiated or irradiated RPV-grade materials. Before the J-Q analysis technique can be applied to RPV analyses, the technique itself needs further verification. In addition, the determination and application of $J_c(Q,T)$ toughness data involve the resolution of several issues, which are summarized in the final section.

7 Conclusions and Recommendations

Studies were described herein that seek to address shortcomings of the conventional one-parameter (K or J) fracture correlation methods through development and evaluation of various two-parameter methods. Two different analytical approaches to the problem were presented in the paper. The K-T or J-Q approach characterizes crack initiation in terms of descriptions of the near crack-tip fields that incorporate effects of the higher-order T-stress for LEFM conditions or the Q-stress for more general EPFM conditions. The second approach is based on a stress contour method, which correlates cleavage crack initiation with the attainment of a critical area

enclosed within a selected maximum principal stress contour surrounding the crack tip. In preliminary evaluations, these methodologies were applied to experimental data taken from several intermediate- and large-scale testing programs. Applications of the methodologies to analytical studies concerning biaxial stress effects on fracture toughness and safety margin assessments of an RPV subjected to PTS transient loadings were also presented.

While the fracture correlation methodologies appear to show promise in being able to model different crack-tip constraint levels, numerous issues were identified in the HSST studies that require further investigation. Recommendations for future work include the following:

1. Resolve different $J_c(Q)$ data. Recent reanalysis of the ORNL wide-plate tests using a 2-D, J-Q analysis and the HSST shallow-crack beam J-Q analysis produced different sets of $J_c(Q)$ data. According to the underlying theory of the J-Q technique, these data sets should have been similar. This discrepancy will have to be explained before the J-Q techniques can be used in RPV fracture methodology.

2. Generate additional $J_c(Q)$ toughness data. The $J_c(Q)$ toughness locus for A 533 B steel needs to be better defined. In particular, Q-stress data between 0 and –0.7 need to be collected. Additional analyses of HSST shallow-crack beams need to be performed. In addition, scatter in the $J_c(Q)$ data exists that needs to be quantified. Finally, the current $J_c(Q)$ data are based on 2-D finite-element analysis and 3-D specimen data. The introduction of 3-D effects not previously considered needs to be assessed.

3. Perform sensitivity analyses of applied J-Q data. Analyses presented in this paper are based on one RPV geometry using one particular transient. Sufficient analyses need to be performed on multiple RPV geometries and PTS transients to determine the sensitivity of the applied J-Q curve to important PTS parameters (such as pressure level and thermal-shock severity).

4. Determine applicability of J-Q approach to irradiated data. Available $J_c(Q,T)$ toughness locus data, including the HSST shallow-flaw data, are limited to unirradiated material properties and simple laboratory-specimen geometries. Results from the HSST shallow-flaw testing program appear to indicate that the "shallow-flaw" or Q-stress effects on unirradiated toughness might be amendable to some form of RT_{NDT} shift. It remains to be determined if an appropriate temperature-shift methodology could be established for irradiated $J_c(Q,T)$ toughness data.

5. Determine influence of biaxial loading. Currently the influence of out-of-plane (biaxial) loading is inferred from HSST thermal-shock and shallow-crack data. The direct influence of biaxial loading needs to be shown analytically and experimentally. Additional analyses and alternate fracture criterion may be required to explain the HSST shallow-crack toughness evaluation and the lack of toughness increase in thermal-shock data.

6. Determine applicability to cleavage/ductile fracture interaction. Studies should be performed to evaluate dual parameter models for predicting ductile tearing initiation followed by cleavage fracture in the transition region. These capabilities are important for improved safety margin assessments of RPVs subjected to PTS loading.

7. Evaluate alternative fracture methodologies. Investigations should be initiated to develop and evaluate other potential fracture correlation methodologies for characterizing constraint conditions.

References

1. W. E. Pennell, "Heavy-Section Steel Technology Program Overview," *Proceedings of 18th Water Reactor Safety Information Meeting*, Rockville, Md., October 22–24, 1990.

2. J. W. Hutchinson, "Singular Behavior at the End of a Tensile Crack in a Hardening Material," *J. Mech. Phys. Solids* 16, 13–31 (1968).

3. J. R. Rice and G. F. Rosengren, "Plane Strain Deformation Near a Crack Tip in a Power-Law Hardening Material," *J. Mech. Phys. Solids* 16, 1–12 (1968).

4. T. J. Theiss, D. K. M. Shum, and S. T. Rolfe, Martin Marietta Energy Systems, Inc., Oak Ridge Natl. Lab., "Experimental and Analytical Investigation of the Shallow-Flaw Effect in Reactor Pressure Vessels," USNRC Report NUREG/CR-5886 (ORNL/TM-12115), July 1992.

5. D. J. Naus et al., Martin Marietta Energy Systems, Inc., Oak Ridge Natl. Lab., "Crack-Arrest Behavior in SEN Wide Plates of Quenched and Tempered A 533 Grade B Steel Tested Under Nonisothermal Conditions," USNRC Report NUREG/CR-4930 (ORNL-6388), August 1987.

6. R. D. Cheverton and D. G. Ball, Martin Marietta Energy Systems, Inc., Oak Ridge Natl. Lab., "Pressurized-Thermal-Shock Evaluation of the H. B. Robinson Nuclear Power Plant," USNRC Report NUREG/CR-4183 (ORNL/TM-9567/V1), pp. 263–306, September 1985.

7. R. D. Cheverton and D. G. Ball, Martin Marietta Energy Systems, Inc., Oak Ridge Natl. Lab., "Pressurized-Thermal-Shock Evaluation of the Calvert Cliffs Nuclear Power Plant," pp. 201–244, USNRC Report NUREG/CR-4022 (ORNL/TM-9408), September 1985.

8. R. D. Cheverton and D. G. Ball, Martin Marietta Energy Systems, Inc., Oak Ridge Natl. Lab., "Preliminary Development of an Integrated Approach to the Evaluation of Pressurized Thermal Shock as Applied to the Oconee 1 Nuclear Power Plant," USNRC Report NUREG/CR-3770 (ORNL/TM-9176), pp. 5.1–5.51, May 1986.

9. M. L. Williams, "On the Stress Distribution at the Base of a Stationary Crack," *J. Appl. Mech.* 24, 109-114 (1957).

10. G. R. Irwin, "Fracture Mechanics," in *Structural Mechanics*, Pergamon Press, New York, 1960.

11. N. P. O'Dowd and C. F. Shih, "Family of Crack-Tip Fields Characterized by a Triaxiality Parameter: Part I—Structure of Fields," *J. Mech. Phys. Solids 39*, 989–1015 (1991).

12. J. Keeney-Walker, B. R. Bass and J. D. Landes, Martin Marietta Energy Systems, Inc., Oak Ridge National Lab., "An Investigation of Crack-Tip Stress Field Criteria for Predicting Cleavage-Crack Initiation," USNRC Report NUREG/CR-5651 (ORNL/TM-11692), September 1991.

13. D. J. Naus et al., Martin Marietta Energy Systems, Inc., Oak Ridge Natl. Lab., "High-Temperature Crack-Arrest Behavior in 152-mm-Thick SEN Wide Plates of Quenched and Tempered A 533 Grade B Class 1 Steel," USNRC Report NUREG/CR-5330 (ORNL/TM-11083), April 1989.

14. D. K. M. Shum et al., Martin Marietta Energy Systems, Inc. Oak Ridge Natl. Lab., "Analytical Studies of Transverse Strain Effects on Fracture Toughness for Circumferentially Oriented Cracks," USNRC Report NUREG/CR-5592 (ORNL/TM-11581), April 1991.

15. B. R. Bass, D. K. M. Shum, and J. Keeney-Walker, Martin Marietta Energy Systems, Inc., Oak Ridge Natl. Lab., "Constraint Effects on Fracture Toughness for Circumferentially Oriented Cracks in Reactor Pressure Vessels," USNRC Report NUREG/CR-6008 (ORNL/TM-12131), September 1992.

16. W. E. Pennell, Martin Marietta Energy Systems, Inc., Oak Ridge Natl. Lab., "Heavy Section Steel Technology Program: Recent Developments in Crack Initiation and Arrest Research," *Proceedings of the U.S. Nuclear Regulatory Commission Nineteenth Water Reactor Safety Information Meeting*, USNRC Proceeding NUREG/CP-0019, October 1991.

17. J. R. Rice, "Limitations to the Small Scale Yielding Approximation for Crack Tip Plasticity," *J. Mech. Phys. Solids* 22, 17–26 (1974).

18. D. M. Parks, "Three-Dimensional Aspects of HRR-Dominance, Defect Assessment in Components—Fundamentals and Applications," pp. 205–231 in *Proceedings of the European Symposium on Elastic-Plastic Fracture Mechanics*, ESIS/EGF Publication 9, 1991.

19. N. P. O'Dowd and C. F. Shih, "Family of Crack-Tip Fields Characterized by a Triaxiality Parameter: Part II—Fracture Applications," *J. Mech. Phys. Solids* 39 (1991).

20. C. F. Shih and N. P. O'Dowd, "A Fracture Mechanics Approach Based on a Toughness Locus," *Proceedings of International Conference on Shallow Crack Fracture Mechanics Tests and Applications*, Cambridge, United Kingdom, September 23–24, 1992.

21. J. D. Sumpter and J. W. Hancock, "Shallow Crack Toughness of HY80 Welds: An Analysis Based on T Stresses," *Int. J. Pres. Ves. & Piping* 45, 207–221 (1991).

22. R. O. Ritchie, J. F. Knott, and J. R. Rice, "On the Relationship Between Critical Tensile Stress and Fracture Toughness in Mild Steel," *J. Mech. Phys. Solids* 21, 395–410 (1973).

23. D. M. Parks, "Interpretation of Irradiation Effects on the Fracture Toughness of a Pressure Vessel Steel in Terms of Crack Tip Stress Analysis," *J. Eng. Mat. and Tech.* 98, 30–36 (1976).

24. R. O. Ritchie, W. L. Server, and R. A. Wullaert, "Critical Fracture Stress and Fracture Strain Models for the Prediction of Lower and Upper Shelf Toughness in Nuclear Pressure Vessel Steels," *Met. Trans. A*, 10A, 1557–1570 (1979).

25. R. A. Wullaert and W. L. Server, "Small Specimen Predictions of Fracture Toughness for Nuclear Pressure Vessel Steels," *Nucl. Eng. Des.* 576, 153–173 (1980).

26. J. Heerens and D. T. Reed, "Fracture Behavior of a Pressure Vessel Steel in the Ductile to Brittle Transition Region," National Institute of Standards and Technology, NISTIR 88/3099 (PB89-189195/AS), December 1988.

27. S. G. Druse, G. P. Gibson, and M. Capel, "Microstructural Control of Cleavage Fracture in an A508 Class 3 Pressure Vessel Steel," paper presented at the 22nd National Symposium on Fracture Mechanics, Atlanta, Georgia, June 26–28, 1990.

28. T. L. Anderson and R. H. Dodds, Jr., "Specimen Size Requirements for Fracture Toughness Testing in the Transition Region," Report MM-6585-90-5, Mechanics and Materials Center, Texas A&M University, College Station, Texas, May 1990.

29. D. E. McCabe and J. D. Landes, "The Effect of Specimen Plan View Size and Material Thickness on the Transition Temperature Behavior of A533 B Steel," Research Report 80-102-REVEM-92, Westinghouse R&D Center, November 1980.

30. G. T. Hahn, A. Gilbert, and C. N. Reid, "Model for Crack Propagation in Steel," *Journal, Iron and Steel Institute (London)* 202, 677–684 (August 1964).

31. R. D. Cheverton et al., Martin Marietta Energy Systems, Inc., Oak Ridge Natl. Lab., "Review of Pressurized-Water-Reactor-Related Thermal-Shock Studies," ASTM Special Technical Publication No. 969, 752-766 (1988).

32. D. L. Selby et al., Martin Marietta Energy Systems, Inc., Oak Ridge Natl. Lab., "Pressurized Thermal Shock Evaluation of the H. B. Robinson Unit 2 Nuclear Power Plant," USNRC Report NUREG/CR-4183 (ORNL/TM-9567/V1 and V2), September 1985.

33. D. Aurich, "The Influence of the Stress State on the Plastic Zone Size," *Eng. Frac. Mech.* 7, 761–765 (1975).

34. D. Aurich et al., "The Influence on the Stress State of K_{Ic}," Paper G 5/2 in *Proceedings of the 4th International Conference on Structural Mechanics in Reactor Technology*, San Francisco, Calif., August 15–19, 1977.

35. D. Aurich et al., "The Influence on Stress State on Fracture Toughness—Further Results," Paper G 2/3 in *Transactions of the 5th International Conference on Structural Mechanics in Reactor Technology*, Berlin, Germany, August 13–17, 1979.

36. J. Olschewski et al., "The Influence of Biaxial Loading on Fracture Toughness—Further Results," Paper G/F 3/3 in *Transactions of 7th International Conference on Structural Mechanics in Reactor Technology*, Chicago, Ill., August 1983.

37. D. Aurich, "Übertragbarkeit von Bruchkennwerten von Probem auf Bauteil im Hinblick auf die Sicherheits-analyses von Kernkrafwerks-komponenten," Report RS 275, BAM, Berlin, Germany, September 14, 1984 (text in German).

38. D. Aurich et al., "The Influence of Multiaxial Stress States on Characteristic Parameters for Cleavage Fracture in the Elastic-Plastic Range," pp. 345–356 in *Proceedings International Conference Applied Fracture Mechanics to Materials and Structures*, 1984.

39. D. K. M. Shum and B. R. Bass, Martin Marietta Energy Systems, Inc., Oak Ridge Natl. Lab., "Absence of Toughness Elevation in Thermal-Shock Experiment TSE-5A: Preliminary Explanation Based on Crack-Tip Constraint," USNRC Report ORNL/NCR/LTR-92/24, September 1992.

40. S. Glasstone and A. Sesonske, in *Nuclear Reactor Engineering*, Van Nostrand Reinhold Co., New York, 1981, p. 458.

41. J. J. McGowan, Martin Marietta Energy Systems, Inc., Oak Ridge Natl. Lab., "Tensile Properties of Irradiated Nuclear Grade Pressure Vessel Plate and Welds for the Fourth HSST Irradiation Series," USNRC Report NUREG/CR-3978 (ORNL/TM-9516), January 1985.

42. D. K. M. Shum, Martin Marietta Energy Systems, Inc., Oak Ridge Natl. Lab., "Implications of Warm Prestressing on Safety-Margin Assessment of Reactor Pressure Vessels," USNRC Report ORNL/NRC/LTR-92/9, March 1992.

Prediction of the First Spinning Cylinder Test Using Continuum Damage Mechanics

by

D.P.G. Lidbury* and A.H. Sherry*; B.A. Bilby**, I.C. Howard** and Z.H. Li**; and C. Eripret***

Paper to be presented at:

IAEA/CSNI Specialists' Meeting on Fracture Mechanics Verification by Large-Scale Testing, Oak Ridge, Tennessee, USA, 26-29 October 1992

Abstract: For many years large-scale experiments have been performed world-wide to validate aspects of fracture mechanics methodology. Special emphasis has been given to correlations between small- and large-scale specimen behaviour in quantifying the structural behaviour of pressure vessels, piping and closures. Within this context, the first three Spinning Cylinder Tests, performed by AEA Technology at its Risley Laboratory, addressed the phenomenon of stable crack growth by ductile tearing in contained yield and conditions simulating pressurised thermal shock loading in a PWR reactor pressure vessel. A notable feature of the test data was that the effective resistance to crack growth, as measured in terms of the J R-curve, was appreciably greater than that anticipated from small-scale testing, both at initiation and after small amounts (a few millimetres) of tearing.

In the present paper, two independent finite element analyses of the First Spinning Cylinder Test (SC 1) are presented and compared. Both involved application of the Rousselier ductile damage theory in an attempt to better understand the transferability of test data from small specimens to structural validation tests. In each instance, the parameters associated with the theory's constitutive equation were calibrated in terms of data from notched-tensile and (or) fracture mechanics tests, metallographic observations and (or) chemical composition. The evolution of ductile damage local to the crack tip during SC 1 was thereby calculated and, together with a crack growth criterion based on the maximisation of opening-mode stress, used as the basis for predicting cylinder R-curves (angular velocity vs. Δa, J -integral vs. Δa). The results show the Rousselier model to be capable of correctly predicting the enhancement of tearing toughness of the cylinder relative to that of conventional test specimens, given an appropriate choice of finite element cell size in the region representing the crack tip. As such, they represent a positive step towards achieving the goal to establish continuum damage mechanics as a reliable predictive engineering tool.

* AEA Technology, Reactor Services, Risley, Warrington, Cheshire, WA3 6AT, UNITED KINGDOM.

** SIRIUS, University of Sheffield, Department of Mechanical and Process Engineering, Sheffield, S1 3JD, UNITED KINGDOM.

*** Electricité de France, Département MTC, Les Renardières, BP1, 77250 Moret-sur-Loing, FRANCE.

Introduction

During the last decade, several large-scale test programmes have been mounted world-wide to validate the fracture mechanics principles employed in the structural integrity assessment of LWR pressure vessels. In particular, the Spinning Cylinder Test Facility *[1]* was designed and constructed to validate the fracture mechanics principles used in UK civil PWR pressure vessel safety cases. To date, six spinning cylinder tests have been conducted. The first three tests were aimed at a progressive demonstration of stable crack growth by ductile tearing in contained yield and conditions simulating pressurised thermal shock loading. Each involved a full length axial defect (fatigue precracked to $a_0/W = 0.55$) in a cylindrical test specimen of modified A508 Class 3 pressure vessel steel preheated to a temperature of 290°C. In the first test ductile crack growth was generated by progressively increasing the rotation speed to simulate pressure loading. In the second it was generated by thermally shocking the inner surface of the cylinder with water at ambient temperature. In the third it was generated by combined rotational and thermal shock loading. In each case a notable feature of the test data was that the effective resistance to crack growth, as measured in terms of the J R-curve, was appreciably greater than that anticipated from small-scale (compact specimen) testing, both at initiation and after small amounts (up to a few millimetres) of tearing. This effect, whilst not explainable in terms of the conventional theory of J-controlled growth *[2]*, must be ultimately understandable in terms of the variation of crack-tip stresses and strains as a function of geometry and loading configuration, and the materials response to these variations. On this basis, the transferability of data from standard compact fracture mechanics specimens to spinning cylinder tests may be investigated numerically by simulating the evolution of ductile damage caused by the nucleation and growth of micro-voids in response to crack-tip stress and strain fields. This enables direct predictions to be made of crack initiation and subsequent growth. By combining the results of the numerical simulation with independent J-integral calculations, J R-curves may be calculated. By performing separate computations for compact specimen and cylinder it is possible to see if their respective crack growth responses may be reconciled in terms of a *transferable* constitutive equation representing the ductile crack growth process.

The purpose of this paper, then, is to compare two recently-published finite element analyses *[3,4]* of the First Spinning Cylinder Test (SC 1), both of which used the above damage mechanics approach. Each involved application of the Rousselier ductile damage theory *[5]* in an attempt to address key questions regarding the transferability of fracture toughness test data to structures. In both instances, the parameters associated with the theory's constitutive equation were calibrated in terms of data from notched-tensile and (or) compact specimen tests, metallographic observations and (or) chemical composition. The evolution of ductile damage in response to the local (crack-tip) values of stress and strain during SC 1 was thereby calculated and, together with a crack growth criterion based on the maximisation of opening-mode stress, used as the basis for predicting cylinder R-curves (angular velocity vs. Δa, J -integral vs. Δa). The results of these studies are therefore examined to see whether the continuum damage mechanics approach has potential for becoming a reliable predictive tool for the transfer of ductile tearing test results to structures.

Outline Details of the First Spinning Cylinder Test

The experimental details of Spinning Cylinder Test 1 are described fully in *[1]*. Briefly, the general arrangement of the apparatus is shown in Fig. 1, where the central feature is an 8-ton cylindrical test specimen (1.3m long, 1.4m OD, 200mm wall thickness) suspended by a flexible shaft from a single pivoted bearing so that it is free to rotate about the vertical axis. The driving power is provided by a 375 kW DC motor mounted on a horizontal pedestal, and is transmitted via a right-angle gearbox with 2:1 step-up ratio (maximum design speed of 3500 rpm at the rotor). A damping device (not shown) is attached to the bearing pivot to stabilise the rotor against aerodynamically induced precessional motion. The cylinder is suspended in a reinforced underground enclosure for safety containment. Eight 3-kW heaters mounted vertically within the test enclosure provided the necessary thermal energy to raise the temperature of the cylinder to a pretest value of 290°C.

The rotation speed of the cylinder was measured by three independent devices. The primary speed indication was an analogue tachometer, which also provided the control signal for the motor servo system. The back-up systems were two digital counters, one electromagnetic and the other optical.

The primary method employed to measure crack growth during the test was the alternating current potential difference technique (ACPD). Three sets of ACPD probes were situated 25mm above the bottom of the machined slot in different axial locations. The crack tip was located at the bottom of this slot. The connections for the driving current (0.4A at 1kHz) were on opposite sides of the slot so that the current between them passed around the crack tip. The voltage probes were deployed similarly. Back up measurements of crack growth were obtained from five back face strain gauges welded on the outer surface of the cylinder behind the slot. Additional instrumentation comprised three pairs of clip gauges to monitor changes in the slot gap closely adjacent to the ACPD stations, and an array of thermocouples to measure the cylinder temperature variations axially, circumferentially and through the thickness.

All instrumentation signals were routed through a data logging system that processed and recorded them at preselected frequencies of up to 0.17Hz. All data were stored to hard disc on line and buffered to a printer. Selected data were also displayed on a visual display unit; in particular, the crack growth signals were further processed by satellite microcomputers to provide a graphical display of growth as a function of speed.

In order to generate a J R-curve from the test result the relationship between rotation speed and crack growth was established by a process of calibration. In particular, the temperature-corrected ACPD signal was plotted against the square of the rotation speed and the point at which a pronounced change of slope occurred was identified as the point of tearing initiation. Values of the J-integral corresponding to a particular value of crack growth were obtained by finite element analysis using the ABAQUS (1984) Code. Version 4.5 was used, in which values of the J-integral are evaluated by the Virtual Crack Extension method using Parks' *[6]* stiffness derivative method. The cylinder was modelled in two-dimensional plane strain using eight-noded biquadratic quadrilateral elements with reduced integration.

The Rousselier Continuum Damage Model

The Rousselier continuum damage model /5/ provides a description of ductile tearing behaviour based on the plastic potential F and the yield criterion F = 0. The resulting constitutive equations, derived using the normality rule /5/ are:

$$F = F_h + F_s \tag{1}$$

$$F_h = \frac{\sigma_{eq}}{\rho} - R(p) \tag{2}$$

$$F_s = DB(\beta)\exp\left(\frac{\sigma_m}{\rho\sigma_1}\right) \tag{3}$$

Here, F_h denotes the hardening term and F_s denotes the softening (or damage) term. The quantity ρ is the material density. R(p) is representative of the material true-stress vs. true-strain curve, D is a constant, σ_m is the mean normal stress and σ_1 is related to the material flow stress. The term B(β) is given by:

$$B(\beta) = \frac{\sigma_1 f_0 \exp(\beta)}{1 - f_0 + f_0\exp(\beta)} \tag{4}$$

where

$$\beta = \ln\left[f(1-f_0)/f_0(1-f)\right] \tag{5}$$

and β is the damage variable. The quantities f and f_0 are respectively the current and initial values of the void volume fraction. Equivalently, β may be calculated from the formula:

$$\beta = \int D\exp\left(\frac{\sigma_m}{\rho\sigma_1}\right) d\ d_{eq}^p \tag{6}$$

where d_{eq}^p denotes the equivalent plastic strain rate.

The evolution of damage in the above model reflects the competition between material hardening and softening behaviour. A dilatational plasticity represents the growth of voids and leads to softening with increasing deformation. Thus, as loading is increased, the term F_h increases and reflects the increase in crack-tip stresses due to work hardening. With further increases in loading, F_s increases at the expense of F_h such that the crack opening stress (σ_{yy}) reaches a maximum and thereafter sharply declines (Fig. 2). In conjunction with a finite element model, this effectively allows crack initiation and propagation to be modelled as a progression of discrete steps without recourse to the more usual technique of nodal release (Figs. 3 and 4). Because the above equations do not model the actual linking of voids as the material fails, a crack growth criterion based on stress is invoked. The crack growth criteria used in Ref. 3 and Ref. 4 respectively are:

1. When the opening stress reaches a maximum in element n+1, the crack tip is considered to move to the boundary of element n, for n = 1, 2, 3, ... Thus initiation occurs when the stress reaches a maximum value in the second element and the crack always moves in steps of L.

2. When the opening stress reaches a maximum at the centroid of element n, the crack tip is considered to move to this location, for n = 1, 2, 3, ... Thus initiation occurs when the stress reaches a maximum in the first element. The crack moves L/2 and thereafter by increments of L.

The L values in 1 and 2 above refer to the size of the deformed mesh.

Calibration of the Rousselier Model

In order to use the Rousselier model, it is necessary to determine the following parameters:

- the initial void volume fraction, f_0
- the characteristic length, λ_c, describing the ductile fracture process
- σ_1 and D

In Ref. 3, and also in Ref. 4, the value of f_0 is equated with the volume fraction of critical inclusions. In both cases, this is taken as the volume fraction of MnS inclusions estimated from Franklin's formula as:

$$f_v = 0.054\left\{S(\%) - \frac{0.001}{Mn(\%)}\right\} \qquad (7)$$

For the modified A508-3 steel in question, S = 0.012% and Mn = 1.32% and so $f_V = f_0 = 6.07 \times 10^{-4}$.

There has been general criticism of damage theories used with finite element calculations because the values of fitted parameters depend on the mesh size, L. Notwithstanding such criticism, the view is taken in Ref. 3 and Ref. 4 that the selection of a particular mesh size represents a process of averaging over an appropriate damage cell relevant to the failure mechanism under discussion. Consequently, the mesh size L is equated with the characteristic length, λ_c, describing the ductile fracture process. This in turn equates with the spacing of the MnS particles controlling the failure process. In Ref. 3 the value of λ_c is estimated to be 550μm, based on data published in Ref. 7. This value was therefore used for the finite element mesh size in modelling ductile damage. In Ref. 4, the best estimate of λ_c is 250μm, based on more detailed metallographic evidence than that available in Ref. 7. However, for the purpose of assessing the sensitivity of predictions to the value of λ_c, finite element mesh sizes of 500, 250 and 125μm were used in Ref. 4 in modelling the ductile damage process. Subsequent further evidence suggested that a size less than 250μm might well have been chosen.

The determination of σ_1 is generally made via mechanical testing of axisymmetric notched-tension specimens. However, data from such tests were not available at the time Ref. 3 was published, and so the authors of that paper calibrated Equation 3 in terms of σ_1 with reference to the J R-curve data for 35mm-thick side grooved compact specimens presented in Ref. 7. The test temperature was 290°C, corresponding to the temperature at which SC 1 was carried out. A value of σ_1 = 350MPa with $f_0 = f_V = 6.07 \times 10^{-4}$ and L = 550μm gave the best overall prediction of this data — Fig. 5.

In Ref. 4 values of σ_1 for a temperature of 290°C were determined ($D = 2\sqrt{3}$) to be 443, 516 and 571MPa for L = 500, 250 and 125μm respectively. These values represent a compromise resulting from predicted curves 'tuned' to fit not only AE10, AE4 and AE2 notched tensile results† but also the results from 35mm-thick side grooved compact specimens — Figs. 6 and 7.

Comparison of Predictions

The finite element analyses in Ref. 3 and Ref. 4 reflect the same set of relevant dimensions for the test cylinder. However, the analysis of Ref. 3 using the ALIBABA Code did not model centrifugal loading; instead, the cylinder was loaded by an internal pressure that would produce in a linear elastic material the same average hoop stress as that in an uncracked rotating cylinder. The numerical simulation of the behaviour of the cracked cylinder thus reflected internal pressure loading; predicted values of crack growth and the J-integral were correlated in terms of the equivalent rotation speed. In the TOMECH Code calculations in Ref. 4, a distribution of body forces was applied to the finite element nodes to simulate the centrifugal loading due to the rotation of the cylinder. Values of the J-integral were obtained by the virtual crack extension method using an area integral and an interpolation function. No significant differences were found in comparisons with corresponding values of the conventional J-integral; moreover, for the particular type of body force loading applied during SC 1, the latter was found to be path independent to within a few percent, even where the integration path passed through plastic regions, provided the path was not too close to the crack tip. Predictions of crack growth are also reported in Ref. 4 as a function of rotation speed. These involve the use of the J-integral in the compact specimen calculations only, where values conform very closely to values using the parameter obtained by standard measurements of load and load-line displacement. The predictions of crack growth as a function of rotation speed are thus independent of any complications that may result from the use of the J-integral in relation to body force loading.

The J R-curves derived for SC 1 are shown in Fig. 8 and Fig. 9. These figures relate to Ref. 3 and Ref. 4 respectively. In addition, Fig. 10 shows the Ref. 4 predicted and experimental curves for rotation speed vs. crack advance. An important point to note is that in Ref. 4 the

---

† Three sets of standard axisymmetrically notched bar specimens were tested; all had a bar diameter of 18mm and a minimum diameter of 10mm. The notations AE10, AE4 and AE2 denote notch radii of 10, 4 and 2mm respectively. Unfortunately only load vs. axial displacement data were available on these notched bars. Figure 6 shows data in respect of AE10 specimens only.

predictions of rotation speed vs. crack advance were made 'blind', with the best estimate being for L = 250μm. In all cases the predictions confirm that the cylinder's resistance to ductile tearing is significantly greater than that measured on 35mm-thick compact specimens. Overall, the predictions represent a significant improvement compared with previous predictions based on standard fracture mechanics techniques and small specimen J R-curve data *[7]*. The best predictions are for mesh sizes ≥ 250μm. In Fig. 8 the prediction of the initiation of ductile tearing and the slope of the tearing resistance curve is in good agreement with the experimental measurements. However, there is an underprediction of the overall extent of ductile tearing. In Figs. 9 and 10 there is a deviation from experiment in the region of crack initiation, although the slope of the tearing resistance curve and the total crack extension is accurately predicted. These latter results suggest the possibility that initiation in the cylinder may occur at a similar J-integral level to that found in the compact specimens, notwithstanding the slope of the J R-curve being greater in the cylinder. This point is currently the subject of an ongoing study that is involving quantitative metallography including detailed post-test measurements of stretch-zone width in both the test cylinder and compact specimens *[8]*.

Lastly, it is noted that in both Ref. 3 and Ref. 4 comparisons are made of the fields ahead of the crack tip in the cylinder and the compact specimen at different stages of crack advance using damage theory. In both cases a higher value of the ratio, σ_m/σ_{eq}, of the mean normal stress to the equivalent stress, is reported in the compact specimen compared with the cylinder, albeit after crack initiation in the case of Ref. 4. Whilst this is consistent with the observation of a higher resistance curve slope in the cylinder, the full explanation of this effect again remains the subject of an ongoing study.

Conclusions

Using the standard Rousselier ductile damage model, comparative predictions have been made of crack growth in the First Spinning Cylinder Test carried out by AEA Technology at its Risley Laboratory. The following conclusions may be drawn:

1. Two independent analyses have correctly predicted the enhancement in tearing toughness of the cylinder relative to that of standard small-scale fracture toughness specimens. This is a significant improvement compared with previous predictions based on standard fracture mechanics techniques and small specimen J R-curve data.

2. The accuracy of predictions is most sensitive to the selection of the finite element mesh size L to represent the process of averaging over a damage zone relevant to the failure mechanism under consideration. In the present case this has meant equating L with a characteristic length λ_C representative of some average spacing between dominant MnS inclusions.

3. The potential for models based on continuum damage mechanics to address more complex materials and structural circumstances requires further validation. However, the present results represent a positive step towards achieving the goal to establish damage mechanics as a reliable predictive engineering tool.

References

1. A.M. Clayton et al., "A Spinning Cylinder Tensile Test Facility for Pressure Vessel Steels", Proceedings Eighth International Conference on Structural Mechanics in Reactor Technology, Brussels, Belgium, August 19-23, 1985, Paper G1/4.

2. R.M. McMeeking and D.M. Parks, "On Criteria for J-Dominance of Crack-Tip Fields in Large-Scale Yielding", Elastic-Plastic Fracture, ASTM STP 668, American Society for Testing and Materials, Philadelphia, Pa., pp. 175-194 (1979).

3. C. Eripret and G. Rousselier, "First Spinning Cylinder Test Analysis by using Local Approach to Fracture", International Conference on Pressure Vessels and Piping, San Diego, June 1991.

4. B.A. Bilby, I.C. Howard and Z.H. Li, "Prediction of the First Spinning Cylinder Test using Ductile Damage Theory", Fatigue and Fracture of Engineering Materials and Structures, **16** (1), 1993. In press.

5. G. Rousselier, "Ductile Fracture Models and their Potential in Local Approach of Fracture", Nuclear Engineering and Design, **105**, pp. 97-111, 1987.

6. D M Parks. "The Virtual Crack Extension Method of Non-Linear Material Behaviour", Computer Methods in Applied Mechanics and Engineering, **12**, pp 353-364, 1977.

7. D J Lacey and R E Leckenby. "Determination of Upper Shelf Fracture Resistance in Spinning Cylinder Test Facility", Trans. Tenth SMIRT Conference, Division F, pp. 1-6, Anaheim, August, 1989.

8. I. J. O'Donnell. Unpublished work, AEA Technology, Risley, 1991.

Figure Captions

1. General view of spinning cylinder test rig.

2. Stress-strain curve showing competition between hardening and softening behaviour. From Reference 3.

3. Normalised hoop stress versus rotation speed. From Reference 3.

4. Normalised hoop stress versus rotation speed. From Reference 4.

5. Predicted and experimental J R-curves for 35mm-thick side grooved compact specimens. From Reference 3.

6. Predicted and experimental load vs. displacement curves for the AE10 notched tensile specimen. From Reference 4.

7. Predicted and experimental J R-curves for 35mm-thick side grooved compact specimens. From Reference 4.

8. Predicted and experimental J R-curves for the first spinning cylinder test. From Reference 3.

9. Predicted and experimental J R-curves for the first spinning cylinder test. From Reference 4.

10. Predicted and experimental curves for rotation speed vs. crack advance in the first spinning cylinder test. From Reference 4.

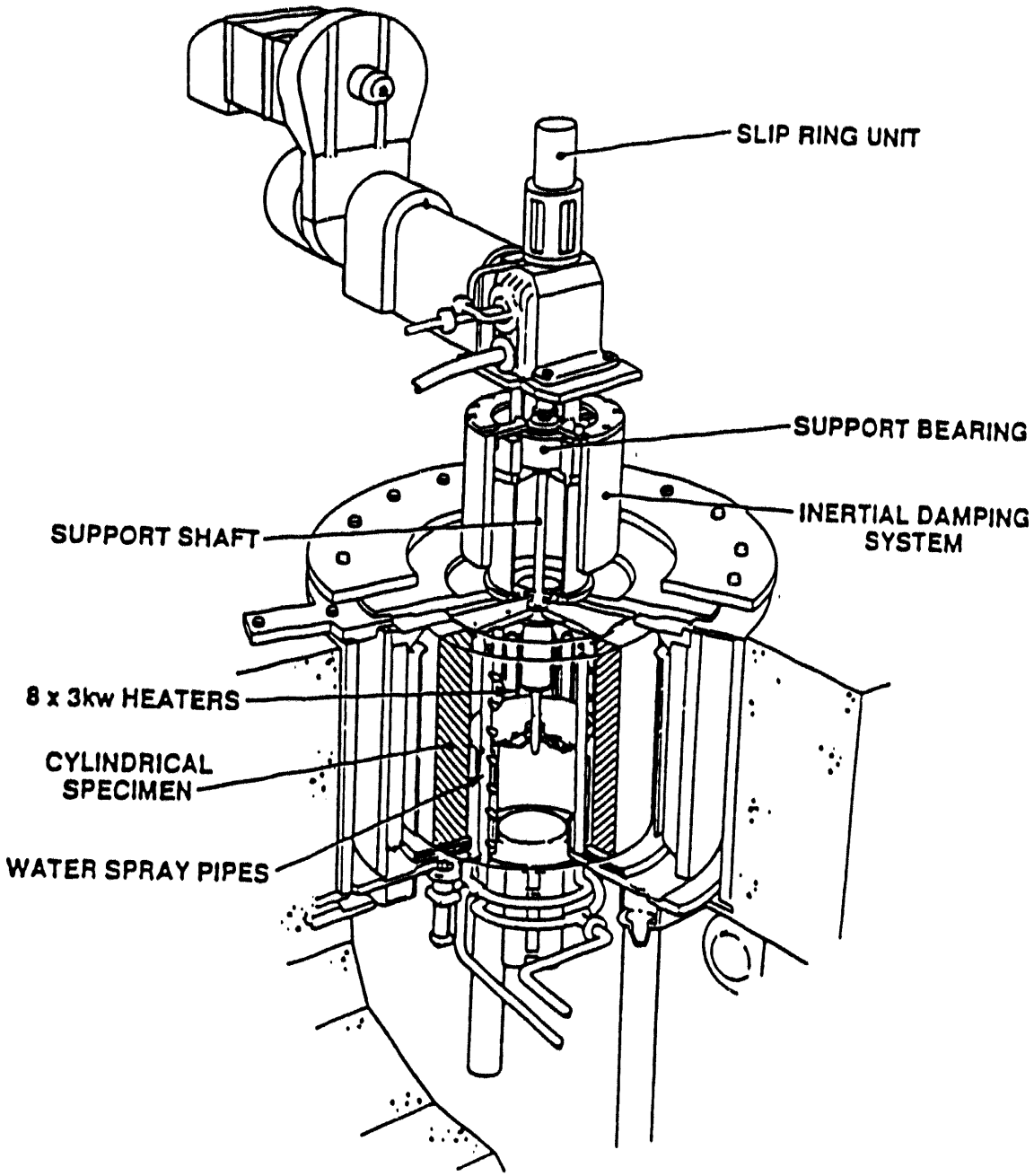

Fig. 1 The Spinning Cylinder Test Facility

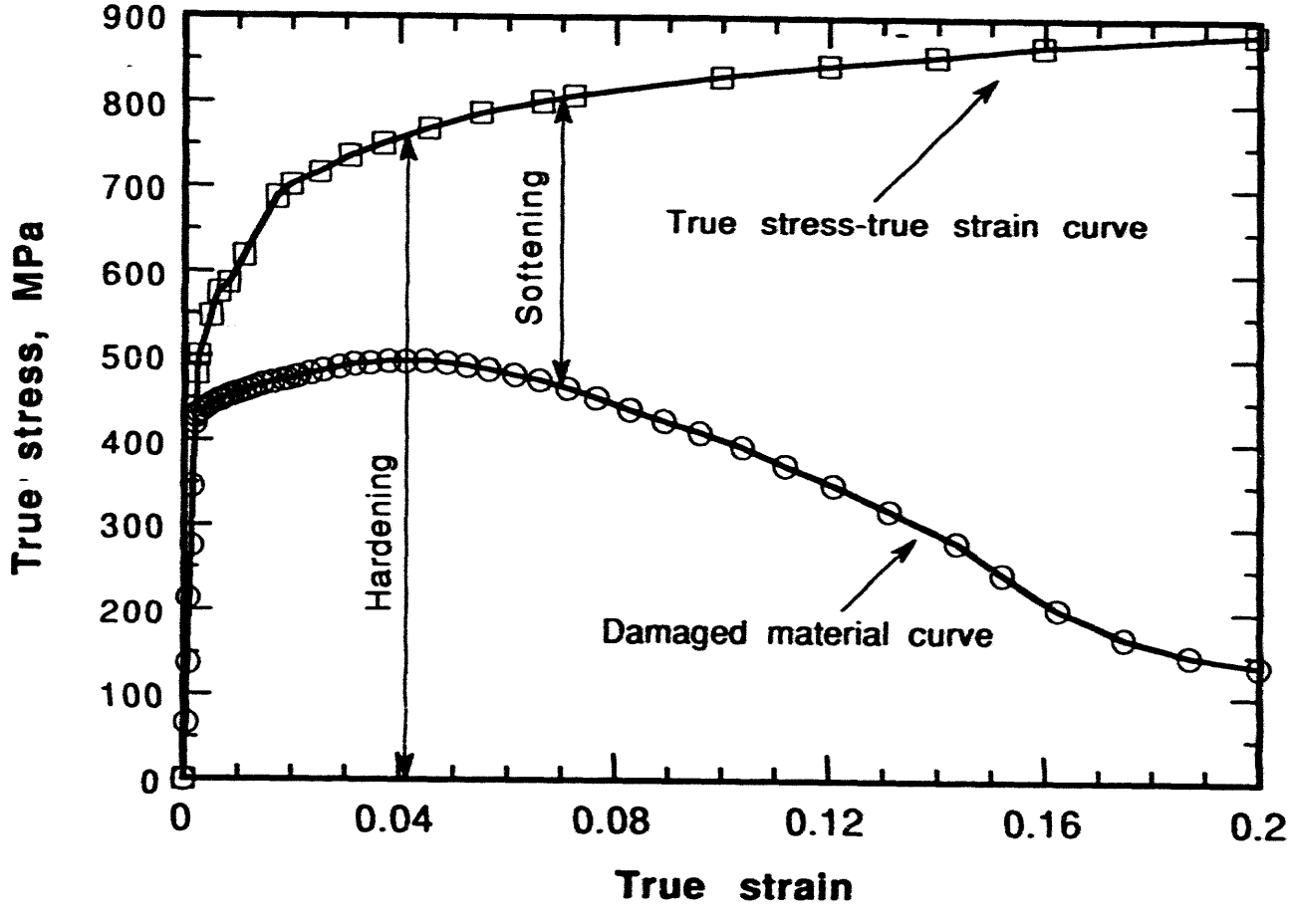

Figure 2: Stress-strain curve showing competition between hardening and softening behaviour. From Reference 3.

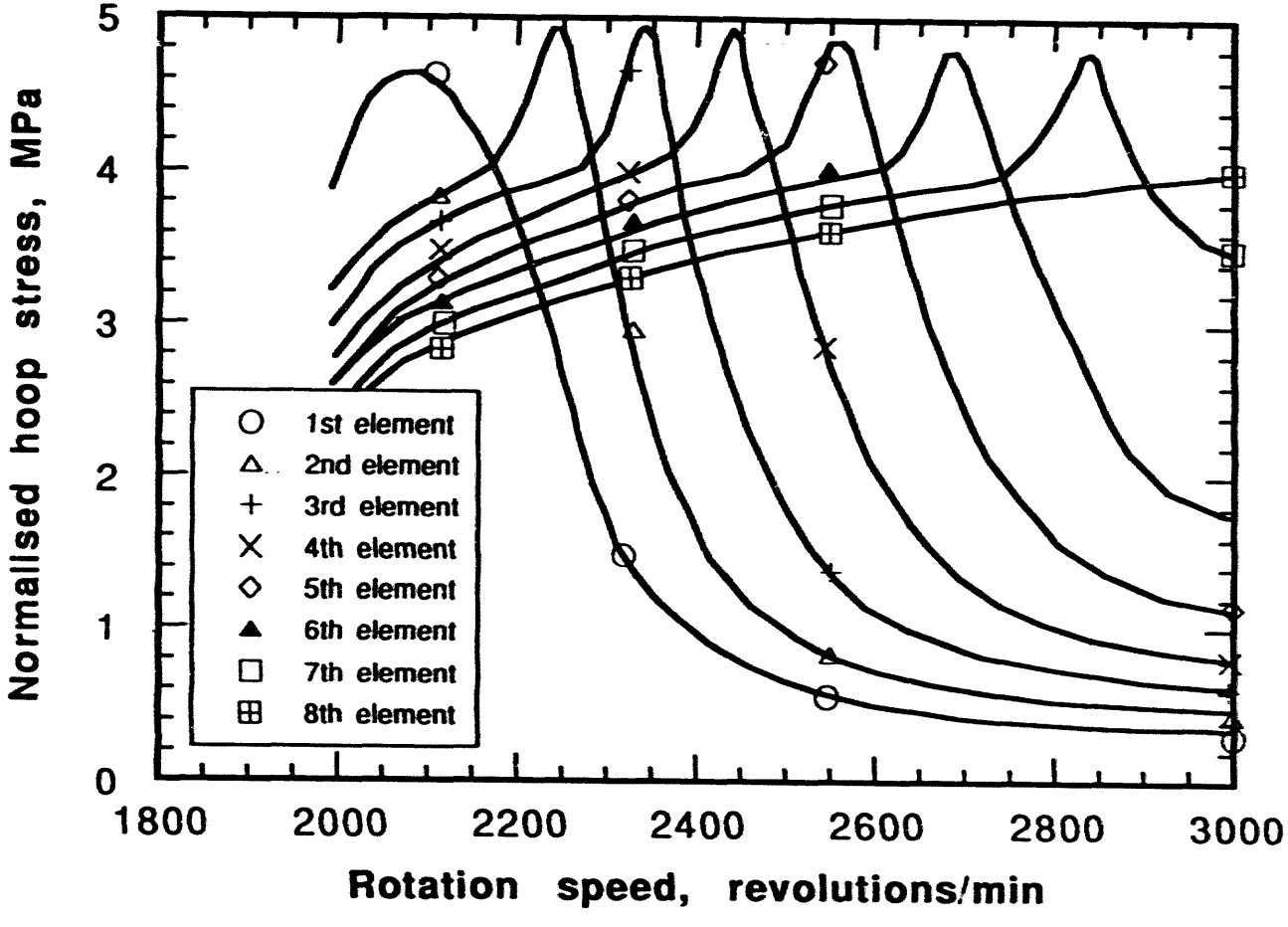

Figure 3: Normalised hoop stress vs. rotational speed. From Reference 3.

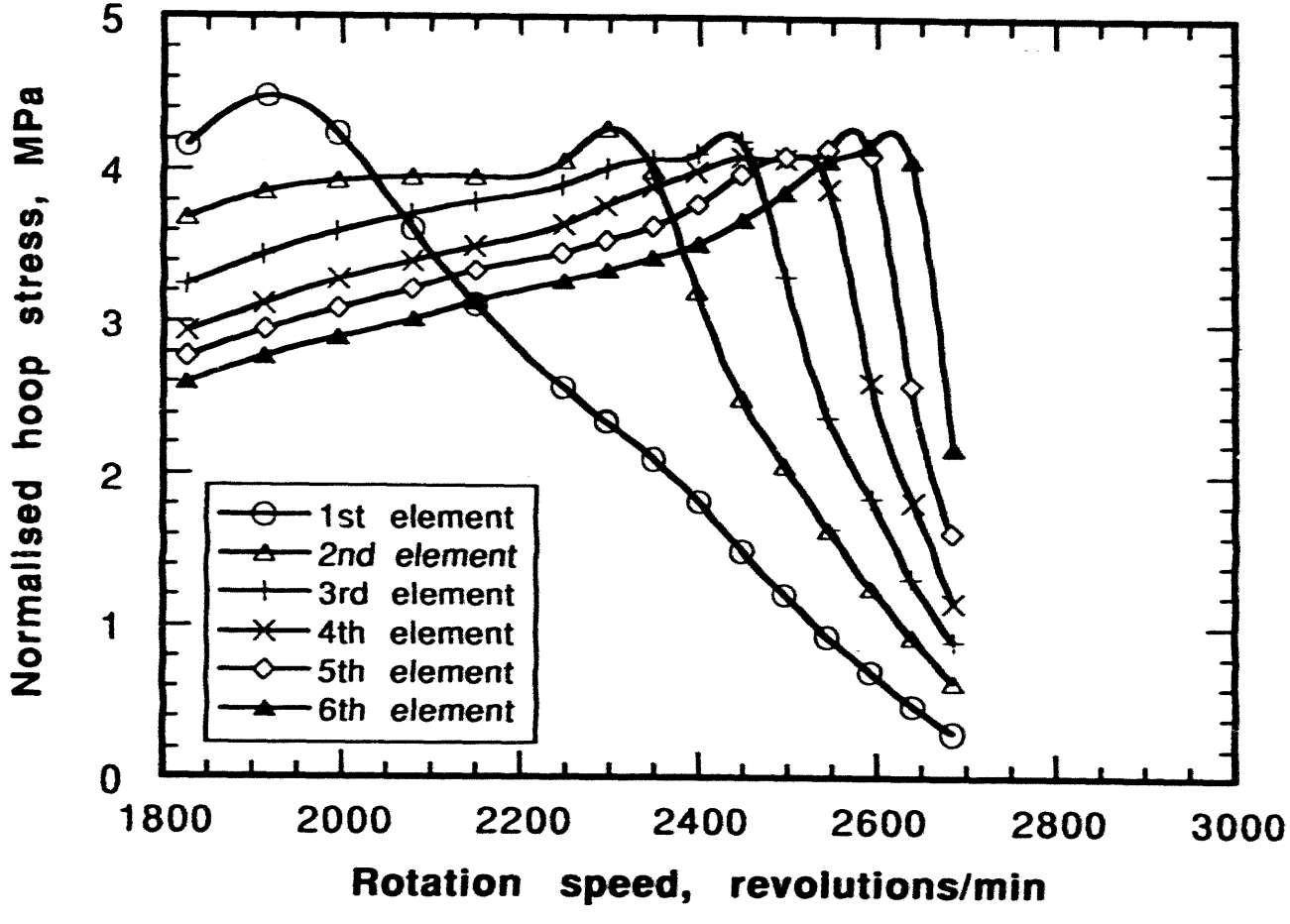

Figure 4: Normalised hoop stress vs. rotational speed. From Reference 4.

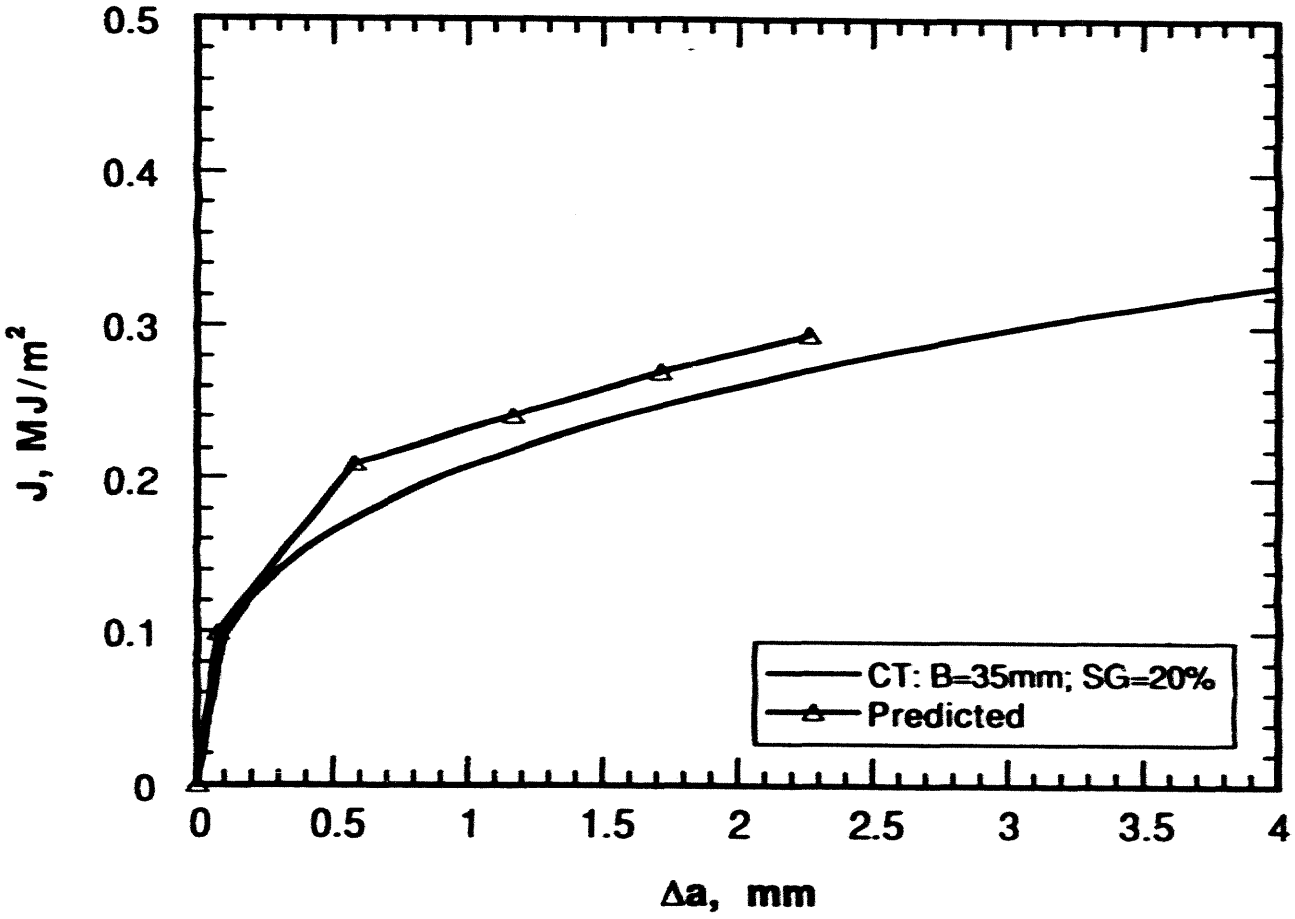

Figure 5: Predicted and experimental J R-curves for compact specimens. From Reference 3.

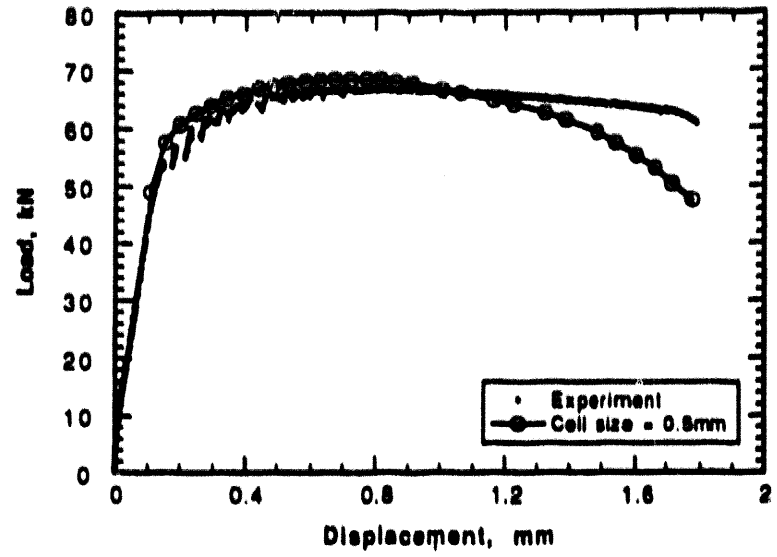

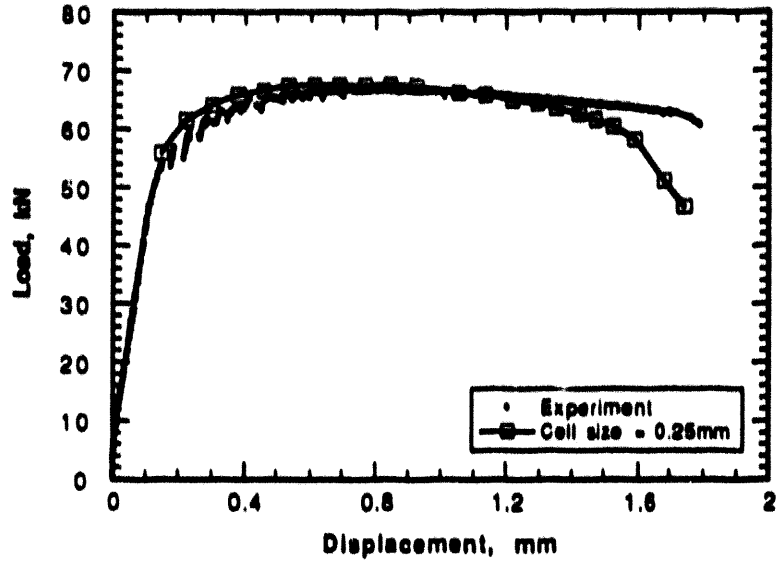

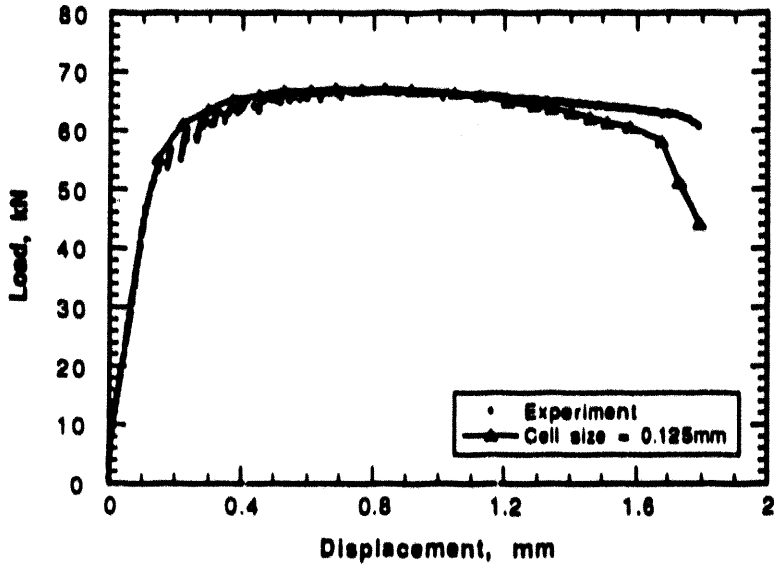

Figure 6: Predicted and experimental load vs. displacement curves for the AE10 notched tensile specimen. From Reference 4.

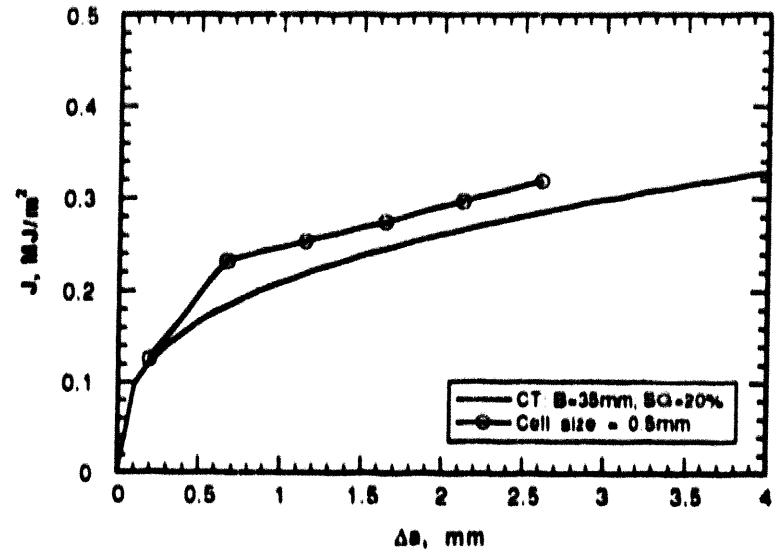

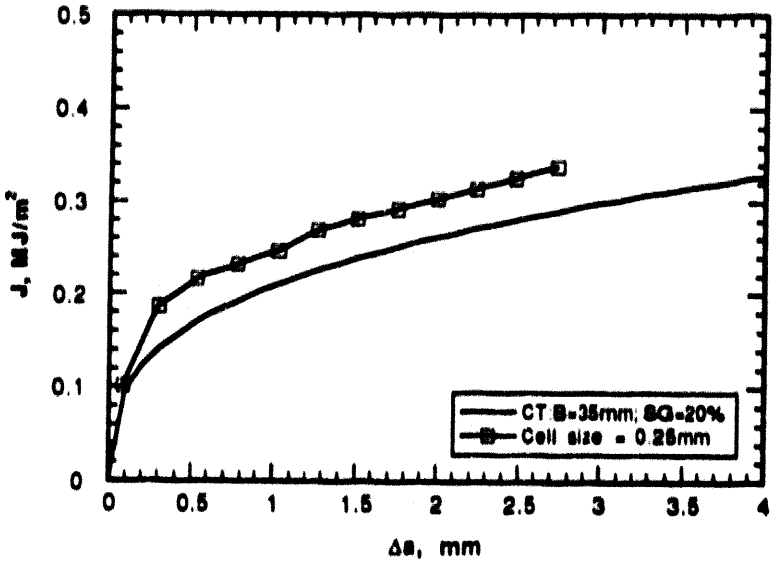

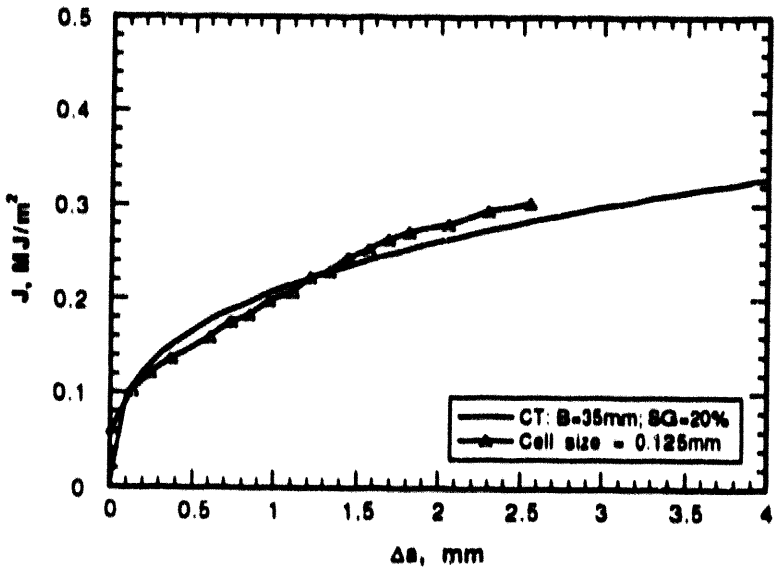

Figure 7: Predicted and experimental J R-curves for compact specimens. From Reference 4.

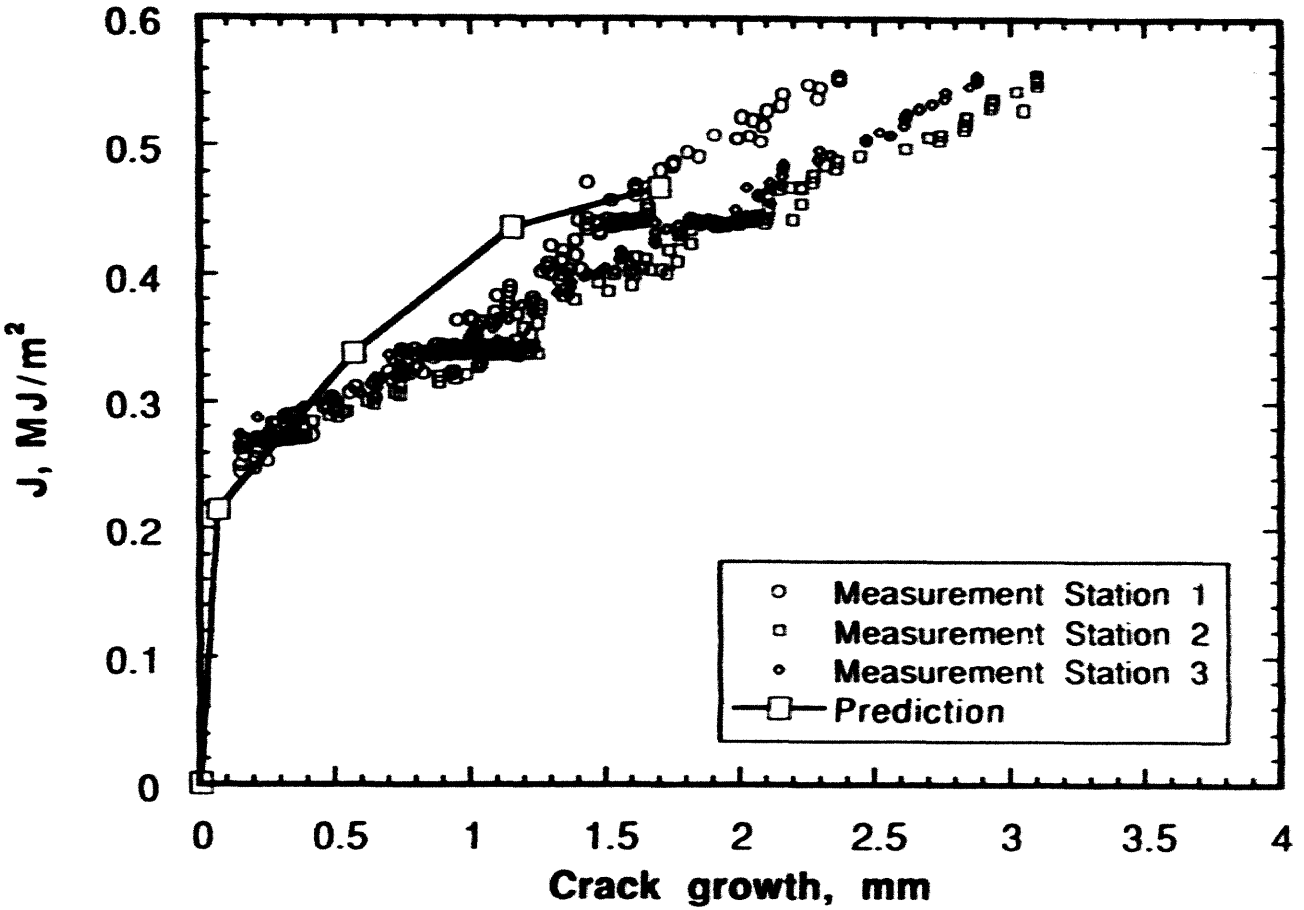

Figure 8: Predicted and experimental J R-curves for the first spinning cylinder test. From Reference 3.

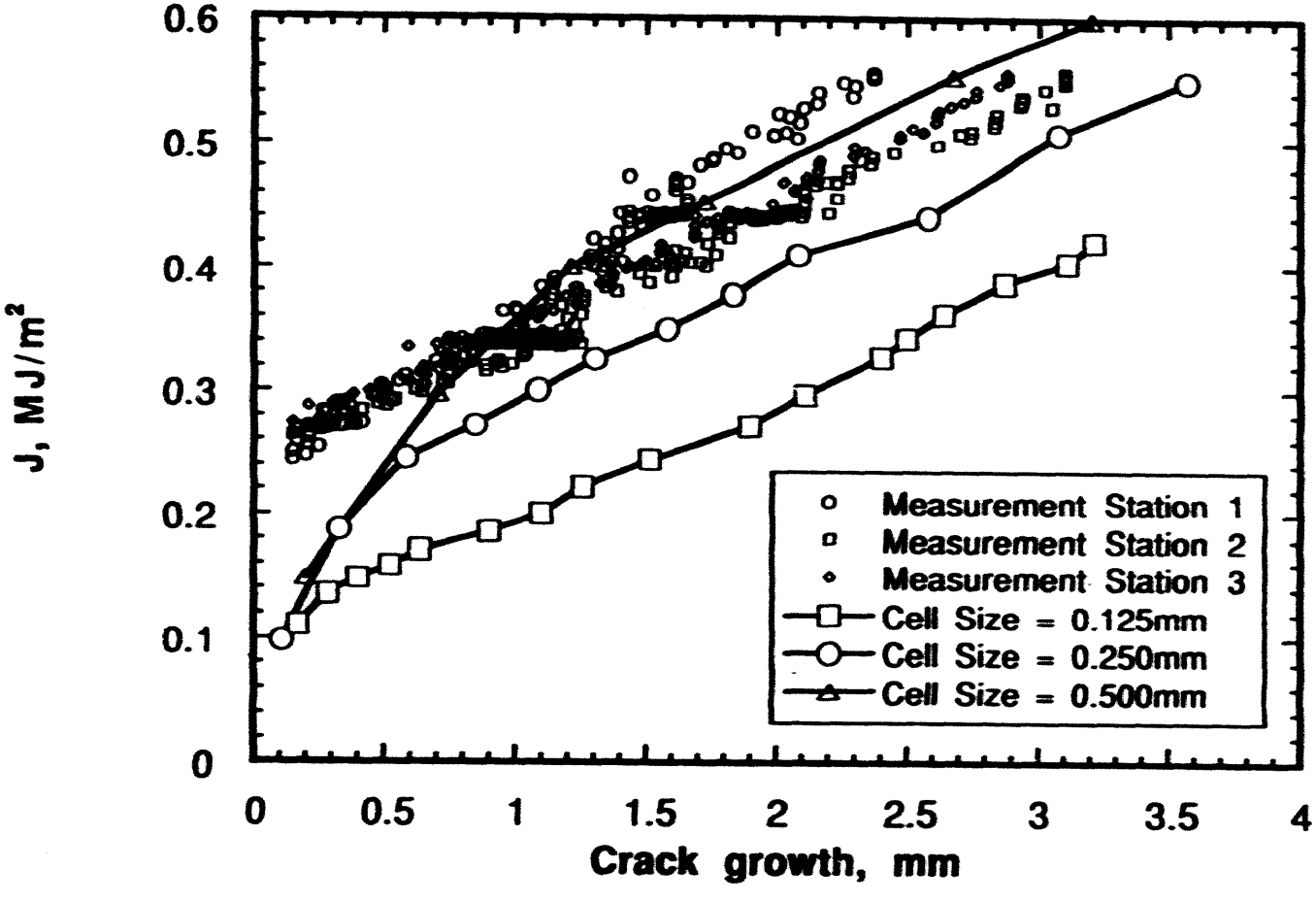

Figure 9: Predicted and experimental J R-curves for the first spinning cylinder test. From Reference 4.

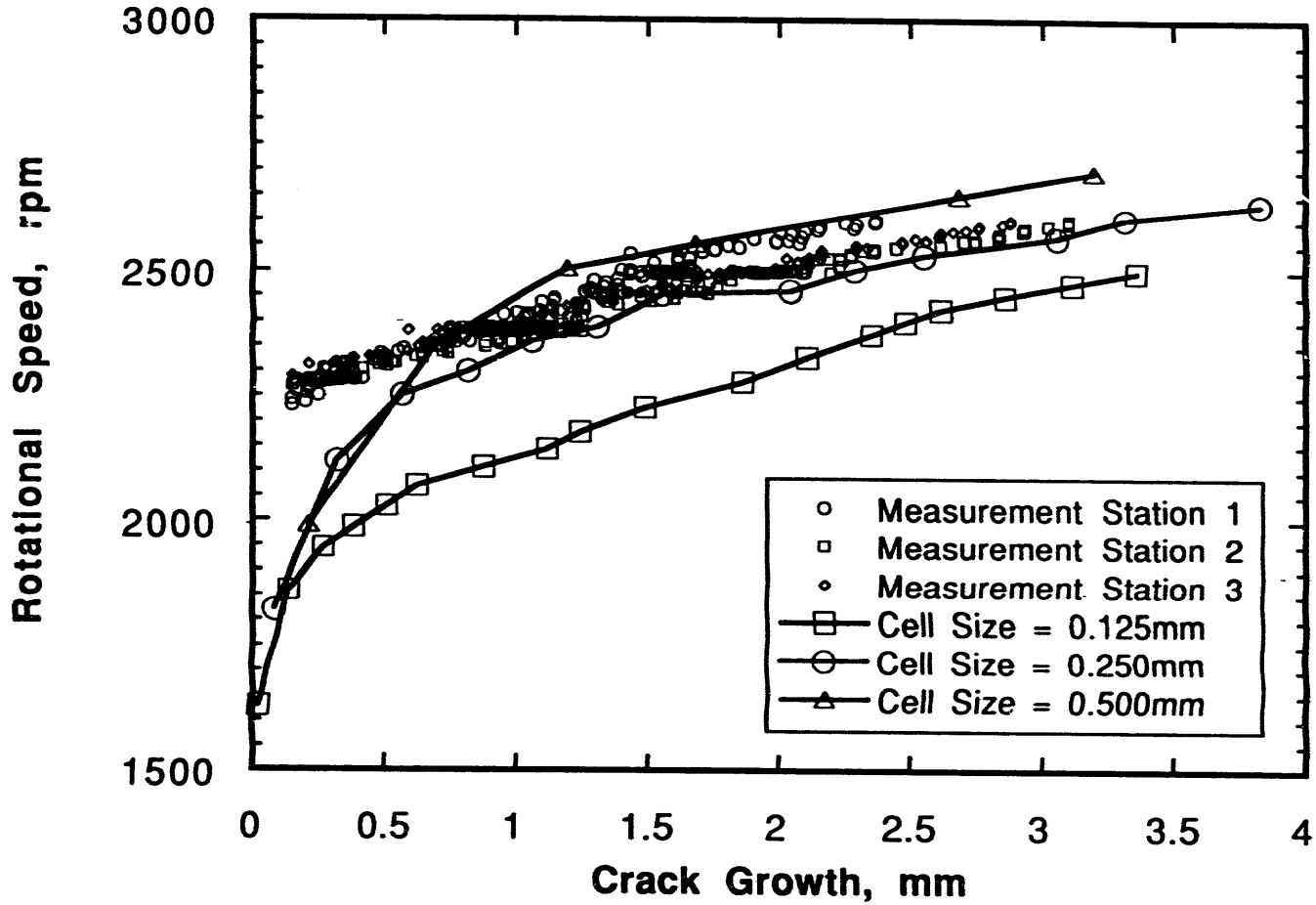

Figure 10: Predicted and experimental curves for rotation speed vs. crack advance in the first spinning cylinder test. From Reference 4.

Full Thickness Crack Arrest Investigations on Compact Specimens and a Heavy Wide-Plate

K. Kussmaul, R. Gillot, T. Elenz

MPA Stuttgart

University of Stuttgart, Federal Republic of Germany

Abstract - *In order to determine the influence of specimen size and testing procedure on the crack arrest toughness K_{Ia} at various temperatures, investigations were carried out on a wide-plate and compact specimens using a highly brittle material. Test interpretation included static as well as dynamic methods. The comparison of the measured K_{Ia}-values shows good agreement although there is a distinct difference in specimen size. In general, the (static) ASTM test method yields a lower and thus conservative estimate of the crack arrest toughness K_{Ia}.*

1 Introduction

Brittle dynamic crack events under special consideration of the crack arrest phenomenology are being investigated within the research project "Behavior of a Low Toughness Pressure Vessel Steel at Fracture Initiation, Unstable Crack Propagation and Crack Arrest". For this program, a MoV-steel was specially heat treated. This heat treatment [1] yielded an isotropic, highly brittle so-called model material (briefly called KS 22) with low upper-shelf C_v-energy and high yield strength. KS 22 represents a worst-case material state with regard to the toughness, being even worse than that which may be found in a reactor pressure vessel at the end of service due to radiation by fast neutrons.

To prove the transferability of crack arrest values determined by small compact specimens, [2], to component-like large specimens, wide-plates are tested. In this case a sophisticated data acquisition system is necessary to exactly measure all boundary conditions during crack propagation as well as the time dependent position of the crack tip. This is of crucial importance with regard to interpretation of test results and numerical calculations.

Similar wide-plate tests - carried out in the USA - have shown that a number of crack run-arrest events can occur during the experiment. This was also intended for the wide-plate experiment GP 1 described here.

2 Material

Special austenitization and temper treatment produced an isotropic material with an upper-shelf C_v-energy of approx. 60 J, a high yield strength ($\sigma_{ys} = 1085$ MPa, $\sigma_{ys}/\sigma_{uts} = 0.93$) and fracture appearance transition temperature FATT 50 $\approx 250°$ C. The chemical composition is shown in Table 1, the mechanical properties in Table 2. Fig. 1 shows a micrograph with details on heat treatment, as well as values of hardness and grain size.

3 Investigations on Compact Specimens

3.1 Static Analysis According to ASTM E 1221-88

The crack arrest toughness is the characteristic parameter which describes the very end of unstable crack propagation. It can be determined by means of modified compact specimens, wide-plates, rotating disks, and component tests. The investigations on transverse wedge-loaded compact specimens have proved to be the simplest and most favorable method with regard to material quantity and costs. The implementation and evaluation of the tests are delineated in ASTM test method E 1221-88 [3]. From specimen dimensions, crack opening and crack length the (static) crack arrest toughness K_{Ia} is calculated as defined in [3]. K_{Ia} represents the stress intensity factor at the crack tip some milliseconds after crack arrest. According to [3], it is considered as the lower and thus conservative estimate of K_{IA}, which is generally agreed to be the minimum value of K_{ID}, the velocity-dependent fracture toughness of a rapidly propagating crack.

Altogether, 20 specimens of various dimensions and orientations were tested at temperatures $20° \text{ C} \leq T \leq 435°$ C. A picture of the four specimen sizes is shown in Fig. 2. The dependence of the K_{Ia}-values on test temperature is plotted in Fig. 3. It is of great significance to realize that according to present results, not only the C_v-energy, but also the crack arrest toughness is attaining an upper-shelf plateau. This is in contradiction to results from HSST wide-plate tests which provide K_{Ia}-values of more than 500 MPa$\sqrt{m}$ without indicating the formation of an upper limit, e.g. [4].

3.2 Dynamic Analysis (FEM)

Dynamic analyses described here are two dimensional plane stress finite element calculations carried out using the computer code VISCRK [5,6]. This program has quasi-static as well as dynamic capabilities and allows the use of thermal as well as mechanical loads. Crack propagation was realized with the node release technique according to the prescribed crack length versus time correlation. The postprocessor uses the T^*-integral developed by Atluri, Brust et al. [7,8,9] and calculates the stress intensity factor K_I for mode I crack opening with

$$K_I = \sqrt{E \cdot T^*} \cdot \sqrt{\frac{B}{B_N}} \qquad (1)$$

This is the conventional plane stress formulation taking the existence of side grooves with the correction factor $\sqrt{B/B_N}$ into account. Because of the extrem low toughness of the material KS 22, the linear-elastic model could be used. In this context the T^*-integral is identical to an enlarged J-integral formulation with additional terms for

dynamic and thermal effects.

Compact specimen KS22CW31 was tested at 350° C according to ASTM E 1221-88 [3] with additional instrumentation to allow for elastodynamic posttest analyses. Youngs modulus was determined from tensile tests to 181,500 N/mm^2. Crack length measured at arrest gave a crack propagation Δa of 124.6 mm, the interpretation of strain gage signals yield a crack velocity v = 200 m/s while the reference curve from Battelle Columbus, USA, for tough materials [10] gives v = 550 m/s.

Considering the knowledge on spurious wave reflections [11] the finite element idealization of half the specimen was realized as shown in Fig. 4. The structure is characterized by small elements in the region of the crack path, a transition region and larger elements for the other areas. In addition, Fig. 4 shows the applied load and the displacement boundary condition at fracture initiation.

Two elastodynamic posttest analyses were carried out using v = 200 m/s (550 m/s) and the displacement was hold constant at the load point during crack propagation. Figs. 5a and b show the resultant K_J-curves as function of the dimensionless crack length a/W together with the static (FEM) solutions and ASTM-calculations : K_{Ja} (ASTM) = 141.8 MPa$\sqrt{m}$, K_{Ja}^{dyn} (v = 550 m/s) = 174.9 MPa$\sqrt{m}$, K_{Ja}^{dyn} (v = 200 m/s) = 167.1 MPa$\sqrt{m}$. Therefore, the elastodynamic analyses give results at arrest that exceed the (static) value according to ASTM E 1221-88 by 18% (v = 200 m/s) or 23 % (v = 550 m/s).

4 Crack-Arrest Test GP 1

4.1 Specimen Preparation

The test plate of material KS 22 having the dimensions 1500 x 1680 x 172 mm^3 (width x height x thickness) was welded to the upper and lower pull plate. To prevent out-of-plane deviation of the pull plates, welding was done alternately on each side of the specimen and bending of the specimen was continuously measured and corrected. The overall dimensions of the wide-plate specimen GP 1 are shown in Fig. 6.

The total initial crack length, notch plus fatigue crack was 543 mm (a/W = 0.36), and the flaw was parallel to the rolling direction. That is a specimen in T-L orientation according to ASTM E 399-81. The fatigue crack was produced by internal pressure acting on the flanks of a slot with a length of 51 mm and a height of 9 mm, machined through the thickness of the plate by spark erosion. At the elevated temperature of 160° C the fatigue crack was produced by alternating internal pressure (f = 4 Hz, 50 bar $\leq$ p $\leq$ 800 bar). After 194,000 cycles the fatigue crack had reached the length of 43 mm (average), being shorter at the plate surface.

Completion of specimen preparation included :

- The cross section of the ligament was reduced by 25 % through side grooves on each face of the specimen, Fig. 7 (plate thickness B=172 mm, notched thickness B_N=129).

- The opening of the ligament between the original notch of length 290 mm and the slot produced the initial crack length a_o, Fig. 8.

4.2 Instrumentation

The complex, dynamic behavior of the wide-plate and the numerical calculations using finite elements made extensive instrumentation necessary. Altogether, there were eleven different types of devices: thermocouples, strain gages, piezoelectric sensors for indirect force measurement, clip gages, accelerometer, electric-optical extensometers, optical displacement transducer, inductiv displacement transducer, force measurement of the maschine, accustic emission, and high speed camera.

Altogether, 58 thermocouples were attached to the test plate of material KS 22 and the upper and lower pull plate to get information of the total temperature field, Fig. 9. The results were monitored periodically and recorded on magnetic tape. Additional thermocouples were used to control heating of the wide-plate. 23 uniaxial strain gages were positioned on the test plate for determination of the crack tip position as function of time, Fig. 10. Because of the temperatures, T > 240° C, special high temperature strain gages of length 28 mm were used.

The lower pull plate was instrumented around the 600 mm borehole with seven strain gages and two piezoelectric sensors. The sensors are shaped like a cylindrical pin and were installed in the depth of a borehole. They were recorded as one signal (labeled QMD). This provided far-field strain measurements for assessing boundary conditions, Fig. 11. The crack opening measurements included clip gages at a/W=0.0 (labeled CMOD), 0.1 (COD2) and 0.3 (COD1) on side B, and two extensometers for detection of the crack opening as function of time at a/W=0.1 (EXD1) and 0.3 (EXD2) on side A. The accelerometer (BS1) was positioned at a/W=0.0 and 67 mm below the crack plane. Two transducer (PSD1 and PSD2) measured the vertical displacement of the specimen relativ to the large columns of the machine, Fig. 12. The inductive transducer (INW) was positioned to provide the horizontal displacement of the crack plane. The high speed camera and the accustic emission system did not provide additional information. They will not be discussed further.

Monitoring fast fracture events was possible through a sophisticated data acquisition system. This includes amplifiers and filters, sample and hold equipment, analog-digital converters. The use of a hard disc having 684 MByte of storage made the problem of triggering the signals obsolete and allowed the continuous data recording. The signals were recorded with an overall sampling rate of 1 MHz. This yields a time difference of 44 μs between two measurements.

4.3 Test Procedure

Heating the specimen and imposing a temperature gradient was achieved with 20 electric-resistance heaters. These cassettes were fixed on the plate of material KS 22 and were oriented in axial direction of the specimen. The desired gradient could be established without cooling devices due to the effects of radiation and convection.

First, the specimen was heated from room temperature to 200°C with a rate of 10° / h. Then, the desired temperature gradient was imposed. This was done with a computer aided control system that allowed to define the temperatures as function of time and position. After completion of an additional system check, heating was switched off to prevent a short-circuit during the test, the high speed camera was started and the tensile load of the 100 MN machine was increased with a rate of 20 MN/min. At a load of 11.9 MN the fracture event began and lasted about 12 seconds. The measured data and the fracture surface indicate that five cleavage crack run-arrest events occured prior to the onset of ductile tearing.

4.4 Test Results

Testing the tension-loaded single edge notched wide-plate specimen GP 1 took place at August 2, 1990. It was the first test of this kind at MPA Stuttgart and at the same time the first crack arrest experiment with this type of specimen employing the low toughness material KS 22.

Fig. 13 is a schematic representation of the temporal sequence of the events during the test. At the time labeled t_o quasi-static loading began. After 35 seconds the crack initiated at the load of 11.932 MN (time t_1). Then, five crack run-arrest events (labeled A to E) occurred within 2.4 seconds (t_{10} - t_1 = 2.4 s) prior to ductile tearing of the remaining ligament. During the test a number of run-arrest events could be clearly heard and could be distinguished by the ear. That means there were at least 20 milliseconds between single events.

Temperature distribution :

The temperatures across the crack plane were in the range of 195° C to 337° C, that is a thermal gradient of 142° C, Fig. 14. At the crack tip there was a temperature of 230° C, 20 K below the FATT 50 of 250° C. In the direction of the pull plates the temperatures were lower. The approximation of the 58 meassured temperature data yield the temperature field shown for the upper half of the specimen in Fig. 15.

Fractografical examination :

Fig. 16 shows the fracture surface for the specimen bottom half. The fatigue crack and the positions of crack-arrest are specially marked. As can be seen, five crack run-arrest events have occured. According to their temporal and geometrical order they are labeled A to E. The crack initiated in the plane of the side grooves. As the crack propagated it deviated from its predetermined path. At a = 850 mm (a/W=0.57) it reached the maximum offset of 23 mm. Then the crack returned gradually reaching the plane of the side grooves again at a = 1350 mm (a/W=0.9).

In addition, the fracture surface was investigated using a raster electron microscope (REM). Fig. 17 shows the microscopic characteristics of crack arrest for run-arrest event A. Crack arrest is characterized by a ductile zone stretching over the plate thickness from one face of the specimen to the other, Fig. 17a. Unstable crack propagation took place in the cleavage mode for all crack jumps. The width of the ductile zone at arrest A is approximately 10 to 30 μm being bigger with arresting at higher temperatures (up

to some millimeters).

Test results during loading and during fracture :

Besides the aforementioned data acquisition system, experimental data were also stored separatly with a frequency of 1 Hz. These data are shown in Figs. 18a - d with time 0 s (35 s) being equal to the moment labeled t_o - that is starting of loading - (t_1, fracture initiation) in the scheme of Fig. 13. In Figs. 18 - 20 the ordinate shows the experimental data relative to time t_o. This corresponds to a zero offset at time t_o. Tension force (F), crack mouth opening (CMOD) and horizontal displacement of the crack plane (INW) vary linear with loading time as shown in Figs. 18. In addition, the test material exhibits nearly linear elastic behavior. This can be seen from the relation of force F to crack opening near the crack tip, Fig. 18d.

A number of result histories during fracture are presented in Figs. 19 and 20. In these figures time = 0.062 s represents the moment of fracture initiation to see the influence of fracture initiation on the signals. Acceleration BS1 is shown in Fig. 19 at two levels of time resolution to make clear that crack jumps A to E occured within 2.4 seconds after fracture initiation. At time 12.4 s the specimen completly broke in two parts. Therefore, the following figures have a time axis of three seconds. The tension force varies during the test as can be seen from Fig. 20a. In addition, the time dependent behavior of other signals are presented in Fig. 20. The piezo-electric sensor QMD shows general agreement with force F and will be used in the next section to derive the force acting on the specimen during the fast crack jumps. The relative displacement (PSD1 + PSD2) increases from 2.4 to 3 mm as a result of crack jump A and B. Afterwards the two points remove approximately with 60 mm/min. Time dependence of crack opening at a/W=0.3 and of the horizontal displacement INW is shown in Fig. 20d-f.

Determination of the boundary conditions :

The boundary conditions must be determined to realize numerical calculations without idealized assumptions and the specimen instrumentation was already chosen to ease this task. Crack arrest test GP 1 has two time-dependent boundary conditions :

1. External force F at the bore-hole
2. Crack length a (derivative is crack velocity v).

The experimental data show that crack jump A and B occured within four milliseconds while crack jump C, D and E can be regarded as separate events. In addition, the specimen geometry with its distance between crack plane to bore-hole of ≈2500 mm yields a run time for the elastic wave of 500 μs. This means 1000 μs after the begin of a crack event the crack tip will be influenced by possible load adjustment. Therefore, the numerical simulation of fast crack propagation with emphasis on crack arrest using the FEM needs the force - time relation during crack jump events A and B. Due to the short time (less than 1000 μs) of crack jump C, D and E the force is constant for the calculation of the latter events.

To gain the true behavior of external force F during the first event (fracture initiation up to crack arrest B) the signal of sensor QMD was used. First the correlation of force

F and QMD during quasi-static loading gives the slope m shown in Fig. 21. Then, the signal of QMD during fracture was multiplied with this value and gives the true force. Fig. 22 summarizes the force boundary conditions for all run-arrest events. As could be shown, there is considerable load decrease after some milliseconds and there is no increase of force F to its value at fracture initiation during the fracture event.

Strain gage records, accelerometer signal BS1, and fracture surface were used to deduce the crack length as function of time during the fracture process. Signal BS1 did exactly show the moments of fracture initiation and reinitiation, except for crack jump B. The strain gage records gave further insights and defined the moments of crack arrest. The crack length at arrest documented here and used for the finite element calculations is the averaged value of the crack length at five positions of varying plate thickness (0, 1/4, 1/2, 3/4, 1). This gives the second boundary condition as shown in Fig. 23.

4.5 Dynamic Analysis (FEM)

The strategy of the numerical calculation is shown in Fig. 24. The moment of fracture initiation was calculated in one quasi-static time step including the influence of the temperature field. Dynamic effects during crack propagation and at arrest were considered by using the dynamic capabilites of VISCRK. Simulation of run-arrest events C, D and E was done with one quasi-static calculation of the moment of reinitiation and dynamic calculation of crack propagation. The linear-elastic material model was used with material properties at 230° C : Youngs modulus is 193,210 N/mm^2 and $\alpha = 13.7 \times 10^{-6}$ 1/K.

The finite element idealization of one half of the specimen was developed under consideration of further perceptions on spurious wave reflections. The 2-D plane stress model, Fig. 25 consists of 402 eight-noded elements and 1298 nodes. In addition, Fig. 25 shows the load at the bore-hole and the area of integration for calculating K_I.

As far as known to the authors it is the first time that posttest analyses of a wide-plate experiment were carried out using the true boundary conditions. Fig. 26 shows the resulting K_I-curves during all crack run-arrest events. The identical feature is that arrest occurs during decreasing K_I-curves. The values at initiation, K_{Io}, and at arrest, K_{Ia}, are summarized in Table 3.

5 Comparison of Test Results

The stress intensity factors at fracture initiation/reinitiation, K_{Io}, are relatively high compared with the scatter band from small scale specimens. Especially the value at fracture initiation, when there are no dynamic effects present, is not totally plausible. The same behavior has been observed at similar wide-plate tests in the USA (HSST Program, WP-1 series, material A533B Cl.1), however a clear explanation is not known so far. According to Keeney-Walker and Bass [12] an explanation of this behavior may be possible by applying a maximum principal stress criterion.

Five crack arrest toughness values K_{Ia}, $3406 \leq K_{Ia} \leq 6146$ N/mm$^{3/2}$ at temperatures $250° \leq T \leq 306°$ C ($0° \leq T$ - FATT 50 $\leq 56°$) could be calculated from test results

by using the finite element based computer code VISCRK, Fig. 27. K_{Ia} from wide-plate GP 1 is calculated including dynamic effects, K_{Ia} from small compact specimens is calculated according to ASTM E 1221-88 [3] and is considered (static) crack arrest toughness. As could be expected, K_{Ia} from wide-plate tests (dynamic FEM) are 10% to 20% higher than K_{Ia} from compact specimens. This behavior is in agreement with the common interpretation, i.e. Kalthoff [13], that E 1221-88 yields the lower bound of K_{Ia}. The numerical calculation of compact specimen KS22CW31 [14] with thickness 170 mm is an additional verification of the statement mentioned before, Fig. 27. In this test K_{Ia} according to ASTM is 18% lower than the value calculated with FEM.

6 Summary

Dynamic crack events, that is initiation, unstable crack propagation and crack arrest of a highly brittle model material have been studied both experimentally as well as by using a sophisticated computer program. To prove the transferability of crack arrest toughness determined from small compact specimens to component-like specimens, wide-plate GP 1 has been tested at $195° \leq T \leq 337°$ C. The results are as follows :

- Crack velocity of material KS 22 is approximately 200 - 500 m/s for wide-plate and compact specimens at temperatures $200° \leq T \leq 350°$ C. There may be a decrease in crack velocity with increasing temperature.
- Unstable crack propagation Δa of 125 mm (compact specimen) and $39 \leq \Delta a \leq 291$ mm (wide-plate) was observed.
- Raster electron fractographs of various regions on the fracture surface show that there was fracture initiation in cleavage. During unstable crack propagation the dominant mode was cleavage. At crack arrest there is an abrupt change from cleavage to ductile tearing.
- The (dynamic) calculated crack arrest toughness of wide-plate GP 1 is higher than the (static) K_{Ia} from small specimens. The same is true for static versus dynamic calculation of crack arrest toughness from compact specimen.

The investigations are being continued at MPA Stuttgart by testing a second wide-plate specimen at temperatures 50 K higher than in the first test.

Acknowledgments

Part of the investigations were sponsored by funds of the Federal Minister for Research and Technology (budget number 150 0787). This support is highly appreciated.

References

[1] Kuppler, D., R. Langer and R. Gillot :
Wärmebehandlungsversuche an Werkstoff 17 MoV 8 4 sur Absenkung der Hochlagenzähigkeit. TWB 3/3, Forschungsvorhaben Komponentensicherheit, Staatliche Materialprüfungsanstalt (MPA) Universität Stuttgart, April 1982.

[2] Kußmaul, K. and R. Gillot:
Determination of Crack Arrest Toughness at High Temperatures Using Compact Specimens. Journal of Pressure Vessel Technology, Vol. 110, pp. 129-136, 1988.

[3] ASTM E 1221-88 :
Standard Test Method for Determining Plane-Strain Crack Arrest Fracture Toughness, K_{Ia}, of Ferritic Steels. Annual Book of ASTM Standards, 1988.

[4] Pugh, C.E., D.J. Naus and B.R. Bass :
Crack arrest behavior of reactor pressure vessel steels at high temperatures, IAEA Specialists Meeting on Fracture Mechanics Verification by large scale testing, Stuttgart, May 25-27 1988.

[5] User's Manual for VISCRK.
A Finite-Element Program for Dynamic Fracture in Viscoplastic Materials.
Southwest Research Institute, San Antonio, Texas, USA, March 1988. Not published thus far.

[6] Kanninen, M.F. et al.:
Elastodynamic and Viscoplastic-Dynamic Fracture Mechanics. Heavy-Section Steel Technology Program Semiann. Prog. Rep. October 1986 - March 1987, NUREG/CR-4219, Vol.4, No. 1, pp. 25-35, August 1987.

[7] Brust, F.W. and S.N. Atluri:
Studies on Crack Growth Using the $\dot{T}^*$-Integral. Eng. Fracture Mechanics, Vol.23, No. 3, pp. 551-574, 1986.

[8] Nishioka, T. and H. Yagami:
Invariance of the Path Independent T^*-Integral in Nonlinear Dynamic Fracture Mechanics, with Respect to the Shape of a Finite Process Zone. Eng. Fracture Mechanics, Vol.31, No. 3, pp. 481-491, 1988.

[9] Cherepanov, G.P. :
A Remark on the Dynamic Invariant or Path-Independent Integral. International Journal of Solids and Structures, Vol. 25, No. 11, pp. 1267-1269, 1989.

[10] Rosenfield, A.R., J. Jung, M.F. Kanninen, A.F. Markworth, C.W. Marschall, P.P Milella, P.N. Mincer and R.L. Shook :
Critical Experiments, Measurements and Analyses to Establish a Crack Arrest Methodology for Nuclear Pressure Vessel Steels. Battelle Columbus Laboratories, Columbus, USA, NUREG/CR-1887, BMI-2071, pp. 3-1 to 3-6, 1981.

[11] Pliesk., M.:
Untersuchung zur Ausbreitung von Spannungswellen bei Verwendung eines dynamischen Finite Elemente (FE) Computerprogramms. Studienarbeit 754 945, MPA Stuttgart, Januar 1989.

[12] Keeney-Walker, J., B.R. Bass and J.D. Landes:
An Investigation of Crack-Tip Stress Field Criteria for Predicting Cleavage-Crack Initiation, NUREG/CR-5651, ORNL/TM-11692, 1990.

[13] Kalthoff, J.K.:
Interpretation of Crack Arrest Fracture Toughness Measured with various Steels. Advances of Fracture Research, Proceedings of the 7th. Int. Conf. on Fracture, pp. 705-714, March 20-24 1989.

[14] Elens, T.W.:
Nachrechnung des Rißstoppversuches mit der Compact-Probe KS22CW31. MPA Stuttgart, Aktennotiz vom 1.3.1990.

Table 1 : Chemical composition of material KS 22 in weight-percent

C	Si	Mn	P	S	Cr	Mo	Ni	Cu	V
0.16	0.3	0.69	0.004	0.026	0.32	1.01	0.25	0.08	0.31

Table 2 : Mechanical properties of material KS 22

temperature ° C	$\sigma_{y,t}$ MPa	$\sigma_{u,t}$ MPa	A_t %	Z %	E MPa	FATT 50 ° C
21	1085	1166	11	41	211 000	
100	1038	1120	12	39	206 000	
250	980	1082	10	39	191 300	250
350	929	1025	13	45	181 500	
450	859	961	13	51	172 000	

Table 3 : Values at initiation and at arrest for wide-plate test GP 1.
Dynamic finite element calculations using VISCRK

event	temperature T ° C	crack length a mm	stress intensity factor K_{Ia} MPa$\sqrt{m}$	K_{Ia} N/mm$^{3/2}$	K_{Ia} MPa$\sqrt{m}$	K_{Ia} N/mm$^{3/2}$
Fracture initiation	230	543	174.5	5518	-	-
1. crack arrest	250	834	-	-	107.7	3406
1. reinitiation	250	834	222.6	7039	-	-
2. crack arrest	272	995	-	-	165.5	5233
2. reinitiation	272	995	226.8	7172	-	-
3. crack arrest	286	1071	-	-	175.8	5559
3. reinitiation	286	1071	249.6	7893	-	-
4. crack arrest	299	1137	-	-	194.3	6145
4. reinitiation	299	1137	220.4	6969	-	-
5. crack arrest	306	1176	-	-	187.3	5924

heat treatment : *1050°C/2h/oil, 640°C/7h/air*
hardness : *370 - 383 HV 10*
grain size : *4 (ASTM E 112)*

Fig. 1 : Microstructure of material KS 22

Fig. 2 : Sp men dimensions (millimeter)

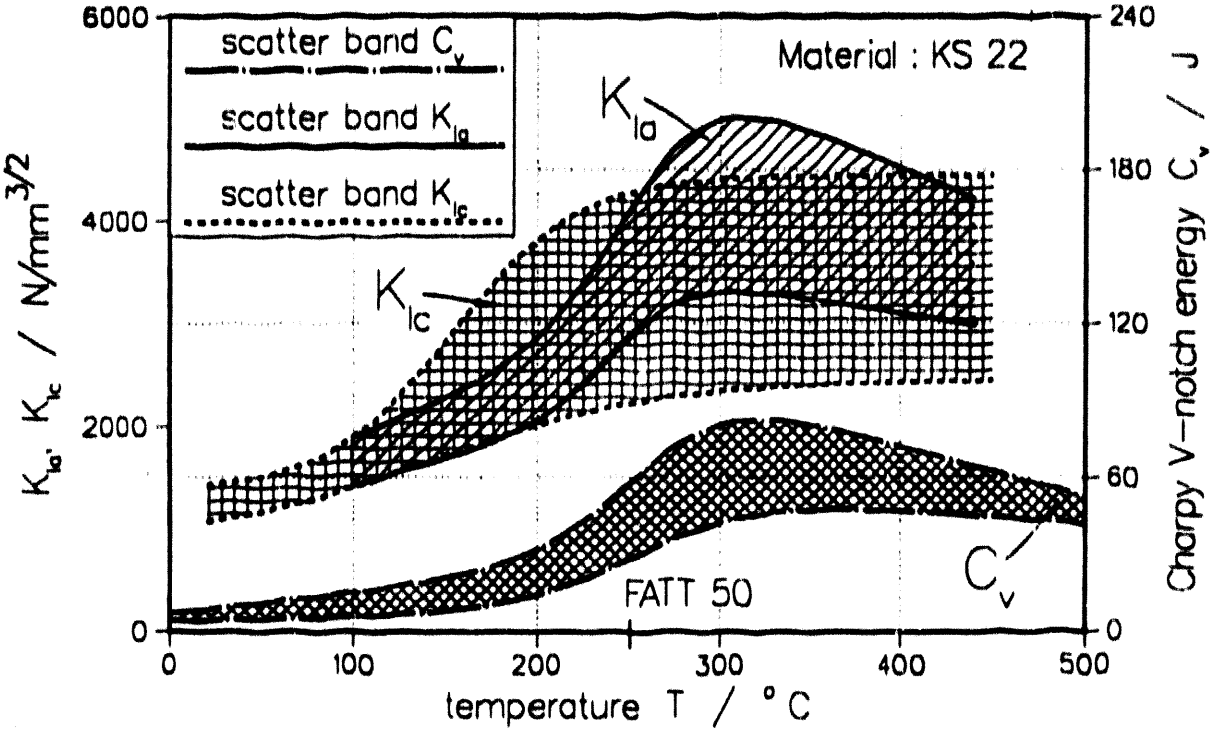

Fig. 3 : Toughness K_{Ia}, K_{Ic} and C_v versus temperature

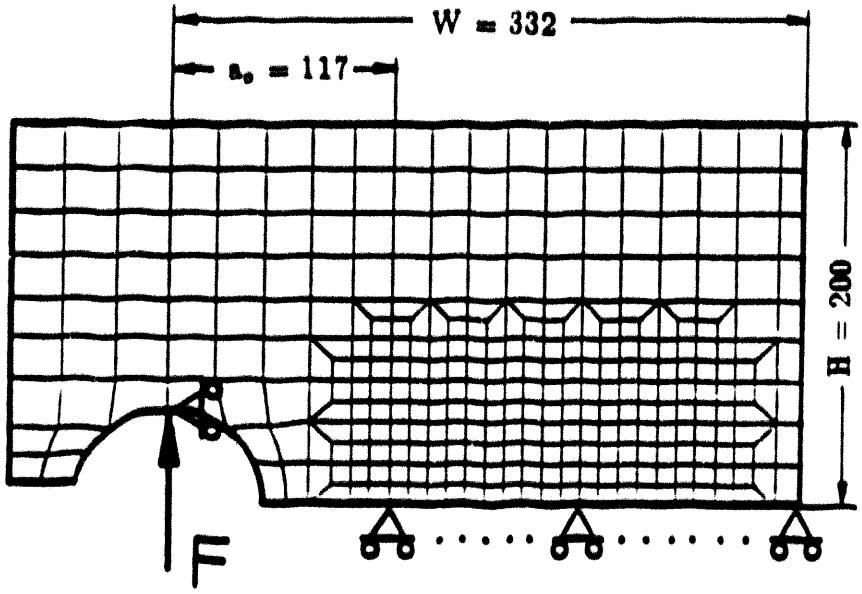

Fig. 4 : FE-idealisation of compact specimen KS22CW31 and displacement boundary conditions at fracture initiation (dimensions in millimeters)

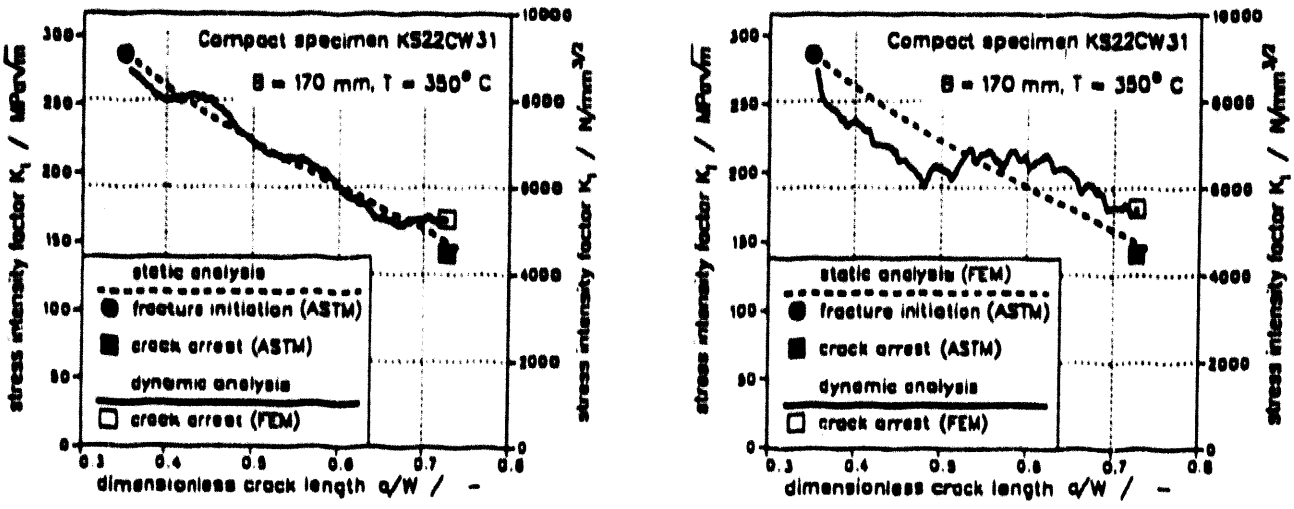

a.) crack velocity 200 m/s *b.) crack velocity 550 m/s*

Fig. 5 : Stress intensity factor $K_I(T^*)$ during unstable crack propagation

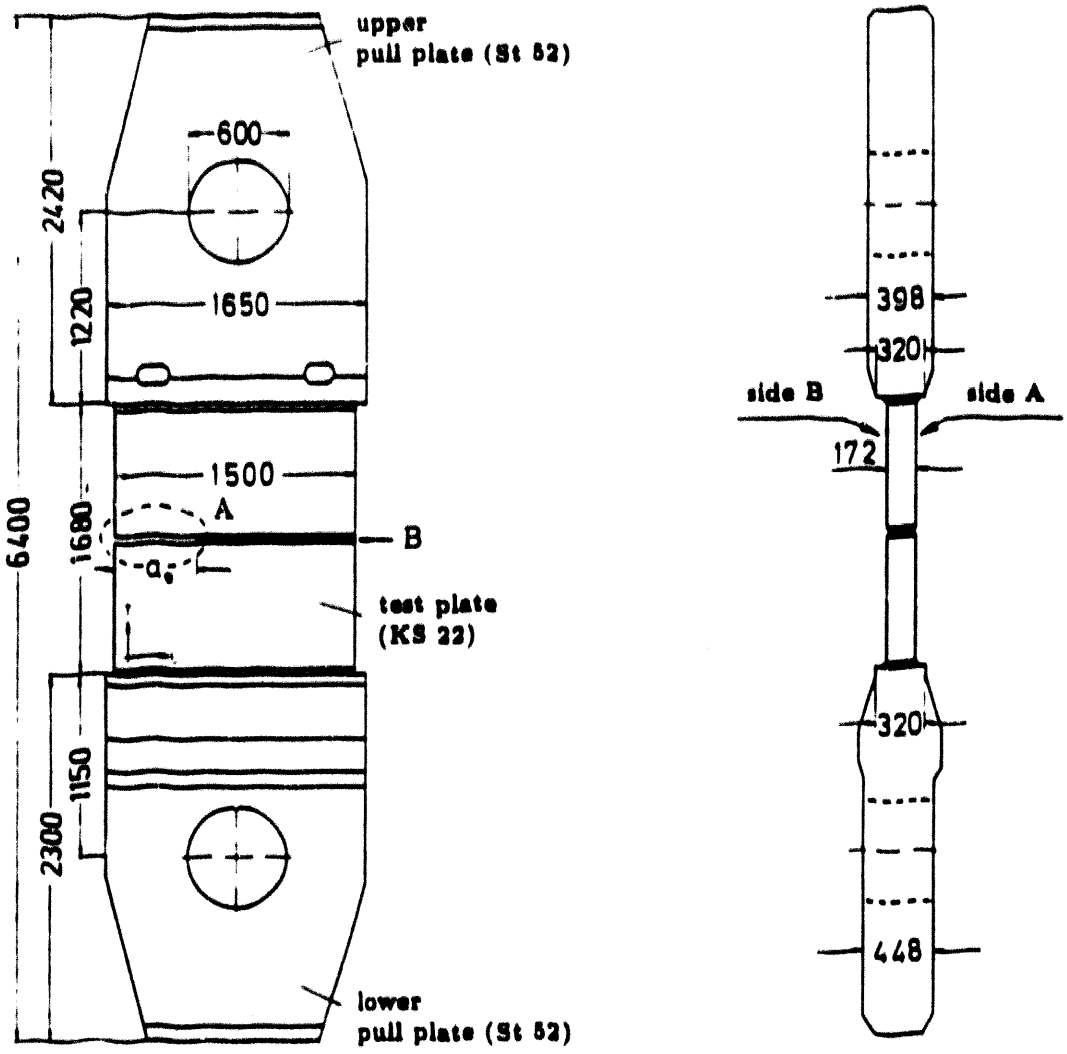

a.) *front view, side A* b.) *side view*

Fig. 6 : Overall dimensions of crack-arrest specimen GP 1 (dimensions in millimeters)

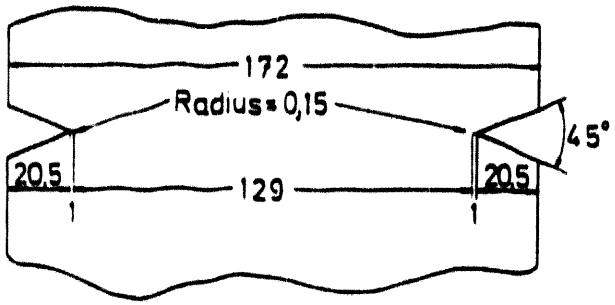

Fig. 7 : Geometry of the side grooves (part B in Fig. 6)

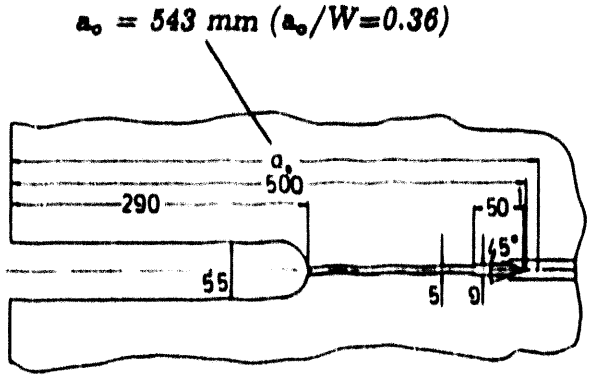

Fig. 8 : Geometry of the initial crack (part A in Fig. 6)

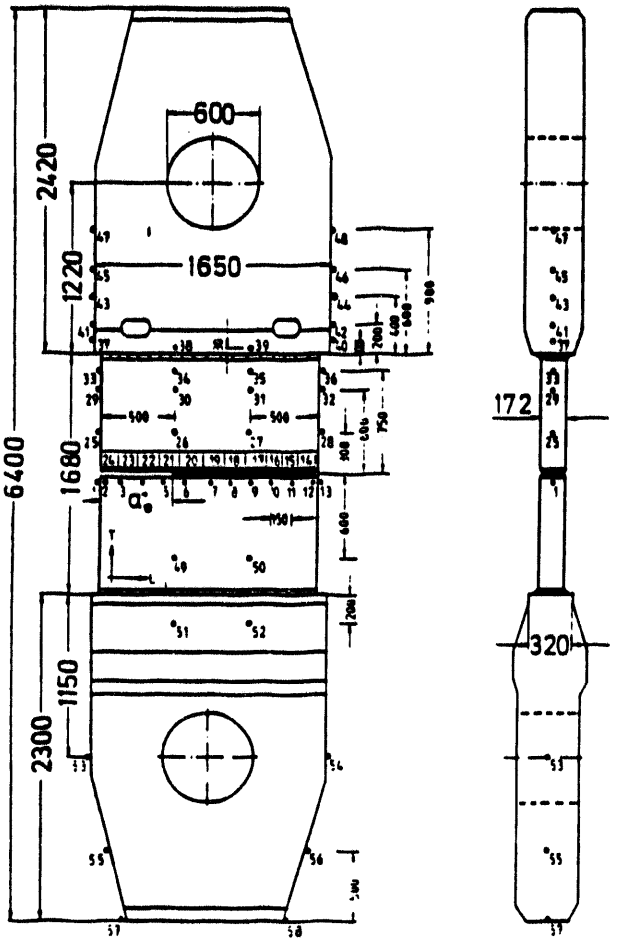

Fig. 9 : Thermocouple locations : test GP 1

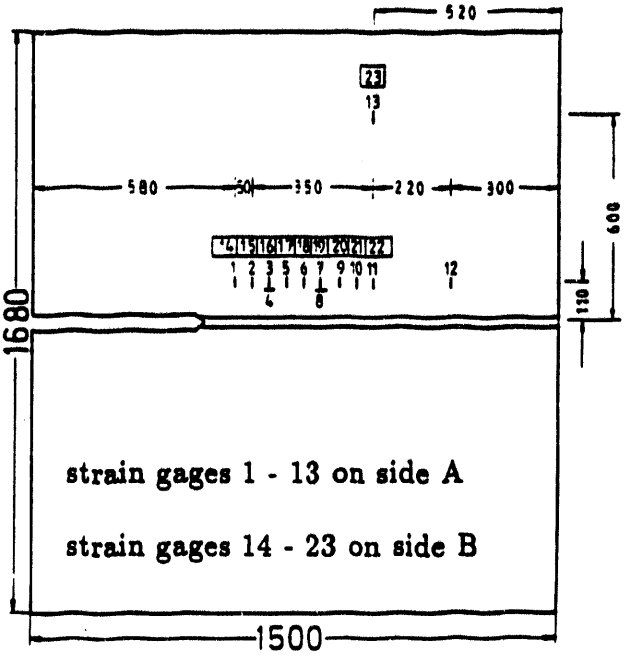

Fig. 10 : Strain gage locations : test GP 1 (plate of material KS 22)

side A

side B

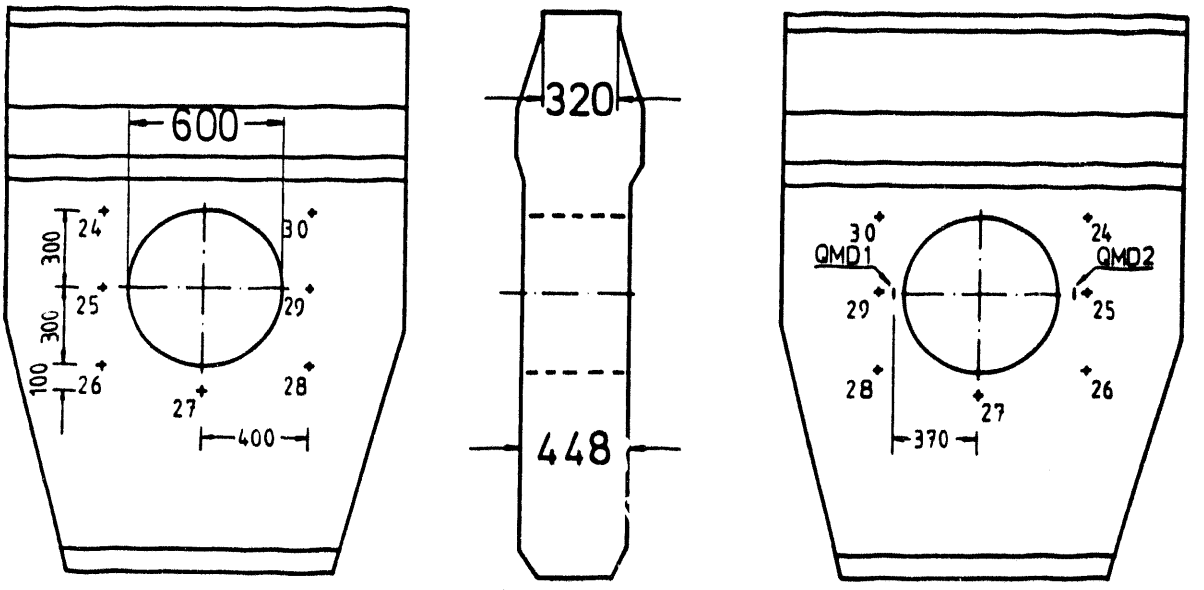

Fig. 11 : Strain gage locations on the lower pull plate : test GP 1

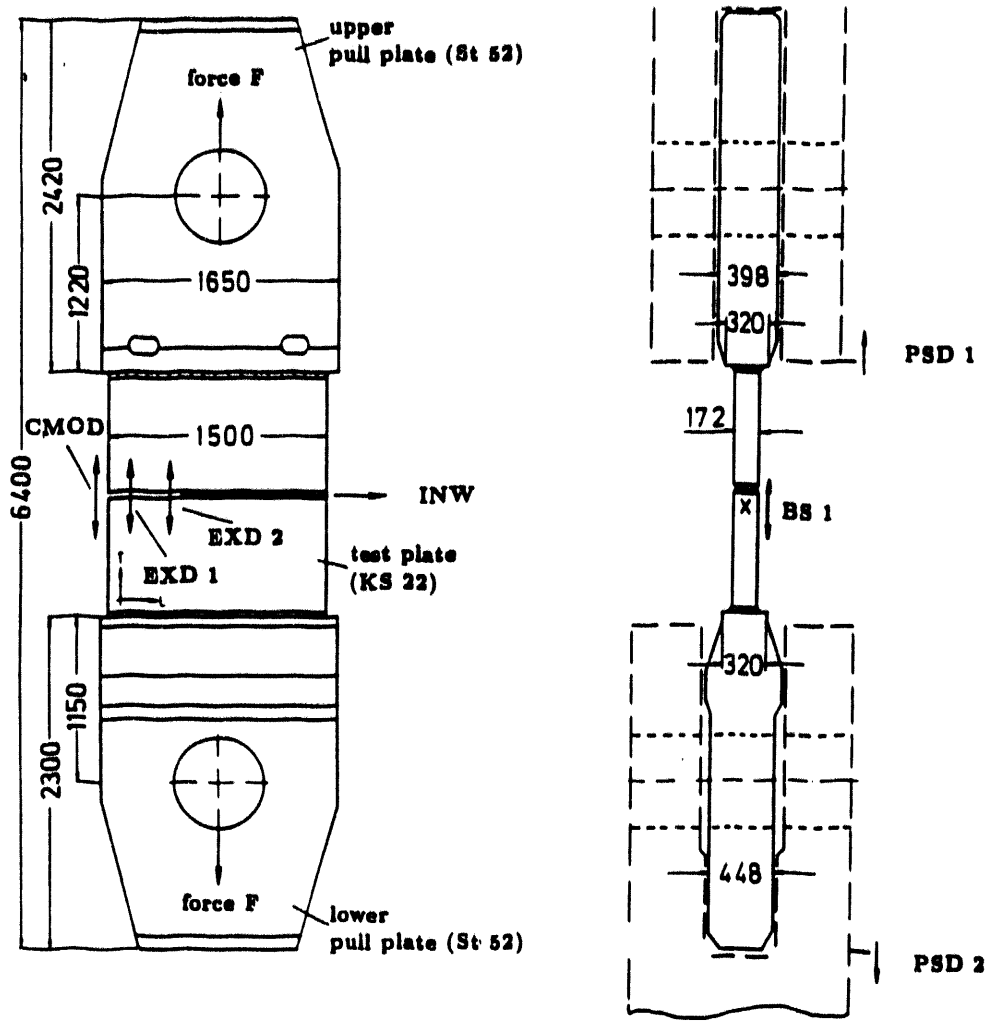

Fig. 12 : Additional instrumentation : test GP 1

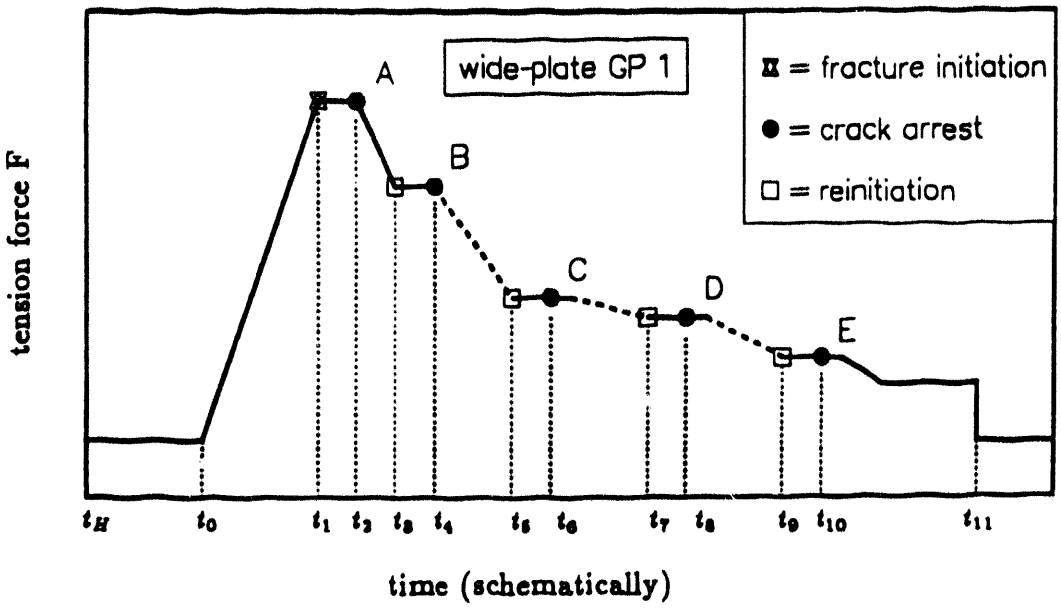

Fig. 13 : Schematic representation of crack-arrest test GP 1 with a tension-loaded single edge notched specimen (t_{10} - t_1 = 2.4 s)

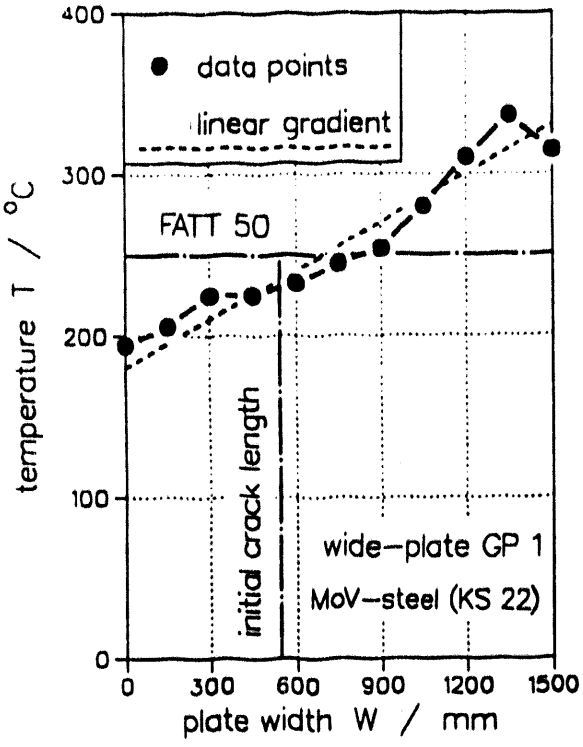

Fig. 14 : Temperatures across the plate width W : test GP 1

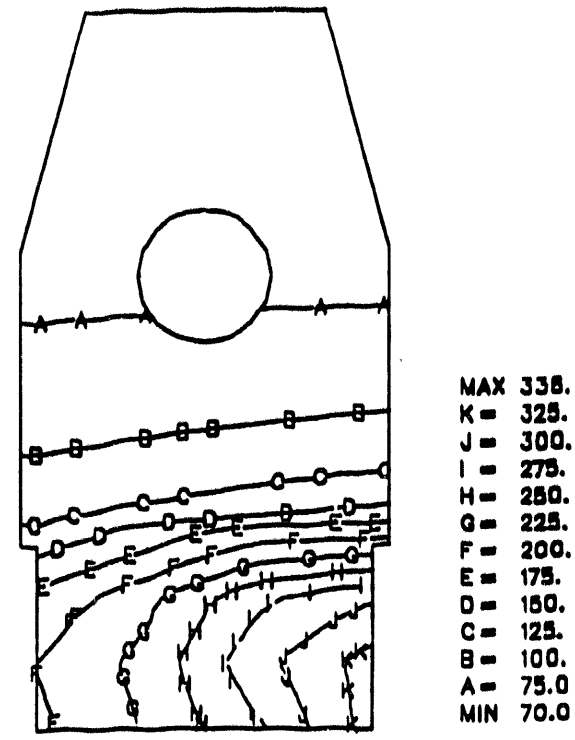

Fig. 15 : Temperature distribution of specimen GP 1

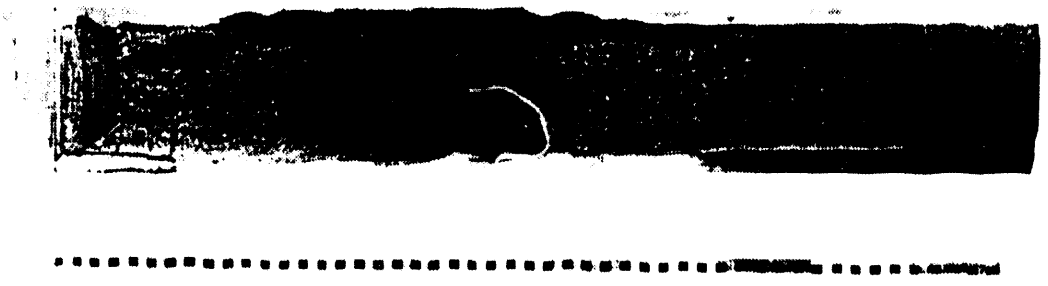

a.) fracture surface

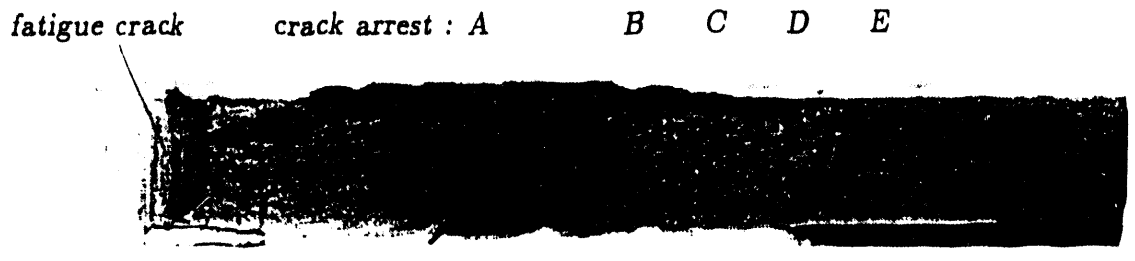

→ direction of crack propagation

b.) fracture surface with front at crack arrest highlighted

Fig. 16 : Fracture surface of bottom half : specimen GP 1

b.) a.) c.)

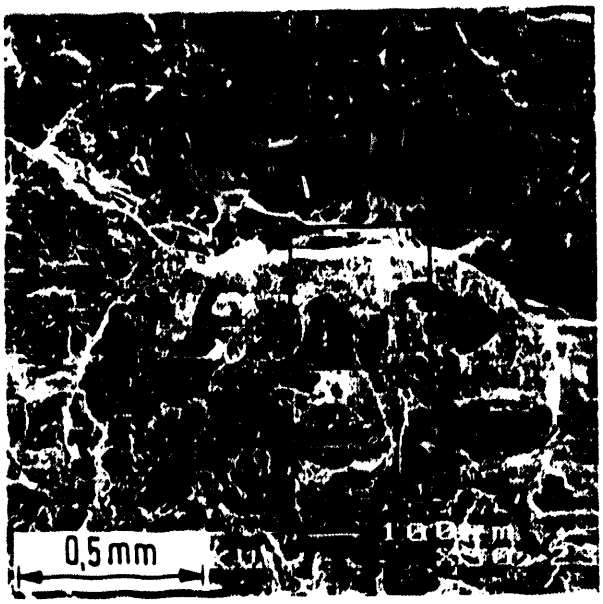

a.) *overview of crack arrest A*

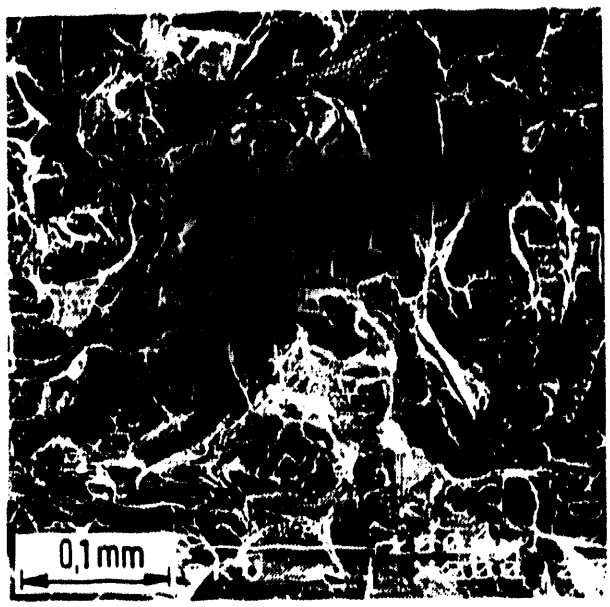

b.) *cleavage crack jump A*

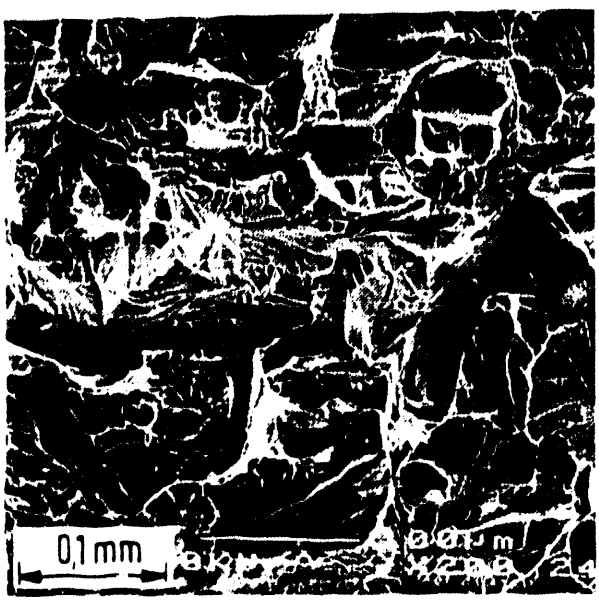

c.) *cleavage crack jump B*

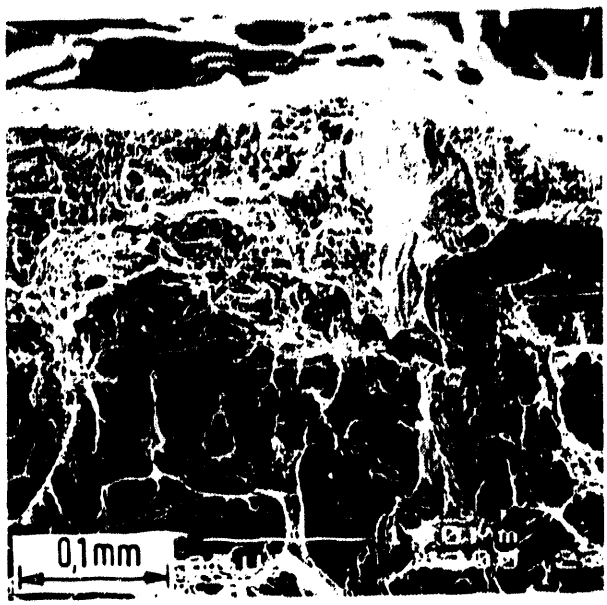

d.) *ductile crack arrest A, part A from a.)*

Fig. 17 : Microscopic examination of the fracture surface in the region of crack arrest A : transition fast fracture (cleavage) - crack arrest A (ductile) - fast fracture (cleavage)

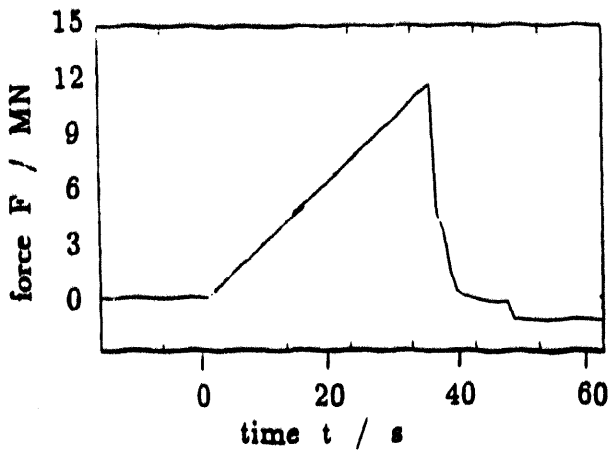

a.) *tension force* **F** *of the machine*

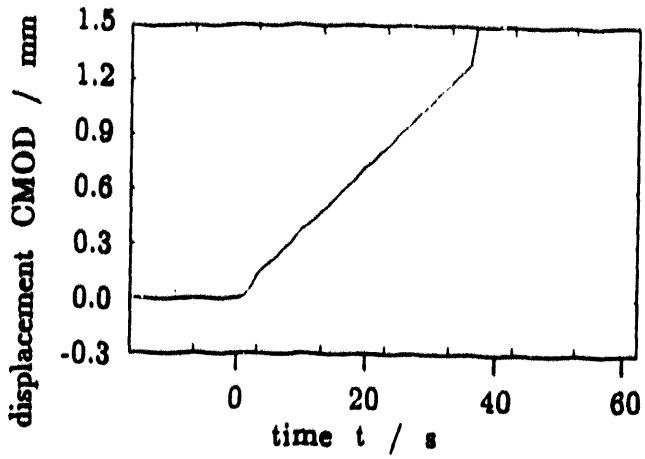

b.) *crack mouth opening* **CMOD**

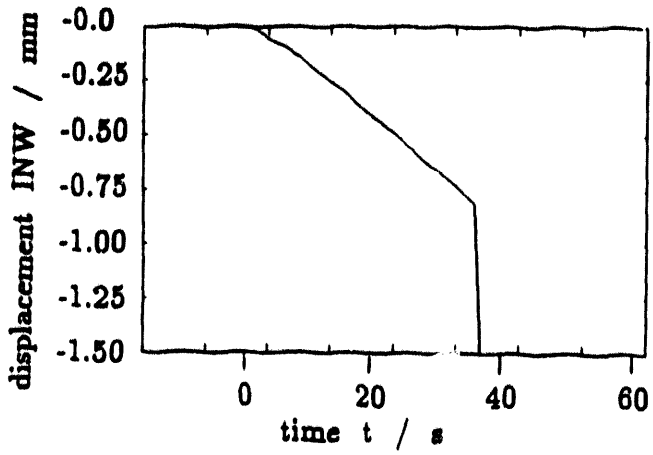

c.) *horizontal displacement* **INW**

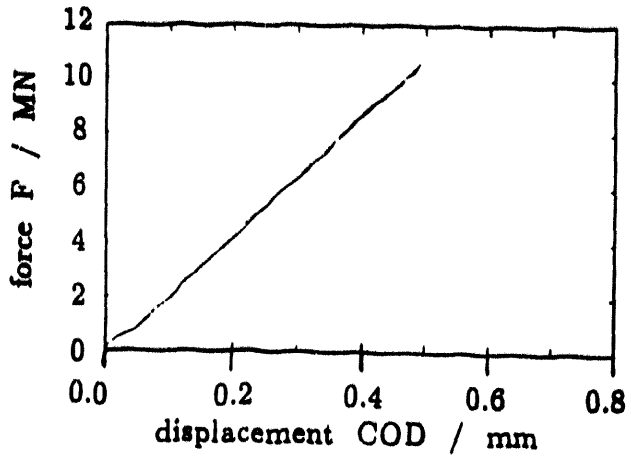

d.) *force* **F** *to crack opening* **COD1***(a/W=0.3)*

Fig. 18 : Results during wide plate test GP 1 (start loading $t_o = 0$ *s, fracture initiation* $t_1 \approx 35$ *s)*

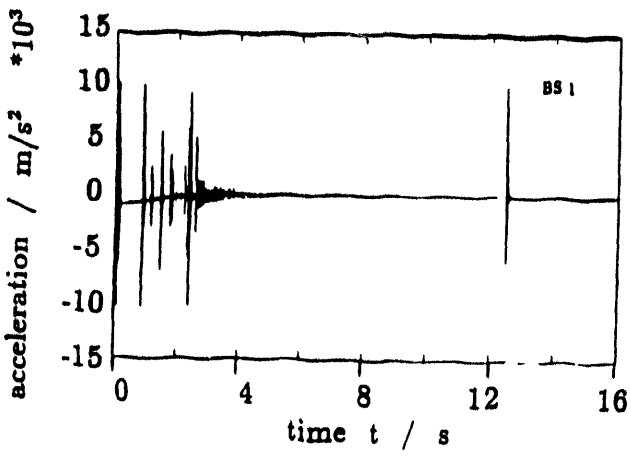

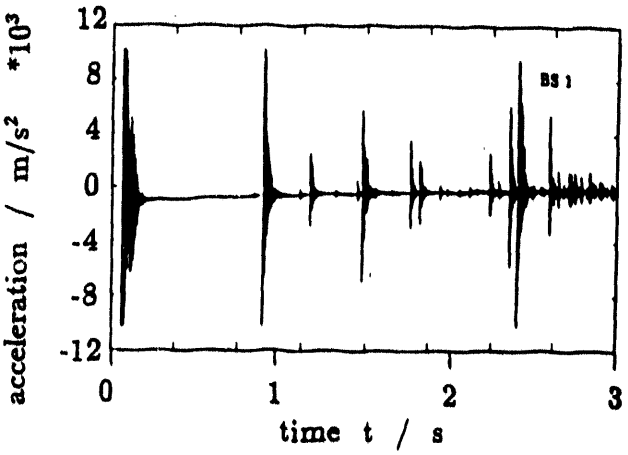

Fig. 19 : Results of wide plate test GP 1 during fracture : longitudinal acceleration **BS1** *at two levels of time resolution (fracture initiation* $t_1 \approx 0.06$ *s)*

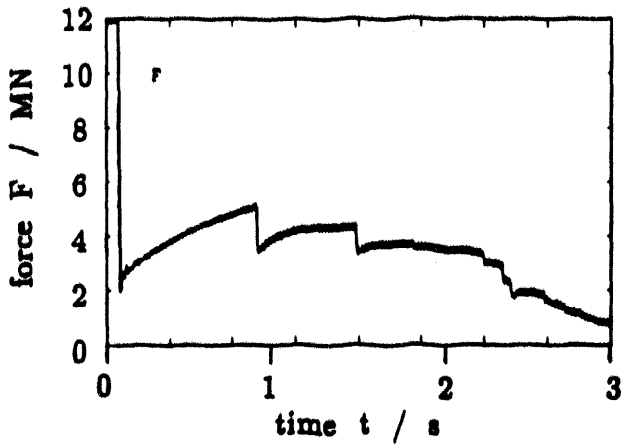

a.) tension force F of the machine

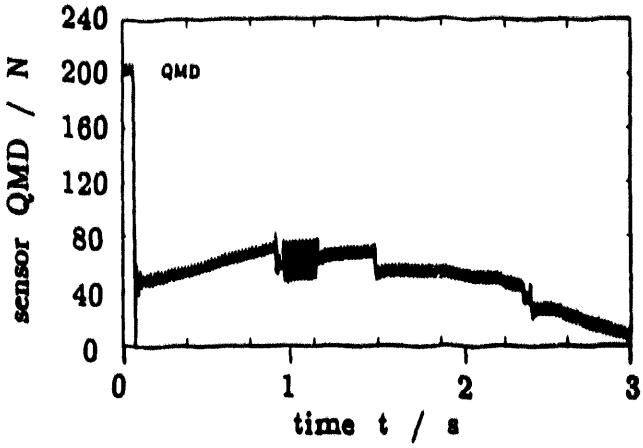

b.) pieso-electric sensor QMD

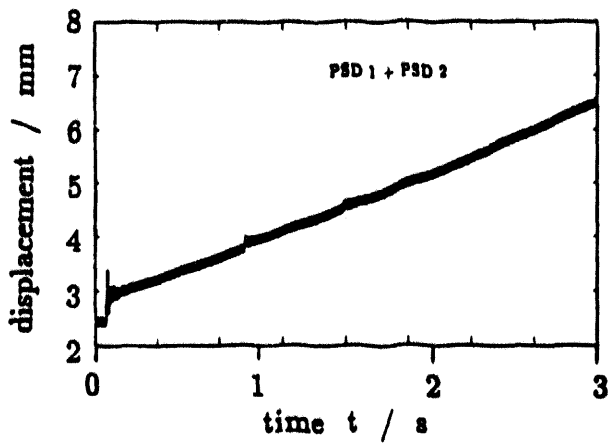

c.) relativ displacement PSD1 + PSD2

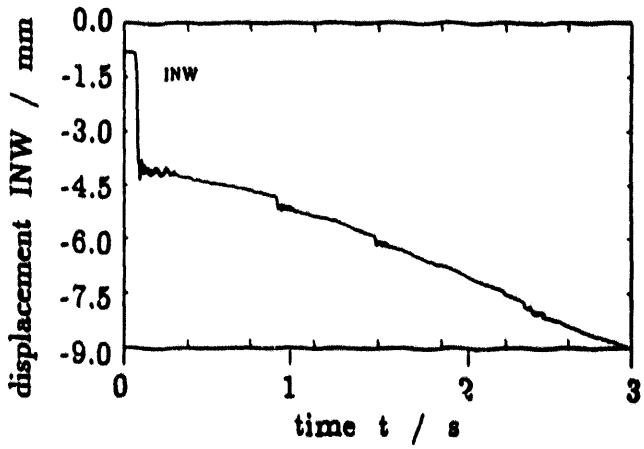

d.) horizontal displacement INW

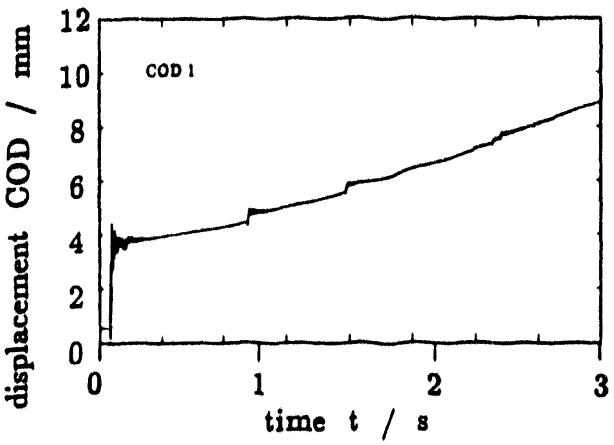

e.) crack opening COD1 (a/W=0.3)

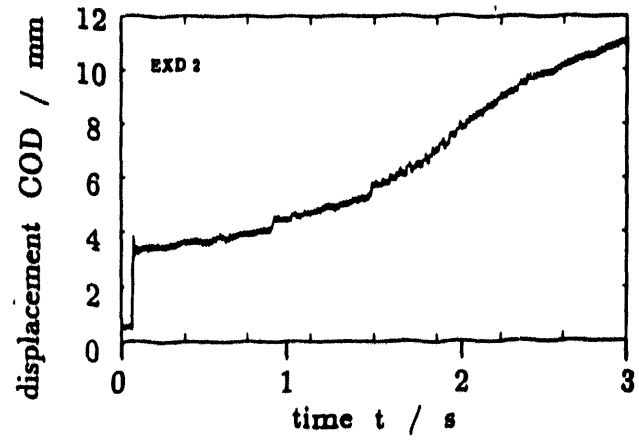

f.) crack opening EXD2 (a/W=0.3)

Fig. 20 : Results of wide plate test GP 1 during fracture : fracture initiation $t_i \approx 0.06$ s

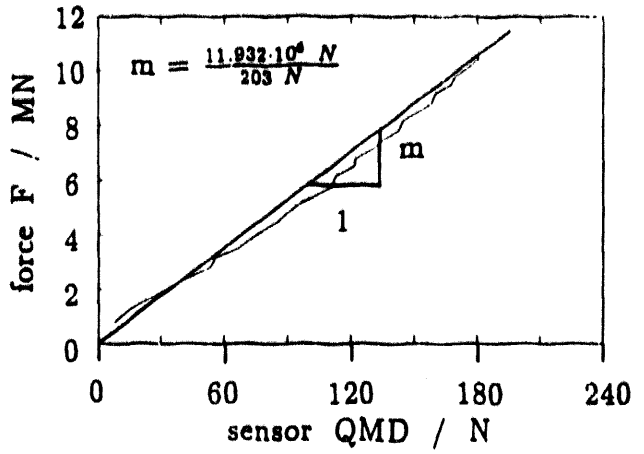

Fig. 21 : Correlation of force F and sensor QMD during quasi-static loading

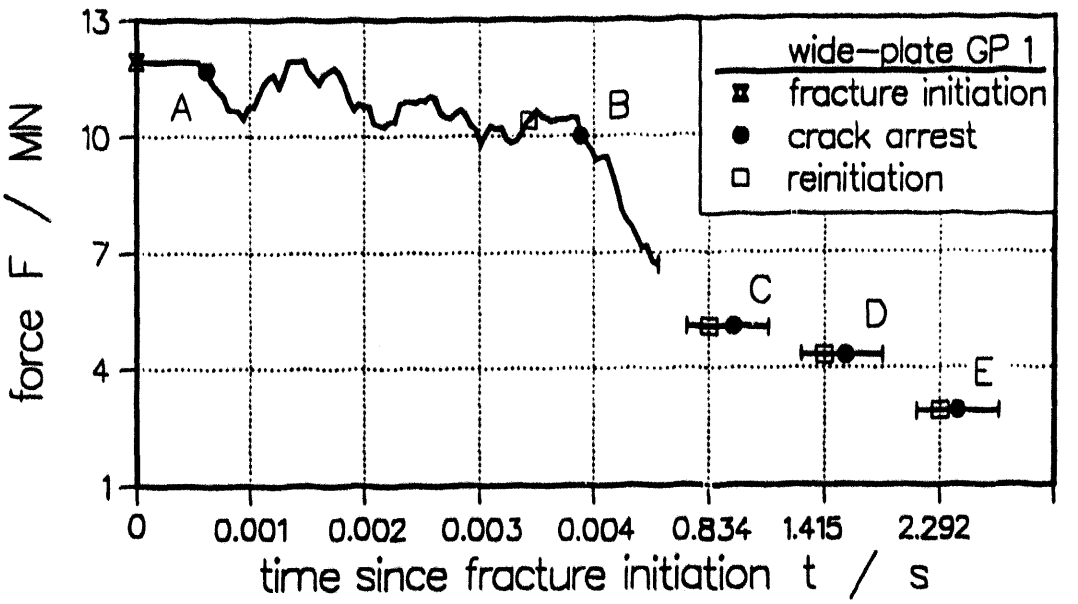

Fig. 22 : Boundary condition of force F used for numerical analyses of test GP 1

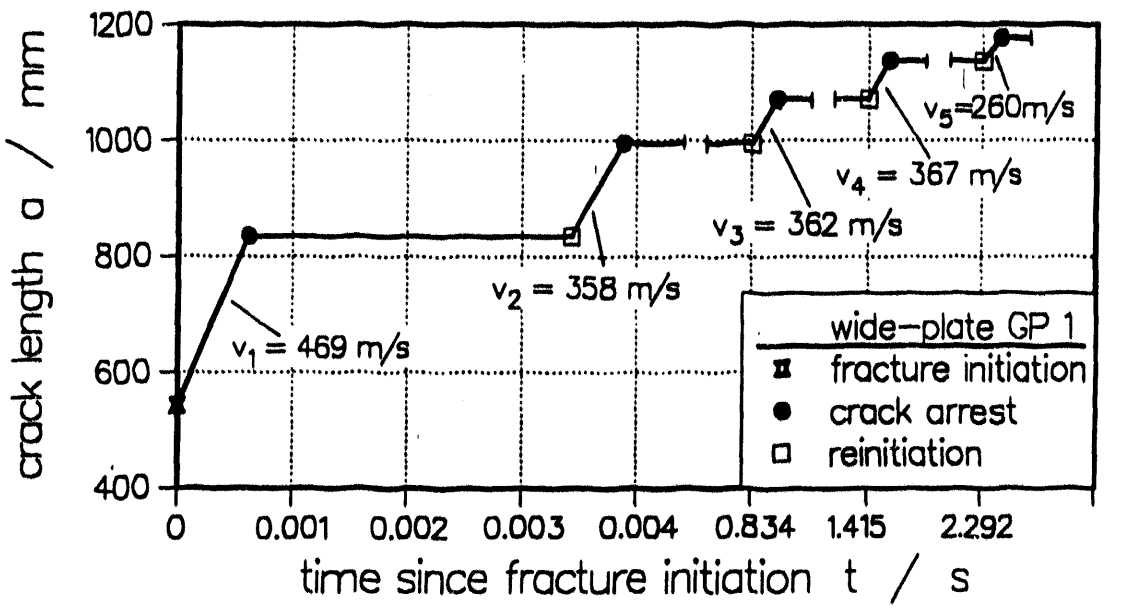

Fig. 23 : Boundary condition of crack length a used for numerical analyses of test GP 1

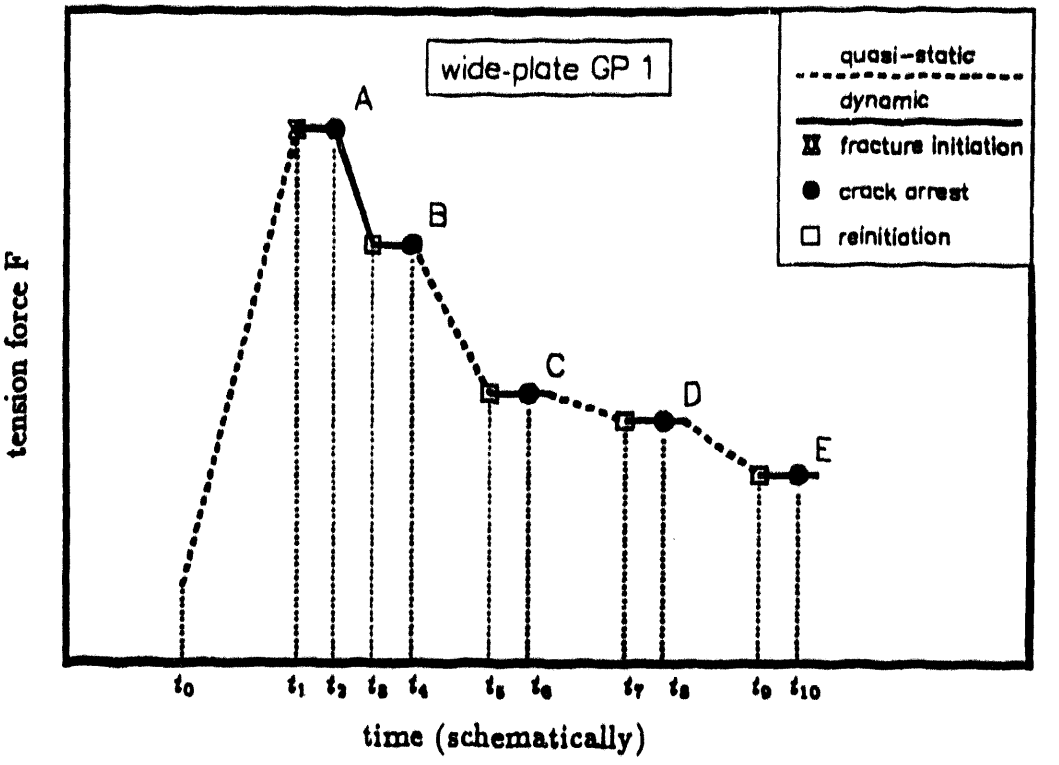

Fig. 24 : Strategy of the numerical simulation of test GP 1

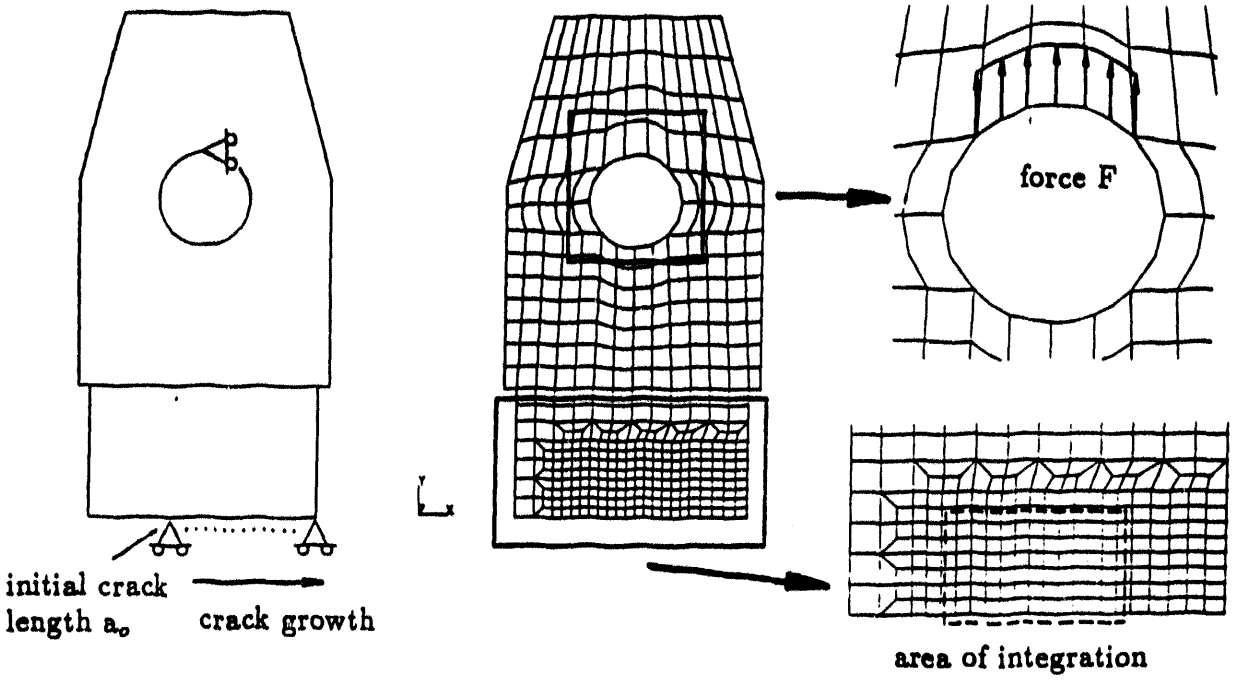

Fig. 25 : Finite element idealization of half the specimen GP 1 and displacement boundary condition at fracture initiation

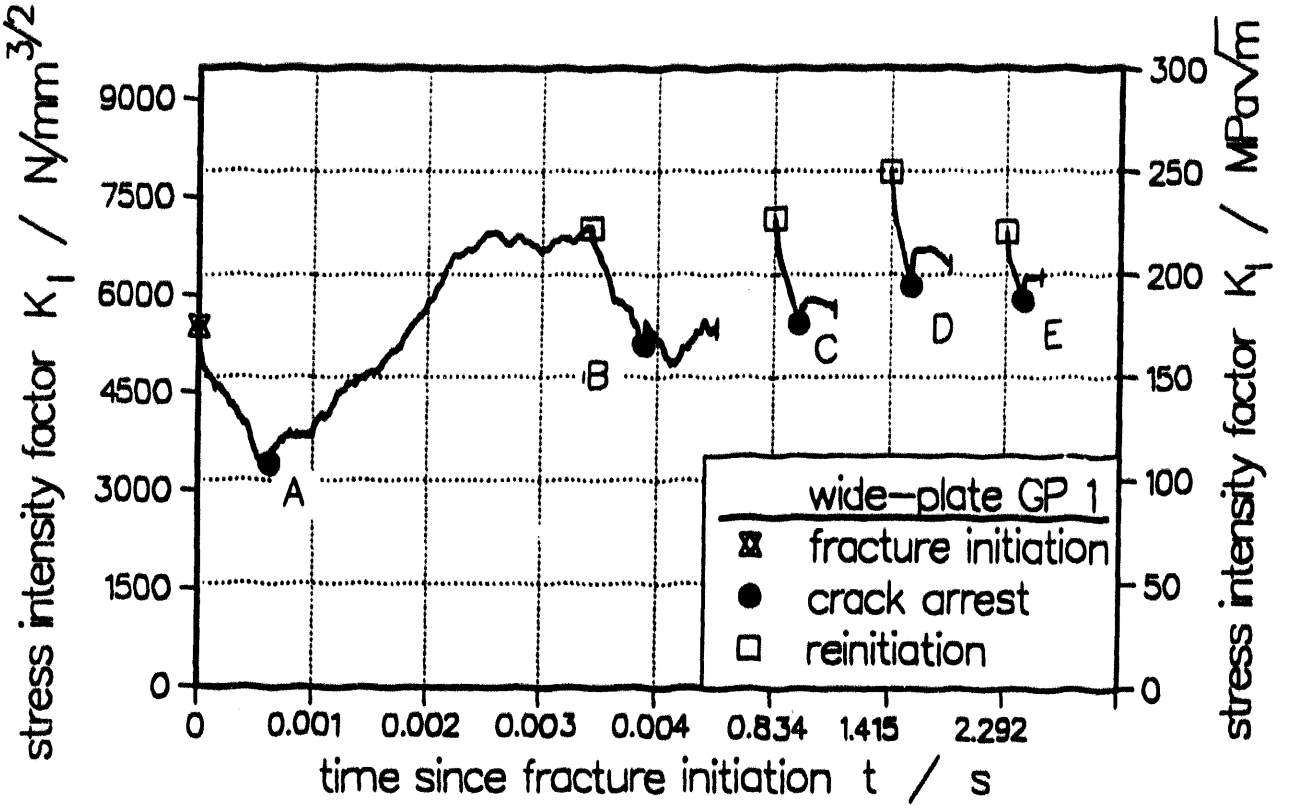

Fig. 26 : Resultant K_I-curves of crack arrest test GP 1 as function of time

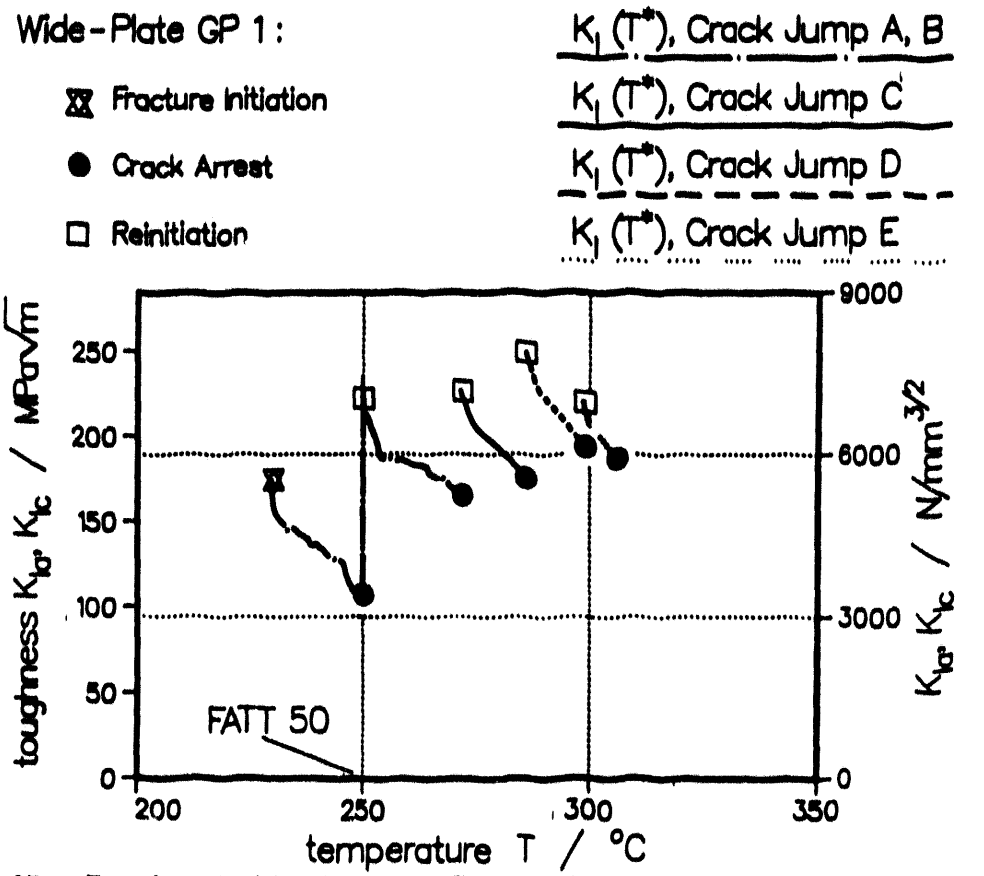

Fig. 27 : Results of wide plate test GP 1 as function of temperature

EFFECT OF LOADING ON STABLE TEARING OF WIDE PLATES

BY

A M CLAYTON*

A series of wide plate tests using a 0.36% carbon steel have been carried out in the AEA Structural Features Test Facility to determine the stable tearing behaviour of cracks under different loading conditions, typical of pressurised components. The majority of the plates were edge cracked. They were tested in pure in-plane bending, pure ligament tension, nominal tension and cyclic tensile loading. These tests can be compared with large centre cracked wide plates, described in a companion paper at this conference. Small scale fracture toughness tests were also made of the same material.

It was found that Failure Assessment Diagrams (FADs) could be used to plot out the results and showed that the assessment line gave a good failure prediction or was conservative. The very conservative evaluation of a plate in bending cannot currently be explained., Where there was combined fatigue and tearing, linearly adding crack growth due to the different processes well predicted the results. For a surface breaking defect, initiation is well predicted from using a local limit load in the FAD, but that as loads increase towards net section yield, the global limit load is more appropriate.

* AEA Technology, Risley, Warrington, UK WA3 6AT

INTRODUCTION

Nuclear pressure vessels need to be shown to be resistant to failure from the unstable growth of flaws in the vessel. Failure depends on the material; for ferritic steels at low temperatures or following extensive irradiation the failure is brittle and crack growth is rapid. For ferritic steels at higher temperature, or for austenitic steels the failure process is ductile. Increasing loads are then needed to cause the crack to extend in a tearing process. Most safety cases for nuclear plant limit loads to those to cause crack initiation and no account is taken of the considerable margins available in tearing. In some instances, for example during a pressurised thermal shock sequence during emergency cooling or due to irradiation reducing the load needed to induce tearing, some allowance for stable tearing is made. This is usually limited to an amount of crack extension which can be shown not to significantly influence the stress field around the region of intense deformation at the crack tip, so called J-controlled growth.

In order to obtain a better understanding of stable tearing, a series of wide plate tests have been carried out in which the loading conditions were varied to cover a range of conditions experienced in pressure vessels. The plates were mainly tested in a 20MN servo hydraulic test machine, Fig 1, now in the Structural Features Test Facility of AEA Technology.

TEST CONDITIONS

The plates were made from a 0.36%C steel, used because of its low upper shelf toughness (a crack initiation toughness of about 100 MPa$\sqrt{m}$) with moderate strength (yield typically of 250 MPa). This combination enables tearing to occur in moderately sized plates before next section yield. This is important because at temperatures below 150°C, the ferritic steels exhibit an elastic - perfectly plastic stress-strain response before subsequent hardening, and thus there are instantaneous major extensions occurring once yield is reached. Since ductile conditions could only be assumed above 100°C, this was used as the test plate temperature. The plates were 70mm thick, and generally of 750mm width. Most were tested with a through thickness crack from one edge. The plates were welded into extension pieces which terminated in flanges so that, end-on, the complete assembly was I-shaped. Loading was between the top and bottom flanges, with two loading stacks, each of up to 500 tonnes (5MN) on each side of the plate. Each loading stack incorporated a servo hydraulically operated actuator, and the control system to each actuator was independent.

Notches were machined in the plates and fatigued to sharpen them prior to the fracture tests being carried out.

The plates were extensively instrumented with strain gauges which were used to determine when yielding from the cracks was nearly across the whole plate. In addition, plate deformation was determined from linear transducers, on the plate itself and in the loading stacks. Crack extension was determined visually when it occurred on the plate faces, and by alternating current potential drop measurements for tearing in the mid-thickness position.

Material from the same batches as the test plates was used for supporting tensile and fracture toughness tests carried out at 100°C. The fracture toughness was found to be somewhat variable from test plate to test plate. The fracture toughness tests produced a resistance curve of crack extension toughness -v- crack extension using unloading compliance techniques on 40mm compact tension (CT) specimens with 20% side grooves. In addition a standard ASTM 3 point bend full thickness fracture toughness test was carried out on one plate. In the CT tests some 2mm of crack growth would be considered as valid and the bend test 3.7mm of crack growth would be valid. The wide plate tests carried out were (Fig 2):

(a) A 3 point bend test on a 500mm wide plate (GNSR2).

(b) A tensile test aimed at producing no net bending in the ligament behind the crack. This was produced by using two loading stacks loaded across the remaining ligament in displacement control and two small actuators attached to the edge of the plate at the crack mouth which had a fixed load ratio (1:10) of the main actuators (GNSR3).

(c) A uniform tensile end load, obtained by making all four main actuators of equal load, 3 following one actuator which was displacement controlled (GNSR7).

(d) A similar test to (c), but with cyclic loading of constant amplitude. This amplitude was increased after blocks of constant amplitude cycles, until the cycles induced tearing as well as fatigue. All loading was tensile (positive R-ratio) (GNSR4).

(e) A plate with a surface breaking thumb nail crack on one face, loaded in monotonic tension (GNSR8).

In addition, there were tests on a centre cracked plate of the same material in uniaxial and biaxial tension, which are described in a companion paper to this conference.

STRESS ANALYSIS

For many of the tests, finite element analysis was carried out, using the large strain option in ABAQUS, in which the J-integral is obtained using a domain integral procedure.

The stress-strain response in tensile test specimens results from the formation of Lüders bands, which cannot be readily modelled in the finite element analysis. The material model used allows for the virtually perfectly plastic initial response beyond yield, but not the localised Lüders band response.

Checks were made to compare loads, displacements and strains with those measured and was found to give generally good agreement. In addition, for GNSR2 the J calculations were compared with J values obtained from the load/load line displacement record using ASTM E813, and again reasonable agreement was obtained. It was found that near maximum load, the J values could be calculated accurately as a

function of load line displacements, but not as a function of load, because of the rapid change in J value with load.

CRACK GROWTH EVALUATION

Considerable reliance is placed on the alternating current potential drop (acpd) measurements to determine the onset of cracking in the tests (final crack size is obtained from breaking open the specimen after the test, which also shows any unloading beachmarks). A detailed study has been carried out of acpd behaviour as it is affected by local straining along the electrical path along the crack flanks. However, these effects have saturated in the tests before crack initiation takes place, and apart from problems due to noise on the signal, the onset of crack growth can be reasonably well determined. In all cases, the crack initiates at the mid thickness before surface growth is observed.

RESULTS

General Approach

The results of the tests have been interpreted in terms of a Failure Assessment Diagram methodology, used by Bloom in the US and developed extensively in the 'R6' procedures in the UK. The Failure Assessment Diagram is a plot of Crack Tip Stress Intensity Factor, K, (normalised to the fracture toughness, K_c to give a ratio Kr), against the load (normalised to the limit load, to give a ratio L_r).

This form of presentation has a number of advantages:

1. It enables the different plate materials properties to be taken into account with no confusion.

2. It enables the data to provide a validation of FAD methods.

3. It enables the onset of cross section yielding to be readily identified ($L_r = 1$).

4. Stable tearing response can be shown as a curve on the diagram.

The shape of the failure assessment diagram is dependent on the shape of the material stress-strain curve, but is not greatly dependent on geometry. In the R6 procedure, it is usual to use a lower bound diagram calculated from:

$$Kr = (1 - 0.14\, L_r^2)\,(0.3 + 0.7 \exp(-0.65\, L_r^6))$$

This is known as option 1. Where the stress strain curve is known option 2 is used calculated from:

$$K_r = [(E\varepsilon_{ref}/L_r\,\sigma_y) + (L_r^3\sigma_y/2E\varepsilon_{ref})]^{-1/2} \text{ for } L_r \le L_r^{max}$$

$$K_r = 0 \text{ for } L_r > L_r^{max}$$

Where E is Young's Modulus, ε_{ref} is the true strain and σ_y the 0.2% proof stress.

Points that lie in the region bounded by the K_r, L_r axes and the FAD line are safe; any test causing failure should therefore lie outside the diagram. As tearing occurs, the locus of K_r, L_r points should move along the FAD line.

Test data

The main test data is given in table 1. Values of the effective fracture toughness K_c are calculated from:

$$K_c = [JE/(1-\nu^2)]^{0.5}$$

where $J(\Delta a)$ is given by $C\Delta a^m$
and ν is Poisson's ratio.

Stress Intensity factors and Limit loads are calculated from handbook relationships.

The resulting K_r, L_r data is plotted in figures 3 and 4.

Edge crack plates in Monotonic Loading

The three edge cracked plates GNSR2, 3R and 7 are shown in Figure 3. These indicate that whilst the tension tests 3R and 7 give results generally very close to the assessment line, the initiation of the tension test 3R and all of the bend test 2 is very conservatively predicted. Since the bend test is the most constrained geometry, and thus most likely to be well predicted from compact tension fracture data, this result is surprising and currently cannot be explained. GNSR7 underwent a control system instability at low load, which continued up to the final load where stability was regained. The marginally unconservative result at this load giving data inside the curve for test GNSR7 is probably due to minor variations in material properties, which are being confirmed by further testing.

Edge crack plate in Cyclic Loading

The data shown for GNSR4 in figure 3 are obtained by taking the total crack growth due to fatigue and due to tearing and subtracting the contribution due to fatigue to give Δa values. This gives results very close to the identical geometry but monotonic loading in GNSR7 and therefore is consistent with the contention that in tearing-fatigue, the contributions to crack growth from both processes can be linearly added.

Surface breaking crack

For a surface breaking crack, there are two possible limit load solutions which could be used, one developed by Merkle for the HSST ITV programme based on a local collapse of the material in the vicinity of the crack using a slip line solution in which the limit load is calculated from:

$$L_r = \sigma bt/\{\sigma_y[(2c+t)t-½\pi ac]\}$$

where σ is the nominal stress in the unflawed section

c is the semi-surface crack length
a is the crack depth
t is the plate thickness
and b is the plate width

The alternative is to assume that all of the remaining area in the plane of the crack can carry a uniform yield value (a global solution). This gives:

$$L_r = \sigma bt/\{\sigma_y(bt-½\pi ac)\}$$

These two possible options are plotted in figure 4. It is clear that at crack initiation, the local solution provides a good prediction (ie is near the FAD line), but a global L_r would be very unconservative. However, once the load has reached the condition where general yielding occurs in the remaining area in the plane of the crack, the global L_r is more appropriate.

CONCLUSIONS

Provisional analyses have been made of a series of wide plate tests in which stable tearing occurs in different loading configurations. Further materials evaluation and assessment, using more advanced fracture assessment methods is ongoing, but from Failure Assessment Diagram (FAD) evaluation, the following conclusions can be drawn:

1. The R6 FAD gives a good representation of stable tearing response, or is conservative. In the case of pure bending, the results are greatly conservative and the reasons for this are not clear.

2. The results from combined fatigue and tearing loading with tensile load cycling are consistent with linearly adding crack growth due to both processes.

3. For ferritic materials containing surface breaking cracks, initiation is best predicted from using a local limit load, but as the net section containing the crack reaches yield, the global limit load is more appropriate.

ACKNOWLEDGEMENTS

This programme has been the result of a dedicated team effort. The author would particularly note the contributions of J K Sharples and D J Lacey to the assessment, and to H G Morgan, L Gardner, G Melvin and D Dobson to the experimental programme. All were members of AEA Reactor Services, but Dr Lacey is now with NII, Bootle, UK. The test programme was sponsored by the UK Department of Energy under the General Nuclear Safety Research Programme Letter. Further testing analysis and reporting was sponsored by the UK Health and Safety Executive.

TABLE 1

Summary of Tests

Ref	plate width b (mm)	plate thickness t (mm)	crack size $a_o(c_o)$ (mm)	yield** stress σ_y (MPa)	ultimate** stress σ_u (MPa)	constants in $J=C\Delta^{m}$** C	m	load at initiation (MN)	max load++ (MN)	Δa at max load (mm)
GNSR 2	500	68	270	264	478	0.12	0.569	0.62*	0.85*	16
GNSR 3R	750	70	420	264	478	0.109	0.605	5.4	5.9	5.9
GNSR 7	850	70.5	250	294	533	0.085	0.398	N/A	6.48	18.5
GNSR 4	850	70	200	264	478	0.109	0.605	5.5+	5.85+	14+
GNSR 8	750	70	56(183)	222	483	0.140	0.512	>4.0	9.5	13

* 3 point bend load on span of 1.5m. All other loads are total axial loads.

\+ Part of fatigue test with increasing load amplitude cycle blocks. Load at initiation is first load producing stable tearing; actual max load was higher, but not used in analysis, crack extension is the total crack extension less fatigue crack growth. At 'initiation', total crack size was 50.6mm with 2mm due to tearing; at 'max load' total crack size was 77.4mm with 14mm due to tearing.

** Provisional values; to be confirmed by further testing.

++ Maximum load is instability load in tests GNSR2, 3R and 8 and is load at termination of test in GNSR7 and 4.

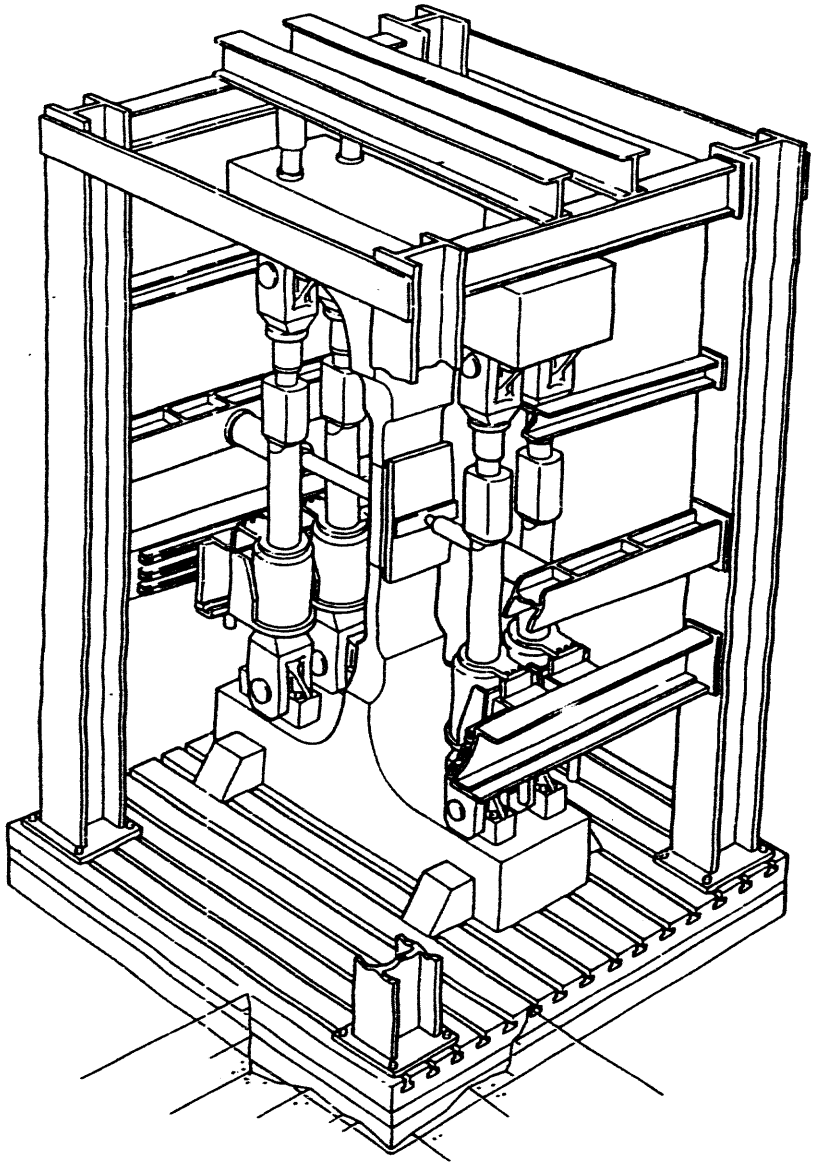

Fig 1 20MN Rig

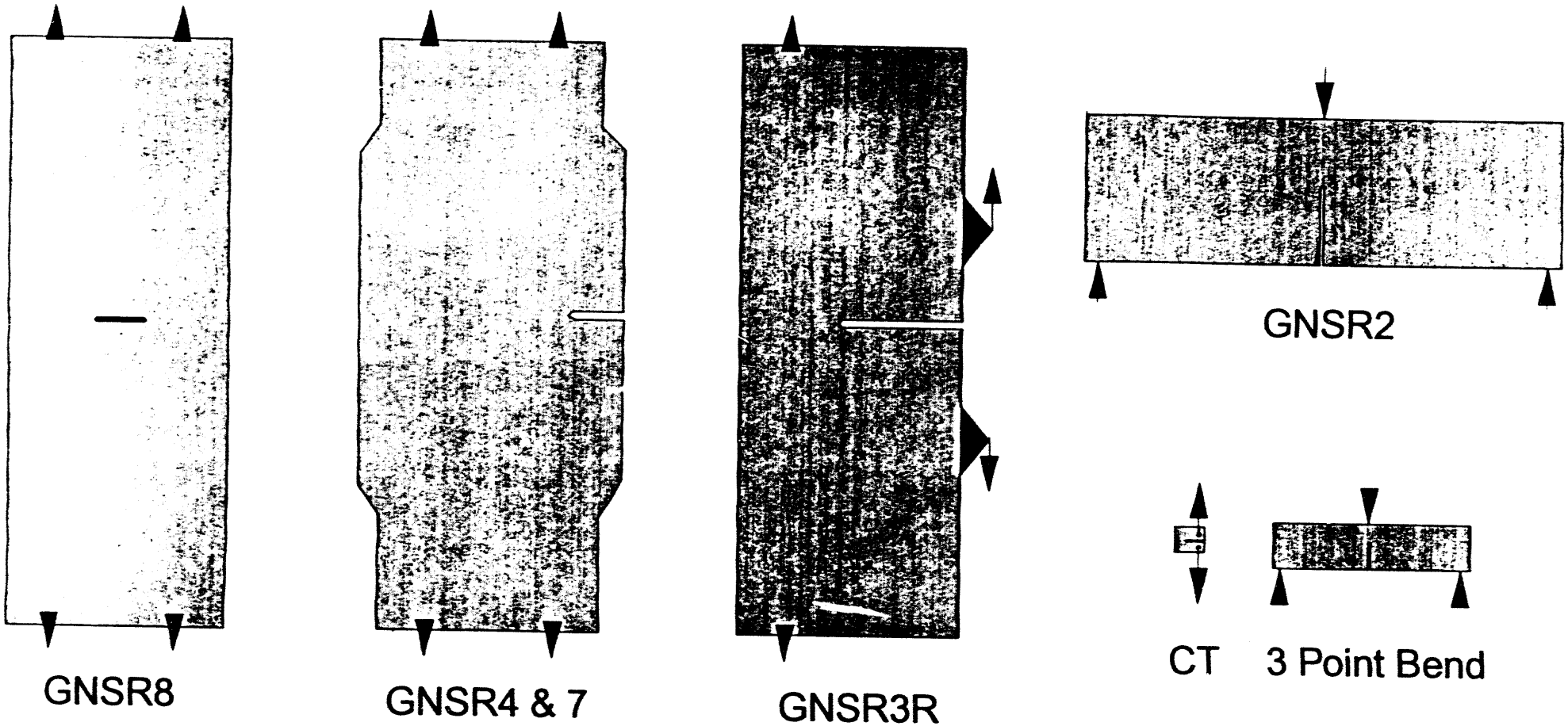

Fig 2 Specimen Geometries

Fig 3 Results of edge crack plate tests plotted on R6 failure assessment diagram

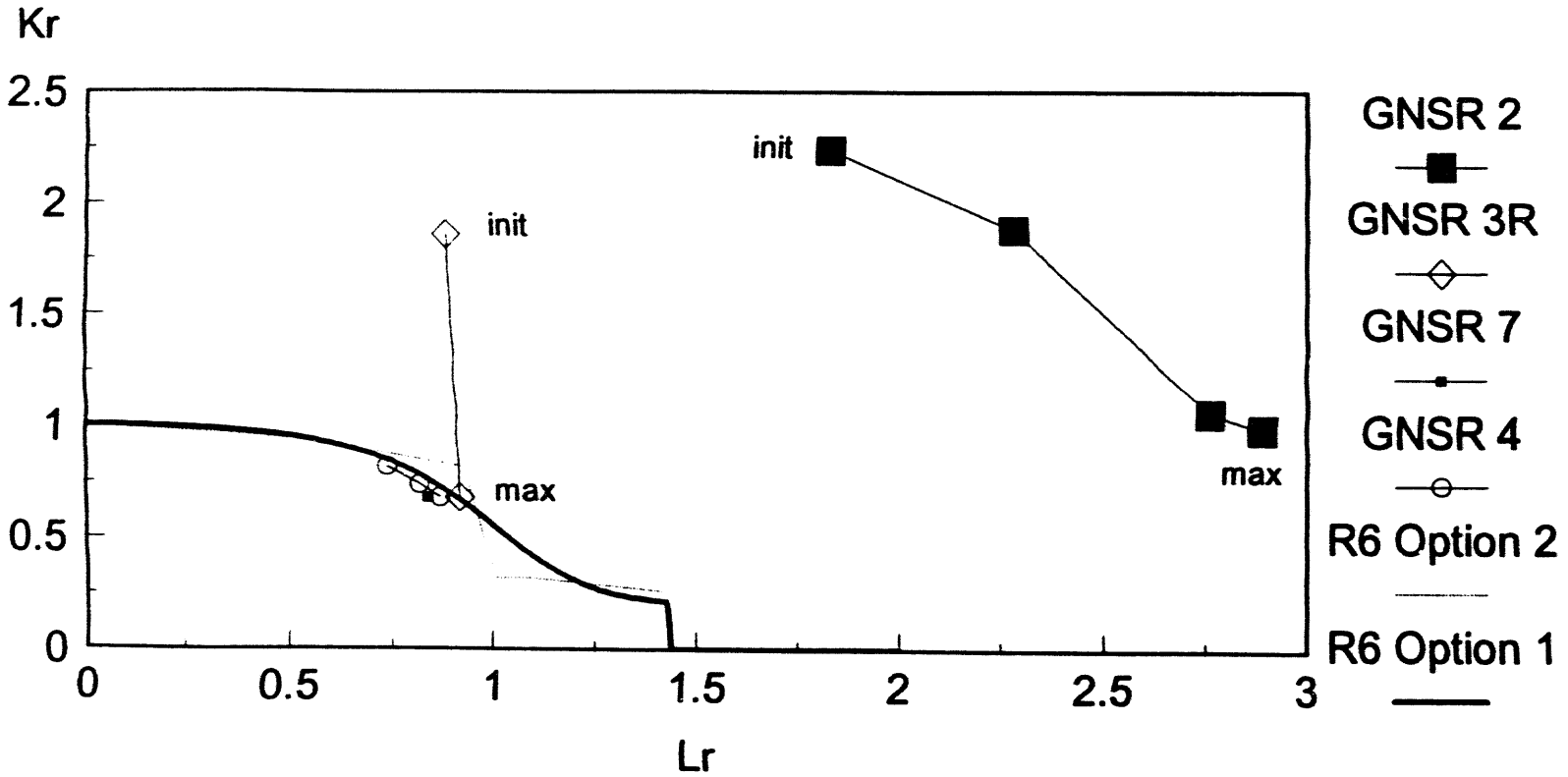

Fig 4 Surface Breaking Crack
Local and Global Limit Loads on R6 FAD

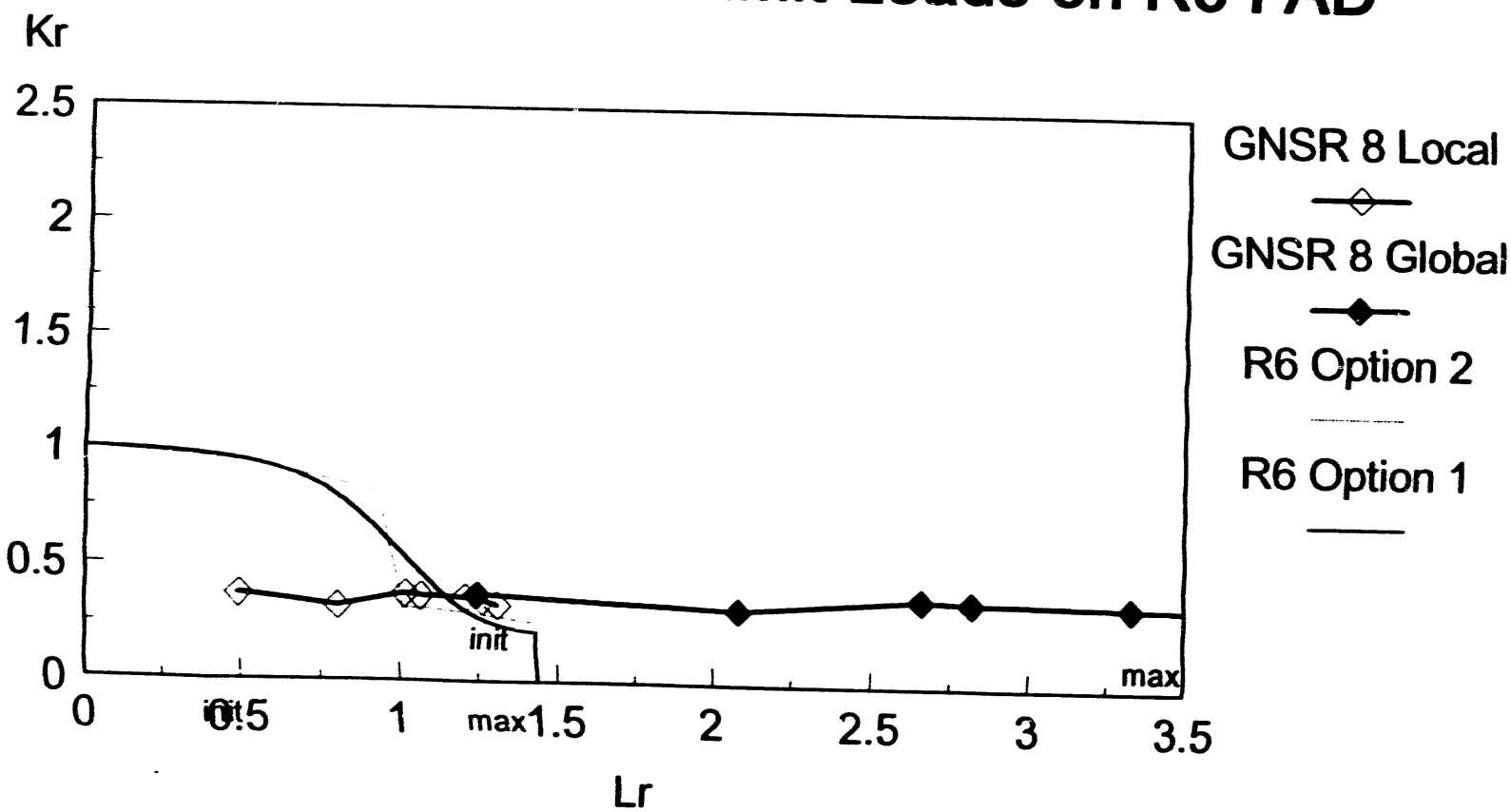

REACTOR VESSEL INTEGRITY ANALYSIS BASED UPON LARGE SCALE TEST RESULTS

by

Dr. David J. Ayres* and Mr. Raymond J. Fabi**

The fracture mechanics analysis of a nuclear reactor pressure vessel is discussed to illustrate the impact of knowledge gained by large scale testing on the demonstration of the integrity of such a vessel. The analysis must be able to predict crack initiation, arrest and re-initiation. The basis for the capability to make each prediction, including the large scale test information which is judged appropriate, is identified and the confidence in the applicability of the experimental data to a vessel is discussed. Where there is inadequate data to make a prediction with confidence or where there are apparently conflicting data, recommendations for future testing are presented.

* ABB Combustion Engineering Nuclear Services
Windsor, CT 06095 U.S.A.

** ABB Combustion Engineering Nuclear Systems
Windsor, CT 06095 U.S.A.

INTRODUCTION

Fracture mechanics analysis is performed to demonstrate that nuclear reactor vessels can safely withstand normal and severe loadings. For some routine evaluations, such as for the normal startup and shutdown of plants, the analysis procedure is well established and codified in detail in the ASME Code [1] and U.S. NRC regulations [2]. For the evaluation of severe transients, such as the pressurized thermal shock of a highly irradiated vessel, there are yet some uncertainties in the analysis method which need to be resolved before it can be comfortably accepted by the entire industry.

The Regulatory Guide 1.154 [3] prescribes a philosophy for a probabilistic analysis of a vessel if the material is anticipated to reach the PTS screening criterion of 10CFR50.61 [4]. Prior to reaching the screening criterion, a vessel is essentially pre-evaluated to be acceptable by analyses performed during the early 1980s.

A probabilistic analysis is the compilation of results from a large number of deterministic analyses performed with varying inputs. Therefore, the probabilistic analysis is only as good as the deterministic analysis assumptions, procedures, and data on which it is based. The regulatory guide presently does not prescribe in detail all of the inputs and procedures for the analysis, so considerable latitude is given to the analyst.

The potential for disagreement between different analysts on what are appropriate inputs and procedures was illustrated by the Yankee Atomic attempt to perform analyses to justify the continued operation of the Yankee Rowe vessel in 1991. After prolonged discussions and revisions of analyses, Yankee Atomic withdrew its efforts to justify the Rowe vessel and the NRC determined that the regulatory requirements and guidance documents needed clarification. Observers throughout the industry, perceived the failure of analysis to justify continued operation at Rowe to be an indication that analysis was an unacceptable method for demonstrating the integrity and continued operability of a reactor vessel.

During the recent NRC/Industry meeting on Coordination of Reactor Vessel Integrity Efforts (September 1992) [5], the NRC reaffirmed that:

a) they intend to revise all the regulatory documents relating to vessel integrity, and

b) analysis will be an acceptable integrity demonstration tool once the details of the methods and inputs are resolved.

To hasten the resolution of the analysis issues, the NRC has requested industry help. Industry, via NUMARC, has agreed to work toward resolution and a state of regulatory stability in the area of reactor vessel integrity.

There are many unsettled issues, some large and some small, and limited resources throughout industry to work on them. Therefore, it is vital that the most important issues be given the highest priority so that the greatest benefit can be attained.

The purpose of this paper is to aid in identifying the issues which, if resolved, would provide the greatest enhancement to the acceptability of the analysis option. In order to do this, some typical deterministic vessel analyses will be addressed, and points of uncertainty will be identified. The impact of the uncertainty on the credibility and acceptability of the results will be discussed so that the various issues can be evaluated with respect to degree of impact and therefore, prioritized for industry attention.

VESSEL ANALYSIS

To make comparisons to other work easier, several generic analyses will be used for discussion. A typical analysis addressing these issues is presented in a recent paper by J. Keeney-Walker and B. R. Bass [6], and several other analyses have been presented during the EPRI/NRC Research Benchmarking meetings [7]. These analyses consider typical severe PTS transients in embrittled vessels. In the analyses, the key issues are:

a) does the crack initiate,

b) if the crack initiates, does it arrest and at what depth into the vessel wall, and

c) if it arrests, will the crack reinitiate due to dynamic response of the structure or at a later time in the transient.

The issues of crack initiation, arrest and reinitiation will be addressed separately in order to focus clearly on one issue at a time. Reference 6 provides a good point of discussion. It analyses a typical PTS transient with a variety of analysis methods.

CRACK INITIATION

Figure 1, which is taken from Reference 6, shows that K_I first exceeds K_{Ic} at a time fairly late in the transient. The value of K_I at this time, is in the range of 60 to 90 ksi$\sqrt{}$in and the crack depth is 0.3 to 0.9 inches. Values of this magnitude are also typical of those found in the probabilistic benchmarking exercise. The issue to be addressed is what is the confidence that a prediction of crack initiation at these conditions is accurate, conservative or unconservative.

Reviewing the variety of large scale test results available from the HSST Wide Plate and PTS tests, we see that, in general, it is hard to initiate a crack, and specifically, the K_I required for initiation is often significantly higher than K_{Ic} which is determined from small specimen tests or is given in the ASME Code. One example of this can be seen in the PTSE-2 experiment [8], where the crack initiation toughness had to be shifted so that the

post test analysis could be compared to the experimental results. A comparison of the potential K_{Ic} values is shown in Figure 2. In the HSST wide plate tests [9], the ratio of the actual load required to initiate the crack to the predicted value is shown in Figure 3.

The cracks of concern for initiation in a PTS transient are typically very small. Mayfield and Wichman [10] indicate that new insight into the behavior of shallow cracks and the apparent toughness elevation of these shallow cracks emphasizes the need for more work in this area. These observations lead to the recognition that an elastic calculation of $K_I = K_{Ic}$ will very conservatively estimate crack initiation.

One phenomenon which could lead to a less conservative prediction of initiation, is the potential for ductile crack extension prior to cleavage. This phenomena was observed in the PTSE2 test, but the values of K_I were considerably higher than in the PTS example (above 150 ksi$\sqrt{in}$). These higher K_I values are typically not the values of concern during the first crack initiation due to a PTS transient. They may be seen for deeper cracks which may be subject to reinitiation which will be discussed later.

- Assessment of Uncertainty

  Based on the data from large specimens, crack initiation appears difficult to predict with a high degree of certainty. However, the error is characteristically on the conservative side for reactor vessel materials in that the load to crack initiation is much higher than predicted. Therefore, two conclusions can be drawn. First, the analysis methodology at present is conservative so it could be used with confidence that a prediction of no initiation would result in a safe structure. Second, more study on this issue may provide sufficient understanding to lead to more accurate predictions and the potential removal or at least quantification of the conservatisms in the existing analysis.

CRACK ARREST

The crack arrest issue has been vigorously discussed since researchers began to synthesize the results of the CE/EPRI Crack Arrest Program and the HSST Wide Plate Test Program [11]. Reference 6 contains the last word in that discussion which indicates that excellent agreement between the results of the CE/EPRI and HSST Programs has been achieved with respect to the prediction of crack arrest. Clearly, crack arrest is a dynamic phenomenon which can best be predicted by dynamic analysis. However, the "static analogy" method provides a good approximization of the dynamic results and is so simple that it can be included in a probabilistic analysis.

- Assessment of Uncertainty

  The agreement of analysis and experimental results of crack arrest tests, indicate that crack arrest may be the best understood phenomenon in the entire analysis chain. Although there is some uncertainty with respect to the precise values of K_{Ia}, the

ASME Section XI Appendix A curve [12] prescribes a lower bound which appears to be conservative. Therefore, present crack arrest analyses per References 6 and 11, can be used to obtain conservative crack arrest predictions.

CRACK REINITIATION

Reinitiation of a crack is an important issue if the acceptance criterion for a vessel allows some amount of crack extension. At the present time, Regulatory Guide 1.154 stipulates that the crack must extend no further than 75% of the way through the wall.

Reinitiation of an arrested crack could occur within milliseconds after arrest due to the dynamic structural response to the presence of the extended crack, or it may occur later in the transient due to higher loads caused by system repressurization.

The difficulty in predicting reinitiation due to the dynamic structural response is discussed in Reference 6. The key issue is the sensitivity of toughness to loading rate which can be very high following arrest. One source of data [13], Figure 4, suggests that the initiation toughness, K_{Id}, decreases significantly with rate, especially at relatively higher temperatures. On the other hand, dynamic analyses of both the CE/EPRI crack arrest specimens and the HSST Wide Plate tests indicated that reinitiation did not occur until significantly higher values of K_I were reached than would be predicted by Reference (13). These analyses were discussed in an EPRI/NRC meeting in San Diego in June of 1991 [12] but were never published.

Two examples of large scale tests which appear to be inconsistent with the Shabbits data are the MMCT tests and the Wide Plate tests. The stress intensity factor, as a function of time after crack arrest, is computed for a MMCT specimen test in Figure 5 [15]. The crack tip loading rate is very high at about $6x10^5$ ksi$\sqrt{}$in/sec. The rate sensitive K_{Id} from Figure 4 is on the order of 120 ksi$\sqrt{}$in which is significantly lower than the calculated value of approximately 360 ksi$\sqrt{}$in when reinitiation was observed to occur. In fact, the computed value is higher than K_{Ic} predicted from the ASME Section XI curve which is consistent with previous observations.

Another example is Wide Plate Test numbers (WP1.5) for which dynamic analyses were also performed [11]. The K_I as a function of time for both an elastic and an elastic-plastic analysis, is shown in Figure 6. In this case, the crack tip loading rate is about $1.8x10^5$ ksi$\sqrt{}$in/sec, and the rate sensitive K_{Id} is estimated to be 170 ksi$\sqrt{}$in. The K_I at the time of crack reinitiation is again very much higher than the rate sensitive value would predict. Additional analyses of crack reinitiation in Wide Plate tests result in similar conclusions.

The HSST Wide Plate and CE/EPRI programs were primarily concerned with studying crack arrest. Since they did not focus on reinitiation, the test specimens were not specifically instrumented to provide the kind of data necessary to characterize crack tip conditions at reinitiation. There is, however, enough large scale test data to demonstrate that the rate effect data [13] are not applicable for predicting reinitiation in these tests.

If a crack does not reinitiate due to the dynamic response of the structure, it may reinitiate later in the transient due to repressurization or some other increased loading. In this situation, since the material is likely to be fairly tough (deeper in the wall, less embrittled and perhaps warmer), ductile tearing may precede cleavage as was observed in PTSE2B [8]. Ductile tearing may also lead to through wall crack extension, also observed as the last phenomenon of PTSE2B.

- Assessment of Uncertainty

  Use of the rate dependent material toughness of Figure 4, appears to underpredict the loading required for reinitiation. Inclusion of this in a vessel analysis would result in a very conservative prediction of crack reinitiation and, therefore, crack extension in the vessel wall. Additional studies may lead to insights which would enable a more realistic reinitiation prediction and therefore, a more useful vessel analysis method.

Reference 6 suggests that the development of an effective model for the complete fracture event is dependent upon substantial progress being made in several of areas including dynamic initiation toughness and pre-cleavage ductile tearing.

SUMMARY OF ISSUES

The critical parts of the fracture analysis of a vessel are the prediction of crack initiation, crack arrest and reinitiation. Present analysis methodology can provide a conservative assessment of initiation, possibly a very conservative assessment of dynamic reinitiation, and a realistic prediction of crack arrest. Therefore, it is clear that a conservative analysis of vessel integrity can be performed. The conservatisms in initiation and reinitiation, however, may result in a failure to be able to demonstrate vessel integrity which could result in the shutdown of a safe vessel. In order to preserve the analysis option as a means of demonstrating that a vessel is safe, conservatisms in the analysis must be eliminated or quantified.

Based on the discussions in this paper, it is clear that the key issues which need to be addressed to enhance the credibility of the present analysis option for reactor vessel integrity demonstration are:

1. Initiation of small cracks in brittle material of large structures;

2. Dynamic reinitiation of deep cracks of brittle or ductile material to test the rate dependence hypothesis; and

3. Static reinitiation of deep cracks in ductile materials with emphasis on the effect of pre-cleavage ductile tearing.

REFERENCES

1. The American Society of Mechanical Engineers Boiler and Pressure Vessel Code Section XI Appendix G and Section III Appendix G

2. Code of Federal Regulations, Title 10, Part 50, Appendix G

3. U.S. Nuclear Regulatory Commission, Regulatory Guide 1,154, *"Format and Content of Plant Specific Pressurized Thermal Shock Safety Analysis Reports for Pressurized Water Reactors"*

4. Code of Federal Regulations, Title 10, Part 50, Section 50.61

5. U.S. Nuclear Regulatory Commission and Industry meeting on Coordination of RV Integrity Efforts, Rockville, Maryland, September 2-3, 1992

6. J. Keeney-Walker, B. R. Bass, *"An Evaluation of Analysis Methodologies for Predicting Cleavage Arrest of a Deep Crack in an RPV Subjected to PTS Loading Conditions"*, PVP Vol 233, *"Pressure Vessel Fracture Fatigue and Life Assessment"*, ASME, 1992

7. EPRI and NRC Research have held several meeting during 1992. Contact: T. Griesbach of EPRI

8. R. M. Bryan, et al, *"Pressurized-Thermal-Shock Test of 6-in-Thick Pressure Vessels. PTSE-2: Investigation of Low Tearing Resistance and Warm Prestressing"*, U.S. NRC Report NUREG CR-4888, ORNL, 1987

9. D. J. Naus, et al, *"Summary of the Eleventh Heavy-Section Steel Technology (HSST) Wide Plate Crack Arrest Test (WP1.7)"*, Oak Ridge National Laboratory, December 7, 1987

10. M. Mayfield, K. Wichman, *"Technical Issues to be Resolved in Assuring Reactor Pressure Vessel Integrity"*, SMiRT-11, Taipei, Taiwan, August 1991

11. R. J. Fabi, D. J. Ayres, *"Calculating Dynamic Crack Arrest by Static Analogy"*, Electric Power Research Institute, NP6223, March 1989

12. The American Society of Mechanical Engineers, Boiler and Pressure Vessel Code, Section XI Appendix A

13. W. O. Shabbits, *"Dynamic Fracture Toughness Properties of Heavy Section A533 Grade B Class 1 Steel Plate"*, Westinghouse R&D Center, WCAP-7623, HSST Technical Report No. 13, December 1970

14. EPRI/NRC Meeting in Crack Arrest Technology, San Diego, California, June 28, 1991

15. *"Tests and Analyses of Crack Arrest in Reactor Vessel Materials"*, Electric Power Research Institute, NP5121M and NP5121-SP, April 1987

PREDICTED CRACK INITIATIONS IN PTS TRANSIENT

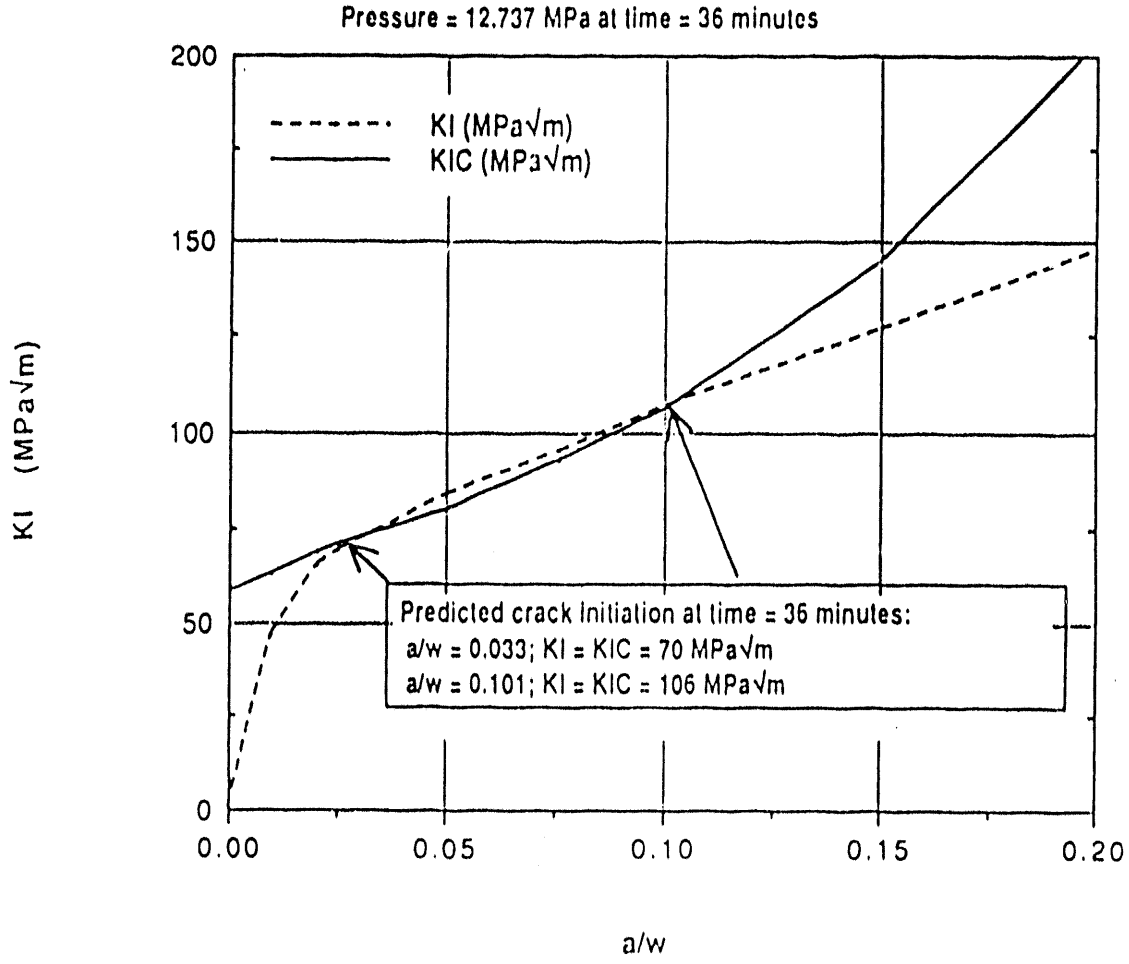

Figure 1: Typical Crack Initiation Prediction for a PTS Transient

J. Keeney-Walker, B. R. Bass, *"An Evaluation of Analysis Methodologies for Predicting Cleavage Arrest of a Deep Crack in an RPV Subjected to PTS Loading Conditions"*, PVP Vol 233, *"Pressure Vessel Fracture Fatigue and Life Assessment"*, ASME, 1992

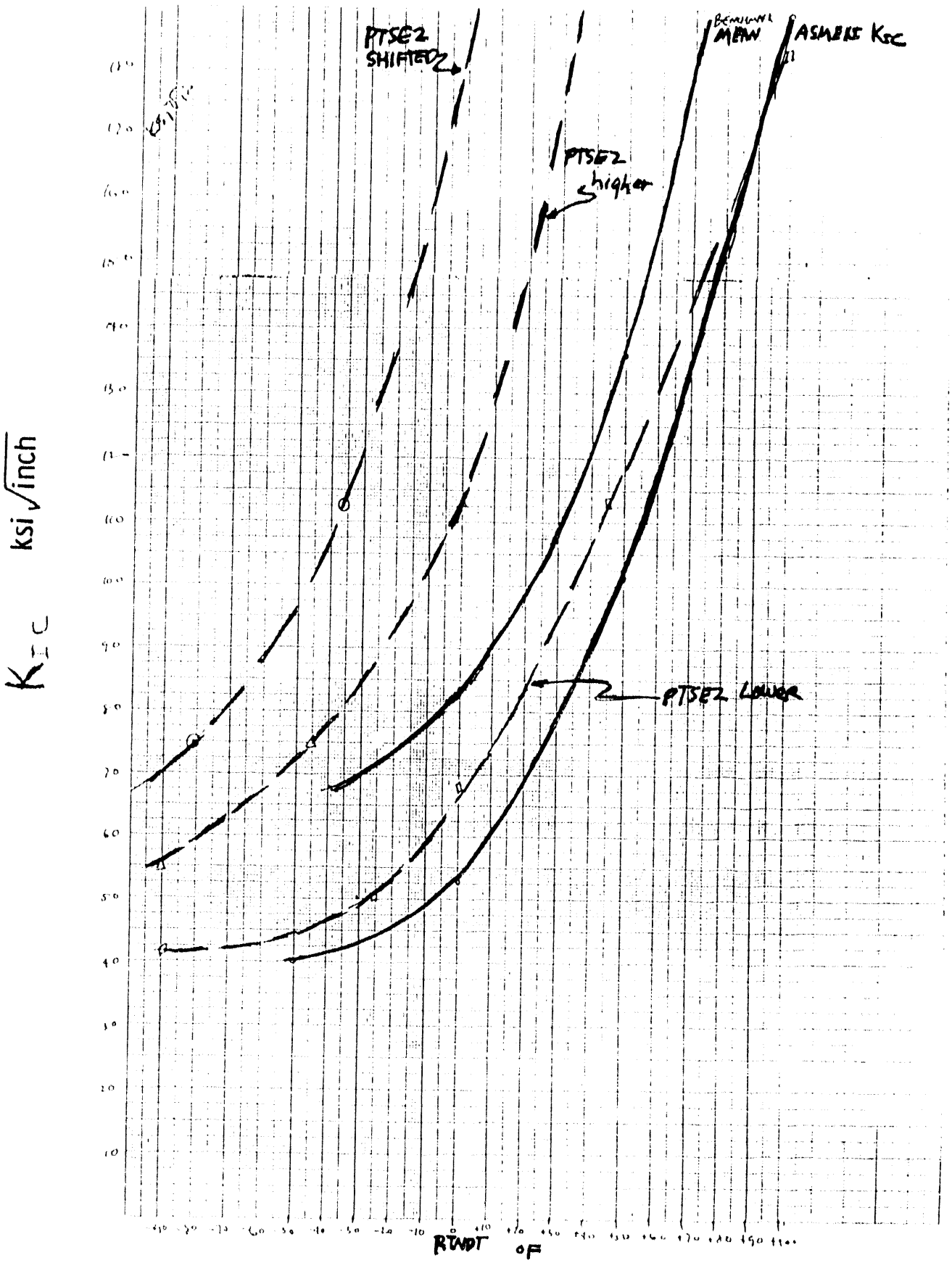

Figure 2: Fracture Toughness Values Considered for PTSE-2 Crack Initiation Prediction

Table 5.1. Initiation stress intensity factor comparisons

Test designation	Crack tip temperature, (°C)	Calculated static K_I[a] (MPa·√m)	Property correlation K_{Ic} (MPa·√m)	K_I/K_{Ic}
WP-1.2	-33	251.5	87.5[b]	2.87
WP-1.3	-51	173.5	70.1[b]	2.48
WP-1.4	-62	213.0	63.9[b]	3.33
WP-1.5	-30	179.8	91.6[b]	1.96
WP-1.6	-19	233.8	111.2[b]	2.10
WP-1.7	-22.7	280.6	103.7[b]	2.71

[a] Computed from 3-D static analysis using ORMGEN/ADINA/ORVIRT.

[b] Calculated from $K_{Ic} = 51.276 + 51.897\ e^{0.036(T - RT_{NDT})}$ using crack tip temperature of initial flaw.

Figure 3: Ratio of Predicted K_{Ic} to Post-Test Computed Value for Wide Plate Tests of 533B Material

D. J. Naus, et al, *"Summary of the Eleventh Heavy-Section Steel Technology (HSST) Wide Plate Crack Arrest Test (WP1.7)"*, Oak Ridge National Laboratory, December 7, 1987

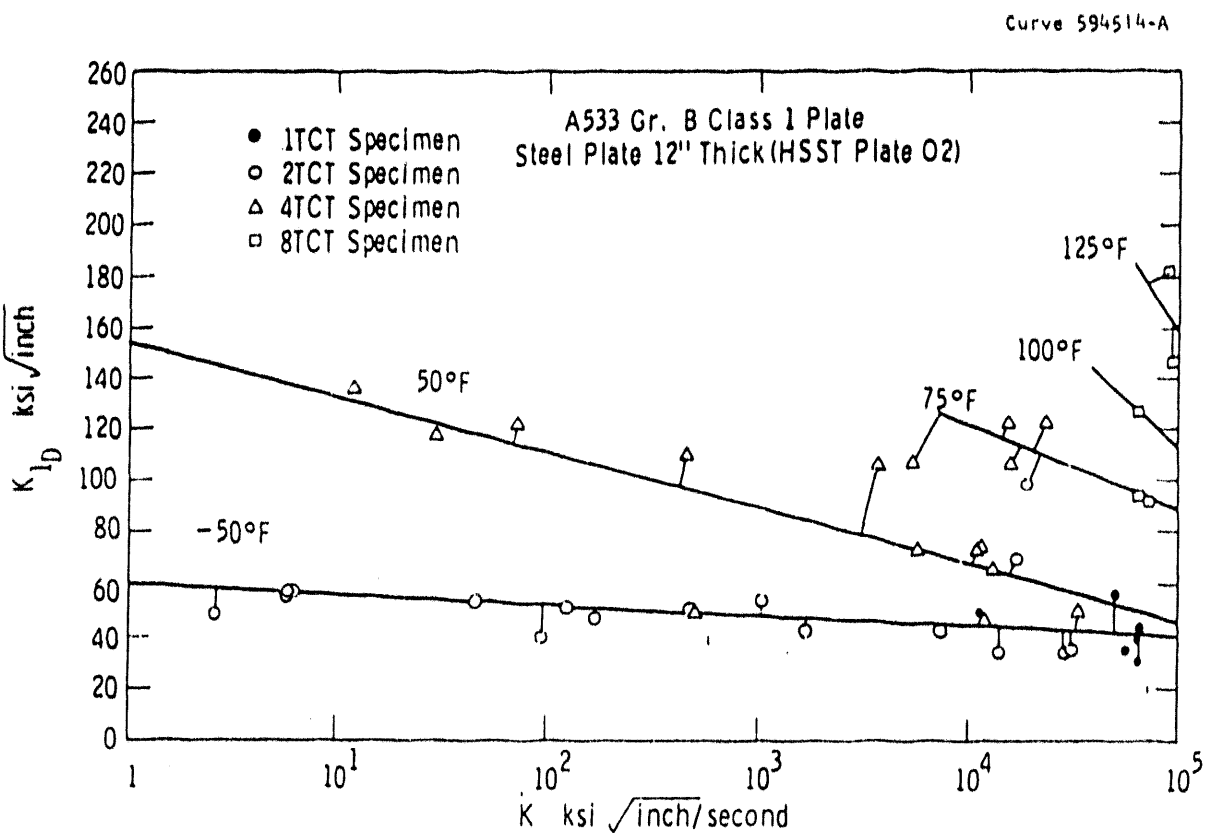

Figure 4: Dynamic Fracture Toughness as a Function of Loading Rate

W. O. Shabbits, *"Dynamic Fracture Toughness Properties of Heavy Section A533 Grade B Class 1 Steel Plate"*, Westinghouse R&D Center, WCAP-7623, HSST Technical Report No. 13, December 1970

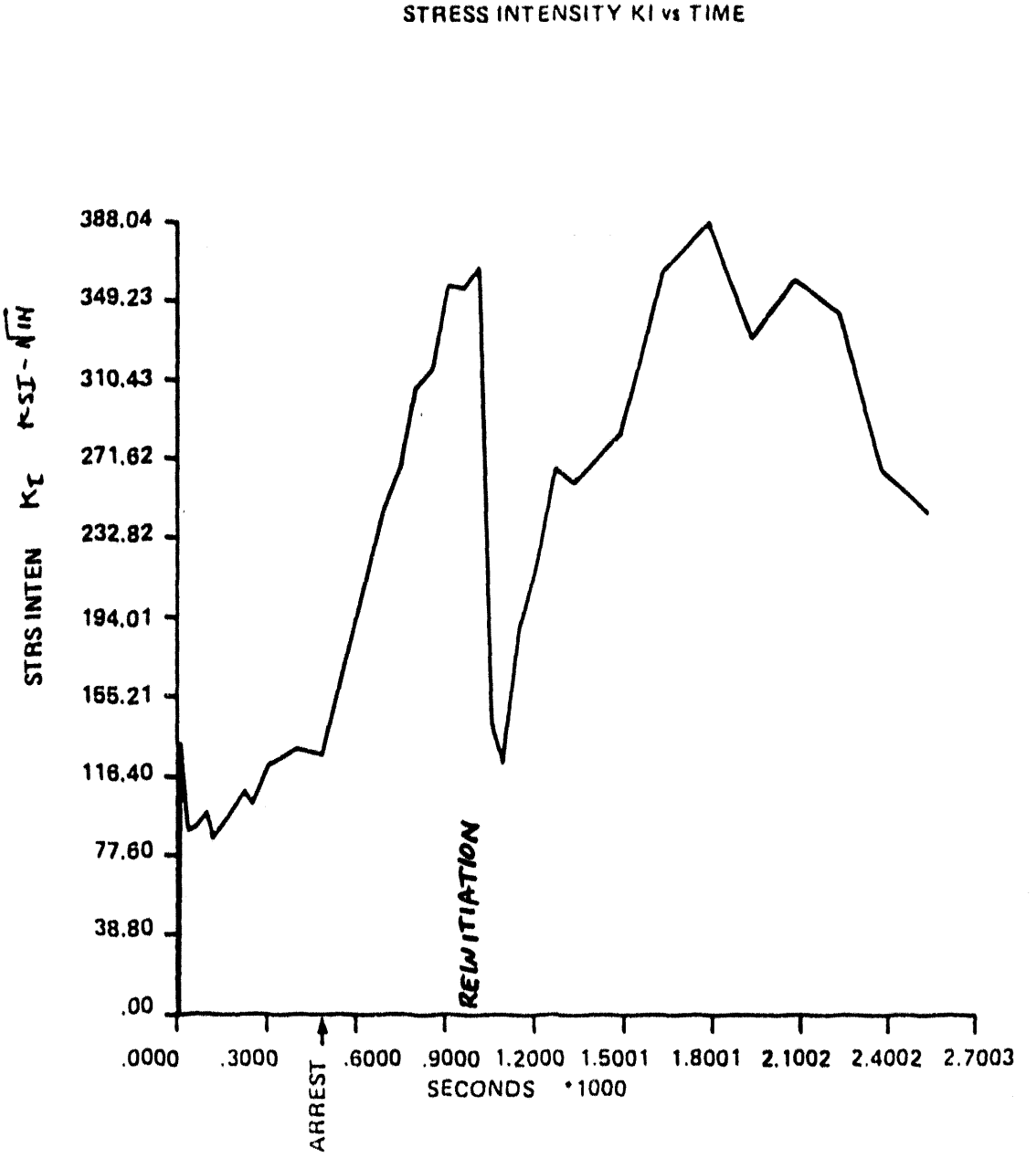

Figure 5: Stress Intensity Factor vs Time for MMCT Test 9a

"Tests and Analyses of Crack Arrest in Reactor Vessel Materials", Electric Power Research Institute, NP5121M and NP5121-SP, April 1987

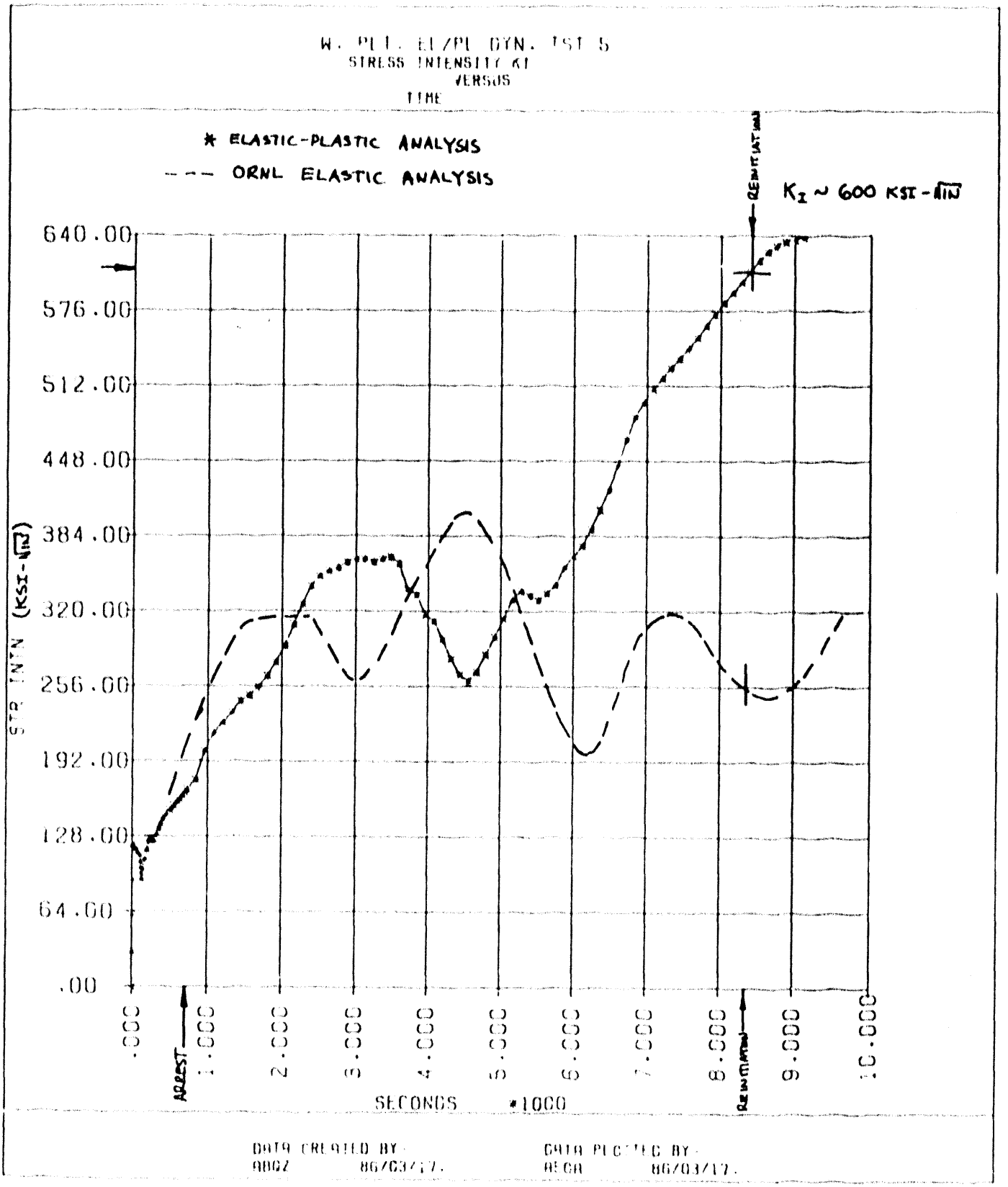

Figure 6: Stress Intensity Factor vs Time for Wide Plate Test WP1.5

R. J. Fabi, D. J. Ayres, *"Calculating Dynamic Crack Arrest by Static Analogy"*, Electric Power Research Institute, NP6223, March 1989

APPLICABILITY OF LABORATORY DATA TO LARGE SCALE TESTS UNDER DYNAMIC LOADING CONDITIONS

by

K. Kußmaul*, A. Klenk*

Abstract

The analysis of dynamic loading and subsequent fracture must be based on reliable data for loading and deformation history. This paper describes an investigation to examine the applicability of parameters which are determined by means of small-scale laboratory tests to large-scale tests. The following steps were carried out:

- Determination of crack initiation by means of strain gauges applied in the crack tip field of compact tension specimens.
- Determination of dynamic crack resistance curves of CT-specimens using a modified key-curve technique. The key curves are determined by dynamic finite element analyses.
- Determination of strain-rate-dependent stress-strain relationships for the finite element simulation of small-scale and large-scale tests.
- Analysis of the loading history for small-scale tests with the aid of experimental data and finite element calculations.
- Testing of dynamically loaded tensile specimens taken as strips from ferritic steel pipes with a thickness of 13 mm resp. 18 mm. The strips contained slits and surface cracks.
- Fracture mechanics analyses of the above mentioned tests and of wide plate tests. The wide plates (960x608x40 mm^3) had been tested in a propellant-driven 12 MN dynamic testing facility. For calculating the fracture mechanics parameters of both tests, a dynamic finite element simulation considering the dynamic material behaviour was employed.

The finite element analyses showed a good agreement with the simulated tests. This prerequisite allowed to gain critical J-integral values. Generally the results of the large-scale tests were conservative.

* Staatliche Materialprüfungsanstalt (MPA)
University of Stuttgart
Pfaffenwaldring 32
D 7000 Stuttgart 80

1 Introduction

The linear-elastic and elastic-plastic fracture mechanics concepts are used in the safety analysis of cracked components. The methodology for the performance and evaluation of fracture mechanics tests is subject to standards and is highly developped in the case of quasi-static loading conditions /1/. Investigations on the applicability of laboratory data to components and methods for the application in this loading case are established. In the case of dynamic and impact loading conditions only first approaches exist for a complete methodology which allows a quantification of the safety margin against catastrophic failure /2-5/. Impact loading conditions can often be found in energy, traffic or manufacturing technology; in the design of nuclear power plants some dynamic loading events are taken into account.

The present investigations comprise the determination of laboratory data with compact tension (CT-) specimens and three-point-bend (TPB-) specimens as well as tests with specimens which are in size and shape similar to components (Fig. 1). The tests with small-scale specimens are used to determine crack initiation and crack resistance curves by means of special measuring and evaluation techniques. They were performed in servohydraulic testing machines, a high energy rotating disk impact machine (Fig. 2) an inverted instrumented impact machine, and a split-Hopkinson-pressure bar. The loading rates varied from 1 MpaÖm/s to 10^7 MPaÖm/s. Dynamic tensile tests with specimens machined in longitudinally oriented strips from a pipe were performed on a servohydraulic testing machine (Fig. 3). The wide plate tests were carried out on a 12 MN propellant-driven dynamic tensile testing facility (Fig. 4).

Fine-grained structural steels with different values of upper shelf Charpy-V notch impact energy (Fig. 5) and the austenitic steel X6 CrNi 18 11 with a Charpy-V notch impact energy of 300 J at room temperature were examined (Table 1). The ferritic specimens were machined from seamless pipes with different diameters the austenitic ones from a plate. The chemical composition of the materials is shown in Table 2.

The fracture mechanics analyses comprise the investigation of crack initiation values and crack resistance curves by means of small-scale specimen tests. A fracture mechanics analysis of the large-scale specimen tests was employed using dynamic finite element calculations. A material characterization by stress-strain-relationships is necessary for an assessment of the results and for the modelling of material behaviour for the numerical analyses. If the applicability of laboratory data to components is to be investigated, an additional analysis of the loading and deformation history will be necessary. In addition to the critical values for crack initiation and the crack resistance curves a characteristic loading rate has

to be determined. The shift of the transition temperature for ferritic steels under dynamic loading has to be taken into account. Therefore a detailed investigation in the temperature range -100 °C to +100 °C was carried out for the material 17 MnMoV 6 4. Other tests and simulations were carried out at room temperature.

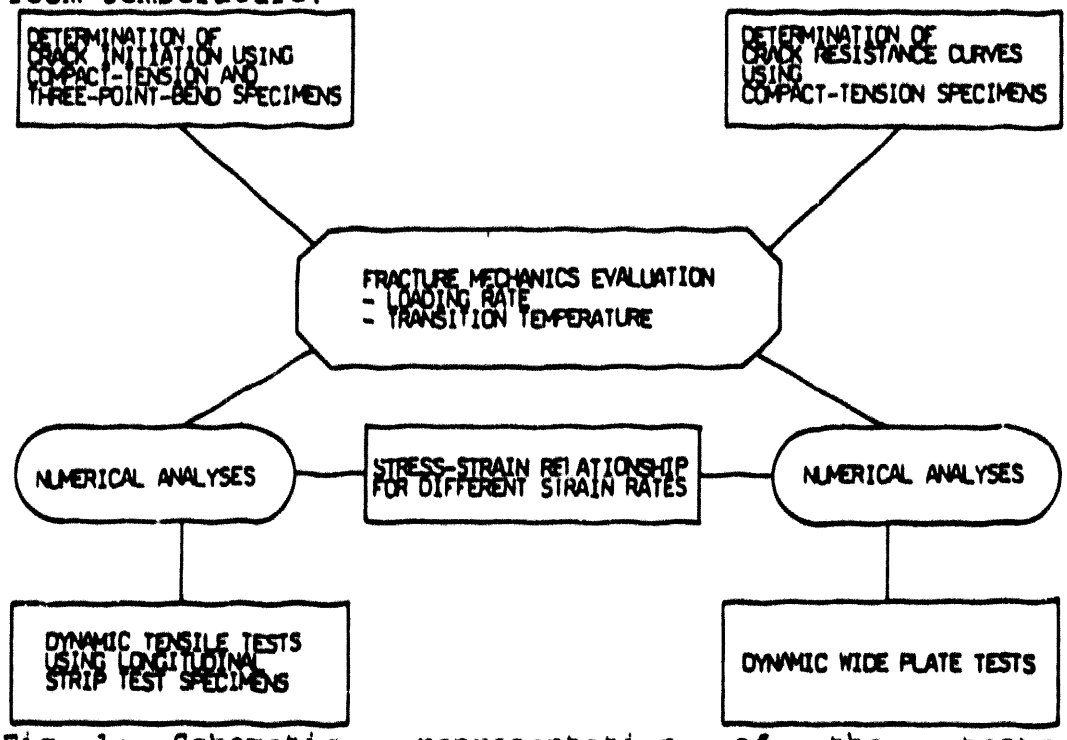

Fig. 1: Schematic representation of the tests and investigations

Material	orientation	NDT-temperature	specimen forms	machined from	inner diameter	wall thickness
20 MnMoNi 5 5 (similar to A508B Cl.3)	TL	-50 °C	CT25	seamless pipe	704 mm	48 mm
17 MnMoV 6 4 (WB35)	LS	-40 °C	TPB stripes	seamless pipe	346 mm	11 mm
	LT	-10 °C	CT10, TPB stripes			
	TL	-10 °C	CT 10			
15 NiCuMoNb 5 (WB36)	LT	0 °C	CT 10, stripes	seamless pipe	434 mm	18 mm
X6 CrNi 18 11	TL	-	CT 25 wide plates	plate	-	40 mm

Table 1: Materials and specimen forms

Material	C	Si	Mn	Cr	Mo	Ni	Al	Cu	Nb
20 MnMoNi 5 5	0.20	0.22	1.32	0.08	0.50	0.72	0.02	0.02	-
17 MnMoV 6 4	0.14	0.34	1.63	0.11	0.37	0.05	0.03	0.07	<0.01
15 NiCuMoNb 5	0.14	0.30	1.04	0.17	0.36	1.18	0.01	0.65	0.02
X 6 CrNi 18 11	0.05	0.56	1.40	18.4	0.02	10.2	0.03	0.06	0.05

Table 2: Chemical composition of the materials

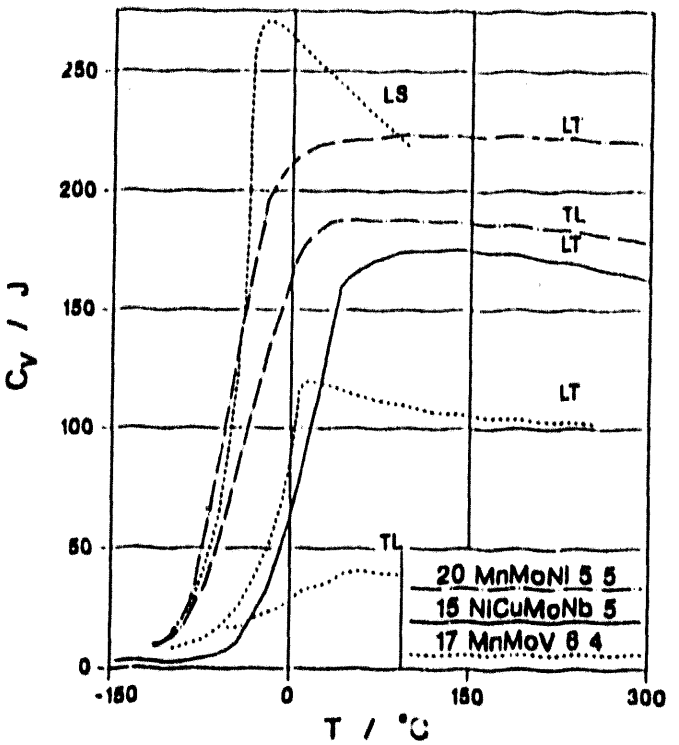

Fig. 2: Charpy-V-notch impact energy for the test materials

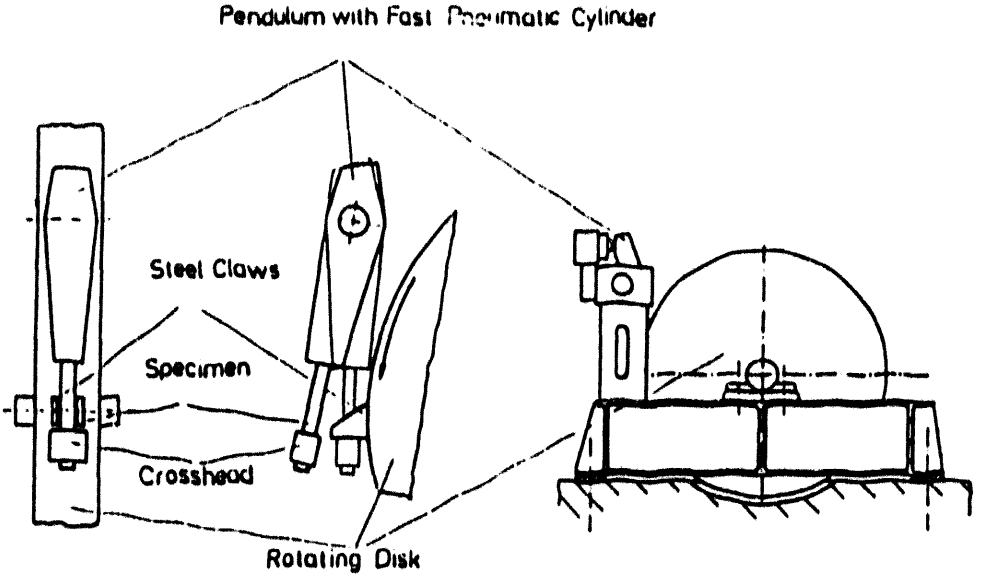

Fig. 3: Rotating disk impact machine

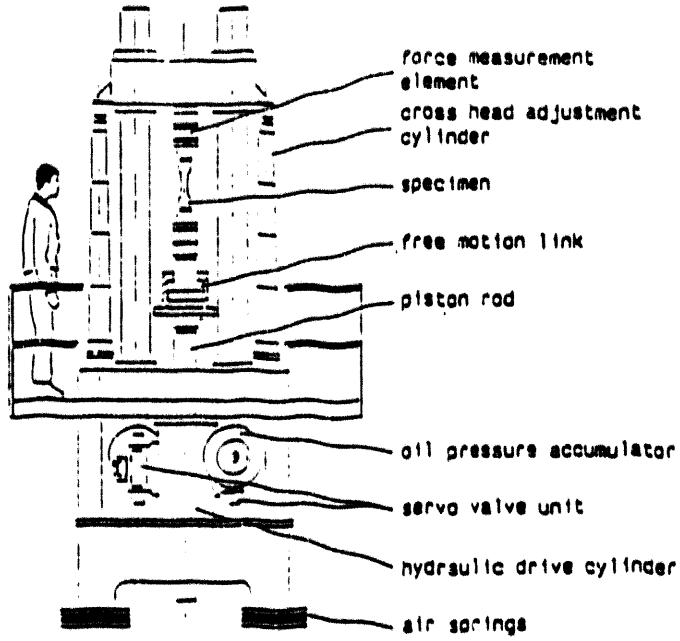

Fig. 4: Servohydraulic testing machine with a maximum speed of 12 m/s for the tensile tests with longitudinal strip test specimens

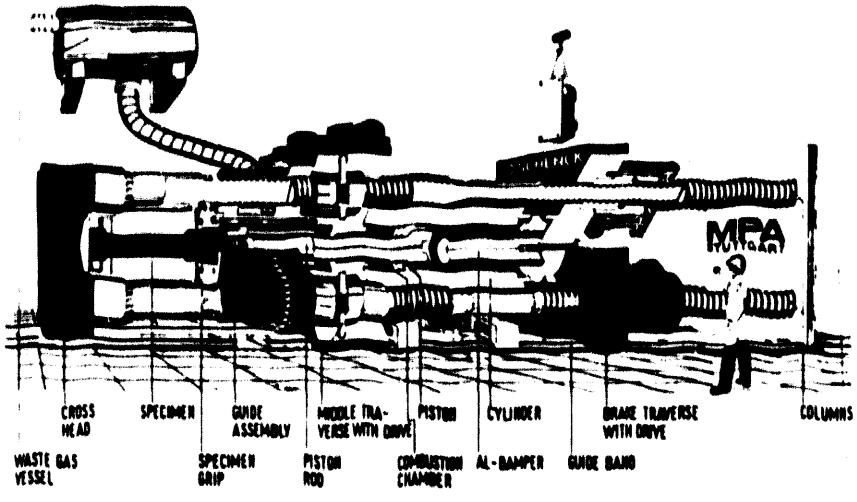

LOAD	12 MN	**WEIGHT**	
STROKE	600 (1300) mm	TOTAL	490 t
VELOCITY		ACCELERATING PARTS	15 t
-AFTER 20 mm STROKE	25 m/s	ACCELERATION FORCE	100 MN
-AFTER 400 mm STROKE	60 m/s		
LOAD FRAME STIFFNESS	10^{10} N/m		
CROSS-SECTIONAL AREA	20000 mm^2	**STRESSES**	
MAX. INTERNAL PRESSURE	200 MPa	PISTON ROD	MAX. 900 MPa
I.D. OF CYLINDER	1200 mm	CYLINDER	MAX. 625 MPa

Fig. 5: 12 MN propellant-driven tensile testing machine

2 Dynamic stress-strain curves

The stress-strain curves have to be determined as a function of the strain rate /6,7/. The maximum strain rate usually occurring in structures without defects can be estimated to be in the magnitude of 10^1 s^{-1}. The mean value of strain rate at the boundary of the plastic zone at a crack tip can be ten times higher than that of the component without defect. Thus strain rates of about 10^3 can be found in the plastic part of the crack tip region /2/. The simulation of cracked structures needs therefore reliable material data for strain rates up to this value. The strain rate should be constant during each test. This prerequisite was fulfiled owing to an optimized testing technique /8,9/. Smooth round bar specimens with a diameter of 6 mm in the gauge length and gauge lengths of 30 mm resp. 10 mm were used. Dynamometer sections instrumented with strain gauges served to determine the stress σ_o via quasi-static calibration. This sections of the specimens were deformed purely elastically during the test. Because of the nonlinear stress-strain behaviour of the austenitic steel, the dynamometer sections were made from a ferritic steel and welded on by electron beam welding. Strain ε was measured with a post-yield strain gauge which allowed the measurement of strain up to 20 percent. By means of an electro-optical extensometer resp. contact-free opto-electronic sensors the strain for larger plastic deformations could be gained. True stress σ and true strain Φ were calculated using

$$\sigma = \sigma_o \ (1 + \varepsilon \ )$$

$$\Phi = \ln \ (1 + \varepsilon \ ).$$

These relations are valid up to the ultimate tensile strength. Fig. 6 shows the true stress-true strain relationship for the material 17 MnMoV 6 4 as a function of strain rate. All materials show an increasing flow stress with increasing strain rate. The increase of stress at the onset of yielding is higher than that for higher strain values. To determine a material model which can be used for the finite element analyses the mean value of the quotient

$$k^* = \sigma_{dyn} \ (\varepsilon, \dot{\varepsilon}) \ / \ \sigma_{stat} \ (\varepsilon)$$

between the lower yield strength and the ultimate tensile strength was determined for each strain rate $\dot{\varepsilon}$. The material model for each material comprises a complete quasi-static stress-strain-curve and the following approximation using the Symonds-Cowper-equation :

$$\dot{\varepsilon} = D \ (k^* - 1)^p \ .$$

The parameters D and p are shown in Table 3. The strain rate sensitivity is smaller for materials of higher strength and

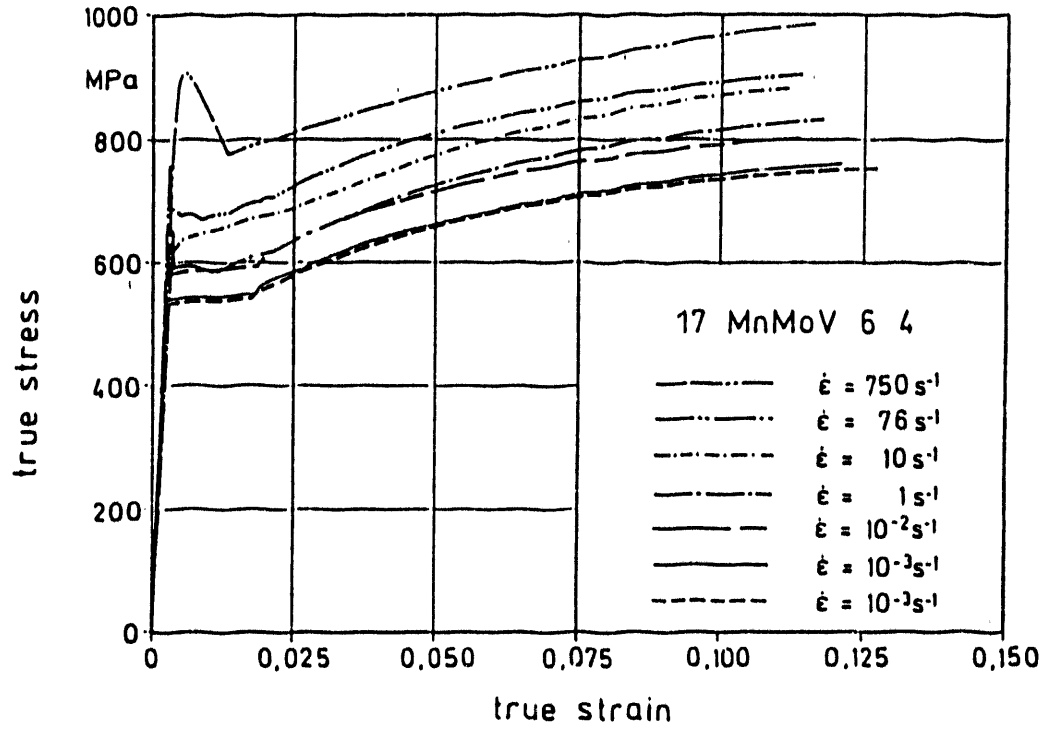

Fig. 6: True stress-true strain curves for the material 17 MnMoV 6 4

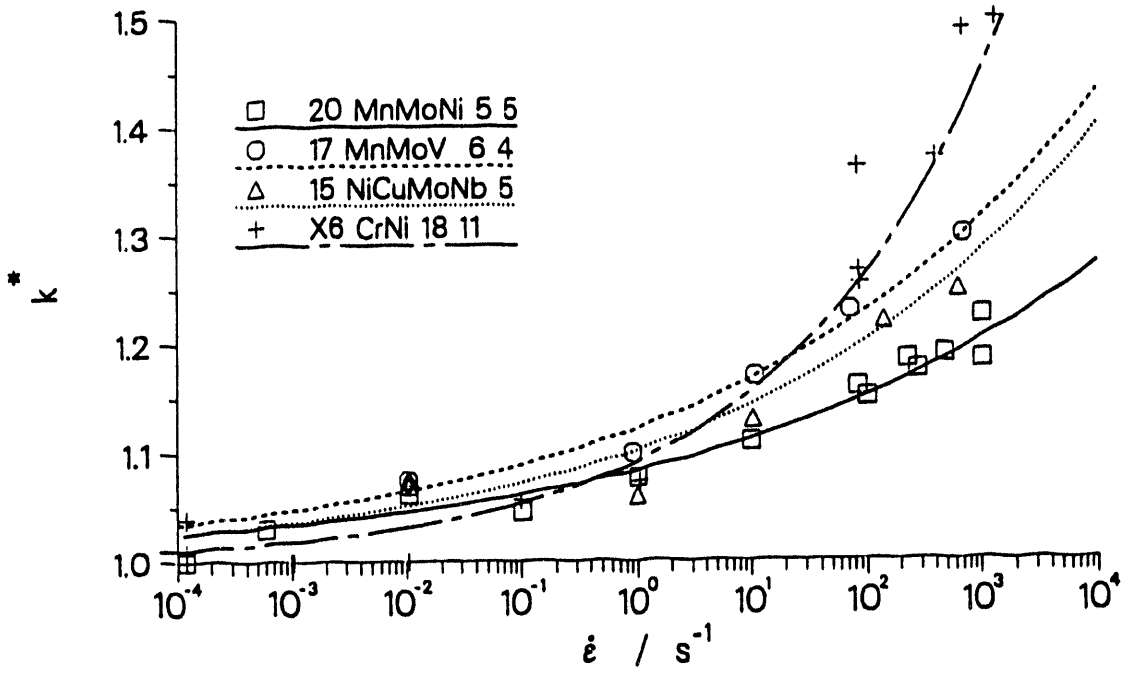

Fig. 7: Approximation for the strain-rate-dependence of the flow stress

material	$R_{e\ stat}$ ($R_{p0,2}$) N/mm²	$R_{m\ stat}$ N/mm²	D s^{-1}	p
20 MnMoNi 5 5	530	658	2.27×10^8	7.74
17 MnMo V 6 4	520	690	4.54×10^6	7.29
15 NiCuMoNb 5	574	730	4.70×10^6	6.73
X6 CrNi 18 11	280	590	3.19×10^4	4.33

Table 3: Parameters for the quasi-static and dynamic material characterization

vice versa (Fig. 7) as shown for a variety of materials in earlier investigations /2/. The characteristic of the rate sensitivity is similar for all the ferritic steels, the austenitic steel shows a stronger increase of flow stress at strain rates greater than 10 s^{-1}.

3 Determination of crack initiation and crack resistance curves with small-scale specimens

Quasi-static tests according to the method of partial unloading were compared with dynamic tests with compact tension specimens (Fig. 8) with a thickness of 10 mm (pipe materials with wall thicknesses of less than 20 mm) and 25 mm and three-point-bend specimens of Charpy-V-notch specimen size. All specimens had a crack depth ratio of 0.5 to 0.6 and fatigue cracks. A number of CT-specimens with eroded "crack" front (notch radius R = 0.15 mm) served for comparison with the large-scale specimen which also had eroded notches of the same radius. The instrumentation of the compact tension specimens comprised strain gauges attached to the bottom and top faces of the specimens for load measurement. This method was optimized for elastic-plastic material behaviour /2/. Quasi-statically determined calibration functions showed a linear relationship between measured strain and load for the ferritic steel. For the austenitic steel the load was calculated via a calibration function which was determined by a quasi-static experiment and was modified by means of dynamic finite element calculations /7/. Crack opening displacement was measured by an opto-electronic extensometer /6,7/. The time of crack initiation was determined from the signal of a strain gauge near the crack tip which shows a significant drop after changing the slope of increase (Fig. 9). The J-integral evaluated according to ASTM E 813-88 at this time is taken as critical value J_i. The quasi-static evaluation by measuring the stretched zone width is described in /10/. Additionally the method of DVM proposed in /11/ was used. The critical J-value is calculated with the aid of a theoretical blunting line.

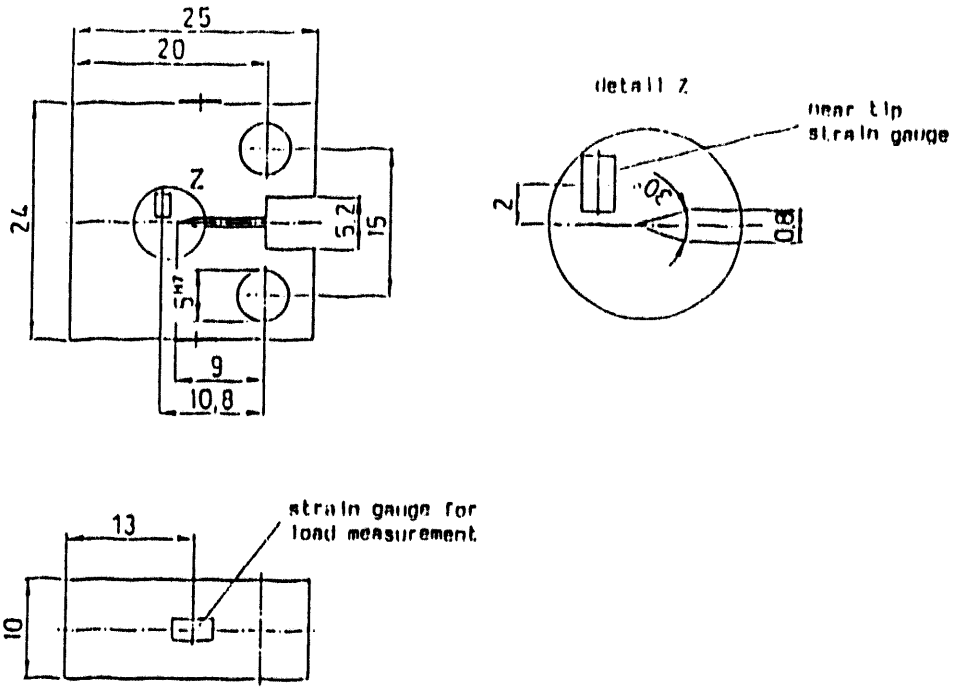

Fig. 8: Compact tension specimen with instrumentation

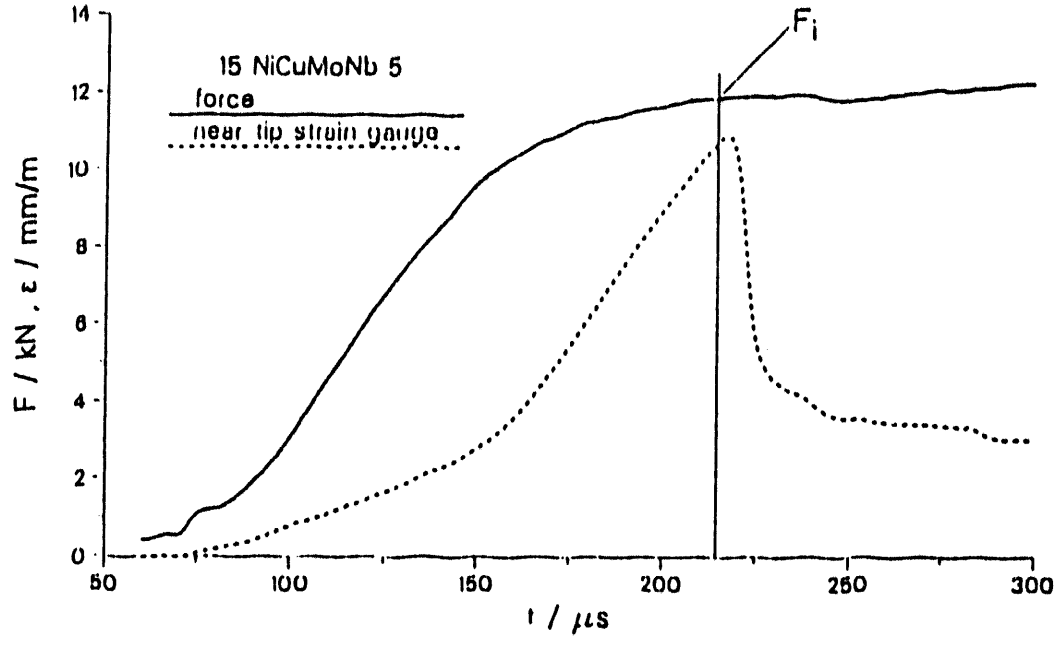

Fig. 9: Strain-time-curve measured by the strain gauge near crack tip and load-time-function of a CT 10 specimen

The calculation of the theoretical blunting lines were performed using the dynamic material characteristics. The three point bend specimens were tested in an inverted impact tester /12/. Crack initiation was determined from the crack opening displacement(COD)-time curve, the COD was measured by means of an optoelectronic sensor /13/.

The relationship

$$K_{IJ} = (J_i \; E \; / \; (1-\mu^2) \;)^{1/2}$$

was used for the calculation of the values shown in the following figures. The time derivative of the stress intensity factor proved to be a useful parameter for the description of the loading rate. Mean values for $\dot{K}$ and $\dot{J}_{pl}$ were determined according to BS 7448. K describes the elastic increase of load and J_{pl} characterizes the loading rate in the plastic range. All the tests showed a similar relationship between $\dot{K}$ and $\dot{J}_{pl}$. Thus K was used as a characteristic parameter for the test.

Ernst et al. /14,15/ proposed a Key-Curve-Method for the determination of crack resistance curves. This method is suitable for the application under dynamic loading. The determination of the key curves by means of finite element analyses applied in /5/ was optimized using calculations considering inertia effects and a strain-rate-dependent material model /7/. The principle is shown in Fig. 10. The comparison of quasi-static and dynamic crack resistance curves showed different results for different materials (Fig. 11). The dynamic J-integral values for the steel 17 MnMoV 6 4 are higher than the quasi-static ones. For the optimized steel 20 MnMoNi 5 5 quasi-static and dynamic J-R-curves lie within the same scatter band.

4 Fracture mechanics analyses of dynamic longitudinal strip tension tests

Specimens machined in longitudinally oriented strips from the pipes made of 15 NiCuMoNb 5 and 17 MnMoV 6 4 were used in a large test program to prove the reliability of evidences for the integrity of structures /16/. Additional tests with strain gauge instrumentation were carried out to determine reliable boundary conditions for the numerical simulations. Besides specimens without defect, the specimens (Fig. 12) tested at a ram speed of 8 m/s disposed of a surface notch or slit. The notch depth to thickness ratio was 0.2 for both geometries. The load measurement by a piezo quartz and a strain gauge dynamometer in the upper specimen grip was controlled by strain gauges attached to the elastic part of the specimen and by quasi-static calibration analogously to the small-scale specimen tests. The results show that the load values measured externally are the same but the force time curve is not exact enough. The crack opening displacement was measured by means

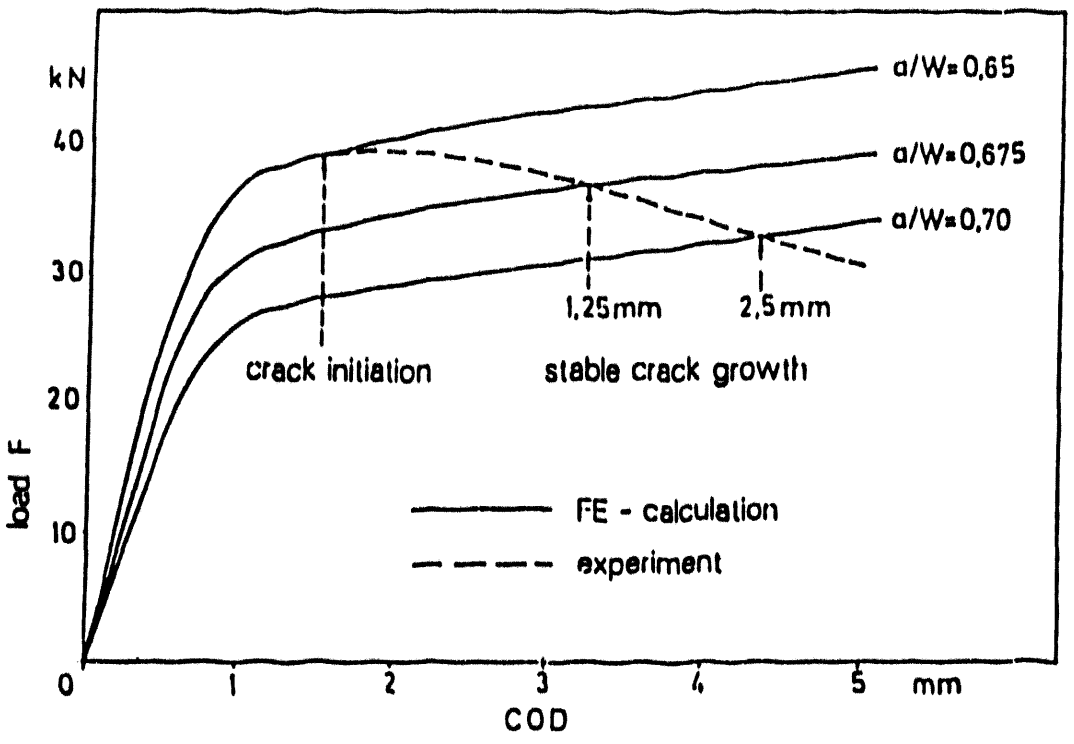

Fig. 10: Principle of the Key-Curve method

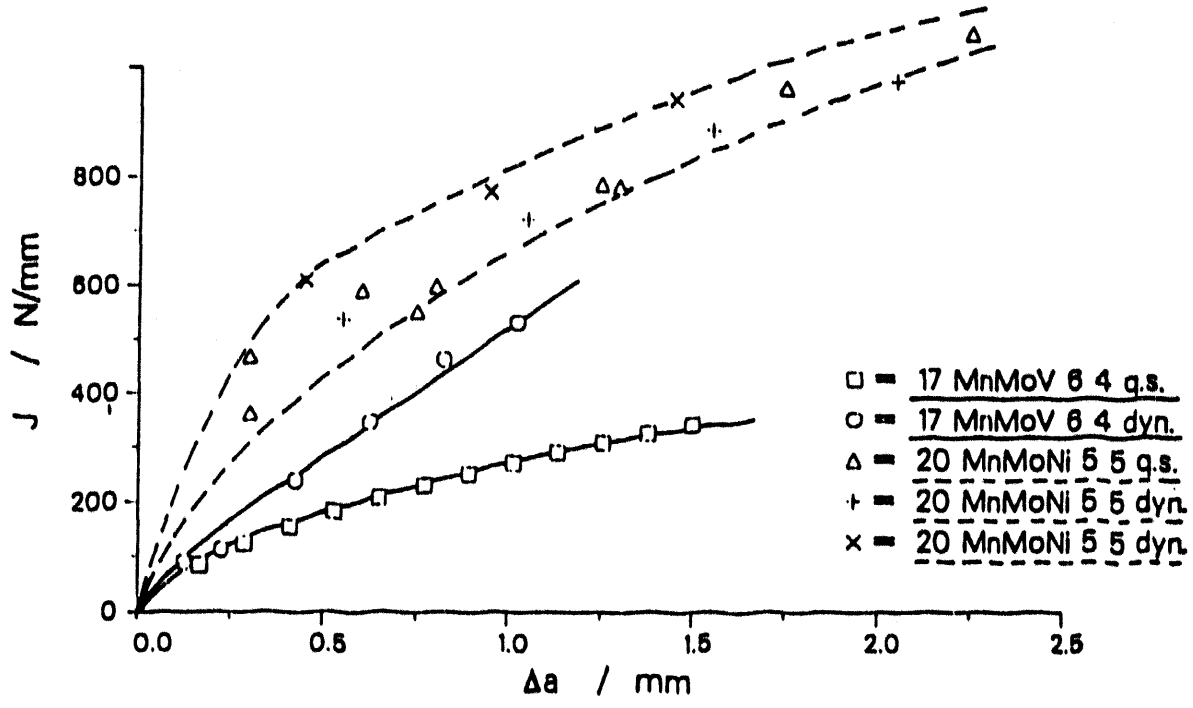

Fig. 11: J-R curves of 17 MnMoV 6 4 and 20 MnMoNi 5 5 under quasi-static and dynamic loading conditions

of an electro-optical extensometer. The specimen elongation measured by an opto-electronic bar code sensor /8/ served as boundary condition for the finite element calculations. Strain gauges in the notch tip area were used to determine crack initiation similar to the CT-specimens.

The finite element calculations were performed with ABAQUS /17/ using an implicit time integration scheme. The dynamic J-integral was determined within the program using the method of virtual crack extension. Due to the symmetry half resp. a quarter of the specimens were modeled with 8 noded isoparametric continuum elements. The comparison of the quarter- and half model (with full length) showed that the inertia effects of the second half of the specimen is negligible. Inertia effects due to the lower specimen grip are included in the boundary conditions. Fig. 13 shows a comparison of measured load and calculated reaction forces for specimens with surface notch and slit. Both types of specimens show the same force--time curve. A good agreement between measured and calculated values even in details is visible. After crack initiation the simulation is not correct any more, because of the missing modelling of the crack propagation. Critical values for crack initiation are determined by the near tip strain gauges. This measuring method is very sensitive and yields lower bound values which are shown in the scatter band in Fig. 14. A second possibility is to take advantage of the difference between measurement and calculation at the onset of crack propagation. This more integral approach yields the upper bound values. The loading rate $\dot{K}$ is determined analogously to the CT-specimens and amounts to 5.0 ... 8.2 x 10^5 MPa$\sqrt{m}$/s. The comparison with small-scale specimen results in Fig. 14 shows the conservativity of these values. The material 15 NiCuMoNb 5 (WB36) shows higher values at small- and large-scale tests than the material 17 MnMoV 6 4 (WB35) as expected from the technological material data. The results of the small-scale tests show a slight increase with increasing loading rate. The initiation values determined for notched CT-specimens are higher than those found for fatigue precracked ones. The difference is more significant for the material 17 MnMoV 6 4. The values determined by means of the theoretical blunting line (designated with DVM) are higher for notched specimens and agree with the results of the crack tip gauge method for fatigue precracked specimens. At high loading rates (> 10^6 MPa$\sqrt{m}$/s) the specimens with fatigue crack of both materials show a decrease of K_{IJ}. An increasing part of brittle fracture can be found at the fracture surface of these specimens. This shows that the transition temperature is reached at these loading rates. The fracture surfaces of the strip specimens and notched CT-specimens do not show any cleavage fracture. A more detailed comparison of transition temperatures /18/ for the material 17 MnMoV 6 4 is presented in Fig. 15.

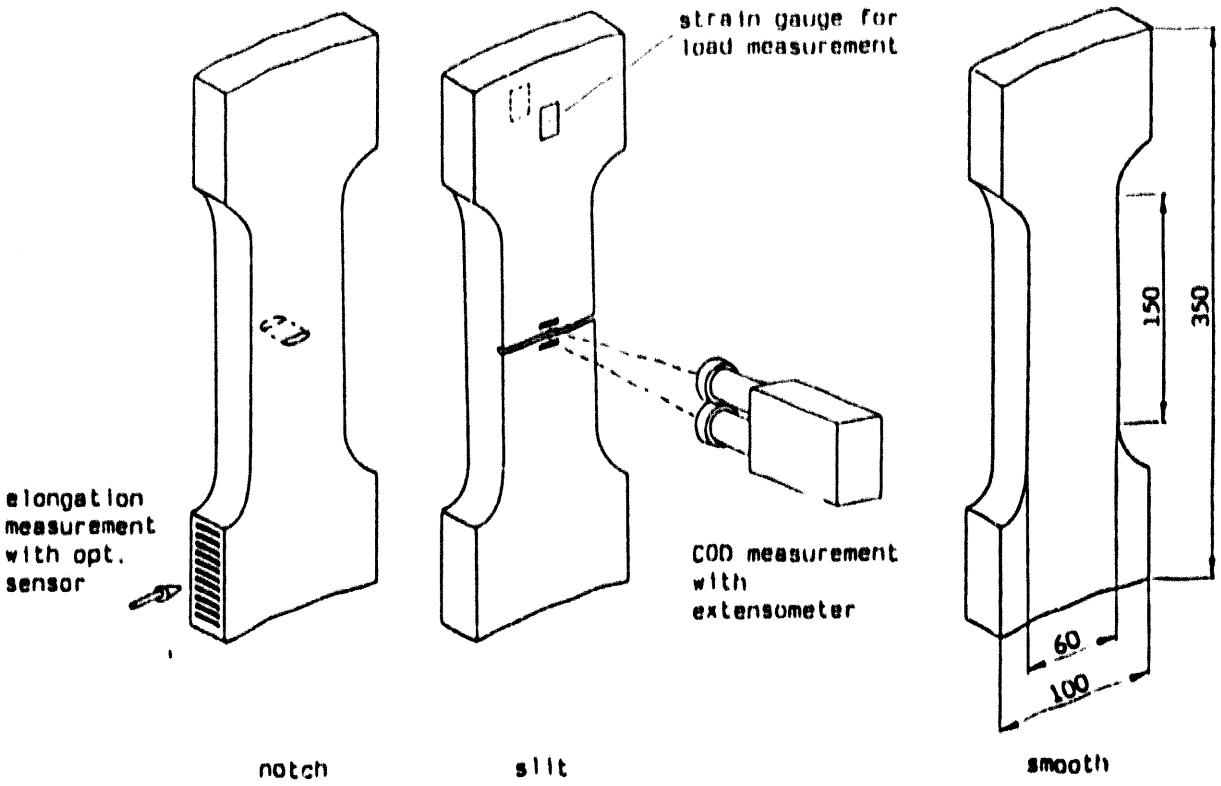

Fig. 12: Specimens machined in longitudinally oriented stripes from a pipe

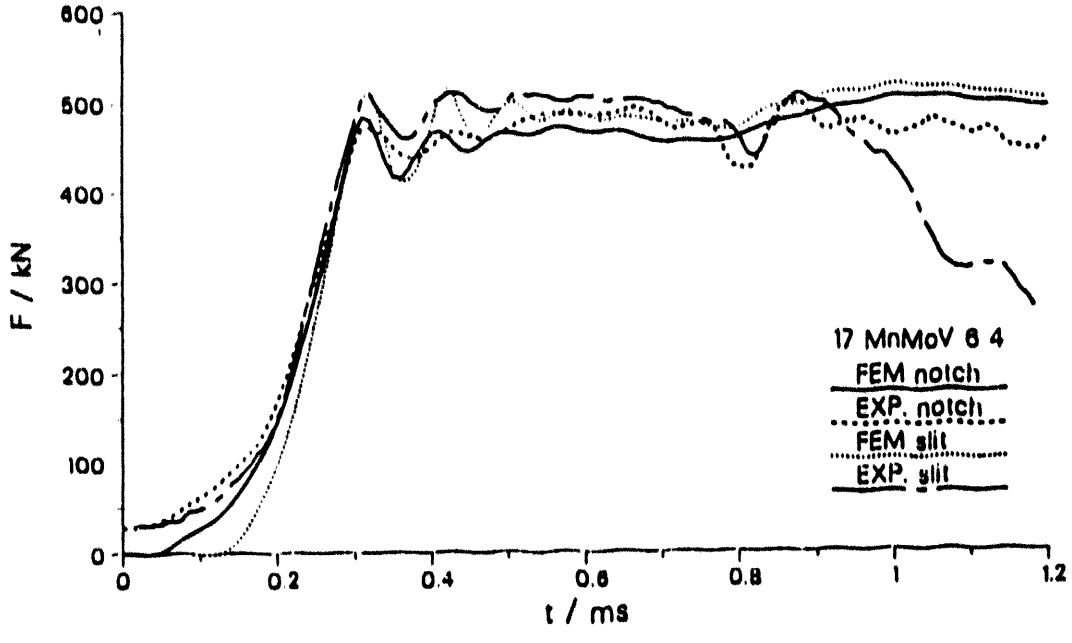

Fig. 13: Comparison of measured load and calculated reaction forces for specimens with surface notch and slit

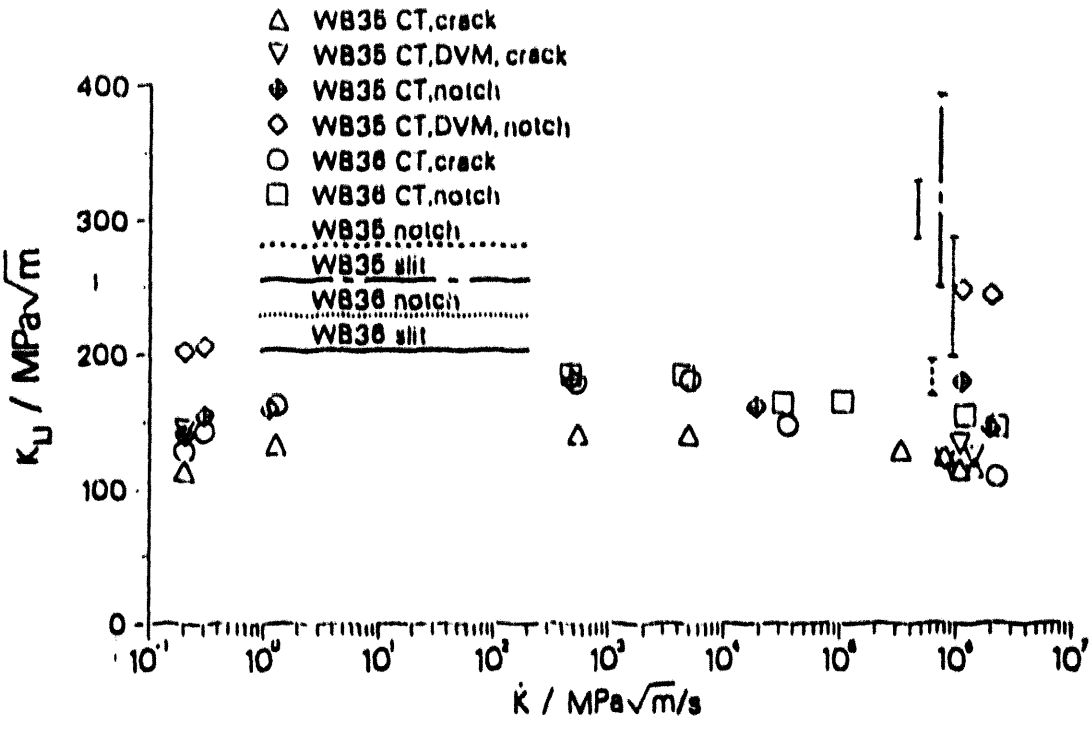

Fig. 14: K_{IJ}-values as a function of loading rate for small- and large-scale specimens

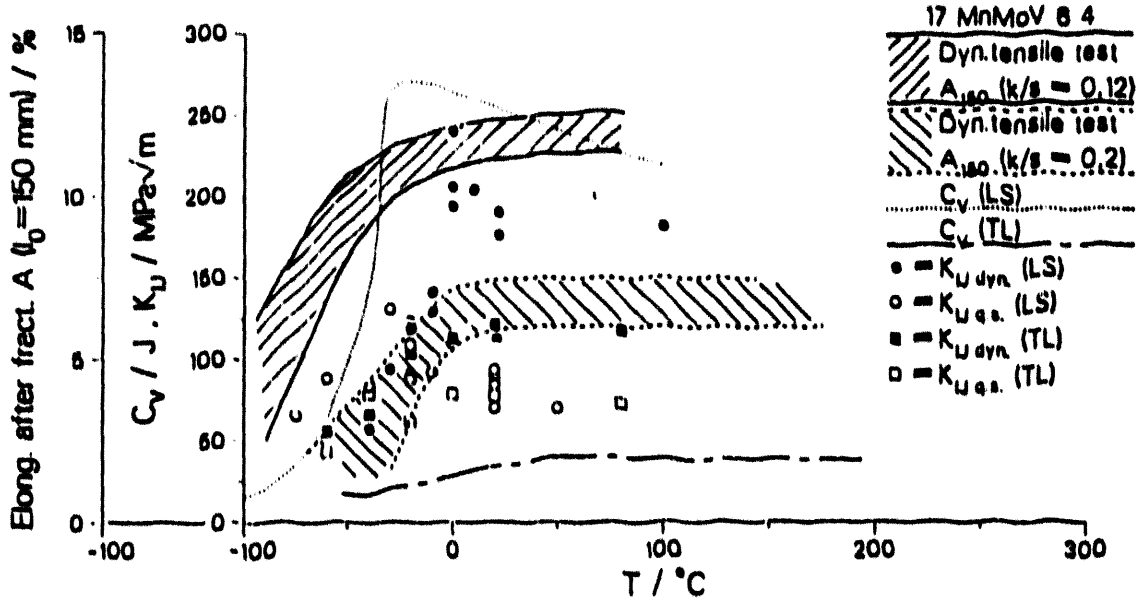

Fig. 15: Comparison of transition temperatures

Emanating from the Charpy V-notch impact energy with a transition temperature of -40 °C (orientation LS) resp. -10 °C (orientation LT and TL) the transition temperature of quasi-static fracture mechanics values is shifted to lower temperatures by about 40 K, that of the dynamic fracture mechanics values to higher temperatures by about 20 K. Elongation after fracture of the dynamic strip tension tests /16/ is shown in Fig. 15. The elongation determined for a notch depth ratio of 0.2 has the same transition temperature as the Charpy energy. The transition determined for a ratio of 0.12 is shifted to -80 °C. These specimens show nearly the same results than smooth specimens.

5 Numerical simulation of the dynamic wide plate tests

Quasi-static and dynamic tensile tests /19/ with wide plates made of the austenitic steel X6 CrNi 18 11 (Fig. 16) were simulated numerically. The simulation was done for plates without defects as well as plates with surface notches of length 21 = 60 mm and a depth of 4 mm and slits of length 21 = 60 mm. The radius of the eroded notches was 0.15 mm. ABAQUS /17/ with implicit time integration was used. Two- and three-dimensional models consist of isoparametric continuum elements. Fig. 16 shows the model of the plate with slit exemplarily. The strain-rate-dependence described in section 2 was used. The experimentally determined displacements of the accelerated specimen grips were prescribed as boundary conditions. The discretization could be qualified using the quasi-static calculations and the calculation of the smooth specimen.

A prerequisite for using numerically determined fracture mechanics parameters is a good agreement of experimental and numerical data. As already found for the smooth plate forces and strains coincide well for the plates with defects. Fig.17 presents the longitudinal strain-time curves of a wide plate with slit. The strain in loading direction was measured by means of strain gauges at 4 measuring points on the upper (1 and 3) and lower (2 and 4) surface of the specimen. In the load-strain-curve (Fig. 18) the pure time shift is eliminated. Up to a strain of 5 % the numerically determined course concurs with the experiment. The beginning of stable crack growth was determined experimentally by the potential drop method /19/, Table 4. Stable crack growth occurs before the numerically and experimentally determined time courses diverge. Thus the specimen behaviour of the plate with slit can be said to change at higher amounts of crack growth only. Within the ABAQUS program the J-integral is determined with the method of virtual crack extension under consideration of dynamic terms. In Fig. 19 the load of the plate with slit versus the numerically determined J-integral is plotted. The value at the onset of stable crack growth is marked and shown in Table 4.

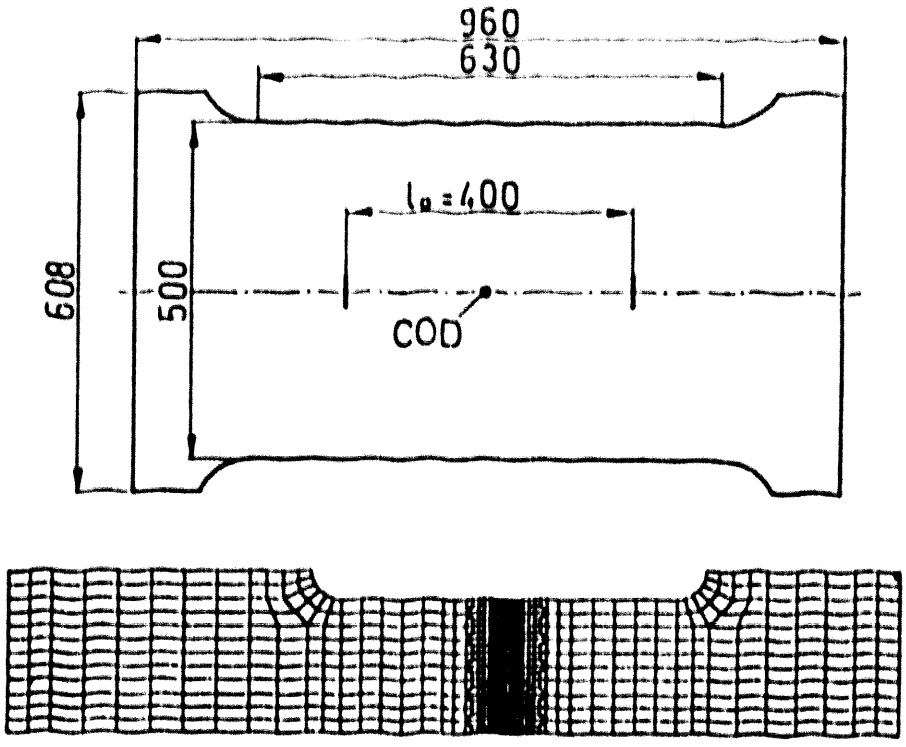

Fig. 16: Wide plate and finite element model

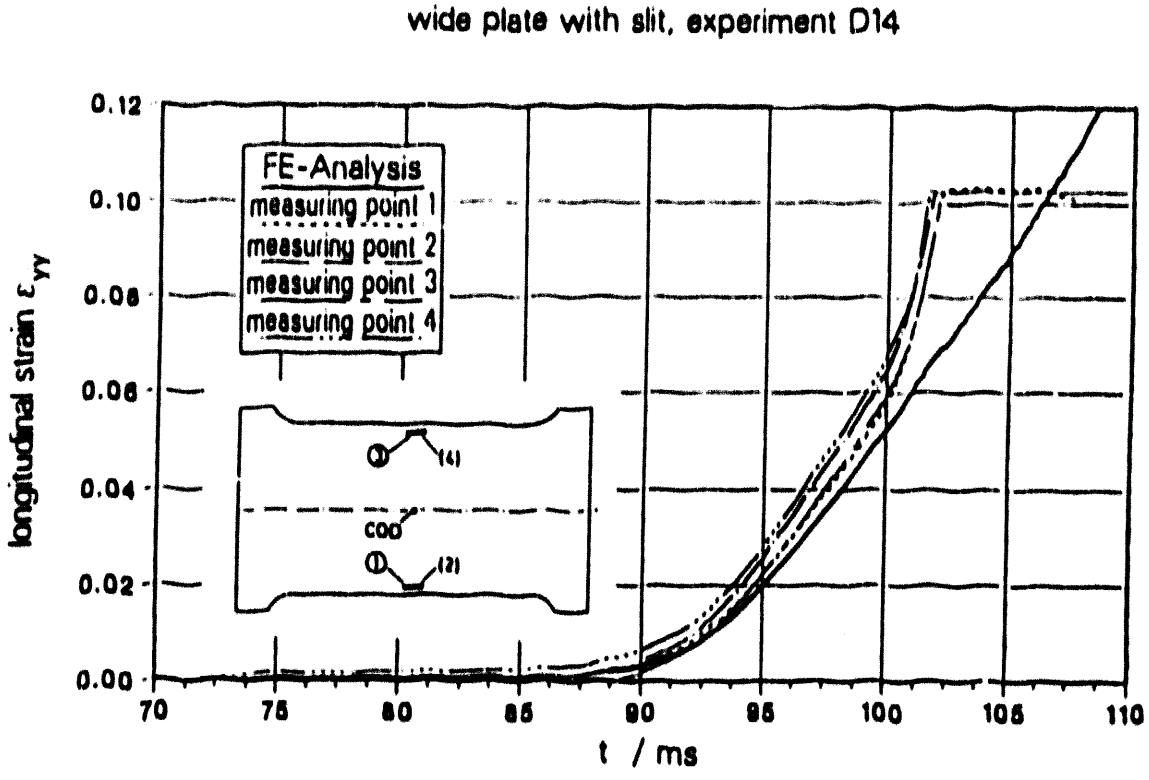

Fig. 17: Experimentally and numerically determined longitudinal strain versus time for the plate with slit

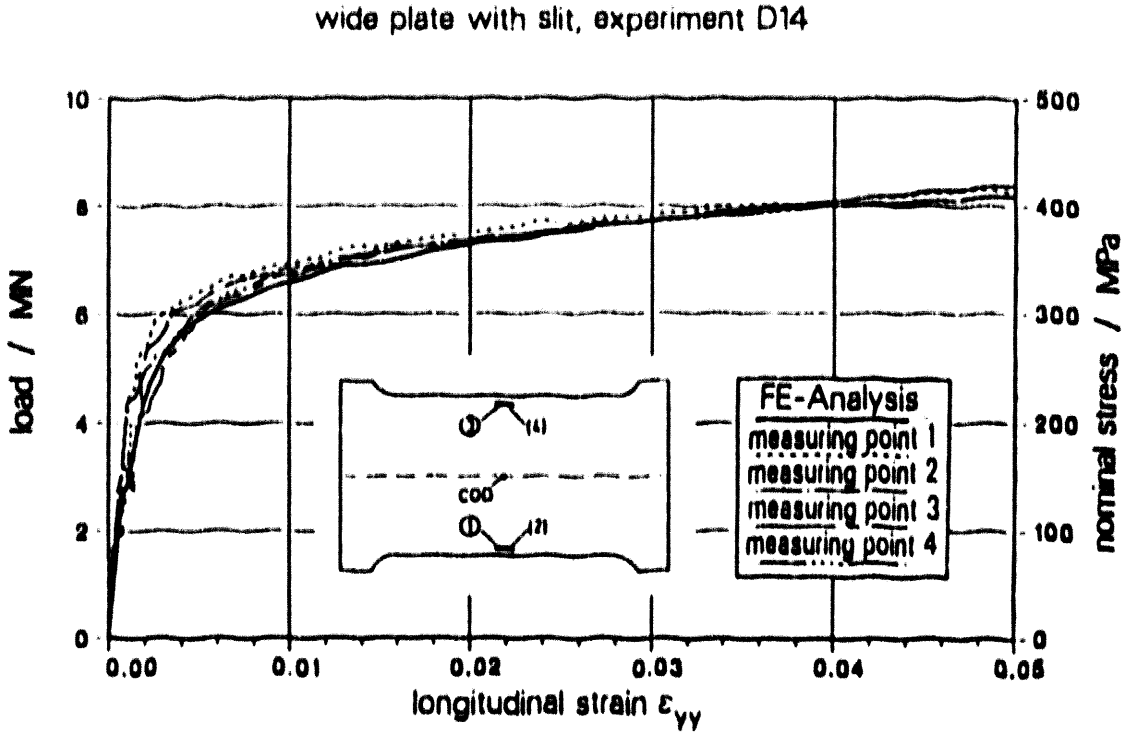

Fig. 18: Load versus longitudinal strain for the plate with slit

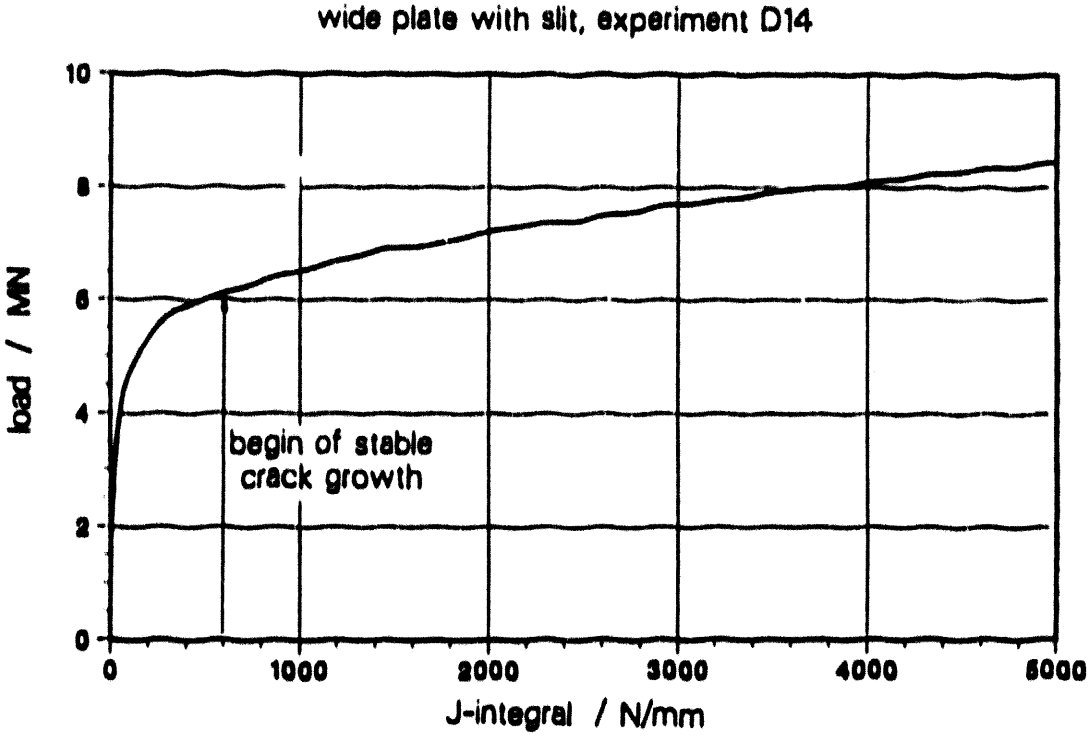

Fig. 19: J-integral for the plate with slit

Experiment	defec	load F MN	time t ms	COD mm	J N/mm
D14	slit	6.2	89.7	1.8	580
D13	surface notch	9.1	41.4	2.1	420

Table 4: Numerically and experimentally determined values for the onset of stable crack growth

The simulation results for the plate with surface notch deviate from the experimental values nearly at the same time as determined by the potential drop method. The J-integral value increases along the notch front and has a maximum at position 1, Fig. 20. The value in table 4 is determined at this position.

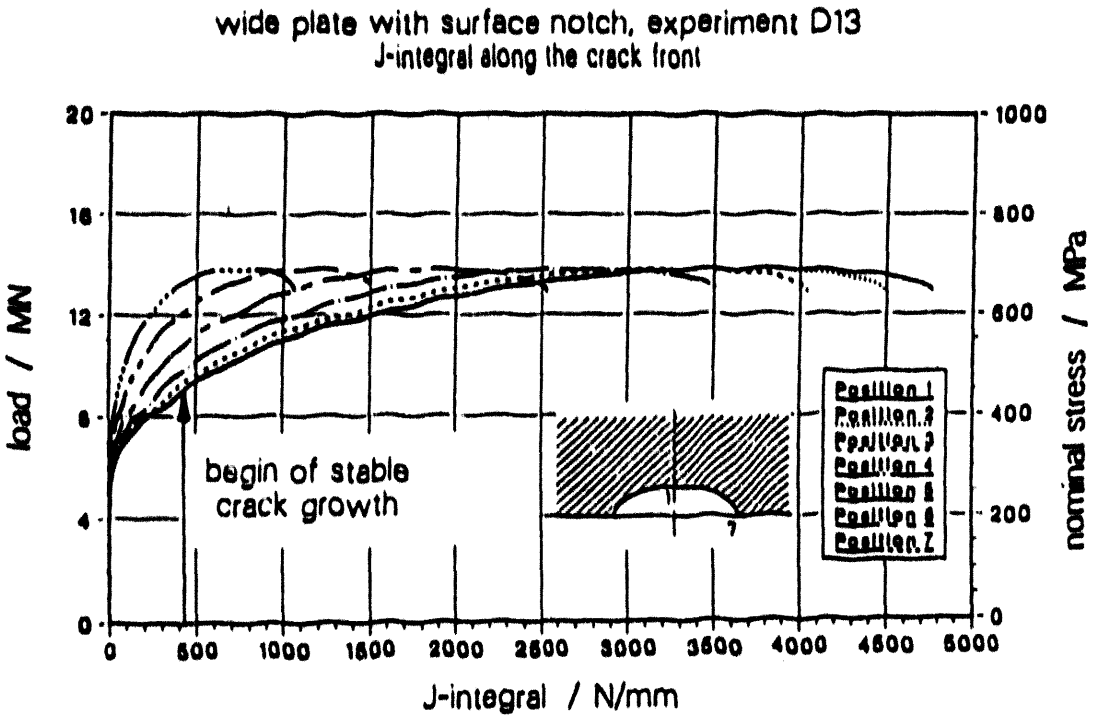

Fig. 20: J-integral along the notch front for the plate with surface notch

6 Conclusions

The dynamic finite element simulations revealed that it is possible to determine fracture mechanics data for dynamic large-scale tests which can be compared with results from small-scale tests. Further evaluations will be made to compare the results with engineering approaches and to prove their applicability to numerical simulations of components.

7 Acknowledgements

The work was financially supported by the Federal Minister for Research and Technology and the Federal Minister for Environment, Nature conservation and Nuclear Safety.
The dynamic tests with three point bend specimens were carried out at the Technical Research Center (VTT), Espoo, Finland.

8 References

/1/ Kußmaul, K.
A Total Structural Integrity Approach to the Fracture Safe Design of Light Water Reactor Pressure Vessels (LW-RPV), ASME Winter Annual Meeting, Atlanta, USA, 27.11.-2.12.1977

/2/ Kußmaul, K. and T. Demler
The Effect of Loading Rate on the Strength and Toughness of Fine-Grained Structural Steels
to be published in Steel Research

/3/ Roos, E., T. Demler, U. Eisele and R. Gillot
Fracture Mechanics Safety Assessment Based on Mechanics of Materials
Steel Research 61, 1990, pp. 172-180

/4/ Hesse, W., K. Brüninghaus and W. Dahl
Yielding and Fracture Behaviour of Fierritic Steels in the Transition Region of Quasistatic to Dynamic Loadin
Nucl.Eng.Des. 96 (1986), pp. 167-172

/5/ Brüninghaus, K., J. Falk, M. Twickler, R. Twickler and W. Dahl
Effect of Loading Rate on Upper Shelf Crack Resistance of Structural Steels with Different Yield Strength and Microstructure
Nucl.Eng.Des. 127 (1991) No. 1, pp. 95-102

/6/ Kußmaul, K., M. Schüle and A. Seibold
Investigations on the Transferability of Fracture Mechanics Parameters under Dynamic Loading
to be published in Nucl.Eng.Des.

/7/ Kußmaul, K., T. Link, A. Klenk and T. Nguyen-Huy
Determination of Crack Initiation and Crack Resistance Using Compact Specimens and Comparison with Results of Numerical Simulations of Dynamically Loaded Wide Plates
to be published in Nucl.Eng.Des.

/8/ Kußmaul, K., T. Demler and A. Klenk
Advanced Testing Methods for Rotating Disk Impact Machines
Int.Phys.Conf.Ser. No.102, Session 4, pp.157-164

/9/ Kußmaul, K., A. Klenk, M. Schüle and H. Klamser
Development and Validation of a Simulation Method for Dynamic Tensile and Fracture Tests Using Explicit and Implicit Finite Element Codes
Journ.de Physique IV, Colloque C3, Vol. 1, 1991, pp. C3-821 - C3-828

/10/ Roos, E. and U. Eisele
Determination of Material Characteristic Values in Elastic-Plastic Fracture Mechanics by Means of J-Integral Crack Resistance Curves
Journ.Test.Eval. 16 (1988), pp. 1-11

/11/ Deutscher Verband für Materialprüfung e.V. (DVM):
Ermittlung von Rinßinitiierungswerten und Rißwiderstandskurven bei Anwendung des J-Integrals
DVM-Merkblatt 002, 1987

/12/ Rintamaa, R., K. Rahka, K. Wallin, K. Ikonen, H. Talja, H. Kotilainen and E. Sirkkola
Instrumented Impact Testing Machine with Reduced Specimen Oscillation Effects

/13/ Rintamaa, R. and C. Zimmermann
Advanced Instrumented Impact Testing Facility for Characterization of Dynamic Fracture Behaviour
Nucl.Eng.Des. 96 (1986) No.2 and 3, pp. 159-166

/14/ Ernst, H. et al.
Analysis of Load-Displacement Relationship to determine J-R curve and Tearing Instability Material Properties
ASTM STP 677, 1979, pp 581-599

/15/ Ernst, H. et al.
Estimations on J-Integral and Tearing Modulus T form a Single Specimen Test Record
ASTM STP 743, 1981, pp. 476-502

/16/ Absicherungsprogramm zum Integritätsnachweis von Bauteilen
Zusammenfassender Bericht mit Bewertung,
MPA Stuttgart, 1989

/17/ ABAQUS User's Manual, Version 4.9, Hibbitt, Karlsson & Sorensen Inc., 1991

/18/ Klenk, A., R. Rintamaa, M. Schüle and K. Wallin
Fracture Mechanics Investigations at Different Loading Rates Using Three-Point-Bend and Compact-Tension Specimens
to be published in Nucl.Eng.Des.

/19/ Julisch,P., H.-J. Hädrich, W. Stadtmüller and D. Sturm
Dynamic Large Scale Testing with a 12 MN High-Speed Propellant Driven Tensile Testing Machine
IAEA-Specialists' Meeting on Large Scale Testing,
May 25-27, 1988, Stuttgart

EFFECT OF BIAXIAL LOADING ON THE FRACTURE BEHAVIOUR OF A FERRITIC STEEL COMPONENT

Mr D J Wright, Mr J K Sharples, Mr L Gardner

ABSTRACT

The effect of biaxial loading on the ductile tearing behaviour of a through-wall crack in a ferritic steel structure under contained yield is of particular interest to the structural integrity argument for reactor pressure vessels. This results from the fact that there are many instances in practice, (for example a crack in a circumferential weld), where a significant applied stress is present in the direction parallel to the crack as well as in the perpendicular direction.

Two large plate ductile tearing tests have been performed on centre through-crack specimens (75 mm by 2 m by 2 m) manufactured from a ferritic steel. The first test specimen was loaded in uniaxial tension and the second test specimen was loaded biaxially. This paper presents experimental details and results of the two wide plate tests and describes the analysis work being undertaken which is required to interpret the experiments satisfactorily. Preliminary results of this analysis work are presented.

AEA Technology, AEA Reactor Services, Risley, Warrington WA3 6AT

1. INTRODUCTION

Pressure vessels by their very nature are subjected to biaxial stress fields. In assessing the significance of a known or postulated flaw in the circumferential direction of a vessel, the contribution to the fracture process of the hoop stress, parallel to the crack, having a magnitude twice the value of the longitudinal, crack opening, stress is currently not properly understood. The R6 method (1) is used in the UK nuclear industry and elsewhere for carrying out such fracture assessment work. Although some guidance is given in this procedure for evaluating limit loads for a biaxial stress field, no account of the stress parallel to the crack is available for fracture toughness data.

In order to examine the influence of biaxial loading on fracture behaviour, AEA Technology has carried out two wide plate tests in the Structural Features Test Facility at Risley. The tests were performed on centre through-crack specimens manufactured from renormalised 0.36% carbon steel, employing a geometry of plate sufficient to provide contained yield conditions in the uncracked ligaments. The first test specimen, designated GNSR1.0U, was loaded in uniaxial tension. The second, designated GNSR1.0B, was loaded in biaxial tension with the higher load acting parallel to the crack to maximise biaxiality effects. Both tests were conducted at an upper shelf temperature of 100°C.

This paper presents the experimental details and results of the two wide plate tests and describes the analysis work being undertaken which is required to interpret the experiments satisfactorily. Preliminary results of this analysis work are presented.

2. EXPERIMENTAL DETAILS

2.1 Test Specimen Design

The two test specimens were manufactured from a renormalised 0.36% carbon steel plate. In each case the specimen was fabricated from two parent plates welded together to give the required width. The dimensions of the uniaxial specimen were 2.3 m by 1.8 m by 75 mm (Fig 1), and the dimensions of the biaxial specimen were 2.5 m by 1.8 m by 75 mm (Fig 2). The effective width of the biaxial specimen after manufacture was 2.3 m, consistent with the uniaxial specimen. Each test plate contained a centrally machined through-thickness crack, 1.15 m in length lying across the seam weld in the test plates. The crack tips were generated with a saw cut and then sharpened by fatigue cycling.

The uniaxial specimen, GNSR 1.0U, was welded between two cast steel cross-heads (Fig 1). The cross-heads were then cut through to the plate in four places to allow unrestricted crack opening along the crack length. In the test, this was achieved by loading each of the equally sized segments in the crosshead independently with five pairs of hydraulic actuators.

The biaxial specimen, GNSR 1.0B, was welded between four cast steel cross-heads (Fig 2) and, in the same way as 1.0U, saw cuts were made through to the test plate. The four corners of the 1.0B specimen were machined to a 100 mm radius and the saw cuts in the cross-heads running parallel to the crack were extended by 100 mm into the plate thus providing a test plate geometry consistent with 1.0U.

2.2 Test Facilities

The 100 MN wide plate rig (Fig 3) in the Structural Features Test Facility at Risley was used to execute both tests. The machine, weighing more than 600 tonnes, has the capability of applying loads up to 100 MN uniaxially or to apply loads biaxially up to 50 MN on each axis. The rig is a multi actuator machine offering twenty 5MN hydraulic actuators with a stroke of 300 mm each. Each actuator is served by a high response two stage servo valve and controlled by state of the art three term controllers. The 20 controllers are grouped into pairs and run from a central computer. The two actuators in a pair are those from either side of the test plate, loading through the same cross-head segment. The control software has been designed to make each actuator pair behave as a single actuator to minimise unwanted bending in the test plate. This effect is achieved by maintaining a fixed total load in each actuator pair but keeping the two displacements the same. When the rig is operated in this fashion the control is said to be in group mode.

Load is transferred from the hydraulic actuators to the test plate via a series of loading beams. There are ten uniaxial beams, designed to carry two or four actuators in pairs horizontally. The ten biaxial beams accept two actuators running vertically. Each of the loading beams are bolted to a single cross-head segment with a pair of actuators mounted across the plate and between the beams as indicated in Figures 4 and 5.

The test plate, cast steel cross-heads, hydraulic actuators, loading beams, and instrumentation form the complete test assembly which is supported by the bottom uniaxial beams sitting on four rollers. This decouples the assembly from the rest of the machine and gives total freedom for both horizontal and vertical displacement of the test plate.

2.3 Instrumentation

Each of the twenty hydraulic actuators is equipped with a strain gauge full bridge load cell calibrated to 0.1% FSD.

An array of 27 strain gauge rosettes and 13 single strain gauges was used on test GNSR 1.0U. The gauges were compensated for mild steel and had an active length of 2 mm. Figures 6 shows the strain gauge pattern adopted during the test to measure plate strains for comparison with the theoretical analysis and allow a yield criterion to be applied when necessary. Test GNSR 1.0B had five extra rosettes to allow for a plastic zone extension moving away from the 45° lines extending from the crack tip as occurs under uniaxial loading, Figure 7.

Thirteen displacement transducers of the potentiometric type were fitted to GNSR 1.0U as shown in Figure 8, to monitor displacement perpendicular to the crack. Seventeen displacement transducers were used for the GNSR 1.0B test, Figure 9; the four additional to GNSR 1.0U were mounted parallel to the crack.

The remaining instrumentation for crack growth and temperature monitoring was identical in both uniaxial and biaxial tests. The data logging system was also a common feature.

Crack growth was monitored by the alternating current potential difference (ACPD) technique using probes fitted as shown in Figure 10. Remote visual

observations of the notch tips on either side of the plate was carried out continuously during the fracture test using video cameras with the images recorded on tape. Still photography was also used to capture details of surface crack extension.

Temperature was maintained at 100°C throughout the fracture tests, to ensure ductile behaviour, using twelve flat plate heater elements arranged so as to generate a uniform temperature. Temperature was monitored and controlled from eight thermocouples.

2.4 Test Procedure

Both tests followed the same procedure for establishing a fatigue crack, approximately 5 mm long, from each of the machined notch tips before the ductile tearing test was undertaken. Fatigue crack sharpening was carried out using a loading cycle having a corresponding stress intensity factor range ΔK_I, of approximately 25 MPa$\sqrt{m}$. With a through crack geometry, the crack tip plastic zone was therefore minimal. The cyclic load was applied at ambient temperature and in the case of GNSR 1.0B, using only the horizontal hydraulic actuators.

For GNSR 1.0U, the ductile tearing test consisted of a monotonic slow ramp increase in the applied tensile force, uniformly distributed across the plate width through the five pairs of actuators. The ramp rate was 50 KN/actuator/minute. The actuators were operated in group mode as described earlier and the total applied load was allowed to peak at 18.4 MN before the specimen was unloaded. The criteria for termination of the test was based on maintaining contained yield conditions for an applied load up to 80% of the theoretically predicted limit load.

Test GNSR 1.0B was loaded with a monotonic slow ramp tensile force, in both the vertical and horizontal actuators. The ratio between the crack opening horizontal force and the vertical force in line with the crack was fixed at 1:1.35. This ratio was evaluated to give a crack tip stress field similar to that of an infinitely large plate. The horizontal load peaked at 17.5 MN before the specimen was unloaded. The same criteria used for terminating the GNSR 1.0U test was again employed here.

A computer controlled data acquisition system was used to monitor and record all the instrumentation signals during the two tests. In addition, an on-line computer graphics display of selected data was available to assist in the assessment of plate behaviour and crack extension.

On completion of the tests, the specimen crack tip sections were broken open to permit measurement of the crack extension.

3. EXPERIMENTAL RESULTS

Displacements and strains were carefully monitored throughout the test to assess whether any significant in-plane or out-of-plane bending was evident in the test plates. This in fact confirmed that a small degree of bending had occurred in both test plates but it was considered that this would have no significant effect on the test results. An example of this bending is shown in Figure 11 where displacements from transducers 6, 10, 12 and 13 are presented.

Assessing crack growth initiation using ACPD is not a simple task in elastic-plastic fracture. This is due to the uncertainties associated with isolating crack growth induced changes in PD from those due to stress. Nevertheless, significant work, so far unpublished, undertaken in the UK in recent years has enabled crack initiation to be monitored by ACPD with a high degree of confidence in large scale structural tests of ferritic steel specimens of the type under consideration in the present study. The ACPD plots all exhibited typical features of response during fracture testing on ferritic materials. An example is given in Figure 12, taken from the GNSR/1.0U test. During initial loading, a sharp increase in voltage occurred which corresponded to the unbutting of the fatigue crack surfaces at each end of the machined defect. This phase was complete at about 4MN applied load. The increase due to crack opening was followed by a reduction in the ACPD with increasing load caused by the effect of material straining on the conducting skin depth. This effect eventually saturated and the subsequent increase in voltage may be attributed to crack growth.

By careful processing of the ACPD results therefore, the initiation load for the uniaxial GNSR/1.0U test was evaluated to be between 15.5 MN and 16 MN at the upper crack tip and 13.5 MN at the lower crack tip. In the same way, the initiation load (in the horizontal direction perpendicular to the plane of the crack) for the biaxial GNSR/1.0B test was evaluated to be 15.5 MN at the upper crack tip and 16 MN at the lower crack tip.

After the specimens had been broken open, it was evident that some crack "tunnelling" had occurred at each of the four crack tips. The nine point weighted average values of ductile tearing for the GNSR/1.U test specimen were 3.5mm and 5.3mm at the upper and lower tips respectively. The corresponding values for the GNSR/1.0B specimen were 3.2mm (upper crack tip) and 1.3mm (lower crack tip).

4. FINITE ELEMENT ANALYSIS

A programme of elastic-plastic finite element stress analysis is currently being performed for both GNSR/1.0U and GNSR/1.0B test specimens using the ABAQUS code (2). The edges of the GNSR/1.0U specimen were welded via 100mm thick transition pieces to loading heads which were slotted to form five independent sections (Figure 1). Equal loads were applied to each section, enabling what approximates to a uniform distributed load to be applied to the specimen. The loading head slots stop approximately 50mm short of the actual specimen. An initial finite element model therefore included a strip 100mm thick and 50mm high across the "top" of the model to which the uniform load was applied.

Figure 13 shows the mesh used initially for the GNSR/1.0U analysis. The mesh, which consisted of second order (eight-noded) quadrilateral plane stress elements with reduced integration, modelled only a quarter of the specimen assuming geometric and material symmetry about two axes. The mesh was refined in the crack tip region and extending away from this at 45 degrees, the expected direction of the spread of plasticity with increasing applied load. The crack length modelled was 1.15m which was that in the experiment prior to the fatigue crack growth.

As with more sophisticated meshes currently being developed, the initial mesh referred to in Figure 13 was designed so that as many nodes as possible would coincide with strain gauge and displacement transducer

locations so that output could be compared directly with the test results. These locations are indicated in Figure 13.

The same mesh as shown in Figure 13 was used for the initial finite element analysis of the GNSR/1.0B test plate. This time of course, the loading was applied in the direction parallel to the crack, as well as perpendicular to the crack, in order to model the biaxial loading with the required load ratio of 1.35. As may be noted from Figure 3, the loading parallel to the crack in the GNSR/1.0B specimen was not distributed over the entire edge of the plate and this was allowed for in the modelling.

Figure 14 gives an example of strain results compared with those obtained experimentally for GNSR/1.0U for the direction perpendicular to the crack. Reasonably good agreement is shown between the experimental and finite element calculated values.

Figure 15 shows applied load (perpendicular to the crack) plotted against the finite element calculated J-integral values obtained for both GNSR/1.0U and GNSR/1.0B specimens. As can be seen, the effect of the biaxial loading is shown to result in the J values being reduced from the uniaxially loaded case of GNSR/1.0U.

The finite element work currently being undertaken as part of this programme models the test plates more accurately by using actual material properties obtained from samples cut from the same plates as the GNSR/1.0U and GNSR/1.0B specimens were manufactured from. Plane strain as well as plane stress analyses are also being considered. This will lead to accurate J-Resistance curves being evaluated by relating the finite element calculated J values to the experimentally determined crack growth versus applied load or plate displacement values for both crack tips in each of the test plates

5. FRACTURE MECHANICS ANALYSIS

R6 Category 3 (1) analyses have been carried out for each of the "crack tips" in the GNSR/1.0U and GNSR/1.0B test plates. The crack growth (Δa) versus applied load predictions obtained by this method were then compared with the experimental results. In all cases, the general Option 1 and mild steel Appendix 8 failure assessment diagrams (FAD's) were employed.

Figure 16 gives an example of an assessment plot. This relates to the bottom crack tip in the GNSR/1.0U plate. (Both the tensile and fracture toughness material properties used in the assessment were obtained from samples cut from the plate relevant to this crack tip).

Crack growth versus applied load "predictions" were obtained by scaling assessment points such as those presented in Figure 16 to the FAD's. In making direct comparisons between the uniaxial test of GNSR/1.0U and the biaxial test of GNSR/1.0B, the bottom crack tip results of the former may be compared with the top crack tip results of the latter, since the material properties for the plates of these two cases were shown to be exactly the same. The GNSR/1.0U specimen was 5mm thicker than the GNSR/1.0B specimen, as it is more meaningful therefore for the comparison to be based on applied nominal stresses rather than applied loads. The results of this comparison are given in Fig 17 which shows crack growth versus applied stress for both the experimental and R6 results. The R6 results for the GNSR/1.0U and GNSR/1.0B specimens are identical when based on applied

stress since no attempt was made to take account of biaxiality for the latter. It can be seen that the "observed" initiation applied stress for GNSR/1.0B was approximately 20% higher than that for GNSR/1.0U. However, the maximum stresses are very similar in the two tests, with that for the biaxial test being slightly higher; 106.7 MPa in GNSR/1.0U for 5.3mm of tearing and 108.7 MPa in GNSR/1.0B for 3.2mm of tearing.

It can be seen that the R6 results conservatively underpredict the applied stress for the amounts of ductile tearing obtained in the tests for the crack tips considered in Figure 17. This was also shown to be the case for the other crack tips (Figures 18 and 19). (Note that for the upper crack tip of GNSR/1.0UB, material specific option 2 and material and geometry specific option 3 analyses were performed. FAD options were also considered, Figure 18). It would seem likely that the conservatism of the R6 results would still apply even if the cracks had been grown up to instability. However, it can be seen from Figure 10, that for the GNSR/1.0U top crack tip, it is likely that the R6 results would be non-conservative for crack extensions of a few millimetres more than was obtained in the test.

Finally, it is worth remembering that all the experimental data points presented in this report have been based only on two results; (i) the initiation load, based on ACPD measurements, and (ii) the maximum load point, based on nine point average measurements taken of the fracture surface. Although this maximum load point measurement is an accurate assessment of the amount of ductile tearing obtained during the tests, further rigorous analysis of the ACPD data will enable more crack growth versus applied load or stress to be obtained by "back-calibrating" from this point.

6. CONCLUSIONS

The following main conclusions may be drawn from the work contained in this report:

1) The initiation applied stress, evaluated by the ACPD method, for the biaxial specimen, GNSR/1.0B, was approximately 20% higher than that for the uniaxial specimen, GNSR/1.0U indicating an effective benefit of biaxial loading.

2) The maximum applied stresses were similar in the two tests with that for the biaxial test being slightly higher than that for the uniaxial test; 106.7 MPa in GNSR/1.0U for 5.3mm of tearing and 108.7 MPa in GNSR/1.0B for 3.2mm of tearing.

3) All the R6 results conservatively underpredicted the applied load for the amounts of ductile tearing obtained in the tests (ie. 3.5mm and 5.3mm in GNSR/1.0U and 3.2mm and 1.3mm in GNSR/1.0B).

4) For the GNSR/1.0U bottom crack tip and both crack tips in GNSR/1.0B, it would seem likely that the conservatism would still apply even if the cracks had been grown up to instability. However, for the GNSR/1.0U top crack tip, it is likely that the R6 results would be non-conservative for crack extensions of a few millimetres more than was obtained at that crack tip in the test.

5) Preliminary elastic-plastic finite element analyses carried out for the test plate designs have shown that the effect of the biaxial loading is to reduce the J-Integral values from the uniaxially loaded case of GNSR/1.0U.

7. ACKNOWLEDGEMENTS

The authors wish to thank the UK Health and Safety Executive for funding the work and for giving permission for the publication of this paper.

The authors also wish to express their gratitude to the following for their valuable technical contribution made to the work contained in this paper:

D Dobson, T J Davenport, P W Winter, S A Fields, R P Birkett and A M Clayton, all of AEA Technology, UK.

8. REFERENCES

1. Milne I, Ainsworth R A, Dowling A R and Stewart A T. (1988) "Assessment Of The Integrity Of Structures Containing Defects". Int Jnl Pressure Vessels & Piping, Vol 32, pp3-105.

2. Hibbitt, Karlsson and Sorensen Inc. ABAQUS Manuals, 100 Medway St, Providence, Rhode Island 02906-4402.

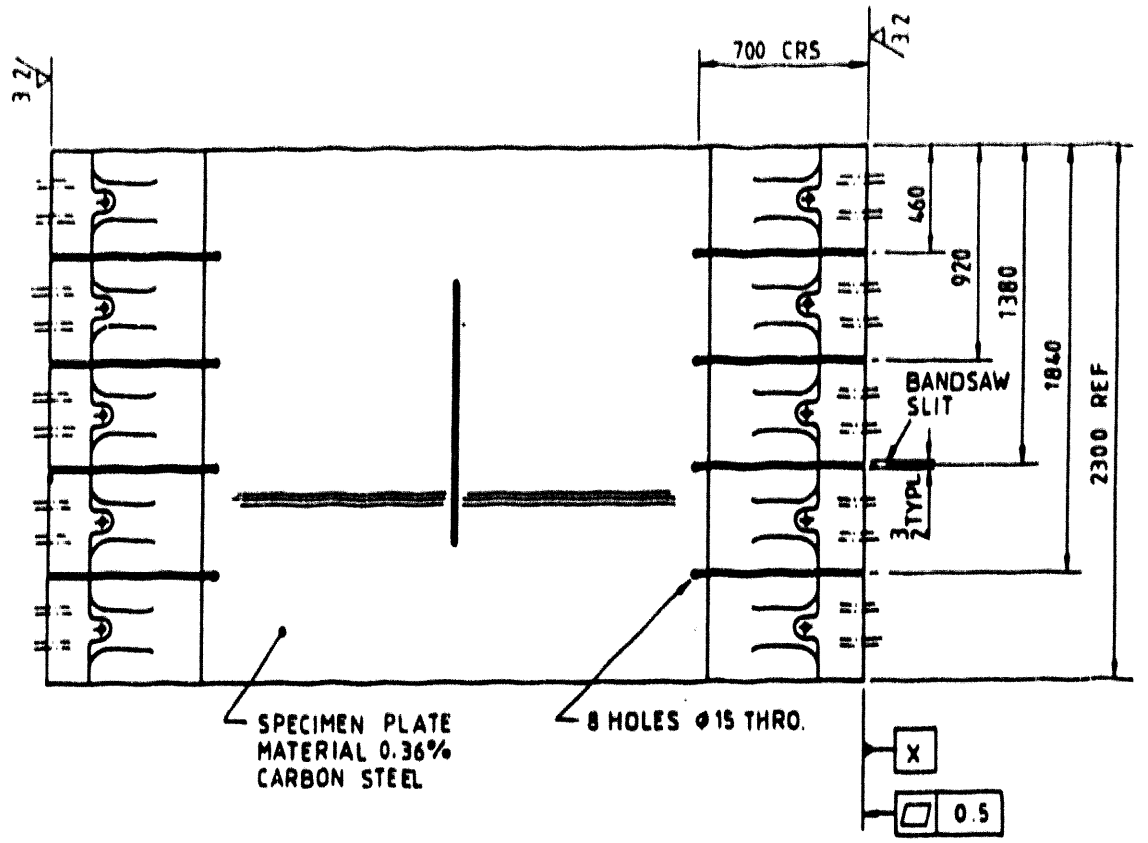

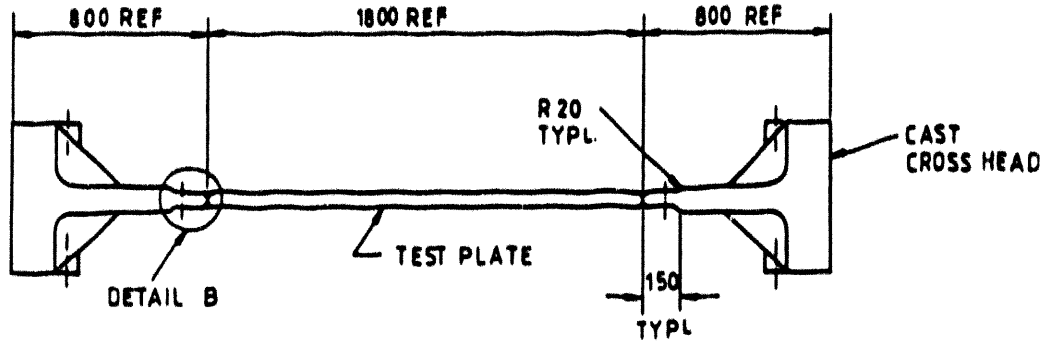

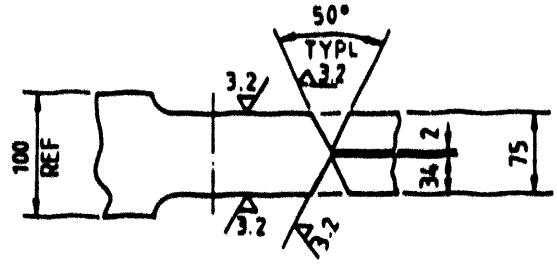

ENLARGED DETAIL B ON 2 PLACES

FIG 1. GHSR 1.0U SPECIMEN ASSEMBLY (FROM DRG. NO. OAE 549635)

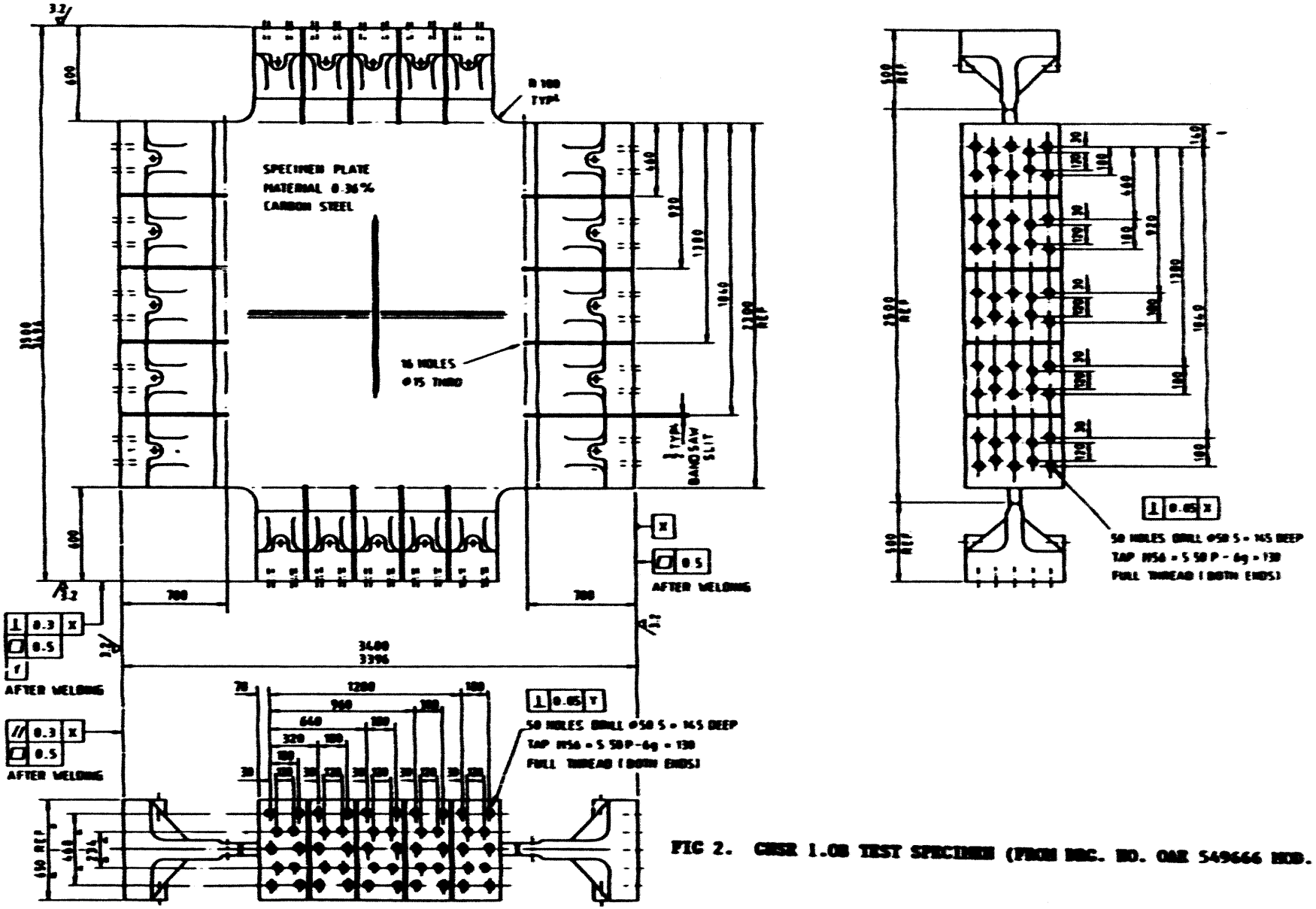

FIG 2. CBSR 1.0B TEST SPECIMEN (FROM DRG. NO. OAR 549666 REV. A

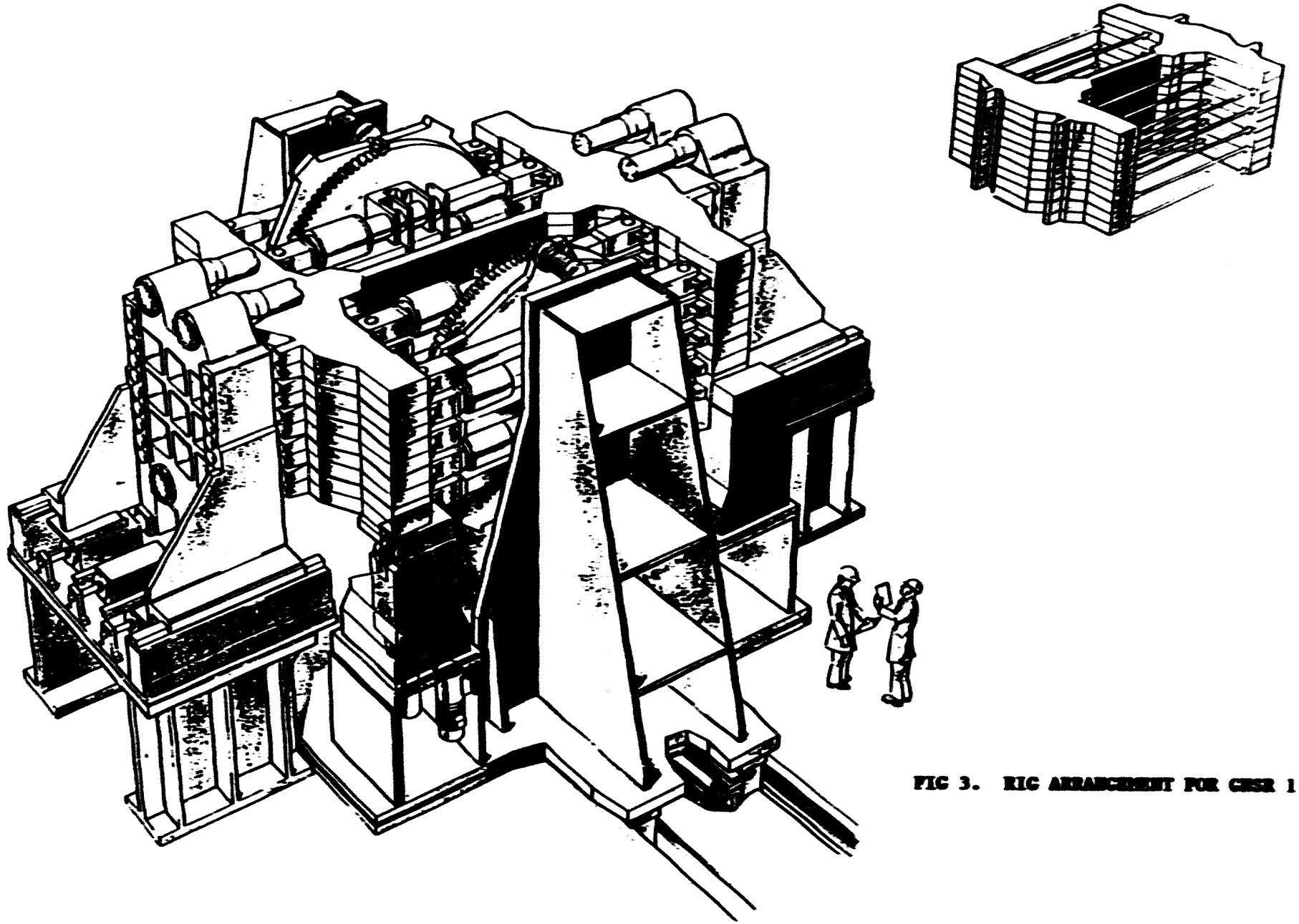

FIG 3. RIG ARRANGEMENT FOR CHSR 1.0M

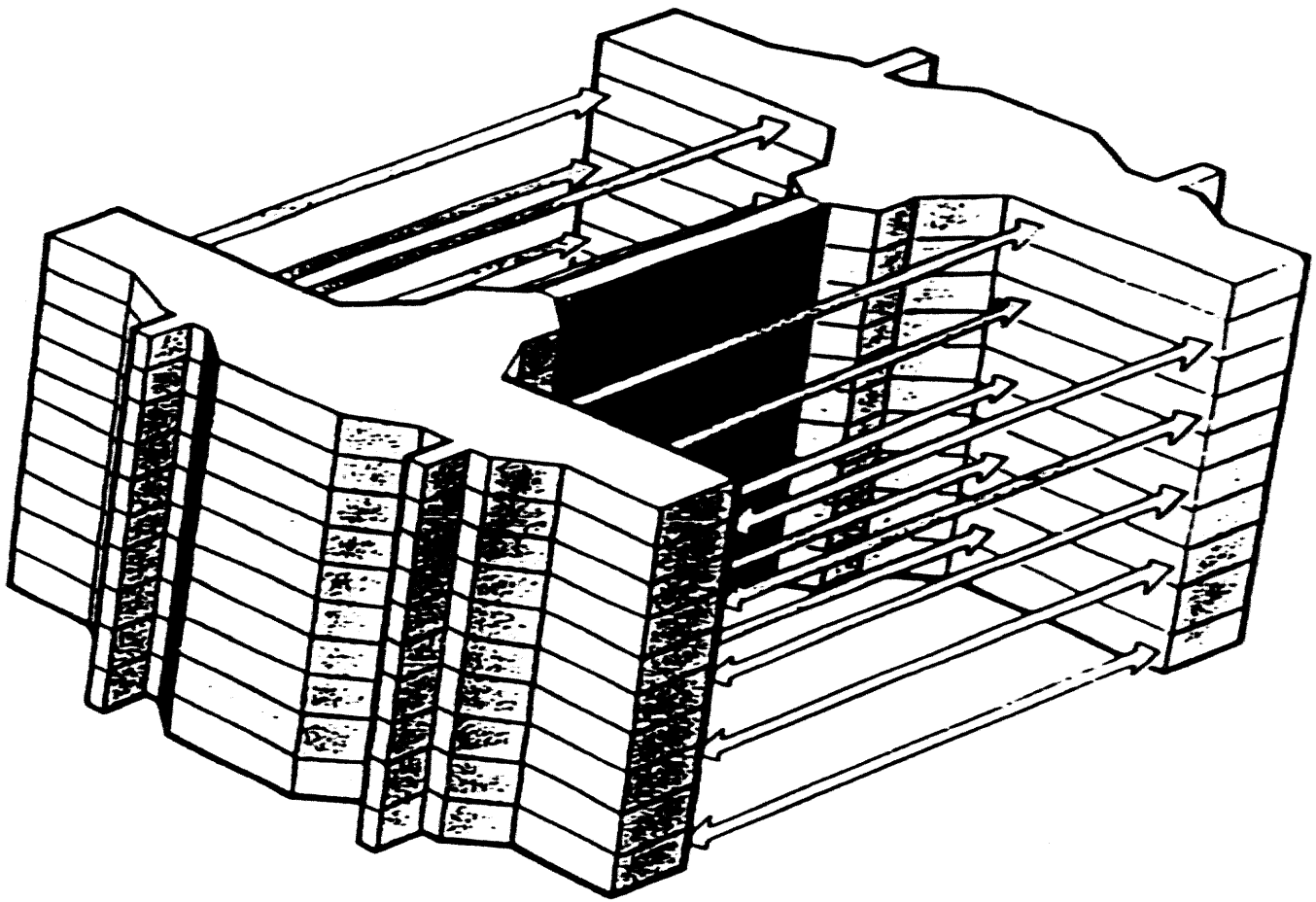

FIG 4. TEST ASSEMBLY ARRANGEMENT FOR UNIAXIAL SPECIMEN GHSR 1.00

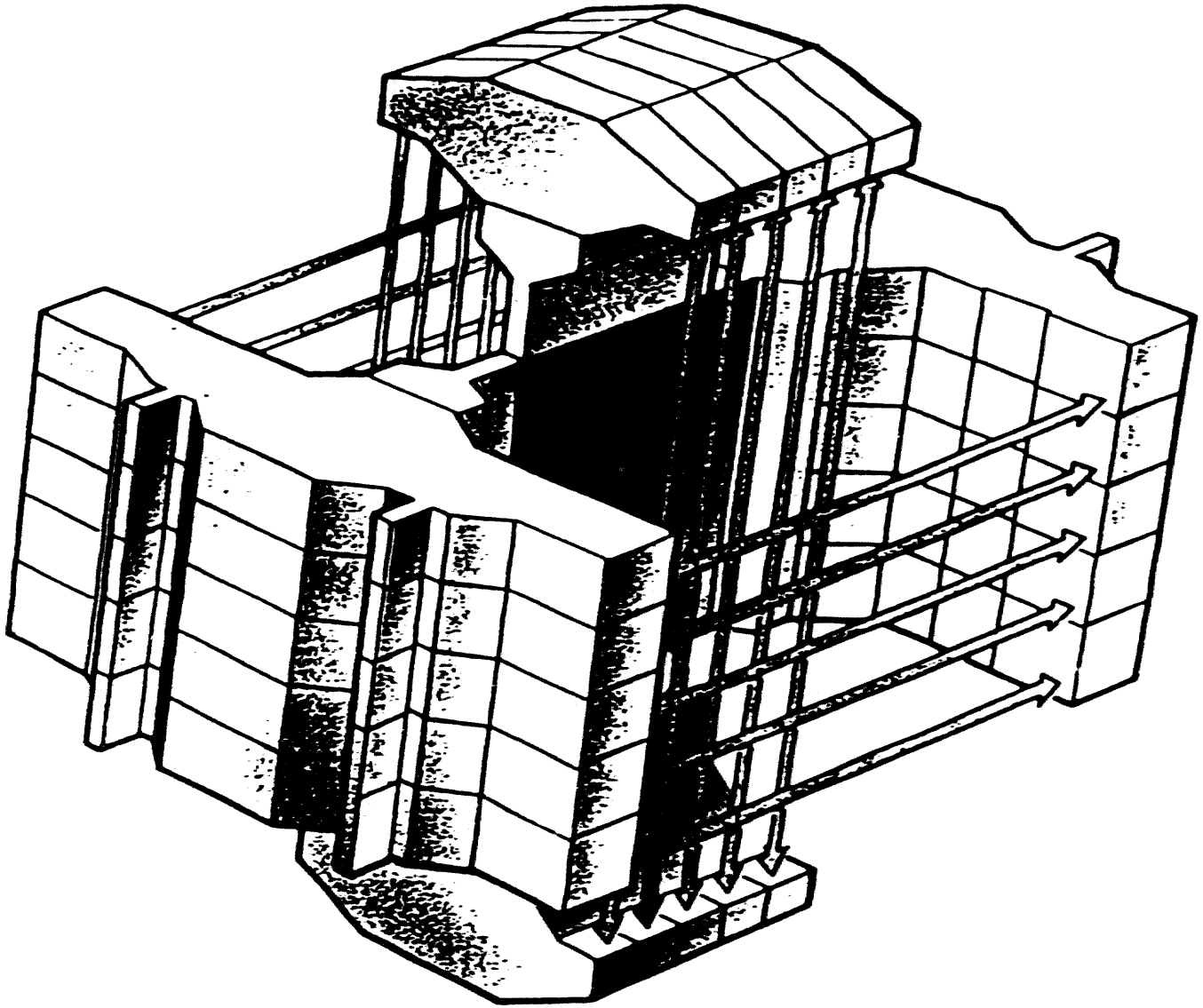

FIG 5. TEST ASSEMBLY ARRANGEMENT FOR BIAXIAL SPECIMEN CBSR 1.0B

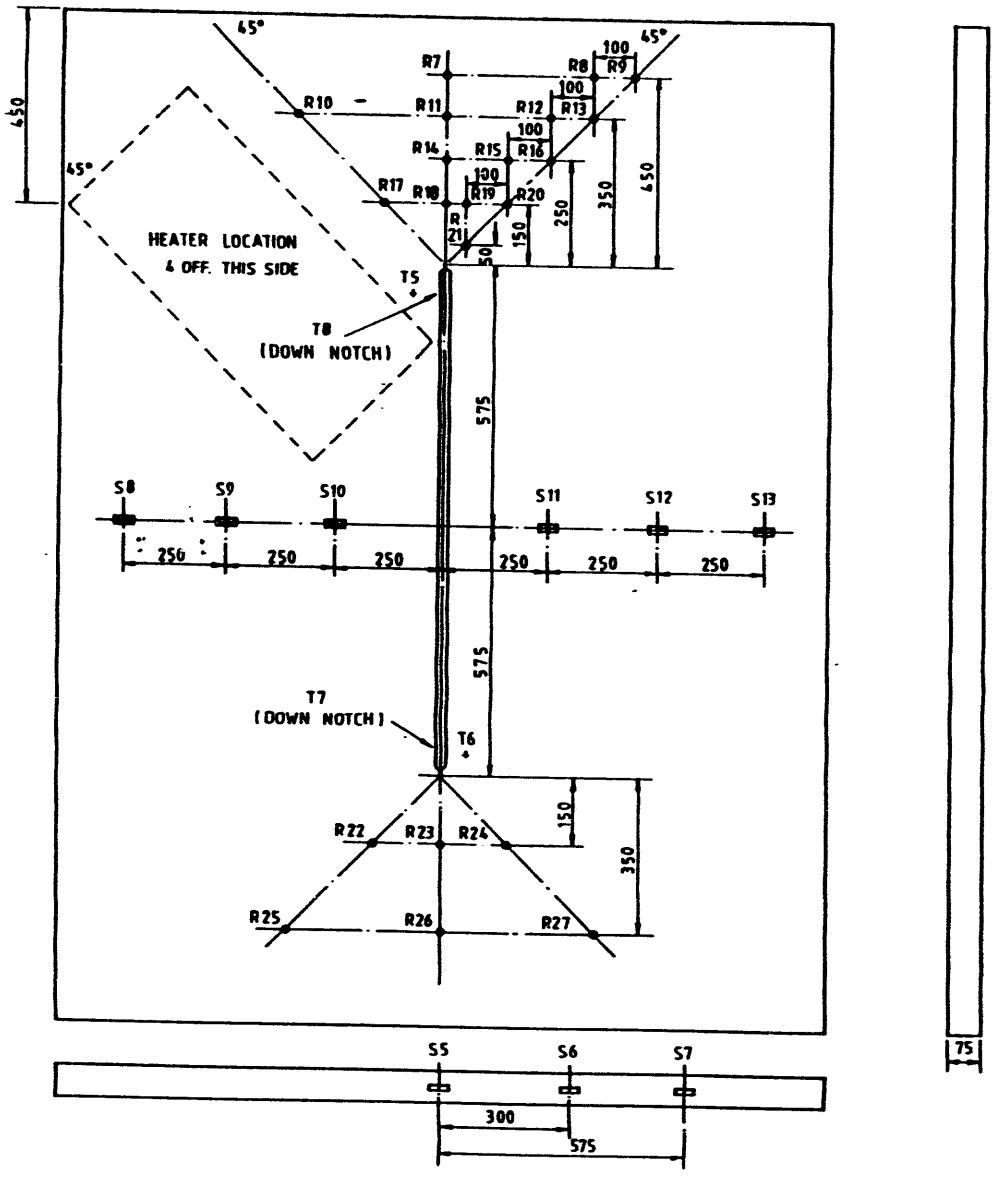

GAUGE ORIENTATION

1 (0°) ——→ FORCE

2 (45°)

3 (90°)

27 ROSETTES R1 ⟶ R27

13 SINGLE GRID GAUGES S1 ⟶ S13

8 THERMOCOUPLES T1 ⟶ T8

FIG 6. SOUTH SIDE STRAIN GAUGE LAYOUT G1.OU

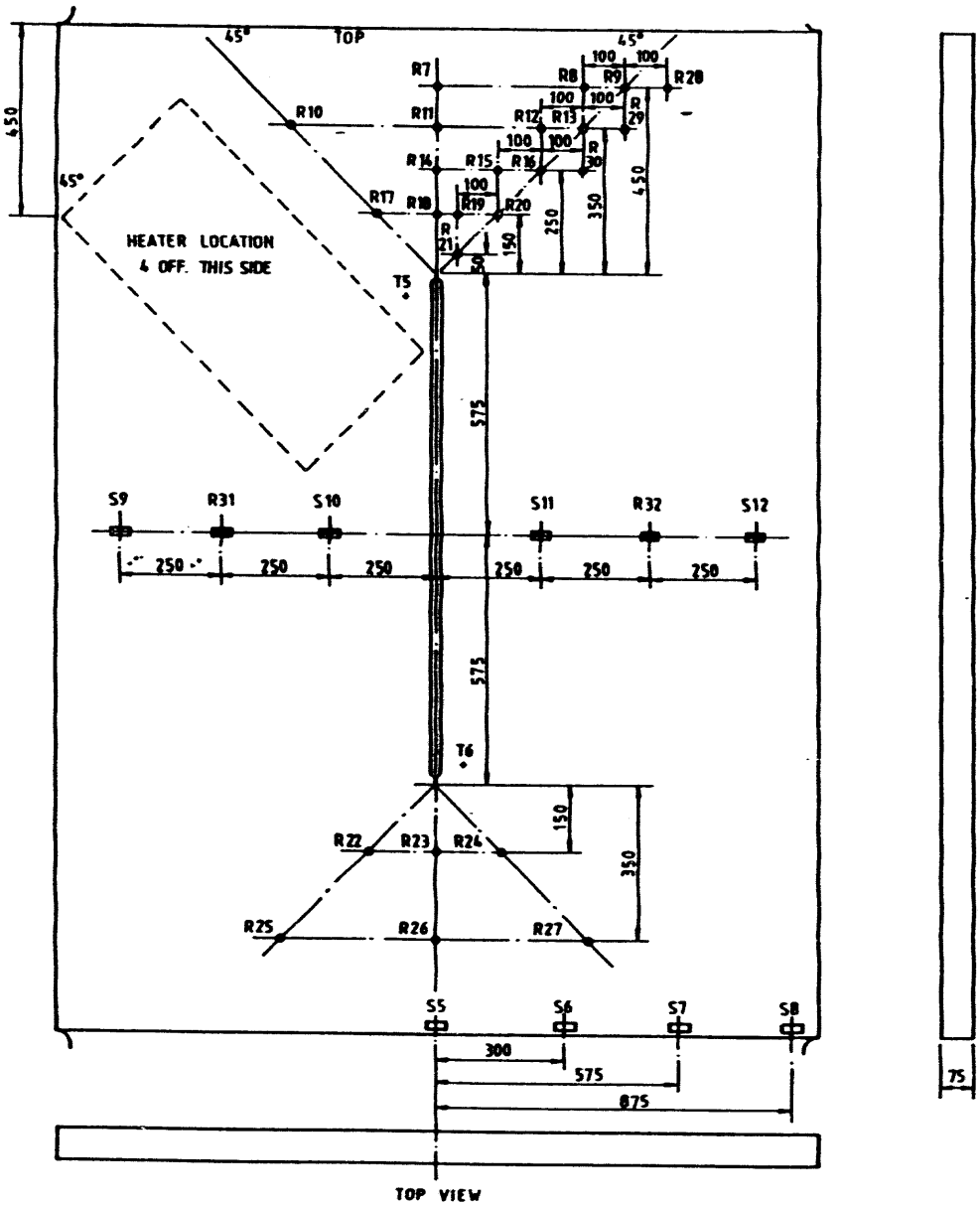

GAUGE ORIENTATION

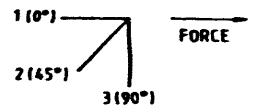

32 ROSETTES R1 ⟶ R27

12 SINGLE GRID GAUGES S1 ⟶ S13

6 THERMOCOUPLES T1 ⟶ T6

FIG 7. SOUTH SIDE STRAIN GAUGE LAYOUT G1.OB

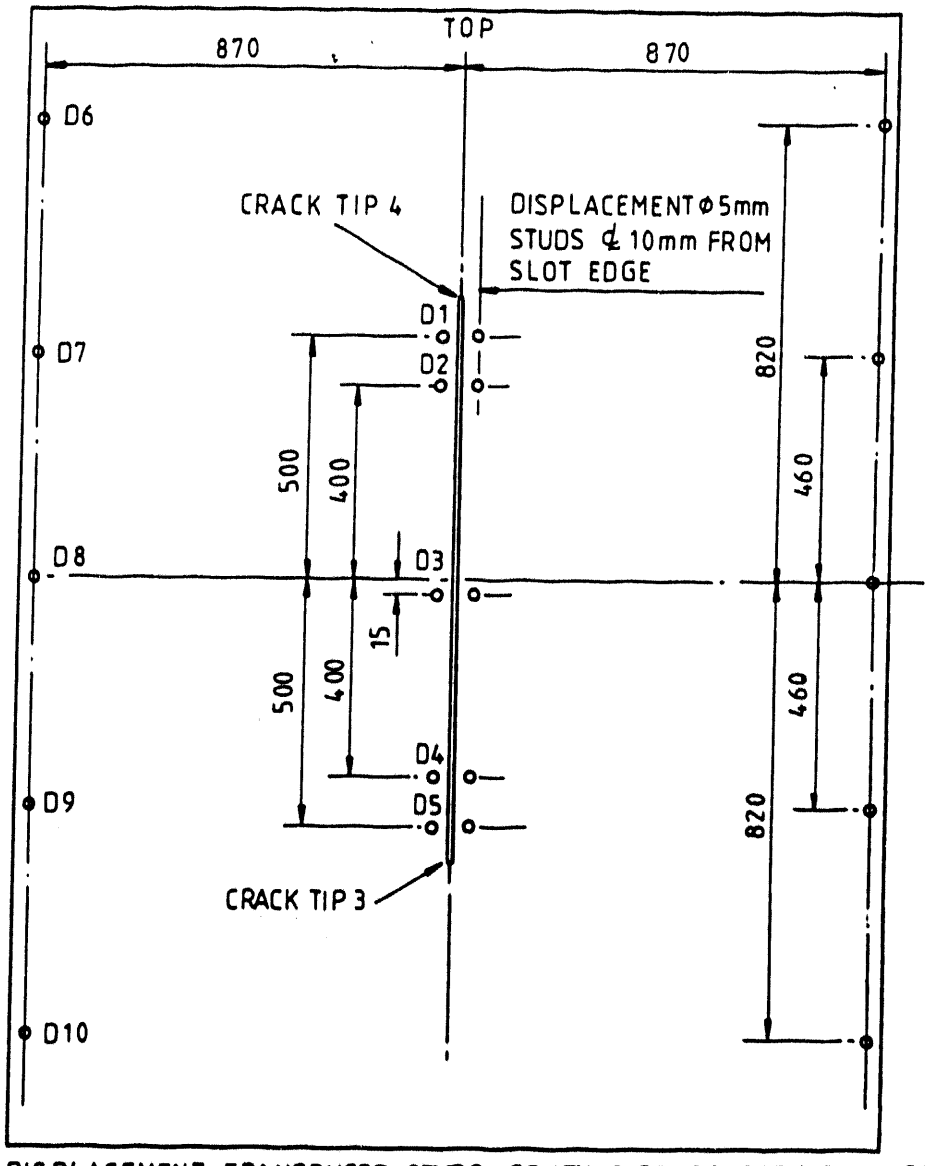

FIG 8. LOCATION OF TRANSDUCER STUDS SOUTH SIDE G1.OU

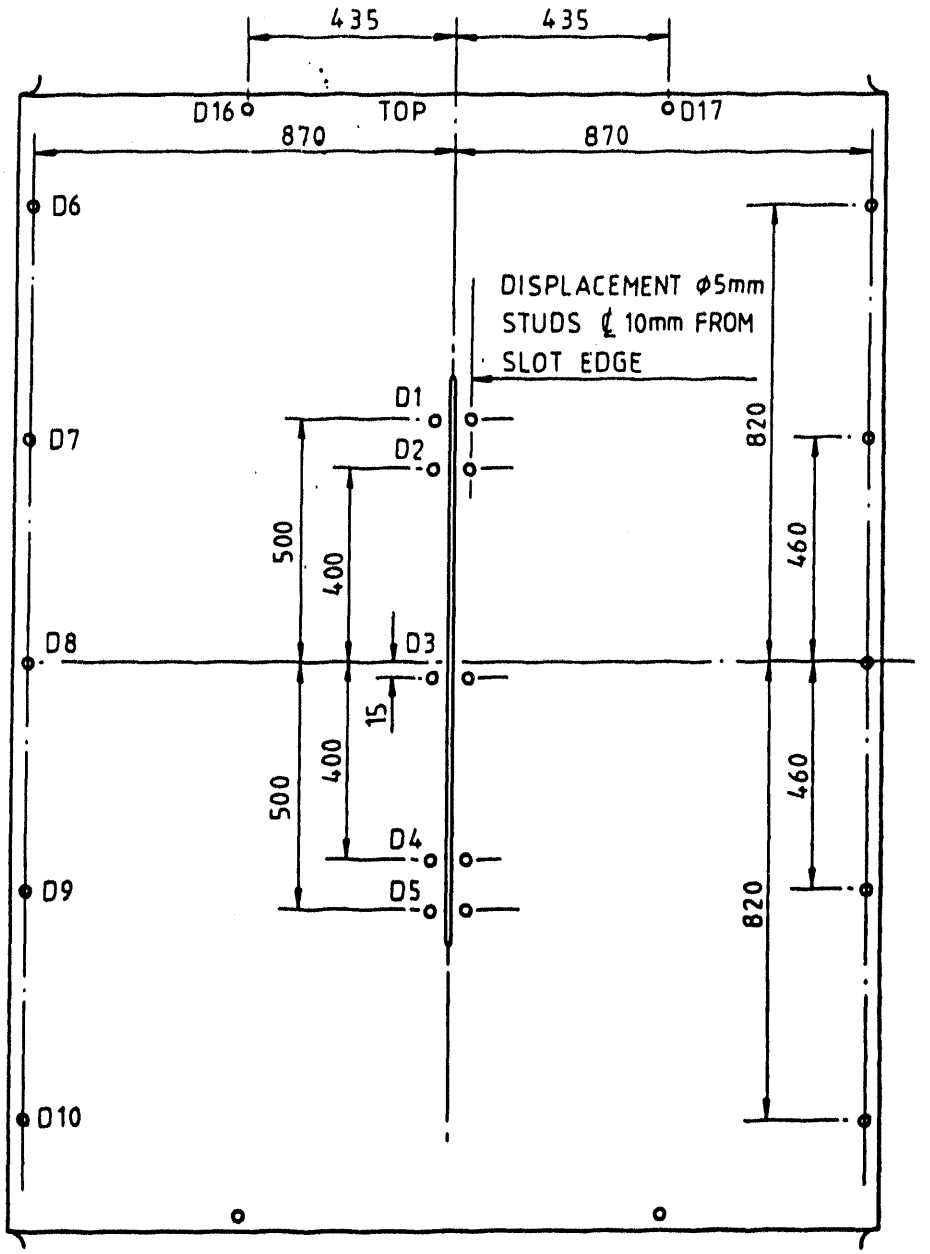

FIG 9. LOCATION OF TRANSDUCER STUDS SOUTH SIDE G1.OB

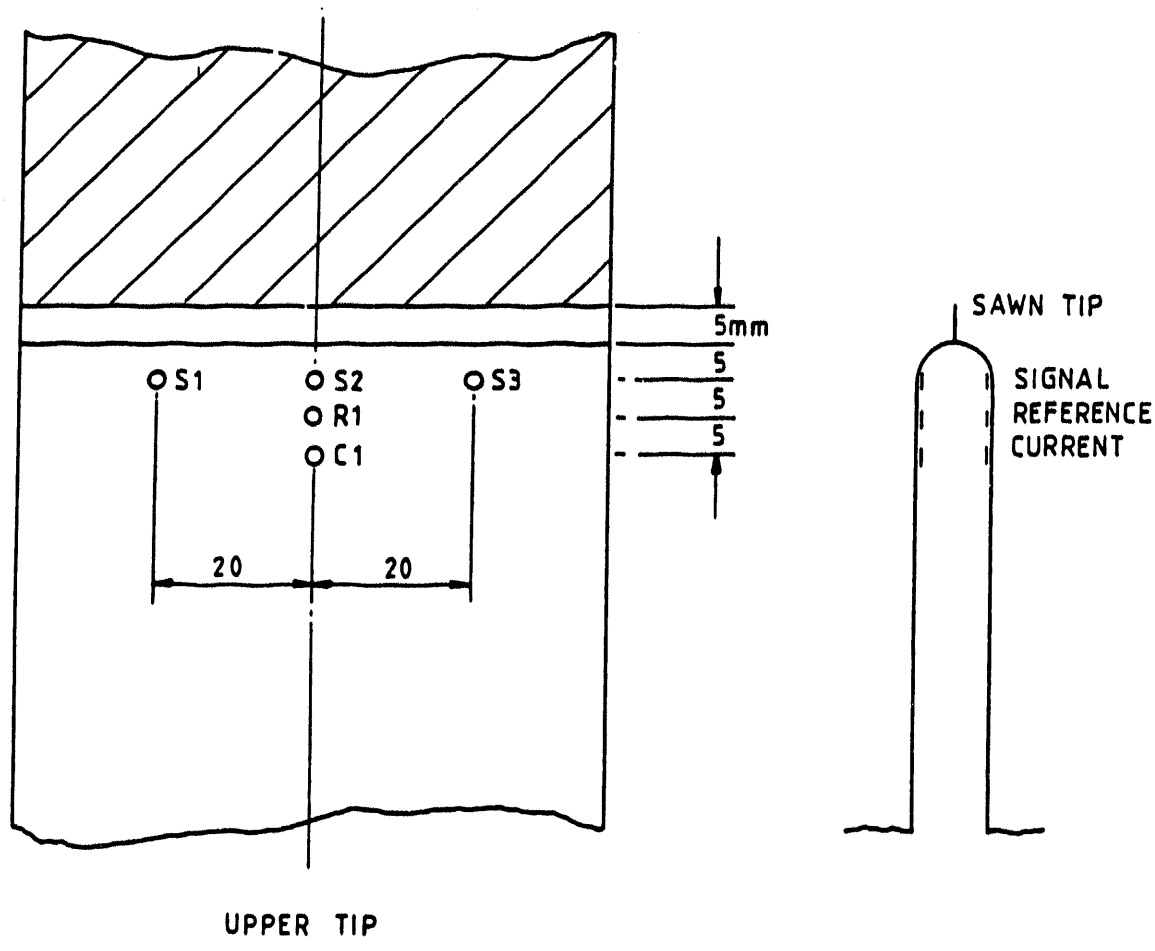

FIG 10. ACPD PROBE ARRANGEMENT G1.OU

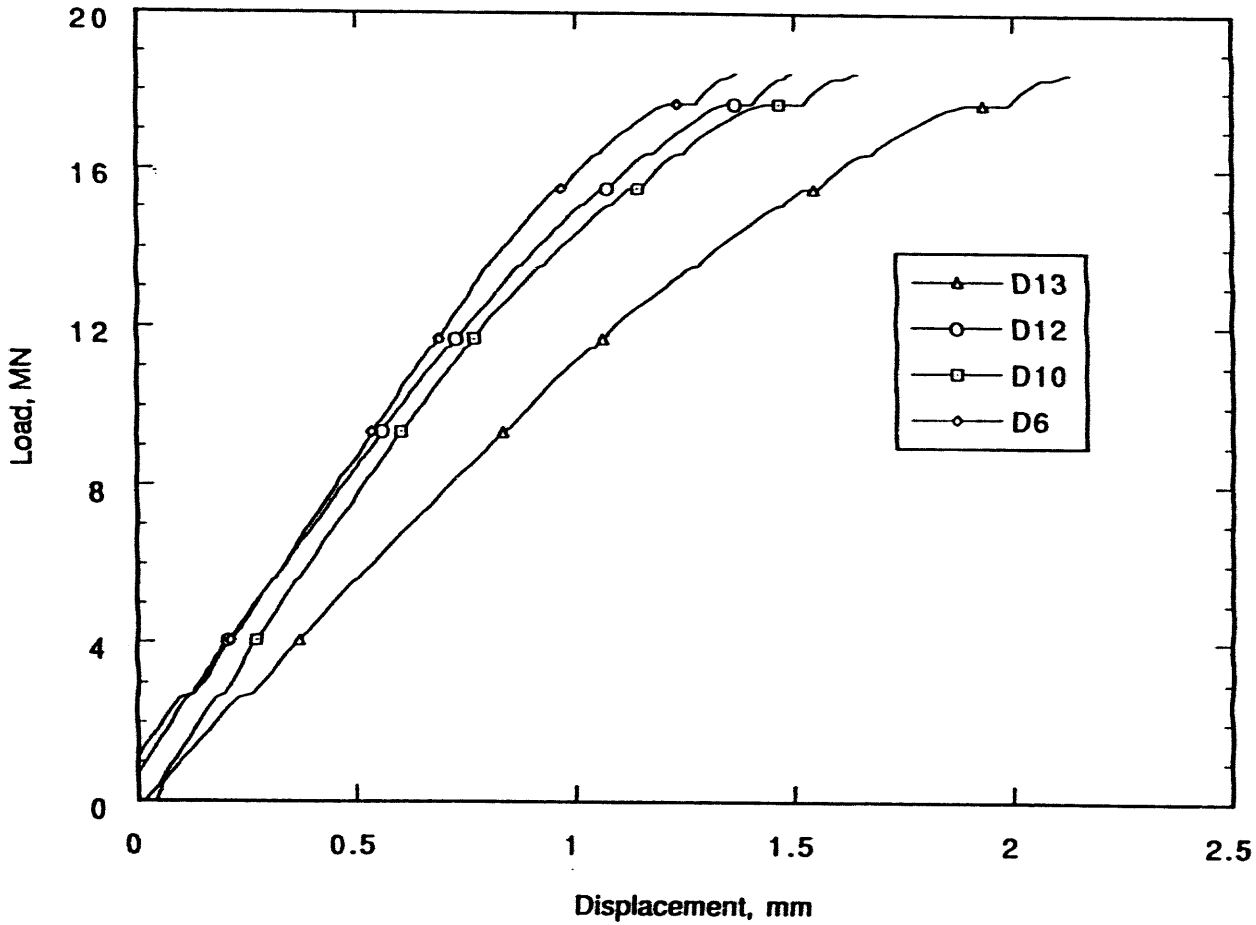

FIG 11. GNSR 1.0U LOAD vs DISPLACEMENT FROM EXPERIMENTAL DATA FOR TRANSDUCERS D6, D10, D12 & D13

FIG 12. GNSR 1.OU TOTAL LOAD v UPPER TIP ACPD PROBE S1

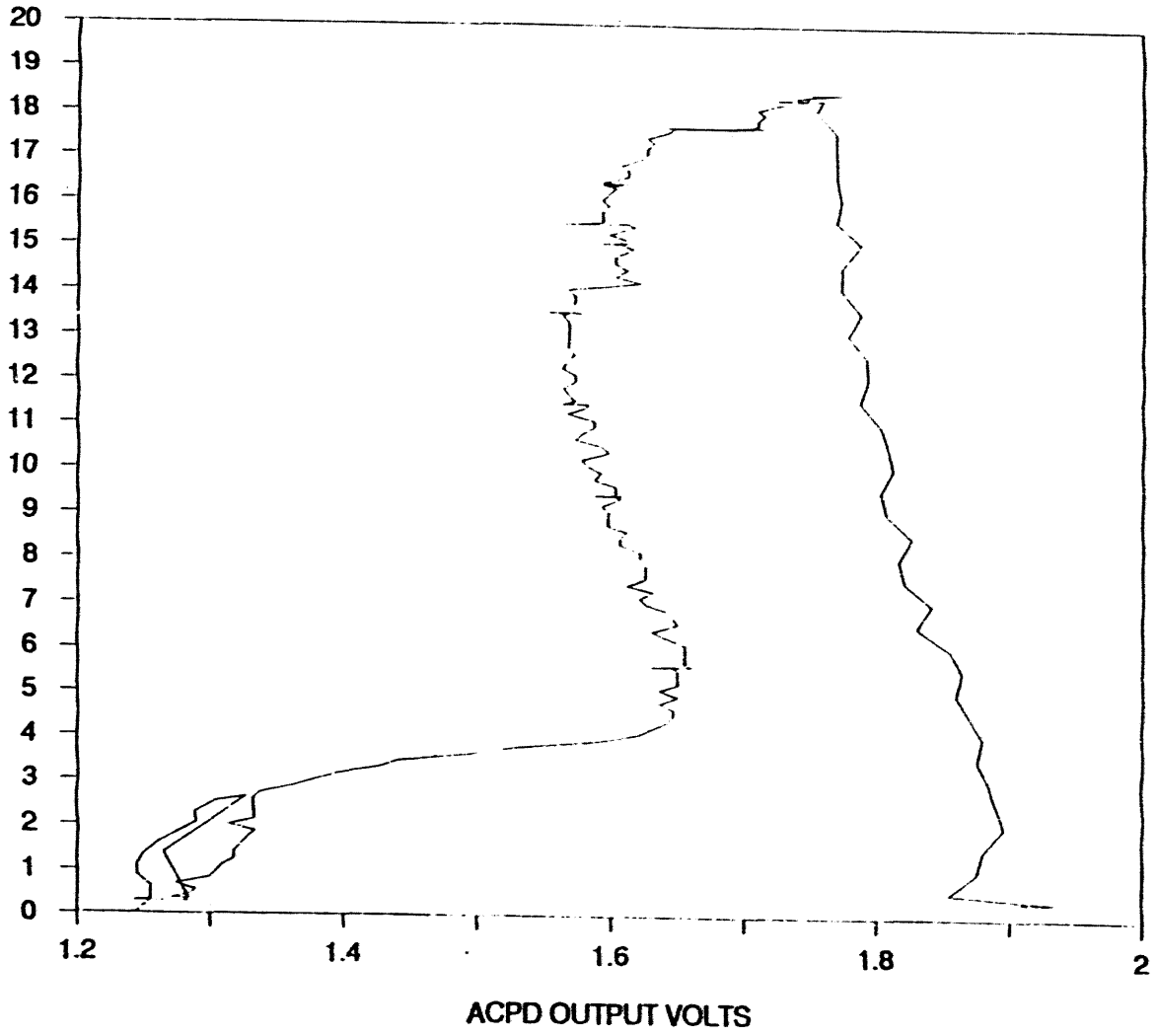

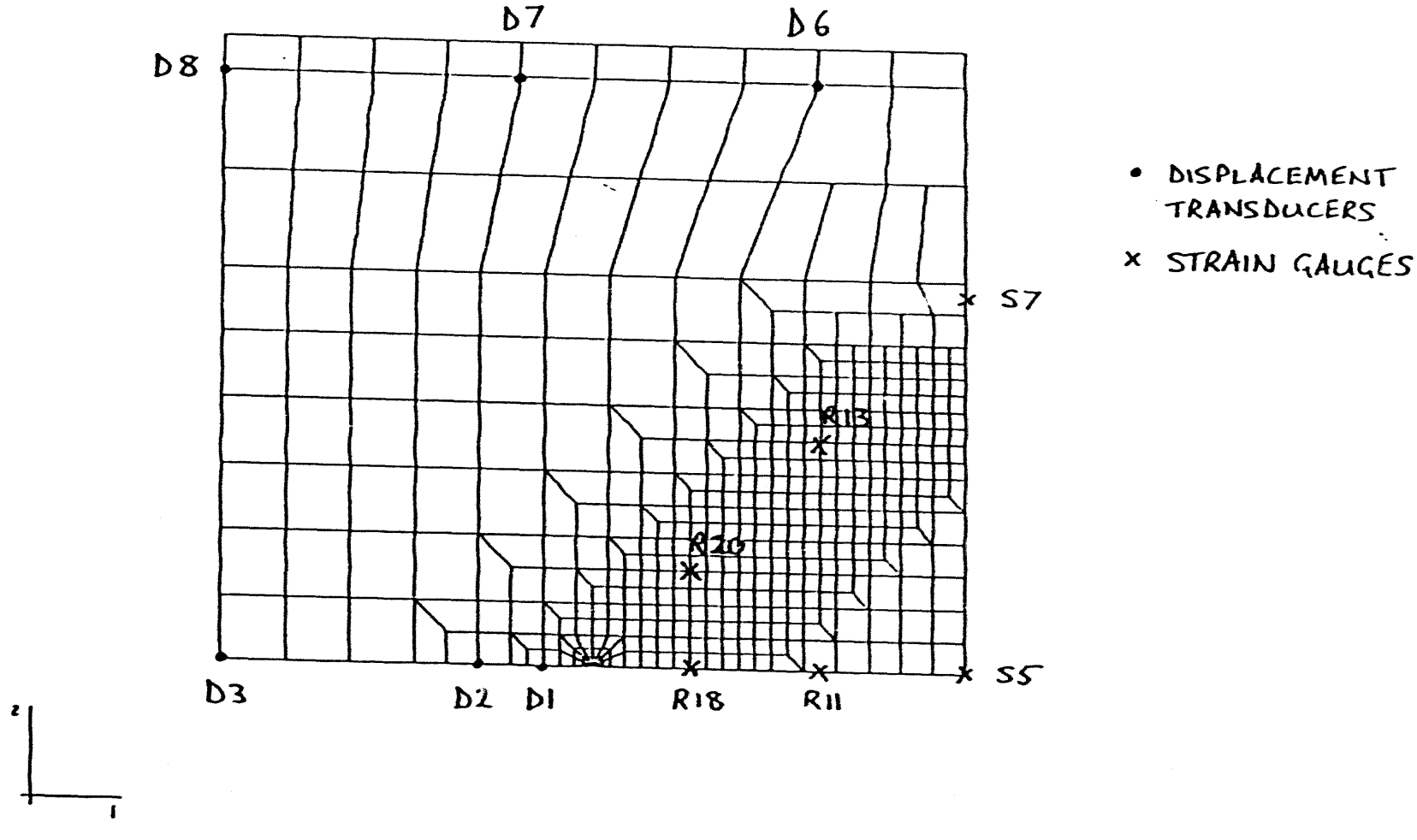

FIG 13. FINITE ELEMENT MESH FOR GRSR/1.0U TEST

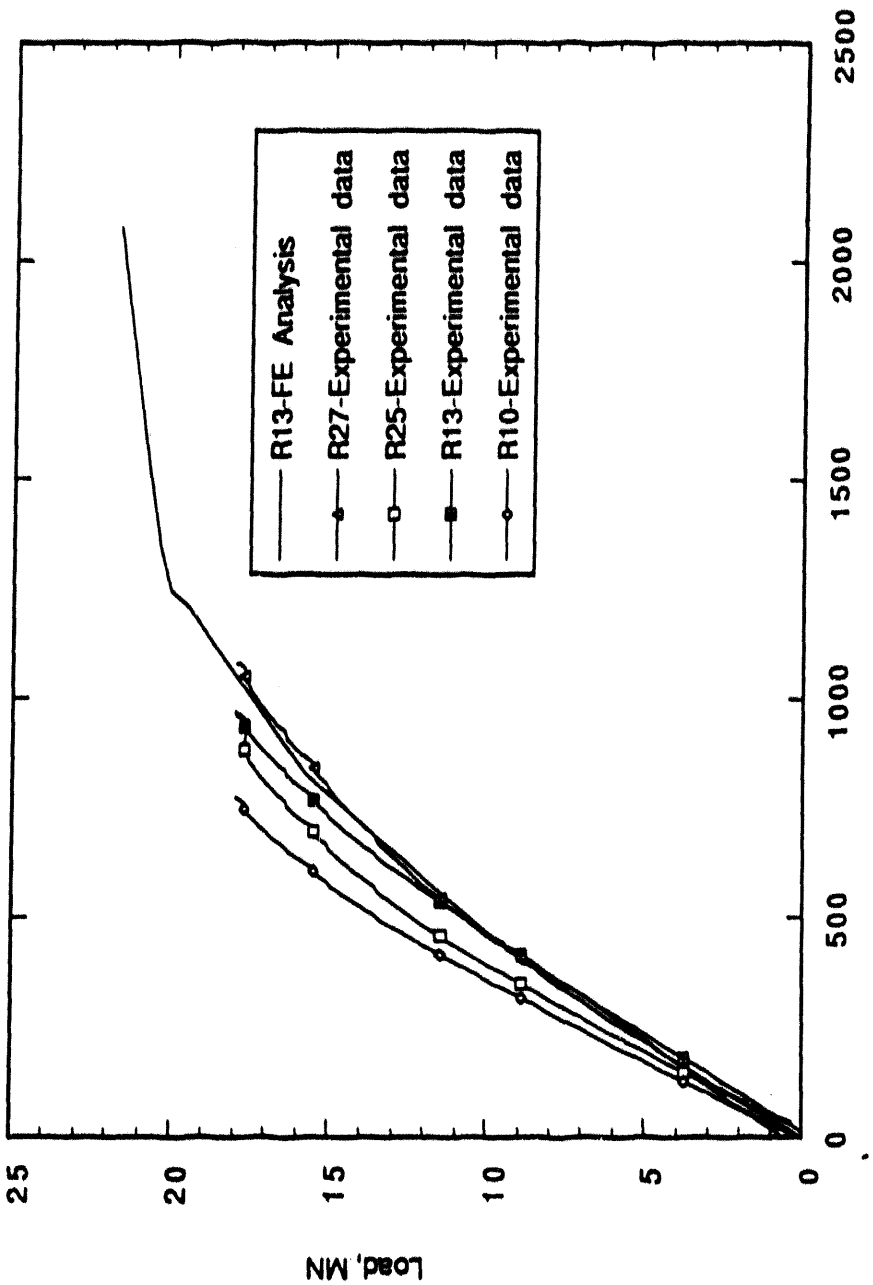

FIG 14. CESR 1.0U LOAD v STRAIN FOR ROSETTES R27, R25, R13 & R10

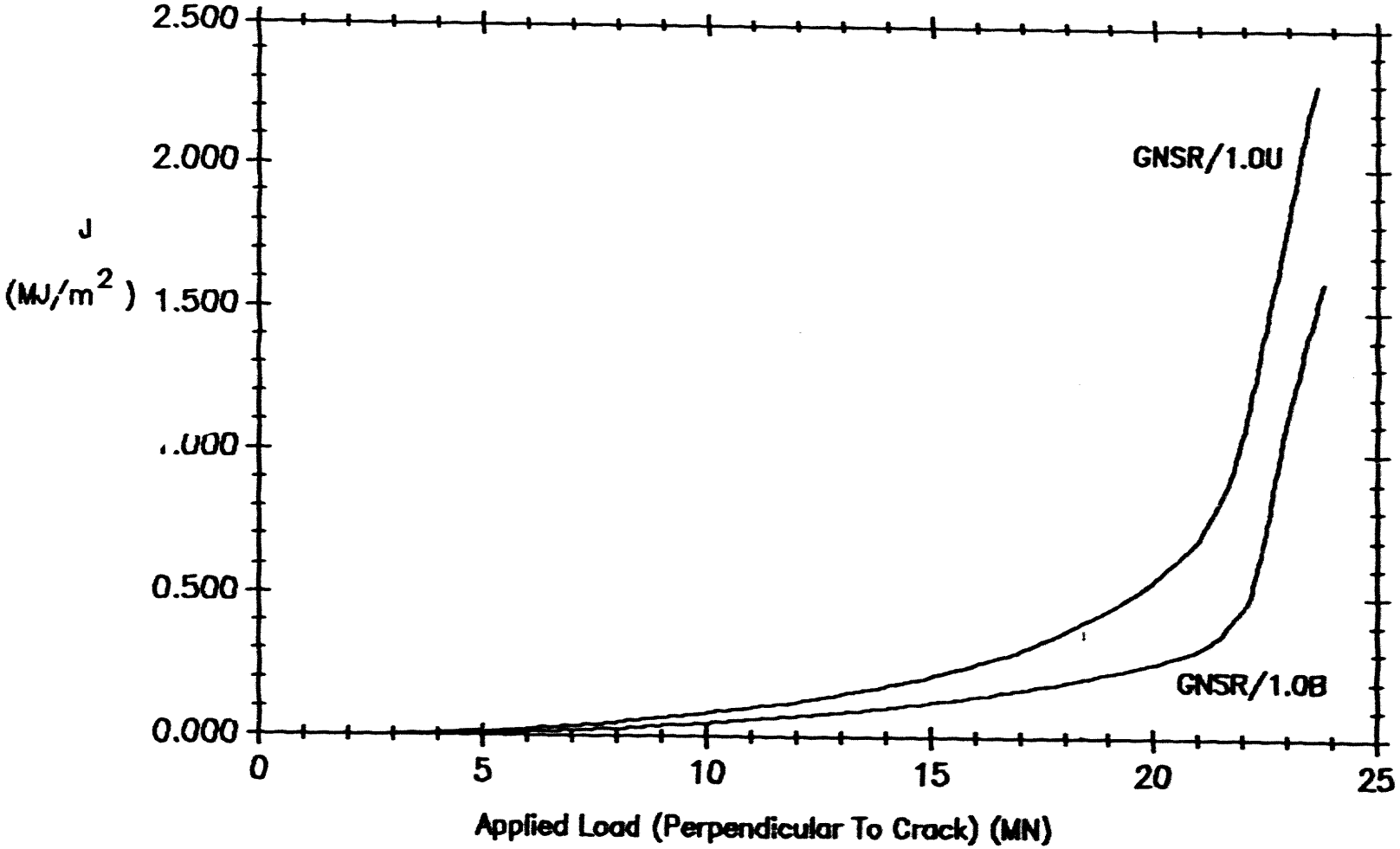

FIG 15. Finite Element Calculated Applied Load Versus J For GNSR/1.0U And GNSR/1.0B Test Specimens

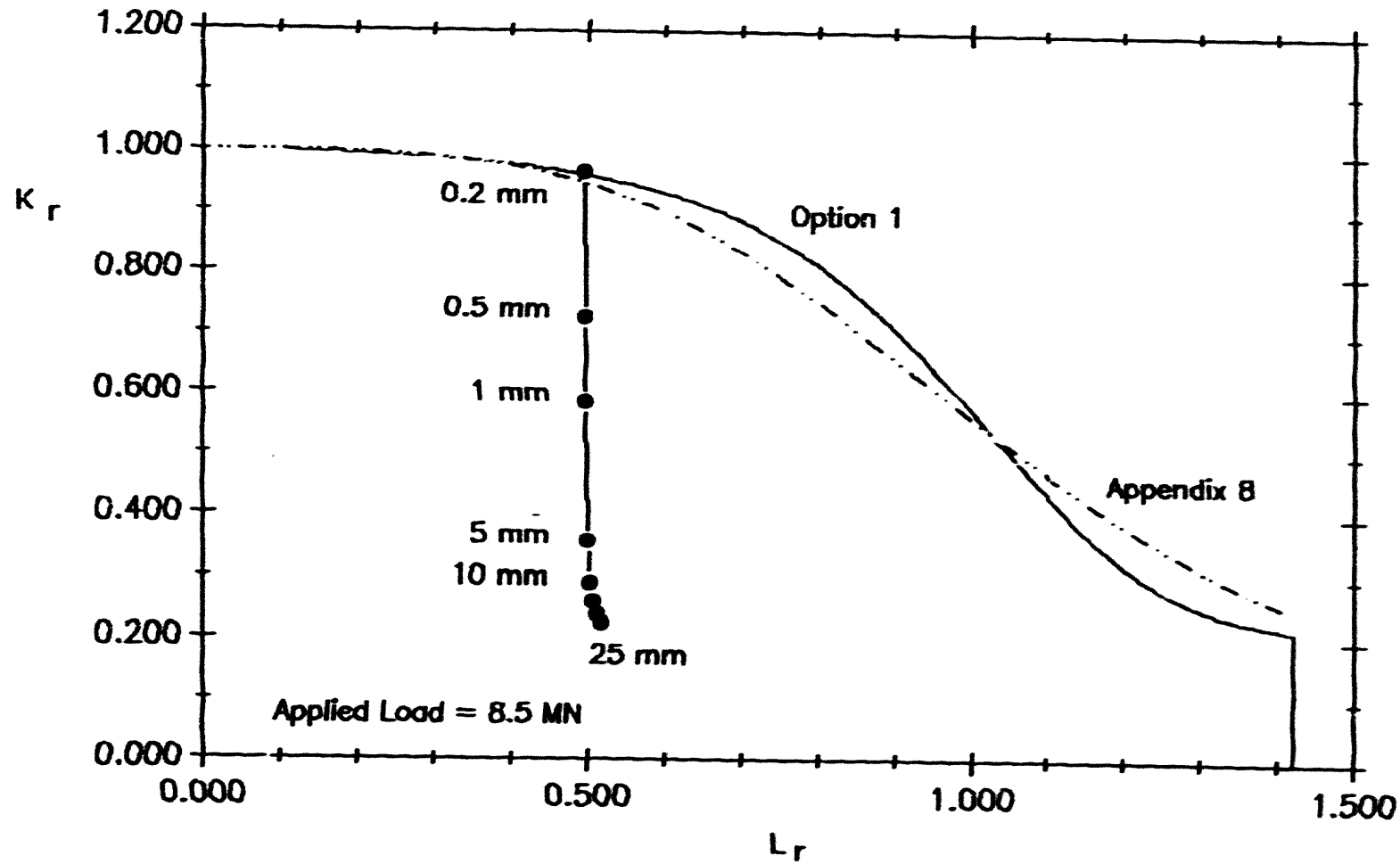

FIG 16. R6/Rev 3 Failure Assessment Diagrams For Test GNSR/1.0U – Bottom Crack Tip

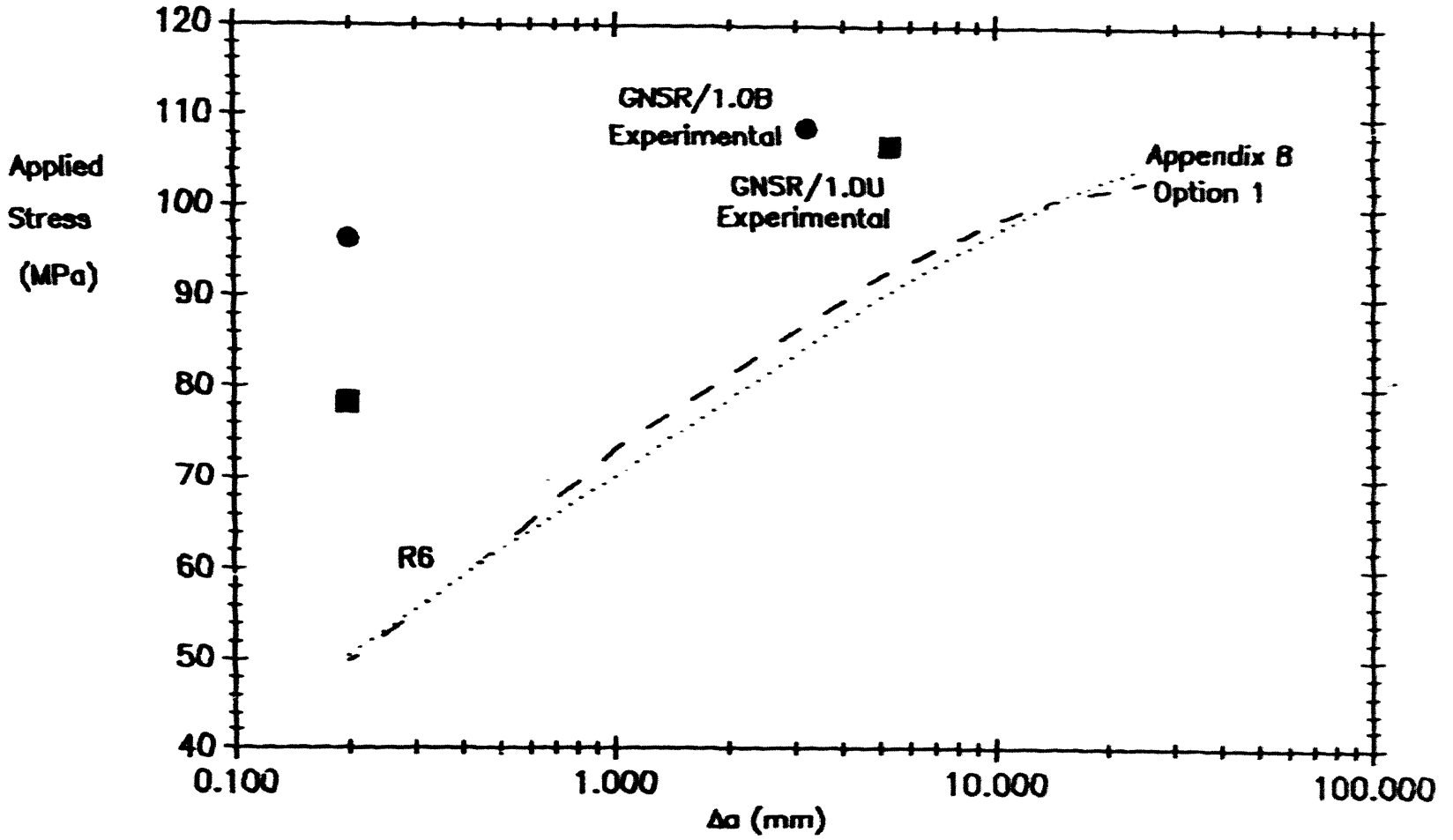

FIG 17. R6/Rev 3 And Experimental Results For GNSR/1.0U – Bottom Crack Tip And GNSR/1.0B – Top Crack Tip

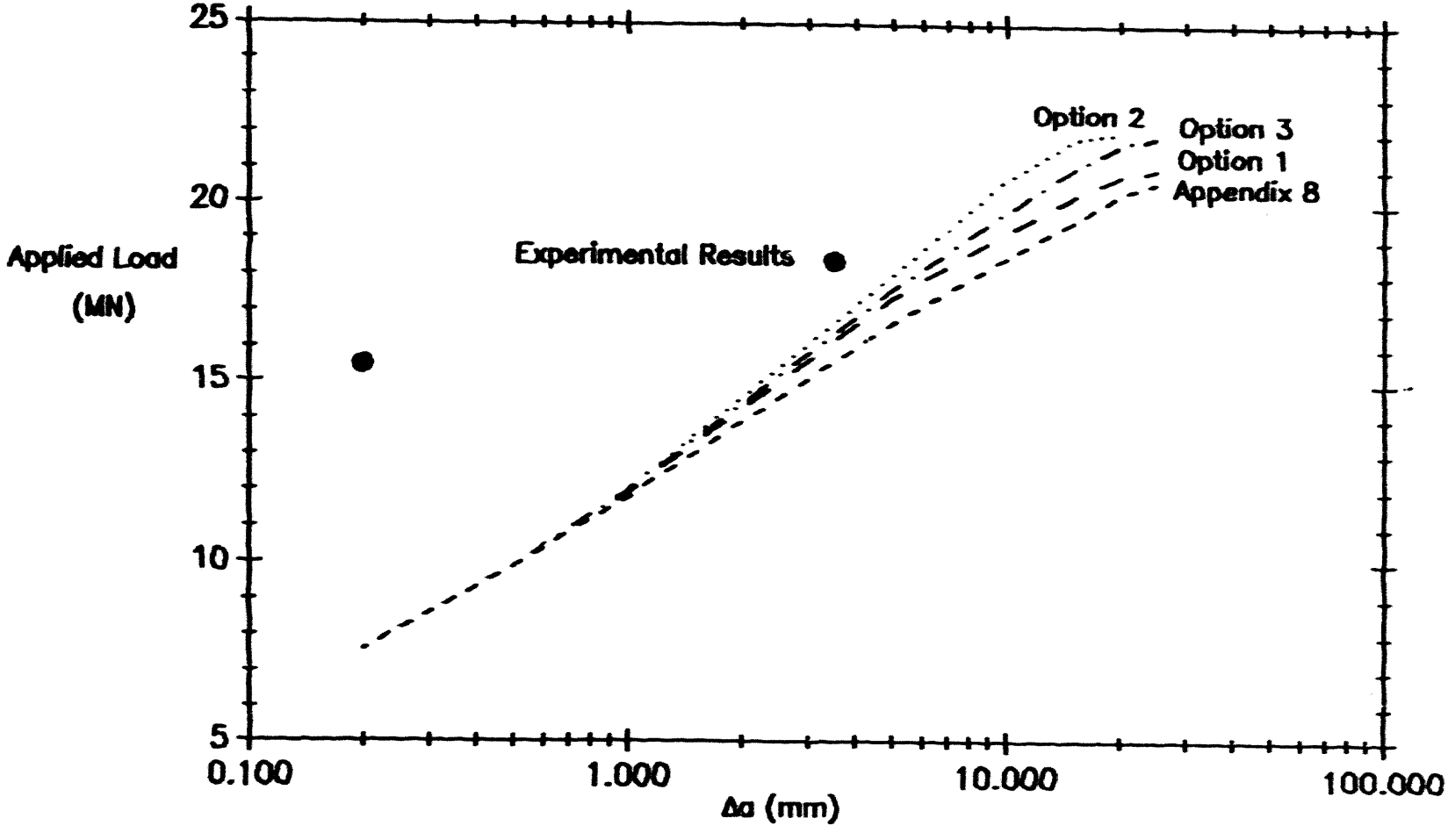

FIG 18. R6/Rev 3 Analyses For GNSR/1.0U – Top Crack Tip

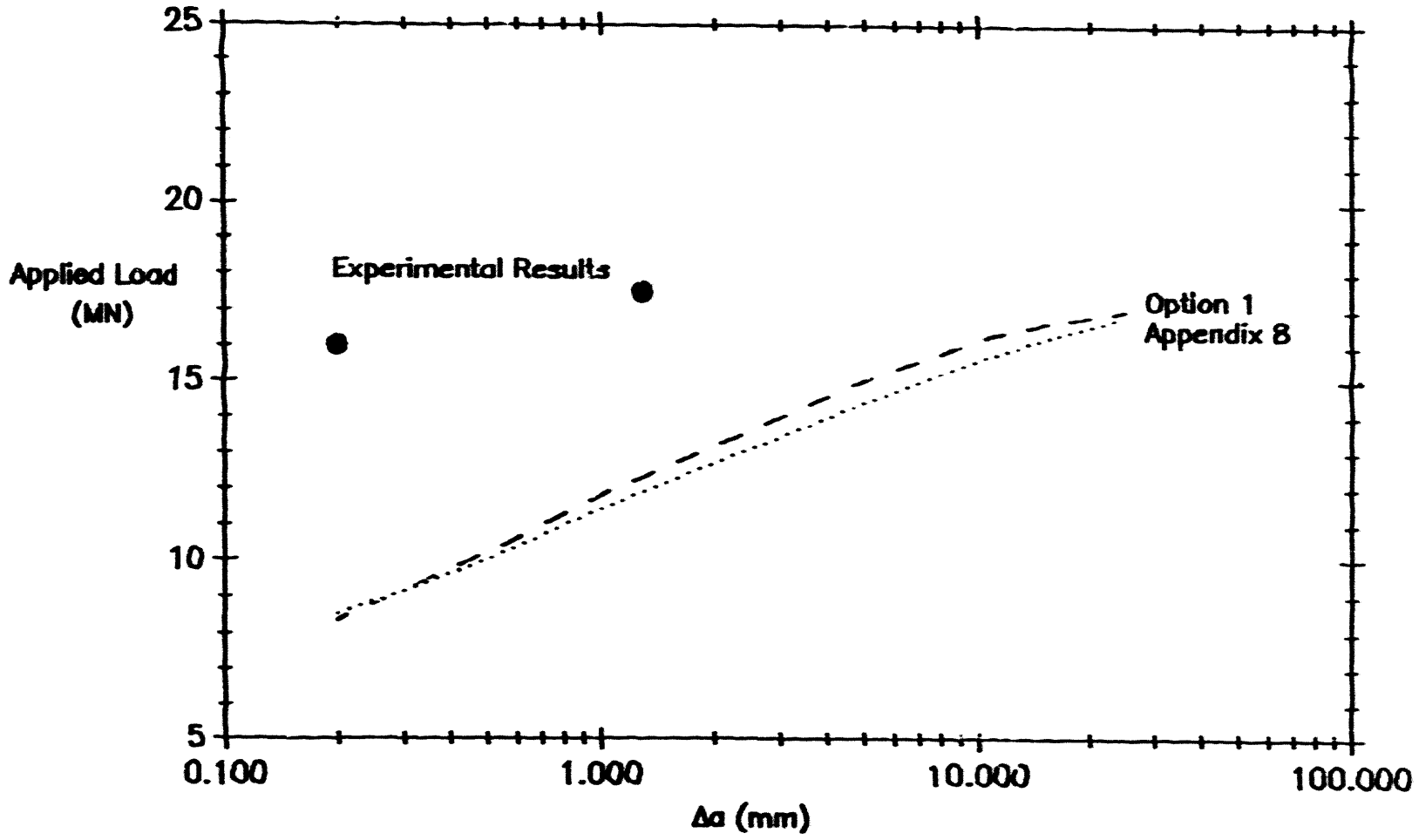

FIG 19. R6/Rev 3 Analyses For GNSR/1.0B – Bottom Crack Tip

VERIFICATION OF DUCTILE FRACTURE MECHANICS ASSESSMENT METHODS BY A WIDE PLATE TEST

by

H. Kordisch*, H. Talja**, L. Hodulak*

Abstract

In order to simulate the behaviour of a circumferential crack in a RPV-cylinder wall under pressurized thermal shock (PTS) conditions a large plate made of RPV-steel 22NiMoCr37 was tested under four point bending. The depth of the surface crack was 35% of the wall thickness with a c/a-ratio of 2.5. J_R-curves for the material were measured from side-grooved and smooth CT-specimens of different dimensions.

The aim of the test was to achieve crack initiation and some amount of ductile crack growth and to verify ductile fracture mechanics analysis and assessment methods, including the transferability of material parameters measured on small-scale specimens to the plate. Therefore, analytical and three-dimensional elastic-plastic finite element analyses had been carried out to predict and to simulate the initiation and stable crack growth. Based on the J-integral concept the agreement between the experiment and the numerical simulation was improved if "constraint-modified" J_R-curves were taken into account.

* Fraunhofer-Institut für Werkstoffmechanik, Wöhlerstr. 11, D-7800 Freiburg, Germany
** VTT, Metals Laboratory, P.O.Box 26, Kemistintie 3, SF-02151 Espoo, Finland

1 INTRODUCTION

For a reactor pressure vessel (RPV) under emergency conditions the most severe loading case is the "pressurized thermal shock" (PTS) with a striplike cooling situation beneath the inlet nozzles. Due to the toughness requirements and the prevailing temperatures, elastic-plastic fracture mechanics methods seem necessary for a realistic analysis and assessment, including the transferability of material parameters measured on small-scale specimens to the real structure.

Therefore at Fh-IWM a method has been developed to take the constraint dependence of the crack growth resistance along the crack front into consideration in the numerical simulation of stable crack growth [3]. The degree of the triaxiality of the stress state is described by a constraint factor h defined as

$$h = \sigma_h/\sigma_v ,$$

quotient of the mean or hydrostatic stress σ_h to the equivalent stress (von Mises reference stress) σ_v. To describe the effect of the geometry three-dimensional finite element analyses have to be performed for the specimens from which the crack growth resistance curves are defined. The over the crack front averaged calculated values h_m are then correlated to the measured J_R-curves. This is consistent with the fact that similarly a J_R-curve also essentially presents the dependence between average J-integral and average crack growth.

In a first stage a linear relationship between h_m and the slope dJ/da is established and used to simulate the local crack growth and it is assumed that the constraint effect does not influence the initiation value J_i, whereas new investigations show a triaxiality influence on J_i [7].

In order to simulate the behaviour of a circumferential crack in a RPV-cylinder wall under pressurized thermal shock (PTS) conditions a large flawed plate made of the reactor pressure vessel steel 22NiMoCr37 was tested under four point bending at the temperature of 70 °C. J_R-curves for the material were measured from side-grooved and smooth CT-specimens having different dimensions.

The aim of the test was to achieve crack initiation and some amount of ductile crack growth and to verify ductile fracture mechanics analysis and assessment methods. Therefore, analytical assesssments and three-dimensional elastic plastic finite element analyses had been carried out to predict and to simulate the initiation and stable crack growth.

2 DESCRIPTION OF EXPERIMENTAL PART

The plate test was performed under four point bending to obtain a stress gradient resembling to that in a RPV wall loaded by a pressurized thermal shock. Stable crack growth of a few millimeters was planned to be reached in the test. The test configuration is illustrated in Figure 1. A semi-elliptical flaw was produced in the plate by machining and sharpened by

fatigue. The depth a of the final surface flaw shown in Fig. 2 was 27.7 mm which is 35 % of the thickness. The length 2c of the flaw was 140.4 mm (a/c = 0.4). The test was performed at a temperature of 70 °C in order to assure upper shelf behaviour.

The plate was extensively instrumented. The values of load, load point displacement and crack mouth opening displacement (CMOD) were measured during the test. Strain fields were measured with strain gages to validate the numerical results. Acoustic emission measurements were made to detect the initiation of crack growth.

The test was stopped at an expected stable crack growth of about 1...2 mm. The final load value was 1.59 MN, the load line displacement as measured from the cylinder was 24.9 mm and CMOD 2.37 mm. Acoustic emission measurement did not show any signal of crack initiation. For further testing of the acoustic emission technique, the plate was fatigued and the test was repeated with the larger crack size. Comparisons can only be made between the calculation and the experimental results from the first test phase.

Stress-strain curves were defined for the material at the test temperature. The yield stress was 443 MPa and the ultimate strength 572 MPa. J_R-curves (shown in Fig. 3) were measured using the partial unloading compliance technique from smooth and side-grooved CT-specimens of different dimensions (Table 1). Additionally, potential drop measurements were made to detect the initiation.

The test programme and the analytical and numerical simulations of the tests are described in [4, 5].

3 DESCRIPTION OF ANALYTICAL AND NUMERICAL PART

Analytical calculations and extensive elastic-plastic three-dimensional finite element analyses have been performed for the plate before and after the test. Three CT-specimens were chosen from the test series for further analyses. Two of them were smooth specimens with different thickness values and one specimen with 20 % side-grooves. The dimensions are given in Table 1. The finite element mesh for the side-grooved CT-specimen is shown in Fig. 4.

To assess the fracture behaviour of the plate analytically the IWM-VERB program was adopted. Three-dimensional elastic-plastic finite element (FE) calculations were made using the FE-program ADINA [1] with IWM-CRACK routines [2] to simulate stable crack growth.

For the plate test three different finite element calculations have been performed: one analysis with the stationary crack and two different analyses simulating stable crack growth, using only the lower bound J_R-curve obtained from a side-grooved CT-specimen and with 'constraint modified' J_R-curves.

Normal 20-noded volume elements were used in the whole model including the crack tip region which is often modeled with collapsed elements to describe the singular strain fields. They can not describe the blunting of the crack tip which is the most important geometric nonlinear effect in the present case. Thus the 'materially nonlinear only (MNLO)' - formulation was used.

The present simulations of crack growth are based on the h-variation calculated at the Gaussian integration points located nearest to the crack front, at the load level corresponding to initiation. It is assumed that the h-value is not essentially affected by a moderate amount of crack growth. CT-specimens and the plate are modeled using finite elements of equal size at the crack front. So the h-values used for the CT-specimens and the plate are consistent.

In a side-grooved CT-specimen the local J-value and triaxiality of stress state do not vary much along the crack front. Thus it is appropriate to use only one J_R-curve in simulating crack growth. This is depicted in Fig. 5 where the estimated and measured crack growth are compared for the side-grooved specimen AED02 at the end of the experiment. The agreement is good even near the bottom of the side-groove which was modeled rather coarsely.

The situation is very different in a smooth specimen. In the analysis for the smooth CT-specimens the effect of the varying constraint was considered. One difficulty was caused by the very low triaxiality level at the outer surface where the stress state is near plane stress. The stress state does thus not correspond there to the average h_m in any of the CT-specimens. In a first stage the ASTM blunting line was used as the J_R-curve at the outer surface. A comparative analysis was made using only the J_R-curve obtained from the thicker smooth specimen AEF01. The results for the specimen AEF01 are compared in Fig. 6. A very clear tunneling can be seen in the middle of the specimen in the experimental result. None of the simulations was able to reproduce this effect accurately, but a clearly better agreement was achieved when the constraint dependent crack growth resistance was considered. At the outer surface the new model improved the agreement remarkably. In case of the thinner specimen AED04 the situation was more complicated because shear fracture occurred at the outer surfaces.

Figure 7 represents the finite element model used in the analysis for the plate with the surface flaw. Due to symmetry only one quarter of the plate was modeled. Equal prescribed vertical displacements were imposed along the load line.

Calculated and measured strains at the crack side of the plate, near the crack end, are compared in Fig. 8. The agreement between those results was good. As shown in Fig. 9, the calculation somewhat overestimated the load. Main reason for that is probably the rather coarse mesh. At the same CMOD level, the calculated load point displacement was clearly smaller than the measured one (Fig. 10). The discrepancies between load, load point displacement and CMOD results may be caused by following reasons:

- The displacement was measured directly from the hydraulic cylinder whereas the finite element model did not include the compliance of the loading.
- The model was somewhat too stiff against bending, because it was rather coarse in the length direction of the plate. The nearest Gaussian integration points had therefore a rather large distance from the support lines and so the model could not consider the local plastic effects there.
- Because the MNLO formulation was used, the possible increase in the distance between support lines making the plate more flexible was ignored. The actual displacement of the support rollers was not measured but the finite element calculations indicated that this displacement is at most 5 mm affecting the load line displacement by less than 1%.

Figure 11 shows calculated h-variations along the crack front in the plate at different load levels. The constraint parameter had a quite uniform value along the front except very near the outer surface. The value was almost the same as in a side-grooved CT-specimen [4]. Thus the lower bound J_R-curve could be applied in the main part of the crack front. Figure 12 compares J-variations at the end of the experiment. As in the case of the smooth CT-specimen, both simulations of crack growth led to very similar results as regards to local J-values. A stationary analysis yielded higher local J-values especially in the middle of the specimen. Thus it may be concluded that a stationary analysis tends to overestimate crack growth at the deepest point of the flaw.

As the final result the estimated and measured crack growth are compared in Fig. 13. The amount of stable crack growth was quite small in the experiment. Thus it was difficult to separate apparent crack growth due to blunting from actual stable crack growth. Therefore the crack extension values in Fig. 13 contain the stretch zone. The agreement between calculation and measurement is good. The consideration of the constraint effect improved the result especially near the outer surface.

Table 2 compares measured stable crack growth (excluding blunting) at the deepest point of the flaw with analytical and numerical results. Different alternative loading parameters were considered. Only the lower bound crack growth resistance curve obtained from a side-grooved CT-specimen was used. Due to the discrepancies between load, load point displacement and CMOD results, which were discussed above, they led to different results. Stable crack growth is underestimated by analytical methods, numerical methods yielded a good agreement when the measured force was used as loading parameter and to an overestimation when CMOD or load line displacement was used.

4 SUMMARY AND CONCLUSIONS

The work was aimed as a supplementary link in assuring the applicability of numerical and analytical fracture mechanics methods to the assessment of the behaviour of real structures. Additionally it was aimed as validation of nondestructive examination methods.

For this purpose a large flawed plate made of a reactor pressure vessel steel was tested. The loading and temperature at the deepest point of the crack as well as the material behaviour during the test were planned to simulate those during a pressurized thermal shock. The material was characterized using stress strain and crack growth resistance measurements. A number of simulations of stable crack growth in the plate test and tests with CT-specimens were made with analytical and numerical methods.

As regards to the plate test, neither the potential measurement method, which has proved very reliable in fracture resistance testing, nor the acoustic emission gave an indication of crack growth. However, some crack growth could be seen in the fracture surface. In calculating stable crack growth, the use of only the lower bound crack growth resistance curve obtained from a side-grooved CT-specimen led to different results when different methods were used: to an underestimation by analytical methods, by numerical methods to a good agreement when the measured load was used as loading parameter and to an overestimation when CMOD or load line displacement were used. In the calculation for a side-grooved CT-specimen, it was

TABLES

Table 1. Dimensions of the CT-specimens.

specimen	thickness (mm)	width (mm)	a/W (-)	side-grooves (%)
AED04	12.5	50	0.60	-
AEF01	40	80	0.61	-
AED02	40	80	0.61	20

Table 2. Estimated and measured stable crack growth in the plate. Stretch zone excluded.

method	loading parameter	stable crack growth (mm)
test	-	0.3
analytical	load	0.1
FE	load	0.3
FE	CMOD	1.1
FE	load line displacement	1.4

appropriate to use only the lower bound crack growth resistance curve, whereas in the case of smooth CT-specimens it proved to be necessary to consider also the differing local stress state triaxiality.

Good results were achieved in the numerical simulation of local stable crack growth under mechanical loading, especially when the constraint dependent crack growth resistance was considered. Stationary analyses overestimated local J-values especially in the middle of the specimen and proved thus to be somewhat conservative.

Unfortunately, the planned verification during a PTS loading was not achieved in the HDR programme [6], because the actual crack size in the long duration PTS test (THEL) was too small to obtain stable crack growth. Thus a similar test with a deeper crack should be performed. Another interesting task would be to try to apply the presented constraint parameter on cleavage fracture for shallow cracks. For that purpose further experimental investigations combined with numerical assessments are necessary.

REFERENCES

/1/ K.J. Bathe, ADINA, a Finite Element Program for Automatic Dynamic Incremental Nonlinear Analysis. Report 82 448-1, MIT, Cambridge Mass., USA, 1980.

/2/ IWM-CRACK, a Subroutine Package for Crack Problems. Fraunhofer-Institut für Werkstoffmechanik, Freiburg, FRG.

/3/ Kordisch, H., Sommer, E., Schmitt, W., The Influence of Triaxiality on Stable Crack Growth. Nuclear Engineering and Design 112, pp 27 - 35, 1989.

/4/ Talja, H., Kordisch, H., Hodulak, L., Assessment of Stable Growth of Surface Flaws. Defect Assessments in Components - Fundamentals and Applications. ESIS/EGF9 (Eds. J.G. Blauel & K.-H. Schwalbe. 1991, Mechanical Engineering Publications, London, pp. 1025 - 1039.

/5/ Talja, H., Hodulak, L., Kordisch, H., Voss, B., Knee, N., Durchführung und Analyse eines Laborversuches zur numerischen Simulation des stabilen Riβwachstums. Report V40/88 of the Fraunhofer-Institut für Werkstoffmechanik, 1988.

/6/ Kordisch, H., Talja, H., Neubrech, G. E., Analysis of Initiation and Growth of Circumferential Crack in the HDR-RPV-Cylinder under Pressurized Thermal Shock. SMiRT-10 Post Conference Seminar No. 2, Monterey, California, U.S.A., August 1989.

/7/ Brocks, W., Schmitt, W., The Role of Crack Tip Constraint for Ductile Tearing. European Conference on Fracture - ECF8, Torino, Italy, October 1 - 5, 1990.

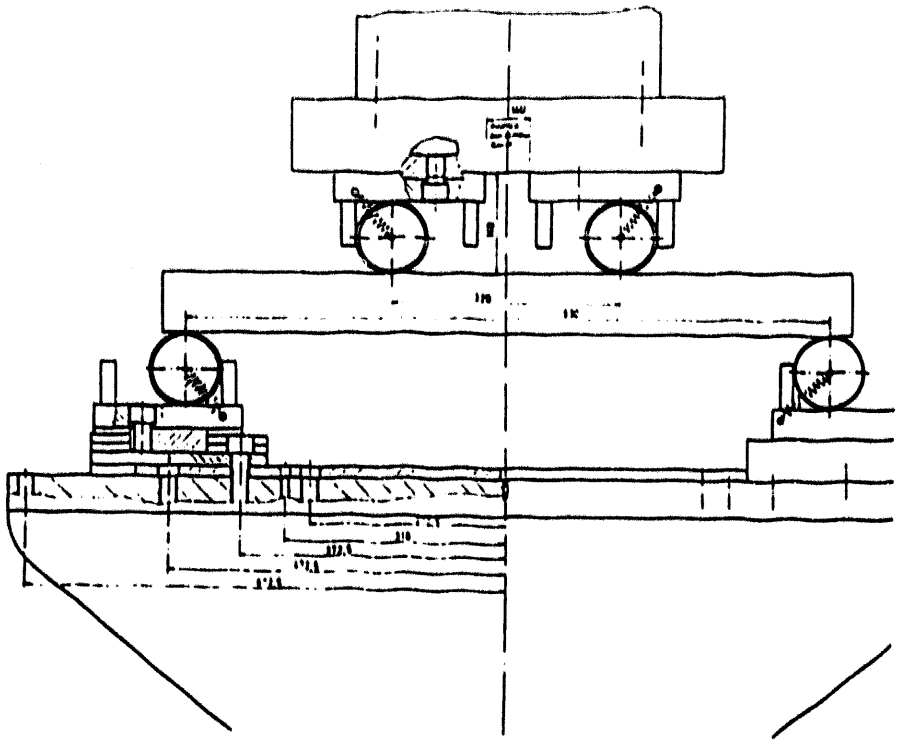

Fig. 1 *The configuration of the four point bending plate test.*

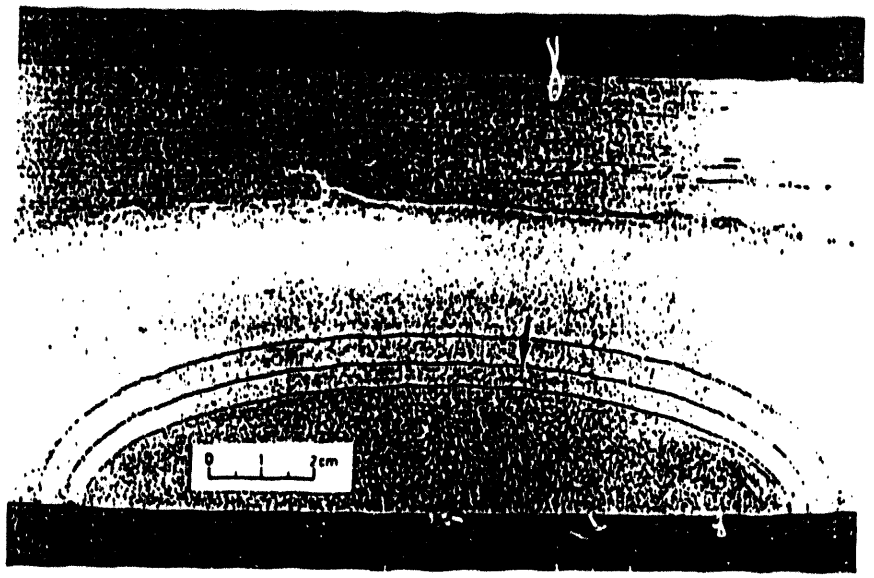

Fig. 2 *Fracture surface of the steel plate.*

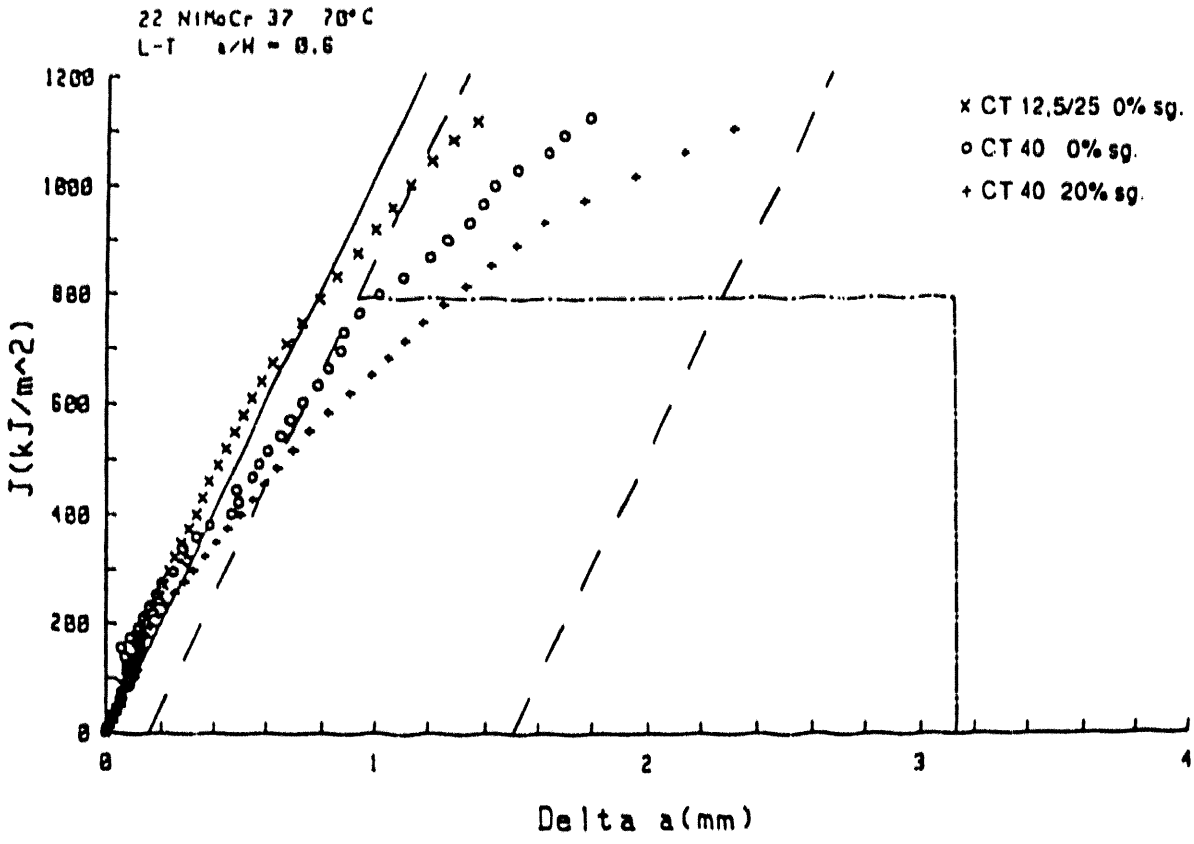

Fig. 3 *Crack growth resistance curves measured for the material 22 NiMoCr 37 in 70 °C.*

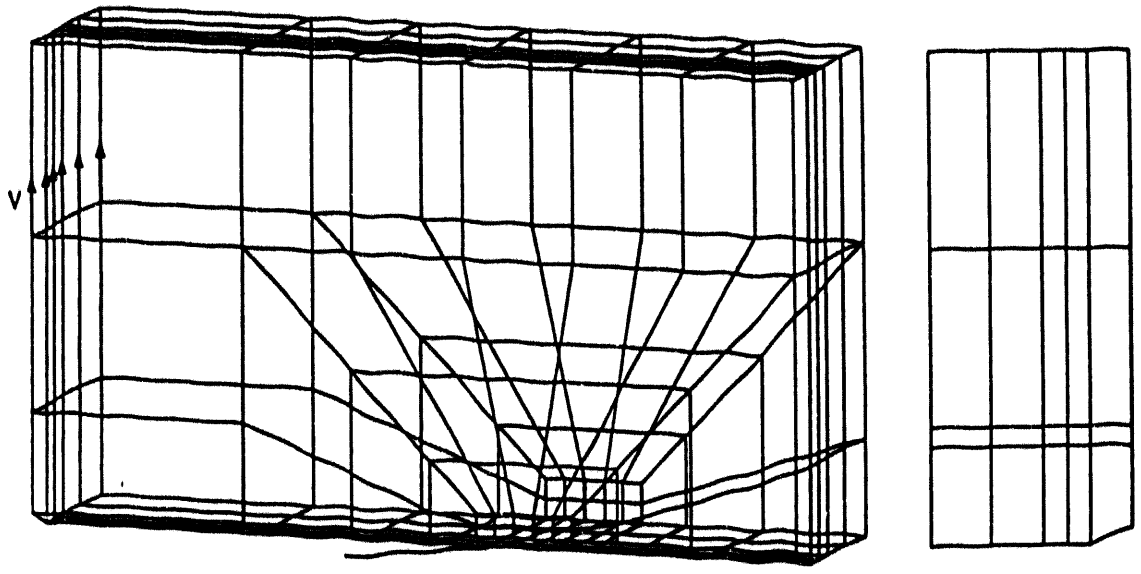

Fig. 4 *Finite element mesh for the side-grooved CT-specimen AED02.*

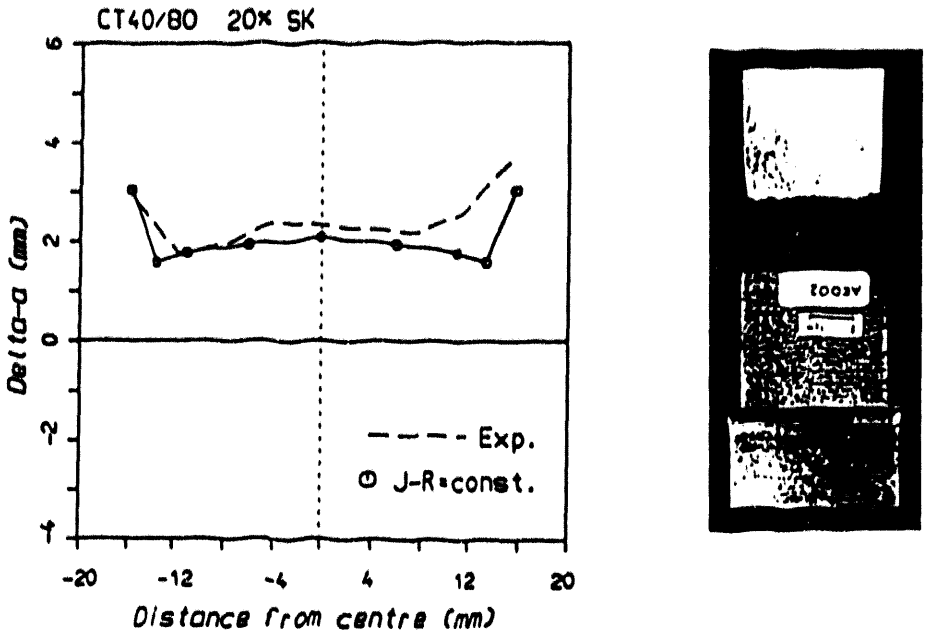

Fig. 5 *Estimated and measured crack growth in the side-grooved specimen AED02.*

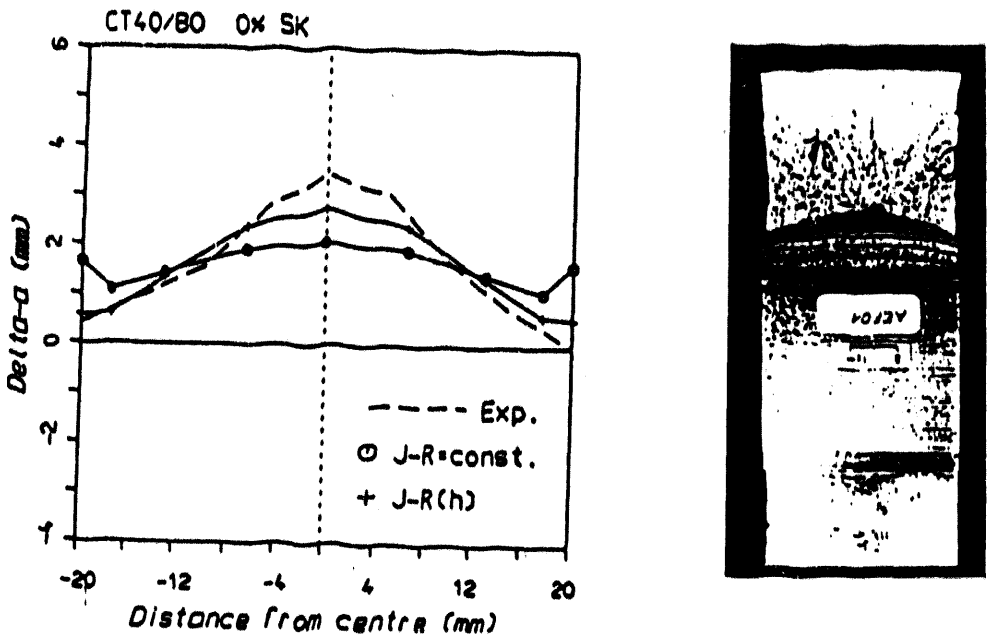

Fig. 6 *Estimated and measured crack growth in the smooth specimen AEF01.*

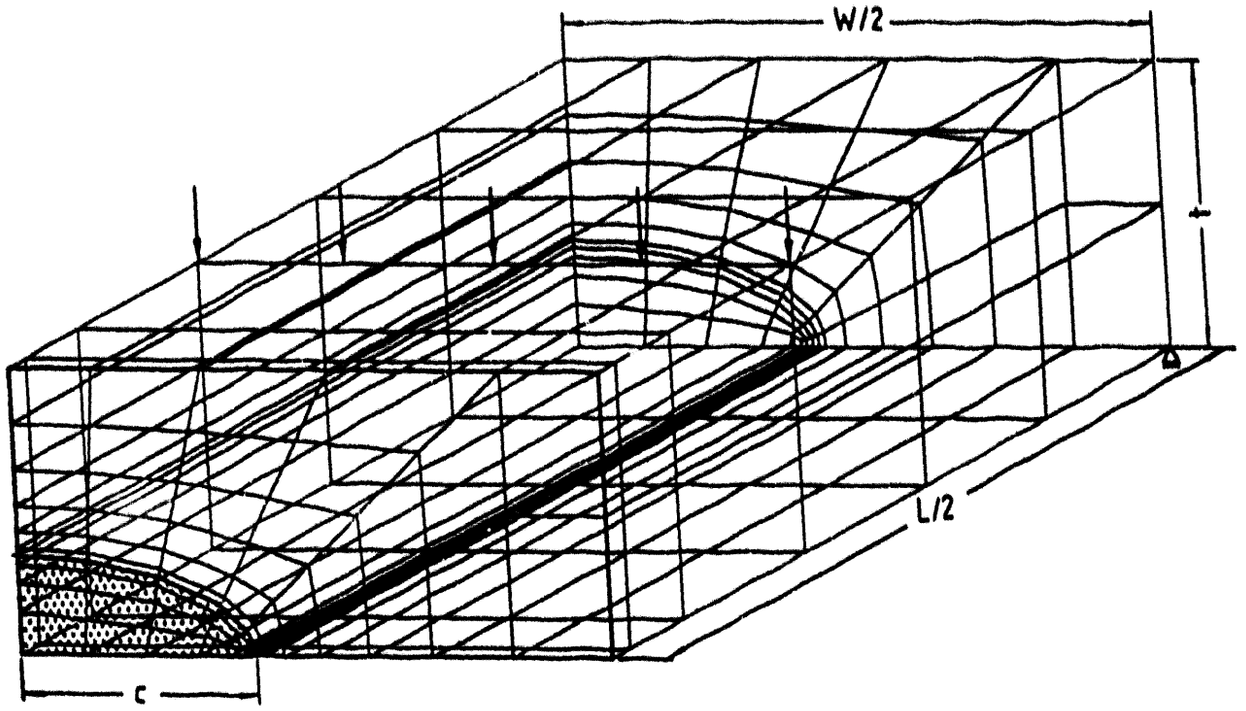

Fig. 7 Finite element mesh for the flawed plate.

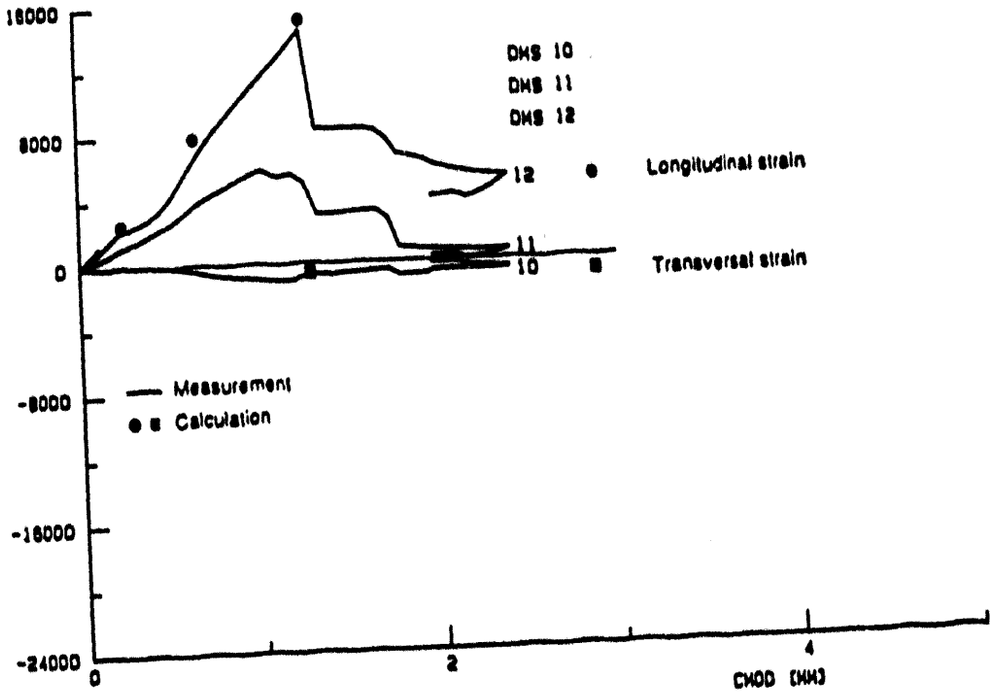

Fig. 8 Comparison of measured and calculated strains in the plate near crack end.

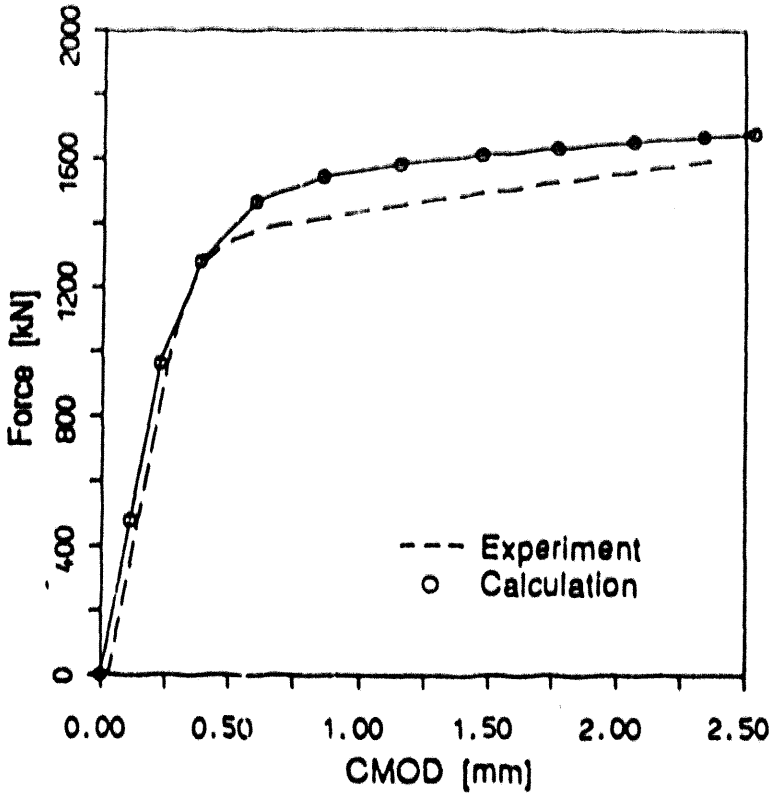

Fig. 9 *Comparison of measured and calculated load vs. load line displacement.*

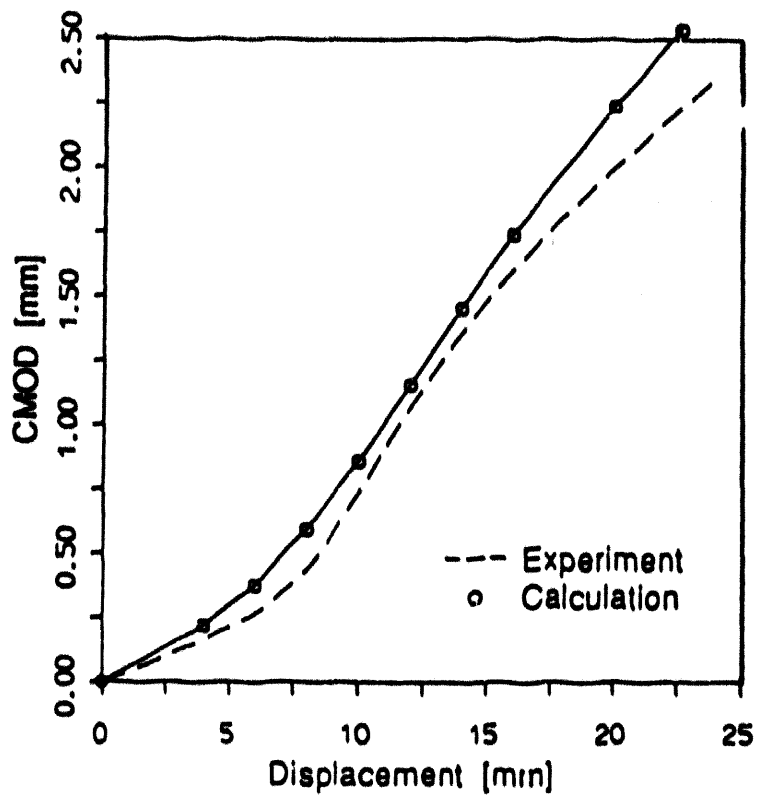

Fig. 10 *Comparison of measured and calculated CMOD vs. load line displacement.*

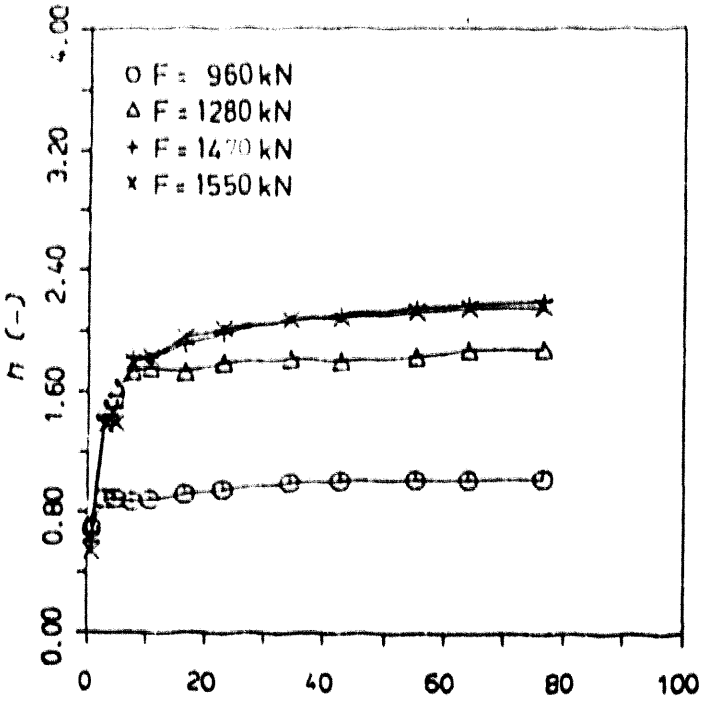

Fig. 11 h-distribution along crack front in the plate.

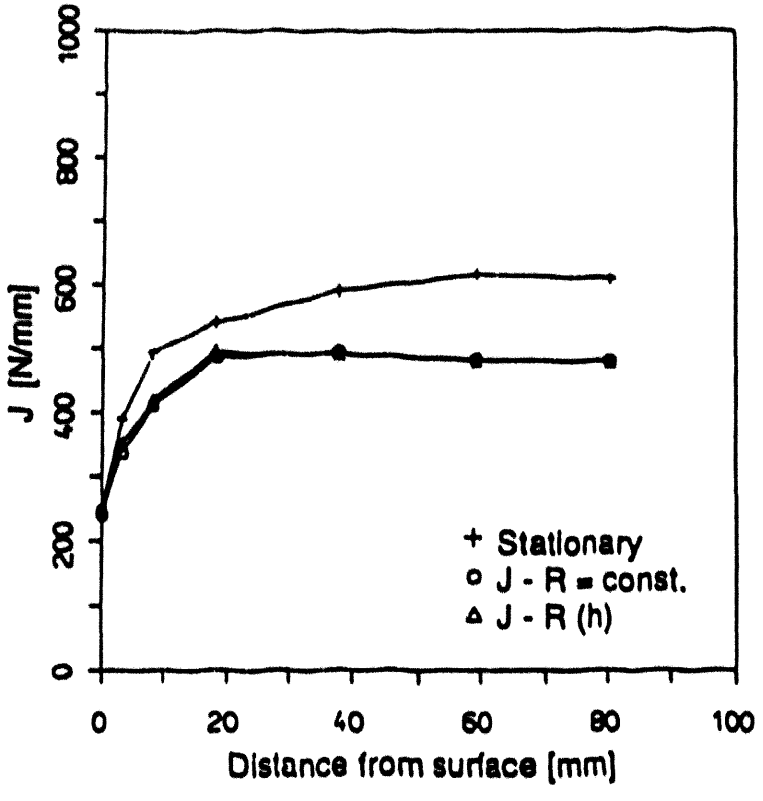

Fig. 12 J-distribution along crack front in the plate.

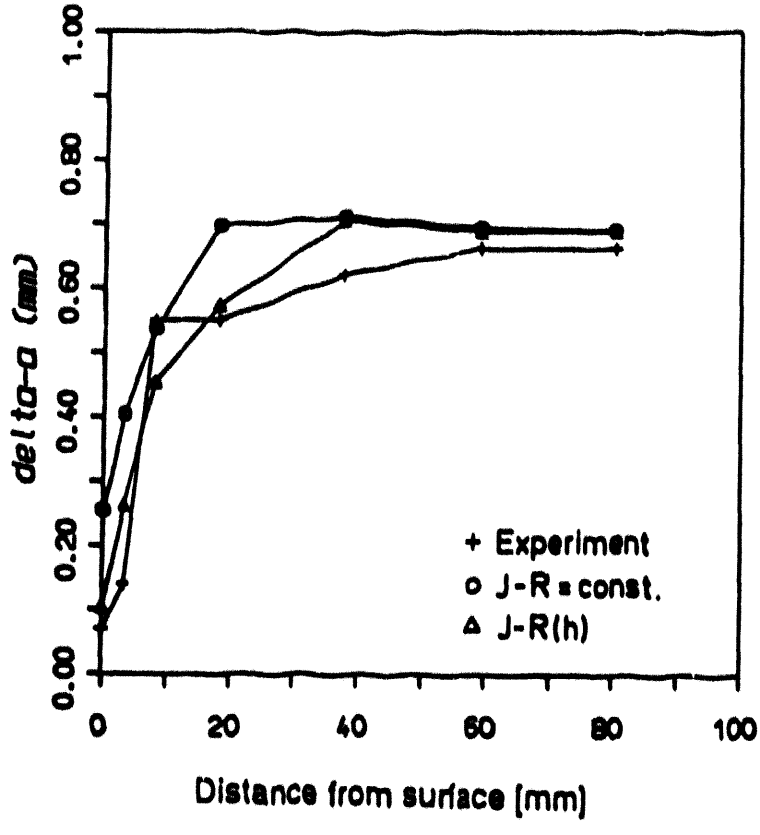

Fig. 13 Comparison of measured and estimated crack growth in the plate.

EXPERIMENTAL INVESTIGATIONS OF THE FRACTURE TOUGHNESS ENHANCEMENT ASSOCIATED WITH SHALLOW FLAWS *

T. J. Theiss[1], D. K. M Shum[1] & S. T. Rolfe[2]

[1]Oak Ridge National Laboratory
Oak Ridge, Tennessee 37831-8056
[2]University of Kansas
Lawrence, KS 66045-2235

ABSTRACT

The Heavy Section Steel Technology Program (HSST) is investigating the influence of flaw depth on the fracture toughness of reactor pressure vessel (RPV) steel. Recently, it has been shown that shallow cracks tend to exhibit an elevated toughness as a result of a loss of constraint at the crack tip. The loss of constraint takes place when interaction occurs between the elastic-plastic crack-tip stress field and the specimen surface nearest the crack tip. An increased shallow-crack fracture toughness is of interest to the nuclear industry because probabilistic fracture-mechanics evaluations show that shallow flaws play a dominant role in the probability of vessel failure during postulated pressurized-thermal-shock (PTS) conditions.

The HSST investigation is a joint analytical/experimental study combining the use of shallow-cracked laboratory specimens with RPV analysis. All tests have been performed on beam specimens loaded in 3-point bending using specimens about 100 mm deep. Primarily two crack depths have been considered: a = 50 and 9 mm (a/W = 0.5 and 0.1). Test results indicate a significant increase in the fracture toughness associated with the shallow flaw specimens in the lower transition region compared to the conventional fracture toughness. The testing has produced a limited database of fracture-toughness values as a function of crack depth which can be used in probabilistic or deterministic fracture mechanics analyses of pressure vessel integrity. Final test results from the shallow-crack fracture toughness program will be included in this paper.

Examination of previously tested thermal shock data reveals that no toughness elevation appears to be present even though the thermal shock cylinders were tested with shallow flaws.

INTRODUCTION

The Heavy-Section Steel Technology (HSST) program sponsored by the Nuclear Regulatory Commission (NRC), is investigating the influence of crack depth on the fracture toughness of A533B material under conditions prototypic of a pressurized-water reactor (PWR) vessel. Specifically, HSST is investigating the significance of the increase in fracture toughness associated with decreasing flaw depth. The elevated toughness associated with shallow-flaws (i.e. shallow-flaw effect) is the result of a loss of constraint at the crack-tip because of the proximity of the crack-tip to the specimen surface. This paper presents the final toughness data from the HSST shallow-crack fracture toughness testing program and posttest analysis of the results. More detailed information on the motivation and objectives of the program, experimental set-up, and verification of the test techniques used can be found in previously published reports [1-4].

---

* Research sponsored by the Office of Nuclear Regulatory Research, U.S. Nuclear Regulatory Commission under Interagency Agreement 1886-8011-9B with the U.S. Department of Energy under Contract DE-AC05-84OR21400 with Martin Marietta Energy Systems, Inc.

The primary application of the HSST shallow-crack fracture toughness program is the pressurized-thermal-shock (PTS) accident scenario which in some cases limits the operating life of a PWR reactor pressure vessel (RPV). Probabilistic fracture-mechanics analyses of an RPV have shown that shallow rather than deep flaws dominate the conditional probability of vessel failure in a PTS evaluation [5-7]. In fact, up to 95% of all initial crack initiations originated from flaws with depths of 25 mm or less. Thus, PTS analyses require that the behavior of shallow flaws be understood. In addition to investigating the shallow-flaw effect for PTS analyses, the shallow-flaw investigation is studying the general influence of constraint on fracture toughness. The HSST shallow-crack program is investigating the influence of both a loss of in-plane constraint (i.e. shallow-flaw effect) and a loss of out-of-plane constraint (i.e. thickness effect). The understanding of constraint is vital to the transferability of small-specimen toughness data to various structural applications (including RPVs). Furthermore, ASTM validity requirements in standard fracture toughness determinations may be appropriately relaxed based on a better understanding of the influence of constraint on fracture toughness.

The HSST shallow-flaw program is a joint experimental/analytical program which has produced a limited data base of shallow-flaw fracture toughness values and analysis to aid in the transferability of the specimen data to an RPV. The experimental portion of the program was divided into two phases: a development phase and a production phase. The development phase established the techniques appropriate for shallow-crack testing, verified the existence of a shallow-flaw effect in A533B beams, and compared beams of three thicknesses to choose the thickness for the production phase of the program. Broken ends of the development-phase beams were subsequently remachined and tested, yielding six additional deep-crack beam tests. The production phase involved developing a limited data base of shallow-crack toughness values at various temperatures. The analytical portion of the shallow-flaw program consisted of both pretest and posttest analyses of the test specimens. The pretest analysis was used to size the instrumentation for the tests and to select an appropriate shallow-crack depth.

EXPERIMENTAL PROGRAM

The specimen configuration chosen for all testing in the shallow-crack program is the single-edge-notch-bend (SENB) specimen with a through-thickness crack (as opposed to the 3D surface crack). A beam approximately 100-mm deep (4-in.) was selected for use in the HSST shallow-crack project. To maintain consistency with ASTM standards, the beams were tested in three-point bending. All testing was conducted on unirradiated reactor material (A533 Grade B, Class 1 steel) with the cracks oriented in the thickness (S) direction to simulate the material conditions of an axial flaw in an RPV. Specimens were taken from the center, homogeneous region of the source plate to minimize metallurgical differences between the material surrounding a shallow and deep flaw.

The specimen thickness was varied in the development phase tests to examine the influence of thickness on toughness. Three beam thicknesses were used: B = 50, 100, and 150 mm (2, 4, and 6 in.). The span for the 50-mm-thick beam was 4W or 406 mm (16 in.). The spans for the 100- and 150-mm beams were increased to assure failure without exceeding the load capacity of the beam loading fixture. Figure 1 shows three of the beam sizes used in the shallow-crack testing. Both shallow- and deep-crack specimens were tested at each thickness. Beams 100 mm thick (4 in.) were used for the production phase tests.

The development and production phases of the HSST shallow-crack testing program resulted in 14 and 18 data points, respectively, and an additional 6 deep-crack beams of varying thickness were tested providing a total of 38 data points. All but one of the development phase-tests were conducted at -60°C, and the 6 additional deep-crack beams were tested at -45°C. The production-phase tests used one beam geometry (100 x 100 mm) but were conducted at various temperatures. Two crack depths (one shallow and one deep) were used for the shallow-crack fracture toughness testing program. The nominal shallow crack depth chosen was ≈ 10 mm (a ≈ 0.4 in.), which is representative of the flaw depths that resulted in a majority of the initiations in the IPTS studies [5-7] and yields a normalized crack depth (a/W) of 0.10. All deep-crack specimens were cracked to an a/W value of approximately 0.5. The total test matrix for the HSST shallow-crack fracture toughness program is shown in Table 1.

Instrumentation was attached to the specimens to permit independent determination of both J-integral and crack-tip opening displacement (CTOD). The J-integral was determined from the load-line-displacement (LLD) vs. load diagram. The LLD was determined using a reference bar attached to the beam fixture and a micrometer attached to the neutral axis of the beam. CTOD was determined from crack-mouth-opening-displacement (CMOD) gages mounted directly on the crack mouth of the specimen. Toughness data are expressed in terms of CTOD according to ASTM E1290-89, Crack-Tip Opening Displacement (CTOD) Fracture Toughness Measurement. ASTM E399, Plane-Strain Fracture Toughness of Metallic Materials, was used to analyze the deep-crack specimens to determine if the test results could be considered "valid" plane-strain (K_{Ic}) data. ASTM E813, J_{Ic}, A Measure of Fracture Toughness, is not applicable to these tests since typically the failures were cleavage events; however, critical J-integral cleavage values (J_c) were determined for each test. The shallow-crack toughness formulations are as similar as possible to the deep-crack ASTM standard toughness formulations.

Material Properties

Two heats of unirradiated A 533 B material were tested in this program. The development phase and six additional deep-crack beams were taken from the HSST-CE plate and were tested in the T-S orientation. The production-phase beams were taken from HSST Plate 13B, were given a final heat treatment (620 °C for 40 hrs) prior to machining, and were tested in the L-S orientation. Material properties used in the analysis of the shallow-crack test results for both the development and production phases are included in Table 2. Additional information on the shallow-crack production-phase material characterization and source material properties can be found in References 8-10.

Crack-Tip Opening Displacement (CTOD), δ_c, Determination

The plastic component of CTOD is determined experimentally from the plastic component of CMOD and the rotation factor (RF), according to ASTM E1290. The plastic displacement of the crack flanks is assumed to vary linearly with distance from the plastic center of rotation. In this way, the plastic CMOD can be related to the plastic CTOD. The plastic center of rotation is located ahead of the crack tip a distance equal to the rotation factor multiplied by the remaining ligament (W-a). The rotation factor in ASTM E1290 is 0.44, but is a function of specimen geometry and material. RF values determined for deep-crack beams are not necessarily applicable for otherwise identical shallow-crack beams.

An experimental technique was utilized in this program to locate the neutral axis of the beam ahead of the crack tip, using strain gages on each face of the beam. Assuming the plastic center of rotation is located at the neutral axis of the beam, the RF can be determined. Since the rotation factor relates the plastic component of CMOD to the plastic component of CTOD, only plastic strains were used to determine the rotation factor. The rotation factors determined using this technique were relatively insensitive to load once plastic strains became nontrivial and were consistent on each face of the beam. The RF for a beam was taken as the average calculated RF from each face. Four deep-crack beams were strain gaged yielding an average RF of 0.44. Eight shallow-crack beams were gaged to yield an average RF of 0.49. The rotation factor used for the CTOD toughness calculation is the average of the values from this technique for the two crack depths.

A parametric evaluation was performed to assess the sensitivity of the calculated CTOD toughness on the RF. This evaluation indicated that the plastic component of CTOD is not sensitive to the value of the rotation factor. Shallow-crack beams are less sensitive to the rotation factor than deep-crack beams. A 25% increase in rotation factor increases the plastic CTOD by about 5% and 17% for the shallow and deep-crack geometries, respectively. The rotation factor is insensitive to beam thickness and absolute beam dimensions, varying only with a/W ratios for a given material and specimen depth. Based on the comparison of deep and shallow RF and the insensitivity of CTOD to RF, the ASTM E1290 value of the RF of 0.44 would appear to be appropriate for deep and shallow-cracked A533B specimens.

Critical CTOD (δ_c) values calculated using the RF values just described and ASTM E1290-89 are included in Table 3. The ratios of the shallow-to-deep-crack lower-bound δ_c at T-RT_{NDT} = -25 °C and -10 °C are 3.3 and 4.9 respectively, which is consistent with the A36 and A517 results [11, 12] Further examination of these data indicate little variation of δ_c as a function of beam thickness for either the deep-crack or shallow-crack beams.

J-Integral, J_c, Determination

The critical J-integral value (J_c) was determined for each beam using LLD data. Little or no crack growth took place in these tests so ASTM E813 was not applicable. The J-integral was calculated by dividing the elastic and plastic components of J and using only the plastic area under the load v. LLD curve and a plastic η factor as proposed by Sumpter [13]. The equations used to determine the shallow-crack J-integral toughness are as follows [13]:

$$J_c = J_{el} + J_{pl} \quad \text{where} \tag{1}$$

$$J_{el} = K_c^2(1-\nu^2) / E \quad \text{and} \tag{2}$$

$$J_{pl} = \eta_{pl} U_{pl} / (B(W-a)) \tag{3}$$

where U_{pl} is plastic area under load v. LLD curve.

The J-integral toughness values for each beam are given in Table 3. J-integral results are consistent with the CTOD results. The ratios of the shallow-to-deep lower bound J_c at T-RT_{NDT} = -25°C and -10°C are 2.4 and 2.9 respectively, which is consistent with the δ_c results.

Comparison of δ_c, and J_c Values

CTOD toughness values can be converted into J-integral values [14] according to $J_c = m \cdot \sigma_f \cdot \delta_c$, where σ_f is the average of the yield and tensile strengths, and m is the constraint parameter. Since J_c and δ_c are known for each specimen, comparison of J_c and δ_c allows m to be determined as a function of crack depth. Plots of J v. CTOD show a linear relationship between the two toughness expressions. The constraint parameter, m, for each test was determined using the critical toughness (J_c and δ_c) values. The constraint parameter as a function of crack depth yields repeatable results as shown in Fig. 2. The average deep-crack constraint parameter is 1.5. The average shallow-crack constraint parameter is 1.0 except for three beams which resulted in a significantly elevated m value. These three shallow-crack beams were tested on the lower shelf where linear-elastic behavior takes place regardless of the crack depth. An average constraint parameter of 1.9 was found for these beams. This value is anticipated on the lower shelf since the elastic CTOD equation is based on conversion from J of $2\sigma_0$ and the plastic component of CTOD is negligible. The constraint parameter values found experimentally are consistent with published analytical results [15]. Critical CTOD was converted into J-integral expressions using the average values of m shown in Fig. 2. J-integral values converted from CTOD will be referred to as J_c (CTOD); J_c (LLD) refers to J-integral values determined directly from LLD records.

Stress-Intensity Factor, K_c, Determination

Typically RPV fracture toughness values are expressed in terms of the critical stress-intensity factor, K_{Jc}. The two J-integral toughness expressions were converted into elastic-plastic K_{Jc} values according to $K_{Jc} = \sqrt{(J\,E')}$ [14]. The plane-strain value of E', $E / (1-\nu^2)$, is justified because thickness had little influence on the resulting toughness values. Figure 3 and Table 3 contain comparisons of K_{Jc} from the two J estimation techniques used (CTOD and LLD). As shown in

Fig. 3, the two J estimation techniques give similar values of K_{Jc}. The maximum difference between the two techniques is about 10%. The average difference is less than 1%.

The toughness data expressed in terms of K_{Jc} (CTOD) vs. normalized temperature ($T\text{-}RT_{NDT}$) are presented in Table 3 and Fig. 4. The data show a significant increase in the fracture toughness for shallow-crack specimens in the transition region of the A533B toughness curve. All but one of the specimens failed in cleavage (the data point indicated in Fig. 4 with the arrow). As expected, the shallow-crack specimens on the lower shelf, where linear-elastic behavior occurs, showed little to no toughness increase. The specimens had crack depths that were deep (a ~ 50 mm) or shallow (a ~ 10 mm) except for one beam with a crack depth of 14 mm. This intermediate crack-depth specimen also appears to show the shallow-crack-toughness elevation.

The shallow-crack toughness increase can be quantified in terms of a ratio of toughness values at one temperature or as a temperature shift. In terms of K_{Jc}, the shallow-crack toughness increase is approximately 60% at $T\text{-}RT_{NDT}$= -25C. Figure 4 shows the shallow-crack and deep-crack test data with approximate lower bound curves. The shallow-crack lower-bound curve was formed using the deep-crack lower bound curve shifted by 35°C (63 °F). The shifte deep-crack lower-bound curve fits the shallow-crack data well at all test temperatures.

Toughness data in terms of K_{Jc} (CTOD) are plotted as a function of beam thickness for all of the tests conducted at $T - RT_{NDT}$ = -25C and -11C (-45F and -20F) in Fig. 5. As indicated in Figs. 4 and 5, the toughness values for the shallow- and deep-crack specimens from the 100- and 150-mm-thick (4- and 6-in.) beams generally are consistent with the 50-mm-thick (2 in.) data. However, there appears to be slightly more data scatter associated with the 50-mm-thick (2 in.) beams than with the 100- and 150-mm-thick (4- and 6-in.) beams. None of the deep-crack tests strictly meet the requirements of ASTM E399 for a valid plane-strain K_{IC} result because of insufficient crack depth. The beams which had otherwise linear-elastic test records and were sufficiently thick for valid results are marked in Fig. 5.

POST-TEST SPECIMEN ANALYSIS

This section presents detailed post-test two-dimensional (2D) plane-strain analysis results for a select number of specimens from the production phase of the shallow-flaw fracture toughness testing program. Specifically, detailed finite-strain, finite element analyses were performed for six specimens that were tested at -40°C. Three of the specimens (Beams # 36, 31, & 25) are deep-flaw specimens with nominal a/W = 0.5, while the remaining three are shallow-flaw specimens (Beams # 38, 37, & 21) with nominal a/W = 0.1. As shown in Table 3, the three shallow-flaw specimens exhibited higher toughness levels than the three specimens with deep flaws. One of the primary objectives of these analyses was to evaluate the J estimation techniques developed to determine shallow-crack toughness.

Material Models

Two material models have been adopted in the analysis of the test specimens. The first material model simulates the unirradiated tensile properties of A533B (HSST Plate 13B) at -40°C (-40°F) as determined from material characterization. The linear-elastic portion of the true stress-true strain curve is characterized by a yield strain of magnitude $\varepsilon_0 = \sigma_0/E = 0.0022$, where the Young's modulus E = 207.2 GPa (30×10^6 psi), the uniaxial yield stress in tension σ_0 = 454 MPa (65.8 ksi) and Poisson's ratio ν = 0.3. The uniaxial true-stress true-plastic-strain curve in tension is modeled in a multi-linear fashion as indicated in Fig. 6. In subsequent discussions this material model is referred to as the unadjusted model.

Post-test analysis results to be presented indicate that finite element models based in part on the unadjusted material model underestimate the displacements of the specimens as compared to experimentally measured values. Various reasonable analysis options to reduce the stiffness of the finite element models have been attempted. One option that, in conjunction with other analysis techniques to be described later, results in good agreement between calculated and measured mechanical responses of the specimens is to reduce both the Young's modulus and the uniaxial

yield stress in tension from their pre-test characterization values. The magnitudes of the reduction are consistent with anticipated variability in tensile material properties. In subsequent discussions this material model is referred to as the adjusted model.

The adjusted material model incorporates adjustments to the unirradiated tensile characteristics of A533B (HSST Plate 13B) in the following manner. Within the linear-elastic region the Young's modulus is reduced by 5% such that E = 196.5 GPa (28500 ksi). The yield stress was reduced by 9% such that σ_0 = 413 MPa (59.9 ksi). A 9% variation in yield and a 5% variation in E are reasonable based on the scatter of material properties. The adjusted yield strain is thus ε_0 = 0.0021, and Poisson's ratio remains ν = 0.3. The uniaxial engineering-stress engineering-strain curve in tension beyond yield is the same as the unadjusted model. The uniaxial true-stress true-plastic-strain curve in tension for the adjusted model is also indicated in Fig. 6.

Minimal differences are observed between the stress-strain curves of these two material models when they are presented in the form indicated in Fig. 6. However, an indication of the relative plastic response of these two material models can be obtained with the stress-strain curves presented in the form indicated in Fig. 7. In Fig. 7, the instantaneous yield stress σ is normalized by the initial yield stress σ_0. The effects of the differences between the two material models on analysis results are expected to become significant as the loading conditions in a specimen approach elastic-plastic behavior.

Finite Element Models and Analysis Assumptions

The finite-strain, elastic-plastic post-test analyses are performed using the finite element code ABAQUS [16]. The analyses assume a rate-independent, J_2 (isotropic-hardening) incremental plasticity theory as implemented in ABAQUS. The planform for both the shallow- and deep-flaw specimen is 102 mm x 610 mm (4-in. x 24-in.). The initial flaw-depth is 10.2 mm (0.4 in.) for the shallow-flaw specimen and 50.8 mm (2 in.) for the deep-flaw specimen. The shallow-flaw specimen geometry is modeled with the finite element mesh indicated in Fig. 8 (a, b and c), which is made up of 914 10-node generalized-plane-strain isoparametric elements with a total of 2883 nodes. The deep-flaw specimen geometry is modeled with the finite element similarly refined mesh made up of 922 10-node generalized-plane-strain isoparametric elements with a total of 2903 nodes. These 10-node elements behave as conventional 8-node isoparametric elements except for an extra degree-of-freedom (DOF) that allows for uniform straining in a direction perpendicular to the plane of the mesh [16]. In a plane strain analysis the out-of-plane DOF is not active. The integration order of the elements is 2x2.

A unique feature of the finite element meshes is the highly refined crack-tip region. The rectangular crack-tip region is made up of 29 (shallow-flaw) or 31 (deep-flaw) "rings" of elements as indicated in Fig. 8(b) for the shallow-crack geometry. The mathematically-sharp crack-tip profile associated with small-strain fracture analysis is replaced, in the present finite-strain context, with an initial root radius prior to the imposition of external loading as indicated in Fig. 8(c). The assumption of a finite value of the initial root radius is necessary to facilitate numerical convergence of the finite element results. The magnitude of the initial root radius is r_0 = 0.6 μm (2.36 x 10^{-5} in.) for the shallow-flaw mesh, while for the deep-flaw mesh r_0 = 1.3 μm (5.03 x 10^{-5} in.). The high degree of mesh refinement is necessary in order to obtain an accurate determination of the crack-tip stress and strain fields ahead of the blunting notch tip.

J-integral values are determined from up to 29 (shallow-flaw) or 31(deep-flaw) paths surrounding the crack tip to verify path independence. A measure of the mesh refinement is that the elastically determined K value using these meshes is within 99.5% of the reported value in the literature [17]. Convergence requirements of the elastic-plastic finite element results to be presented are specified by means of limiting the maximum value of the residual nodal force per unit thickness at any node. Specifically, the maximum value is required to be less than 0.1% of the product between the yield stress and the smallest element dimension in the finite element mesh.

Comparison of Calculated and Measured Mechanical Responses

Experimental measurements for the load (P), LLD and CMOD are available for the six specimens considered in these analyses. Comparison of the calculated and measured mechanical responses provides a means to gage the general accuracy of the analysis results, and provide an additional basis for establishing confidence in the calculated fracture mechanics parameters. Results of the comparison can be found in Ref. 4. As an example, Fig. 9 indicates the extent of the agreement between the calculated and measured P-LLD response for the shallow-flaw specimens.

Figure 9 presents two sets of calculated responses along with the measured responses for the three shallow-flaw specimens (Beams # 38, 37, 26). The measured responses of these specimens appear to indicate the presence of general-yielding conditions at the onset of crack initiation. The two sets of calculated curves correspond to two cases of analysis conditions labeled as Case A and B. The calculated P-LLD curve corresponding to Case A was determined based on a/W = 0.1 and the unadjusted material model. The finite element analysis was carried out under "load-control" in that reaction forces were specified along the back-side of the specimen ahead of the crack tip.

From Figs. 9 it is observed that at a given value of applied load the calculated LLD response is below the measured values both in the elastic and plastic regimes. Analysis options that have been attempted to reduce the stiffness of the finite element models include reasonable adjustment of the material model and/or refinement of the flaw depth. Post-test examination of the fracture surfaces for the three shallow-flaw specimens, along nine locations on the crack front, indicate that the actual flaw depth is 10.8 mm (a/W = 0.106) rather than the assumed value of 10.2 mm (a/W = 0.10).

Analysis results for Case B were determined based on a flaw depth of a = 10.8 mm and the adjusted material model described previously. The finite element analysis was carried out under "displacement-control" as displacements were specified along the back-side of the specimen ahead of the crack tip. As evident from Fig. 9, analysis conditions for Case B appear to result in better agreement between the calculated and measured mechanical responses both in the elastic and plastic regimes.

Comparison for the a/W = 0.5 geometry have been carried out in a similar fashion with details presented in Ref. 4. Discrepancies are observed between results based on the unadjusted material model, a/W = 0.5 and the measured responses. Post-test examination of the fracture surfaces for the three deep-flaw specimens indicate that the actual flaw depth is 51.6 mm (a/W = 0.502) rather than the assumed value of 51 mm (a/W = 0.50) or an increase of only 1%. Analysis results determined based on the nominal flaw depth of a/W = 0.50 and the adjusted material model appear to result in better agreement between the calculated and measured mechanical responses both in the elastic and plastic regimes. In subsequent discussions these are referred to as Case D conditions.

Comparison of J-Integral Values From Finite Element Analysis and J-Estimation Schemes

Fracture toughness is often expressed as the magnitude of the J-integral or the stress intensity factor (K) at the onset of crack initiation. The J-integral values have been determined as a part of the post-test analysis of the specimens. The magnitude of critical values of P and LLD (P_c, LLD_c) for the three shallow-flaw specimens at crack initiation are indicated in Table 4. The magnitude of the analytical J-integral based on attaining LLD_c are denoted as J_{LLDc}. Since the calculated P-LLD curve for the shallow-flaw specimen under-estimates the measured value of LLD at a given value of P, J_{LLDc} can be regarded as an upper bound to the actual value of the J-integral at the onset of crack initiation. On the other hand, the magnitude of the J-integral based on attaining P_c can be regarded as a lower bound to the actual value of the J-integral. These J-integral values are denoted as J_{Pc}. In terms of the stress intensity factor, magnitudes of K_{LLDc} and K_{Pc} are also listed in Table 4. Analogous results for the deep-flaw geometry based on Case D conditions are listed in Table 5.

J-estimation schemes based on the magnitude of the experimentally determined LLD and CMOD for both the shallow- and deep-flaw geometry have been presented. The J-integral values based on

these estimation scheme, denoted here as J_{EXP} (LLD) and J_{EXP} (CMOD) are listed in Tables 4 and 5 for the shallow and deep-crack beams. In terms of the stress intensity factor, magnitudes of K_{EXP} (LLD) and K_{EXP} (CMOD) are also listed in Tables 4 and 5.

Results in Tables 4 and 5 indicate that both values of J_{EXP} calculated from measured values of LLD compare favorably with the finite element results. The general accuracy of the LLD-based J-estimation scheme for the deep-flaw geometry is verified by the observation that all of the deep-flaw J_{EXP} (LLD) values are between J_{LLDc} and J_{Pc}. A similar degree of accuracy is observed for the case of the shallow-flaw geometry, although one of the J_{EXP} (LLD) values is slightly higher than the upper-bound J_{LLDc} value. The J-integral estimation scheme based on CMOD appears to overestimate the fracture toughness for these shallow-flaw specimens since all three values of J_{EXP} (CMOD) were above the upper-bound value of J_{LLDc}.

THERMAL SHOCK TESTS

Reexamination of previous HSST thermal-shock experiment (TSE) data [18] is necessary when considering the implications of the shallow-flaw effect on RPVs during PTS transients. Thermal-shock tests were conducted to determine the fracture response of an RPV to thermal-shock loading with various flaw configurations and depths. The initial flaws ranged from 11 to 19 mm deep in a vessel wall that was 152 mm thick. These flaws are roughly the same depth as those tested in the HSST shallow-flaw program. The key result of the TSE data is that the initial initiation values were mostly within the scatter band of the ASME data base. In other words, the TSE data appear to show no substantial increase in the effective fracture toughness due to any shallow-flaw effect.

The first crack initiation in the TSE and the shallow-flaw data are presented in Fig. 10 with the ASME lower-bound curve. As can be seen, the TSE data fall near the ASME lower-bound curve, while the HSST shallow-crack data are elevated over both the deep-crack data and ASME lower-bound curve. Figure 10 also indicates that the HSST deep-crack data are significantly elevated over the ASME lower-bound curve.

A possible explanation for the lack of a shallow-crack elevation in the thermal-shock data is the presence of out-of-plane stresses, which are not present in the HSST shallow-flaw specimens. Out-of-plane (biaxial) loading has been shown to decrease the effective fracture toughness in other applications [19]. The current hypothesis being investigated is that the thermal shock tests were subjected to two offsetting influences: a "shallow-flaw effect," which increases the toughness, and a "biaxial loading effect," which decreases the toughness. The net result is that the TSE data appear consistent with the uniaxially loaded deep-crack data used to generate the ASME lower-bound curve.

SUMMARY

Results from the HSST shallow-crack fracture toughness program to date can be summarized as follows:

1) Thirty-eight relatively large laboratory beam specimens were tested to compare the behavior of specimens with shallow-flaws to that of specimens with deep flaws.
2) The results showed conclusively that A 533 B shallow-flaw beam specimens have a significant increase in CTOD or J_C toughness and K_{JC} toughness in the transition region. All specimens were approximately 100 mm deep (W). Shallow-crack beams had crack depths ranging from 9-14 mm (a/W ~ 0.1 to 0.14), while deep-crack beams had 50 mm deep cracks (a/W ~ 0.5).
3) There is little or no difference in toughness on the lower shelf where linear-elastic conditions exist for specimens with either deep or shallow flaws.
4) Varying the beam thickness from 50 to 150 mm had little or no influence on the toughness in both the shallow- and deep-crack specimens in spite of the fact that the ASTM E-399 requirement for valid plane-strain results were not met.
5) In the transition region, the increase in shallow-flaw toughness compared with deep-flaw results appears to be well characterized by a temperature shift of 35°C (63°F).
6) Post-test two-dimensional (2D) plane-strain analyses were performed on both shallow-flaw and deep-flaw specimens. The analytical J-integral results were consistent with experimental J-

integral results confirming the validity of the J-estimation schemes used and the effect of flaw depth on fracture toughness.

7) Previous HSST thermal-shock data failed to show any substantial toughness increase in spite of the fact that the tests were conducted on large, unclad cylindrical vessels with a shallow, initial flaw. There is no reason to believe that the thermal-shock cylinders would not have shown a toughness elevation if the cylinders had been subjected to the same loading conditions as the shallow-crack beams, namely, no biaxial stress.

REFERENCES

[1] T. J. Theiss, "Recommendations for the Shallow-Crack Fracture Toughness Testing Task Within the HSST Program," USNRC Report NUREG/ CR-5554 (ORNL/TM-11509), August 1990.

[2] T. J. Theiss, G. C. Robinson, and S. T. Rolfe, "Preliminary Test Results from the Heavy-Section Steel Technology Shallow-Crack Toughness Program," *Proceedings of the ASME Pressure Vessel & Piping Conference*, Pressure Vessel Integrity, PVP Vol. 213/MPC-Vol. 32, pp. 125–129, ASME 1991.

[3] T. J. Theiss and J. W. Bryson, "Influence of Crack Depth on Fracture Toughness of Reactor Pressure Vessel Steel,"*Constraint Effects in Fracture ASTM STP 1171*, E. M Hackett, Ed., American Society for Testing and Materials, Philadelphia, (to be published).

[4] T. J. Theiss. D. K. M. Shum, and S. T. Rolfe, "Experimental and Analytical Investigation of the Shallow-Flaw Effect in Reactor Pressure Vessels" USNRC Report NUREG/ CR-5886 (ORNL/TM-12115), July 1992.

[5] R. D. Cheverton and D. G. Ball, "Pressurized-Thermal-Shock Evaluation of the H. B. Robinson Nuclear Power Plant," pp. 263–306, USNRC Report NUREG/CR-4183 (ORNL/TM-9567/V1), September 1985.

[6] R. D. Cheverton and D. G. Ball, "Pressurized-Thermal-Shock Evaluation of the Calvert Cliffs Nuclear Power Plant," pp. 201–244, USNRC Report NUREG/CR-4022 (ORNL/TM-9408), September 1985.

[7] R. D. Cheverton and D. G. Ball, "Preliminary Development of an Integrated Approach to the Evaluation of Pressurized Thermal Shock as Applied to the Oconee 1 Nuclear Power Plant," pp. 5.1–5.51, USNRC Report NUREG/CR-3770 (ORNL/TM-9176), May 1986.

[8] R. K. Nanstad and S. K. Iskander, "Material Characterization and Properties," in *HSST Program Semiann. Prog. Rep. April–September 1991*, USNRC Report NUREG/CR-4219, Vol. 9, No. 1 (ORNL/TM-9593/V9&N1), (to be published).

[9] D. J. Naus et al., "SEN Wide-Plate Crack-Arrest Tests Using A 533 Grade B Class 1 Material: WP-CE Series," USNRC Report NUREG/CR-5408 (ORNL/TM-11269), November 1989.

[10] D. J. Naus et al., "Crack Arrest Behavior in SEN Wide Plates of Quenched and Tempered A 533 Grade B Steel Tested Under Nonisothermal Conditions," USNRC Report NUREG/CR-4930 (ORNL-6388), August 1987.

[11] W. A. Sorem, R. H. Dodds, Jr., and S. T. Rolfe, "An Analytical Comparison of Short Crack and Deep Crack CTOD Fracture Specimens of an A36 Steel," *WRC Bulletin 351*, Welding Research Council, New York, February 1990.

[12] J. A. Smith, and S. T. Rolfe, "The Effect of Crack Depth to Width Ratio on the Elastic-Plastic Fracture Toughness of a High-Strength Low-Strain Hardening Steel," *WRC Bulletin 358*, Welding Research Council, New York, November 1990.

[13] J. D. G. Sumpter and J. W. Hancock, "Shallow Crack Toughness of HY80 Welds: An Analysis Based on T Stresses," *Int. J. Pres. Ves. & Piping* 45, 207–221 (1991).

[14] J. M. Barsom and S. T. Rolfe, *Fracture and Fatigue Control in Structures*, Prentice-Hall, Englewood Cliffs, N.J., 1987.

[15] M. T. Kirk, and R. H. Dodds, Jr., "J and CTOD Estimation Equations for Shallow Cracks in Single Edge Notch Bend Specimens," Civil Engineering Studies, Structural Research Series No. 565, Dept. of Civil Engineering, Univ. of Illinois, UILI-ENG-91-2013, Jan. 1991.

[16] ABAQUS *Theory Manual*, Version 4-8, Hibbitt, Karlson and Sorensen, Inc., Providence, R.I., 1989.

[17] H. Tada, P. C. Paris and G. R. Irwin, *The Stress Analysis of Cracks Handbook*, Del Research Corporation, Hellertown, Pa., 1973.

[18] R. D. Cheverton, S. K. Iskander, and D. G. Ball, "Review of Pressurized-Water-Reactor-Related Thermal Shock Studies," pp. 752–766 in *Fracture Mechanics: Nineteenth Symposium, ASTM STP 969*, American Society for Testing and Materials, Philadelphia, 1988.

[19] D. Aurich et al., "The Influence of the Stress State on K_{Ic}," Transactions of the 4th International Conference on Structural Mechanics in Reactor Technology, Vol. G, August 1977.†

TABLE 1--Test matrix for the HSST shallow-crack program

Phase	Temp (°C)	Crack Depth (mm)	Thickness (mm)	No. Tested Beams	Total	
Development	-60	~50	50	3		
	-60	~50	100	1		
	-60	~50	150	1		
	-60	~50	50	3		
	-60	~10	100	2		
	-60	~10	150	2		
	-60	~14	50	1		
	-35	~10	50	1	14	
6 Add. Beams	-45	~50	50	2		
	-45	~50	100	2		
	-45	~50	150	2	6	
Production	-105	~10	100	3		
	-40	~50	100	3		
	-40	~10	100	3		
	-23	~10	100	3		
	-6	~50	100	3		
	-6	~10	100	3	18	
						38

TABLE 2--Material properties for A 533 B steels used in HSST shallow-crack program

Development phase and six deep-crack beams	*Production phase*
HSST CE-WP	HSST Plate 13B after postweld heat treatment
$E = 202 - 0.0626\ T$, GPa	$E = 202 - 0.0626\ T$, GPa
$\nu = 0.3$	$\nu = 0.3$
$\sigma_0 = 211 + 55{,}000 / (T + 273)$, MPa	$\sigma_0 = 430 - 0.223\ T + 0.014\ T^2$, MPa
$\sigma_u = 371 + 55{,}000 / (T + 273)$, MPa	$\sigma_u = 609 + 0.618\ T + 0.00927\ T^2$, MPa
$\sigma_f = 1/2\ (\sigma_0 + \sigma_u)$	$\sigma_f = 1/2\ (\sigma_0 + \sigma_u)$
$RT_{NDT} = -35°C$	$RT_{NDT} = -15°C$ (center material)

T = temperature, °C.

TABLE 3--HSST shallow-crack test data

HSST beam No.	Temperature (°C)	S (mm)	B (mm)	W (mm)	a (mm)	Failure load (kN)	CTOD total (mm)	J integral (MPa-mm)	K_c from CTOD (MPa·$\sqrt{m}$)	K_c from J (MPa·$\sqrt{m}$)
					Development phase					
3	−36	406	51	100	10.0	600.0	0.586	261	265	243
4	−61	406	51	100	51.8	128.1	0.048	42	96	97
5	−55	406	51	99	51.2	139.7	0.049	48	97	105
6	−59	406	51	100	51.9	184.6	0.117	102	149	152
7	−59	406	51	94	10.2	483.5	0.137	92	132	144
8	−60	406	51	94	9.6	657.4	0.476	284	245	254
9	−62	406	51	94	9.5	552.4	0.352	173	212	198
10	−60	406	51	94	14.0	489.3	0.235	143	180	180
11	−57	864	102	94	8.4	472.4	0.196	101	157	152
12	−57	864	102	95	49.8	116.5	0.061	50	108	106
13	−60	864	102	94	8.8	501.7	0.357	208	213	217
14	−60	864	152	93	8.7	723.2	0.346	225	209	226
15	−59	864	153	94	8.7	684.1	0.146	85	136	139
16	−58	864	153	94	50.0	170.4	0.060	46	107	102
					Six deep-crack beams phase					
12A	−44	406	102	94	51.0	251.8	0.077	60	120	117
13A	−46	406	102	94	50.8	293.1	0.111	86	144	140
14A1	−44	406	51	93	50.2	135.2	0.121	93	150	145
14A2	−44	406	51	93	50.8	102.7	0.043	39	90	94
15A	−47	406	153	94	50.7	435.0	0.096	79	133	134
16A	−43	406	153	94	51.9	348.3	0.062	51	107	108
					Production phase					
17	−6	610	102	102	52.6	245.1	0.116	98	144	147
18	−24	610	101	102	10.6	777.1	0.468	238	239	231
20	−4	610	101	101	10.8	823.3	1.733	987	453	469
21	−23	610	101	102	10.7	724.1	0.306	152	194	185
22	−7	610	101	102	10.9	793.5	0.942	566	334	355
24	−7	610	102	102	52.0	269.1	0.367	270	253	245
25	−39	610	102	102	52.0	238.4	0.110	85	145	138
26	−40	610	102	102	11.0	740.1	0.355	175	213	199
27	−22	610	101	102	10.7	787.3	0.559	242	261	233
28	−6	610	101	102	10.3	832.7	1.242	788	384	419
31	−40	610	102	102	51.5	205.5	0.063	51	110	108
32	−103	610	102	102	11.1	417.7	0.016	20	69	68
33	−103	610	102	102	10.7	339.8	0.009	13	53	54
34	−106	610	101	102	10.4	431.0	0.017	21	72	70
35	−7	610	102	102	51.7	244.2	0.121	97	147	147
36	−38	610	102	102	51.6	176.1	0.042	35	89	89
37	−39	610	102	102	10.8	745.9	0.263	135	183	175
38	−39	610	102	102	10.8	755.3	0.206	106	162	155

TABLE 4--Experimental and analytical results of fracture toughness for the shallow-flaw (a/W = 0.1) specimen based on Case B conditions

Beam No.	P_C (kN)	LLD_C (mm)	J_{LLDC} (kN/m)	J_{PC} (kN/m)	J_{EXP} (LLD) (kN/m)	J_{EXP} (CTOD) (kN/m)
38	756	2.71	115	112	106	116
37	746	3.08	142	108	135	148
26	740	3.45	169	105	175	201

TABLE 5--Experimental and analytical results for the fracture toughness for deep-flaw (a/W = 0.5) specimens based on Case D conditions

Beam No.	P_C (kN)	LLD_C (mm)	J_{LLDC} (kN/m)	J_{PC} (kN/m)	J_{EXP} (LLD) (kN/m)	J_{EXP} (CTOD) (kN/m)
36	176	1.24	44	35	35	34
31	206	1.41	57	49	51	53
25	238	1.82	91	71	85	93

Fig. 1--Three specimen thicknesses used in the shallow-crack program to investigate size effects.

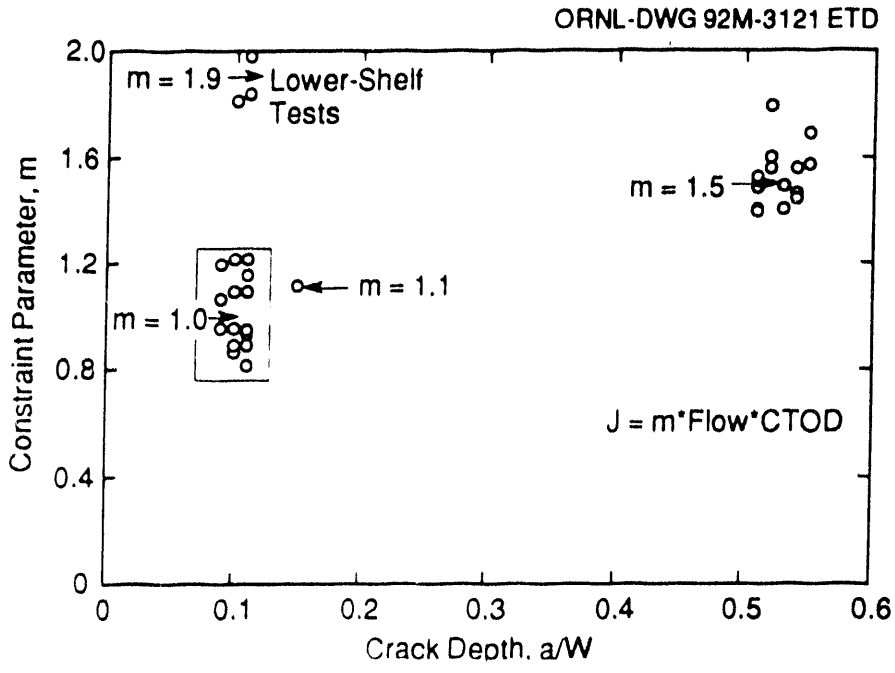

Fig. 2--Constraint parameter (m) values as a function of crack depth (a/W).

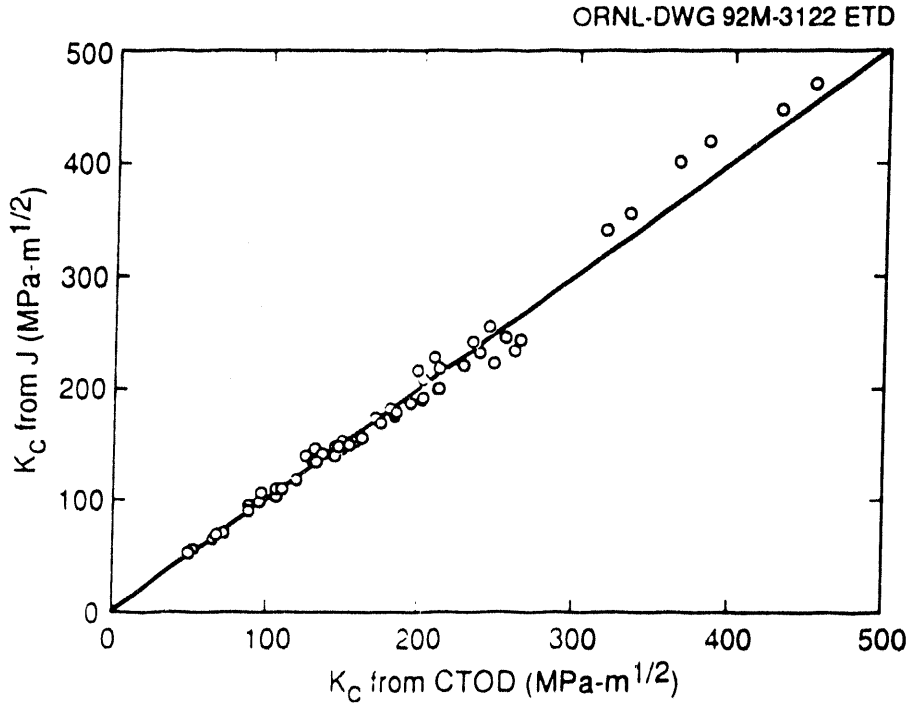

Fig. 3--Comparison of K_c (LLD) and K_c (CTOD) toughness values

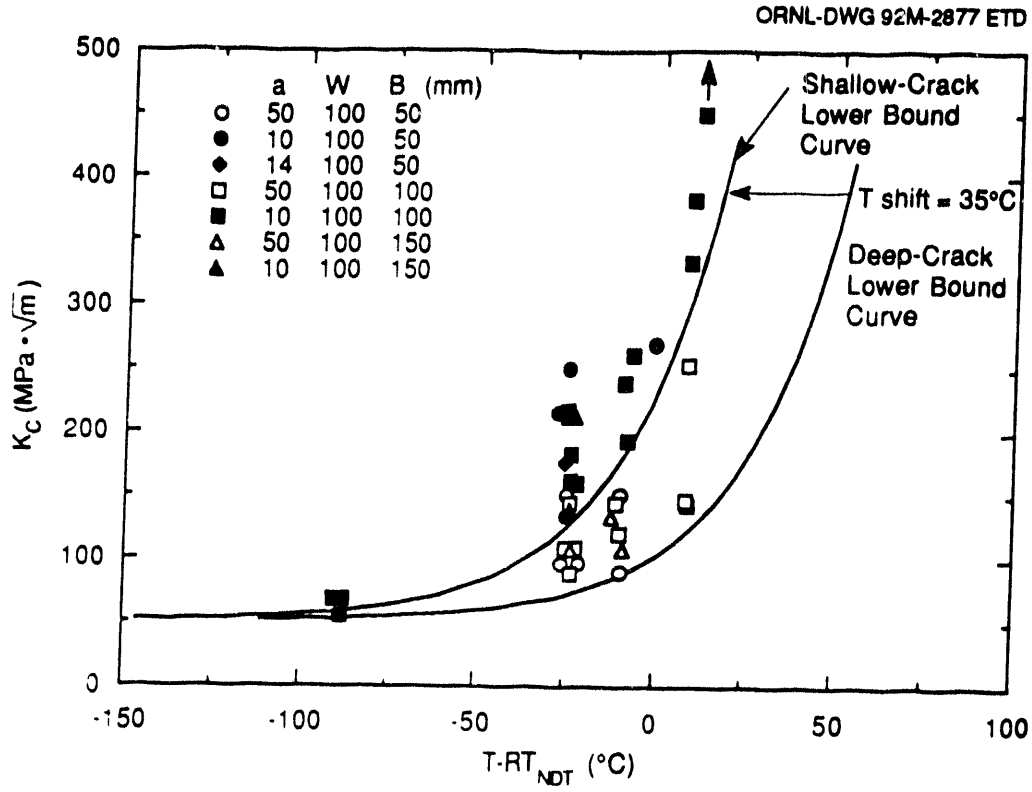

Fig. 4--Toughness (K_C) data vs. normalized temperature for the shallow and deep-crack specimens with lower bound curves

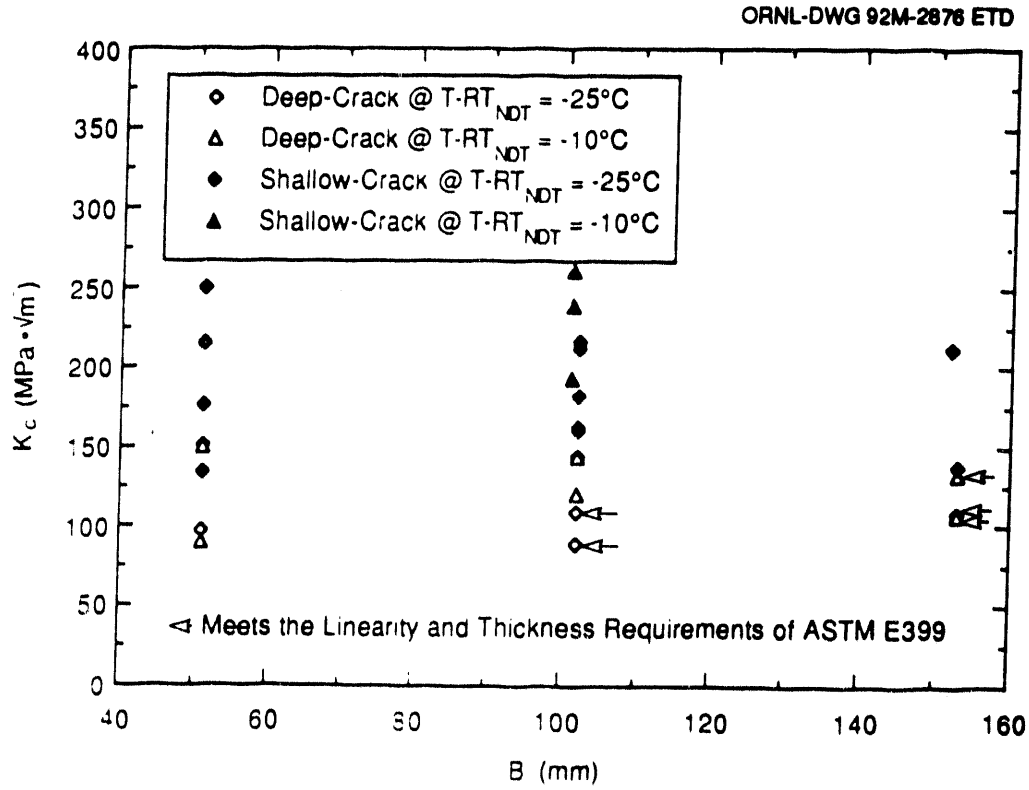

Fig. 5--Toughness (K_C) data vs. beam thickness for the shallow and deep-crack specimens at T-RT_{NDT} = -25 °C & -10 °C

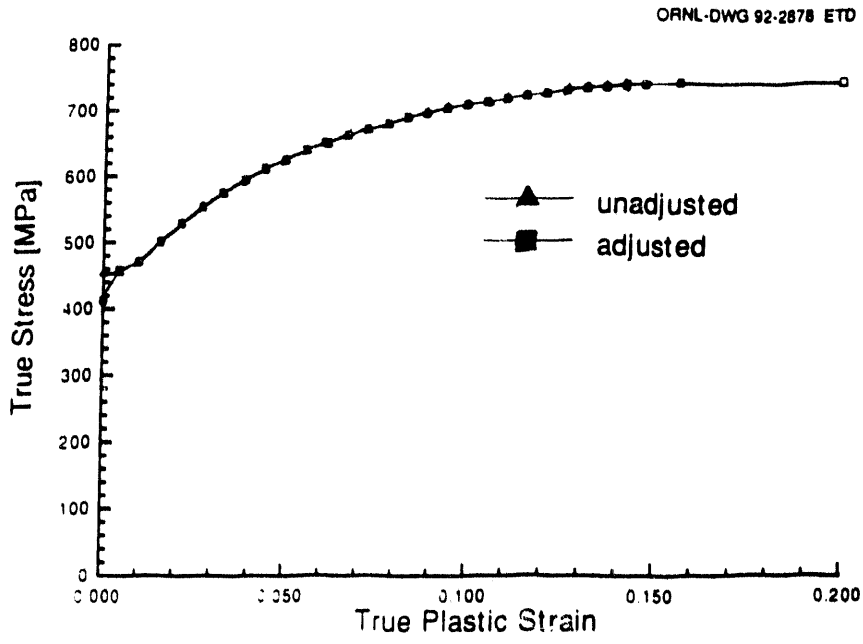

Fig. 6--Uniaxial true stress-true plastic strain curve in tension for unadjusted and adjusted material models.

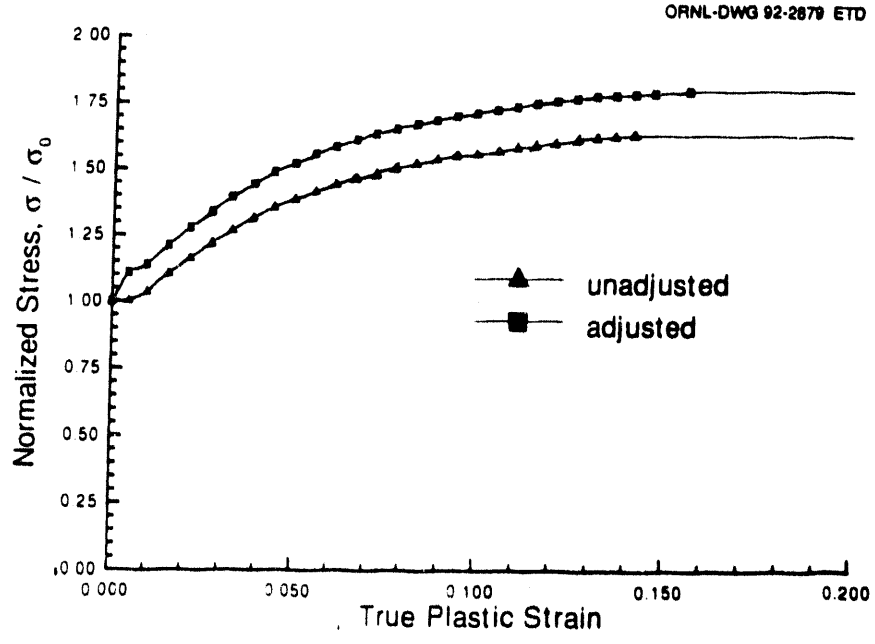

Fig. 7--Normalized stress-strain curves for unadjusted and adjusted material models.

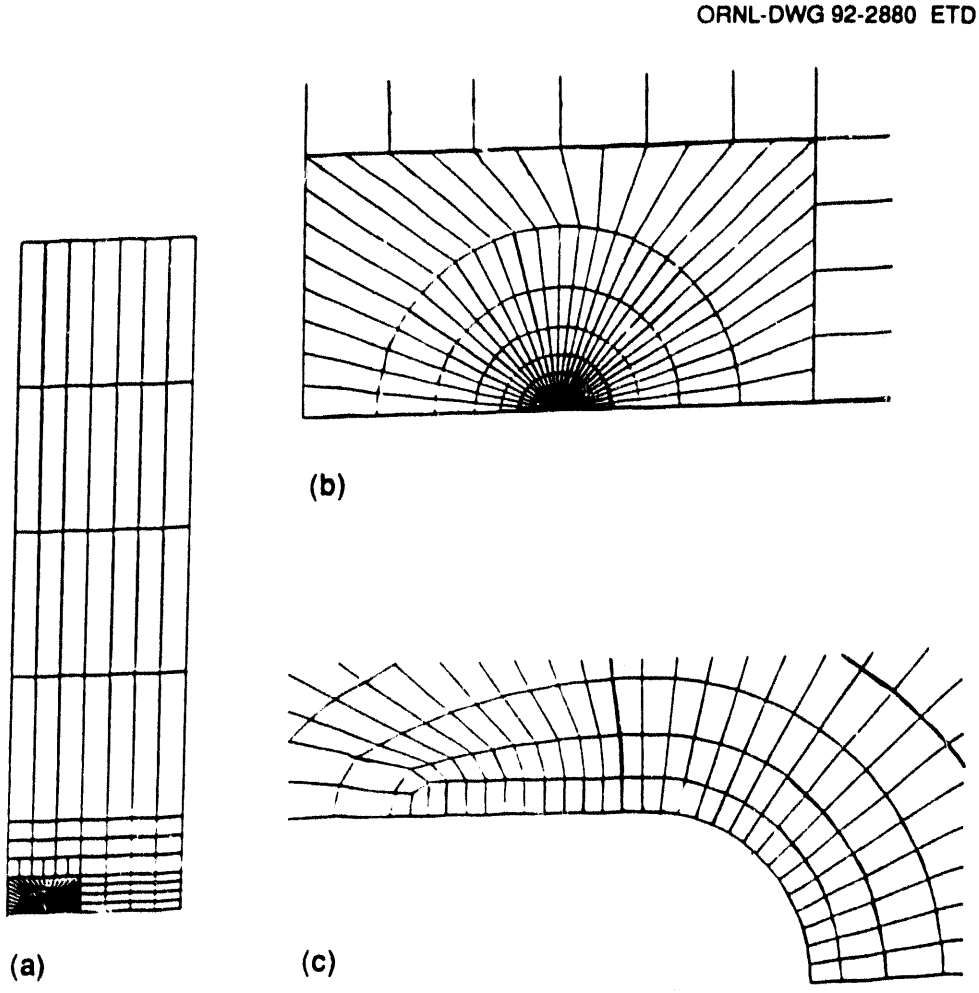

Fig. 8--FEA mesh for a/W = 0.1.

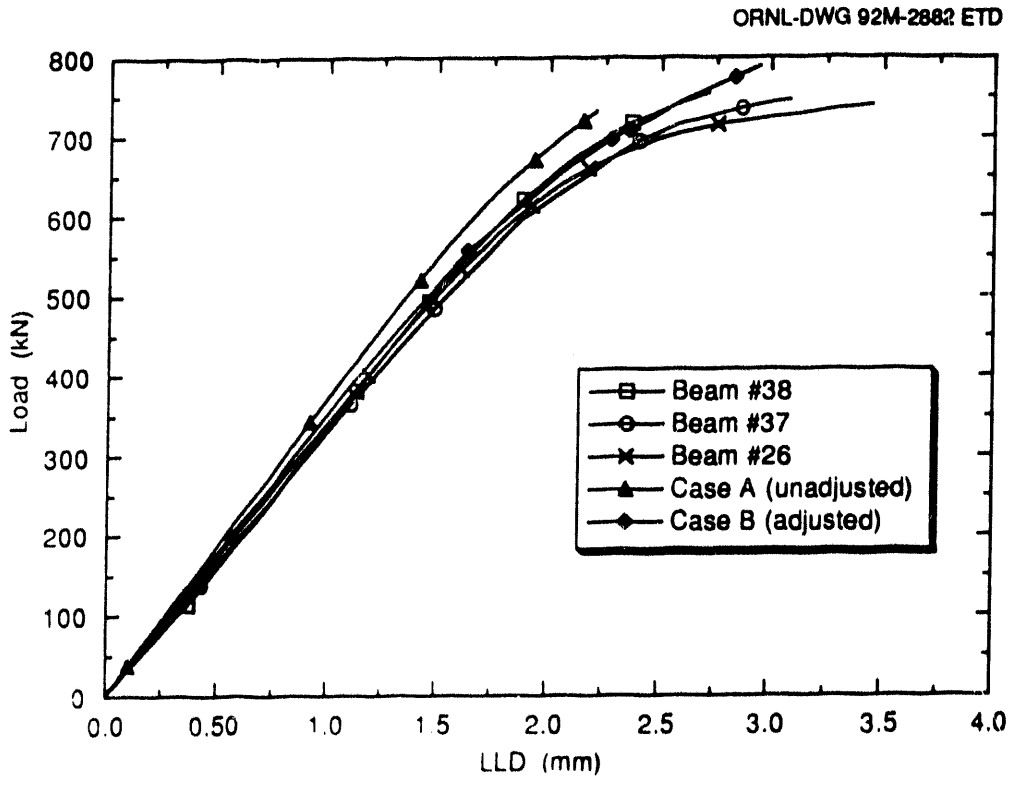

Fig. 9--P-LLD for a/W = 0.1.

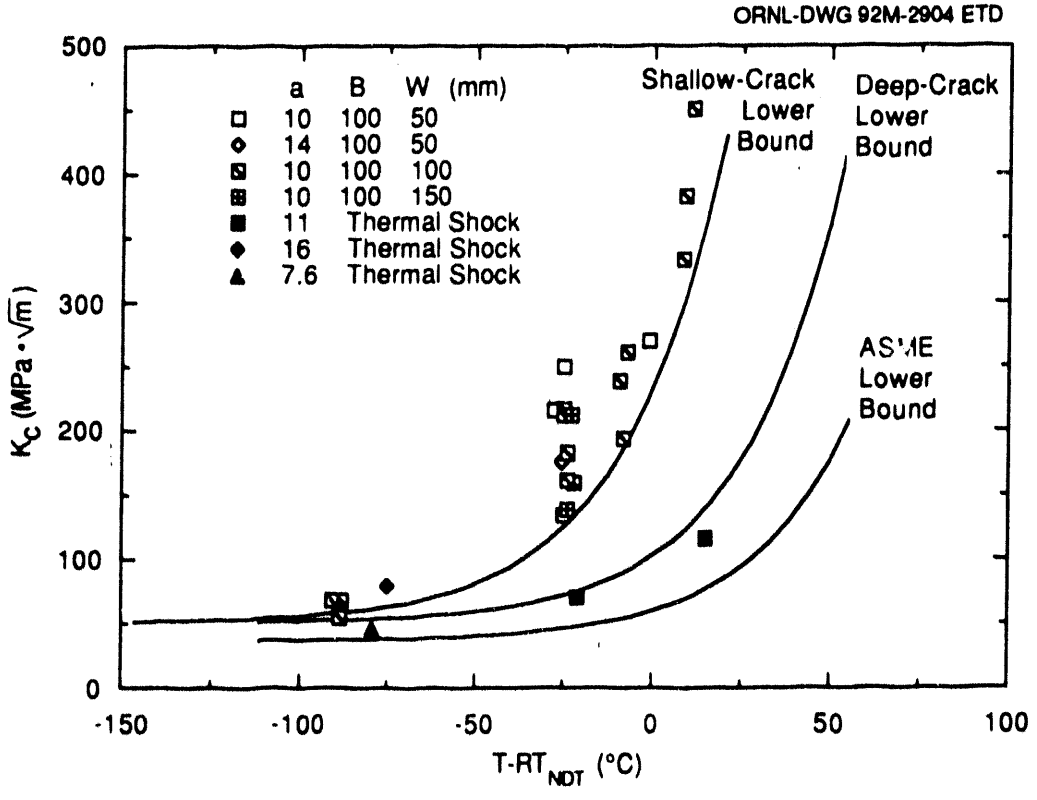

Fig. 10--HSST shallow-crack and thermal-shock data with ASME lower-bound curve

STABLE CRACK GROWTH BEHAVIORS IN WELDED CT SPECIMENS - FINITE ELEMENT ANALYSES AND SIMPLIFIED ASSESSMENTS -

by

Dr. Genki Yagawa [1], Dr. Shinobu Yoshimura [1],
Dr. Shigeru Aoki [2], Dr. Masanori Kikuchi [3],
Dr. Yoshio Arai [4], Dr. Koichi Kashima [5],
Dr. Takayuki Watanabe [6] and Mr. Takashi Shimakawa [7]

This paper describes stable crack growth behaviors in welded CT specimens made of nuclear pressure vessel A533B class 1 steel, in which initial cracks are placed to be normal to fusion line.

At first, using the relations between the load-line displacement (δ) and the crack extension amount (Δa) measured in experiments, the generation phase finite element crack growth analyses are performed, calculating the applied load (P) and various kinds of J-integrals.

Next, the simplified crack growth analyses based on the GE/EPRI method and the reference stress method are performed using the same experimental results. Some modification procedures of the two simplified assessment schemes are discussed to make them applicable to inhomogeneous materials.

Finally, a neural network approach is proposed to optimize the above modification procedures.

1) University of Tokyo, 7-3-1 Hongo, Bunkyo, Tokyo 113, Japan
2) Tokyo Institute of Technology, 1-21-1 Ohokayama, Meguro, Tokyo152, Japan
3) Science University of Tokyo, 2641 Yamazaki, Noda, Chiba 278, Japan
4) Saitama University, 225 Shimo-Ookubo, Urawa, Saitama 338, Japan
5) Central Research Institute of Electric Power Industry, 11-1-2 Iwatokita, Komae, Tokyo 201, Japan
6) CRC Research Institute, Ltd., 1-3-D17 Nakase, Chiba, Chiba 261-01, Japan
7) Kawasaki Heavy Industries, 4-25-2 Minamisuna, Koto, Tokyo 136,Japan

1. INTRODUCTION

Nonlinear fracture mechanics based on the J-integral concept [1] is widely utilized in the assessment of structural integrity of ductile materials [2, 3]. The J-integral was originally derived on the assumption that materials and structures be homogeneous. This is not always the case in practical situations. The assessment of Elastic-Plastic fracture phenomena of Inhomogeneous materials and structures, named here as "EPI Problems", is one of critical issues to assure the structural integrity of nuclear structural components such as irradiated, welded and cladded pressure vessels and welded piping. Thus various studies have been performed in these respects [4-12]

Among others, the researchers belonging to the EPI Subcommittee (Chairman : G. Yagawa) of the Japan Welding Engineering Society have performed a series of numerical and experimental studies on stable crack growth in welded CT specimens made of a nuclear pressure vessel A533B class 1 steel [7-11], aiming at the development of the simplified estimation schemes for crack growth resistance in inhomogeneous materials and structures. In the experiments, it was intended that crack grows in the direction normal to the phase boundary of the base metal (BM) and the weld metal (WM). This configuration of specimens was selected to simulate crack growth across irradiated pressure vessel, crack growth across the clad/base material interface and crack growth across the weld/base material interface. In the previous studies, elastic-plastic finite element analyses of stationary cracks in the welded CT specimens were first performed by parametrically varying the material properties of the weld metal and the distance between the crack-tip and the phase boundary. The influences of these factors on the J-integral evaluations were examined in detail. Next, using the relations among a crack extension amount (Δa), an applied load per unit thickness (P) and a load-line displacement (δ) measured in experiments, generation phase crack growth simulations were performed using the finite element method (FEM), and detailed discussions were made on the behaviors of fracture mechanics parameters during crack growth phenomena in the welded CT specimens. In the third, round-robin studies on simplified assessment of the above crack growth behaviors were performed.

This paper first summarizes generation phase crack growth analyses of the welded CT specimens using the finite element method. Then, simplified crack growth simulations based on the GE/EPRI method [13] and the reference stress method [14] are presented. Some modification procedures of these simplified assessment schemes are discussed to make them applicable to an inhomogeneous material. Finally, a neural network approach [15, 16] is proposed to optimize the modification procedures of the conventional estimation schemes.

2. FINITE ELEMENT ANALYSES

2.1 Materials and Structures

The one homogeneous CT specimen which is denoted here as M5G, and the two

welded CT specimens D5G and H5G were analyzed. The details of experimental results of these specimens are given in EPI report (III) [17]. In experiments, a fatigue precrack was introduced by a servo-hydraulic testing machine under the stress intensity factor range ΔK of 25MPa$\sqrt{m}$ and the stress ratio R of 0.05. The final location of the precrack was about 0.6 in terms of a/W, where a is an initial crack length and W is a specimen width. After the precracking, side grooves of 20 % depth were machined. In the analyses, the welded specimens were simply modeled to be bimaterial as shown in Fig. 1. In the H5G specimen, an initial crack-tip was placed about 3mm behind the phase boundary, i.e. in the heat affected zone (HAZ), while in the D5G specimen, about 3mm ahead the phase boundary.

The materials #1 and #2 in the figure correspond to the base metal (BM) and the weld metal (WM), respectively. The orientation of crack is normal to the phase boundary.

The uniaxial stress-strain relation of the material #1, i.e. BM, was given as follows :

$$\sigma \le \sigma_{YS} \qquad \varepsilon = \frac{\sigma}{E} \tag{1a}$$

$$\sigma > \sigma_{YS},\ \varepsilon^p \le 0.02153 \qquad \varepsilon = \frac{\sigma}{E} + \left\{\left(\frac{\sigma}{E'}\right)^n - \left(\frac{\sigma_{YS}}{E'}\right)^n\right\} \tag{1b}$$

$$\sigma > \sigma_{YS},\ \varepsilon^p \ge 0.02153 \qquad \varepsilon = \frac{\sigma}{E} + \left\{\left(\frac{\sigma}{E''}\right)^{n'} - \left(\frac{\sigma'_{YS}}{E''}\right)^{n'}\right\} + \varepsilon_o^p \tag{1c}$$

where E = 206GPa, σ_{YS} = 550MPa, n = 2 and E' = 500MPa, E'' = 850MPa, n' = 10, $\sigma_{YS'}$ = 554.9MPa and ε_o^p = 0.02153.

For the material #2, i.e. WM, the following relation was used :

$$\sigma \le \sigma_{YS} \qquad \varepsilon = \frac{\sigma}{E} \tag{2a}$$

$$\sigma > \sigma_{YS} \qquad \varepsilon = \frac{\sigma}{E} + \left\{\left(\frac{\sigma}{E'}\right)^n - \left(\frac{\sigma_{YS}}{E'}\right)^n\right\} \tag{2b}$$

where E = 175GPa, σ_{YS} = 630MPa, n = 8 and E' = 950MPa. The stress-strain relations of both materials are shown in Fig. 2. The Poisson's ratio ν was set to be 0.3 for both metals.

2.2 Analysis Procedure

The generation phase crack growth analyses were performed using the measured load-line displacement (δ) vs Δa curves as input data. The eight-noded isoparametric plane strain or plane stress elements were used. The line integration technique was used for the J-integral calculation. The nodal release technique was employed to simulate the stable crack growth. The following four different J-integrals were evaluated :

J_{path} : the J-integral calculated by the above finite elements,
$J_{M\text{-}C}$: the J-integral of the Merkle-Corten's formula [18] defined as :

$$J_{M\text{-}C} = \frac{2A}{bB}\frac{(1+\alpha)}{(1+\alpha^2)} \tag{3}$$

J_M : the modified J-integral of Ernst [19] defined as :

$$J_M = J_{M\text{-}C} + \int_{a_0}^{a} m\frac{J_{pl}}{b}\,da \tag{4}$$

J_D : the deformed J-integral of Ernst et al. [20] defined as :

$$J_{D(i+1)} = (J_{D(i)} + (\frac{\eta}{b})_i A_{i,i+1}\,)\,(1 - (\frac{\gamma}{b})_i (a_{i+1} - a_i)) \tag{5}$$

where

A : Area of load vs load-line displacement curve
B : Specimen thickness
a_0 and a : Initial and current crack lengths, respectively
W : Width of CT specimen
$b = \begin{cases} W - a_0 \text{ for } J_{M\text{-}C} \\ W - a \text{ for } J_M \text{ and } J_D \end{cases}$: Uncracked ligament length
α : A positive solution of $\alpha^2 + 2\alpha\,(2a/b + 1) - 1 = 0$
$m = 1 + 0.76(b/W)$
$J_{pl} = J_{M\text{-}C} - G$
G : Elastic strain energy density
$\eta = 2 + 0.522\,(b/W)$
$\gamma = 1 + 0.76\,(b/W)$
$J_{D(i)}$, $(\eta/b)_i$, $(\gamma/b)_i$: Values at i-th step
$A_{i,i+1}$: Area of load vs load-line displacement curve between (i) and (i+1)-th steps

It is well known that the J_{path} looses a physical meaning and a path independent feature when large-scale crack growth occurs. Nevertheless, we calculated the values along various integration paths because one of the purposes of the present analyses was to study the correlation of J_{path} with other empirical formulae such as $J_{M\text{-}C}$, J_M and J_D during crack growth in inhomogeneous materials.

2.3 Results and Discussions

Figures 3(a) through (c) show the measured and the calculated P-δ curves of the three specimens. The experimental results agree relatively well with the numerical ones under the plane strain condition. Figures 4(a) through (c) show the calculated and the measured J-Δa curves of the same specimens, where solid circles indicate the measured values of J_D, and the others are the calculated J values, i.e. J_D (open circles), J_M (open squares), $J_{M\text{-}C}$ (open triangles), J_{path} calculated along the farthest path (dashed

line). The Jpath values showed a reasonably good path independence feature (not shown here) and agreed well with calculated J_D, J_M and $J_{M\text{-}D}$ values in small crack growth even for welded CT specimens. The calculated and measured J_D values agreed well with each other within 10 % difference. The order of magnitudes of the three J values was as follows : $J_M > J_{M\text{-}C} > J_D$.

3. SIMPLIFIED ASSESSMENTS

To study the applicability of some conventional simplified estimation schemes to crack growth phenomena in inhomogeneous materials, simplified crack growth analyses were performed on the three CT specimens of M5G, D5G and H5G mentioned previously. Among others, the GE/EPRI method [13] and the reference stress method [14], both of which are applicable to the assessment of three-dimensional cracks,were examined here.

3.1 GE / EPRI Method

3.1.1 Analysis Procedure

The GE / EPRI estimation scheme is based on the J2-deformation theory of plasticity and the power-law hardening constitutive relationship. In this scheme, the J-integral (J) and the load-line displacement (δ) are defined as follows :

$$J = J_e + J_p \tag{6a}$$

$$\delta = \delta_e + \delta_p \tag{6b}$$

where J_e and J_p are the elastic and the fully plastic solutions of J, and δ_e and δ_p are the elastic and the fully plastic solutions of δ, respectively. J_p and δ_p are defined as follows :

$$J_p = \alpha \times \sigma_o \times \varepsilon_o \times b \times h_1(a/W, n) \times (P/P_o)^{n+1} \tag{7a}$$

$$\delta_p = \alpha \times \varepsilon_o \times a \times h_3(a/W, n) \times (P/P_o)^{n} \tag{7b}$$

where

α, n	:	Constants of the Ramberg-Osgood type relation
σ_o	:	Proportional limit stress of material (= yield stress)
ε_o	:	Proportional limit strain of material (= yield strain)
a	:	Crack length
W	:	Width of CT specimen
b = W - a	:	Uncracked ligament length
h_1, h_3	:	Fully plastic solutions of J and δ, respectively
P	:	Applied load per unit thickness
P_o	:	Limit load per unit thickness

The material constants of the base and the weld metals corresponding to Fig. 2, α, n, σ_o and ε_o, are given in Table 1. The present analyses were conducted under the plane strain condition. To analyze crack growth behaviors in the D5G and H5G specimens, we tested several combinations of material properties described later.

The Generation Phase Simulations (GPS) were performed as illustrated in Fig. 5. Using the measured δ vs Δa curve as input data, the applied load P was iteratively calculated from Eq. (6b), and then the J value was calculated by substituting the applied load P into Eq. (6a).

3.1.2 Results

(1) M5G Specimen (Homogeneous)

Figure 6(a) shows the comparison of the measured and the estimated P-δ curves. The estimated curve under the plane strain condition agrees relatively well with the measured one. Figure 6(b) shows the comparison of the measured and the estimated J-Δa curves. The measured J values here are J_D or $J_{M\text{-}C}$, which are almost the same. The J-Δa curve estimated under the plane strain condition also agrees rather well with the measured one. It is concluded that in the present homogeneous case, the GE / EPRI method assuming the plane strain condition gives us good estimation.

(2) D5G Specimen (Inhomogeneous)

The simplified generation phase crack growth analyses were performed under the plane strain condition. Figure 7(a) shows the comparison between the measured and the estimated P-δ curves. Figure 7(b) shows the measured and the estimated J-Δa curves. In the analyses, the following three kinds of analyses were performed with different material constants as :

(a) Materials constants of the base metal
(b) Material constants of the weld metal
(c) Simply averaged values of the material constants of the base and the weld metals

It is noted from Figs. 7(a) and 7(b) that the estimated values obtained with the material constants of the base metal underestimate the applied load and J value, while those with the material constants with the weld metal are larger than the experimental values. On the other hand, the estimated values obtained with the simply averaged material constants seem to give appropriate results.

The detailed observation of the P-δ curves in Fig. 7(a) gives us more interesting features. The measured P-δ curve is rather close to the curve estimated with the material constants of the base metal in the beginning stage of crack growth, and then it gradually approaches the curve with the material constants of the weld metal as the crack grows. Such a behavior of P-δ curve seems reasonable from the material arrangement as shown in Fig. 1 (b).

(3) H5G Specimen (Inhomogeneous)

Figure 8(a) shows the comparison between the measured and the estimated P-δ curves, and Fig. 8(b) the measured and the estimated J-Δa curves. The tendency of the H5G specimen is basically the same as that of the D5G specimen, irrespective of different crack-tip locations.

Although it is difficult to obtain a general conclusion only from the above two cases, the utilization of averaged material properties could make the GE / EPRI scheme applicable to crack growth phenomena in the welded CT specimens.

3.2 Reference Stress Method

3.2.1 Analysis Procedure

The flow of the reference stress method employed here [14] is as follows. At first, we determine the applied load P corresponding to the measured load-line displacement δ by means of the GE / EPRI method as described in 3.1.1. Then, we determine the reference stress σ_r and the elastic stress intesity factor K corresponding to the applied load P. Finally, the J value is obtained as follows :

$$J = J_e \, \varepsilon_r / (\sigma_r / E) \qquad (8)$$

where ε_r is the reference strain and E the Young's modulus. The present analyses were conducted under the plane strain condition.

3.2.2 Results

(1) M5G Specimen (Homogeneous)

Figure 9(a) shows the comparison of the measured and the estimated P-δ curves. The estimated curve under the plane strain condition agrees well with the measured one. Figure 9(b) shows the comparison of the measured and the estimated J-Δa curves. The J-Δa curve estimated under the plane strain condition also agrees well with the measured one. It is concluded that in the present homogeneous case, the reference stress method assuming the plane strain condition gives us good estimation.

(2) D5G Specimen (Inhomogeneous)

Figure 10(a) shows the comparison between the measured and the estimated P-δ curves. Figure 10(b) shows the measured and the estimated J-Δa curves. The three different analyses were performed using, respectively

(a) Materials constants of the base metal
(b) Material constants of the weld metal
(c) Simply averaged values of the material constants of the base and the weld metals

As the results, the estimated values obtained with the material constants of the base metal underestimate the applied load and J values, while those with the material

constants of the weld metal agree well with the measured ones. The analysis results using averaged material properties of both metals are inbetween the other two results.

(3) H5G Specimen (Inhomogeneous)

Figure 11(a) shows the comparison between the measured and the estimated P-δ curves, and Fig. 11(b) the measured and the estimated J-Δa curves. The tendency of the analysis results of the H5G specimen is basically the same as that of the D5G specimen.

The comparison between the results of the GE / EPRI method and those of the reference stress method shows that the latter method is slightly less sensitive to the difference of material properties.

4. NEURAL NETWORK FOR MODIFICATION OF SIMPLIFIED ASSESSMENT SCHEMES

As shown previously, there are some possibilities that some mixture of different material constants makes the conventional simplified assessment schemes applicable to an inhomogeneous material. However, it is easily expected that the degree of the best mixture of material constants might depend on that of inhomogeneity of specimen. To find the best or optimum mixture of material constants, we propose here an inverse analysis approach based on the hierarchical neural network [15, 16]. The main features of the hierarchical neural network may be summarized as follows.

(1) One can construct automatically a nonlinear mapping relation between one multiple data and the other multiple data in the network through a learning process of a number of sets of learning patterns.
(2) The network has a capability of the so-called "generalization", i.e. a kind of interpolation, that the trained neural network can estimate appropriate output data even for unlearned patterns.
(3) Once the network is trained, it operates quickly in an application process. The CPU power required for the operation of the trained network may be equivalent to only that of a personal computer.

The flow to determine the optimum combination of different material constants by the neural network is illustrated in Fig. 12. By fixing the stress-strain relationships of two materials, i.e. base metal and weld metal, and changing δ-Δa curves and the ratios of mixture of material constants, we parametrically calculate P-δ curves and J-Δa curves by means of the GE / EPRI or the reference stress method (Part 1). The obtained data sets among the δ-Δa, P-δ and J-Δa curves and the ratio of mixture are called here the "learning data". A hierarchical neural network is trained then using a number of learning data above (Part 2). In this training process, the δ-Δa, P-δ and J-Δa curves are given to the input units of the network, while the ratio of mixture is given to the output units of the network as teaching data as shown in Fig. 13. By providing the measured δ-

Δa, P- δ and J-Δa curves to the input units of the trained network, we can determine the best ratio of mixture (Part 3). By accumulating such data, we will be able to formulate the correlation between the best ratio of mixture and the degree of inhomogeneity of specimen, such as volume fraction of base metal and weld metal.

5. CONCLUSIONS

(1) The use of simple average of material constants of the base metal and weld metal may be effective to make the GE / EPRI method and the reference stress method applicable to the assessment of crack growth behaviors in the welded CT specimens.
(2) The mixing procedure above could be optimized by using an inverse analysis approach based on the hierarchical neural network.

ACKNOWLEDGMENTS

This study was performed as an activity of the Japan Welding Engineering Society, Subcommittee for the Study on Elastic-Plastic Fracture Mechanics in Inhomogeneous Materials and Structures (EPI program), and financially supported by Japanese utilities, fabricators, universities, research institutes and the Martin Marietta Energy Sytems, Inc. under USNRC Subcontract No.19X-SD561V.

REFERENCES

1. Rice, J. R., "A Path-Independent Integral and the Approximate Analysis of Strain Concentration by Notches and Cracks", Trans. ASME., J. Appl. Mech., 35, pp. 376-386, 1968.
2. Yagawa, G., Takahashi, Y. and Ueda H, "Three-Dimensional Fully Plastic Solutions for Plates and Cylinders with Through-Wall Cracks", Trans. ASME, J. Appl. Mech., 52, pp. 319-325, 1985.
3. Yagawa, G. and Ishihara, K., "Cleavage and Ductile Thermal Shock Fractures of Corner-Cracked Nozzles", Trans. ASME, J. Press. Vess. Tech., 111, pp. 241-246, 1989.
4. Okamura, H., Yagawa, G., Kawakami, T., Sano, J., Urabe, Y. and Sato, M., "A Crack Arrest Test Using a Toughness Gradient Steel", Proc. 1991 ASME PVP Conf., San Diego, PVP-Vol.213 / MPC-Vol.32, pp. 47-52, 1991.
5. Pennell, W. E., "Heavy-Section Steel Technology Program Fracture Issues", Proc. 1991 ASME PVP Conf., San Diego, PVP-Vol.213 / MPC-Vol.32, pp.15-24, 1991.
6. Pellissier-Tanon, A., Bhandari, S. and Vagner, J., "Practical Methods for Surface and Sub-Surface Cracks in Reactor Pressure Vessels", Proc. 1991 ASME PVP Conf., San Diego, PVP-Vol.213 / MPC-Vol.32, pp. 131-140, 1991.
7. Miura, N., Kashima, K., Michiba, K. and Shimakawa, T., "Ductile Fracture of Stainless Steel Welds at Elevated Temperature", Proc. 1991 ASME PVP Conf., San Diego, Vol. 215, pp. 81-86, 1991.

8. Yagawa, G., Yoshimura, S., Pyo, C.-R. and Yoshioka, A., "Analysis of Large-Scale Crack Growth in Welded Plate Using Computer Image Processing", Proc. 1991 ASME PVP Conf., San Diego, Vol. 215, pp.93-98, 1991.
9. Yagawa, G., Yoshimura, S., Kikuchi, M., Aoki, S., Miyazaki, N., Nakagaki, M., Nishioka, T., Mukaimachi, N., Sasaki, S., Shimakawa, T. and Watanabe, T., "Japanese Round-Robin Analyses of Stable Crack Growth in Inhomogeneous CT Specimen", Proc. 6th Int. Conf. Mechanical Behaviour of Materials, Kyoto, Vol. 1, pp. 609-614, 1991.
10. Kikuchi, M., Yoshimura, S., Yagawa, G., Aoki, S., Nishioka, T., Nakagaki, M., Miyazaki, N., Mukaimachi, N., Sasaki, S., Shimakawa, T. and Watanabe, T., "Analysis of Stable Crack Growth across Welded Fusion Line : Japanese Round-Robin", Trans. 11th SMiRT, Tokyo, Vol. G2, pp. 75-85, 1991.
11. Yoshimura, S., Yagawa, G., Pyo, C.-R., Kashima, K., Shimakawa, T. and Takamatsu, S., "Stable Crack Growth Phenomena of Welded CT Specimens and Their Simplified Assessment", Proc. 1992 ASME PVP Conf., New Orleans, Vol. 215, pp.93-98, 1992.
12. Keeney-Walker, J., Bass, B. R. and Pennell, W. E., "Evaluation of the Effects of Irradiated Cladding on the Behavior of Shallow Flaws Subjected to Pressurized-Thermal-Shock Loading", Trans. 11th SMiRT, Tokyo, Vol. G1, pp. 195-200, 1991.
13. Kumar,V., German, M. D. and Shih, C. F., "An Engineering Approach for Elastic-Plastic Fracture Analysis", NP-1391, Project 1237-1, Topical Report, EPRI, 1981.
14. Roche, R. L., "Modes of Failure Primary and Secondary Stresses, Design and Analysis of Piping, Pressure Vessels, and Components", Proc. 1987 ASME PVP Conf. San Diego, PVP-Vol. 120, pp. 171-176, 1987.
15. Mochizuki, Y., Yagawa, G. and Yoshimura, S., "Inverse Analyses by Means of the Combination of Multilayer Neural Network and Computational Mechanics", Trans. Japan Society of Mechanical Engineers, Vol. 57A, pp.1922-1929, 1991 (in Japanese).
16. Yoshimura, S., Hishida, H. and Yagawa, G., "Parameter Optimization of Visco-Plastic Constitutive Equation Using Hierarchical Neural Network", Proc. 7th Int. Conf. Experimental Mechanics, Las Vegas, Vol. I, pp.296-301, 1992.
17. Yagawa, G., (ed.) "Study on Elastic-Plastic Fracture Mechanics in Inhomogeneous Materials and Structures (III), CRC-EPI-3, 1991.
18. Merkle, J. G. and Corten, T. H., "A J-integral Analysis for the Compact Specimen, Considering Axial Force as well as Bending Effects", Trans. ASME, J. Press. Vess. Tech., 96, pp. 286-292, 1974.
19. Ernst. H. A., "Material Resistance and Instability beyond J-Controlled Crack Growth", ASTM STP 803, pp. I-191-213, 1983.
20. Ernst, H. A., Paris, P. C. and Landes, J. D., "Estimations on J-Integral and Tearing Modulus T from a Single Specimen Test Record", ASTM STP 743, pp.476-502, 1981.

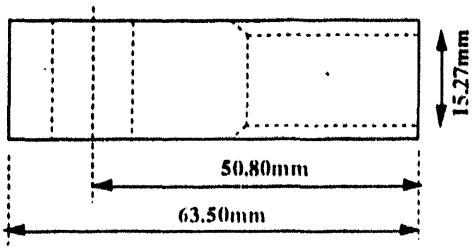

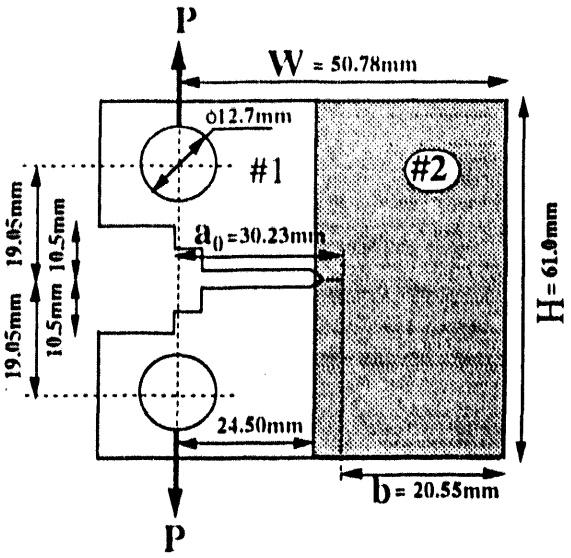

Fig. 1(b) D5G Specimen

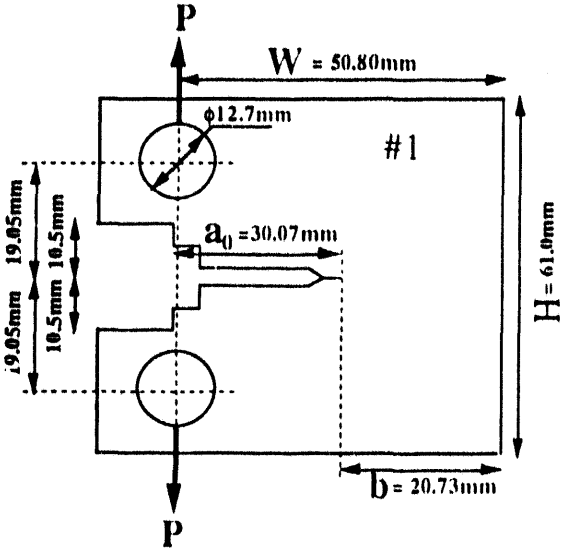

Fig. 1(a) M5G Specimen

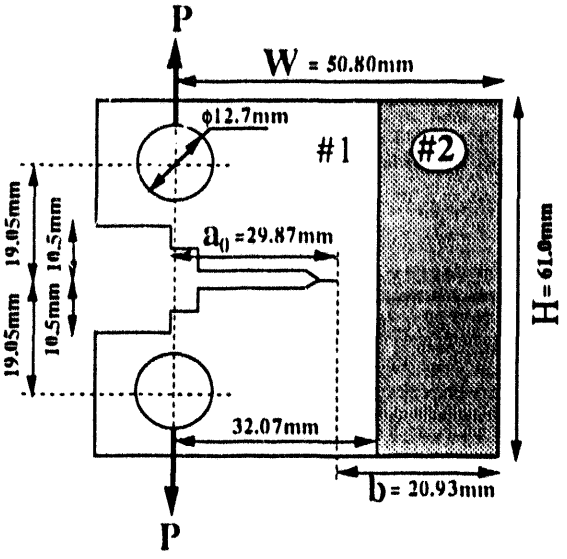

Fig. 1(c) H5G Specimen

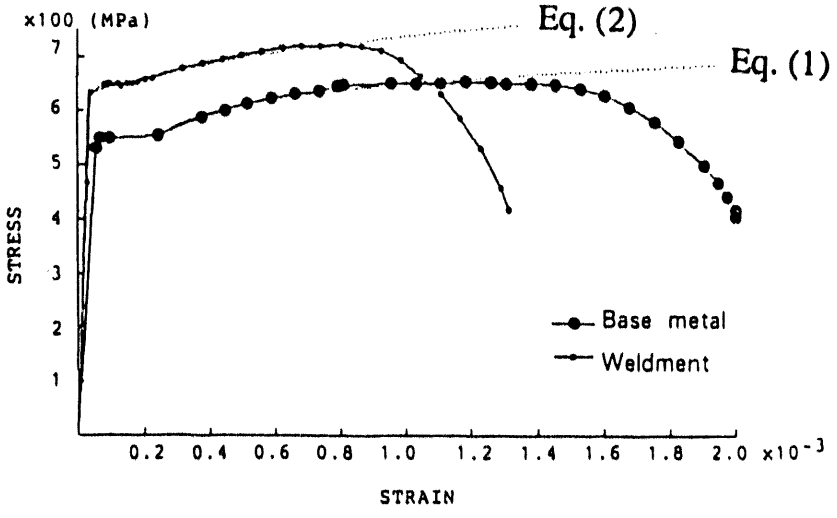

Fig. 2 Uniaxial Stress vs Strain Relation of A533B class 1 Steel and Its Weldment

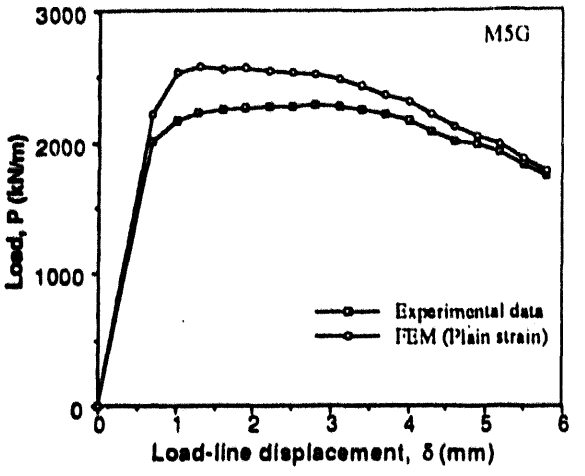

Fig. 3(a) P-δ Curves (M5G)

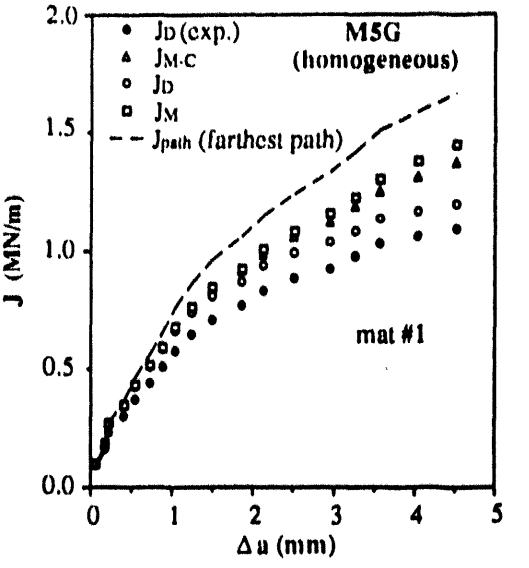

Fig. 4(a) J-Δa Curves (M5G)

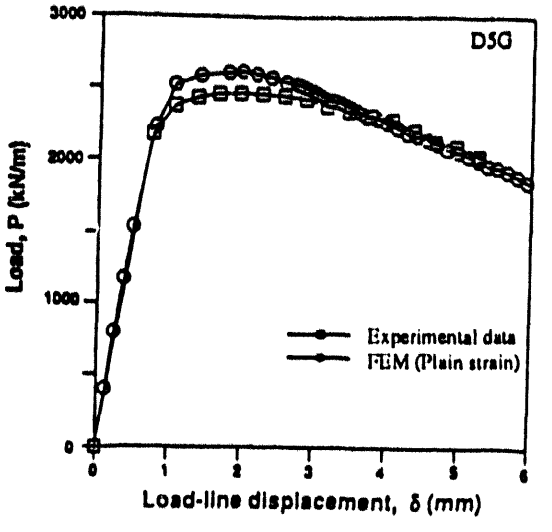

Fig. 3(b) P-δ Curves (D5G)

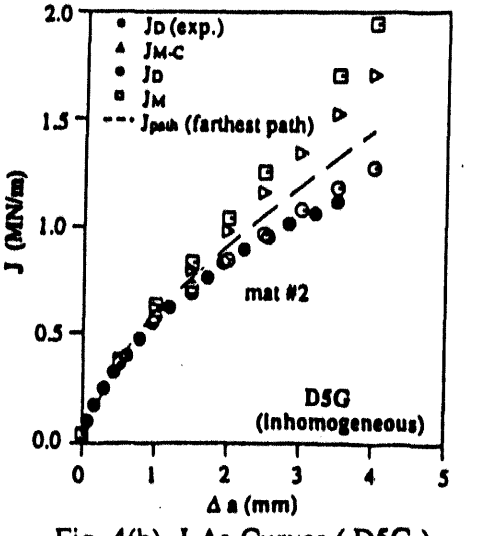

Fig. 4(b) J-Δa Curves (D5G)

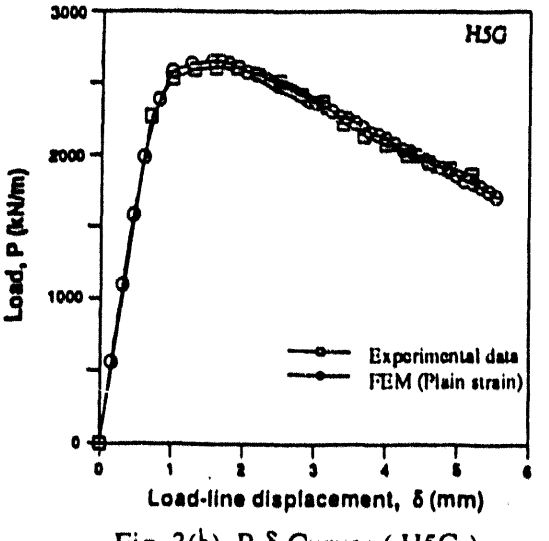

Fig. 3(c) P-δ Curves (H5G)

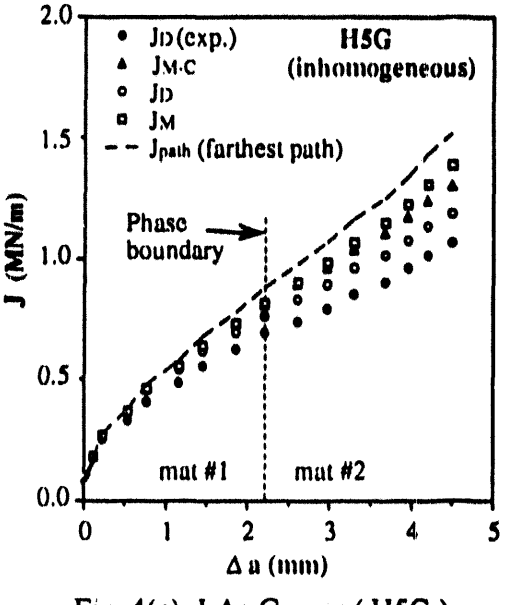

Fig. 4(c) J-Δa Curves (H5G)

Table 1 Materisal Constants of Base and Weld Metals

	Base Metal	Weld Metal
σ_o	550 MPa	630 MPa
ε_o	0.267 %	0.360 %
α	6.478	0.892
n	9.997	24.50

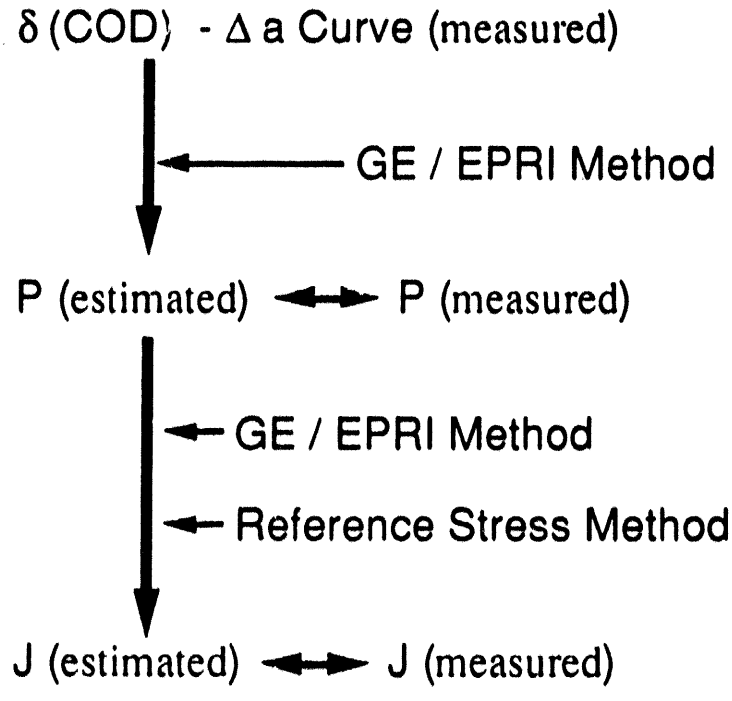

Fig. 5 Flow of Simplified Generation Phase Crack Growth Analyses

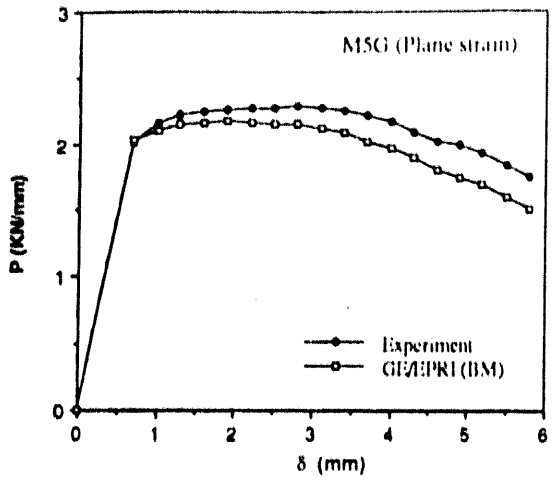

Fig. 6(a) P-δ Curves (M5G)

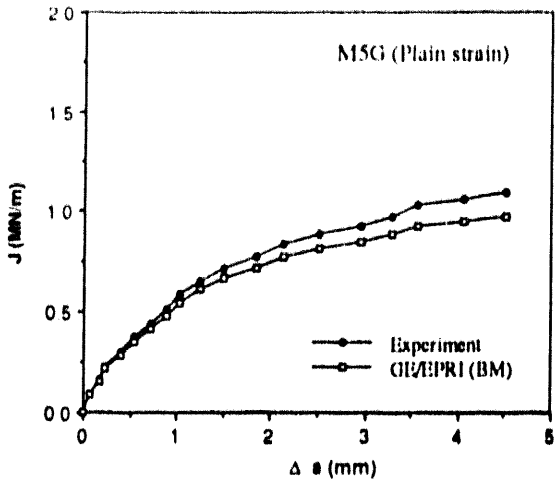

Fig. 6(b) J-Δa Curves (M5G)

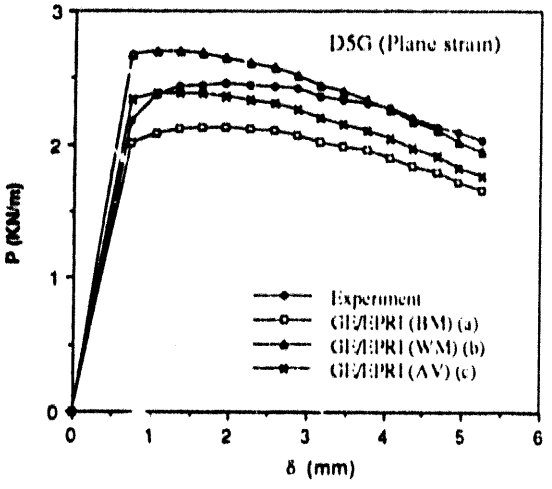

Fig. 7(a) P-δ Curves (D5G)

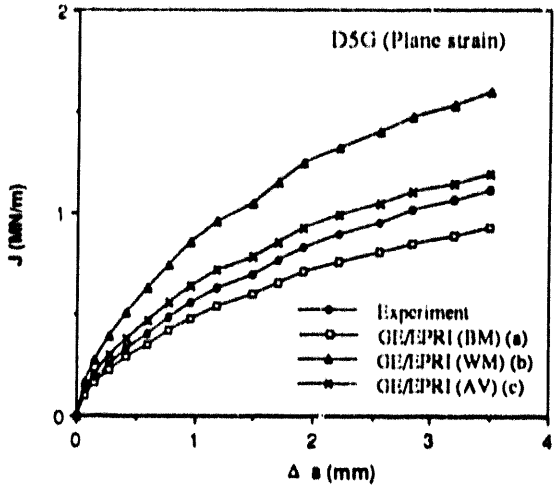

Fig. 7(b) J-Δa Curves (D5G)

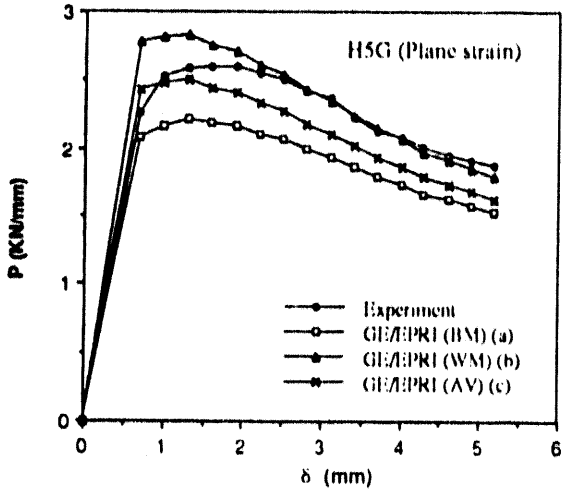

Fig. 8(a) P-δ Curves (H5G)

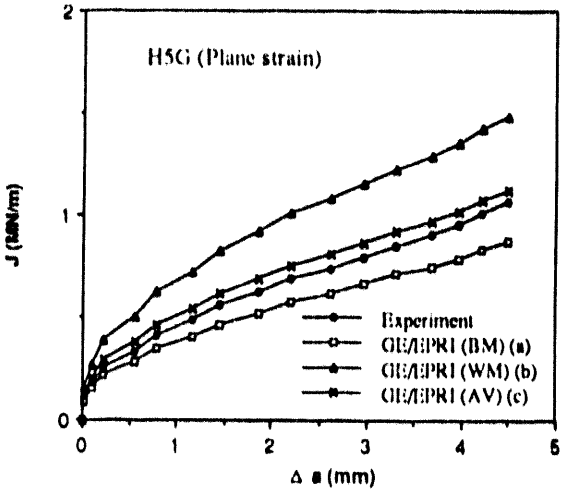

Fig. 8(b) J-Δa Curves (H5G)

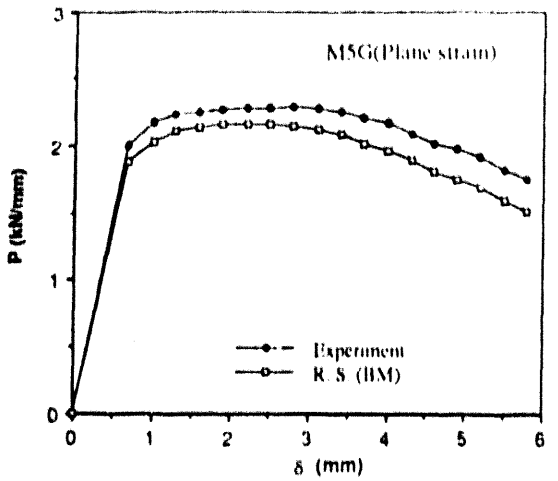

Fig. 9(a) P-δ Curves (M5G)

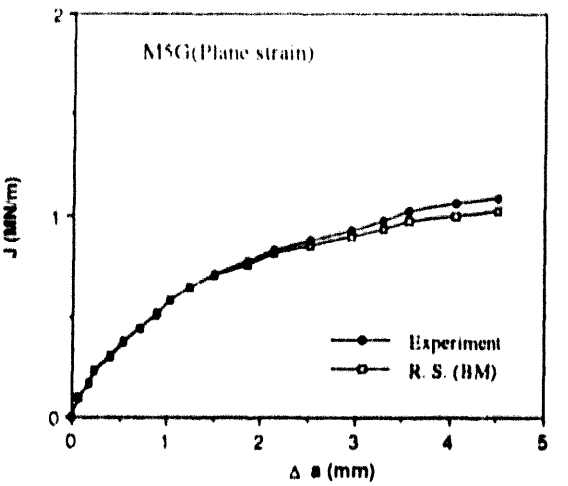

Fig. 9(b) J-Δa Curves (M5G)

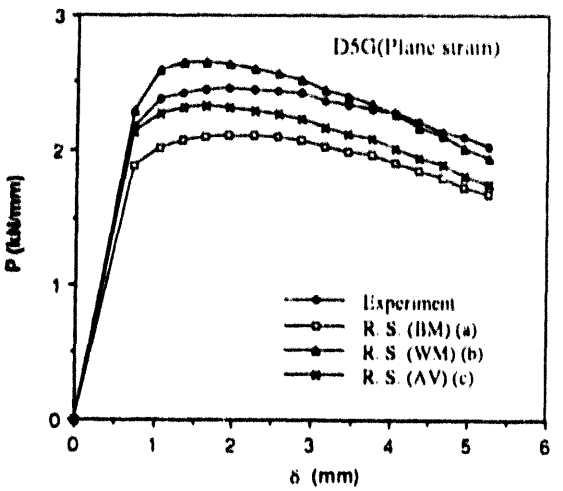

Fig. 10(a) P-δ Curves (D5G)

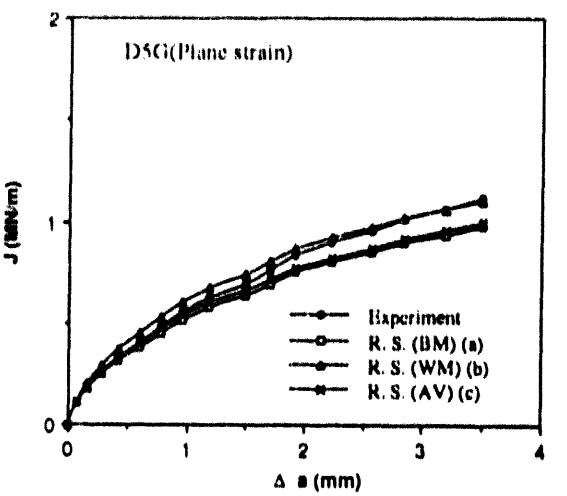

Fig. 10(b) J-Δa Curves (D5G)

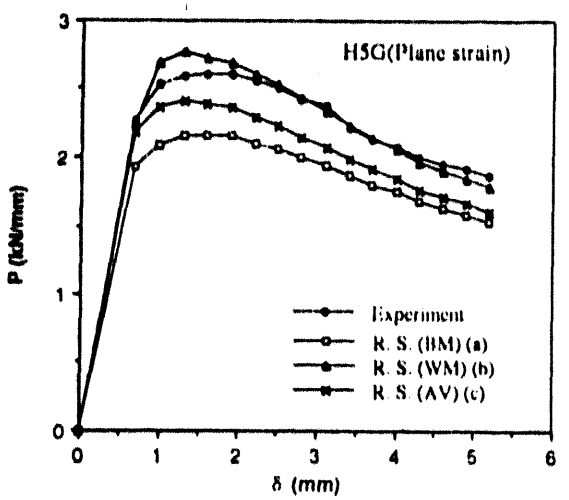

Fig. 11(a) P-δ Curves (H5G)

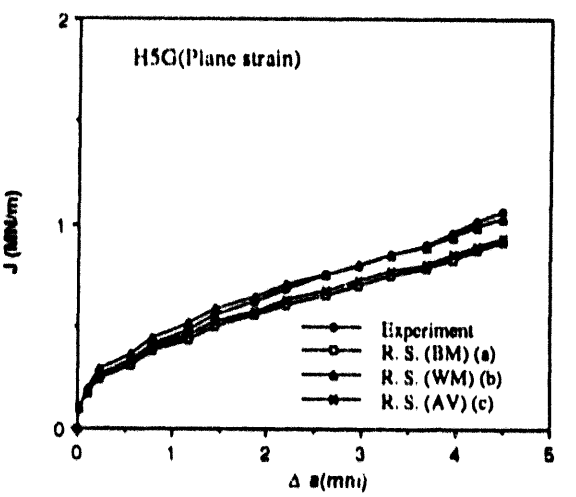

Fig. 11(b) J-Δa Curves (H5G)

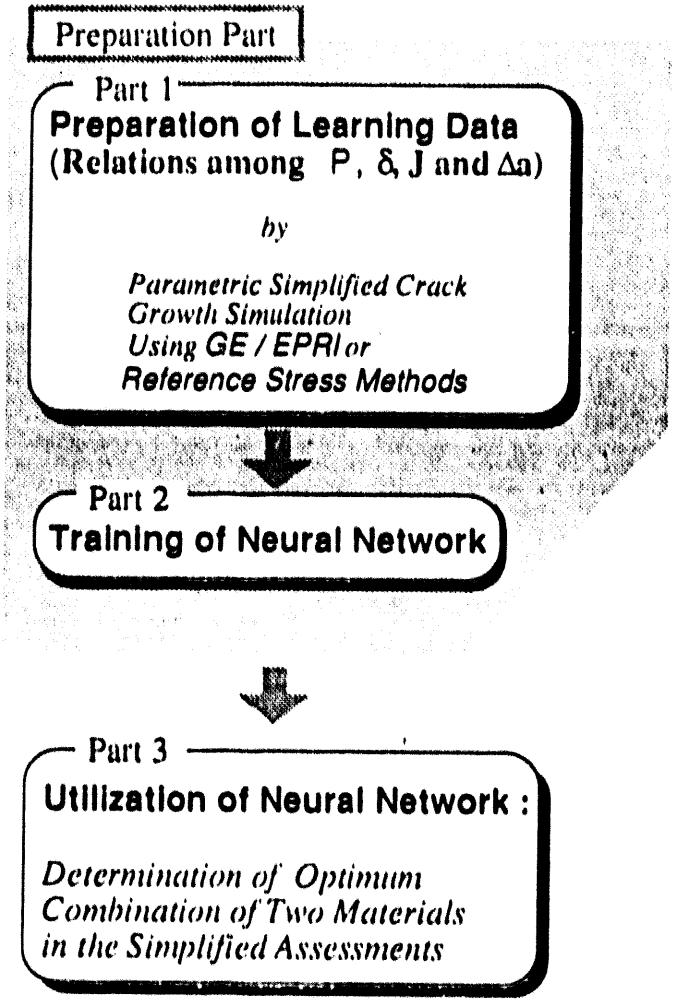

Fig. 12 Flow of Neural Network for Determination of Optimum Combination of Different Material Constants in Simplified Assessments

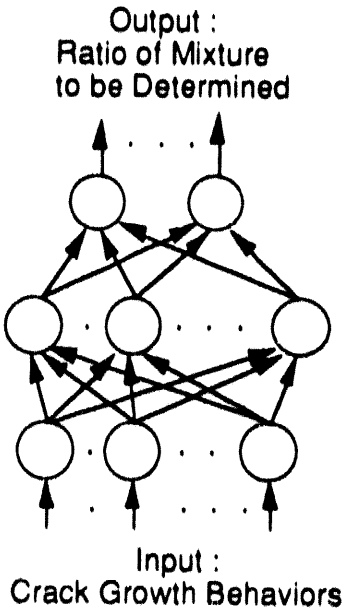

Fig. 13 Schematic View of Present Neural Network

LARGE-SCALE FRACTURE MECHANICS TESTING - REQUIREMENTS AND POSSIBILITIES

Milan BRUMOVSKÝ
ŠKODA Concern, Nuclear Machinery Plant
Czech and Slovak Federal Republic

A B S T R A C T

Application of fracture mechanics to very important and/or complicated structures, like reactor pressure vessels, brings also some questions about the reliability and precision of such calculations. These problems become more pronounced in cases of elastic-plastic conditions of loading and/or in parts with non-homogenous materials (base metal and austenitic cladding, property gradient changes through material thickness) or with non-homogenous stress fields (nozzles, bolt threads, residual stresses etc.). For such special cases some verification by large-scale testing is necessary and valuable.

Paper discusses problems connected with planing of such experiments with respect to their limitations, requirements to a good transfer of received results to an actual vessel.

In the same time, an analysis of possibilities of small-scale model experiments is also shown, mostly in connection with application of results between standard, small-scale and large-scale experiments. Experience from 30 years of large-scale testing in ŠKODA is used as an example to support this analysis.

INTRODUCTION

Development of nuclear power together with other manufacturing directions (aeronautics, austronautics, ship-building etc.) initiated further development of many other scientific disciplines, one of the most important of them is *fracture mechanics*. From the point of view of ŠKODA Concern, we concetrated to the most important parts of primary circuit of nuclear power plants - nuclear reactor and expecially to the reactor pressure vessel and its internals.

One of the most important task at this time is to ensure a sufficient reliability and safety of nuclear reactors and especially of their pressure vessel. Thus, large requirements are then put on realization of proper calculations and supporting research programmes that might support the aforementioned requirements.

In case of reactor pressure vessels, it is not possible, from the technical and economical point of view, to simulate all operational regimes on geometrical similar models in scale 1:1, the only possibility is to carry out tests on some large-scale specimens (or models), supplemented by standard type of tests.

For realization of such important but complex testing there is necessary to design and built several special large testing equipments.

PROBLEMS OF MODEL TESTING

Requirement of nuclear reactor pressure vessel safety are concentrated, first of all, to ensure their resistance against brittle and fatigue failure during complex loading conditions during whole nuclear reactor operation. Solving this problem is complicated by large dimensions of pressure vessels and large thicknesses of their walls on one side, and by not fully corresponding calculation methods on the other one. Calculation of structural resistance against failure is based mainly on standard characteristics of materials received by testing of small, standard specimens of small dimensions. Codes and standards for calculations of

strength and reliability of pressure vessels and other components, as well, contain so-called guaranteed values of individual material characteristics. These values represent, as a rule, boundary (upper or lower) curves of material properties on safe side, they are received by testing of a large set of material products of the same type. In some cases, these values are valid only for certain class of materials or type of welding joint. Results of calculations, carried out using these characteristics are in most cases considerably conservative. On contrary, some components, working rallably for long time, appear to be non-acceptable according to these calculations. For some complicated structures only approximated methods can be used, it is not fully understood if they are conservative or optimistic ones. from these reasons it is necessary that these calculations must be supplemented by suitably chosen experiments to serve for precising up-to-date calculation methods and at the same time to be a basis for new ones.

Another reason for carrying out tests of large-scale testing specimens (up to thicknesses of real products) and models is to eliminate the size effect (material and geometrical ones) on received results.

"Material size effect" represents the existence of :

- non-homogenity of properties and microstructures of base material, welding joint and austenitic cladding (this effect is normally pronounced in cases when:
  - small specimens are cut from different places of material thickness,
  - surface, non-through defects are situated in specimens,
  - through-thickness defects are situated in large specimens

- residual stresses that are mostly released during cutting and machining of small testing specimens (they exist mainly in welding weldments and bimetallic joints - cladding materials etc.),

- statistical distribution of defects in material (effect of defects in standard specimens testing is not taken into account as results of such specimens are excluded from their evaluation).

"Geometrical size effect" includes the following:

- effect of the ratio between base material and austenitic cladding thicknesses and of absolute values of both material thicknesses,

- effect of the ratio between welding metal and heat affected zone widths to the total width of testing speciman,

- effect of plastic zone size in case of testing specimens and model with stress concentrators (holes, nozzles, artiticial defects, etc.),

- *aspects of linear elastic fracture mechanics :*

  - plane strain conditions (for which, only, fracture toughness K_{IC} is valid) are fulfilled only, if

$$a, B \geq 2.5 \left(K_{IC} / R_p 0.2 \right) \qquad (1)$$

  where a - characteristical crack size in direction of thickness,
  B - thickness of testing specimen or model in the place of defect,

  - fracture stress should fulfill the relation :

$$\sigma_c \leq 0.8 \left(R_p 0.2 \right) \qquad (2)$$

  - stress intensity factor K_I depends on defect size as

$$K_I = \sigma \cdot C \left(\pi a / Q^2 \right)^{1/2} \qquad (3)$$

  where σ - nominal stress in specimen,
  thus plastic zone size in the vicinity of crack tip is equal to :

$$r_y = \begin{cases} \frac{1}{6\pi}\left(\frac{K_{IC}}{R_p 0.2}\right)^2 \text{ for plain strain} \\ \frac{1}{2\pi}\left(\frac{K_{IC}}{R_p 0.2}\right)^2 \text{ for plain stress} \end{cases} \quad (4)$$

It means that for testing of geometrical reduced specimens failure will occur at substantial higher stresses than in cases of real structures, in most cases these specimens will fail under conditions of elastic-plastic loading conditions. At the same time the ration between plastic zone size at crack tip and specimen (structure) thickness will be different, not mention that conditions (1) and (2) are very difficult to realize. Very complicated will be also a transfer of results from testing of model with defects in the region of stress concentrators such as in nozzles, threads etc. Generally, it can be concluded that for obtaining approximately same critical stresses on models and structures it is necessary to realize tests of models at substantially lower temperatures in comparison with operational ones, in most cases even below - 100 ^{o}C, it is is necessary to fulfill conditions of linear elastic fracture mechanics, i.e. (1) and (2). This temperature shift is not so large in the cases of elastic-plastic region of loading, but it is also not negligible. At these case it is necessary to take into account different stress-strain diagrams of tested materials at different temperatures, first of all their different yield strengths and strain hardening. Example of such situation is demonstrated in Fig.1, which represents the "Fracture Analysis Diagram" for 15Kh2MFA type of steel. This diagram was received by testing specimens of 150 mm thickness as well as small-scale specimens in scale 1:8 and 1:12, all with surface defects of different depths.

- *aspects of fatigue failure :*

  - crack growth rate during repeating loading depends on fulfillement of conditions (1) a (2), i.e. on specimen thickness,

  - in case of testing specimens and models with stress concentrators, main role plays not only crack size but also crack placing in stress gradient, and in some cases also the effect of austenitic cladding,

  - "geometrical size effect" takes place in testing of reduced models with defects. Failure stresses will be generally higher in reduced models than in real structures and for the same nominal stress its crack growth rate will be also higher,

- *during testing of large-scale specimens and model the following effects and situation can take place :*

  - dependence of crack arrest temperature on specimen thickness, i.e. basement of "temperature approach of safety",

  - possibility of testing the "leak-before-break" type of failure and approach,

  - effect of plastic zone size in crack tip in stress field,

  - testing of complex operational conditions and their influence of material and structurel behaviour (transients, pressurized thermal shock, etc.),

  - effect of tolerances from specimen (structure) manufacturing, first of all of bolts and nuts.

Besides these effects, during testing of large-scale specimens it is also possible to measure and estimate (in comparison with small specimens) :

- distribution of stresses and strains in the vicinity of stress concentrators,

- redistribution of stresses in the region of stress concentrators during loading in elastic-plastic region of loading,

- interaction of close defects in the field of stress gradient or even in the field of non-monotonic stress field etc.

TESTING POSSIBILITIES - EQUIPMENTS

Large-scale testing requires unique testing equipments, mostly of special design and with high loading capacities. Of course, additional requirements can arose, for example need of fast loading, biaxial loading etc. Thus, for such experiments special equipments are designed and manufactured, mostly only as prototypes.

In ŠKODA Concern three equipments were designed and manufactured and still are used in our laboratories:

- ZZ 8000 : hydraulic tensile testing machine with maximum capacity of 80 MN in tension
  maximum section of specimen (connection by welding) is 1,200 x 350 mm
  maximum length of specimens - up to 4 m
  flat tensile specimens are commonly used, but also crack arrest temperature on plate specimens were determined, as well as repeating loading of large bolting joints (M 240 mm) can RPV parts like nozzles etc.

- ZÚ 1000/1000 : servohydraulic testing machine for repeating loading with maximum capacity +/- 10 MN in tension and compression, maximum specimen elongation is +/- 200 mm
  specimen are welded to specimen heads or mounted directly to machine planes

- ZŠ 1000 : servohydraulic tensile testing machine with maximum capacity of 10 MN in tension
  this machined is designed for testing by uniaxial tension of axisymetrical type of specimens, mainly bolting joints (up to M 140 mm for RPV of VVER-440 MW unit)

CONCLUSIONS

There exists a unreplaceable role of large-scale material testing, mainly from the existence of :
- material size effect,
- geometrical size effect.

Such type of tests can also demonstrate special loading conditions and lifetime of complicated structures and their parts, particularly in elastic-plactic type of loading.

Large-scale testing should be used also for verification of calculation models as well as for preparation and/or backfitting of new codes for calculations.

Planning of such type of tests needs fulfillment of some special requirements to their defect size, configuration, defect ratio and to specimen general dimensions - all these parameters depends on aspects of testing, material conditions and overall geometry of specimens and structures.

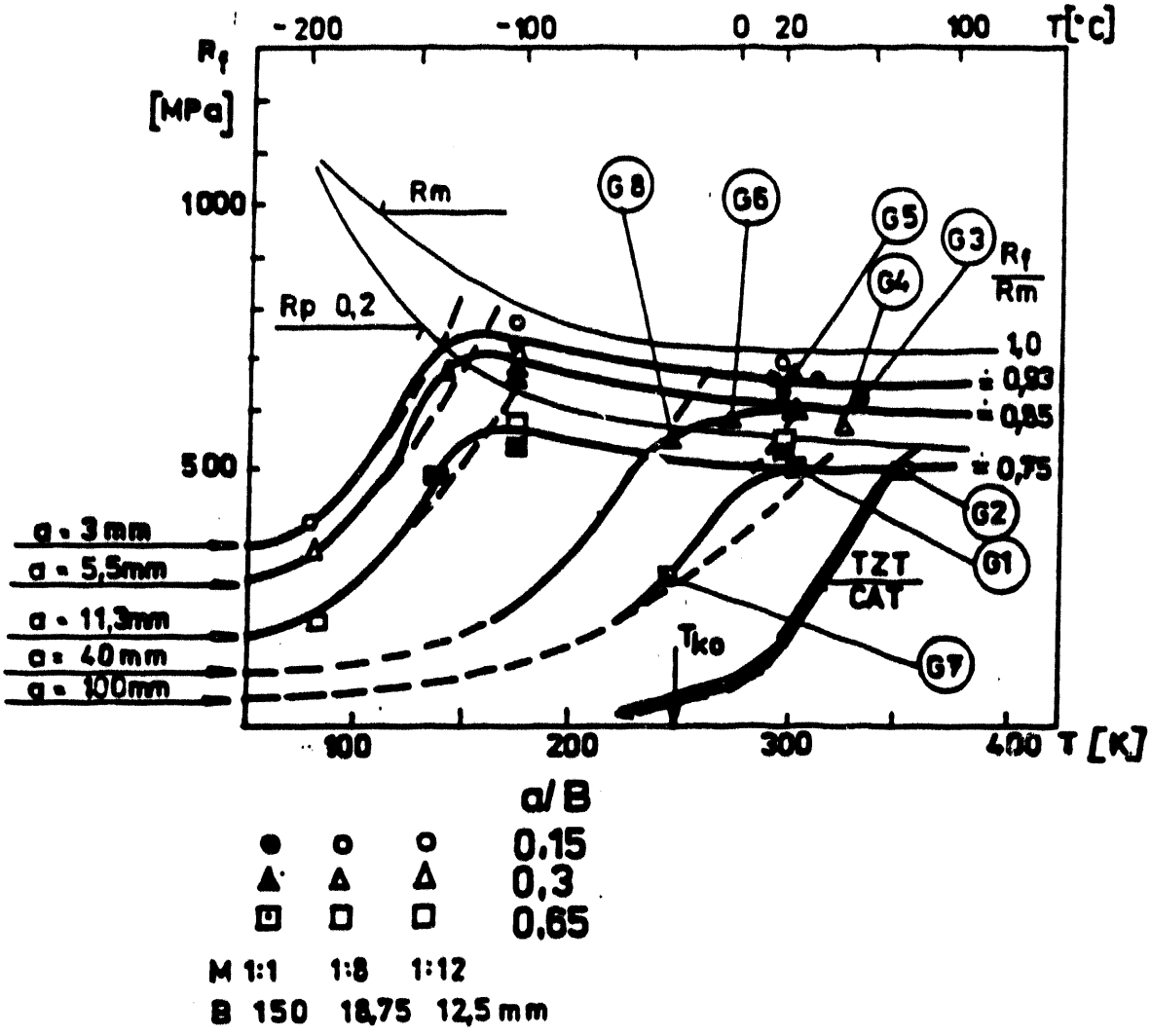

Fig.1. Fracture Analysis Diagram of 15Kh2MFA type of steel - 150 mm thickness

3D-CALCULATIONS OF A TYPICAL NUCLEAR PRESSURE VESSEL SUBJECTED TO THERMAL SHOCK LOADING

Dr. Seth Swamy*, Mr. John Schmertz*, Mr Mario Recinella**, Mr Joseph Boucau**

*Westinghouse Nuclear and Advanced Technology Division
P.O. Box 355, Pittsburgh, PA 15230 USA

**Westinghouse Energy Systems International
73 Rue de Stalle, 1180 Brussells, Belgium

ABSTRACT

The phenomenon associated with High Pressure Safety Injection (HPI) following a Small Break LOCA has received considerable attention in recent years. Particularly, thermal mixing following an accident condition such as a Small Break LOCA has been examined experimentally throughout the world. Data from various experiments are available now, some on scale models while others are full scale tests. Specifically, tests conducted by Battelle Institute at the HDR facility and the tests conducted by Kraftwerk Union at the UPTF facility in Germany were full scale tests. Available test data indicate localized cooldown or a stratified condition in the reactor vessel following the safety injection. Such behavior cannot be described by a traditional simple thermal hydraulic model. The need to simulate observed test data in the analysis has led to the development of multi-dimensional computer codes such as TEMPEST, COMMIX-1B, SOLA-PTS and other regional mixing models based on a fundamentally oriented zonal approach, such as REMIX, NEWMIX[1].

In this paper the results of a Small Break LOCA evaluation for a typical PWR are presented. The effect of High Pressure Safety Injection was evaluated using the TEMPEST code. The axial and azimuthal fluid temperature distributions were determined following the safety injection. The temperature distribution clearly indicated localized temperature gradients directly below the primary loop cold leg, indicating a stratified condition. A 3-dimensional finite element model was constructed to evaluate the thermal and stress response. The effects of the stress fields on the fracture behavior of the reactor vessel were investigated.

INTRODUCTION

In Pressurized Water Reactor (PWR) plants the accidents of concern with regard to the reactor pressure vessel are known as the pressurized thermal shock (PTS) which allow cool water to come in contact with the hot inner-surface of the reactor vessel, where the fast-neutron fluence and thus the radiation-induced reduction in fracture toughness in the wall is a maximum.

In addition to postulated accidents, PTS events can result from a variety of causes. These include system transients, some of which are initiated by instrumentation and control system malfunctions, e.g., stuck open valves in either the primary or secondary system.

Specifically, the PTS events are system transients in PWRs that can cause severe overcooling followed by immediate repressurization to a high level. The thermal stresses caused by rapid cooling of the reactor pressure vessel inside surface combine with the pressure stresses to increase the potential for fracture if an initial flaw is present in low toughness material. Low fracture toughness material can be a result of the neutron irradiation in the beltline region of the reactor pressure vessel.

The phenomena associated with High Pressure Safety Injection (HPI), and associated stratification/cooldown effects when this injection is under stagnant loop flow conditions, have received considerable attention in recent years. Particularly, thermal mixing following an accident condition such as a Small Break LOCA has been examined experimentally throughout the world. Data from various thermal mixing experiments related to pressurized thermal shock are available now. These include [1]:

- Tests conducted by Creare, Inc. for EPRI on a 1/5 scale model
- Tests conducted by Imtram Voima Oy (Finland) for USNRC on a 2/5 scale model
- Tests conducted by Purdue University for USNRC on a 1/2 scale model
- Tests conducted by Creare, Inc. for EPRI/NRC on a 1/2 scale model
- Full scale tests conducted by Battelle Institute at the HDR facility
- Full scale tests conducted by Kraftwerk Union at the UPTF facility in Germany

A unified interpretation of the data obtained from the above tests is presented in Reference 1. None of the fluid system codes such as TRAC, RELAP and RETRAN have the ability to account for thermal stratification and thermal mixing phenomena [1,2]. The need to simulate observed test data in the analysis has led to the development of multi-dimensional computer codes such as TEMPEST, COMMIX-1B, SOLA-PTS [5,9,10] and other regional mixing models such as, REMIX and NEWMIX [1,3,4].

In this paper the results of a Small Break LOCA evaluation for a typical PWR are presented. The reactor pressure vessel thermal, stress and fracture mechanics evaluation procedure and the associated steps of evaluation are pictorially depicted in Figure 1.

THERMAL HYDRAULIC ANALYSIS

In this analysis a Small Loss-of-Coolant Accident (Small LOCA) is evaluated. A small-break LOCA is characterized by a rapid cooldown and depressurization of the Reactor Coolant System (RCS). The primary temperature remains just above the steam generator saturation temperature for a while until the combined effects of cold Safety Injection (SI) water addition and energy loss from the break exceed the energy addition rate from decay heat production. After that time, RCS pressure and temperature should both decrease slowly. If the SI flow is less than the break flow, the RCS experiences a net loss of inventory, leading eventually to flow stagnation in the cold leg/downcomer region. The fluid temperature in this region drops rapidly as the cold SI water replaces the warmer RCS water through the break. While the fluid temperature in the downcomer region continues to decrease, the RCS pressure remains fairly high when the break is small.

For this evaluation, a system code was used to determine the transient conditions as long as national circulation does exist. During loop flow stagnation, a three dimensional thermal hydraulic analysis was performed using the TEMPEST computer code, which is described in References 5 and 6. Figure 2 shows a typical circumferential fluid temperature distribution at the core mid-plane, plotted at one-hundred seconds into the small break LOCA transient. The figure shows the abrupt drop in the water temperature below the inlet cold leg nozzle centerline.

FINITE ELEMENT THERMAL ANALYSIS

A three-dimensional (3D) finite element model (see Figure 3) of a typical reactor pressure vessel was constructed to perform the finite element thermal and stress analysis. In the thermal version, the external surface is insulated and the internal surface is subjected to the LOCA fluid temperatures, which vary with time and location. Material properties for the vessel are obtained from Section III of the ASME Code ('89 including '90 addenda).

Heat transfer coefficients developed by TEMPEST vary with space and time. A typical surface temperature distribution is shown in Figure 4.

FINITE ELEMENT STRESS ANALYSIS

Obtained in the stress analysis are the thermal stresses due to the thermal expansion effects associated with the temperature gradients and the mechanical stresses due to internal pressure. A plot of internal pressure versus time is given in Figure 5. A representative stress contour plot is shown in Figure 6. This plot corresponds to the time for which the temperature distribution of Figure 4 was provided. Figure 7 shows the through-wall hoop stress distribution at a selected location for the Small LOCA transient.

Mechanical properties are obtained from Section III of the ASME Code ('89 including '90 addenda).

FRACTURE MECHANICS EVALUATION

For the fracture evaluation, linear elastic stress intensity factor (K_I) solutions were used. The computed K_I values are compared with the toughness (K_{IC}) values to determine the critical flaw sizes.

Shown in Figure 8 is the geometry of the reference flaw used in developing the Stress Intensity Factor (SIF) expression applicable to typical PWR vessel beltlines. The flaw is semielliptical in shape and its depth and length are denoted by a and 2c, respectively. The aspect ratio, defined by the ratio of 2c/a, is assumed to be 6 consistent with industry practice. The beltline inside radius and wall thickness are denoted by R and t, respectively.

The crack opening through-wall stress σ is represented by a third degree polynomial as follows:

$$\sigma(x) = A_0 + A_1 x + A_2 x^2 + A_3 x^3$$

where A_0, A_1, A_2, and A_3 are the coefficients of the polynomial and x is the linear coordinate as shown in Figure 8. Denoting the dimensionless distance α by

$$\alpha = x/t$$

the crack opening stress defined above can be written as:

$$\sigma(\alpha) = B_0 + B_1\alpha + B_2\alpha^2 + B_3\alpha^3$$

where:

$B_0 = A_0$
$B_1 = A_1 t$
$B_2 = A_2 t^2$
$B_3 = A_3 t^3$

The stress intensity factor, K_I, at any point P on the crack front (Figure 8) can be expressed by the relation:

$$K_I = \left(\frac{\pi a}{Q}\right)^{1/2} \left(\cos^2\phi + \frac{a^2}{c^2}\sin^2\phi\right)^{1/4} \left[B_0 H_0 + \frac{2}{\pi}\xi B_1 H_1 + \frac{1}{2}\xi^2 B_2 H_2 + \frac{4}{3\pi}\xi^3 B_3 H_3\right]$$

where $\xi = a/t$, and the influence functions H_0, H_1, H_2, and H_3 are obtainable from the methods given in reference 7.

The lower bound toughness K_{Ic} curve as defined in Reference 8 was used as allowable toughness, in this evaluation, as follows:

$$K_{Ic} = 33.2 + 2.806 \exp [0.02 (T-RT_{NDT})] \quad \text{ksi } \sqrt{\text{in}}$$

where RT_{NDT} = reference nil-ductility transition temperature (°F)
T = material temperature (°F)

Neutron irradiation has the effect of shifting the RT_{NDT} of the beltline material to higher temperatures. When the RT_{NDT} values are known, the allowable K_{Ic} at any location of the reactor vessel can be easily obtained by the equation. The upper shelf toughness value is chosen to be 200 ksi $\sqrt{\text{in}}$ consistent with the industry practice.

Figure 9 shows a typical plot of the stress intensity factor for a finite circumferential flaw during the small LOCA transient. It is easily seen that the critical flaw size is very large - more than 80% through the wall.

DISCUSSION AND CONCLUSION

A vital ingredient for performing integrity analyses is the knowledge of the stresses that develop in the structure when subjected to various loadings such as the transient loadings. In recent years thermal mixing phenomena following an accident condition such as a small break LOCA has been examined throughout the world. Data from various experiments are available now, some on scale models while others are on full scale tests. Specifically, tests conducted by Battelle Institute at the HDR facility and the tests conducted by Kraftwerk Union at the UPTF facility in Germany were full scale tests. Available test data indicate localized cooldown or a stratified condition in the reactor vessel following the safety injection. Such behavior cannot be described by a traditional simple thermal hydraulic model.

The input temperatures used in this evaluation were obtained by three-dimensional thermal-hydraulic analysis. Thus, the vessel wall was subjected to fluid temperatures which varied both in the axial as well as the azimuthal direction, thus providing a more realistic representation of the transients.

A three dimensional finite element model was constructed for the thermal and stress analyses. Analytical results clearly indicated the plume effect caused by localized cooldown or a stratified condition as was observed in the experiments. The maximum stresses occurred in the reactor vessel practically along the centerline of the inlet nozzle.

Fracture mechanics analyses were performed. Both longitudinal and circumferential flaws were considered. Location of the lowest toughness in the reactor vessel identified by the highest RT_{NDT} was also evaluated by postulating flaws at such a location. The calculated

critical flaw sizes were rather large, mainly because in this case the material RT_{NDT} was on the low side. The smallest critical flaw size was about 80 percent through the wall.

In conclusion, realistic thermal hydraulic and finite element thermal and stress analyses were performed for a typical reactor pressure vessel. Using the results of stress analyses, fracture mechanics evaluations were performed as discussed above. The results demonstrate integrity of a typical reactor pressure vessel when subjected to a small LOCA transient.

ACKNOWLEDGEMENT

The authors gratefully acknowledge the motivation and encouragement provided by Mr. T. R. Mager and Mr. D. C. Adamonis. The authors wish to thank Mr. J. F. Petsche for providing the computer analyses results and illustrations for this paper.

REFERENCES

1. Theofaneous, T. G., Yan, H., "A Unified Interpretation of One-Fifth to Full Scale Thermal Mixing Experiments Related to Pressurized Thermal Shock," NUREG/CR-5677, April 1991.

2. Wolf, L., Schygulla, U., Görner, F., Neubrech, G. E., "Thermal Mixing Processes and RPV Wall Loads for HPI-Emergency Core Cooling Experiments in the HDR-Pressure Vessel," Nuclear Engineering and Design, Volume 96, pp 337-362, 1986.

3. Theofanous, T., La Chance, J. L., Williams, K. A., "The Thermal Hydraulics of Small-Break Loss-of-Coolant Accidents Relative to Pressurized Thermal Shock," Nuclear Science and Engineering, Vol. 102, pp 74-100, 1989.

4. Eyler, L. L., Trent, D. S., "Pressurized Thermal Shock: TEMPEST Computer Code Simulation of Thermal Mixing in the Cold Leg and Downcomer of a Pressurized Water Reactor," NUREG/CR-3564, April 1984.

5. Trent, D. S., Eyler, L. L., and Budden, M. J., "TEMPEST - A Three-Dimensional Time-Dependent Computer Program for Hydrothermal Analysis, Volume I: Numerical Methods and User Input Instructions," PNL-4348, Vol. I, Pacific Northwest Laboratory, Richland, Washington, September 1983.

6. Eyler, L. L., Trent, D. S., and Budden, M. J., "TEMPEST - A Three-Dimensional Time-Dependent Computer Program for Hydrothermal Analysis, Volume II: Assessment and Verification Results," PNL-4348, Vol. II, Pacific Northwest Laboratory, Richland, Washington, September 1983.

7. McGowan, J J. and Raymund, M., Stress Intensity Factor Solutions for Internal Longitudinal Semi-elliptical Surface Flaws in a Cylinder under Arbitrary Loadings, STP-677, ASTM, pp. 365-380, 1979.

8. ASME Boiler and Pressure Vessel Code, Section XI, Appendix A, "Evaluation of Flaw Indications", ASME, New York, 1971.

9. Domanus, H. M., et al., COMMIX-1A: A 3-D Transient Single-Phase Computer Program for Thermal Hydraulic Analysis of Single and Multicomponent Systems, NUREG/CR-2896, 1983.

10. Daly, B. J., Torrey, M. D., SOLA-PTS: A Transient, Three-Dimensional Algorithm for Fluid-Thermal Mixing and Wall Heat Transfer in Complex Geometries, NUREG/CR-3822, July 1984.

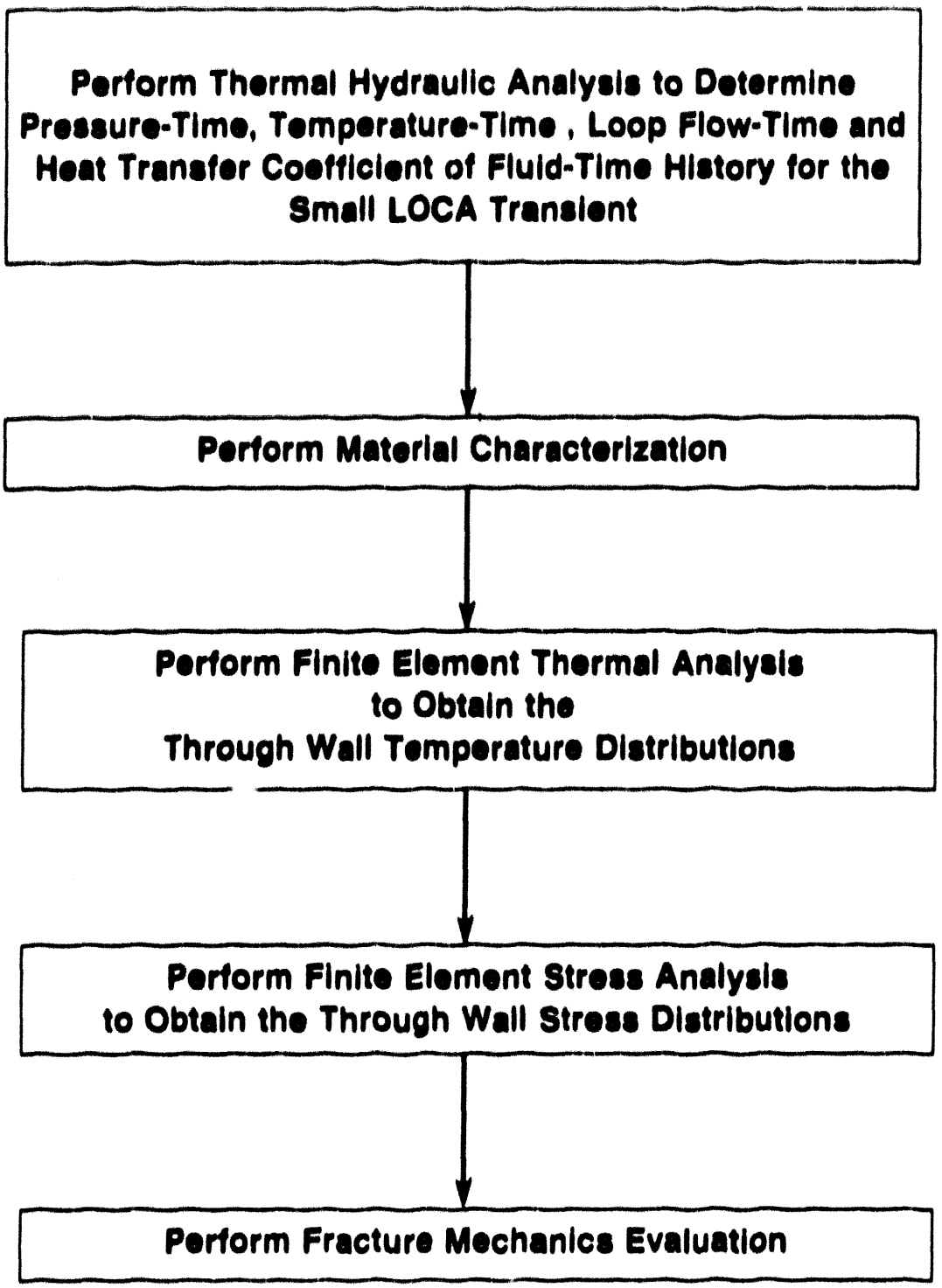

Figure 1: Thermal, Stress and Fracture Mechanics Evaluation Procedure

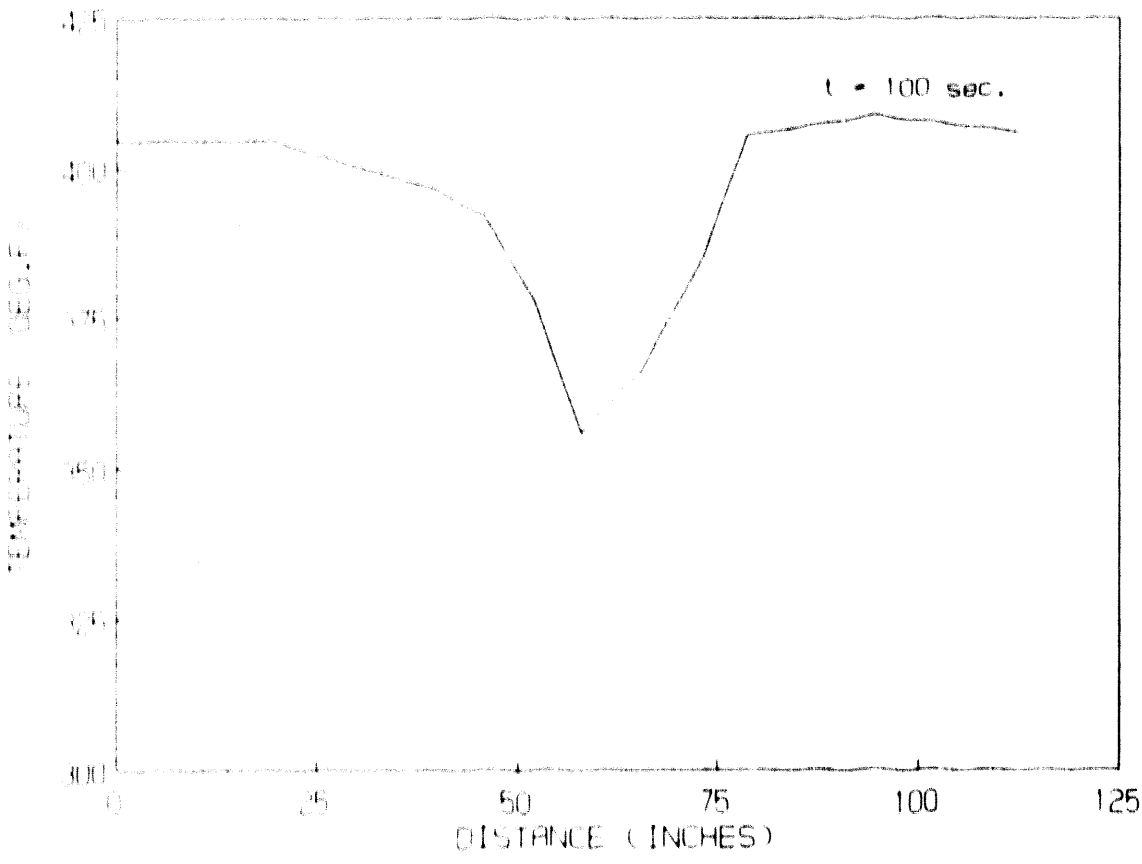

Figure 2 Circumferential Fluid Temperature Distribution in Downcomer (Core Midplane)

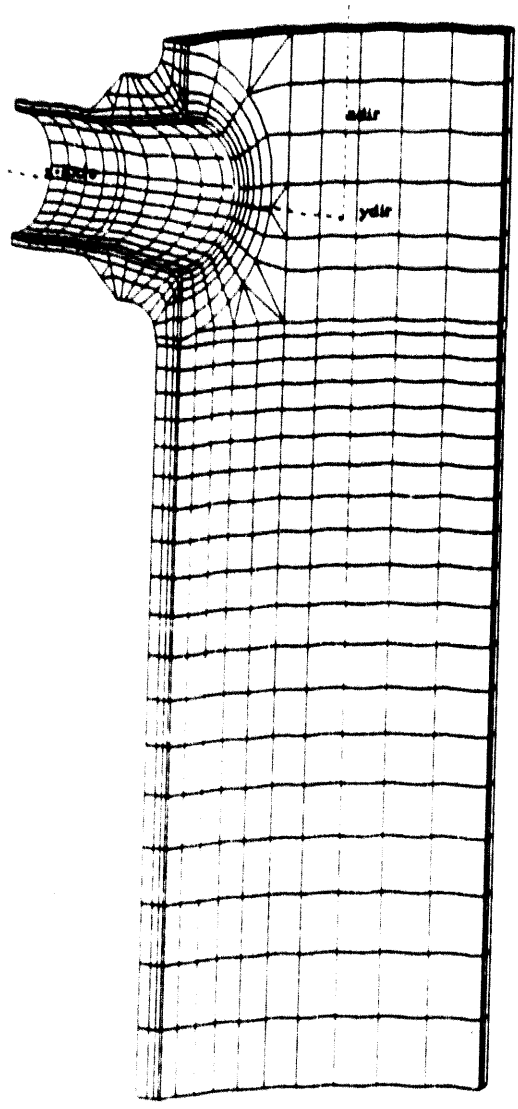

Figure 3 Finite Element Model Inside View

X1285.1b 092292-10

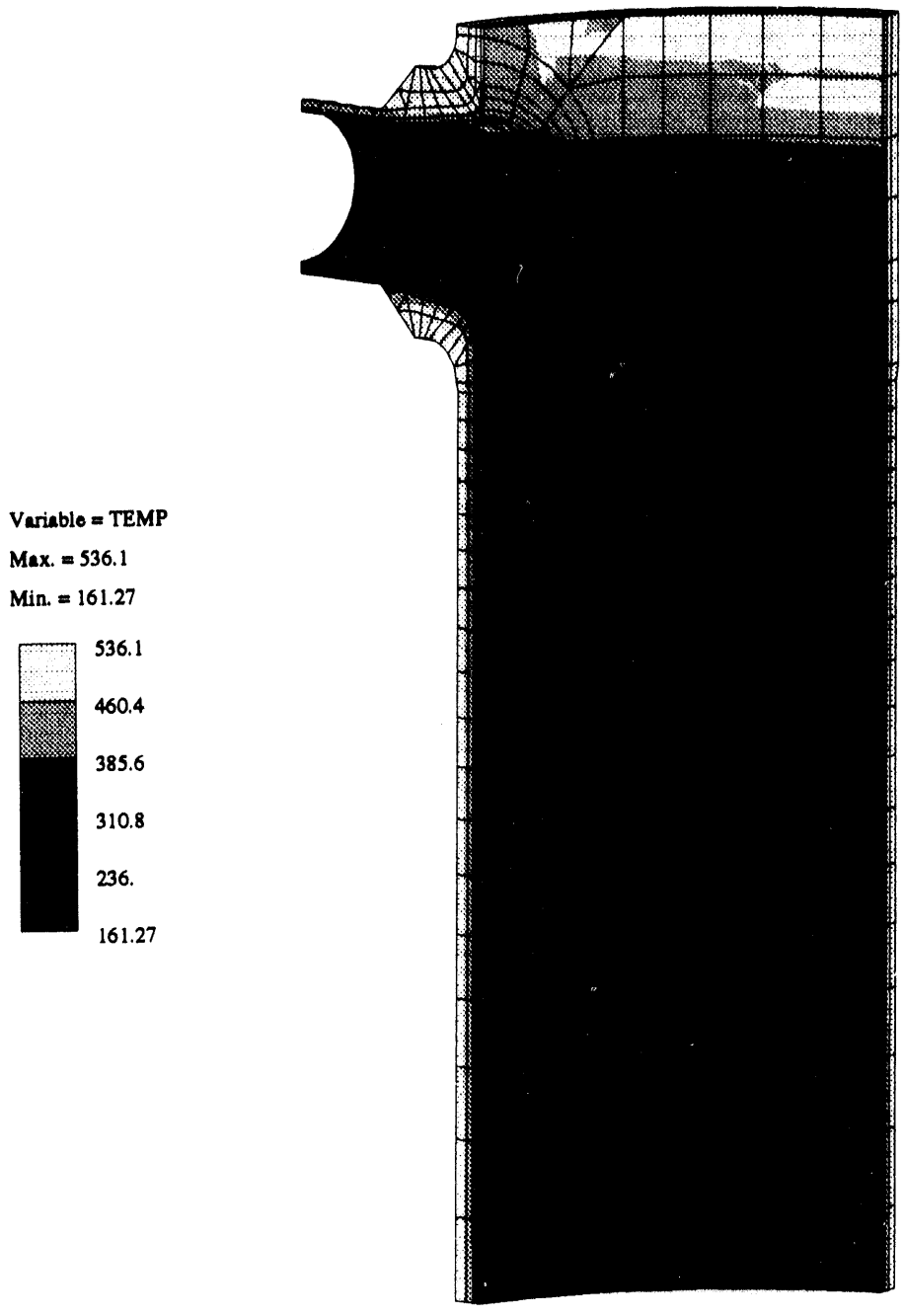

Figure 4 Typical Reactor Vessel Surface Temperature Distribution

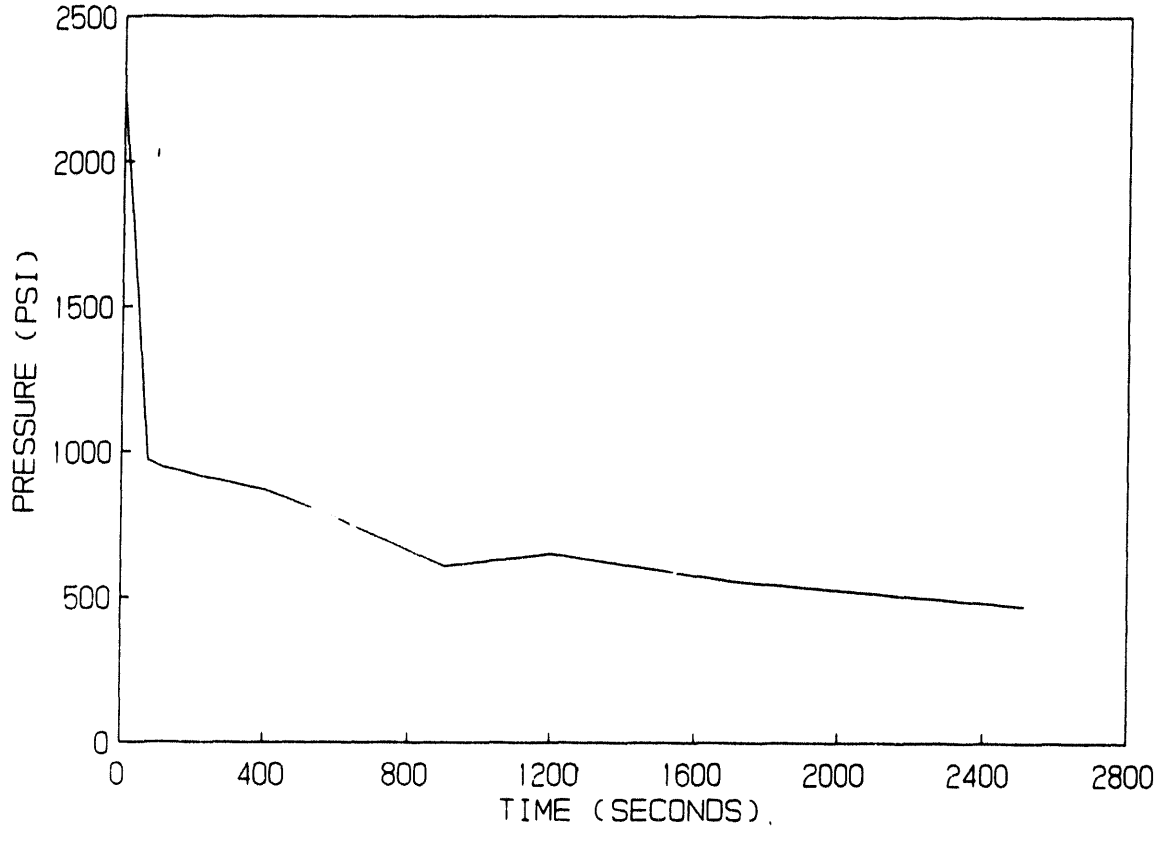

Figure 5 Pressure versus Time for Small LOCA Transient

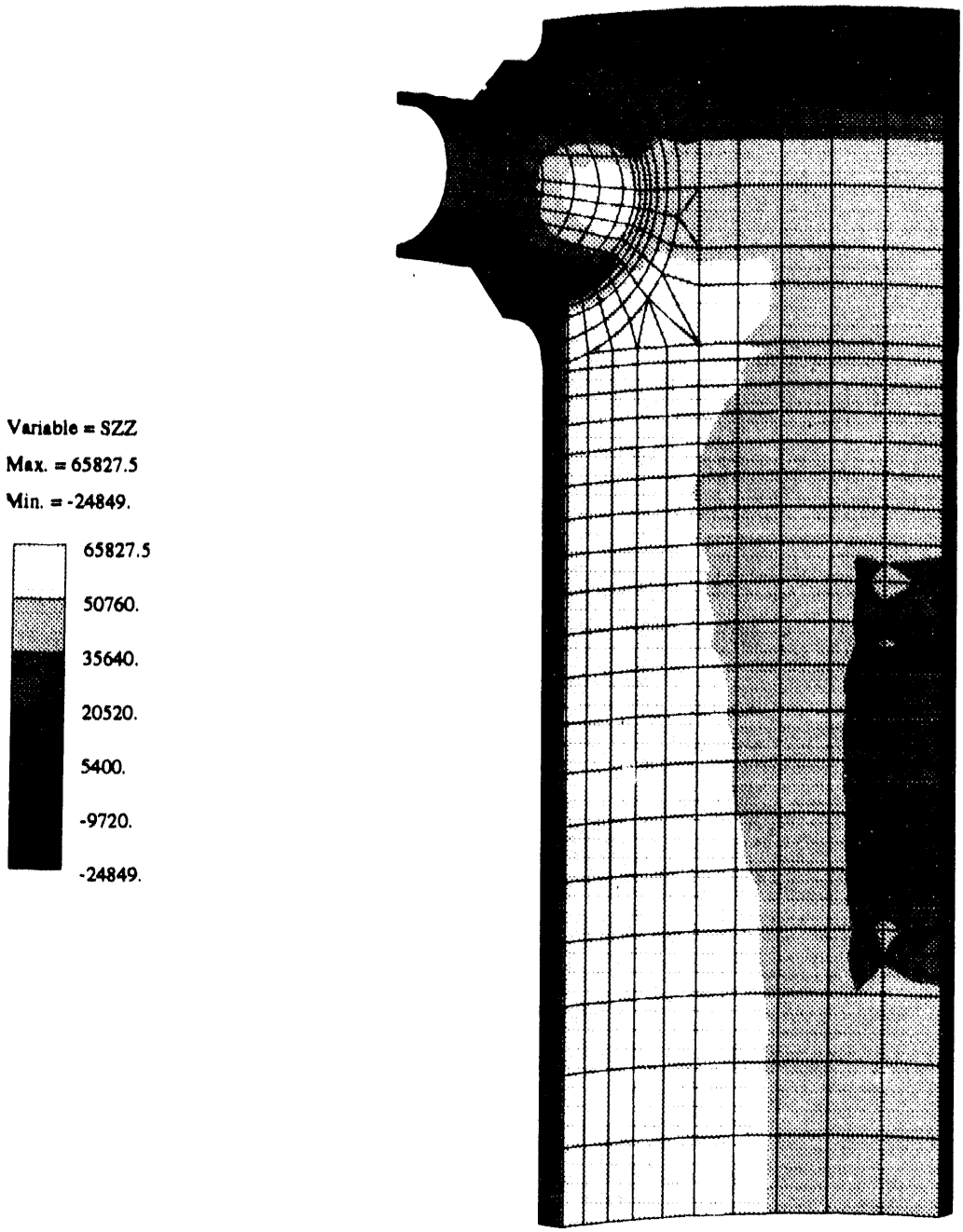

Figure 6 Representative Stress Contour Plot

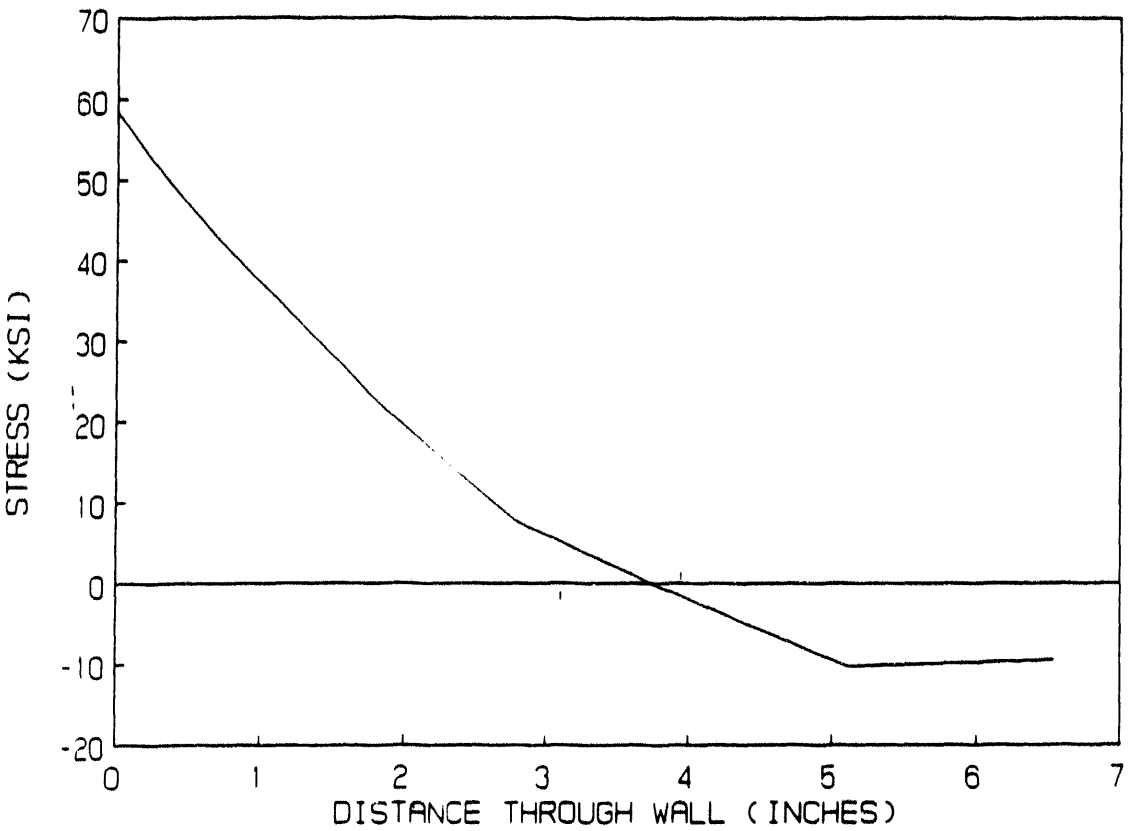

Figure 7 Through-Wall Hoop Stress Distribution of a Critical Location

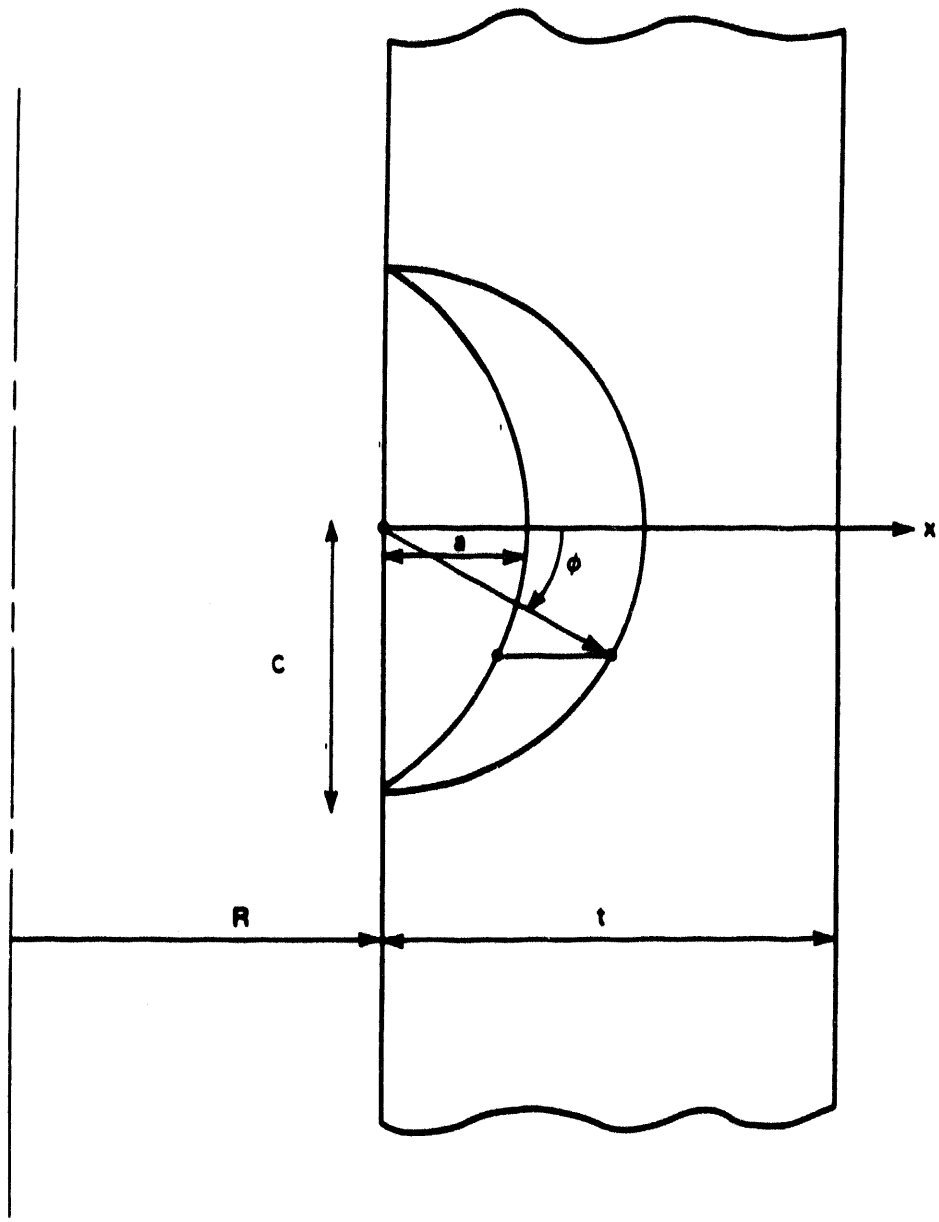

Figure 8 Geometry of Finite Flaw

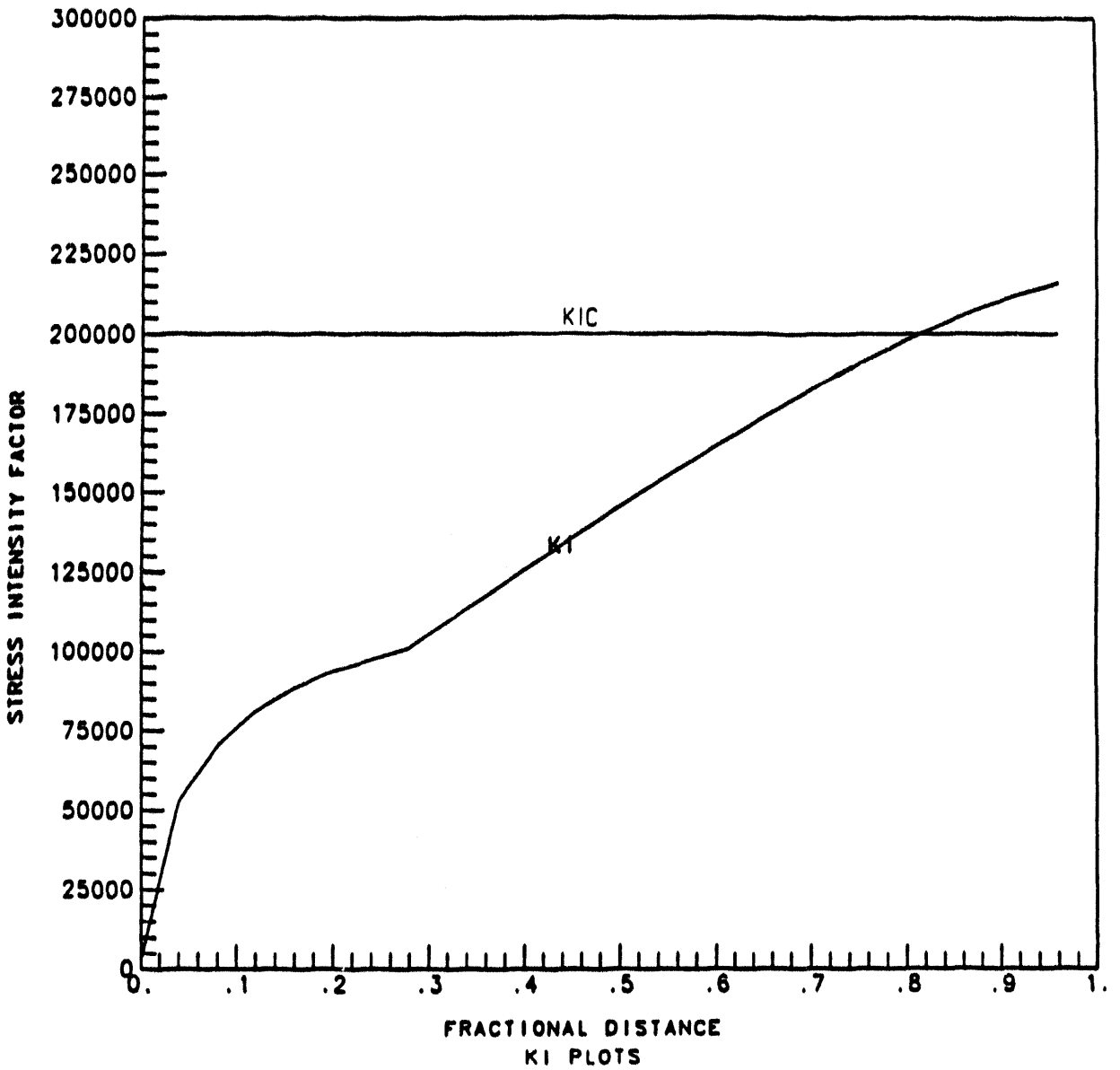

Figure 9 Stress Intensity Factors for Circumferential Finite Flaws

THE CAUSES OF GEOMETRY EFFECTS IN DUCTILE TEARING

by

Dr. Robert J. Dexter* and Dr. Tim J. Griesbach**

An adequate understanding of geometry effects in ductile tearing can only be achieved when the different causes of the effects are distinguished and these geometry effects are linked to particular micromechanical fracture processes or global deformation mechanisms. It is shown that the micromechanical process of ductile (fibrous) fracture is dependent on achieving a critical strain, which is only slightly dependent on the stress state for the range of triaxiality conditions in pressure vessels and through-cracked plates. Under certain conditions, the crack tip strain can be shown to scale with the value of the J integral and there is a direct connection between J and the underlying micromechanical process. This connection is lost for significant crack extension or large-scale plasticity. Nevertheless the J integral may still be used on an empirical basis under some conditions. Under fully-plastic conditions the primary source of geometry dependence in the J-R curves is due to the geometry dependence of the shape and volume of the plastic region that develops around the uncracked ligament. This occurs because J is essentially proportional to the total plastic work done on the specimen. If it can be assured that the fracture mode in both the test specimen and the structure will remain fully fibrous, it is conservative to extrapolate J-R curves generated from small compact specimens for the analysis of pressure vessel crack stability.

*Lehigh University, Center for Advanced Technology for Large Structural Systems
117 ATLSS Drive, Bethlehem, PA, USA 18015-4729

**Electric Power Research Institute, 3412 Hillview Ave., Palo Alto, CA, USA 94303

INTRODUCTION

The recent report on project FALSIRE [1] noted the significant uncertainty associated with the effect of geometry on the analyses of large-scale fracture experiments [1]. Most recent ductile fracture analyses in the electric-power industry have been based on the J integral [2]. The J-integral methodology allows a prediction of ductile crack initiation in various components using the value of J at crack initiation (J_{Ic}) as a material property that can be measured in small specimens [3-4]. (The J integral is directly proportional to the crack-tip-opening displacement (CTOD) [5-8], therefore the two approaches for crack initiation are essentially equivalent.)

A plot of the J integral vs. crack extension (J-R curve) has also been used as a material property to predict ductile crack extension (tearing) in various components [9,10]. To evaluate possible specimen geometry effects, J-R curves from various specimen sizes are required. Such data for reactor pressure vessel (RPV) materials up until 1987 included J-R curves from A533B and A508 base plate material and the Linde 80 weld metal in the original and irradiated conditions, e.g. references [11-13]. The J-R curves in Figure 1 [11,13] were measured on standard compact (CT) specimens. The specimens are different sizes but the proportions are constant. The 0.5T specimen is nominally 13 mm (0.5 inch) thick and the distance from the initial crack tip to the back face of the specimen (the ligament) is also nominally 13 mm (0.5 inch). The thickness and the ligament of the 4T specimen is nominally 100 mm (4 inches). The slope of a linear fit to the J-R curves between the dashed lines (i.e. for the first few millimeters of crack extension) is called the tearing modulus. The apparent J_{Ic} and tearing modulii for these test specimens are shown in Table 1. As shown in Table 1, the J_{Ic} values vary by less than 25 percent and the tearing modulii vary by less than 36 percent. The standard for what constitutes reasonable agreement in fracture mechanics is very generous due to the high degree of natural variation that would be exhibited between replicate specimens. This level of agreement is typical for most moderate toughness steels, i.e. steels that can meet the specimen size requirements of the ASTM specification [10].

If the J-R curves are given in terms of a modified J proposed by Ernst [12], even better agreement is obtained. In any case, it is important to note that the trend in the size dependence is that larger specimens have a higher tearing modulus, i.e. that larger specimens have a higher apparent resistance to crack extension. Therefore, under these conditions and for these materials, the ASTM J-R curve is an empirically demonstrated material property that can be conservatively applied to predict crack extension (up to 10% of the ligament size) as a function of load and displacement in larger geometrically-similar specimens. For example, Table 1 shows the crack extension in each size specimen at a particular level of applied J. The J level for each material for this example is the J level which would cause 3 mm of crack extension in the smaller specimen. As shown in Table 1, the crack extension at this applied J level in the larger specimen is 1.5 mm in the A533B (at J of 625 kJ/m^2) and 1.7 mm in the Linde 80 weld metal (at J of 220 kJ/m^2). The actual crack extension is only 50 to 57 percent of predicted crack extension, i.e. 3 mm.

A distinction must be made between variation of specimen "geometry" (changes in shape and ratio of tension to bending as well as size) and specimen "size" (proportional specimens of a particular type). Note that the data in Figure 1 do not show that the J-R curve for this material is independent of geometry, only that the J-R curve is reasonably independent of size for a particular proportional geometry. In a CT specimen, the remaining ligament is loaded primarily in bending, with a small axial tension component. Similar J-R curves are also obtained from single-edge-notched bend bars (SENB specimens) in which the remaining ligament is loaded entirely in bending. In a center-cracked tension panel (CCT specimens)

the ligament is loaded entirely in tension. When J-R curves are obtained from CCT specimens, the resulting tearing modulus is typically significantly greater than the tearing modulus measured on CT or SENB specimens.

Figures 2 and 3 show J-R curves from CT specimens compared to J-R curves for CCT specimens for two different pipeline steels [22]. These steels are very tough and the specimens were only 9 mm thick. Therefore tests on this material cannot meet the ASTM size requirements. The bottom plot in these figures shows the same data on a much larger range of crack extension. The J_i and tearing modulus values are shown in Table 1. The tearing modulus for the CCT specimen is 72 to 85 percent greater than the tearing modulus for the CT specimens. Table 1 shows the crack extension in the CCT specimen at a level of J which would cause crack extension of 3 mm in the CT specimens. The actual crack extension in the CCT specimens at this J level is only 1.0 mm in the X46 steel and 0.6 mm in the X70 steel. These calculations show that applying the J-R curve from the CT specimen is unreasonably conservative, the actual crack extension is only 20 to 33 percent of the predicted crack extension. Similar differences between CCT and CT specimens have been shown by Garwood [14] and by Zahoor and Kanninen [15].

The trend in the geometry effects depends on the micromechanical failure mode. For example, in 1988 Hiser and Terrell [16,17] reported the results of many tests on an A302B plate. This particular A302B plate was specially rolled to be similar to plates used in early reactor pressure vessel construction and to yield a low upper-shelf Charpy energy, i.e., below 68 J. The minimal cross rolling applied to the plate and the high sulfur content (0.025%) resulted in a high proportion of longitudinally oriented manganese-sulfide inclusions. In the fracture tests in the T-L orientation (the crack extends in the rolling direction), these inclusions manifest as separations (often called delaminations or splits) perpendicular to the fracture surfaces and parallel to the plate surfaces.

The J-R curves for a series of proportional specimens for this material at 82°C are shown in Figure 4. The thickness and initial remaining ligament of the 0.5T specimen is nominally 13 mm (0.5 inch) while the thickness and the remaining ligament of the 6T specimen is nominally 150 mm (6 inches). The geometry dependence of these curves is very significant. But, of much greater concern, the trend in the tearing modulus with specimen size that can be seen in Figure 4 is the opposite of that for the Linde 80 welds and the A533B steel as shown in Figure 1. Table 1 shows that the tearing modulus for the 6T specimen is only 30 percent of the tearing modulus for the 0.5T specimen. If the J-R curve from the 0.5 specimen were used to predict 3 mm of crack extension in the 6T specimen, the actual crack extension would exceed 80mm (the limit of the data in Figure 1) and the result would be unconservative by a factor of greater than 27. Data from Joyce for an HY-100 material (reported in reference [18]) that also became available in 1988 showed the same trend as the A302B steel. This steel also revealed separations perpendicular to the fracture surface [18].

Tearing stability analyses have been applied to several critical safety problems in the nuclear power industry. The stability of a part-through crack in piping is assessed to demonstrate that the pipe will develop a noticeable leak before break so that it can be detected and repaired before catastrophic bursting [19-21]. Another critical application is the assessment of surface cracks in pressure vessels [19]. It is necessary to analyze ductile tearing in the pressure vessel for up to 200mm of crack extension [16]. In this case, the restriction of valid J-R curves to 10% of a test specimen ligament would require full-scale specimens. Since the data must be obtained from small surveillance (irradiated) specimens, it is necessary to use J-R curves beyond the range considered valid by the ASTM specifications. In fact, it may be necessary to extrapolate the J-R curve to crack extension greater than the ligament size of

the test specimens. Obviously, under these conditions, there is no theoretical basis for using the J-R curve. However, an empirical basis for the J-R curve can be established for engineering purposes. If there is to be confidence in this empirical basis, the geometry effects must be predictable. This paper discusses the causes of geometry dependence of J-R curves and attempts to outline the conditions under which the trends in the geometry effects will be predictable.

FRACTURE MICROMECHANISMS

Fracture criteria can only be effective if there is some connection to the micromechanical processes leading to fracture. For ductile fracture (also referred to as fibrous fracture), these processes are void initiation, growth, and coalescence [23]. Other mechanisms can intervene during the course of an otherwise ductile process to cause premature separation of part or all of the fracture surface, e.g. separations or cleavage. Fracture criteria are generally not applicable to more than one type of fracture mechanism. Therefore, if one or more of these other mechanisms intervene, the geometry independence and validity of the fracture criteria will generally be adversely affected.

Void Growth from Inclusions

Ductile fracture mechanisms and models were recently reviewed in a book by Thomason [23]. In order to hypothesize the connection of global fracture criteria to the mechanics of ductile fracture, mathematical models of these ductile fracture processes are required. There are independent models for void initiation, growth and coalescence [23]. However, the void initiation phase typically represents less than 15 percent of the total strain at fracture (for C-Mn pressure vessel steels [24,25]) and is therefore commonly ignored in the development of fracture criteria.

Void coalescence can occur either by impingement of growing voids or by sudden void sheeting. The criteria for void impingement generally involve non-continuum models that account for the actual voids rather than smearing out the effects of the voids. The development of void sheets depends on the loading and structural configuration as well as the strain hardening, strain-rate hardening, and plastic anisotropy [26]. Therefore, mathematical criteria for void coalescence are difficult to implement in the type of numerical simulations employed in fracture research. Therefore, fracture criteria are typically developed empirically as some critical value of a parameter related to void growth.

Numerous micromechanical models have been developed to characterize the void growth process [27-34]. Atkins and Mai [35,36] and Clift et al [37] have recently reviewed most of the published models. The useful models are variations of an incrementally defined function of the effective plastic strain that is postulated to be a controlling factor in void growth. The increment of effective plastic strain is typically multiplied by some nonlinear function of the constraint factor or other stress quantities that can be derived from the constraint factor.

There are various definitions of constraint factors which are all derivable from one another [38]. The term "constraint" is often used with many different meanings. In this paper it will have a very specific meaning according to the following definition of the constraint factor:

$$constraint\,factor = \frac{\sigma_m}{\sigma_e} \tag{1}$$

where: σ_m is the mean or hydrostatic stress $= \frac{1}{3}\sigma_{kk}$

and σ_e is the Von-Mises effective stress $= \sqrt{\frac{3}{2}S_{ij}S_{ij}}$

where S_{ij} is the deviatoric stress $= \sigma_{ij} - \sigma_m \delta_{ij}$

where $\delta_{ij} = 1$ when $i = j$, and 0 otherwise.

The constraint factor reflects the ratio of the stress quantity that effects the dilatational growth of voids (the hydrostatic stress) with respect to the stress quantity that effects their distortion (the effective stress) [36]. Table 2 shows some typical values of constraint factor for various test specimens as well as surface cracks in pressure vessel geometries [39-43]. In fracture test specimens and surface cracks in pressure vessels, the constraint factor typically ranges from one to two. (Note that this definition of the constraint factor is equal to one third the triaxiality coefficient "q" that is used in the project FALSIRE report [1]).

In this paper the term strain will be taken to mean the effective plastic strain unless specifically stated otherwise. The effective plastic strain increment is defined as follows [44]:

$$d\varepsilon^p = \sqrt{\frac{2}{3}d\varepsilon^p_{ij}d\varepsilon^p_{ij}} \tag{2}$$

The results of analyses by McClintock [27,28] and Rice and Tracey [29] have been used to formulate a simplified model for void-growth intended primarily for relatively high constraint factors only. The Rice and Tracey analysis represents the growth of the average diameter of an isolated two-dimensional void in an infinite medium.

$$ln(R/R_0) = 0.283 * D \tag{3}$$

where R = average radius of the void,

R_0 = original average radius of the void,

0.283 is an empirically derived constant, and

$$D = \int_0^{\varepsilon_p} \exp\left(\frac{1.5\sigma_m}{\sigma_e}\right) d\,\varepsilon^p$$

The integral D often appears in the form of a hyperbolic sine or hyperbolic cosine (with an appropriate change in the constants) rather than the exponential and is postulated to be a measure of damage [27,28]. Local failure is predicted when the level of D, i.e. the level of damage, reaches a critical value associated with void coalescence. Thus the fracture criterion is stated as an integral which depends on the history of the deformation. As a fracture criterion, the critical value should therefore be independent of the history of constraint during deformation. For example, the critical value of the integral should be the same for an experiment with high constraint resulting in low fracture strains and an experiment with low constraint resulting in high fracture strains.

The strain-energy density has been used by Sih [45,46] and Nemat-Nasser [47] as a fracture criterion. Often, this criterion has been employed as simply a critical plastic-work density [48-52]. This criterion is readily calculated and can be related to macroscopic fracture criteria as discussed later. Gillemot [53] has suggested that a critical strain energy density of plain carbon steels is from 500-700 MJ/m^3 and for vacuum-remelted steels is from 1000-1050 MJ/m^3. For large strain, the strain energy density is approximately equal to plastic work density, i.e.:

$$\text{SED}(t) = \int_0^t \sigma_{ij} d\varepsilon_{ij} \approx W^p \text{ (the plastic work density)} \tag{4}$$

$$W^p = \int_0^{\varepsilon^p} \sigma_{ij} d\varepsilon_{ij}^p = \int_0^{\varepsilon^p} \sigma_e d\varepsilon^p = \sigma_f \int_0^{\varepsilon^p} d\varepsilon^p = \sigma_f \varepsilon^p$$

where $\varepsilon^p = \sqrt{\frac{2}{3}\varepsilon_{ij}^p \varepsilon_{ij}^p}$ for proportional straining and σ_f = flow stress ≈ engineering ultimate stress.

Atkins and Mai [36] show that for the special case of constant constraint factor (proportional loading), all of the integrated functions of stress and strain reduce to a constant (reflecting the hydrostatic stress term) times the critical plastic work per unit volume (W^p). This relationship may be approximately correct for loading that is roughly proportional. Therefore, for loading that is roughly proportional, there is approximately a one-to-one correspondence between the damage integral, the plastic-work density, and the effective plastic strain. It is therefore approximately equivalent to specify a critical value of a damage integral, the critical plastic-work density, or the critical effective plastic strain.

Various investigators have evaluated the applicability of these models [37,54-56]. It can be concluded from these investigations that simple damage integrals (void growth models) can, in certain materials over a limited range of strain states, approximately capture the influence of the important variables in fibrous fracture. The applicability of a particular void growth model to a given material and loading condition must always be carefully considered. The void growth models have been used successfully in C-Mn steels with relatively high impurities (by modern standards) and relatively large and closely spaced Mn-S inclusions, like most pressure vessel steel. However, there are sometimes conflicting successes and failures of the void growth models which indicates that the appropriate choice of void growth criterion is dependent on the material.

Empirical Fracture-Strain/Constraint-Factor Locus

Hancock and Mackenzie [57] and others [58-63] have found it useful to correlate fracture strains from various tensile tests according to some function of the constraint factor. Hancock and Mackenzie show that at least at the higher values of constraint factor, the data can be fit by:

$$\varepsilon^f = C\exp\left(\frac{-1.5\sigma_m}{\sigma_e}\right) \tag{5}$$

where: ε^f = effective plastic strain at fracture (typically obtained from the reduction in area)

and C = a constant.

Equation 5 implies the Rice and Tracey [29] model (Equation 3) applies and the loading is proportional, i.e., the constraint factor is constant and can be taken outside the integral of Equation 3.

Figure 5 shows some data for various steels from Hancock and Mackenzie [57,60], Miyata et al [61], Reuter et al [59], and from Dexter and Roy [64]. Some of the data, particularly those with low fracture strains as studied by Hancock and MacKenzie, form an approximately straight line on the semi-log plot, i.e., these data can be fit with Equation 5. However, data at higher fracture strain levels do not fit Equation 5, in fact the data of Dexter and Roy are not significantly affected by the constraint factor. This indicates that a particular functional form of a void growth model may only be adequate for a narrow range of materials.

Miyata et al [61] make the useful observation that many of these steels exhibit a plateau for constraint factors greater than 1.0. (The plateau is much more apparent on a linear plot.) This observation leads to the conclusion that a critical strain (actually only appropriate for high constraint conditions) could be conservatively used in simplified fracture models. As shown in Table 2, the range of constraint factors for the pressure vessel [41-43] and test specimens [39-42] is always greater than 1.0 and typically less than 2.5. Therefore, the critical strain value for ductile fracture in these geometries would not be expected to be very sensitive to changes in stress state in these geometries.

Many investigators have noted approximate relations between the fracture strain and global fracture criteria such as J and CTOD. Green and Knott [65] expressed the CTOD as the product of the fracture strain times a microstructural gage length equal to the participating inclusion spacing (the critical distance for ductile fracture).

$$CTOD \cong l^*\varepsilon^f \tag{6}$$

This simple relation is based on the notion that the process zone is approximately triangular with a base equal to the CTOD and a height equal to the critical distance. Ritchie and Thompson [66] pointed out that if this relation is multiplied by the flow stress it expresses a link between the plastic work density in the fracture process zone (which relates these quantities to Sih's strain-energy density theory [46,53]) and J_{IC}:

$$J_{IC} \sim \sigma_f CTOD \cong l^* \sigma_f \varepsilon^f \cong l^* SED \sim S_c \quad (7)$$

Equation 7 rationalizes the empirical correlation between J_{Ic} and the product of the flow stress and the fracture strain (i.e. an approximation of the strain energy density or the plastic work density). These relationships show the fundamental importance of the fracture strain (or equivalently the plastic work density) as a fracture criterion. Equation 7 is quite a useful relationship because it would allow an estimate of J_{Ic} based on tensile test data alone.

Miyata et al [61] showed that J_{Ic} ought to be a linear function of the fracture strain times the yield stress. They plotted the correlation for various steels at upper shelf temperatures and found the data could be described by two lines, i.e. one for alloy steels and one for low-carbon steels. Figure 6 shows their correlations along with data from two very tough pipeline steels. (The J-R curves for these pipeline steels were shown in Figures 2 and 3). The data from the pipeline steels fit very well along an extrapolation of their line for low-carbon steels.

Cleavage

The mechanisms of cleavage fracture have been reviewed in detail [67-70]. Cleavage propagation is governed by a critical principal stress [71,72]. The cleavage stress is independent of temperature [71-73,75] and constraint [73,74]. (Note that the constraint may still have an indirect effect in being responsible for raising the stress to the level of the cleavage stress. However, the cleavage will occur at a particular stress level, regardless of the level of hydrostatic stress at that stress level.) Strain rate may have an effect on the cleavage stress. For example, a change from slow-bend to impact strain rates had the effect of raising the cleavage stress of pressure vessel steel from 9 to 15% [75]. Orowan [72] discussed the statistical "weakest-link" argument for a size effect in cleavage fracture. It has recently been recognized that there is a statistical size effect and that the critical cleavage stress is maximum for sharp crack specimens, decreases for blunt notch specimens due to the higher volume exposed to the cleavage stress, and decreases further for uniaxial tensile specimens [76].

Formation of Separations

Formation of separations (delaminations or splitting) is one example of how limited cleavage can influence a ductile fracture process. Separations are generally parallel to the plate surface and appear perpendicular to the fracture surface when specimens are tested in the T-L orientation in a temperature range including the transition and lower temperatures of the upper-shelf region [16,77,78]. Separations are given special attention here due to their key role in the unusual geometry dependence exhibited by the A302B steel J-R curves [16,18,78,79]. There are many possible causes for the appearance of separations: 1) decohesion of long thin (lamellar) inclusions, 2) a transgranular cleavage due to a preferred crystallographic texture parallel to the plate surface, or 3) cleavage of banded microstructures (regions of coarse-grained and/or alloy rich ferrite lying parallel to the plate surface) [80-83].

Separations in hot-rolled steels is usually due to inclusions [81] or banded microstructure [84]. Both of these causes have been mentioned in the discussion of the A302B plate [17]. The decohesion of inclusions leaves a unique fracture surface that is described as "woody" [81] and persists into the upper-shelf ductile fracture region [81,83]. The transition in the Charpy energy curve is abrupt when the separations are caused by inclusions and there is little difference in the transition temperature between orientations [81]. The transition is quite gradual when the separations are caused by microstructure [83]. The Charpy transition in the

T-L orientation was not gradual for the A302B plate [16]. The fracture surface of the A302B has been described as woody and otherwise seems to be consistent with decohesion of Mn-S inclusions, although probably the banded microstructure also plays a role [16,17]. There are several cases of separations reported in the literature in which inclusions and microstructure played a combined role in separations [80,82].

Baldi and Buzzichelli studied the cleavage stress in three directions for a steel exhibiting separations due to inclusions and microstructure [80]. These experiments showed that separations appeared at a critical level of through-thickness tensile stress independent of temperature. Their analysis explained the disappearance of separations at low temperatures due to the exceedence of the normal cleavage stress prior to the attainment of the through-thickness separation stress in this case [80].

The Local Approach to Fracture

The local micromechanical criteria for fracture can be expressed in mathematical models, e.g. critical stress or a more complex statistical model for cleavage and critical strain or a more complex void growth model for ductile fracture. If these local criteria are implemented in numerical models of fracture specimens [56,85-92], the problems with geometry effects in global criteria like the J integral can be avoided [89,91]. However, such simulations of fracture are currently impractical for extended quasi-static crack propagation [88,89]. Therefore the J integral and related global fracture criteria are currently the only practical method of predicting ductile crack extension. Problems arise with global criteria when sufficient attention is not given to the underlying micromechanical fracture mode and how the fracture mode and the global criteria might be affected by changes in specimen and structure size. The best approach to the pressure vessel problem is to use global criteria supported by the local approach, i.e. the local approach may be used to define the limitations and expected geometry effects in the global criteria. Multiple criteria will be required when there is a possibility of transition of fracture modes. The optimum criteria for fracture will in general depend on the material, the history and condition of the material (irradiation, warm prestressing, and strain ageing), and temperature [75].

THE EFFECT OF SPECIMEN GEOMETRY ON THE J INTEGRAL

Table 3 shows a summary of the causes of geometry effects in J-R curves. The list in Table 3 is not exclusive, and some simplifications have been made. The list reflects the difference between causes that can be attributed to micromechanics as well as those attributed to the global deformation mechanism. It is convenient to discuss the effects of specimen geometry in terms of two-dimensional generalized plane strain conceptual models. Therefore, it is useful to define a group of "three-dimensional" effects that cannot be discussed in terms of two-dimensions and to discuss these effects later. Much of the literature pertaining to size effects in fracture is motivated by these three-dimensional effects, e.g. crack tunneling and the development of shear lips. In this paper, it is useful to distinguish these phenomena, which arise from variations of stress-state through the thickness and are defined as "three-dimensional", from the "two-dimensional" effects on a particular plane. For example, a change in the stress state at a particular plane in the specimen, e.g. the center plane at midthickness, is considered as a two-dimensional effect even if this change in the stress state were brought about by a change in thickness. Obviously, there are complex interactions between the three-dimensional and two-dimensional effects. However, if the interactions are ignored and these three-dimensional effects are treated separately, it becomes much easier to rationalize geometry effects in terms of simple two-dimensional idealizations.

Each manifestation of geometry effects can be associated with and rationalized by one or more of these local modes and/or global mechanisms noted in Table 3. It is submitted that if the local mode and global mechanism can be assured to remain the same between test specimen and structure, that J-R curves can be used and possibly even extrapolated with confidence. The confidence is not that J-R curves will be a true geometry independent material property, but rather that the trend in the tearing modulus with changing specimen size (and application of test data to the pressure vessel) is known. For example, if it is known that in certain material and test-specimen/component systems that the test specimen will always give a lower bound to the tearing modulus, then this tearing modulus can be used without an excessive factor of safety. If this trend cannot be assured or if the test specimen will always give an upper-bound tearing modulus (which is sometimes the case), then taking advantage of an increase in tearing resistance above J_{Ic} cannot be easily justified in a safety assessment unless full-scale test specimens are used.

Two-Dimensional Micromechanical Effects

As discussed above, ductile fracture is controlled by the attainment of a critical strain at some small distance from the crack tip. (The magnitude of the critical strain is mildly dependent on the state of stress over the range of stress states associated with surface cracks in pressure vessels and single through cracks in plates.) Since local crack-tip strain is difficult to compute and measure, various global fracture parameters have been used as indices of this crack-tip strain.

Figure 7 shows the crack-tip stress and strain fields for a single-edge-notch-bend specimen in plane strain computed using large-deformation finite-element analysis [8]. As shown in Figure 7, for specimens larger than certain minimum specimen ligament size, the stress and strain fields at the tip of the crack scale approximately with the magnitude of J. Since both the stress and strain scale with J, it is clear that J (or equivalently CTOD) should be a useful fracture criterion for ductile crack initiation under these conditions. These conditions are incorporated in the ASTM test specification [4,10] as restrictions on minimum specimen size that are proportional to J.

The theoretical basis of the J integral as a fracture criterion derives primarily from the relationship between J and the crack tip fields. The relationship between J and the crack-tip fields can only be established for small-scale yielding (SSY), but the J integral is still useful and geometry independent (transferable) beyond SSY conditions. However, the variation in the relationship between J and the crack tip fields can lead to geometry effects. These effects are most significant for cleavage fracture and low-toughness ductile fracture. For the fully-plastic conditions for very tough steel, this effect is usually not very significant.

Most of the research on "size effects" or "constraint effects" in fracture pertains to cleavage or to mixed cleavage/ductile fracture crack initiation. On a micromechanical level, cleavage is controlled by the attainment of a critical stress at a particular distance from the crack tip. Since the stress fields scale with J, cleavage fracture may also be predicted using the value of the J integral at the initiation of fracture. However, as shown in Figure 7, the stress fields are more sensitive to changes in specimen geometry. Therefore, in order to have geometry independent J values for cleavage fracture, test specimen size must be about eight times bigger than specified in the ASTM standard for J_{Ic} [93,94]. (This may account for the greater interest in size effects for cleavage fracture.)

Despite the fact that the same parameter (J) may be used to predict both ductile and cleavage fracture, it is very important to remember that cleavage and ductile fracture are completely different phenomena governed by different micromechanisms. Too often in the literature this distinction is not made, and generalizations are made about size effects in "fracture". In fact, the effect of inadequate specimen size are typically completely opposite for cleavage than for ductile fracture. Typically, for ductile fracture, the smaller the ligament size the smaller the J value at crack initiation. (There are exceptions to this generalization which will be explained later.) For cleavage fracture, the smaller the ligament size the greater the apparent fracture toughness [93,94].

This difference in trends in specimen geometry effects on the apparent fracture toughness is easily explained by looking at the effect of inadequate specimen size on the crack-tip fields in Figure 7. As the specimen size decreases, the crack-tip strain increases above the ideal fields. Therefore, smaller J values will be required to cause the initiation of ductile crack extension at a particular critical-strain value. On the other hand, crack-tip stress decreases as the specimen size decreases. Therefore, larger J values will be required to cause cleavage fracture at a particular critical-stress value. This argument illustrates the importance of considering the underlying micromechanics of fracture.

Another reason that ductile fracture is less sensitive to loss of SSY is that ductile fracture is controlled by an integral of the product of stress and strain as in Equation 3. Therefore, for ductile fracture, there are two opposing effects of loss of constraint that will cancel each other out to a certain extent [95]. As the specimen size decreases and conditions of SSY are gradually lost, the strain increases. This would tend to make the smaller specimens yield lower critical J values as the fracture strain is attained at a lower value of J in the smaller specimens. However, the fracture strain may be increased in the smaller specimens due to the decrease in the hydrostatic stress [96,97].

Cleavage may be induced in highly constrained specimens of one material where other specimens of the same material behave in a ductile manner. Generally, this material would have to be close to the lower shelf of the transition region for such a transition. This effect is due to a loss in SSY in the ductile specimens, where in the highly constrained specimens, the SSY fields are achieved and the stresses are higher, thus the critical stress for cleavage can occur instead of yielding. Three-dimensional analyses of test specimens show that it is conservative to use a CT specimen in most cases. Specifically, as shown in Table 2, the CT specimen produces a maximum constraint factor that typically ranges from two [42] to three [41]. In most test geometries including the CT specimen, the constraint factor typically drops off to slightly greater than one across most of the ligament. On the other hand, the DENT specimen can produce a constraint factor which may peak as high as three and remain higher than 2 across the small ligament between the cracks [39,40]. At certain temperatures some materials that exhibited ductile fracture in compact specimens failed in cleavage in such a DENT geometry [38-40]. However, the high a/W DENT is an extreme case and is not applicable to most structural geometries.

The competition between micromechanical criteria for cleavage and ductile fracture modes explains the effects of temperature, constraint, strain rate, irradiation, warm pre-stressing, and strain ageing on the transition between different fracture modes (brittle-ductile transition behavior) [75,98-100]. However, sorting out the effect of specimen size for mixed cleavage/ductile fracture in the transition region may be hopelessly complicated and is beyond the scope of this paper.

Correction and Indexing Schemes for SSY Effect

Kirk et al [101] have recently reviewed the many schemes that are being investigated for dealing with geometry effects on the global criteria which arise from loss of SSY. The schemes generally can be classified as either correction schemes or indexing schemes. Correction schemes seek to correct the measured toughness data back to some transferable geometry-independent value. The transferable toughness value is usually equivalent to that which would be obtained under SSY conditions. The SSY value can then be uncorrected if necessary if the application is not essentially SSY. A correction scheme often requires accurate determination of the stress and strain fields in both the test specimen and structure and therefore is computationally intensive.

If this level of analysis is required, the correction scheme offers little advantage relative to the local approach. In other words, a global fracture criterion is a vehicle to express the more complex actual underlying local fracture criteria. If the underlying criteria must be used to correct the global criterion the global criterion has lost its usefulness. It would make more sense to abandon this troublesome vehicle and deal directly with the local fracture criteria in a computationally intensive scheme.

It should be noted that a factor which is used in a correction scheme could also be used in an indexing scheme. Indexing schemes categorize fracture toughness data according to some measure of constraint. In this "two-parameter" approach, a locus of fracture toughness values is obtained in terms of J (or equivalently CTOD) and the index parameter which corresponds to the particular conditions under which the J was measured. A measure of the index parameter in the application is required and a fracture toughness value that was generated in a specimen with a similar value of the parameter is selected. Indexing schemes obviously are experimentally intensive because data are required for the entire range of index parameters encountered in the application. Significant computations may also be required to define the index parameter for the test specimens and the applications.

Indexing schemes are close to demanding that the conditions of the test and the application are the same, i.e., that full-scale elements must be tested. However, the indexing schemes offer the advantage of correlating constraint effects from different sources, e.g., loading, in-plane dimensions, or crack length. For example, a small bend specimen can be used to simulate the conditions in a large tension specimen.

Irwin's β_{I_c} correction for thickness effects on K_{Ic} [102] is an early example of a correction scheme. The β_{I_c} factor is essentially proportional to the plastic zone size divided by the thickness. Kirk et al [101] proposed a modified factor which is the ratio of the SSY equation for the plastic zone (half) height to the smallest of the crack length, the ligament, or half the thickness. The plastic zone size equation is used even for fully-plastic cases when the plastic zone has engulfed the ligament and thus represents only an index of the deformation. A corrected J value is obtained by dividing the apparent J by one plus this factor. Kirk et al showed this to be an effective correction scheme for cleavage fracture of A515 and A36 steel. It has the advantage of requiring only minimal computations.

$$\frac{r_y}{L_{\min}} = \frac{\frac{1}{6\pi}\left(\frac{K_c}{\sigma_y}\right)^2\left(\frac{n-1}{n+1}\right)}{\min(a,b,B/2)} \tag{8}$$

Anderson and Dodds [93,103] have developed the concept of equivalent stress contour areas described above. A ratio J/J_{SSY} is used to quantify the J required to achieve a stress contour area equal to that which would be achieved by J_{SSY} under SSY conditions. Using this technique J values measured in a variety of configurations could be converted to equivalent J_{SSY} values. It is actually a critically stressed volume of material that is required, therefore this correction must be used between specimens and applications that are the same thickness. The Anderson and Dodds correction scheme [94] is equally effective as the Kirk et al scheme but has the disadvantage of being computationally intensive.

O'Dowd and Shih [104,105] have proposed that the amplitude of the second term in the expansion for the crack-tip fields for power-law hardening material can be used as an indexing parameter. The first term is the HRR singularity and this second term was shown to be approximately constant and given the name Q. Under a slightly different definition, the product of Q times the yield stress is the difference between the SSY fields and the actual fields for a given finite specimen geometry. Like the Anderson and Dodds scheme, the evaluation of Q requires a detailed elastic-plastic finite element analysis of the crack-tip fields for both the test specimen and the application. Kirk et al [101] evaluated the usefulness of Q in a correction scheme where the fraction 1-Q was used in a manner analogous to the ratio of J/J_{SSY}. They found the Q based correction scheme to be less effective than the modified β_{Ic} scheme or the Anderson and Dodds scheme.

Al-Ani and Hancock [106] have suggested the first nonsingular term in the expansion of the elastic stress field, the T stress, is an effective index parameter. The T stress is a constant stress parallel to the crack but has an effect on the actual crack-tip stresses normal to the crack. It has the advantage of being relatively easy to calculate because only a linear-elastic analysis of the test specimen and application are required [107]. However, it cannot be used in a correction scheme because the connection to the crack-tip fields is not direct.

The above schemes treat only the stress and are therefore only applicable to cleavage. Various schemes have been devised to treat fibrous initiation and even tearing. Anderson et al [95] extended the concept of J/J_{SSY} ratio by comparing the profile of the damage parameter given by Equation 3 in finite specimens to that in SSY. The ratio of the distances from the crack tip to the profiles at 45° at a particular value of the damage parameter was equated to J/J_{SSY}. This ratio was not very sensitive to the value of the damage parameter at which it was evaluated. The value of the damage parameter for the evaluation was chosen such that the distance associated with the damage parameter was between 2 and 4 CTOD. This approach was based on small-strain analyses and thus was only qualitative in view of the fact that ductile fracture typically takes place in the large-strain zone. The results confirmed that ductile fracture would be less sensitive to constraint than cleavage.

Sun Jun et al [108] have proposed a correction scheme for fibrous initiation values of J_{IC}. The correction factor is a simple function of the Poisson ratio and the maximum constraint factor in the ligament at the instant of crack initiation. Their corrected J values were able to correlate some data generated with different notch angles (and corresponding different levels of constraint).

The Effect of Crack Extension (Modified J)

The way J is defined, J values increase during the test due to the increase in the applied displacements. At the same time, J values decrease slightly due to crack extension [12]. This decrease due to crack extension evolves in a way that is dependent on the ligament length. For the moderate toughness steel for which J can be applied, the effect of crack extension may be the dominant geometry effect in CT specimens. As shown in Figure 1, the J-R curve from the smaller (0.5T) specimens seems to level out as the crack extension exceeds 2 or 3 mm. The limit of 10% of the ligament size for these specimens is about 1.3 mm. The levelling out is due to this decrease in J due to crack extension, which becomes noticeable when the crack extension limits are exceeded.

As the crack extends, the connection between J and the crack-tip strain field is difficult to establish analytically or numerically. However, some work has shown that under certain conditions the rate of increase of the strains at a fixed point ahead of the crack is proportional to the rate of increase of J [109,110]. This expanding J-dominated strain field ahead of the crack can be thought of as similar to the strain field that would occur if the loading had continued without crack extension. The actual strain field ahead of a propagating crack can be thought of as a combination of the J-dominant strain field and disturbance of that strain field due to the local unloading associated with the crack extension. The conditions for J dominance [66] require that the rate of increase of J must be large enough such that the J-dominant zone has expands more rapidly than the disturbance from unloading. The connection between J and the crack-tip strains (and therefore the validity of J as a material property for tearing) is therefore tenuous. However, if an empirical basis can be established, the J-R curves can be used outside the range of J dominance for engineering purposes.

In specimens where the loading is predominantly bending (bend or compact-tension specimens) the crack extension effect can be avoided through the use of Ernst's modified J [12]. The modified J is a history dependent parameter that essentially does not allow the decrease in J for crack extension. A J value obtained from a load-displacement record involving crack extension is transformed by Ernst's procedure into the J that would have been obtained had the crack length always been equal to the current crack length. Within the 10% ligament crack extension limits the difference between J and modified J is negligible. It is important to note that outside these limits, neither parameter is fundamentally based. Therefore, the best parameter to use is that which can be shown empirically to correlate crack growth among different size specimens to the greatest crack extension. Joyce et al [111-113] have investigated the possibility of using J-R curves with crack extension beyond these limits and even extrapolating the J-R curves from small specimens [113].

The Effect of the Shape of the Remote Plastic Region

The global fracture parameters discussed above and the schemes for correcting or indexing the geometry effects are applicable to elastic-plastic fracture mechanics, i.e. for materials of moderate toughness where the strains are small if not elastic on most of the remaining ligament. Another type of geometry effect arises in fully-plastic fracture, i.e. for very tough materials where there are large strains across most of the ligament. The geometry effect dominating such fully-plastic fracture is due to the geometry dependence of the remote plasticity. The J-R curves for the two pipeline steels shown in Figures 2 and 3 are an example of fully-plastic fracture. Often the ASTM specimen size requirements for elastic-plastic fracture mechanics cannot be met due to the limited dimensions of the product or other practical considerations. It is still necessary to make fracture predictions for these situations.

When the specimen size requirements are violated, the effect due to the geometry dependence of the remote plasticity becomes increasingly apparent. It is easiest to discuss this effect for specimens that are far too ductile and too thin to be characterized by valid J procedures. However, the size dependence mechanism involved may sometimes be involved (albeit in a less apparent way) in fracture that is within the valid J limits.

Dependence of J on Total Plastic Work

In order to understand this effect, it is useful to adopt the simplifications of rigid-plastic fracture mechanics as proposed by Atkins and Mai [36,114,115]. In rigid-plastic fracture mechanics, the elastic contributions to the total fracture energy are deemed small and can be ignored. Broberg [116-118] suggested that the plastic region can be separated into a process zone and a remote plastic region which screens the process zone. Following Broberg's work, Cotterell and Reddel [119] suggested that only the energy consumed in the process zone was independent of specimen geometry and this was called the essential work of fracture. The essential work of fracture is practically equivalent to J_{IC} [120,121].

Figure 8a shows the load-displacement curve for a typical J-R curve test. The load-displacement curve can be thought of as the projection of the general curve in load displacement crack-extension space. The sectors shown on the curve show the differential change of energy with crack extension or dU/da. The differential dU/da is the definition of J [2]. Following the above argument, the energy in fully-plastic cases can be separated into essential work of fracture and energy for remote plasticity, and this separation is shown in the differential energy sectors in Figure 8a.

The J values can be computed from the load displacement curves in terms of the energy and complementary energy integrals [79,122]. The J and modified J for the case of the growing crack can be derived from these expressions for the stationary crack [79]. Smith and Griesbach [79] have shown that for the CT or bend specimens, the expressions for the plastic component of J for the growing crack can be approximately expressed as a single function (eta factor) times the area under the load displacement curve or the work done on the specimen. (For tension specimens, they showed these relations were only reliable for small ligament length.)

The area under the J-R curve is therefore a monotonic function of the total energy. For the purposes of identifying the effects of specimen geometry, it is useful to conceptually separate this relationship between the J-R curve and the total energy into parts due to essential work of fracture and parts due to remote plasticity as shown in Figure 8b. For the purposes of this illustration, three-dimensional effects such as shear lip formation are ignored. It has been shown empirically [120,121] that J_{IC} times the crack area is equal to the essential work of fracture. The energy consumed by remote plasticity corresponds conceptually to the tearing modulus times the crack area, as shown in Figure 8b.

The effect of remote plasticity is most apparent after significant crack extension, although remote plasticity may influence initiation values as well. The effect of remote plasticity occurs form interactions of the plastic field with the boundaries of the test specimen and the structure. Figure 9 shows qualitatively the shape of the region of large plastic strains in CCT, CT, and DENT specimens. Assume for the sake of argument that the average plastic-work density in the plastic zones in these specimens is approximately constant. Then it is clear that the total plastic work to deform and grow a crack through these specimens will increase with ligament length. It is also clear why it takes additional work to fracture CCT specimens than CT specimens with an equal ligament area.

By this argument, the plastic work in the remote plastic region is dependent on the specimen geometry and is responsible for the geometry effects. Figure 9 shows the shape of the plastic flow fields for various specimen configurations. Various specimen configurations exhibit different shapes of these plastic regions. If the average plastic work density in these regions is approximately constant, then this variation in shape could explain how the total work of fracture depends on specimen geometry. Further, through the connection between the work and the J-R curve, one effect of geometry (the effect of the shape of the flow fields) on the J-R curves can be rationalized.

Figure 10 shows some results of total fracture energy per original ligament area for DENT and CT specimens as well as a conventional J-R curve for a ductile aluminum alloy [121]. The total energy scales linearly with the ligament length in both specimens. The intercept in either case is equal to J_{IC}. Also note that for any specific ligament length, the DENT specimen requires less energy than the CT specimen.

Rigid-plastic fracture mechanics is valid only for very ductile materials. The elastic energy may not be negligible in many of these experiments. Analysis of the scaling of the total energy does not reveal the development of this energy as a function of crack extension as a J-R curve does, although the theory is being extended for crack extension [36,115]. However, rigid-plastic fracture mechanics is not dependent on the vagaries of J control and is not subject to limitations on crack extension.

Indexing Fully-Plastic Fracture

The only schemes to account for the effect of remote plasticity that are applicable to the fully-plastic case are variations on indexing schemes. Figure 11 shows the results of Holmes, Priest, and Walker [123] from bend tests on specimens of various ligament lengths. The results for these ductile pipeline steels are generally plotted in terms of the total fracture energy divided by the ligament area as a function of ligament length or area. After a ligament length of about 20mm, the results are usually remarkably linear suggesting that the fracture energy per unit area increases linearly with ligament length as was shown in Figure 10. Different lines are obtained for dynamic drop weight tests and static tests.

These investigators have named the intercept R_c and stated that this must be the work to create fracture surface and should scale directly with ligament length (i.e., crack area). The slope, S_c, is the rate of increase of fracture energy due to remote plasticity. S_c scales with ligament length squared as does the volume of the remote plasticity region in Figure 9. The total fracture energy (U) is given by:

$$\frac{U}{Bb} = R_c + S_c b \tag{9}$$

where B is the thickness and b is the ligament length.

Other investigators have found similar results and given different names to the two terms. Atkins, Cotterell, and Mai have developed an area of fracture they refer to as fully-plastic fracture mechanics [36,96,97,114,115,119,120]. Their studies are based on the scaling principles shown in Figure 10 and rigid-perfectly-plastic analysis methods. Cotterell et al [96] have used this scaling method and found that R_c is equivalent to the CTOD at initiation and that S_c is related to the rate of increase of CTOD with crack extension or CTOA. Atkins et al

have also made the connection between the R_c and the essential work of fracture [36]. R_c and the essential work to fracture can therefore be related to the J at initiation or the energy in region A in Figure 8.

Researchers at CSM in Italy have observed these trends and equated the R_c to a parameter they call "neck" or a necking displacement equivalent to an initiation CTOD [124,125]. The S_c parameter is equal to the CTOA in their analysis. Various researchers have shown the relation between the CTOA and the tearing modulus [126]. Thus these parameters of fully-plastic fracture can be related back to J and the tearing modulus from conventional elastic-plastic fracture mechanics. Therefore, elastic-plastic fracture mechanics is a special case of the fully-plastic fracture mechanics wherein J-dominance can be assured and the convenient laboratory techniques can be used to measure geometry independent J-R curves.

The above approaches appear to be new fracture criteria. It is important to note that they all involve a parameter such as the ligament length to account for the effect of geometry. Therefore, these are indexing schemes. Zahoor and Kanninen [15] emphasized the importance of using a J-R curve that is appropriate for the "constraint" of the application in their tearing instability analyses of circumferentially cracked pipe. Brocks et al [41,43] and Kordisch et al [42] have taken the constraint factor as an indexing parameter. Brocks et al take the maximum value of the constraint factor from a large-strain analysis. Kordisch et al have extrapolated the linear part of the constraint factor profile from a small-strain analysis back to the crack tip.

The constraint factor may not be the best indexing parameter, however. For example, the peak constraint factor for the DENT and the CT specimen are approximately equal whereas the MPA data show that lower tearing modulii can be obtained with the DENT specimens. The additional plastic work done on CT specimens can account for this difference.

The Variation in Plastic Flow in Weldments

In fully-plastic fracture the height of the zone of plastic deformation increases with increasing specimen width as shown in Figure 9. Due to the relationships between plastic work and J discussed above, the additional plastic work is reflected in larger J values at a given level of crack extension, i.e., a larger tearing modulus. Remote plasticity can also cause a geometry effect in tests with a weld zone of different strength than the base metal. Because of the strength difference, the plastic work density in the weld will be different than in the base metal. The weld zone will comprise different proportions of the plastic region as the specimen size changes. Therefore, the proportion of the plastic work from the weld zone will change and have an influence on the J-R curve [127-129].

Kirk and Dodds [130] have reviewed many finite-element analyses of welds with different strength weld and base metal. The objective of these analyses was to calculate the applied J integral as a function of applied load or displacement. Consideration of the appropriate test specimen and J-estimation scheme was treated in this report. It was concluded that the only simple means to determine J for welds is by testing deeply cracked bend specimens where only the weld metal is plastified. In this case the specimen can be idealized as a homogeneous monolithic bend bar made entirely of weld metal. The total plastic work (and therefore J) will depend in a geometry dependant way on the flow stress in both the base and weld metal. Therefore, any configuration besides the deeply cracked bend bar requires complex analysis including explicit consideration of the size and properties of the weld and base metal.

Kirk and Dodds' conclusions have wide implications. Unless the structure that the J analysis is applied to is also deeply cracked, the application will also require complex analysis. In most cases, the structural integrity analyses will involve shallow cracks. Since the J and CTOD are proportional, any of these conclusions about the measuring or application of the J integral also apply to the CTOD. The connection between the CTOD and remote plasticity is not as easily seen as it is for the J integral. The primary reason the CTOD is affected by remote plasticity and therefore will not be independent of test specimen and application configuration is that the simple formula for calculating CTOD from CMOD will also be strongly dependent on the plastic properties of both the weld metal and base metal. Finally, since the testing and analysis for cracks in weld metal is so problematic, the fracture testing and analysis associated with cracks in the HAZ must be even more uncertain.

Separations

The data on steel exhibiting separations are unusual and add to the controversy over geometry effects. It was shown in Figure 4 that these separations lead to a unique fracture mode. Because of this unique fracture mode, the size effects in this steel are unique and do not fit the above explanations. However, if it can be assured that the fracture mode in both the test specimen and the structure will remain fully fibrous, it will be conservative to use J-R curves generated from small compact specimens for the analysis of crack stability in larger structures. If the fracture mode in the structure is partly cleavage or includes other unusual characteristics such as separations, the effect of hydrostatic stress (constraint effects) in the larger specimens may reduce the apparent tearing modulus in larger specimens. This trend would make the use of small specimens unconservative as was shown in Table 1. The possibility of change in the fracture mode must be considered when applying data from small specimens to larger structures.

Lereim [131] developed a conceptual micromechanical model that can be used to explain the J or CTOD values during crack propagation for material which exhibits separations. As shown in Figure 12, the material in front of the main crack behaves like a set of laminates. Lereim's model can be extended to predict the reduction in tearing modulus as the delaminations propagate farther ahead of the main crack. As shown in Figure 12, the separations occur well in front of the main crack. In general, specimens with larger width or thickness build up greater through-thickness stress over greater distances ahead of the main crack [9,93]. Furthermore, if only a small level of through thickness stress is required to open the separations (as was likely the case of this A302B steel), the separations may extend over most of the tension zone of the remaining ligament. The extent of the through-thickness tension zone is limited by the location of the neutral axis on the remaining ligament of the specimens, which will obviously be a direct function of the size of the remaining ligament. Thus the separations travelled farther ahead of the main crack in the bigger specimens. The sequence in which the events occurred is not apparent on the fracture surface, hence the lack of fractographic clues for the reasons for this size effect [16,17].

The tangent of the bending angle for these specimens is defined by the critical displacement (which should be independent of specimen geometry) and the depth of the separations ahead of the crack. The depth of the separations is governed by the strain gradient or the specimen width. In the case of these necking laminates, the bending angle is practically equivalent to the crack-tip-opening angle (CTOA). The CTOA is equal to the rate of change of the CTOD at the initial crack tip with respect to crack extension. Therefore, as the CTOD is directly proportional to J, so the CTOA is directly proportional to the tearing modulus. Therefore, since in the wider specimens the bending angle is less than in the smaller specimens, the tearing modulus would be expected to be less in the larger specimens. This mechanism explains the trend of decreasing slope of the J-R curves with larger specimens in this special

steel. There might also be an effect of the thickness on the development of through-thickness tension and therefore on the depth of the separations. Since the thickness was varied with the width, it is not yet possible to separate these effects. It is important to note that there is no theoretical connection between J and the strains ahead of the crack in this material. In fact, the process zone becomes so diffuse that it would be impossible to precisely define the location of the crack tip. While it may be possible to use the J-R curve on an empirical basis in some materials, use of J-R curves for this material is not recommended.

Three-Dimensional Effects

Researchers at MPA in Stuttgart have questioned the present understanding of the trends in geometry effects (i.e. bigger specimens give greater tearing modulus such as in Figure 1). These researchers presented some J-R curves where the tearing modulus decreased as the thickness only was increased in compact specimens with and without sidegrooves. The effect was most significant in the specimens without sidegrooves. In the specimens with sidegrooves, there is a small effect of increasing thickness which saturates (i.e. there is no further effect for greater thickness) for specimens thicker than 50mm. These trends in the J-R curves and the influence of sidegrooves on the severity of the trends are consistent with typical three-dimensional effects in fracture.

The maximum constraint factor at the center plane decreases as the thickness decreases and this may lead to a "two-dimensional" effect, i.e. loss of small-scale yielding, that was discussed above. For reasonably thick specimens, the constraint at midthickness reaches a constant and the effect of thickness on the constraint at the midthickness saturates. As previously discussed, the peak constraint at midthickness is significant for cleavage and low toughness ductile fracture but is not expected to be significant for fully-plastic fracture. The primary influence of the thickness of laboratory specimens on the J-R curve for elasto-plastic and fully-plastic fracture arises not from changes in the peak constraint but from the variation in constraint through the thickness. The stress state through most of the specimen is nearly plane strain. However, even in sidegrooved specimens, there is a decrease in constraint near the plate surfaces. The decreased constraint means the strain required for void growth and fracture at that location along the crack front is increased. Due to compatibility requirements, the strain is essentially constant along lines perpendicular to the plate surfaces. Therefore the crack front at the plate surfaces tends to lag behind that at the center of the specimen.

This curved crack front is referred to as crack tunnelling. In specimens without sidegrooves, the thin region lagging behind the crack front often fails like a thin sheet and a region of slant fracture called shear lips may develop on the surfaces. In a series of tests on C-Mn steel compact specimens without sidegrooves similar to the series run at MPA, Gibson, et al [132] showed that the presence of these shear lips could account for the thickness effect on the J-R curves. The constraint gradient and associated lagging crack front and shear lips are confined to a region close to the surfaces. Therefore, the proportion of the length along the crack front influenced by the constraint gradients is significant for thinner specimens. This proportion and the significance of the thickness effect diminish as the thickness increases.

Changes in crack shape are an obviously important geometry effect and must be dealt with in fracture assessments. However, sidegrooved specimens meeting ASTM requirements [10] on the thickness and the maximum deviation of the crack front from straightness should be in the regime where these thickness effects have saturated.

CONCLUSIONS

1. The conflicting observations regarding the effect of fracture test specimen geometry on J-R curves and other related fracture criteria can be rationalized by separating phenomena according to the underlying physical cause of the geometry effect.

2. The case of the A302B steel shows that compliance with ASTM specifications does not preclude unconservative application of the J-R curve and emphasizes that it is imperative to examine the local fracture mode and possible changes in fracture mode with geometry before any fracture criteria may be employed with confidence.

3. The dominant size effect for fully-plastic fracture is due to additional work of remote plasticity, and therefore higher J values, in larger specimens or in specimens loaded primarily in tension rather than bending.

4. None of the various schemes to correct J for geometry effects can account for this particular geometry effect due to remote plasticity.

5. If it can be assured that the fracture mode in both the test specimen and the structure will remain fully fibrous, it is conservative to extrapolate J-R curves generated from small compact specimens for the analysis of pressure vessel crack stability.

ACKNOWLEDGEMENTS

The author wishes to express his appreciation of the support of EPRI through contract RP2975-20. The authors also acknowledge the useful discussions with Andre Pellisier-Tanon of Framatome, Karl Frank of the University of Texas at Austin, George Irwin of University of Maryland, and Ted Anderson of Texas A&M University. This work is primarily an assimilation and review of the work of others who have been duly acknowledged in the text.

REFERENCES

1. Bass, B.R., et al, "Final Report on Phase I of the CSNI Multi-National Project for Fracture Analyses of Large-Scale International Reference Experiments (FALSIRE), *Oak Ridge National Laboratory*, June 1992.
2. Rice, J.R., "A Path Independent Integral and the Approximate Analysis of Strain Concentration by Notches and Cracks," *Journal of Applied Mechanics*, Vol. 35, pp. 379-386, June 1968.
3. Landes, J.D., and Begley, J.A., "Recent Developments in J_{IC} Testing," *Developments in Fracture Mechanics Test Methods Standardization, ASTM STP 632*, W.F. Brown, Jr. and J.G. Kaufmann, Eds. pp. 57-81, 1977.
4. ASTM, Standard Test Method for J_{IC}, a Measure of Fracture Toughness, E813-87, ASTM, Philadelphia, 1987.
5. De Castro, P.M.S.T. Spurrier, J., and Hancock, P., "Comparison of J Testing Techniques and Correlation J-COD Using Structural Steel Specimens," *International Journal of Fracture*, Vol. 17., pp. 83-95, 1981.
6. Dexter, R.J., "Fracture Toughness of Underwater Wet Welds," *Fatigue and Fracture Testing of Weldments, ASTM STP 1058*, H.I. McHenry, and J.M. Potter, Eds., American Society for Testing and Materials, Philadelphia, Vol. 1058, pp. 256-271, 1990.

7. Shih, C.F., "Relationships Between the J-Integral and the Crack Opening Displacement for Stationary and Extending Cracks," *Journal of the Mechanics and Physics of Solids*, Vol. 29, No. 4, pp. 305-326, 1981.
8. McMeeking, R.M., and Parks, D.M., "On Criteria for J-Dominance of Crack-Tip Fields in Large-Scale Yielding," *Elastic-Plastic Fracture, ASTM STP 688*, J.D. Landes, J.A. Begley, and G.A. Clarke, Eds., American Society for Testing and Materials, pp. 175-194, 1979.
9. Paris, P.C., Tada, H. Zahoor, A., and Ernst, H., "The Theory of Instability of the Tearing Mode of Elastic-Plastic Crack Growth," *Elastic-Plastic Fracture, ASTM STP 668*, J.D. Landes, J.A. Begley, and G.A. Clarke, Eds., American Society for Testing and Materials, pp. 5-36, 1979.
10. ASTM, Standard Test Method for Determining J-R Curves, E1152-87, ASTM, Philadelphia, 1987.
11. Loss, F.J., Ed., "Structural Integrity of Water Reactor Pressure Boundary Components, Annual Report for 1983," Materials Engineering Associates, Report for U.S. Nuclear Regulatory Commission, NUREG/CR-3228, MEA-2051, Vol. 2, September 1984.
12. Ernst, H.A., "Materials Resistance and Instability Beyond J-Controlled Crack Growth," *Elastic-Plastic Fracture, ASTM STP 803*, Vol. 1, American Society for Testing and Materials, Philadelphia, PA, pp. 191-213.
13. Hiser, A.L., Loss, F.J., and Menke, B.H., "J-R Curve Characterization of Irradiated Low Upper Shelf Welds," Materials Engineering Associates, Report for U.S. Nuclear Regulatory Commission, NUREG/CR-3506, MEA-2028, April 1984.
14. Garwood, S.J., "Geometry and Orientation Effects on Ductile Crack Growth Resistance," *International Journal of Pressure Vessel & Piping*, Vol. 10, pp. 297-319, 1982.
15. Zahoor, A., and Kanninen, M.F., "A Plastic Fracture Mechanics Prediction of Fracture Instability in a Circumferentially Cracked Pipe in Bending—Part I: J-Integral Analysis," *Journal of Pressure Vessel Technology*, Vol. 103, pp. 352-358, November 1981.
16. Hiser, A.L., and Terrell, J.B., "Size Effects on J-R Curves for A302-B Plate," Materials Engineering Associates, Report for U.S. Nuclear Regulatory Commission, NUREG/CR-5265, MEA-2320 RF, R5, January 1989.
17. Hiser, A.L. Jr., "Specimen Size Effects on J-R Curves for RPV Steels," Presented at *ASTM Symposium on Constraint Effects in Fracture*, Indianapolis, May 8-9, 1991.
18. Merkle, J.G., "An Overview of the Low-Upper-Shelf Toughness Safety Margin Issue," Oak Ridge National Laboratory, Report for U.S. Nuclear Regulatory Commission, NUREG/CR-5552, ORNL/TM-11314, August 1990.
19. Wessel, E.T., Server W.L., and Kennedy, E.L., "Primer: Fracture Mechanics in the Nuclear Power Industry," Electric Power Research Institute, EPRI NP-5792-SR, Revision 1, May 1991.
20. Nichols, R.W., ed., "Special Issue: Leak-Before-Break in Water Reactor Piping and Vessels," *International Journal of Pressure Vessels and Piping*, Vol. 43, No. 1-3, pp. 1-433, 1989.
21. Klecker, R., Brust, F., and Wilkowski, G., "NRC Leak-Before-Break (LBB.NRC) Analysis Method for Circumferentially Through-Wall Cracked Pipes Under Axial Plus Bending Loads," Battele's Columbus Division, Report for U.S. Nuclear Regulatory Commission, NUREG/CR-4572, BMI-2134, May 1986.
22. Dexter, R.J., "Investigation of Criteria for Ductile Fracture Under Fully-Plastic Conditions", Dissertation, The University of Texas at Austin, December 1992.
23. Thomason, P.F., Ductile Fracture of Metals, Pergamon Press, Oxford, UK, 1990.

24. Beremin, F.M., "Cavity Formation from Inclusions in Ductile Fracture of A508 Steel," *Metallurgical Transactions*, Vol. 12A, pp. 723-731, 1981.
25. Beremin, F.M., "Experimental and Numerical Study of the Different Stages in Ductile Rupture: Application to Crack Initiation and Stable Crack Growth," *Three-Dimensional Constitutive Relations and Ductile Fracture*, S. Nemat-Nasser, Ed., North-Holland Pub. Co., Amsterdam, pp. 185-209, 1981.
26. Backofen, W.A., *Deformation Processing*, Addison-Wesley, Reading MA, 1972.
27. McClintock, F.A., "A Criterion for Ductile Fracture by the Growth of Holes," *J. Applied Mech., Trans. ASME Series E*, Vol. 35, pp. 363-371, June 1968.
28. McClintock, F.A., Kaplan, S.M., and Berg, C.A., "Ductile Fracture by Hole Growth in Shear Bands," *International Journal of Fracture Mechanics*, Vol. 2, No. 4, pp. 614-627, 1966.
29. Rice, J.R., and Tracey, D.M., "On the Ductile Enlargement of Voids in Triaxial Stress Fields," *Journal of the Mechanics and Physics of Solids*, Vol. 17, pp. 201-217, 1969.
30. Gurson, A.L., "Continuum Theory of Ductile Rupture by Void Nucleation and Growth: Part 1 — Yield Criteria and Flow Rules for Porous Ductile Media," *Journal of Engineering Materials and Technology*, Vol. 99, p. 2-15, 1977.
31. Oyane, M., Sato, T., Okimoto, K., and Shima, S., "Criteria for Ductile Fracture and Their Applications," *J. Mech. Work. Tech.* Vol. 4, p. 65, 1980.
32. Norris, D.M. Jr., Reaugh, J.E., Moran, B., and Quinones, D.F., "A Plastic-Strain, Mean-Stress Criterion for Ductile Fracture," *Journal of Engineering Materials and Technology*, Vol. 100, pp. 279-286, July 1978.
33. Cockroft, M.G., and Latham, D.J., "Ductility and the Workability of Metals," *Journal of the Institute of Metals*, Vol. 96, pp. 33-39, 1968.
34. Berg, C.A., "Plastic Dilation and Void Interaction," *Inelastic Behavior of Solids*, McGraw-Hill, New York, pp. 171-210, 1970.
35. Atkins, A.G., and Mai, Y.W., "Fracture Strains in Sheet Metalforming and Specific Essential Work of Fracture," *Engineering Fracture Mechanics*, Vol. 27, No. 3, pp. 291-297, 1987.
36. Atkins, A.G., and Mai, Y.W., Elastic and Plastic Fracture, Ellis Horwood/John Wiley, Chichester UK, 1985.
37. Clift, S.E., Hartley, P., Sturgess, C.E.N., and Rowe, G.W., "Fracture Prediction in Plastic Deformation Processes," *Int. J. Mech. Sci.*, Vol. 32, pp. 1-17, 1990.
38. Roos, E., Eisele, U., and Silcher, H., "Effect of Stress State on the Ductile Fracture Behavior of Large Scale Specimens," Presented at *ASTM Symposium on Constraint Effects in Fracture*, Indianapolis, May 8-9, 1991.
39. Roos, E., Eisele, U., Silcher, H., and Spaeth, F., "The Influence of the Material Toughness and the State of Stress on Fracture of Large Scale Specimens," *Nuclear Engineering and Design*, Vol. 102, pp. 439-449, 1987.
40. Clausmeyer, H., Kussmaul, K., and Roos, E., "Influence of Stress State on the Failure Behavior of Cracked Components Made of Steel," *Applied Mechanics Review*, Vol. 44, No. 2, pp. 77-92, February 1991.
41. Brocks, W., Kunecke, W.B., Noack, H.-D., and Veith, H., "On the Transferability of Fracture Mechanics Parameters from Specimens to Structures Using FEM," *Nuclear Engineering and Design*, Vol. 112, pp. 1-14, 1989.
42. Kordisch, H., Sommer, E., and Schmitt, W., "The Influence of Triaxiality on Stable Crack Growth," *Nuclear Engineering and Design*, Vol. 112, pp. 27-35, 1989.

43. Brocks, W., Krafka, H., Kunecke, G., and Wobst, K., "Ductile Crack Growth of Semi-Elliptical Surface Flaws in Pressure Vessels," *International Journal of Pressure Vessel & Piping*, Vol. 43, 301-316, 1990.
44. Malvern, L.E., *Introduction to the Mechanics of a continuous Medium*, Prentice-Hall, Englewood Cliffs, NJ, 1969.
45. Sih, G.C., and Madenci, E., "Prediction of Failure in Weldments - Part 1: Smooth Joint," *Theoretical and Applied Fracture Mechanics*, Vol. 3, pp. 23-29, 1985.
46. Sih, G.C., and Madenci, E., "Fracture Initiation Under Gross Yielding: Strain Energy Density Criterion," *Engineering Fracture Mechanics*, Vol. 18, No. 3, pp. 667-677, 1983.
47. Nemat-Nasser, S., "Overview of the Basic Progress in Ductile Fracture," *Transactions of the Fourth International Conference on Structural Mechanics in Reactor Technology (SMIRT-4)*, San Francisco, August 1977, pp. L2/1-11, 1977.
48. Sih, G.C., and Madenci, E., "Crack Growth Resistance Characterized by the Strain Energy Density Function," *Engineering Fracture Mechanics*, Vol. 18, No. 6, pp. 1159-1171, 1983.
49. Matic, P., "Numerically Predicting Ductile Material Behavior from Tensile Specimen Response," *Theoretical and Applied Fracture Mechanics*, Vol. 4, pp. 13-28, 1985.
50. Matic, P., and Jolles, M.I., "The Influence of Weld Metal Properties, Weld Geometry and Applied Load on Weld System Performance," *Naval Engineers Journal*, March 1988.
51. Matic, P., and Jolles, M.I., "Defects, Constitutive Behavior and Continuum Toughness Considerations for Weld Integrity Analysis," NRL Memo. Rpt. No. 5935, 1987.
52. Matic, P., Kirby, G.C. III, and Jolles, M.I., "The Relation of Tensile Specimen Size and Geometry Effects to Unique Constitutive Parameters for Ductile Materials," *Proc. R. Soc. London*, Vol. A 417, pp. 309-333, 1988.
53. Gillemot, L.F., "Criterion of Crack Initiation and Spreading," *Engineering Fracture Mechanics*, Vol. 8, pp. 239-253, 1976.
54. Tomkins, B., and Atkins, A.G., "Crack Initiation in Expanded Fully Plastic Thick-Walled Rings and Rotating Discs," *Int. J. Mech. Sci.*,, Vol. 23, No. 7, pp. 395-412, 1981.
55. Barnby, J.T., Shi, Y.W., and Nadkarni, A.S., "On the Void Growth in C-Mn Structural Steel During Plastic Deformation," *International Journal of Fracture*, Vol. 25, pp. 273-283, 1984.
56. Shockey, D.A., Dao, K.C., Seaman, L., Burback, R., and Curran, D.R., "Computational Modeling of Microstructural Fracture Processes in A533B Pressure Vessel Steel," NP-1398, Final Report, EPRI, 1980.
57. Hancock, J.W., and Mackenzie, A.C., "On the Mechanisms of Ductile Failure in High-Strength Steels Subjected to Multi-Axial Stress-States," *Journal of the Mechanics and Physics of Solids*, Vol. 24, pp. 147-269, June 1976.
58. Lindholm, U.S., and Johnson, G.R., "Strain-Rate Effects in Metals at Large Shear Strains," *Material Behavior Under High Stress and Ultrahigh Loading Rates*, J. Mescall and V. Weiss, Eds., Plenum Pub. Corp., pp. 61-79, 1983.
59. Reuter, W.G., Lloyd, W.R., Williamson, R., Smith, J.A., and Epstein, J.S., "Relationship Between Stress or Strain and Constraint for Crack Initiation," Presented at the *ASTM 23rd National Symposium on Fracture Mechanics*, June 18-20, 1991, College Station Texas, ASTM, 1991.
60. MacKenzie, A.C., Hancock, J.W., and Brown, D.K., "On The Influence of State of Stress on Ductile Failure Initiation in High Strength Steels," *Engineering Fracture Mechanics*, Vol. 9, pp. 167-188, 1977.
61. Miyata, T., Otsuka, A., Mitsubayashi, M., Haze, T., and Aihara, S., "Prediction of Fracture Toughness by Local Fracture Criterion," Presented at *ASTM 21st National Symposium on Fracture Mechanics*, Annapolis MD, June 28-30, 1988.

62. Clausing, D.P. "Effect of Plastic Strain State on Ductility and Toughness," *International Journal of Fracture Mechanics*, Vol. 6, No. 1, pp. 1-6, March 1970.
63. Hancock, J.W., and Cowling, M.J., "Role of State of Stress in Crack-tip Failure Processes," *Metal Science*, pp. 293-304, August-September 1980.
64. Dexter, R.J. and Roy, S., "The Conditions at Ductile Fracture in Tensile Tests," Presented at the *ASTM 23rd National Symposium on Fracture Mechanics* (accepted for publication in an STP), June 18-20, 1991, College Station Texas, ASTM, 1991.
65. Green, G., and Knott, J.F., "The Initiation and Propagation of Ductile Fracture in Low Strength Steels," *Journal of Engineering Materials and Technology*, pp. 37-46, January 1976.
66. Ritchie, R.O., and Thompson, A.W., "On Macroscopic and Microscopic Analysis for Crack Initiation and Crack Growth Toughness in Ductile Alloys," *Metallurgical Transactions A*, Vol. 16A, pp. 233-248, February 1985.
67. Vitek, V., "Executive Summary, Chapter 1: Mechanics and Micromechanics of Fracture, and Chapter 2: Microstructural and Microscopic Aspects of Fracture," *Materials Science and Engineering*, Vol. 94, pp. 7-30, 1987.
68. Knott, J.F., "The Toughness of Steel," *Transactions Iron and Steel Institute of Japan*, Vol. 21, p. 306, 1981.
69. Knott, J.F. "Metallurgical Aspects of the Toughness of Engineering Alloys," *Phil. Trans. R. Soc. Lond., A*, Vol. 299, pp. 45-57, 1981.
70. Bates, R.C., "Mechanics and Mechanisms of Fracture," Proceedings, USA-China Bilateral Conference, Metallurgical Society of AIME, 1981.
71. Knott, J.F., "Some Effects of Hydrostatic Tension on the Fracture Behavior of Mild Steel," *Journal of the Iron and Steel Institute*, Vol. 204, No. 2, pp. 104-111, February 1966.
72. Orowan, E., "Fracture and Strength of Solids," Rep. Prog. Phys., Vol. 12, pp. 185-232
73. Curry, D.A., "Influence of Hydrostatic Tension on Cleavage Fracture of Bainitic Pressure Vessel Steel," *Metal Science*, Vol. 16, pp. 435-440, September 1982.
74. Griffith, A.A., "The Phenomena of Rupture and Flow in Solids," *Philosophical Transactions of the Royal Society*, Vol. 221-A, pp. 163-198, 1920.
75. Ritchie, R.O., Server, W.L., and Wullaert, R.A., "Critical Fracture Stress and Fracture Strain Models for the Prediction of Lower and Upper Shelf Toughness in Nuclear Pressure Vessel Steels," *Metallurgical Transactions A*, Vol. 10A, pp. 1557-1570, October 1979.
76. Lin, T, and Ritchie, R.O., "On the Effect of Sampling Volume on the Microscopic Cleavage Fracture Stress," *Engineering Fracture Mechanics*, Vol. 29, No. 6, pp. 697-703, 1988.
77. Engl, B., and Fuchs, A., "The Cause of Separations and its Effects on Fracture Toughness," The Proceedings of the 4th European Conference on Fracture, *Fracture and the Role of Microstructure*, Leoben, Austria, September 22-24, 1982, K.L. Maurer and F.E. Matzer, Eds., Engineering Materials Advisory Services Ltd., Warley, West Midlands UK, pp. 335-342, 1982.
78. Firrao, D., Doglione, R., and Ilia, E., "Thickness Constraint Loss by Delamination and Pop-In Behavior," Presented at *ASTM Symposium on Constraint Effects in Fracture*, Indianapolis, May 8-9, 1991.
79. Smith, E., and Griesbach, T.J., "Quantifying the Crack Growth Resistance of Materials Using J-R Curves," Presented at the *17th MPA Seminar*, Stuttgart, October 10-11, 1991.
80. Baldi, G., and Buzzicheli, G., "Critical Stress for Delamination Fracture in HSLA Steels," *Metal Science*, p. 459, October 1978
81. Morrison, W.B., "Influence of Testing Direction on the Mechanical Properties of Wrought Steel," *Metals Technology*, pp. 33-41, January 1975.

82. Schofield, R., Rowntree, G., Sarma, N.V., and Weiner, R.T., "'Arrowhead' Fractures in Controlled-Rolled Pipeline Steels," *Metals Technology*, pp. 325-331, July 1974.
83. Hawkins, D.N., "Cleavage Separations in Warm-Rolled Low-Carbon Steels," *Metals Technology*, pp. 417-421, September 1976.
84. Almond, E.A., "Delamination in Banded Steels," *Metallurgical Transactions*, Vol. 1, pp. 2038-2041, July 1970.
85. Marston, T., Smith, R.E., Hahn, G.T., Wilkinson, J.P.D., Norris, D.M. Jr., and Shockey, D.A. "EPRI Ductile Fracture Research Review Document," Special Report No. NP-701-SR, February 1978.
86. Norris, D.M. Jr., Reaugh, J.E., Moran, B., and Quinones, D.F., "Computer Model for Ductile Fracture: Applications to the Charpy V-Notch Test," EPRI Report NP-961, Research Project 603, January 1979.
87. Bethmont, M.G., Rousselier, G., Kusmaul, K., Sauter, A., and Jovanovic, A., "The Method of 'Local Approach of Fracture' and its Application to a Thermal Shock Experiment," *Nuclear Engineering and Design*, Vol. 119, pp. 249-261, 1990.
88. Batisse, R., Bethmont, M., Devesa, G., and Rousselier, G., "Ductile Fracture of A508 Cl 3 Steel in Relation with Inclusion Content: The Benefit of the Local Approach of Fracture and Continuum Damage Mechanics," *Nuclear Engineering and Design*, Vol. 105, No. 1, pp. 113,120, December, 1987.
89. Schmitt, W., Sun, D.-Z., and Kienzler, R., "Application of Micro-Mechanical Models to the Prediction of Ductile Fracture," Localized Damage Computer-Aided Assessment and Control, Vol. 1: Fatigue and Fracture Mechanics, Proceedings, First International Conference on Computer-Aided Assessment and Control of Localized Damage, Portsmouth, UK, June 26-28, 1990.
90. Sun, D.-Z., Siegele, D., Voss, B., and Schmitt, W., "Application of Local Damage Models to the Numerical Analysis of Ductile Rupture," *Fatigue and Fracture of Engineering Materials and Structures*, Vol. 12, No. 3, pp. 201-212, 1989.
91. Bethmont, M., Rousselier, G., and Devesa, G., "Effect of Specimen Geometry on J-Resistance Curves in Near Small-Scale Yielding Conditions," Advances in Fracture Research, Proceedings of the 7th International Conference on Fracture (ICF7), Houston, Texas, March 20-24, 1989, K. Salama et al Eds., Pergamon Press, 1989.
92. d'Escatha, Y., and Devaux, J.C., "Numerical Study of Initiation, Stale Crack Growth, and Maximum Load, with a Ductile Fracture Criterion Based on the Growth of Holes," *Elastic-Plastic Fracture, ASTM STP 668*, J.D. Landes, J.A. Begley, and G.A. Clarke, Eds., American Society for Testing and Materials, pp. 229-248, 1979.
93. Anderson, T.L., and Dodds, R.H. Jr., "Specimen Size Requirements for Fracture Toughness Testing in the Transition Region," *Journal of Testing and Evaluation, JTEVA*, Vol. 19, No. 2, pp. 123-134, March 2, 1991.
94. Anderson, Ted L., "Crack Tip Parameters for Large Scale Yielding and Low Constraint Configurations," *International Journal of Fracture*, Vol. 41, pp. 79-104, 1989.
95. Anderson, T.L., Vanaparthy, N.M.R., and Dodds, R.H. Jr., "Predictions of Specimen Size Dependence on Fracture Toughness for Cleavage and Ductile Tearing," Presented at *ASTM Symposium on Constraint Effects in Fracture*, Indianapolis, May 8-9, 1991.
96. Cotterell, B., Li, Q.-F., Zhang, D.-Z., and Mai, Y.-W., "On The Effect of Plastic Constraint on Ductile Tearing in a Structural Steel," *Engineering Fracture Mechanics*, Vol. 21, No. 2, pp. 239-244, 1985.
97. Matsoukas, G., Cotterell, B., and Mai, Y.-W., "Crack Opening Displacement and Hydrostatic Stress," 6th International Conference on Fracture (ICF6), New Delhi, India, Vol. 6, pp. 1543-1551, December 4-10, 1984.

98. Parks, D.M., "Interpretation of Irradiation Effects on the Fracture Toughness of a Pressure Vessel Steel in Terms of Crack Tip Stress Analysis," *Journal of Engineering Materials and Technology*, pp. 30-35, January 1976.
99. Beremin, F.M., "Numerical Modelling of Warm Prestress Effect Using a Damage Function for Cleavage Fracture," Proceedings of the 5th International Conference on Fracture (ICF5), *Advances in Fracture Research*, Cannes, France, 1981, D. Francois, Ed., Pergamon Press, Oxford UK, pp. 825-832, 1981.
100. Curry, D.A., "Predicting the Temperature and Strain Rate Dependences of the Cleavage Fracture Toughness of Ferritic Steels," *Materials Science and Engineering*, Vol. 43, pp. 135-144, 1980.
101. Kirk, M.T., Koppenhoefer, K.C., and Shih, C.F., "Effect of Constraint on Specimen Dimensions Needed to Obtain Structurally Relevant Toughness Measures," Presented at the ASTM Symposium on Constraint Effects in Fracture, Indianapolis, IN, May 8-9, 1991.
102. Irwin, G.R., "Fracture Mode Transition for a Crack Traversing a Plate," *Journal of Basic Engineering*, Vol. 82, No. 2, pp. 417-425, 1960.
103. Dodds, R.H. Jr., Anderson, T.L., and Kirk, M.T., "A Framework to Correlate a/W Ratio Effects on Elastic-Plastic Fracture Toughness (J_c)," *International Journal of Fracture*, Vol. 48, pp. 1-22, 1991.
104. O'Dowd, N.P., and Shih, C.F., "Family of Crack-Tip Fields Characterized by a Triaxiality Parameter: Part I - Structure of Fields," *Journal of Mechanics and Physics of Solids*, to appear, 1991.
105. O'Dowd, N.P., and Shih, C.F., "Family of Crack-Tip Fields Characterized by a Triaxiality Parameter: Part II - Fracture Applications," *Journal of Mechanics and Physics of Solids*, to appear, 1991.
106. Al-Ani, A.M., and Hancock, J.W., "J-Dominance of Short Cracks in Tension and Bending," *Journal of Mechanics and Physics of Solids*, Vol. 39, pp. 23-43, 1991.
107. Sumpter, J.D.G., and Hancock, J.W. "Shallow Crack Toughness of HY-80 Welds: An Analysis Based on T Stresses," *International Journal of Pressure Vessels and Piping*, Vol. 45, pp. 207-221, 1991.
108. Sun J., Deng Z., Li Z., and Tu M., "Constraint Intensity in Crack Tip Field and Elastic-Plastic Fracture Criterion," *Engineering Fracture Mechanics*, Vol. 34, No. 2, pp. 413-418, 1989.
109. Rice, J.R., Proceedings of the Conference *Mechanics and Mechanisms of Crack Growth*, Cambridge UK, April 1973, M.J. May, Ed., British Steel Corp. Physical Metallurgy Centre Publication, pp. 14-39, 1975.
110. Hutchinson, J.W., and Paris, P.C., "Stability Analysis of J-Controlled Crack Growth," *Elastic-Plastic Fracture, ASTM STP 668*, J.D. Landes, J.A. Begley, and G.A. Clarke, Eds., American Society for Testing and Materials, pp. 37-64, 1979.
111. Joyce, J.A., Davis, D.A., Hackett, E.M., and Hays, R.A., "Application of the J-Integral and the Modified J-Integral to Cases of Large Crack Extension," U.S. Nuclear Regulatory Commission, NUREG/CR-5143, February 1989.
112. Joyce, J.A., and Hackett, E.M., "Development of an Engineering Definition of the Extent of J Singularity Controlled Crack Growth," Report for the U.S. Nuclear Regulatory Commission, NUREG/CR5238, May 1989.
113. Joyce, J.A., and Hackett, E.M., "Extension and Extrapolation of J-R Curves and Their Application to the Low Upper Shelf Toughness Issue," Report for the U.S. Nuclear Regulatory Commission, NUREG/CR-5577, March 1991.
114. Atkins, A.G., "Scaling in Combined Plastic Flow and Fracture," *International Journal of Mechanics Sciences*, Vol. 30, No. 3/4, pp. 173-191, 1988.

115. Atkins, A.G., "Scaling of J_R Curves," *International Journal of Fracture*, Vol. 43, pp. R43-R46, 1990.
116. Broberg, K.B., "Crack Growth Criteria and Non-Linear Fracture Mechanics," *Journal of the Mechanics and Physics of Solids*, Vol. 19, pp. 407-418, 1971.
117. Broberg, K.B., *International Journal of Fracture Mechanics*, Vol. 4, pp. 11-19, 1968.
118. Broberg, K.B., *Journal of the Mechanics and Physics of Solids*, Vol. 23, pp. 215-237, 1975.
119. Cotterell, B., and Reddel, J.K., "The Essential Work of Plane Stress Ductile Fracture," *International Journal of Fracture*, Vol. 13, No. 3, pp. 267-277, June 1977.
120. Mai, Y.W., and Cotterell, B., "Effect of Specimen Geometry on the Essential Work of Plane Stress Ductile Fracture," *Engineering Fracture Mechanics*, Vol. 21, No. 1, pp. 123-128, 1985.
121. Wnuk, M.P., and Read, D.T., "Essential Work of Fracture (w_e) Versus Energy Dissipation Rate (J_C) in Plane Stress Ductile Fracture," *International Journal of Fracture*, Vol. 31, pp. 161-171, 1986.
122. Smith, E., "An Appraisal of a Recent Analysis for Estimating the Plastic Component of the Deformation J Integral for a Stationary Crack," *Journal of Engineering Materials and Technology*, Vol. 113, pp. 344-349, 1991.
123. Holmes, B., Priest, A.H., and Walker, E.F., "Prediction of Linepipe Fracture Behaviour from Laboratory Tests," *International Journal of Pressure Vessels & Piping*, Vol. 12, pp. 1-27, 1983.
124. Demofonti, G., and Rizzi, L., "Experimental Evaluation of CTOA in Controlling Unstable Ductile Fracture Propagation," European Symposium on Elastic-Plastic Fracture Mechanics: Elements of Defect Assessment,: Freiburg, Germany, October 9-12, 1989.
125. Demofonti, G., Cole, I., and Venzi, S., "Fracture Mechanics Concepts for Modeling Ductile Crack Propagation in Gas Pipelines," Proceedings at ECF8, ECF 8 Fracture Behavior and Design of Materials and Structures.
126. Ogasawara, M., "The Crack Tip Opening Angle (CTOA) of the Plane Stress Moving Crack," *Engineering Fracture Mechanics*, Vol. 18, No. 4., pp. 839-849, 1983.
127. Devaux, J.C., Mottet, G., Houssin, B., and Pellissier-Tanon, A., "Prediction of Overall Toughness of Bimetallic Welds Through Numerical Analysis According to the Local Approach of Tearing Fracture," pp. 325-335.
128. Zhang, J.X., Shi, Y.W., and Tu, M., "Studies on the Fracture Mechanics Parameters of Weldment with Mechanical Heterogeneity," *Engineering Fracture Mechanics*, Vol. 34, No. 5/6, pp. 1041-1050, 1989.
129. Yagawa, G., "Study on Elastic-Plastic Fracture Mechanics in Inhomogeneous Materials and Structures (II)," Report for Martin Marietta Energy Systems, Inc., CRC-EPI-2, May 1990.
130. Kirk, M.T., and Dodds, R.H., Jr., "The Effect of Weld Metal Strength Mismatch on the Deformation and Fracture Behavior of Steel Butt Weldments", Report to David Taylor Research Center, Metals and Welding Division, Annapolis, MD, by the Department of Civil Engineering, University of Illinois at Urbana-Champaign, Civil Engineering Studies, Structural Research Series No. 559, January 1991.
131. Lereim, J., "Ductile Fracture Mechanisms of Structural Steel," The Proceedings of the 4th European Conference on Fracture, *Fractures and the Role of Microstructure*, Leoben, Austria, September 22-24, 1982, K.L. Maurer and F.E. Matzer, Eds., Engineering Materials Advisory Services Ltd., Warley, West Midlands UK, pp. 11-22, 1982.

132. Gibson, G.P., Druce, S.G., and Turner, C.E., "Effect of Specimen Size and Geometry on Ductile Crack Growth Resistance in a C-Mn Steel," *International Journal of Fracture*, Vol. 32, pp. 219-240, 1987.

Table 1
Evaluation of Geometry Dependence of J-R Curves for Several Types of Steel

Material	Specimen	Jic		Tearing Modulus		Example: 3 mm Crack Extension			
		Jic (kJ/m**2)	Variation* (% of small specimen)	dJ/da (MJ/m**3)	Variation* (% of small specimen)	Applied J** (kJ/m**2)	Crack Extension (mm)	Actual da** / Predicted da	(%)
A533B	4T-CT	300	125	260	136	630	1.5		50
	0.5T-CT	240	-	190	-	630	3.0		-
Linde 80	4T-CT	110	110	83	133	220	1.7		57
	0.5T-CT	100	-	62	-	220	3.0		-
X46	CCT	490	100	190	172	800	1.0		33
	CT	490	-	110	-	800	3.0		-
X70	CCT	1200	129	260	185	1500	0.6		20
	CT	930	-	140	-	1500	3.0		-
A302B	6T-CT	25	59	14	30	250	>80		>2700
	0.5T-CT	42	-	46	-	250	3.0		-

* In the case of the X46 and X70 steels, the CT specimen is considered the smaller specimen.

** The applied J level for this example was selected such that 3 mm of crack extension would occur in the smaller specimen. If the J-R curve from the smaller specimen is used, a prediction of 3 mm of crack extension at this level of J would be made for the larger specimen as well. The ratio shown is the actual crack extension at this level of J in the larger specimen divided by the prediction, i.e. 3 mm.

TABLE 2

Range of Constraint Factor for Typical Experimental Geometries

Specimen Type [Reference]	Constraint factor (h) $\frac{\sigma_m}{\sigma_e}$	Constraint factor (q) $\frac{3\sigma_m}{\sigma_e}$	Comments
uniaxial tension	0.33	1.0	prior to necking
plane strain	2.3	7.0	$\sigma_2 = \sigma_3$
CCT [40,41]	1.5 - 2	4.5 - 6	range of typical peak value
CT [41,42]	2 - 3	6 - 9	range of typical peak value
DENT [39,40]	2.5 - 3	7.5 - 9	range of typical peak values very high values across the entire ligament > 2.0
Surface Crack [41-43]	2 - 2.5	6 - 7.5	reaches peak near surface, decreases to less than 2.0 at middepth

range.wq1

Table 3
Causes of Test Specimen Geometry Effects in Ductile Fracture

Cause	Comments
Two-Dimensional Effects	
Micromechanical Effects	
Loss of SSY	May dominate in cleavage fracture. Typically not significant in ductile fracture.
Crack extension effect	May dominate J-R curves from CT specimens at large crack extension for moderate toughness steel. Use modified J.
Global Deformation Effects	
Shape of the remote plastic region	May dominate in fully-plastic fracture.
Plastic flow in heterogeneous weld	Weld zone comprises different proportion of the plastic volume for different specimen widths.
Separations	Separations effect the bending angle of the specimens.
Three-Dimensional Effects	
Tunnelling, curved crack front, development of shear lips	Minimize by using thick sidegrooved specimens meeting ASTM requirements.

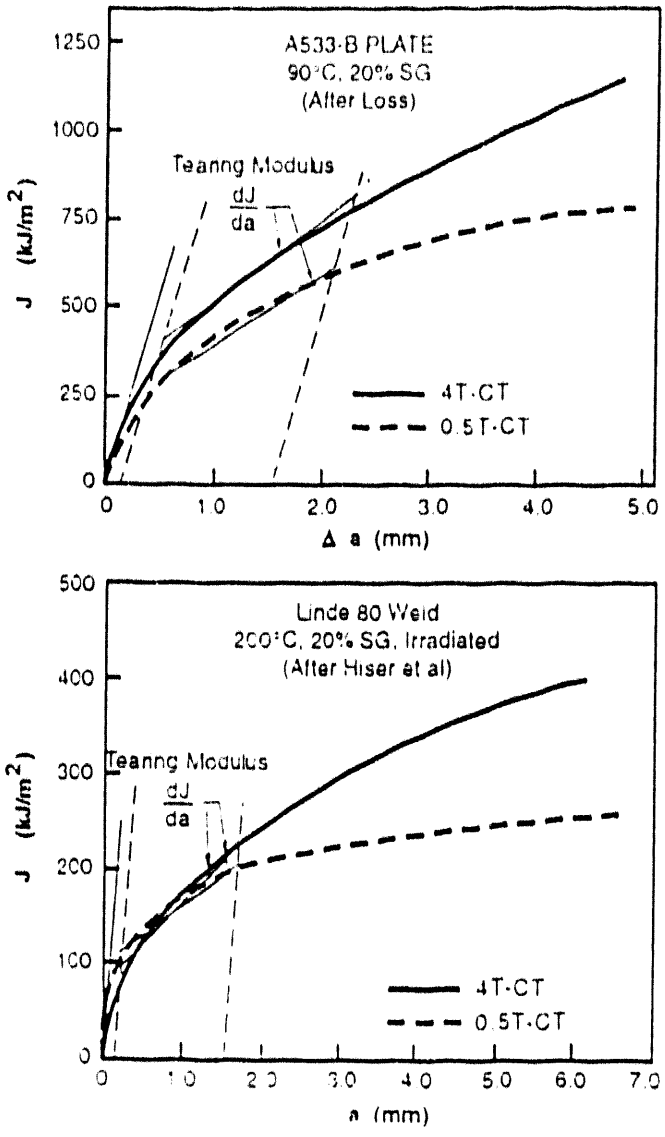

Figure 1. Comparison of J-R Curves for Several Proportional Compact Specimens of a A533B Base Plate and Line 80 Weld Metal Showing Usual Size Effect of Greater Tearing Modulus for Bigger Specimens (0.5 and 4 are the thicknesses in inches).

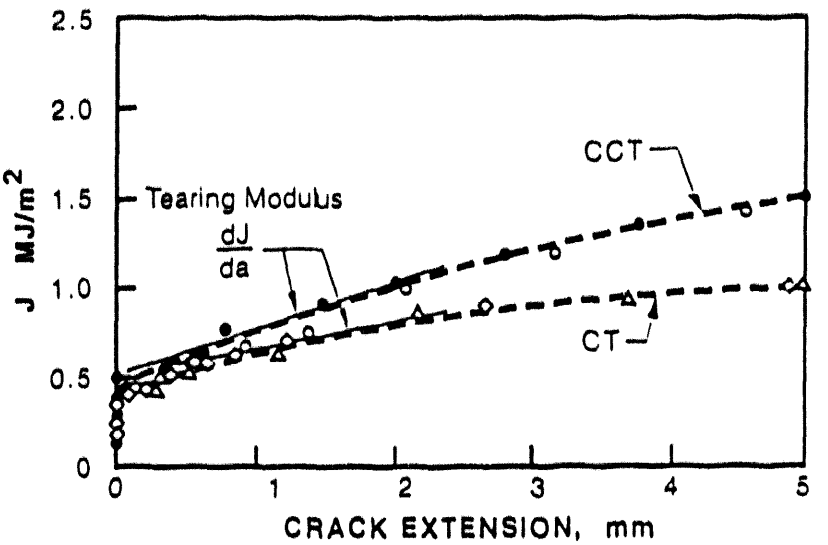

(a) Small Crack Extension

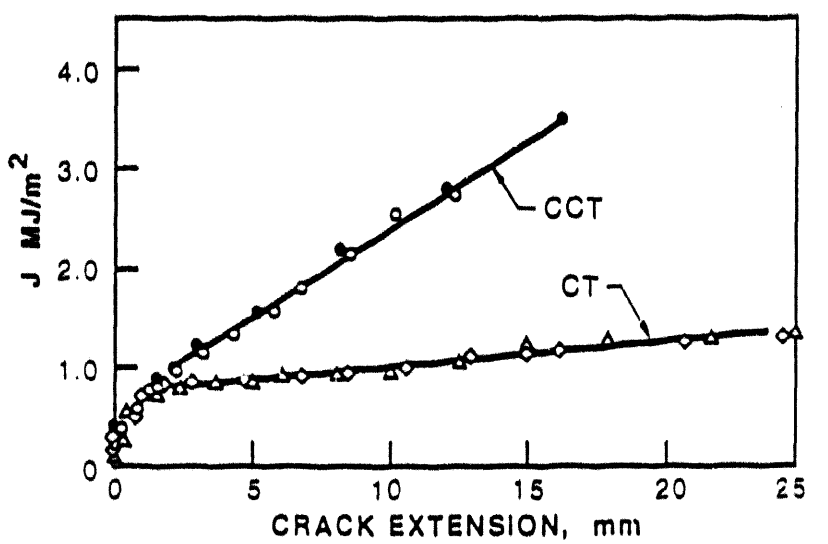

(b) Full Resistance Curve

Figure 2. J-Resistance Curve for X46 Steel.

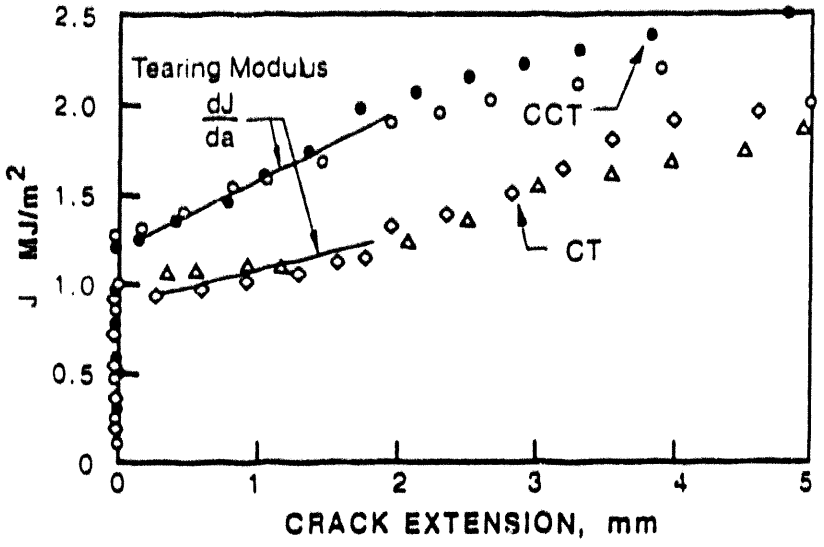

(a) Small Crack Extecnsion

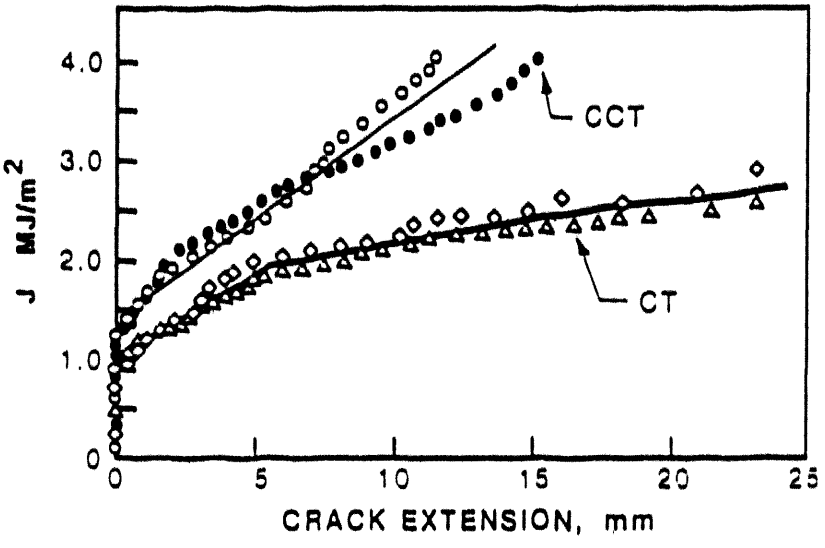

(b) Full Resistance Curve

Figure 3. J-Resistance Curve for X70 Steel.

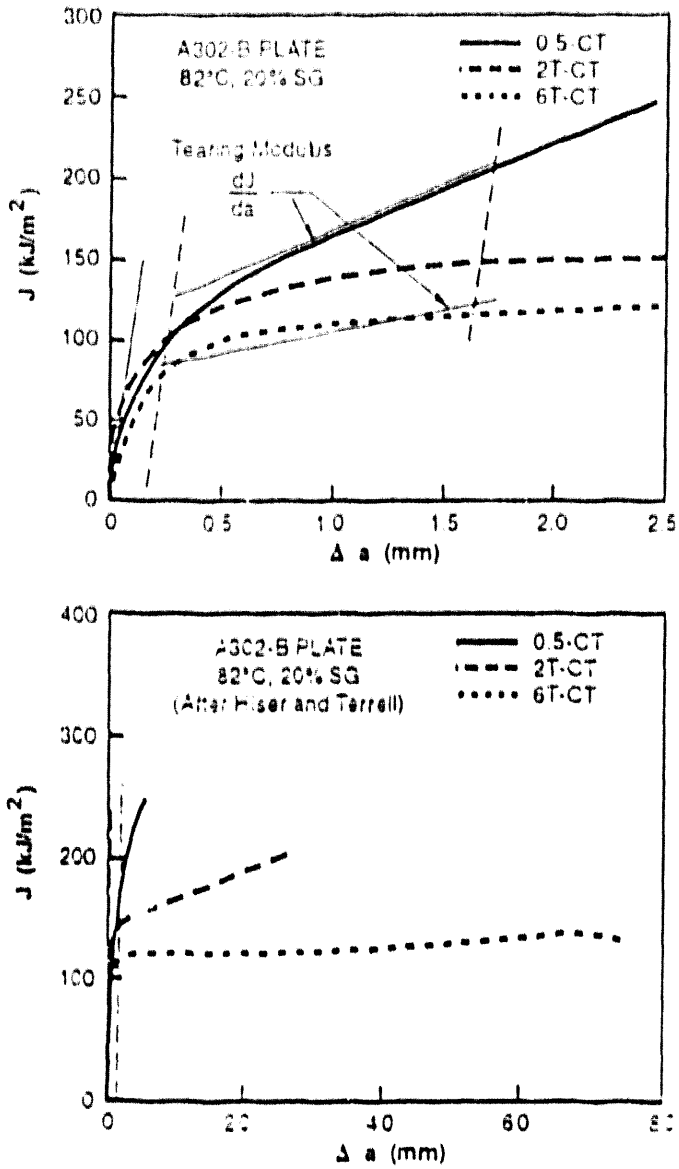

Figure 4. Comparison of J-R Curves for Several Proportional Compact Specimens of A302B Steel Showing Unusual Size Effect of Lower Tearing Modulus for Bigger Specimens (The same tests are shown for two ranges of crack extension, 0.5, 2, and 6 are the thickness in inches).

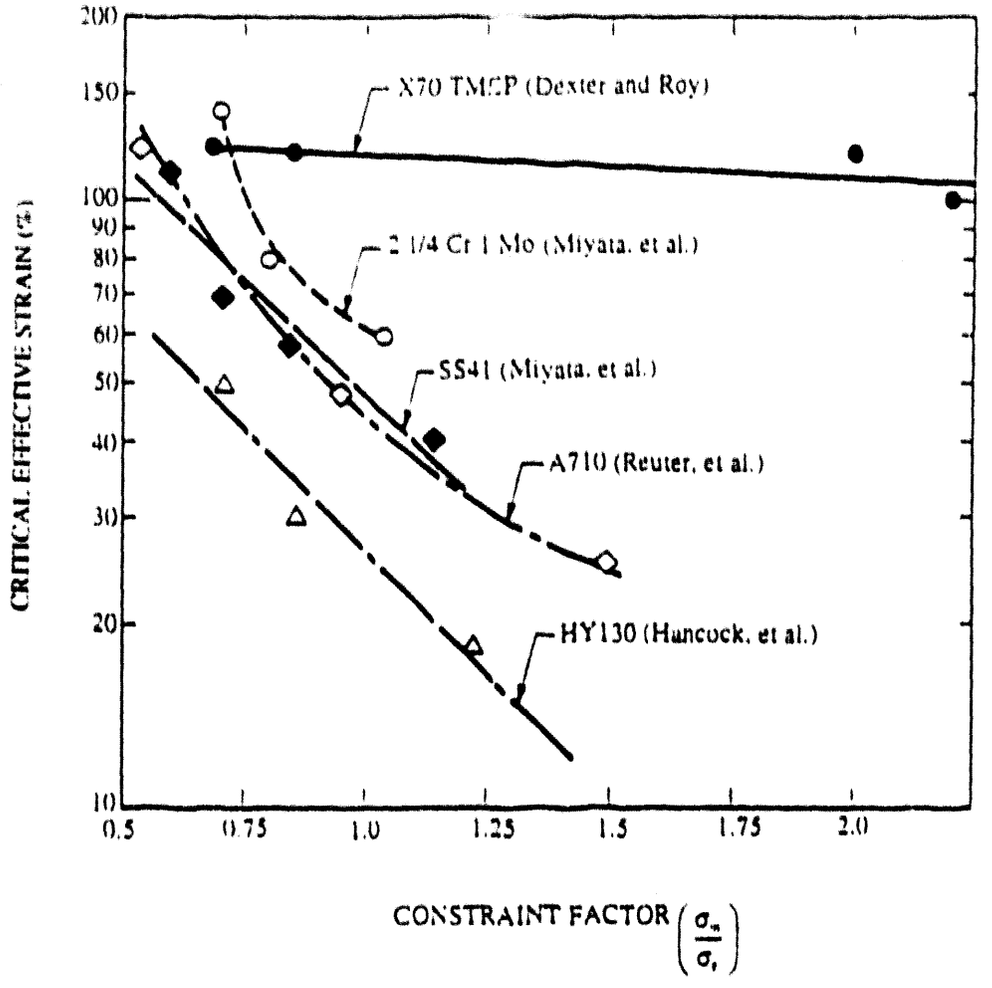

Figure 5. Empirical Fracture-Strain/Constraint-Factor Loci for a Variety of Steels.

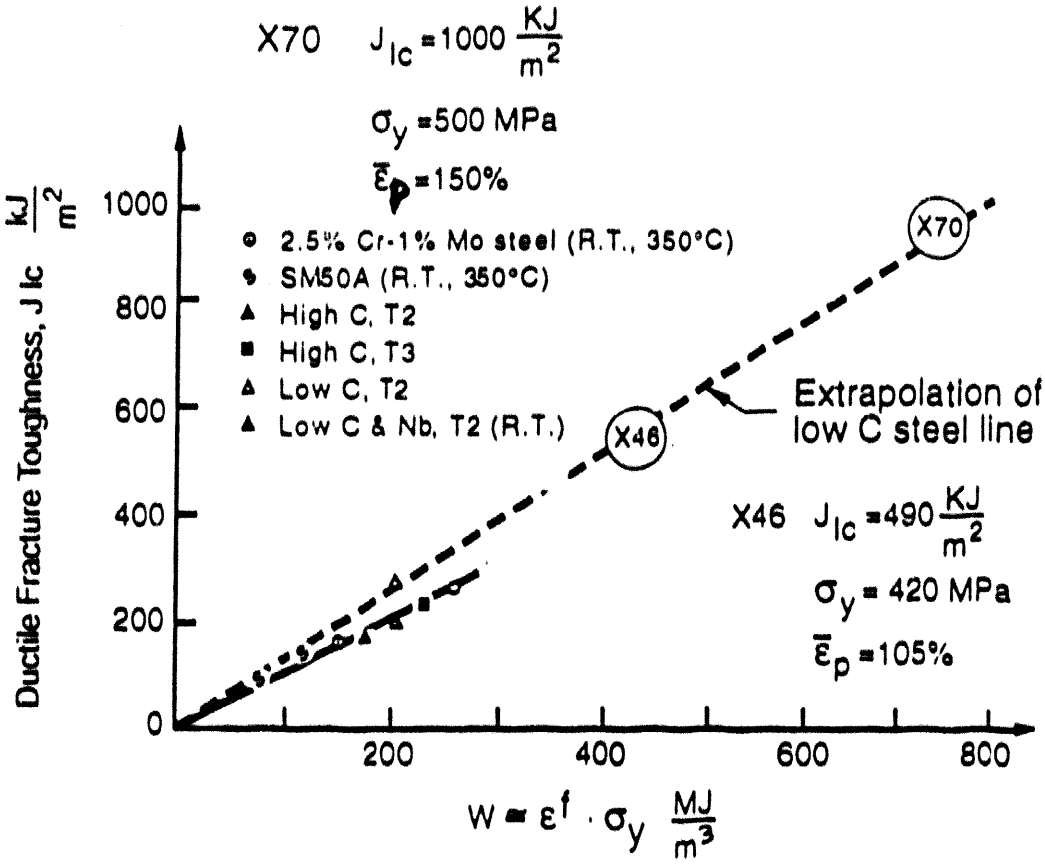

Figure 6. Empirical Correlation Between Fibrous Initiation Toughness J_i and the Average Critical Strain from a Notched Specimen Times the Yield Strength (after Miyata, et al).

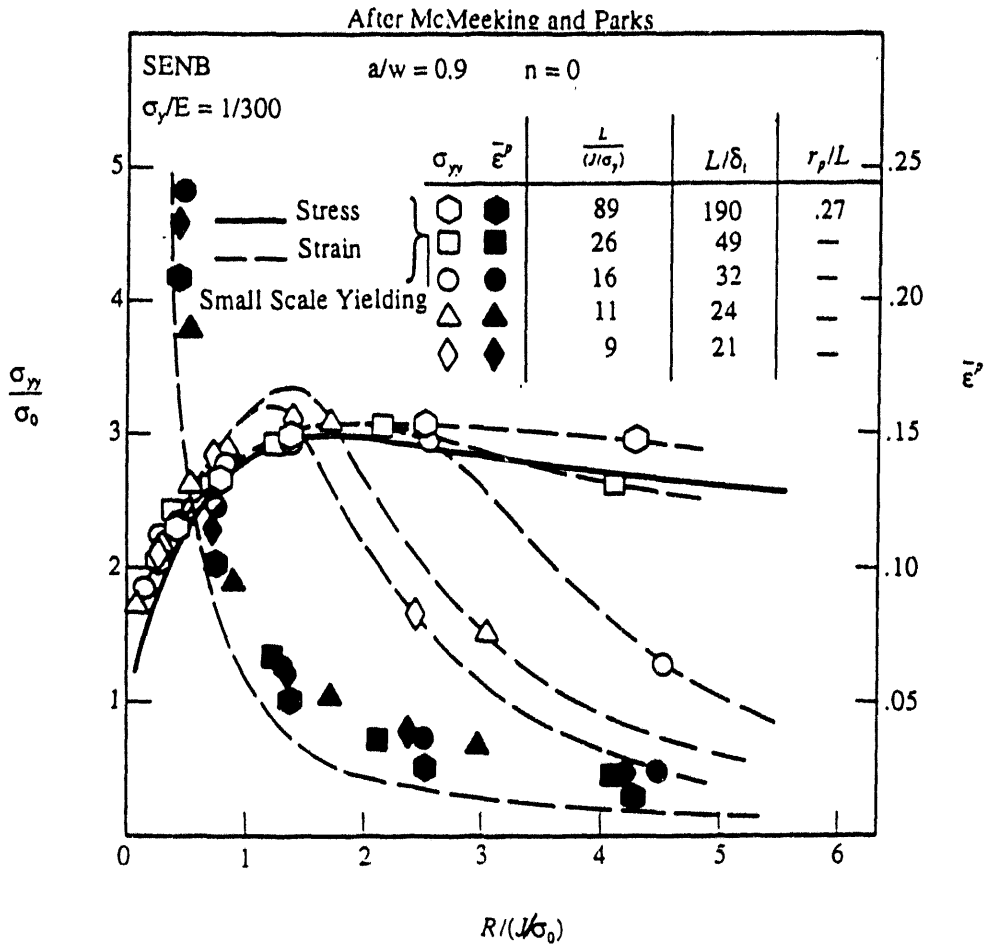

Figure 7. Distribution of Normal Stress on the Crack Plane and Equivalent Strain on a Plane Inclined at 45° for a Single-Edge-Notched Bend Specimen for No Strain Hardening (n = 0). Note that L is the remaining ligament.

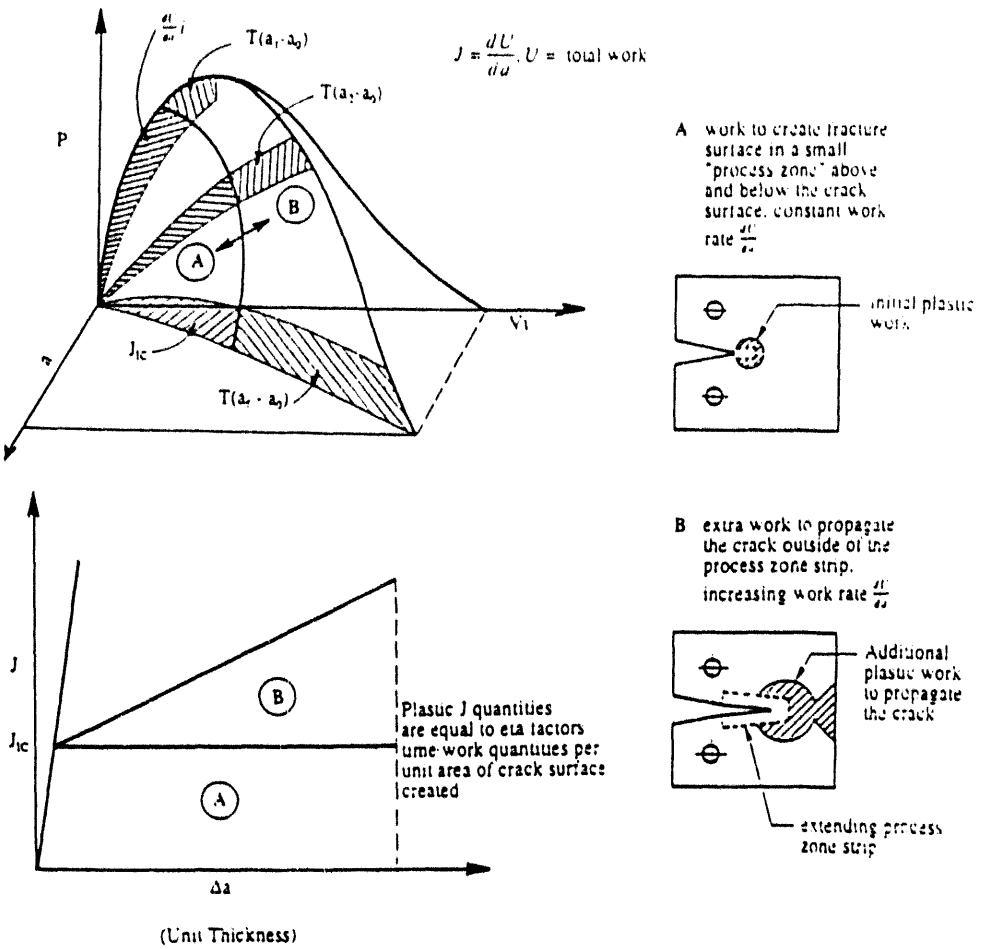

Figure 8. Interpretation of J in Terms of Energy Quantities to Create Fracture Surface and to Create Remote Plastic Work and the Load Displacement, Crack Growth Curve.

Note: This schematic is for an idealized unit thickness slice of a specimen in plane strain. In a three-dimensional specimen, B would also include the work consumed in developing shear lips.

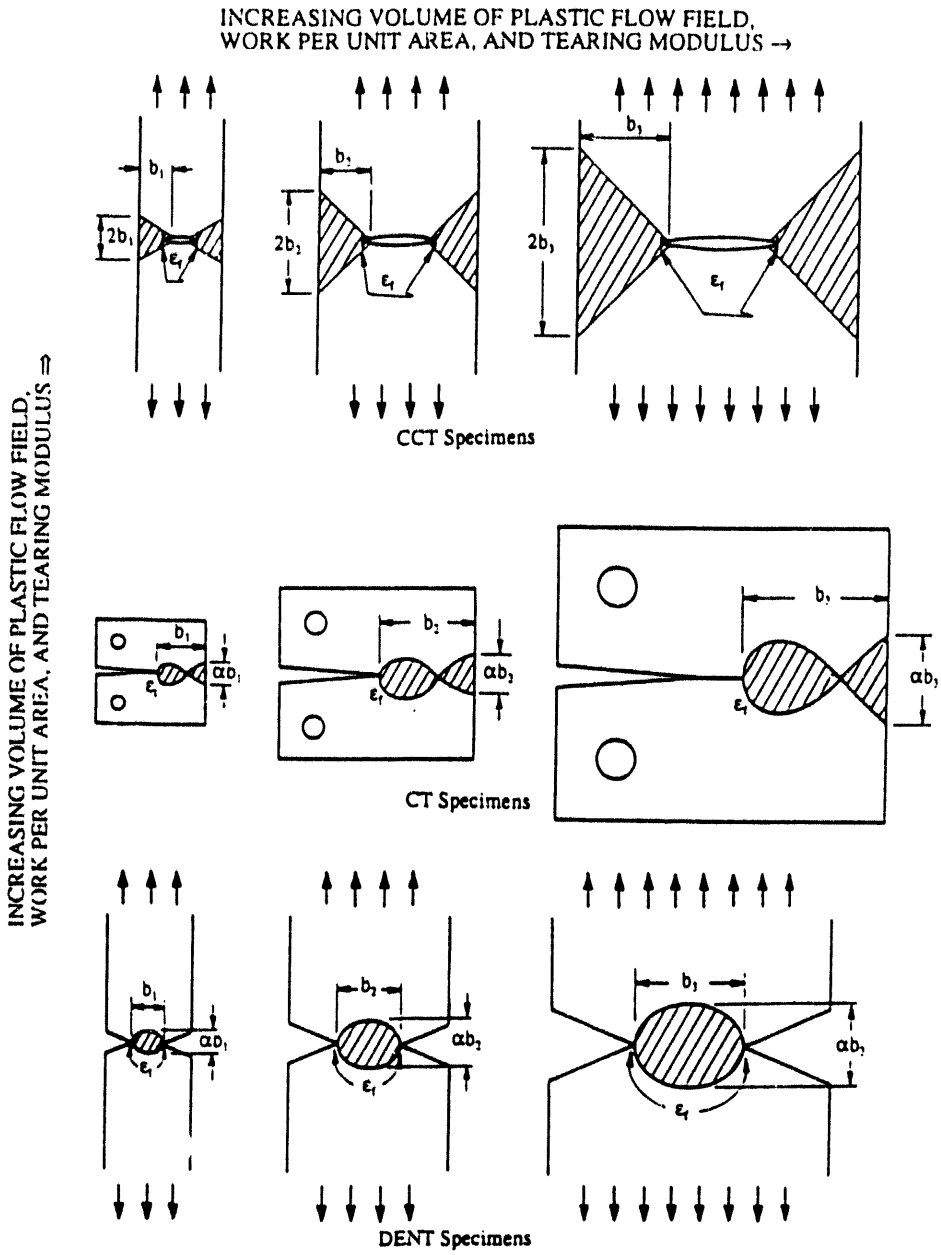

Figure 9. Proportional Test Specimens Showing How the Height of the Plastic Flow Field Increases Proportionally with Ligament Size and Showing Differences in the Shape of the Plastic Flow Field for Various Specimen Types. Note that the local fracture strain is constant in all of these cases although the remote plasticity has a significant effect on the global fracture criterion J.

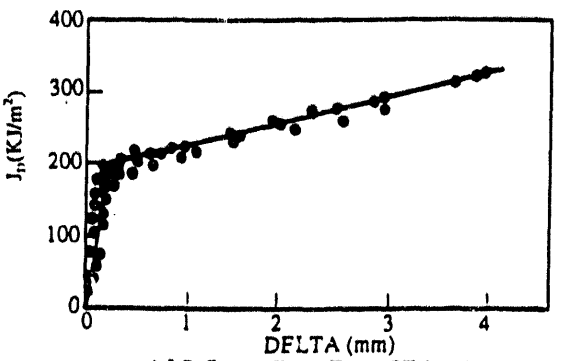

a) J-R Curves From Three CT Specimens

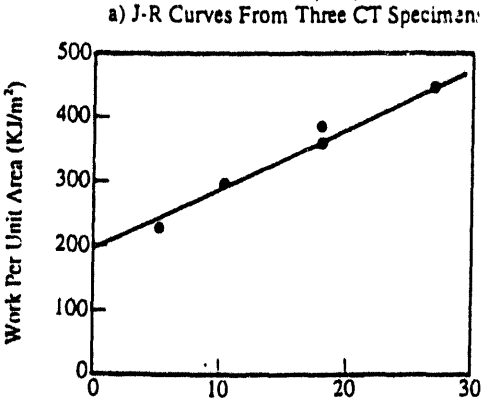

b) Total Fracture Energy From DENT Specimens

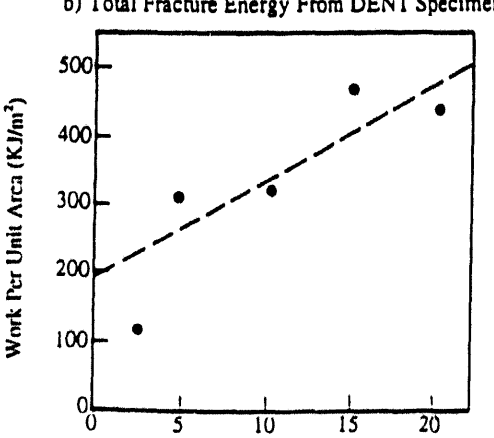

c) Total Fracture Energy From CT Specimens

Figure 10. **Comparison of J-R Curve and Total Fracture Energy vs. Ligament Length for Several Specimen Types Showing Agreement Between J_{IC} and Specific Work of Fracture for 5052-H32 Aluminum.**

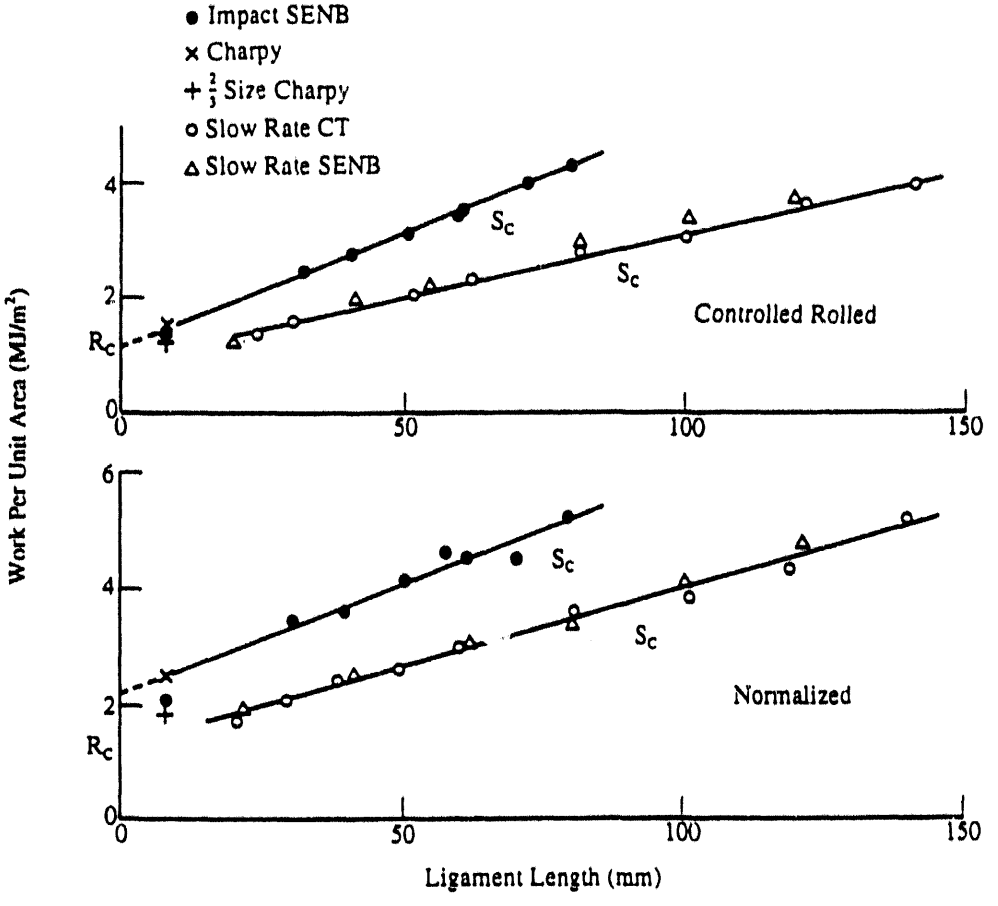

Figure 11. Impact and Slow Bend Fracture Energy for a Steel in Two Finishing Conditions Showing Linear Increase in Work Done per Unit Area with Ligament Length.

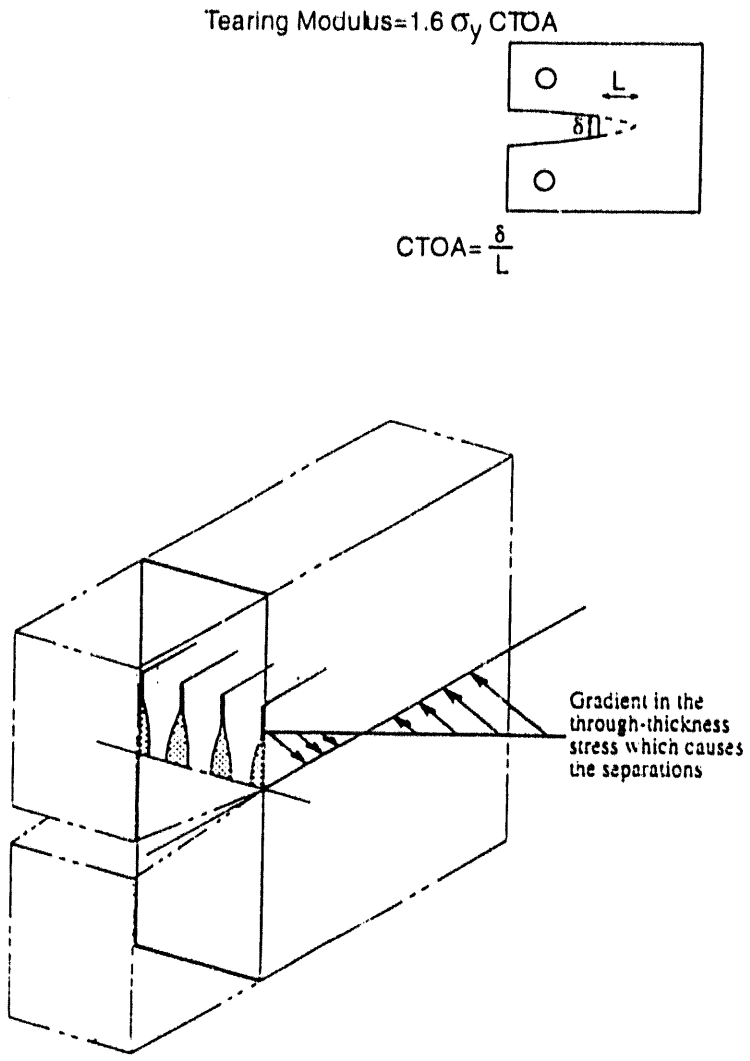

Figure 12.Schematic of Ductile Failure Process of Steel Exhibiting Separations Showing Individually Necking Laminates Ahead of the Crack. Note that the length of the region where separations extenc ahead of the crack is governed by the location of the stress reversal or hinge.

PROGRESS IN GENERATING FRACTURE DATA BASE AS A FUNCTION OF LOADING RATE AND TEMPERATURE USING SMALL-SCALE TESTS

by

Dr. Hervé Couque and Dr. Stephen J. Hudak, Jr.

Structural integrity assessment of nuclear pressure vessels requires small specimen fracture testing to generate data over a wide range of material loading, and temperature conditions. Small scale testing is employed since extensive testing is required including small radiation embrittled samples from nuclear surveillance capsules. However, current small scale technology does not provide the needed dynamic fracture toughness relevant to the crack arrest/reinitiation events that may occur during pressurized thermal shock transients following emergency shutdown. This paper addresses the generation of this much needed dynamic toughness data using a novel experimental-computational approach involving a coupled pressure bars (CPB) technique and a viscoplastic dynamic fracture code. CPB data have been generated to testing temperatures never before reached: 37 to 100°C - 60 to 123°C above the nil ductility transition temperature. Fracture behavior of pressure vessel steel from lower shelf to upper shelf temperatures and previous toughness estimates for the 10^6 MPa$\sqrt{m}$ s^{-1} loading rate regime are assessed in light of the new CPB data.

Southwest Research Institute, 6220 Culebra Road, San Antonio, Texas 78228.

INTRODUCTION

To prevent catastrophic failure of engineering structures, fracture properties have been measured under dynamic loading conditions to consider the effect of inertia as well as rate sensitivity of the material. These properties are relevant to the structural integrity assessment of nuclear pressure vessels where small specimens are needed to obtain fracture toughness data over a wide range of material, loading, and environmental (temperature) conditions. The most critical event to the integrity of a nuclear pressure vessel is a loss of coolant accident which results in an emergency shutdown of the reactor system. The sudden ingress of emergency cooling water which accompanies such a shutdown can cause the vessel to be thermally shocked while still under pressure. During such a pressurized thermal shock (PTS) event, the combination of thermal and pressure stresses would likely cause surface cracks on the interior of the vessel to grow as the static toughness (K_{Ic}) is exceeded. The integrity of the vessel would then depend on the ability of the material to arrest the crack as it propagates through the vessel wall and encounters less-embrittled, tougher material. During this process, cracks can arrest and reinitiate under stress-wave loading.

Although relevant data have largely been generated using elastic-plastic fracture mechanics technology which evolved over the past two decades, these data do not include the influence of dynamic effects. Evidence that such effects are important and need to be considered can be found in recent wide-plate tests conducted under the Heavy Section Steel Technology (HSST) Program [1]. These large-scale experiments were designed to provide crack arrest data in the transition and upper-shelf regimes. Dynamic measurements of crack growth and displacement boundary conditions clearly showed that cracks actually initiate, propagate at high velocities, temporarily arrest, and reinitiate. This scenario, which often occurred more than once in a given experiment, is understandable if one considers dynamic effects. Specifically, crack arrest/reinitiation occurs by reflected stress wave in the specimen. Similar effects can also be expected in actual pressure vessels.

Recognition of the above events may have been the motivation for the generation of dynamic initiation data at Westinghouse in 1970 as part of the HSST Program [2]. These data are shown in Figure 1. Critical data could not be generated at elevated temperatures and higher strain rates because of the limitations of the technology to measure toughnesses of 200-400 MPa$\sqrt{m}$ in the temperature range 23-80°C [1]. These values exceed the already high upper-shelf static toughness. Until recently, experimental technology involving laboratory specimens has successfully measured toughnesses up to 230 MPa$\sqrt{m}$ [3-5]. Beyond 230 MPa$\sqrt{m}$, large specimen fracture tests have been the only reliable experimental approach [1]. Another challenge related to nuclear pressure vessel steels is the identification of a reliable procedure for the dynamic testing of small coupons from surveillance capsule programs. A need exists to develop techniques to characterize high-toughness materials using small specimens, not only for economic reasons, but also for situations where only a limited quantity of material is available. The present investigation describes dynamic fracture data generated with a relatively new coupled pressure bars (CPB) technique. It will be shown that the CPB technique is a reliable small specimen technology for the dynamic fracture characterization of pressure vessel steel over the full temperature range encompassing cleavage and fibrous fracture. Finally, the CPB data are compared to previous toughness estimates for the 10^6 MPa$\sqrt{m}$ s^{-1} loading rate regime.

EXPERIMENTAL ANALYTICAL PROCEDURE

A nuclear pressure vessel steel, A533B plate steel (ORNL plate 13A) [6], was used in this investigation. The composition and heat treatment of this steel are summarized in Table 1. This steel has a nil-ductility transition temperature of -23°C and a static yield stress at room temperature of 445 MPa [6]. Tensile tests were conducted parallel to the plate rolling direction. The direction of crack propagation for the fracture specimens was in the LT orientation, i.e., transverse to the rolling direction.

Dynamic fracture testing of the A533B steel at temperatures varying from 37 to 100°C was conducted with the CPB technique. This technique has been successfully applied to materials covering a wide range of toughnesses, 10-350 MPa$\sqrt{m}$, and fracture modes [7,8,9]. For the background on the design and development of the experimental apparatus, the reader is referred to Refs. 7 and 9. Figure 2 shows a schematic of the CPB experiment. The primary components consist of two pressure bars to store energy, a notched round starter specimen to rapidly release the stored energy, and two prefatigued compact fracture specimens. These experiments were conducted by preloading the pressure bars and starter specimen to a load between 311 to 623 kN corresponding to an applied stress in the bars of between 273 to 546 MPa. The test specimens were then inserted into slots in the bars and secured with wedges, as shown in Figure 2. Fracture of the starter specimen was subsequently initiated by introducing a sharp cut into the circumferential notch of the starter specimen using a cutter wheel and high-speed air drill. Failure of the starter specimen initiates an unloading (compressive) pulse in the pressure bars which transmits a rapid axial displacement rate to the specimen arms. This pulse has a rise time of 60 to 120 μs corresponding to the failure duration of the starter and, is followed by a relatively constant specimen displacement rate associated with the unloading of the two separated pressure bars. The latter period lasts about 380 μs for a bar length of 1m. During this event, the unloading pulse imposes a constant load-line displacement rate, $\{\dot{COD}_{LL}\}_{\text{late time}}$, to the specimens. Based on one-dimensional stress wave analysis of the bar, $\{\dot{COD}_{LL}\}_{\text{late time}}$ is approximated by:

$$\{\dot{COD}_{LL}\}_{\text{late time}} = 2C_o\sigma_o/E \qquad (1)$$

where C_o is the sound wave velocity of the bar, E is the Young's modulus of the bar, and σ_o is the prestress in the pressure bar. This constant displacement rate can be easily varied either by using a bar material of different sound velocity or by applying a different prestress to the pressure bars. Using Eq. 1, a load-line displacement rate of about 19 m s^{-1} is reached with steel bars (C_o = 5200 m s^{-1} and E = 2 x 10^5 MPa) prestressed to 390 MPa.

Prefatigued compact specimens of planar size W = 44 mm and crack length a_o = 24 mm were employed. Two thicknesses, B, were used, specifically, 15 mm for the tests performed at 37 and 50°C, and 20 mm for the tests performed at 75 and 100°C. The specimens were also side-grooved to 25 percent of the thickness, B, resulting in net thicknesses, B_N, of 11.4 and 15.0 mm, respectively. This side-grooving served to maximize the through-thickness constraint for a given nominal specimen thickness. The test specimens were heated to the testing temperature with electrical resistance heaters. Two specimens of the same thicknesses were tested simultaneously with the CPB technique as shown in Figure 2 for the 20 mm thick specimens, i.e., 75 and 100°C specimens. The crack opening displacement history, $COD_X(t)$, was monitored at a distance X = 12.5 mm from the load line using an eddy current transducer, as shown in Figure 2. In addition, one strain gage was mounted on each specimen above the prefatigued crack-tip location. The crack

initiation time was deduced from this strain gage record, $\varepsilon_{yy}(t)$, by identifying the unloading compressive wave resulting from the initiation of the prefatigued crack. Crack propagation history, a(t), was monitored on one side of each compact specimen using a crack gage having five to ten lines, spaced 3 mm apart.

Finite-element simulations of the CPB specimens were conducted with a dynamic viscoplastic fracture code VISCRCK [10] implemented with the elastic-viscoplastic constitutive model formulated by Bodner-Partom [11]. Appropriate constants for the Bodner-Partom constitutive model were developed from A533B tensile data obtained at strain rates varying from 10^{-3} to 3×10^{3} s^{-1} over the temperature range -60 to 175°C and incorporated in the dynamic fracture code [12]. A mesh composed of 387 elements having linear dimensions of 2 mm was used.

RESULTS

Planar crack growth was obtained for each specimen, with deviations less than 1 mm over a distance of 14 mm or greater. This is illustrated in Figure 3 with a specimen tested at 100°C. Figure 4 compares the computed crack opening displacement history, COD_X, with the experimental data for the specimen tested at 100°C. Good agreement was obtained between the computed and experimental values up to initiation. Two fracture criteria for ductile materials, were considered: the dynamic J′ integral [13,14], and the T* integral [15]. The J′ and T* integrals are equivalent for monotonic loading up to crack initiation. The T* integral is an incremental formulation that was proposed to handle the effects of viscoplasticity and unloading that occur during dynamic crack propagation. Both crack-tip integrals, J′ and T*, were calculated and found to coincide during the process of crack initiation. Consequently, from the evaluation of the crack-tip integral, the equivalent elastic stress intensity factor K_I is deduced by considering the small scale yielding relation under plane strain conditions:

$$K_{IJ} = \sqrt{E J'_I / (1 - \nu^2)} \tag{2}$$

where E and ν are Young's modulus and Poisson's ratio, respectively.

The influence of mesh size was investigated using two mesh sizes of linear dimension, 2 mm and 3 mm, for analyses at 100°C. The measured toughness were found to converge up to initiation, see Figure 5, indicating the relevance of the fracture parameter, J′, to quantify dynamic fracture initiation. This procedure was repeated for each specimen over the temperature range 37-100°C, and the results are summarized in Table 2.

The validity of the results were evaluated based on an adaptation of Paris' static criterion to dynamic loading conditions [16]:

$$a_o, b, B \geq \alpha J_{Id} / \sigma_{yd} \tag{3}$$

where a_o, b, B, and σ_{yd} are the initial crack length, the remaining ligament, the thickness, and the dynamic yield stress, respectively, and $\alpha = 25$, see Reference 17 and ASTM Standard Test Method for J_{Ic}, A Measure of Fracture Toughness E813. The relevance of using this criterion for dynamic ductile fracture has been recently demonstrated by Moran *et al.* [18]. The strain rate corresponding

to the dynamic yield stress of Eq. 3 was taken to be the average strain rate reached at the plastic zone boundary, defined at 0.002 strain. This strain rate was estimated using Costin *et al.* [19], approach and calculated to be 30 s^{-1} for A533B steel.

For data not satisfying Eq. 2, the overestimation of the toughness was deduced using the procedure developed by Couque *et al.* [20], based on the data of Landes and Begley [17] for a steel of similar flow stress and static toughness to the A533B steel. Using dynamic yield stresses at a strain rate of 30 s^{-1} over the temperature range of interest (see Reference 12) the values of α, and eventual toughness corrections, were calculated and are reported in Table 2. Also indicated in Table 2 is a margin of error for the corrected toughnesses deduced from Landes and Begley's data.

The dynamic upper-shelf regime of the A533B steel used in the present study occurred at 100°C. As shown in Figure 6, no cleavage was observed at this temperature, either at initiation or during propagation. Even with this fully fibrous fracture crack velocities up to 1000 m s^{-1} were reached as shown in Figure 7. The higher crack velocity reached during the early crack propagation event is related to the initiation event. The release of a large amount of strain energy stored during the blunting process of the prefatigued crack, along with the rapid loading rate imposed by the pressure bars, provides the highest dynamic loading conditions early in the crack growth process. Therefore, higher crack velocities are expected just after crack-initiation. Crack-arrest occurred under a fibrous failure mode at about 15 mm from the prefatigued crack tip.

By continuing the analysis beyond the initiation time, it is theoretically possible to obtain, the dynamic fracture toughness of a rapidly propagating "fibrous" crack. This would require iterative analyses to be performed until the experimental and analytical crack opening displacements (COD_X) are matched. However, before this can be done, several difficulties need to be overcome to measure a crack-arrest toughness. First, the use of a finer crack gage technique needs to be developed to identify the precise time of arrest. Secondly, cracks need to be arrested before they become too deep since the large rotations and deformations associated with high toughness materials result in ill-defined boundary conditions. This can be achieved by using pressure bars of different lengths to obtain controlled crack arrest lengths. And last, but not least, a fracture criterion for ductile crack growth which is independent of specimen geometry will need to be developed. Two potential candidates are the crack-tip integrals previously mentioned, J′ and T*.

Figure 8 compares the dynamic fracture-initiation toughness obtained with the coupled pressure bars with the quasi-static fracture toughness [21]. With increased loading rate, the transition temperature is increased by about 25°C, while the upper-shelf fracture toughness increases by at least 70 percent. This increase of the transition temperature and upper-shelf toughness with loading rate seems to be typical of ductile steels exhibiting a strong strain-rate sensitivity [20].

Dynamic fracture-initiation toughness and crack-arrest toughness obtained from the recent series of 1m x 9.6 m wide-plate crack arrest experiments, conducted as part of the Heavy Section Steel Technology (HSST) Program [1] are compared in Figure 9. The dynamic initiation toughness can be seen to be similar to the crack-arrest toughness in the transition regime (37 to 50°C). At temperatures above 50°C, the dynamic initiation toughness rises with the crack-arrest toughness. The dynamic initiation toughness appears to provide an estimate of the crack-arrest toughness, at least up to 75°C.

Table 3 summarizes the failure modes involved in crack initiation, propagation, and arrest for the specimens tested over the temperature range 37-100°C. These observations match those made in the HSST Program [1], in that cleavage fracture was observed at temperatures lower than 92°C. Additional dynamic initiation and crack-arrest experiments are needed at elevated temperatures to establish if this correspondence prevails over the upper-shelf regime. The expectation of a relationship between K_{Id} and K_{Ia} is based on the view that crack arrest occurs when a crack fails to reinitiate, thus K_{Ia} should be related to the properties of a stationary crack being loaded dynamically. This hypothesis need to be examined not only for arresting cracks preceded by a rapid cleavage fracture, but also by a rapid fibrous fracture [22].

DISCUSSION

The CPB technique has been demonstrated to promote rapid crack propagation successfully in small A533B specimens at temperatures never before reached with other experimental techniques (37 to 100°C -- 60 to 123°C above the nil-ductility transition temperature). Based on an observed levelling of the upper-shelf dynamic initiation toughness of certain low-strength steels [19], we anticipate that the technique can be used to evaluate the dynamic fracture properties of A533B steel up to 320°C, the service temperature of nuclear pressure vessels.

The CPB technique presents other unique features with regard to the characterization of dynamic fracture properties. The technique has the potential for extracting dynamic initiation, propagation, and arrest toughnesses from the analysis of a single specimen with a dynamic viscoplastic fracture simulation code. The analysis will be optimum since the specimen size will be minimized with regard to the criteria for valid plane-strain fracture toughness. These small specimens enable finely discretized meshes to be used thereby facilitating more accurate finite element results. This technology provides a tool for further investigation of the correlation between dynamic initiation toughness and crack-arrest toughness, as well as the relation between dynamic propagation toughness and crack velocity, particularly for fibrous fracture. Furthermore, since energy storage is independent of specimen size, the possible influence of specimen size on dynamic fracture toughness of high-toughness steels can also be examined systematically for the first time.

Insights into the potential of the CPB experiment to study the influence of specimen size on the dynamic upper shelf toughness of A533B steel were provided from a final experiment. TI is experiment involved two A533B specimens of large planar size, W = 89 mm, and of thickness, B = 44 mm, and net thickness, B_N = 33 mm. These specimens were tested at upper shelf temperatures of 100 and 300°C and at a loading rate of about 2×10^6 MPa$\sqrt{m}$ s^{-1} with a bar preload of 390 MPa. The experimental set-up, shown in Figure 10, involves a new load transfer mechanism to accommodate the large size of the compact fracture specimens. From this experiment, no dynamic measurements were recorded but the static crack opening displacement, δ_i, was measured from the sectioned specimen. Figure 11 shows the blunted prefatigued crack tip along with a growth of 2 mm. Using the formulation of the fracture toughness at initiation as a function of the critical crack-tip opening, δ_i^* derived in Reference 23:

$$K_{Id} = \sqrt{1.89 \sigma_{yd} E \delta_i^*} \qquad (4)$$

and a measured δ_i of 720 μm, a dynamic initiation toughness, K_{Id}, of 359 MPa$\sqrt{m}$ was calculated for the specimen tested at 100°C. This toughness agrees well with the corrected toughness of 337 MPa$\sqrt{m}$ measured from the dynamic simulation of the A533B specimen tested with a specimen of planar size, W = 44 mm. The specimen tested at 300°C exhibited no crack growth, but a blunted crack, 500 μm in height was observed. Using Eq. 4 with σ_{yd} = 460 MPa [12] and δ_i = 500 μm, a stress intensity, K_I, of 300 MPa$\sqrt{m}$ was calculated. This indicates that the dynamic initiation toughness at 300°C exceeds 300 MPa$\sqrt{m}$ and, therefore, is greater than the static initiation toughness, K_{Ic}, of 200 MPa$\sqrt{m}$ [21]. Increase of the bar prestress from 390 MPa to 546 MPa will most likely promote growth in such a specimen at 300°C. These results are another indication that the CPB technique can be used to evaluate the dynamic fracture properties of A533B steel up to 320°C, the service temperature of nuclear pressure vessels. It is estimated that these specimens of planar size, W = 89 mm, will be adequate for such characterization since according to Eq. 3 they will provide valid toughness data up to 500 MPa$\sqrt{m}$.

The extrapolation of the Westinghouse data, Figure 1, to higher loading rates appears to be in reasonable agreement with available lower-shelf crack arrest data [24]. In fact, this observation may have influenced the positioning of the original trend lines, particularly for the limited high temperature data. However, this interpretation did not recognize the strong temperature-loading rate interactions which can occur, consequently extrapolated K_{Id} values in the high-temperature, high loading rate regime are significantly underestimated. The later fact can be seen by adding the present CPB data to the Westinghouse data as shown in Figure 12. This rather complex behavior can be better understood by also considering the accompanying schematics in Figure 12b and 12c.

The upturn in K_{Id} at the higher loading rates is not an artifact of the CPB technique. This strong strain rate dependence is also supported by the data of Kalthoff shown in Figure 13 which were obtained with a very different technique -- impact loading combined with high speed photography and the shadow optic method of caustics [25]. Although these data are limited to room temperature, they clearly show the same trend as the elevated temperature CPB data in Figure 12.

Combining all of the above results provides a three-dimensional view of the interactive dependence of fracture toughness on temperature and loading rate as shown in Figure 14. This view is also consistent with the notion that crack arrest occurs when the crack fails to reinitiate when acted upon by reflected stress waves. Thus, it would appear that the present limited high temperature K_{Id} data, along with improper static, linear elastic interpretations of small-scale crack arrest data, may combine to result in overly conservative estimates of the materials' resistance to crack growth at elevated temperature.

It is important to recognize that Figure 12 will also be influenced by another important variable -- material aging due to irradiation embrittlement. The extent of this aging is tracked through the nuclear surveillance program which requires exposure of tensile, Charpy and fracture toughness specimens to the irradiation which occurs in the critical beltline region of reactors. In this regard, the CPB technology is significant in that it enables dynamic fracture/crack arrest toughness data to be obtained for the first time using the small specimens which are available from surveillance capsules. For example, based on the Eq. 3, and a room temperature dynamic yield strength of 645 MPa for A533B steel [26] (with an irradiation fluence of 6.5 x 10^{19} n cm^{-2}) would enable a valid toughness measurement of up to 300 MPa$\sqrt{m}$ for a typically sized surveillance specimen (W = 29 mm).

As continued aging occurs and more vessels exhibit unacceptable levels of upper-shelf static toughness, it will become increasingly advantageous to develop more precise, and less conservative, assessment procedures that take full advantage of emerging technology -- such as the CPB technique, as well as advances in computational fracture mechanics.

SUMMARY AND CONCLUSIONS

The utility of a novel approach to generating dynamic initiation and propagation fracture toughness has been demonstrated using an integrated experimental/analytical approach. This approach, termed the Coupled Pressure Bar (CPB) technique, uses stress wave loading to achieve loading rates for crack initiation of about 10^6 MPa$\sqrt{m}$ s^{-1}. These high loading rates are applicable to situations where cracks initiate, run, arrest, and are subsequently *reinitiated* by reflected stress waves -- a scenario which can occur in nuclear pressure vessels during a pressurized thermal shock event. Results demonstrate that dynamic toughness data can be generated for the sizes and toughness levels of interest for small specimens of embrittled pressure vessel steels which are found in nuclear surveillance capsules. Somewhat larger specimens sizes can also be used with this technique to determine fracture toughness levels in the transition- and upper-shelf regimes of higher toughness unirradiated pressure vessel steels. Specific conclusions based on this study are as follows:

1) The CPB technique provides a unique tool for determining dynamic fracture toughness of high-toughness materials over the full temperature range encompassing cleavage to fully-fibrous fracture. Additional advantages are as follows:

   a) small specimen size
   b) efficient energy storage external to the specimen
   c) stress waves provide high loading rates ($\dot{K} > 10^6$ MPa$\sqrt{m}$ s^{-1})
   d) well-behaved boundary conditions facilitate analysis
   e) specimen displacement and/or energy input can be specified independent of specimen size
   f) both dynamic initiation and propagation toughnesses can be measured with a single specimen
   g) crack arrest measurements are feasible (with minor modification of the existing system)

2) Since the CPB technique enables extremely high dynamic initiation and propagation toughness levels to be achieved with small specimens, requirements for specimen size are dictated by the validity criteria given in Eq. 3, and not by the need to promote rapid, unstable crack propagation by storage of a large amount of energy within the specimen.

3) Application of the CPB technique to A533B steel was used to demonstrate the loading rate sensitivity of A533B steel; specifically, increasing the loading rate from 1 (quasi static) to 2×10^6 MPa$\sqrt{m}$ s^{-1} resulted in a 25°C increase in the transition temperature, while the upper-shelf initiation toughness increased by 70%. These effects have important implications for dynamic reinitiation of cracks during hypothesized pressurized thermal shock events in nuclear pressure vessels.

4) The high-rate dynamic initiation toughness appears to provide an estimate of the crack arrest toughness, thereby supporting the notion that crack arrest corresponds to failure of the crack to reinitiate under loading from reflected stress waves.

5) Dynamic viscoplastic analysis is needed to extract dynamic fracture properties from high toughness materials using small specimens. Such analyses are presently tractable for crack initiation under high rate loading. However, analyses of dynamic crack propagation and arrest in viscoplastic materials are presently hampered by uncertainty regarding the proper crack driving force.

REFERENCES

1. Bass R. B., Pugh C. E., Merkle J. G., Naus D. J., and Keeney-Walker J., ASTM-STP 969, 1988, p. 691.

2. Shabitts W. O., Heavy Section Steel Technology Program, Technical Report No. 13, Westinghouse R&D, December 1970.

3. Hahn G. T., Hoagland R. G., Lereim J., Markworth A. J. and Rosenfield A. R., ASTM-STP 711, 1980, p. 289.

4. Rosenfield A. R., Mincer P. N., and Marschall C. W., ASTM-STP 945, 1988, p. 73.

5. Kussmaul K. and Gillot R., *J. Pres. Ves. Tech.*, Vol. 110, 1988, p. 129.

6. Naus D. J., Keeney Walker J., Bass B. R., Bolt S. E., Fields R. J., de Wilt R., and Low S. R., NUREG/CR 5330 (ORNL-TM 11083), Oak Ridge National Laboratory, Oak Ridge, Tennessee, 1989.

7. Couque H., Hudak Jr. S. J., and Lindholm U. S., *J. Phys.*, Suplément N°9, Tome 49, 1988, p. 347.

8. Couque H. and Lankford J., *Inst. Phys.*, Series 102, p. 89, 1989.

9. Couque H., Dexter R. J., and Hudak Jr. S. J., ASTM STP 1130, p. 24, 1992.

10. Dexter R. J., Hudak Jr., S. J., Reed K. W., Polch E. Z., and Kanninen M. F.: *Numerical Methods in Fracture Mechanics*, Luxmore A. R. *et al.*, eds, 1987, p. 173.

11. Bodner S. R. and Partom Y., ASME *J. Appl. Mech.*, Vol. 42, p. 176, 1968.

12. Dexter R. J. and Chan K. S., *J. Pres. Ves. Tech.*, Vol. 112, 1990, p. 218.

13. Kostrov B. V. and Nikitin L. V., *Archiwum Mechaniki Stovowanej*, 22, p. 749, 1970.

14. Freund L. B., *J. Elast.*, 2, p. 341, 1972.

15. Atluri S. N., *Eng. Fract. Mech.*, Vol. 16, p. 341, 1982.

16. Paris P. C., In written discussion to Landes J. D. and Begley J. A., ASTM-STP 514, p. 1, 1972.

17. Landes J. D. and Begley J. A., ASTM STP 632, p. 57, 1977.

18. Moran B., Asaro R. J., and Shih C. F., *Met. Trans. A*, Vol. 22A, 1991, p. 161.

19. Costin L. S., Duffy J., Freund L. B., ASTM STP 627, 1976, p. 301.

20. Couque H., Asaro R. J., Duffy J., and Lee S., *Met. Trans. A*, Vol. 19A, 1988, p. 2179.

21. Edmonds D. P. and McGowan J. J., Report NUREG/CR-3744, Vol. 2, Oak Ridge National Laboratory, Oak Ridge, TN, Vol. 2, 1984, p. 96.

22. Irwin G. R., ASTM-STP 627, 1983, p. 7, [11].

23. Couque H., Hudak S. J., Jr., Leung C. P., and Dexter R. J., EPRI final report RP 2426-22, March 1992.

24. Bass B. R. and Keeney-Walker J., EPRI/NRC-Sponsored Meeting on Dynamic Fracture Analysis, San Diego, June 1991.

25. Kalthoff J. F., *Eng. Fract. Mech.*, Vol. 23, p. 58, 1986.

26. Steichen J. M. and Williams J. A., Heavy Section Steel Technology Program, Technical Report No. 32, Westinghouse Electric Company, 1973.

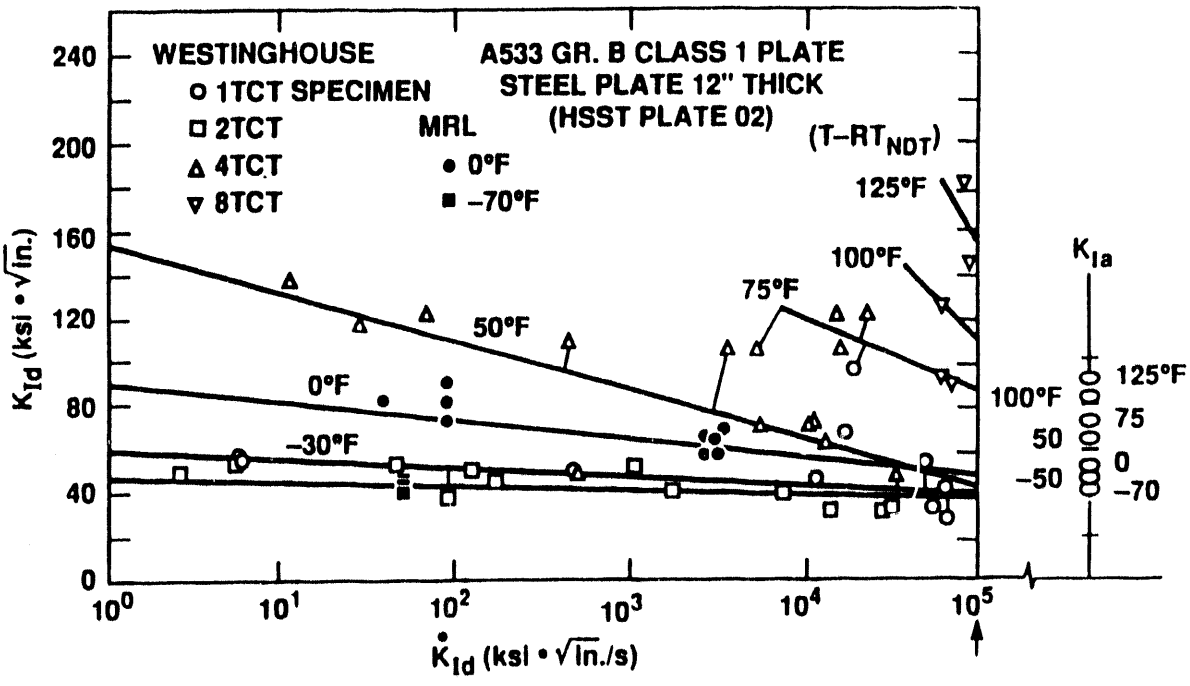

Figure 1. Westinghouse initiation data base[1]. Available lower shelf crack arrest data is also indicated[2].

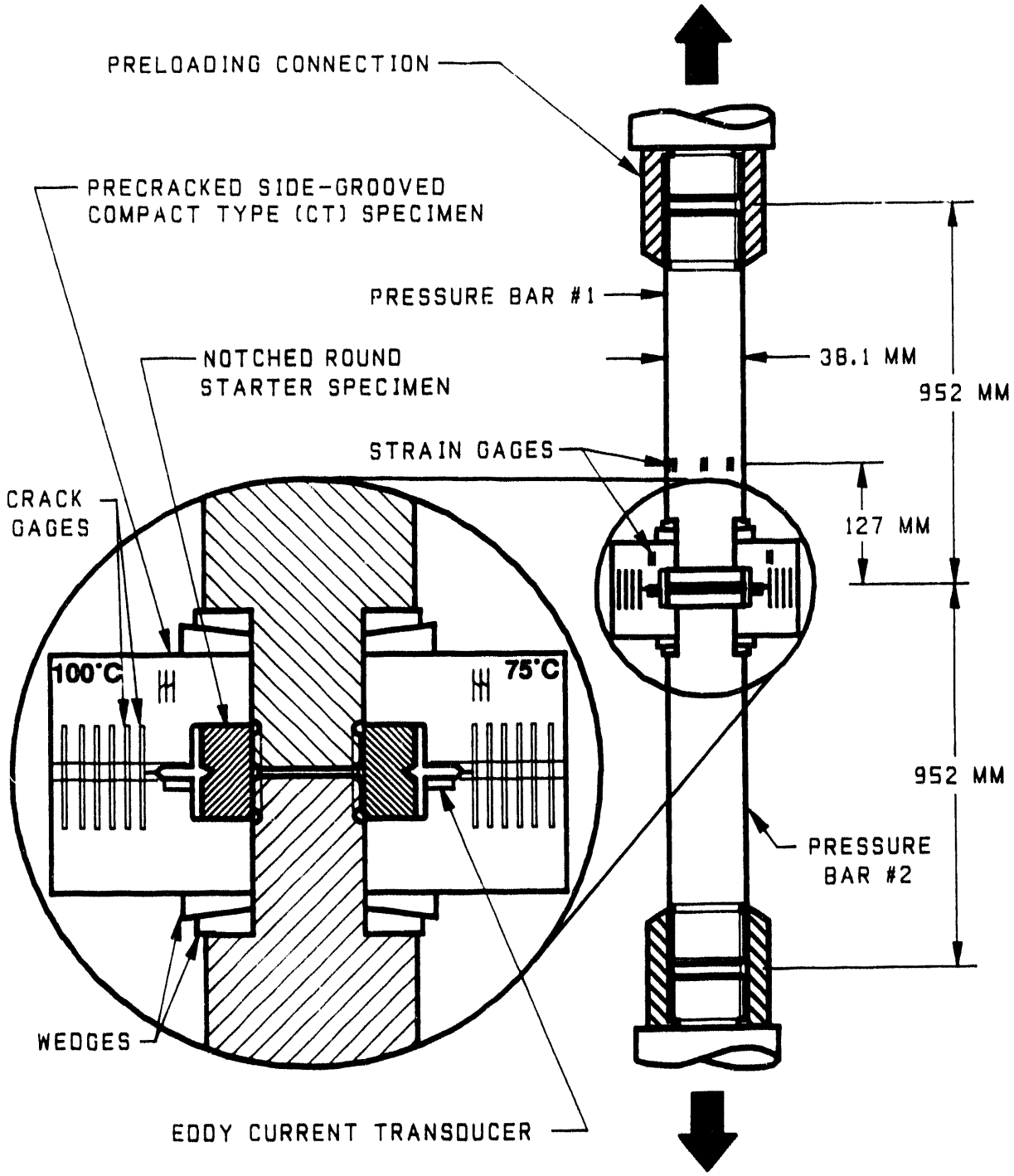

Figure 2. Schematic of the couple pressure bars experiment used with A533B specimens.

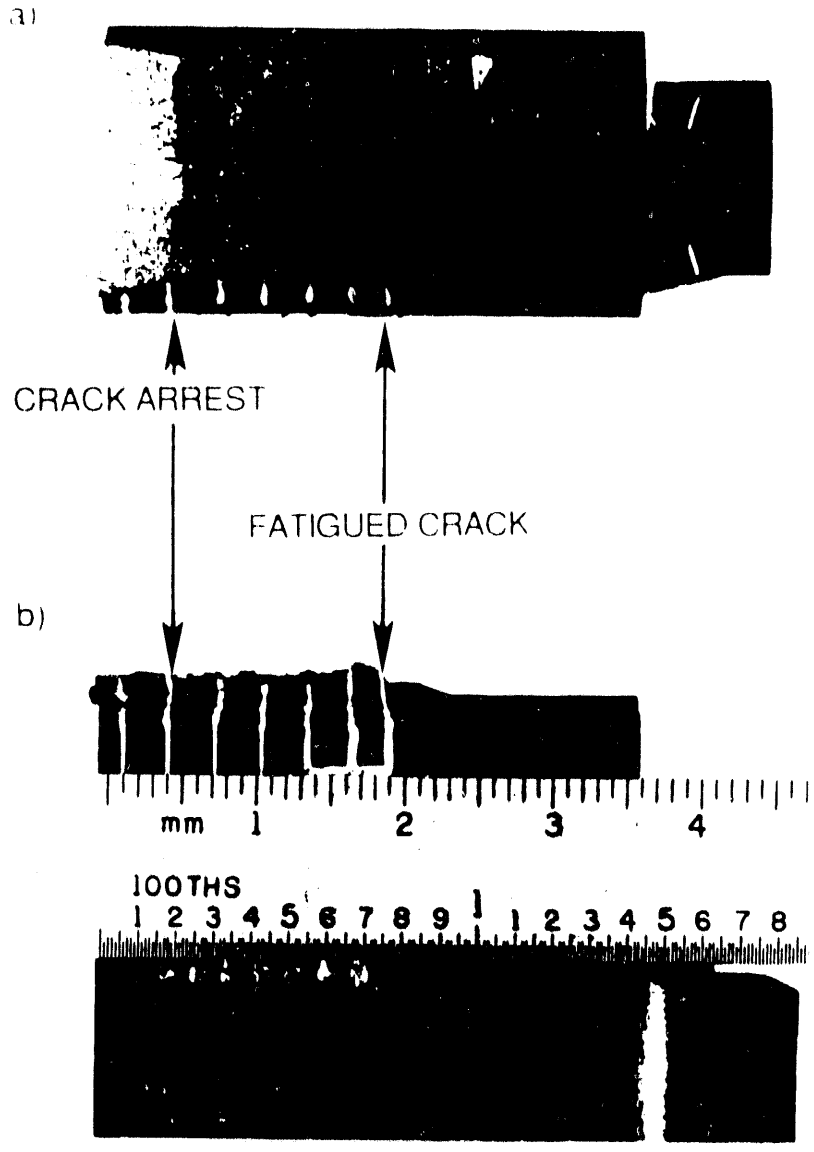

Figure 3. A533B specimen tested at 100°C: a) fracture surface, b) crack profile.

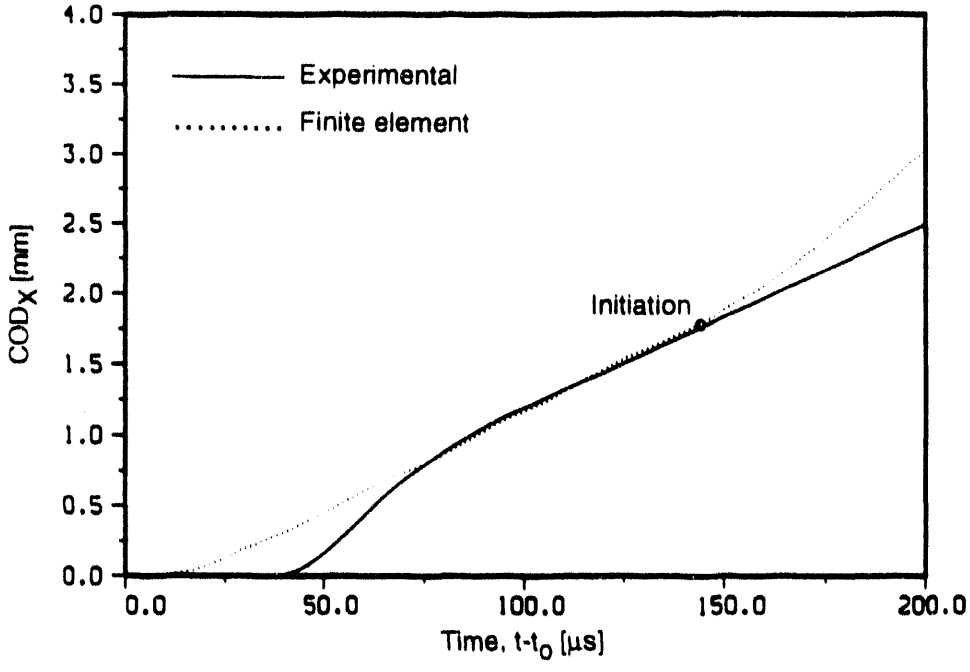

Figure 4. Comparison of measured and calculated crack opening displacement records $COD_X(t)$ for the A533B tested at 100°C.

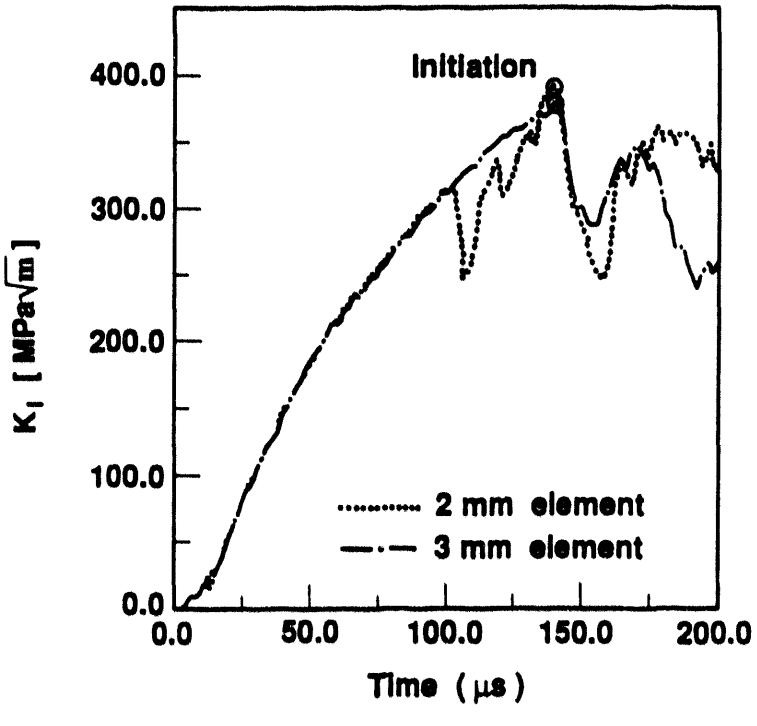

Figure 5. History of the crack driving force, $K_I(t)$, calculated with two mesh sizes of linear dimension 2mm and 3mm, for the A533B tested at 100°C.

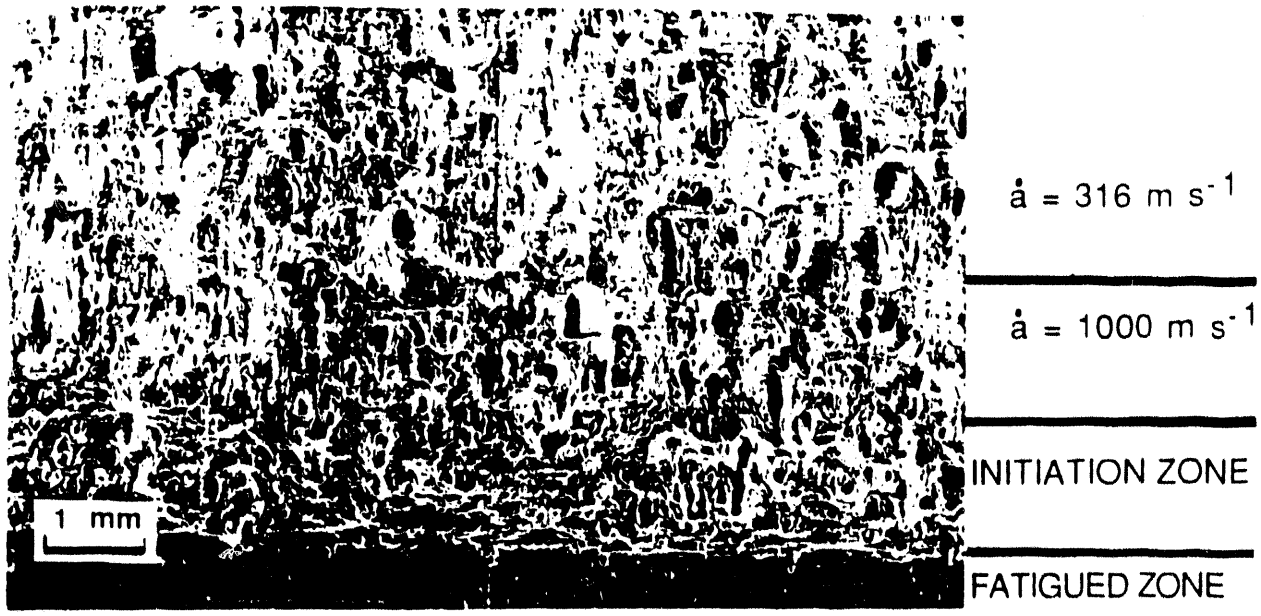

Figure 6. Scanning electron fractograph adjacent to the prefatigued crack-tip of the A533B tested at 100°C. The crack velocities reached during the early stage of the rapid crack propagation event are also indicated.

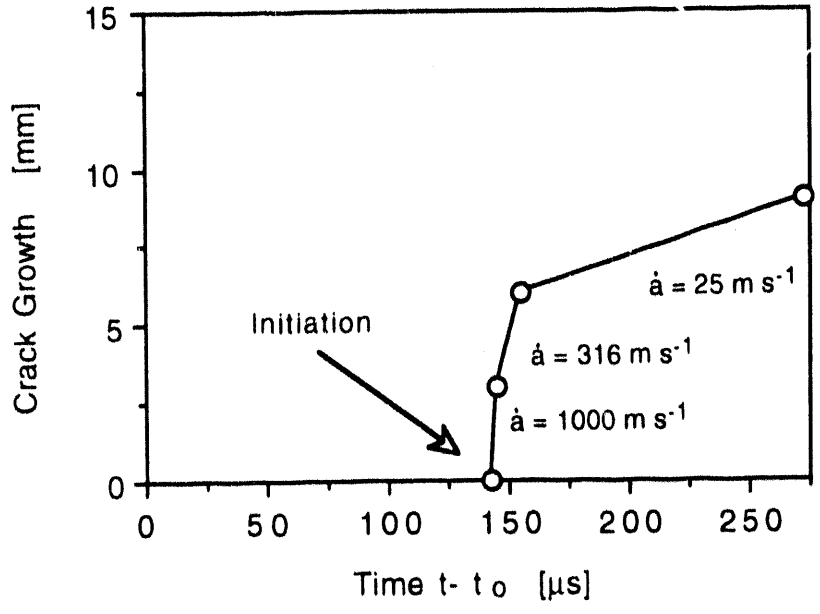

Figure 7. Crack growth history of the A533B tested at 100°C.

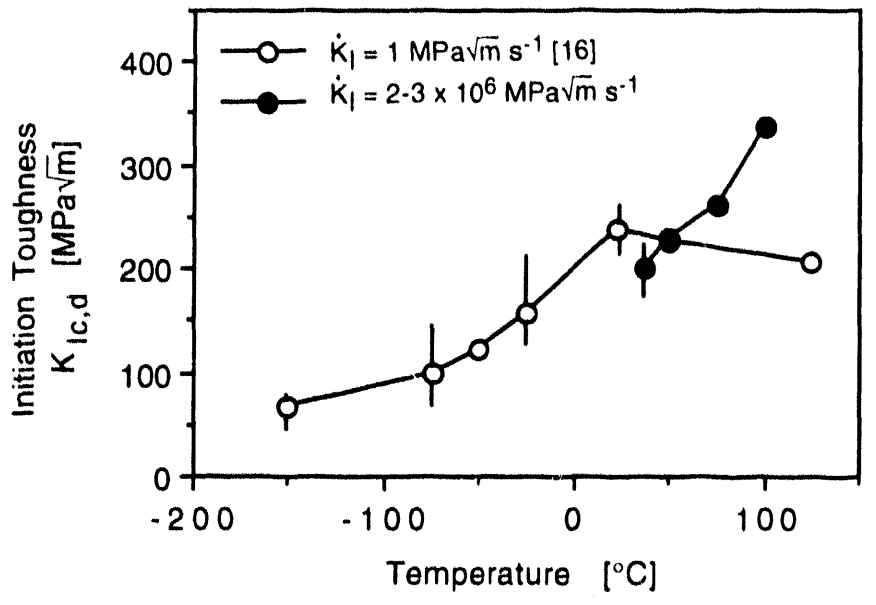

Figure 8. Comparison of A533B static and dynamic fracture initiation toughness over the temperature range 37 to 100°C.

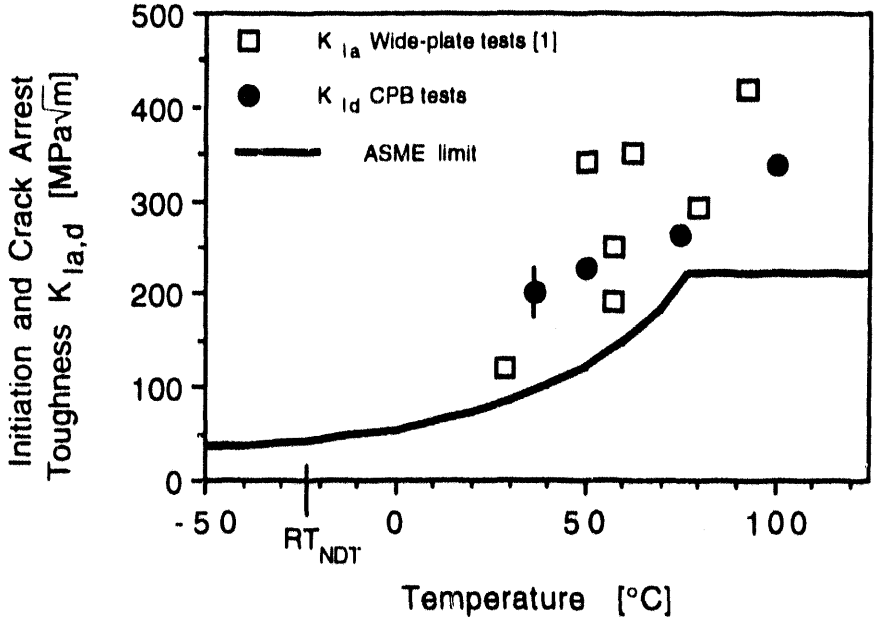

Figure 9. Dynamic fracture initiation toughness (K_{Id}) and crack-arrest toughness (K_{Ia}) of A533B steel. The fracture toughness values prescribed by Section XI of the ASME boiler and pressure vessel code are also indicated.

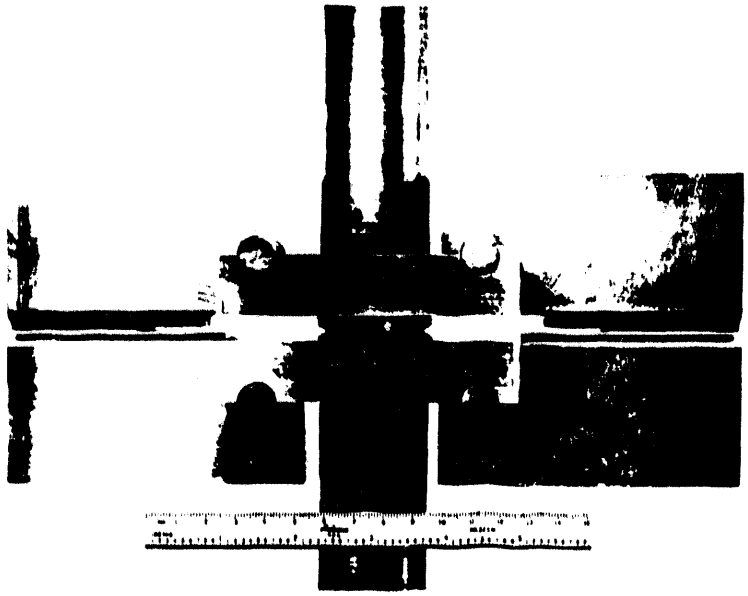

Figure 10. Coupled pressure bars experimental set-up with fracture specimens of large planar size, W = 89 mm.

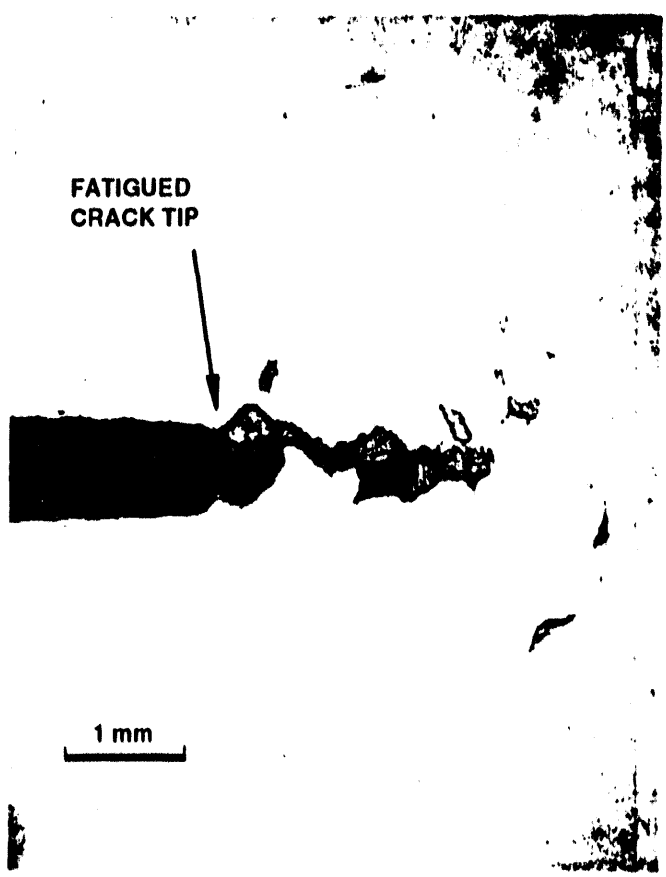

Figure 11. Enlarged view of the prefatigued crack for the large A533B specimen size, W = 89 mm, tested at 100°C showing crack growth of 2 mm.

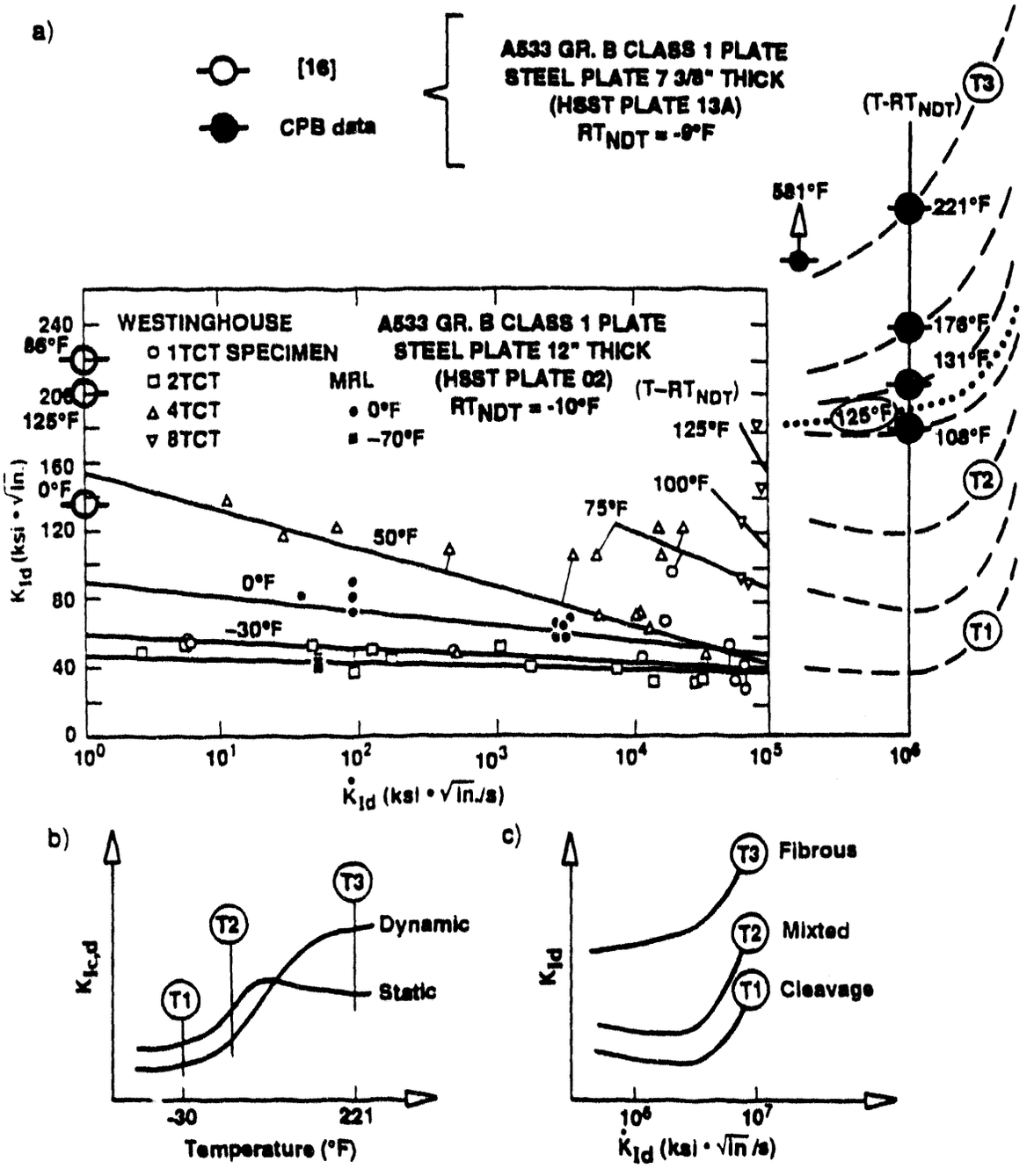

Figure 12. Extension of Westinghouse initiation data base (A533B, HSST plate 02)[1] to the $10^{6\text{-}7}$ ksi$\sqrt{m}$ s^{-1} loading rate regime using CPB data (A533B, HSST plate 13A) at transition and upper shelf temperatures and Kalthoff[3] toughness-loading rate relationship for lower-shelf temperatures of a rate-sensitive steel. The toughness-loading rate dependance for cleavage (T1), mixed fracture (T2), and fibrous fracture (T3) are schematically represented: a) initiation toughness versus temperature, and b) initiation toughness versus dynamic loading rates.

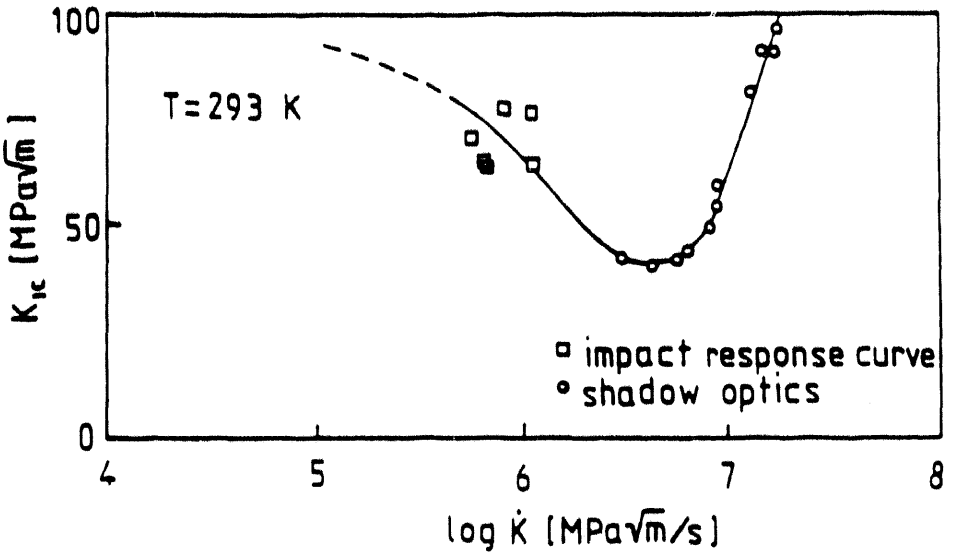

Figure 13. Toughness lower bound of a steel X_2NiCoMo 1895 (German Standards) reached at a loading rate $\dot{K}_I$ of 3 x 10^6 MPa$\sqrt{m}$ s^{-1} [3].

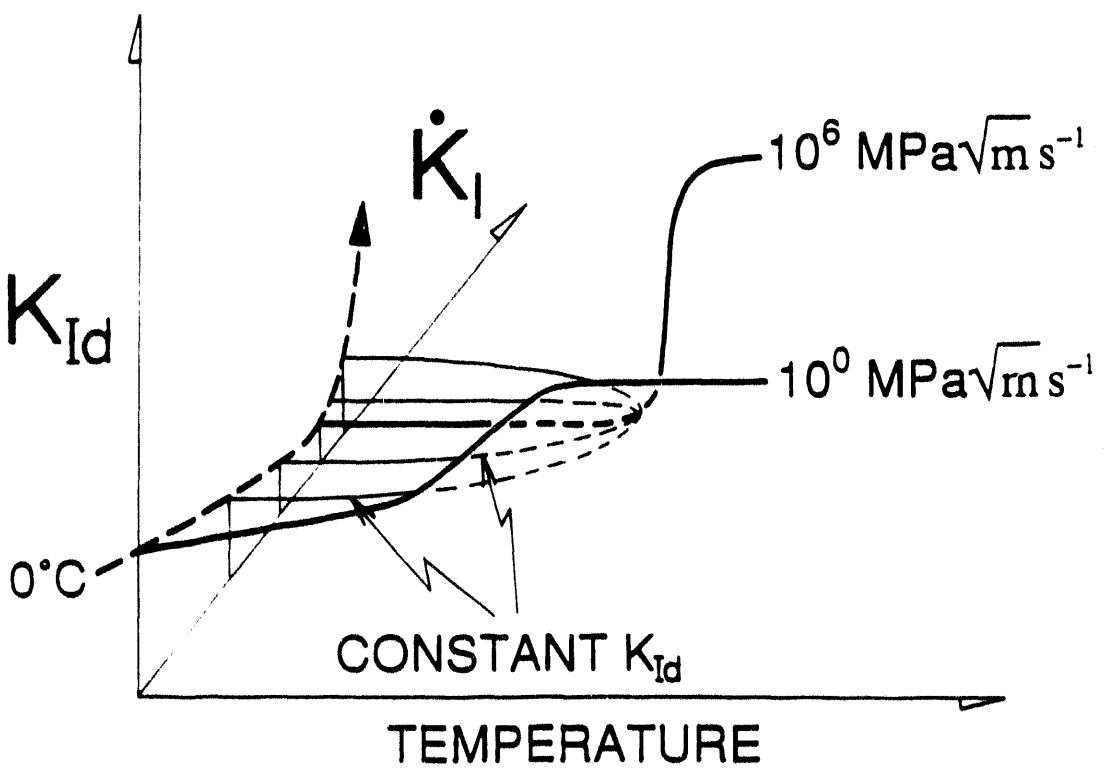

Figure 14. Dynamic crack initiation data (K_{Id}) as a function of loading rate ($\dot{K}_I$) and temperature.

Table 1

Chemical Composition and Heat Treatment of A533B Steel Grade B Class 1 Steel Plate 13A[a]

Chemistry in Weight Percent						
C	Mn	P	S	Si	Ni	Mo
0.19	1.28	0.012	0.013	0.21	0.65	0.55

Heat Treatment

Normalized 7.5 h at 893°C, water quenched;
Austenitized 8.5 h at 671°C, water quenched;
Tempered 4 h at 565°C, air cooled;
Stress relieved 50 h at 621°C, furnaced cooled to 316°C.

Table 2

Dynamic Initiation Fracture Toughness Results

Testing Temperature [C°]	Fibrous Mode[a] [%]	K_{Id} Uncorrected [MPa$\sqrt{m}$]	σ_{yd} [MPa]	α	B_N [mm]	K_{Id} Corrected [MPa$\sqrt{m}$]	$\dot{K}_I$ [10^6 MPa $\sqrt{m}s^{-1}$]
37	30	220	501	27	11.5	220	2.2
37	30	180	501	40	11.5	180	2.0
50	85	250	491	21	11.5	228±8	2.4
75	100	262	480	24	15.0	262	2.1
100	100	398	476	10	15.0	337±16	2.8

a) Percentage of initiation zone, defined as region within one calculated crack-tip-opening displacement using procedure outlined in Reference 20 and A533B dynamic tensile data

Table 3

Summary of the Failure Modes Involved in the CPB Specimens of A533B Steel

Testing Temperature [°C]	Initiation	Propagation	Arrest
	Fibrous Mode [%]	Failure Mode as a Function of Crack Extension $a-a_0$	Fibrous Mode [%]
37	30	cleavage for $a-a_0$ varying from 0.5 to 12.5 mm	100
50	85	cleavage for $a-a_0$ varying from 0.5 to 12.0 mm	100
75	100	cleavage for $a-a_0$ varying from 1 to 9.5 mm	100
100	100	no cleavage observed (total growth 15 mm)	100

ENERGY RELEASE RATE FOR CRACKS IN NON HOMOGENEOUS MEDIA

J. BROCHARD, A. COMBESCURE
CEA/CEN SACLAY, 91191 GIF-SUR-YVETTE CEDEX, FRANCE

X.Z. SUO
EUROSIM SARL, Av. des Andes, 91952 LES ULIS CEDEX, FRANCE

H. HOROWITZ
CEA/CEN FONTENAY, BP 6, 92265 FONTENAY-AUX-ROSES CEDEX, FRANCE

1. INTRODUCTION

In this paper, we give two new results that allow to compute the energy release rate G in a media with spatially varying elastic properties.

In this special case, it is shown that the classical G or J formulae are not appropriate and that auxiliary terms should be added to the expressions to keep their independance with the contour of integration. The new integrals have been implanted in the finite element computer code CASTEM 2000, and the efficiency of the additional terms is presented on some examples.

2. CRACKED BODY WITH CONTINUOUSLY VARYING MATERIAL PARAMETERS

2.1. Theoretical expression for G

For a non homogeneous cracked body Ω, under general loading conditions in the elastic range, the following analytical expression for the energy release rate can be derived [1], where G_{hom} represents the energy release rate when the material is considered as homogeneous, and G_{add} an additional contribution when the material is non homogeneous.

$$G = G_{hom} + G_{add} \qquad (1)$$

with $G_{hom} = \int_\Omega Tr(\sigma\ \nabla U\ \nabla\Theta)d\Omega - \int_\Omega w\ div\Theta\ d\Omega + \int_\Omega Tr(\sigma)\ \alpha\ \nabla T\ \Theta\ d\Omega - \int_\Omega F\ \nabla U\ \Theta\ d\Omega$

and $G_{add} = \int_\Omega Tr(\sigma)\ \nabla\alpha\ \Theta\ T\ d\Omega - \frac{1}{2}\int_\Omega Tr(\nabla R\ \Theta\ \varepsilon\ \varepsilon)\ d\Omega$

Notations :

ε : total strain tensor,
σ : stress tensor,
U : displacement vector,
w : strain energy density,
F : body force vector,
T : temperatures (variation in comparison with the reference state),
Θ : mapping function (explained below),

α : thermal expansion coefficient,

R : elastic constitutive tensor.

and ∇ : gradient operator.

$Tr(c) = \sum C_{ii}$: operation Tr on a matrix C_{ij}

The mapping function Θ is a normalized displacement field, oriented in the direction corresponding to a crack length increase.

For example, in a bidimensionnel configuration (figure 1), it is equal to (1, 0) in all region A near the crack tip, varies continuously from (1, 0) to (0, 0) in a surrounding crown, and is equal to (0, 0) outside.

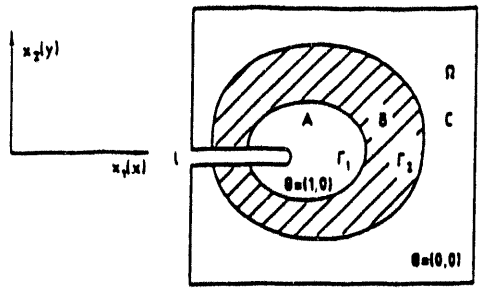

Figure 1 : Mapping function Θ for a bidimensionnel configuration

2.2. Application : center-cracked plate with varying material parameters

Let us consider the problem of a center-cracked plate, with non homogeneous elastic material parameters, and under plane-stress condition.

The plane is assumed to be subjected to two systems of loadings :

1) a uniform tensile stress σ = 50 MPa,
2) a linear thermal gradient, ΔT = 330°C, between the crack faces and the plate boundary (figure 2).

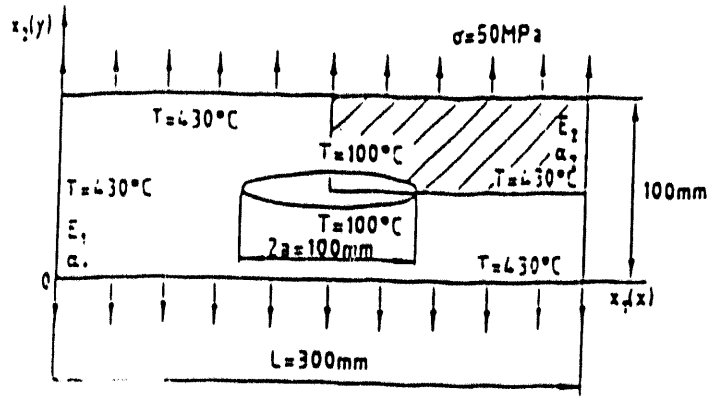

Figure 2 : Center-cracked plate with a non homogeneous material

Young's modulus E and thermal expansion coefficient α are assumed to vary linearly in the x-direction :

$$E(x, y) = E_1 + \frac{x}{L}(E_2 - E_1)$$

$$\alpha(x, y) = \alpha_1 + \frac{x}{L}(\alpha_2 - \alpha_1),$$

the extreme values on left and right boundaries being fixed to :

$$E_1 = 1.2\ 10^5\ \text{MPa} \qquad E_2 = 3.8\ 10^5\ \text{MPa}$$

$$\alpha_1 = 6.0\ 10^{-6}\ °C^{-1} \qquad \alpha_2 = 25.0\ 10^{-6}\ °C^{-1}$$

The calculation was performed using CASTEM 2000 computer code, on one quarter of the plate modelled with 370 constant strain triangular elements (figure 3).

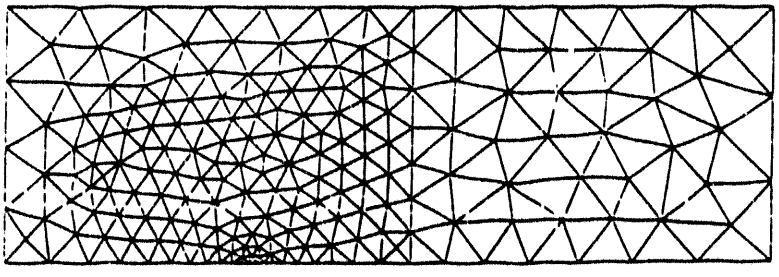

Figure 3 : Finite element model

Θ contours, around the crack tip (notation Γ_1 on figure 1) were defined to analyse the stability of the computed G-values (figure 4).

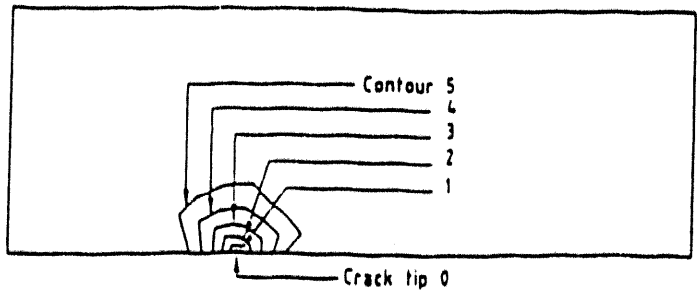

Figure 4 : 5 contours limiting the region A for the 5 Θ-fields

Thermal and mechanical loading were independantly taken into account. In each case, the influence of the additional term G_{add} in the ernergy release rate formula was studied. Results are depicted on figures 5 and 6, and we may concluded that :

- the additional term G_{add} guarantees the stability of the computed G values with more and more extended Θ displacement fields,
- the additional term G_{add} is not negligible.

The second point is particularly true in the thermal loading case, where the omission of the additional term can lead to an important error.

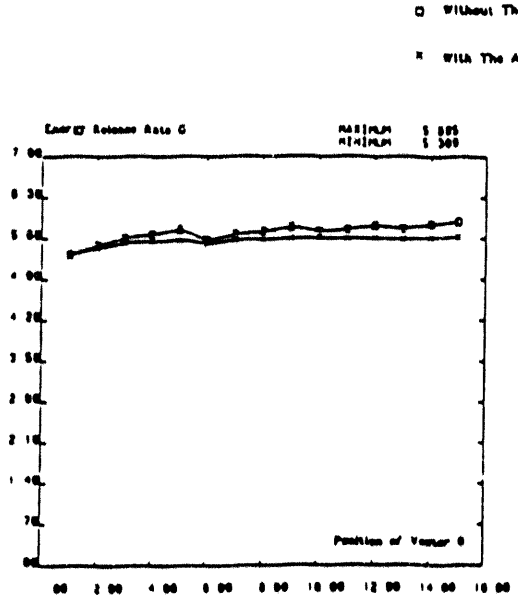

Figure 5 : G as function of the Θ vector mechanical loading

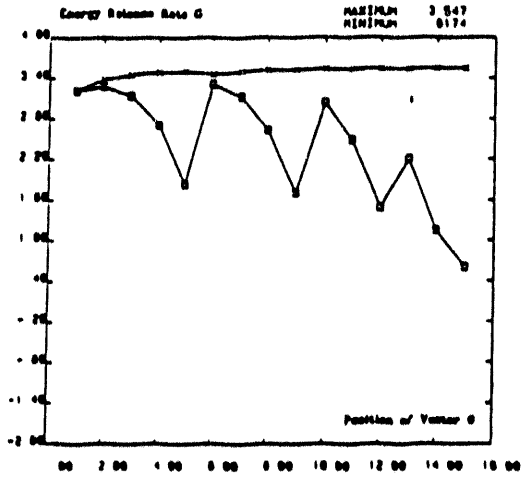

Figure 6 : G as function of the Θ vector thermal loading

3. CRACKED BODY WITH A BIMETALLIC INTERFACE

3.1. Theoretical expression for G

Refering to the formulation of Delale and al. [2], the cracked body with a bimetallic interface is divised into three parts, and the integration over the whole body Ω is the sum of the integrations over the three parts (figure 7) :

$$\int_{\Omega} d\Omega = \int_{\Omega_1} d\Omega + \lim_{\xi \to 0} \int_{\Omega^*} d\Omega + \int_{\Omega_2} d\Omega$$

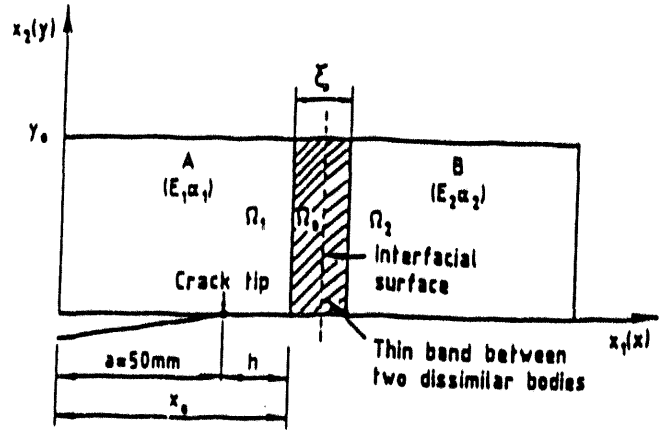

Figure 7 : Cracked body with a bimetallic interface

Volume integrations over Ω_1 and Ω_2 correspond to the formula (1), since material parameters in the two media are assumed continuous.

For the integration over Ω^*, with ξ tending to zero, it has been demonstrated that this term corresponds to a line integral along the interface. In a bidimensionnel case, with a straight interface along the y-axis, the G_{line} term is expressed by (2) :

$$G_{line} = \int_0^{y_0} (w_a - w_b)\Theta_x \, dy + \int_0^{y_0} \left[\sigma_b \, n \, \frac{\partial U}{\partial x}\Big|_b - \sigma_a \, n \, \frac{\partial U}{\partial x}\Big|_a \right] \Theta_x \, dy \qquad (2)$$

with w : elastic energy density,
U : displacement vector,
n : normal to the discontinuity.

a and b subscripts design left and right side of the discontinuity.

3.2. Application : crack perpendicular to a bimetallic interface

Erdogan and Lu ([3] and [4]) give analytical solutions of the stress intensity factor, for cracks perpendicular to and on the interface of bonded elastic layers. Results are given in diagrams for fixed material combinaison or layer dimensions. More specifically, we analysed the case of a pressurized edge crack, with a tip located near the interface (figure 8).

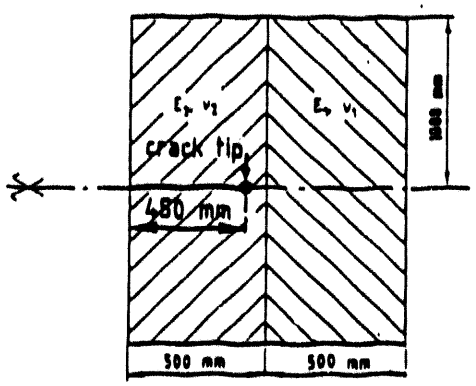

Figure 8 : Pressurized edge crack perpendicular to a bimetallic interface

Due to the symetry condition, one half of the plate was modelled with quadratic elements (figure 9).

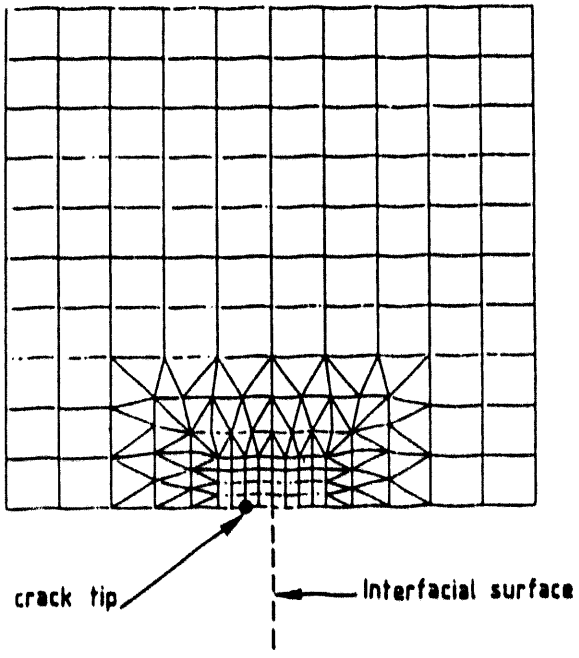

Figure 9 : Mesh for the pressurized edge crack

Computer G value agrees very well with that readed in Erdogan's diagram :

K/p $\sqrt{\pi a}$ values :	- computed	2.16
	- Erdogan's diagram	2.17

with $K = \sqrt{\frac{E_2\ G}{1 - \nu_2^2}}$

Furthermore, the stability of the G-values for Θ-fields crossing the interface is verified.

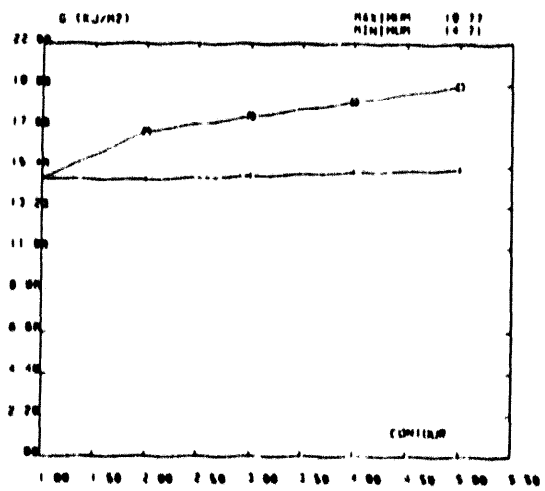

□ without additional term

+ with additional term

Figure 10 : G-values stability analysis

4. CRACKS PARALLEL TO OR LYING ALONG BIMATERIAL INTERFACES

For a crack parallel to or lying along bimaterial interfaces, no corrector term has to be added to the classical formula G_{hom}, since a virtual crack advance does not lead to cross the discontinuity. This application is presented just as an example to verify the precision of the computed G-values in this special case.

Let us consider the problem of a pressurized crack lying along a bimaterial interface, in an infinite plate (figure 11).

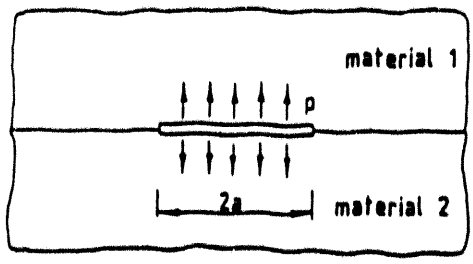

Figure 11 : Pressurized crack lying along a bimaterial interface

England [5] gave the expression of the complex stress concentration vector Q, for this case :

$$Q = Q_1 + i\,Q_2 = p\sqrt{\pi a}\,(1 + i\,2\varepsilon)$$

with :

$$\varepsilon = \frac{1}{2\pi} \ln \left\{ \frac{\frac{k_1}{G_1} + \frac{1}{G_2}}{\frac{1}{G_1} + \frac{k_2}{G_2}} \right\}$$ (bimetallic constant introduced by Williams [6])

G shear modulus and $k = 3 - 4\alpha$ in plane strain condition.

Shih and As.. [7] had identified the relation between the complex stress concentration vector Q and the energy release rate G :

$$G = \frac{(Q_1^2 + Q_2^2)\left(\frac{1 - \nu_1}{G_1} + \frac{1 - \nu_2}{G_2}\right)}{4 \cosh^2 \pi \varepsilon}$$

A calculation was performed with the G-Θ method using always the computer code CASTEM 2000. Properties of the two materials was choosen strongly different (figure 12).

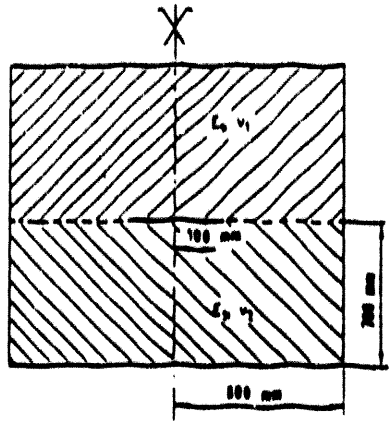

$E_1 = 2\ 10^4$ MPa
$\mu_1 = 0.45$

$E_2 = 2\ 10^5$ MPa
$\mu_2 = 0.15$

p = 10 MPa

Figure 12 : Geometry and material parameters for the pressurized interface crack

Taking into account the symetry condition, one half of the plate was modelled with quadratic elements (figure 13 and 14).

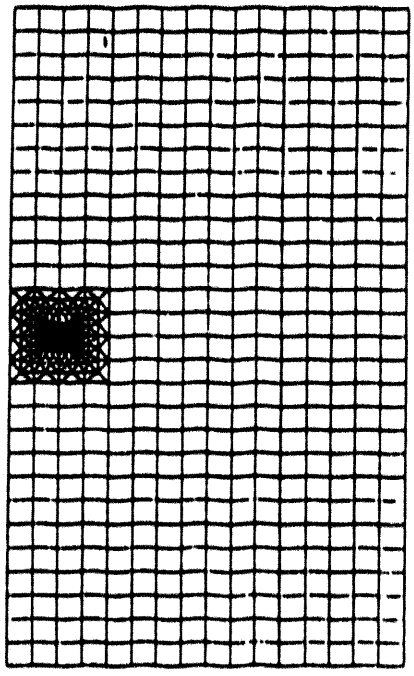

Figure 13 : Mesh for the interface crack

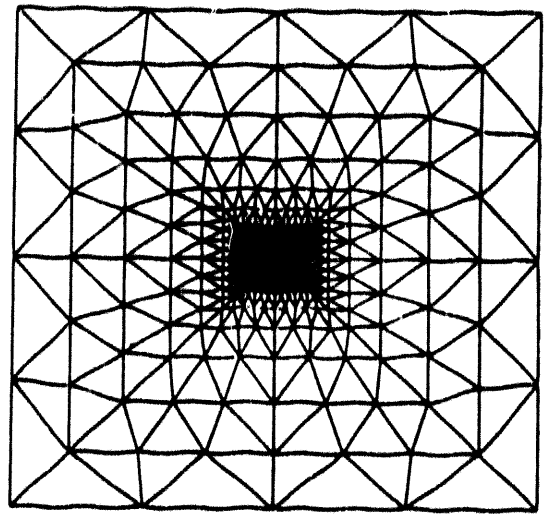

Figure 14 : Zoom near the crack tip of the interface crack mesh

The calculated G-value is in good agreement with the analytical solution (difference < 0.5 %) :

analytical value : $G = 0.702$ KJ/m^2
calculated value : $G = 0.705$ KJ/m^2

and the stability of the computed G-values is well verified (figure 15).

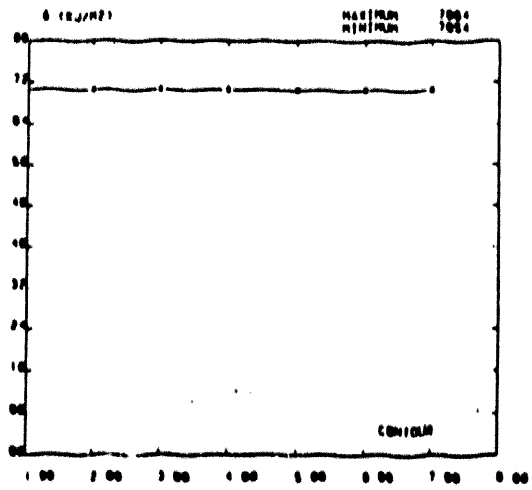

Figure 15 : Stability analysis fot the interface crack

5. CONCLUSION

The interest of the new formulations of the G-Θ method to take into account spatial variations of the elastic material properties, either continuous variations or brutal discontinuity, has been demonstrated on some examples.

In the case of a crack parallel to or lying along a bimaterial interface, no corrector term has to be added, and the classical formulation gives precise results.

But when the crack is not parallel to the interface, and the crack tip is exactly at the discontinuity of material, there is a special difficulty, not mentionned in the paper. In this particular case, the order of the elastic stresses singularity ($r^{\lambda-1}$ with $0 < \lambda < 1$) leads to indefined terms in the expression of G. However the stress intensity factor remains defined, and analytical solutions are given in references (for example [4]).

REFERENCES

[1] Suo, X. Z., and Combescure, A., "Energy Release Rate and J-Integral for any non homogeneous material." PVP New Orleans, Vol. 233, pp. 173-180 (1992).

[2] Delale, F., and Erdogan, F., "On the Mechanical Modeling of the Interfacial Region in Bonded Half-Planes." Journal of Applied Mechanics, Vol. 55, pp. 317-324 (1988).

[3] Ming-Che, Lu, and Erdogan, F., "Stress Intensity Factors in Two Bonded Elastic Layers Containing Cracks Perpendicular To And On The Interface. I. Analysis." Engineering Fracture Mechanics, Vol. 18, No. 3, pp. 491-506 (1983).

[4] Ming-Che, Lu, and Erdogan, F., "Stress Intensity Factors in Two Bonded Elastic Layers Containing Cracks Perpendicular To And On The Interface. II. Solution." Engineering Fracture Mechanics, Vol. 18, No. 3, pp. 507-528 (1983).

[5] England, A. H., "A Crack Between Dissimilar Media," ASME Journal of Applied Mech., Vol. 32, pp. 400-402 (1965).

[6] Williams, M. L., "The Stresses Around a Fault or Crack in Dissimilar Media," Bulletin of the Seism. Society of America, Vol. 49, pp. 199-204.

[7] Shih, C. F., and Asaro, R. J., "Elastic-Plastic Analysis of Cracks in Bimaterial Interfaces: Part I - Small Scale Yielding." Journal of Applied Mechanics, Vol. 55, pp. 299-316 (1988).

MATHEMATICAL MODELLING OF STRESS-DEFORMATION STATE OF THE STEAM GENERATOR COLLECTOR (WWER-TYPE) UNDER PRESSURE LOADING DURING FRACTURE MECHANICS CALCULATIONS

M. Zaitsev, V. Lyssakov
Nuclear Safety Institute of Russian Academy of Sciences

Description of Construction

The steam generator collector (WWER-type) is a thick cylindrical shell with a constant inner diameter of 850 mm and a height of 4970 mm. The wall thickness of the lower part of the shell is 78 mm. The wall thickness of the perforated part is 163 mm. The wall thickness is slightly increasing from the lower part of the shell to the perforated part. A wall perforation presents a system of holes to connect the steam generator heat exchanging tubes. The holes are disposed as in a chess-board-like order with a step along the height equal to 38 mm and with an angle of 3 degrees. The perforation zone starts from a height of 789 mm and finishes at a height of 2841 mm. Below the height of 1239 mm one half of the shell is nonperforated on this figure elements of nonperforated zone are shown within the thick line area. Above this height the nonperforated zone is smoothly decreasing and after a height of 1839 mm the regular perforated zone is located. Such type of perforated zone structure was chosen due to the design of the steam generator since the space between the wall of the lower part of the steam generator and the collector is rather small and there is no possibility to install heat exchanging tube therefore the collector has no perforations. Thus a nonperforated wedge in the perforated zone causes stress concentration. Inner pressure equals 16 MPa.

Mathematical Modelling

Fracture mechanics calculations demand an exact definition of a stress-deformation state of a large scale construction. A finite element method for stress and structure analysis is widely used for such definition of the stress state. However, certain designs like the WWER steam generator

collector are rather difficult to analyze. A large number of holes, a nonperforated wedge in perforated zone and appearance of a penetrating fracture in the collector wall are three actual concentrators of stresses. There is no versatile finite element model to describe this state. The first cause of this fact is the large amount of holes and the large wall thickness. A well known rule for finite element models creation gives the specific size of the element which is of hole radius. The ratio of the whole volume of the collector and the volume of one element gives the number of elements in this finite element model. This number of about 100,000. The above model actually requires super computing. The numerical definition of stress in the collector structure with a penetrating fracture to facilitate computation using PCS was based on a number of finite element models.

The first model defines the stresses in the collector, which is presented as a structure consisting of two materials. The second material possesses an average property of the perforated structure. Since the first model is a very rough approach, the stress of one section with two materials was analyzed in detail with the help of the second finite element model.

The third finite element model is necessary to define the real stress in the hole region. Following models describe the stress concentrations with the presence of a crack and without it. These calculations are needed to define the critical length of the crack.

Definition of 3-D Stress State

The finite element model consists of 1512 solid 8-node elements and 2204 nodes. During calculations more crude models with lower number of elements were used. The cylindrical shell was made of 18 elements in the direction of length of cylindrical shell. Since only the lower and middle parts were under consideration, the upper surface of the finite element model was loaded by negative pressure of -16.2 MPa. The connection of the collector with the steam generator was modeled by fixing all the degrees of freedom in the lower part of the collector. The symmetry plane was created

by the collector axis and the top point of the nonperforated wedge. The finite element model is shown on Fig. 1.

The stress intensity is shown on Fig. 2 and Fig. 3. The discrepancy between the stress in the wedge region and the stress evaluated by the exact analytical solution of the thick tube shell (a theoretical solution does not depend on the elastic Young modulus and defines stress on the external surface of 42 MPa and on the internal surface as 51 MPa) is negligibly small. Some increase in stress intensity was found in the region of boundary between perforated and nonperforated zones (Fig. 3). On the internal surface the stress is greater than it is on the external surface (which is described by the theoretical solution of a thick cylindrical tube). Since the number of finite elements was limited due to the computer capabilities, in order to validate this finite element model a plane finite element model with a big number of elements in the direction of wall thickness was used. The stress intensity for this model caused by inner pressure is shown on the Fig. 4. The 14 elements on the left side in each layer (from 0 to 45 degrees) are those of the nonperforated zones. The results of the stress calculations of this more detailed model show a negligible increase of stress in the joint of the perforated and nonperforated materials. Thus, common stress distribution does not depend on the nonconformity of the properties of this structure. It was found that the increase in stress on the external surface of more elastic perforated materials was caused by the bending character of deformation of this particular design structure. Therefore, one may conclude that stress distribution of the thick cylindrical tube with uniform properties is not a distinct one with nonuniform properties. The average stress of such structure may be approximated by an exact theoretical solution for the thick cylindrical tube. This fact gives the possibility to investigate the stress concentration of the structure with a crack using a plane finite element model. A condition of the use of this finite element model transformation is in the application to the plane of the finite element model of maximal tensile stress in thick tubes.

There are also problems to define the real stress in the perforated zones of the collector structure for this transformation from a defined average stress of the thick tube. While defining the 3-D stress distribution in the collector structure shell finite element models were used. This model gave an intolerable distinction in the stress distribution comparing with the theoretical stress distribution of thick cylindrical tube. A detailed consideration of this distinction and the results of this 3-D stress calculation, using 3-D elements, has shown that the shell finite element models should not be used for a thick cylindrical tube. The numerical effects of the shell finite element models caused great increase of stress in the joint region of materials with different properties. Therefore it was found that thick shells with contemporary increasing properties were impossible to calculate by the shell finite element model.

Real Stress Definition in the Regular Perforated Zone

Real stress definition in the regular perforated zone was made with the help of two finite element models (Figs. 5-6). The reason of the use of two models is due to the influence of planes of their symmetry. The small angle between the planes of symmetry (the first model has an angle of 3 degrees) and the algorithm of the elastic plane would give some numerical effects in stress distribution. The results of the modelling with one and two holes (the angles between the planes are 3 and 6 degrees) give identical data for stress. The loading pressure equals to 32 MPa. The finite element model was restricted by the four planes of symmetry, two of the above planes are perpendicular to the collector axis and the two other planes had an angle of 3 degrees. The maximum stress intensity in those models reaches 231 MPa. A similar solution for the uniform media gives a value of 92.7 MPa. The coefficient of concentration equals to the stress ratio multiplied by the loaded area ratio and equals to 4.1. Thus the real stress in the perforated zone is greater than the average stress by the factor of 4.12. The intolerable numerical effect of finite element modelling

of those stress calculations is caused by the influence of the elasticity of the boundary planes of symmetry. A large angle between the planes of symmetry is to be used.

Definition of a Stress Concentrator in a Structure with a Through Failure

The finite element model for calculations of the stress in a structure with a failure is shown on Fig. 8 (stress intensity).

The tensile stress on the boundary in the X-direction is greater than the tensile stress in the Y-direction. The stress intensity wedge region is shown on Fig. 7. One may conclude that the stress in wedge region is regular in the model without failure and is intolerable and irregular in the model with failure (Fig. 8). The stress concentration coefficient is equal to the ratio of the maximal stress in the model with failure and the maximal stress in the model without failure and reaches the value of 3.1. This fact is in agreement with the experimental data obtained on the photoelastic models, manufactured in scales 1:10 and 1:17.5. A numerical effect in this modelling may be performed if the displacement of the boundaries is large enough.

References

R. D. Cook, "Concepts and Applications of Finite Element Analysis," Second Edition John Wiley & Sons, New York.

K. J. Bathe, E. L. Wilson, and R. Iding, "NONSAP - A Structural Analysis Program for Static and Dynamic Response of Nonlinear Systems, SESM Report Number 74-3, University of California, Berkeley, 1974.

O. C. Zienkiewics, The Finite Element Method, McGraw-Hill, Book Co. Ltd., 1977.

"Results of Investigation Crack Opening and Stress State of Primary Circuit Collector of PGV-1000M using Optical Model," Report 8.14-12363. OKB "Gidropress", 1990.

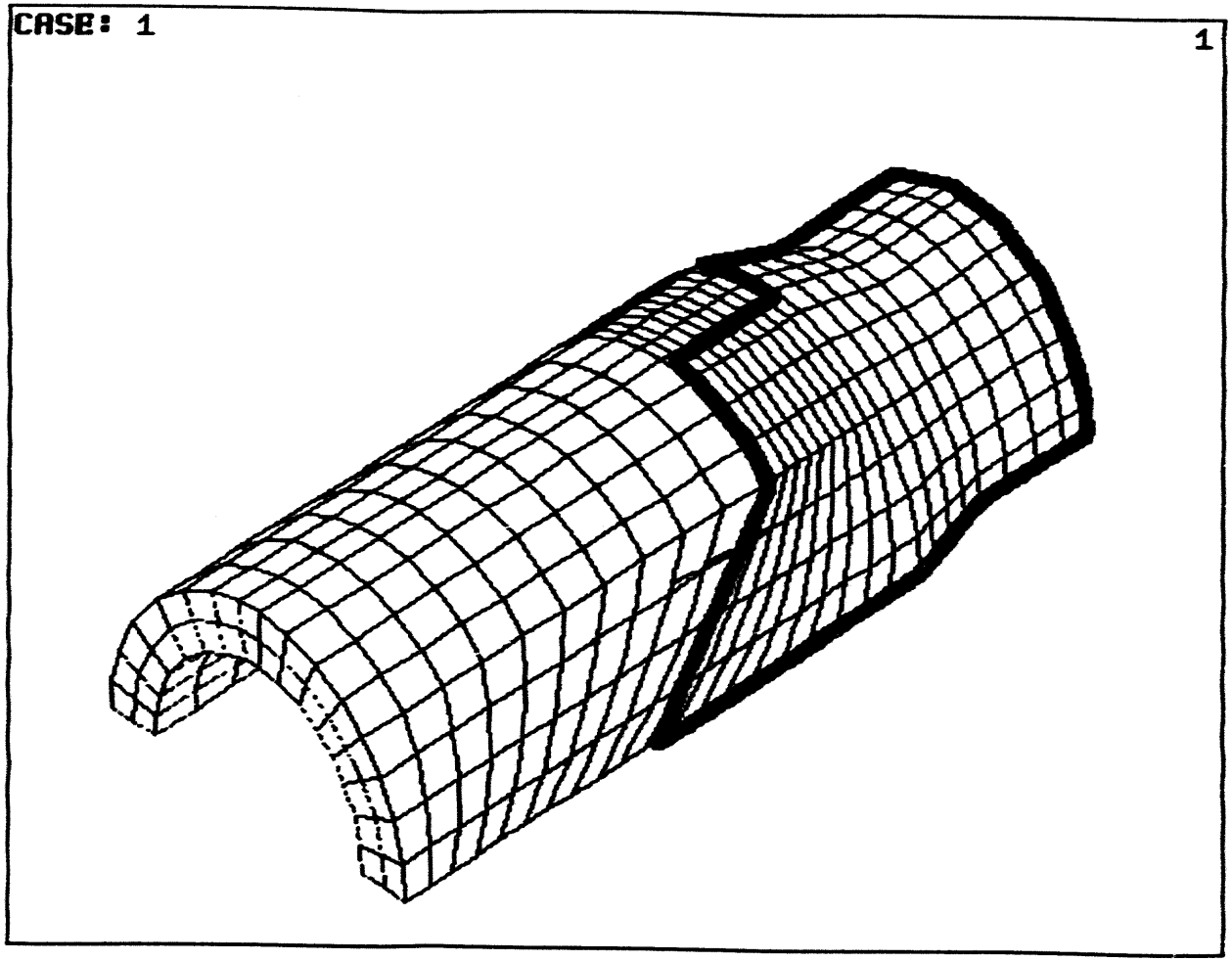

Fig. 1 Finite Element Model

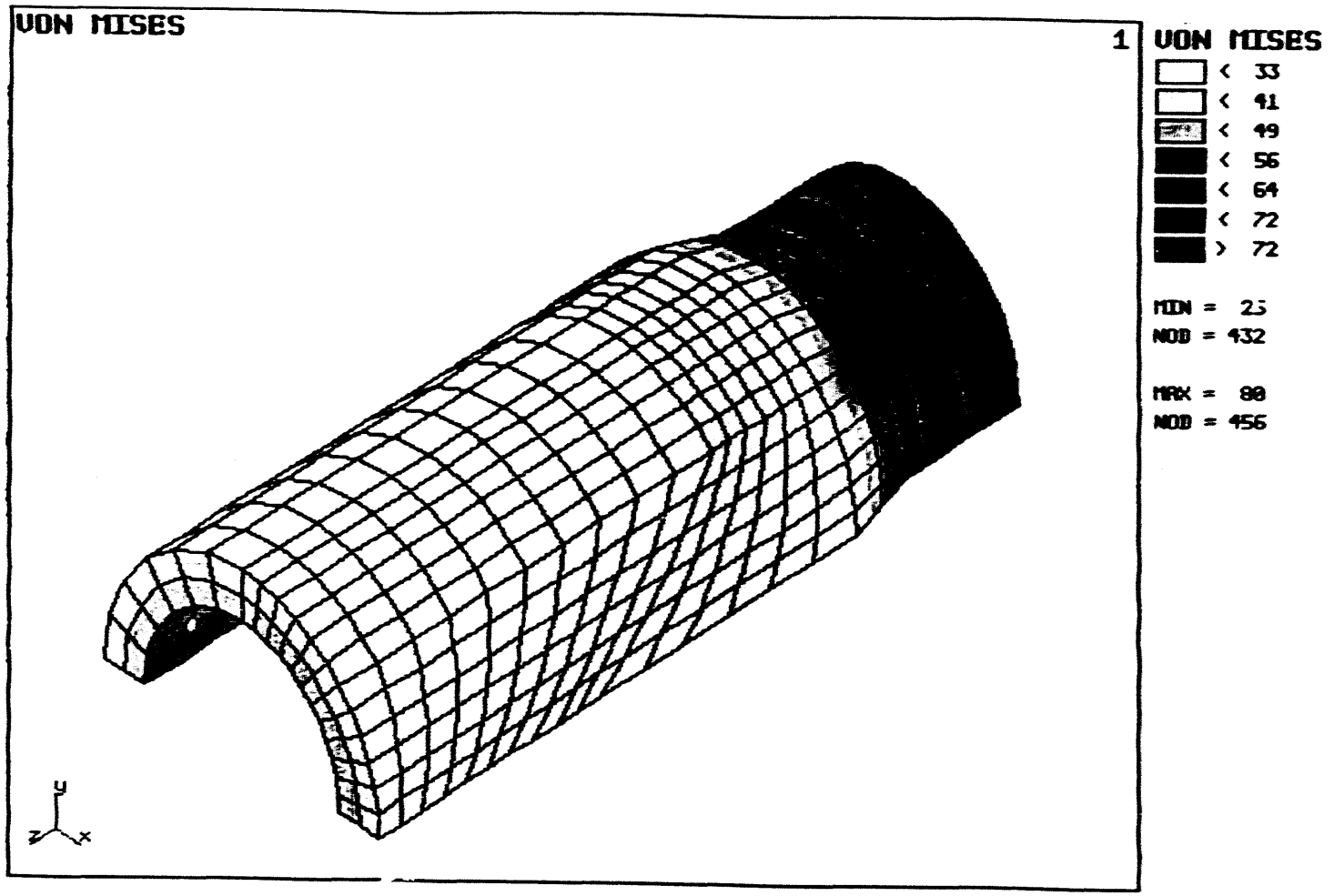

Fig. 2 Stress distribution.

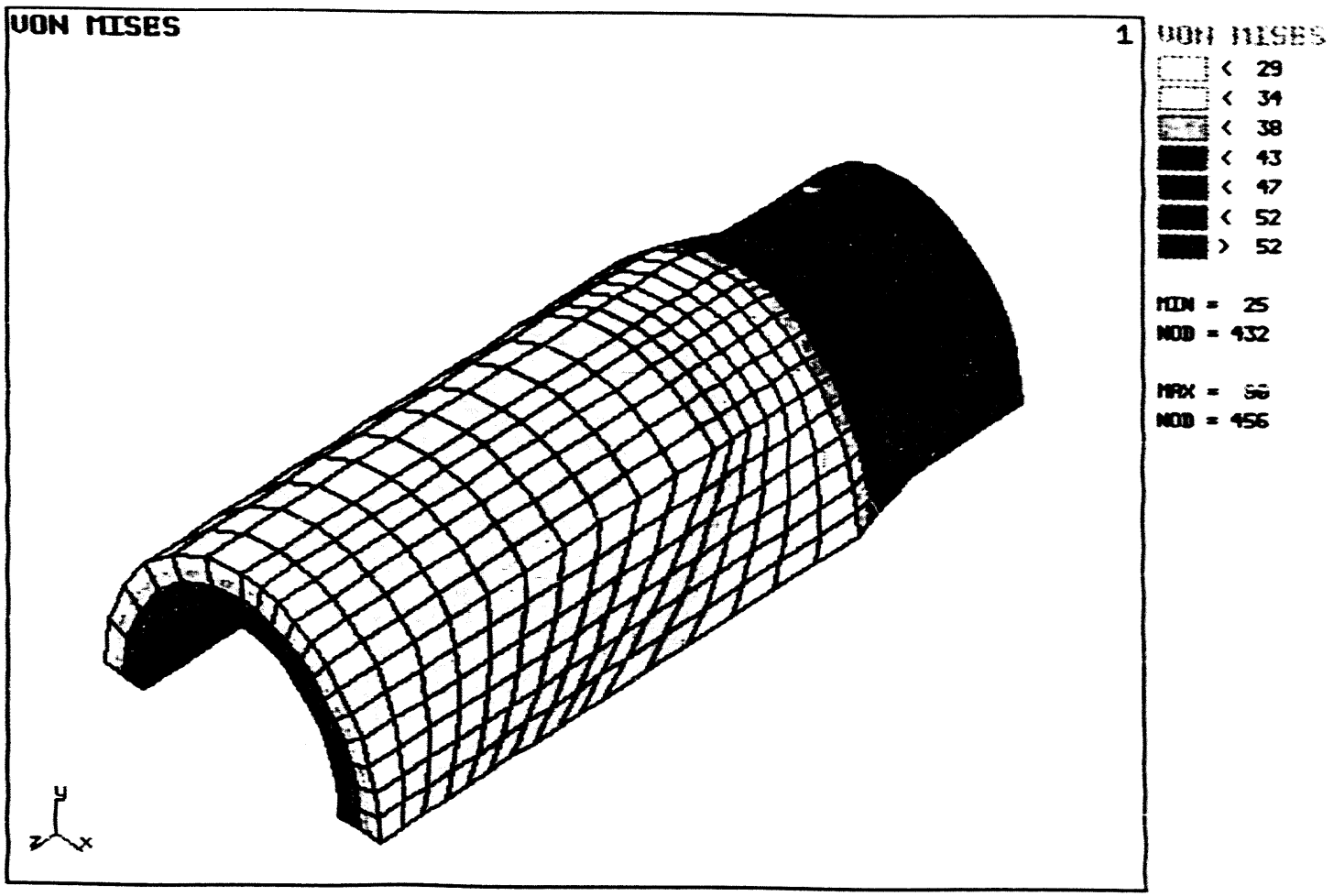

Fig. 3 Stress Distribution of Collector.

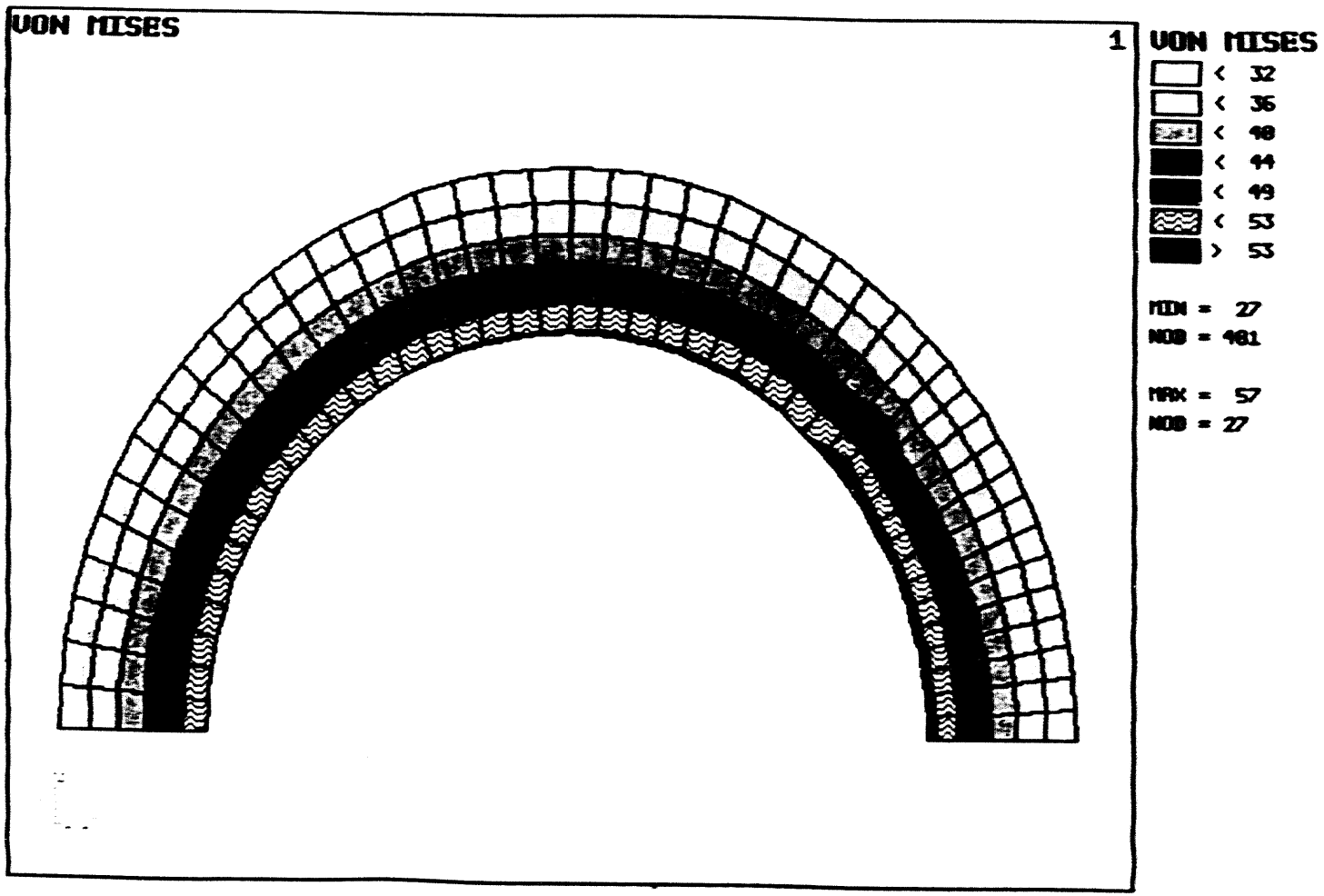

Fig. 4 Plane Stress Distribution.

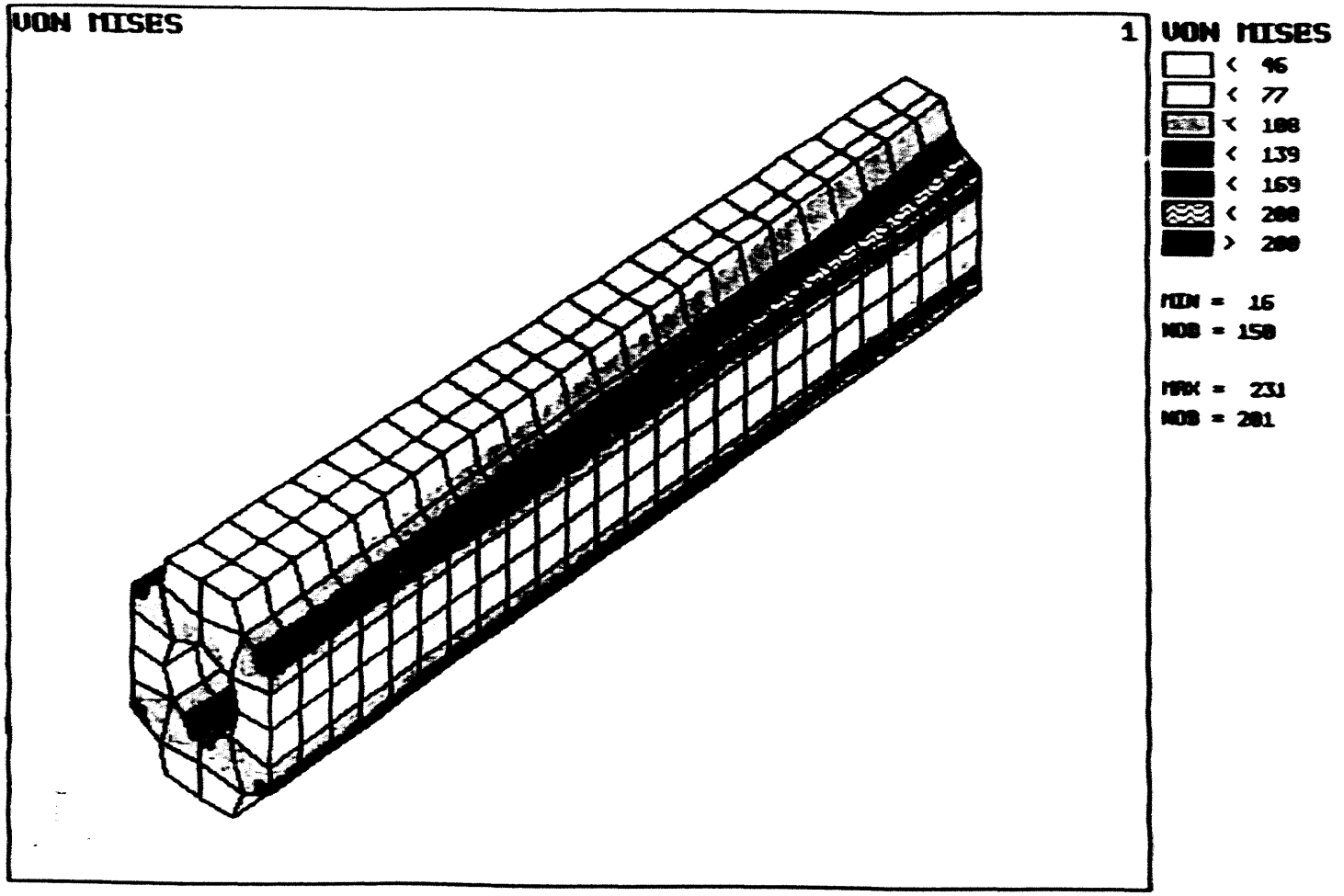

Fig. 5 Stress Distribution of the Hole.

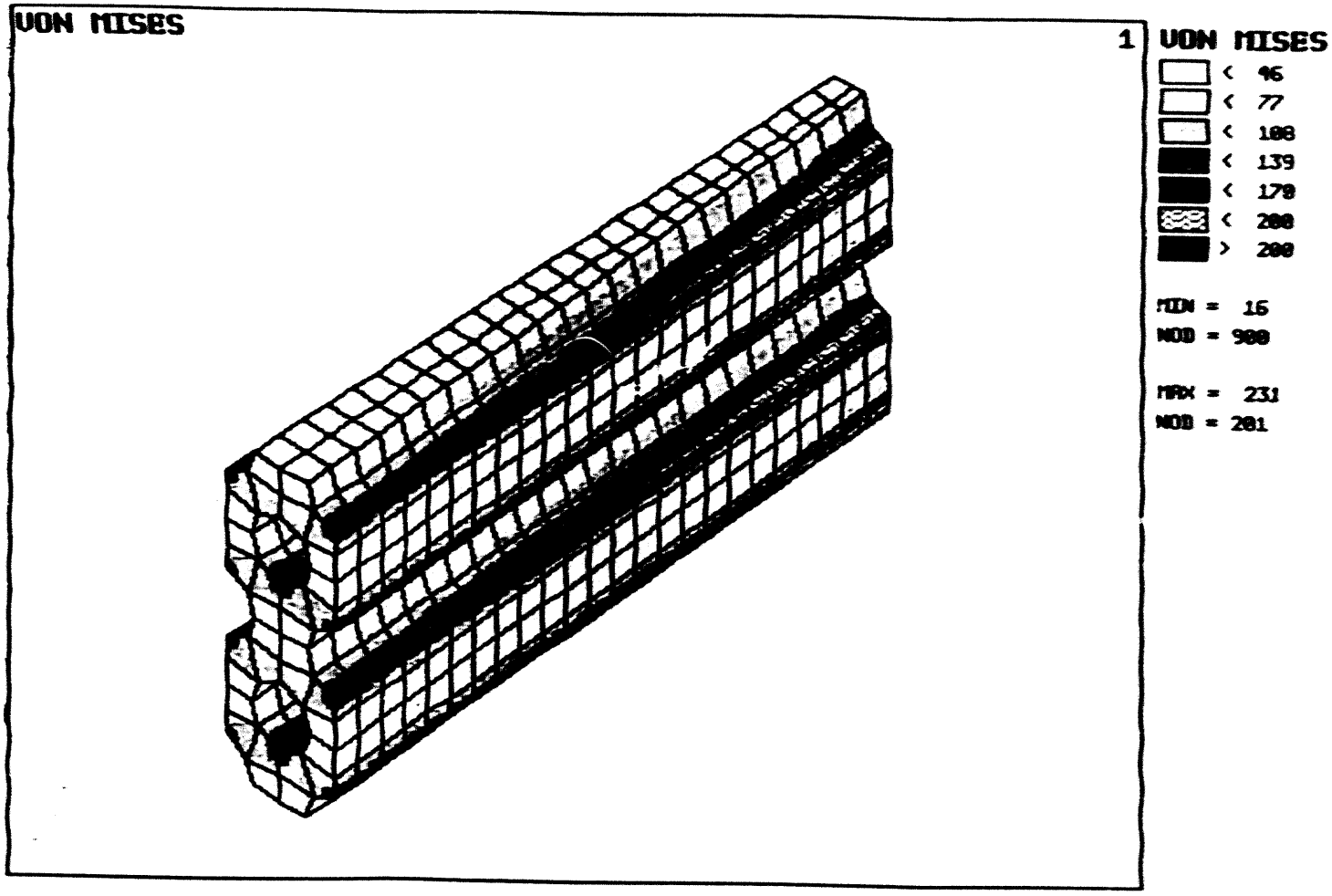

Fig. 6 Stress distribution of Holes.

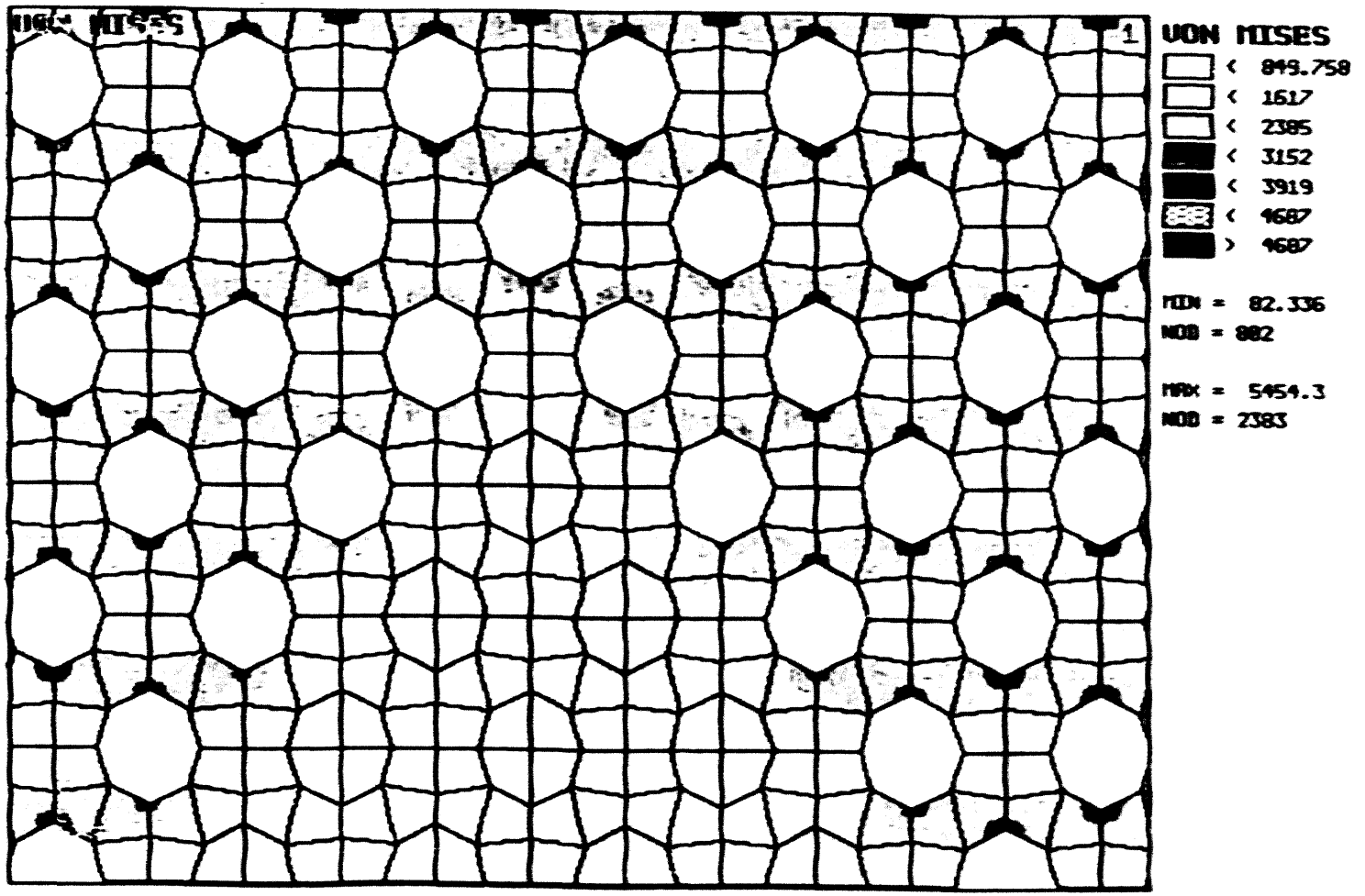

Fig. 7 Plane Problem.

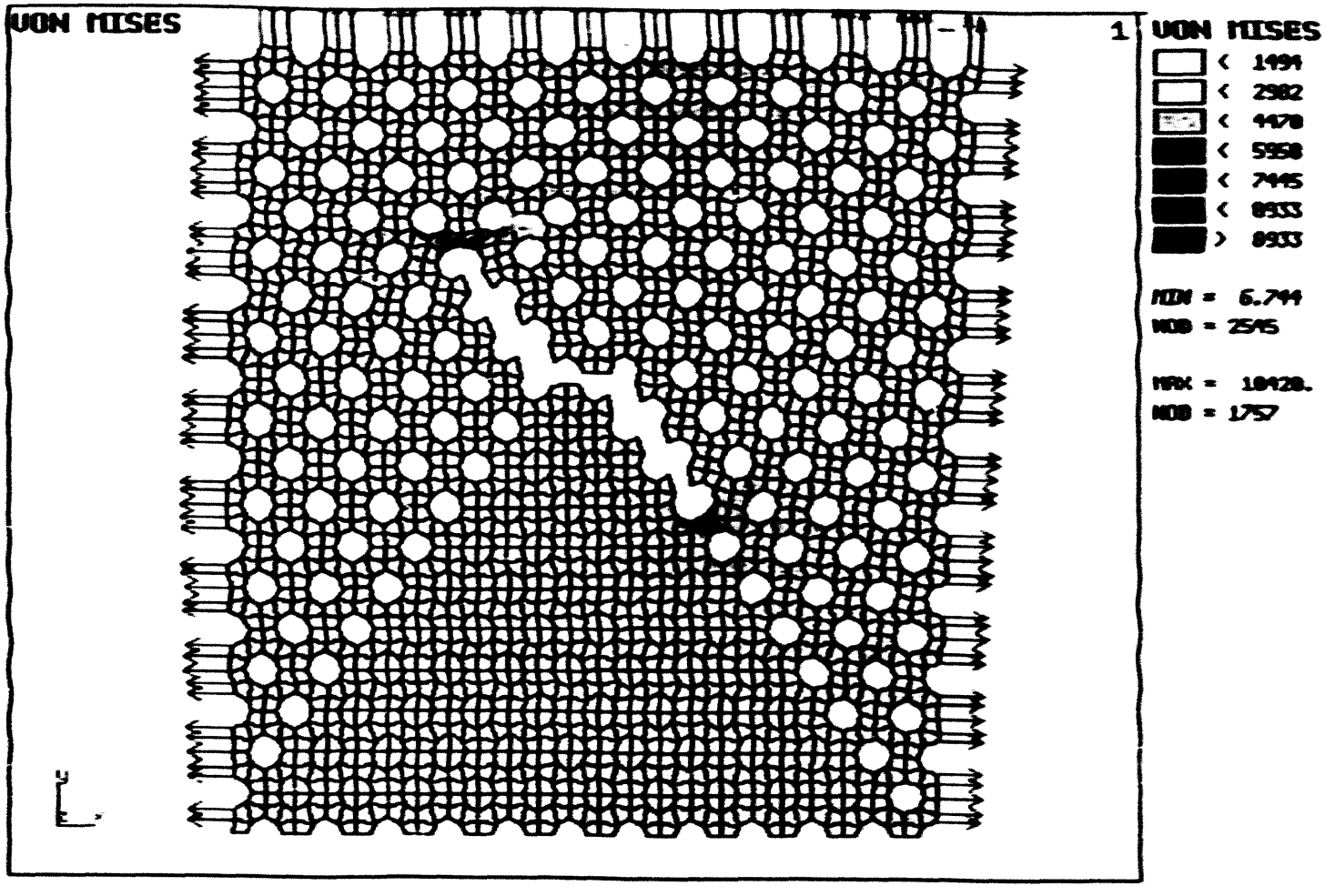

Fig. 8 Plane Problem with Crack.

LOW CYCLE FATIGUE OF PRESSURIZED PIPES WITH CIRCUMFERENTIAL FLAWS UNDER CYCLIC BENDING MOMENT

Waldemar Stoppler and Dietmar Sturm

Staatliche Materialprüfungsanstalt Universität Stuttgart, Pfaffenwaldring 32, D–7000 Stuttgart 80, Germany

Abstract

Pipes of 706 mm inner diameter, 47 mm wall thickness and about 5000 mm in length were provided with circumferential surface cracks and loaded by internal pressure of 15 MPa whilst being simultaneously subjected to an alternating external bending moment. Usually a load ratio R of –1 (M_{min}/M_{max}), in one case R=0.1, was applied. The pipes were fabricated of two types of ferritic steel: one, grade 20 MnMoNi 5 5, with a high upper shelf impact energy of about 200 J and one, MnMoNiV–special melt, with a low upper shelf impact energy of about 60 J. Deformation and crack growth in the wall thickness and circumferential direction were determined and compared with calculated values.

Introduction

The test programme which is described in the following is intended to provide a further contribution to the proof of integrity of piping of dimensions up to those of the main cooling loop of a 1300 MW_e pressurized water nuclear power plant (PWR). It is the logical continuation of tests carried out in Phase I and II of the research project "Phenomenological Pressure Vessel and Pipe Burst Tests", in which the failure and fracture behaviour of pipes containing longitudinal or circumferential defects were investigated in detail and which already furnished important results for the proof of integrity /1, 2, 3/. Figure 1 gives an overview of the main objectives investigated within the research programme.

Objective

In Phase III of this research project it is now intended to enlarge the knowledge about the failure behaviour of circumferentially cracked pipes loaded by a static internal pressure and simultaneously applied cyclic external bending moment. Figure 1 also represents the aims of investigation of this part of the project. For the design, calculation and construction of primary cooling systems of light water reactors the KTA–rules 3201.1 and .2 /4/ are applicable and demand also a fatigue analysis, which is limited to the determination of a maximum permissible number of load cycles based on linear–elastic or simplified elasto–plastic calculated stress amplitudes. Should upset conditions occur then loadings can arise which cause local plastic deformations in the components. In the case of earthquakes or water hammers etc. additionally low cycle fatigue crack growth has to be considered.Therefore the projected tests focus on the determination of the fatigue life of artifical cracked pipes subjected to high loads which cause an overall nominal equivalent strain range up to 20 mm/m. Furthermore the rules governing the transferability of properties obtained from small specimens to components are to be determined. The calculational procedures required for this are to be so refined that an analytical description of component behaviour during cyclic loading, even in the plastic range, is possible.

The present paper describes the testing equipment neccessary for the performance of bending fatigue tests, the material employed, test results and results by means of FE–calculations.

Description of the 12 MNm bending device

In order to investigate crack growth during slow cyclic bending in the frequency range between 1 load cycle per 3 hours (10^{-4} Hz) and 30 cycles per hour (0.01 Hz) the four point bending device shown in Figure 2 was constructed and taken into operation. Both ends of the test pipe are provide with cylindrical bearings which are mounted into slide blocks supported by the upper and lower plate of the machine frame. Two servo–hydraulically controlled actuators, having a maximum stroke of 700 mm, generate a bending moment of up to +12 MNm. The force to the pipe is applied by means of two load distributing saddles. Because of the symmetry of both the system and loading at the pipe centre, a constant bending moment results over a distance of +500 mm of the centreline.

Test pipes and test parameters

For the bending fatigue tests with the 12 MNm bending device pipes with an inner diameter of 706 mm and a wall thickness of 47.2 mm were used. To avoid geometrically influenced effects, both the inner and

outer surface had been turned by means of a lathe. Therefore the pipes showed little standard deviation in diameter (0.525 mm) and wall thickness (0.72 mm). The pipes were fabricated of two types of ferritic steel. One was grade 20 MnMoNi 5 5 with a high upper shelf impact energy of 200 J. The pipes of this material were seamless. To produce pipes with a low upper shelf impact energy of 60 J with nearly the same strength properties a special melt with a special heat treatment was used. The pipes of this material were made of rolled plates with the rolling direction in circumferential direction. The two longidutinally welding joints were positioned in the neutral axis during the fatigue bending tests. The pipes were weakened by artificial circumferential cracks by means of spark eroding (electric discharge machining). Figure 3 shows an example of the shape of the starter crack. Growth behaviour of cracks with various lengths, depths and under various loadings (described in the test parameters, Figure 4) was investigated. It should be mentioned here, that in an other part of the programme, not covered in this paper, pipes with smaller dimensions are loaded by resonance excitation /5, 6/. The test parameters for this part of the programme are also included in Figure 4.

Material properties

As seen in Figure 4 the pipes were made of a ferritic material with high upper shelf impact energy of 200 J and also one of low upper shelf impact energy of 60 J both having similar strength and deformation properties. The very ductile material was of grade 20 MnMoNi 5 5, a most common material in German nuclear power plants. The most important properties of both materials such as chemical composition, mechanical properties and course of impact energy (Charpy–V) are shown in Figure 5. The course of the crack growth curves (mm per load cycle) depending on the range of stress intensity factor DK, determined with CT–specimens according to ASTM E 647, lay slightly right of the reference curve of ASME Boiler and Pressure Vessel Code Sect. XI for the high toughness material and otherwise slightly left, Figure 6. The curves were obtained from averaging results of tests carried out at temperatures of 20 ^{0}C and 90 ^{0}C. The influence of the test temperature to the crack growth was not significant.

Test results

The calculated component bending moment – equivalent strain curve /7/ for the unweakend pipe, shown graphically in Figure 7, agree very well with the experimentally determined equivalent strain at the maximum bending moment. The equivalent strain due to internal pressure is not taken into consideration in this plot. The equivalent strain is calculated from the principle strains using v. Mises equations. The range of bending moment, resp. the range of equivalent strain was chosen with respect to the failure moment of the considered crack for a steadily increasing moment. The range of the strain $2\varepsilon_a$ in the unweakened cross section at the mostly stressed fibre serves as a basis for the assessment of the crack growth behaviour. The strain range $2\varepsilon_a$ is determined from the bending moment–equivalent strain curve, Figure 7, and the range of the bending moment applied in the fatigue test. The tests were performed at a temperature when the upper shelf impact energy level was reached, i. e. 20 ^{0}C for the high and 80 ^{0}C for the low thoughness material. The results of 15 fatigue bending tests performed so far together with the test parameters such as crack size and shape and level of loading are listed in Figure 8 and plotted as a function of the numbers of load cycles to through cracking and equivalent strain range. Also plotted is a scatterband (load cycles to incipient crack) determined of smooth fatigue specimens of various materials which is known from published works /7, 8/. The test results for smooth fatigue specimens of the two here applied materials also lie within this scatterband.

The tests in which the circumferential crack in the pipe had an initial depth of 4.7 mm (a/t = 0.1) and a length of 292 mm (42 degrees) gave through–crack cycle numbers which lie about one decade below the incipient crack growth curve for smooth fatigue test bars. There was also no significant difference between the fatigue crack growth starting from a crack on the outer or inner surface (test BVZ 210). On the other hand for pipes with deeper notches, e. g. a/t = 0.5, the numbers of cycles to through cracking lie up to three decades lower than the incipient crack curve for smooth fatigue bars.

The numbers of load cycles for through cracking are influenced by the crack length. Comparing the results of pipes with a crack length of 40 degrees, resp. 20 degrees there is a one decade shift of the fatigue life curves. But for length more than about 40 degrees the fatigue life curve is not affected anymore (test BVZ 290 and BVS 230, crack length: 120 degrees).

The test results of BVZ 250, BVZ 270, BVS 200 and BVS 220 imply an influence of the material toughness to the numbers of load cycles to through cracking. Temperature effects may negligible in this case. But it could be also an effect of the scatterband, which we have to face in this range of low cycle fatigue tests. Further investigations should prove this special point.

As shown in Figure 9 in some cases a canoe–shaped and in some cases a semi–elliptical–shaped fracture surface were formed. The mechanism leading to the different shapes is not fully understood up to now.

Comparison of calculation and measurement to the deformation behaviour

The deformation behaviour was verified by means of calculation and experiment. The strain distribution calculated was based on the finite–element programme ABAQUS and S8R–shell elements (thick–walled) and LS3S–line–spring elements shown in Figure 10 in immediate vicinity to the notched pipe cross–section. The distribution of the circumferential strain demonstrates that the measured circumferential strain could be met only with the calculation model which takes into account the reinforcing effect of the load distribution saddle (extended course of the curve). The calculation model which assumes a direct load input without impeding the deformation provides values (dashed line) not showing such a good agreement with the measured circumferential strain.

Furthermore, the calculations indicate that the longitudinal strain decisve for mode I of the crack in the relevant cross–section is largely independent of the hypothesis of the load input. The longitudinal strain running exactly cosine shaped over the circumference according to the bending theory (Bernoulli) was additionally included in figure 10 (see the dotted line). All the curves agree well with the measured longitudinal strains. In the area of tension where the pipe does not experience any reinforcing effect due to the load distribution saddle, longitudinal strains only negligibly smaller than in the area of compression occur on the outer surface.

Calculation of the stress–intensity factor on the crack front

For the purpose of calculating the stress intensity factors in the notched area of pipe BVZ 210, the shell FEM model was used also with line–spring elements for modelling the crack. The line–spring–method /9/ is based on the thought of a defined surface crack in a plate or shell to be idealised by a slit having equally distributed springs between the slit surfaces, Figure 11. The slit length corresponds to the maximum length of the surface flaw. The remaining load capacity of the plate or the shell in the crack cross–section is represented by the rigidity of the spring. This enables normal forces N and moments M to be transferred each as function of the local crack depth to wall thickness relation a/t per unit of flaw length. These local internal forces and moments correlate with the relatively normal displacements s and the rotations θ of the slit edges.

The course of the stress intensity factor K_I along the crack front calculated for variously deep flaws (a/t = 0.1; 0.5 and 0.9) and for a bending moment of 10 MNm is represented in Figure 12. The top of figure 12 shows the course of the stress intensity factor K_I for a pressurized pipe (15 MPa) only. For the sake of comparison, the course of the stress intensity factors were also determined by ABAQUS–3D and SOLVIA–3D calculations for the same flaw configurations and loads. Despite the area around the end of the flaw the individual curves show no considerable differences.

Comparison of calculated and experimentally determined crack growth

The cyclic crack growth of two experiments BVZ 240 and BVZ 250 was calculated by means of the above descriped FE–methods taking the tension part of the loading into consideration (the compression part was neglected). The elasto–plastic calculation was based on a true stress – true strain curve of the used material and the appropriate crack growth curve of figure 6. But, the crack growth curve had had to be linear extrapolited because no experimentally determined data exceeding a range of stress intensity factor ΔK of 2,000 $N/mm^{3/2}$ were available. As shown in Figure 13 a satisfactory agreement was achieved between calculated and experimentally determined crack growth for both tests.

Summary

Low cycle fatigue life curves were experimentally determined with pipes of the dimensions of main cooling pipes of a 1300 MW_e–PWR (inner diameter: 706 mm, wall thickness: 47.2 mm). The pipes were provided with spark–eroded cracks with a length between 20 degrees and 120 degrees and a depth between 4.7 mm (a/t = 0.1) and 23.6 mm (a/t = 0.5). The pipes were subjected to a statically internal pressure of 15 MPa and superimposed an alternating bending moment with an amplitude between 3 MNm and 12 MNm.To investigate the influence of material toughness the pipes were fabcricated of two types of ferritic steels: one, grade 20 MnMoNi 5 5, with a high upper shelf impact energy of about 200 J and MnMoNiV–special melt, with a low upper shelf impact energy of about 60 J.

In order to verify the load capacity and to determine the stress intensity factors along the crack front comparison calculations were carried out by means of FE–calculation with the aid of shell models with line–spring elements. The rsults otained correspond well with the experimentally determined ones. Even calculated cyclic crack growth curves agree satisfactorily with experimentally dtermined. But further investigations have to be done to proof this statement.

Acknowlegdments

We greatly appreciate the financial support of this project by the Federal Minister for Research and Technology, Bonn, and the technical support by the Gesellschaft für Reaktorsicherheit (GRS), Köln.

References

/1/ Sturm, D. und Stoppler, W., 1985, "Forschungsvorhaben Phänomenologische Behälterberstversuche – Versuche zum Traglast– und Bruchverhalten von Rohren mit Längsfehlern. Förderkennzeichen 150 279, Phase I", Forschungsbericht MPA Stuttgart.

/2/ Sturm, D. und Stoppler, W., 1987, "Forschungsvorhaben Phänomenologische Behälterberstversuche – Versuche zum Traglast– und Bruchverhalten von Rohren mit Umfangsfehlern – Förderkennzeichen 150 279, Phase II", Forschungsbericht MPA Stuttgart.

/3/ Sturm, D. und Stoppler, W., 1989, "Forschungsvorhaben Phänomenologische Behälterberstversuche – Versuche zum Versagens– und Bruchverhalten von Rohren mit Umfangsfehlern – Förderkennzeichen 150 279", Abschlußbericht MPA Stuttgart.

/4/ "Sicherheitstechnische Regel des Kerntechnischen Ausschusses KTA Nr. 3201.1 und .2 Komponenten des Primärkreises von Leichtwasserreaktoren. Teil 1: Werkstoffe, Teil 2: Auslegung, Konstruktion und Berechnung, Fassung 3/84", Carl Heynmanns Verlag KG, Köln.

/5/ Kerkhof, K., W. Stoppler, D. Sturm and R. Zirn, 1990, "Resonant Excitation of Pipe Section", *Nuclear Engineering and Design*, Vol. 119, pp. 361–370.

/6/ Stoppler, W., D. Sturm, K. Hippelein, A. de Boer, K. Kerkhof and H. Sommer, 1990, "Crack Growth Tests on Pipes with Circumferential Defects under Internal Pressure and Superposed, Alternating Bending Load", 16. MPA–Seminar, Stuttgart.

/7/ Wellinger, K. und H. Dietmann, 1969, "Festigkeitsberechnung", A. Kröner Verlag Stuttgart.

/8/ Luft, G., 1968, "Zeitfestigkeitsverhalten von Stählen", Technisch–wissenschaftl. Bericht MPA Stuttgart.

/9/ Parks, D. M., 1981, "Inelastic Analysis of Surface Flaws Using the Line–Spring Model", in Advances in Fracture, Ed. D. Francois, Vol. 5 (Pergamon, Oxford, 1981), pp. 2589–2598.

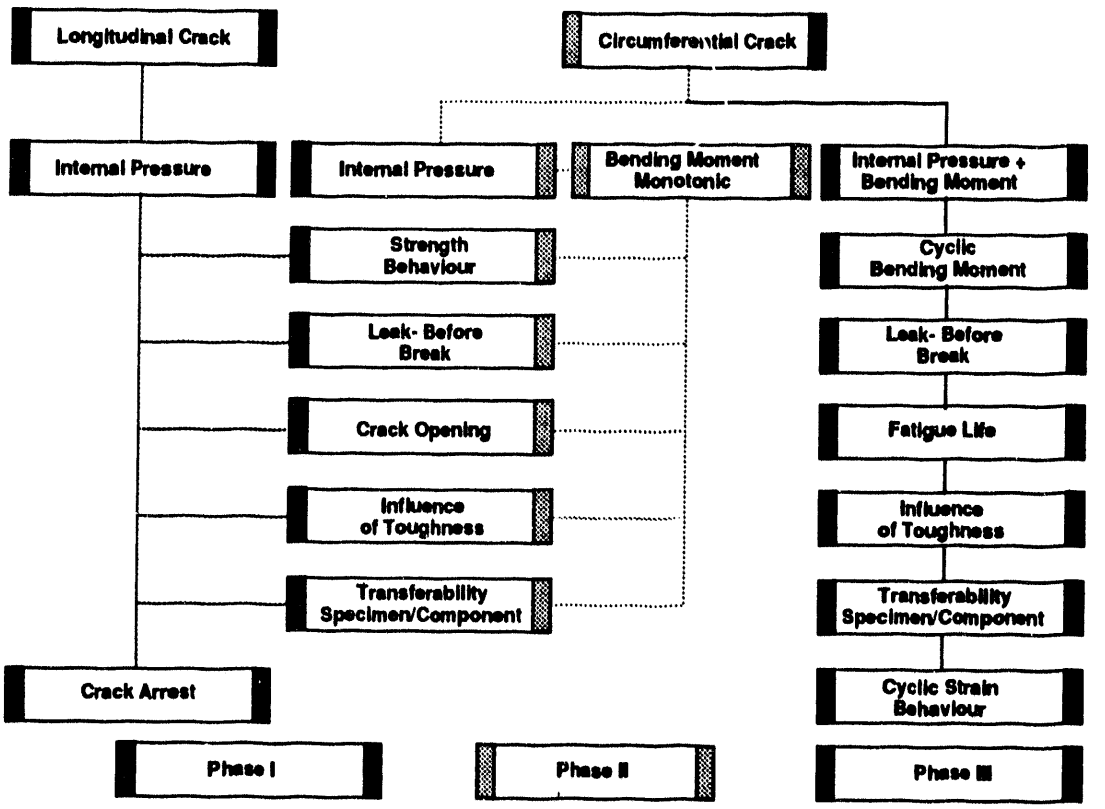

Figure 1: Main Objectives of the Research Programme "Phenomenological Pressure Vessel and Pipe Burst Tests"; Phase III Subject of Actual Investigation

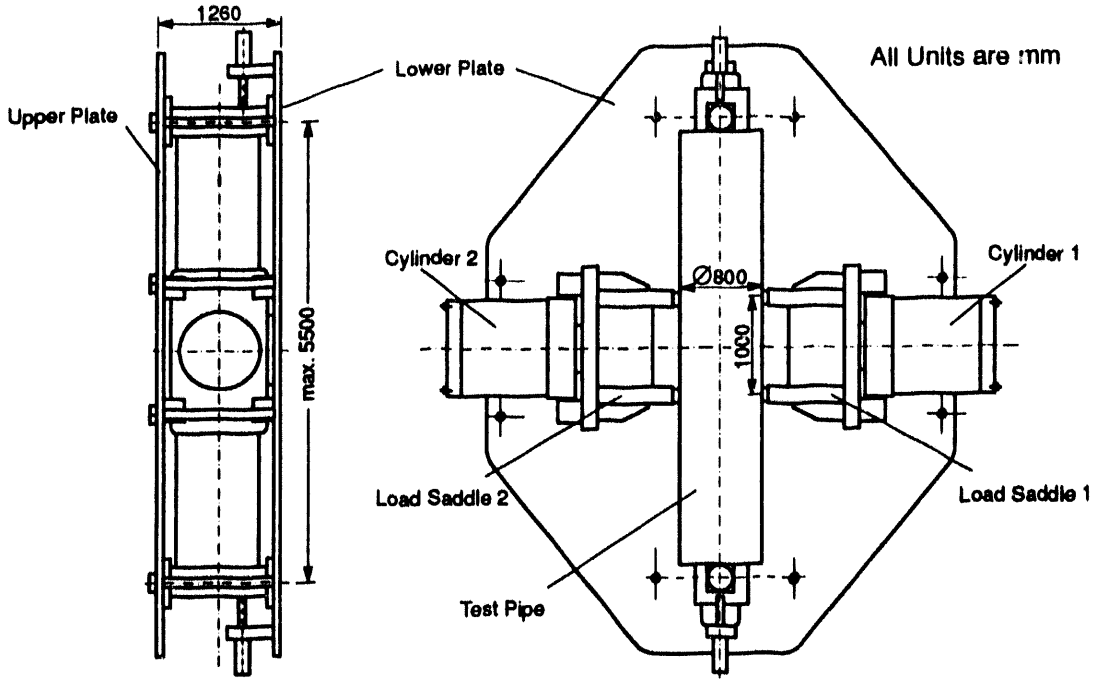

Figure 2: 12 MNm Four–Point Bending Device

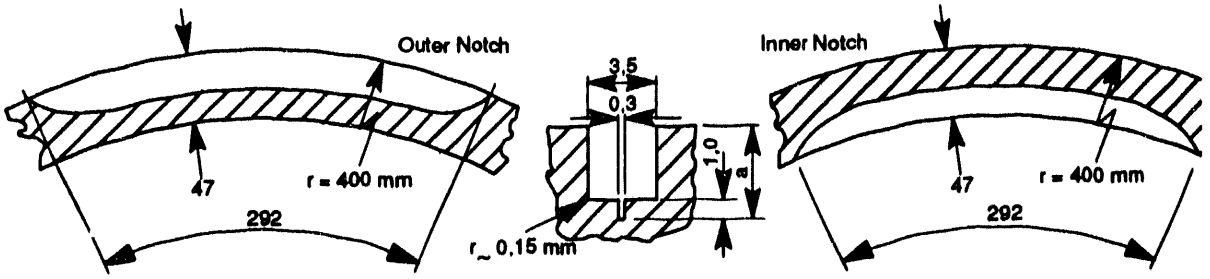

Figure 3: Example of Spark – eroded Starter Crack (Electric Discharge Machining)

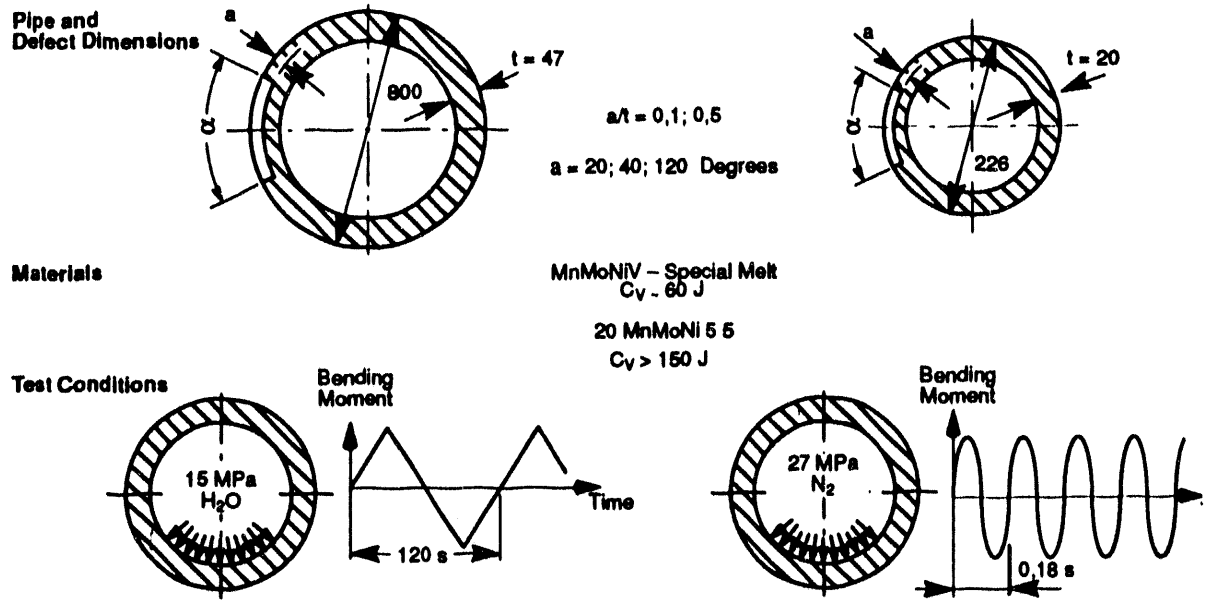

Figure 4: Test Parameters for Slow Cycle Fatigue Tests (Left) and Eigenfrequency Excitation (Right)

Material 20 MnMoNi 5 5

Mechanical Properties			20°C R_{eH} MPa	20°C R_m MPa	20°C E MPa	20°C A_5 %	20°C Z %	300°C $R_{p0,2}$ MPa	300°C R_m MPa	300°C E MPa	300°C A_5 %	300°C Z %
Cast 107 854 and 107 873	Mean Value from	L – Specimen	556	664	208 000	24	74	457	658	181 000	26	74
		C – Specimen	547	658	207 000	24	70	455	657	184 000	25	67
		L– and C– Specimen	552	662	207 000	24	72	456	658	182 000	25	70
	Standard Deviation of Mean Value from L– and T– Specimen		18	23	2 000	1	2	20	19	6 000	1	4

Chem. Composition %		C	Si	Mn	P	S	Cr	Mo	Ni	Al	Cu	V	Sn
VDTÜV – Specification 401 / 2 07.83	Min.	0,17	0,15	1,20	–	–	–	0,40	0,50	0,010	–	–	–
	Max.	0,23	0,30	1,50	0,012	0,008	0,20	0,55	0,80	0,040	0,12	0,02	0,011
Cast 107 854		0,20	0,22	1,33	0,012	0,003	0,08	0,51	0,74	0,022	0,02	0,01	0,002
Cast 107 873		0,20	0,22	1,32	0,010	0,002	0,02	0,49	0,69	0,022	0,02	0,01	0,002

R_{eH}=Yield Point $R_{p0,2}$=Y. Strength 0.2 % Offset R_m=Tensile Strength E=Modulus of Elasticity A_5=Total Elongation Z=Reduction in area

Material MnMoNiV–Special Melt

Mechanical Properties			20°C R_{eH} MPa	20°C R_m MPa	20°C E MPa	20°C A_5 %	20°C Z %	90°C $R_{p0,2}$ MPa	90°C R_m MPa	90°C E MPa	90°C A_5 %	90°C Z %
Cast 63 809	Mean Value from	L – Specimen	527	693	207 000	19	49	541	710	203 000	18	48
		C – Specimen	531	698	207 500	20	56	515	689	204 000	20	55
		L– and C– Specimen	529	696	207 000	19	52	529	701	203 000	19	51
	Standard Deviation of Mean Value from L– and T– Specimen		27	32	1 700	1,4	4,4	43	46	3 000	1	4

Chem. Composition %	C	Si	Mn	P	S	Cr	Mo	Ni	Al	Cu	V	Sn
Cast 63 809	0,17	0,37	1,35	0,023	0,020	0,26	0,41	1,17	0,049	0,15	0,11	0,006

R_{eH}=Yield Point $R_{p0,2}$=Y. Strength 0.2 % Offset R_m=Tensile Strength E=Modulus of Elasticity A_5=Total Elongation Z=Reduction in area

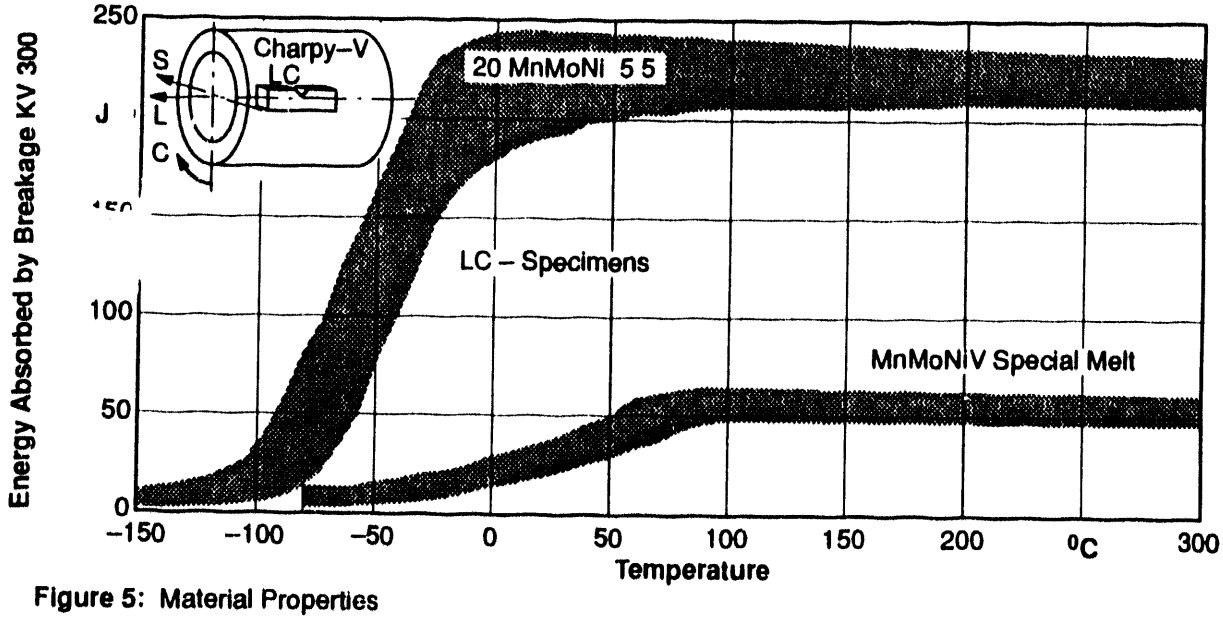

Figure 5: Material Properties

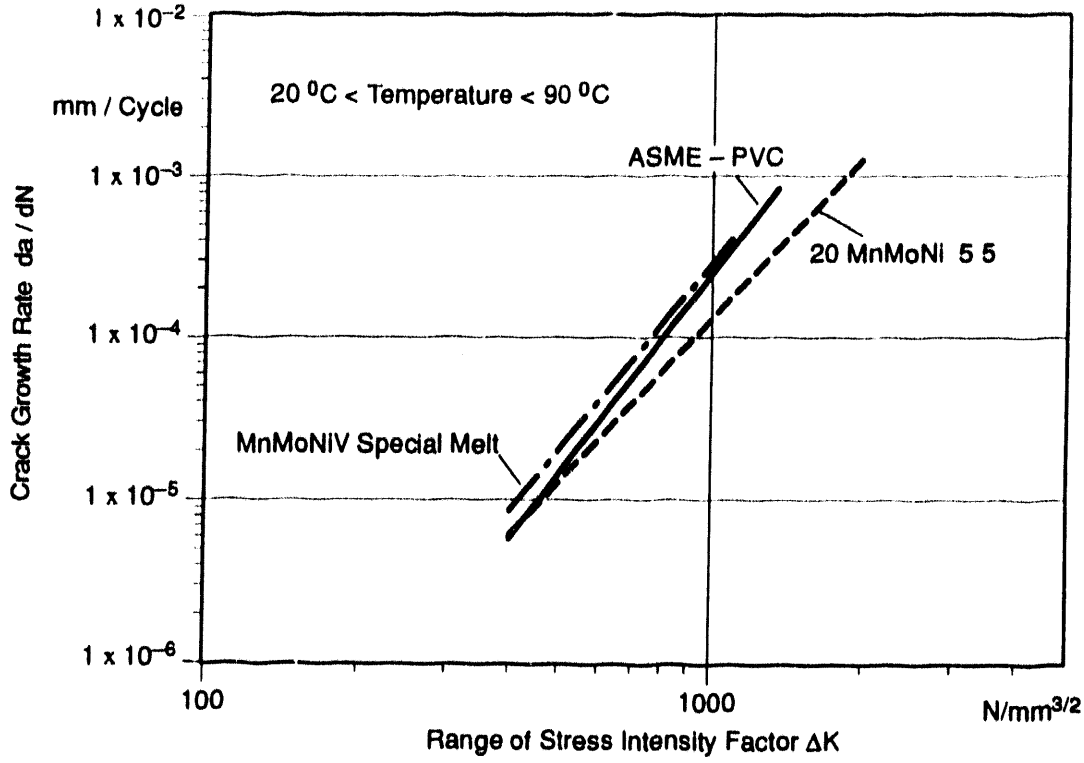

Figure 6: Crack Growth Behaviour of CT – Specimens

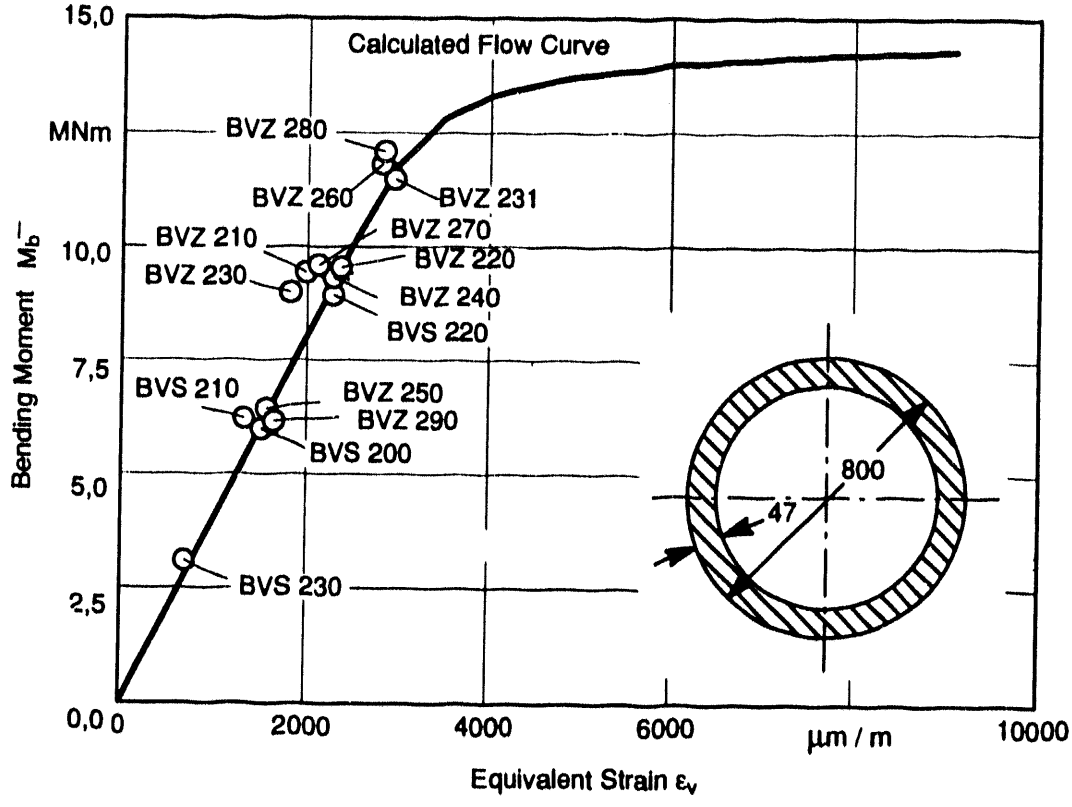

Figure 7: Bending Moment – Equivalent Strain Curve

Pipe No.	Defect			Test conditions				Equivalent Strain Range	Load cycles	Remarks
	Depth a	Length α	Position	Temperature	Internal Pressure	Bending Moment				
	mm	mm	Spark Eroded (EDM)	°C	MPa	MNm Max.	MNm Min.	$2\varepsilon_e$ mm/m	N_B	
BVZ 210 ◆	4,7 a/t = 0,1	292 (.40 Deg.)	outer + inner surface	20	0	+ 9,5	− 9,50	4,00	2200	Outer Notch: Through Crack Devel.
									2316	Inner Notch: Defect Depth = 35 mm
BVZ 220 ◆			outer surface		15			4,80	1000	Through Crack Devel.
BVZ 230 ◆							+ 0,50	1,80	7998	Test Discontinued Defect Depth: 9,8 mm
BVZ 231 ■	9,8 a/t = 0,2	294 (.40 Deg.)				+ 11,5	+ 0,25	2,80	724	Test Discontinued Defect depth: 12,8 mm
BVZ 240 ●	23,6 a/t = 0,5	292 (.40 Deg.)				+ 9,5	− 9,5	4,80	30	Through Crack
BVZ 250 ●				20		+ 6,5	− 6,5	3,16	238	Developed
BVZ 300 ●									320	
BVZ 260 ●						+ 11,9	− 11,9	5,71	4	
BVS 200 ○				80		+ 6,0	− 6,0	2,92	69	
BVS 210 △		140 (.20 Deg.)							663	
BVS 220 △						+ 9,0	− 9,0	4,60	41	
BVZ 270 ▲				20		+ 9,5	− 9,5	4,80	274	
BVZ 280 ▲						+12,1	−12,1	5,96	13	
BVZ 290 ▼		838 (.120 Deg.)				+ 6,0	− 6,0	3,25	84	
BVS 230 ▽				80		+ 3,0	− 3,0	1,45	606	

BVZ Material: 20 MnMoNi 5 5 BVS Material: MnMoNiV – Special Melt

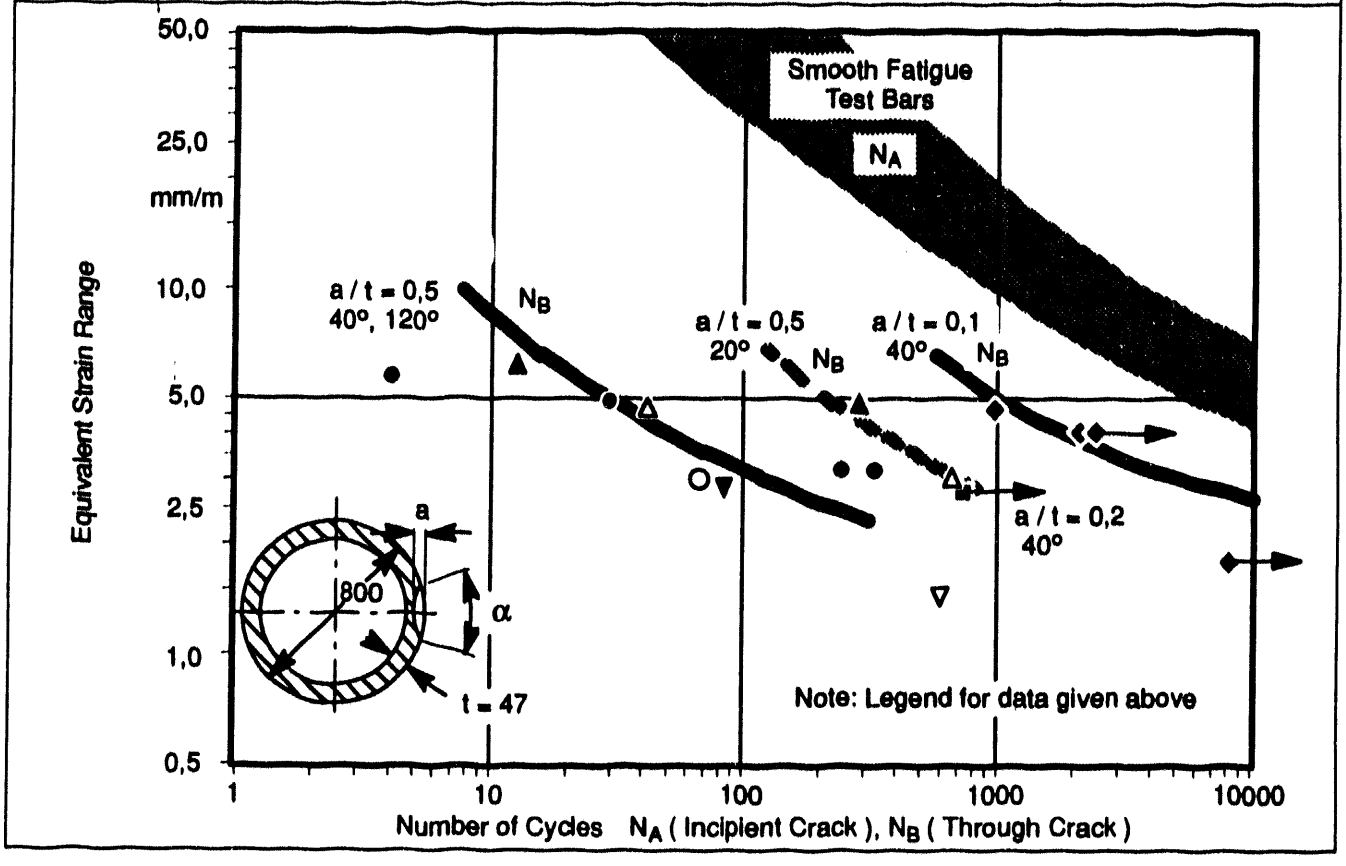

Figure 8: Test Results

BVZ 210

a) Outer Surface Notch 292 mm (41,8 Degrees) Length, 4,7 mm Depth

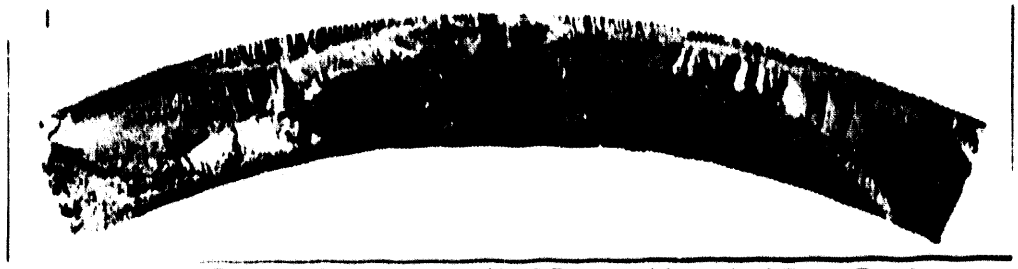

BVZ 210

b) Inner Surface Notch 292 mm (47,3 Degrees) Length, 4,7 mm Depth

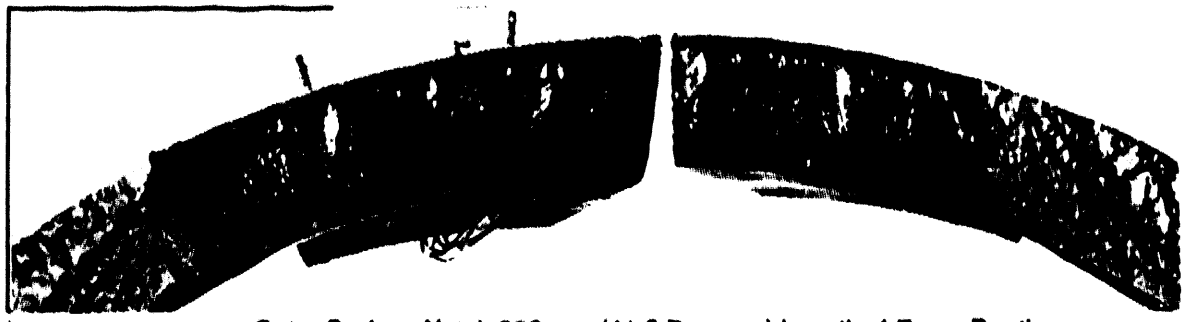

BVZ 220

c) Outer Surface Notch 292 mm (41,8 Degrees) Length, 4,7 mm Depth

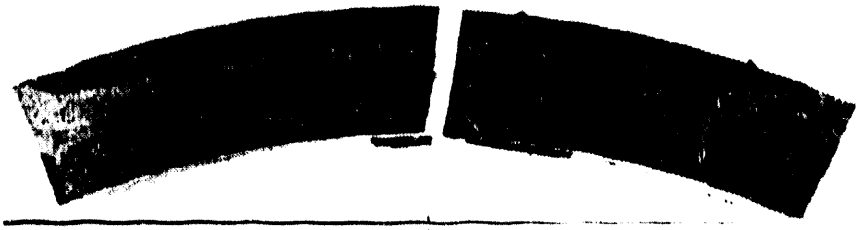

BVZ 230/231

d) Outer Surface Notch 294 mm (41,8 Degrees) Length, 4,7 mm Depth resp. 9,8 mm Depth

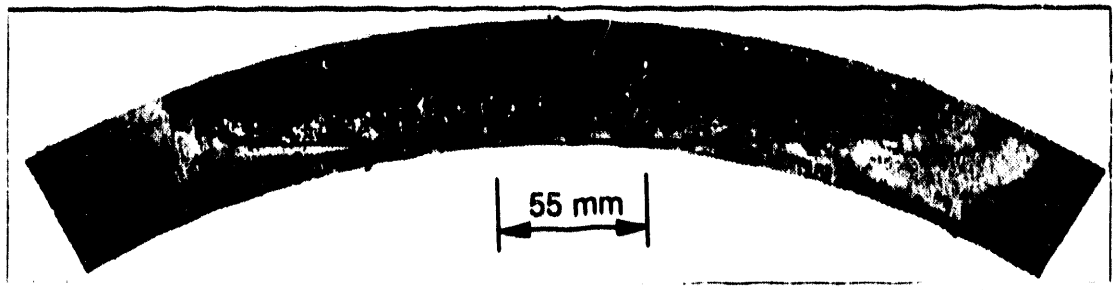

BVZ 240

e) Outer Surface Notch 292 mm (41,8 Degrees) Length, 23,6 mm Depth

Figure 9: Exposed Fracture Surfaces of Tested Pipes

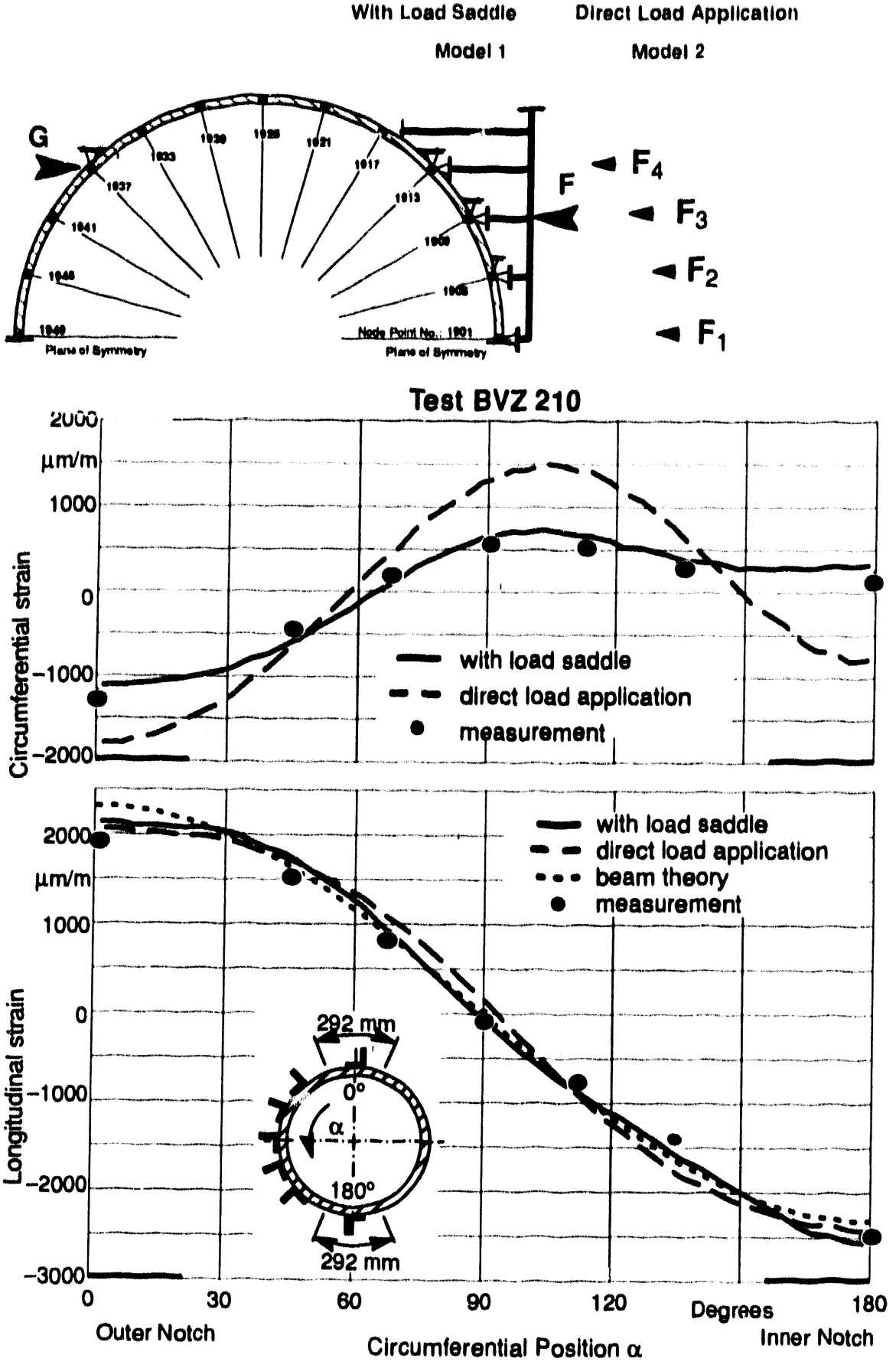

Figure 10: Influence of Load Initiation Model on the Numerically Determined Strain in the Pipe Centre Compared with the Measured Strains of the Test Pipe BVZ 210

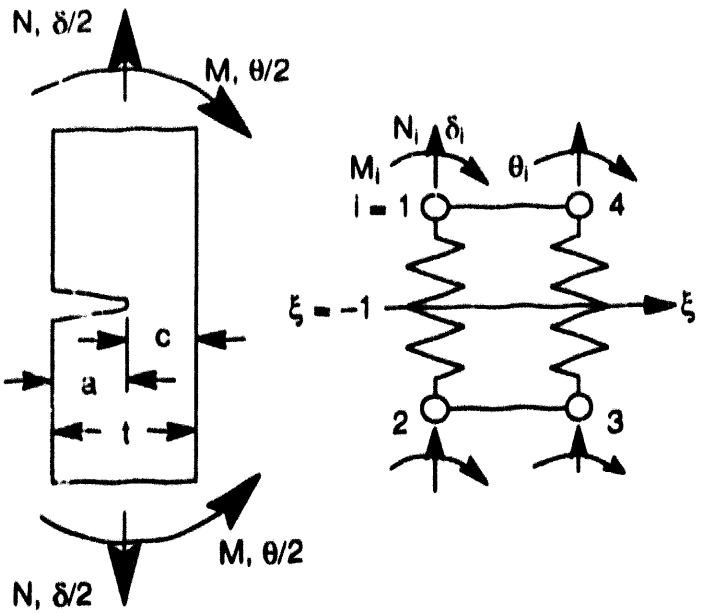

Figure 11: Order of the Forces and Moments and Representation of a "Line–Spring" Element to Calculate the Stress Intensity Factor K_I

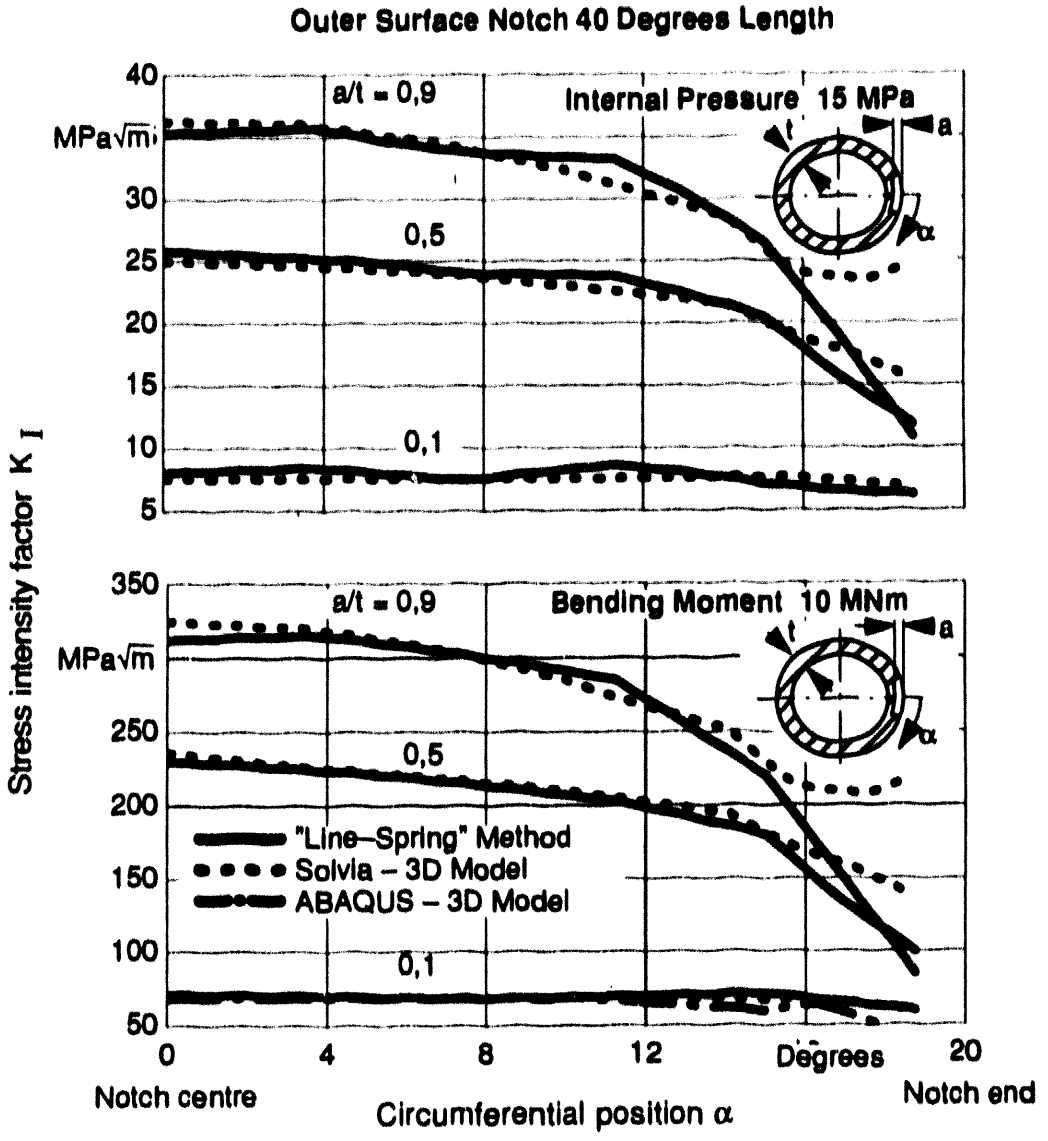

Figure 12: Calculated Course of the Stress Intensity Factor K_I along the Notch

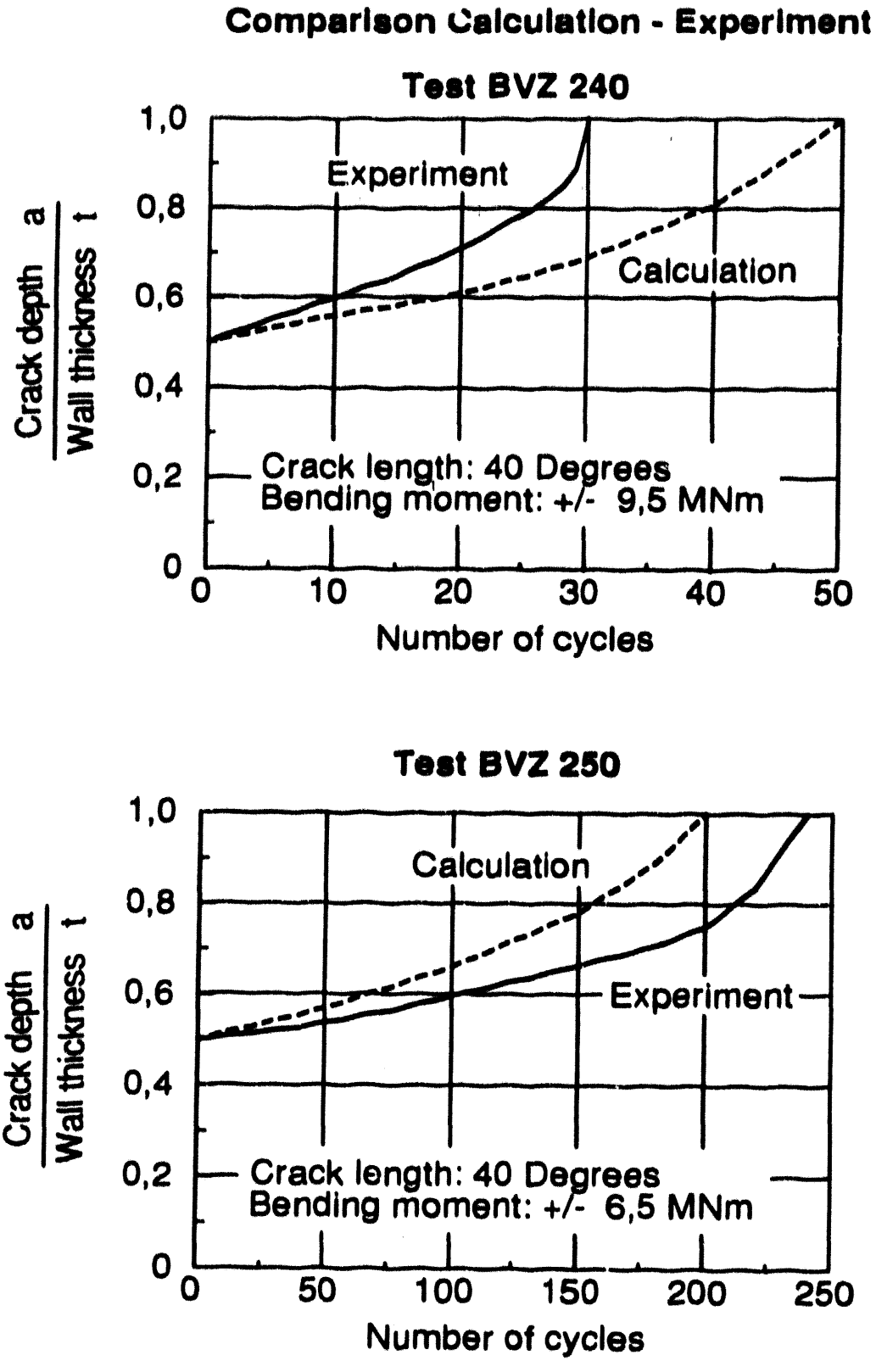

Figure 13: Comparison Calculated and Experimentally Determined Crack Growth Curves of Test BVZ 240 and Test BVZ 250

Crack Resistance of Austenitic Pipes with Circumferential Through-Wall Cracks

K. Förster, L. Grüter*, W. Setz, Siemens, 5060 Bergisch Gladbach, FRG

S. Bhandari, J.-P. Debaene, Novatome, 69398 Lyon, France

C. Faidy, Electricité de France, 69628 Villeurbanne, France

K.-H. Schwalbe, Forschungszentrum Geesthacht GmbH, 2054 Geesthacht, FRG

ABSTRACT

For monotonously increasing load the correct evaluation of the crack resistance properties of a structure is essential for safety analyses. Considerable attention has been given to the through-wall case, since this is generally believed to be the controlling case with regard to complete pipe failure. The maximum load conditions for circumferential crack growth in pipes under displacement-controlled loadings has been determined. The need for crack resistance curves, measured on circumferentially through-wall cracked straight pipes of austenitic stainless steel 316 L under bending, is emphasized by the limitation in the data range on small specimens and by the differences in the procedures. To answer open questions and to improve calculational methods a joint fracture mechanics programme is being performed by Electricité de France, Novatome and Siemens-Interatom. The working programme contains experimental and theoretical investigations on the applicability of small-specimen data to real structures.

* Present address: Office of the German Reactor Safety Commission, 5300 Bonn, Germany

INTRODUCTION

Within a cooporative fracture mechanics programme between Electricité de France (EdF), Novatome and Interatom bending tests on circumferentially cracked straight pipes of typical " Liquid Metal Fast Breeder Reactor" (LMFBR) main piping dimensions were performed[1] with the following objectives:

- Derivation of the crack resistance curves (R-curves) based on the J-integral and the δ_5 type Crack Tip Opening Displacement (CTOD) for original LMFBR geometries. This objective involves the definition of the usable scope of the R-curves as well as the structural and material effects. It is known from the literature[2] that the lowest J_R-curves have been obtained for piping structures.
- Check of the transferability of laboratory specimen crack growth characteristics to circumferentially cracked pipes. Beside the general influence of geometry this problem occurs if the small specimen fracture resistance properties which represe it only a few mm crack growth have to be extrapolated to real structures where the crack growth can be by two orders of magnitude higher.
- Check of the applicability of certain theoretical methods for the prediction of the crack instability in particular with the Engineering Treatment Model (ETM). The latter method has been established in a separate research programme by GKSS.

EXPERIMENTAL INVESTIGATIONS

The bending experiments on straight L-T orientated pipes of austenitic stainless steel 316 L with a nominal pipe diameter D = 700 mm and a nominal wall thickness t = 11 mm and circumferential through-wall cracks varying in size and location have been performed at room temperature (about 20°C) in air. Table 1 gives the actual geometries and material conditions (BM = Base Material, HAZ = Heat Affected Zone, WM = Weld Material). Note, that in the case of pipes 3 and 4 the wall-thickness t is the thickness of the weldment itself.

Table 1

Summary of the Pipes Tested at Room Temperature (RT)

Test	*Symbol*	*D* [*mm*]	*t* [*mm*]	*Initial crack* *angle* [°]	*location*
1	◆	701	12.2	61.6	BM
2	▲	698	11.5	124.2	HAZ
3	x	695	14.3	120.9	WM
4	+	698	13.4	175.4	WM
5	●	700	11.6	120	BM
6	■	697	10.4	120.6	BM

Table 2 gives the actual material data of the six pipes tested so far (R_e = yield strength, R_m = ultimate tensile strength, E = Young's modulus, n = strain hardening exponent after eqn (5)). The pipes of tests 1 to 5 have been fabricated from sheets of the austenitic stainless steel 316 L SPH used for the Superphenix Reactor, wereas the pipe of test 6 has been fabricated from the German version of this steel, 316 L mod. These are type 316 stainless steels with a carbon content lower than 0.03 percent and a controlled nitrogen content between 0.06 and 0.08 percent.

Table 2

Material Data Used For Calculations

Test	*Material*	R_e [*MPa*]	R_m [*MPa*]	*E* [*MPa*]	*n* [ ]
1	316 L SPH BM	297	613	192300	0.15
2	316 L SPH HAZ	410	638	192300	0.15
3	316 L SPH WM	379	639	192300	0.15
4	316 L SPH WM	379	639	192300	0.15
5	316 L SPH BM	297	613	192300	0.15
6	316 L mod BM	239	594	192300	0.15

Additionally eight C(T)-specimens with a width of 50 mm and a thickness of 10.5 mm (corresponding to the wall-thickness of the pipes) have been tested.

With no internal pressure in the pipe the pre-fatigued crack was opened by a monotonically quasi-static increasing displacement controlled loading of the two hydraulic actuators acting as a bending moment. The bending plane bisects the crack symmetrically. The partial unloading technique was used to measure the compliance of the cracked pipe. Fig. 1 shows the test set-up.

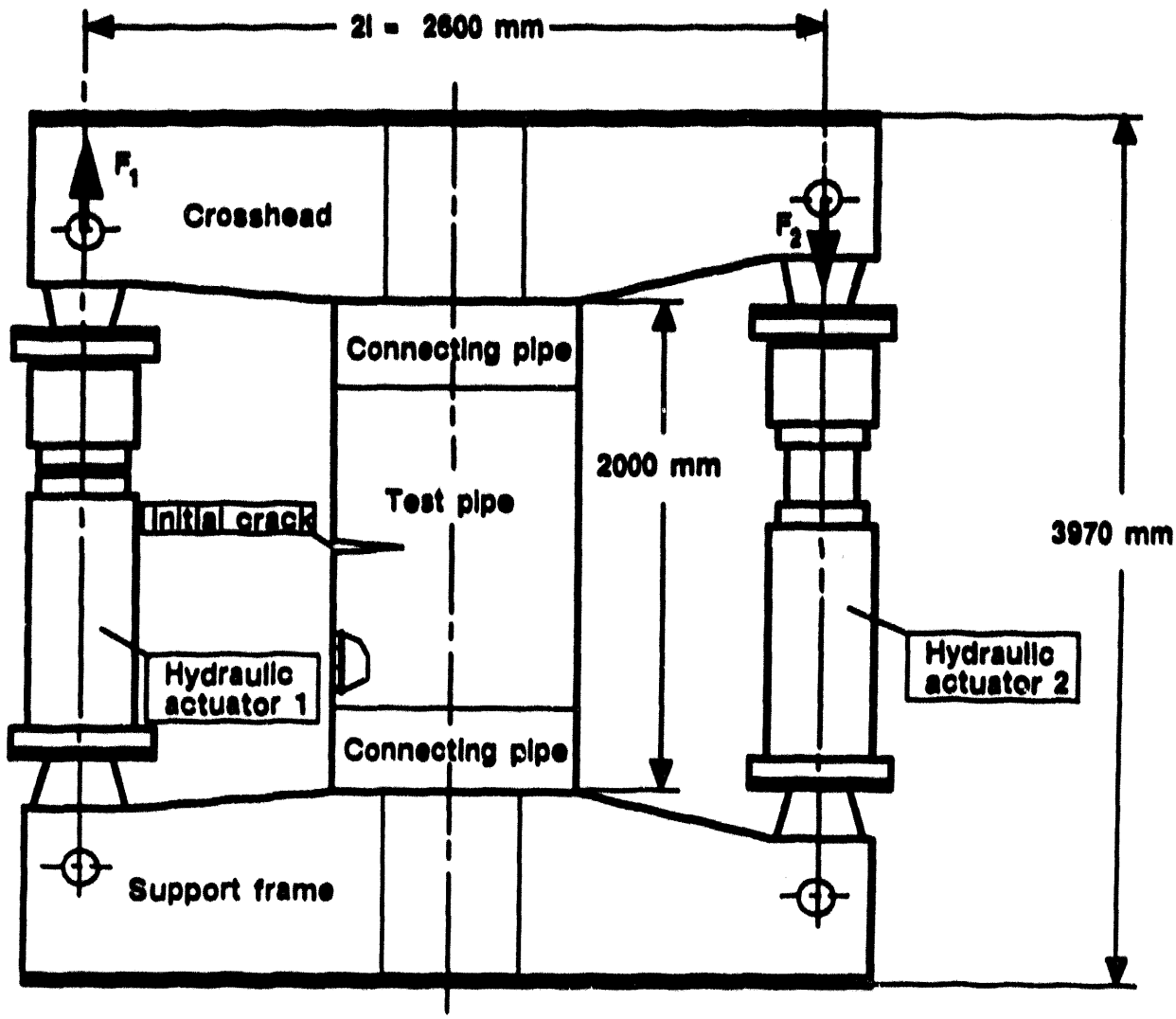

Fig. 1. Test facility

In general the following measurements were performed:

- Prior to the test: The geometry of the pipe and the crack
  The mean values of the geometry are listed in Table 1.
- During the test: Actuator forces and displacements,
  strains on the pipe surface, crack opening, crack
  extension, crack length, ovalization, begin of buckling
- After the test: The geometry of the pipe and the crack; the wall thickness in the
  crack plane if the cracks were located in the base material

DERIVATION OF R-CURVES

As a result of the tests the realistic J_R-curves and δ_R-curves have been evaluated.The calculated J_R-curves are shown in Fig. 2.1 (Δc = semi crack extension) together with the J_R-range of small specimens.

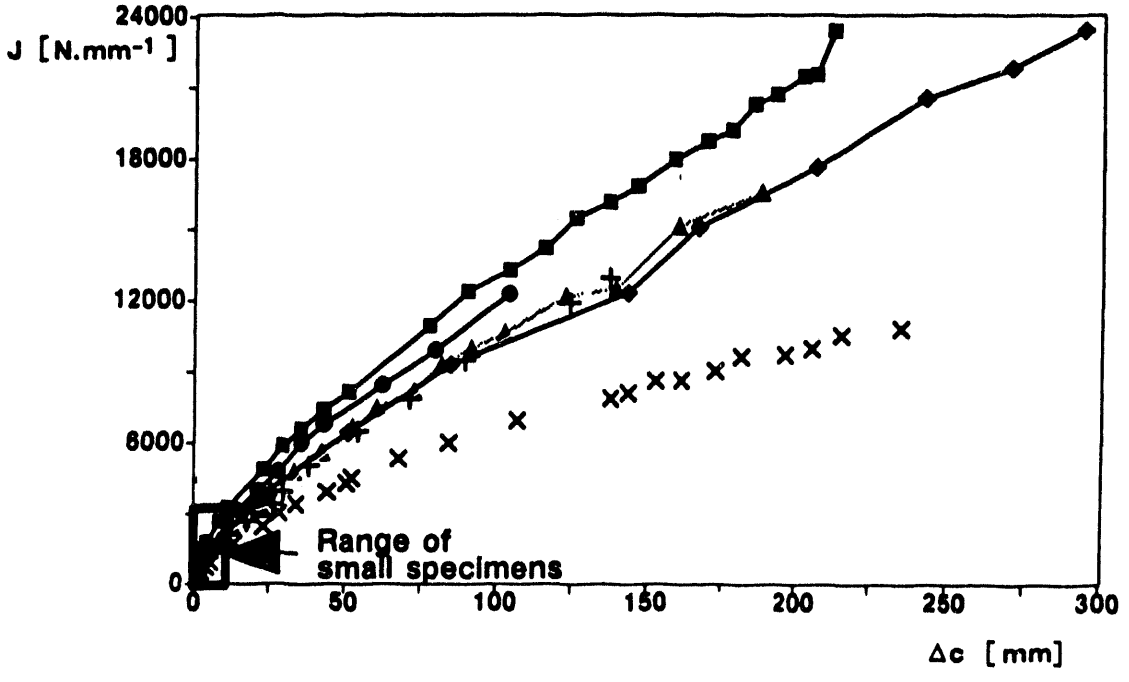

Fig. 2.1 J_R-curves for the pipes including the buckling range, Legend in Table 1

As can be seen for 316 L SPH pipes with the initial cracks of 120^0 the J_R-curve of the third experiment (WM) is well below the curve of the fifth experiment (BM). This toughness-effect can be seen also as a result of small specimen tests[3]. The J_R-curve of the second experiment (HAZ) lies between those of the third (WM) and the fifth (BM) experiment but near those of the BM. The J_R-curves rise monotonically up to a total crack extension of 600 mm. The shapes of the curves are non-linear.

J is calculated according to the basic formular

$$J = -\int_0^{\psi} \left(\frac{\partial F}{\partial A}\right) d\psi \qquad (1)$$

(ψ = load point displacement). The results of the present tests correspond to the application of

$$J = J^{el} + J^{pl} \qquad (2)$$

J^{el} is the elastic and J^{pl} is the plastic part of the J-integral

A light microscope was used to measure the crack tip opening displacement δ of the crack edges at the original crack tip on the photos taken during the pipe tests. δ_5 (Fig. 2.2 and eqn (5)) is not subject to such strong limitations on the allowable ligament and crack extension when compared to the parameters CTOA and COA[1]. Fig. 2.2 shows the linear correlation of δ and the crack extension which begins after a short initial non-linear part and ends after the initiation of buckling; the small specimen range is also shown.

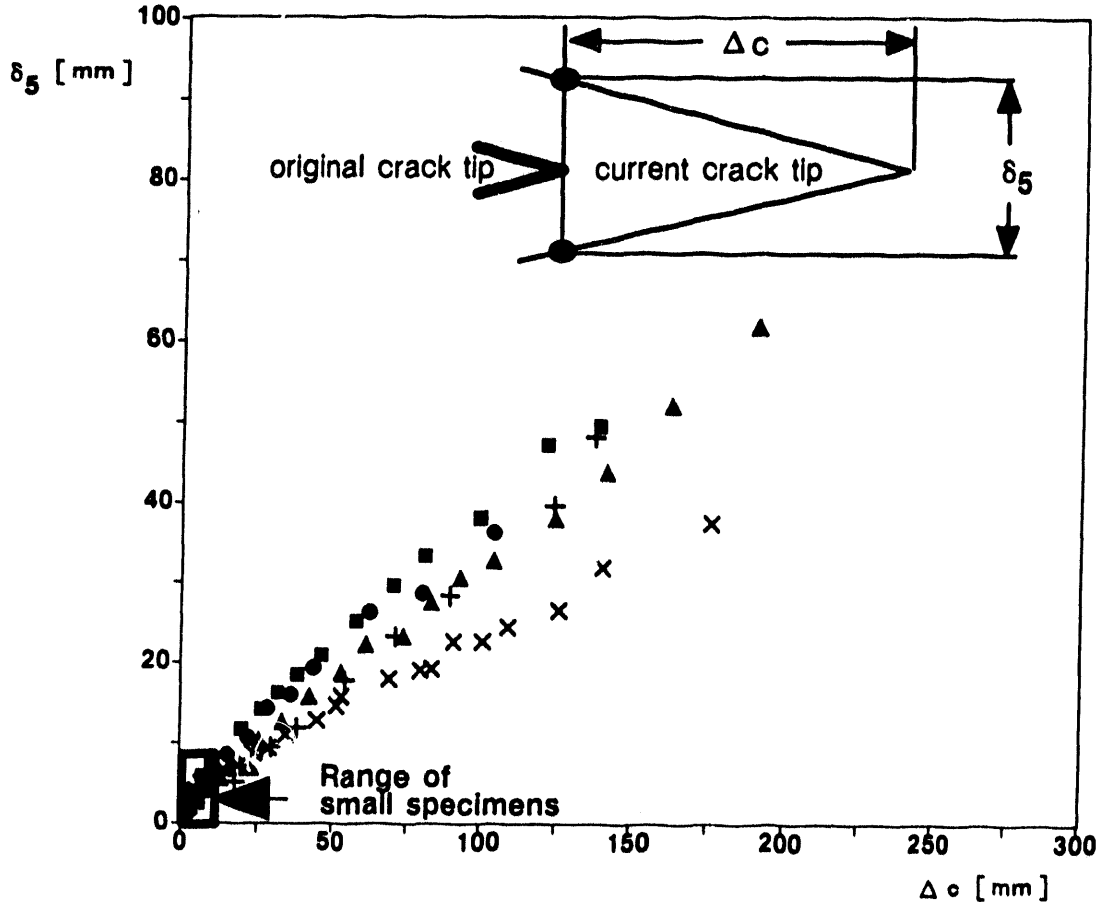

Fig. 2.2 δ_R-curves for the pipes including the buckling range. Legend in Table 1

The fundamental idea is that - for a given thickness - the measured R-curves are material constants. By the pipe tests the diversion of the forces around the crack leads to compressive stresses transverse to the applied forces. This leads to ovalization of the pipe shortly after starting the test. The diameter D_V (Fig. 3.1) is increased while the diameter D_H (Fig. 3.1) is decreased; this type of behaviour is in contrast to that of an uncracked pipe. This ovalization of the pipes is a geometrical effect which leads to a lowering of the R-curves and of the maximum moment[4]. Interim calculations using correction formulas after[6] have shown that a slight but small decrease of the J_R-curve has to be expected. Concerning effects of ovalization finite element studies[5] have shown that due to the acceptable correspondence between the finite element results and the results of the experiments the stress intensity calibration function Y is not affected.

The failure mechanism working finally is buckling on the backwall side of the pipe which is under compression. A summary of the ovalization measurements is shown in Table 3. To compare the buckling of the tested pipes the minimum of the decreasing pipe diameter D_H can be regarded as the initiation of buckling.

Table 3

Summary of the ovalization measurements

Test 2			*Test 3*			*Test 4*			*Test 5*		
Φ [°]	D_H [mm]	D_V [mm]	Φ [°]	D_H [mm]	D_V [mm]	Φ [°]	D_H [mm]	D_V [mm]	Φ [°]	D_H [mm]	D_V [mm]
124.2	703	710	120.9	702	709	175.4	705	711	120	706	714
126	679	723	122.5	686	718	175.5	698	718	120.2	697	727
128.6	678	726	137.5	675	730	175.9	694	722	120.7	693	734
131.8	676	729	148.7	670	731	177.9	688	728	121.5	688	733
132.6	673	731	166.2	672	733	185.1	686	733	123.6	681	736
138.1	670	734	180.7	674	738	198.7	687	734	129.2	674	740
148	667	738	198.3	676	736				134.2	671	749
157.8	668	745									

D_H and D_V see Fig. 3.1; Φ see Fig. 5

As a result Figs. 3.1 and 3.2 show the usable parts of the J- respectively δ - values of the measured R-curves. The question-marks characterise those ranges for which measurements are not available.

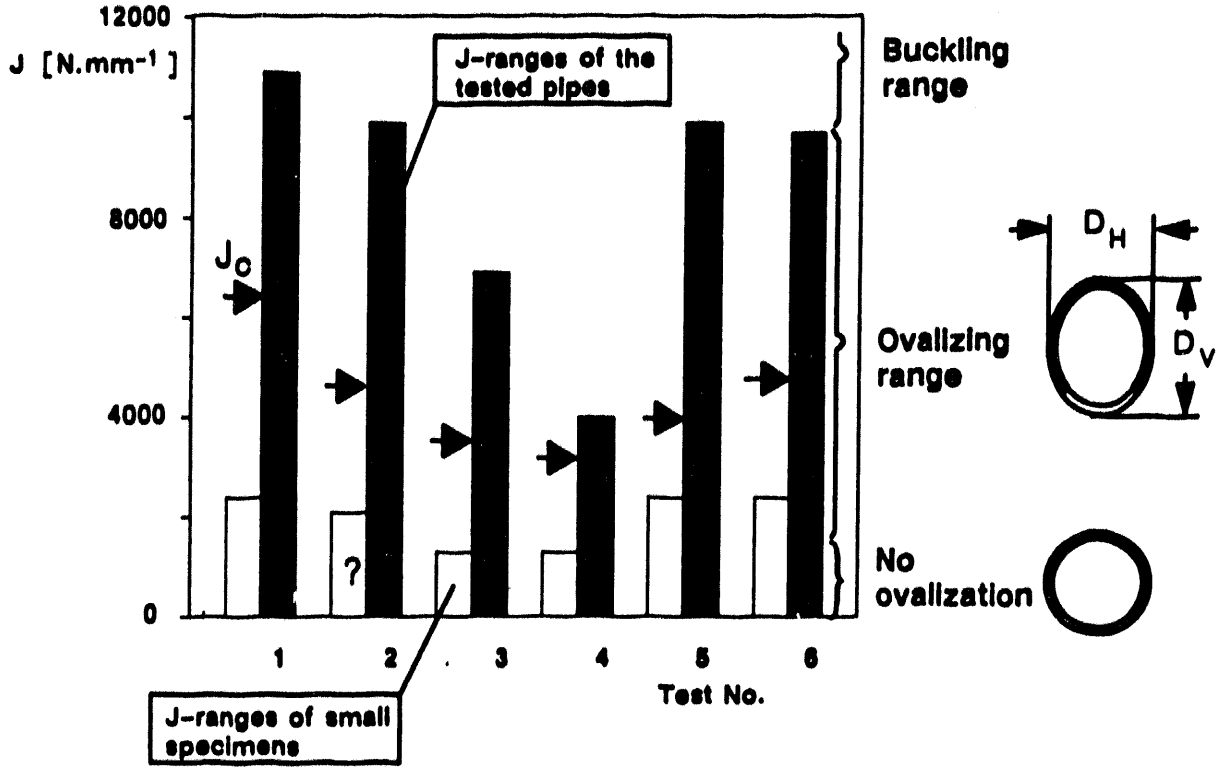

Fig. 3.1 Ranges of J values excluding the buckling range, J_c is the J-value at the maximum applied moment M

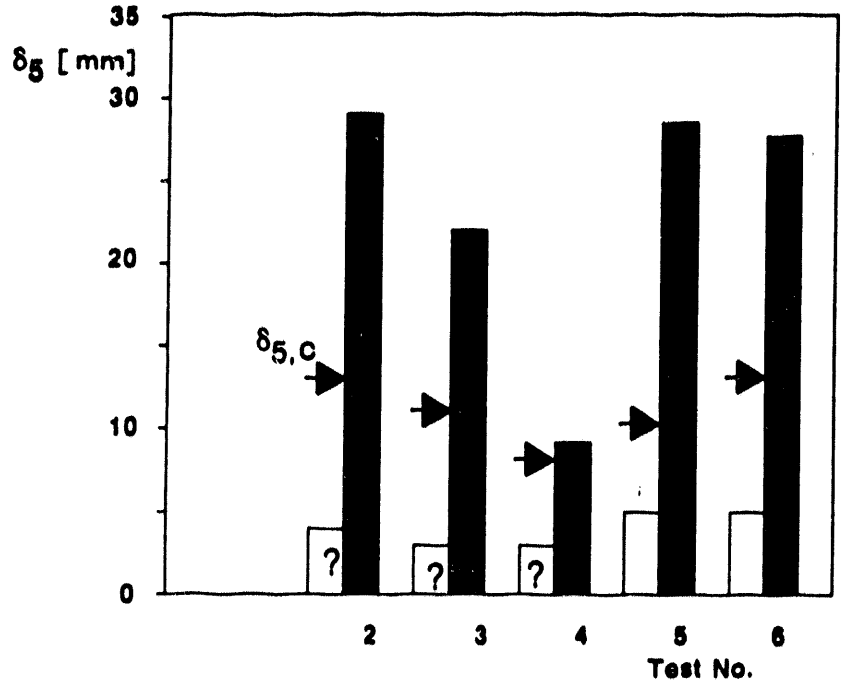

Fig. 3.2 Ranges of the Delta values excluding the buckling range

TRANSFERABILITY OF THE SPECIMEN CHARACTERISTICS

To test the transferability of R-curves from small specimens to large structures, J_R-curves of C(T)-specimens were determined by using standard test procedures after DVM, EGF and ASTM[7]. Results of J calculations are affected by the calculation procedure (see Fig.4.1a). In the present case the J_R-curves of the pipes must be referred to the EGF_{corr} J_R-curve, because in both cases the same formulas have been used.

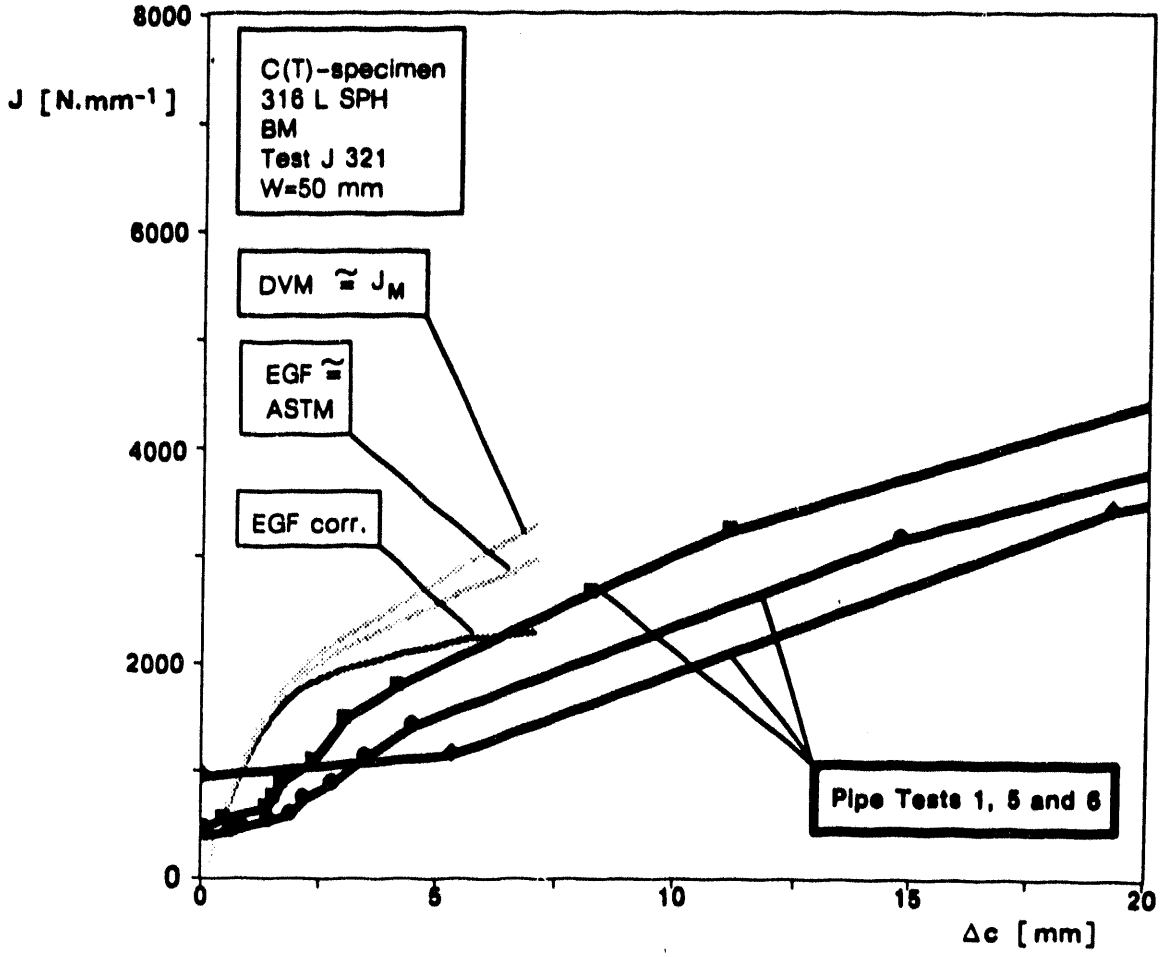

Fig. 4.1a Comparison of the J_R -curves of three pipes with those of one C(T)-specimen of the same material, Legend in Table 1

As shown in Fig. 2.1 the J_R-curves of the pipes are non-linear. This means that any extrapolation from small specimens to large structures is impeded. Further more, it is immediately clear that any extrapolation from small specimen data will be difficult due to the small crack extension of only a few mm in these specimens.

In this context another point of interest is the effect of the material toughness on the R-curve. From small specimen results it is well known, that the J_R-curves of weldments are lower than those of base material. This is also a result of J_R-curves taken from the pipe tests; see Fig. 2.1, test 3 and 5. On the other hand, as a result of some size effect, in the crack initiation area the J_R-curves of the tested pipes are generally lower than those of the tested small specimens; an example is shown in Fig.4.1a. This supposition is supported by the different reduction in wall-thickness t, shown in Fig.4.1b.

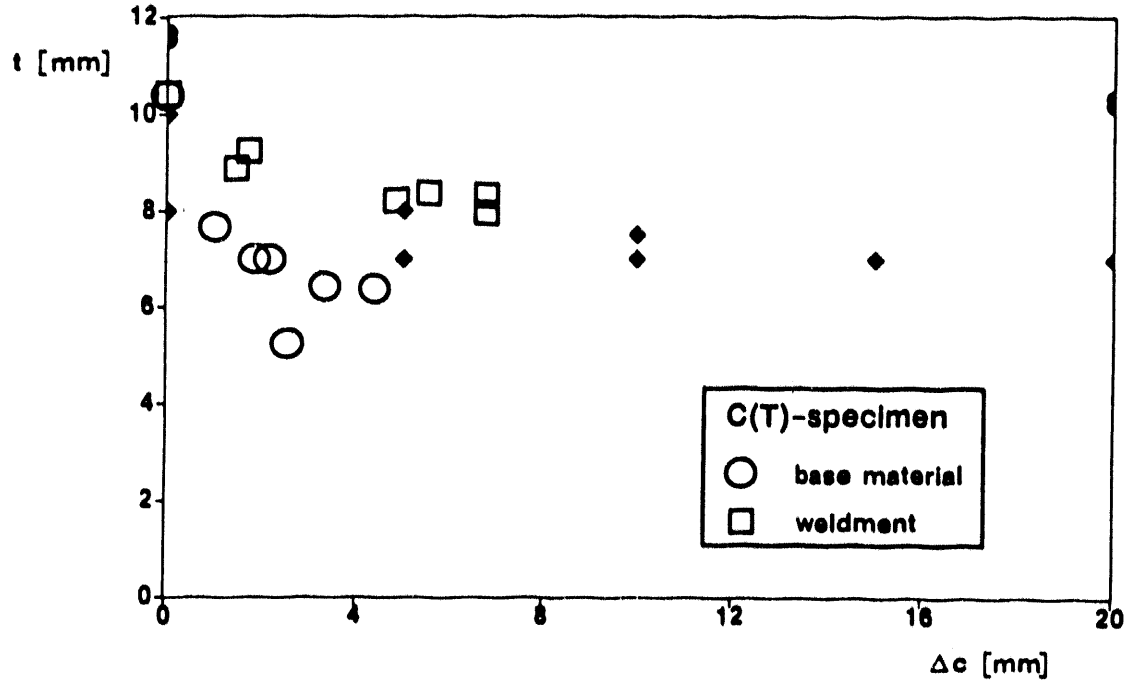

Fig. 4.1b Comparison of the reduction in wall-thickness of the pipes (Legend in Table 1) in tests 1, 5 and the C(T)- specimens

During the same tests the crack tip opening displacement at the original pre-fatigue crack tip over a gauge span of 5 mm (a schematic drawing is shown in Fig. 2.2) was measured by using two special clip gauges. In Fig. 4.2 the $\delta_{5,R}$-curves measured on eight C(T)-specimens are shown together with the comparable δ_R-curve of pipe test 5. The small specimen data are available for crack extensions up to 5.8 mm. The C(T)-specimen data are at the upper bound of the pipe data, following the non-linear trend curve up to the maximum observed crack extension. The linear part of the δ_R -curve measured on the pipe is within the range of possible extrapolations from the small specimen measurements.

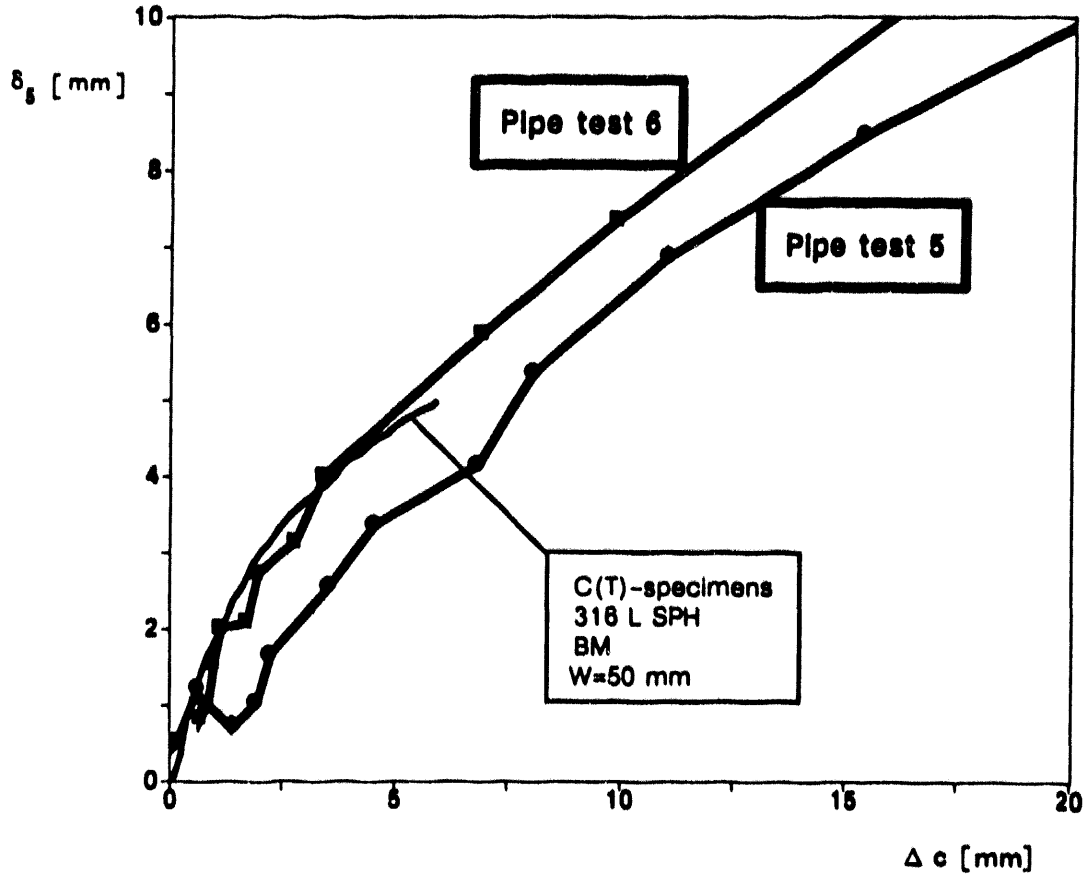

Fig. 4.2 Comparison of the δ_R -curves of two pipes with those of eight C(T) - specimens of the same material

APPLICABILITY OF THEORETICAL METHODS FOR PREDICTION

The necessity for making quick assessments for the severity of a crack-like flaw in a structure led to the development of a number of failure assessment methods[8] which are easy to apply, provided that the relevant input information are available. Two of these are investigated for predicting the point of instability.

It has been observed experimentally that the applied moments M are well below the limit moments M_L (based on $\sigma_F = (R_e + R_m) / 2$, σ_F = flow stress) of the pipes. The plasticity in the remaining ligament was investigated by Wilkowski et al.[9] who proposed an empirical criterion called the "Screening Criterion", which shows relation between the ratio of maximum experimental moment M_{max} (M_o if load controlled) to limit moment M_L and a dimensionsless plastic zone parameter incorporating the toughness of the material. The results of the pipe tests seem to support this criterion (see Fig.5, J_0 = initial value of J, σ_F = flow stress).

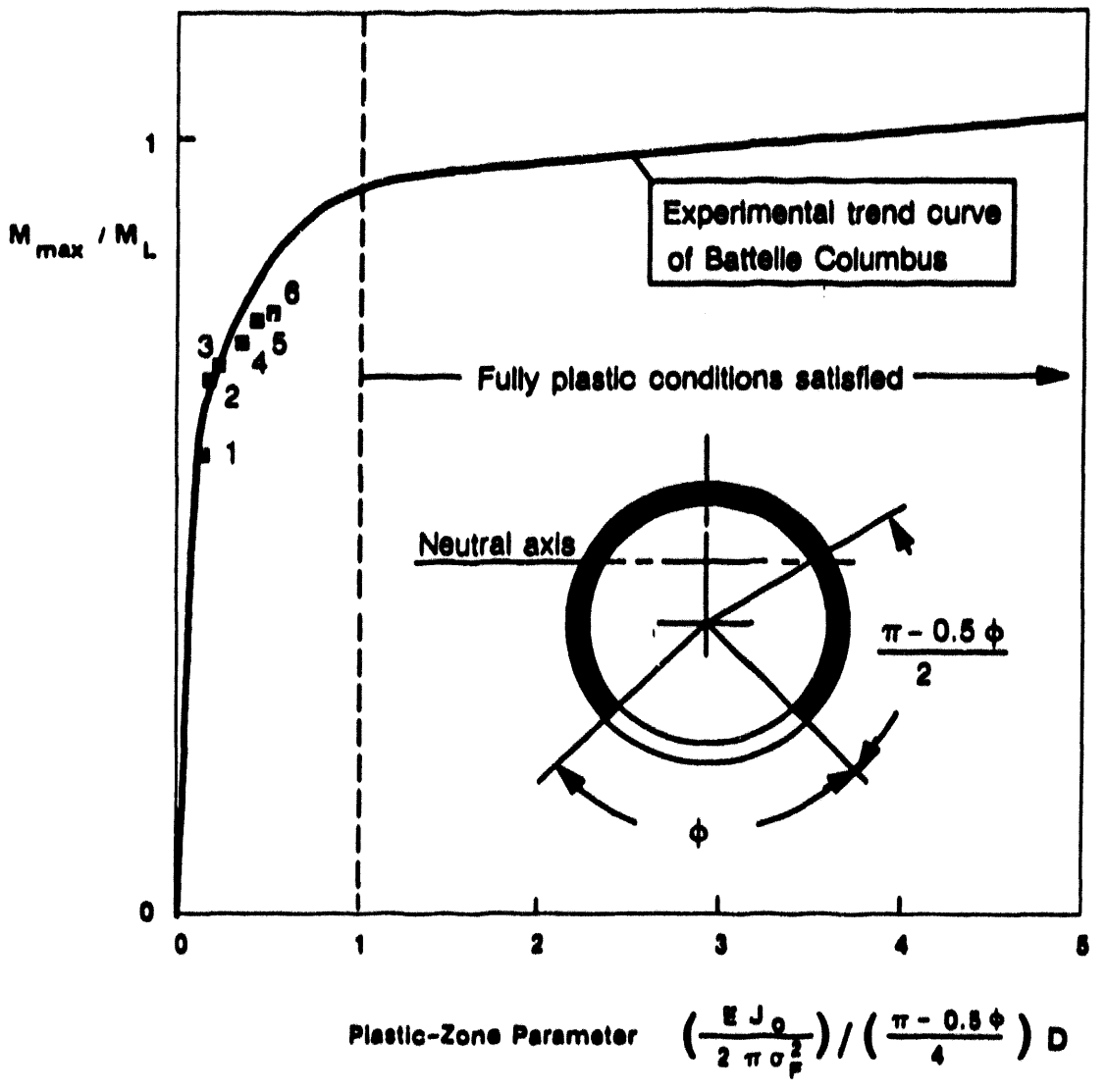

Fig. 5 Comparison of the "Screening Criterion" with the results of the pipe tests

The ETM is aimed at estimating the mechanical behaviour of a cracked structure by closed form solutions[10]. The ETM distinguishes between the load ranges $F < F_e$ and $F > F_e$, where F_e is the yield load which is related to the attainment of net section yielding.

In the load range $F < F_e$ the CTOD is given for bending configurations by the plastic corrected small-scale yielding solution:

$$\delta = \frac{[\,0.5\,(K_{eff} + K)\,]^2}{E \cdot R_e} \qquad (3)$$

with

$$K_{eff} = \sigma \cdot Y \sqrt{(\pi \cdot c_{eff})}$$

$$c_{eff} = \frac{K^2}{2 \cdot \pi \cdot R_e^2\,(1+n)}$$

$$K = \sigma \cdot Y \sqrt{(\pi \cdot c)}$$

(δ = displacement, c = semi crack length, K = stress intensity factor, Y = stress intensity calibration function). In the net section yielding regime the applied load $F > F_e$, the area of interest for this paper, the CTOD is given by:

$$\delta = \delta_e \left\{ \frac{F}{F_e} \right\}^{1/n} \qquad (4)$$

where δ_e designates the value of δ at $F = F_e$ and n is the strain hardening exponent of a piece-wise power law representing the material's engineering stress-strain curve:

$$\epsilon = \epsilon_e \left\{ \frac{\sigma}{R_e} \right\}^{1/n} \qquad (5)$$

As these formulations have already been successfully applied to laboratory specimens, it was intended to use ETM for predicting the behaviour of the pipes tested.

In the case of the pipes eqn (4) can be rewritten as follows:

$$\delta_5 = \delta_e \left\{ \frac{M}{M_e} \right\}^{1/n} \qquad (6)$$

(M = applied bending moment). According to the rules of ETM the input value n (Table 2) is an average slope of the σ-ϵ values going through R_e/ϵ_e and touching the σ-ϵ at its upper end as a tangent.

$$M = F \cdot l$$

$$M_e = R_e \cdot t \cdot D^2 \left(\cos \frac{\Phi}{4} - \frac{1}{2} \sin \frac{\Phi}{2} \right)$$

δ_e from eqn (3) with $\sigma = \dfrac{4 \cdot M}{\pi \cdot t \cdot D^2}$

(Φ = Crack Angle). The tensile data are listed in Table 2. Y was determined by using the compliance measurements during the tests[5].

For all six pipes the maximum (in the case of load control: critical) moment M_e and the related crack extension Δc_e were predicted using eqn 4 as the driving force expression for the R-curve analysis. For a sensitivity study the critical values have been determined in a systematic manner (Table 4) by the tangency condition between the driving force curves and the R-curves. Category 1 in Table 4 means, for example: The critical values of pipe 3 ($\Phi = 120^0$, WM) have been determined with the driving force expressions using the tensile data for the weldment (Test 3) and the R-curve of test 3 itself. The driving force expression and the R-curve are based on the same parameters. Category 2 means, for example: The critical values of pipe 3 ($\Phi = 120^0$, WM) have been determined with the driving force expressions using the tensile data for the weldment and the R-curve of test 5 ($\Phi = 120^0$, BM); the material as an R-curve parameter changes against category 1. It seems to be more difficult to get the correct prediction than in category 1. Category 3 means: The critical values of pipe 4 ($\Phi = 180^0$, WM) have been determined with the driving force expressions using the tensile data for the weldment (Test 4) and the R-curve of test 5 ($\Phi = 120^0$, BM); against category 2 the level of confidence of the results decreases once more.

Table 4

Categories for the Prediction of Instability

Category	*Load Configuration*	*Geometry*	*Initial Crack*	*Material*
1	same	same	same	same
2	same	same	same	different
3	same	same	different	different

Figs. 6.1 and 6.2 show the results of the predicted critical values of semi crack length c and bending moment M. It can be seen, that in category 2 and 3 the crack lengths are underpredicted and the moments are overpredicted.

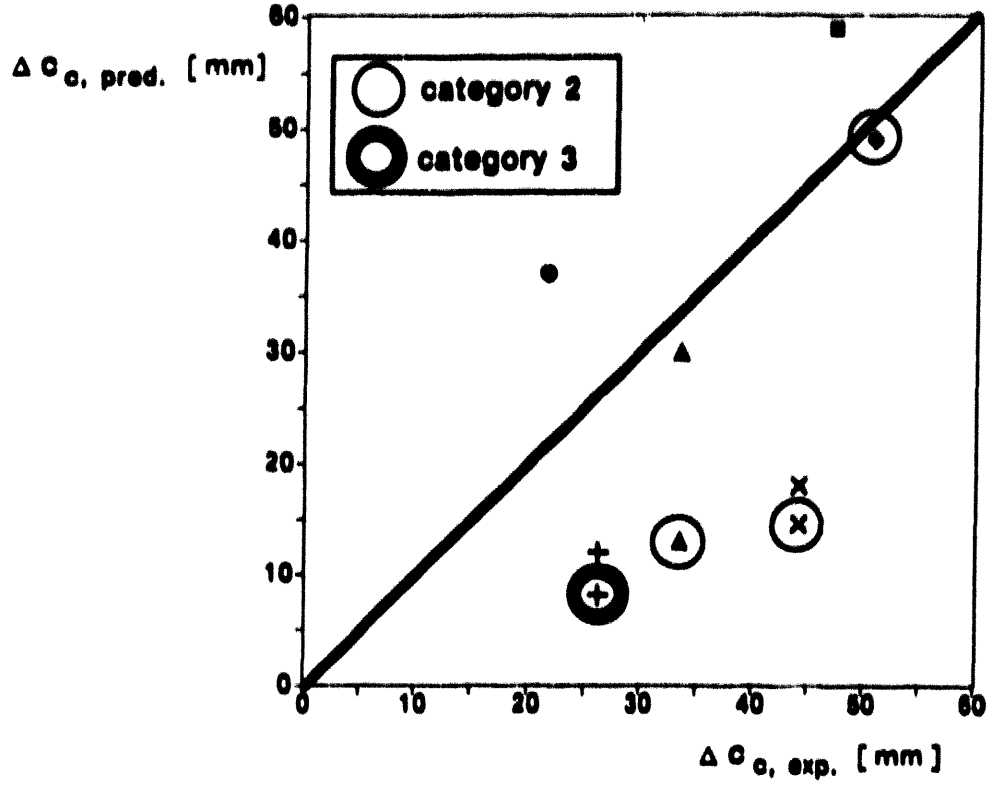

Fig. 6.1 Predicted critical crack extensions, Legend in Table 1

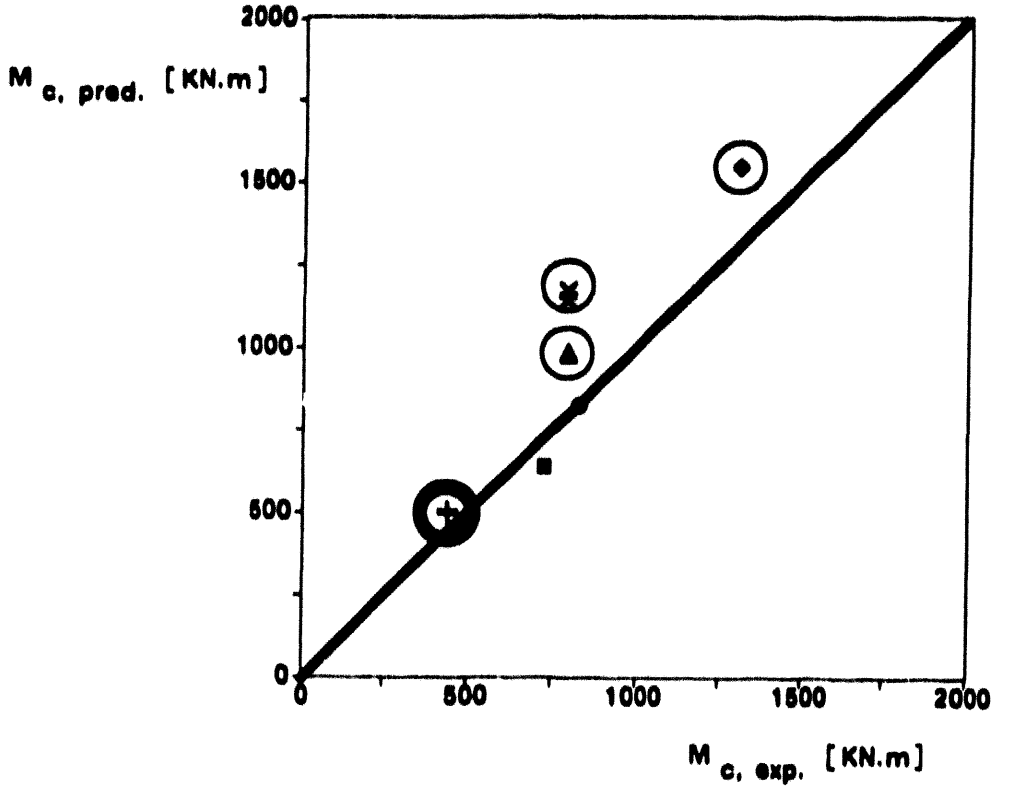

Fig. 6.2 Predicted value of the critical moment, Legend in Table 1

CONCLUSIONS

- R-curves based on the J-integral and the Crack Tip Opening Displacement have been established for circumferentially cracked thin-walled straight pipes. It has been emphasized that the usable range of the R-curves is limited by the beginning of buckling.
- The results of checking the transferability of laboratory specimen crack growth characteristics to circumferentially cracked pipes demonstrated on the austenitic stainless steel 316 L SPH, that the fracture mechanics concept for a reliable transfer of crack resistance data from small specimen geometries to large structures is still to be qualified for high toughness materials.
- Two methods, the "Screening Criterion" and in particular the "Engineering Treatment Model" ETM, have been checked for their usefulness in predicting the point of crack instability. The results presented in this paper show an overestimation of the maximum moment and in the most cases an underestimation of the corresponding crack extension Δc_e.

REFERENCES

1. Grûter, L., Fortmann, M., Bhandari, S., Faidy, C., Crack resistance properties of through-cracks in austenitic straight pipes DN 700 under bending, Nucl. Eng. and Design 108 (1988) 447-456

2. Kotter, K.H., Chang and Zahoor A., Application of tearing modulus stability concepts to nuclear piping, EPRI-NP 2261 (1982)

3. Grûter, L., Debaene, J.P., Faidy, C., Stable crack growth in large austenitic pipes under bending, Proc. ASME-PVP Conf., Pittsburgh (19.-23. Juni 1988), ASME-PVP 135, 65-70

4. Bucci, R.J., Sha, G.T., Effect of Antibuckling Constraint on Determination of Critical Stress Intensity Factor of Aluminum Sheet, Journal of Testing and Evaluation 5, No. 2, (1977) 94-95

5. Grûter, L., Setz, W., Bhandari, S., Deschanels, H., Faidy, C., Stress intensity factor solution for thin-walled straight pipes DN 700 under bending, Int. J. Pres. Ves. & Piping, 52 (1992)

6. Zahoor, A., Kanninen, M.F., A Plastic Fracture Mechanics Prediction of Fracture Instability in a Circumferentially Cracked Pipe in Bending - Part I: J-Integral Analysis, Trans. ASME, J. Pres. Ves. Technol., 103 (1981) 352-358

7. Grûter, L., Huthmann, H., Cornec, A., Transferability of laboratory specimen crack growth characteristics to circumferentially cracked pipes, *Defect assessment in components - fundamentals and applications*, ESIS/EGF 9 (Edited by J.G. Blauel and K.-H. Schwalbe), Mechanical Engineering Publications, London (1991) 723-737

8. Bhandari, S., Nesa, D., Faidy, C., Grûter, L., Initiation and instability behaviour of cracked LMFBR piping: Comparison of different approaches and experiments, Nucl. Eng. and Design 119 (1990) 337-345

9. Wilkowski, G., Degraded piping programm - phase II progress, Nucl. Eng. and Design 98 (1987) 195-217

10. Schwalbe, K.-H., Grûter, L., Application of the Engineering Treatment Model (ETM) to the prediction of the behaviour of a circumferantially cracked pipe, *Defect assessment in components - fundamentals and applications*, ESIS/EGF 9 (Edited by J.G. Blauel and K.-H. Schwalbe), Mechanical Engineering Publications, London (1991) 1125-1133

COMPARISON OF FRACTURE TOUGHNESS VALUES FROM LARGE-SCALE PIPE SYSTEM TESTS AND C(T) SPECIMENS

by

R. Olson, P. Scott, C. Marschall, and G. Wilkowski
BATTELLE
505 King Avenue
Columbus, Ohio 43201
U.S.A.

ABSTRACT

Within the International Piping Integrity Research Group (IPIRG) program, pipe system experiments involving dynamic loading with intentionally circumferentially cracked pipe were conducted. The pipe system was fabricated from 406-mm (16-inch) diameter Schedule 100 pipe and the experiments were conducted at 15.5 MPa (2,250 psi) and 288 C (550 F). The loads consisted of pressure, dead-weight, thermal expansion, inertia, and dynamic anchor motion.

Significant instrumentation was used to allow the material fracture resistance to be calculated from these large-scale experiments. A comparison of the toughness values from the stainless steel base metal pipe experiment to standard quasi-static and dynamic C(T) specimen tests showed the pipe toughness value was significantly lower than that obtained from C(T) specimens. It is hypothesized that the cyclic loading from inertial stresses in this pipe system experiment caused local degradation of the material toughness. Such effects are not considered in current LBB or pipe flaw evaluation criteria.

INTRODUCTION

The first phase of the International Piping Integrity Research Group (IPIRG-1) program was an international group program managed by the U.S. Nuclear Regulatory Commission (USNRC) and funded by a consortium of organizations from nine nations: Canada, France, Italy, Japan, Sweden, Switzerland, Taiwan, the United Kingdom, and the United States. The objective of the IPIRG-1 program was to develop data needed to verify engineering methods for assessing the integrity of nuclear power plant piping that contains circumferential defects. The primary focus was experiments that investigated the behavior of circumferentially flawed piping and piping systems subjected to loading typical of seismic events.

In nuclear piping system applications, the fracture resistance of a material is typically expressed in terms of the J-integral fracture parameter versus crack extension, i.e, the J-resistance (J-R) curve. Typically, J-R curves are developed using compact (tension), C(T), specimens with monotonic loading. In these tests, applied load, specimen displacement, and crack growth are measured and

used to generate the J-R curve. Another method of developing J-R curves is to measure crack growth, load, and displacement from a pipe fracture experiment. Again, using suitable analyses, a pipe J-R curve can be developed.

In the ideal case, C(T) specimen and pipe J-R curves would be quite compatible. If this ideal state always existed, then only specimen tests would be required to supply the data for piping fracture analyses. Unfortunately, the ideal case does not always exist. The effect of constraint on toughness is currently a high priority topic, even though it was recognized long ago that a bend-bar or C(T) specimen would give a lower toughness than a center-cracked plate. Under monotonic loading, numerous programs determined that bend or C(T) specimens yield lower bound results. However, other mechanisms, such as cyclic and/or dynamic loading, may influence the fracture toughness of a material. The following paper compares the standard C(T) specimen and dynamic pipe fracture experiment J-R curves from the IPIRG-1 stainless steel base metal pipe system experiment. It will be shown that the C(T) specimen J-R curve is significantly higher than the pipe test J-R curve leading to speculation that cyclic loading in this pipe system experiment has caused some degradation of the material toughness.

DESCRIPTION OF EXPERIMENTS

The main experimental effort in the IPIRG-1 program consisted of both "separate effects" experiments on simple small-diameter 152-mm (6-inch) pipe and combined inertial- and displacement-controlled load experiments on a larger diameter 406-mm (16-inch) piping system tested at nominal pressurized water reactor (PWR) conditions. The pipe system experiments were conducted to investigate the complex interaction of loading conditions and system dynamics on pipe fracture behavior. Results from these experiments provide an important data base that can be used for the critical assessment of analytical procedures.

There were five cracked and one uncracked pipe system experiments conducted as part of IPIRG-1. The crack in each cracked pipe experiment was an internal circumferential surface crack with a crack size approximately 66 percent of the wall thickness in depth and approximately 50 percent of the pipe circumference in length.

The pipe system used in the conduct of these experiments was fabricated as an expansion loop with over 30.5 m (100 feet) of straight pipe and five (5) long radius elbows, see Figure 1. Special care was taken in the design and construction of this pipe system to ensure that the boundary conditions could be properly modeled in a finite element analysis. At the two fixed ends (Nodes 1 and 31 in Figure 1), the pipe was attached to 1500-pound class weld neck flanges which were bolted to a large steel frame that was buried in a large, heavily reinforced concrete mass. At the two hanger locations (Nodes 6 and 26), the pipe was supported by spherical bearings which allowed the pipe to translate in the direction along the pipe axis and to freely rotate in all three rotational degrees-of-freedom while constraining the pipe in the vertical and horizonal directions perpendicular to the pipe axis. At the actuator location, lateral displacements were prescribed. Because a spherical bearing was also incorporated at the actuator location, the pipe was constrained vertically but was free to translate along its axis and free to rotate in any direction. Finally, at the two vertical supports, the pipe

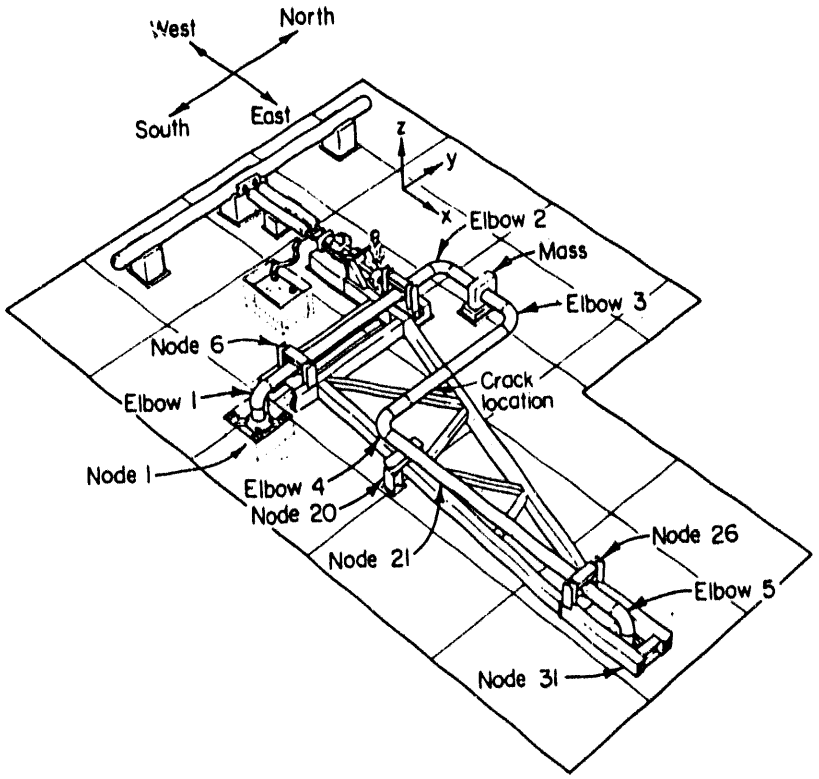

Figure 1 Artist's conception of the IPIRG pipe system test configuration

QL/1.3-4/F1

floated on a thin film of oil from hydrostatic bearings which supported the pipe in an essentially frictionless manner.

The actuator displacement-time history for the stainless steel base metal experiment was an increasing amplitude sinusoid with an increasing ramp superimposed. The equation of motion for the actuator was:

$$U_x = St + A[1-e^{-bt}]\sin(\omega t) \qquad (1)$$

where

U_x = actuator displacement
t = time
S,A,b = equation constants
ω = 24.82 rad/sec (3.95 Hz).

The forcing function frequency used in this experiment, 3.95 Hz, is 90 percent of the first natural frequency of the pipe system, 4.41 Hz. As a result of this load history and test conditions (PWR), the cracked section experienced a variety of stress components, i.e., thermal expansion, dead weight, pressure induced membrane, and a mixture of displacement-controlled (seismic anchor motion) and inertial bending stresses.

For each of the IPIRG-1 pipe system experiments, crack section moment data were measured using a series of strain gages attached to the pipe loop on each side of the crack section. In addition, rotation data were recorded using an LVDT-based device mounted across the crack, see Figure 2. Figure 3 is a plot of the moment-rotation response from the IPIRG-1 stainless steel base metal experiment.

Prior to conducting the cracked pipe experiments, quasi-static and dynamic tensile tests and quasi-static and dynamic J-R curve tests were conducted using laboratory-scale-size test specimens for each of the materials tested in a pipe system experiment. The monotonic tensile test results (quasi-static and dynamic) for this stainless steel material are shown in Figure 4. The monotonic J-R curves (quasi-static and dynamic) for this material are shown in Figure 5.

Figure 2 Photograph of LVDT-based rotation device used on three stainless steel experiments

F1.3-3/91-F3.52

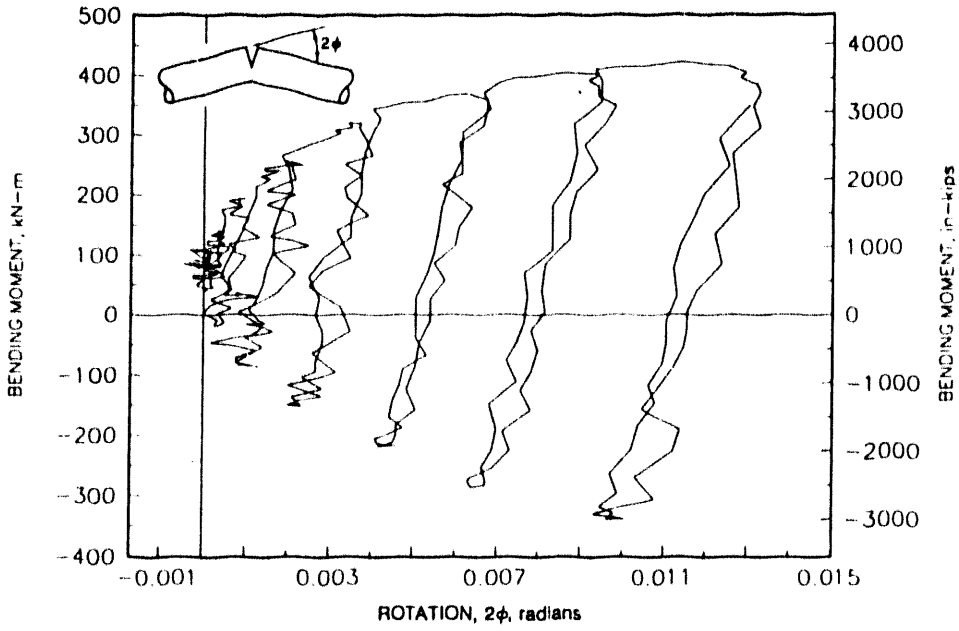

Figure 3 Crack section moment-rotation behavior from the IPIRG-1 stainless steel base metal experiment (1.3-3)

I1.3-10/90-F3.133

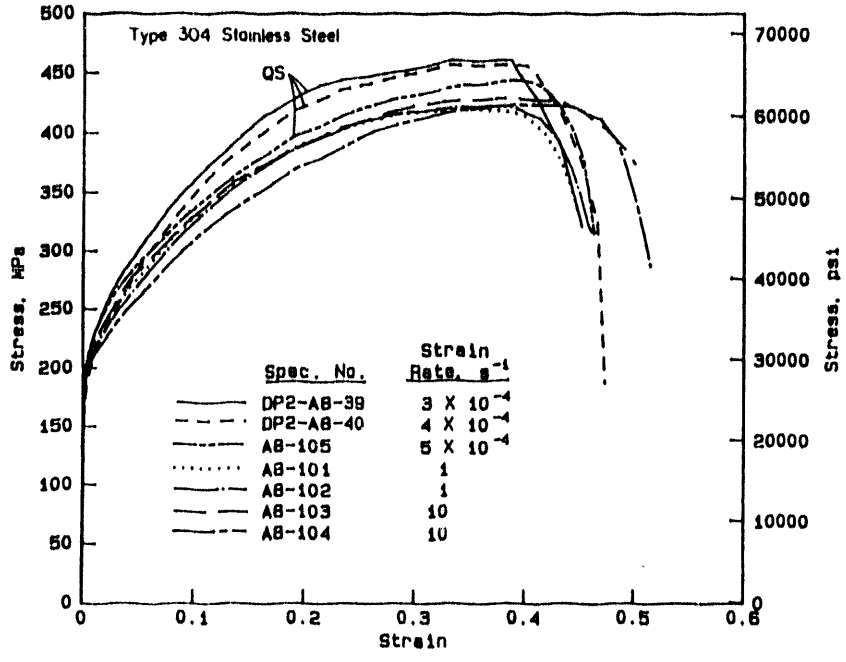

Figure 4 Engineering stress-strain curves at 288 C (550 F) for A358 Type 304 stainless steel pipe (DP2-A8) tested at several different strain rates

I1.3-10/90-F2.2.5

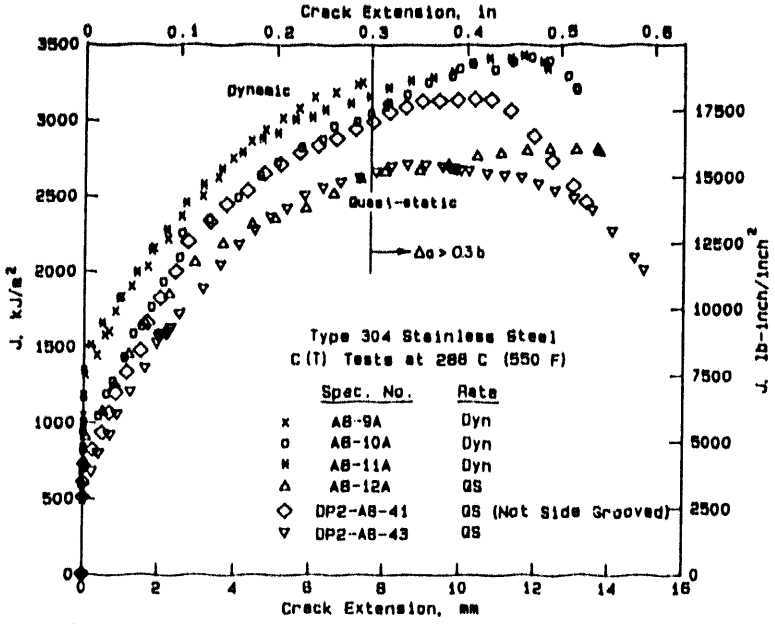

Figure 5 J-resistance curves for compact specimens from A358 Type 304 stainless steel pipe (DP2-A8) tested at 288 C (550 F)

I1.3-10/90-F2.3.3

ANALYSIS OF EXPERIMENTS

One aspect of the analysis of the IPIRG-1 stainless steel base metal surface-cracked pipe system experiment involved comparing the envelope of the experimental moment-rotation response to the predicted moment-rotation response from the SC.TNP J-estimation scheme[1]. SC.TNP is a finite length surface crack J-estimation scheme developed at Battelle as part of the USNRC's Degraded Piping Program. The SC.TNP approach uses the EPRI/GE 360-degree surface-cracked pipe solution[2] for pure tension to develop new h-functions for calculating the plastic component of J, J_p, for a finite length surface crack subjected to pure bending loads.

The effect of internal pressure is addressed in the analysis in an approximate way by ignoring possible loading path effects on plastic deformation, and replacing the axial tension in the uncracked ligament ahead of the crack by an additional applied moment. The equivalent moment, M_{eq}, from the pressure-induced axial tensile stress is approximated as being equal to the difference of the Net-Section-Collapse predicted moment under pure bending and the Net-Section-Collapse predicted moment under combined bending and tension due to the internal pressure.

The material property data needed for J-estimation scheme analyses are the yield and ultimate strengths, Ramberg-Osgood parameters for the stress strain curve, and the J-R curve for the material. Stainless steel is a difficult material to have a good fit of the tensile test data with a Ramberg-Osgood curve. Figure 6 shows four different Ramberg-Osgood stress-strain curve fits used in the following fracture analysis. Table 1 lists the Ramberg-Osgood coefficients for each of four fits to the measured stress-strain curve data.

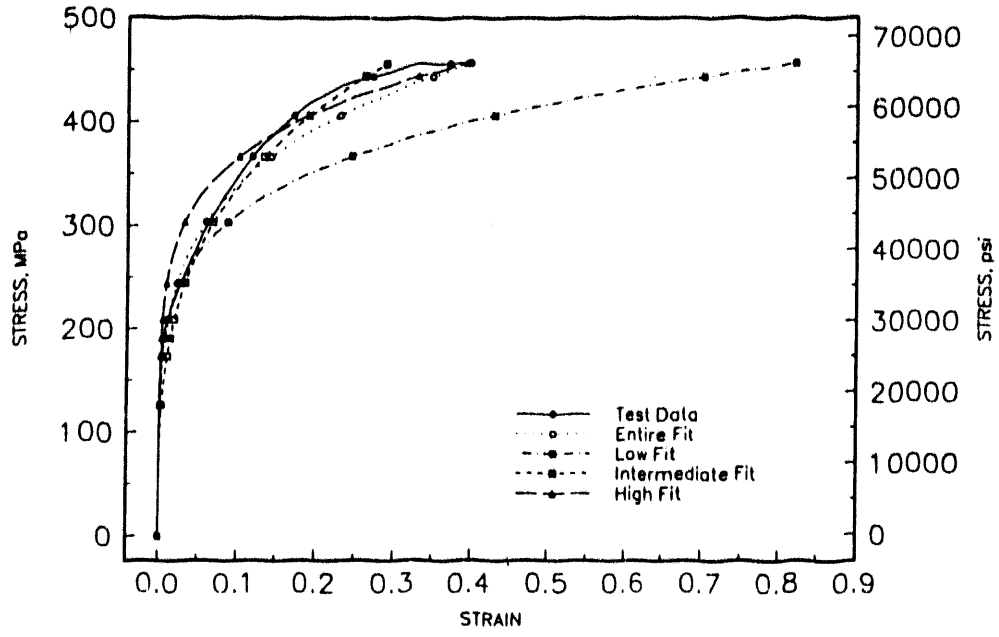

Figure 6 Engineering stress-strain curve for stainless steel base metal material at 288 C (550 F) showing four strain ranges considered in Ramberg-Osgood regression analysis

IAEA-10/92-F6

Table 1 Tensile properties of stainless steel base metal with four different fits of stress-strain data to Ramberg-Osgood equation

	Entire Curve	Low Strain Region	Intermediate Strain Region	High Strain Region
alpha (α)	3.529	3.181	8.328	0.724
exponent (n)	4.715	5.534	3.551	6.264
Regression Coefficient (R)	0.982	0.949	1.001	0.996
Yield Strength	24.8 ksi			
Ultimate Strength	66.2 ksi			
Reference Strain	0.000936			

Figure 7 compares the envelope of the experimental moment-rotation curve for the stainless steel base metal pipe system experiment with the predicted moment-rotation response from the SC.TNP J-estimation scheme using the four different fits of the quasi-static stress-strain curve to the Ramberg-Osgood equation. In each case, the predicted moment-rotation response is based on quasi-static J-R curve data from monotonically loaded C(T) specimens. The predicted maximum moments from the SC.TNP analysis for each of these cases are significantly higher than the maximum experimental moment. Furthermore, except for the case where the predicted moment-rotation response is based on Ramberg-Osgood coefficients from a fit of the stress-strain data in the intermediate strain region, the predicted moment-rotation response is higher than the experimental data in the elastic region. Because it is essential to compare well in the purely elastic region, only the intermediate strain region coefficients will be considered from hereon.

Figure 8 compares the envelope of the experimental moment-rotation curve to the predicted response using the intermediate strain range coefficients. The agreement between prediction and experiment is quite good up to a rotation value of approximately 0.0045 radians. After that point, the analysis significantly overpredicts the experiment. One possible explanation for this deviation between the experimental and predicted response is due to a difference in the J-R curves between the pipe experiment and the C(T) specimen test. A logical assumption is that the crack initiated at the point where the two curves began to deviate. If one examines the output file for the SC.TNP analysis, one finds that the J value at the point where the two curves deviate, 0.0045 radians of rotation, is 215 kJ/m^2 (1,230 in-lb/in^2). This is 29 percent of the average J_i value from the quasi-static

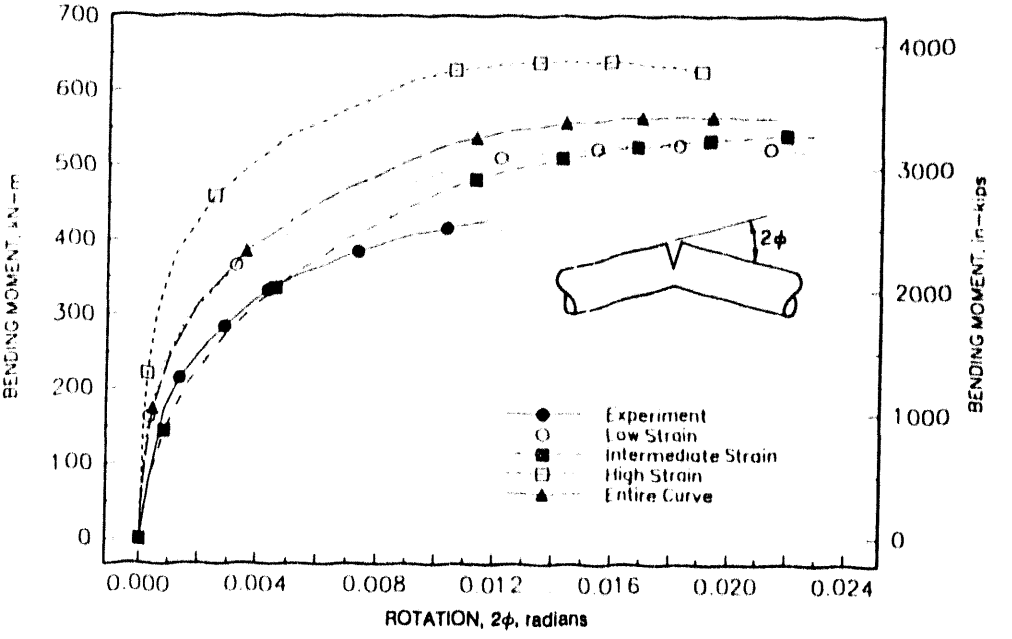

Figure 7 Comparison of the envelope of the experimental moment-rotation response for the stainless steel base metal pipe system experiment with the SC.TNP predicted moment-rotation response using four different fits of the quasi-static stress-strain curve to the Ramberg-Osgood equation

IAEA-10/92-F7

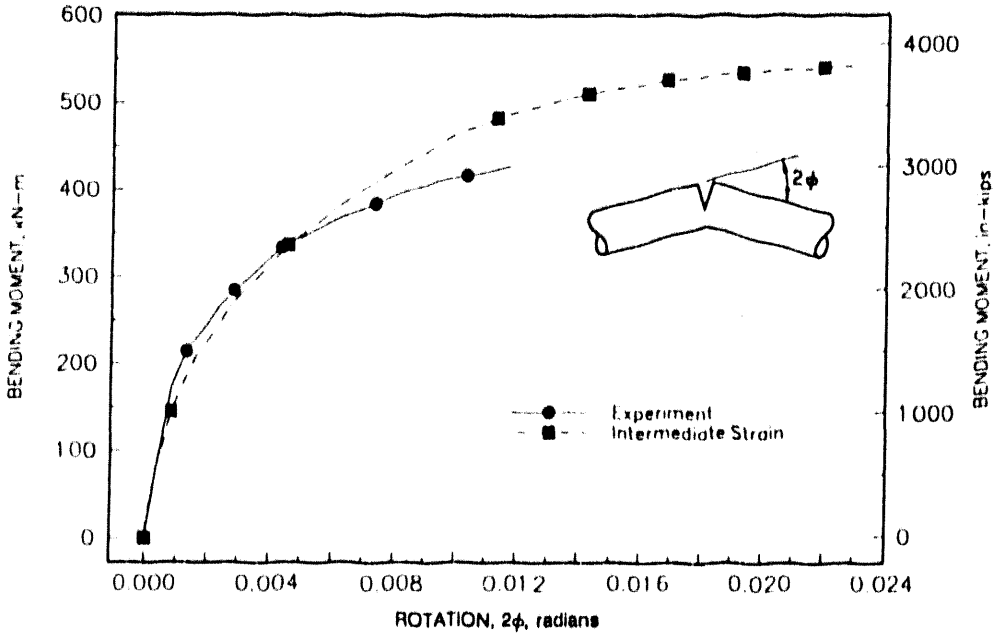

Figure 8 Comparison of the envelope of the experimental moment-rotation response for the stainless steel pipe system experiment with the SC.TNP predicted response using the intermediate range Ramberg-Osgood coefficients

IAEA-10/92-F8

monotonically loaded C(T) specimen tests, 738 kJ/m^2 (4,215 in-lb/in^2), and only 18 percent of the average dynamic monotonic J_i value of 1,215 kJ/m^2 (6,933 in-lb/in^2). If one lowers the slope of the J-R curve, i.e., dJ/da, to account for the lower slope of the experimental moment-rotation response, and one assumes that J_i is lower, one should be able to match the predicted and experimental curves past crack initiation. Through an iterative process, it was found that if the J-R curve used in the SC.TNP analysis was modified so that the J_i value was set at 738 kJ/m^2 (1,230 in-lbs/in^2) and the dJ/da value was decreased by a factor of approximately 1.7, then the agreement between the predicted and experimental response is exceptional, see Figure 9. The modified J-R curve used in this analysis along with the J-R curve from the quasi-static, monotonic C(T) specimen test are shown in Figure 10. Clearly, the pipe system J-R curve in Figure 10 suggests that some degrading mechanism has affected the pipe's fracture toughness.

One possible explanation for the experimental moment-rotation curve for the stainless steel base metal experiment being low compared to the moment-rotation behavior using C(T) data is a lowering of the material's fracture resistance due to cyclic loading effects. The SC.TNP predictions are predictions of monotonic loading behavior using laboratory specimen data generated under monotonic loading conditions, whereas the loading for the experiments was cyclic in nature, see Figure 3. In fact the effective stress ratio (R) for this experiment, considering the membrane stress contribution due to internal pressure, was -0.34. This was the lowest stress ratio of all the IPIRG-1 pipe system experiments.

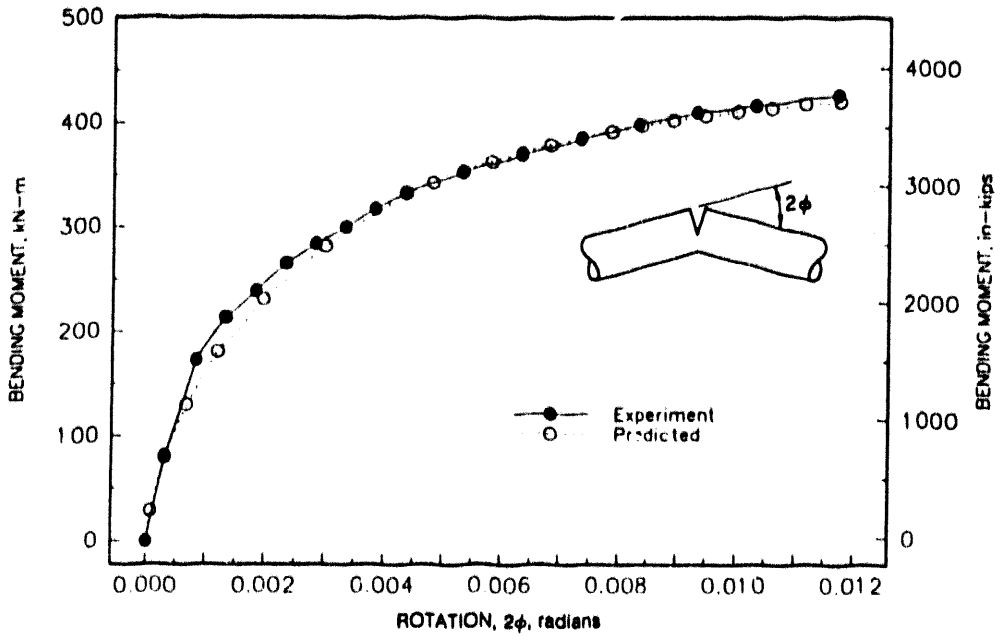

Figure 9 Comparison of the envelope of the experimental moment-rotation response for the stainless steel base metal pipe system experiment with the SC.TNP predicted moment-rotation response using the intermediate range Ramberg-Osgood coefficients and the modified J-R curve

IAEA-10/92-F9

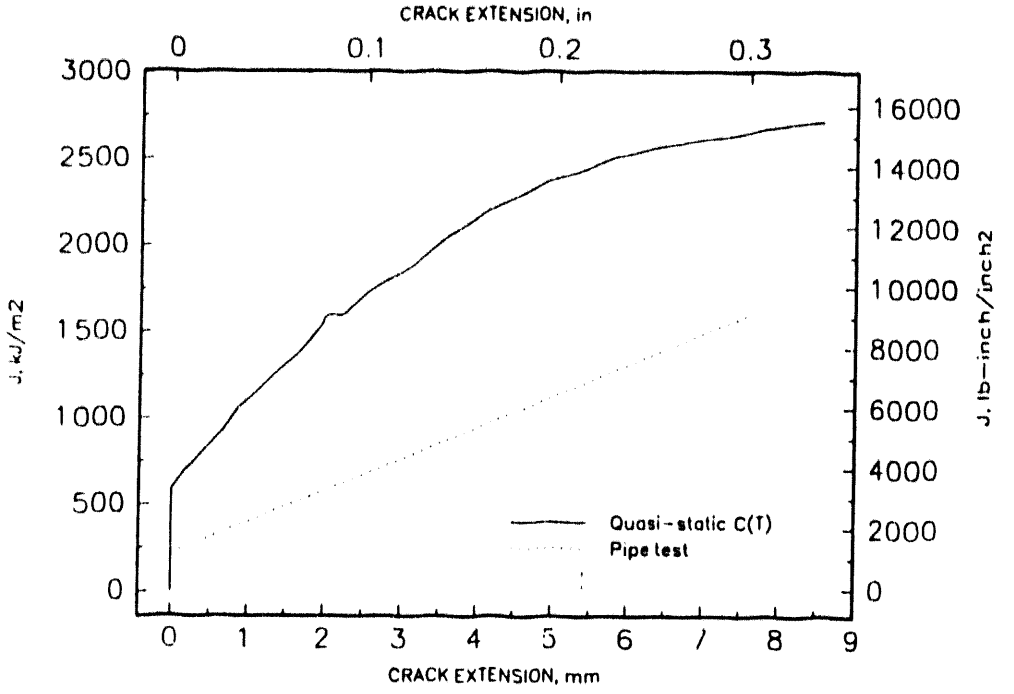

Figure 10 Comparison of the modified J-R curve from the pipe experiment with the quasi-static, monotonic C(T) specimen J-R curve

IAEA-10/92-F10

Further evidence supporting the possible reduction in the material's fracture resistance due to cyclic loading can be seen in Figure 11. Figure 11 shows the Dimensionless Plastic Zone Parameter (DPZP) analysis developed at Battelle with a large amount of experimental data. The DPZP analysis is a semi-empirical analysis where the ratio of the experimental stress to the Net-Section Collapse (NSC) analysis predicted stress is a function of the DPZP. The DPZP is the ratio of the plastic-zone size, which is a function of the material's fracture toughness, to the remaining tensile ligament, i.e., the distance between the crack and the neutral bending axis. (If the plastic zone encompasses the entire remaining tensile ligament, i.e., the DPZP equals 1.0, then fully plastic conditions exist and the failure stress should approach the NSC stress.) For the stainless steel base metal pipe system experiment, if the quasi-static C(T) specimen J_i value is used to calculate the DPZP, then the actual failure stress is significantly less than predicted, see Figure 11. However, if the quasi-static C(T) specimen J_i value is reduced by a factor of 3.0, 215 kJ/m^2 versus 738 kJ/m^2 (1,230 in-lb/in^2 versus 4,215 in-lb/in^2), then the stainless steel base metal experimental results are more consistent with the rest of the experimental data, see Figure 11. This further supports the contention that the stainless steel in this surface-cracked pipe experiment behaved as if it had a much lower toughness than it exhibited in the C(T) specimen tests.

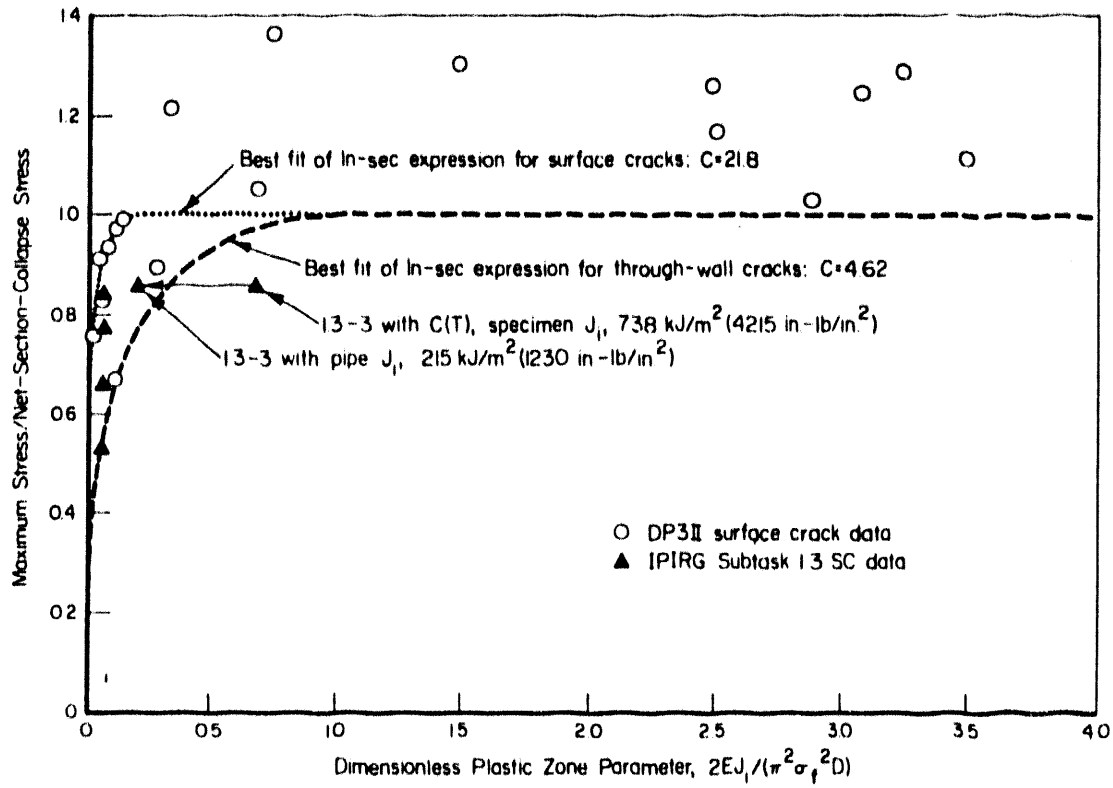

Figure 11 Effect of using Experiment 1.3-3 surface-cracked pipe J_i rather than quasi-static side-grooved C(T) specimen J_i value

11.3-10/90-F5.8

DISCUSSION

It has been shown that for at least one material evaluated in IPIRG-1, the J-R curve from the pipe experiment appears to be significantly lower than the J-R curve from the corresponding C(T) specimen test. In support of this finding, Landes and McCabe[3] showed that the effect of cyclic loading was markedly dependent on the material. For the case of an HY-130 steel, there was no discernible effect of cyclic loading on the J-R curve, see Figure 12. On the other hand, for an A508 Class 2 steel, there was a strong effect of cyclic loading on the J-R curve, see Figure 13. In addition, as part of Subtask 1.2 of the IPIRG-1 program[4], it was shown that cyclic loading lowered the crack-tip-opening angle (CTOA), which is related to the material's toughness, in a cyclically loaded stainless steel through-wall crack pipe experiment. The reduction in CTOA was related to the stress ratio (R) and the incremental plastic displacement between cycles, see Figure 14. Similarly, Landes and McCabe[3] reported that the smaller the increment of plastic strain between cycles, the greater the effect of the cyclic loads on the J-R curve. These findings raise the question of how well can quasi-static, monotonically loaded C(T) specimen data (which are probably the best toughness information one would have available for use in an analysis) represent the fracture response of a material in a piping system subjected to complex dynamic, cyclic loading. Obviously, such effects are not considered in current Leak-Before-Break (LBB) or in-service flaw evaluation criteria.

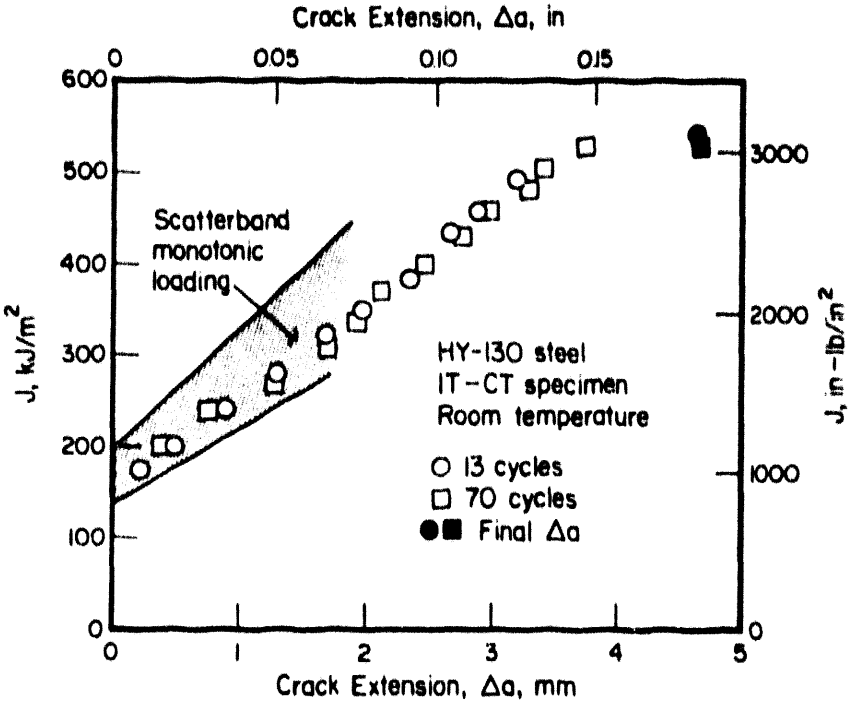

Figure 12 J versus Δa for HY-130 steel loaded cyclically to develop the J-R curve (Ref. 3)

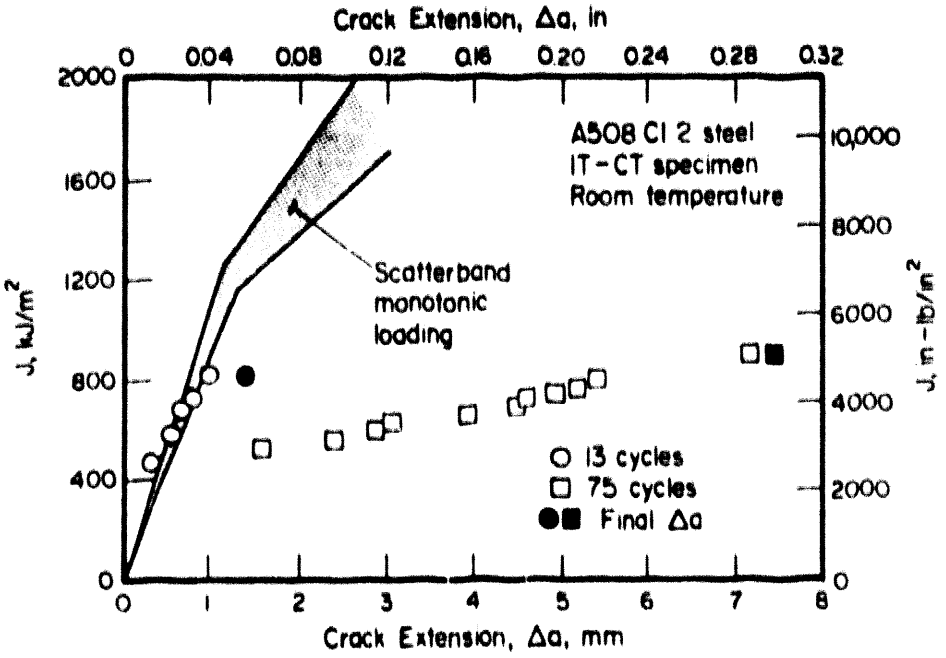

Figure 13 J versus Δa for A508 Cl 2 steel loaded cyclically to develop the J-R curve (Ref. 3)

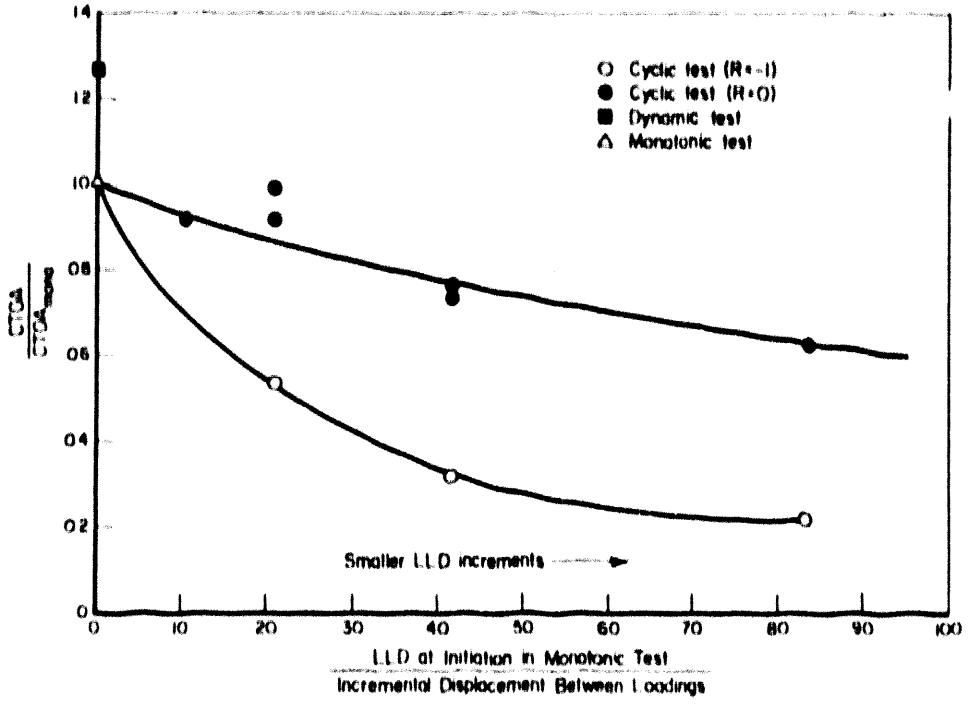

Figure 14 Crack-tip-opening-angle data from IPIRG Subtask 1.2 stainless steel pipe experiments

DRB/1.2-5/F25

REFERENCES

(1) Scott, P. M. and Ahmad, J., "Experimental and Analytical Assessment of Circumferentially Surface-Cracked Pipes under Bending," NUREG/CR-4872, April 1987.

(2) Kumar, V. and German, M., "Elastic-Plastic Fracture Analysis of Through-Wall and Surface F'aws in Cylinders," EPRI report NP-5596, January 1988.

(3) Landes, J. D. and McCabe, D. E., "Load History Effects on the J_R-Curve," Elastic-Plastic Fracture: Second Symposium, Volume II-Fracture Resistance Curves and Engineering Applications, ASTM STP 803, C. F. Shih and J. P. Gudas, Eds., American Society for Testing and materials, 1983, pp. II723-II738.

(4) Wilkowski, G. M., Vieth, P., Kramer, G. Marschall, C., and Landow, J., "Results of Separate-Effects Pipe Fracture Experiments," Post SMiRT-11 Conference, August 1991.

OECD/IAEA Joint International Specialists Meeting on Fracture Mechanics Verification by Large Scale Testing

October 26-29, 1992, Oak Ridge, Tennessee

A. Bruce Poole[1]
J. A. Clinard[1]
R. L. Battiste[1]
W. R. Hendrich[1]

FRACTURE MECHANICS AND FULL SCALE PIPE BREAK TESTING FOR DOE'S NEW PRODUCTION REACTOR-HEAVY WATER REACTOR[2]

[1]Senior Development Staff, Oak Ridge National Laboratory, Mail Stop 8051, Oak Ridge, TN 37831

[2]Research sponsored by the Office of New Production Reactor Programs, U. S. Department of Energy, under contract DE-AC05-84OR21400 with Martin Marietta Energy Systems, Inc.

ABSTRACT

Oak Ridge National Laboratory (ORNL) is completing a major task for the Department of Energy (DOE) in the demonstration that the primary piping of the New Production Reactor-Heavy Water Reactor (NPR-HWR), with its relatively moderate temperature and pressure, should not suffer an instantaneous Double-Ended-Guillotine-Break (DEGB) under design basis loadings and conditions. The growth of possible small pre-existing defects in the piping wall was estimated over a plant life of 60 years. This worst case flaw was then evaluated using fracture mechanics methods. It was established that this worst case flaw would increase in size by at least 14 times before pipe instability during an earthquake would even begin to be possible.

The approach to showing the improbability of an instantaneous DEGB for HWR primary piping required a major facility (Pipe Impact Test Facility, PITF) to apply all possible design loads, including an equivalent major earthquake (called the SSE earthquake). The facility was designed and built at ORNL in six months. The test article, a 20-ft (6.1 m) long 16-in. (406 mm) diameter SCH-40 pipe of stainless steel 316LN material was fabricated to exacting standards and inspections following the nuclear industry standard practices. A flaw was machined and fatigued into the pipe at a TIG butt weld (ER316L weld wire) as an initial condition. The flaw/crack was sized to be beyond the worst-case flaw that HWR piping could see in 60 years of service—if all leak detection systems and if all crack inspection systems failed to notice the flaw's existence.

Since October 1991, the first test article was subjected to considerable overloadings. The pipe was impacted 104 times at levels equal and well beyond the SSE loadings. In addition, over 560,000 fatigue cycles and numerous purposeful static overloads were applied in order to extend the flaw to establish the data necessary to confirm fracture mechanics theories, and, more importantly, to simply demonstrate that instantaneous DEGB is highly improbable for the relatively moderate energy system.

KEY WORDS: fatigue crack growth, J-R curves, elastic-plastic fracture, nuclear piping, cracks, fracture mechanics. Type 316L stainless steel, TIG welding

INTRODUCTION

DOE was in the process of designing a new generation of production reactors intended to replace the aging production reactors at the Savannah River Site (SRS) in Aiken, South Carolina. A heavy water reactor was one of the options being pursued during the Title 1 design phase. The increases in understanding and the vast experience gained from existing production reactors and commercial nuclear power plants led to proposed improvements in several areas of the design for the NPR-HWR.

One such area of improvement was to show that the tough austenitic piping of the NPR-HWR at the relatively moderate temperatures and pressures could provide a design that was not susceptible to a DEGB.

The PITF at ORNL was designed to load pipes in bending. The maximum bending stress being located at the center of the pipe. The pipe is loaded in four point bending. This loading condition provides a constant bending stress across the 3 ft (914 mm) long center section of the pipe. The flaw under test was at a weld in the exact center of the constant bending section of piping. Both static and dynamic loadings were produced to bend the pipe. These bending loads tended to open the flaw. Therefore, the PITF was used to show crack stability in tough austenitic piping.

INITIAL FLAW DESIGN

A fatigue crack growth analysis was part of the design process for the NPR-HWR primary pressure piping. This analysis was completed using weld residual stress levels in order to predict crack growth through the piping wall over 60-years of operation. A conservative approach to this analysis was to assume an existing flaw at the piping inside wall surface. For this analysis, that initial flaw was chosen to be 9% of the wall thickness and located at the inner surface. This value was chosen because it represents a general lower bound on flaw detectability using non-destructive testing methods at welded joints in 316 stainless steel material.

Using the crack growth rate methodology discussed in Ref. 1, the worst case 60 year flaws were established. For the welded pipe, a 0.17 in. (4.45 mm) deep 360° circumferential crack at the pipe inside diameter is assumed to exist and was determined to be the worst case complex crack condition where a 1 in. (25.4 mm) long thru-wall flaw intersects the 360° inside surface circumferential flaw. The dynamic testing program was designed to prove the existence of large failure margins for this initially flawed pipe.

PIPE LOADING CONDITIONS

An analysis of the NPR-HWR primary piping was completed using the current design basis. This loading condition is assumed to be present at a circumferential weld in the primary piping cold leg. In order to represent the seismic bending load in the pipe, a combined bending moment was established using the square root of the sum of the squares (SRSS) method. This moment is provided in the test pipe by four point bending. The actual test pipe is pressurized to 250 psi (1.72 MPa), which is a conservative over test condition. The water temperature during impact testing was approximately 135°F(57°C) and represents the NPR-HWR cold leg temperature.

As discussed in Ref. 1, a value of 110 ft-kips (149 KN·m) was established to represent the safe shutdown earthquake (SSE) pipe bending moment. Based upon the geometry of the PITF, this 110 ft-kip (149 KN·m) bending moment is applied to the test pipe when the load cell reads a value of 27.5 kips (122.3 KN). Therefore, a load cell value of 27.5 kips (122.3 KN) is considered 1 SSE loading. The loading methodology and instrumentation locations for the pipe test are shown on Figure 1. Figures 2 through 5 show details of the test facility. The location of stain gages and crack propagation gages on the test pipe are shown on Figure 6. The bending moment can also be measured by strain gage XE-100 on the back side of the pipe. A compression strain of 0.0455% at gage XE-100 represents 1 SSE loading.

TEST FACILITY DESIGN

The piping impact test facility is shown in Figs. 2-5. The test piece is a 16-in. (406 mm) diameter schedule 40 stainless steel pipe. This pipe is approximately 20 ft (6.1 m) long and has a circumferential weld at the center. The center weld was completed using a TIG weld joint design that provided a lack of penetration 360 degrees around the pipe and 0.17 in. (4.45 mm) deep at the inside surface. This represents a worst case 60-year flaw at the pipe inside diameter. At the center of the pipe weld, a 0.03 in. (0.76 mm) wide by 1 in. (25.4 mm) long slot was machined by metal disintegration from the outside pipe surface totally through the 0.5 in. (12.7 mm) thick pipe wall. This provided a worst case initial complex crack.

The test facility design is such that the pipe can be loaded in bending using a hydraulic ram and/or a 3100 lb (13.79 KN) swing weight. After the initial thru-wall flaw was machined into the pipe, it was covered over at the pipe surface by a 0.006 in. (1.52 mm) deep weld along the slot. The pipe was then fatigued in bending until a crack was developed completely along the cover weld. This

crack was then extended along the circumferential weld by fatigue using the hydraulic ram. At various crack lengths the flaw was tested by a dynamic impact loading using the swing weight. This dynamic load method has provided loads up to twice the seismic bending load calculated for the NPR-HWR plant (2 times SSE).

DATA COLLECTION INSTRUMENTATION

A high speed data system collects data during the 0.1 second dynamic event. The significant features of this system are as follows:

- 32,000 Synchronous scans/sec
- 24 channels, nominally as below:
  - 1 Load cell
  - 1 Pressure cell
  - 2 Crack extension gages
  - 1 Crack opening gage
  - 5 Displacement measuring devices
  - 7 Accelerometers
  - 7 Strain gages
- Pretriggers for exact t = 0
- Sophisticated display software
- Data management software with built-in QA features
- Backup each night to tape
- Some analytical features, e.g. integration & differentiation

TESTING HISTORY AND RESULTS

From October 1991 to August 1992, the test article was subjected to considerable overloadings. The pipe was impacted 104 times at levels equal to and beyond the SSE loadings. In addition, over 560,000 fatigue cycles and numerous static overloads were applied in order to extend the flaw and to establish the data necessary to confirm fracture mechanics theories. The pipe did not part into two pieces until the crack was 94% around the circumference.

This paper will provide and review some of the data taken during 10 hammer drops and 5 static loadings. The outside diameter crack length in these tests varied from 4.1 in. (104 mm) to 7.6

in. (193 mm). The fracture surface of the test pipe is shown on Figure 7. This fracture surface picture starts at 2 inches from the front pipe centerline and shows approximately 4 inches of the final surface. The pipe wall dimensions and initial subsurface flaw are shown on Figure 7. The location of 4 strain gages are also shown on Figure 7.

The flaw was located at the center of a TIG weld. Based on small specimen test data, the material characteristics of the weld are as provided in Table 1.

Table 1. Tig weld metal data

Test Temperature	Yield Strength	Ultimate Strength	J_{IC} (L-C)	Tearing Modulus (L-C)
140° F	51.15 ksi	74.95 ksi	4,163 in-lb/in^2	268
(60° C)	(352 Mpa)	(516 Mpa)	(729 kJ/m^2)	

The first test data provided here was taken during static load test T7C2. For this load test the crack length was 4.1 in. (104 mm). Prior to this test the pipe had experienced the following load history:

265,555 Fatigue Cycles

30 Hammer Drops

13 Static Overloads

The strain data at gage XE-112 for various pipe center loads is shown on Figure 9. The maximum load during test T7C2 was 42.5 kips (189 KN). The strain at gage XE-112 was elastic with load during test T7C2. The crack tip was located approximately 1.6 in. (40.6 mm) from gage XE-112 during test T7C2.

After T7C2 was completed, the pipe was fatigued for 36,600 cycles. This fatigue loading grew the crack to a total length of 4.18 in. (106 mm). At this crack length, three hammer drops (T7HO-2) were completed at a pipe center load of approximately 40.5 kips (180 KN). No observable crack growth occurred during these dynamic loadings. Next, the hammer was dropped from a higher point and the pipe center load was increased to 46.0 kips (205 KN). After the first higher impact load, the crack was observed to grow to 4.6 in. (117 mm). Over the next 6 impacts (T7H3-9) at this loading condition, no additional crack growth was observed. Aft 'his series of dynamic loads, the pipe was

fatigue loaded for 56,000 cycles. This fatigue loading grew the crack to an observed length of 7.3 in. (185 mm).

With the crack at a length of 7.3 in. (185 mm), a series of static compliance loads were completed. A significant amount of blunting was seen at the crack tip during these compliance tests, but no tearing was observed at the top crack tip until load T8C7. During the blunting loadings, a long plastic zone was established beyond the crack tip along the circumferential weld. This crack tip and plastic zone are shown on Figure 8. Tearing was observed when center loads of 50 kips (222 KN) and 55 kips (245 KN) were applied to the pipe. This tearing is shown on Figure 8.

During load tests T8C1 through T8C11, the strain values for gage XE-112 departed from linearity with pipe load. This load versus strain data is shown on Figure 9. During these ever increasing loadings, a hysteresis loop is observed in the gage XE-112 measurements.

For loading T8C7, a strain of 0.02 was measured before gage XE-112 failed. During this loading condition, it is estimated that the subsurface flaw was essentially along the fatigue line labeled number 3 as shown on Figure 7. This subsurface crack face extended approximately 2 inches (50.8 mm) beyond the observable surface crack at each end of the crack tip. Thus, a 7.3 in. (185 mm) surface crack extended to an approximate length of 11.3 in. (287 mm) length through the pipe wall.

Gage XE-113 did not function during the compliance tests. However, gage XE-114 did function and strain versus load data is provided on Figure 10. The data was nearly linear with load, however, plasticity at the gage location was evident. During the higher loadings minus strain values were measured at XE-114. Thus, gage XE-114 was clearly impacted by the plastic zone. Gage XE-115 was beyond the plastic zone during this testing.

CONCLUSIONS

Testing of flaws in the weld metal confirms that crack growth under dynamic SSE load levels is stable and demonstrates that the instantaneous DEGB is not probable for the moderate energy system of the NPR-HWR when loaded at a 1 SSE loading condition. This testing indicates crack stability for a worst case 60-year flaw at the 1 SSE level. Tearing of a 7.6 in. (193 mm) crack did not occur until a load of 50 kips (222 KN) was achieved. This tearing was stable. Fatigue crack growth was shown to provide significant subsurface crack extension. Additional testing is planned for flaws located in the weld heat affected zone (HAZ). The HAZ has been shown to have lower J_{IC} and Tmat values than the weld metal or the base metal for this piping.

ACKNOWLEDGEMENTS

The author wishes to acknowledge the help and interest provided by Mr. J. J. Jicha of the Office of new Production Reactors Program, Department of Energy.

REFERENCES

1. Poole, A. B., Battiste, R. L., Clinard, J. A., and Hendrich, W. R., "Pipe Break Testing of Primary Loop Piping Similar to Department of Energy's New Production Reactor-Heavy Water Reactor," Oak Ridge National Laboratory, Report ORNL/NPR-92/8, January 1992.

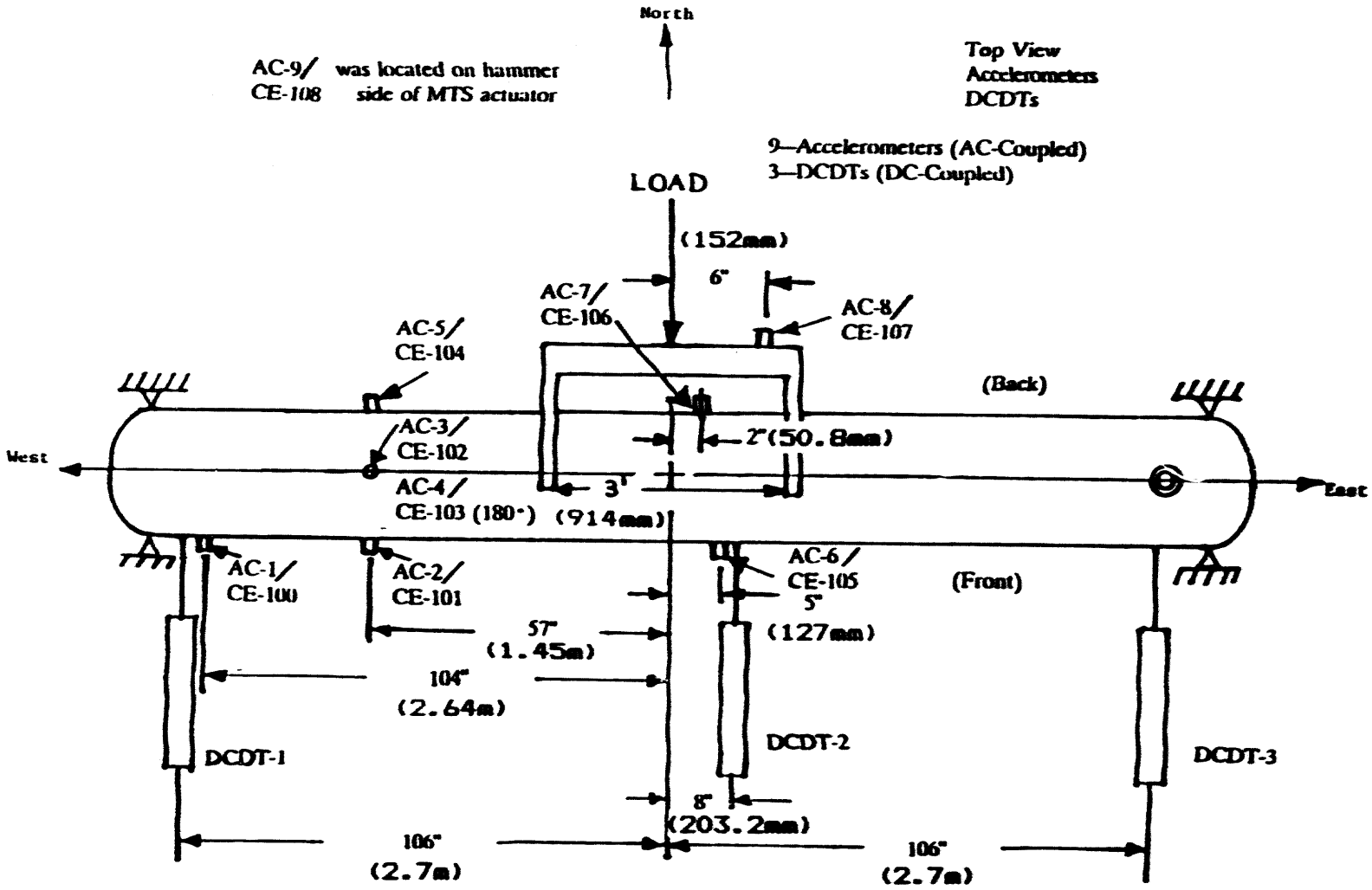

Fig. 1. Pipe Loading Diagram and Location of Accelerometers and DCDTs on Pipe.

Photo 8498-91

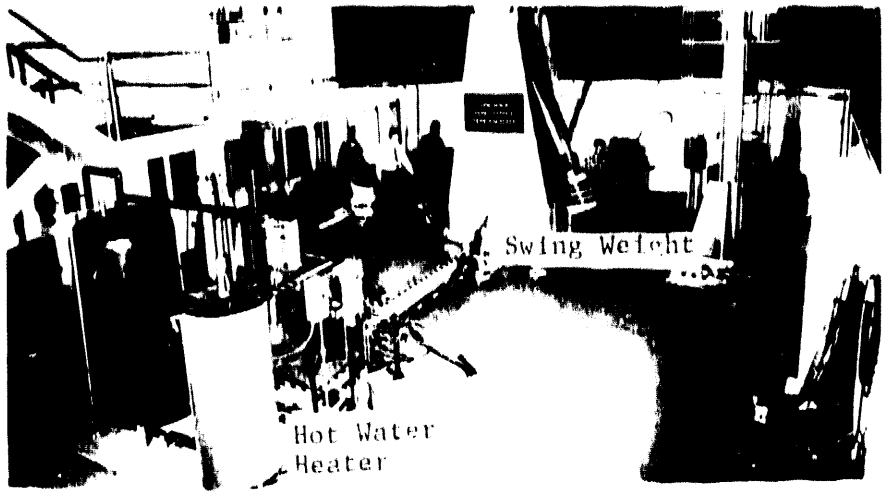

Fig. 2. Pipe Impact Test Facility at ORNL.

Photo 8500-91

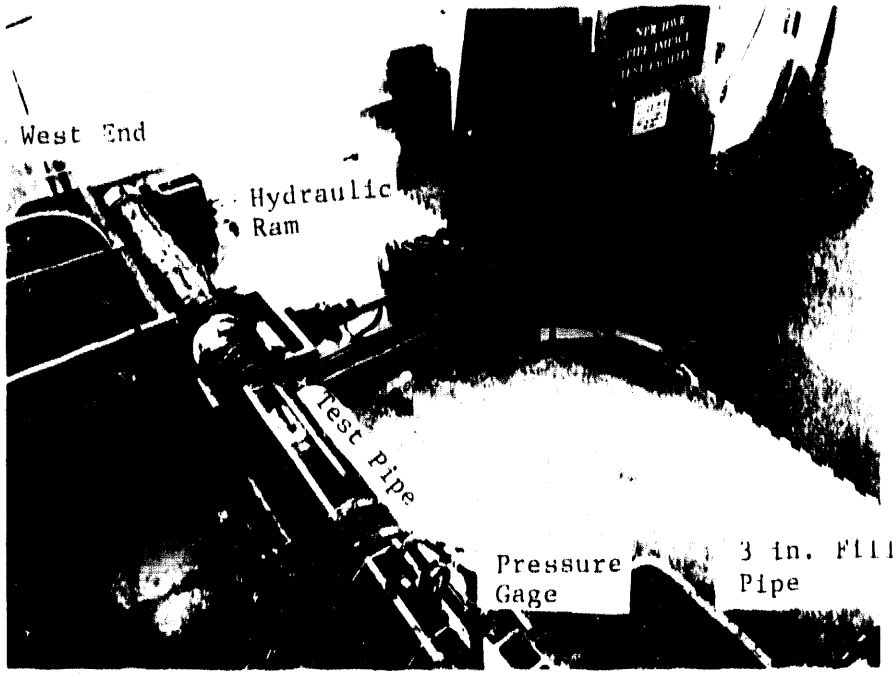

Fig. 3. Pipe Impact Test Facility at ORNL.

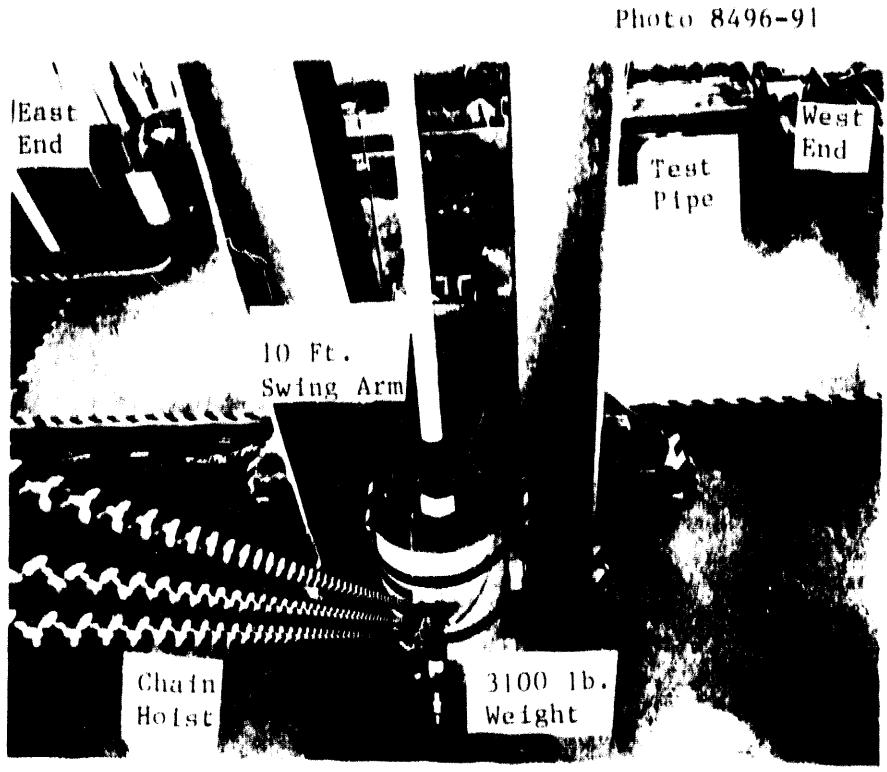

Fig. 4. Pipe Impact Test Facility at ORNL.

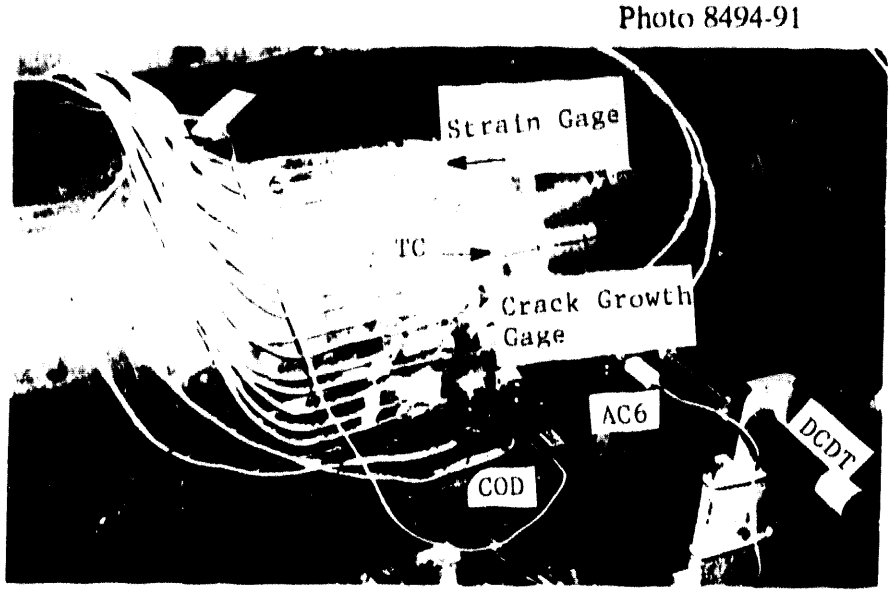

Fig. 5. Pipe Test Specimen at ORNL.

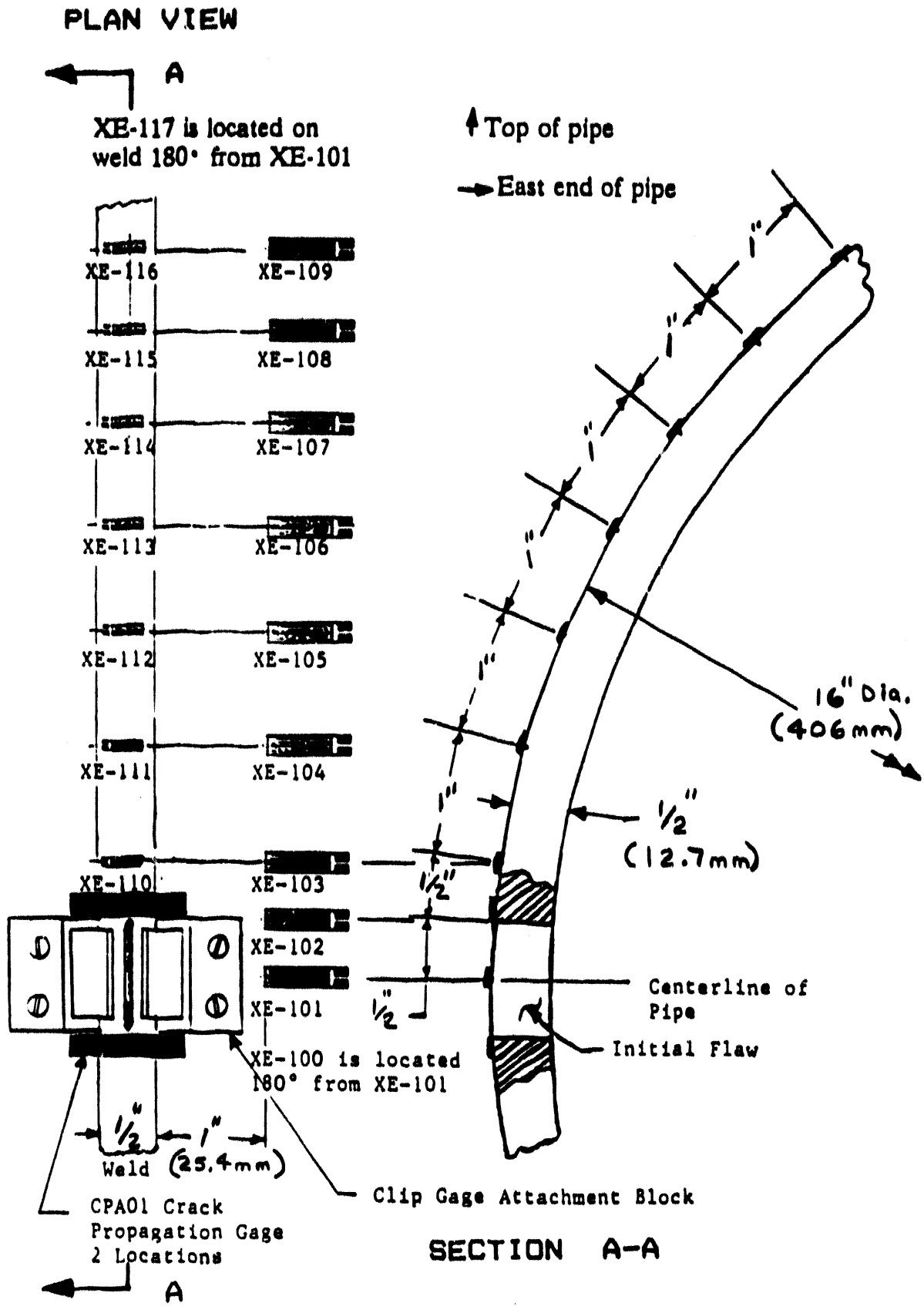

Fig. 6. Strain Gage and Crack Propagation Gages Located on Pipe.

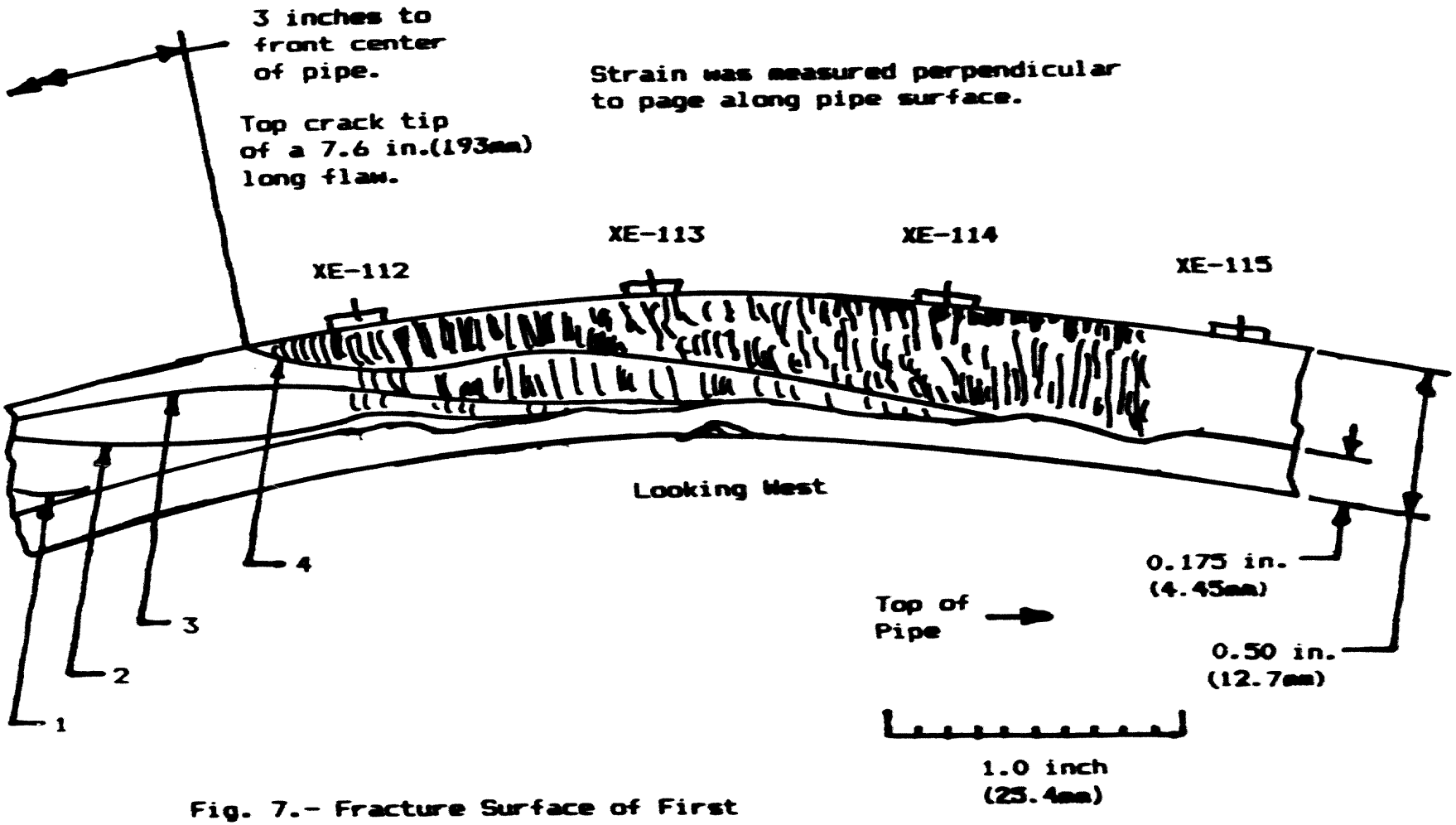

Fig. 7.- Fracture Surface of First Test Pipe

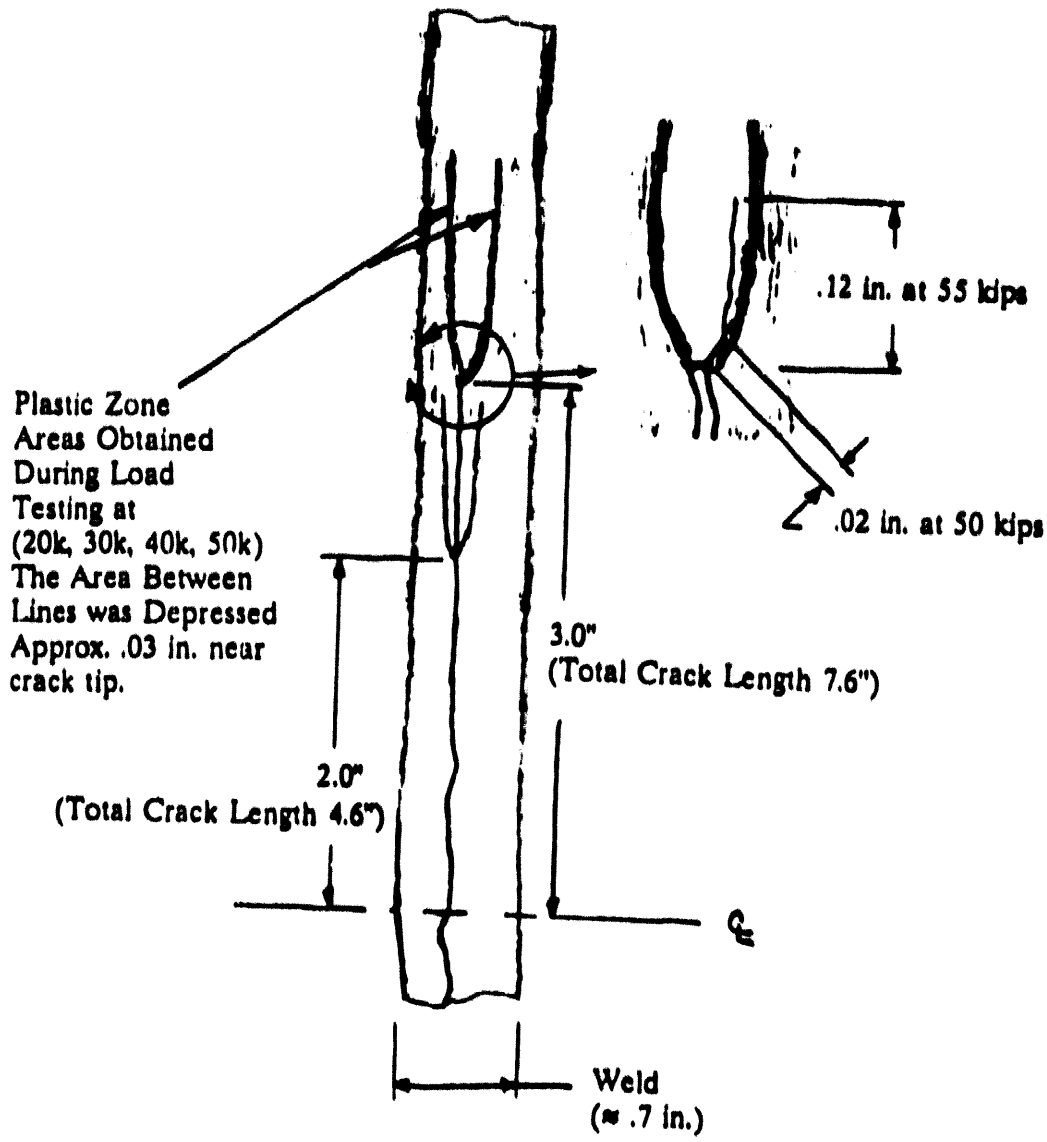

Fig. 8. Crack Extension and Plastic Zone Deformation During Compliance Loading

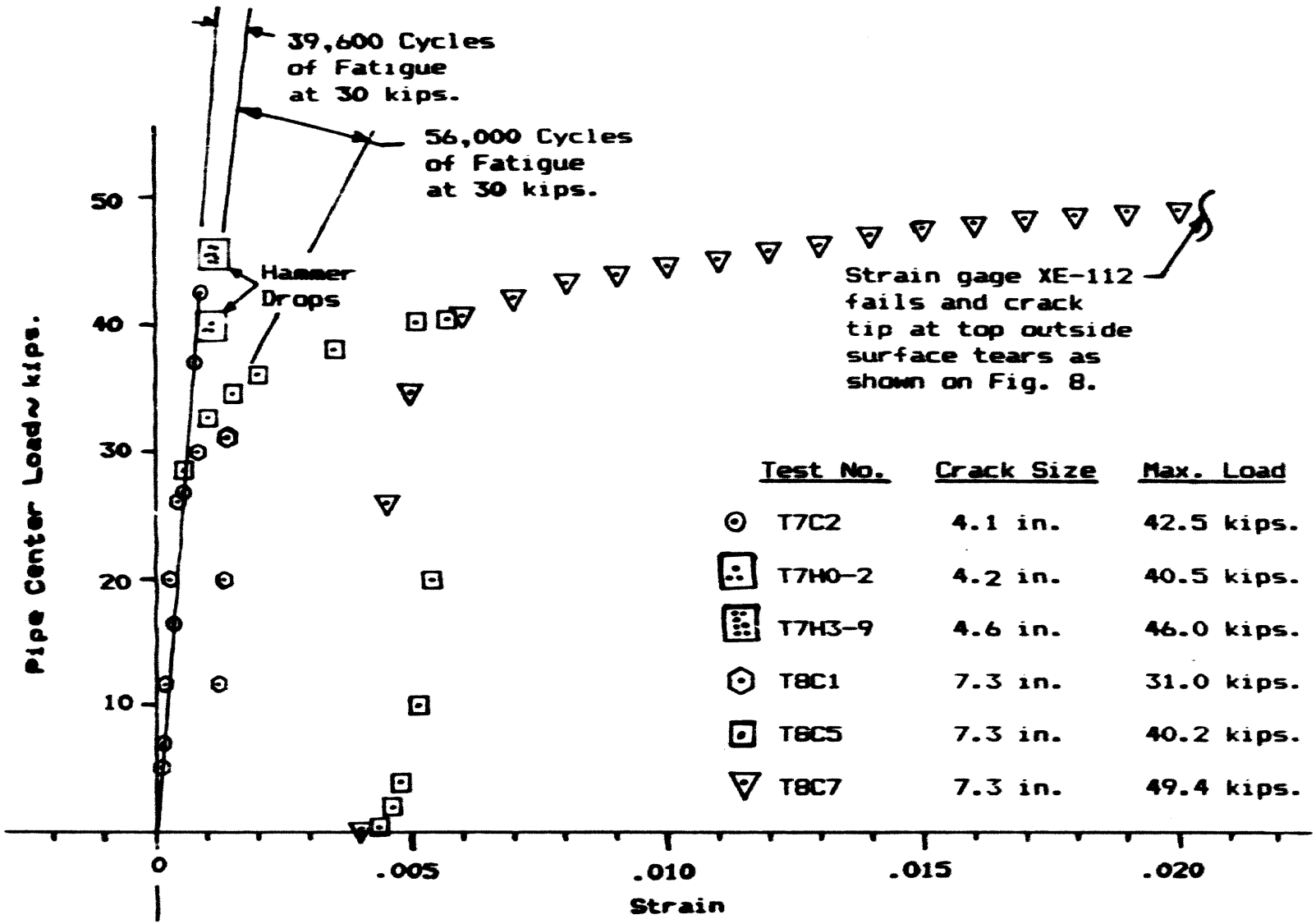

Fig. 9. Pipe Load versus Strain at Gage XE-112

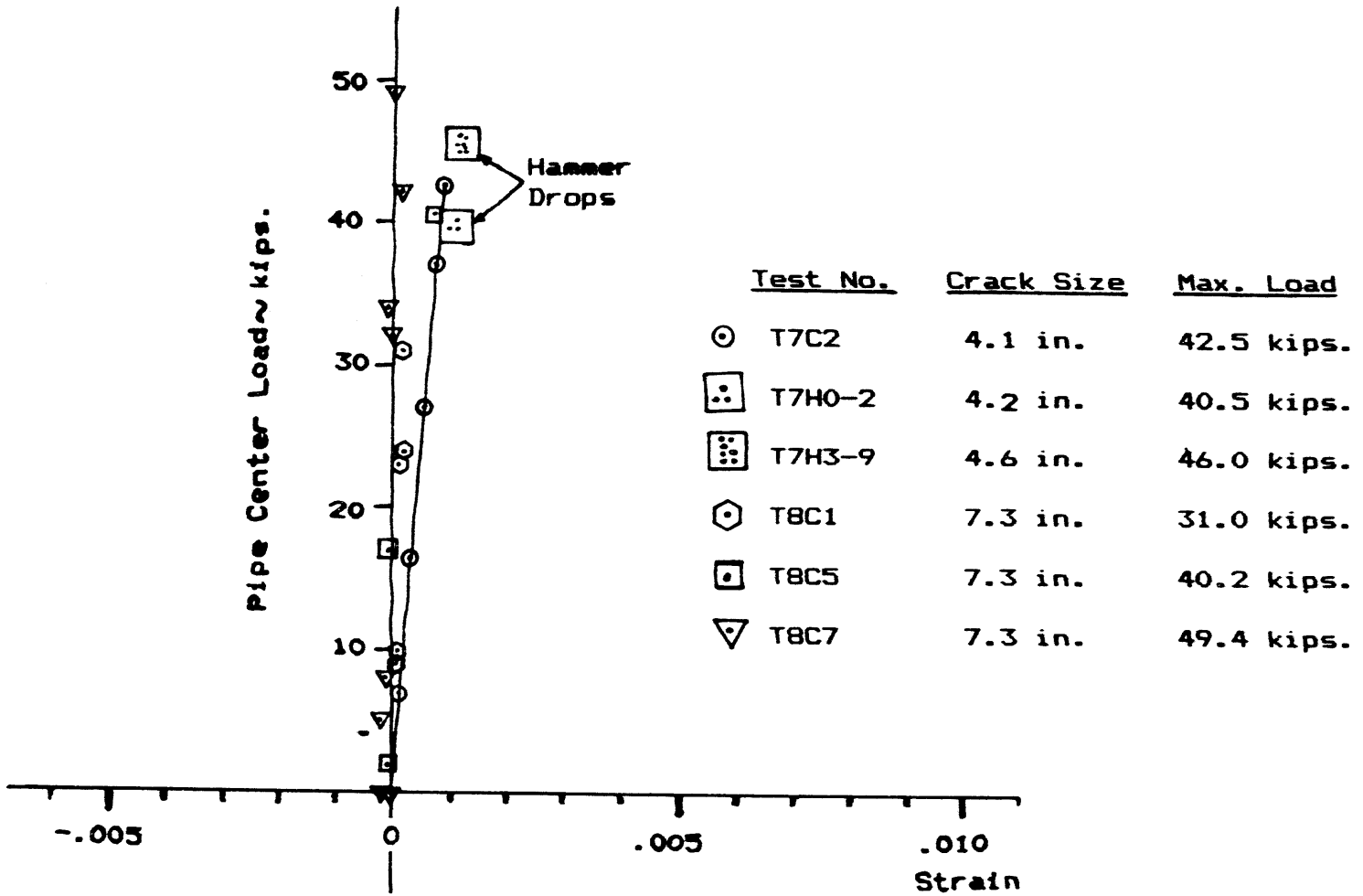

Fig. 10. Pipe Load versus Strain at Gage XE-114

MEETING SUMMARY

This section is comprised of informal summaries of the papers presented in each session of the Specialists' Meeting. These summaries were prepared by rapporteurs for each session and, consequently, reflect their assessment and interpretation of the presentations the day the papers were delivered.

SESSION I. CSNI PROJECT FALSIRE

H. Schulz and R. Bass - Chairmen

Description

The objective of the FALSIRE project was to evaluate present fracture prediction capabilities through interpretative analysis of selected large scale fracture experiments.

Six experiments with different material properties were analyzed to examine various aspects of crack growth under mainly pressurized-thermal-shock loading conditions. Besides the PTSE-2A/B test which showed multiple crack events, the other tests showed only stable crack extension in a range of 1 to 6 percent of the initial crack depth. The initial crack depth in these experiments had an a/W ratio that ranged between 0.1 to 0.54.

Thirty-nine analyses were performed, giving this exercise a truly international picture. The methods applied did include various engineering estimation schemes as well as extensive finite-element calculations.

Following a workshop in Boston two years ago, more extensive comparisons and detective work to clarify discrepancies have been performed and presented.

Observations and Recommendations to FALSIRE

1. The FALSIRE project has been extremely useful to bring the large scale experiments with combined mechanical and thermal loading to the attention of a large international community.
2. The results of the analyses showed good capabilities to predict crack initiation, but for some experiments the available information on measurements for crack initiation were not available in time or were insufficient.
3. As a technique to predict crack extension, J_R methodology was partially successful in some cases (NKS experiments) but not in others (PTSE-2, spinning cylinder).
4. Root causes which account for differences in the analysis results could be identified in many cases. Thus, the report can be used as a good reference document in the future. It is necessary to go on in this effort, especially for clarification of remaining differences for PTSE2 and more extensive comparison with newer data for the spinning cylinder tests.
5. As capabilities of the analyses methods improved (ability to account for multi-linear stressstrain curves, full temperature dependence, inhomogeneous property models), it was obvious that former material characterization was partly insufficient. Limited supplementary programs could improve the situation.
6. Work presently going on to improve the understanding of "constraint" may give a large benefit for future analyses to improve crack growth predictions.

7. Phase II of FALSIRE will start by the end of 1992 with the selection of tests, and a call for participation for the analyst will go out in the spring of 1993. The intention is to select:
   - two or three specimens preferably showing two stages of crack growth.
   - comparing first the results of the structural analyses to clarify differences originated by the modeling of the load and elastic-plastic material behavior.
   - comparing second results of the fracture mechanics analyses.

SESSION II. LARGE-SCALE EXPERIMENTS AND APPLICATIONS

C. Pugh and E. Hackett - Chairmen

This session focused primarily on two technical areas: (1) evaluation and analyses of largescale PTS thermal shock tests with particular regard to flaw geometry effects and; (2) use of fracture mechanics estimation schemes for defect assessments in reactor pressure vessels.

(1) The papers by Keinanen, Cheverton, and Keeney-Walker highlighted the effect of surface flaws and surface flaw characteristics (a/T, a/c, clad and unclad) on PTS thermal shock analyses. Keeney-Walker concluded that generally deeper flaws are required for PTS crack initiation for the 3-D flaw as opposed to the 2-D flaw. Probabilistic failure assessments using OCA-P showed a significant reduction in conditional failure probability of the RPV for the 3-D flaw case. Cheverton concluded that LEFM worked well for analysis of the ORNL thermal shock tests, but that the beneficial effect on fracture toughness for the short cracks in these experiments was not in evidence. Possible explanations for lack of the "short crack effect" included biaxial loading and the steep K gradients produced in these tests. Keinanen noted a strong effect of flaw aspect ratio on the probability for crack arrest in the VTT PTS analyses, short cracks having a greater propensity to arrest than deep cracks.

Brumovsky reported on plate and spinning disc tests for VVER pressure vessel steels. These CSFR tests show that base metal with flaws smaller than 40 mm and weld metal with flaws smaller than 15 to 20 mm behave as though the flaws are not present. As with some other experiments, Brumovsky reported that multiaxial stresses at failure were lower than for the uniaxial case.

(2) The papers presented by Bloom and Dowling/Morland were concerned with using flaw estimation schemes (calibration functions and R6, respectively) for RPV defect assessments. Bloom presented the results of ABAQUS FEM J-integral solutions in terms of calibration constraints as a function of a/W, a/c, r/t and Ramberg-Osgood strain hardening behavior. The primary conclusion of this work is that use of FEM formulations for RPV defect assessments can be minimized in favor of calibration function approaches. The Dowling/Morland presentation emphasized that, although conservative, the CEGB R6 methodology has also been shown to be reasonable for RPV defect assessments. Areas in which reduced conservatism now appears justified included allowance for stable ductile tearing and an improved definition of limit load for ductile materials.

SESSION III. ASSESSMENT OF FRACTURE MECHANICS ANALYSIS METHODS

G. Yagawa and J. Landes - Chairmen

This session dealt with the development of methods to predict fracture behavior in structural components and the actual application of some of these methods. The consensus among presenters was that traditional approaches to fracture characterization may not be adequate to predict fracture in complex geometries. The first paper "Perspectives on Fracture: Correlation versus First Principles and Length Scales" by Professor Shih, suggested a framework for fracture assessment contrasting a mechanistic approach versus a phenomonological approach labeled correlation approach. He pointed out that fracture behavior was controlled by the exceptional behavior of atoms rather than the average behavior, causing many mechanistic models to predict incorrect fracture trends. The correlation approach attributed to Irwin did not in its present format describe effects of all factors involved in fracture. Mixing the two approaches gave a common ground which could take the philosophies of both the mechanism approach to fracture and correlation approach. This mixed approach is labeled the constraint correction approach. Fracture behavior is governed by two crack-tip stress states, a deformation stress state, and a triaxial stress state. These states are independent, requiring different parameters to describe their behavior; therefore, a single parameter correlation approach should not be adequate to characterize fracture; a two parameter approach is needed. For this, J describes the deformation stress state and Q the triaxial stress state. These parameters must be calibrated for a given geometry and crack aspect ratio; a handbook of these solutions is planned. To predict fracture behavior, a locus of J-Q points is needed, rather than a simple J for fracture.

The second paper "Continuum and Micro-Mechanics Treatment of Constraint in Fracture" presented by Professor Dodds continued the theme of the first paper. He stated that in order to transfer the results of a laboratory test to the fracture prediction of a component structure, four factors affecting constraint must be considered; a/W, size, thickness, geometry. His method for dealing with constraint is to take a reference constraint state, essentially an infinite body where Q = 0, and reference all other constraint states to that. This is done by characterizing the principal stress and a size parameter for fracture in the reference stress state; this gives fracture corresponding to a crack-tip field characterized by the global parameter J_0. To determine the condition for fracture in a component, it must have a crack-tip field equivalent to the J_0 field in the infinite body. A component with a constraint less than the infinite body would have a global applied J which is not J_0 for this corresponding field; for lower constraint, the applied J is greater than J_0. Through numerical calibration, the applied J, which gives a crack-tip field corresponding to the one at J_0 in the infinite body, can be determined. This applied J then is the one that can be used to determine fracture for the lower constraint. Dodds showed data of Sumpter which had a large toughness variation due to differences of constraint. When analyzed by the equivalent J_0 approach, these data were consistent.

Dodds continued by showing for the first time J-Q calibrations for the three-dimensional part through surface crack. Q varies around the crack edge being low at the surface, $\phi = 0$, and rising to a high value at about $\phi = 17°$. The addition of a biaxial stress component changes this distribution of Q. Fracture prediction for the part-through crack could be done by choosing a two-dimensional fracture specimen that has an equivalent constraint, characterized by Q, to the part-through crack.

The third paper "Recommendations for the Application of Fracture Toughness Data for Structural Integrity Assessment" by Dr. Wallin discussed which data are appropriate to apply in fracture prediction models. Since fracture toughness data in the transition have extensive scatter, it is not easy to determine the appropriate values to use for a safe assessment of fracture in a structural component. Dr. Wallin characterized the scatter by a three-parameter Weibull equation. This distribution was representative of data scatter for a single specimen size. Size differences could be accounted for by a second equation

based on a Weibull statistics which adjusted toughness means for size. Wallin showed that all fracture toughness data in the transition for steel alloys would fall along a common curve when adjusted to a common temperature, T_0, which is defined as the temperature where mean toughness is 100 MPa$\sqrt{m}$. Based on his analysis, he suggested a size criterion given by

$$b = \frac{1}{\pi^2}\left(\frac{K_{Jc}}{\sigma_{ys}}\right)^2$$

where b is the specimen uncracked ligament, K_{Jc} the fracture toughness expressed as K, and σ_{ys} the yield stress of the material.

The fourth paper by B. R. Bass, et al "Constraint Effects in Heavy-Section Steels" presented by Dr. Shum describes two different analytical approaches to attempt to address shortcomings of conventional one-parameter methods. These are applied to experimental data and some analytical studies. For example, the J-Q models were applied to some actual component test results like the wide-plate tests. Dr. Shum showed that planar constraint adjustment may not always be adequate; thickness constraint adjustment may also be needed. As concluded by the authors, many issues still seem to remain to be solved to establish the two-parameter methods in practical situations.

The fifth paper by Dr. Lidbury "Prediction of the First Spinning Cylinder Test Using Continuum Damage Mechanics" presents the FE analyses of the SC-I Test, where the Rousselier ductile damage theory is employed to better understand the transferability of test data from small specimens to structural tests. The results show that the model can predict the observed enhancement of tearing toughness of the cylinder to that of small specimens with the appropriate crack-tip mesh size, i.e. mesh size >250 m. It is considered that the present results show a positive step toward achieving the goal to establish damage mechanics as an efficient tool.

In summary, this session showed that traditional single parameter fracture correlation methods are not adequate; new models which account for constraint must be used. These models show promise of solving the classic problem of transferring laboratory data measured at high constraint to predict fracture of a component structure at lower constraint. In addition to solving the problem of constraint, the scatter of fracture toughness data in the transition must be accounted for by statistical models.

SESSION IV. LARGE-SCALE PLATE EXPERIMENTS AND ANALYSES

D. Miannay and A. Hiser - Chairmen

Dr. L. Stumpfrock of MPA described a program to assess the transferability of crack arrest toughness from small compact specimens to wide-plate specimens at high temperature for a steel thermally embrittled. The results show that multiple reinitiation and arrest occur. During unstable propagation the dominant mode was cleavage. At arrest there is an abrupt change from cleavage to ductile tearing. A fairly good agreement between the two types of specimens is observed. However, this general behavior is in discrepancy with previous results of ORNL on wide-plate specimens. No reason can be given.

Dr. D. Lidbury of AEA Technology described a program to determine the stable tearing behavior of cracks under different loading conditions by testing wide plate specimens of a carbon steel and by using the failure assessment diagram approach. For the edge cracked plates, the assessment gives a good failure prediction or is conservative. The very conservative evaluation in bending cannot currently be explained. The results from combined fatigue and tearing loading in tension are consistent with linearly adding crack

growth. For the surface cracked plate, initiation is best predicted from using a local limit lead. This program is now planned for nuclear steels.

Mr. R. Fabi of ABB reviewed the knowledge gained by large scale testing to demonstrate integrity. He highlighted the key issues to be addressed, initiation of small cracks in brittle material of large structures, the dynamic reinitiation of deep cracks in brittle or ductile materials and the static reinitiation of deep cracks in ductile materials.

Professor K. Kussmaul of MPA described a program to investigate the application of small specimen laboratory test data to large-scale tests, under dynamic loading conditions. Overall the results demonstrated good comparability of the results for stable tearing; additional analyses are under way for comparison to component sections.

Mr. D. Wright of AEA Technology reviewed work in progress examining biaxial loading effects on the ductile tearing behavior of a ferritic steel. Overall the results indicate a benefit of biaxial loading from the standpoint of higher stress of initiation (by 20 percent) and slightly higher maximum stress (by 2 percent). No comparisons of J levels at initiation or maximum load were presented, although the speaker thought that the J levels were higher for the biaxial loading geometry. A comment was made from the audience that the observed benefits of biaxial loading were applicable for ductile tearing and not necessarily for cleavage fracture.

Dr. H. Kordisch of IWM-Freiburg described a program to assess the transferability of data from small specimens to a larger plate specimen, for the case of ductile crack initiation and growth in an RPV steel. Results from this program indicate that good agreement in crack growth profiles can be found between numerical simulations using small specimens and large plate experimental results if the constraint dependance of crack growth resistance is accounted for in the numerical simulations.

SESSION V. FRACTURE MODELING AND TRANSFERABILITY

K. Kussmaul and W. Pennell - Chairmen

The first paper (T. Theiss, ORNL) was entitled "Experimental and Analytical Investigations of the Fracture Toughness Enhancement Associated with Shallow Flaws." The ORNL shallow flaw fracture toughness testing program has as its objective a definition of the shift in the nil ductility transition temperature produced by relaxation of crack-tip constraint for shallow flaws. Test results from this program have the potential to influence RPV pressurizedthermal-shock (PTS) analysis, where shallow flaws are a primary source of predicted crack initiations. Three point SEN benching specimens of A533B material were used in the test program. The beam section for most of the tests was 100 mm deep and 100 mm wide. Crack defects were in the range of 10 mm to 14 mm, with 50 mm crack defects used in the control specimens. Results from the lower transition region of the fracture toughness showed a toughness increase of approximately 60 percent (K_{Jcs}/K_{Jcd}) for shallow flaws, when compared with the deep-flaw data. As expected, deep flaw and shallow flaw data were coincident at lower-shelf temperatures. The shallow-flaw fracture toughness test is shifted by approximately 35°C relative to the deep flaw data. Follow-up work will investigate the effects of biaxial (out-of-plane) stress field and full-scale geometries on shallow-flaw fracture toughness. Feedback from the audience questioned the use of RT_{NDT} to characterize shallow-flawfracture toughness extension for a reactor vessel when cladding was present. The author explained that the ΔRT_{NDT} impact of the shallow-flaw constraint relaxation was a convenient way of summarizing the effect in a single number, cladding effects were however included in the application models.

The second paper (Professor G. Yagawa, University of Tokyo) was entitled "Stable Crack Growth Behaviors in Welded CT Specimens - Finite Element Analyses and Simplified Assessment". Investigations

have been conducted on homogeneous A533B and composite A533B/weld material IT-CT specimens. In the composite specimens the crack-tip was located both in the parent material HAZ and in the weld metal. The GE-EPRI method and the reference stress methods were used to estimate J from the CMOD-P curves. These estimates were then compared with measured values. Mean values of coefficients were used in the material power law hardening equation to represent the weld material behavior. The coefficients for parent material were set at 1.0. Coefficients in the range 0 to 1 were used for the weld material. A coefficient of 0.5 gave a close match to the measured J- Δ a curve for weld material. Neural network technology is being applied to refine the selection of material coefficients. In an example, training data for the neural network were taken from elastic-plastic cyclic stress-strain test hysteresis loops. The neural network analysis permits the optimization of the stress-strain curve representation. The positive impact of this optimization was evident in a comparison of interpretation of the test data for the composite specimens. It was apparent from the discussion of this paper that the use of neural networks for test data interpretation was a novel concept for much of the audience.

The third paper (M. Brumovsky, CSFR) was entitled "Large-Scale Fracture Mechanics Testing - Requirements and Possibilities." Large-scale testing provides the means of optimizing and validating pressure vessel fracture margin assessment technology. There are however a number of factors which must be considered when planning a large-scale test in order to avoid producing non-prototypic results. Size effects are often underestimated in tests. Plate thickness was given as an example. Surface inhomogenities occupy a greater portion of the test specimen when the specimen is cut from a non-prototypic plate thickness. Loss of residual stress effects can occur when test specimens are cut from large plate or components. Examples were given of (a) cracks which initiated from unanticipated locations in prototypic structures and (b) crack-arrest data which were influenced by environment, thickness and also the total energy stored within the structural system. Feedback from the audience was generally supportive of the concerns and recommendations summarized by the author. The ongoing HSST program shallow flaw fracture toughness tests on full-scale three-point bend SEN specimens cut from the wall of a reactor pressure vessel from a canceled nuclear plant were cited as an endorsement of the recommendations made by the author.

The fourth paper (S. A. Swamy, Westinghouse) provided insight into thermal mixing phenomena in case of a small LOCA. It is important to know that the safety injection into the cold leg results in a stratified mass flow through the nozzle and downwards in a striplike manner. This causes localized high stresses in a highly inhomogeneous stress field. The maximum loading occurs in the nozzle region. In the beltline region the axial stress might become as high or even higher as the hoop stress.

A critical review (R. Dexter, Lehigh) of the causes of geometry effects in ductile tearing clarifies the importance of the geometry dependence of the shape and volume of the plastic zone in the ligament, ranging from local to remote plasticity. It is therefore imperative to examine the local fracture mode before any fracture criteria may be adequately employed. On a micromechanical level, ductile fracture is controlled by a critical fracture strain. This parameter is not very sensitive to both high triaxiality and surface-type cracks. Therefore, constraint based approaches will not work for ductile fracture.

The understanding of PTS events requires investigation of highly dynamic events (H. Couque SWRI). The generation of respective fracture mechanics data is possible using a novel experimental-computational approach involving a coupled pressure bar technique and a viscoplastic dynamic fracture code. Fracture data have been generated up to upper-shelf temperatures with loading rates of 10^6 MPa$\sqrt{\text{m/s}}$.

The paper on nonhomogeneous media (F. Brochard, CEA/CEN) focuses on drastically changing material properties, e.g., bimetallic joints and nonhomogeneous temperature distributions, where a correction term is needed for the calculation of the energy release rate. This fact is important for PTS events, where the temperature distribution is nonhomogeneous. An open question remains if the crack tip lies on an interface.

SESSION VI. LARGE-SCALE PIPING EXPERIMENTS AND ANALYSES

G. Wilkowski and M. Kozluk - Chairmen

The first paper by W. Stoppler and D. Sturm (presented by L. Stumpfrock), presents the results of cyclic loading tests on pressurized, large diameter ferritic pipes containing circumferential flaws. The testing program addressed a number of parameters, including: inside surface versus outside surface flaws, three flaw lengths were used 20°/40°/120°, three flaw depths were used 10%/20%/50%, upper versus lower shelf material, and rate of cyclic loading. A majority of the 15 test results reported were pressurized and tested under full reversal cyclic loading (R-ratio of -1). The authors report that reasonable agreement with test results were obtained by finite element analysis based growth rates. The results of the tests indicate that the fatigue growth rates increase with increasing flaw size and the number of cycles to failure are also influenced by the toughness of the material.

The second paper by Förster et. al. (presented by S. Bhandari), describes bending tests performed on through-wall circumferential cracks in thin-walled, large diameter austenitic pipes for liquid metal fast breeder reactor applications. In the 6 test results reported, the enclosed angle of the crack ranged from 60°-175° with three of the tests having the crack located in base metal and the remaining tests having the crack located in either the weld center-line or in the HAZ. The J_R-curves from the pipe tests were over-predicted by C(T) specimen tests of the same material. The bending moment for the tests was applied as a quasi-static monotonically increasing load. Because of the larger size of the pipe specimens the J_R-curves obtained much greater amounts of crack extension than are available with C(T) specimens. The lowest J_R-curve from the pipe tests was for a specimen in which the machined crack was located in the center-line of the weld and grew by turning into the fusion line of the weld. Because of the relatively large diameter-to-thickness ratio of the pipe specimens, all of the specimens exhibited buckling in the compressive region of the speci nen but the buckling did not occur until after maximum load was reached. The authors obtained good prediction of the maximum load using the Battelle plastic-zone screening criteria (worst error being 9%). The engineering treatment model (ETM) used by the authors over-predicted the maximum moment (worst error being 45%) and underestimated the amount of crack extension.

The third paper by Olson et. al., presents the analysis methodology used for the piping system tests performed as part of the first International Piping Integrity Research Program (IPIRG-1). The results of the tests for a long surface flaw in austenitic base metal are presented. The loading consisted of pressure, thermal expansion, inertia, and dynamic anchor motion. The piping system loading is an increasing amplitude sinusoid with an increasing ramp superimposed. The paper concludes that this austenitic base metal experiences a reduction in fracture toughness (J_R and CTOA) because of cyclic loading. The paper raises the question on the applicability of quasi-static, monotonically loaded C(T) specimen data for analysis of piping systems. The paper also addresses the difficulty of using a Ramberg-Osgood material characterization for austenitic steels, and the importance of using a suitable fit. The paper presents that for these types of application the goodness of fit is best determined by examining the moment-rotation curve for the cracked piping section.

The fourth paper by Poole et. al., presents an engineering demonstration of the large margins available in the design procedures to grow cracks from their detectable size to a length corresponding to final collapse of the pipe. Loading was applied to the piping segment to simulate seismic and impact loadings, and it also included load-controlled cyclic loading. As with the earlier paper by K. Föster et. al., when a crack was put in the center-line of the weld it eventually grew to the fusion line during ductile tearing.

The papers presented in this session appear to indicate that J_R-curves derived from C(T) specimens may not be conservative when applied to actual piping systems containing circumferential cracks. It

appears that: C(T) specimens over-predict the J_R-curves for thin-walled pipes with circumferential through-wall cracks, cyclic loading appears to reduce the apparent toughness of austenitic materials, and confirms that crack growth rates are strongly dependent on the size of flaws. It appears that the cyclic effects cause damage in the local region of the crack tip and this may change the constraint conditions at the crack tip. Under cyclic loading, the crack extends in increments (of either stable tearing or crack jumps) which position the crack tip once again in a region of undamaged material. In spite of these potential non-conservatisms it appears that initiation of flaws can be reasonably predicted and that nuclear grade piping is extremely tough and that the only apparent way to obtain double ended guillotine ruptures is through repeated application of large bending loads to progressively tear the pipe into two pieces.

NUREG/CP-0131
ORNL/TM-12413
Dist. Category RF

ORNL Internal Distribution

1-5. B. R. Bass
6. J. W. Bryson
7. E. W. Carver
8. R. D. Cheverton
9. J. A. Clinard
10. J. M. Corum
11. W. R. Corwin
12. T. L. Dickson
13. W. Fulkerson
14. S. K. Islander
15. J. E. Jones Jr.
16-20. J. A. Keeney
21. W. J. McAfee
22. D. E. McCabe
23. J. G. Merkle
24. R. K. Nanstad
25. D. J. Naus
26-30. D. G. O'Connor
31-32. W. E. Pennell
33. A. B. Poole
34-38. C. E. Pugh
39-41. S. J. Ranney
42. D. K. M. Shum
43. T. J. Theiss
44. G. E. Whitesides
45. ORNL Patent Section
46. Central Research Library
47. Document Reference Section
48-49. Laboratory Records
50. Laboratory Records (RC)

External Distribution

51-111. Meeting Attendees
112-138. IAEA IWG/LMNPP Members
139-171. CSNI PWG-3 Members
172. P. Albrecht, University of Maryland, Department of Civil Engineering, College Park, MD 20742
173. A. M. Clayton, AEA Technology, Reactor Services, Risley, Warrington, Cheshire WA3 6AT, UNITED KINGDOM
174. A. R. Dowling, Nuclear Electric, Barnett Way, Barnwood, GOS GL4 7RS, UNITED KINGDOM
175. C. Eripret, Electricite de France, Les Renardieres, 77250 Moret-sur-Loing, FRANCE
176. L. Hodulak, Frauhofer Institute fur Werkstoffmechanik, Wohlerstr 11, 7800 Freiburg, FRG
177-181. L. Ianko, International Atomic Energy Agency, Wagramerstrassee 5, P.O. Box 100, A-1400 Vienna, Austria
182. G. P. Karzov, Prometey, Central Research Institute of Structural Mechanics, 193167 Monastyrka River Quay 1, St. Peterburg, RUSSIA
183. D. J. Lacey, AEA Technology, Risley, Warrington WA3 6AT, ENGLAND
184. A. L. Lowe, P.E., B&W Nuclear Technologies, P.O. Box 10935, Lynchburg, VA 24506-0935
185. V. Lyssakov, Academy of Sciences, Nuclear Safety Institute, Bolshaya Tulskaya str., 52, Moscow, 113191, RUSSIA

186. T. R. Mager, Westinghouse Electric Corp. Nuclear and Advanced Technologies Division, Box 355, Pittsburgh, PA 15230-0355

187-191. M. E. Mayfield, RES, Division of Engineering, U.S. Nuclear Regulatory Commission, Mail Stop NLS-007, Washington, DC 20555-0001

192-196. A. G. Miller, CSNI, Nuclear Safety Division, OECD Nuclear Energy Agency, Le Seine Saint-Germain, 12, Boulevard Des Iles, F-92130 Issy-Les-Moulineaux, France

197. S. T. Rolfe, Department of Civil Engineering, 2006 Learned Hall, The University of Kansas, Lawrence, KS 66045-2225

198-199. C. Z. Serpan, Jr., RES, Division of Engineering, U.S. Nuclear Regulatory Commission, Washington, DC 20555-0001

200. L. C. Shao, Director, RES, Division of Engineering, U.S. Nuclear Regulatory Commission, Washington, DC 20555-0001

201. A. Sherry, AEA Technology, Reactor Services, Risley, Warrington, Cheshire WA3 6AT, UNITED KINGDOM

202. L. E. Steele, 7624 Highland Street, Springfield, VA 22150-3931

203. A. Taboada, RES, Division of Engineering, U.S. Nuclear Regulatory Commission, Washington, DC 20555-0001

204. H. Talja, Technical Research Centre of Finland (VTT), Nuclear Engineering Laboratory, Lonnrotinkatu 37, 00180 Helsinki, FINLAND

205. T. Timofeev, CRISM "Prometey," Monastryrka River Quay 1, St. Petersburg, 193167, RUSSIA

206. A. A. Tutnor, Kurchatov Institute of Atomic Energy, I.V. Kurchatov Place, 123182 Moskow, RUSSIA

207. T. Uga, Japan Atomic Energy Research Institute, Tokai Research Establishment, Tokai-mura, Naka-gun, Ibaraki-ken 319-11, JAPAN

208. M. Vagins, RES, Division of Engineering, U.S. Nuclear Regulatory Commission, Washington, DC 20555-0001

209. J. B. Wintle, Principal Engineer, AEA Technology, Harwell Laboratory, Oxfordshire OX 11 ORA, UNITED KINGDOM

210. Office of Assistant Manager for Energy Research and Development, DOE-OR, Oak Ridge, TN 37831

211-212. Office of Scientific and Technical Information, P.O. Box 62, Oak Ridge, TN 37831

NRC Form 335 (2-89) U.S. NUCLEAR REGULATORY COMMISSION

BIBLIOGRAPHIC DATA SHEET

See instructions on the reverse

1 REPORT NUMBER (Assigned by NRC, Add Vol., Supp., Rev., and Addendum Numbers, if any.)

NUREG/CP-0111
ORNL/TM-12413

2 TITLE AND SUBTITLE

Proceedings of the Joint IAEA/CSNI Specialists' Meeting on Fracture Mechanics Verification by Large-Scale Testing

3 DATE REPORT PUBLISHED

October 1991

4 FIN OR GRANT NUMBER

B5703

5 AUTHOR(S)

C. E. Pugh, B. R. Bass, J. A. Keeney

6 TYPE OF REPORT

Conference Proceedings

7 PERIOD COVERED (Inclusive Dates)

8 PERFORMING ORGANIZATION - NAME AND ADDRESS (If NRC, provide Division, Office or Region, U.S. Nuclear Regulatory Commission, and mailing address; if contractor, provide name and mailing address.)

Oak Ridge National Laboratory
Oak Ridge, TN 37831-8063

9 SPONSORING ORGANIZATION - NAME AND ADDRESS (If NRC, type "Same as above"; if contractor, provide NRC Division, Office or Region, U.S. Nuclear Regulatory Commission, and mailing address.)

Division of Engineering
Office of Nuclear Regulatory Research
U.S. Nuclear Regulatory Commission
Washington, DC 20555-0001

10 SUPPLEMENTARY NOTES

11 ABSTRACT (200 words or less)

This report contains 40 papers that were presented at the Joint IAEA/CSNI Specialists' Meeting - Fracture Mechanics Verification by Large-Scale Testing held at the Pollard Auditorium, Oak Ridge, Tennessee, during the week of October 26-29, 1992. The papers are printed in the order of their presentation in each session and describe recent large-scale fracture (brittle and/or ductile) experiments, analyses of these experiments, and comparisons between predictions and experimental results. The goal of the meeting was to allow international experts to examine the fracture behavior of various materials and structures under conditions relevant to nuclear reactor components and operating environments. The emphasis was on the ability of various fracture models and analysis methods to predict the wide range of experimental data now available. The international nature of the meeting is illustrated by the fact that papers were presented by researchers from CSFR, Finland, France, Germany, Japan, Russia, U.S., and the U.K. There were experts present from several other countries who participated in discussing the results presented. The titles for some of the final papers and the names of the authors have been updated in this report and may differ slightly from those that appeared in the final program of the meeting.

12 KEY WORDS/DESCRIPTORS (List words or phrases that will assist researchers in locating the report.)

fracture mechanics
reactor pressure vessels
brittle fracture toughness
ductile fracture
reference experiments
piping analysis
certification

13 AVAILABILITY STATEMENT

Unlimited

14 SECURITY CLASSIFICATION

(This Page)
Unclassified

(This Report)
Unclassified

15 NUMBER OF PAGES

16 PRICE

END

DATE FILMED

12/6/93